

AD-A189 673 GALLIUM ARSENIDE AND RELATED COMPOUNDS 1986(U) ILLINOIS 1/7  
UNIV CHAMPAIGN W T LINDLEY 1986 AFOSR-IR-87-1800  
AFOSR-86-0169

UNCLASSIFIED

F/G 20/2 NL



2

R

30/2

30

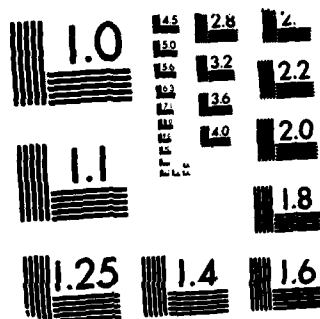
30

30

30

30

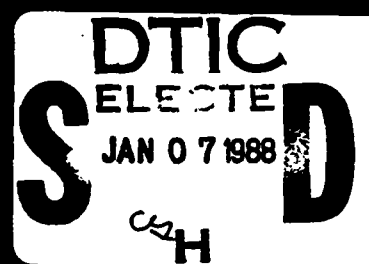
30



MICROCOPY RESOLUTION TEST CHART  
NATIONAL BUREAU OF STANDARDS-1963-A

AD-A189 673

2



# GALLIUM ARSENIDE and RELATED COMPOUNDS 1986

## DISTRIBUTION STATEMENT A

Approved for public release;  
Distribution Unlimited

83

Institute of Physics Conference Series

SECURITY CLASSIFICATION OF THIS PAGE

## REPORT DOCUMENTATION PAGE

|   |  |  |                          |
|---|--|--|--------------------------|
| 1a. REPORT SECURITY CLASSIFICATION<br><b>UNCLASSIFIED</b>   |  | 1b. RESTRICTIVE MARKINGS   |                          |
| 2a. SECURITY CLASSIFICATION AUTHORITY   |  | 3. DISTRIBUTION / AVAILABILITY OF REPORT<br>Approved for public release,<br>distribution unlimited |                          |
| 2b. DECLASSIFICATION / DOWNGRADING SCHEDULE   |  | 5. MONITORING ORGANIZATION REPORT NUMBER(S)<br><b>AFOSR-TR-87-1800</b>                             |                          |
| 4. PERFORMING ORGANIZATION REPORT NUMBER(S)   |  | 7a. NAME OF MONITORING ORGANIZATION<br>AFOSR/NE  |                          |
| 6a. NAME OF PERFORMING ORGANIZATION<br>University of Illinois   | 6b. OFFICE SYMBOL<br>(If applicable)             | 7b. ADDRESS (City, State, and ZIP Code)<br>Bldg 410<br>Bolling AFB, DC 20332-6448                  |                          |
| 6c. ADDRESS (City, State, and ZIP Code)<br>Champaign, IL 61801  |  | 9. PROCUREMENT INSTRUMENT IDENTIFICATION NUMBER<br>AFOSR-86-0169                                   |                          |
| 8a. NAME OF FUNDING / SPONSORING ORGANIZATION<br>AFOSR  | 8b. OFFICE SYMBOL<br>(If applicable)<br>NE       | 10. SOURCE OF FUNDING NUMBERS  |                          |
| 8c. ADDRESS (City, State, and ZIP Code)<br>Bldg 410<br>Bolling AFB, DC 20332-6448   |  | PROGRAM ELEMENT NO<br>61102F   | PROJECT NO<br>2306       |
|   |  | TASK NO<br>B1  | WORK UNIT ACCESSION NO   |
| 11. TITLE (Include Security Classification)<br>1986 International Symposium on Gallium Arsenide and Related Compounds   |  |  |                          |
| 12. PERSONAL AUTHOR(S)<br>Professor Stillman  |  |  |                          |
| 13a. TYPE OF REPORT<br>Final Report   | 13b. TIME COVERED<br>FROM 01 Aug 86 TO 30 Jul 87 | 14. DATE OF REPORT (Year, Month, Day)  | 15. PAGE COUNT           |
| 16. SUPPLEMENTARY NOTATION  |  |  |                          |
| 17. COSATI CODES  |  | 18. SUBJECT TERMS (Continue on reverse if necessary and identify by block number)                  |                          |
| FIELD   | GROUP  | SUB-GROUP  |                          |
|   |  |  |                          |
| 19. ABSTRACT (Continue on reverse if necessary and identify by block number)<br>The 13th International Symposium on Gallium Arsenide and Related Compounds was held in Las Vegas, Nevada from September 28 through Oct 1, 1986. There were 360 participants from 15 countries. There were 180 regular papers and 16 late news papers submitted from which the Technical Program Committee selected 91 regular papers and 8 late news papers to be presented at the conference. The significant recent growth and development of the field is well illustrated by the scope of the papers printed included are: bulk growth, epitaxial growth, characterization, processing, quantum wells, optoelectronic devices and high-speed devices. |  |  |                          |
| 20. DISTRIBUTION / AVAILABILITY OF ABSTRACT<br><input checked="" type="checkbox"/> UNCLASSIFIED/UNLIMITED <input type="checkbox"/> SAME AS RPT <input type="checkbox"/> DTIC USERS  |  | 21. ABSTRACT   |                          |
| 22a. NAME OF RESPONSIBLE INDIVIDUAL<br>CAPT. VALLOY   |  | 22b. TELEPHONE (Include Area Code)<br>(202) 767-4931   | 22c. OFFICE SYMBOL<br>NE |

DD FORM 1473, 84 MAR

83 APR edition may be used until exhausted.  
All other editions are obsolete.

SECURITY CLASSIFICATION OF THIS PAGE

87 12 29 263



**AFOSR-TX- 87 - 1840**

**AIR FORCE OFFICE OF SCIENTIFIC RESEARCH (AFOSR)  
NOTICE OF TRANSMITTAL TO DTIC**  
This technical report has been reviewed and is  
approved for public release IAW AFR 190-12.  
Distribution is unlimited.  
R. J. KERPER  
Chief, Technical Information Division

**87 12 29 263**

**Gallium Arsenide and Related Compounds 1986**

**Conference Committee**

D W Shaw (Chairman), C M Wolfe (Secretary), L F Eastman, G E Stillman,  
R E Enstrom, H B Kim

**Organising Committee**

A Y Cho, L R Dawson, J S Harris, W T Lindley, C G Kirkpatrick, Y S Park,  
D W Shaw, D E Stillman, C M Wolfe

**International Advisory Committee**

J V DiLorenzo, L F Eastman, C Hilsum, J Magarshack, T Nakahara, D W Shaw,  
T Sugano, H Thim, M Uenohara, K H Zschauer

**Technical Program Committee**

W T Lindley (Chairman), R D Burnham, A Y Cho, L R Dawson, J P Duchemin,  
C G Fonstad, M Fujimoto, H Goronkin, J S Harris, C G Kirkpatrick, F L Leonberger,  
P Norris, Y S Park, N Thomas, G Witt, J M Woodall

**Honorary Editor**

W T Lindley

**Sponsors**

The Symposium was sponsored by the Air Force Office of Scientific Research in  
cooperation with the IEEE Electron Devices Society and The Electrochemical  
Society.

2

## Gallium Arsenide and Related Compounds 1986

Proceedings of the Thirteenth International Symposium on  
Gallium Arsenide and Related Compounds held in Las Vegas,  
Nevada, 28 September - 1 October 1986

Edited by W T Lindley

DTIC  
ELECTE  
JAN 07 1988  
S H D



|                    |                                     |
|--------------------|-------------------------------------|
| Accession For      |                                     |
| NTIS GRA&I         | <input checked="" type="checkbox"/> |
| DTIC TAB           | <input type="checkbox"/>            |
| Unannounced        | <input type="checkbox"/>            |
| Justification      |                                     |
| By _____           |                                     |
| Distribution/      |                                     |
| Availability Codes |                                     |
| Dist               | Avail and/or<br>Special             |
| A-1                |                                     |

**DISTRIBUTION STATEMENT A**  
Approved for public release;  
Distribution Unlimited

Institute of Physics Conference Series Number 83  
Institute of Physics, Bristol

87 12 29 263

Copyright © 1987 by IOP Publishing Ltd and individual contributors. All rights reserved. Multiple copying of the contents or parts thereof without permission is in breach of copyright but permission is hereby given to copy titles and abstracts of papers and names of authors. Permission is usually given upon written application to IOP Publishing Ltd to copy illustrations and short extracts from the text of individual contributions, provided that the source (and, where appropriate, the copyright) is acknowledged. Authorisation to photocopy items for internal use, or the internal and personal use of specific clients in the USA, is granted by IOP Publishing Ltd for libraries and other users registered with the Copyright Clearance Center (CCC) Transactional Reporting Service, provided that the base fee of \$2.50 per copy per article is paid directly to CCC, 27 Congress Street, Salem, MA 01970, USA.  
0305-2346/87 \$2.50+.00

CODEN IPHSAC 83 1 - 594 (1987)

*British Library Cataloguing in Publication Data*

International Symposium on Gallium Arsenide  
and Related Compounds. (*13th: 1986: Las Vegas*)  
Gallium arsenide and related compounds  
1986: proceedings of the Thirteenth  
International Symposium on Gallium Arsenide  
and Related Compounds held in Las Vegas,  
Nevada, 28 September - 1 October 1986.  
(Institute of Physics conference series,  
no. 83).  
I. Gallium arsenide semiconductors  
I. Title II. Lindley, W.T. III. Series  
537.6'22 QC611.8.G4  
ISBN 0-85498-176-4

Published under the Institute of Physics imprint by IOP Publishing Ltd  
Techno House, Redcliffe Way, Bristol BS1 6NX, England

Printed in Great Britain by J W Arrowsmith Ltd, Bristol

## **Preface**

The 13th International Symposium on Gallium Arsenide and Related Compounds was held in Las Vegas, Nevada from September 28 through October 1, 1986. There were 360 participants from 15 countries.

There were 180 regular papers and 16 late news papers submitted from which the Technical Program Committee selected 91 regular papers and 8 late news papers to be presented at the conference. In addition to the submitted papers, there was a plenary session with three invited speakers.

The papers from the plenary session are in Chapter 1. The submitted papers are arranged in the remaining seven chapters. The late news papers are included in the chapters dealing with their subject. As an example, the work on quantum well structures is included in the chapter with that name as well as the chapters on high-speed devices, optical sources, characterisation and epitaxial growth. Readers looking for papers on a particular topic are encouraged to explore chapters on related subject areas.

**W T Lindley**

## **GaAs Symposium Award and Heinrich Welker Gold Medal**

The Gallium Arsenide Symposium Award was initiated in 1976. Candidates for the Award are selected by the GaAs Symposium Award Committee from those who have distinguished themselves in the area of III-V compound semiconductors. The Award consists of \$1000 and a plaque citing the recipient's contribution to the field. In addition, the Heinrich Welker Gold Medal, sponsored by Siemens, is also presented to the award recipient.

The 1976 Award was presented to Nick Holonyak of the University of Illinois for his work leading to the development of the first practical light-emitting diodes and his continuing research on III-V compound semiconductors. The second Award was received by Cyril Hilsum of the Royal Signals and Radar Establishment (now at GEC Research Laboratories) for his contributions in the field of transferred-electron logic devices and the advancement of GaAs MESFETs. In 1981 the Award and Medal were presented to Gerald L. Pearson, Stanford University, for his research and teaching in the field of compound semiconductor physics and new device technology. In 1982 the Award and Medal were presented to Herbert Kroemer, University of California at Santa Barbara, for his contributions to hot-electron effects, the Gunn Oscillator, and III-V heterojunction devices including the heterojunction laser. The 1984 Award and Medal were presented to Izuo Hayashi (now at Optoelectronics Joint Research Laboratories) for his contributions to the development and understanding of room temperature operation double-heterojunction lasers. In 1985 the recipient was Heinz Beneking, Technical University of Aachen, in recognition of his distinguished contributions to the development of III-V compound semiconductor technology and new structure devices.

At this conference, the 1986 GaAs Symposium Award and Medal were presented to Alfred Y. Cho, AT&T Bell Laboratories, for his pioneering work in the development of molecular beam epitaxy and his contributions to III-V compound semiconductor research.



Alfred Y Cho is Head of the Electronics and Photonics Materials Research Department of AT&T Bell Laboratories, Murray Hill, New Jersey. He received a BS, MS and PhD in Electrical Engineering from the University of Illinois in 1960, 1961 and 1968, respectively. He joined AT&T Bell Laboratories in 1968 where he pioneered the development of molecular beam epitaxy (MBE). He has published more than 200 scientific and technical papers and holds 27 patents related to MBE. His original work included observation of surface reconstruction during crystal growth. He also defined the Ga- and As-stabilised surface structures of GaAs which led to the first construction of a surface phase diagram. Other topics include the first demonstration of an MBE superlattice structure, the first application of MBE to microwave devices, such as FETs, Mixer and IMPATT diodes, and the fabrication of optical devices, such as the laser, LED and photodetectors.

Dr Cho was elected to membership in both the National Academy of Sciences and the National Academy of Engineering. He is a Fellow of the Institute of Electrical and Electronics Engineers and the American Physical Society. He was the recipient of the Electrochemical Society Electronics Division Award, the American Physical Society International Prize for New Materials, and the IEEE Morris N Liebmann Award.



## Young Scientist Award

The International Advisory Committee of the GaAs Symposium has established a Young Scientist Award to recognise technical achievements in the field of III-V compound semiconductors by a scientist under the age of 40. The award consists of \$1000 and a plaque citing the recipient's contributions. The first Young Scientist Award was presented at the 1986 Symposium to Russell D Dupuis for his work in the development of organometallic vapour phase epitaxy for III-V compound semiconductors.



After earning his PhD in Electrical Engineering in 1973 at the University of Illinois at Urbana-Champaign, Russell Dupuis joined the Semiconductor Research and Development Laboratory of Texas Instruments in Dallas, Texas where he worked on liquid-phase epitaxy of GaAs and GaP for LED's. He joined the Electronics Research Division of Rockwell International in 1975 where he worked on MOCVD of GaAs and AlGaAs for lasers and solar cells. In 1979, he joined the Solid State Electronics Research Laboratory of AT&T Bell Laboratories. He has continued his work on MOCVD growth of III-V compound semiconductors, including GaAs, AlGaAs, InP, InGaAs and InGaAsP materials. He was promoted to Distinguished Member of the Technical Staff of Bell Labs in 1985. For his work in developing the MOCVD process, he was given the IEEE Morris Liebmann Award in 1985.

## Contents

- v Preface
- vi GaAs Symposium Award and Heinrich Welker Gold Medal
- viii Young Scientist Award

### Chapter 1: Plenary papers

- 1 – 8 Atomic layer epitaxy  
*H Watanabe and S Usui*
- 9 – 16 Impurity-induced disordering and its applications in optoelectronics  
*R D Burnham, R L Thornton, N Holonyak Jr, J E Epler and T L Paoli*
- 17 – 25 Resonant tunneling transistors and superlattice devices by band-gap engineering  
*F Capasso*

### Chapter 2: Bulk growth

- 27 – 32 Improvement in the uniformity of electric properties of semi-insulating 3"  $\phi$  In-mixed GaAs single crystal by high magnetic field applied liquid encapsulated Czochralski technique  
*T Kawase, A Kawasaki and K Tada*
- 33 – 38 Distribution coefficient of carbon in gallium arsenide  
*U V Desnica and L M Pawlowicz*
- 39 – 44 The effects of residual acceptors on the electrical properties of low pressure LEC GaAs: a comparison of theory and experiment  
*W M Duncan and G H Westphal*
- 45 – 50 Role of boron in LEC semi-insulating GaAs  
*T Kikuta and K Ishida*
- 51 – 56 A TEM study of precipitates in As-grown semi-insulating indium-doped GaAs  
*B-T Lee, T Sands, R Grosky and E Bourret*
- 57 – 62 Correlation between melt stoichiometry and activation efficiency in Si-implanted GaAs  
*A R Von Neida, S J Pearton, M Stavola and R Caruso*
- 63 – 68 The use of selective pair luminescence to characterize semi-insulating GaAs  
*E S Koteles, J Kafalas, S Zemon and P Norris*

- 69 – 74 InP doped with isoelectronic impurities  
*R L Henry and R L Gorman*

### Chapter 3: Epitaxial growth

- 75 – 80 Isobutylphosphine and tertiarybutylphosphine sources for OMVPE growth of InP  
*C H Chen, C A Larsen and G B Stringfellow*
- 81 – 86 High mobility, low compensation GaAs grown by OMVPE  
*S K Shastry, S Zemon and P Norris*
- 87 – 92 Rare-earth ion-doped InP grown by metalorganic chemical vapor deposition  
*K Uwai, H Nakagome and K Takahei*
- 93 – 98 Chemical beam epitaxial growth of very high quality  $\text{Ga}_{0.47}\text{In}_{0.53}\text{As}$ /InP quantum wells and superlattices: photoluminescence and photoluminescence excitation spectroscopies  
*W T Tsang, E F Schubert, S N G Chu, K C Tai, R Sauer, T H Chiu, J E Cunningham and J A Ditzenberger*
- 99 – 104 Formation of DX centers by heavy Si doping in MBE-grown  $\text{Al}_x\text{Ga}_{1-x}\text{As}$  with low Al content  
*T Ishikawa, T Yamamoto, K Kondo, J Komeno and A Shibatomi*
- 105 – 110 Nonradiative recombination process at deep levels in AlGaAs grown by MBE  
*M O Watanabe, Y Ahizawa, N Sugiyama and T Nakanisi*
- 111 – 116 MBE growth of GaAs on Si using thermally strained layers  
*J W Lee*
- 117 – 122 Properties of AlGaAs grown by molecular beam epitaxy on lenticular substrates  
*G D Kramer, R K Tsui, J A Curless and M S Peffley*
- 123 – 128 The electrical properties of In-doped and low-temperature-grown MBE GaAs  
*M Missous and K E Singer*
- 129 – 134 Atomic layer epitaxy of III – V compounds by hydride VPE  
*A Usui and H Sunakawa*
- 135 – 140 Atomic layer epitaxy of III – V materials and quantum-well structures  
*M A Tischler, N G Anderson and S M Bedair*
- 141 – 146 Optical characterization of stress effects in GaAs/Si  
*S Zemon, C Jagannath, E S Koteles, S K Shastry, P Norris, G Lambert, A N M Choudhury and C A Armiento*
- 147 – 152 Impurity gettering and dislocation reduction by GaAs(In) and InP(As) strained layer epitaxy and related device effects  
*T Tilli, R Schummers, P Narozny, N Emeis, H Beneking and H Klapper*

- 153 – 158 AlN on GaAs and InP for application to MIS structure – low temperature growth of AlN using TMAI and hydrazine  
*M Mizuta, S Fujieda, T Jitsukawa and Y Matsumoto*
- 159 – 164 Ordered structures in OMVPE grown  $\text{GaAs}_{1-x}\text{Sb}_x$  and  $\text{Ga}_{1-x}\text{In}_x\text{As}_{1-y}\text{Sb}_y$  alloys  
*H R Jen, M J Cherng, M J Jou and G B Stringfellow*
- 165 – 170 Growth behaviors and characterization of plasma-assisted epitaxial InSb and InAs on different substrates  
*T Hariu, S F Fang, K Shida and K Matsushita*
- 171 – 176 Laser selective deposition and direct writing of single crystal III – V compounds films  
*N H Karam, N A El-Masry and S M Bedair*
- 177 – 182 Optical characterisation of high purity GaAs and InP grown by vapor levitation epitaxy  
*B J Skromme, H M Cox and S G Hummel*
- 183 – 186 Growth of  $\text{Ga}_{1-x}\text{In}_x\text{As}$  layers with excellent compositional uniformity on InP by OMVPE  
*H Kamei, G Sasaki, T Kato, H Hayashi, K Ono and K Yoshida*

#### Chapter 4: Characterisation

- 187 – 192 Double-injection induced conductivity between n and p contacts to semi-insulating GaAs: Experiment and numerical simulation  
*L D Flesner, M O'Brien, A K Nedoluha, R Zuleeg, A H Guerrero and C M Penchina*
- 193 – 196 Scanning laser photoluminescence imaging technique for nondestructive evaluation of direct bandgap materials  
*D L Parker and N Moon*
- 197 – 202 GaAs wafer investigation by near-infrared transmission and photoluminescence topography techniques  
*J Windscheif and W Wettling*
- 203 – 208 Characteristics of deep electron-traps in Te-doped AlGaSb on GaSb substrate  
*Y Takeda, Y Zhu and A Sasaki*
- 209 – 214 Correlation of structural, chemical and optical properties of GaInAs quantum wells  
*R Hull, K W Carey, J E Fouquet, G A Reid, S J Rosner, D Bimberg and D Oertel*
- 215 – 220 Photoluminescence studies of single GaAs quantum wells with extended monolayer-flat regions  
*B A Wilson, R C Miller, S K Sputz, T D Harris, R Sauer, M G Lamont, C W Tu and R F Kopf*

xii      *Contents*

- 221 – 226 Spectroscopic investigation of the properties of III – V quantum well structures at high carrier densities  
*G Tränkle, A Forchel, E Lach, F Scholz, M H Pilkuhn, G Weimann, H Kroemer, S Subbanna, G Griffiths and M Razeghi*
- 227 – 232 Magneto-luminescence measurements in InGaAs/GaAs single-strained-quantum-wells  
*E D Jones, I J Fritz, J E Schirber, M C Smith and T J Drummond*
- 233 – 238 Hole transport and charge transfer in GaAs/InGaAs/GaAs single strained quantum well structures  
*I J Fritz, J E Schirber, E D Jones, T J Drummond and G C Osbourn*
- 239 – 244 Characterization of modulation-doped FET's using the Shubnikov – de Haas oscillations  
*S Y Chou, C S Lam, D A Antoniadis, H I Smith and C G Fonstad*
- 245 – 250 Growth parameter dependence of 2DEG mobility in selectively doped n-AlGaAs/GaAs grown by MO-CVD  
*H Tokuda, A Tanaka, H Kawasaki, I Inami, M Higashiura, S Hori and K Kamei*
- 251 – 256 Characterization of simultaneous diffusions of zinc and indium into GaAs, and (AlAs)<sub>n</sub>(GaAs)<sub>m</sub> superlattice surfaces and its device applications  
*J R Shealy, K Kavanagh and P M Enquist*
- 257 – 262 Characterization by Raman spectroscopy of GaInP, AlInP and GaAs single layers and superlattices  
*G W Wicks, D P Bour, J R Shealy and J T Bradshaw*
- 263 – 266 Effects of internal stress on the thermal stability of superlattice and alloy semiconductors  
*T Katoda and N Hara*
- 267 – 270 Electron beam measurement of band discontinuities at heterostructure interfaces  
*A Lechner, M Kneidinger, K Lübke and H Thim*

**Chapter 5: Processing**

- 271 – 276 Activation and characterization of MeV n-type implants in GaAs  
*P E Thompson and H B Dietrich*
- 277 – 282 High activation transient annealing of Si- and Mg-implanted GaAs using improved graphite heater  
*W D Fan, X Y Jiang, G Q Xia and W Y Wang*
- 283 – 288 Regrowth of amorphized InP  
*G Bahir, J L Merz, J R Abelson and T W Sigmon*

- 289 – 294 Hydrogen passivation of shallow level impurities and deep level defects in GaAs  
*S J Pearton, W C Dautremont-Smith, C W Tu, J C Nabity, V Swaminathan, M Stavola and J Chevallier*
- 295 – 300 Submicron processing of III – V semiconductors by focused ion beam technology  
*T Hiramoto, T Odagiri, P Oldiges, T Saito and T Ikoma*
- 301 – 306 A self-aligned technology using refractory metals for GaAs/GaAlAs heterojunction bipolar transistors  
*K Daoud-Ketata, J F Bresse and C Dubon-Chevallier*
- 307 – 312 Low resistance refractory metal WAg/W gate self-aligned GaAs MESFETs  
*G Q Xia and W Y Wang*
- 313 – 318 Influence of the InAs – GaAs miscibility gap on the In/GaAs reaction  
*J Ding, J Washburn, T Sands and V G Keramidas*

#### Chapter 6: Quantum Wells

- 319 – 324 Observation of coupled states in AlGaAs/GaAs coupled quantum well  
*H Q Le, J J Zayhowski, W D Goodhue and J Bales*
- 325 – 330 Magneto-optical studies of GaAs –  $\text{Al}_x\text{Ga}_{1-x}\text{As}$  multi-quantum-well structures  
*K K Bajaj, D C Reynolds, C W Litton, R L Greene, P W Yu, C K Peng and H Morkoc*
- 331 – 336 GaAs/ $\text{In}_x\text{Al}_{1-x}\text{As}$  ( $0 \leq x \leq 0.006$ ) indirect bandgap superlattices  
*T J Drummond, E D Jones, H P Hjalmarson and B L Doyle*
- 337 – 342 The observation of the expansion of electron – hole plasma in GaAs –  $\text{Al}_x\text{Ga}_{1-x}\text{As}$  multiple quantum well structures  
*K T Tsen and H Morkoc*

#### Chapter 7: Optoelectronic Devices

- 343 – 348 Surface emitting lasers with slant edge mirrors and multilayer reflectors  
*M Ohshima, N Takenaka, N Hirayama, Y Toyoda and N Hase*
- 349 – 354 Angular chlorine ion-beam-assisted etching of GaAs and AlGaAs  
*W D Goodhue, G D Johnson and T H Windhorn*
- 355 – 360 GaAs/AlGaAs double-heterostructure diode lasers on (110) GaAs substrates  
*H K Choi and M K Connors*

xiv      *Contents*

- 361 – 366 Si-induced disordering and its application to fabrication of index-guided AlGaAs MQW lasers  
*Koji Ishida, K Matsui, T Fukunaga, T Takamori, J Kobayashi, Koichi Ishida and H Nakashima*
- 367 – 372 GaAs/AlGaAs waveguide with grating coupler fabricated by selective superlattice intermixing  
*J D Ralston, L H Camnitz, G W Wicks and L F Eastman*
- 373 – 378 Device structures for high power 0.83  $\mu\text{m}$  superluminescent diodes  
*J Niesen, C Morrison and L Zinkiewicz*
- 379 – 384 Reliable high power 1.3 micron DCPBH laser diodes  
*E A Rezek, D Tran and L Yow*
- 385 – 390 Growth and modelling of InAsPSb/InAs double heterostructures  
*J L Benchimol, B Sermage and J Primot*
- 391 – 394 First fabrication of CW high power phase-locked laser arrays emitting at 1.3  $\mu\text{m}$  grown by LP-MOCVD  
*M Razezghi and R Blondeau*
- 395 – 398 Fe-doped InP hydride vapor phase epitaxy for high speed buried heterostructure laser diodes  
*Y Kato, A Usui, T Kamejima, S Sugou and K Kasahara*
- 399 – 404 Observation of novel step-like structure in the photocurrent and dark current of a superlattice: charge collection by successive depletion of quantum wells  
*J Allam, F Capasso, M B Panish and A L Hutchinson*
- 405 – 410 Impact ionization across the band-edge discontinuity with very large ionization rate ratio in a superlattice with graded wells  
*J Allam, F Capasso, K Alavi and A Y Cho*
- 411 – 416 III – V superlattice photodiodes  
*F-Y Juang, W Li, P K Bhattacharya, U Das, A Chin, D J Jackson and D L Persechini*
- 417 – 422 High quality lattice matched InGaAs/InP heterostructures prepared by atmospheric pressure MOVPE for high speed photodetectors  
*J P André, J N Patillon, J L Gentner, E P Menu, D Moroni and G M Martin*
- 423 – 428 Single-crystal integration of an optical interference filter and photodiode  
*P L Gourley, R M Biefeld and T E Zipperian*
- 429 – 434 A (Ga,Al)As semiconductor scintillator with monolithically integrated photodiode: a new X-ray detector  
*P A Glasow, W W Rühle and K D Schwarzmichel*
- 435 – 440 Electro-optic effect in a GaAs/AlGaAs quantum well structure at room temperature  
*Y Kan, M Yamanishi, H Nagai and I Suemune*

**Chapter 8: High-Speed Devices**

- 441 – 446 Very short channel GaAs MESFETs obtained using an overlapped gate configuration  
*A Colquhoun and G Ebert*
- 447 – 452 Analysis of narrow channel effect in small-size GaAs MESFET  
*T Uenoyama, S Odanaka and T Onuma*
- 453 – 458 Characterization and physics of low-field electron transport in GaAs MESFETs  
*K Shenai and R W Dutton*
- 459 – 464 Effects of thin and high-carrier concentration active layer for GaAs MESFET performance  
*Y Matsuoka, S Sugitani, N Kato and H Yamazaki*
- 465 – 470 A GaAs high-electron-confinement transistor (HECT)  
*S P Kwok, M Feng and H B Kim*
- 471 – 476 Ion-implanted submicron MESFET's with high transconductance  
*H Jaeckel, V Graf, B J Van Zeghbroeck, P Vettiger and P Wolf*
- 477 – 482 Ultrahigh transconductance, tin doped, spike channel GaAs MESFETs grown by MOCVD  
*K H Hsieh, J D Parsons, L S Lichtmann, L Jelloian and F G Krajenbrink*
- 483 – 488 High gain step-graded InGaAs(P)/InP heterostructure bipolar transistors for high current drive – high frequency applications  
*R N Nottenburg, M B Panish and H Temkin*
- 489 – 492 GaAs E/D MESFET 1K-bit static RAM fabricated on silicon substrate  
*H Shichijo, J W Lee, W V McLevige and A H Taddiken*
- 493 – 496 W-band characterization of high electron mobility transistor  
*J Schaffner, K Moeller, H Fetterman, J Berenz and K Nakano*
- 497 – 502 15 GHz-band power InP MISFETs  
*H Tokuda, H Kamo, F Sasaki and M Higashiura*
- 503 – 508 Correlation of undoped, In-alloyed and whole ingot annealed semi-insulating GaAs substrates for low noise microwave amplifiers  
*H Kanber and D C Wang*
- 509 – 514 Evaluation of the theoretical maximum fabrication yield of GaAs 1K bit SRAM's  
*C Rocher, J Maluenda, B Gabillard, T Ducourant, M Prost and M Rocchi*
- 515 – 520 High performance inverted HEMT and its application to LSI  
*S Nishi, T Saito, S Seki, Y Sano, H Inomata, T Itoh, M Akiyama and K Kaminishi*
- 521 – 526 Multiple-input and -output OR/AND circuits for VLSI GaAs ICs  
*T Vu, K Lee, A Peczalski, G Lee, H Somal and W Betten*



xvi      *Contents*

- 527 – 532    Total dose effects of gamma ray on GaAs ICs  
*K Aono, T Shimura, M Komaru, M Katsumata, O Ishihara and K Fujikawa*
- 533 – 538    A novel rapid thermal annealing for GaAs digital ICs  
*A Tamura, T Uenoyama, K Inoue and T Onuma*
- 539 – 544    Hot electron resonant tunneling through a quantum well: a new electron spectroscopy  
*F Capasso, S Sen, A Y Cho and A L Hutchinson*
- 545 – 550    Resonant tunneling in a double GaAs/AlAs superlattice barrier heterostructure  
*M A Reed and J W Lee*
- 551 – 556    New quantum interference effects in GaAs/AlAs resonant tunneling structures  
*N Tabatabaie and M C Tamargo*
- 557 – 562    Mobility and parasitic resistance measurements in AlGaAs/GaAs and AlGaAs/InGaAs MODFET structures  
*D C Look, T Henderson, C K Peng and H Morkoc*
- 563 – 568    Improved 77K performance of AlAs/GaAs superlattice heterostructure field-effect-transistors (SLHFET)  
*M Heuken, W Prost, S Kugler, K Heime, W Schlapp and G Weimann*
- 569 – 574    Strained N-Ga<sub>0.7</sub>Al<sub>0.3</sub>As/In<sub>0.23</sub>Ga<sub>0.77</sub>As/GaAs 2DEG FET with large band offset  
*A Okamoto, H Toyoshima and K Ohata*
- 575 – 580    Selectively doped AlInAs/GaInAs heterostructures grown by MOCVD and their application to HIFETs (Hetero-Interface FETs)  
*M Kamada, H Ishikawa, M Ikeda, Y Mori and C Kojima*
- 581 – 586    DC and RF characterization of a planar-doped double heterojunction MODFET  
*Y K Chen, D C Radulescu, P J Tasker, G W Wang and L F Eastman*
- 587 – 590    Novel resonant tunneling diodes with an In<sub>x</sub>Ga<sub>1-x</sub>As strained layer deep quantum-well  
*H Toyoshima, Y Ando, A Okamoto and T Itoh*
- 591 – 594    Author Index

## Atomic layer epitaxy

H. Watanabe and A. Usui

Fundamental Research Laboratories, NEC Corporation  
1-1, Miyazaki 4-chome, Miyamae-ku, Kawasaki, Japan

**Abstract.** Atomic layer epitaxy (ALE), a new growth technique with control at the monolayer level, is reviewed with reference to the importance of the degree of surface coverage ( $\theta$ ) of the adsorbed vapor species. In ALE growth of GaAs using a metal chloride (GaCl) process,  $\theta$  is observed to be unity and insensitive to the GaCl partial pressure and substrate temperature. A similar result is obtained in ALE growth using a metalorganic source such as  $\text{Ga}(\text{CH}_3)_3$ , but under more restricted conditions. We call these ALE processes "digital epitaxy" because precise control of analogue parameters such as pressure, temperature and growth time is not required. In comparison with MBE and MOCVD, ALE offers advantages of greater thickness uniformity, fewer surface defects, less edge growth in selective epitaxy, and monolayer control in sidewall epitaxy. The electronic properties of GaAs grown by ALE are also discussed.

### 1. Introduction

Various kinds of multilayer structures requiring monolayer-level control have been proposed for high speed or optical devices. At present, these devices are discussed in discrete forms but, they will be eventually integrated to higher performance functional ICs. Atomic layer epitaxy (ALE), originally proposed by Suntola et al (1980), seems to be attractive as an epitaxial technique to make such monolayer-level controlled IC wafers because of its potentially unique characteristics.

The present paper describes (1) the principle and the current status of GaAs ALE with reference to the importance of the degree of surface coverage ( $\theta$ ) of the adsorbed vapor species, (2) the proposal of the novel idea "digital epitaxy", (3) unique advantages of ALE over MBE or MOCVD, and (4) some electronic properties of GaAs grown by ALE.

### 2. Principle and review of GaAs ALE

A general review was recently made for ALE of II-VI and III-V compounds (Goodman and Pessa 1986). Therefore the present paper focuses on such topics as GaAs ALE (including the latest papers) and concentrates on the study of the surface coverage kinetics and also unique advantages of ALE.

Figure 1 shows a single sequence in GaAs ALE. An essential point in ALE is the alternative supply of two kinds of source gases, such as trimethylgallium (TMG) and  $\text{AsH}_3$  (Nishizawa et al 1985, Bedair et al 1985, Doi et al 1986a, Mori et al 1986), triethylgallium (TEG) and  $\text{AsH}_3$  (Nishizawa et al 1986, Kobayashi et al 1985), or GaCl and  $\text{AsH}_3$  (Usui and Sunakawa 1986a, 1986b). Although adsorbed vapor species in step 1 have not been identified, they are considered to

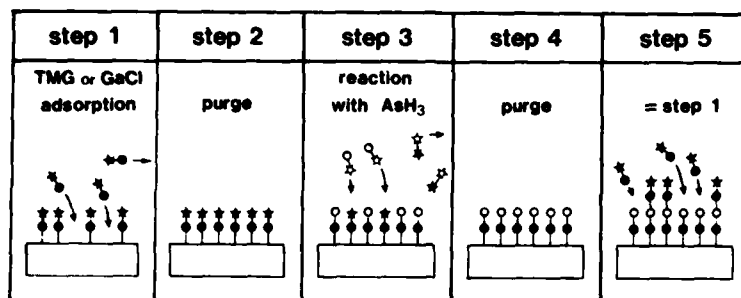


Fig. 1 Sequence of GaAs ALE

be organic gallium radicals containing mono- or di-methyl molecules in TMG-ALE (Nishizawa and Kurabayashi 1986, Tischler and Bedair 1986, Bedair et al 1986). In GaCl-ALE, it is believed that the GaCl source gas is directly adsorbed on the substrate surface on the basis of the growth kinetic studies of GaAs chloride transport VPE (Shaw 1975, Cadoret and Cadoret 1975). A crucial factor in ALE as a monolayer-accurate growth method is the surface coverage ( $\theta$ ) of the adsorbed vapor species. The surface coverage after the purge process (step 2) must be kept unity in order to achieve the monolayer abruptness. Since no direct measurement has been made of the surface coverage after (or before) the purge step, we estimate the surface coverage from the grown thickness per single ALE cycle, i.e. the total grown thickness divided by the number of ALE cycles.

Figure 2 shows grown thickness per cycle as a function of the partial pressures of TMG, TEG and GaCl source gases. In TMG-ALE by Nishizawa et al (1985) (they call it MLE: molecular layer epitaxy) growth was carried out in vacuum chamber, while all the other ALE works were done in H<sub>2</sub> carrier gas CVD systems at total pressures of 760 Torr (Tischler, Doi, Usui), 90 Torr (Kobayashi) and 100 Torr (Mori). Tischler et al used a type of reactor whose substrate holder makes it difficult to determine TMG partial pressure over the substrate, which, therefore, is plotted as half of that in the TMG inlet.

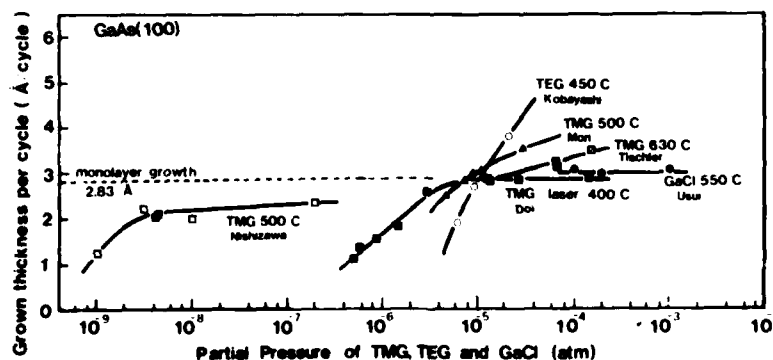


Fig. 2 Source gas pressure dependence of ALE growth

Nishizawa et al observed that grown thickness per cycle saturates to a value smaller than the monolayer thickness of 2.83 Å. This may be due to insufficient supply of AsH<sub>3</sub> in step 3. By increasing the AsH<sub>3</sub> partial pressure it approaches 2.83 Å. Similar saturation was observed in ALE by Tischler et al. As discussed by Nishizawa and Kurabayashi (1986) and Tischler and Bedair (1986)

there must be a self-limiting process in TMG-ALE, but the saturation seems to be not perfect. A similar result is also obtained by Mori et al (1986).

Doi et al (1986a) found that no growth takes place if the substrate temperature is lowered to 400°C. They irradiated the substrate with an Ar-laser light to enhance the TMG decomposition on the surface, and obtained a cycle thickness of 2.83Å. They explained their series of experiments that Ar-laser light decomposes TMG to gallium atom at limited surface sites (arsenic sites) which are decreased with increase of adsorbed gallium and no more decomposition nor radical adsorption occurs after the complete monolayer coverage of gallium atoms. They named this particular ALE process "SME by SL-MOVPE" (stepwise monolayer epitaxy by switched-laser MOVPE).

TEG-ALE by Kobayashi et al (1985) exhibits no saturation in the growth thickness per cycle indicating the absence of the self-limiting mechanism. TEG is thermally unstable, and homogeneous pyrolytic decomposition by the  $\beta$ -elimination mechanism starts at 300°C or below (Yoshida et al 1985). No stable adsorbed radical is generated after TEG decomposition, which leads to adsorption of gallium atoms on gallium atoms, resulting in  $\theta > 1$ .

Usui and Sunakawa (1986a) carried out GaCl-ALE and observed no GaCl pressure dependence, from which they conclude that GaCl adsorption is very stable, and no decomposition, hydrogen reduction of adsorbed GaCl, or adsorption on GaCl takes place, resulting in unity coverage of GaCl.

### 3. Surface coverage in ALE

#### a. Adsorption mechanism

The dependence of the surface coverage ( $\theta$ ) of adsorbed vapor species on its partial pressure ( $P$ ) has been interpreted by several different formulae such as Henry's Eq.  $\theta \propto P$ , Freundlich's Eq.  $\theta \propto P^{1/n}$  ( $n$ : integer), or Langmuir's Eq.

$$\theta = KP/(1 + KP) , \quad \dots\dots\dots(1)$$

where  $K$ , the adsorption constant, is a function of temperature  $T$ . We assume that the grown thickness per single ALE cycle is equivalent to the surface coverage in step 2 in Fig. 1. The experimental curves in Fig. 2 seem to be well explained by one of these formulae. In order to determine which adsorption type is applicable to the above experiments, temperature dependences are studied and summarized in Fig. 3.

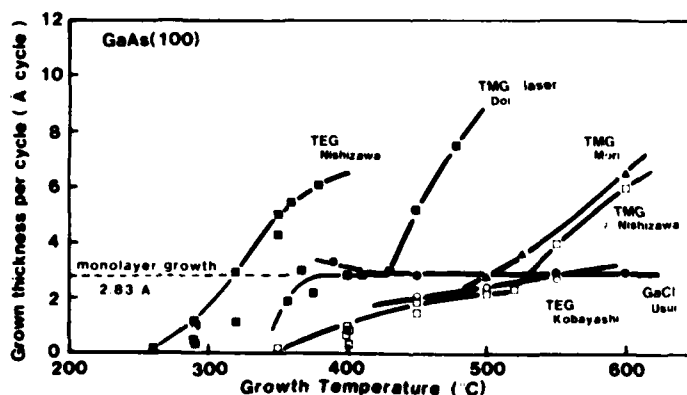


Fig. 3 Growth temperature dependence of ALE growth

Unlike GaCl-ALE, all ALEs using metalorganic sources (MO-ALE) show increasing  $\theta$  with  $T$  which is not likely in the normal adsorption types described above, where the temperature increase causes reduction in surface coverage. We can not use conventional simple adsorption equations for MO-ALE. Although more detailed study is needed, we can say that in MO-ALE at least two processes take place simultaneously on the substrate surface. One is the thermal decomposition process, enhanced by a temperature increase, which forms not only radicals but also atomic gallium. The other is the adsorption process where adsorbed species (radicals or gallium atoms) are generated by thermal decomposition, and hence the concentration increases with increasing partial pressure of source gases (TMG) but saturates due to the limited adsorption site. A consistent explanation for MO-ALE in Figs. 2 and 3 is possible in this way.

For GaCl-ALE we assume that GaCl adsorption obeys the Langmuir Eq. (1), where  $\theta$  approaches unity by increasing  $P$  and becomes insensitive to not only  $P$  but also temperature. The adsorption layer thickness measurement in chloride transport GaAs VPE and the surface coverage calculation of GaCl by Cadoret (1980) support the Langmuir mechanism. The fact that the grown thickness per cycle exhibits no dependence on GaCl partial pressure and growth temperature is well explained by Eq. (1) in the limit  $KP \gg 1$ .

#### b). Coverage calculation

Adsorption constant  $K$  is expressed by

$$K = \exp \left( - \frac{\Delta H + T\Delta S}{RT} \right),$$

where  $\Delta H$  and  $\Delta S$  are enthalpy and entropy changes due to the adsorption,  $R$  the gas constant. We assume that  $\Delta H$  of GaCl adsorption is 35.2 Kcal/mol (Cadoret 1980) or 55.7 Kcal/mol (Korec 1982), and  $\Delta S$  is enthalpy change from vapor to liquid, 22 cal/deg. At 450°C,  $K = 6.3 \times 10^5$  (Cadoret) or  $1.1 \times 10^{12}$  (Korec). Therefore, we obtain  $1 - \theta = 2 \times 10^{-3}$  (Cadoret) or  $1 \times 10^{-8}$  (Korec) when GaCl pressure is  $1 \times 10^{-4}$  atm. Although the assumptions used here must be discussed further, we believe that the GaCl coverage is more than 99%, which is also supported by extrapolating the result by Theeten and Hottier (1976).

#### 4. Cycle speed in ALE

One of the disadvantages in ALE is the slow speed of a single cycle. In Table 1, calculated impinging rates ( $R_i$ ) of TMG, TEG or GaCl in ALE experiments are shown. Degrees of excess supply,  $R_i t / N_s$ , are fairly large in all ALE works where  $t$  and  $N_s$  are the exposure time and surface lattice sites of GaAs (100),  $6.4 \times 10^{14}$  cm $^{-2}$ , respectively. This calculation suggests that we can reduce the exposure time, at least, by 1~2 orders of magnitude. However, because of the mechanical limit of gas valves or the substrate transfer system and also because of the limits of adsorption speed in step 1 and reaction speed in step 3 in Fig. 1, it seems

|                         | Gas  | atmosphere      | Impinging rate                            | Exposure             | $R_i t / N_s$     |
|-------------------------|------|-----------------|---|----------------------|-------------------|
|                         |      |                 | $R_i$<br>(molecules cm $^{-2}$ sec)       | time<br>$t$ (second) |                   |
| Nishizawa et al<br>1985 | TMG  | vacuum          | $2.0 \times 10^{13} - 3.9 \times 10^{15}$ | 4                    | 0.12 - 25         |
| Kobayashi et al<br>1985 | TEG  | 90 Torr H $_2$  | $3.1 \times 10^{16} - 2.2 \times 10^{17}$ | 1                    | 50 - 350          |
| Dor et al<br>1986       | TMG  | 76 Torr H $_2$  | $5.5 \times 10^{15} - 2.5 \times 10^{18}$ | 1                    | 8 - 4000          |
| Usui et al<br>1986      | GaCl | 760 Torr H $_2$ | $1.3 \times 10^{18} - 1.3 \times 10^{19}$ | 6                    | 12000<br>- 120000 |

Table 1 Impinging rate in step 1  $R_i = N \bar{v} = N \cdot \frac{T}{T} \cdot \left( \frac{8kT}{\pi M} \right)^{1/2}$

difficult to reduce the ALE cycle to less than 1 second. 1 second per monolayer is equal to conventional MBE or MOCVD growth rates.

### 5. Digital epitaxy

As discussed in Section 3, the surface coverage of adsorbed species is usually a function of the substrate temperature and the partial pressure of the adsorbed species, and, hence, we need precise controls of the temperature, the pressures and the flow rates to obtain a desired thickness. On the other hand, under the particular conditions in Figs. 2 and 3, the grown thickness per cycle is not dependent on source gas pressure and growth temperature and is equal to a monolayer thickness. Total thickness is determined only by the number of ALE cycles, and no control of the partial pressures or the growth temperature is required. ALE is classified to analogue and digital ALEs.

$$\begin{aligned} \text{Analogue ALE: } \theta &= f(T, P, \text{flow rates}) \\ \text{Digital ALE: } \theta &\neq f(T, P, \text{flow rates}) \end{aligned}$$

We need digital ALE with  $\theta=1$ . Digital ALE with  $\theta<1$ , which is realized when an adsorbed species is so large that it covers more than one lattice sites, is less useful because a grown interface has no atomic abruptness.

Since growth time is irrelevant in determining the grown thickness, now we are free from the requirement to control any analogue quantities and, hence, ALE under this particular mode (digital ALE) can be called "digital epitaxy" (Watanabe 1986, Usui and Sunakawa 1986c). Doi et al (1986c) also call their SME by SL-MOVPE digital epitaxy. The advantages of ALE described below are particularly clear under the digital epitaxy condition. As shown in Figs. 2 and 3, the range of source gas pressure and growth temperature to assure digital epitaxy is remarkably wide in GaCl-ALE as compared with TMG-ALE.

### 6. Advantages of ALE

#### a) Accurate thickness control and reproducibility

The grown thickness in digital epitaxy is simply determined by the number of ALE cycles. No precise control of temperatures, pressures, flow rates or growth time is required. Furthermore, no careful design of reactor, especially the substrate holder and its surroundings, is necessary even for a multiwafer epitaxial reactor. This situation is of particularly significance in mass-production of multiple large wafers with a high reproducibility.

#### b) Excellent thickness uniformities

Thickness nonuniformity in conventional CVD is caused by the non-uniform boundary layer distribution along the flow direction and also by the depletion effect of the source gases. MBE needs substrate rotation to minimize inhomogeneous flux distributions. In ALE, the growth rate is not influenced by these parameters and hence in principle uniformity must be excellent, independent of the susceptor structure, flow pattern or flux distribution. This is confirmed in MO-ALE on a 3-inch substrate by Mori et al (1986) as shown in Fig. 4.

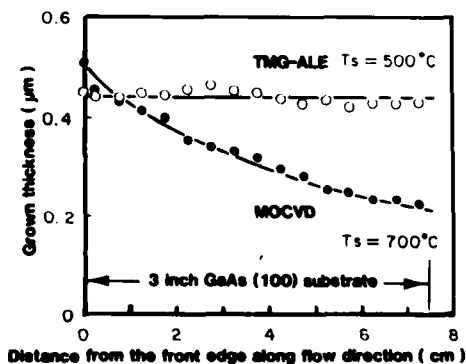


Fig. 4 Thickness uniformity by TMG-ALE

Because of the very narrow space between substrate and reactor wall, the non-uniformity in the conventional MOCVD mode is particularly large. However, by simply switching to ALE mode, i.e. switching from simultaneous to alternative supply of TMG and AsH<sub>3</sub>, the non-uniformity is drastically improved. No fluctuation is observed within experimental error in the ALE mode, which supports the growth kinetics explained above.

**c) Mirror surface of grown layers**

ALE process in the digital epitaxy mode offers high quality mirror of grown surface. No additional surface texture is observed after ALE growth. No terraces, hillocks, or oval defects are developed during digital epitaxy. This is confirmed for the substrate orientations of (100), 2° off (100), (511), (211) and (111) A,B (Usui and Sunakawa 1986a). This is explained as follows. Because the lattice sites are completely occupied with the adsorbed species (GaCl), the adsorbed species are unable to migrate and aggregate, causing an irregularity. GaAs decomposition is negligibly small at low temperatures of 400~500°C.

**d) No edge growth in selective epitaxy**

Selective epitaxy, growth through the window of a SiO<sub>2</sub> mask on the substrate, has been adopted for several reasons, for instance, to reduce source and drain contact resistances in GaAs FETs. In conventional epitaxial methods, the growth rate in the window is enhanced and determined by the window area. This is due to the reactant flow from the mask surface to the window area. Figure 5 shows optical photographs of selective epitaxy of source and drain regions (white areas) in a GaAlAs/GaAs 2DEG FET (Miyamoto et al 1986). Edge growth or facet development are frequently observed in conventional selective epitaxy by VPE. GaCl-ALE in the digital epitaxy mode solves these problems. Mirror surface without edge growth nor facet development are seen in ALE. Grown thickness in selective epitaxy is readily controlled by the number of ALE cycles, independent of the window area.

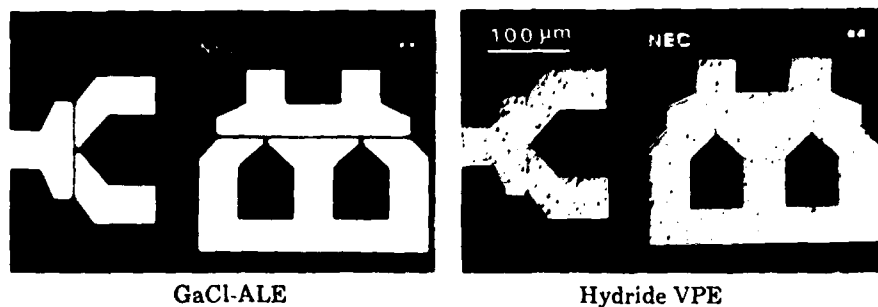


Fig. 5 Selective epitaxy of source and drain regions of GaAs 2DEG FET

**e) Sidewall epitaxy**

In GaCl-ALE, it was confirmed that a single ALE cycle offers a monolayer growth on (111)A,B, (211) and (511) as well as (100) (Usui and Sunakawa 1986a). Therefore, epitaxial growth at the monolayer level on sidewalls of a structured substrate such as shown in Fig. 6, is possible if the source gas partial pressure is sufficiently high for the coverage to be unity on all exposed surfaces of the fabricated substrate. By carrying out such sidewall epitaxy on a previously processed epitaxial multilayer wafer, we can obtain three-dimensionally confined low-dimension structures for use in novel devices. This is difficult to obtain by MBE or MOCVD.

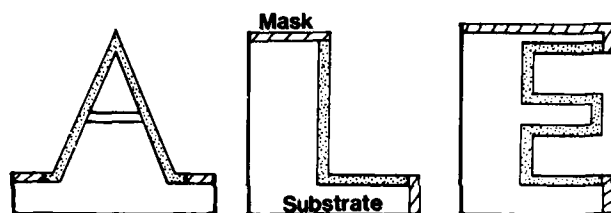


Fig. 6 Sidewall epitaxy

## 7. Electronic properties of GaAs layers grown by ALE.

### a) MO-ALE

GaAs epitaxial layers grown by ALE with metalorganic source gases frequently show p-type conduction. Hole concentrations are  $10^{17}\sim 10^{19}\text{cm}^{-3}$  with mobilities of  $60\sim 200\text{cm}^2/\text{vsec}$ . (Nishizawa et al 1986, Doi et al 1986b). To obtain high purity n-type layers, Kobayashi et al (1985) introduced a small amount of  $\text{AsH}_3$  during the TEG-exposure step (step 1 in Fig. 1). They call this technique FME (flow-rate modulation epitaxy). They succeeded in growth of n-type materials having carrier concentrations of  $10^{14}\sim 10^{16}\text{cm}^{-3}$  and mobilities at 77K as high as  $4.2\times 10^4\text{cm}^2/\text{vsec}$ . They also successfully obtained a modulation-doped structure with a 2DEG mobility of  $7\times 10^4\text{cm}^2/\text{vsec}$  at 6K. Additional  $\text{AsH}_3$  introduction during TEG suppresses carbon contamination and explains the excellent properties (Makimoto et al 1986).

### b) Chloride-ALE

The best among GaAs grown by GaCl-ALE is n-type with carrier concentration of  $6\times 10^{15}\text{cm}^{-3}$  and mobility of  $1.6\times 10^4\text{cm}^2/\text{vsec}$  at 77 K, where photoluminescence at 5 K suggests carbon acceptor compensation (Matsumoto and Usui 1986). A striking fact is that this sample shows no electron trap signal in DLTS within the detection limit of  $1\times 10^{13}\text{cm}^{-3}$ . (N. Iwata 1986). The major electron trap EL2 was not detected in this ALE sample. It is in remarkable contrast with conventional VPE or MOCVD samples which exhibit EL2 in the concentration range of  $10^{14}\sim 10^{15}\text{cm}^{-3}$ . When the GaCl coverage is not perfect, for example  $1-\theta=10^{-6}$ , and arsenic atoms occupy these vacant sites, antisite arsenic ( $\text{As}_{\text{Ga}}$ ) concentration becomes as high as  $\sim 10^{16}\text{cm}^{-3}$ . It has been frequently said that  $\text{As}_{\text{Ga}}$  acts as a deep donor defect EL2. The absence of EL2 signal in DLTS measurement means that (1) the GaCl coverage is almost perfect ( $1-\theta<10^{-9}$ ), (2) arsenic atoms are hardly incorporated to GaCl vacant sites, or (3) the EL2 defect does not have a simple form of  $\text{As}_{\text{Ga}}$  but rather it is a complex defect (EL2 family) as proposed by Ikoma and Mochizuki (1985). Further defect study using ALE samples will aid in the identification of EL2.

## 8. Summary

Atomic layer epitaxy of GaAs is reviewed with emphasis on the surface coverage of adsorbed species. A digital epitaxy concept is proposed for ALE under the particular condition where grown thickness is insensitive to any analogue quantities such as source gas pressures, growth temperature and growth time, and is determined only by the digital quantity ALE cycle. Several advantages of ALE, especially as digital epitaxy, are demonstrated. These advantages will be particularly useful for obtaining large diameter IC wafers containing monolayer-level-controlled, three-dimensionally-confined devices. Some preliminary results of electronic properties of the GaAs grown by ALE are discussed.



Acknowledgement

The authors are much indebted to H. Sunakawa, T. Matsumoto, K. Mori and N. Miyamoto for supplying recent ALE data, N. Iwata for measurement of DLTS, M. Yoshida, T. Inoshita and H. Terao for useful discussions. They appreciate F. Saito, D. Shinoda and S. Asanabe for their continuous encouragements.

References

- Bedair S M, Tischler M A, Katsuyama T and El-Masry N A 1985 Appl. Phys. Lett. **47** 51
- Bedair S M, Tischler M, El-Masry N and Katsuyama T 1986 This Symposium
- Cadoret R and Cadoret M 1975 J. Cryst. Growth **31** 142
- Cadoret R 1980 Current Topics in Materials Science, vol. 5, edited by E. Kaldis (North-Holland, Amsterdam, 1980) p.219
- Doi A, Aoyagi Y, Iwai S and Namba S 1986a Extended Abstracts of the 18th (1986 International) Conf. Solid State Devices and Materials, Tokyo, p. 739
- Doi A, Aoyagi Y and Namba S 1986b Appl. Phys. Lett. **48** 1787
- Doi A, Aoyagi Y, Iwai S, Mihara M and Namba S 1986c Abstracts of Riken Symposium, Tokyo, p.13
- Goodman C H L and Pessa M V 1986 J. Appl. Phys. **60** R65
- Ikoma T and Mochizuki Y 1985 Japan. J. Appl. Phys. **24** L935
- Iwata N 1986 Unpublished
- Kobayashi N, Makimoto T and Horikoshi Y 1985 Japan. J. Appl. Phys. **24** L962
- Korec J 1982 J. Cryst. Growth **60** 297
- Makimoto T, Kobayashi N and Horikoshi Y 1986 Japan. J. Appl. Phys. **25** L513
- Matsumoto T and Usui A 1986 Abstracts of 1986 Fall Meeting of Japan. Soc. Appl. Phys.
- Miyamoto H, Sunakawa H, Usui A and Ohata K 1986 Abstracts of 1986 Fall Meeting of Japan. Soc. Appl. Phys.
- Mori K, Ogura A, Yoshida M and Terao H 1986 Extended abstracts of the 18th (1986 International) Conf. Solid State Devices and Materials, Tokyo, p. 743
- Nishizawa J, Abe H and Kurabayashi T 1985 J. Electrochem. Soc. **132** 1197
- Nishizawa J, Abe H, Kurabayashi T, and Sakurai N 1986 J. Vac. Sci. Technol. A **4**(3) 706
- Nishizawa J, and Kurabayashi T 1986 J. Crystallographic Soc. Japan **28** 133
- Shaw D W 1975 J. Cryst. Growth **31** 130
- Suntola T, Antson J, Pakkala A and Lindfors S 1980 SID 80 Digest 108
- Theeten J B and Hottier F 1976 Surf. Sci. **58** 583
- Tischler M A and Bedair S M 1986 Appl. Phys. Lett. **48** 1681
- Usui A and Sunakawa H 1986a Japan. J. Appl. Phys. **25** L212
- Usui A and Sunakawa H 1986b This Symposium
- Usui A and Sunakawa H 1986c Proceedings of 2nd Meeting of the 151st Committee of Nippon Gakujutu Shinkokai
- Watanabe H 1986 The Physics and Fabrication of Microstructures and Microdevices, edited by M. J. Kelly and C. Weisbuch (Springer-Verlag, Heidelberg, 1986) p.158
- Yoshida M, Watanabe H and Uesugi F 1985 J. Electrochem. Soc. **132** 677

## **Impurity-induced disordering and its applications in optoelectronics**

\*R. D. Burnham, R. L. Thornton,  
\*\*N. Holonyak Jr., J. E. Epler, and T. L. Paoli

Xerox Palo Alto Research Center  
3333 Coyote Hill Rd., Palo Alto, CA 94304

\*Present Address: Amoco Research Center, P.O. Box 400  
Warrenville Rd., Naperville, IL 60566

\*\*University of Illinois at Urbana-Champaign  
Electrical Engineering Research Laboratory  
and Materials Research Laboratory, Urbana, IL 61801

**Abstract.** The technology and applications of impurity-induced disordering have been rapidly advancing. Many different impurities, as well as vacancies, have proven capable of enhancing the disordering. So far, three different approaches — diffusion from the surface, ion implantation, and doping during epitaxial growth — have been used to introduce the impurity source. High performance devices have already been demonstrated using either Zn or Si as the impurity. These results demonstrate clearly that impurity-induced disordering will play a key role in future integrated optoelectronics.

### **1. Disordering Mechanisms**

In the five years that have elapsed since the first demonstration of the phenomenon of impurity induced disordering (IID) (Laidig et al 1981b) and the obvious implication to integrated optoelectronics (Holonyak et al 1981), considerable effort has been devoted to studying and utilizing this effect. It is becoming increasingly apparent that the effect is an almost universal one, being observed in a wide variety of III-V alloy systems as well as being induced by a wide variety of impurity species. Studies have been carried out using surface diffusion, ion implantation and doping during epitaxial growth. The results of this work indicate that the mechanisms are at least as complicated as the technique is universal. IID is especially attractive because it significantly enhances the disordering compared to thermally induced disordering (Chang and Koma 1976, Fleming et al 1980, Laidig et al 1981a and 1982), although thermal annealing has been used successfully to modify the wavelength of the laser emission (Camras et al 1983b, Meehan et al 1983 and 1984c).

Numerous studies have been performed using surface diffusion of impurities to facilitate IID. In Table 1 are indicated some of the conditions that were first used in order to achieve IID in a variety of III-V materials. Of particular interest is the work demonstrating disordering on the column V site i.e., GaP/GaAs<sub>1-x</sub>P<sub>x</sub> and InP/Ga<sub>1-y</sub>In<sub>y</sub>As<sub>1-x</sub>P<sub>x</sub>. This work illustrates that the disordering phenomena are not unique to the column III site species. In the InP/Ga<sub>1-y</sub>In<sub>y</sub>As<sub>1-x</sub>P<sub>x</sub> material system, it is possible to achieve disordering effects on both sites by using the appropriate annealing temperature range. In this work disordering first occurs on the column III site at temperatures between 450-550 °C, shifting the photoluminescence to a lower energy. At higher temperatures of 550-700 °C, disordering on the column V site occurs, resulting in an increase in photoluminescence energy.

In addition to atomic species, vacancies on column III sites have been used to effect disordering as indicated in Table 1. By providing a surface condition that allows Ga to be preferentially removed from the surface of the crystal, an effective surface source of Ga vacancies was created, and disordering as a result of this vacancy "species" diffusing into the crystal has been observed. The

| III-V Material  | Impurity Species | ~T (°C) | First Reported           |
|---|------------------|---------|--------------------------|
| $\text{Al}_x\text{Ga}_{1-x}\text{As}/\text{Al}_y\text{Ga}_{1-y}\text{As}$ | Zn               | 500-600 | Laidig W D et al (1981b) |
|   | Si               | 850     | Meehan K et al (1984d)   |
|   | Ge               | 750     | Kaliski R W et al (1985) |
|   | S                | 850     | Rao E V K et al (1985)   |
|   | Cu               | 700     | Shimizu N et al (1985)   |
|   | V <sub>III</sub> | 825-875 | Deppe D G et al (1986)   |
| $\text{GaP}/\text{GaAs}_{1-x}\text{P}_x$                                  | Zn               | 825     | Camras M D et al (1983a) |
| $\text{GaAs}/\text{In}_x\text{Ga}_{1-x}\text{As} (x \sim 0.15)$           | Zn               | 615-680 | Laidig W D et al (1983)  |
| $\text{In}_x\text{Ga}_{1-x}\text{As}/\text{In}_y\text{Al}_{1-y}\text{As}$ | Zn               | 550     | Kawamura Y et al (1985)  |
| $\text{InP}/\text{Ga}_{1-y}\text{In}_y\text{As}_{1-x}\text{P}_x$          | Zn               | 450-700 | Razeghi M (1986)         |

Table 1 A list of III-V structures along with the corresponding impurity species and temperature conditions in which impurity induced disordering via diffusion was first reported.

combination of vacancies with other diffusing species can enhance (II). For example Si diffuses more rapidly when excess arsenic is present (Kavanaugh et al 1985) and (Omura et al 1986). The excess arsenic is a mechanism for providing Ga vacancies which enhance the Si diffusion.

Ion implantation has also received considerable attention as a method for introducing the disordering species. Implantation is advantageous because it permits use of species for which there are no surface diffusion sources. Table 2 contains a list of the wide variety of species that have been implanted followed by heat treatment in disordering studies in the AlGaAs alloy system. As can be seen, disordering has been observed not only with common dopants such as Si, Zn, Be, Mg and Se, but also with implanted lattice constituents such as Ga, Al, and As, and even with non-electrically active species such as Kr. The process of implantation is complicated greatly by the issue of implant damage, which may create disordering of its own as well as interfere with the diffusion kinetics of the implanted species which is intended to disorder, thereby blocking the disordering process. Heat treatment after implanting plays a significant role in implantation disordering. In one study it has been observed that concentrations of  $3 \times 10^{18}/\text{cm}^3$  are required for Si implant disordering (Kobayashi et al 1986), whereas other workers (Guido et al 1986a) have observed disordering at lower concentrations under different conditions. Recent work has revealed that disordering is suppressed not only by defects, but also by the presence of additional implanted species. Be has been shown to suppress disordering due to Ge when both species are introduced by ion implantation and to cause disordering when implanted alone. To complicate matters even further, these disordering suppression effects have a dependence on the order in which the two species were implanted (Venkatesan et al 1986b). The fact that other workers (Ralston J et al) obtain different results for Be as a disordering species is an indication that all relevant process parameters have not yet been fully characterized. All of these observations suggest an interplay of several mechanisms at work in the disordering process.

Disordering with complex mechanisms has also been observed in structures that have been doped during epitaxial growth. An AlAs-GaAs superlattice with uniform Si doping has been shown to have a threshold to disordering somewhere between  $2$  and  $4 \times 10^{18}/\text{cm}^3$  with annealing at  $800^\circ\text{C}$  for 2 hours (Kawahe et al 1984). Selectively doping only the GaAs layers in such a structure to  $3 \times 10^{18}/\text{cm}^3$  has also been shown to yield disordering of the entire structure when annealed at temperatures above  $650^\circ\text{C}$  (Iwata et al 1985). Also the  $(\text{Si}_2)_x(\text{GaAs})_{1-x}$  alloy has been used as an internal Si source for alloy disordering (Guido et al 1986b). In addition, very promising results have been achieved by using laser scanning to enhance the Si diffusion process in a selective, patterned manner (Epler et al 1986). Again, the variations reported in the concentrations required to produce

| III-V Material  | Ion Species  | ~T (°C)                                  | First Reported             |
|---|--|--|----------------------------|
| $\text{Al}_x\text{Ga}_{1-x}\text{As}/\text{Al}_y\text{Ga}_{1-y}\text{As}$ | Si <sup>+</sup>  | 675                                      | Coleman J J et al (1982)   |
|   | Zn <sup>+</sup>  | 575                                      | Camras M D et al (1982)    |
|   | S <sup>+</sup><br>Al <sup>+</sup><br>Kr <sup>+</sup>                       | 850<br>850<br>850                        | Gavrilovic P et al (1985b) |
|   | Ga <sup>+</sup>  | 750                                      | Hirayama Y et al (1985a)   |
|   | B <sup>+</sup><br>F <sup>+</sup><br>Ar <sup>+</sup> (1)<br>As <sup>+</sup> | 750-800<br>750-800<br>750-800<br>750-800 | Hirayama Y et al (1985b)   |
|   | Be <sup>+</sup> (1)<br>Mg <sup>+</sup><br>Se <sup>+</sup>                  | 660<br>660<br>660                        | Ralston J et al (1986)     |
|   | Be <sup>+</sup><br>Ge <sup>+</sup><br>Be <sup>+</sup> , Ge <sup>+</sup>    | 850                                      | Venkatesan T et al (1986b) |
|   |  |  |                            |

Table II A list of III-V structures along with the corresponding impurity species and temperature conditions in which disordering by ion implantation followed by heat treatment was first reported. (1) indicates no disordering observed.

the disordering effect vary due to the complex nature of the process. Similar to the work with Be implantation previously mentioned, Be has been shown to suppress disordering due to Si when both species are dopants grown in multilayer structures (Kawabe et al 1985). For example, Figure 1 shows that a region doped only with Si disorders as expected, while the superlattice structure remains unaffected in a portion of the same material also doped with  $1 \times 10^{19}/\text{cm}^3$  of Be.

## 2. Device Applications

In the field of IID, device results have followed very rapidly on the heels of process development. Although photopumped laser samples were first used to study the quality of the disordered material (Meehan et al 1984a), buried heterostructure lasers have received the most attention thus far. IID of the active region stripe by Zn diffusion in AlGaAs multiple quantum well laser material (Meehan et al 1984b) and AlGaAs single quantum well material (Fukuzawa et al 1984) resulted in the first device applications of IID, prompting extensive investigation (Nakashima et al 1985a) and (Semura et al 1985a and 1985b) into this system for the realization of an easily fabricated laser source with low threshold and high efficiency. Laser devices with thresholds as low as 20mA have been reported by these techniques. These devices were typically fabricated on p-type substrates, in order to simplify device contacting after performing the p-type zinc disordering diffusion. Oxide isolation stripes required for very narrow stripe widths resulted in a relatively complicated device process.

In 1983, a technique was demonstrated for diffusing Si into GaAs from a thin film source of elemental Si (Greiner et al 1984). This technique was quickly exploited to achieve IID (Meehan et al 1984d), and buried heterostructure lasers using Si-IID were demonstrated (Meehan et al 1985a and 1985b). Figure 2 shows an SEM cross-section of a buried heterostructure stripe formed by Si IID. These devices offered the potential advantage of utilizing the more typical n-type GaAs substrate in their fabrication. In addition, techniques have been developed to fabricate extremely narrow stripes without correspondingly high resolution lithography. As a result, threshold currents as low as 1.5-

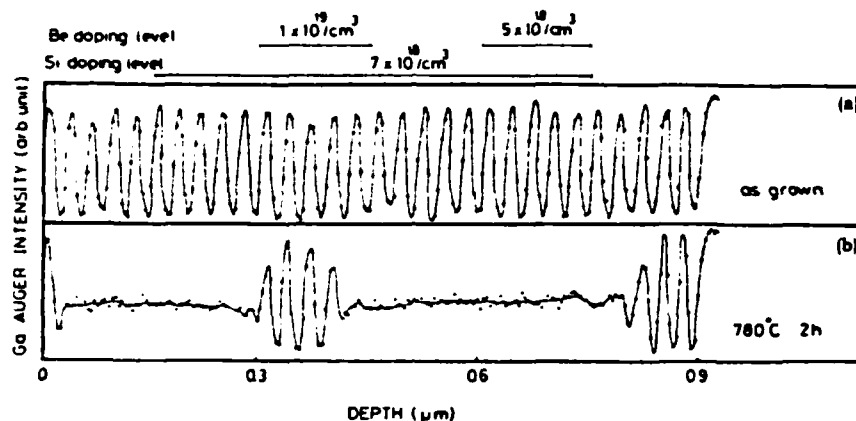


Fig. 1 Auger profile of Ga in the superlattice doped with Be and Si. Doping profiles are shown above the figure. (a) is the as-grown and (b) is after annealing at 780 C for 2 h (Kawabe et al 1985).

3mA have been achieved (Deppe et al 1985) and (Thornton et al 1985). In addition, these devices have been shown to be capable of high efficiencies (Thornton et al 1986a) as well as long life (Thornton et al 1986b). The data indicates that useful device lifetimes in the tens of thousands of hours can be achieved.

The relative suitability of Zn and Si for the purpose of IID has also been studied (Thornton et al 1986c). This study observed that the process using Zn has the advantages of lower diffusion temperature, shorter diffusion time and better characterized properties of Zn diffusion. The silicon diffusion process has the advantages of lower carrier concentration required to produce disordering, more abrupt interface transitions between ordered and disordered material, and compatibility with n type substrates. For specific device applications, one or the other of these species may be preferred.

The buried heterostructure laser device can easily be extended to its high power array analog. The optical waveguiding is sufficiently strong such that very closely spaced stripes remain uncoupled (Thornton et al 1986a), but various mechanisms may be introduced into these structures to induce phase-locking (Gavrlovic et al 1985a).

The simplicity of ion implantation compared to diffusion has encouraged the extensive investigation of implantation disordering described above. To date, however, the applications of these techniques to device fabrication are few. Si ion implantation has been used to make buried heterostructure lasers in the AlGaAs system (Gavrlovic et al 1985c), and Zn ion implantation has been used to make electroluminescent diodes in the (InGa)As/GaAs strained layer superlattice system (Myers et al 1986). Results, however, have not yet reached the same level of device performance as by conventional diffusion, partly because very high implant energies, typically several Mev, are required to realize the deep implants necessary to achieve the potentially simple device fabrication. The

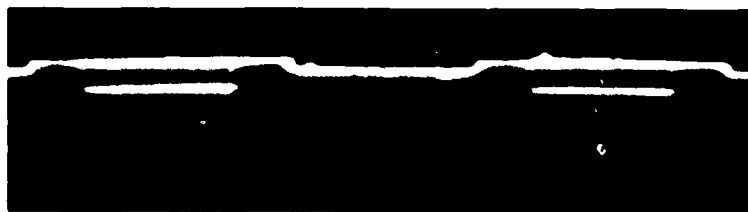


Fig. 2 SEM cross-section of a portion of a heterostructure array laser fabricated by impurity induced disordering. Each filament is 3.2 μm wide.

lattice damage resulting from high energy, high dose implants into a complex III-V crystal lattice structure (Gavrilovic et al 1985b, Guido et al 1986a, Kirillov et al 1986, Matsui et al 1986, Ralston et al 1986, Schwarz 1986a and 1986b, and Venkatesan et al 1986a) are difficult to anneal out. Nevertheless, the great deal of effort in this area will no doubt prove fruitful in this extremely promising technique.

In addition to the buried heterostructure laser, IID has been also utilized to fabricate Transverse Junction Stripe (TJS) lasers with improved performance (Yang et al 1986). Figure 3 shows a sketch of the structure for a recently demonstrated Zn-IID TJS laser, which gains improved performance from the disordering of the active region to reduce carrier diffusion away from the active portion of the multiple quantum well active region. This device has the significant advantage of being realizable on a semi-insulating type substrate, lending itself much more readily to integration with present GaAs integrated circuits.

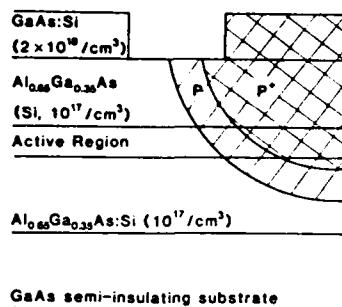


Fig. 3 Schematic diagram of a transverse junction stripe laser fabricated by Zn impurity induced disordering (Yang et al 1986).

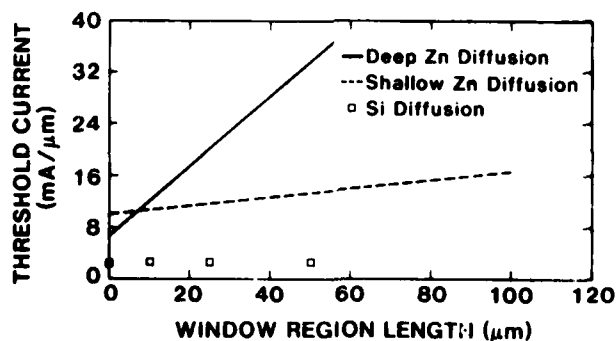


Fig. 4 Variation of threshold current with window region length for zinc (Nakashima et al 1985b) and silicon (Thornton et al 1986d) disordered window laser devices.

Another type of device which has received some attention from the IID technique is the window laser (Yonezu et al 1979). Designed for high optical output power per unit area of the emission facet, the window laser minimizes absorption at the output facet by making the material at the cleaved facet have a bandgap wider than the emission energy of the laser cavity. These devices have been successfully fabricated by both Zn (Laidig et al 1984, Suzuki et al 1984, Semura et al 1985a and Nakashima et al 1985b) and Si (Thornton et al 1986d) IID. Due to the higher carrier concentrations required to achieve disordering with Zn, propagation loss due to free carrier absorption in the window regions becomes an increasingly significant problem. Figure 4 shows a comparison of the increase in threshold with window region length for Zn and Si window laser structures. The effects of free carrier absorption on Zn-diffused window lasers are clearly evident in this data. Both deep (strongly disordered) and shallow (weakly disordered) Zn window lasers are shown for comparison. The Si disordered devices show no significant tendency towards increasing threshold current with increasing window region length, reflecting the low carrier concentration and low free carrier absorption level in this structure.

The effectiveness of Si IID in the creation of the window region is shown in figure 5, where the

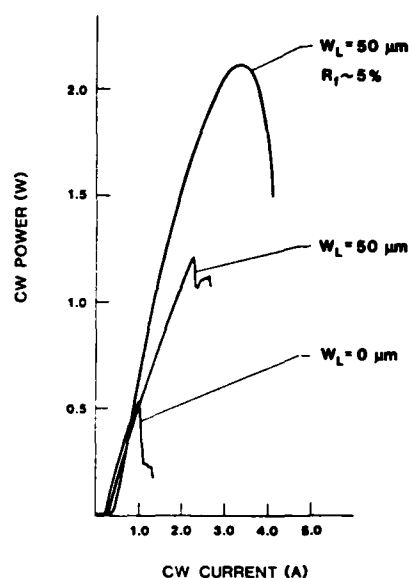


Fig. 5 Light versus current characteristics for a typical control device and a typical window device driven to their catastrophic limits, as well as an antireflection coated device that does not exhibit catastrophic damage up to 2.1 watts (Thornton et al 1986d).

Light versus Current characteristics for a control device with no window facet, an uncoated window facet, and a window facet with a quarter wave facet coating are shown. As can be seen, the laser with a window region exhibits a catastrophic facet damage level which is 2.3 times higher than the non-window device. Even more importantly, the coated facet window laser device does not exhibit catastrophic damage even up to 2.1 watts cw from a  $100 \mu\text{m}$  aperture. The power limitation on this device is no longer catastrophic facet damage, but thermal effects due to the large heat dissipation in the device. Thus it can be seen that IID techniques can dramatically improve the high power performance of these devices.

In conclusion, there is a tremendous amount of research yet to be done in the field of Impurity Induced Disorder. The alloy systems to be disordered, disordering species, and device applications are all receiving a great deal of attention. The field promises to provide many revolutionary processing techniques to the world of III-V semiconductors.

The authors gratefully acknowledge the technical assistance of H. Chung, R. Donaldson, F. Endicott, N. Mainzer, W. Mosby, S. Nelson, D. Taylor, T. Tjoe, and D. Treat of Xerox PARC.

## References

- Camras M D, Coleman J J, Holonyak N Jr, Hess K, Dapkus P D and Kirkpatrick C G 1982 International Symposium on GaAs and Related Compounds (London, Inst. of Physics) pp 233-9
- Camras M D, Holonyak N Jr, Hess K, Ludowise M J, Dietze W T and Lewis C R 1983a Appl. Phys. Lett. **42** 185-7
- Camras M D, Holonyak N Jr, Burnham R D, Streifer W, Scifres D R, Paoli T L and Lindström C 1983b J. Appl. Phys. **54** 5637-41
- Chang L I and Koma A 1976 Appl. Phys. Lett. **29** 138-41
- Coleman J J, Dapkus P D, Kirkpatrick C G, Camras M D and Holonyak N Jr, 1982 Appl. Phys. Lett. **40** 904-6
- Deppe D G, Hsieh K C, Holonyak N Jr, Burnham R D and Thornton R L 1985 J. Appl. Phys. **58** 4515-20
- Deppe D G, Guido I J, Holonyak N Jr, Hsieh K C, Burnham R D, Thornton R L and Paoli T L 1986 (To be published)
- Epler J E, Burnham R D, Thornton R L, Paoli T L and Bashaw M C (Submitted to Appl. Phys. Lett.)
- Fleming R M, McWhan D B, Gossard A C, Wiegmann W and Logan R A 1980 J. Appl. Phys. **51** 357-63
- Fukuzawa T, Semura S, Saito H, Ohta T, Uchida Y and Nakashima H 1984 Appl. Phys. Lett. **45** 1-3
- Gavrilovic P, Meehan K, Epler J E, Holonyak N Jr, Burnham R D, Thornton R L and Streifer W 1985a Appl. Phys. Lett. **46** 857-9
- Gavrilovic P, Deppe D G, Meehan K, Holonyak N Jr, Coleman J J and Burnham R D 1985b Appl. Phys. Lett. **47** 130-2
- Gavrilovic P, Meehan K, Guido I J, Holonyak N Jr, Eu V, Feng M and Burnham R D 1985c Appl. Phys. Lett. **47** 903-5
- Greiner M E and Gibbons J F 1984 Appl. Phys. Lett. **44** 750-52
- Guido I J, Hsieh K C, Holonyak N Jr, Kaliski R W, Eu V, Feng M and Burnham R D 1986a (To be published in J. Appl. Phys.)
- Guido I J, Holonyak N Jr, Hsieh K C, Kaliski R W, Baker J E, Deppe D G, Burnham R D, Thornton R L and Paoli T L 1986b (Submitted to J. Appl. Phys.)
- Hirayama Y, Suzuki Y, Tarucha S and Okamoto H 1985a Jpn. J. Appl. Phys. **24** L516-8
- Hirayama Y, Suzuki Y and Okamoto H 1985b Jpn. J. Appl. Phys. **24** 1498-502
- Holonyak N Jr, Laidig W D, Camras M D, Coleman J and Dapkus P D 1981 Appl. Phys. Lett. **39** 102-4
- Iwata N, Matsumoto Y and Baba T 1985 Jpn. J. Appl. Phys. **24** L17-20
- Kaliski R W, Gavrilovic P, Meehan K, Gavrilovic J, Hsieh K C, Jackson G S, Holonyak N Jr, Coleman J J, Burnham R D, Thornton R L and Paoli T L 1985 J. Appl. Phys. **58** 101-7
- Kavanagh K L, Mayer J W, Magee C W, Sheets J, Fong J, and Woodall J M 1985 Appl. Phys. Lett. **47** 1208-10
- Kawabe M, Matsuura N, Shimizu N, Hasegawa F and Nannichi Y 1984 Jpn. J. Appl. Phys. **23** L623-4
- Kawabe M, Shimizu N, Hasegawa F and Nannichi Y 1985 Appl. Phys. Lett. **46** 849-50
- Kawamura Y, Asahi H, Kohzen A and Wakita K 1985 Electron. Lett. **21** 218-9
- Kirilov K, Ho P and Davis G A 1986 Appl. Phys. Lett. **48** 53-5
- Kobayashi J, Nakajima M, Bamba Y, Fukunaga T, Matsui K, Ishida K, Nakashima H and Ishida K 1986 Jpn. J. Applied Physics **25** L385-7
- Laidig W D, Holonyak N Jr, Camras M D, Vojak B A, Hess K, Coleman J J and Dapkus P D 1981a Solid State Commun. **38** 301-4
- Laidig W D, Holonyak N Jr, Camras M D, Hess K, Coleman J J, Dapkus P D and Bardeen J 1981b Appl. Phys. Lett. **38** 776-8
- Laidig W D, Holonyak N Jr, Coleman J J and Dapkus P D 1982 J. Electron. Mater. **11** 1-20



- Laidig W D, Lee J W, Chiang P K, Simpson I W and Bedair S W 1983 *J. Appl. Phys.* **54** 6382-4
- Laidig W D, Lee J W and Caldwell P J 1984 *Appl. Phys. Lett.* **45** 485-7
- Matsui K, Takatani S, Fukunaga T, Narusawa T, Bamba Y and Nakashima H 1986 *Jpn. J. Appl. Phys.* **25** 1391-3
- Meehan K, Holonyak N Jr, Burnham R D, Paoli F I and Streifer W 1983 *J. Appl. Phys.* **54** 7190-7191
- Meehan K, Brown J M, Camras M D, Holonyak N Jr, Burnham R D, Paoli F I and Streifer W 1984a *Appl. Phys. Lett.* **44** 428-30
- Meehan K, Brown J M, Camras M D, Holonyak N Jr, Burnham R D, Paoli F I and Streifer W 1984b *Appl. Phys. Lett.* **44** 700-2
- Meehan K, Brown J M, Gavrilovic P, Holonyak N Jr, Burnham R D, Paoli F I and Streifer W 1984c **55** 2672-2675
- Meehan K, Holonyak N Jr, Brown J M, Nixon M A, Gavrilovic P and Burnham R D 1984d *Appl. Phys. Lett.* **45** 549-51
- Meehan K, Gavrilovic P, Holonyak N Jr, Burnham R D and Thornton R I 1985a *Appl. Phys. Lett.* **46** 75-7
- Meehan K, Gavrilovic P, Epler J E, Hsieh K C, Holonyak N Jr, Burnham R D, Paoli F I and Streifer W 1985b *J. Appl. Phys.* **57** 5345-8
- Myers D R, Arnold G W, Zipperian J E, Dawson I R, Biefeld R M, Fritz I J and Burnes C F 1986 *J. Appl. Phys.* **60** 1131-4
- Nakashima H, Semura S, Ohta T, Uchida Y, Saito H, Fukuzawa T, Kuroda T and Kobayashi K I 1985a *IEEE J. Quantum Electron.* **QJ-21** 629-33
- Nakashima H, Semura S, Ohta T and Kuroda T 1985b *Jpn. J. Appl. Phys.* **24** 1647-9
- Omura F, Wu X S, Vawter G A, Coldren L, Hu F and Merz J J 1986 *Electron Lett.* **22** 436-38
- Rao E V K, Thibierge H, Brillouet F, Alexandre F and Azoulay R 1985 *Appl. Phys. Lett.* **46** 867-9
- Ralston J, Wicks G W, Eastman L F, DeCoonan B C and Carter C B 1986 *J. Appl. Phys.* **59** 120-23
- Razeghi M 1986 (Private Communication)
- Schwarz S A, Venkatesan T, Bhat R, Koza M, Yoon H W and Arakawa Y 1986a (To be published)
- Schwarz S A, Venkatesan T, Hwang D M, Yoon H W, Bhat R and Arakawa Y 1986b (Submitted to *Appl. Phys. Lett.*)
- Semura S, Ohta T, Kuroda T and Nakashima H 1985a *Jpn. J. Appl. Phys.* **24** 1463-5
- Semura S, Ohta T, Kuroda T and Nakashima H 1985b *Jpn. J. Appl. Phys.* **24** 1548-50
- Shimizu N, Kawabe M and Nannichi Y 1985 32nd Spring Meeting of the Japan Society of Applied Physics (Tokyo)
- Suzuki Y, Horikoshi Y, Kobayashi M and Okamoto H 1984 *Electron. Lett.* **20** 383-4
- Thornton R I, Burnham R D, Paoli F I, Holonyak N Jr and Deppe D G 1985 *Appl. Phys. Lett.* **47** 1239-41
- Thornton R I, Burnham R D, Paoli F I, Holonyak N Jr and Deppe D G 1986a *Appl. Phys. Lett.* **48** 7-9
- Thornton R I, Burnham R D, Paoli F I, Holonyak N Jr and Deppe D G 1986b *Appl. Phys. Lett.* **49** 133-34
- Thornton R I, Burnham R D, Paoli F I, Holonyak N Jr and Deppe D G 1986c (To be published in *J. Cryst. Growth*)
- Thornton R I, Welch D E, Burnham R D, Paoli F I and Cross P S 1986d (To be published in *Appl. Phys. Lett.*)
- Venkatesan T, Schwarz S A, Hwang D M, Bhat R, Koza M, Yoon H W, Mei P, Arakawa Y and Yaris A 1986a (Submitted to *Appl. Phys. Lett.*)
- Venkatesan T, Schwarz S A, Hwang D M, Bhat R, Yoon H W and Arakawa Y 1986b (To be published in *Proc. of 1986 IBMM*)
- Yang Y J, Lo Y C, Lee G S, Hsieh K Y and Kolbas R M 1986 (submitted to *Appl. Phys. Lett.*)
- Yonezu H O, Ueno M, Kamejima T and Hayashi I 1979 *IEEE J. Quantum Electron.* **QJ-15** 775-81

## **Resonant tunneling transistors and superlattice devices by band-gap engineering**

(Invited Paper)

Federico Capasso  
AT&T Bell Laboratories  
600 Mountain Avenue  
Murray Hill, NJ 07974

### **Abstract**

Recent advances in quantum well (QW) tunneling optoelectronic and electron devices are discussed. These include the first realization of a resonant tunneling (RT) bipolar transistor; infrared lasers and detectors based on sequential RT and superlattice effective mass filters.

### **1. Resonant Tunneling Heterostructures.**

#### **1.1 Resonant Tunneling through Double Barrier Structures.**

Recently, Solnier et al. (1984) and Brown et al. (1986) have demonstrated negative differential resistance (NDR), microwave and millimeter wave operation in double-barrier (DB) QW structures. Since the pioneering work of Chang et al. (1974) on RT in DBQW structures, the material quality has improved to the point that negative differential resistance (NDR) can be observed at room temperature (Tsuchiya et al., 1985; Shewchuk et al., 1986). Recently peak-to-valley ratios in current of nearly 3:1 were obtained at room temperature by these authors. Ratios of 9:1 at 77 K have been demonstrated by Morkoc et al. (1986). As shown by Luryi (1985), the NDR in DBQW diodes is a consequence of the dimensional confinement of states in a QW, and the conservation of energy and lateral momentum in tunneling. In addition to that, the operation of these structures has often been discussed in connection with a RT effect analogous to that in a Fabry-Perot resonator. This *coherent* effect is presumed to occur when the energies of incident electrons in the emitter match those of unoccupied states in the QW. Under such conditions, the amplitude of the resonant modes builds up in the QW to the extent that the electron waves leaking out in both directions cancel the reflected waves and enhance the transmitted ones. This can lead to much higher peak currents than in the case when phase coherence of the electrons waves is destroyed by scattering. In the latter case collisions in the double barrier region randomize the phase of the electron waves and prevent the build-up of the probability density in the well. No resonant enhancement of the transmission is then possible and the electrons must be viewed as tunneling into and out of the well *sequentially* without preserving the phase coherence of the incident wave. One should distinguish therefore coherent (Fabry-Perot like) RT from incoherent (sequential) RT. It is the ratio of the intrinsic resonance width to the total scattering width (collision broadening) that determines which of the two mechanisms controls RT, as recently shown by Capasso et al. (1986 a). If the latter ratio is  $\gg 1$  the probability density can build-up in the well to the

resonant value in a time much smaller than the scattering time. In the opposite case instead the build-up time of the wave in the Fabry-Perot ( $\approx \hbar/\text{intrinsic resonance width}$ ) is long compared to the scattering time, so that collisions tend to randomize the phase of the wave function and prevent the resonant enhancement of the transmission.

Recently, Reed et al (1986) showed that the replacement of AlGaAs in the barriers with an AlAs/GaAs superlattice with the same average composition considerably improves the IV characteristics of RT diodes, by making it symmetric. Nakagawa et al., (1986) have also reported RT in triple barrier diodes.

### 1.2 Resonant Tunneling Bipolar Transistors

The physical picture of coherent RT has lead to a design strategy intended to optimize the Fabry-Perot resonator conditions. In particular, Davis and Hosack (1963) and Ricco and Azbel (1984) pointed out that achievement of a near-unity resonant transmission requires equal transmission coefficients for both barriers at the operating point - a condition not fulfilled for barriers designed to be symmetric in the absence of an applied field. To counter that, a RT structure was proposed by Capasso and Kiehl (1985) in which a symmetric DBQW was built in the base of a bipolar transistor, and the Fabry-Perot conditions were maintained through the use of minority-carrier injection (Fig. 1 and 2). Thus, this novel geometry maintains the crucial, structural symmetry of the double barrier, allowing near unity transmission at all resonance peaks and higher peak-to-valley ratios and currents compared to conventional RT structures. Both tunneling and ballistic injection in the base are considered (Fig. 1 and 2).

Shortly after this initial proposal, Yokoyama et al. (1985) reported the low temperature operation (70 K) of a *unipolar* RT hot electron transistor (RHET) [12]. This structure contains a double barrier in the emitter.

Recently, we have demonstrated the room temperature operation of the first RT bipolar transistor (RTBT) (Capasso et al. 1986 b). The band diagram of the transistor under operating conditions is sketched in Fig. 3, along with a schematics of the composition and doping profile of the structure (bottom). The DB consists of a 74 Å undoped GaAs QW sandwiched between the two undoped 21.5 Å AlAs barrier and that the AlGaAs graded emitter is doped to  $\approx 3 \times 10^{17} \text{ cm}^{-3}$ . The portion of the base ( $\text{Al}_{0.07}\text{Ga}_{0.93}\text{As}$ ) adjacent to the emitter was anodically etched off, while the rest of the base was contacted using AuBe. These base processing steps are essential for the operation of the device.

There is an essential difference with respect to the previously discussed RT transistors. These structures rely on *quasi-ballistic or hot-electron* transport through the base. These schemes place stringent constraints on the design and make it difficult to achieve room temperature operation due to the small electron mean free path ( $\leq 500$  Å at 300 K), since electrons that have suffered a few phonon collisions cannot reach the collector. The key to the present structure is that electrons are *thermally* injected into and transported through the base, thus making the device operation much less critical. This new approach has allowed

us to achieve for the first time RT transistor action at room temperature. Thermal injection is achieved by adjusting the alloy composition of the portion of the base adjacent to the emitter in such a way that the conduction band in this region lines up with the bottom of the ground-state subband of the QW (Fig. 3a). For a 74 Å well and 21.5 Å AlAs barriers the first quantized energy level is  $E_1 = 65$  meV. Thus the Al mole fraction was chosen to be  $x = 0.07$  (corresponding to  $E_g = 1.521$  eV) so that  $\Delta E_c \approx E_1$ . This equality need not be rigorously satisfied for the device to operate in the desired mode, as long as  $E_1$  does not exceed  $\Delta E_c$  by more than a few  $kT$ . The QW is undoped; nevertheless it is easy to show that there is a high concentration ( $\approx 7 \times 10^{11} \text{ cm}^{-2}$ ) two-dimensional hole gas in the well. These holes have transferred from the nearby  $\text{Al}_{0.07}\text{Ga}_{0.93}\text{As}$  region, by tunneling through the AlAs barrier, in order to achieve Fermi level line-up in the base. Consider a common emitter bias configuration. Initially the collector-emitter voltage  $V_{CE}$  and the base current  $I_B$ , are chosen in such a way that the base-emitter and the base-collector junctions are respectively forward and reversed-biased. If  $V_{CE}$  is kept constant and the base current  $I_B$  is increased, the base-emitter potential also increases until flat-band condition in the emitter region is reached (Fig. 3b left). In going from the band configuration of Fig. 3a to that of Fig. 3b the device behaves like a conventional transistor with the collector current increasing with the base current (Figs. 3a-3b right). The slope of this curve is, of course, the current gain  $\beta$  of the device. In this region of operation electrons in the emitter overcome, by thermionic injection, the barrier of the base-emitter junction and undergo RT through the double barrier. If now the base current is further increased above the value  $I_{BTH}$  corresponding to the flat band condition, the additional potential difference drops primarily across the first semi-insulating AlAs barrier (Fig. 3c), between the contacted and uncontacted portions of the base, since the highly doped emitter is now fully conducting. This pushes the conduction band edge in the  $\text{Al}_{0.07}\text{Ga}_{0.93}\text{As}$  above the first energy level of the well, thus quenching the RT. The net effect is that the base transport factor and the current gain are greatly reduced. This causes an abrupt drop of the collector current as the base current exceeds a certain threshold value  $I_{BTH}$  (Fig. 3c, right). The devices were biased in a common emitter configuration at 300 K and the I-V characteristics were displayed on a curve tracer. For base currents  $\leq 2.5$  mA the transistor exhibits normal characteristics, while for  $I_B \geq 2.5$  mA the behavior previously discussed was observed. Fig. 4 shows the collector current versus base current at  $V_{CE} = 12$  V, as obtained from the common emitter characteristics. The collector current increases with the base current and there is clear evidence of current gain ( $\beta = 7$  for  $I_C > 4$  mA). As the base current exceeds 2.5 mA, there is a drop in  $I_C$  because the current gain is quenched by the suppression of RT. Figure 5 illustrates the common emitter characteristics at 100 K. It is apparent that in addition to the previously discussed dependence of  $I_C$  on  $I_B$  (see Fig. 4), there is also a large negative conductance in the  $I_C$  vs  $V_{CE}$  curve for base currents in excess of the threshold value ( $= 4$  mA at 100 K). This is easy to understand by noting that in order to reach the band configuration of Fig. 3c and quench RT (at a fixed  $I_B > I_{BTH}$ ) the collector-emitter voltage  $V_{CE}$  must be large enough for the collector-base junction to be reverse biased and draw a significant collector current. Single frequency

oscillations (at 25 MHz, limited by the probe stage) have been observed in these devices when biased in the negative conductance region of the characteristics. One important advantage of this device compared to the RHET is that it has much higher current gain in its "on" state. Other RT transistors have also been proposed ranging from Stark effect RT's (Bonnefoi et al., 1985) to quantum wire unipolar RTs (Capasso and Luryi, 1985).

RT transistors are potentially very valuable for many logic and signal processing applications. These include new ultrahigh-speed analog-to-digital converters, parity generator circuits, high density memories using multiple valued logic (Capasso, 1985).

### **1.3 Sequential Resonant Tunneling and Effective Mass Filtering in Superlattices.**

In a strong electric field in a superlattice the miniband picture breaks down when the potential drop across the superlattice period exceeds the miniband width. When this condition is satisfied the quantum states become localized in the individual wells. In this limit an enhanced electron current will flow at sharply defined values of the external field, when the ground state in the  $n$ -th well is degenerate with the first or second excited state in the  $(n+1)$ -th well, as illustrated in Fig. 6a. Under such conditions, the current is due to electron tunneling between the adjacent wells with a subsequent de-excitation in the  $(n+1)$ -th well, by emission of phonons. In other words, electron propagation through the entire superlattice involves sequential RT.

Experimental difficulties in studying this phenomenon are usually associated with the non-uniformity of the electric field across the superlattice and the instabilities generated by negative differential conductivity. To ensure a strictly controlled and spatially uniform electric field, Capasso et al. (1986 c) placed the superlattice in the  $i$  region of a reverse-biased  $p^+ - i - n^+$  junction. This structure allowed for the first time to observe the sequential RT predicted by Kazarinov and Suris (1972). Two NDR peaks observed in the photocurrent characteristics, Fig. 7, correspond to the resonances shown schematically in Fig. 6. For the sequential RT regime, Kazarinov and Suris (1972) had predicted the possibility of a laser action at the inter-subband transition frequency - an effect not yet observed experimentally in superlattice (Fig. 6b). Another interesting possible application of sequential RT is a narrow band (a few meV) ir detector which uses absorption between the first two subbands of the wells (Capasso et al. 1986). The applied voltage is such the first and second excited states of adjacent wells are resonant. Thus the photoexcited electrons tunnel to the nearby well and give rise to a photocurrent.

Capasso et al. (1985a,b), recently reported the observation of a few extremely large photocurrent amplification phenomenon at very low voltages in a superlattice of  $\text{Al}_{0.48}\text{In}_{0.52}\text{As}/\text{Ga}_{0.47}\text{In}_{0.53}\text{As}$  in the quantum coupling regime (35 Å wells, 35 Å barriers). Room temperature responsivities at  $\lambda = 1.3 \mu\text{m}$  are typically  $2 \times 10^3$  and 300 Amps/Watt, at 0.3 Volt and 0.08 Volts bias respectively, while the highest measured value is  $4 \times 10^3$  A/W, corresponding to a current gain of  $2 \times 10^4$ . This effect, which represents a new quantum type photoconductivity, is

caused by the extremely large difference in the tunneling rates of electrons and heavy holes through the superlattice layers (*effective mass filtering*; Fig. 8). When thickness and compositional fluctuations cause fluctuations in the subband energies of the order or greater than the miniband width  $\Delta E$  miniband conduction cannot be sustained and hence conduction will proceed by phonon-assisted tunneling between adjacent wells, (hopping conduction). Since electrons have a much smaller mass than holes, their tunneling rate between adjacent wells is much larger (*effective mass filtering*). Photogenerated holes therefore remain relatively localized in the wells (their hopping probability is negligible) while electrons propagate through the superlattice (Fig. 8a). This effective mass filtering effect produces a photocurrent gain, given by the ratio of the lifetime to the electron transit time. The gain strongly decreased with increasing  $\text{Al}_{0.48}\text{In}_{0.52}\text{As}$  barrier layer thickness and becomes unity when this exceeds 100 Å. This confirms effective mass filtering as the origin of the large gain, since, as the barriers are made thicker, electrons also eventually tend to become localized, thus decreasing the tunneling probability and increasing the recombination rate. The temperature dependence of the responsivity conclusively confirmed hopping conduction.

For superlattices made of the same two materials with wider electron minibands (achieved by using thinner barriers) the electron transport is by miniband conduction, while holes are still localized (Fig. 8b). Such superlattice effective mass filters will have a much greater gain-bandwidth product than the other kind (Fig. 8a) due to the much shorter electron transit time.

#### REFERENCES

- Bonnefoi, A. R., Chow, D. H., and McGill, T. C., 1985, *Appl. Phys. Lett.* **47**, 888-890.
- Brown, E. R., Sollner, T. C. L. G., Goodhue, W. D., Clifton, B. J., and Tannenwald, P. E., Technical Digest of the 1986 Device Research Conference, Paper IV-B1.
- Capasso, F. and Kiehl, R. A., 1985, *J. Appl. Phys.* **58**, 1366-1369.
- Capasso, F., 1985, in "Picosecond Electronics and Optoelectronics", Springer Series in Electrophysics Vol. 21, G. A. Mourou, D. M. Bloom and C. H. Lee, Eds. pp. 112-130.
- Capasso, F., Mohammed, K., Cho, A. Y., Hull, R. and Hutchinson, A. L., 1985 a, *Appl. Phys. Lett.* **47**, 420-422.
- Capasso, F., Mohammed, K., Cho, A. Y., Hull, R., and Hutchinson, A. L., 1985 b, *Phys. Rev. Lett.* **55**, 1152-1155.
- Capasso, F., Mohammed, K., and Cho, A. Y., 1986 a, *IEEE J. Quantum Electronics*, **QE-22**, 1853-1855.

Capasso, F., Sen, S., Gossard, A. C., Hutchinson, A. L., and English, J. E., 1986 b, IEEE Electron Device Lett., *EDL7*, 573-576.

Capasso, F., Mohammed, K., and Cho, A. Y., 1986 c, Appl. Phys. Lett. *48*, 474-476.

Chang, L. L., Esaki, L., and Tsu, R., 1974, Appl. Phys. Lett. *24*, 593-595.

Davis, R. H. and Hosack, H. H., 1963, J. Appl. Phys. *34*, 864-866.

Kazarinov, R. F., and Suris, R. A., 1972, Sov. Phys. Semicond. *6*, 120-131.

Luryi, S., 1985, Appl. Phys. Lett. *47*, 490-492.

Luryi, S. and Capasso, F., 1985, Appl. Phys. Lett. *47*, 1347-1349.

Morkoc, H., Chen, J., Reddy, U. K., Henderson, T., Coleman, P. D., and Luryi, S., 1986, Appl. Phys. Lett. *42*, 70-72.

Nakagawa, T., Imamoto, H., Kojima, T. and Ohta, K., 1986, Appl. Phys. Lett. *49*, 73-75.

Reed, M. A., Lee, J. W. and Tsai, H.-L., 1986, Appl. Phys. Lett. *49*, 158-160.

Ricco, B. and Azbel, M. Ya., 1984, Phys. Rev. *B 29*, 1970-1981.

Shewchuk, T. T., Chapin, T. C., Coleman, P.D., Kopp, W., Fischer, R. and Morkoc, H., 1985, Appl. Phys. Lett. *46*, 508-510.

Sollner, T. C. L. G., Tannenwald, P. E., Peck, D. D. and Goodhue, W. D., 1984, Appl. Phys. Lett. *45*, 1319-1322.

Tsuchiya, M., Sakaki, H. and Yoshino, J., 1985, Jpn. J. Appl. Phys. *24*, L466-468.

Yokoyama, N., Imamura, K., Muto, S., Hiyamizu, S. and Nishi, H., 1985, Jpn. J. Appl. Phys., *24*, L583-584.

Figures are on the next page.

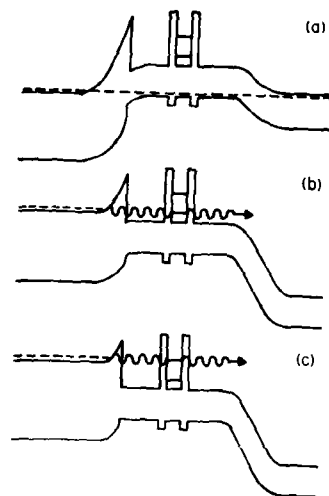


Fig. 1 Band-diagram of RBT with tunneling emitter and quantum well base.

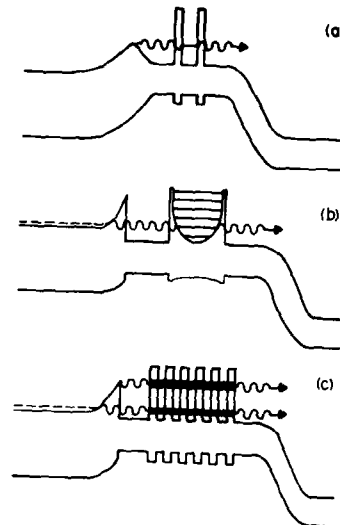


Fig. 2 Band diagram of RBTs with (a) ballistic injection, (b) parabolic QW, (c) superlattice base.

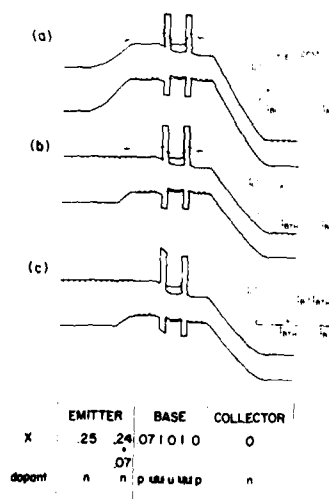


Fig. 3 Energy band diagrams of RBT with thermal injection and corresponding schematics of collector current  $I_C$  for different base currents at a fixed collector-emitter voltage  $V_{CE}$ . Shown is also the composition and doping profile of the structure; u stands for undoped.



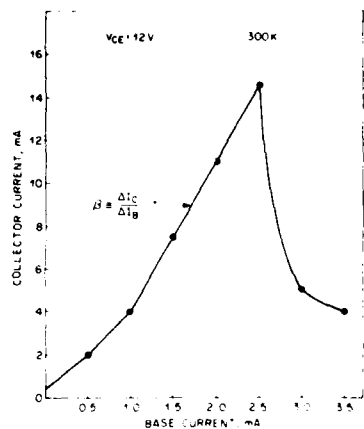


Fig. 4  $I_C$  vs  $I_B$  in the common emitter configuration, at room temperature, with the collector-emitter voltage held constant. The line connecting the data points is drawn only to guide the eye.

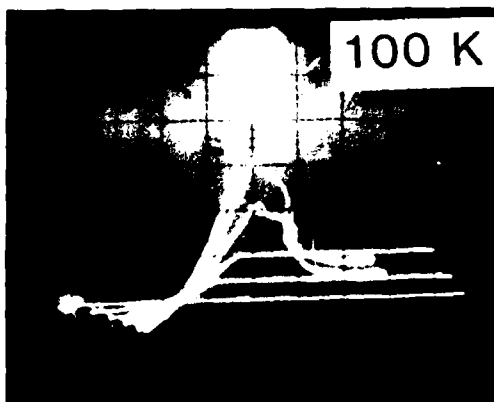


Fig. 5 Common emitter characteristics of the RBT bipolar at 100 K. The vertical scale is 10 mA/div, while the horizontal scale is 2 V/div. Each step in the base current is 2 mA.

The emitter area is  $1.5 \times 10^{-5} \text{ cm}^2$ .

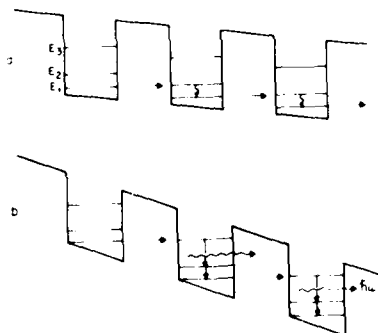


Fig. 6 a. Band diagram of sequential RT of electrons through a superlattice (SL).  
b. Band-diagram of far ir four level laser based on sequential RT.

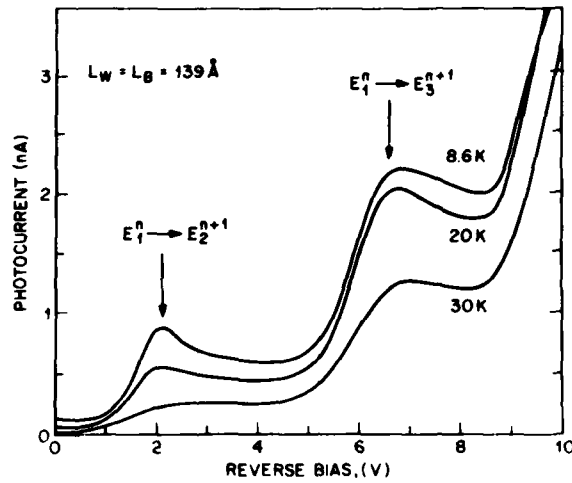


Fig. 7 Photo I-V for a SL with 139 Å thick wells and barriers and 35 periods. The two peaks correspond to RT between the ground and first two excited states of a adjacent wells. (See Fig. 6a and 6b).

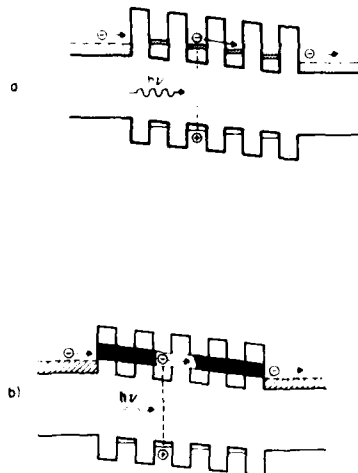


Fig. 8 Band diagram of effective mass filtering in the case of  
a. phonon assisted tunneling and  
b. miniband conduction

### **Improvement in the uniformity of electric properties of semi-insulating 3" $\phi$ In-mixed GaAs single crystal by high magnetic field applied liquid encapsulated Czochralski technique**

T. Kawase, A. Kawasaki, K. Tada  
Sumitomo Electric Industries, Ltd.  
1-3, Shimaya 1-chome, Konohana-ku, Osaka 554, Japan

**Abstract.** 3"; semi-insulating indium-mixed GaAs single crystals were grown by vertical magnetic field applied liquid encapsulated Czochralski technique. We found that application of a magnetic field strongly affected solid-liquid interface shape, slip-dislocation length, indium concentration distribution, and neutral EL2 distribution.

#### **1. Introduction**

The dislocation-free semi-insulating LEC GaAs single crystals with large diameter have been successfully obtained by mixing indium (Jacob et al. 1983, Kimura et al. 1984, Nakanishi et al. 1984, Tada et al. 1984). Some authors have previously reported the effects of magnetic field application on the impurity concentration and the electrical properties of GaAs single crystal (Fukuda et al. 1983, Terashima et al. 1986a). Recently a notable effect on carbon contamination with high magnetic field application has been investigated by Terashima et al. (1986b).

We applied the high magnetic field in the growth of In-mixed GaAs single crystals, and found the following effects: (1) reduction of the slip dislocations propagating from the crystal surface, (2) improvement of the uniformity in the distribution of indium concentration, (3) improvement of the uniformity in the distribution of the neutral EL2 concentration, [EL2]. In this report, we discuss the relationship between those effects and the changes of the thermal environment in the melt, especially near the melt surface, by applying magnetic field.

#### **2. Experiments**

3";  $\langle 100 \rangle$  oriented In-mixed GaAs single crystals were grown by vertical magnetic field applied liquid encapsulated Czochralski (VMLEC) technique. The GaAs melts (about 3.6kg) including 1.6wt% indium were prepared from GaAs polycrystals and metal indium in 6"  $\phi$  pBN crucibles. The crystals and the crucibles were counterrotated at rates of 5 rpm and 20 rpm, respectively. The crystals were grown at a constant pull rate of 6.0 mm/h under 15 ~ 25 atm nitrogen atmosphere. Magnetic fields were applied to the melts up to 6000 Oe.

The solid-liquid interface shapes were observed by X-ray topography. The indium concentrations in the crystals were determined by inductively coupled plasma atomic emission spectrometry (ICP) analysis. [EL2] were evaluated from the optical absorption at  $\lambda = 1 \mu\text{m}$  (Martin et al. 1980). The infrared ray (IR) transmission images were observed by conventional

type IR apparatus and video image processing system (Katsumata et al. 1985). The temperature gradients and the temperature fluctuations in the GaAs melt without crucible rotation were measured by using W5%Re-W26%Re thermocouples at three points aligned along radial direction of the crucible.

### 3. Results

Figure 1 shows the average vertical temperature gradient between depths of 0 mm and 15 mm under the melt surface. Figure 2 shows the temperature fluctuations at a depth of 15 mm. The average temperature gradient is low, but also the temperature fluctuation is extremely large at the crucible center at  $H = 0$  Oe ( $H$ : magnetic field strength). In a higher magnetic fields, the temperature gradient becomes higher, and the temperature fluctuation becomes smaller at the crucible center. Temperature gradient in the melt increases from  $25^\circ\text{C}/\text{cm}$  (at  $H = 0$  Oe) to  $35^\circ\text{C}/\text{cm}$  (at  $H = 3000$  Oe) at the center of the crucible. On the other hand, temperature gradient, at a position of 40 mm apart from the center of the crucible, decreases by applying a magnetic field. It follows from this fact that the turbulent free convective flow at the crucible center at  $H = 0$  Oe is suppressed by the magnetic field application. The measurement at 6000 Oe gave the result similar to that at 3000 Oe. Therefore, the magnetic fields higher than 3000 Oe don't give drastic further changes. Figure 3 shows the X-ray topographs at the center region of the crystals grown at  $H = 0$  Oe and  $H = 3000$  Oe. The growth striations of the crystal grown at  $H = 0$  Oe are intersected each other, and are random in spacing. These behaviors represent that growth and remelt are randomly repeated due to a large temperature fluctuation at the center region. The striations of crystals grown at  $H = 3000$  Oe appear to be aligned parallelly and regularly.

From the striation pattern, the magnetic field application is found to make a convex shaped interface flatter. The value of  $\Delta/D$  ( $\Delta$ : deviation of the solid-liquid interface from the flat plane,  $D$ : diameter of the crystal), which is introduced in order to evaluate the interface shape, is about 1% at  $H = 6000$  Oe, while it is about 8% at  $H = 0$  Oe. Figure 4 shows the variation of the value of  $\Delta/D$  with magnetic field strength. X-ray topographs also show that a magnetic field application affects the slip dislocations in the periphery regions of the crystals. Figure 5 shows the X-ray topographs of (100) wafers (indium concentration: 2500 wtppm) perpendicular to the growth axis. The length of slip dislocations of the crystal grown at  $H = 3000$  Oe is much shorter than that at  $H = 0$  Oe.

Figure 6 shows the radial distribution of indium concentrations on (100) wafers where the indium concentrations are about 2500 wtppm (the fraction solidified ( $g$ ) of 0.3). This figure suggests that the indium on the solid-liquid interface concentrates at the center of the crystals. On the other hand, by applying magnetic field, the indium distribution is relatively flat at the center of the crystals.

Figure 7 shows the radial  $[\text{EL2}^\circ]$  distribution in the as-grown crystals. The crystal grown at  $H = 3000$  Oe has the wider region with uniform  $[\text{EL2}^\circ]$  distribution than the crystal grown at  $H = 0$  Oe. The region with uniform  $[\text{EL2}^\circ]$  is coincide with the dislocation free region. Figure 8 shows the IR topographic images of the longitudinal section in the center region of the crystals. These images reveal the similar striation patterns as shown in the X-ray topographs.

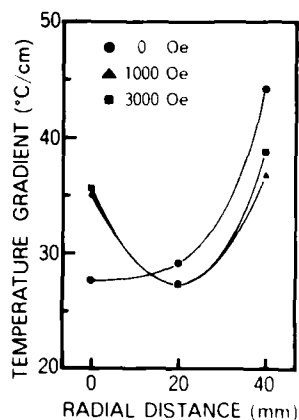


Figure 1 Average vertical temperature gradients in the melt without crucible rotation, at  $H = 0$  Oe, 1000 Oe, 3000 Oe.

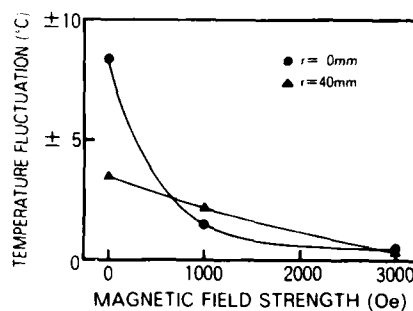


Figure 2 Amplitudes of the temperature fluctuations in the melt without crucible rotation versus magnetic field strength.

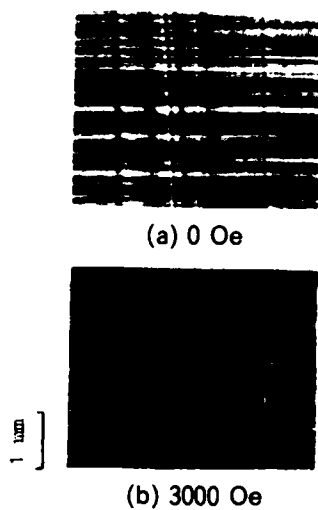


Figure 3 X-ray topographs of the longitudinal section at the center region of the crystals grown at (a)  $H = 0$  Oe and (b)  $H = 3000$  Oe.

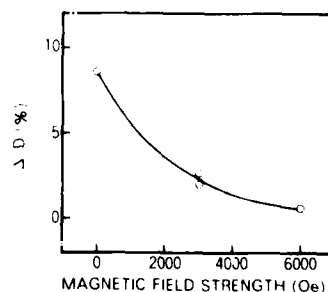


Figure 4 The value of  $\Delta/D$  versus magnetic field strength.  $\Delta$ : deviation of the solid-liquid interface from the flat plane,  $D$ : diameter of the crystal.

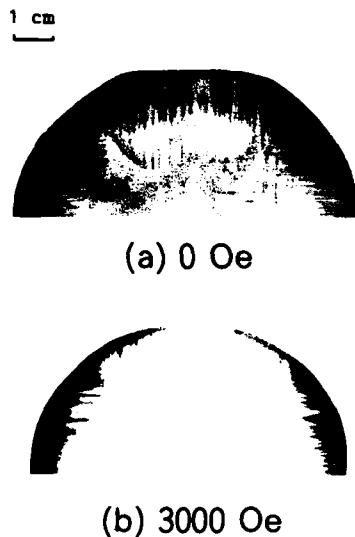


Figure 5 X-ray topographs of (100) wafer of the crystals grown at (a)  $H = 0$  Oe and (b)  $H = 3000$  Oe.

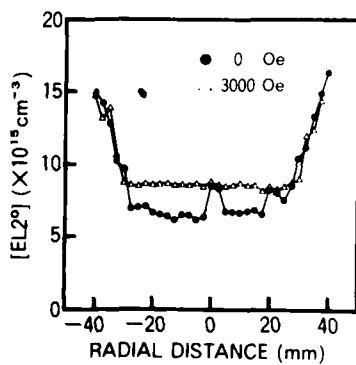


Figure 7 Radial distribution of EL2 of the crystals grown at  $H = 0$  Oe and  $H = 3000$  Oe.

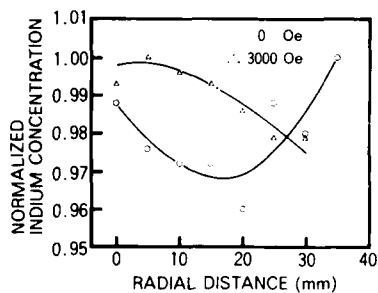


Figure 6 Radial distribution of indium concentrations of the crystals grown (normalized by the maximum value) at  $H = 0$  Oe and  $H = 3000$  Oe.

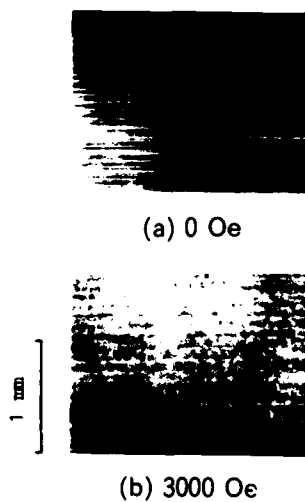


Figure 8 IR images of the longitudinal section at the center region of the crystals grown at (a)  $H = 0$  Oe and (b)  $H = 3000$  Oe.

#### 4. Discussion

The flow modes of the melt change drastically and become stable by applying a magnetic field to the GaAs melt. The temperature fluctuation results in the striations, and the changes of temperature gradient along axial direction are reflected on the change of solid-liquid interface shape from the convex to the flat by applying a magnetic field. Therefore, as shown in Figure 4, the solid-liquid interface shape ( $\Delta/D$ ) doesn't change largely above 3000 Oe. These results are confirmed from the striation patterns of the X-ray topographs and IR absorption images. Melt flow also affects the distribution of impurity concentration in the crystal. There are differences between the indium concentration distribution along the radial direction in the crystal grown at  $H = 0$  Oe and in the crystal grown at  $H = 3000$  Oe. At zero magnetic field, the high indium concentration at the center region is probably caused by the following two reasons. The dominant natural convection, which flows from the periphery of the growing crystal to the center, accumulates indium atoms swept out from the interface at the center region. Or the high indium concentration region is confined under the interface region which is called the Taylor-Praudman cell (Carruthers et al. 1968). In a magnetic field if crystal rotation is changed by an appropriate rate, indium concentration becomes uniform due to the melt flow induced by a forced convection from the center to the periphery of crystal.

From the results of X-ray topograph, IR absorption image and EPD distribution, it is found that magnetic field application reduces the length of slip dislocations along radial direction on the wafer. Since magnetic field little affects on the thermal environments above the melt surface, the reduction of the length of slip dislocations is attributable to the change of the temperature gradient in the melt, especially along radial direction. Radial temperature gradient at the interface is lower under the growth conditions resulting in the flat solid-liquid interface than those resulting in the convex one. Therefore, a magnetic field shortens the length of the slip dislocations since the thermal stress in the crystal is reduced in the low temperature gradient.

These slip dislocations give a large effect to the  $[EL2^{\circ}]$  distribution. It is reported that  $[EL2^{\circ}]$  are affected by dislocations in the region where dislocation densities are more than  $1000 \text{ cm}^{-2}$  (Takebe et al. 1985). High  $[EL2^{\circ}]$  at the periphery is related to the slip dislocations. Therefore, the uniform  $[EL2^{\circ}]$  regions are broadened considerably, since dislocation free regions without slip dislocation are expanded by applying a magnetic field. This broadening of uniform  $[EL2^{\circ}]$  regions is confirmed by IR absorption images of the (100) wafers cut perpendicular to the growth direction. The IR absorption images also show similar results as the X-ray topograph in which the contrast of the striations become weaker by applying magnetic field. What contributes to the absorption, especially striation pattern, in IR image is not yet fully understood. However, the striations in IR image may influence the microscopic  $[EL2^{\circ}]$  distributions in the crystal along the radial direction as well as the axial direction.

#### 5. Conclusion

We have grown 3"  $\phi$  semi-insulating indium-mixed GaAs single crystals by vertical magnetic field (up to 6000 Oe) applied liquid-encapsulated Czochralski technique. We have found that the change of the flow modes in the melt by applying a magnetic field affects the inhomogeneity of

the indium concentration and [EL2°] distribution, and the length of the slip dislocations. Improvement of macroscopic [EL2°] distribution was attributed to the broadening of the dislocation free region which was achieved by the reduction of the temperature gradient in the melt applied magnetic field.

#### Acknowledgements

The authors would like to thank the people of the Semiconductor Division, The Analytical Characterization Center, and the Semiconductor Materials R & D Dept. of Sumitomo Electric Industries, Ltd. for precious experimental cooperation and discussion.

#### References

- Carruthers J R and Nassau K 1968 J. Appl. Phys. 39 5205  
 Fukuda T, Terashima K, Katsumata T, Orito F, and Kikuta T 1983 Extended Abstracts of the 15th Conf. on Solid State Devices and Materials 153  
 Jacob G, Duseaux M, Farges J P, Van Den Boom M M B, and Roksnoer J P 1983 J. Crystal Growth 61 417  
 Katsumata T, Obokata T, Nakajima M, and Fukuda T 1985 Defect Recognition and Image Processing in III-V Compounds (Montpellier) p149  
 Kimura H, Afable C B, Olsen H M, Hunter A T, Miller K T, and Winston H V 1984 Extended Abstracts of the 16th Conf. on Solid State Devices and Materials 63  
 Martin G M, Jacob G, Poiblaud G, Goltzene A, and Schwab C 1980 Defects and Radiation Effects in Semiconductors (Oslo) Inst. Phys. Conf. Ser. 59 281  
 Nakanishi H, Kohda H, Yamada K, and Hoshikawa 1984 Extended Abstracts of the 16th Conf. on Solid State Devices and Materials 63  
 Tada K, Murai S, Akai S, and Suzuki T 1984 Proc. of IEEE GaAs IC Symposium (Boston) p49  
 Takebe T, Murai S, Tada K, Akai S 1984 Proc. of 12th Int. Symposium on GaAs and Related Compounds (Karuizawa) Inst. Phys. Conf. Ser. 79 283  
 Terashima K, Yahata A, and Fukuda T 1986a J. Appl. Phys. 59 982  
 Terashima K, Washizuka S, Nishio J, Shimada H, Yasuami S, and Watanabe M 1986b Presented at 4th Conf. on Semi Insulating III-V Materials (Hakone)



## **Distribution coefficient of carbon in gallium arsenide**

U. V. Desnica and L. M. Pawlowicz\*

Cabot Corporation, Billerica Technical Center, Billerica, MA 01821  
\*Massachusetts Institute of Technology, Cambridge, MA 02139

**Abstract.** We performed a systematic study of the distribution coefficient of carbon in LEC GaAs crystals grown with different pulling rates,  $R$ . The concentration of  $C_{As}$  along the ingots was determined using carbon-related IR-LVM absorption. We found that the measured effective distribution coefficient of carbon strongly depends on pulling rate, ranging from 1.15 for  $R = 5$  cm/h up to 2.5 for  $R = 0.63$  cm/h. This indicates that the value of the equilibrium distribution coefficient of C in GaAs exceeds 3, which is considerably higher than has been previously estimated.

### 1. Introduction

Carbon is one of the major electrically active chemical contaminants in "undoped" semi-insulating (SI) GaAs grown by the liquid encapsulated Czochralski (LEC) method [Brozel (1986), Holmes et al. (1980)]. In GaAs lattice carbon occupies arsenic sites where it acts as a shallow acceptor,  $C_{As}$ . Its concentration generally exceeds the total concentration of residual donor impurities in LEC GaAs, which would result in p-type GaAs. Semi-insulating behavior is obtained because of the native compensating deep donor defects known as EL2. It is believed [Kirkpatrick et al. (1985)] that the balance of carbon shallow acceptors and EL2 deep donors governs macro- and microscopic properties of GaAs, especially its high electrical resistivity, as well as the uniformity of relevant properties; therefore radial and axial distribution of both carbon and EL2 need to be known in detail. In spite of its obvious importance, the data on the distribution of carbon in GaAs crystals are inconsistent and contradictory: reported values for  $k$  vary from 0.8-2.0.

Here we present the results of a detailed investigation of distribution coefficient of carbon in GaAs. The carbon concentration was measured using the carbon-related localized vibrational mode (LVM) absorption. The carbon distribution was determined along the growth axis of 5 LEC GaAs crystals, which were grown at different pulling rates. We have found that the  $k_{eff}$  for carbon strongly depends on the pulling rate, so that the equilibrium distribution coefficient,  $k_0$ , (for infinitesimally small pulling rate) is very large, exceeding 3. Thus, for low pulling rates, a very pronounced non-uniformity of C has to be expected along the ingot, which may account for some of the non-uniformity observed in the electrical and other properties of GaAs ingots.

2. Experimental

All GaAs ingots used in this study were grown by the LEC method in the same high-pressure growth apparatus. Pre-synthesized GaAs was used as the charge source: the same source material was used for all crystals measured. The charge material was cleaned in organic solvents, and etched in 3:1:1  $\text{H}_2\text{SO}_4 : \text{H}_2\text{O}_2 : \text{H}_2\text{O}$ . The crystals were grown in PBN crucibles, 1.4-inch diameter by 1.5-inch depth; the standard charge size was approximately 70 g. Crystals were pulled in  $\langle 111 \rangle$  directions. The typical dimensions of the grown crystals were 1.25 cm in diameter, 10 cm in length. The growth time varied from approximately 3 hours for the fastest-pulled crystal (5 cm/h) to approximately 12 hours for the slowest (0.625 cm/h).

The concentration of carbon was determined using a Fourier Transform Infrared (FTIR) spectrometer (Nicolet MX-1), with a spectral resolution of  $0.6 \text{ cm}^{-1}$ , at room temperature. The IR absorption at room temperature due to the excitation of localized vibrational modes of  $\text{C}_{\text{As}}$  results in an absorption peak at  $580 \text{ cm}^{-1}$ , with a half width about  $1.3 \text{ cm}^{-1}$ . At low temperatures absorption spectrum of carbon is very sharp (less than  $1 \text{ cm}^{-1}$ ), but it splits into at least five peaks, which makes it rather inconvenient for determination of the area under the carbon-related peaks. At present, LVM absorption is the most sensitive method for determination of carbon in GaAs: the sensitivity limit is in the range of  $10^{14} \text{ C-atoms/cm}^3$  [Homma Y and Ishii Y (1984)].

3. Results

In all GaAs ingots we found that the concentration of  $\text{C}_{\text{As}}$  decreases from the seed toward the tang end. The distribution coefficient of  $\text{C}_{\text{As}}$  in GaAs is, therefore, definitely larger than 1. The concentration distribution of carbon along the pulling direction (axial distribution) was measured, and plotted against  $(1-g)$ , where  $g$  denotes the fraction of the GaAs melt which has been solidified. Changes of carbon concentration along the ingots are presented in Figure 1, with the pulling rate,  $R$ , as the parameter. It is clearly seen that the distribution function is quite different for different pulling rates. It is seen that small pulling rates give more pronounced changes in carbon concentration and vice versa, indicating that the measured, effective distribution coefficient of carbon depends strongly on the pulling rate.

For a LEC grown crystal  $k$  can be generally expressed by the equation:

$$C_s = k_{\text{eff}} C_L = k_{\text{eff}} C_{\text{LO}} (1-g)^{k_{\text{eff}} - 1}$$

where  $C_s$  and  $C_L$  are the carbon impurity concentrations in the solid and the melt respectively, while  $C_{\text{LO}}$  is the initial carbon concentration in the melt. Measured changes in all ingots follow formula (1) so that for every pulling rate the effective distribution coefficient can be determined from the slope of  $\log C_s$  vs.  $(1-g)$  plots. The results are presented in Table 1:

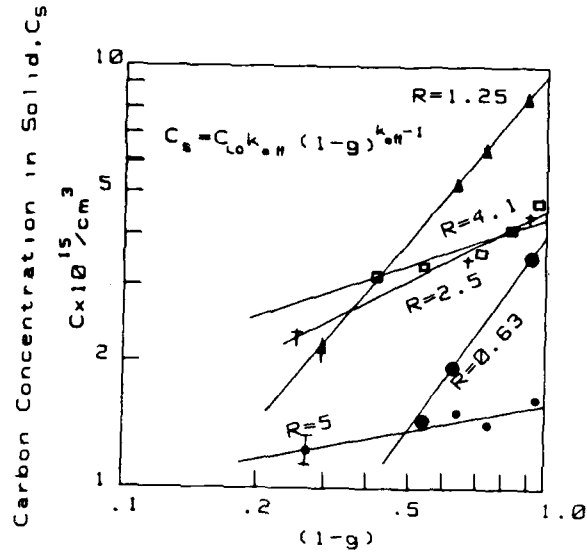


Fig. 1 Longitudinal distribution of C concentration in LEC GaAs crystals grown with different pulling rates,  $R$ (cm/h)

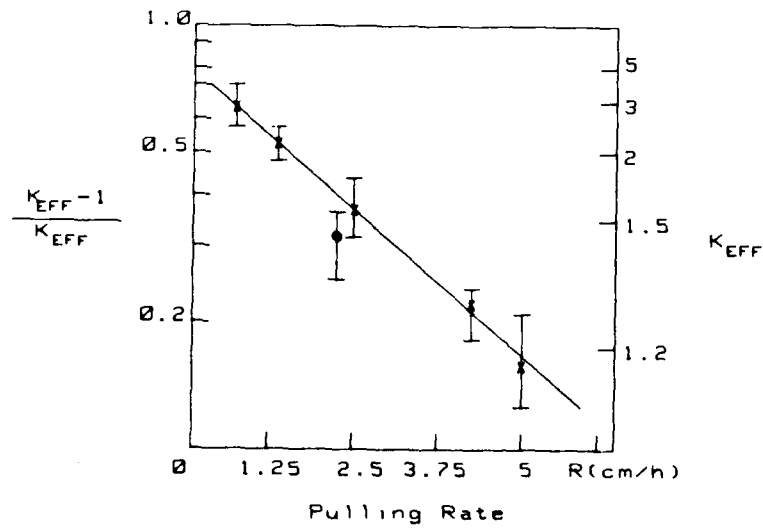


Fig. 2 Effective distribution coefficient of C in LEC GaAs as a function of pulling rate  
 ●=Kobayashi & Oseka (1985), ×=Present work  
 Line=Calculated from eq. (2) with  $k_0 = 3.5$  and  $S/D = 0.28$

Table 1  
Effective Distribution Coefficients For Carbon in GaAs

|  |       |      |     |     |      |
|--|-------|------|-----|-----|------|
| Pulling Rate, R(cm/hr)                       | 0.625 | 1.25 | 2.5 | 4.1 | 5    |
| Effective Distribution Coefficient $K_{eff}$ | 2.5   | 2.1  | 1.5 | 1.3 | 1.15 |

Present results extrapolated to  $R=0$  can be used for the determination of the equilibrium distribution coefficient  $k_0$ . The relationship between effective and equilibrium distribution coefficients can be expressed by:

$$k_{eff} = \frac{k_0}{k_0 + (1-k_0) \exp(-R\delta/D)} \quad (2)$$

where  $\delta$  is the effective diffusion layer thickness and  $D$  is the diffusion constant of the impurity in the dilute liquid. Consequently:

$$\ln \left( \frac{k_{eff}-1}{k_{eff}} \right) = \ln \left( \frac{k_0-1}{k_0} \right) - R\delta/D \quad (3)$$

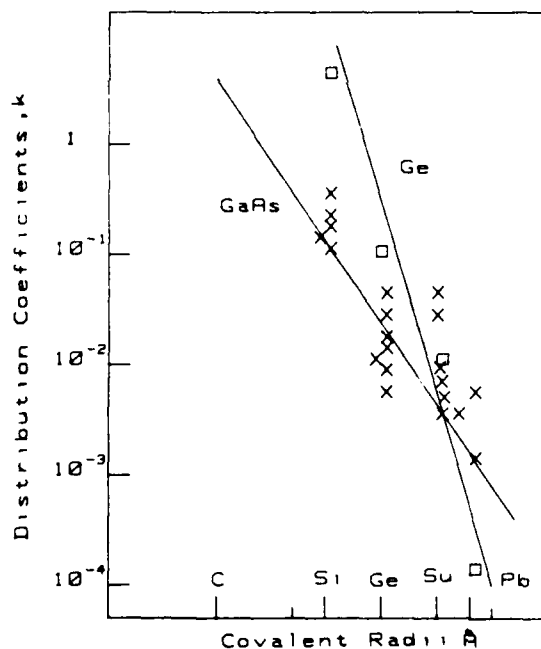


Fig.3 Correlation between distribution coefficients and covalent radii for group IV elements in Ge and GaAs.

Figure 2. depicts the dependence of  $\ln[(k_{eff}-1)/k_{eff}]$  on  $R$ . To the limits of experimental error this dependence is linear. By extrapolating to  $R=0$ , one finds a value  $k_0$  of approximately 3.5. The linearity of the  $\ln[(k_{eff}-1)/k_{eff}]$  dependence on  $R$  also indicates that  $\delta/D$  remains more or less constant, i.e. that the  $\delta/D$  ratio is not considerably disturbed by changes in the pulling rate. From the same data  $\delta/D$  is estimated to be 0.28 (h/cm). If we assume the diffusion constant to be of the order of magnitude  $10^{-5} \text{ (cm}^2/\text{sec)}$ , one can estimate the effective diffusion layer thickness to be 0.1mm.

In order to compare the distribution coefficient of carbon with predictions based on chemical trends we plotted in Figure 3 measured values of  $k$  for group IV elements in GaAs against their covalent radii. Correlation of this type was observed for Ge [Willardson and Allred (1967)]. In spite of a considerable scatter in reported experimental values of  $k$  in GaAs it is evident from Figure 3 that same type of correlation holds for GaAs as well. Extrapolation of this trend from Pb, Sn, Ge and Si to C indicates that one should indeed expect a high  $k$  value for C in GaAs, in accordance with our experimental finding of  $k_0=3.5$ .

#### 2. Discussion

The value of 3.5 for  $k_0$  which we have obtained in this work is considerably higher than up to now published data for  $k_{eff}$ . In earlier reported results based on indirect methods of carbon determination [Willardson and Allred (1967), Thomas et al. (1984)], the effective distribution coefficient,  $k_{eff}$ , for carbon in GaAs was estimated to be 0.8 and 0.9, respectively, indicating an almost uniform concentration of carbon along the ingot with only a slight increase from seed to tang end. Conversely, Chen et al. (1984) found the carbon concentration in the seed end to be approximately three times larger than in the tang end, which indicates that carbon tends to segregate from liquid into solid phase of GaAs. In their work, the carbon concentration was determined by far infrared localized vibrational mode (LVM) absorption, and was in the range of  $0.8-2.5 \times 10^{16} \text{ C atoms/cm}^3$ . (IR-LVM absorption can detect only  $C_{As}$ , but up to now there is no evidence that carbon occupies any other place in the GaAs lattice, and in particular not for the case of low carbon concentrations.) Applying the LVM method to two carbon doped (up to  $4 \times 10^{16} \text{ C/cm}^3$ ) LEC GaAs ingots, pulled at a rate of 2 cm/h, Kobayashi and Osaka (1985) determined  $k_{eff}$  to be 1.44. Kirkpatrick et al. (1985) also found that the distribution coefficient for carbon in GaAs is larger than 1, but that it is a strong function of the carbon concentrations ranging from 1.3 to 2.3 for a concentration range of  $5 \times 10^{15}$  to  $3 \times 10^{16} \text{ /cm}^3$ . Within the narrow range of initial melt carbon concentration in our samples ( $1-4 \times 10^{15} \text{ /cm}^3$ ) we did not observe such a trend (Figure 1). However, even if there is some concentration dependence of  $k_{eff}$  in our case, it is obviously insignificant in comparison with the much stronger influence of pulling rate on carbon distribution along the ingot.

In this work, we have shown that  $k_{eff}$  is strongly dependent on the pulling rate. The value of  $k_{eff} = 1.44 \pm 0.08$  obtained by Kobayashi and Osaka (1985) at a pulling rate of 2 cm/h, is in good agreement with the

results at a similar pulling rate in this work, as shown in Figure 2. The carbon distribution in ingots grown by Chen et al. (1984) also showed that  $k$  must be larger than 1, but we were not able to compare quantitatively their results with ours since their pulling rate was not specified. The earlier published values of 0.8 and 0.9 were estimated from Hall analysis. The presence of other donors and acceptors can easily mislead the interpretation of the Hall experimental data. In addition, the GaAs crystals analysed by Thomas et al. (1984) were p-type, Ga-rich GaAs material, and one can not exclude the possibility that C behaves differently in non-stoichiometric material.

Large equilibrium distribution coefficient of C in GaAs can have serious practical consequences: for compensation mechanism and especially for n- to p-type conversions. Wafers cut from the tang end of the ingot will have a considerably lower carbon concentration than wafers cut from the seed end, especially in ingots grown at low pulling rates. If carbon is really the main shallow acceptor and thus responsible for compensation of residual shallow donors, then its presence is crucial to obtain semi-insulating GaAs. A considerable decrease in its concentration at tang end should then lead to n-type conductivity in that part of ingots. This effect should be further enhanced by the fact that all important shallow donor impurities (Si, Se, Te) have distribution coefficients lower than 1, i.e. they tend to accumulate toward the tang end of the ingot. Experimentally, however, just the opposite behavior is observed; LEC grown GaAs Si ingots often tend to become p-type at the tang end. Present results obviously rule out the possibility that the accumulation of carbon at tang end can significantly contribute to n- to p-type conversion. Therefore, it seems that some other acceptors (perhaps native defects) play an important role in the compensation mechanism observed in SI GaAs, and that those defects may be responsible for SI behavior in at least the tang end of LEC GaAs crystals.

#### Acknowledgements

The authors would like to thank J. Lagowski for his continual encouragement and many useful comments. They wish to thank M. Cretella and M. Skowronski for helpful discussions and D. Smith for his kind collaboration in FTIR measurements.

#### References

- Brozel M R 1986 EMIS Datareviews Series No. 2, (London & New York: INSPEC) pp 13.1.
- Chen R T, Holmes D E, and Asbeck P M, 1984 Appl. Phys. Lett. **45** 459
- Holmes D E, Chen R T, Eliot K R and Kirkpatrick C G 1980 Appl. Phys. Lett. **40**, 46.
- Homma Y and Ishii Y 1984, J. Appl. Phys. **57**, 2931.
- Kirkpatrick C G, Chen R T, Holmes D E, and Eliot K R 1985, Gallium Arsenide, Materials, Devices and Circuits (New York: Wiley) pp 39-94.
- Kobayashi T and Osaka J 1984, J. Crystal Growth, **71**, 240.
- Thomas R N, Hobgood H M, Eldridge G W, Baret D L, Baggins T T, Ta L B and Wan S K 1984, Semiconductors and Semimetals (Orlando: Academic Press Inc.) pp 1-87.
- Willardson R K and Allred W P 1967, GaAs and Related Compounds (London: Inst. Phys.) pp. 35-40.

## **The effects of residual acceptors on the electrical properties of low pressure LEC GaAs: a comparison of theory and experiment**

W.M. Duncan and G.H. Westphal

Texas Instruments Incorporated, Central Research Laboratories,  
Dallas, Texas 75265

### **ABSTRACT**

In this study we have determined the concentration of residual impurities and defects, and electrical properties of undoped and In doped GaAs ingots grown using the low pressure liquid encapsulated (LP-LEC) Czochralski technique. A novel approach of using a combination of photoluminescence and infrared absorption measurements to quantitatively measure total acceptor concentration is presented. Variation in the residual acceptor concentration is found to be the dominant variable in determining the electrical properties of LP-LEC GaAs. Deep donor concentrations are shown to be relatively invariant within ingots and from ingot-to-ingot. A multilevel model was also developed to calculate the electrical properties of these ingots from the measured concentrations of electrically active centers. Using the multilevel model, the calculated resistivities are in good agreement with those measured experimentally. Calculations also show that the resistivity is a very sensitive function of deep donor activation energy.

### **INTRODUCTION**

Undoped semi-insulating GaAs grown by the liquid encapsulated Czochralski (LEC) technique is receiving much attention as a substrate material for fabricating monolithic microwave and digital integrated circuits. Although high-pressure in situ synthesis and LEC growth of GaAs is currently in common use, low pressure in situ synthesis and LEC growth (Pekarek 1970, Hughes and Li 1982, Duncan 1983) is an efficient alternative to the high-pressure method. The quality of low-pressure LEC (LP-LEC) GaAs, however, has not been well established. Furthermore, no detail studies have been reported to date as to the residual impurity and defect characteristics of low pressure material.

Since the early work by Haisty, et al. (1962) on high resistivity behavior in GaAs, there have been numerous papers which have undertaken to explain the electrical properties of GaAs based on measured impurity concentrations or on intentional doping. The first indications that the phase extent of GaAs is electrically active were presented by Lombos, et al. (1982) resulting from a comparison of impurity and transport measurements to Fermi level calculations. At about the same time, the importance of stoichiometry on the electrical properties of GaAs was demonstrated from high pressure LEC growth experiments (Holmes et al 1982, Ta et al 1982). In the current work we have grown undoped and In doped LP-LEC GaAs crystals from melts compounded in situ at low pressure. Impurity and defect assessments of the LP-LEC material were carried out using a combination of spectroscopic techniques. In addition, the Fermi energy and, hence, the electrical properties of these ingots were calculated from the spectroscopically measured concentrations of electrically active centers using the charge neutrality equation and statistical expressions for ionized impurity and carrier concentrations.

Calculated electrical properties were compared to those determined from Hall measurements.

#### EXPERIMENTAL

The low-pressure material used in this study was synthesized and grown in a modified silicon crystal puller at pressures less than 30 psig (207 kPa). The crystals were pulled in the  $\langle 100 \rangle$  direction from unintentionally doped or isovalent In doped melts. The melts were synthesized in situ at low pressure just prior to growth. A resistively heated arsenic injection cell was used to introduce arsenic gas into the liquid Ga melt held at the melting point of GaAs. Pyrolytic BN crucible liners and dry boric oxide ( $\sim 120$  ppmw water, Rasa grade "D") encapsulant were used in all cases. Melts were arsenic rich (As/Ga of 1.005) with volumes of 3500 to 7000 grams starting with 7 nines Ga (Alusuisse) and 6 nines double refined As (Cominco). Due to the controlled compounding reaction obtained using arsenic injection, melts with repeatable stoichiometry were prepared. These crystals were grown with nominal body diameters of 3.3 inches. Crystal rotations of 8 rpm CCW and crucible rotations of 4 rpm CW were typically used. All crystals were post annealed at 850°C for 24 hours prior to wafering. Dislocation densities as delineated using KOH etching varied from 6,000 to 80,000 per  $\text{cm}^2$  in these crystals.

The chemical properties of the low pressure GaAs were determined using secondary ion mass spectroscopy (SIMS), localized vibrational mode (LVM) absorption, near infrared (NIR) electronic optical absorption and photoluminescence (PL). The SIMS measurements were performed using a Cameca IMS-3F ion microanalyser. The localized vibrational mode analysis of carbon employed an IBM Instruments IR-98 Fourier Transform Infrared (FTIR) spectrometer. Carbon measurements were made at 77 K on 80 to 120 mil thick slabs. The carbon absorption coefficient,  $\alpha$ , at  $583\text{ cm}^{-1}$  was calculated using the expression,  $\ln(T/T_0) = \alpha x$ , where  $T$  and  $T_0$  are the peak and baseline transmittances at  $583\text{ cm}^{-1}$ , respectively, and  $x$  is the specimen thickness. The optical absorption cross-section of Hunter, et al. (1984) was used to convert from carbon absorption strength to concentration. The material was also analysed using photoluminescence (PL) measurements. An unfocused  $\text{Ar}^+$  ion ion-pump laser at  $5145\text{ Å}$  with incident power density of approximately  $1\text{ W/cm}^2$  was used for exciting the luminescence. The emitted light was collected and then analyzed using either a Michelson interferometer or a 0.8 M dispersive double monochromator. Near infrared absorption measurements were made using a Cary 14R spectrophotometer at room temperature on 80 to 120 mil thick slabs. The absorption coefficient,  $\alpha$ , at  $1.097\text{ eV}$  was calculated using the expression,  $\ln(T/T_0) = \alpha x$  where  $T$  and  $T_0$  are the transmittances at  $1.097\text{ eV}$  and  $0.60\text{ eV}$ , respectively, and  $x$  is the sample thickness. The conversion coefficient of Martin (1981) was used to convert the  $1.1\text{ eV}$  absorption coefficient to deep donor concentration. Resistivity and mobility values of as-grown material were determined using low current van der Pauw-Hall effect measurements (Hemenger 1973). Sample contacts were formed by alloying with In.

#### RESULTS AND DISCUSSION

Impurity, defect and electrical measurements were made on seed and tail samples from six undoped and two indium doped ingots (0.1% by weight in the melt). The concentration of residual shallow donors Si, S, Se and Te were determined from SIMS. The concentrations of the shallow donors Si, S and Te were always found at the background of SIMS on any given day. Average concentrations were  $3 \times 10^{14}$ ,  $5 \times 10^{14}$  and  $2 \times 10^{13}\text{ cm}^{-3}$  for Si, S and Te, respectively. Residual Se levels were found between  $9 \times 10^{12}$  and  $2 \times 10^{14}\text{ cm}^{-3}$ , an order of magnitude higher than the SIMS



background. Therefore, from the SIMS, an upper limit of  $5 \times 10^{14}$  to  $1 \times 10^{15} \text{ cm}^{-3}$  is expected for the total residual shallow donors concentration in this material.

The shallow acceptors C, Mg(Be), Zn, Si, were analysed using a combination of LVM absorption and photoluminescence. Carbon was first measured quantitatively from its LVM absorption. Photoluminescence measurements were then used to determine the relative intensities of the free-electron-to-neutral acceptor,  $F-A^0$ , transition for C, Mg(Be), Zn and Si. Magnesium and beryllium are indistinguishable in PL due to their nearly equal ionization energies (Ashen et al 1975). Based on quantum mechanical calculations for shallow acceptors in direct gap semi-conductors (Dumke 1963),  $F-A^0$  transition probabilities are proportional to the impurity concentration. A small correction in calculating shallow acceptor concentrations from PL intensity ratios is required due to the differences in transition probability resulting from the different activation energies for each impurity. In order to avoid contributions from neutral donor-to-neutral acceptor ( $D^0-A^0$ ) transitions to the manifold of acceptor bands, impurity ratios must be extracted from spectra taken at sufficiently high temperatures (typically 25°K) such that the donors are predominately ionized. Shown in Figure 1 is the PL spectrum of a low carbon sample which also contains Mg(Be), Zn and Si residual acceptors. A four Gaussian fit (dashed line) has been used to approximate the individual acceptor contributions to the acceptor manifold. Contributions due to impurities other than C have been found significant only for low carbon material ( $[C] < 1 \times 10^{15} \text{ cm}^{-3}$ ). The presence of Ge, Sn, Cu and Mn acceptors can also be detected by PL, but these impurities have not been observed in any LP-LEC GaAs studied to date. Total shallow acceptor concentrations in these ingots measured using LVM absorption and PL are found to vary from  $1 \times 10^{15}$  to  $1.5 \times 10^{16} \text{ cm}^{-3}$ .

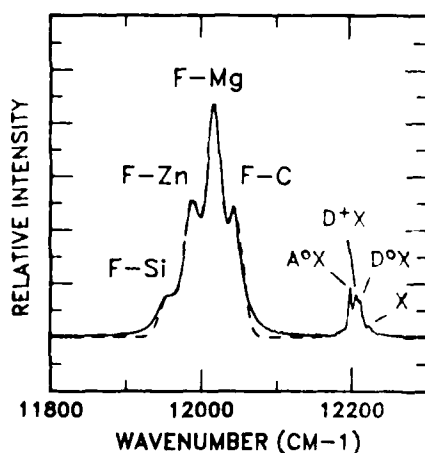


FIGURE 1. PL Spectrum (—) and Gaussian fit (---) of a low carbon specimen at 4.2 K. Free-electron-to-neutral acceptor,  $F-A^0$ , band positions are indicated for C, Mg(Be), Zn and Si. Free exciton and bound exciton recombinations are also shown.

Deep acceptor concentrations have also been determined for these ingots using SIMS measurements. The deep acceptors were found at the background of SIMS on any given day. The average SIMS backgrounds are  $2 \times 10^{14} \text{ cm}^{-3}$  for both Cr and Mn and  $1.5 \times 10^{15} \text{ cm}^{-3}$  for Fe. From consideration of segregation coefficients, these metal impurities would be expected to accumulate in the last to freeze region of the crystal. However, transition metals in samples taken from the tails of these crystals are also observed at or below the background of SIMS. Therefore, transition metal impurities are expected to be present at levels well below the SIMS background in these crystals.

Deep donor concentrations have been determined using the near infrared absorption method of Martin (1981). Although the nature of the deep center (i.e., EL2 vs. ELO) is not defined from the near IR measurement, Skowronski, et al. (1986) have shown that the deep donor optical cross-sections are nearly equal for EL2 and ELO. The mean neutral deep donor concentration (EL2 plus ELO) in these ingots was found to be  $1.5 \times 10^{16} \text{ cm}^{-3}$  and varied  $\pm 22\%$  ( $\pm 1$  sigma relative to mean). The uncertainty due to measurement signal-to-noise is  $\pm 2 \times 10^{15} \text{ cm}^{-3}$  or  $\pm 13\%$  of the mean and no systematic variations were observed from seed-to-tail in these crystals.

From consideration of the relative concentrations of shallow donors and shallow acceptors in this material, the electrical conductivity of these crystals have been calculated based on the presence of three level types, deep donor, shallow acceptors and shallow donor. We have not included the deep acceptors in this treatment as the shallow acceptor concentration exceeds the shallow donor concentration. Since at room temperature, deep centers ionize only as a result of trapping excess carriers of the opposite charge type, deep acceptors would not contribute to conductivity in the presence of excess shallow acceptors. Furthermore, the deep acceptor concentrations in this material have been shown indirectly to be present at very low levels.

The position of the Fermi energy,  $E_F$ , as a function of impurity concentration can be determined from the charge neutrality condition.

$$n + \sum_i N_{ai}^- = p + \sum_j N_{dj}^+ \quad (1)$$

where  $n$  and  $p$  are the free electron and hole concentrations, respectively, and  $N_{ai}^-$  and  $N_{dj}^+$  are the ionized acceptor and ionized donor concentrations, respectively. Assuming nondegenerate carrier concentrations, Fermi-Dirac statistics can be used to determine the quantities in the charge neutrality equation. The free electron and free hole concentrations are given under these conditions by:

$$n = N_c \exp[-(E_g - E_F)/kT] \quad (2)$$

and

$$p = N_v \exp[-(E_F)/kT] \quad (3)$$

where  $N_c$  and  $N_v$  are the conduction band and combined light and heavy hole valence band density of states, respectively,  $E_g$  is the 295 K bandgap of GaAs,  $E_F$  is the Fermi energy,  $k$  is Boltzman's constant and  $T$  is temperature. The  $N_c$  and  $N_v$  values given by Blakemore (1982) are used in the calculation. The ionized acceptor concentration is given by:

$$N_{ai}^- = N_{ai} \{1 + (1/g) \exp[(E_{ai} - E_F)/kT]\}^{-1} \quad (4)$$

and the ionized donor concentration given by

$$N_{dj}^+ = N_{dj} \{1 + g \exp[(E_F - E_{dj})/kT]\}^{-1} \quad (5)$$

where  $N_{ai}$  and  $N_{dj}$  are the specific doping concentrations and  $E_{ai}$  and  $E_{dj}$  are the respective activation energies. The degeneracy factor,  $g$ , is taken to be 4 for shallow acceptors and 2 for both the deep and shallow donors.

In the case of deep donors, concentrations were calculated from the absorption coefficient,  $\alpha$ , at  $1.1 \mu\text{m}$ . Since the  $1.1 \mu\text{m}$  absorption is due to the electronic transition between neutral deep donor states and the conduction band, the absorption coefficient depends both on total deep donor concentration and the Fermi energy (Walukjewicz 1983). Therefore, the deep donor contribution is entered into the calculation as an absorption coefficient rather than a concentration. The absorption coefficient at  $1.1 \mu\text{m}$  is given by:

$$\alpha = N_{dd}^T(1-f)\sigma \quad (6)$$

where  $N_{dd}^T$  is the total deep donor concentration,  $\sigma$  is the absorption cross-section and  $f$  is the deep donor Fermi function:

$$f = \{1 + (g \exp[(E_F - E_{dd})/kT])\}^{-1} \quad (7)$$

Hence, the ionized deep donor concentration is given by:

$$N_{dd}^+ = (\alpha/\sigma)f/(1-f) \quad \text{where } f \neq 1 \quad (8)$$

With these equations, the known physical constants, the measured shallow impurity concentrations, and the deep donor absorption coefficient, a unique value for the Fermi energy can be found.

Once the Fermi energy has been determined, the resistivity can be calculated using equations 2 and 3 and the resistivity equation:

$$\rho = [q(e\mu_e + p\mu_h)]^{-1} \quad (9)$$

where  $\mu_e$  and  $\mu_h$  are the conductivity (drift) mobilities for electrons and holes, respectively. Although drift mobilities in general are expected to vary with ionized impurity concentration, all of the material studied has low free carrier concentrations (less than  $10^8 \text{ cm}^{-3}$ ) and low total ionized impurity concentrations (less than  $2 \times 10^{16} \text{ cm}^{-3}$ ). Hence, the weak doping mobilities cited by Blakemore (1982) are used in the calculations.

Shown in Figure 2 is the resistivity versus shallow acceptor concentration behavior for three deep donor activation energies calculated based on the three level model. The curves in Figure 2 were calculated for a near IR absorption coefficient of  $1.20 \text{ cm}^{-1}$  ( $N_{dd}$  of  $1.52 \times 10^{16} \text{ cm}^{-3}$  for an  $f$  of zero in equation 6 above) and for a shallow donor concentration of  $5 \times 10^{14} \text{ cm}^{-3}$ . Also shown in the figure is the experimental resistivity versus total acceptor concentration data. As can be seen from the figure, the resistivity in this regime is very sensitive to the deep donor activation energy. The experimental data agree with a deep donor activation energy of about 0.65 eV. Not unexpectedly, calculated resistivities are independent of both shallow donor activation energy over the range of 5 to 7 meV and shallow acceptor activation energy over the range of 25 to 40 meV.

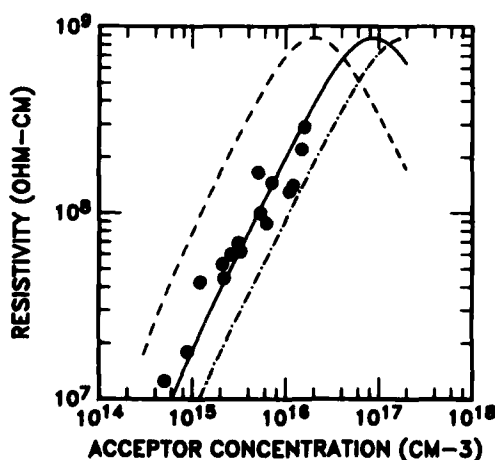


FIGURE 2. Resistivity versus total acceptor concentration determined experimentally (●) and calculated from three level model. Calculated curves are for deep donor activation energies of 0.69 meV (---), 0.65 meV (—) and 0.63 meV (-.-).

Using a deep donor activation energy of 0.65 eV and a shallow donor concentration of  $5 \times 10^{14} \text{ cm}^{-3}$ , the Fermi energy has been calculated for each sample from the total shallow acceptor concentration and the near IR absorption. The calculated Fermi energies vary from 0.754 to 0.823 eV. From these Fermi energies and equations 7 and 8 above, the deep donor centers are calculated to be less than 1% ionized in these crystals.

#### CONCLUSIONS

From impurity and defect evaluations of high purity LP-LEC GaAs ingots, variations in the total shallow acceptor concentration are found to be the dominant variable in determining the resistivity of as grown material. The carbon shallow acceptor is found in all ingots with Zn, Mg(Be) and Si also contributing to the resistivity in low carbon material. Variations in total deep donor concentrations in this material are small. Good agreement is demonstrated between electrical properties calculated from measured impurity concentrations and those determined from Hall measurements.

#### ACKNOWLEDGEMENT

This work was supported in part by the Air Force Wright Aeronautical Laboratories under contract No. F33615-83-C-5134.

#### REFERENCES

- Ashen D. J., Dean P. J., Hurde D. T. J., Mullen J. B., White A. M., and Greene P. D. 1975 J. Phys. Chem. Solids 36 1041  
 Blakemore J. S. 1982 J. Appl. Phys. 53 R123  
 Dumke W. P. 1963 Phys. Rev. 132 1998  
 Duncan W. M., Westphal G. H., and Sherer J. B. 1983 IEEE Elect. Dev. Lett. EDL-4 199  
 Haisty R. W., Mehal E. W. and Stratton R. 1962 J. Phys. Chem. Solids 23 829  
 Hemenger P. M. 1973 Rev. Sci. Instrum. 44 698  
 Holmes D. E., Chen R. T., Elliott K. R., and Kirkpatrick C. G. 1982 Appl. Phys. Lett. 40 46  
 Hughes B. and Li C. 1983 GaAs and Related Compounds 1982 (Inst. Phys. Conf. Ser. 65) pp 57-64  
 Hunter A. T., Kimura H., Baukus J. P., Winston H. V. and Marsh O. J. 1984 Appl. Phys. Lett. 44 74  
 Lombos B. A., Yermenidjian N. and Averous M. 1982 Can. J. Phys. 60 35  
 Martin G. M. 1981 Appl. Phys. Lett. 39 747  
 Pekarek L. 1970 Czech. J. Phys. B20 857  
 Skowronski M., Lagowski J. and Gatos H. C. 1986 J. Appl. Phys. 59 2451  
 Ta L. B., Hobgood H. M., Rohatgi A., and Thomas R. N. 1982 J. Appl. Phys. 53 5771  
 Walukiewicz W., Lagowski J., and Gatos H. C. 1983 Appl. Phys. Lett. 43 192

## **Role of boron in LEC semi-insulating GaAs**

Toshio Kikuta\* and Koichi Ishida

Optoelectronics Joint Research Laboratory,  
1333 Kamikodanaka, Nakahara-ku, Kawasaki 211 Japan

\*Present address: The Furukawa Electric Co., Ltd.,  
2-5-1 Okano, Nishi-ku, Yokohama 220 Japan

**Abstract** The main acceptor in undoped LEC SI-GaAs has been considered to be carbon. However, the crystal with a low carbon concentration ( $< 1 \times 10^{15} \text{ cm}^{-3}$ ) even revealed a high resistivity ( $> 1 \times 10^8 \Omega \text{ cm}$ ). This suggests that acceptors other than carbon should be considered to explain the semi-insulating mechanism. The highly Si- or Al-doped crystals with the high B concentration ( $> 1 \times 10^{18} \text{ cm}^{-3}$ ) were p-type. Infrared absorption, SIMS and Hall effect measurements were carried out to estimate the  $B_{\text{As}}$  concentration. We have found that the 3 - 4% to the total boron concentration occupies the arsenic site and acts as acceptors. In SI-crystals with the high B concentration ( $> 1 \times 10^{17} \text{ cm}^{-3}$ ), the presence of  $B_{\text{As}}$  possibly contributes to the SI-mechanism.

### **1. Introduction**

Undoped semi-insulating (SI) GaAs is promising to fabricate high-speed integrated circuits and microwave devices. The SI-mechanism has been explained by the compensation of the deep donor EL2 with the excess acceptors over shallow donors (Martin et al. 1980, Holmes et al. 1982a). The main acceptor has been suggested as carbon (Holmes et al. 1982a, Ta et al. 1982). However, the crystal with a very low carbon concentration ( $< 1 \times 10^{15} \text{ cm}^{-3}$ ) also revealed a high resistivity ( $> 1 \times 10^8 \Omega \cdot \text{cm}$ ). Furthermore, it has been reported that the conversion factor from the absorption coefficient to the carbon concentration conventionally obtained by FTIR is a few times larger than the result obtained by secondary ion mass spectroscopy (SIMS) (Homma et al. 1985). These suggest that acceptors other than carbon should be considered to explain the SI-mechanism. Boron on the arsenic site ( $B_{\text{As}}$ ) is the most possible candidate for the acceptor, but there have been no detailed studies. In this paper, we describe the role of the  $B_{\text{As}}$  acceptors in LEC SI-GaAs based on the results obtained infrared absorption (IR), SIMS and Hall effect measurements.

Table I Characteristics of Si- or Al-doped crystals with a high B concentration.

|            | $\rho$ | [Si]  | [EL2] | [B <sub>As</sub> ] | [B]  | [B <sub>As</sub> ]/[B] |
|------------|--------|-------|-------|--------------------|------|------------------------|
| Si - doped | 2E16   | 1E17  | —     | 1.2E17             | 3E18 | 0.04                   |
| Al - doped | 2E16   | <1E15 | ~1E16 | 3E16               | 1E18 | 0.03                   |
| Al - doped | 1.2E16 | <1E15 | ~1E16 | 1.3E16             | 3E18 | 0.04                   |

## 2. Experimental

The crystals used in this study were grown in an Ar ambient from PBN crucibles using a high pressure puller by the LEC technique with in situ synthesis. The infrared absorption spectra were acquired with the FTIR spectrometer with CsI beamsplitters. The measurements were carried out at 10 K by using a temperature-variable Dewar with KRS-5 windows. The carbon concentrations were determined by using the LVM IR method at room temperature. The conversion factor reported by Brozel et al. was used to obtain the absolute carbon concentration (Brozel et al. 1978). The concentrations of boron, silicon and other impurities were measured by SIMS. The absorption coefficient at 1.1  $\mu\text{m}$  was determined by the method reported by Martin et al. (1979). The carrier concentration was determined by Hall measurements at room temperature.

## 3. Results and Discussion

Highly Si- or Al-doped crystals were grown under the growth conditions similar to those of Si-crystals except for doping. The initial arsenic atom fraction ( $x=\text{As}/\text{As}+\text{Ga}$ ) of the melts was 0.503. It was expected that the Si-doped crystal is n-type conductive, while the Al-doped crystal is semi-insulating, since Al is electrically inactive in GaAs. However, contrary to the expectation, all the crystals were conductive with p-type conductivity. The characteristics of the crystals are summarized in Table I. Note that all the crystals contain the high boron concentration ( $>1 \times 10^{18} \text{ cm}^{-3}$ ). The boron was unintentionally incorporated into the crystals by deoxygenation of  $\text{B}_2\text{O}_3$  encapsulant by Si or Al, since  $\text{SiO}_2$  and  $\text{Al}_2\text{O}_3$  are more stable than  $\text{B}_2\text{O}_3$  near the melting point of GaAs. In these crystals, the carbon concentrations were less than  $2 \times 10^{15} \text{ cm}^{-3}$ , other residual acceptor concentrations were less than  $1 \times 10^{15} \text{ cm}^{-3}$ . However, the free hole concentrations  $\rho$  were more than  $2 \times 10^{16} \text{ cm}^{-3}$ . These results show that acceptors other than impurities such as C, Mg, Mn and Zn must be present in these crystals.

The presence of the native acceptor defect  $\text{Ga}_{\text{As}}$  was studied by infrared absorption. Figure 1 shows the infrared absorption spectra of three crystals (A)~(C). (A) was the undoped Ga-rich crystal. (B) and (C) were Si- and Al-doped crystals shown in Table I, respectively. The infrared absorption around  $574 \text{ cm}^{-1}$  has been reported to be related to  $\text{Ga}_{\text{As}}$  antisite defects (Elliott 1983). The peak is clearly observed for

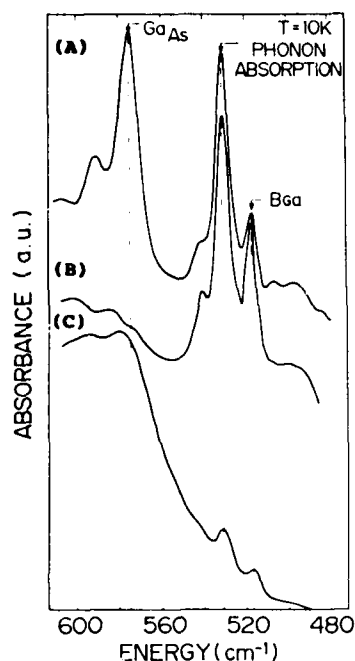


Fig. 1 Infrared spectra of three crystals (A)~(C).

keep charge neutrality:  $N_A^- = p + N_D^+ + N_{DD}^+$ , where  $p$  is the free hole concentration,  $N_A^-$ ,  $N_D^+$  and  $N_{DD}^+$  are the concentrations of shallow acceptors, shallow donors Si and deep donors EL2, respectively. The EL2 concentration was neglected in the highly Si-doped crystal (Lagowski et al. 1982). The contribution of carbon is also neglected, since the carbon concentrations of these crystals are lower than  $p$  ( $> 2 \times 10^{16} \text{ cm}^{-3}$ ) by one order of magnitude. Thus, we can estimate the  $B_{As}$  concentration  $[B_{As}]$  by assuming  $[B_{As}] = N_A^-$ . The total B concentration  $[B]$  was measured by SIMS. The calculated results shown in Table I indicates that the 3 - 4 % to the total boron concentration occupies the As-site.

When undoped LEC SI-crystal is grown using dry  $B_2O_3$  ( $< 100 \text{ ppm wt H}_2\text{O}$ ), the high B concentration ( $> 1 \times 10^{17} \text{ cm}^{-3}$ ) is incorporated into the crystal. Then, from the above estimation,  $B_{As}$  acceptors in the order of  $10^{15} \text{ cm}^{-3}$  may be present in the crystal. This amount would be large enough to contribute to the SI-mechanism.

To clarify the contribution of  $B_{As}$  to the SI-mechanism, we compared the characteristics of SI-crystals containing definitely different order of boron concentration but with similar carbon concentration. Emori et al.

(A), but not for (B) and (C). The  $B_{As}$  concentrations of (B) and (C) are estimated to be less than  $1 \times 10^{15} \text{ cm}^{-3}$  from the peak height (Elliott et al. 1982). This is consistent with the initial melt composition. This result suggests that no specific stoichiometry change was occurred by the high doping material of Si or Al.

Boron is understood to occupy the Ga- or As-site in GaAs, but not the interstitial, since no change in the depth profile of the implanted boron has been observed during annealing temperature up to  $900^\circ \text{C}$  (Toulouse et al. 1979). The  $B_{Ga}$  is electrically inactive, while the  $B_{As}$  acts as acceptors. Thus, the observed p-type conversion of Si- or Al-doped crystals can only be explained by occupation of the highly doped boron on the arsenic site.

We next estimate the ratio of the  $B_{As}$  concentration to the total B concentration for the crystals shown in Table I. In p-type crystals, the following equation can be realized to

Table II Characteristics of samples (A) and (B) in Fig. 2.

|   | As MOLE FRACTION | B <sub>2</sub> O <sub>3</sub> (ppm) | BORON (cm <sup>-3</sup> ) | CARBON (cm <sup>-3</sup> ) | $\rho$ ( $\Omega \cdot \text{cm}$ ) | $\alpha_{1.1}$ (cm <sup>-1</sup> ) |
|---|------------------|-------------------------------------|---------------------------|----------------------------|-------------------------------------|------------------------------------|
| A | 0.46             | ~2000                               | $1 \times 10^{15}$        | $1.2 \times 10^{15}$       | $7 \times 10^7$                     | 1.0                                |
| B | 0.50             | <100                                | $2 \times 10^{17}$        | $1.5 \times 10^{15}$       | $8 \times 10^7$                     | 1.5                                |

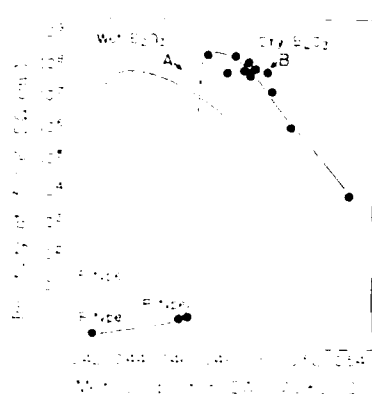
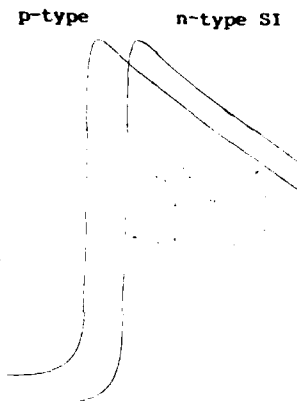
Fig. 2 Melt composition dependence of resistivity in the crystals grown from the wet and dry B<sub>2</sub>O<sub>3</sub> (Emori et al. 1985).

Fig. 3 Calculated resistivity as a function of the EL2 concentration.

(1985) have found that the initial melt composition dependence of the resistivity is definitely different for the crystals grown using wet (2000 ppm) and dry (100 ppm) B<sub>2</sub>O<sub>3</sub>. Hereafter, we call the former W-crystals and the latter D-crystals. Their results are shown in Fig. 2 for the comparison with the calculated results given below. Note that the critical melt composition changing the conductivity from n-type SI to p-type is distinctly smaller for the W-crystals than the D-crystals.

The characteristics of two typical W- and D-crystals, (A) and (B) arrowed in Fig. 2 are summarized in Table II. Note that the boron concentration of (A) ( $1 \times 10^{15} \text{ cm}^{-3}$ ) is by two order of magnitude lower than that of (B) ( $2 \times 10^{17} \text{ cm}^{-3}$ ), while the carbon concentrations are similar to each other. The absorption coefficient at  $1.1 \mu\text{m}$  ( $\alpha_{1.1}$ ), which is corresponding to the EL2 concentration ( $N_{\text{EL2}}$ ), is smaller in (A) than in (B). Since these samples reveal the similar resistivity, the Fermi level



is also located at the similar position. Thus, the smaller  $\alpha_{1.1}$  of (A) shows the lower concentration of EL2, since the effect of the correction factor attributed to the electron occupancy function of EL2 is neglected (Walukiewicz et al. 1983). The difference of  $\alpha_{1.1}$  between (A) and (B) is due to the melt composition change, since  $N_{EL2}$  decreases with decreasing As mole fraction (Holmes et al. 1982b).

Figure 3 shows the calculated resistivity as a function of the  $N_{EL2}$  under the conditions of  $N_A - N_D = 2 \times 10^{15} \text{ cm}^{-3}$  and  $5 \times 10^{14} \text{ cm}^{-3}$  (Johnson et al. 1983, Kikuta et al. 1984). This indicates that the critical EL2 concentration changing the conductivity from p- to n-type increased with increasing  $N_A - N_D$ . Figures 2 and 3 suggest that  $N_A - N_D$  is large in D-crystals than in W-crystals. The  $N_D$  of D-crystals has been found to be similar to that of W-crystals, indicating that large  $N_A - N_D$  means large  $N_A$ . Since the carbon concentrations of D-crystals are similar to those of W-crystals, the presence of acceptors other than carbon should be required in D-crystals. As shown above, if the 3 - 4 % of total boron atoms occupies the arsenic site, the  $B_{As}$  concentration is high enough to explain the large  $N_A$  of D-crystals. Therefore, we conclude that the large  $N_A - N_D$  of D-crystals is due to the large  $B_{As}$  concentration, indicating the contribution of the boron acceptors  $B_{As}$  to the SI-mechanism in the LEC GaAs crystals with the high boron concentration ( $> 1 \times 10^{17} \text{ cm}^{-3}$ ).

It has been speculated that the melt composition becomes more As-rich with increasing in the water content in the  $B_2O_3$  encapsulant to explain the smaller critical melt composition for the W-crystals (Emori et al. 1985). About 30 g decrease in Ga is needed to explain the shift in Fig. 2, when 500 g Ga is initially charged in the crucible. However, such a large amount of Ga loss during the growth was not observed in our experiments. Therefore, the melt composition change seems not to be the main reason for the critical melt composition shift in Fig. 2.

Boron on arsenic site has been observed using LVM spectroscopy (Gredhill et al. 1984). The appearance of  $B_{As}$  by LVM depends on the charge state of  $B_{As}$ , i.e., the negative charge state is only detectable. Thus, in p-type material, no LVM absorption is detectable since the charge state of  $B_{As}$  is neutral. Accordingly, the LVM peak of  $B_{As}$  was not observed in the Si- or Al-doped crystals in spite of the high B concentration. The more direct evidence of the presence of  $B_{As}$  would be obtained from the LVM observation for the crystals shown in Table I changing the charge state by the neutron irradiation.

#### 4. Summary

The main acceptor in undoped LEC SI-GaAs has been considered to be carbon. However, the crystal with a low carbon concentration ( $< 1 \times 10^{15} \text{ cm}^{-3}$ ) even revealed a high resistivity ( $> 1 \times 10^8 \Omega \text{ cm}$ ). This suggests that acceptors other than carbon should be considered to explain the semi-insulating mechanism. We have investigated the role of boron in the crystals and have found that the 3 - 4 % to the total boron concentration occupies the As-site and acts as acceptors.

Acknowledgements

The authors wish to thank S. Ozawa and H. Okada for supplying the samples examined in this study. We also wish to thank J. Kobayashi for SIMS measurements and T. Iizuka for useful discussions. The present research effort is part of the large-scale project "Optical measurement and control system" conducted under a program set up by the Agency of Industrial Science and Technology, Ministry of International Trade and Industry.

References

- Brozel M R, Clegg J B and Newman R C 1978 J. Phys. D11 1331  
Ellicott K R, Holmes D E, Chen R T and Kirkpatrick C G 1982 Appl. Phys. Lett. 40 898  
Elliott K R 1983 Appl. Phys. Lett. 42 274  
Emori H, Kikuta T, Inada T, Obokata T and Fukuda T 1985 J. Appl. Phys. 24 L291  
Gledhill G A, Newman R C and Woodhead J 1984 J. Phys. C:Solid State Phys. 17 L301  
Holmes D E, Chen R T, Elliott K R and Kirkpatrick C G 1982a Appl. Phys. Lett. 40 46  
Holmes D E, Chen R T, Elliott K R, Kirkpatrick C G and Yu P W 1982b IEEE Trans. Electron. Devices ED-29 1045  
Homma Y, Ishii Y, Kobayashi T and Osaka J 1985 J. Appl. Phys. 57 2931  
Johnson E J, Kafalas L A and Davies R W 1983 J. Appl. Phys. 54 204  
Kikuta T, Katsumata T, Obokata T and Ishida K 1984 Proceeding of 11th International Symposium on GaAs and Related Compounds, Biarritz, pp 47  
Lagowski J, Gatos H C, Parsey J M, Wada K, Kaminska M and Walukiewicz W 1982 Appl. Phys. Lett. 40 342  
Martin G M, Verheijke M L, Jansen J A J and Poiblaud G 1979 J. Appl. Phys. 50 467  
Martin G M, Farges J P, Jacob G and Hallais J P 1980 J. Appl. Phys. 51 2840  
Ta L B, Hobgood H M, Rohatagi A and Thomas R N 1982 J. Appl. Phys. 53 5771  
Toulouse B, Favennec P N, Guivarch A and Pelous G 1979 Inst. Phys. Conf. Ser. 45 501  
Walukiewicz W, Lagowski J and Gatos H C 1983 Appl. Phys. Lett. 43 192

## **A TEM study of precipitates in As-grown semi-insulating indium-doped GaAs**

Byung-Teak Lee\*, Tim Sands\*\*, Ron Gronsky\*\*\*, and Edith Bourret\*

\* Center for Advanced Materials, B77G, Lawrence Berkeley Laboratory, Berkeley, CA 94720

\*\* Bell Communications Research Inc., Red Bank, NJ 07701 \*\*\* Materials and Molecular Research Division, LBL

**Abstract** Precipitation in as-grown semi-insulating In-doped GaAs crystal has been studied using transmission electron microscopy. Hexagonal As precipitates that exhibit a very simple orientation relationship with the GaAs matrix were found, although the crystal showed no evidence of In-containing particles. Precipitates of quite different phase(s), very likely a new As-rich Ga-As phase, have also been observed with very large interplanar spacings. The number density of these particles is estimated to be approximately  $1.5 \times 10^{10} \text{ cm}^{-3}$ .

### **1. Introduction**

Precipitates in as-grown GaAs are believed to affect the properties of GaAs both structurally and electronically. Often they are studied in relation to the behavior of grown-in dislocations (Stirland et al. 1984, for example) and in fact have been suspected to be a potential source of dislocations (Cornier et al. 1981A). They are also believed to be important to the homogeneity of crystals, related in general to the distribution of point defects. In fact, the precipitates are suspected to be responsible, at least partially, for the fact that the  $\text{EL}_2$  concentration in a GaAs crystal becomes much more homogeneous after annealing at certain temperatures (Holmes et al. 1981).

Observations of precipitates have been reported in several articles (Markov et al. 1984, for example). A few TEM studies to characterize the particles have been also published, generally identifying them as hexagonal arsenic phase (Cullis et al. 1980, Lodge et al. 1985). No detailed study, however, has been done on precipitation in In-doped crystals despite the important fact that In-doping reduces dislocation density drastically without apparent change in electronic properties (VonNeida and Jordan, 1986). In the present research program, a battery of TEM techniques has been applied in an effort to more completely characterize the precipitates and to extend the analysis to the doped crystals. Results on precipitates in the In-doped materials are presented and discussed here.

### **2. Experimental**

The crystal investigated in this work was grown by an LEC technique at a low axial thermal gradient of about  $6^\circ\text{C/cm}$ , fully encapsulated in  $\text{B}_2\text{O}_3$ . The indium concentration in the melt was  $2.8 \times 10^{19} \text{ cm}^{-3}$ . The crystal was mainly dislocation-free except an annular region of about 10mm at the periphery where the dislocation density was about  $5000 \text{ cm}^{-2}$ . It was also semi-insulating with resistivity of  $10^4 \Omega\text{cm}$ . Further details of the growth conditions and results of macroscopic characterization have been reported elsewhere (Elliot et al. 1984). Both chemical thinning (chlorine in methanol) and ion milling were used to prepare suitable TEM samples and no significant differences were found between samples made by these different techniques. Prepared samples were first observed and screened using a Philips EM301 TEM followed by more detailed analysis in a JEOL 200CX TEM equipped with ultrahigh resolution goniometer. A Philips EM400 TEM/STEM was used for most of the

chemical analysis although a JEOL 200CX AEM with an ultra-thin window detector was also employed for light element Energy Dispersive X-ray Spectrometry (EDXS) analysis ( $Z > 5$ ).

Due to their low density and relatively large size, the precipitates presented many experimental difficulties. In particular, two conflicting conditions had to be satisfied at the same time: the specimen had to be thin enough to give meaningful results and yet had to contain the precipitate within the probed volume. Fortunately, when the precipitates were coupled to dislocations, they were more readily found in the thicker regions of the sample, allowing "controlled thinning" with the ion mill while monitoring the thickness periodically in the TEM. Figure 1 is an example of this procedure, where the decreasing length of the dislocation clearly shows the decrease in thickness of the sample.

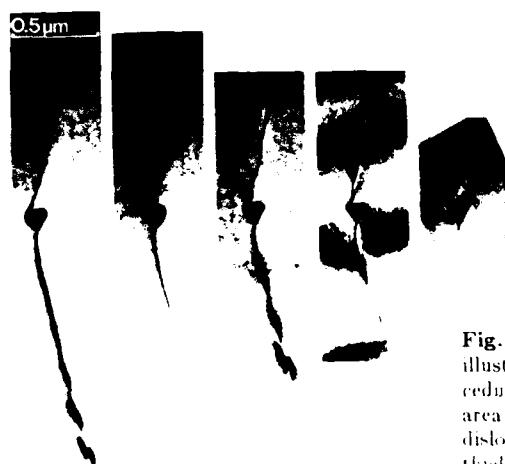


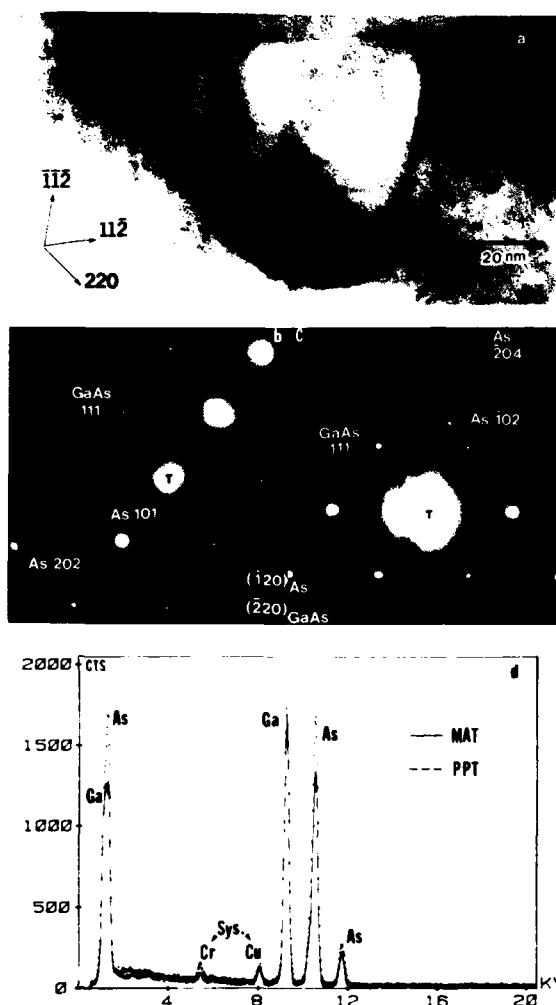
Fig.1 Series of images of same precipitate illustrating the sample preparation procedure to result in a precipitate in the thin area of sample. Decrease in the length of dislocation lines reflects the reduction in thickness.

### 3. Results of General Observation

About 65 TEM samples were prepared from various parts of an In-doped GaAs crystal. By surveying this large number of specimens, it was estimated that the precipitate number density is approximately  $1.5 \times 10^8 \text{ cm}^{-3}$ , which is slightly lower than but comparable to the value reported for dislocated undoped crystals (Cornier et al. 1984B). Most of the precipitates were found in the dislocated regions of the crystal and were coupled with nominally straight dislocations (see Fig. 1 for example). Isolated precipitates, however, were also found in the relatively dislocation-free regions. They were all observed to have a tetrahedral shape bounded by  $\{111\}$  matrix planes and to vary in size from a few tens to over two hundred nanometers. Their tetrahedral shape can be easily visualized from the fact that their projected shape on the  $\{110\}$  matrix plane is an isosceles triangle with two inside angles of  $55^\circ$  and one of  $70^\circ$  (Fig. 2(a) and Fig. 3(a)) and that the projected shape on the  $\{111\}$  matrix plane is an equilateral triangle (Fig. 4(a)).

### 4. Characterization of Observed Precipitates

Figure 2(a) shows a multibeam image of a typical precipitate found in In-doped GaAs and Figs. 2(b) and (c) are corresponding selected area diffraction patterns (SADP) with extra spots indicated and indexed. Notice the two SADP's were taken from slightly different crystallographic orientations near a same  $\langle 110 \rangle$  matrix pole. This approach was necessary to accentuate weak diffraction spots associated with the particle. Measured interplanar spacings



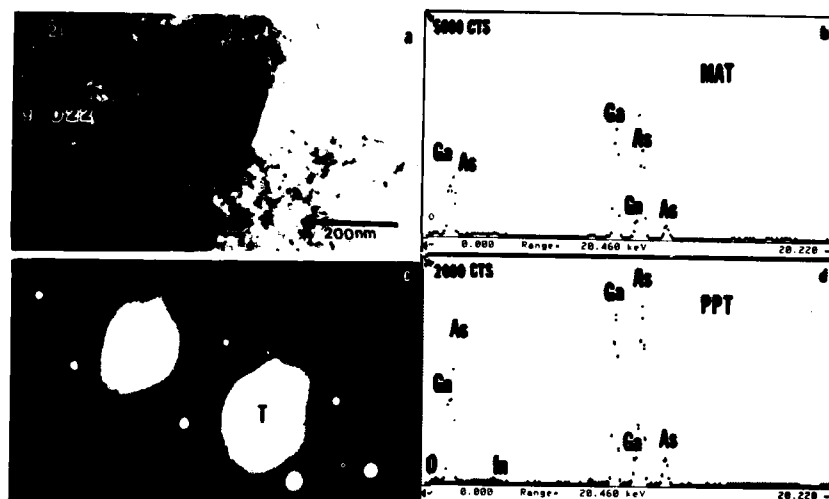
and angles, summarized and compared with the theoretical values in Table 1, clearly indicate that this is a hexagonal arsenic precipitate.

In agreement with this conclusion, results of the chemical analysis by EDXS in TEM, Fig. 2(d) show excess As compared to the matrix but no major element other than Ga and As in the precipitate. It should be stressed that the EDXS spectra presented in this work may not represent quantitative values because of the likelihood that the precipitates are completely surrounded by the GaAs matrix. It is very interesting that a simple orientation relationship exists between this particle and matrix GaAs and this point will be discussed in more detail in next section.

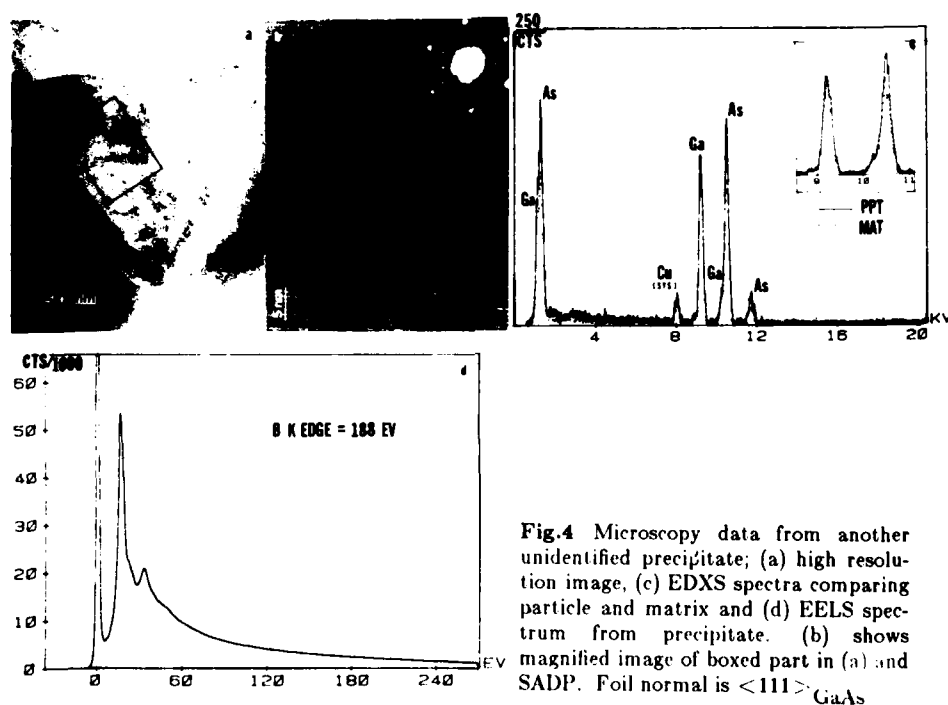
**Fig.2** Multibeam image, (a), and SADP's, (b) and (c), obtained from a hexagonal As precipitate in In-doped GaAs. Foil planes are  $(120)_{As}$  and  $(\bar{2}20)_{GaAs}$ . In (d) an EDXS spectrum from the precipitate is compared with one from nearby matrix.

**Table 1** Analysis of diffraction patterns.

|               | Measured<br>Spacings(nm) | Included<br>Meas | Angles<br>Theor | Theor<br>Spgs(nm) | Planes in<br>Hex As      |
|---------------|--------------------------|------------------|-----------------|-------------------|--------------------------|
| Fig. 2(b)&(c) | 0.31<br>0.275            | 131°             | 131°            | 0.311<br>0.277    | (101)<br>( $\bar{1}02$ ) |
| Fig. 3(c)     | 1.9<br>0.68              | 91°              |                 |                   |                          |
| Fig. 4(b)     | 0.58<br>0.67             | 94°              |                 |                   |                          |



**Fig.3** Information from an unidentified precipitate; (a) BF image at 220 matrix two beam condition, (b) corresponding SADP with extra spots arrowed, (c) EDXS spectrum from matrix and (d) EDXS spectrum from the precipitate (d). Note a very small spacing in SADP which corresponds to 1.9 nm of interplanar spacing in real space.



**Fig.4** Microscopy data from another unidentified precipitate; (a) high resolution image, (c) EDXS spectra comparing particle and matrix and (d) EELS spectrum from precipitate. (b) shows magnified image of boxed part in (a) and SADP. Foil normal is  $\langle 111 \rangle$  GaAs

Figures 3 and 4 contain information obtained from other particles. Four interplanar spacings and two included angles measured from the diffraction patterns, Figs. 3(c) and 4(b), are summarized in Table 1. Note that an interplanar spacing as large as 1.9 nm is detected. The two patterns also show that a certain orientation relationship exists between the matrix and precipitates although there is no apparent consistency between them. The observed variation in intensities of the diffracted spots furthermore suggests an ordering in a direction parallel to the  $\langle 112 \rangle$  matrix direction. This is also apparent in the high resolution image, Fig. 4(b). Precipitate EDX spectra, Figs. 3(b), 3(d) and 4(c), show that the precipitates are As-rich and do not contain any other major elements with  $Z > 10$ , except Ga and As. The spectrum in Fig. 3(d) shows an indium peak, but it is too small in amplitude to be related to any kind of compound. Figures 3(b) and 3(d) show the results of an EDX analysis with an ultra-thin window detector and Fig. 4(d) the result of Electron Energy Loss Spectrometry (EELS) analysis employed to detect the existence of light elements. It is clear from these data that large amounts of light elements are not present in the precipitates. A thorough search has been performed but no good match with all the information given has yet been found. It is suggested that the precipitates are an ordered compound of Ga and As which is As-rich. Although no such compound has been reported in the literature, the formation of a metastable phase may be possible under the high local pressure and high temperature growth conditions experienced by the crystal. Such a metastable phase may also be stabilized by a very small amount of impurities, possibly below the detectability limits of EDXS or EELS.

## 5. Discussion

There are very few reports of precipitates in In-doped GaAs except one of As-rich particles in In-doped crystals grown from an As-rich melt (Barrett et al, 1984). Since no In-bearing phase has been found even in this work, it may be concluded that indium is not involved in formation of precipitates in GaAs at the concentration level studied in this work and precipitation hardening is not a major mechanism for the observed reduction in dislocation density caused by In doping. However, it is still very interesting that a number of precipitates, all of them related to excess As, have been observed because this can give clues to the behavior of As-related defects in a growing crystal, for example to agglomeration phenomena of the defects. Most of all, the existence of unidentified complex phases which would not be formed at the normal environment illustrates the complicated behavior of these defects.

**Table 2** Lattice mismatch between hexagonal As and matrix

| Planes                      | $d_{hkl}(\text{nm})$ | Mismatch(%) |
|-----------------------------|----------------------|-------------|
| $\{003\}_{\text{As}}$       | 0.352                | 7.7         |
| $\{111\}_{\text{GaAs}}$     | 0.326                |             |
| $\{\bar{1}20\}_{\text{As}}$ | 0.188                | 6.2         |
| $\{220\}_{\text{GaAs}}$     | 0.1998               |             |

A very simple orientation relationship can be deduced from the SADP's in Fig. 2 between the As precipitate and matrix, namely  $(001)_{\text{As}} \parallel (111)_{\text{GaAs}}$  and  $(\bar{1}20)_{\text{As}} \parallel (202)_{\text{GaAs}}$ . Note that the position of the 003 As spot can be estimated to be on the line connecting the transmitted beam and the 111 GaAs spot, even though the spot does not appear very bright under these diffracting conditions. Table 2 shows that differences in planar spacings, or lattice mismatch, are quite small in both directions suggesting that this orientation relationship is energetically favorable. In fact the As atoms in the (001) plane of arsenic are in an arrangement similar

to that of As atoms in the (111)B plane of GaAs. Since the same orientation relationship has been observed by Sands et al (1985) between the matrix and hexagonal As precipitates formed by the thermal oxidation of GaAs, it is believed that this kind of orientation relationship is generally taken by a hexagonal As precipitate in GaAs although Cullis et al (1980) reported they observed no simple orientation relationship between an As particle and its undoped GaAs matrix.

It is also interesting that the precipitates have a tetrahedral shape while particles in undoped GaAs reported previously show round or somewhat cylindrical shape (Cullis et al, 1980; Cornier et al, 1984A), suggesting that the interfacial energies and/or formation mechanism is altered by In-doping. Experiments to obtain more precise information on the precipitation phenomena in GaAs and to clarify uncertainties remaining in this work are in progress.

## 6. Conclusions

As a result of an extensive TEM work, a low density -about  $1.5 \times 10^8 \text{ cm}^{-3}$ - of precipitates has been observed in In-doped GaAs crystals. None of particles was found to contain significant amount of In, however all were found to be As-rich. One phase in particular was identified as hexagonal As. Analysis of diffraction patterns from these precipitates shows a very simple orientation relationship between the precipitates and matrix. Unidentified As-rich particles, with an interplanar spacing as large as 1.9 nm, have been also observed.

## 7. Acknowledgement

The crystal used in this investigation was kindly provided by Dr. A. G. Elliot of HP-OED in San Jose, CA. The authors are indebted to Mr. M. Kundmann for his help in EELS analysis. This work was supported by the Director, Office of Basic Energy Science Division of the U. S. Department of Energy under contract No. DE-AC03-76SF00098.

## References

- Barrett D L, McGuigan S, Hobgood H M, Eldridge G W, and Thomas R N, 1984 *J. Crystal Gr.* **70** 179
- Cornier J P, Duseaux M and Chevalier J P, 1984A *Appl. Phys. Lett.* **45** 1105
- Cornier J P, Duseaux M and Chevalier J P, 1984B *Inst. Phys. Conf. Ser.* **74** 95
- Cullis A G, Augustus P D and Stirland D J, 1980 *J. Appl. Phys.* **51** 2556
- Elliot A G, Wei C, Farraro R, Woolhouse G, Scott M, and Hiskes R, 1984 *J. Crystal Gr.* **70** 169
- Holmes D E, Kuwamoto H, Kirkpatrick C G, and Chen R T, 1984 *Semi-insulating III-V Materials*; Kaneeta 205
- Lodge E A, Booker G R, Warwick C A and Brown G T, 1985 *Inst. Phys. Conf. Ser.* **76** 217
- Markov A V, Mil'vidskii M G and Shifrin S S, 1984 *Sov. Phys. Crystallogr.* **29** 205
- Sands T, Washburn J, and Gronsky R, 1985 *Mat. Lett.* **3** 247
- Stirland D J, Augustus P D, Brozel M R and Foulkes E J, 1984 *Semi-insulating III-V Compounds*; Kaneeta 91
- VonNeida A R and Jordan A S, 1986 *J. Metals* June 35



## **Correlation between melt stoichiometry and activation efficiency in Si-implanted GaAs**

A. R. Von Neida, S. J. Pearton, M. Stavola, and R. Caruso

AT&T Bell Laboratories, Murray Hill, New Jersey 07974, USA

**Abstract.** The net donor activation efficiency of Si implanted in undoped, semi-insulating, Liquid Encapsulated Czochralski grown GaAs is found to be a strong function of the melt stoichiometry. The net activation efficiency after annealing of 100 keV  $^{29}\text{Si}$  ions implanted at a dose of  $5 \times 10^{12} \text{ cm}^{-2}$  ranged from 26% in material grown from a melt containing 47½ atom % As to 91% for a sample from a 65 atom % As melt. DLTS on conducting samples from crystals grown in a similar manner show much higher concentrations of stoichiometry-related defects like EL2 in material from As-rich melts, indicating that melt stoichiometry differences are reflected in the stoichiometry of the resulting crystal. The results are consistent with an increased occupation probability for Si on a Ga site in As-rich material.

### **1. Introduction**

The need for uniform and reproducible activation of implanted Si in semi-insulating GaAs is paramount if an implantation-based technology for high-speed integrated circuits in this material is to succeed. The channel layers comprising the field effect transistors in these circuits are formed by implanting Si at low doses ( $1-7 \times 10^{12} \text{ cm}^{-2}$ ) to give shallow ( $\leq 1000\text{\AA}$ ), n-type ( $\sim 10^{17} \text{ cm}^{-3}$ ) regions in the semi-insulating substrates. There are generally quite significant variations in the net donor activation efficiency over the wafer area, and from wafer-to-wafer and ingot-to-ingot. There are some obvious reasons for these variations, such as non-uniform compensating acceptor backgrounds in the material, which may be different from one crystal to another. These variations can be accentuated during the implant activation anneal, in which contamination from the surface or encapsulant-induced stresses can alter the doping profile. Another parameter which may be critical in determining implant activation is the stoichiometry of the semi-insulating substrate. Several attempts to examine this dependence have employed material with a relatively small range of As atom fractions in the melt ( $\text{As}/(\text{As} + \text{Ga}) = 0.488 - 0.509$ ) leading to somewhat inconclusive results (Sato et al 1984, 1985). In this experiment, the activation efficiency of  $^{29}\text{Si}$  ions implanted at a low dose ( $5 \times 10^{12} \text{ cm}^{-2}$ , 100 keV) into GaAs grown from melts of widely varying stoichiometries ( $\text{As}/(\text{As} + \text{Ga}) = 0.475 - 0.650$ ) was investigated.

### **2. Experimental**

The samples for implantation were prepared from the seed end of undoped high resistivity crystals which were grown by the Liquid Encapsulated Czochralski (LEC) technique. The four crystals were grown in the  $\langle 111 \rangle_B$  direction from charges containing As concentrations of 47½, 50, 52½ and 65 atom % respectively. In order to stabilize the As-rich compositions, high pressures were used in the melt formation phase ( $\approx 100 \text{ atm.}$ ) and subsequent pulling procedure (35 atm.). This is obviously a crucial requirement if the melt stoichiometry variations are to be reflected in the crystal. Low growth rates were required to minimize the development of constitutional supercooling. Typically, the crystals weighed 30-80g with a maximum diameter of 20mm.

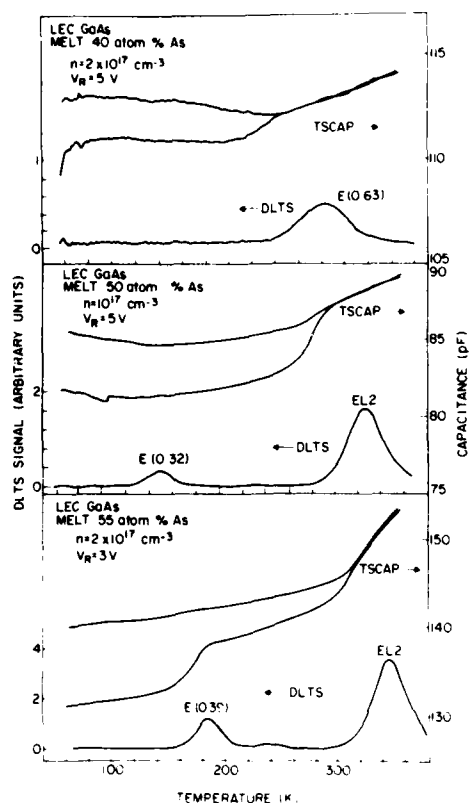


Fig. 1 DLTS spectra and TSCAP scans from conducting GaAs samples taken from crystals grown from melt containing 40, 50 and 55 As atom % respectively. The increasing EL2 concentration indicates that the resultant crystal stoichiometry reflects the increasing As concentrations in the different melts.

### 3. Results and Discussion

The electrical characteristics of the high resistivity samples were determined by Hall measurements, and the dislocation densities were obtained by preferential etching and counting. These are given in Table 1. The As deficient charge gave rise to material with low p-type conductivity; all other crystals displayed n-type conductivity. The major acceptor in our material is C, typically present at the  $5 \times 10^{15} \text{ cm}^{-3}$  level. Shallow donors such as S and Si incorporated during growth are also present at the  $10^{15} \text{ cm}^{-3}$  level.

Three other crystals were grown under similar conditions but were intentionally doped with Si to give n-type ( $\sim 10^{17} \text{ cm}^{-3}$ ) conducting GaAs. The charges for these crystals contained 40, 50 and 55 atom % As respectively. Deep level concentrations in this material were examined on Au-Schottky barrier contacted samples by standard deep level transient spectroscopy (DLTS) analysis in a system based on a PAR model 410 capacitance meter and lock-in amplifier. The spectrum from each sample is shown in Figure 1. In the As-deficient material a level at  $E_c - 0.63 \text{ eV}$  is present at a concentration of  $7 \times 10^{15} \text{ cm}^{-3}$ , determined from the accompanying Thermally Stimulated Capacitance (TSCAP) scan. The difference in such scans under bias-on and bias-off conditions gives a measure of the ionized trap concentration in the material.

TABLE 1. Characteristics of high resistivity GaAs crystals used for implantation

| As atom % | $\rho_{300} (\Omega \text{ cm})$ | $\mu_{300} (\text{cm}^2 \text{ V}^{-1} \text{ s}^{-1})$ | $N_{300} (\text{cm}^{-3})$ | Dislocation Density ( $\text{cm}^{-2}$ ) |
|-----------|----------------------------------|---|----------------------------|--|
| 47½       | $1.8 \times 10^5$                | 374   | $9.4 \times 10^{10}$       | $3 \times 10^4$                          |
| 50        | $6.2 \times 10^5$                | 4073  | $2.5 \times 10^9$          | $6 \times 10^4$                          |
| 52½       | $5.7 \times 10^7$                | 4619  | $2.4 \times 10^7$          | $1 \times 10^5$                          |
| 65        | $2.6 \times 10^6$                | 3914  | $6.1 \times 10^8$          | $2 \times 10^4$                          |

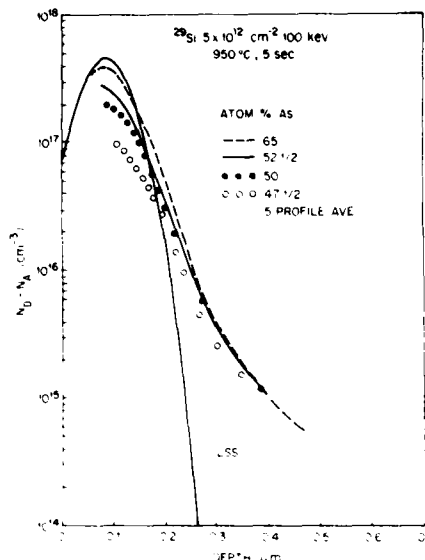


Fig. 2 Net free carrier profiles in GaAs samples taken from crystals grown from widely varying melt stoichiometries, after  $^{29}\text{Si}$  implantation ( $5 \times 10^{12} \text{ cm}^{-2}$ , 100 keV) and activation ( $950^\circ\text{C}$ , 5 sec).

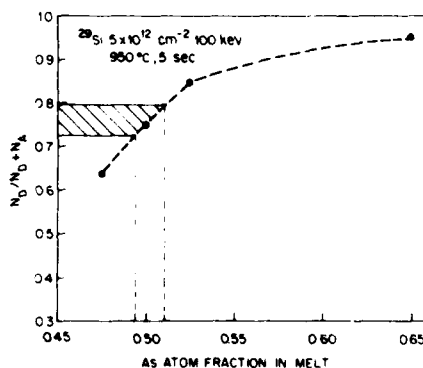


Fig. 3 Relative donor ratio in Si implanted GaAs samples grown from different Ga or As-rich melts. The cross hatched area is the range of relative donor concentration across the diameter of a commercial wafer. This wafer has net donor activations of 46-56%. The range of melt stoichiometry this represents under our growth conditions is 0.485-0.508 atom % As.

The density of the well-known stoichiometry related level EL2 ( $E_c - 0.80\text{eV}$ ), generally assumed to be related to  $\text{As}_{\text{Ga}}$  defects, is  $< 10^{14} \text{ cm}^{-3}$ . By contrast, in the sample taken from the 50 As atom % melt material, EL2 is present at a concentration of  $\sim 6 \times 10^{15} \text{ cm}^{-3}$ , with another lower concentration ( $\sim 1.5 \times 10^{15} \text{ cm}^{-3}$ ) level at  $E_c - 0.32\text{eV}$ , possibly EL7, also evident. In the 55 As atom % sample EL2 is even more dominant, with a concentration of  $\sim 1.4 \times 10^{16} \text{ cm}^{-3}$ . This is a good indication that the trend in stoichiometry variation in the melt is reflected by the stoichiometry of the resultant crystal. Also present in the As-rich material is a level at  $E_c - 0.39\text{eV}$ , possibly EL5, at a concentration of  $\sim 4 \times 10^{15} \text{ cm}^{-3}$ .

Armed with this knowledge we are justified in looking for implant activation variations in the semi-insulating samples. After mechanical polishing with Br-methanol and etching for 5 min in 5:1:1  $\text{H}_2\text{SO}_4:\text{H}_2\text{O}_2:\text{H}_2\text{O}$  at  $70^\circ\text{C}$ , these were implanted at room temperature to a dose of  $5 \times 10^{12} \text{ cm}^{-2}$ . Ion channeling effects were minimized by tilting the samples with respect to the beam. Implant activation was achieved at  $950^\circ\text{C}$  for 5 sec in a Heatpulse 410T furnace, with the sample of interest placed face-down on another GaAs substrate to minimize As loss from the surface. (Malbon 1976) This technique avoids possible complications that can arise from stress induced in the near-surface region by encapsulants such as  $\text{SiO}_2$  (Pearton and Cummings 1985) (Nishi 1985) and that lead to enhanced diffusion of the implant Si.

Carrier concentration profiles in each sample were obtained by 10 kHz capacitance-voltage (C-V) measurements using a mercury probe (1.5mm diameter dot size) as a Schottky contact. The series resistance was monitored simultaneously with the C-V data, and showed the resultant carrier profiles to be affected only on the bulk side of the profile below a concentration of  $\sim 5 \times 10^{15} \text{ cm}^{-3}$ . This effect, together with unavoidable channeling during implantation and Debye tailing of the electrons into the semi-insulating substrate leads to extended, low-concentration tails on the carrier profiles.

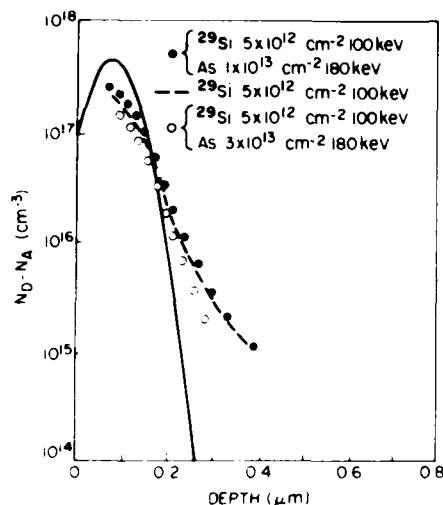


Fig. 4 Net free carrier profiles in 50 atom % As samples co-implanted with Si + As, compared to a Si-only implanted sample. Beyond an optimum dose ( $\sim 10^{13} \text{ cm}^{-2}$ ) of As, the Si activation begins to decrease.

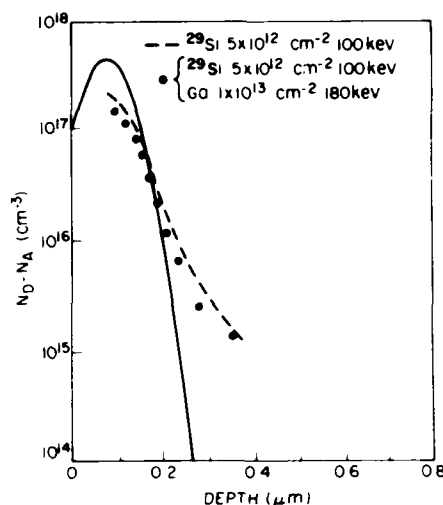


Fig. 5 Net free carrier profiles in 50 atom % As samples co-implanted with Si + Ga, compared to a Si-only sample. The effect is opposite to that of As co-implantation.

Figure 2 shows carrier profiles measured in the center of each sample after implantation and annealing. Each curve is the average of five separate profiles taken across the diameter of the sample. The variation of the profile does not exceed the range shown by the error bar. There is a clear and dramatic dependence of Si donor activation efficiency on melt stoichiometry, a much more convincing demonstration than previously observed (Sato *op cit* 1984, 1985), that Si donor activation efficiency increases as crystals become arsenic rich. The surface-depletion corrected donor activation efficiency ranged from 26% for the 47½ atom % As material to 91% for the 65 atom % As composition.

Hall mobilities measured at 77K in the Si implanted material were used to obtain average compensation ratios in the implanted region by comparison with the calculated values of Walukiewicz *et. al.* (1982). This was done by integrating under the respective carrier profiles to obtain an average carrier density, which together with the 77K mobility leads to a value for  $N_A/N_D$  (acceptor-to-donor ratio). Assuming that all of the Si ions are substitutional and that the charge in the implanted region is due either to  $\text{Si}_{\text{Ga}}$  ( $N_D$ ) or  $\text{Si}_{\text{As}}$  ( $N_A$ ), then we can calculate the fraction of Si donors as shown in Figure 3. The trend with increasing As atom fraction suggests the cause of the increased donor activation in As-rich material is simply the preferential occupation by Si of Ga sites. This trend is physically reasonable, as in very As-rich material, Ga site occupation will asymptotically tend towards unity.

Also shown in Figure 3 is the range of activations measured across the diameter of a standard (2"φ), commercially obtained wafer after a similar implantation and annealing cycle. There are two points to note. First, the range of activations measured for our Ga or As-rich material is much larger than the variation within a particular melt-stoichiometry sample, and

secondly this latter variation makes it very difficult to draw conclusions based on the use of slightly Ga or As-rich material. (Sato et al 1984, 1985). Several other possible explanations for the dependence of activation on crystal stoichiometry are ruled out. For example, there could be more compensating acceptors present as the As concentration decreases. However, significant differences in the background acceptor concentrations between the various samples would also affect the shape of the implant carrier profiles. On the bulk side of the implanted distribution the profile would be much sharper for samples with significant acceptor densities, a situation common to Cr-compensated GaAs. Certainly, in our samples the acceptor concentrations are much below the  $10^{17} \text{ cm}^{-3}$  level needed to affect the implant activation. To ensure that the implantation and annealing cycle did not cause the break-up of previously neutral impurity complexes, Ar was implanted to a similar dose and range as for the Si, and the samples were subjected to an annealing treatment. There was no significant change in carrier concentration or mobility in any of the samples after this procedure. In common with the results of Sato et. al. (1984, 1985) we did not notice any correlation of peak implant doping concentration or profile shape with dislocation density in the samples, so that gettering of compensating acceptor impurities to dislocation cores is not a feasible explanation for the variation in Si activation efficiency.

We can also attempt to increase the occupation probability for Si on Ga sites by co-implanting Si and As into stoichiometric GaAs (Krautle 1981) (Park et al 1981). The effect of various As doses (180 keV ions) on the carrier profiles from our standard Si implants ( $5 \times 10^{12} \text{ cm}^{-2}$ , 100 keV) is shown in Figure 4. The net donor activation efficiency increased from 50% to 68% for optimum As doses. As the arsenic dose is increased above  $3 \times 10^{13} \text{ cm}^{-2}$ , damage related compensation begins to become significant as shown by the decrease in the peak carrier concentration. In this case the As implant leads to the formation of local regions of nonstoichiometry (Christel and Gibbons 1981). No significant effect was found in the order of the co-implantation, or whether the As implant was annealed prior to the Si implant. Therefore, although an artificial increase in the occupation probability of Si on Ga sites by As co-implantation can lead to enhanced donor activation, it is not as effective as a standard Si implant into As-rich material. This would be expected from a consideration of the relative As excess introduced by the two methods; one cannot simulate by implantation a very As-rich sample because the remnant damage after annealing tends to compensate the low dose Si donor activity. In contrast to the enhanced donor activation for As co-implantation, Ga + Si implantation into 50 atom % As samples leads to a decrease in net electron concentration after annealing as shown in Figure 5. These results were not duplicated when the donor species used was selenium which occupies an As sub-lattice site. Because Se is not an amphoteric dopant its lattice location for low doses remains essentially unaffected.

The As co-implantation results can be used to make a simple estimate of the actual stoichiometry in the crystals, as opposed to the melt stoichiometries we have quoted. An As dose of  $10^{11} \text{ cm}^{-2}$  at 180 keV, corresponds to an excess introduced into the implanted region of the order of  $10^{18} \text{ cm}^{-3}$ . This is equivalent to an As atom fraction of  $\sim 50.001\%$ . The activation in this co-implanted sample increased from 59 to 68%, and is approximately the same as that in the 52½ atom % As melt stoichiometry material. Assuming a linear dependence of net activation on crystal stoichiometry we can also estimate the As deficiency in the 47½ atom % As melt material to be  $\sim 2.5 \times 10^{18} \text{ cm}^{-3}$ , and similarly, an As excess of  $\sim 5 \times 10^{18} \text{ cm}^{-3}$  for the 65 atom % As melt sample. As expected from the GaAs phase diagram, (Hurle 1979) very little of the As excess in the melt is carried over to the crystal. While these point defect concentrations in the crystal correspond to a very small fraction of the melt stoichiometry they are sufficiently large to have an important effect on the Si activation efficiency. This trend in crystal stoichiometry with melt stoichiometry is qualitatively similar to that measured by Terashima et. al. (1985) using a coulometric titration method on crystals grown from melts of widely varying composition.

**4. Conclusions**

The data reported here emphasize that local variations in As concentration can have a profound effect on the activation of low dose ( $\sim 10^{12} \text{ cm}^{-2}$ ) Si implants into GaAs. We also note that there may be other contributions in determining the uniformity of the donor implant activation such as spatial variations in background acceptor concentration. This effect has been more widely recognized than that produced by local variation in stoichiometry. The relative importance of these two phenomena in the final activated profile will be a function of the purity of the crystal and its thermal history. Indeed, local stoichiometry variations can also be induced by non-uniform heating during the implantation activation step, which can lead to increased loss of As from the hotter sections of the wafer. In conclusion, we demonstrate a strong dependence of implanted Si donor activation efficiency in semi-insulating GaAs on the stoichiometry of the initial melt. To achieve reproducible activation, not only across the whole substrate, but from wafer-to-wafer, close attention must be paid to the crystal stoichiometry.

**Acknowledgements**

The authors acknowledge illuminating discussions with J. M. Parsey, Jr., and the encouragement of A. S. Jordan and A. M. Glass.

**REFERENCES**

- Christel, L. H. and Gibbons, J. F. 1981 *J. Appl. Phys.* **52** 5080.
- Hurle, D. J. T. 1979 *Phys. Chem. Solids* **40** 613.
- Co-implantation of a lattice constituent and amphoteric dopant has been studied in some detail; see for example H. Krautle, *Nucl. Instr. Meth.* **82** 625, and Park, Y. S., Yea, Y. K., and Pedrotti, F. L., *ibid* p. 617.
- Malbon, R. M., Lee, D. H., and Whelan, J. M., 1976 *J. Electro Chem. Soc.* **123** 1413.
- Nishi, H. 1985 *Nucl. Instr. Meth.* **B7/8** 395.
- Pearton, S. J. and Cummings, K. D. 1985 *J. Appl. Phys.* **58**, 1500.
- Sato, T., Terashima, K., Ozawa, S., Nakajima, M., Fukuda, T. and Ishida, K. 1984 *Proc. GaAs IC Symposium* (published IEEE, NY) pp. 53-56.
- Sato, T., Terashima, K., Emori, H., Ozawa, S., Nakajima, M., Fukuda, T. and Ishida, K. 1985 *Jap. J. Appl. Phys.* **24**, L488.
- Terashima, K., Washizuka, S., Nishio, J., Okada, A., Yasuami, S. and Watanabe, M. 1985 *Proc. Int. Symp. GaAs and Related Compounds 12*, Inst. Phys. Conf. Ser. No. **79** 37.
- Walukiewicz, W., Lagowski, J. and Gatos, H. C. 1982 *J. Appl. Phys.* **53** 769.

## **The use of selective pair luminescence to characterize semi-insulating GaAs**

Emil S. Koteles, James Kafalas, Stanley Zemon and Peter Norris

GTE Laboratories Incorporated  
40 Sylvan Rd.  
Waltham, Massachusetts 02254

**Abstract.** Selective pair luminescence (SPL) has been shown to be a powerful technique for investigating excited levels of shallow acceptors in semi-insulating LEC-grown GaAs. We now illustrate its usefulness as a nondestructive characterization tool for studying variations of crystal quality due to differing growth conditions, postgrowth treatments, as well as spatial variations within a given boule. A direct correlation is demonstrated between the quality of a sample as indicated by SPL spectra and as determined by room temperature mobility measurements.

### **1. Introduction**

Gallium arsenide (GaAs) is, perhaps, one of the most studied and most technologically important members of the family of III-V compound semiconductors. Efforts are continually being made to improve the crystal quality and purity of this material. An area of critical importance is that of bulk grown GaAs, because it is used both as the starting material for a host of devices and integrated circuits and as a substrate for epitaxial layers. Ideally, for these uses, undoped GaAs wafers, usually grown by the liquid encapsulated Czochralski (LEC) technique, should be of high purity and of uniform quality. These attributes are usually determined by transport measurements (generally resistivity and Hall effect measurements to determine total impurity-generated carrier concentrations) and low temperature photoluminescence measurements (which provide information on acceptor identities and relative concentrations). However, transport measurements have their limitations in these materials. In many cases, it is difficult to make good ohmic contacts at the low temperatures required to obtain usable information about impurity concentrations and charge carrier mobilities. In addition uniformity studies necessitate the fabrication of many samples requiring much time and effort and the destruction of the wafer. On the other hand, optical studies, since they do not require contacts and are nondestructive, are much more attractive. Also, it is possible in principle, and increasingly in practice, to raster-scan a whole wafer and thus obtain a rapid determination of the uniformity of PL intensity over a wafer. This is equivalent to uniformity of wafer purity or quality since PL intensity can be assumed proportional to impurity concentration (Yokogawa et al 1984a,b).

It has recently been demonstrated that added sensitivity and resolution for acceptor identification is possible when a semi-insulating GaAs sample is studied using the

selective pair luminescence (SPL) technique. This process has been discussed in detail by Tews et al 1979 and has been studied in GaAs by Hunter and McGill 1982, Kisker et al 1983 and Koteles et al 1986.

SPL is a low temperature photoluminescence process which takes place in semi-insulating semiconductors and which involves the resonant excitation of pairs of donor and acceptor impurity atoms separated by a particular spatial distance. This selective excitation is possible since the donor-acceptor pair transition energy (which depends on the Coulomb interaction) is a function of the pair separation. A resonant incident photon generates an electron-hole pair with the hole in an excited state. Then, since the decay of excited holes to their ground states is much more rapid than donor-acceptor recombination rates, the emitted photon is down-shifted by an energy amount equal to the energy difference between the excited and ground states of the acceptor impurity. These differences are quite sensitive to the chemical nature of the acceptor and thus provide an accurate and sensitive method for studying excited levels of acceptors in these materials.

In this paper we will show that it is also possible to utilize this technique as a characterization tool for detecting small changes in material properties due to changing growth conditions and annealing. It has been suggested recently (Wagner et al 1986) that electronic Raman scattering is useful for quantitative analysis of shallow acceptors in these materials. However, since this is a nonresonant technique, in order to obtain a spectrum comparable in signal-to-noise to that of a resonant SPL spectrum, the input power must be increased by more than six orders of magnitude.

## 2. Experimental

The GaAs samples used in this study were grown at GTE Laboratories using the liquid encapsulated Czochralski (LEC) method in a Malvern MSR-6-R high pressure crystal puller with a PBN crucible. Cross-sectional (100) wafers were cut from various positions along the length of the one kilogram undoped boules (which were approximately 15 cm long and 5 cm in diameter) and polished. For the annealing study one half of a boule was subsequently annealed for 20 hours in an argon atmosphere at 900 °C. Results from wafers cut from the end of this boule were then compared with results obtained from nearly adjacent wafers cut from the control (unannealed) boule half.

Hall measurements were made in the Van der Pauw configuration using indium contacts alloyed into the sample in a hydrogen atmosphere. Typically, the transport measurements indicated the semi-insulating nature of these materials. Room temperature resistivities were in the  $10^7 \Omega\text{cm}$  range with mobilities of the order of  $10^3 \text{ cm}^2/\text{Vsec}$  and net carrier concentrations of the order of  $10^7 \text{ cm}^{-3}$  (n-type). Attempts to directly measure residual acceptor concentrations of zinc using neutron activation analysis were unsuccessful since the concentrations were below the detection limit of the technique (i.e., less than  $5 \times 10^{16} \text{ cm}^{-3}$ ).

The optical studies were performed with a double grating spectrometer coupled with a cooled GaAs photomultiplier tube and photon counting system. The samples were mounted strain-free in an exchange gas LHe cryostat and excited with about 100 mW/cm<sup>2</sup> of power from a Kr ion laser pumped tunable dye laser. The laser beam was



focused to a spot size of about 100  $\mu\text{m}$  diameter and for spatial dependence studies the spot was moved across the sample in steps of about 3 mm.

### 3. Results and Discussion

Figure 1 presents the 5K SPL spectra of nominally undoped semi-insulating LEC-grown GaAs wafers obtained from five different sources. The energy of the exciting laser beam ( $\sim 1.510$  eV) was chosen so as to maximize the intensity of  $2S_{3/2}$  to  $1S_{3/2}$  transitions in order to simplify the identification and increase the sensitivity of the technique (Koteles et al 1986). Thus, for example, in the top spectrum (sample 311) the strong, narrow peaks are identified as being due to these transitions from carbon, zinc and silicon/cadmium (it is not possible to distinguish between Si and Cd using excited impurity energy levels). The weak peak at higher energy is due to  $2P_{3/2}$  to  $1S_{3/2}$  transitions in carbon. Although the total emission efficiency is approximately the same in all these samples and room

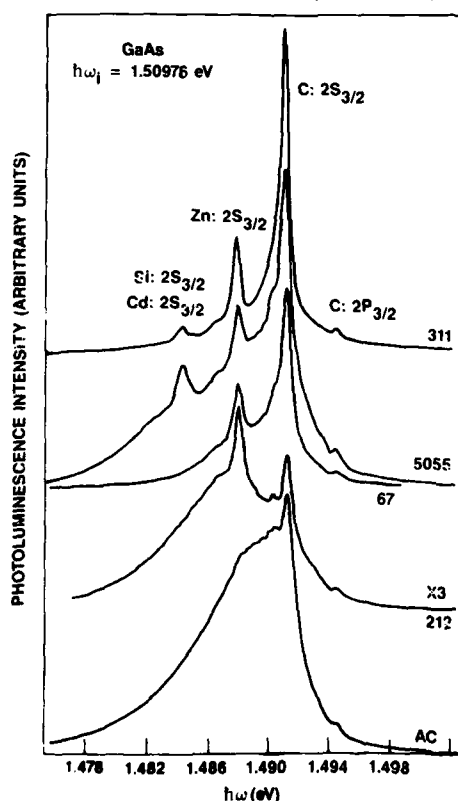


Figure 1 5K SPL spectra of five semi-insulating, nominally undoped LEC-grown GaAs samples from different boules or manufacturers.

temperature transport measurements yielded similar electrical results, the ratio of SPL intensity (the narrow peaks) to PL intensity (the broad background) varies considerably. In some spectra (e.g. Fig. 1 bottom) PL dominates while in others (e.g. Fig. 1 top) SPL features dominate. From other spectroscopic data in the exciton region it appears that better quality samples yield stronger SPL features. This finding is in agreement with studies of the change of crystal quality as a function of distance from the head (seed end) to tail of a typical boule discussed below.

To study the ability of SPL to monitor changes in crystal quality as a boule is being grown from a seed, sample wafers from the head and tail ends of two boules (numbers 13 and 20) were measured both with room temperature Hall effect and SPL. The results from both boules exhibited similar trends. Transport measurements indicated that wafers from the tail end of the boule were of better quality than those from the head end with mobilities as large as 5780  $\text{cm}^2/\text{Vsec}$  (as much as a factor of two greater than the head end). Tail end resistivities were somewhat smaller but still in the  $10^7 \Omega\text{cm}$  range. The change in the SPL spectra, as shown in Figure 2,

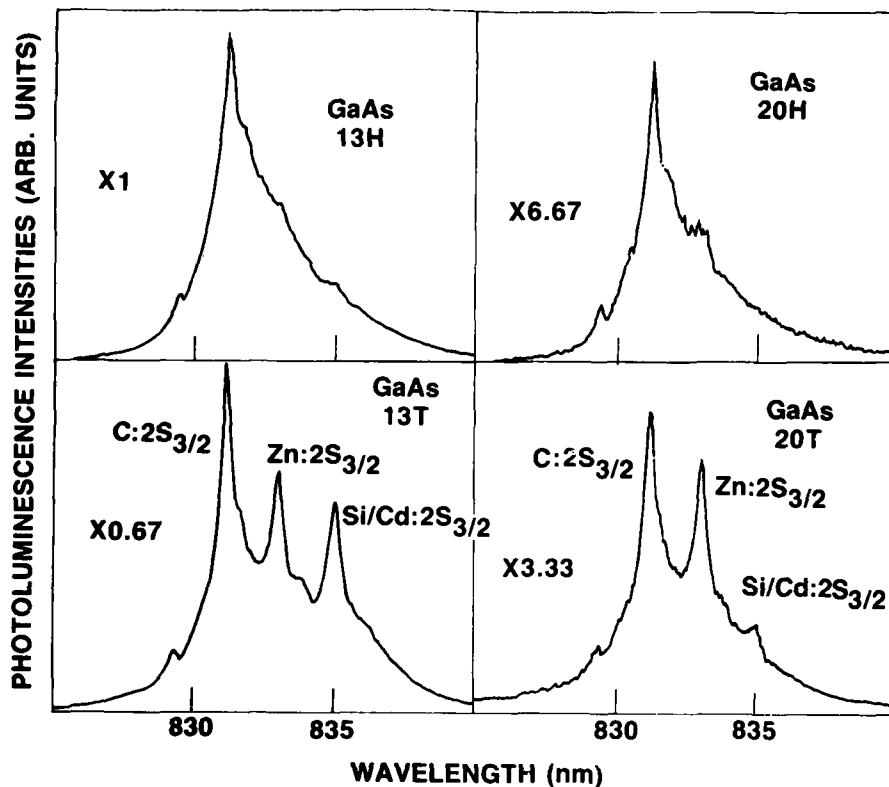


Figure 2 5K SPL spectra obtained from GaAs wafers cut from near the head (H) or tail (T) of two different LEC-GaAs boules (numbers 13 and 20) grown at GTE Laboratories.

was much more dramatic. The spectra of the head wafer from both boules (labelled by 13H and 20H in Figure 2) were dominated by PL with a small SPL peak due to carbon superimposed on top. Only weak SPL structure due to other impurities was observable. The spectra of the tail wafers (labelled 13T and 20T) were stronger, by about a factor of two, and possessed much more intense SPL peaks. The increase in the carbon peak intensity with respect to the PL background (perhaps as much as a factor of three) was smaller than that of the other two acceptor impurities (as much as a factor of 20 in the case of zinc in boule 13). This can be understood in terms of the increasing concentration of zinc and silicon/cadmium atoms in the melt due to the low incorporation rate of these impurities into the solid boule. However, as growth proceeds the liquid melt reservoir becomes depleted thereby increasing the impurity atom concentration and the incorporation of impurities into the boule. The change in the relative concentrations of carbon versus zinc and silicon/cadmium between the head and tail of the boule is a direct consequence of differences in the segregation coefficients of these impurities. By performing a careful study of changes in the SPL spectrum along a boule from head to tail it should be possible to derive unknown segregation coefficients with respect to a known standard (e.g. carbon) in dilute systems.

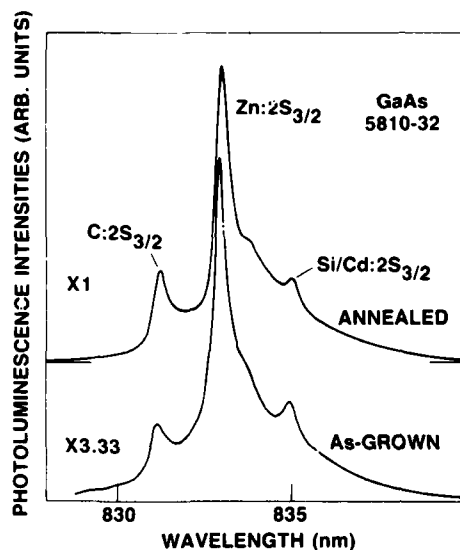


Figure 3 5K SPL spectra of an as-grown (bottom) and annealed (top) GaAs wafer.

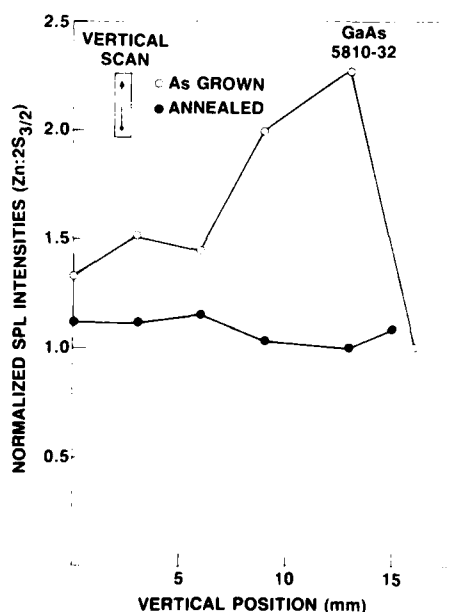


Figure 4 Intensity of Zn:2S<sub>3/2</sub> SPL peak as a function of the distance from the center of a wafer for an as-grown (open circles) and annealed (closed circles) GaAs wafer.

It is also interesting to study changes in the SPL spectrum as a result of bouie annealing. In Figure 3, a comparison of SPL spectra from wafers taken from annealed and as-grown (control) bouie halves (of bouie 5810-32) is presented. Again, the increase in PL emission efficiency (about 3X) of the annealed sample with respect to the as-grown sample is taken to be an indication of improved crystal quality. This is in agreement with transport measurements which show an increase in the average mobility of the annealed bouie over the unannealed of a factor of two (to about 5200 cm<sup>2</sup>/Vs). The cause of the changes in the relative intensities of the zinc and silicon/cadmium peaks compared with that of carbon between the two spectra will be discussed later. Changes in the wafer uniformity due to annealing are easily monitored using SPL. In Figure 4 the intensity of the Zn:2S<sub>3/2</sub> peak (normalized to the smallest value measured) as a function of distance across a wafer is presented for both annealed and as-grown wafers. Over a distance of 15 mm (starting from the center of the wafer which is taken to be 0 mm) the intensity of the peak in the as-grown sample changes by as much as 230% in a characteristic M (or half M in this case) pattern. In the annealed sample however, the intensity of the peak changes by less than 15%, an indication of much better bouie uniformity. Again, this is in agreement with transport results which show more uniform mobilities across the annealed wafer than across the unannealed wafer. Across the unannealed wafer, the exact form of the acceptor distribution varies slightly depending on the chemical nature of the impurity. The cause of this variation is not clear but may be related to the effect of differences in growth conditions along the growth front on acceptor incorporation rates. However, in the annealed wafers, all the different acceptors are similarly uniformly

distributed over the wafer. Thus, in comparing SPL spectra of annealed as opposed to unannealed wafers, significant modifications in the relative peak intensities of Zn and Si/Cd to C acceptors at certain places on the wafer are observed as shown in Figure 3. Finally, it would be straightforward to couple this measurement with a rastering technique such as that demonstrated by Yokogawa et al 1984a,b to obtain a complete two dimensional map of acceptor impurity distributions over a wafer.

#### 4. Summary

We have previously demonstrated the utility of selective pair luminescence for the identification of acceptor impurities in semi-insulating GaAs and determinations of their relative abundances. We have now shown that SPL can also be utilized for monitoring changes in the crystal quality of LEC-grown GaAs as a function of growth parameters (e.g., by comparing SPL spectra from samples taken near the head and tail ends of a boule) and as a function of postgrowth treatment (e.g., the effect of annealing on SPL spectra).

Acknowledgements: We should like to thank E. Hartmann and J. Alexander for help with the growth and treatment of the GaAs boules and wafer preparation.

#### References

- Hunter A T and McGill T C 1982 *Appl. Phys. Lett.* **40** 169  
 Kisker D W, Tews H and Rehm W J. 1983 *J. Appl. Phys.* **54** 1332  
 Koteles Emil S, Zemon S and Norris P 1986 **International Symposium on GaAs and Related Compounds, Karuizawa, Japan, 1985** (Bristol:Adam Hilger) pp 259-64  
 Tews H, Venghaus H and Dean P J 1979 *Phys. Rev* **B19** 5178  
 Wagner J, Seelewind H and Kaufmann U 1986 *Appl. Phys. Lett.* **48** 1054  
 Yokogawa M, Nishine S, Matsumoto K, Akai S and Okada H 1984a *Jpn. J. Appl. Phys.* **23** 663  
 Yokogawa M, Nishine S, Sasaki M, Matsumoto K, Fujita K and Akai S 1984b *Jpn. J. Appl. Phys.* **23** L339

## **InP doped with isoelectronic impurities**

R. L. Henry and R. J. Gorman

Naval Research Laboratory, Washington, DC 20375-5000

### **1. Introduction**

Large diameter InP crystals grown by the LEC technique typically have a dislocation density exceeding  $5 \times 10^4 \text{ cm}^{-2}$ . Jordan, Von Neida, and Caruso (1984) have shown that the dislocation densities are related to strain arising from temperature gradients between the crystal and its surroundings during the growth process. The calculations of Jordan et al (1985) show that only very small temperature gradients can be tolerated to grow undoped dislocation free InP. As a practical matter crystal growth problems such as diameter control, solid-liquid interface shape and twinning become more severe when growth is attempted using small temperature gradients. One additional method of lowering the dislocation density is to harden the lattice via the addition of impurities. Zinc and sulfur dopants have been shown by Seki, Watanabe, and Matsui (1978) and germanium has been shown by Brown, Cockayne, and MacEwan (1981) to produce InP crystals with a low dislocation density. These dopants do affect the electrical conductivity such that semi-insulating InP cannot be obtained when the required quantities of the above dopants are added to yield a low dislocation density. Jacob (1982) has reported the use of isoelectronic impurities to lower the dislocation density of GaAs and InP. One of the attractions of Group III or Group V dopants is that the conductivity of a crystal containing high concentrations of dopant would not be substantially different from the conductivity of an undoped crystal. Thus semi-insulating low dislocation density crystals are attainable and semi-insulating In-doped GaAs crystals have been grown by many laboratories. Much less work has been done on InP doped with isoelectronic impurities. The purpose of this paper is to expand on the early work of Jacob (1982) and to do the investigation using InP melts of 450g size rather than the 70-80g melts used by Jacob.

### **2. Experimental Procedure**

The InP crystals were grown by the liquid encapsulation Czochralski procedure using polycrystalline InP as the starting material. The size of the melts, the shape and size of the boules and the growth conditions were reproduced for the various experiments in order to assess which of the Group III or Group V impurities was most effective at lowering the dislocation density. So as not to alter the ratio of Group III: Group V atoms within the melts, all dopants were added in the form of IIIP or InV compounds. The crystals were grown in the (111)P direction with a pull rate of 14 mm/hr. The puller was

pressurized to 38 atm with dry argon and a 60g pellet of  $B_2O_3$  with  $H_2O$  content of less than 100 ppm was used for each experiment. The depth of the  $B_2O_3$  was approximately 12 mm in the 50 mm diameter pyrolytic BN crucible. Subsequent experiments used a  $B_2O_3$  depth of 20 mm in order to lower the thermal gradient and make additional improvements in the dislocation density of As-doped InP. For the etching studies, (111) oriented wafers were cut from the boules at the point where approximately 50% of the melt had been solidified. Etch pits were produced following the procedures of Akita et al (1979)

### 3. Arsenic-Doped InP

Boules were grown with InAs additions to the melt of 1%, 4%, 6% and 8% by weight. Single crystals were readily grown with up to 6% by weight additions of InAs, although there was some evidence of constitutional super-cooling during the growth of the last to freeze portions of the 6% crystals. The crystal that was doped with InAs at 8% by wt. became polycrystalline before the boule reached the full diameter and single crystal growth could not be achieved using the 14 mm/hr pull rate. The etch pit densities for the middle wafers of an Fe-doped crystal and crystals doped with InAs at 1% and 4% are shown in Figure 1. It is apparent that the crystal grown from the 4% InAs-doped melt contains a central core approximately 8mm in diameter with a very low dislocation density. The etch pit density outside the central core is similar to that of the Fe-doped crystal. Figure 2 shows a micrograph of the etched central core region. We are at a loss to explain the abruptness with which the etch pit density plunges to zero. Figure 3 shows micrographs of an etched (110) wafer cut from the As-doped boule. The growth striations indicate that the center part of the boule experienced faceted growth. Hulme and Mullen (1962) had shown that faceted growth of Te-doped InSb resulted in the segregation coefficient being up to nine times larger for growth in the faceted region compared to growth off the facets. SIMS analyses were made to test whether As behaves similarly in faceted growth of InP and to calculate a segregation coefficient for As. The SIMS results are shown in Table 1. The As concentration was measured in the central core region and near the edge for 2 different wafers. The As concentration did not differ significantly between the central facet and the edge of the wafers. SIMS results are also shown for a wafer from the top and bottom of the 1% crystal. A segregation coefficient of .4 was calculated using the As concentrations determined from SIMS. X-ray diffraction and Vegards law were also applied to As-doped InP. The As concentrations determined by the X-ray technique are shown in Table 1 for the 6% crystal. A segregation coefficient of .6 was calculated using the X-ray determined As concentrations.

Figure 4 shows the EPD of a wafer from a crystal doped with InAs at 6% and Fe at 200 ppm by weight. This crystal was grown using 90g of  $B_2O_3$  and an RF coil containing two more turns than the coil used for the other crystals. The EPD is  $< 5 \times 10^3 \text{ cm}^{-2}$  over approximately 75% of the wafer diameter and it also has a central core of zero dislocation density. The crystal is semi-insulating with a room temperature resistivity of  $4 \times 10^6 \text{ ohm-cm}$  at the top and  $2 \times 10^7 \text{ ohm-cm}$  at the bottom of the crystal. The electrical properties of the As-doped crys-

tals are listed in Table 2. Smaller temperature gradients in addition to the As-doping will be required to achieve a lower dislocation density.

#### 4. Antimony-Doped InP

Single crystal growth was achieved from a melt doped with InSb at 1.4% by weight. After approximately 75% of the melt had been solidified, the boule abruptly became polycrystalline. The etch pit density for the Sb-doped boule is shown in Figure 5. This crystal has a small central core with an etch pit density of zero and the etch pit density of the remaining part of the wafer is similar to that for an undoped boule. We have been unable to achieve single crystal growth with larger concentrations of InSb in the melt. SIMS analysis indicate an Sb concentration of  $2 \times 10^{18} \text{ cm}^{-3}$  for the first grown area and  $5 \times 10^{18} \text{ cm}^{-3}$  for the last grown single crystal area. Using the SIMS results a segregation coefficient of .01 is calculated for Sb in InP.

#### 5. Gallium-Doped InP

Tohno et al (1984) have published EPD and  $K_{\text{eff}}$  results for Ga-doped InP in which they concluded that in order to grow a low dislocation density crystal with diameter larger than 15mm, a Ga concentration of at least  $10^{20} \text{ cm}^{-3}$  would be needed. They also reported that twinning is a problem when Ga concentrations exceed  $5 \times 10^{19} \text{ cm}^{-3}$ . For our work one crystal was grown with GaP added at .05% by weight which would give  $5 \times 10^{19} \text{ Ga cm}^{-3}$  at the top of the boule. The EPD as seen in Figure 6 is slightly lowered at the seed end of the boule while the EPD for wafers from lower in the boule are not significantly different from an undoped boule. Several attempts were made to grow a boule doped with both Ga (.05 wt%) and As (4 wt%). Crystal growth was difficult but we finally achieved a full diameter single crystal boule which became polycrystalline after approximately 30% of the melt had been solidified. The EPD was similar to that for an undoped boule but double crystal X-ray diffraction rocking curves indicated that the boule was composed of many grains with small angles of misorientation.

#### 6. Conclusions

The results show that As is the isoelectronic dopant which is most suitable for lowering the dislocation density of InP. Both Ga and Sb do lower the EPD but the EPD is lower still for As-doped material. Arsenic is more effective because it can be used at higher concentrations than either Ga or Sb. The high concentrations of dopants enable the observation of growth striations within the boules evidencing faceted growth. Semi-insulating InP can be achieved by adding Fe in addition to the isoelectronic dopants otherwise the carrier concentrations and mobilities are similar to those of undoped InP.

#### 7. References

- Akita K, Kusynoki T, Komiya S, and Kotani T 1979 J. Cryst. Growth 46 783.
- Brown G T, Cockayne B, and MacEwan W R 1981 J. Cryst. Growth 51 369.
- Hulme K F and Mullen J B 1962 Solid State Electronics 5 211.
- Jacob G 1982 Proc. 2nd Intern. Conf. on Semi-Insulating III-V Compounds 2.

Jordan A S 1985 J. Cryst. Growth 71 559.

Jordan A S, VonNeida A R, and Caruso R 1984 J. Cryst. Growth 70 555.

Tohno S, Kubota E, Shinogama S, Katsui A, and Uemura C 1984 Jap. J.

Appl. Phys. 23 672.

Seki Y, Watanabe H and Matsui J 1978 J. Appl. Phys. 49 822.

Table 1 Measured Arsenic Concentrations

| InAs (wt%) | $\frac{\text{As}(\text{cm}^{-3})}{\text{SIMS}}$ | $\frac{\text{As}(\text{cm}^{-3})}{\text{X-ray}}$ | Location      |
|------------|---|--|---------------|
| 1%         | $6 \times 10^{19} \pm .5$                       |  | top           |
| 1%         | $1.8 \times 10^{20} \pm .5$                     |  | bottom        |
| 4%         | $2.7 \times 10^{20} \pm .5..$                   |  | top center    |
| 4%         | $2.7 \times 10^{20} \pm .5$                     |  | top edge      |
| 4%         | $3.9 \times 10^{20} \pm .5$                     |  | middle center |
| 4%         | $3.3 \times 10^{20} \pm .5$                     |  | middle edge   |
| 6%         |   | $5.7 \times 10^{20}$                             | top           |
| 6%         |   | $6.0 \times 10^{20}$                             | middle        |
| 6%         |   | $7.9 \times 10^{20}$                             | bottom        |

Table 2 Electrical Properties of InP Crystals

| Dopant      | $N_D - N_A (\text{cm}^{-3})$ | $\mu_{77} \text{cm}^2/\text{Vs}$ | $\rho (\text{ohm-cm})$ |
|-------------|------------------------------|----------------------------------|------------------------|
| None        | $3.3 \times 10^{15}$         | 36,600                           |                        |
| None        | $5.2 \times 10^{15}$         | 33,200                           |                        |
| InAs (1%)   | $3.3 \times 10^{15}$         | 36,400                           |                        |
| InAs (4%)   | $3.8 \times 10^{15}$         | 33,000                           |                        |
| InAs (8%)   | $3.6 \times 10^{15}$         | 31,600                           |                        |
| InSb (1.4%) | $4.5 \times 10^{15}$         | 31,200                           |                        |
| GaP (05%)   | $3.4 \times 10^{15}$         | 34,700                           |                        |
| GaP, InAs   | $3.5 \times 10^{15}$         | 36,100                           |                        |
| InAs, Fe    |                              |                                  | $4 \times 10^6$        |



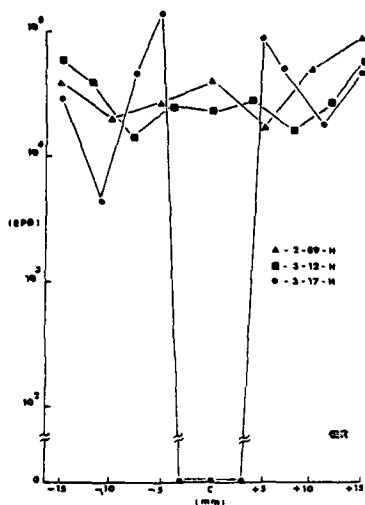


Fig. 1 Etch Pit Densities for Doped InP Crystals  
A. 2-87-H Fe-Doped  
B. 3-12-H 1% by wt. InAs  
C. 3-17-H 4% by wt. InAs



Fig. 2 Micrograph Showing Edge of Central Core for As-Doped Crystal.



Fig. 3 Micrographs of Etched (110) Wafer.

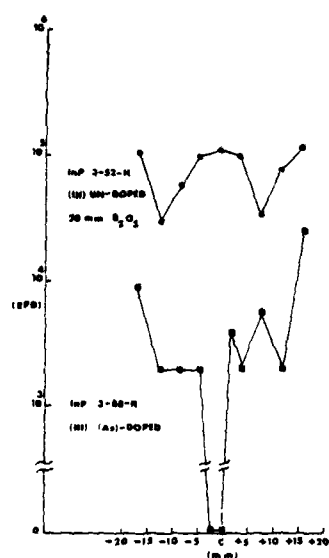


Fig. 4 Etch Pit Density for InP Doped With InAs at 6% by wt.

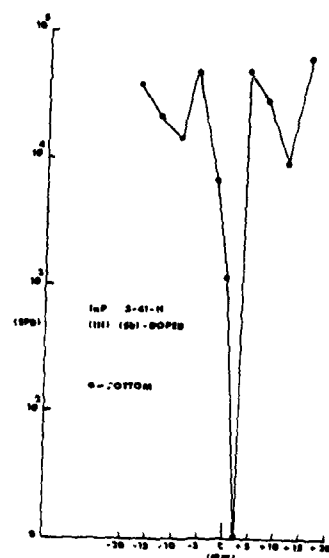


Fig. 5 Etch Pit Density for InP Doped With InSb at 1.4% by wt.

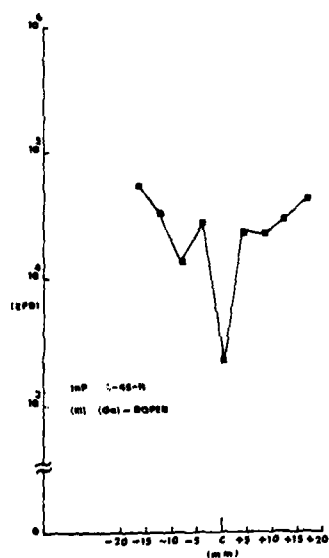


Fig. 6 Etch Pit Density for InP Doped With GaP at .05 wt. %.

## **Isobutylphosphine and tertiarybutylphosphine sources for OMVPE growth of InP**

C.H. Chen, C.A. Larsen, G.B. Stringfellow

Department of Materials Science and Engineering, University of Utah, Salt Lake City, UT 84112, USA

**Abstract:** Isobutylphosphine (IBP) and tertiarybutylphosphine (TBP) are less toxic than phosphine and have been used to grow InP. Excellent morphologies are achieved for IBP at high V/III ratios and low growth temperatures. For TBP, low V/III ratios can be used. Carbon is the dominant acceptor and its incorporation is suppressed at higher temperatures and higher V/III ratios. The carbon concentration is much less with TBP than with phosphine or IBP. Best mobilities are 2800 and 3100 cm<sup>2</sup>/V-sec for IBP and TBP, respectively, with minimum electron densities in the mid 10<sup>16</sup> cm<sup>-3</sup> range.

### **INTRODUCTION**

In less than a decade, organometallic vapor phase epitaxy (OMVPE) has become a leading contender for producing both ultra-pure III/V semiconductors and superlattices (Kawai et al 1985). Problems associated with the purity of group III methyl and ethyl organometallic sources are largely in the past. A major obstacle to further progress in OMVPE and the commercialization of this growth technique lies with the group V sources. The group V hydrides, AsH<sub>3</sub> and PH<sub>3</sub>, have been known for some years to sporadically contain O<sub>2</sub> and H<sub>2</sub>O which results in poor material quality, especially for Al containing alloys (Wagner et al 1981 and Dapkus et al 1981). Even more difficult to deal with is the hazard of using high pressure cylinders of these extremely toxic materials (Cole-Hamilton et al 1984). As a result, costly equipment is needed to make OMVPE systems "absolutely" safe. A third problem for PH<sub>3</sub> is its slow pyrolysis rate (Stringfellow 1984a). This makes it necessary to use high V/III ratios to prevent morphological problems (Stringfellow 1984b). The slow pyrolysis of PH<sub>3</sub> compared with AsH<sub>3</sub> also gives compositional non-uniformity for compounds containing P and As if a temperature gradient exists across the wafer (Stringfellow 1983).

A potential solution for these problems is the use of group V organometallic sources. They are liquids contained in small stainless steel bubblers at atmospheric pressure. This automatically decreases the toxic hazard tremendously. Since they are liquids they should be easily purified and may

ultimately be as pure as the group III organometallic sources. In principle, the molecules might be engineered to pyrolyze at lower temperatures than the hydrides. However, the problem to date has been that the organometallic P sources, triethylphosphine and trimethylphosphine, do not pyrolyze significantly at ordinary growth temperatures (Moss et al 1981 and Renz et al 1980).

We recently reported the first use of IBP and TBP for the growth of device quality InP (Larsen et al 1986 and Chen et al 1986a). The use of these liquid organometallic phosphorus sources reduces the toxic hazard and handling problems associated with the group V hydrides. The material quality is similar to that obtained using  $\text{PH}_3$ . The problem with slow pyrolysis is improved using TBP. Both sources produce  $\text{PH}_3$  which, for IBP, is the primary phosphorus source for the growth process. Preliminary results indicate that TBP produces phosphorus directly, thus allowing the growth of high quality InP layers at lower V/III ratios than either  $\text{PH}_3$  or IBP.

#### EXPERIMENTAL

The reactor, which has been described in detail (Kuo et al 1985), was of the horizontal, atmospheric pressure, cold wall type. The sources used were TMIn, IBP\* and TBP\*. For growth of InP using TMIn and IBP, typical flow rates were 300 cc/min at 17C for TMIn and 500 cc/min at 1-20C for IBP. For growth using TMIn and TBP, typical flow rates were 100-260 cc/min at 7C for TBP and 200 cc/min at 17C for TMIn. The carrier gas was Palladium-diffused hydrogen with a flow rate of 2.5 liter/min. The substrates were semi-insulating InP or GaAs oriented 3 degrees off the (100) orientation toward (110). The morphologies, photoluminescence (PL) spectra, and electrical properties were evaluated on epilayers grown on InP substrates. The epilayers grown on GaAs were used only to determine the epilayer thicknesses. Prior to loading into the reactor, the substrates were etched in A-etch ( $\text{H}_2\text{SO}_4:\text{H}_2\text{O}:\text{H}_2\text{O}_2=5:1:1$ ) for 4 minutes at room temperature.

A He-Ne laser was used in low temperature PL measurements. The excitation intensity was about  $10 \text{ W/cm}^2$ . The conventional lock-in technique was used with a Ge detector cooled to 77K. The van der Pauw method was used to measure the mobility and carrier concentration. The magnetic field intensity was 5 kGauss and the current was 10  $\mu\text{A}$ .

#### RESULTS

InP layers grown using IBP at temperatures of  $580 \leq T \leq 630\text{C}$ , at the proper V/III ratio, have a smooth mirror-like appearance. The values of V/III ratio necessary to obtain good surface morphologies are found to increase with increasing temperature, from a value of 60 at 580C to 110 at 630C.

For InP layers grown using TBP, smooth morphologies could be obtained at lower values of V/III ratio. For example, at 610C, good morphology InP could be grown at a V/III ratio of 26. The ability to grow good morphology layers using TBP with lower values of V/III ratio than for either IBP or  $\text{PH}_3$  is apparently due

to the direct production of phosphorus, as inferred from the data of Larsen et al (1986) and Chen et al (1986a). Using  $\text{PH}_3$ , growth at 650C and a V/III ratio of  $\geq 30$  is routine (Hsu et al 1986 and Fry et al 1985).

6K PL spectra for InP grown using IBP at 600C and values of V/III ratio of 90, 126 and 217 are shown in Fig. 1. Two peaks are observed. The shortest wavelength peak at approximately 873 nm, is attributed to bound exciton (BX) recombination. The peak located at approximately 892 nm is attributed to a donor to acceptor pair transition(DAP), probably involving carbon, as deduced from earlier studies of InP grown using ethyldimethylindium and phosphine (Fry et al 1985). Since Zn also introduces a peak at a similar position in InP, the dependence of intensity on V/III ratio is necessary to make a definitive identification. We see a marked decrease in the ratio of the DAP to the BX peaks with increasing V/III ratio. Since C resides on the P sublattice and Zn on the In sublattice, this V/III ratio dependence indicates the acceptor to be C. The full width at half maximum of the BX peak also becomes narrower for larger V/III ratios, changing from 8.8 meV for a V/III ratio of 90 to 7.8 meV for a V/III ratio of 217. In general, the PL spectra from InP grown using IBP are very similar to samples grown under similar conditions using  $\text{PH}_3$  (Hsu et al 1986 and Fry et al 1985). As reported by Larsen et al (1986) and Chen et al (1986a) the carbon peak decreases rapidly with increasing growth temperature. These results are similar to the decrease in the carbon peak observed in GaInAs grown using TMIn, trimethylgallium (TMGa), and  $\text{AsH}_3$  (Kuo et al 1985), and in InP grown using ethyldimethylindium (EDMIn) and  $\text{PH}_3$  (Fry et al 1985).

9K PL spectra for InP layers grown using TMIn and TBP are shown in Fig. 2 for growth temperatures of 550, 600 and 620C with a constant V/III ratio of 60. Similar to the results for IBP (Larsen et al 1986 and Chen et al 1986a) increasing growth temperature results in a reduction in the ratio of the intensities of the DAP to BX peaks. From the V/III ratio dependence of the DAP peak seen in Fig. 3, we conclude that the acceptor involved is again carbon. The full width at half maximum is about 5 meV for these three samples. These spectra are very different than those presented in Fig. 1. Using TBP the carbon concentration is markedly less than using IBP. This is more clearly seen in Fig. 4 where three spectra are plotted for samples grown at 600C using TMIn and  $\text{PH}_3$ , TBP or IBP using the V/III ratios indicated in the figure. Even though a high V/III ratio is used, the IBP grown InP contains appreciable amount of carbon. But for TBP grown InP, much less carbon is detected using a V/III ratio similar to that for  $\text{PH}_3$ .

The room temperature free electron concentrations for InP samples grown using TMIn and IBP ( 2 different sources) or TBP are plotted versus input V/III ratio during growth in Fig. 5. The V/III ratio dependence of carrier concentration and mobility was measured only for the second, less pure bottle of IBP giving carrier concentrations in the  $10^{17} \text{ cm}^{-3}$  range. The carrier concentration appears to decrease slightly at higher values of V/III ratio. The mobility shows a definite

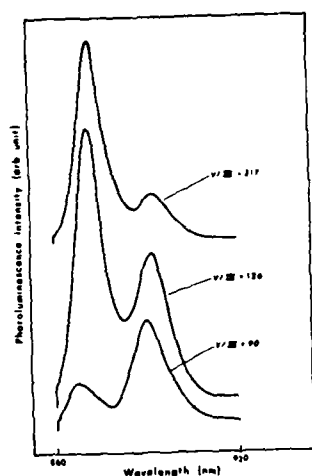


Fig. 1. 6 K photoluminescence spectra of layers of InP grown using TMIn and IBP at three values of V/III ratios: 90, 126, and 217.

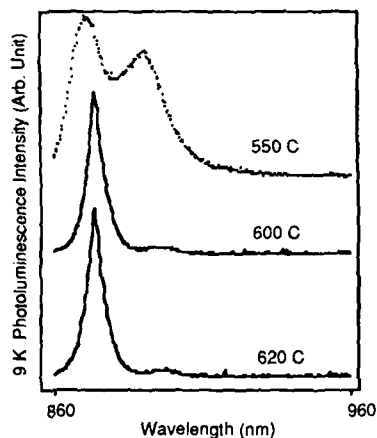


Fig. 2. 9 K photoluminescence spectra for layers of InP grown using TMIn and TBP at a V/III ratio of 60 and several values of growth temperature.

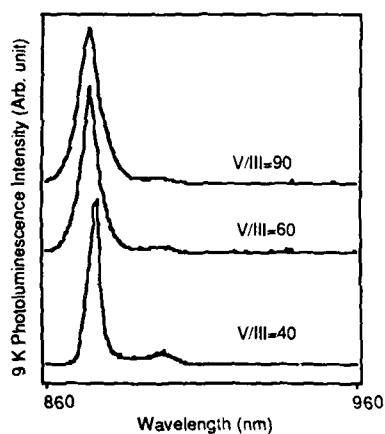


Fig. 3. 9 K photoluminescence spectra for 3 InP epilayers grown using TMIn and TBP at 600 C and values of V/III ratio of 40, 60, and 90.

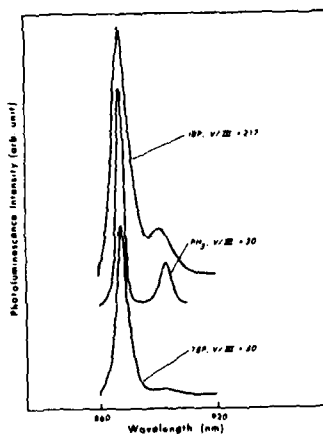


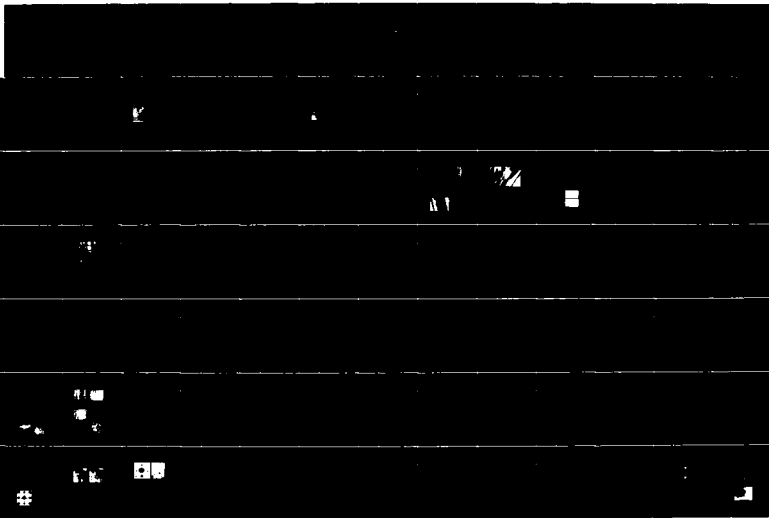
Fig. 4. 9 K photoluminescence spectra for 3 InP samples grown at 600 C using TMIn and IBP, TBP or phosphine.

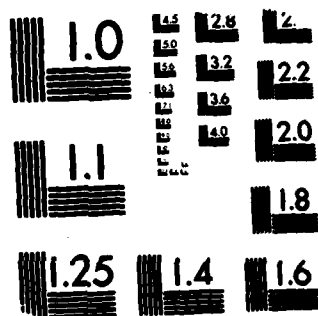
AD-A189 673

GALLIUM ARSENIDE AND RELATED COMPOUNDS 1986(U) ILLINOIS 2/7  
UNIV CHAMPAIGN W T LINDLEY 1986 AFOSR-IR-87-1888  
AFOSR-86-0169

UNCLASSIFIED

F/G 28/2 NL





MICROCOPY RESOLUTION TEST CHART  
NATIONAL BUREAU OF STANDARDS-1963-A



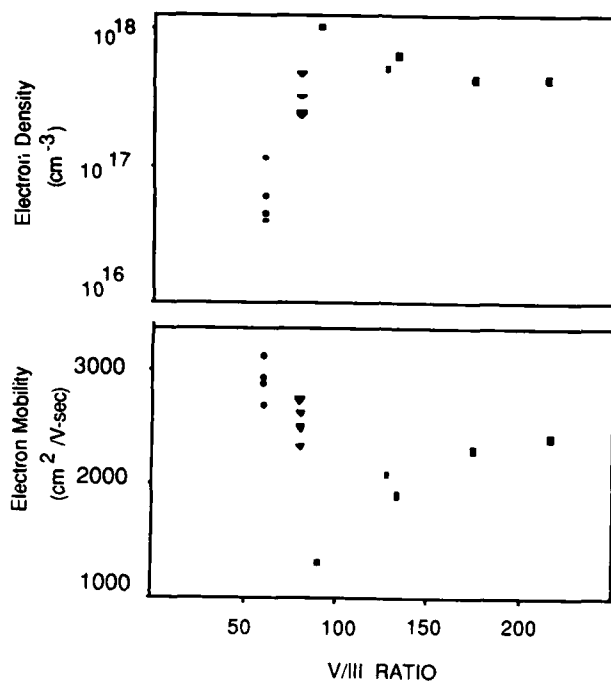


Fig. 5. Electron density and mobility measured at 300 K versus input V/III ratio during growth for InP grown at 600 C and using: (▽) IBP bottle #1, (■) IBP bottle #2, and (●) TBP.

increase with increasing V/III ratio. However, the highest mobilities obtained using the 2nd bottle of IBP are only 2400 cm<sup>2</sup>/Vs. The highest mobility values measured to date were 2800 cm<sup>2</sup>/Vs for the first bottle of IBP and 3100 cm<sup>2</sup>/Vs for TBP, both at low values of V/III ratio. These values are consistent with a total ionized impurity concentration of approximately 5 × 10<sup>16</sup> cm<sup>-3</sup> (Walukiewicz et al 1980). Using TMIn and PH<sub>3</sub>, typical 300 K electron mobilities of 3500 cm<sup>2</sup>/Vs are observed, although the very best TMIn yields room temperature mobilities in excess of 5000 cm<sup>2</sup>/Vs and carrier concentrations of 10<sup>14</sup> cm<sup>-3</sup> (Hsu et al 1986 and Chen et al 1986b) in the same reactor used for the present study.

#### SUMMARY

In conclusion, IBP and TBP have been studied in terms of their potential use as sources for OMVPE growth. The compounds have been used effectively to produce epitaxial layers of InP. The layer purity is found from both Hall effect and low temperature photoluminescence studies to improve dramatically as the V/III ratio is increased to 217 and as the growth temperature is increased from 580 to 630C for IBP. Higher values of V/III ratio are also required to obtain good surface morphologies at higher temperatures. Using TBP, a dramatic increase in layer quality was observed with increasing growth temperature. Somewhat lower values of V/III ratio of approximately 26 can be used to yield excellent morphology layers. In addition, the carbon concentrations for InP layers grown at

a value of V/III ratio of 40 were lower than layers grown at much higher values of V/III ratios using IBP and layers grown using  $\text{PH}_3$  at a similar V/III ratio. For growth temperatures between 600 and 630°C, the best layers have optical and electrical properties which are comparable to similar layers grown with phosphine as the phosphorus source, except that lower values of V/III ratio can be used for TBP due to its more rapid pyrolysis rate. However, neither the IBP nor TBP purity is quite as good as the best  $\text{PH}_3$ . The best values for carrier concentration were in the low  $10^{16} \text{ cm}^{-3}$  region with mobilities of  $2800 \text{ cm}^2/\text{Vs}$  for growth using IBP and  $3100 \text{ cm}^2/\text{Vs}$  for TBP. Due to the much lower safety risks of IBP and TBP, and the potential for higher purity compared to phosphine, it is expected that they may fill a significant need in the OMVPE growth of phosphorus containing III/V semiconductors.

#### Acknowledgements

This research at the University of Utah was supported by a grant from American Cyanamid Company. We also thank D. Brown of American Cyanamid Company for supplying the isobutylphosphine and tertbutylphosphine.

#### References

- \*CYPURE \*\* : Isobutylphosphine and tertbutylphosphine CVD sources are available in electronic grade purity from Electronics Chemicals Department, American Cyanamid Company, Wayne New Jersey.  
 \*\*Trademark of American Cyanamid Company.
- Chen C H, Larsen C A, Stringfellow G B, Brown D W and Robertson A J 1986 a J. Crystal Growth (to be published).  
 Chen C H, Kitamura M, Cohen R M and Stringfellow G B 1986b Appl. Phys. Lett. (to be published).  
 Cole-Hamilton D J 1984 J. Cryst. Growth 68, xi  
 Dapkus P D, Manasevit H M and Hess K L 1981 J. Cryst. Growth 55, 10  
 Fry K L, Kuo C P, Cohen R M and Stringfellow G B 1985 Appl. Phys. Lett. 46, 955  
 Hsu C C, Yuan J S, Cohen R M, and Stringfellow G B 1986 J. Crystal Growth 74, 535  
 Kawai H, Kaneko J, and Watanabe N 1985 J. Appl. Phys. 58, 1263  
 Kuo C P, Cohen R M, Fry K L, and Stringfellow G B 1985 J. Electron. Mater. 14, 231  
 Larsen C A, Chen C H, Kitamura M, Stringfellow G B, Brown D W and Robertson A J 1986 Appl. Phys. Lett. 48, 1531  
 Moss R H and Evans J S 1981 J. Cryst. Growth 55, 129  
 Renz H, Weidlein J, Benz K W and Pilkuhn M H 1980 Electron. Lett. 16, 6.  
 Stringfellow G B 1983 J. Crystal Growth 62, 225  
 Stringfellow G B 1984a J. Crystal Growth 68, 111  
 Stringfellow G B 1984b J. Crystal Growth 70, 133  
 Wagner E E, Horn G and Stringfellow G B 1981 J. Electron. Mater. 10, 239  
 Walukiewicz W, Lagowski J, Jastrzebski L, Rava P, Lichtensteiger M, and Gatos C H 1980 J. Appl. Phys. 51, 2659

## High mobility, low compensation GaAs grown by OMVPE

S.K. Shastri, S. Zemon, and P. Norris

GTE Laboratories Incorporated, 40 Sylvan Road, Waltham, MA 02254

**Abstract:** High purity epitaxial GaAs with very high electron mobility ( $190,000 \text{ cm}^2/\text{V.s}$  at 77 K) and low compensation ( $N_A/N_D < 0.05$ ,  $N_D = 1.21 \times 10^{14} \text{ cm}^{-3}$ ) has been reproducibly grown by low pressure organometallic vapor phase epitaxy.

### 1. Introduction

The utility of GaAs and related compounds for high-speed electronic and optoelectronic device applications is well known. These applications require high carrier mobility, and therefore high purity and low compensation material. However, high mobility, epitaxial GaAs layers grown on (100)GaAs substrates by liquid-phase epitaxy (Miki and Otsubo 1971), vapor-phase epitaxy (Wolfe and Stillman 1975), or molecular beam epitaxy (Larkins et al 1986) are often compensated ( $N_A/N_D = 0.15-0.6$  where  $N_A$  and  $N_D$  are the acceptor and donor concentrations, respectively). Further, these layers are obtained only after quite elaborate baking of the epitaxial growth systems. Epitaxial GaAs layers grown by organometallic vapor-phase epitaxy (OMVPE) have thus far fared poorly ( $N_A/N_D = 0.4-0.8$ ), with total impurity concentrations being about  $1 \times 10^{15} \text{ cm}^{-3}$ , and often more (Nakanishi et al 1981, Dapkus et al 1981, Bhat et al 1982, Shealy et al 1983, Roth et al 1983, Kuech and Potemski 1985). The only reported work on low compensation ( $N_A/N_D = 0.06$ ) GaAs was on (211)A-substrates grown by  $\text{AsCl}_3$  VPE (Colter et al 1983), and this precludes direct comparison to results obtained with the commonly used (100)-substrates.

We have grown high purity ( $N_D - N_A = N_D = 1.21 \times 10^{14} \text{ cm}^{-3}$ ) GaAs layers by low pressure OMVPE in a vertical reactor. Previously, epitaxial GaAs layers with 77 K electron mobilities of  $130,000-140,000 \text{ cm}^2/\text{V.s}$  were grown in this reactor (Black et al 1985). These layers were, however, compensated ( $N_A/N_D = 0.7$ ,  $N_A = 2 \times 10^{14} \text{ cm}^{-3}$ ), and the dominant residual impurity was carbon. We have now obtained higher purity ( $N_A < 10^{13} \text{ cm}^{-3}$ ) GaAs layers by eliminating system leaks and reducing contamination sources. The present layers are reproducibly and routinely grown on 2-in. diameter substrates without extensive baking or purging of the OMVPE system. In this paper, we report on the factors contributing to the growth of such high purity material.

### 2. Experimental Procedure

The epitaxial layers were grown on undoped LEC semi-insulating GaAs substrates. They were (100)-oriented with  $2^\circ$  off toward (110) and a quoted dislocation density of  $5 \times 10^4 \text{ cm}^{-2}$ . The polished, as-purchased GaAs substrate was dipped in dilute (10%) HCl, blown dry, and loaded into the vertical, RF-heated reactor via a load-lock arrangement. The substrate was then heat-treated at  $600^\circ\text{C}$  for 10 minutes under arsine (56 sccm) and hydrogen (5 slm) flows. Using triethylgallium (TEG), a  $0.5\text{-}\mu\text{m}$  thick GaAs buffer layer was then grown at  $600^\circ\text{C}$ ; growth was further continued for 4-5 hours at a desired temperature, between  $550^\circ\text{C}$  and  $700^\circ\text{C}$ , with a growth rate of about  $40 \text{ nm/min}$ . This amounted to an arsine:TEG mole ratio of 17.5 at the inlet of the reactor. (This is referred to as the V:III or As:Ga ratio in this paper.) Some experiments were carried out at different V:III ratios, between 8 and 65, by varying the arsine flow rate. All the experiments were carried out at 50 Torr.

Hall and Van der Pauw measurements were made at 300 K and 77 K under room light with magnetic flux densities of  $0.2-0.5 \text{ T}$  and sample currents of  $2.5-100 \text{ }\mu\text{A}$  using an automated measurement system. The layer thicknesses were measured by cleaving and staining, and corrections were made for interface and surface depletions (Chandra et al 1979). Carrier

concentrations were also measured by C-V profiling to confirm the Hall effect measurements. Compensation was estimated using the empirical curve of Wolfe et al (1970). Photoluminescence (PL) and magnetophotoluminescence (MPL) measurements were made at 4.2 K (Zemon et al 1986).

### 3. Results and Discussion

In the initial stages of this study, it was found that using molecular sieve filters at the outlet of the arsine tank and at the inlet of the vacuum pump was essential to improve the purity of the GaAs layers. The former filter caused a reduction mainly in the donor concentration while the latter reduced the acceptor concentration. PL measurements indicated this acceptor to be carbon. All the work reported in this paper was carried out by incorporating these filters. The epitaxial layers thus grown were smooth, featureless, and uniform in thickness within  $\pm 10\%$ . They were n-type with net carrier concentrations ranging from about  $2 \times 10^{13} \text{ cm}^{-3}$  to  $4 \times 10^{14} \text{ cm}^{-3}$ . Hall data on layers grown between  $550^\circ\text{C}$  and  $700^\circ\text{C}$  with V:III ratio of 17.5 are shown in Table I. A reduction in 77 K mobility and an increase in the impurity concentrations are seen for layers grown below  $600^\circ\text{C}$  and above  $650^\circ\text{C}$ . Figure 1 shows the residual donor and acceptor concentrations as a function of growth temperature over the range of  $550^\circ\text{C}$  to  $700^\circ\text{C}$ . The open circles and closed triangles represent  $N_D$  and  $N_A$ , respectively.  $N_D$  increases with an activation energy ( $E_D$ ) of about 2.8 eV for growths above  $650^\circ\text{C}$ . This value of  $E_D$  is close to the dissociation energy of silane or organosilane species (Weast 1984); thus, the donor species could be Si.  $N_A$  increases with an activation energy ( $E_A$ ) of about 6 eV. This is unusually high, and hence is unlikely to be due to a simple surface activated process. We note that in the vertical RF-heated reactor, even at 50 Torr, convection flows of vapors increasingly take place above  $650^\circ\text{C}$ . Thus, the rapid increase in  $N_A$  could be due to the recycling of reaction products onto the growth surface or due to the formation of defect complexes at the higher growth temperatures.

For layers grown below  $600^\circ\text{C}$ , both  $N_D$  and  $N_A$  increase as the growth temperature is decreased, with  $E_D$  of about 1.8 eV and  $E_A$  of about 3.2 eV. This temperature dependence is similar to that of S (Bass and Oliver 1977) and Zn (Bass and Oliver 1977, Glew 1984) doping in OMVPE GaAs. Additionally,  $E_A$  of 3.2 eV is close to the C-H bond strength (Weast 1984). Thus the residual impurities in these layers could be S, Zn, and C. The layer grown at  $550^\circ\text{C}$  is nearly compensated, though its 77K mobility is unusually high for such low growth. This is probably due to the still comparatively low impurity concentration ( $<10^{15} \text{ cm}^{-3}$ ) and the associated long relaxation time for the ionized impurity scattering process.

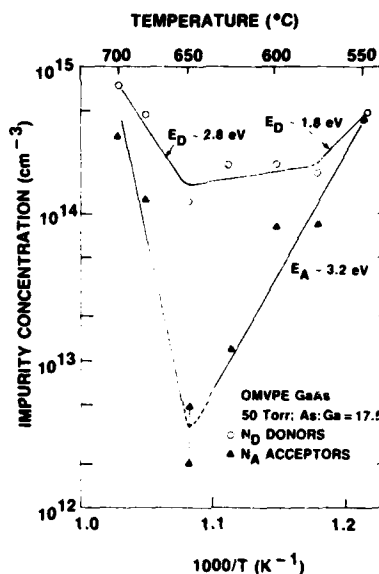


Fig. 1 Variation of residual impurity concentrations as a function of growth temperature for V:III ratio of 17.5

Table I Hall data on 10- to 12- $\mu\text{m}$  thick OMVPE GaAs layers (V/III = 17.5)

| Growth temp ( $^\circ\text{C}$ ) | $N_D$ ( $10^{14} \text{ cm}^{-3}$ ) | $N_A/N_D$ | $\mu_{77}^*$ ( $\text{cm}^2/\text{V.s}$ ) |
|----------------------------------|-------------------------------------|-----------|---|
| 550                              | 4.60                                | 0.95      | 98,000                                    |
| 575                              | 1.78                                | 0.46      | 149,000                                   |
| 600                              | 2.20                                | 0.36      | 153,000                                   |
| 625                              | 2.12                                | 0.06      | 166,000                                   |
| 650                              | 1.21                                | <.05      | 190,000                                   |
| 675                              | 4.75                                | 0.26      | 111,400                                   |
| 700                              | 7.50                                | 0.4       | 86,000                                    |

\*  $\mu_{300} = 6800\text{--}8500 \text{ cm}^2/\text{V.s}$

The layers grown between 600°C and 650°C exhibit high 77 K electron mobility and very low residual acceptor concentration.  $N_D$  is typically  $1-2 \times 10^{14} \text{ cm}^{-3}$  while  $N_A$  is an order of magnitude or more lower in these layers. The highest mobility layer (grown at 650°C) had a  $\mu_{77}$  of 190,000  $\text{cm}^2/\text{V}\cdot\text{s}$ , the highest reported for OMVPE GaAs at this temperature. The estimated value of  $N_A$  is not more than  $5 \times 10^{12} \text{ cm}^{-3}$ , while  $N_D$  is  $1.21 \times 10^{14} \text{ cm}^{-3}$ . The uniformity over the 2-in. diameter wafer is excellent, with  $\mu_{77}$  varying by about 12%. Such low compensation layers have been reproducibly grown over 6 times in the present work.

Figure 2 shows the 4.2 K PL spectra of the GaAs layers grown at 550°C, 600°C, and 650°C with a V:III ratio of 17.5. It is seen that the PL amplitude in the acceptor region is very much less than that in the exciton region. This is indicative of low shallow acceptor concentration in these layers. Figure 3 shows on an expanded scale the exciton region for a sample grown at 625°C with V:III ratio of 17.5. We note that the acceptor bound exciton line ( $A^0$ , X) is over two orders of magnitude smaller than the donor bound exciton line ( $D^0$ , X), indicating very low compensation consistent with the Hall data. Additionally, the PL line widths are sharp [0.15 meV full-width-half-maximum for the ( $D^0$ , X) line], and the excited states [ $(D^0, X)^*$ ] of the ( $D^0$ , X) line are well delineated, characteristic of material with impurity concentration in the low  $10^{14} \text{ cm}^{-3}$  range (Skromme et al 1985). These results are similar to those reported for low compensation, high purity hydride (Abrokwa et al 1983) and chloride (Colter et al 1983, Dorrity et al 1985) VPE GaAs.

Figure 4 shows the PL and MPL data for our high purity sample of Fig. 3. The three sharp acceptor MPL (2.5 T) lines are denoted (Zemon et al 1986) as free-to-bound acceptor lines ( $e, A^0_C$ ), ( $e, A^0_{Mg/Be}$ ), and ( $e, A^0_{Zn}$ ), while the remaining three broad lines (Ashen et al 1975) are the companion donor-to-acceptor lines ( $D^0, A^0_C$ ), ( $D^0, A^0_{Mg/Be}$ ), and ( $D^0, A^0_{Zn}$ ). The TO and LO phonon replicas of the free exciton emission ( $X_{TO}$  and  $X_{LO}$ ) and the LO phonon replica of the ( $D^0$ , X) line are also identified (Skromme et al 1983). Another demonstration of the reductions in the acceptor PL intensity in the low compensation GaAs can be seen from comparing the PL amplitude of the acceptor lines to that of  $X_{LO}$  transition. The latter is a higher order intrinsic process. Thus, it is expected to be weak and independent of the degree of compensation. From Fig. 4, the ratio is on the order of 10:1, while for typical high purity compensated material, the ratio is much larger, on the order of 400:1 (Zemon and Lambert 1986). Preliminary MPL results for donor identification via the "two electron" replica of the donor bound exciton (Dean

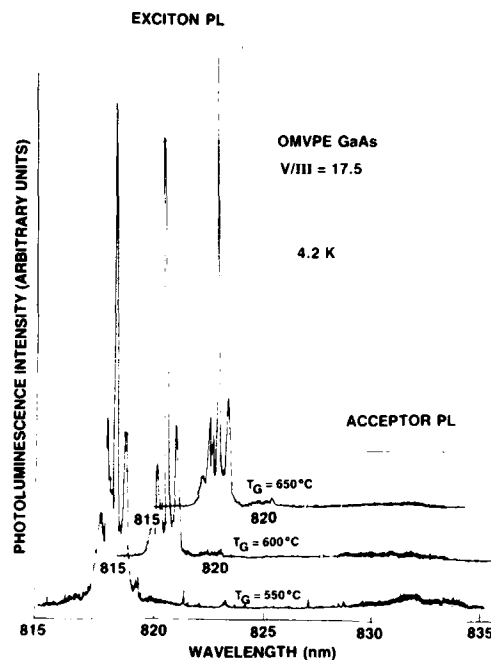


Fig. 2 4.2-K PL spectra for high purity OMVPE GaAs grown at 550°C, 600°C, and 650°C (V:III = 17.5). The excitation intensity was  $0.5 \text{ mW}/\text{cm}^2$ . For clarity, the x-axis for the exciton spectra is shifted.

et al 1984, Reynolds et al 1984) indicate that the residual donors are mainly Si and Ge with sulphur often present in lesser amounts.

Acceptor region MPL spectra of GaAs layers grown at temperatures  $> 675^\circ\text{C}$  did not reveal any sharp ( $e$ ,  $A^0$ ) structure, suggesting that the concentration of shallow acceptors is further decreased. The high concentration of residual acceptors as determined from the Hall data (Table I) therefore signifies the presence of compensating defect complexes in these layers. The MPL spectra of layers grown at temperatures  $\leq 600^\circ\text{C}$  revealed Zn and C as the main acceptors present. An activation energy  $E_A$  of 3.2 eV derived from Fig. 1 also suggests that this is the case.

Table II shows the Hall effect data of GaAs layers grown at  $575^\circ\text{C}$  for different V:III ratios. All the layers have low total impurity concentration ( $< 5 \times 10^{14} \text{ cm}^{-3}$ ), and hence high 77 K electron mobility. They are, however, compensated. Here, both  $N_D$  and  $N_A$  slightly increase with increasing V:III ratio. PL spectra indicate that Zn and C are the main acceptors in these layers, the latter being reduced at the higher V:III ratio. Compensation in the present GaAs layers grown at the low temperature ( $< 600^\circ\text{C}$ ) appears to be due to shallow acceptors other than defect complexes.

Table III shows the Hall effect data of the layers grown at  $650^\circ\text{C}$  for different V:III ratios. Layers grown at low V:III ratios ( $< 40$ ) have low total impurity concentration ( $< 3 \times 10^{14} \text{ cm}^{-3}$ ) and low compensation. Both  $N_D$  and  $N_A$  initially decrease (around  $V/\text{III} = 17.5$ ) and then increase with increasing V:III ratio. PL spectra indicate Zn as the main residual acceptor in layers grown at low V:III ratio. However, no shallow acceptor could be identified by PL in layers grown at high V:III ratios ( $\geq 50$ ), although electrical measurements indicate an increasing amount of acceptors. This could be due to defect complexes formed under high V:III ratio growth conditions. The dominant residual donors in these layers appear to be Ge and Si. These assignments satisfactorily agree with the impurity activation energies derived from Fig. 1.

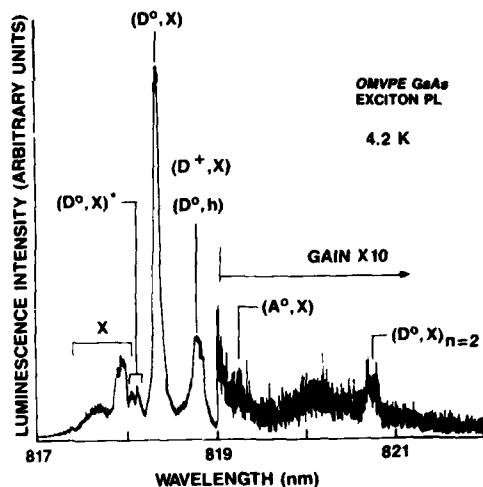


Fig. 3 A high resolution (0.01 nm) PL spectrum of a sample grown at  $625^\circ\text{C}$  with V:III ratio of 17.5

Table II Hall data for GaAs layers grown at  $575^\circ\text{C}$

| V:III ratio | $N_D$<br>( $10^{14} \text{ cm}^{-3}$ ) | $N_A/N_D$ | $\mu_{77}^*$<br>( $\text{cm}^2/\text{V.s}$ ) |
|-------------|--|-----------|--|
| 17.5        | 1.78                                   | 0.46      | 149,000                                      |
| 45.0        | 1.00                                   | 0.40      | 160,000                                      |
| 65.0        | 2.96                                   | 0.53      | 133,000                                      |

\* $\mu_{300} = 6800\text{--}7700 \text{ cm}^2/\text{V.s}$

#### 4. Summary

High purity, low compensation GaAs layers have been grown reproducibly on 2-in. diameter substrates by low pressure OMVPE. The highest purity sample had total impurity concentration of  $1.24 \times 10^{14} \text{ cm}^{-3}$  and compensation of less than 0.05. The 77 K electron mobility was 190,000  $\text{cm}^2/\text{V.s.}$  Zn, C, S, and Ge are the main impurities for layers grown below 600°C; amounts of C and S decrease for growths at higher temperatures. Compensation in layers grown at lower ( $\leq 600^\circ\text{C}$ ) temperatures appears to be due to shallow acceptors, while in layers grown at higher ( $>650^\circ\text{C}$ ) temperatures, it appears to be due to defect complexes. Nonetheless, almost all the layers have low ( $< 5 \times 10^{14} \text{ cm}^{-3}$ ) total ionized impurities, and the PL spectra show features typical of such high purity GaAs.

#### Acknowledgments

We thank Drs. P. Haugsjaa and H. Lockwood for support and encouragement, M. DeAngelis and G. Lambert for assistance and measurements, and P. Tavilla and F. Lisherness for manuscript preparation.

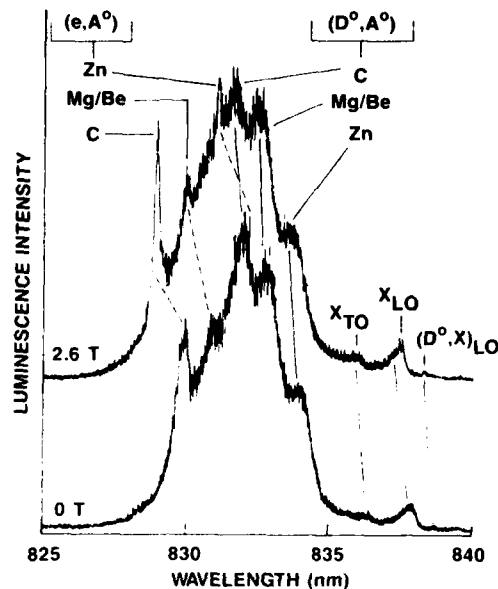


Fig. 4 4.2-K PL of the acceptor region in zero magnetic field and at 2.6 T for the sample of Fig. 3. The MPL spectrum was taken with the sample in the Faraday configuration for left circularly polarized luminescence. Lines are drawn between the zero field and 2.6-T spectra connecting equivalent luminescence transitions.

Table III Hall data for GaAs layers grown at 650°C

| V:III ratio | $N_D$<br>( $10^{14} \text{ cm}^{-3}$ ) | $N_A/N_D$ | $\mu_{77}^*$<br>( $\text{cm}^2/\text{V.s.}$ ) |
|-------------|--|-----------|---|
| 8.0         | 2.70                                   | 0.11      | 150,500                                       |
| 17.5        | 1.21                                   | <.05      | 190,000                                       |
| 40.0        | 2.27                                   | 0.03      | 130,000                                       |
| 50.0        | 3.10                                   | 0.35      | 124,000                                       |

\* $\mu_{300} = 7800\text{--}8500 \text{ cm}^2/\text{V.s.}$

**References**

- Abrokwha J K, Peck T N, Walterson R A, Stillman G E, Low T S, and Skromme B J 1983 *J. Electron. Mater.* **12** 681
- Ashen D J, Dean P J, Hurle D T J, Mullin J B, and White A M 1975 *J. Phys. Chem. Solids* **36** 1041
- Bass S J and Oliver P E 1977 *Gallium Arsenide and Related Compounds 1976* (Inst. Phys. Conf. Ser. No 33b) pp. 1-10
- Bhat R, O'Connor P, Temkin H, Dingle R, and Keramidas V C 1982 *Gallium Arsenide and Related Compounds 1981* (Inst. Phys. Conf. Ser. No. 63) pp. 101-106
- Black J, Norris P, Koteles E, and Zemon S 1985 *Gallium Arsenide and Related Compounds 1984* (Inst. Phys. Conf. Ser. No. 74) pp. 683-684
- Chandra A, Wood C E C, Woodard W, and Eastman L F 1979 *Solid State Electronics* **22** 645
- Colter P C, Look D C, and Reynolds R C 1983 *Appl. Phys. Lett.* **43** 282
- Dapkus P D, Manasevit H M, Hess K L, Low T S, and Stillman G E 1981 *J. Cryst. Growth* **55** 10
- Dean P J, Skolnick M S, and Taylor L L 1984 *J. Appl. Phys.* **55** 957
- Dorrity I A, Hewins D, and Medland J D 1985 *Gallium Arsenide and Related Compounds 1984* (Inst. Phys. Conf. Ser. No. 74) pp. 211-216
- Glew R W 1984 *J. Cryst. Growth* **68** 44
- Kuech T F and Potemski R 1985 *Appl. Phys. Lett.* **47** 821
- Larkins E C, Hellman E S, Schlom D G, Harris Jr. J S, Kim M H, and Stillman G E 1986 *Appl. Phys. Lett.* **49** 391
- Miki H and Otsubo M 1971 *Japan. J. Appl. Phys.* **10** 509
- Nakanisi T, Udagawa T, Tanaka A, and Kamei K 1981 *J. Cryst. Growth* **55** 255
- Reynolds D C, Colter P C, Litton C W, and Smith E B 1984 *J. Appl. Phys.* **55** 1610
- Roth A P, Charbonneau S, and Goodchild R G 1983 *J. Appl. Phys.* **54** 5350
- Shealy J R, Kreismanis V G, Wagner D K, Xu Z Y, Wicks G W, Schaff W J, Ballantyne J M, Eastman L F, Skromme B J, and Stillman B J 1983 *Gallium Arsenide and Related Compounds 1982* (Inst. Phys. Conf. Ser. No. 65) pp. 109-116
- Skromme B J, Low T S, Roth T J, Stillman G E, Kennedy J K, and Abrokwha J K 1983 *J. Electron. Mater.* **12** 433
- Skromme B J, Bose S S, Lee B, Low T S, Lepkowski T R, DeJule R Y, Stillman G E, and Hwang J C M 1985 *J. Appl. Phys.* **58** 4685
- Weast R C 1984 *CRC Handbook of Chemistry and Physics* (Boca Raton, Florida: CRC) pp. F172-F183
- Wolfe C M, Stillman G E, and Dimmock J O 1970 *J. Appl. Phys.* **41** 504
- Wolfe C M and Stillman G E 1975 *Appl. Phys. Lett.* **27** 564
- Zemon S, Norris P, Koteles E S, and Lambert G 1986 *J. Appl. Phys.* **59** 2828
- Zemon S and Lambert G 1986 (Private Communication)



## **Rare-earth ion-doped InP grown by metalorganic chemical vapor deposition**

Kunihiko Uwai, Hiroshi Nakagome and Kenichiro Takahei

NTT Electrical Communications Laboratories  
3-9-11, Midori-cho, Musashino-shi, Tokyo 180, Japan

**Abstract** Yb is doped into InP epitaxial layers by metalorganic chemical vapor deposition for the first time. The Yb-doped InP shows n-type conductivity. Sharp photoluminescence lines due to Yb intra 4f shell transitions are observed at 4.2K, showing a marked increase in linewidths with increasing temperatures. Above 80K, the Yb emission intensity is found to decrease more rapidly with increasing temperatures than the near band-edge emission intensity.

### **1. Introduction**

Rare-earth ions are known to exhibit sharp emission lines due to intra 4f shell transitions and have been used for laser materials such as Nd in yttrium aluminum garnet (YAG) (Kaminskii 1981). Though the hosts of rare-earth-doped laser materials have been limited to insulators, semiconductor hosts have an advantage because of the possibility of fabricating light emitting devices using minority carrier injection. Rare-earth ions in II-VI semiconductors have been extensively studied for applications as electroluminescent devices (Anderson et al 1965, Anderson 1966). However, III-V semiconductors are potentially superior to II-VI semiconductors as host materials for rare-earth doping because most rare-earth elements take a trivalent state, or an isovalent state at cation sites when doped into III-V materials. Moreover, advanced technology of III-V semiconductor crystal growth and processing allows suitable material tailoring for fabricating rare-earth doped optical devices.

However, in spite of the obvious advantages mentioned above, rare-earth ion doping into III-V semiconductors was not realized until the late 1970s and early 1980s when two groups began studying the optical properties of several rare-earth ions in binary III-V semiconductors (Kasatkin et al 1978, Ennen et al 1983). These two groups successfully synthesized rare-earth doped III-V semiconductors and observed characteristic sharp lines arising from 4f electrons of rare-earth ions at low temperatures. However, the possibility of growing high-quality epitaxial layers doped with rare-earth elements has not been extensively explored except in a few pioneering experiments (Haydl et al 1985).

Epitaxial growth of high-quality rare-earth doped III-V semiconductors is essential for the fabrication of thin film optical devices. Furthermore, the use of epitaxial layers for definite material characterization is advantageous because the quality of epitaxial layers is usually superior to that of bulk crystals. Since a lower background doping level can be achieved by epitaxial growth owing to lower growth temperatures (usually

lower than 600°C), the possible association of rare-earth ions with unintentionally doped elements can be avoided. Thus, optical spectra from epitaxial layers are more likely to be caused by isolated rare-earth elements. This greatly simplifies the identification of the origin of these spectra.

Liquid phase epitaxy (LPE) is usually the simplest method for growing high-quality layers. However, low solubility of rare-earth atoms into a molten column III-B metal and small distribution coefficients of rare-earth materials prevent us from growing highly doped epitaxial layers by LPE. Moreover, the higher growth temperatures needed to overcome these obstacles probably cause increased contamination from the apparatus.

Growth processes controlled by mass transport such as metalorganic chemical vapor deposition (MOCVD) and molecular beam epitaxy are suitable for doping elements with small distribution coefficients. We have successfully grown rare-earth (Yb) doped InP by MOCVD using cyclopentadienyl compounds of ytterbium. MOCVD has some advantages over other growth methods. Using metalorganics of rare-earth elements, we can avoid exposing these highly active metallic elements to oxygen and hydrogen when growing epitaxial layers. Furthermore, a variety of purifying methods can be used at stages of synthesizing metalorganics. This paper describes the growth procedure and the electrical as well as optical characteristics of Yb-doped InP.

## 2. Experimental

Yb-doped InP epitaxial layers were grown on Fe-doped semi-insulating InP substrates by low-pressure (0.1atm) MOCVD using triethylindium ( $\text{In}(\text{C}_2\text{H}_5)_3$ ), phosphine ( $\text{PH}_3$ ) and tris-cyclopentadienyl ytterbium ( $\text{Yb}(\text{C}_5\text{H}_5)_3$ ). The undoped layers were of the n-type with electron concentrations of  $10^{15} \sim 10^{16} \text{cm}^{-3}$  at room temperature. Growth conditions for undoped layers have been described elsewhere in detail (Uwai et al 1985).

Yb was doped by sublimating and transporting  $\text{Yb}(\text{C}_5\text{H}_5)_3$  with  $\text{H}_2$  flow. Doping concentrations were varied by varying container temperatures of  $\text{Yb}(\text{C}_5\text{H}_5)_3$ . Typical growth temperatures were in the range from 550 to 650°C.

Yb concentrations in grown layers were determined by secondary ion mass spectroscopy (SIMS) calibrated by inductively coupled plasma (ICP) atomic emission spectroscopy. The calibration method is described elsewhere (Uwai et al 1986). Electrical characteristics were examined by the van der Pauw method using rectangularly shaped samples.

PL was excited with a He-Ne laser operating at 632.8nm and analyzed with a 1.25-m monochromator coupled with a cooled Ge p-i-n detector. Detailed structures due to intra 4f shell transitions in Yb were measured at 4.2K with a wavelength resolution of 0.1nm. Temperature dependence of PL spectra was also investigated between 4.2K and 200K. No corrections for monochromator and detector response have been made.

## 3. Results

Surface morphology of grown layers was inspected using a differential interference microscope. The layers with rare-earth concentrations below  $10^{15} \text{cm}^{-3}$  show specular featureless surfaces. With increasing Yb concentrations up to  $5 \times 10^{16} \text{cm}^{-3}$ , epitaxial layer surfaces show a wavy structure. Further increases in Yb concentrations to  $1 \times 10^{18} \text{cm}^{-3}$  results in a rough surface. Although growth conditions are not yet optimized, these results

suggest that the epitaxial growth process is seriously affected by Yb incorporation during growth. However, it is noteworthy that the shape of a PL spectrum due to intra 4f shell transitions measured at 4.2K is not affected by Yb incorporation in this concentration range in spite of the significant change of the surface morphology and the PL intensity.

The effect of rare-earth doping on electrical characteristics of the grown layers was investigated by varying doping concentrations. All of the Yb-doped layers show n-type conductivity, irrespective of Yb concentrations. Table I summarizes carrier concentrations and Hall mobilities of two layers with different Yb concentrations. The measurements were made at 300K and 77K by the van der Pauw method. Ratios of carrier concentrations at 77K to those at 300K  $n(77K)/n(300K)$ , which indicate the degree of carrier freeze-out, are also shown. Yb concentrations determined by SIMS are shown in the right-hand column of the table.

Table I. Electrical characteristics of Yb-doped layers

| Sample | Carrier Concentrations<br>( $10^{16}\text{cm}^{-3}$ ) |     | $n(77K)/n(300K)$ | Hall Mobilities<br>( $10^3\text{cm}^2/\text{Vs}$ ) |      | Yb Concentrations*<br>( $\text{cm}^{-3}$ ) |
|--------|---|-----|------------------|--|------|--|
|        | 300K  | 77K |                  | 300K   | 77K  |  |
| MOJ    | 2.1   | 1.5 | 0.7              | 3.7  | 13.0 | $4 \times 10^{14}$                         |
| MOL    | 4.0   | 1.7 | 0.4              | 3.4  | 7.6  | $5 \times 10^{16}$                         |

\*determined by SIMS.

Sample MOJ, which is lightly doped with Yb, shows carrier concentrations and mobilities similar to those of undoped layers without serious carrier freeze-out at 77K ( $n(77K)/n(300K) \sim 0.7$ ). In contrast, sample MOL, which shows only a slight increase in the carrier concentration at 300K from the value of MOJ, shows a significant carrier freeze-out ( $n(77K)/n(300K) \sim 0.4$ ).

PL characteristics are investigated for sample MOL at temperatures between 4.2K and 200K. At 4.2K the sample exhibits sharp emission lines characteristic of Yb intra-4f-shell transitions near 1.23eV (Ennen et al 1983) with weaker near band-edge emissions which consist of free exciton (or band-to-band) recombination and band-to-acceptor recombination, as shown in Fig.1. Figure 2 shows an enlargement of Yb lines. As can be seen from the figure, a few distinct zero-phonon lines (ZPL's) are observed with acoustic phonon sidebands. One- and two-phonon replicas appear at lower energies as shown in Fig.3. Lines are numbered using the notation given by Ennen et al (1983). (Lines 18 and 19 have not been resolved for ion implanted samples (Ennen et al 1983).)

If we assume that the contributing phonon energy is  $310.2 \pm 1\text{cm}^{-1}$  ( $38.5 \pm 0.1\text{meV}$ ), which is close to the energy of the local phonon in InP (Tapster et al 1981, Tapster et al 1982, Skolnick et al 1983), we can make the assignment of phonon replicas as shown in Fig.3. (The notation " $n-m\omega$ " in Fig.3 means the  $m$ -phonon replica of ZPL # $n$ .) Line 12 is located  $347.5\text{cm}^{-1}$  ( $43.1\text{meV}$ ) below ZPL 4. This energy is close to the longitudinal optical phonon energy in InP (Mooradian and Wright 1966). Furthermore, we observed a small shoulder at the higher energy side of line 12 and a peak between lines 12 and 13, which are not yet identified.

Temperature dependence of the Yb-related spectrum is shown in Fig.4. In this figure, ZPL's 3, 4, and 8 at 4.2K, 28K, 43K and 82K are shown together

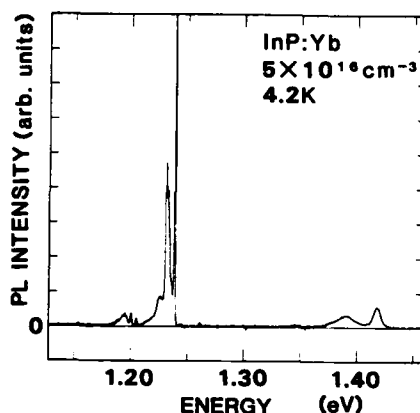


Fig.1 PL spectrum of sample MQL (Yb concentration  $\sim 5 \times 10^{16} \text{ cm}^{-3}$ ) at 4.2K.

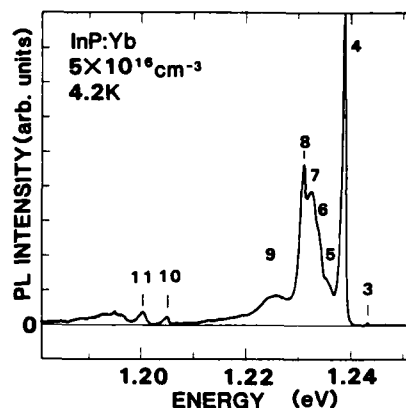


Fig.2 Yb PL lines of sample MQL at 4.2K. Lines are numbered following Ennen et al (1983).

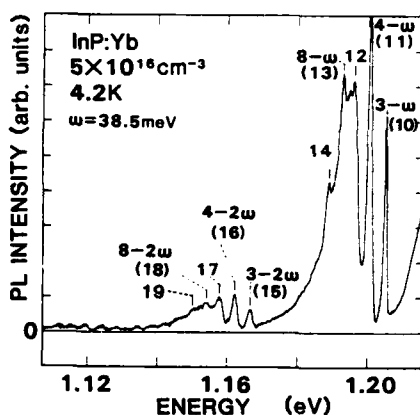


Fig.3 One- and two-phonon replicas of Yb lines shown in Fig.2 at 4.2K. The notation "n-w" means the n-phonon replica of ZPL #n due to the local phonon with the energy of 38.5 meV.

with the phonon sidebands. At temperatures from 4.2K to 10K, the spectrum as well as its intensity remain essentially unchanged. At 43K, however, two ZPL's denoted by 4 and 8 decrease in peak height and notably increase in full width at half maximum (FWHM). At this temperature, ZPL 8 can not be observed as a distinct peak because it merges with an acoustical phonon sideband of ZPL 4. The FWHM of ZPL 4 increases to 3.26 meV at 82K from 0.86 meV at 4.2K. In spite of the marked increase in FWHM, the peak energies of ZPL 4 and 8 remain 1.238 eV and 1.231 eV, respectively, the shift being less than 1 meV between 4.2K and 82K.

Although both the Yb lines and the near band-edge emissions show a decrease in intensity as the temperature rises, the Yb lines become remarkably quenched as the temperature rises above 100K. Figure 5 shows the temperature dependence of the integrated intensities of the Yb lines and the near band-edge emissions above 80K. The near band-edge emissions include a band-to-band (or exciton) transition and a band-to-acceptor transition while the Yb lines include all the phonon sidebands as well as ZPL's.

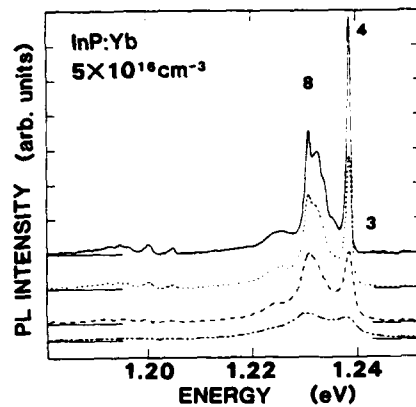


Fig.4 Temperature dependence of Yb lines of sample MOL. Measurement temperatures are 4.2K(—), 28K(.....), 43K(-----), and 82K (-.-.-.-).

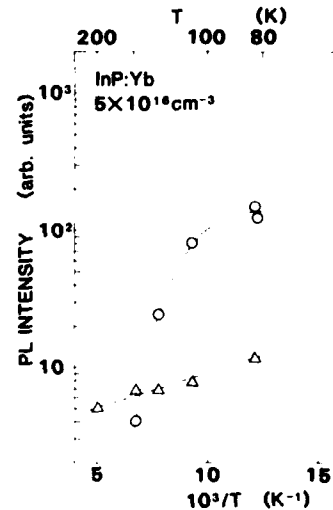


Fig.5 Temperature dependence of integrated intensities of Yb lines (O) and near band-edge emissions (Δ) above 80K. The broken line corresponds to an activation energy of 10meV. Solid line is to guide the eye.

The Yb emission intensity remains nearly the same between 4.2K and 43K, while the near band-edge emissions begin to decrease above 20K. On the other hand, as can be seen in Fig.5, the near band-edge emissions decrease in intensity with increasing temperatures above 80K with an activation energy of  $\sim 10$ meV, while the Yb emissions decrease rapidly above 100K and their activation energy cannot be precisely defined. The Yb emissions are scarcely observed above 200K.

#### 4. Discussions

In contrast to Yb-doped epitaxial layers grown by liquid phase epitaxy (Haydl et al 1985), MOCVD-grown InP invariably shows n-type conductivity. It is possible that p-type conductivity observed for LPE-grown layers is caused by impurities in Yb metal used for doping. For example, impurities such as Zn and Mg are often observed as contaminants in rare-earth metals. They are easily incorporated into epitaxial layers because they have much larger distribution coefficients than that of Yb, thus contributing to p-type conductivity.

PL results at 4.2K (Fig.2) and 82K (Uwai et al 1986) confirm that MOCVD-grown layers contain less amount of the unintentionally doped acceptor compared with the ion-implanted (Ennen et al 1985) or LPE-grown layers (Haydl et al 1985). The band-to-band emission is stronger than the acceptor-related emission both at 4.2K and 82K in MOCVD-grown layers, while in the ion-implanted or the LPE-grown layers the acceptor-related emission dominates the near band-gap emission.

The carrier freeze-out observed in sample MOL suggests that unknown deep

levels are incorporated into our MOCVD-grown epitaxial layers. SIMS measurements reveal that transition metals such as Fe and Mn are incorporated into the layers together with Yb. Therefore, at present, we cannot determine to what extent Yb affects the electrical properties of the layers.

The mechanism of the temperature dependence of the PL spectrum is not clear at present. Though the FWHM of ZPL 4 at 4.2K is as narrow as 0.86meV, this line broadens considerably as the temperature increases from 4.2K to 82K. This broadening is considered to be related to the Debye temperature of the host and the coupling strength between phonons and impurity ions (Yb) (Kushida 1969). The reason for the rapid decrease in the Yb emission intensity with increasing temperatures above 80K is not fully understood either. It should be noted that in contrast to InP:Yb studied here, Yb emissions in CdS do not decrease in intensity with increasing temperatures, although the linewidths increase considerably (Anderson 1966). A comparison of these two hosts might shed light on the energy relaxation mechanism in rare-earth doped semiconductors.

### 5. Conclusions

Yb has been doped into InP epitaxial layers by MOCVD for the first time. The Yb-doped InP shows n-type conductivity in contrast to the LPE-grown layers. Sharp ZPL's due to Yb intra 4f shell transitions were observed at 4.2K with phonon sidebands at lower energies, showing a marked increase in linewidths with increasing temperatures. Above 80K the Yb-related emission intensity decreases drastically and Yb emission is scarcely observed above 200K.

### Acknowledgments

We would like to thank Dr. Hiroshi Kanbe for helpful discussions and encouragement.

### References

- Anderson W W, Razi S and Walsh D J 1965 J. Chem. Phys. **43** 1153
- Anderson W W 1966 J. Chem. Phys. **44** 3283
- Ennen H, Kaufmann U, Pomrenke G, Schneider J, Windscheif J and Axmann A 1983 J. Cryst. Growth **64** 165
- Ennen H, Pomrenke G and Axmann A 1985 J. Appl. Phys. **57** 2182
- Haydl W H, Müller H D, Ennen H, Körber W and Benz K W 1985 Appl. Phys. Lett. **46** 870
- Kaminskii A A 1981 Laser Crystals (Springer, Berlin) p 322
- Kasatkin V A, Kesamanly F P and Samorukov B E 1978 Sov. Phys. Semicond. **12** 974
- Kushida Takashi 1969 Phys. Rev. **185** 500
- Mooradian A and Wright G B 1966 Solid State Comm. **4** 431
- Skolnick M S, Dean P J, Kane M J, Uihlein Ch, Robbins D J, Hayes W, Cockayne B and MacEwan W R 1983 J. Phys. C **16** L767
- Tapster P R, Skolnick M S, Humphreys R G, Dean P J, Cockayne B and MacEwan W R 1981 *ibid.* **14** 5069
- Tapster P R, Skolnick M S, Dean P J, Reed L J, Cockayne B and MacEwan W R 1982 Semi-Insulating III-V Materials (Evian) p 208
- Uwai K, Mikami O and Susa N 1985 Electron. Lett. **21** 131
- Uwai K, Nakagome H and Takahei K 1986 to be submitted to Appl. Phys. Lett.

# **Chemical beam epitaxial growth of very high quality $\text{Ga}_{0.47}\text{In}_{0.53}\text{As}/\text{InP}$ quantum wells and superlattices: photoluminescence and photoluminescence excitation spectroscopies**

W. T. Tsang<sup>a)</sup>, E. F. Schubert<sup>a)</sup>,  
S. N. G. Chy<sup>b)</sup>, K. C. Tai<sup>b)</sup>,  
R. Sauer<sup>b)</sup>, T. H. Chiu<sup>a)</sup>,  
J. E. Cunningham<sup>a)</sup>, and J. A. Ditzenberger<sup>a)</sup>  
AT&T Bell Laboratories  
a) Holmdel, NJ 07733  
b) Murray Hill, NJ 07974

## **1. Introduction**

In all kinds of chemical vapor depositions (CVD),<sup>1,2</sup> because the pressure inside the reactor is typically greater than  $10^{-2}$  torr and up to atmospheric, the flow of the gaseous reactants is viscous. If however, the pressure is sufficiently reduced (down to  $< 10^{-4}$  torr) so that the mean-free paths between molecular collisions becomes longer than the source in-let and substrate distance, the gas transport becomes molecular beam. Such thin-film deposition process is called chemical beam deposition or chemical beam epitaxy (CBE) (Tsang, 1984) if the thin film is an epitaxial layer. Thus, CBE is the newest development in epitaxial growth technology. It combines many important advantages of molecular beam epitaxy (MBE) (Arthur, 1968) and organo-metallic chemical vapor deposition (OM-CVD) (Manasevit, 1968), both of which were first developed in 1968. And, therefore, it promises to advance the epitaxial technology beyond both techniques.

In CBE, unlike MBE which employs atomic beams (e.g. Al, Ga, and In) evaporated at high temperature from elemental sources, all the sources are gaseous at room temperature. They can be organo-metallic or inorgano-metallic compounds. For III-V semiconductors the Al, Ga and In are derived by the pyrolysis of their organo-metallic compounds, e.g. trimethylaluminum, triethylgallium and trimethylindium, at the heated substrate surface. The  $\text{As}_2$  and  $\text{P}_2$  are obtained by the thermal decomposition of their hydrides passing through a heated baffled cell. The use of hydrides was first introduced into the MBE process in 1974 by Morris and Fukui (1974) and later applied to the growth of GaAs and InGaAsP by Calawa (1981) and Panish (1980). Unlike OM-CVD, in which the chemicals reach the substrate surface by diffusing through a stagnant gas boundary layer above the substrate, the chemicals in CBE are admitted into the high vacuum growth chamber in the form of a beam. Further, in OM-CVD, most of the pyrolysis of the organo-metallics is believed to occur in the gas phase, while in CBE there is no gas-phase reaction.

The system design and growth conditions have been described previously (Tsang 1984, 1986 a, b) and so are their advantages over MBE and OM-CVD (Tsang and Miller, 1986c). Thus, we shall describe here a summary of the results obtained from the characterizations of CBE-grown  $\text{Ga}_{0.47}\text{In}_{0.53}\text{As}/\text{InP}$  quantum wells and superlattices.

## 2. Single Quantum Wells

$\text{Ga}_{0.47}\text{In}_{0.53}\text{As}$  QW's have been prepared by many growth techniques including MOCVD (Razeghi et al. 1983; Kuo et al. 1985) chloride transport vapor phase epitaxy (VPE), (Kodama et al. 1983) MBE using solid arsenic and phosphorous sources (Tsang, 1984; Marsh et al. 1985) and arsine and phosphine sources (Temkin et al. 1985; Panish 1986). Recently, it was shown that GaInAs QW's prepared by CBE are of extremely high quality, superior in many respects to those made by MOCVD, VPE, or MBE. The optical emission from these QW's is intense and of narrow linewidth (Tsang et al. 1986a). Figure 1 shows a transmission electron microscopy (TEM) photograph of the cross-sectional view of a stack of single  $\text{Ga}_{0.47}\text{In}_{0.53}\text{As}$  QW's separated by InP down to a thickness of  $\sim 10\text{\AA}$ .

Extremely high quality  $\text{Ga}_{0.47}\text{In}_{0.53}\text{As}/\text{InP}$  quantum wells with thickness as thin as  $6\text{\AA}$  have also been prepared by CBE. Emission as short as  $1.09\text{ }\mu\text{m}$  at 2K ( $1.14\text{ }\mu\text{m}$  at 300K) was obtained. Very sharp intense efficient luminescence peaks due to excitonic transitions were obtained from all quantum wells as shown by an example in Figure 2.

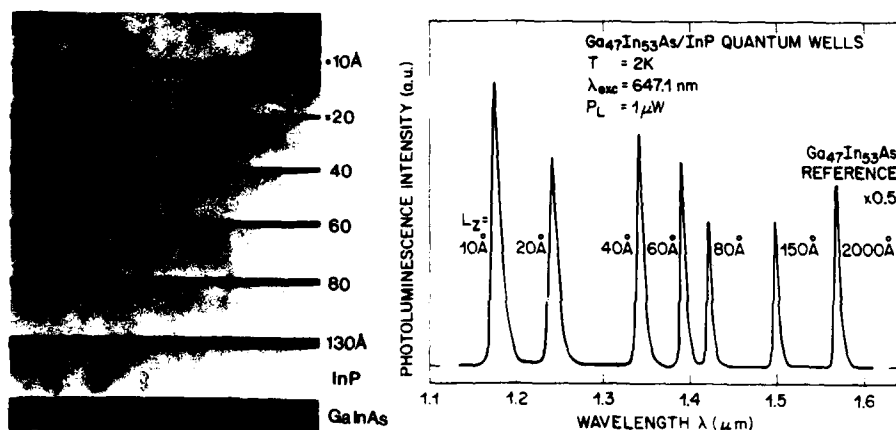


Fig. 1 A cross-sectional TEM of a stack of GaInAs/InP QW's of different thicknesses.

Fig. 2 A typical photoluminescence spectrum from a stack of quantum wells with different thicknesses separated by  $700\text{\AA}$  InP barriers at 2K. The pumping power is  $1\text{ }\mu\text{W}$  and pumping area is  $\sim 50\text{ }\mu\text{m}$  diameter.

The PL linewidths at 2K were the narrowest that have been ever reported for  $\text{Ga}_{0.47}\text{In}_{0.53}\text{As}$  quantum wells grown by any technique (Marsh et al. 1985; Panish et al. 1986; Miller et al. 1986; Razeghi et al. 1983, 1984) as compared in Figure 3.



Fig. 3 Represents a compilation of PL linewidths (FWHM) as a function of well thickness for the best published  $\text{Ga}_{0.47}\text{In}_{0.53}\text{As}/\text{InP}$  quantum wells grown by OM-CVD and MBE together with present results grown by CBE. The dashed curve was calculated broadening due to band-filling from impurities. A sheet carrier density of  $2 \times 10^{11} \text{ cm}^{-2}$  was used. The dotted curve was calculated broadening due to "effective" interface roughness,  $L_z$ , of  $a_0/2$  assuming finite-height barriers.

In fact, such narrow linewidths for  $\text{Ga}_{0.47}\text{In}_{0.53}\text{As}$  quantum wells are, for the first time, at least equal to the narrowest linewidths ever reported for the perfected GaAs/AlAs and GaAs/ $\text{Al}_{1-x}\text{Ga}_x\text{As}$  quantum wells. These linewidths indicate the "effective" interface roughness to be 0.12 lattice constant, which can be interpreted as that the quantum well was largely consisting of a big domain of the same thickness  $L_z$  perforated with small domains of  $(L_z + a_0/2)$ , where  $a_0 (=5.86\text{\AA})$  is the lattice constant. No broadening due to band filling from impurities was found. Alloy broadening in  $\text{Ga}_{0.47}\text{In}_{0.53}\text{As}$  was limited to the intrinsic value of 1.3 meV (Tsang, et al. 1986a, 1986b). Also, for the first time in  $\text{Ga}_{0.47}\text{In}_{0.53}\text{As}$  quantum wells, the measured PL energy upshifts were in excellent agreement with theoretical values.

For GaAs/ $\text{Al}_x\text{Ga}_{1-x}\text{As}$  single and multiquantum well heterostructures, studies (Tsang et al. 1986c) using low temperature photoluminescence and excitation spectroscopy techniques also show that on the average the samples are similar in quality to similar structures grown by MBE and in certain characteristics superior to the MBE ones. For example, unusually sharp excitation peaks have been obtained up to quantum transition levels as high as  $E_{3h}$ . Further, in some important respects, especially the absence of band-filling due to impurities they are also superior to those grown by OM-CVD (Miller et al. 1985).

Compared to AlGaAs/GaAs QW's, almost no photoluminescence excitation spectroscopy (PLE) has been reported on GaInAs quantum wells although such data could give valuable information on important parameters such as band offsets and relevant electron and hole masses. (Claxton et al. 1986, Kodama et al. 1986). Taking advantage of the narrow and extremely intense emission of excitons confined to InGaAs quantum wells grown by the CBE technique. PLE (Sauer et al. 1986) spectra were excited by a 100W halogen lamp in conjunction with a 0.3m McPherson grating monochromator at a blaze wavelength of 1.6  $\mu\text{m}$ . The photoluminescence (PL) light was detected at 90 degrees by a 0.6m Jobin-Yvon grating single monochromator with 1.5  $\mu\text{m}$  blaze wavelength. Figure 4 shows the PLE spectra from a seven-layer quantum well structure grown on an InP substrate wafer.

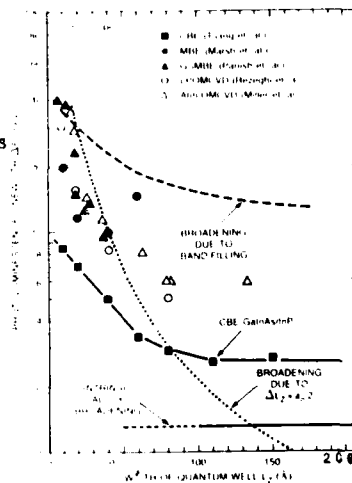


Fig. 3 PL linewidth versus QW thickness

Next to the substrate a 0.5  $\mu\text{m}$  InP buffer layer was grown followed by a 1520 $\text{\AA}$  wide InGaAs control layer, and six wells of thickness  $L_z = 130\text{\AA}$ , 76 $\text{\AA}$ , 60 $\text{\AA}$ , 30 $\text{\AA}$ , and 23 $\text{\AA}$ . The InP barriers separating the wells are 600 $\text{\AA}$  thick. The control layer serves as a reference for the PL spectra from which precise energy upshifts of the QW emission can be calculated. All the transition levels can be clearly assigned for the first time demonstrating indeed the excellent quality of the CBE-grown GaInAs/InP QW's. Fits to the spectra suggest that the band offsets are  $Q_c \sim 60\%$  and  $Q_v \sim 40\%$  with masses  $m_e^* = 0.041 m_0$ ,  $m_{ph}^* = 0.465 m_0$  and  $m_{eh}^* = 0.085 m_0$ . Energy dependent corrections for  $m_e^*$  due to conduction band nonparabolicities are essential for a good fit and yield  $y_e = 3.3 \times 10^{-15} \text{ cm}^{-2}$  for the  $y_e k$  correction term in the energy dispersion.

In Figure 5, we compare PL energy shifts, as a function of well thickness  $L_z$ , with data from other works. Our experimental points lie substantially higher than the points compared, and are in good agreement with the three calculated curves displayed.

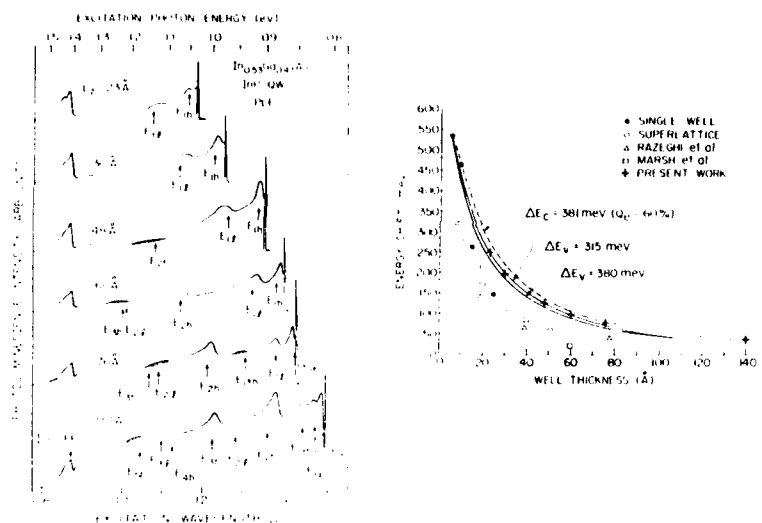


Fig. 4 Photoluminescence excitation (PLE) spectra of the multi-layer sample at 2K. Light detection is at the PL energy positions. An area of  $\sim 1.5 \times 1.5 \text{ mm}^2$  is excited. Weak peaks are shown hatched for clarity.

Fig. 5 Experimental and theoretical energy shifts from the  $\text{In}_{0.53}\text{Ga}_{0.47}\text{As}$  band edge and comparison with data from other works (redrawn from Panish et al., 1986). (Razeghi et al. 1983; Marsh et al. 1985)

Although the origin of the discrepancies between experimental upshifts and theory in the previous works is not known the agreement in the present case gives evidence for the superior quality of the samples grown by CBE. The relatively small differences between our calculated curve (dashed line in Fig. 5) and the two other curves (full lines) result from

the assumption of different conduction or valence band offsets, respectively, as shown in Fig. 5 and different boundary conditions: The full lines refer to the Bastard model (1981) assuming conservation of current whereas we have neglected effects due to mass differences in the well and barrier material. In all three cases the electron and hole masses in InGaAs are the same, with the energy dependent NP corrections of the electron mass for the dashed curve as discussed above. The near coincidence of the three calculated curves shows that the PL energy positions are not sensitive to the mass values and band offsets chosen as expected for the  $n = 1$  electron-heavy hole transitions.

### 3. Superlattices

$\text{Ga}_{0.47}\text{In}_{0.53}\text{As}/\text{InP}$  superlattices were also grown by CBE and characterized by low temperature photoluminescence, room-temperature absorption and photocurrent spectroscopies. Figure 6 shows a cross-sectional TEM of a portion of a 100-period  $\text{GaInAs}$  (110Å)/ $\text{InP}$  (130Å) superlattice. The general picture of interface abruptness and smoothness are clearly conveyed. Room-temperature absorption spectroscopy was performed on several samples of different well thicknesses. Figure 7 shows two typical spectra.

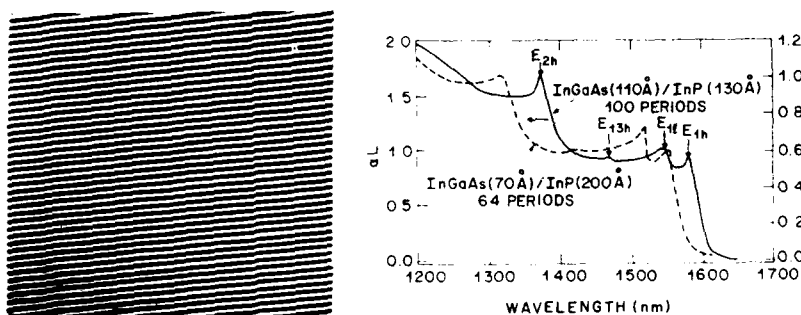


Fig. 6 A cross-sectional TEM of a portion of a 100-period  $\text{GaInAs}$  (110Å)/ $\text{InP}$  (130Å) superlattice.

Fig. 7 Two typical room-temperature absorption spectra of CBE-grown superlattices.

Not only are the various principal quantum transitions clearly identified, the forbidden  $E_{13h}$  transition can also be identified for the first time from absorption spectra.

Photocurrent (PC) measurements were also performed at room-temperature and 77K. Spectra from a typical superlattice sample is given in Figure 8. Again, all quantum transitions even  $E_{13h}$  and as high as  $E_{3h}$  (for the first time in PC) were clearly resolved. In addition to these measurements, low-temperature PL of these superlattices also gave FWHM similar to those of single QW's.

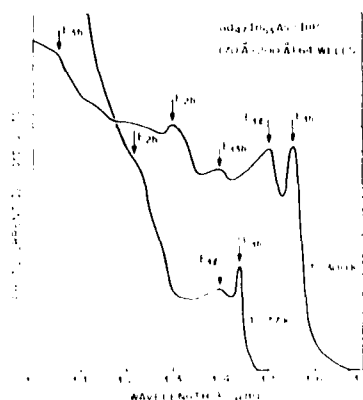


Fig. 8 Photocurrent spectra at 300K and 77K from a typical superlattice.

#### References

- Arthur J R 1968 *J. Appl. Phys.* **39** 4032  
 Bastard G 1981 *Phys. Rev.* **B24** 5693  
 Calawa A R 1981 *Appl. Phys. Lett.* **38** 701  
 Claxton P A, Roberts J S, David J P R, Sotomayor C M,  
 Skolrik M S, Tapster P R, and Nash K J 1986  
 (to be published)  
 Kodama K, Ozeki M, and Komeno J, 1983 *J. Vac. Sci. Technol.* **B1** 696  
 Kodama K, Komeno J, Hoshino M, and Ozeki M 1986 *Japn. J. Appl. Phys.* **25** 558  
 Kuo C, Fry K L, and Stringfellow G B, 1985 *Appl. Phys. Lett.* **47** 855  
 Manasevit H M 1968 *Appl. Phys. Lett.* **12** 156  
 Marsh J H, Roberts J S, and Claxton P A, 1985 *Appl. Phys. Lett.* **46** 1161  
 Miller B I, Schubert E F, Koren U, Ourmazd A, Dayem A H,  
 and Capik R J, 1986 (to be published)  
 Miller R C and Kleinman D 1985 *J. Lumin.* **30** 520  
 Morris F J and Fukui H 1974 *J. Vac. Sci. Technol.* **11** 506  
 Panish M P 1980 *J. Electrochem. Soc.* **127** 2729  
 Panish M P, Temkin H, Hamm R A, and Chu S N G 1986 *Appl. Phys. Lett.* **49** 164  
 Razeghi M and Duchemin J P 1984 *J. Cryst. Growth* **70** 145  
 Razeghi M, Hirtz J P, Ziemelis U O, Delalande C, Etienne B,  
 and Voos M 1983 *Appl. Phys. Lett.* **43** 585  
 Sauer R, Harris T D and Tsang W T 1986 *Phys. Rev. B* (to be published)  
 Temkin H, Panish M P, Petroff P M, Hamm R A, Vandenberg J M,  
 and Sumski S, 1985 *Appl. Phys. Lett.* **47** 394  
 Tsang W T 1984 *Appl. Phys. Lett.* **45** 1234  
 Tsang W T and Schubert E F 1986a *Appl. Phys. Lett.* **49** 220  
 Tsang W T, Dayem A H, Chiu T H, Cunningham J E,  
 Schubert E F, Ditzemberger J A, and Shah J  
 1986b *Appl. Phys. Lett.* **49** 170  
 Tsang W T and Miller R C 1986c *Appl. Phys. Lett.* **48** 1238  
 Tsang W T 1984 *Appl. Phys. Lett.* **44** 288

## Formation of DX centers by heavy Si doping in MBE-grown $\text{Al}_x\text{Ga}_{1-x}\text{As}$ with low Al content

T. Ishikawa, T. Yamamoto, K. Kondo, J. Komeno and A. Shibatomi

FUJITSU LABORATORIES LIMITED  
10-1 Wakamiya, Morinosato, Atsugi 243-01, Japan

**Abstract.** The dependence of shallow donors and DX centers on the Si doping concentration in  $\text{Al}_x\text{Ga}_{1-x}\text{As}$  layers grown by MBE has been investigated. In the shallow-to-DX transition region around  $x=0.2$ , the concentration ratio of DX centers to shallow donors was found to be closely related to the Si doping concentration. While few DX centers were observed in the samples with a Si concentration of about  $1 \times 10^{17} \text{ cm}^{-3}$ , DX centers became dominant in those samples with a doping concentration above  $1 \times 10^{18} \text{ cm}^{-3}$ , as used in HEMTs. These results can be explained by the effect of electron distribution between  $\Gamma$ -valley and DX center level.

### 1. Introduction

The DX centers in  $\text{N-Al}_x\text{Ga}_{1-x}\text{As}$  layers have recently been the subject of much research since they influence the performance of important devices such as high electron mobility transistors (HEMTs). Reports show that n-type dopants in  $\text{Al}_x\text{Ga}_{1-x}\text{As}$  layers form two types of donors, shallow donors mainly in the composition region below  $x=0.2$  and DX centers above  $x=0.3$  (Watanabe et al. 1984, Schubert et al. 1984). These results indicate that, in order to avoid the undesirable influence of DX centers on HEMT performance, AlGaAs layers with a composition of less than  $x=0.2$  are preferred. However, the above conclusion is based on experiments on rather lightly-doped  $\text{N-Al}_x\text{Ga}_{1-x}\text{As}$  layers (about  $1 \times 10^{17} \text{ cm}^{-3}$ ). In HEMT applications, more heavily doped  $\text{N-Al}_x\text{Ga}_{1-x}\text{As}$  layers (about  $1 \times 10^{18} \text{ cm}^{-3}$ ) are used. In this work, therefore, we investigated the dependence of shallow donors and DX centers on Si doping concentration mainly in the shallow-to-DX transition region around  $x=0.2$ .

### 2. Sample Preparation

Samples were grown by conventional MBE on semi-insulating GaAs substrates at a substrate temperature of  $680^\circ\text{C}$ . They included  $0.2\text{-}\mu\text{m}$  undoped GaAs;  $0.3\text{-}$  or  $0.5\text{-}\mu\text{m}$  undoped  $\text{Al}_x\text{Ga}_{1-x}\text{As}$  buffer layers, which can prevent two-dimensional-electron-gas formation; and  $1\text{-}\mu\text{m}$  Si doped  $\text{Al}_x\text{Ga}_{1-x}\text{As}$  layers. The doping concentration was varied from  $8 \times 10^{16} \text{ cm}^{-3}$  to  $3 \times 10^{18} \text{ cm}^{-3}$ . In this work, the composition of the AlGaAs layers was carefully controlled as the maintenance of the constant composition with various doping concentrations is very important. It was precisely determined from the thickness of AlAs and GaAs epitaxial layers grown just before the sample growth, and also determined by x-ray diffraction, consistency of the obtained results

being within  $\pm 2.5\%$ . These epitaxial layers were characterized by van der Pauw Hall and DLTS measurements.

### 3. Results

For  $N\text{-Al}_x\text{Ga}_{1-x}\text{As}$  layers around  $x=0.2$  with various doping concentrations, the concentrations of shallow donors and DX centers were estimated from Hall measurements at 77 K. Figure 1 shows the electron concentrations of  $N\text{-Al}_{0.195}\text{Ga}_{0.805}\text{As}$  (a) and  $N\text{-Al}_{0.22}\text{Ga}_{0.78}\text{As}$  (b) layers in darkness (solid circles) and five minutes after being exposed to light (open circles), as a function of the reciprocal temperature of the Si effusion cell. Even for  $N\text{-Al}_{0.195}\text{Ga}_{0.805}\text{As}$ , the persistent-photoconductivity (PPC) effect was observed in heavily-doped samples. The electron concentration changed little after exposure to light in the samples with a doping concentration of less than  $3 \times 10^{17} \text{ cm}^{-3}$ . In the more heavily-doped samples, however, the electron concentration increased considerably after being exposed to light and persisted after the light source was removed. The heavier the doping, the more significant this PPC effect became. For  $N\text{-Al}_{0.22}\text{Ga}_{0.78}\text{As}$ , on the other hand, a persistent increase in electron concentration was observed even in the slightly-doped samples, but became significant in the more heavily doped samples. While the electron concentration in darkness implies a shallow donor concentration which can ionize at 77 K, the persistent increase in electron concentration after exposure to light is thought to indicate the DX center concentration, because of its very small capture cross

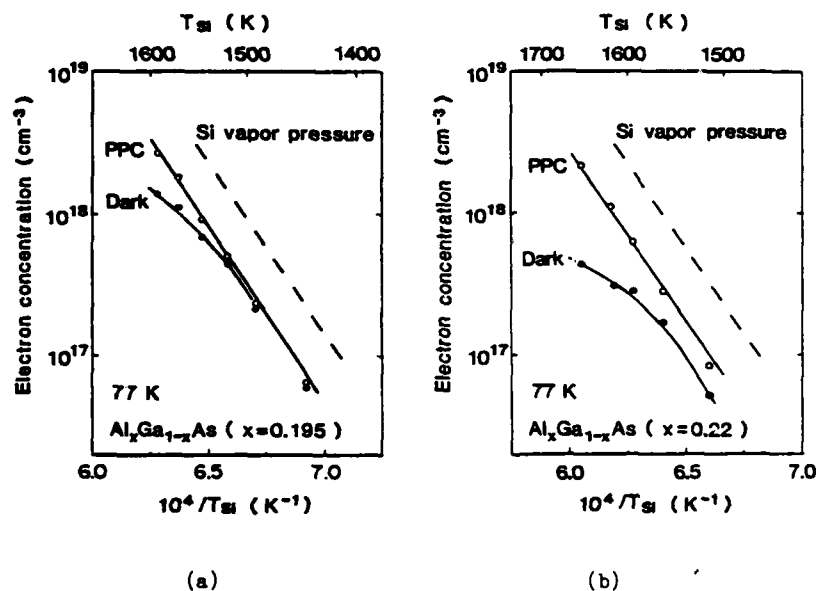


Fig. 1 Electron concentration of  $N\text{-Al}_{0.195}\text{Ga}_{0.805}\text{As}$  (a) and  $N\text{-Al}_{0.22}\text{Ga}_{0.78}\text{As}$  (b) layers at 77 K as a function of reciprocal temperature of the Si effusion cell.

section at 77 K (Zhou et al. 1982). Around  $x=0.2$ , therefore, the formation of DX centers is thought to depend on the doping concentration, and a considerable amount of DX centers are thought to be formed by heavy doping even in the  $N\text{-Al}_{0.195}\text{Ga}_{0.805}\text{As}$  layers which were believed to have only a small amount of DX centers (Watanabe et al. 1984, Schubert et al. 1984). It should also be noted that the electron concentration after exposure to light is proportional to the Si vapor pressure (broken line) both for  $x=0.195$  and  $x=0.22$ . This indicates that almost all the incorporated Si atoms act as either kind of donor and that the auto-compensation effect does not seem to be important.

To assure DX center formation in these heavily doped, low Al content samples, the temperature dependence of Hall measurement and DLTS measurement were made for the same samples as in Fig. 1 (a). Figure 2 shows the temperature dependence of electron concentration in  $N\text{-Al}_{0.195}\text{Ga}_{0.805}\text{As}$  layers with three typical doping concentrations. As in Fig. 1, solid circles represent electron concentration in darkness and open circles after light exposure. The sample with the slightly-doped concentration of  $8 \times 10^{16} \text{ cm}^{-3}$  exhibited a behavior similar to n-type GaAs with shallow donors: a weak dependence of electron concentration on temperature and no PPC effect (Tachikawa et al. 1985). With increased Si concentration, however, below 150 K the PPC effect became significant, indicating an increase in the concentration of DX centers. Moreover, the increase in the activation energy of the carrier concentration above 150 K,  $E_a$ , with the Si doping concentration is thought to imply an increase in the DX-center-to-shallow-donor concentration ratio rather than the increased carrier compensation suggested by Chand et al. (1984).

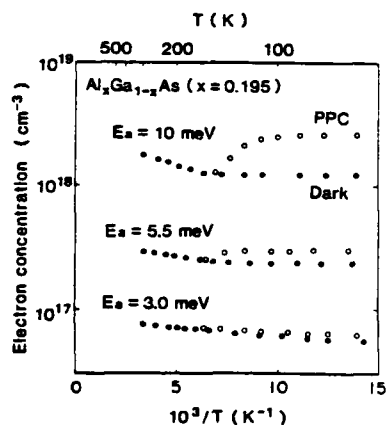


Fig. 2 Electron concentration for  $N\text{-Al}_{0.195}\text{Ga}_{0.805}\text{As}$  layers with three doping concentrations ( $8 \times 10^{16}$ ,  $3 \times 10^{17}$ ,  $2.6 \times 10^{18} \text{ cm}^{-3}$ ) as a function of reciprocal temperature.

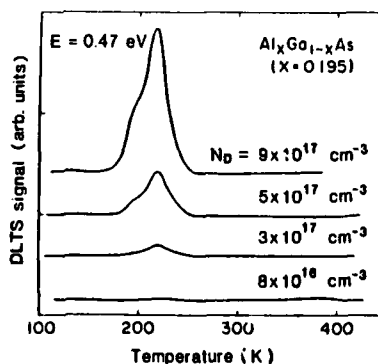


Fig. 3 DLTS spectra for  $N\text{-Al}_{0.195}\text{Ga}_{0.805}\text{As}$  layers with various doping concentrations ( $8 \times 10^{16}$  to  $9 \times 10^{17} \text{ cm}^{-3}$ ).

Figure 3 illustrates DLTS spectra for four samples with a doping concentration,  $N_D$ , of less than  $9 \times 10^{17} \text{ cm}^{-3}$ . Schottky contacts to all of the samples had a sufficiently low leakage current to allow DLTS measurement. The rate window was 5.77 ms. While no DLTS signals corresponding to electron traps were observed in the slightly-doped sample of  $8 \times 10^{16} \text{ cm}^{-3}$ , a small signal appeared at  $3 \times 10^{17} \text{ cm}^{-3}$  and increased significantly with increased doping concentration. These signals had the characteristic two-peak feature often observed for DX centers, and the activation energy of electron emission obtained from these signals is 0.47 eV, nearly equal to the reported values for DX centers of Si-doped  $\text{Al}_{0.3}\text{Ga}_{0.7}\text{As}$  (for example, Zhou et al. 1982). Besides, the electron trap concentration estimated from these DLTS signals was roughly consistent with the persistent increase in electron concentration in Fig. 1(a). Therefore, it can be concluded that DX centers are formed in the  $\text{Al}_{0.195}\text{Ga}_{0.805}\text{As}$  layer as a result of heavy Si doping and thus cause the PPC effect.

We also examined the dependence of DX centers and shallow donors on the doping concentration for other compositions. The concentration of shallow donors,  $N_{SD}$ , and that of DX centers,  $N_{DX}$ , were estimated by Hall measurement at 77 K in the same manner as in Fig. 1. Figure 4 summarizes the concentration ratio of DX centers to total donors as a function of the total donor concentration. The result for  $x=0.34$  reported by Watanabe et al. (1984) is also shown. The DX centers are dominant above  $x=0.3$  and are independent of the doping concentrations. Around  $x=0.2$ , however, the ratio proved to be strongly dependent on the doping concentration. Moreover, the DX centers appeared at the higher doping concentration for lower Al contents. It should be noticed that even in the  $\text{N-Al}_{0.15}\text{Ga}_{0.85}\text{As}$  layers, which were firmly believed to include no DX centers, the PPC effect was observed in the samples doped more heavily than  $2 \times 10^{18} \text{ cm}^{-3}$ . The concentration of DX centers estimated from this PPC effect is significantly high, about 10% of the total donor concentration for the sample with an Si content of  $3 \times 10^{18} \text{ cm}^{-3}$ .

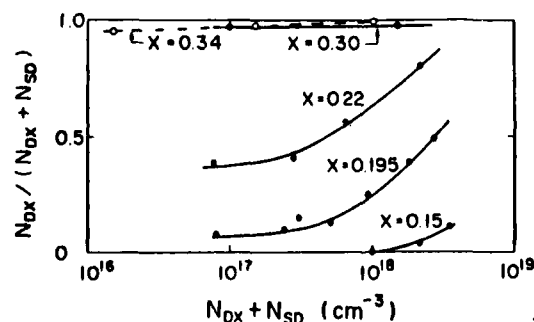


Fig. 4 Concentration ratio of DX centers to total donors for various  $\text{N-Al}_x\text{Ga}_{1-x}\text{As}$  layers as a function of the total donor concentration.  $N_{DX}$  represents the DX center concentration, and  $N_{SD}$  that of the shallow donors. The data for  $x=0.34$  was originally reported by Watanabe et al.



#### 4. Discussion

These results can be explained by the effect of electron distribution between the  $\Gamma$ -valley and the DX center level. We can see from Fig. 4 that the ratio of DX centers to the total donors is determined both by the  $\text{Al}_x\text{Ga}_{1-x}\text{As}$  composition and the doping concentration. Moreover, the ratio was independent of MBE growth conditions (Ishikawa et al. 1985). These results suggest the importance of the band structure effect in the formation of the DX center. Thus, we can explain our results in terms of the band structure. The DX centers in AlGaAs are believed to be the deep levels associated with the L-valley (Mizuta et al. 1985) or X-valley (Lang et al. 1979). Around  $x=0.2$  the energy level of the DX centers associated with such a non- $\Gamma$ -valley is expected to be just above the bottom of the  $\Gamma$ -valley. Therefore, at light doping concentrations such as  $1 \times 10^{17} \text{ cm}^{-3}$ , electrons occupy mainly the  $\Gamma$ -valley. However, increasing the doping concentration to about  $1 \times 10^{18} \text{ cm}^{-3}$  raises the Fermi level 50 or 60 meV and electrons will begin to populate the DX center levels. Thus, as the doping concentration increases, the DX centers become significant at around  $x=0.2$ . Figure 5 schematically shows this situation. For  $x=0.15$ , the energy level of the DX centers is expected to be further above the  $\Gamma$ -minimum, so the DX center appears at a higher doping concentration. For  $\text{Al}_x\text{Ga}_{1-x}\text{As}$  above  $x=0.3$ , in contrast, the DX centers are dominant, regardless of the doping concentration because the energy level is considered to be much lower than  $\Gamma$ -minimum.

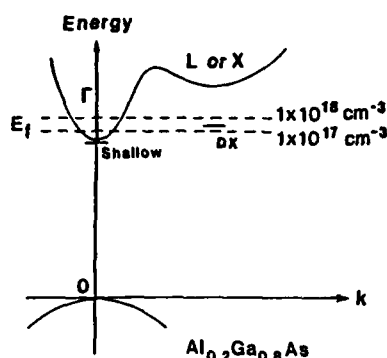


Fig. 5 Schematic energy diagram showing position of the Fermi level and DX center level for  $\text{N-Al}_{0.2}\text{Ga}_{0.8}\text{As}$ .

Based on these interpretations, DX center formation, depending on the doping concentration, can be observed in other alloy systems with an energy configuration as shown in Fig. 5, where the energy of the DX center level is very close to that of  $\Gamma$ -minimum. Recently, donor-related deep centers, which have very similar characteristics to those of the DX centers in AlGaAs, were reported by Kitahara et al. for S-doped  $\text{Ga}_{0.52}\text{In}_{0.48}\text{P}$  grown by chloride VPE. The concentration ratio to the donor total also proved to increase as the doping concentration increased (Kitahara et al. 1986). Since the energy level of these centers is expected to be just above  $\Gamma$ -minimum, the results can be explained in the same way as the present case.

Finally, the influence of DX centers on HEMTs should be mentioned. Even in the case of low Al content epitaxial layers where  $x$  is less than 0.2, DX centers are expected to influence the performance of HEMTs because of the heavily doped AlGaAs layers of more than  $1 \times 10^{18} \text{ cm}^{-3}$ . For  $x=0.2$ , a considerable amount of shift in the threshold voltage of HEMT between 300 K and 77 K was observed, the DX center concentration being estimated to be about 30 % of the total donors (Suzuki et al.). This is consistent with the present result.

### 5. Summary

The dependence of shallow donors and DX centers on the Si doping concentration in  $\text{Al}_x\text{Ga}_{1-x}\text{As}$  layers has been investigated in detail by means of Hall measurement and DLTS measurement. The DX-center-to-shallow-donor concentration ratio was found to increase with the doping concentration in the transition region around  $x=0.2$ , and the formation of DX centers by heavy Si doping in  $\text{Al}_x\text{Ga}_{1-x}\text{As}$  layers with a low Al content ( $x<0.2$ ) was confirmed for the first time. These results were explained by the effect of electron distribution between the  $\Gamma$ -valley and the DX center level.

### Acknowledgments

The authors would like to express their thanks to Y. Sugiyama for the measurement of x-ray diffraction and to M. Kobayashi and T. Misugi for supporting this work.

### References

- Chand N, Henderson T, Klem J, Masselink W T, Fischer R, Chang Y and Morkoç H 1984 Phys. Rev. B 30 4481.  
 Ishikawa T, Kondo K, Hiyamizu S and Shibatomi A 1985 Jpn. J. Appl. Phys. 24 L408.  
 Kitahara K, Hoshino M, Kodama K and Ozeki M 1986 Jpn. J. Appl. Phys. 25 L534.  
 Lang D V, Logan R A and Jaros M 1979 Phys. Rev. B. 19 1015.  
 Mizuta M, Tachikawa M, Kukimoto H and Minomura S 1985 Jpn. J. Appl. Phys. 24 L143.  
 Schubert E F and Ploog K 1984 Phys. Rev. B. 30 7021.  
 Suzuki M et al. to be published.  
 Tachikawa M, Fujisawa T, Kukimoto H, Shibata A, Oomi G and Minomura S 1985 Jpn. J. Appl. Phys. 24 L893.  
 Watanabe M O, Morizuka K, Mashita M, Ashizawa Y and Zohta Y 1984 Jpn. J. Appl. Phys. 23 L103.  
 Zhou B L, Ploog K, Gmelin E, Zheng X Q and Schultz M 1982 Appl. Phys. A.28 223.

## **Nonradiative recombination process at deep levels in AlGaAs grown by MBE**

Miyoko O. Watanabe, Yasuo Ahizawa, Naoharu Sugiyama and Takatosi Nakanisi

Research and Development Center, Toshiba Corporation  
1, Komukai Toshiba-cho, Saiwai-ku, Kawasaki 210, Japan

**Abstract** Recombination at deep levels in MBE-grown AlGaAs has been studied by DLTS. Temperature dependences of both electron and hole capture cross sections were measured for observed deep levels (DX center,  $E_{\text{c}} - 0.60\text{eV}$  and  $E_{\text{c}} - 0.66\text{eV}$ ). The capture cross sections were thermally activated and were found to be very large ( $10^{-15} - 10^{-14}\text{cm}^2$ ) at  $T = \infty$ , suggesting that these levels are nonradiative recombination centers. Based on the capture cross sections, recombination lifetimes were estimated. The results indicated that  $E_{\text{c}} - 0.60\text{eV}$  acts as the most efficient nonradiative recombination center.

### **1. Introduction**

It is well known that, in AlGaAs, both photoluminescence intensity and deep level concentration are sensitive to the growth condition (Lang et al 1976, Yamanaka et al 1984). The presence of deep nonradiative centers is often inferred, either from decreased radiative efficiency or from increased deep level concentration. However, definite experiments, which unambiguously identify nonradiative recombination at deep levels in AlGaAs, have not yet been reported.

The nonradiative recombination mechanism has been studied for GaAs and GaP using various junction capacitance techniques (Lang and Henry 1975, Henry and Lang 1977, Lang 1974a). It was shown that estimation of both electron and hole capture cross sections for individual deep levels were essential for understanding the recombination process. Most of the measurements made, using these techniques, have been on both n-type and p-type samples. Such method is suitable for measuring definite deep levels, that can be identified to be the same in n-type and p-type materials. However, for undefined deep levels it is only necessary to measure both electron and hole capture cross sections either in n-type or p-type samples.

This paper presents nonradiative recombination processes at deep levels in MBE-grown AlGaAs. Both the electron and hole capture cross sections were measured for n-type materials.

### **2. Experiment**

The  $\text{Al}_{0.3}\text{Ga}_{0.7}\text{As}$  p<sup>+</sup>n structures were prepared by MBE on (100) oriented n<sup>+</sup> GaAs substrates. A cross-sectional view of the p<sup>+</sup>n AlGaAs diode is shown in Fig.1. The doping concentration,  $N_{\text{D}}$ , in the n-AlGaAs layer, which was the layer under investigation, was varied between  $5 \times 10^{15}$  and

$5 \times 10^{17} \text{ cm}^{-3}$ . Epitaxial layers were grown at a substrate temperature of  $600^\circ\text{C}$ , with  $\text{As}_4/\text{Ga}$  flux ratio of 2, and at a growth rate of  $1 \mu\text{m/h}$ .

The  $p^+n$  diodes, with various diameters, were fabricated for DLTS measurements by wet etching mesas, followed by deposition of  $\text{AuZn}/\text{Au}$  and  $\text{AuGe}/\text{Au}$  on the  $p$ -side and  $n$ -side, respectively. The metals were alloyed at  $420^\circ\text{C}$  for one minute.

Doping concentration in the  $n\text{-AlGaAs}$  layers was measured by C-V profiling at room temperature. The capacitance measurement frequency was  $1\text{MHz}$ . For characterizing deep levels, DLTS was used, with which both majority carrier (electron) traps and minority carrier (hole) traps could be detected. DLTS was performed at temperatures ranging from 100 to  $450\text{K}$ .

### 3. Deep Level Characteristics

#### 3.1. Deep Level

Typical DLTS spectra obtained for  $n\text{-Al}_{0.3}\text{Ga}_{0.7}\text{As}$  are shown in Fig. 2, where the reverse bias voltage of  $-1\text{V}$  was applied to the  $p^+n$  junction. The solid curve shows the spectrum taken for the pulse bias voltage of  $0\text{V}$ , the condition under which only electron traps could be obtained. Three electron traps ( $0.44\text{eV}$ ,  $0.67\text{eV}$  and  $0.77\text{eV}$ ) were detected, corresponding to DX center,  $E_{\text{C}}-0.60\text{eV}$  and  $E_{\text{C}}-0.66\text{eV}$ , which will be discussed in 3.2. The dashed curve in Fig. 2 shows the spectrum taken under a condition where holes were injected into the  $n\text{-AlGaAs}$  layer by  $20\text{msec}$  saturation injection pulses. Comparing the two spectra shown in Fig. 2, we find that the detected electron trap concentrations varied with injected hole concentrations, which will be discussed in 3.3, and no hole traps are detected. The three deep levels observed here are the same as the reported deep levels in MBE-grown  $\text{AlGaAs}$  (Mooney et al 1985, Yamanaka et al 1984). Typical concentrations are listed in Table I.

#### 3.2. Electron Capture Cross Section

We will confine our discussion to the carrier capture cross section of each deep level shown in Fig. 2. Electron capture cross section  $\sigma_n$  values

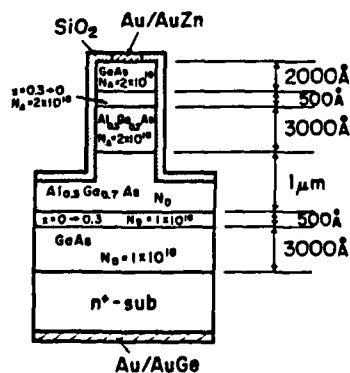


Fig. 1. Cross-sectional view of the sample.

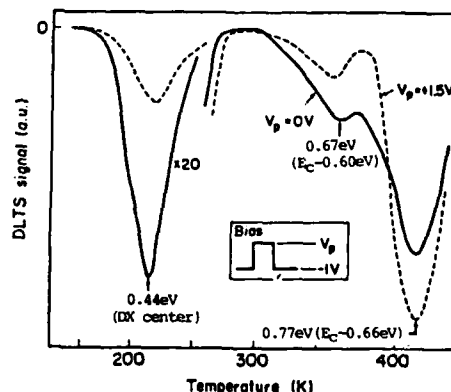


Fig. 2. DLTS spectra for  $n\text{-Al}_{0.3}\text{Ga}_{0.7}\text{As}$ .

were obtained by measuring DLTS signals ( $\Delta C$ ) for various trap filling times, which is a conventional method that was first developed by Lang (1974b). Figure 3 shows the temperature dependence of  $\sigma_n$  for deep levels in n-AlGaAs. One can see a general trend: all the levels have electron capture cross sections, which increase exponentially with temperature and are very large,  $\sigma_n = 10^{-15} \sim 10^{-14} \text{ cm}^2$  at  $T = \infty$ . Furthermore, the obtained values were found to be independent of carrier concentration. These facts suggest that the electron capture is a non-radiative process by lattice-relaxation multiphonon emission at  $T > 200\text{K}$  (Henry and Lang 1977). The energy depth values for the three levels were found to be 0.14eV, 0.60eV and 0.66eV from the conduction band minimum.

### 3.3. Hole Capture Cross Section

In order to obtain the values for hole capture cross section  $\sigma_p$  of deep levels observed as electron traps, first, let's consider a more basic model involving electron and hole capture in a deep level. For simplicity, we will describe the situation in n-type material, which has a lower-concentration of a deep level, in an asymmetric p-n junction. Consider a hole-injection condition for a pulse-biased state. The electron-occupied deep level concentration,  $N_T^0$ , is given by (Lang 1979)

$$N_T^0(t, p_N) = N_T \frac{\sigma_n v_n n}{\sigma_n v_n n + \sigma_p v_p p_N} (1 - e^{-(\sigma_n v_n n + \sigma_p v_p p_N)t}), \quad (1)$$

where a donor-type deep level is assumed to have one of two states,  $N_T^0$  or  $N_T^+$ . In Eq. (1),  $t$  is time during which the forward bias voltage is applied,  $N_T$  is the total deep level concentration ( $N_T = N_T^0 + N_T^+$ ),  $v_n$  ( $v_p$ ) is the thermal velocity for electrons (holes), and  $n$  ( $p_N$ ) is the free electron (injected hole) concentration. At  $t = \infty$ , we obtain

$$N_T^0(p_N) = N_T \frac{\sigma_n v_n n}{\sigma_n v_n n + \sigma_p v_p p_N}. \quad (2)$$

This concentration is described as  $fN_T$ , where  $f$  is the ratio of the electron-occupied deep level concentration to the total deep level concentration. This factor is approximately obtained as

$$f \equiv \frac{N_T^0(p_N)}{N_T} = \frac{\Delta C(p_N)}{\Delta C_{\max}}. \quad (3)$$

Table I. Measured deep level concentration and estimated minority-carrier lifetimes ( $T=300\text{K}$ ).

|  | DX center                            | $E_c - 0.60\text{eV}$                | $E_c - 0.66\text{eV}$                |
|--|--------------------------------------|--------------------------------------|--------------------------------------|
| $N_T$  | $1.0 \times 10^{17} \text{ cm}^{-3}$ | $3.5 \times 10^{15} \text{ cm}^{-3}$ | $6.5 \times 10^{15} \text{ cm}^{-3}$ |
| $\tau_{p16}$<br>( $n = 6 \times 10^{16} \text{ cm}^{-3}$ ,<br>$p = 1 \times 10^{15} \text{ cm}^{-3}$ ) | 250nsec                              | 6.5nsec                              | 180nsec                              |
| $\tau_{p17}$<br>( $p = 1 \times 10^{17} \text{ cm}^{-3}$ ,<br>$n = 1 \times 10^{15} \text{ cm}^{-3}$ ) | 56μsec*                              | 14nsec                               | 42nsec                               |

\* This was calculated for  $N_T(\text{DX center}) = 1.0 \times 10^{16} \text{ cm}^{-3}$ .

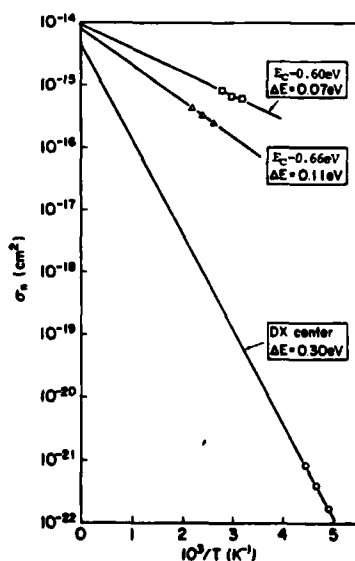


Fig. 3. Temperature Dependence of electron capture cross sections.

Here,  $\Delta C_{\max}$  is the DLTS signal, taken under the condition where all the deep levels,  $N_D$ , are occupied by electrons, and  $\Delta C$  is the DLTS signal corresponding to  $N_D$ . An increase in injected hole concentration leads to a decrease in  $f$ . Figure 4 shows the pulse bias voltage  $V_p$  dependence of the observed DLTS signal for the DX center. Initially, signal  $\Delta C$  increased with increasing  $V_p$  for  $V_p = 0 \sim 1.3V$ . This is considered to be due to the effect of decreasing depletion width with  $V_p$ . Then,  $\Delta C$  decreased with  $V_p$  ( $V_p > 1.3V$ ), due to increased hole concentration. Therefore, the maximum value for  $\Delta C$  is expected to correspond to  $\Delta C_{\max}$ . From Eqs. (2) and (3), a factor  $(1-f)/f$ , which determines the hole to electron capture cross section ratio, is simply expressed by

$$\frac{1-f}{f} = \frac{C_p V_p p_N}{q n v_n n} \quad (4)$$

Equation (4) gives the means of obtaining  $\sigma_p$  by plotting  $(1-f)/f$  vs.  $p_N$ . Figure 5 shows the plot of  $(1-f)/f$  vs.  $p_N$  obtained from the data in Fig. 4. Here, the injected hole concentration  $p_N$  was evaluated from the measured current  $I$  of the diode, as follows:  $p_N = \gamma I / (q S (\tau / D_p))^{1/2}$ , where  $\gamma$  is the hole injection efficiency,  $S$  is the junction area,  $\tau$  is the hole lifetime, and  $D_p$  is the hole diffusion coefficient.  $D_p$  was evaluated as  $D_p = \mu_p kT$ , where  $\mu_p$  the injected hole mobility was assigned at each electron concentration by using the hole mobility obtained in a p-type sample of the same carrier concentration. In the calculation of  $p_N$ ,  $\gamma$  was between 0.7 and 0.9 (Lang 1979), and we assumed  $\tau = 10 \text{ nsec}$  (Casey 1976). A linear relationship between  $p_N$  and  $(1-f)/f$  is obtained in Fig. 5. From the slope of this plot, the hole capture cross section  $\sigma_p$  for the DX center was found to be  $1.3 \times 10^{-17} \text{ cm}^2$  at  $T = 204K$ . The temperature dependence of the hole capture cross section was obtained from the same measurements, but with different rate windows for DLTS corresponding to different peak positions, the technique being similar to that in obtaining the temperature dependence of the electron capture cross section.

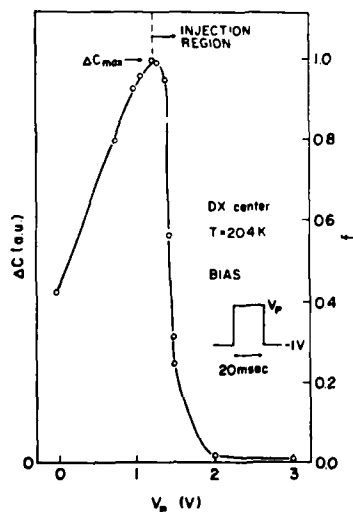


Fig. 4. DLTS signal vs. pulse bias voltage.

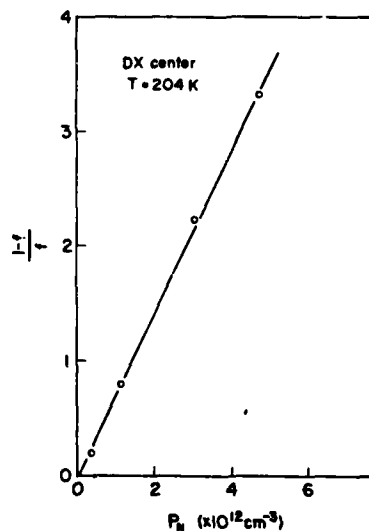


Fig. 5.  $(1-f)/f$  as a function of injected hole concentration.

Figure 6 shows the temperature dependence of the hole capture cross sections for the three deep levels observed in n-AlGaAs. The DX center and E-0.66eV level had thermally activated cross sections. The activation energy for the DX center was 0.14eV, which is in reasonable agreement with the c.c. diagram of the DX center formed by Si (Lang and Logan 1978). Extrapolation in Fig.6 yielded the hole capture cross sections of  $\sigma_p = 10^{-15} \sim 10^{-14} \text{ cm}^2$ , which are similar to the electron capture cross sections, suggesting that the hole capture processes are also multiphonon emission

#### 4. Recombination Lifetime

The recombination lifetimes (electron  $\tau_n$  and hole  $\tau_p$ ) were estimated (Shockley and Read 1952), using the capture cross section values obtained at room temperature, which were extrapolated from the temperature dependence of  $\sigma_n$  and  $\sigma_p$ . Lifetime values,  $\tau_n$  and  $\tau_p$ , were estimated for the observed deep level concentrations shown in Table I.

The hole lifetime associated with a deep level, which plays an important role in n-type material, is expressed by

$$\tau_p = (\sigma_p v_p N_T^0)^{-1} \quad (5)$$

The value of  $N_T^0$  for each deep level was obtained from Eq.(2). Quantity  $\tau_p$  was calculated from the measured values of  $N_D (1 \times 10^{17} \text{ cm}^{-3})$ ,  $n (6 \times 10^{16} \text{ cm}^{-3})$  and  $p (1 \times 10^{15} \text{ cm}^{-3})$ , where  $N_D \gg n$  because of the dominant traps being the DX center (Watanabe 1984). Calculated values of  $\tau_p$  are listed in Table I.

Similarly, the electron lifetime, which is important in p-type material,

$$\tau_n = (\sigma_n v_n N_T^+)^{-1} \quad (6)$$

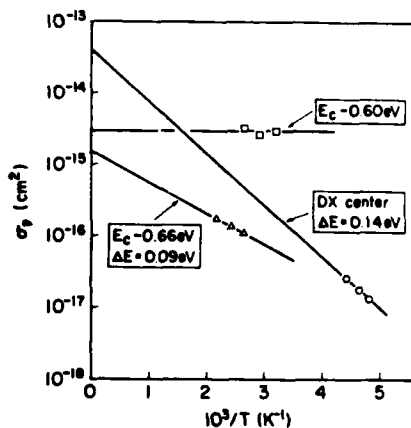


Fig.6. Hole capture cross sections vs. inverse temperature.

was calculated for the conditions where  $p = 1 \times 10^{17} \text{ cm}^{-3}$  and  $n = 1 \times 10^{15} \text{ cm}^{-3}$ . Here, the DX center concentration was assumed to be  $1 \times 10^{16} \text{ cm}^{-3}$ . The electron lifetime calculated values are also listed in Table I.

These results indicate that  $\tau_n, \tau_p$  for E-0.60eV level was the shortest, both in n-type and p-type materials. These values were considered to be comparable to the radiative recombination lifetimes estimated for these conditions (Casey 1976). An increase in E-0.60eV level concentration results in a decrease in a nonradiative recombination lifetime. As a result, reduction of E-0.60eV level concentration is very important to obtain high-quality AlGaAs. It was experimentally confirmed that normalized photoluminescence intensity ( $I_{PL}/n$ ) decreased with an increase in the E-0.60eV level concentration.

Previously,  $E_{-0.66\text{eV}}$  level has been proposed as a nonradiative recombination center in AlGaAs grown by MBE (Yamanaka et al 1984, Akimoto et al 1986). This was based only on experimental results, where the PL intensity decreased with an increase in the concentration of  $E_{-0.66\text{eV}}$  level. This level concentration usually increases with the concentration of  $E_{-0.60\text{eV}}$  level, therefore it can be considered that the decreased PL intensity, observed by Yamanaka et al and Akimoto et al, was due to the increased  $E_{-0.60\text{eV}}$  level concentration.

### 5. Summary

Recombination at deep levels in MBE-grown AlGaAs was investigated by DLTS. Detected deep levels were the DX center,  $E_{-0.60\text{eV}}$ , and  $E_{-0.66\text{eV}}$ . The temperature dependence of the electron capture cross section  $\sigma_n$  was measured for each deep level by a conventional method. The temperature dependence of the hole capture cross section  $\sigma_p$  was also measured by analyzing recombination process. All of the deep levels had capture cross section described as  $\sigma_{np} = \sigma_0 \exp(-\Delta E/kT)$ , where the  $\sigma_0(T=0)$  and  $\Delta E$  values obtained were  $10^{-13} \sim 10^{-14} \text{ cm}^2$  and  $0 \sim 0.30\text{eV}$ . These facts suggest that these recombination processes are nonradiative. Based on the values of the capture cross sections obtained, recombination lifetime  $\tau$  values at room temperature were estimated. The  $\tau$  value for  $E_{-0.60}$  level was found to be the shortest. Reduction in  $E_{-0.60\text{eV}}$  level concentration is essential to obtain high-quality AlGaAs. In conclusion, the present experiments offer a highly efficient tool for characterization of electrical and optical quality of AlGaAs layers.

### Acknowledgment

The authors are indebted to Mr.M.Azuma and Dr.J.Yoshida for providing the initial motivation for this work and Dr.R.S.Mand for critical reading of the manuscript.

### References

- Akimoto K, Kamada M, Taira K, Arai M and Watanabe N 1986 J.Appl.Phys. 59 2833
- Casey H L, Jr. 1976 J.Appl.Phys. 47 631
- Henry C H and Lang D V 1977 Phys.Rev. 15 989
- Lang D V 1974a J.Appl.Phys. 45 3014
- Lang D V 1974b J.Appl.Phys. 45 3023
- Lang D V and Henry C H 1975 Phys.Rev.Lett. 35 1525
- Lang D V, Cho A Y, Gossard A C, Ilegems M and Wiegmann W 1976 J.Appl. Phys. 47 2558
- Lang D V and Logan R A 1978 Physics of Semiconductors (Inst.Phys.Conf. Ser. 43 1979) pp 433
- Lang D V 1979 Thermally Stimulated Relaxation in Solids (Berlin: Springer-Verlag) pp 93
- Mooney P M, Fischer R and Morkoc H 1985 J.Appl.Phys. 57 1928
- Shockley W and Read W T Jr 1952 Phys.Rev. 87 835
- Watanabe M O, Morizuka K, Mashita M, Ahizawa Y and Zohta Y 1984 Jpn.J. Appl.Phys. 23 L103
- Yamanaka K, Naritsuka S, Mannoh M, Yuasa T, Nomura Y, Mihara M and Ishii M 1984 J.Vac.Sci.Technol. B2 229



## **MBE growth of GaAs on Si using thermally strained layers**

J. W. Lee

Texas Instruments Incorporated, Central Research Laboratories,  
P.O. Box 225936 M/S 147, Dallas, TX 75265

**ABSTRACT.** A thermally strained GaAs layer has been used as a buffer layer in MBE growth of GaAs layers on Si substrates. To grow such buffer layer the substrate temperature was cycled with a short period. The as-grown GaAs layers were extremely smooth and flat, and compatible with ion implantation and thermal annealing processes. After annealing the total defect density was reduced at least 1000 x.

### **1. Introduction**

The GaAs epitaxy on Si substrates is now considered to be a practically important technology in both Si and GaAs device fields. The monolithic integration of GaAs devices with Si circuits (Choi et al 1986) and the large area GaAs integrated circuits on Si substrates (Nonaka et al 1984, Shichijo et al 1986) are the two major goals of this time. One of the major difficulties in reaching these goals is the high defect density in the epitaxial GaAs layer. Previous transmission electron microscopy (TEM) studies by Metz et al (1985), Fischer et al (1986), and Lee and Tsai (1986) indicate that misfit dislocations, stacking faults, and twins are the major defects in MBE grown GaAs-on-Si layers. The usual defect density is  $10^8 \sim 10^9/\text{cm}^2$  at the top of a 3  $\mu\text{m}$  epilayer grown using the conventional GaAs growth condition. Assuming a one dimensional concept, this may be interpreted as one defect per every 1  $\mu\text{m}$ .

For defect reduction in GaAs-on-Si layers Akiyama et al (1984) and Masselink (1985) proposed low temperature growth initiation procedures and Metz et al (1985), Fischer et al (1986), and Lee (1986) claimed the use of tilted Si substrates. Relatively smooth surface morphologies have been achieved by them. Strained layer superlattice (SLS) such as InGaAs/GaAs (Fischer et al 1986, Lee 1986) or GaP/GaAsP (Soga et al 1985) have also been used for defect reduction since it is generally known that a variation of lattice strain results in a deviation of the dislocation direction. The dislocation densities of GaAs-on-Si layers grown with InGaAs/GaAs SLS buffer layers ranges between  $\sim 10^6$  and  $10^7/\text{cm}^2$ , depending on growth conditions and defect counting method.

The other approach for defect reduction is post growth thermal annealing. Lee et al (1986) have found that the true defect densities of any GaAs-on-Si layers can be reduced by several orders of magnitude by proper thermal annealing. However, in most cases many cracks or slips are found in the annealed surfaces. This may be ascribed to the film stress release during the high temperature annealing. Therefore, it is necessary to minimize residual film stress. In this paper, a new type of homojunction buffer layer is proposed for this purpose. This layer can provide an extremely

flat and smooth surface for the final GaAs-on-Si layer which is compatible with thermal annealing process. Both the as-grown and the annealed layers are characterized, and the annealing properties are compared with the layer grown on an InGaAs/GaAs SLS buffer layer.

## 2. Thermally strained layer.

In the usual SLS the lattice strain is produced by the enforced lattice match of two crystals with different lattice constants. Another way to introduce strain into a heteroepitaxial layer structure is by varying the growth temperature without changing the material choice. For instance, in molecular beam epitaxy (MBE) or organo-metallic chemical vapor deposition (MOCVD), if the substrate temperature can be alternated within a short period of time, the epitaxial film may be either contracted or expanded periodically due to the dissimilarity of thermal expansion coefficients between the substrate material and the epitaxial material. This bimetallic crystal deformation brings a dynamic strain variation into the epitaxial layer with the same period as the substrate temperature cycle. Since the strain is induced by thermal variation, we may call such a layer 'thermally strained layer (TSL)'. The strain in the TSL will be constant whenever the substrate temperature is kept constant. The strain variation during the TSL growth depends on the difference between the thermal expansion coefficient of the substrate crystal and that of the epilayer crystal as well as the amplitude of the temperature cycle. Since the GaAs expansion coefficient is  $\sim 2.6$  times larger than the Si, the GaAs TSL may introduce a relatively large strain variation into the GaAs-on-Si layer during the epitaxy. With this idea the TSL may be used as a defect filtering buffer layer in MBE growth of GaAs-on-Si layers.

## 3. MBE growth of GaAs-on-Si with TSL

For this work, all GaAs-on-Si layers were grown on 2-inch diameter (100) Si substrates tilted by 3-4 degrees toward a (011) zone. The Si substrate cleaning procedure was described previously (Lee 1986). Each substrate was introduced into the MBE chamber using an indium-free mounting substrate holder, and heated at 1000°C for 3 minutes to provide an oxide-free surface just before the growth. The first 50 Å thick GaAs layer was deposited at a substrate temperature of 580°C with a growth rate of 0.3  $\mu\text{m/hr}$ . After this, the growth rate was raised to 0.9  $\mu\text{m/hr}$  and the substrate temperature was cycled five times between 425°C and 625°C every 600 Å growth period, as illustrated in Figure 1. Following the 0.3  $\mu\text{m}$  thick buffer layer growth, the substrate temperature and growth rate were set at 580°C and 0.9  $\mu\text{m/hr}$ , respectively, to grow 3  $\mu\text{m}$  thick GaAs layers.

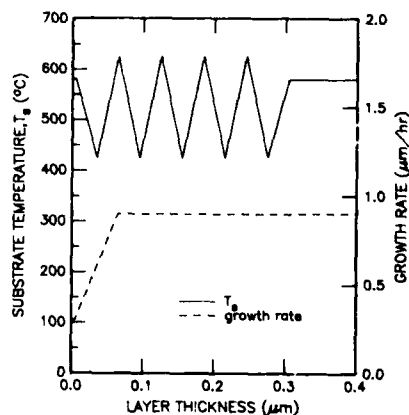


Fig.1. Substrate temperature and growth rate control for TSL growth

#### 4. Characterization of an as-grown layer.

Figure 2 shows the typical surface morphology of a 3  $\mu\text{m}$  thick GaAs-on-Si layer grown with the TSL buffer layer. The surface looks very smooth; no grains were observed in this phase contrast optical micrograph with a 850x magnification. Surface defect density was  $\sim 50/\text{cm}^2$ , including the oval type defect density of  $\sim 30/\text{cm}^2$ . This value is much less than the typical surface defect density of GaAs layers grown on GaAs substrates in the same MBE system,  $\sim 500/\text{cm}^2$ . The wafer flatness was measured by a direct surface profilometer (Taylor-Hobson model Talysurf 4). The profile showed 1.1  $\mu\text{m}$  warpage on the center of the 2 inch wafer. The radius of curvature is estimated to be  $\sim 284$  m from that profile, indicating that the residual thermal stress of this GaAs layer is negligible.

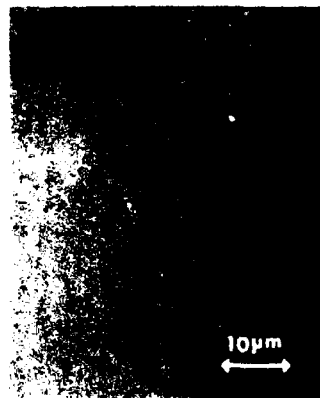


Fig.2. Surface morphology of the GaAs-on-Si layer grown with a TSL buffer.

Detailed defect structure was investigated using TEM. Figure 3 shows a TEM image from the TSL cross section. The area near the GaAs/Si interface has too many dislocations to define the density. Over the first 0.25  $\mu\text{m}$  the dislocation density is reduced quickly, and near the 3  $\mu\text{m}$  top layer it appears to be less than  $10^8/\text{cm}^2$ . Besides the dislocations, several stacking faults (or twins) are seen in this micrograph as straight lines. Small surface ripples are observed on the top surface; the heights of them are less than 200 Å. It should be noted that in this cross sectional image the dislocations over 0.25  $\mu\text{m}$  from the GaAs/Si interface are discrete and short in lengths. The dislocations have deviated from the growth direction and only the short portion of their paths are seen through this thin TEM specimen (less than 1  $\mu\text{m}$ ). Since the dislocation paths are observed over 0.25  $\mu\text{m}$  the deviations may have happened during the TSL epitaxy. This may be an evidence that the TSL acted like a SLS by deflecting the dislocation paths due to thermally induced strain variation.

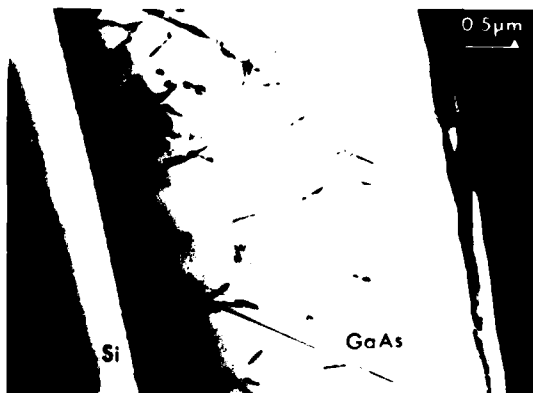


Fig.3. TEM cross section of GaAs-on-Si layer with a TSL buffer. Dislocation paths are discrete over 0.25  $\mu\text{m}$  from the GaAs/Si interface, indicating dislocations were deflected during the TSL epitaxy.

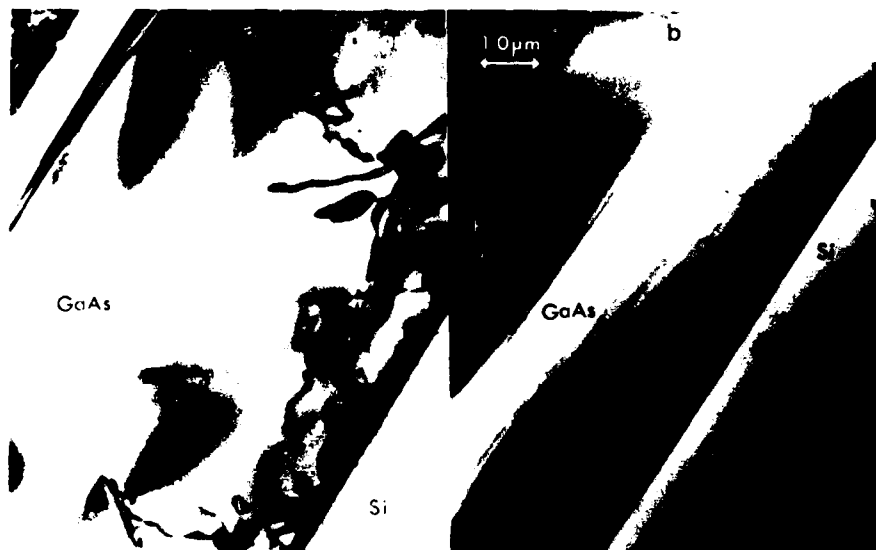


Fig. 4. TEM cross sections of the annealed GaAs-on-Si layer with a TSL before ion-implantation (a) and after ion-implantation at 850°C for 15 minutes.

#### 5. Annealing properties of GaAs-on-Si with TSL buffer

For defect reduction, the GaAs-on-Si wafer with the TSL buffer was annealed in a conventional quartz furnace with As over pressure at 850°C for 15 minutes. Another wafer with Si ion-implantation was also annealed simultaneously. After annealing, no morphological change was observed under optical microscope; no film cracks or slips were found, and the warpage change was negligible.

Figure 4(a) shows the TEM image obtained from the annealed GaAs-on-Si layer specimen. Compared with the as-grown layer, the annealed layer has few defects in the top 2  $\mu\text{m}$  and has no twins and stacking faults. Figure 4(b) shows another TEM cross section of the ion-implanted and annealed specimen. The defect density in this GaAs layer seems to be lower than the annealed only layer. No implantation damage was observed. A wide view of the TEM cross section indicates that the defect free space extends over 20  $\mu\text{m}$  in the near surface region. If we assume that the two dimensional defect density (defect/ $\text{cm}^2$ ) is simply a square of the one dimensional defect (defect/cm), then the total defect density in that area is less than  $3 \times 10^5/\text{cm}^2$ .

#### 6. Comparison with an $\text{In}_{0.15}\text{Ga}_{0.85}\text{As}/\text{GaAs}$ SLS

For the comparison, one 5  $\mu\text{m}$  thick GaAs-on-Si layer was grown with a four-period of  $\text{In}_{0.15}\text{Ga}_{0.85}\text{As}/\text{GaAs}$  (30 Å/200 Å) SLS buffer layer. The SLS was grown at 510°C with a growth rate of 0.3  $\mu\text{m}/\text{hr}$  and the continuing GaAs layer was grown at 580°C with a growth rate of 0.9  $\mu\text{m}/\text{hr}$ . One piece of this layer was annealed simultaneously with a TSL sample.

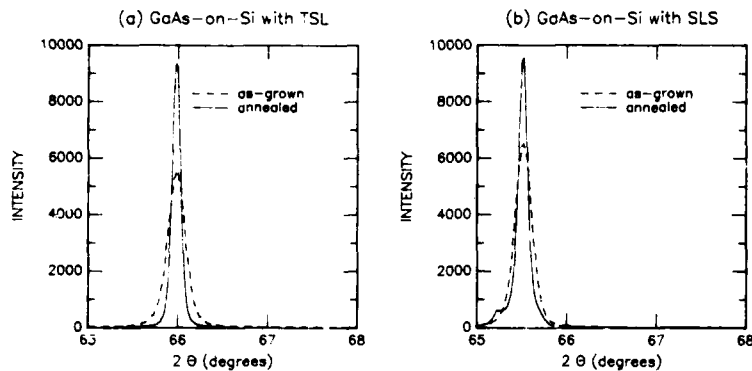


Fig.5 X-ray diffraction patterns of the GaAs-on-Si with a TSL buffer layer (a) and an  $\text{In}_{0.15}\text{Ga}_{0.85}\text{As}$ /GaAs SLS buffer layer (b).

Figure 5 shows (400) x-ray diffraction patterns obtained from the TSL sample (a) and the  $\text{In}_{0.15}\text{Ga}_{0.85}\text{As}$ /GaAs SLS sample (b) both before and after annealing. There are not any significant differences in terms of the GaAs peak linewidths or relative intensities between the TSL sample and SLS sample, indicating that their GaAs epilayer crystallinities are very similar to each other. In both cases, the linewidths of GaAs peaks were significantly reduced after annealing. Combined with the TEM data these linewidth reductions of x-ray peaks proved that thermal annealing truly improved the overall crystallinity of the GaAs-on-Si layers.

The x-ray diffraction proved that the TSL was as good as the SLS as a buffer layer. However, the real advantage of the TSL buffer layer was found after annealing. Figure 6 shows the surface morphologies of the annealed samples. The TSL sample surface (a) remains unchanged, while the SLS sample surface (b) has many cracks or slips with (011) orientations. The reason may be explained by curvature measurements. The radius of curvature of the SLS wafer was 20 m before annealing, while it was 36 m after annealing. From this curvature change it is easily said that the film stress released by thermal annealing induced those cracks or slips. The radius of curvature of the as-grown layer with TSL buffer was 284 m long. It is now under investigation which combination of the TSL results in the minimum stress in the as-grown GaAs-on-Si layers.

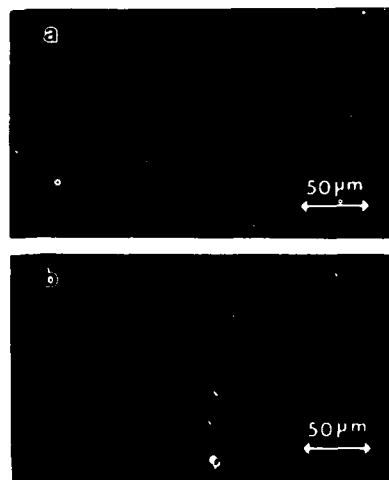


Fig.6. Morphology Comparison of annealed GaAs-on-Si layers with a TSL (a) and SLS (b)

## 7. Conclusion

TSL has been used as a buffer layer for the MBE growth of GaAs-on-Si layers. The as-grown GaAs layers were superior to the other layers in wafer flatness and surface morphology. TEM micrographs indicate that the TSL acted as an effective buffer layer to confine the threading dislocations. The usual defect densities of the as-grown layers were less than  $10^8/\text{cm}^2$ . The defect density was reduced by factor of  $\sim 10^3$  after thermal annealing. The GaAs crystallinity grown on the TSL was comparable to that grown on an  $\text{In}_{0.15}\text{Ga}_{0.85}\text{As}/\text{GaAs}$  SLS; however, the TSL wafer was more resistive to high temperature annealing. After annealing, the surface morphology of the TSL layer sample did not change, while the SLS sample layer had many cracks and slips. This result indicates that the TSL system is more compatible with conventional device processing associated with ion implantation and annealing. To compromise the defect filtering function with the annealing compatibility, it may be useful to combine a low composition ( $\sim 5\%$ )  $\text{InGaAs}/\text{GaAs}$  superlattice with the TSL growth.

## ACKNOWLEDGMENTS

The author is indebted to H. L. Tsai for his TEM works, to R. J. Matyi for his x-ray diffraction measurements, to D. L. Plumton for his careful manuscript reading and valuable suggestions. He is grateful to H. Shichijo, A. J. Purdes, and D. W. Shaw for valuable suggestions and discussions. He thanks J. R. Thomason and K. Tilton for their technical assistant, R. K. Veanueva and J. J. Lorange for their final typing of this manuscript.

## REFERENCES

- Akiyama M, Kawarada Y, and Kaminish K 1984 Jpn. J. Appl. Phys. **23**, L843.  
 Choi H K, Tuner G W, Windhorn T H, and Tsaur B-Y 1986 IEEE Electron Device Lett. **EDL-7**, 500.  
 Fischer R, Neuman D, Zabel H, Morkoc H, Choi C, and Otsuka N 1986 Appl. Phys. Lett. **48**, 1223.  
 Lee J W 1986 Proceedings of Materials Research Society Symposium A, Heteroepitaxy on Si, April 1986, Palo Alto, CA.  
 Lee J W et al 1986 (will be published).  
 Lee J W and Tsai H L 1986 7th MBE Workshop, Oct. 1986, Boston, MA.  
 Masselink W T, Henderson T, Klem J, Fischer R, Pearah P, Morkoc H, Hafich M, Wang P D, and Robinson G Y 1984 Appl. Phys. Lett. **45**, 1309.  
 Metz G M, Choi H K, and Tsaur B-Y 1984 Appl. Phys. Lett. **45**, 1107.  
 Nonaka T, Akiyama M, Kawarada Y, and Kaminish K 1984 Jpn J. Appl. Phys. **23**, L919.  
 Soga T, Hattori S, Sakai S, Takeyasu M, and Umeno M 1985 J. Appl. Phys. **57**, 4578.  
 Shichijo H, Lee J W, McLevige W V, and Taddiken A 1986 IEDM Technical Digest (will be published in December 1986).

## **Properties of AlGaAs grown by molecular beam epitaxy on lenticular substrates**

G. D. Kramer, R. K. Tsui, J. A. Curless and M. S. Peffley

Motorola, Inc., Semiconductor Research and Development Laboratories,  
5005 East McDowell, Phoenix, Arizona, 85008, USA

**Abstract** AlGaAs grown by MBE on GaAs substrate orientations close to (100) has been studied by using lenticular substrates to determine the effect of misorientation on surface morphology and photoluminescence efficiency. Growth parameters which were investigated are aluminum-arsenide mole fraction (0.3 & 0.4), V/III BEP ratio (11 & 6) and substrate temperature (620°C & 650°C). There is two-fold symmetry in the surface morphology about the <100> axis. The smoothest areas, which also have the best photoluminescence, are centered 6° off <100> toward <111>A, i.e., where growth occurs on monatomic steps terminated by gallium atoms.

### **1. Introduction**

Smooth morphology and good optical quality are important properties of semiconductor epitaxial layers that are necessary to optimize device performance. Aluminum gallium arsenide (AlGaAs) is an epitaxial material that has been studied extensively because of its desirable properties, that is, a wide band-gap material lattice matched to gallium arsenide (GaAs). However, AlGaAs grown by Molecular Beam Epitaxy (MBE) has a rough surface and poor optical characteristics when grown under certain conditions that are desirable for device applications (Alexandre et al 1985, Petroff et al 1984, Stall et al 1985). Improved surface and optical quality can be achieved by using high growth temperatures and low V/III BEP ratios (Tsui et al 1984); however, at these higher temperatures there are problems of diffusion and gallium desorption. Recently, we reported that misorienting the GaAs substrate from <100> in a proper direction yields greatly improved structural and optical properties of AlGaAs epitaxial films (Tsui et al 1985, 1986). We also presented evidence of a specific misorientation, that is, a critical angle which gives better-quality epitaxial material. We now report the results of an experiment to more accurately define this critical angle and to determine how the critical angle changes with growth conditions.

The experiment was to grow epitaxial AlGaAs on a convex GaAs substrate which allows all orientations within a certain number of degrees (depending on geometry) to be studied in the same growth run. Four epitaxial layers were grown under different conditions. The growth parameters which were varied were the growth temperature (620°C and 650°C), V/III BEP ratio (6 and 11) and aluminum arsenide (AlAs) mole fraction  $x$  ( $\text{Al}_x\text{Ga}_{1-x}\text{As}$  where  $x \approx 0.3$  and 0.4). The epitaxial films were evaluated by observing the surface morphology and photoluminescence spectrum.

**2. Experimental Procedure**

Four substrates were cut with a (100)-orientation from the same silicon-doped (n+) horizontal Bridgman grown GaAs ingot. They were ground to a plano-convex shape and have a radius of curvature of 100.76 mm, a diameter of 51 mm and a thickness of  $\approx 5$  mm. The convex surface was then polished to a specular finish. This shape allows all orientations within  $14^\circ$  (i.e. out to  $\langle 511 \rangle$ ) of the  $\langle 100 \rangle$ -direction to be studied in one growth run.

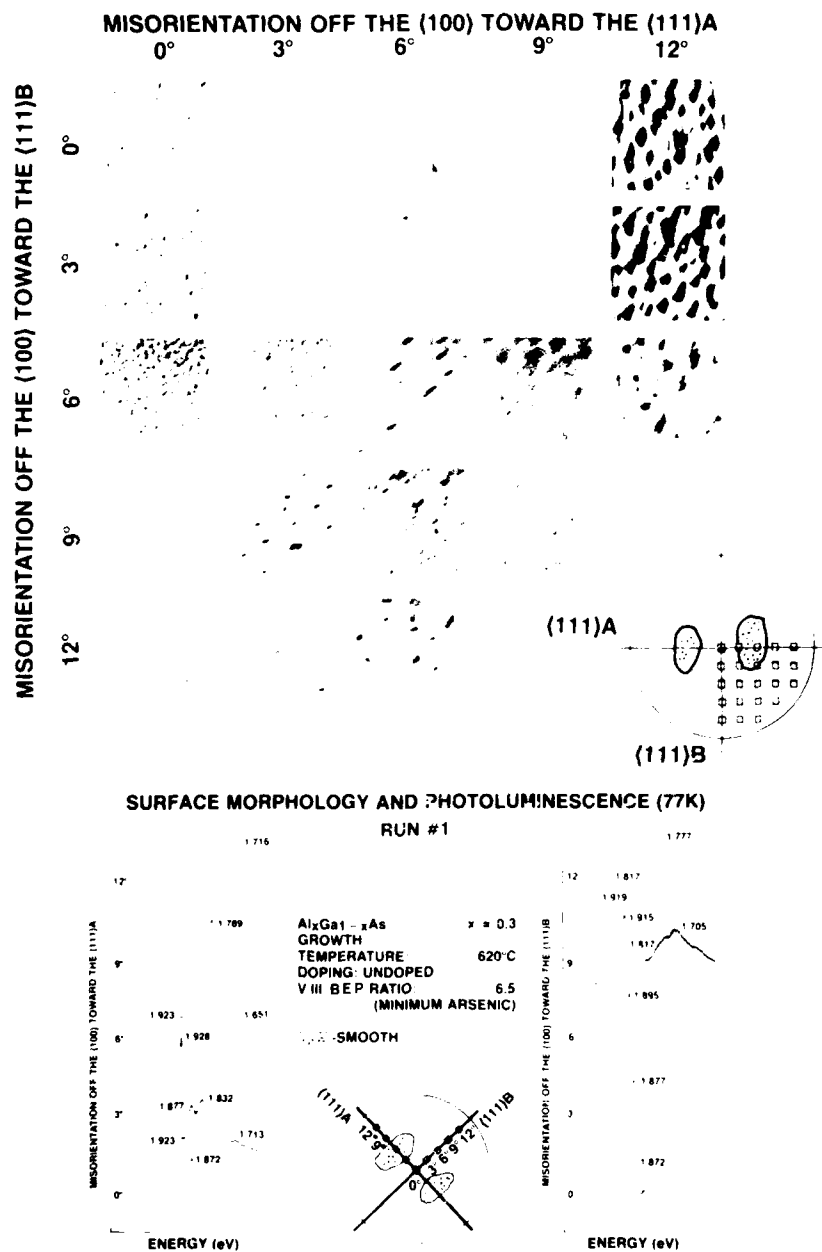
Before epitaxial growth the substrates were solvent cleaned sequentially with two rinses each of: toluene, acetone and 2-propanol heated to just below the boiling point. The lenses were then rinsed in deionized water and etched in a 4:1:1  $\text{H}_2\text{SO}_4 : \text{H}_2\text{O}_2 : \text{H}_2\text{O}$  solution heated to  $100^\circ\text{C}$ . The lenses were etched for a total of 5 minutes, and for the first minute, the solution was stirred. The substrate lenses were removed from the etch solution, rinsed in deionized water and blown dry with nitrogen. After this preparation, the surface of the lens-shaped substrate appears visually to be nearly as good as standard (100) GaAs wafers prepared for epitaxial growth in our laboratory. The lenses were mounted on molybdenum substrate carrier blocks using molten indium and stored in the ultra high vacuum (UHV) of the MBE system until ready for use (usually within 24 hours). There was some initial concern that the thicker, heavier lens-shaped substrates might either slide off the mounting block or crack as they were heated, but this did not turn out to be a problem.

A Varian GEN II MBE system was used to grow the AlGaAs epitaxial layers. This UHV system has two vacuum-locks in series with the growth chamber. Pumping is done by titanium sublimation pumps, ion-pumps and cryo-pumps. There are eight source furnaces arranged radially and pointed toward the substrate holder. The group III furnaces are adjacent to one another to reduce the possibility of a periodic compositional variation as the substrate is rotated. The uniformity of composition  $x$  was evaluated with electron microprobe over the surface of the lens toward the  $\langle 111 \rangle$ A-direction. The variation was found to be  $x \pm 0.012$  over the diameter of the lens.

There are several terms used in the following discussion that should be clarified. The Beam Equivalent Pressure (BEP) is defined as the pressure measured by an ion gauge that is rotated into the growth position; the ion gauge position is then adjusted to maximize the reading. To measure the arsenic BEP, the ion gauge is first exposed to 10 seconds of gallium, then with the gallium shutter open, the arsenic shutter is opened, and the BEP read immediately. The gallium background is subtracted to give the arsenic BEP. The gallium and aluminum BEPs are measured by opening the shutters individually and subtracting the background with the shutters closed. The BEP ratio is defined as the arsenic BEP divided by the sum of the gallium and aluminum BEPs. The arsenic is called minimum when the V/III BEP ratio is set at the lowest level where AlGaAs can be grown without metal-rich morphology.

The AlGaAs in all four runs was grown at a rate of 1 micron per hour to a thickness of  $\approx 4$  microns. The first three runs were grown using an AlAs composition of  $x \approx 0.3$ . Run #1 was grown at  $620^\circ\text{C}$  with minimum arsenic (V/III BEP ratio of 6.5). The BEP readings were: arsenic,  $3.2 \times 10^{-6}$  torr; aluminum,  $1.2 \times 10^{-7}$  torr; and gallium,  $3.7 \times 10^{-7}$  torr. Fig. 1 shows a composite picture of phase contrast micrographs taken of the surface of the epitaxial layer. A quarter of the lens is representative of the surface morphology of the whole lens for all of these growth runs





**Fig. 1.** Surface morphology and photoluminescence (77K) of AlGaAs grown on convex GaAs substrates (growth conditions shown). Smooth morphology and hand-to-hand emission are only found around 6° off <100> toward <111>A.

because of the two-fold symmetry about the  $\langle 100 \rangle$  axis. The micrographs show that growth on the  $\langle 100 \rangle$  orientation is rough as expected. The only smooth regions are located about 6 degrees off  $\langle 100 \rangle$  toward  $\langle 111 \rangle_A$ . The surface becomes rough again as the angle increases even more toward the  $\langle 111 \rangle_A$ -direction indicating that the amount of misorientation is critical. The critical angle is  $6^\circ$  and was determined by observing the smoothest area of the lens using a Nomarski-contrast microscope. The photoluminescence was measured using the 5145 angstrom line of an argon-ion laser with an intensity of  $20 \text{ W/cm}^2$  and a photomultiplier with S-1 response. The 77K photoluminescence spectra were taken at three degree intervals of misorientation off  $\langle 100 \rangle$  toward  $\langle 111 \rangle_A$  and  $\langle 111 \rangle_B$  and correspond to the positions illustrated by the diagram in Fig. 1. The results presented in Fig. 1 show that the areas with the smoothest surface morphology also have the best photoluminescence. Band-to-band emission is visible only toward the  $\langle 111 \rangle_A$  direction. The deeper-level defect-related peaks are reduced or even eliminated in the smooth region.

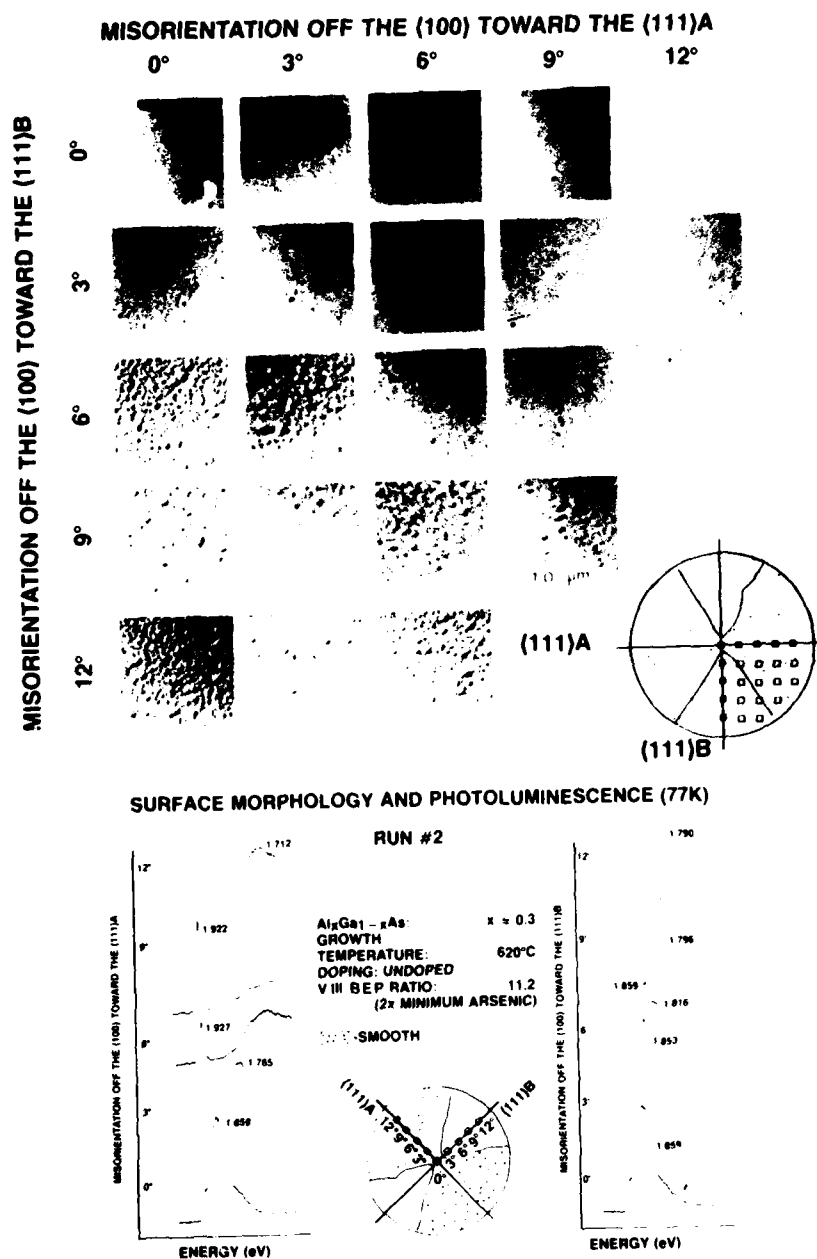
Run #2 used the same growth temperature of  $620^\circ\text{C}$  and  $x \approx 0.3$  but the arsenic flux was increased to yield a V/III BEP ratio of 11.2. The BEPs were: arsenic,  $5.6 \times 10^{-6}$  torr; aluminum,  $1.3 \times 10^{-7}$  torr; and gallium,  $3.7 \times 10^{-7}$  torr. Surface morphology is shown by the composite Nomarski-contrast micrographs in Fig. 2. Run #2 has a large smooth area compared to Run #1 that is triangular shaped. Notice that the surface is fairly smooth in the  $\langle 100 \rangle$  direction and for misorientations toward the  $\langle 111 \rangle_A$  out to  $14^\circ$ , but the orientations toward  $\langle 111 \rangle_B$  all have rough surfaces. The PL spectra (Fig. 2) show band-to-band emission only toward the  $\langle 111 \rangle_A$  direction. The strongest emission is from  $6^\circ$  to  $9^\circ$  which is within the region of smoothest morphology. There is some evidence of much weaker band-to-band emission from  $0^\circ$  to  $6^\circ$ , also within the smooth region. In this instance, the defect-related band near 1.712 eV is still evident.

For the third run, the temperature was increased to  $650^\circ\text{C}$  with  $x \approx 0.3$  and the minimum V/III BEP ratio of 6.7. The BEP readings were: arsenic,  $3.2 \times 10^{-6}$  torr; aluminum,  $1.2 \times 10^{-7}$  torr; and gallium,  $3.6 \times 10^{-7}$  torr. The smooth area is slightly smaller than for Run #1, and again located off  $\langle 100 \rangle$  toward  $\langle 111 \rangle_A$ . The PL spectra show band-edge emission only from the smooth regions.

Finally, in Run #4 the aluminum mole fraction was increased to  $x \approx 0.4$  with growth temperature of  $650^\circ\text{C}$  and V/III BEB ratio of 6.1. The BEP readings were: arsenic,  $3.3 \times 10^{-6}$  torr; aluminum,  $1.7 \times 10^{-7}$  torr; and gallium,  $3.7 \times 10^{-7}$  torr. The surface morphology pattern is very similar to the other minimum arsenic growth runs. The PL spectra again show band-edge emission only from the smooth regions.

### 3. Discussion and Summary

A pictorial summary of the surface morphology of the four AlGaAs epitaxial growth runs is shown in Fig. 3. These smooth regions were determined carefully by a subjective study of the surface using a Nomarski-contrast microscope. The critical angle of misorientation which produces the smoothest morphology in all cases studied is  $6^\circ$  off  $\langle 100 \rangle$  toward  $\langle 111 \rangle_A$  i.e.  $(13,1,1)_A$  to  $(14,1,1)_A$ . The region with smooth morphology changes shape over the range of conditions studied. The strongest effect was in Run #2 when the arsenic flux was doubled. This variation increased the area of the smooth region about the critical angle and produced a wedge-



**Fig. 2.** AlGaAs grown by MBE on a lens shaped GaAs substrate (growth conditions shown) has smooth morphology only off  $\langle 100 \rangle$  toward the  $\langle 111 \rangle$ A. The best PL is also found in the smooth area around  $6^\circ$  misorientation toward the  $\langle 111 \rangle$ A.

## SUMMARY OF REGIONS WITH SMOOTH MORPHOLOGY

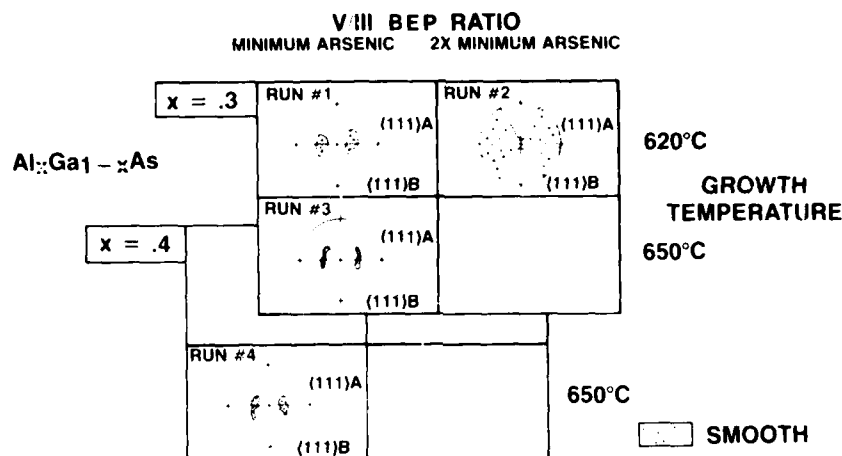


Fig. 3. Comparison of smooth areas for different growth conditions.

shaped smooth area that expands from the center  $\{100\}$ -orientation of the substrate. There are small variations in the shapes of the smooth regions of Runs 1, 3 and 4. It is not clear whether these variations are significant due to the difficulty of precisely controlling the growth conditions. The 77K photoluminescence indicates that the best AlGaAs, as evidenced by band-to-band emission is only found in the regions of smoothest morphology. In the case of increased arsenic flux the best PL is only in the region around the  $6^\circ$  critical angle. Substrate misorientation by the critical angle will result in better-quality AlGaAs being grown at lower temperatures (620°C and 650°C). This misorientation should also lead to improvements in the quality of heterojunction interfaces.

**Acknowledgments** We would like to thank Prof. D. L. Rode (Washington University) for helpful discussions. Also, thanks to T. F. Tracey (Galaris, Phoenix) for his special effort in supplying the substrate blanks, T. P. Rempel for the microprobe analysis, J. S. Escher for providing the PL set-up, K. W. Hansen and H. M. Liaw for their help and support.

### References

- Alexandre F, Goldstein L, Leroux G, Joncour M C, Thibierge H and Rao F V K 1985 J. Vac. Sci. Technol. **B 3** 950
- Morkoc H, Drummond T J, Kopp W and Fischer R 1982 J. Electrochem. Soc. **129** 824
- Petroff P M, Miller R C, Gossard A C and Wiegmann W 1984 Appl. Phys. Lett. **44** 217
- Stall R A, Zilko J, Swaminathan V and Schumaker N 1985 Vac. Sci. Technol. **B 3** 524
- Tsui R K, Curless J A, Kramer G D and Peffley M S 1984 Mat. Lett. **3** 63
- Tsui R K, Curless J A, Kramer G D, Peffley M S and Rode D L 1985 J. Appl. Phys. **58** 2570
- Tsui R K, Curless J A, Kramer G D, Peffley M S and Wicks G W 1986 J. Appl. Phys. **59** 1508

## **The electrical properties of In-doped and low-temperature-grown MBE GaAs**

M. Missous and K.E. Singer

Department of Electrical Engineering and Centre for Electronic Materials  
University of Manchester Institute of Science and Technology,  
PO Box 88, Manchester M60 1QD, U.K.

**Abstract** This work reports the electrical properties of MBE GaAs grown at low temperature. It is demonstrated that the use of indium doping increases the measured free electron concentration and reduces the compensation ratio. The use of  $As_2$  allows good electrical quality GaAs to be grown down to  $430^\circ C$  at  $0.2 \mu m/hour$ . Excellent doping control is exhibited down to  $1 \times 10^{16} cm^{-3}$  and mobilities  $\sim 2/3$  of that for the best MBE material are reported.

### **1. Introduction**

The growth of high electrical and optical quality GaAs epitaxial films is well established, and under the most carefully controlled conditions it is now possible to produce low-doped n-type material whose peak mobility approaches that obtainable by liquid phase epitaxy. For example, Moustakas (1986) has grown intentionally silicon-doped material with a net free electron concentration of  $9 \times 10^{13} cm^{-3}$  and a 55K Hall mobility in excess of  $200,000 cm^2/vs$ . The production of such high quality material requires careful attention to reducing the level of background CO in the MBE system, as well as optimising the growth conditions of arsenic to gallium flux ratio and substrate temperature. The latter of these two is typically in the range  $580$  to  $600^\circ C$  for a growth rate of  $\sim 1 \mu m/hour$ . Whilst these substrate temperatures cause no difficulties in the growth of the majority of structures based on the GaAs and  $Al_xGa_{1-x}As$  material system, there are a number of important areas where a reduction would be desirable.

The object of the work described in this paper was to investigate two possible approaches to the practical growth of acceptable device quality GaAs at lower substrate temperatures. The first of these techniques was the use of the isoelectronic impurity indium introduced into the epilayer at concentrations in the range  $0.05$  to  $0.5$  atomic %; the second was to use  $As_2$  rather than  $As_4$ .

A number of investigations have been made of the low temperature growth of GaAs. Wood et al (1978) found that below  $500^\circ C$  the material became increasingly resistive owing to the presence of compensating defects. Good crystal quality epilayers - as judged from the RED pattern during growth - have been grown at temperatures as low as  $260^\circ C$ , whilst at even lower temperatures ( $\sim 90^\circ C$ ) the surfaces remained smooth but showed no reconstruction (Neave et al 1978). A more detailed study of the electrical and photoluminescence properties has been made by Metze et al (1983). They

demonstrated that a dramatic increase in the film properties could be achieved by reducing the growth rate. For example, they found that for material doped to  $\sim 1 \times 10^{16} \text{cm}^{-3}$ , a reduction in growth rate to  $0.2 \mu\text{m}/\text{hour}$  allowed the substrate temperature to be reduced to  $450^\circ\text{C}$ , whilst at  $0.02 \mu\text{m}/\text{hour}$ ,  $\sim 10^{18} \text{cm}^{-3}$  material could be grown at  $380^\circ\text{C}$ . These measurements were made using  $\text{As}_4$  and silicon as the n-type dopant. More recently a technique entitled Migration-Enhanced Epitaxy (MEE) has been demonstrated (1986) in which the incident beams are interrupted at approximately the monolayer growth frequency. This has allowed material with good PL properties to be grown down to  $200^\circ\text{C}$  at average growth rates of  $0.2 \mu\text{m}/\text{hour}$ . However, as yet no electrical data on these films have been reported.

## 2. Experimental

Growth was performed in a MBE system based on a Riber 2300 growth chamber. Conventional substrate preparation techniques were used (Missous et al 1986) and elemental sources were used for Ga, In,  $\text{As}_4$  and Si. The arsenic dimer was generated from a cell containing nominally undoped, semi-insulating LEC GaAs. The substrate temperature during growth was estimated from the oxide desorption temperature as determined by observation of the appearance of clear RED streaks during initial heating of the substrate in an arsenic flux. For the substrate preparation procedure and heating rates used we have determined this desorption temperature to be  $580 \pm 10^\circ\text{C}$ ; the calibration of the substrate molybdenum block thermocouple having been done previously by observation of the Al-Si eutectic temperature. After oxide desorption the substrate temperature was reduced by a chosen amount for epilayer growth. Beam fluxes were measured using a monitor ion gauge. For  $\text{As}_4$ , and growth at  $580^\circ\text{C}$ , the minimum  $\text{As}_4$  flux for arsenic stable growth gave a beam equivalent pressure ratio of 5:1 ( $\text{As}_4:\text{Ga}$ ). We have denoted this as a flux ratio (J) of 1. Similarly, the minimum beam equivalent pressure ratio for  $\text{As}_2$  growth was 2:1 and the equivalent flux ratio for this species has also been denoted 1.

Assessment of the epilayer has been made by conventional room temperature and 77K Van den Pauw Hall measurements and by C-V profiling using the Polaron PN4200 Electrochemical profiling system.

## 3. Results and Discussion

There were five variables available to us in this work: indium doping or no indium doping,  $\text{As}_2$  or  $\text{As}_4$ , substrate temperature during growth, group V to group III flux ratio and growth rate. The experimental evidence shows that all these factors, singly or in combination, affect the electrical properties of the epilayers. To systematically vary each parameter in various combinations with the others would generate a vast matrix of samples, and consequently we have sought to establish the trends by a careful selection of conditions for each growth run. At this stage of the work we have decoupled the investigations of indium doping and the use of  $\text{As}_2$ .

The results of this work thus fall into the following two categories:

- (i) Effect of indium doping  
The substrate temperature was kept relatively high ( $540$  to  $550^\circ\text{C}$ ), although below the normal GaAs growth temperature in order to reduce indium re-evaporation. Only  $\text{As}_4$  has been used.

(ii) Effect of  $\text{As}_2$ 

For all these epilayers the growth temperature was held at an estimated  $430^\circ\text{C}$ . Comparisons were made between layers grown under nominally identical conditions apart from the choice of group V species. In another series of growth runs the effect of the V:III flux ratio was investigated.

## 3.1 Indium doping

The most obvious effect of indium doping was to increase the measured free electron concentration. This effect is illustrated in figure 1 which is a

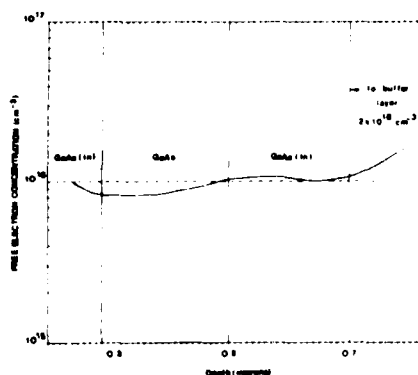


Fig. 1

Profile of film with alternate In and non In-doped layers.

C-V profile of an epitaxial film consisting of alternate indium-doped and non indium-doped layers. Apart from shuttering the indium source, all conditions were kept constant throughout growth. The effect of the indium was to increase the free electron concentration from  $8 \times 10^{15}$  to  $1 \times 10^{16} \text{ cm}^{-3}$ . We have also grown homogeneous films both with and without indium doping on semi-insulating substrates for Hall analysis. The results are shown in table 1 and it can be seen that even though the free electron concentration is higher in the indium-doped layer, the mobility (at both 300 and 77K) is also higher, indicating a substantial decrease in the compensation ratio.

|          | $n_{300}$<br>$\text{cm}^{-3}$ | $\mu_{300}$<br>$\text{cm}^2/\text{V.s}$ | $n_{77}$<br>$\text{cm}^{-3}$ | $\mu_{77}$<br>$\text{cm}^2/\text{V.s}$ | $\eta = \frac{N_D + N_A}{N_D - N_A}$ |
|----------|-------------------------------|---|------------------------------|--|--------------------------------------|
| GaAs     | $1.2 \times 10^{16}$          | 6460                                    | $1.1 \times 10^{16}$         | 16,730                                 | 1.9                                  |
| GaAs(In) | $2.0 \times 10^{16}$          | 6760                                    | $1.9 \times 10^{16}$         | 17,100                                 | 1.4                                  |

Table 1

We have also reported (Missous et al 1986b) an increase in the excitonic PL intensity and reductions in the deep level concentrations measured by DLTS. The increase in free electron concentration was observed for doping from  $10^{16}$  to  $\sim 7 \times 10^{18} \text{ cm}^{-3}$ ; the percentage increase being similar

over the entire range. This observation precludes two possibilities: first, that any observed increase in free electron concentration is simply caused by an additional dopant being present in the indium source, or second, that the indium reduces the concentration of some compensating deep levels. If either of these effects were dominant the increase in the observed free electron concentration would be constant, rather than being proportional to the doping level as we observed. Instead, the magnitude of the effect must be related to the silicon concentration, and this suggests that the indium brings about a reduction in the amphoteric nature of the dopant. Rytova et al (1982) have suggested that as the tetrahedral radius of indium is greater than gallium, the strain introduced in the lattice changes the ratio of gallium to arsenic vacancies. Clearly, any reduction in the concentration of arsenic vacancies relative to gallium will increase the tendency for the silicon atoms to occupy gallium sites, leading to an increase in free electron concentration.

### 3.2 Non indium-doped low temperature growth.

The starting point for these measurements was the data of Metz et al (1983). We have grown a series of three samples using  $\text{As}_4$  and growth rates between 0.25 and 0.12  $\mu\text{m}/\text{hour}$ . The  $\text{As}_4:\text{Ga}$  flux ratio was  $\sim 1$  for all the layers, and the substrate temperature was 430°C. Figure 2 shows the electrochemical C-V profile for a layer grown at 0.2  $\mu\text{m}/\text{hour}$ . It can be seen that whilst it was possible to dope at  $\sim 1.2 \times 10^{18}$  and only just possible to dope at  $4 \times 10^{17}$ , the lower doped (target was  $5 \times 10^{16}$ ) layer is heavily compensated. Similar results were obtained from the layer grown at 0.12  $\mu\text{m}/\text{hour}$ . According to the data shown in Figure 3 of Metz et al (1983), the maximum growth rate for a substrate temperature of 430°C is  $\sim 0.12 \mu\text{m}/\text{hour}$ . However, that figure should be used with caution as it is a compilation of data from epilayers grown in the range  $2 \times 10^{15}$  to  $2 \times 10^{18} \text{ cm}^{-3}$ . It is clear from our results that for a given growth rate the transition temperature between growth of electrically active and non-active layers is dependent on the level of intentional doping. Taking this into account and remembering that the transition is very sharp, the results from our measurements are in reasonable agreement with those of Metz et al (1983).

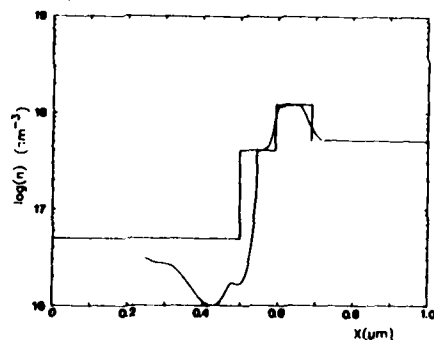


Fig. 2 GaAs grown at 430°C with  $\text{As}_4$  and  $J = 1$

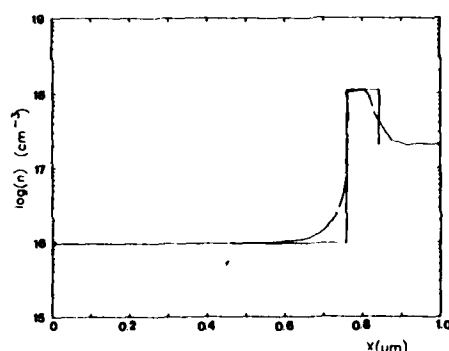


Fig. 3 GaAs grown at 430°C with  $\text{As}_2$  and  $J = 1$

The effect of switching to the use of  $\text{As}_2$  is illustrated by the profile shown in Figure 3. This shows a layer grown under identical conditions to that in Figure 2 apart from the choice of arsenic species. The target



doping of  $\sim 1 \times 10^{16}$  is easily achieved and taking account of the thermal response of the silicon source and Debye smearing effects, the required profile is closely followed.

As with  $\text{As}_4$ , we have found the electrical quality using  $\text{As}_2$  also to be dependent on the V to III flux ratio. This is illustrated by the profile (Figure 4). This film was grown under identical conditions to that in Figure 3 apart from the arsenic:gallium flux ratio which was 3.8 compared to  $\sim 1$  and the target doping which was increased to  $5 \times 10^{16}$ . Even at this increased doping level the layer is seen to be heavily compensated. We have also prepared films with different flux ratios on semi-insulating substrates for Hall analysis. The results are shown in table 2

| J( $\text{As}_2:\text{Ga}$ ) | Tsub( $^{\circ}\text{C}$ ) | $n_{\text{A}}(\text{cm}^{-3})$ | $\mu_{\text{A}}(\text{cm}^2/\text{V.s})$ |
|------------------------------|----------------------------|--------------------------------|--|
| 3.8                          | 430                        | $7.3 \times 10^{16}$           | 2600                                     |
| 1.1                          | 430                        | $6.8 \times 10^{16}$           | 4000                                     |

Table 2

Like the other layers these were grown at  $430^{\circ}\text{C}$  using  $\text{As}_2$  and with flux ratios of 3.8 and 1.1. The improved mobility of the layer grown with the lower flux ratio again points to the importance of this parameter. The mobility of  $8 \times 10^{16} \text{ cm}^{-3}$  GaAs grown under conventional conditions is typically  $6000 \text{ cm}^2/\text{Vs}$ , so whilst our best low temperature growth layers fall short of this figure, the material quality is nevertheless adequate for a number of device applications.

Additional evidence of the electrical quality of the layers can be obtained from the I-V characteristics of Schottky diodes formed on the material. The ideality of the contact is sensitive to the presence of deep levels in the semiconductor which can give rise to space charge recombination/generation current. This effect is shown in the  $\log I$  vs.  $V$  characteristics in figure 5. Both devices exhibit good logarithmic behaviour, but it is clear that the ideality of the layer grown using  $\text{As}_4$  ( $n = 1.22$ ) is considerably worse than that using  $\text{As}_2$  ( $n = 1.04$ ). The reverse current at  $-1\text{V}$  is also about  $100 \times$  greater in the  $\text{As}_4$  grown device.

Preliminary PL and DLTS studies on these layers support the picture that

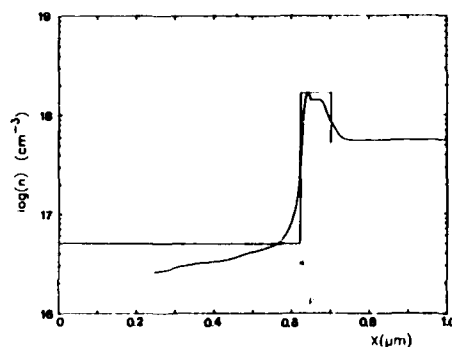


Fig.4 GaAs grown at  $430^{\circ}\text{C}$  with  $\text{As}_2$  and  $J = 3.8$

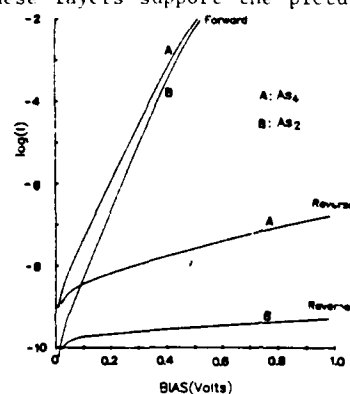


Fig.5  $\ln I$ -V of samples with  $\text{As}_2$  and  $\text{As}_4$

emerges from our results. A significant reduction in the deep level concentrations are observed in DLTS, and PL has shown an increase in the intensity of near band edge excitonic features. These results will be published in more detail shortly.

Neave et al (1980) have reported a reduction in trap concentrations by using  $\text{As}_2$  for GaAs grown at conventional temperatures. They proposed that the simpler surface chemistry involved when using the dimer leads to fewer vacancies being incorporated owing to the higher steady-state arsenic surface coverage. Our results support their observation and demonstrate that the beneficial effect of  $\text{As}_2$  is even more important at lower growth temperatures.

#### 4. Conclusions

The use of the isoelectronic dopant indium at concentrations in the range 0.05 to 0.5 at.% has been shown to improve the electrical quality of GaAs grown at 540-550°C. Apart from a reduction in the trap concentration and increase in the exciton-related PL intensity, the indium also brings about ~ 25% increase in the free electron concentration and reduces the compensation ratio from ~ 2 to 1.4. We suggest that the most important role of the indium is to modify the vacancy concentration in the material, thus reducing the amphoteric nature of the silicon dopant.

Growth at lower temperatures (430°C) is shown to be possible by the use of  $\text{As}_2$ . Although the electrical quality is inferior to the best MBE GaAs grown at higher temperatures, by careful control of the flux ratio we have been able to grow layers with controllable doping down to  $1 \times 10^{16}$  and with Hall mobilities of ~ 2/3 of the best reported values. An important practical point is that the procedures we have adopted do not require unrealistically low growth rates, nor, as in Migration Enhanced Epitaxy (Horikoshi et al 1986), many thousands of shutter operations per micron of growth.

#### References

- Bowler C O and Alley G D 1980 IEEE Trans. Electron Devices **ED-27** pp 1128-1141  
 Horikoshi Y, Kawashima M and Yamaguchi H (1986) IV Int. MBE Conf. York  
 Metze G M, Calawa A R and Mavroides J G 1983 J Vac. Sci. Technol **B1(2)** pp 166-169  
 Missous M, Rhoderick E H and Singer K E 1986a J. Appl. Phys. **59** pp 3189-3195  
 Missous M, Singer K E and Nicholas D J 1986b Proc IV Int. Conf. on MBE York (1986) In press J Cryst. Growth  
 Moustakas T and Friedman R A 1986 In press J Appl. Phys.  
 Neave J H and Joyce B A 1978 J Cryst. Growth **43** pp 387-397  
 Neave J H, Blood P and Joyce B A 1980 Appl. Phys. Letters **36** 4 pp 311-312  
 Rytova N S, Solov'eva E V and Mil'ridsku M G 1982 Sov. Phys. Semicond. **16** pp 951-953  
 Wood C E C, Woodcock J and Harris J J 1978 7th Inst. of Physics Conf. on GaAs and Related Compounds St. Louis. Inst. of Physics Conf. Ser. **45** pp 28-37

#### Acknowledgements

This work has been supported by the U.K. Science and Engineering Research Council.

## **Atomic layer epitaxy of III-V compounds by hydride VPE**

Akira Usui and Haruo Sunakawa

Fundamental Research Laboratories., NEC Corporation,  
1-1, Miyazaki 4-chome, Miyamae-ku, Kawasaki, Kanagawa 213, Japan

**Abstract.** Atomic layer epitaxy(ALE) of III-V compound semiconductors InAs, InP, GaP and InGaP is carried out by the chloride ALE method. It is confirmed that the growth is indeed digital, i.e. the grown thickness per ALE cycle is almost equal to the monolayer thickness and is nearly independent of growth conditions. A Langmuir type adsorption model for chloride gases is employed to discuss the mechanism of the digital epitaxy and the growth under mixed chloride gas conditions. The method is also applied to the growth of GaAs/GaGe heterostructures.

### **1. INTRODUCTION**

Recently, in the growth of III-V compound semiconductors, atomic layer epitaxy(ALE)(Suntola et al. 1980) has been introduced as a new method to control grown thickness with one monolayer accuracy and to make heterostructures with very abrupt interfaces(Nishizawa et al. 1985, Bedair et al. 1985, Doi et al. 1986). In the conventional MBE, MOCVD and VPE methods, these conditions have been realized by the accurate control of growth time, flow rates and temperatures. In contrast, the ALE can achieve layer-by-layer growth without such a fine control of growth conditions. We have already reported the ALE of GaAs using GaCl and AsH<sub>3</sub> over a wide range of GaCl partial pressure and growth temperatures(Usui and Sunakawa 1986). It was shown that the grown thickness per one ALE cycle is approximately equal to the monolayer thickness and the total grown thickness depends solely on GaCl adsorption cycles. This type of growth is called a digital epitaxy, because no analogue parameters such as mentioned above need be controlled precisely(Watanabe and Usui 1980). In the chloride ALE method we used, it was possible to realize digital epitaxy of GaAs over a wider range of growth conditions than the MO-ALE methods so far reported. This is perhaps because the chloride ALE growth involves only a Langmuir type adsorption of GaCl in contrast to the MO-ALE growth where dissociation reactions of hydrocarbons (such as methyl group) take place together with adsorption. This is an advantage of the present method.

In the present paper, the chloride ALE is widely applied to the growth of III-V compound semiconductors other than GaAs such as InP, InAs, GaP and InGaP. We show here that the digital epitaxy has been confirmed on these materials and that the growth can be well understood by the Langmuir type adsorption model. Furthermore, we report on the growth of GaAs/GaGe heterostructures and the incorporation mechanism of selenium and the electrical properties of grown layers.

### **2. EXPERIMENTAL**

© 1987 IOP Publishing Ltd

The reactor used was a horizontal multi-chamber reactor as previously reported (Usui and Sunakawa 1986). This reactor has a high-temperature source zone containing In and Ga source metals, and a low-temperature substrate zone. HCl gas supplied from upstream reacts with the metal sources producing GaCl or InCl, which in turn is carried with  $H_2$  to the substrate zone kept at the atmospheric pressure.  $AsH_3$ ,  $PH_3$  and  $H_2$  were supplied to another chamber and the substrate holder was switched between the two chambers automatically. The substrate was exposed to GaCl for 6 seconds and to  $As_4$  for 10 seconds alternatively. One ALE cycle, consisting of a single round of gas exposure, purge of  $AsH_3$  or  $PH_3$  and substrate transfer, completed in 45 seconds. The  $AsH_3$  or  $PH_3$  flow was suspended during the substrate transfer to prevent the extraneous deposition on the substrate. The above cycle was repeated 200 times typically. The growth temperature and the metal source temperature were 450°C and 750°C, respectively unless stated otherwise.

### 3. RESULTS AND DISCUSSIONS

Figure 1 shows the relationship between the HCl gas partial pressure over In and Ga source metals, and the growth rate of III-V compound semiconductors by the present method. Monolayer thicknesses for those materials, which are indicated in the ordinate, are 3.50 Å, 3.26 Å, 2.93 Å, 2.83 Å and 2.73 Å for InAs(100), GaAs(111), InP(100), GaAs(100) and GaP(100), respectively. The HCl gas partial pressure was varied from  $4 \times 10^{-5}$  to  $10^{-3}$ . The growth rates of these layers were found to agree well with calculated monolayer thicknesses and were almost independent of the HCl gas partial pressure within the accuracy of the measurements ( $\pm 5\%$ ), except the growth of GaP for lower HCl partial pressure. All obtained surfaces were completely mirror-like free from any surface defects as in the case of GaAs previously reported (Usui and Sunakawa 1986). Thus we have confirmed that digital epitaxy can be successfully applied to In-containing or P-containing materials as well. To realize digital epitaxy, monolayer adsorption of GaCl and InCl should take place on the growing surface. Such monolayer adsorption of adsorbates can be well understood by a Langmuir type adsorption mechanism. The isothermal equation of the Langmuir adsorption is simply expressed as  $\theta = Kp / (1 + Kp)$  ( $\theta$ : coverage,  $K$ : adsorption equilibrium constant). This equation indicates that  $\theta$  is nearly equal to unity when  $Kp \gg 1$ , i.e., the amount of adsorption hardly depends on the partial pressure of adsorbates and the temperature. The condition  $Kp \gg 1$  is considered to be applicable to the present system for a wide range of growth conditions. The validity of this assumption will be discussed elsewhere (Watanabe and Usui 1986).

The Langmuir type adsorption model was found to explain well another experimental results when two adsorbates exist in the same gas phase. In the InP ALE on InP(100), it was found that addition of free-HCl to InCl

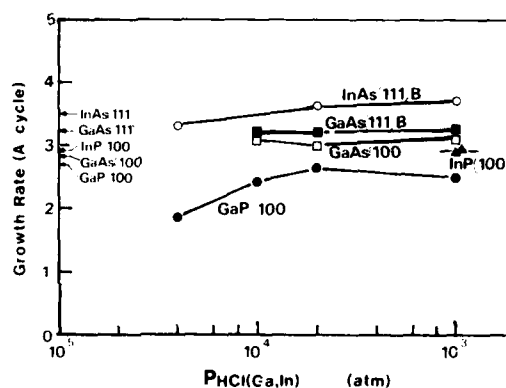


Fig. 1 Growth rate dependence on the HCl partial pressure to transport Ga or In for various III-V compounds. The values in the ordinate represent monolayer thicknesses for these materials.

resulted in a remarkable decrease in the grown thickness. Closed circles in Figure 2 show grown thicknesses normalized by the thickness without free-HCl 3.0 Å. This value was approximately identical to the monolayer thickness. By adding 5% of free-HCl, the grown thickness decreased to about 1/3 and with 20% of free-HCl, practically no growth was observed. These results can be well understood by a Langmuir type competitive adsorption model for mixed gases as follows. By Markham-Benton equation, the adsorbate concentration of species  $i$  can be written in the form

$$v_i = bK_i p_i / (1 + \sum K_i p_i)$$

where  $b$  is the saturation adsorbate concentration,  $K_i$  and  $p_i$  are the adsorption equilibrium constant and the partial pressure of species  $i$ , respectively. Applying this equation to the present system, we obtain

$$v_{\text{InCl}} = bK_{\text{InCl}} p_{\text{InCl}} / (1 + K_{\text{InCl}} p_{\text{InCl}} + K_{\text{HCl}} p_{\text{HCl}})$$

$$v_{\text{HCl}} = bK_{\text{HCl}} p_{\text{HCl}} / (1 + K_{\text{InCl}} p_{\text{InCl}} + K_{\text{HCl}} p_{\text{HCl}})$$

Using  $x$  and  $y$  defined by the relation

$$x = v_{\text{InCl}} / (v_{\text{InCl}} + v_{\text{HCl}}), \quad y = p_{\text{HCl}} / (p_{\text{InCl}} + p_{\text{HCl}})$$

These equations can be rewritten as

$$1/(1-x) = (1 + K_{\text{InCl}}/K_{\text{HCl}})(1/y)$$

Here  $y$  denotes the ratio of HCl to the total chlorides. Furthermore,  $x$  is equal to the surface coverage of InCl if we assume that the adsorption sites are occupied by either InCl or HCl (i.e. no vacant site). The solid lines in Fig. 2 present calculated  $x$  as a function of  $y$  for several different values of the parameter  $K_{\text{InCl}}/K_{\text{HCl}}$ . The curve can be best fitted to the experimental results when  $K_{\text{InCl}}/K_{\text{HCl}}$  is 0.02. A similar comparison was made on the ALE of GaAs. Substrates used in the growth were (100)GaAs and the growth temperature was 450 °C. In Fig. 3, experimental results are shown together with the curves calculated assuming mixed adsorption of GaCl and HCl. In the case of GaAs, the effect of free-HCl on the growth was found to be very small in contrast to the case of InP and was almost negligible for  $y < 0.9$ . The value of  $K_{\text{GaCl}}/K_{\text{HCl}}$  that gives the best fit was as high as 120. These results indicate that the heat of adsorption ( $q_{\text{GaCl}}$ ) of GaCl molecules on an As surface is considerably larger than that of HCl while  $q_{\text{InCl}}$  is fairly smaller on a P surface. Since the heat of adsorption is a measure of the binding energy between the adsorbate and underlying atoms, the bond

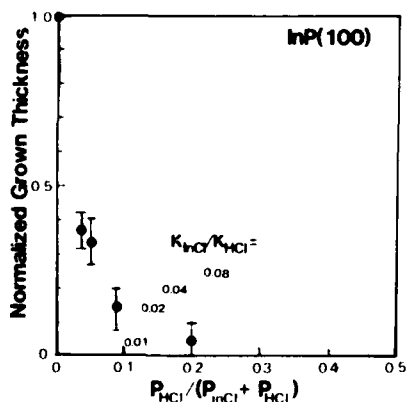


Fig. 2 Effect of free-HCl on the grown thickness of ALE InP. The solid lines represent calculated results.

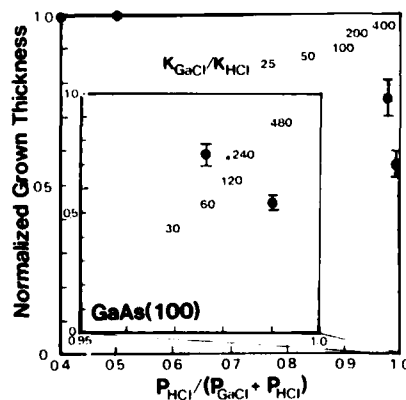


Fig. 3 Effect of free-HCl on the grown thickness of ALE GaAs. The solid lines represent calculated results.

between In and P is considered to be much weaker than between Ga and As. Actually, InP has a relatively large dissociation pressure among the III-V compounds at the present growth temperature. In any case, these results strongly support that the adsorption process in the present system is of the Langmuir type.

Now let us discuss our preliminary result of the ALE growth of InGaP. Both of GaCl and InCl were supplied simultaneously in the present growth. The substrates were GaAs(100) and the growth temperature was 450°C. The partial pressure of  $\text{PH}_3$  was  $2.1 \times 10^{-3}$ . As for the GaCl to InCl ratio  $p_{\text{GaCl}}/(p_{\text{GaCl}} + p_{\text{InCl}})$  in the gas phase, two different values 0.17 and 0.077 were adopted. Microphotographs of grown surfaces are shown in Fig. 4 together with that of the conventional hydride VPE InGaP grown at 550°C. In the case of the conventional method, the surface obtained revealed very rough morphology as shown in Fig. 4(c). Furthermore, the half width of the x-ray rocking curve was greater than 1000 seconds although the lattice-mismatch ( $\Delta a/a$ ) was approximately as low as  $3 \times 10^{-3}$ , and the peak intensity was also very weak in spite of relatively large layer thickness ( $t=2.4 \mu\text{m}$ ). In contrast, completely mirror-like surfaces were obtained by the present method as shown in Fig. 4(a). When the GaCl to InCl ratio was 0.17, line-hatched patterns due to the large lattice-mismatch ( $\Delta a/a = 1.8 \times 10^{-2}$ ) were observed as shown in Fig. 4(b). Thus, in the ALE, InGaP growth is possible even at low temperatures as low as 450°C, which is the lowest temperature so far reported in the InGaP epitaxial growth. The grown thickness of the layer in Fig. 4(a) was about 840 Å. Dividing by the ALE cycle 300, the growth rate of 2.8 Å/ALE cycle is obtained. This is consistent with the monolayer thickness of  $\text{In}_{0.5}\text{Ga}_{0.5}\text{P}$ . Accordingly, the monolayer adsorption of the Langmuir type is considered to take place in this case as well. The alloy composition is determined by the competitive adsorption of GaCl and InCl. The fact that even a small GaCl fraction of 0.17 in the gas phase resulted in a rather large Ga fraction of 0.75 in the solid phase may be attributed to the strong adsorption of GaCl on the growing surface as compared to the InCl adsorption.

In the ALE of GaAs, since arsenic molecules such as  $\text{As}_4$  and  $\text{As}_2$  have very high vapor pressures, the incorporation into the crystal is considered to be governed by the Eley-Rideal surface process, in which Ga-As bonds are formed by the reaction between adsorbed GaCl and the arsenic gas. We introduced  $\text{H}_2\text{Se}$ , which easily decomposes to Se and  $\text{H}_2$  at the present growth temperature, into the reactor instead of  $\text{AsH}_3$ . It is known that Se makes a bond with Ga to form gallium selenides such as  $\text{GaSe}$ ,  $\text{Ga}_2\text{Se}_3$  and  $\text{Ga}_2\text{Se}$ . This indicates that selenium incorporation also obeys the Eley-Rideal process. Selenium is also an n-type dopant in III-V compound semiconductors. The growth procedure was as follows; first, on the GaAs substrate, nine layers of GaAs were grown, then, the source gas

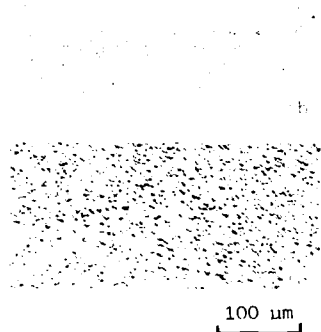


Fig. 4 Microphotographs of InGaP as-grown layers: (a) nearly lattice-matched ALE InGaP, (b) lattice-mismatched ( $\Delta a/a = 1.8 \times 10^{-2}$ ) ALE InGaP, (c) conventional VPE InGaP grown at 550°C.

in the  $\text{AsH}_3$  chamber was switched from  $\text{AsH}_3$  to  $\text{H}_2\text{Se}$  whose partial pressure was  $4 \times 10^{-4}$ . After exposure to  $\text{GaCl}$ , the substrate was carried into a  $\text{H}_2\text{Se}$  atmosphere. The exposure time to  $\text{H}_2\text{Se}$  was identical to that of  $\text{AsH}_3$ . After that, nine GaAs layers were again grown and the whole cycle was repeated 20 times. In this experiment, (100), (111)A and (111)B substrates were used. Figure 5 shows the dependence of selenium concentration from the SIMS measurements on the growth temperature for (100) and (111)B substrates. The growth temperature was varied from 350 °C to 550 °C. The concentrations were calibrated using SIMS intensity obtained from conventional VPE-grown Se-doped ( $n = 1.8 \times 10^{18} \text{ cm}^{-3}$ ) GaAs, assuming that all of the incorporated Se act as donors. The selenium concentration increased rapidly with decreasing growth temperature and the maximum value was on the order of  $10^{21} \text{ cm}^{-3}$ . Although the selenium concentration for (111)B is much larger than for (100) surface, both exhibit almost the same tendency. If we assume that exactly one Se layer is formed and replaces an  $\text{As}_2$  plane in the present structure, the Se concentration should be  $2.2 \times 10^{21} \text{ cm}^{-3}$ . The experimental results are in good agreement with this value for lower growth temperature. This suggests that selenium is actually incorporated in the form of monolayers, but further investigations should be carried out to establish this point. X-ray rocking curve revealed lattice-mismatch of  $5.5 \times 10^{-3}$  for the sample grown on (100)GaAs substrate at 350 °C. However, no surface morphology such as hillock, pit or hatched-pattern due to the lattice-mismatch was observed and a completely mirror-like surface was obtained.

The carrier concentration was measured by the van der Pauw method on those samples. The growth temperature dependence of the carrier concentration for various samples is shown in Fig. 6. The carrier concentration has a peak at around 450 °C for (100) and (111)A samples. The highest value was obtained for (111)A and was as high as  $1.4 \times 10^{19} \text{ cm}^{-3}$ . The carrier concentrations of GaAs(100) samples were slightly below those of (111)A. The carrier concentration decreased drastically on both sides of 450 °C. The decrease in the higher temperature side is clearly

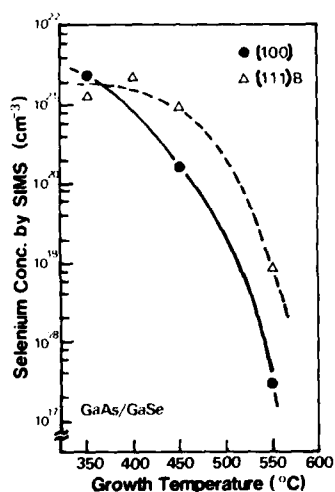


Fig. 5 Growth temperature dependence of the Se concentration of GaAs/GaSe heterostructures by the SIMS measurements.

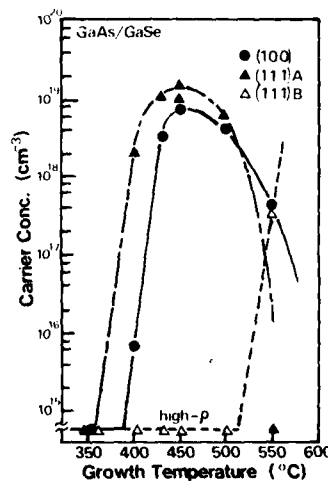


Fig. 6 Growth temperature dependence of the free carrier concentration of GaAs/GaSe heterostructures on various planes.

related to the reduced incorporation of Se as shown in Fig.5. On the lower temperature side, heavily incorporated Se presumably forms gallium selenide layers. As a result, Se does not work as a donor in GaAs and the carrier concentration is decreased. In the case of (111)B, carriers are not generated up to around 550 °C presumably because Se is incorporated in higher concentration than for (100)GaAs and gallium selenide layers may be formed. At the temperature region where selenium layers are considered to be formed, obtained layers revealed high-resistive characteristics. To explain the difference in the amount of incorporated Se between substrates, we propose a simple model. When the substrate, after adsorption of GaCl, is exposed to H<sub>2</sub>Se and Se is incorporated into the As sites, a Se atom is surrounded by three Ga atoms on (111)B surface while it has only one and two neighboring Ga atoms on (111)A and on (100) surfaces, respectively. This suggests that Se atoms on (111)B are most stable and the stability decreases in the order of (100) and (111)A. The experimental results shown in Fig. 5 and 6 can be well explained by this model. Thus, using the present method, new structure such as GaAs/GaSe, which are very difficult to grow by the conventional growth methods, can be readily grown. This is another advantage of the chloride ALE growth.

#### 4. CONCLUSIONS

The atomic layer epitaxial method using chlorides was applied to the growth of III-V compound semiconductors InAs, InP, GaP. InGaP was also grown by the present method at a low growth temperature of 450 °C. Grown thicknesses per ALE cycle were found to be almost identical to their monolayer thicknesses and the digital nature of the epitaxy was confirmed over a wide range of chloride partial pressure. A Langmuir type monolayer adsorption model was employed to explain the mechanism of the digital epitaxy. The ALE growth of GaAs and InP layers under the condition of simultaneous existence of HCl and GaCl or InCl was also discussed. The obtained results also strongly support that the adsorption of chlorides is of the Langmuir type. Furthermore, it was shown that Se planes can be inserted during the growth of GaAs by supplying H<sub>2</sub>Se instead of AsH<sub>3</sub>. These results indicate that the present technique has a wide range of applications in the growth of various new materials and structures.

#### ACKNOWLEDGMENTS

The authors would like to thank Miss T. Jitsukawa for the SIMS measurements and Mr. T. Sasaoka for his assistance in the experiment. They also thank Drs. S. Asanabe, D. Shinoda, F. Saito, H. Watanabe and Y. Matsumoto for their continuous encouragement.

#### REFERENCES

- Suntola T, Anton J, Pakkala A and Lindfors S 1980 SID International Symposium Digest of Technical Papers 11 108
- Nishizawa J, Abe H and Kurabayashi T 1985 J. Electrochem. Soc. 132 1197
- Bedair S M, Tischler M A, Katsuyama T and El-Masry N A 1985 Appl. Phys. Lett. 47 51
- Doi A, Aoyagi Y, Iwai S and Namba S 1986 Extended Abstract the 18th(1985 International) Conf. on Solid State Devices and Materials, Tokyo, p 739
- Usui A and Sunakawa H 1985 Jpn. J. Appl. Phys. 25 L212
- Watanabe H and Usui A, this conference



## **Atomic layer epitaxy of III-V materials and quantum-well structures**

M A Tischler, N G Anderson and S M Bedair

Electrical and Computer Engineering Department  
North Carolina State University  
Raleigh, NC 27695-7911

**Abstract.** The growth of GaAs, InAs and  $\text{In}_x\text{Ga}_{1-x}\text{As}$  ( $0 < x < .43$ ) by atomic layer epitaxy is reported along with the presence of a self-limiting mechanism which controls the deposition to one monolayer per cycle over a wide range of growth conditions. InAs/GaAs single-quantum-well structures with well widths of 2 and 4 monolayers exhibit intense luminescence with very narrow linewidths of 12 and 17 meV respectively.

### 1. Introduction

In the past year or two, there have been a number of reports of III-V semiconductor growth techniques which may conveniently, if somewhat inaccurately be listed under the name atomic layer epitaxy (ALE) (Nishizawa 1985, Usui 1985, Kobayashi 1985 and Tischler 1985). Although they do not all conform to the ideal ALE mode (one monolayer deposited per cycle (Goodman 1986)), they do have in common the fact that some variable of the growth process is cycled and the film thickness then becomes dependent on the growth per cycle and not a growth rate as in conventional growth techniques. In this paper, the growth of GaAs, InAs and  $\text{In}_x\text{Ga}_{1-x}\text{As}$  ( $0 < x < .43$ ) is described. A self-limiting mechanism is present which limits the deposition to one monolayer per cycle. A model is presented to explain this self-limiting mechanism. Extremely thin InAs/GaAs single-quantum-well (SQW) heterostructures grown by ALE are also described. Photoluminescence spectra from these structures are intense with very narrow linewidths indicating high quality material and sharp interfaces.

### 2. ALE of GaAs, InAs and InGaAs

The experimental setup and growth conditions for the ALE of GaAs (Tischler 1986a), InAs and InGaAs (Tischler 1986b) have been described previously. Basically an atmospheric pressure metal-organic chemical vapor deposition (MOCVD) system was modified by the addition of a new susceptor and growth chamber. The growth chamber has separate inlet tubes for the column III and column V species. The substrate is continuously rotated between the two gas streams and thus is alternately

exposed to the column III and column V species. This cycle is repeated as desired with one cycle resulting in the deposition of one monolayer of material ( $2.83 \text{ \AA}$  for GaAs). Thus the total thickness is determined only by the lattice constant of the material and the number of cycles. A cycle takes 2.6 seconds and each exposure time is about 0.3 seconds.

Figure 1 shows the GaAs film thickness per cycle as a function of TMG flow (Tischler 1986a). It is evident that there is a self-limiting mechanism present which allows only one monolayer to be deposited independent of the TMG or  $\text{AsH}_3$  flux. The self-limiting mechanism is also present at growth temperatures from 450 to  $700^\circ\text{C}$  and for substrates oriented (100),  $2^\circ$  towards  $\langle 011 \rangle$ , (111)A and (111)B. The surfaces of all these layers were shiny and mirror-like. The self limiting mechanism was also present in the growth of InAs and  $\text{In}_x\text{Ga}_{1-x}\text{As}$  ( $0 < x < .43$ ) (Tischler 1986b), especially for layers with compositions near the binary endpoints. The film thickness per cycle is somewhat greater than one monolayer (but less than two) for  $x > .4$ .

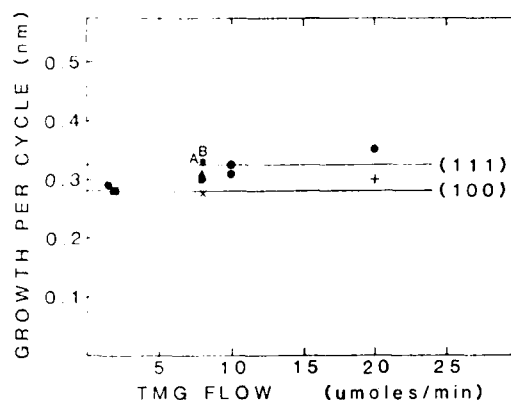


Figure 1: Thickness of GaAs per cycle versus TMG flow.

(100) Substrates

- $T_g = 630^\circ\text{C}$ ,  $\text{AsH}_3 = 52 \mu\text{mole/min}$ ;
- $T_g = 450^\circ\text{C}$ ,  $\text{AsH}_3 = 156 \mu\text{mole/min}$ ;
- +  $T_g = 450^\circ\text{C}$ ,  $\text{AsH}_3 = 110 \mu\text{mole/min}$ ;
- $T_g = 630^\circ\text{C}$ ,  $\text{AsH}_3 = 110 \mu\text{mole/min}$ ;
- ×  $T_g = 700^\circ\text{C}$ ,  $\text{AsH}_3 = 52 \mu\text{mole/min}$ .

(111) Substrates: A = (111)A; B = (111)B

$T_g = 630^\circ\text{C}$ ,  $\text{AsH}_3 = 52 \mu\text{mole/min}$

The thickness of conventionally grown GaAs was investigated as a function of TMG flux in the same system. This was done with and without rotation. The TMG and  $\text{AsH}_3$  were introduced together into the growth chamber through one inlet tube, and the substrate was either held stationary in the gas stream or rotated through the gas stream. The rotation scheme was the same as that used for ALE. In both cases, the amount deposited increased with the TMG flux. This is in contrast to the ALE results where the deposition per cycle was independent of the reactant fluxes and is an indication that ALE growth is proceeding by a different mechanism than conventional bulk MOCVD.

The effect of rotation rate was also investigated. This was done in two ways. In the first case, the actual rotation rate was lengthened. This was done by changing the pause time between each step of the stepping motor which drove the rotating part of

the susceptor. In the second case, the actual exposure time was lengthened, but the time to rotate from one inlet tube to the other was kept constant. This was done by briefly stopping the substrate under each inlet tube. Almost all of the layers were partially hazy and this hazy area increased as the exposure time was increased. In the shiny areas of the substrate the growth was still about one monolayer per cycle, whereas it was larger (but generally less than two monolayers) in the hazy areas. This non-uniformity may have its origins in the asymmetrical design of the susceptor. Gases are more readily heated and trapped near the inside edge of the substrate. This would result in premature cracking of the TMG and possibly deposition of more than one monolayer per cycle. Additionally, as the exposure time is increased, the thermal boundary layer develops more fully allowing cracking of the TMG in the gas phase, with the result that greater than one monolayer per cycle would be deposited. It is probable that the exposure-time window for monolayer deposition could be opened some by changing the design to remove areas in which gases can be trapped.

GaAs was also grown with a shorter exposure time,  $\sim .16$  seconds. The total rotation rate was increased by reducing the pause time between each step of the stepping motor. One rotation occurred in about 1.3 seconds which is about twice as fast as the normal rotation rate. The surface was shiny and the thickness was about one monolayer per cycle.

### 3. Self-Limiting Mechanism and Growth Model

A possible explanation for the self-limiting mechanism may be derived from the growth conditions (Tischler 1986a, 1986d). Since the thermal boundary layer is quite thin, the TMG molecule may not decompose until it is close to, or on the substrate surface. There, the TMG molecule can acquire enough thermal energy from the substrate to partially or fully decompose or to re-evaporate undissociated.

At least a coverage of one monolayer of chemically adsorbed species on the GaAs substrate will take place. It may be that some fragment, or radical, of the TMG molecule is what is adsorbed on the surface. A possible example of this situation is shown in Figure 2. In this case, the TMG radical is attached to the surface where one of the methyl radicals used to be. At this point, the surface is not GaAs, but is covered with a layer of TMG species. It is known that the GaAs surface catalyzes the decomposition of  $\text{AsH}_3$  and  $\text{PH}_3$  (Leys 1981, Nishizawa 1983 and Stringfellow 1984) and there is evidence that it also may catalyze the decomposition of TMG (Schlyer 1976). Thus while the cracking efficiency of TMG on the GaAs surface for these temperatures can be fairly high (Nishizawa 1983), when the GaAs

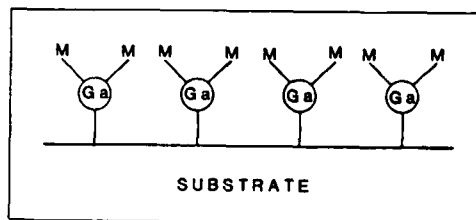
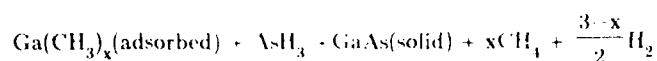


Figure 2: Schematic of the growth model showing TMG radicals adsorbed on the surface.

surface is covered with a monolayer of Ga species, the cracking efficiency or condensation coefficient may then be very small and additional TMG molecules may then re-evaporate before they have a chance to decompose.

At this point, there is a monolayer of TMG radicals on the surface. When this is exposed to the  $\text{AsH}_3$ , an exchange reaction occurs between  $\text{AsH}_3$  and the TMG fragment:



with the methane and hydrogen liberated as a gas. This process is repeated in each cycle.  $\text{AsH}_3$  is not expected to continue to deposit on the surface because of its high vapor pressure. If the self-limiting mechanism is indeed a result of the molecular nature of the sources, one might expect that ALE in a MBE-type system with elemental sources (such as Ga or As) would not produce the same results. More work is needed to verify these assumptions.

#### 4. InAs/GaAs Single-Quantum-Well Structures

The SQW structures were grown on GaAs:Si substrates, oriented (100),  $2^\circ$  towards  $\langle 011 \rangle$ . A  $1 \mu\text{m}$  thick GaAs buffer layer was grown by conventional MOCVD; that is, with the  $\text{AsH}_3$  and TMG arriving simultaneously at the substrate. The GaAs confining layers and the InAs wells were grown by ALE. The details of the ALE growth process have been previously reported (Tischler 1986c). To ensure that the InAs was deposited pseudomorphically (elastically strained), the well widths were kept below the critical thickness  $h_c$  for the onset of dislocation generation (Matthews 1974). For this large lattice mismatch ( $\sim 7.4\%$ ),  $h_c$  is

about  $20 \text{ \AA}$ . The single quantum wells were characterized by photoluminescence (PL) spectroscopy at 19 K. The PL spectra is very sensitive to material and interface quality (Welch 1983 and 1985, Tsang 1986). High quality SQW's typically

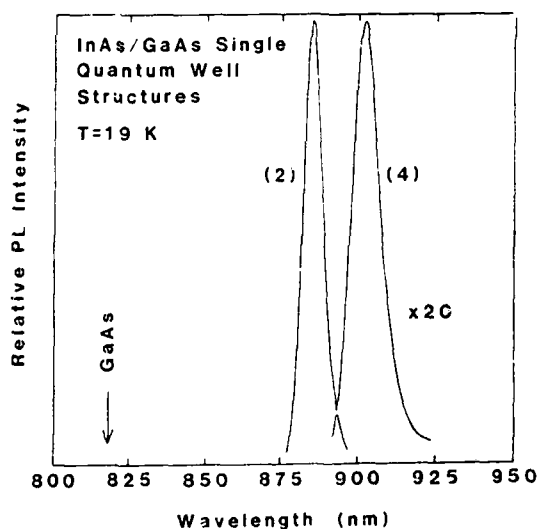


Figure 3: Photoluminescence spectra for the 2 and 4 cycle single quantum wells. The integer next to each spectra corresponds to the number of InAs monolayers in the well.

exhibit sharp, intense peaks (Deveaud 1984, Ohta 1986 and Tsang 1986).

The spectra for the 2 and 4 cycle wells {corresponding to 6.6 and 13.1 Å (Asai 1983)} are shown in Figure 3. The luminescence is strong with very narrow spectral widths, indicating the high quality of the material and the interfaces. The well thicknesses are calculated from the growth per cycle measured on thicker samples (170 Å to 0.34 µm) using transmission electron microscopy. The full width at half maximum (FWHM) of the spectra are 12 and 17 meV (for the 2 and 4 cycle wells respectively). These are shown in Figure 4 which is a plot of the PL FWHM versus well width. Also listed are data for SQW's in many different material systems grown by molecular beam epitaxy (MBE), MOCVD and chemical beam epitaxy (CBE). It can be seen that the ALE results are among the narrowest reported for such thin SQW's in this or other material systems.

A second, identical 2 cycle SQW structure, grown 7 months after the first one, has almost identical spectral characteristics. Peak energies and FWHM for these two samples are within 8 and 0.5 meV of each other, respectively. The photoluminescence peak energy, FWHM and photoluminescence peak energy variation across each sample (1.5 by 1.5 cm) are very uniform which indicates a high degree of control of layer thickness and interface quality. The peak energy variation across each sample is only 5-7 meV. These results indicate that ALE has the ability to produce thin uniform layers, high quality material and sharp interfaces.

### 5. Conclusions

The ALE of GaAs, InAs and  $\text{In}_x\text{Ga}_{1-x}\text{As}$  ( $0 < x < .43$ ) has been demonstrated. A self-limiting mechanism is present which controls the deposition to only one monolayer per cycle independent of the input fluxes, growth temperature and substrate orientation. The deposited thickness is found to be more sensitive to the rotation rate. InAs/GaAs single-quantum-well structures grown by ALE show photoluminescence spectra which are intense with very narrow linewidths. Additionally the PL

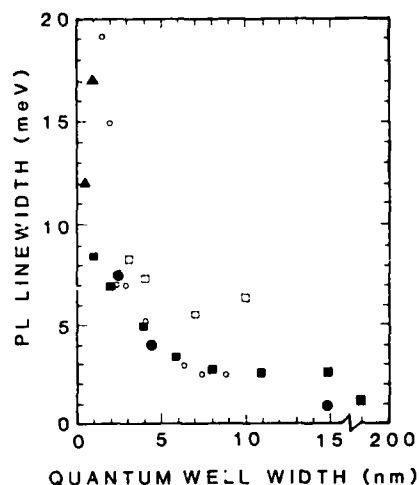


Figure 4: Photoluminescence linewidth as a function of well width.

- ▲ ALE InAs/GaAs (19K, this work)
- MBE AlAs/GaAs (2K, Tsang 1986)
- MBE-PL AlGaAs/GaAs (2K, Ohta 1986)
- MOCVD AlGaAs/GaAs (2K, Deveaud 1984)
- CBE  $\text{In}_{.53}\text{Ga}_{.47}\text{As}/\text{InP}$  (2K, Tsang 1986).

peak variation is very small across the entire substrate. These results indicate that ALE has the capability to controllably produce thin uniform layers with abrupt interfaces.

## 6. References

- Asai H and Oe K 1983 *J. Appl. Phys.* **54** 2052  
 Deveaud B, Emery J, Chomette A, Lambert B and Baudet M 1984 *Appl. Phys. Lett.* **45** 1078  
 Goodman C and Pessa M 1986 *J. Appl. Phys.* **60** R65  
 Kobayashi N, Makimoto T and Horikoshi Y 1985 *Inst. Phys. Conf. Ser. No. 79* 737  
 Leys M and Veenvliet H 1981 *J. Cryst. Growth* **55** 145  
 Matthews J and Blakeslee A 1974 *J. Cryst. Growth* **27** 118  
 Nishizawa J and Kurabayashi T 1983 *J. Electrochem Soc.* **130** 413  
 Nishizawa J, Abe H and Kurabayashi T 1985 *J. Electrochem Soc.* **132** 1197  
 Ohta K, Funabashi H, Sakamoto T, Nakagawa T, Kawai N, Kojima T and Kawashima M 1986 *J. Electron. Mat.* **15** 97  
 Schlyer D and Ring M 1976 *J. Organometallic Chem.* **114** 9  
 Stringfellow G 1981 *J. Cryst. Growth* **68** 111  
 Tischler M, Anderson N, Katsuyama T and Bedair S 1985 *Electronic Materials Conf. Boulder, CO June 19-21*  
 Tischler M and Bedair S 1986a *Appl. Phys. Lett.* **48** 1681  
 Tischler M and Bedair S 1986b *Appl. Phys. Lett.* **49** 274  
 Tischler M, Anderson N and Bedair S 1986c *Appl. Phys. Lett.* Nov.  
 Tischler M 1986d PhD thesis North Carolina State University  
 Tsang W and Schubert E 1986 *Appl. Phys. Lett.* **49** 220  
 Usui A and Sunakawa H 1985 *Inst. Phys. Conf. Ser. No. 79* 753  
 Welch D, Wicks G and Eastman L 1983 *Appl. Phys. Lett.* **43** 762  
 Welch D, Wicks G and Eastman L 1985 *Appl. Phys. Lett.* **46** 991

## Optical characterization of stress effects in GaAs/Si

S. Zemon, C. Jagannath, E.S. Koteles, S.K. Shastry, P. Norris,  
G. Lambert, A.N.M. Choudhury, and C.A. Armiento

GTE Laboratories Incorporated, 40 Sylvan Road, Waltham, MA 02254.

**Abstract:** The dependence of the two excitonic features in GaAs/Si on external uniaxial stress has been found to be in good agreement with theory. A photoluminescence (PL) study of layers of varying thickness shows that the tensile stress is constant between 1 and 10  $\mu\text{m}$ . PL measurements further indicate that the acceptor binding energy is reduced in GaAs/Si, consistent with literature deformation potentials. Rapid thermal annealing is found to cause a stress increase.

### 1. Introduction

GaAs grown directly on Si (GaAs/Si) is of intense current interest because of the many device applications (Fischer et al 1986a, b and references therein). We have found that optical spectra provide not only an insight into important material properties, but also a simple and rapid way to characterize the material (Zemon et al 1986). In a recent publication (Zemon et al 1986) the spectra have been interpreted in terms of a model in which the light hole ( $m_j = \pm 3/2$ ) and heavy hole ( $m_j = \pm 1/2$ ) valence band degeneracy has been removed by the biaxial tensile stress generated by the thermal expansion mismatch between GaAs and Si.

At 4.2 K the PL spectrum consists of four lines (Zemon et al 1986) which are often reported in the literature (Wang 1984, Metze et al 1984, Masselink et al 1984, Fischer et al 1985, Duncan et al 1986). We have identified the two higher energy lines as the heavy- and light-hole exciton features. In this paper we confirm and further explore our model by means of PL excitation spectra of samples subjected to an applied uniaxial stress. Furthermore, we report on the stress uniformity and reproducibility for five layers of differing thicknesses from 1  $\mu\text{m}$  to 10  $\mu\text{m}$  employing photoluminescence (PL) techniques. Finally, we present the results of acceptor studies on undoped GaAs/Si as well as on layers implanted (Mg, Zn, Si) and annealed using rapid thermal annealing (RTA).

### 2. Experimental Details

Our GaAs/Si growth techniques have been previously reported (Shastry and Zemon 1986). Samples used for the PL study of implanted acceptors were 4- $\mu\text{m}$  thick.  $^{24}\text{Mg}^+$  was incorporated into the layer by ion implantation having two implant schedules of dose and energy,  $1 \times 10^{12} \text{ cm}^{-2}$  at 100 keV and  $2.5 \times 10^{12} \text{ cm}^{-2}$  at 400 keV, respectively.  $^{66}\text{Zn}^+$  was implanted with a  $1 \times 10^{12} \text{ cm}^{-2}$  dose at 100 keV and a  $3 \times 10^{12} \text{ cm}^{-2}$  dose at 400 keV.  $^{29}\text{Si}^+$  ions which are amphoteric dopants in GaAs, were implanted in another layer with a dose of  $2 \times 10^{12} \text{ cm}^{-2}$  at 100 keV. The samples were then annealed by a capless RTA technique using an enhanced overpressure proximity method (Armiento and Prince 1986). All the samples were annealed in  $\text{N}_2$  ambient with an AG Heatpulse 410 System.  $\text{Mg}^+$  and  $\text{Zn}^+$

implanted samples were annealed at 950°C for 10 sec, whereas the Si<sup>+</sup> implanted samples were annealed at 950°C for 30 sec just to allow the implants to show acceptor-like behavior. The carrier concentrations were determined to be  $\approx 6 \times 10^{16} \text{ cm}^{-3}$  to a depth of  $\approx 1 \mu\text{m}$  for Mg<sup>+</sup> and Zn<sup>+</sup> and to a depth of 0.2  $\mu\text{m}$  for Si. The experimental techniques involving uniaxial stress and PL excitation spectroscopy (Jagannath and Koteles 1986) and PL (Zemon et al 1986) have been described previously.

### 3. External Uniaxial Stress Experiments

We preface the discussion of our present work with a summary of the pertinent results reported earlier (Zemon et al 1986). From high temperature PL studies (the line shape, the spectral width, the temperature dependence of the energy peaks, dependence of PL intensity upon excitation power) as well as 4.2 K PL, PLE and selective excitation studies, it was proposed that the spectra are dominated by conduction-band-to-light-hole ( $m_j = \pm 3/2$ ) transitions for  $300 \text{ K} \geq T \geq 150 \text{ K}$ , with conduction-band-to-heavy-hole ( $m_j = \pm 1/2$ ) transitions dominating below 100 K. At 4.2 K both lines are excitonic. In addition, at  $60 \text{ K} \geq T \geq 4.2 \text{ K}$ , two impurity lines can be observed, the shallower one identified with carbon. The split valence band model qualitatively accounted for the peak energies of the intrinsic lines assuming a stress of 2-3 kbar.

The two 4.2 K exciton lines were further studied as a function of an external uniaxial stress along a (100) direction applied in the plane of the layer. In the presence of an applied uniaxial stress  $X$ , in addition to the residual biaxial tension  $X_0$ , the eigenvalues of the strain Hamiltonian are

$$E_{\pm} = E_0 + A(X+2X_0) \pm B[(X+X_0)^2 - XX_0]^{1/2} \quad (1)$$

with  $A = a(S_{11} + 2S_{12})$  and  $B = b(S_{11} - S_{12})$  where  $a$ ,  $b$  are the hydrostatic and shear deformation potentials respectively, and  $S_{11}$  and  $S_{12}$  are the elastic compliance constants.  $E_0$  is the exciton energy in GaAs in the absence of any stress and is taken to be 1.5152 eV.

In Fig. 1, we plot (as solid circles) the variation of the exciton peaks with uniaxial stress up to a value of 6 kbar. The solid lines represent the theoretical fit to the data using Eq. 1 with  $A = -3.5 \text{ meV/kbar}$ ,  $B = -2.4 \text{ meV/kbar}$  and  $X_0 = 3 \text{ kbar}$ . Following the normal convention,  $X$  is negative (positive) for compressive (tensile) stress. These values of  $A$  and  $B$  are in good agreement (within 10%) with the experimental values found in literature (Chandrasekhar and Pollak 1977). The

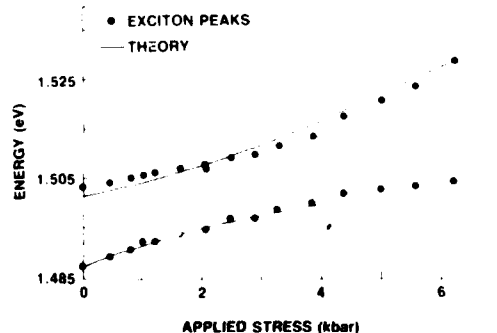


Fig. 1 Data and theoretical fit for the external uniaxial stress measurement at 4.2 K. The applied stress is compressive.



agreement between the experimental points and theory is good, further confirming our identification of the peaks.

#### 4. PL Spectra for Layers 1 $\mu\text{m}$ - 10 $\mu\text{m}$ Thick

PL data were taken on five samples grown to various thicknesses, i.e., 1, 2, 3, 4 and 10  $\mu\text{m}$ . Spectra for the 10- $\mu\text{m}$  sample are shown in Fig. 2 with identifications based upon previous work (Zemon et al 1986). Note that the 4.2 K spectrum is dominated by a ( $\pm 1/2$ )-exciton transition at  $\approx 832.5$  nm. The 4.2 K acceptor and deep level PL amplitudes beyond  $\approx 840$  nm are reduced by about a factor of 40 below that of the dominant exciton transition. [A similar low level of acceptor PL is observed for our homoepitaxial material (Shastry et al 1987).] The PL spectra from all five samples had weak impurity features, in contrast with the results obtained by others (Metze et al 1984, Masselink et al 1984, Fischer et al 1985, Duncan et al 1986) in which impurity features are much stronger. The 4.2 K spectral width of the ( $\pm 1/2$ ) exciton for the 10- $\mu\text{m}$  sample is 4.3 meV, comparable to that reported by Duncan et al (1986) for MBE-grown material. When the excitation intensity is increased (not shown), the ( $\pm 3/2$ )-exciton peak can be detected at 824.4 nm and a ( $e, A^0_C$ ) peak at 843.0 nm. The latter is determined to be a ( $e, A^0_C$ ) and not a ( $D^0, A^0_C$ ) transition from the behavior with power density at 4.2 K [a ( $D^0, A^0_C$ ) transition at 845.0 nm is observed at 4.2 K for the lower excitation densities used in Fig. 2] and at 25 K where donors become ionized. Carbon is identified as the dominant shallow acceptor in undoped GaAs/Si (Zemon et al 1986). We will return to the discussions of the ( $e, A^0_C$ ) transition in a subsequent section.

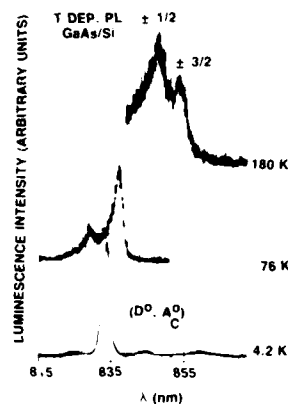


Fig. 2 PL spectra for a 10- $\mu\text{m}$  sample at several temperatures. At 4.2 K,  $I_e$  is  $\approx 50$  mW/cm $^2$ .

The ( $\pm 1/2$ )-exciton peak as well as the other peaks are essentially the same for all five samples. Since the exciton peaks can serve as a measure of biaxial tensile stress [through Eq. (1) with  $X = 0$ ], it is clear that all five layers are subjected to substantially the same stress near the surface excitation region. Thus, for these layers no substantial stress gradients exist, at least for distances greater than 1  $\mu\text{m}$  from the interface. Of course, this is the expected result for all practical cases where the film thickness is much, much less than the radius of curvature (typically  $\approx 10$ -30 m).

#### 5. Acceptor PL

In order to examine the PL behavior of acceptors in GaAs/Si, implanted and annealed layers were used. Figure 3 shows the PL for a Mg-implanted sample at three temperatures, 20.4 K, 70.6 K and 159 K. We identify the longest wavelength line with ( $e, A^0_{Mg}$ ) since it shows the characteristic reduction in PL amplitude due to thermal ionization as the temperature approaches 70 K. Based on the trends seen in previous work (Zemon et al 1986), we identify the two short wavelength lines as intrinsic transitions associated with the ( $\pm 1/2$ )- and the ( $\pm 3/2$ )-valence bands. Data taken at 9 K as a function of excitation intensity ( $I_e$ ) are shown in Fig. 4. The shifting of the peak of the longest wavelength line as  $I_e$  is increased from the lowest to highest values is interpreted in terms of

the expected shift from ( $D^0$ ,  $A^0_{Mg}$ ) to ( $e$ ,  $A^0_{Mg}$ ). The fact that the ( $\pm 1/2$ ) transition increases nonlinearly with  $I_e$ , typical for p-doped material, is due to strong hole trapping by acceptors at low  $I_e$ . When the spectrum is extended to 880 nm, a line situated ( $36.7 \pm 0.5$ ) meV below the ( $e$ ,  $A^0_{Mg}$ ) peak is observed at an intensity two orders of magnitude below that of the [ $e$ ,  $A^0_{Mg}$ ] line. This weak signal is identified with the longitudinal optical phonon replica.

Data obtained for the Zn- and Si-implanted layers were similar to those of the Mg layers except that the acceptor lines were shifted to longer wavelengths. Table I summarizes the pertinent results. We list the estimated biaxial stress  $X_0$  [obtained from using Eq. (1) for  $X = 0$  in conjunction with the peak energy of the ( $\pm 1/2$ )-exciton transition], the energy difference  $\Delta E(X_0)$  between the ( $\pm 1/2$ )-exciton transition and the ( $e$ ,  $A^0_{Mg}$ ) transition, and the energy difference  $\Delta E(0)$  obtained from bulk (unstressed) GaAs. Note that  $\Delta E(0) - \Delta E(X_0) = 4.5$  meV, an indication that the acceptor binding energy in GaAs/Si has decreased with respect to that of GaAs/GaAs.

Stress data have appeared in the literature for carbon acceptors,  $A^0_C$ , in GaAs (Bhargava and Nathan 1967). For  $A^0_C$  transitions, Bhargava and Nathan reported that the hydrostatic deformation potential is equal to that of the valence band while the shear deformation potential ( $b'$ ) is less than the valence band value ( $b$ ), i.e.,  $b' = 0.56 b$ . Using  $b'$  in Eq. 1 (with  $X = 0$ ) we plot the theoretical variation of the ( $e$ ,  $A^0_C$ ) transition energies in Fig. 5 along with the two exciton energies. The fact that the splitting of the two acceptor peaks has a weaker stress dependence than that of the two

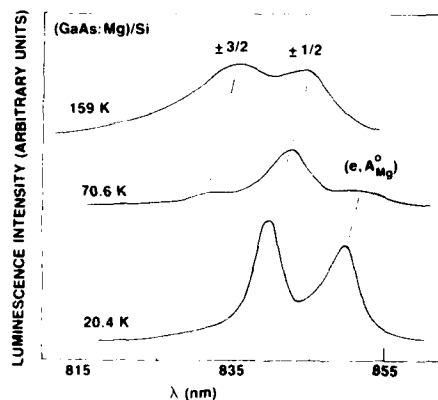


Fig. 3 Mg-implanted GaAs/Si spectra at several temperatures.

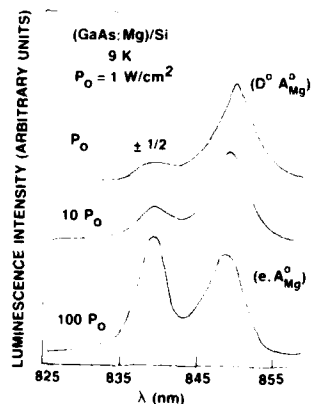


Fig. 4 Mg-implanted GaAs/Si spectra at 9 K for several excitation powers.

| $A^0$ | $X_0$<br>(kbar) | $\Delta E(X_0)$<br>meV | $\Delta E(0)$<br>meV |
|-------|-----------------|------------------------|----------------------|
| Mg    | 3.4             | 17.1                   | 21.7                 |
| Zn    | 3.6             | 20.4                   | ---                  |
| Si    | 3.5             | 23.2                   | 27.6                 |

Table 1 Acceptor ( $A^0$ ) PL data for samples implanted and annealed.  $\Delta E(X_0) = E(\pm 1/2) - E[(e, A^0)]$ .

exciton peaks causes the acceptor binding energy to decrease with increasing  $X_0$ . The crosses represent the peak energies obtained for the 10- $\mu\text{m}$  sample (see Fig. 2).  $X_0 \approx 2.5$  kbar was obtained by fitting the ( $\pm 1/2$ )-exciton peak to the theoretical curve. The fact that the ( $\pm 3/2$ )-exciton data point falls very close to the theoretical line demonstrates the good agreement obtained between theory and experiment. Note that the ( $e, A_0^0$ ) data point falls on the theoretical curve for the ( $\pm 1/2$ ) acceptor level, confirming that the acceptors in GaAs/Si have a reduced binding energy. The data for the samples of other thicknesses are in good agreement with that for the 10- $\mu\text{m}$  sample. We note that a ( $\pm 3/2$ )-acceptor transition is not observed at 4.2 K, presumably due to thermal depopulation and the fact that the PL peak falls on the long wavelength tail of the much stronger ( $\pm 1/2$ )-exciton line.

#### 6. Rapid Thermal Annealing of GaAs/Si

It is apparent from the data of Table I that GaAs/Si which has been implanted and annealed using RTA at 950°C has undergone an increase in stress of about 1 kbar from the  $\approx 2.5$  kbar value found before processing. In order to further investigate this phenomenon, an unimplanted 4- $\mu\text{m}$  layer was processed using RTA at 950°C for 10 s. The resultant ( $\pm 3/2$ )- and ( $\pm 1/2$ )-exciton PL peaks for 4.2 K are plotted as closed circles in Fig. 5. Note that again the biaxial tensile stress has increased about 1 kbar to  $\approx 3.5$  kbar. Using the model of Ishida et al (1986) and assuming stress relief at the annealing temperature (950°C) instead of the growth temperature (600°C), a calculation of the strain induced by the GaAs and Si differential thermal contraction between 950°C and 600°C gives a value of about 0.1%. This corresponds to a stress of about 1 kbar, thus accounting for at least a major part of the stress increase during RTA. Thus, it is clear that after high temperature processing (Inomata et al 1985, Nonaka et al 1984), GaAs/Si will be subjected to an increase in the biaxial tensile stress.

#### 7. Summary

External uniaxial stress experiments have confirmed the split valence band picture suggested by Zemon et al (1986). The sample stress is found to be independent of thickness for layers between 1  $\mu\text{m}$  and 10  $\mu\text{m}$ . Furthermore, acceptor binding energies in GaAs/Si are shown to be reduced from those for homo-epitaxial material. Finally, rapid thermal annealing of GaAs/Si is found to cause a stress increase in the material.

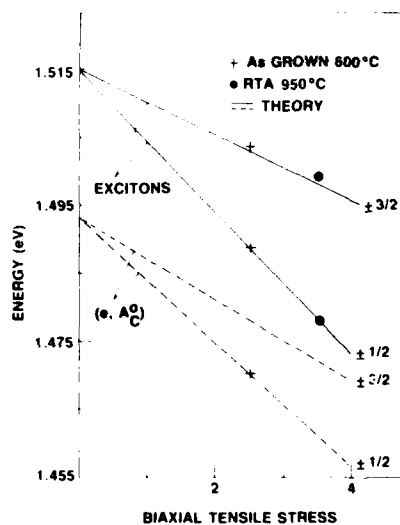


Fig. 5 Comparison of PL peaks of as-grown and RTA GaAs/Si at 4.2 K with theory.

Acknowledgements

We thank Drs. P. Haugsjaa and H. Lockwood for their continued support, and M. DeAngelis, J. Cambriello and L. Lehman for technical assistance.

References

- Armiento C A and Prince F C 1986 Appl. Phys. Lett. 48 1623  
 Bhargava R N and Nathan M I 1967 Phys. Rev. 161 695  
 Chandrasekhar M and Pollak F H 1977 Phys. Rev. B 15 2127  
 Duncan W M, Lee J W, Matyi R J and Liu H-Y 1986 J. Appl. Phys. 59 2161  
 Fischer R, Masselink W T, Klem J, Henderson T, McGlinn T C, Klein M Y, Morkoc H, Mazur J H, and Washburn J 1985 J. Appl. Phys. 58 374  
 Fischer R J, Kopp W F, Gedymin J S, and Morkoc H, 1986a IEEE Trans. Electron Devices ED-33, 1407  
 Fischer R J, Chand N, Kopp W F, Peng C-K, Morkoc H, Gleason K R and Scheitlin D 1986b IEEE Trans. Electron Devices ED-33 206  
 Inomata H, Nishi S, Akiyama M, Itok M, Takahashi S and Kaminishi K 1986 Gallium Arsenide and Related Compounds, Karuizawa 1985 (Bristol: Inst. of Physics) Inst. Phys. Conf. Ser. 79 481  
 Ishida, K, Akiyama M and Nishi S 1986 Jpn. J. Appl. Phys. 25 L288  
 Jagannath C and Koteles E 1986 Solid State Commun. 58 417  
 Masselink W T, Henderson T, Klem J, Fischer R, Pearah P, Morkoc M, Hafick M, Wang P D and Robinson G Y 1984 Appl. Phys. Lett. 45 1309  
 Metze G M, Choi H K and Tsaur B-Y, 1984 Appl. Phys. Lett. 45 1107  
 Shastry, S K and Zemon S 1986 Appl. Phys. Lett. 49 467  
 Shastry S K, Zemon S and Norris P 1987 Gallium Arsenide and Related Compounds 1986 (to be published)  
 Wang W I 1984 Appl. Phys. Lett. 44 1149  
 Zemon S, Shastry S K, Norris P, Jagannath C and Lambert G 1986 Solid State Commun. 58 457

## **Impurity gettering and dislocation reduction by GaAs(In) and InP(As) strained layer epitaxy and related device effects**

T.Tilli, R.Schummers, P.Narozny, N.Emeis, H.Beneking, H.Klapper\*

Institute of Semiconductor Electronics, Aachen University of  
Technology, Sommerfeldstraße, D-5100 Aachen, FRG

\*Institute of Crystallography, Jägerstraße 17-19, D-5100 Aachen, FRG

**Abstract:** It is shown that strained isoelectronically doped buffer layers grown on GaAs and InP substrates reduce the dislocation density due to the formation of a dislocation network at the interface. Applied to bipolar transistors a great improvement in current gain is found in comparison to conventionally fabricated devices.

### **1. Introduction**

It is known that the performance of III-V-devices is significantly influenced by dislocations. For example Roedel et al. (1979) have found that the external efficiency of Si-doped GaAlAs LEDs is reduced with increasing dislocation density. Petroff et al. (1973) show that in short wavelength GaAlAs lasers a high density of point defects formed by pair recombination causes the grown-in dislocations to punch out loops. This dislocation multiplication leads to dark-line-defects, a primary cause of laser failure. Kasahara (1985) has found that the threshold voltage of GaAs FETs imitates the dislocation distribution of the substrate. This leads to the conclusion that for highly-integrated GaAs-ICs the dislocation density must be lower than  $200\text{cm}^{-2}$  as pointed out by Di Lorenzo et al. (1984).

Many investigations have been made to achieve GaAs and InP substrates with low dislocation density. Jordan et al. (1984,1985) have studied the dislocation generation in GaAs and InP. Two methods have been reported to reduce the dislocation density: (a) low temperature gradient during growth, (b) impurity hardening by doping with excessive amounts of S or Ge in InP or similarly Si, Te or In in GaAs. This was experimentally confirmed by Kimura et al. (1984), who have grown low dislocation indium-alloyed GaAs and by Kohda et al. (1985), who have grown completely dislocation-free In-alloyed GaAs. The influence of the temperature-gradient was experimentally determined by Jordan et al. (1984). But there remain some problems with this methods as pointed out by Jordan et al. (1984). A low temperature gradient leads to instability during the crystal growth and the excessive doping is not possible when semi-insulating substrates are needed.

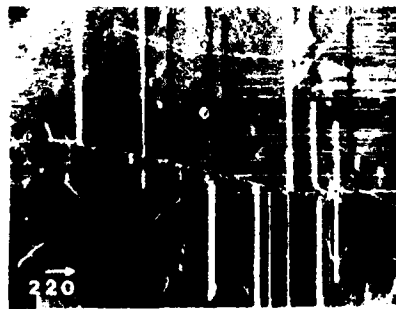
Therefore some other methods have been reported to reduce the dislocation density in the active layer of devices. Matthews et al. (1976) show how threading dislocations can be removed away from the epitaxial layer using misfit strain. This was shown experimentally for

example in  $\text{Ga}_{1-x}\text{Al}_x\text{As}$ -multilayer structures by Bartels et al. (1977), in  $\text{Ga}_{1-x}\text{Al}_x\text{As}_{1-y}\text{P}_y$ -layers on GaAs by Rozgony et al. (1974), in compositionally graded  $(\text{In,Ga})\text{P}$  by Abrahams et al. (1975) and in GaAlAs superlattice structures by Osbourn (1982). Using such strained layers not only the dislocation density is reduced but also a gettering effect takes place. Beneking et al. (1985b) show that the outdiffusion of Cr from the substrate is suppressed. Salih et al. (1985) have shown that the misfit dislocations network at the interface between a Ge containing Si epitaxial layer onto Si getter Cu and Au. Beneking et al. (1985a) and Kalukhov et al. (1985) show that also the intrinsic deep levels can be reduced by isoelectronic impurities.

We have used isoelectronically doped epiaxial layers, especially GaAs(In)-layers on GaAs grown by LPE and MOCVD and InP(As) layers on InP grown by LPE with a lattice mismatch between layer and substrate in the range  $10^{-5}$ ... $10^{-4}$ . The behavior of threading dislocations and the misfit dislocation network has been studied by X-ray-topography and etching methods. To demonstrate the device quality achievable with those strained layers GaAs-Schottky-diodes based on LPE material (Narozny et al. 1985), GaAs- and InP-pn-diodes based on LPE and MOCVD material (Beneking et al. 1985b, 1986), and GaAs-double-Schottky-interdigitated photodetectors based on LPE material (Schumacher et al. 1986) have been fabricated. They confirmed the prediction of better material uniformity as well as device relevant data. The reduction of deep levels leads to an excellent  $1/f$  noise behavior and the minority carrier lifetimes are about double as high as for similar diodes fabricated without strained layer epitaxy. Correspondingly the diffusion length is enhanced.

## 2. Dislocations

It has been found by etching experiments recently (Beneking 1985a, 1985b) that the EPD in the epitaxial layer can be reduced by a factor of 20 with an isoelectronic doping in the range 0.15%-0.3%. Several microns of growth must be performed to achieve the desired EPD reduction (Beneking 1985a). X-ray transmission topographs were obtained by the Lang method using a MoK $\alpha$  source. The GaAs samples were grown by LPE on Si and Cr doped substrates with low dislocation density to observe individual dislocations. The thickness of the layers were 10  $\mu\text{m}$  and 15  $\mu\text{m}$ , the In concentration in the epitaxial layer of different samples was 0%, 0.15%, 0.30% and 0.5%. Therefore it was possible to study the influence of layer thickness and In concentration on the misfit dislocation network and the bending of threading dislocations. Fig. 1a-1d show the influence of the In-doping on the misfit dislocation network density.



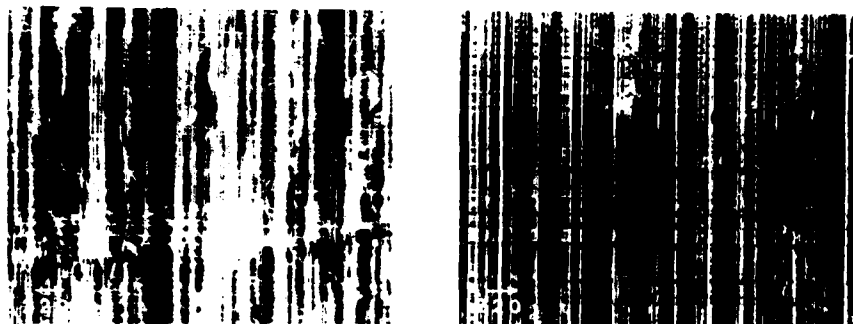


Fig. 1: Misfit dislocation network for different In-concentrations  
a) 0%, b) 0.15%, c) 0.3%, d) 0.5% (Si-doped GaAs-Substrate)

Fig. 1a shows the absence of a dislocation network because no In-doping was performed. Fig. 1b to 1d illustrate the increasing dislocation network density with increasing In-doping (and therefore lattice mismatch). All misfit dislocations run either in  $[110]$  or  $[1\bar{1}0]$  directions and originate either from the wafer edges (fig. 1b), scratches (fig. 1b) or from substrate dislocations (fig. 2, arrows).

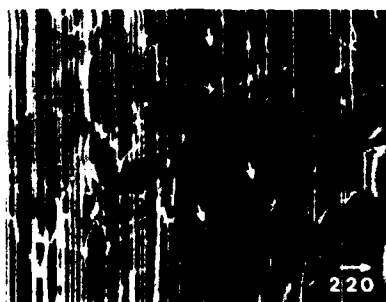


Fig. 2: Bending of dislocations at the interface. (0.3% In)

Further experiments have shown that the misfit dislocation network density increases with increasing substrate dislocation density, because many misfit dislocations originate from substrate dislocations (fig. 2). Therefore it can be concluded that the epitaxial dislocation density is reduced because many substrate dislocations are bent at the interface to form misfit dislocations which run to the wafer edges.

In the case of InP strained layers the dislocation reduction was studied by etching methods (Beneking 1985a, 1985b). It was shown that the EPD can be reduced by a factor of 20. We have also applied X-ray topography, but the poor quality of InP substrates reduces the usefulness of this method. Fig. 3 shows an example. The misfit dislocation network can be seen, but the very rough substrate backside leads to a very strong background. By polishing the backside, the resolution should be improved.



Fig. 3: Dislocation network for As-doped InP

3. Devices

The current gain of a bipolar transistor is determined by the emitter efficiency and the base transport factor. An improvement in the base transport factor can be achieved by increasing the minority carrier diffusion length. Since the diffusion length is related to the crystal quality and the deep level impurities, one has to improve the layer quality.

In order to show the effect on the current gain of bipolar transistors, In-doped (0.15%) and conventionally npn transistors have been fabricated. A homojunction transistor has been chosen instead of a heterojunction transistor to exclude interface recombination effects. A  $8\mu\text{m}$  buffer layer has been grown on a (100)  $\text{n}^+$ -substrate followed by the collector, base and emitter layers with  $1\mu\text{m}$ ,  $0.15\mu\text{m}$ ,  $0.5\mu\text{m}$  thickness and a doping level of  $10^{16}\text{cm}^{-3}$ ,  $10^{17}\text{cm}^{-3}$ , and  $10^{16}\text{cm}^{-3}$ , respectively. For the strained layer device all epitaxial layers are doped with 0.15% In.

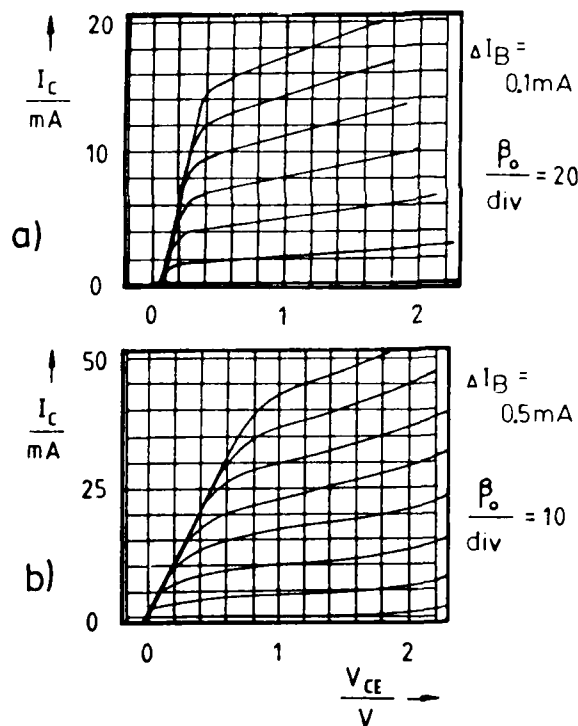


Fig. 4a shows the I-V characteristic of an In-doped device whereas Fig. 4b shows the curves of a conventionally fabricated transistor. An enhanced current gain by a factor 2.5 can be seen from the characteristics. The same breakdown voltage and the same Early voltage indicate identical base widths and doping concentrations so that the enhanced current gain is caused by the improved diffusion length. Furthermore a steep breakdown behavior of the I-V characteristic of the In-doped transistor indicates a homogeneous layer quality.

Fig. 4: I-V characteristics of bipolar transistors  
a) In-doped b)conventional

To show that a carrier lifetime enhancement occurs by isoelectronic doping epitaxial pn-diodes have been investigated. First a lightly doped ( $n=10^{16}\text{cm}^{-3}$ )  $15\mu\text{m}$  n-layer was grown on a  $\text{n}^+$ -substrate followed by a highly doped ( $p=5 \times 10^{18}\text{cm}^{-3}$ ) p-layer. Devices with different (0%, 0.15%, 0.3%, 0.5%) In-concentrations have been fabricated to study the influence of the In-doping concentration. Fig. 5 shows the I-V-characteristic of a conventionally fabricated GaAs-diode in comparison to an



In-doped device (0.3%). The recombination current with an ideality factor of  $n=2$  is reduced by the In-doping so that the diffusion current with an ideality factor  $n=1$  appears at a higher current level. The minority carrier lifetime and diffusion length can be determined by measuring the recombination current  $I_{rec}$  of the diode in forward direction at a current level where recombination determines the I-V-characteristics.

$$I_{rec} = n_1 A e d / 2 \tau_p \exp\left(\frac{V}{2V_T}\right)$$

where  $n_1$  is the intrinsic carrier concentration,  $A$  is the diode area,  $e$  is the electron charge and  $d$  is the depletion layer width. The diffusion length of the holes can then be calculated by

$$L_p = \sqrt{D_p \tau_p}$$

where  $D_p$  is the diffusion coefficient.

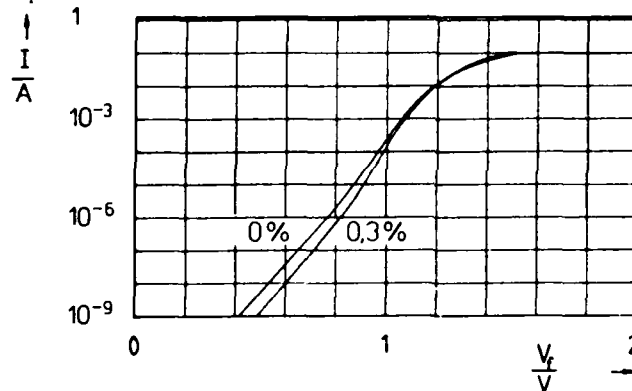


Fig. 5: Forward characteristics of an (0.3%) In-doped pn-diode in comparison to a conventionally fabricated diode

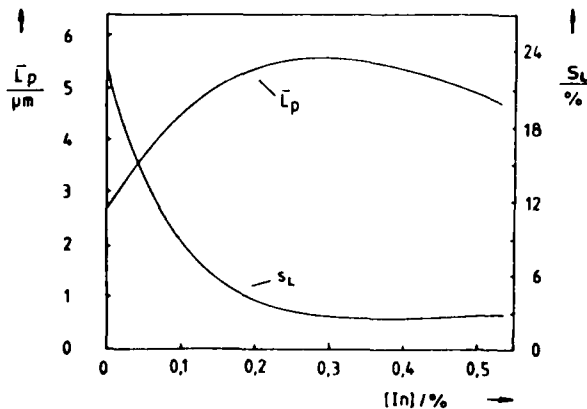


Fig. 6: Hole diffusion length  $L_p$  and standard deviation  $s_L$  against In concentration

Fig. 6 shows the diffusion length and the scattering of the value for different In concentrations measured with a series of diodes placed on a  $1\text{cm}^2$  sample. An improved diffusion length can be seen from the diagram which reaches its maximum value at 0.3% In and decreases when further increasing the In concentration. Beside an increase in diffusion length a decrease of the standard deviation takes place

which indicates a homogenous layer quality.

#### 4. Summary

It has been demonstrated that the epitaxial layer quality and uniformity of GaAs and InP wafers can be improved by applying a single strained epitaxial layer, because the dislocation density and the deep levels are reduced drastically. The method presented is not restricted to the presented examples and will be a very promising tool in III-V technology.

#### References

- Abrahams M S, Buiocchi C J, Olsen G H, 1975 J. Appl. Phys. 46 (10) 4259
- Bartels W J, Nijman W, 1977 J. of Crystal Growth 37 204
- Beneking H, Narozny P, Emeis N, 1985a Appl. Phys. Lett. 47 828
- Beneking H, Narozny P, Emeis N, 1985b, presented at the Int. Symp. on GaAs and Related Compounds, Karuizawa, Japan, Paper II-5, 12
- Beneking H, Narozny P, Roentgen P, Yoshida M, 1986 IEEE Electr. Device Lett. 2 (EDL-7) 101
- Booker G R, Hitchmarsh J M, Fletcher J, Darby D B, Hockley M, Al-Jassim M, 1978 J. of Crystal Growth 45 407
- Jordan A S, Von Neida A R, Caruso R, 1984 J. of Crystal Growth 70 555
- Jordan A S, Brown G T, Cockayne B, Brasen D, Bonner W A, 1985 J. Appl. Phys. 58 (11), 4583
- Kalukhov V A, Chikichev S I, 1985 Phys. Stat. Sol. (a) 88, K 59; (a) 1985 89 K 115
- Kasahara J, 1985 Electronic Letters 21 1040
- Kimura H, Afable C B, Olsen H M, Hunter A T, Winston H V, 1984 J. of Crystal Growth 70 185
- Kohda H, Yamada K, Nakanishi H, Kobayashi G, Osaka J, Hoshikawa K, 1985 J. of Crystal Growth 71 813
- Dilorenzo A V, Jordan A S, Von Neida A R, C'Connor P, 1984 in: Semi-Insulating III-V-Materials, Warm Springs OR (Shiva, 1984)
- Merwe J H van der, Ball C A B, 1983 in: Dislocations in Solids, Vol. 6, Editor: F.R.N. Nabarro North Holland Publishing Company, Amsterdam, New York, Oxford
- Matthews J W, Blakeslee A E, Mader S, 1976 Thin Solid Films 33 253
- Narozny P, Beneking H 1985, Electr. Lett. 21 (22) 1050
- Osbourn G C, 1982 J. Appl. Phys. 53 1586
- Petroff P, Hartman R L, 1973 Appl. Phys. Letters 23 469
- Roedel R, Neida A R, Caruso R, Dawson L R, 1979 J. Elektrochem. Soc. 126 637
- Rozgonyi G A, Petroff P M, Panish M B, 1974 J. of Crystal Growth 27 106
- Salih A S, Kim H J, Davis R F, Rozgonyi G A, 1985 Appl. Phys. Lett. 46 (4), 419
- Schumacher H, Narozny P, Werres Ch., Beneking H, 1986 IEEE Electr. Device Lett. 1 (EDL-7) 26

## **AlN on GaAs and InP for application to MIS structure – low temperature growth of AlN using TMAI and hydrazine**

M. Mizuta, S. Fujieda, T. Jitsukawa and Y. Matsumoto

Fundamental Research Labs., NEC Corporation  
Miyamae-ku, Kawasaki, Kanagawa 213, JAPAN

**Abstract.** Aluminum nitride on n-GaAs and n-InP was successfully grown at low temperature. For both MIS (metal-insulator-semiconductor) systems the surface-state density ( $N_{ss}$ ) was greatly reduced:  $N_{ss} < 10^{11}$  for InP and  $< 10^{12} \text{ cm}^{-2} \text{ eV}^{-1}$  for GaAs. For GaAs the reduced  $N_{ss}$  was confirmed by the ICTS (isothermal capacitance transient spectroscopy) measurement. The abnormal C-V characteristics of GaAs MIS diode is discussed by a model of  $N_{ss}$  distribution with two discrete levels.

### 1. Introduction

There has been a demand for the control of the surface band bending of III-V semiconductors upon metal deposition and/or insulator deposition, specifically for GaAs and InP. This is because precise manipulation of the Schottky barrier height or Fermi level at the surface ( $E_{fs}$ ) would make MESFET or MISFET performance much more reliable. Presently, however, the surface or interface of GaAs is pinned around 0.8eV below the conduction band (CB) regardless of what foreign atoms are deposited (Spicer 1980). Surface depletion other than under the gate due to this pinning also degrades the MESFET performance, such as the side gating effect. Therefore a proper passivation of the surface is a requisite for these devices. To date, however, practical interface and/or surface properties are insufficiently controlled experimentally and also are not reasonably understood theoretically. Several models have been proposed for the Fermi level pinning of the deposited metal Schottky barrier (Tersoff 1985, Sapkey 1985, Spicer 1980), for which required  $N_{ss}$  is estimated to be around  $10^{14} \text{ cm}^{-2} \text{ eV}^{-1}$ . For the case of semiconductor-insulator interfaces pinning usually takes place. However, because of lack of screening by the metal, much smaller  $N_{ss}$  could easily pin the surface. As a consequence, although the MISFET device has several advantages over the MESFET or HEMT type devices, poor interface quality in terms of electrically active states does not allow large excursion of  $E_{fs}$ . We explore here the possibility of an unpinned insulator-semiconductor system.

Up to now, most of MIS-type structure have been fabricated utilizing deposited dielectrics since the complex phases of the native oxides, especially for GaAs (Schwartz 1983), prohibits the control of their dielectric properties. Among several candidate insulators, nitrogen-based materials have received attention since the nitridization is known to occur, which might produce a smooth interface change. In fact the nitridization of the GaAs surface by the nitrogen-plasma has been reported to reduce surface recombination velocity (Pankove 1983), and diode leakage current (Pearson 1984). The nitridization or nitride-deposition have been conducted by  $\text{NH}_3$  or  $\text{N}_2$  plasma previously. We believe, however, that the high-energy plasma-particle could introduce defects at the surface to degrade the interface property.

In this study, we use the low-temperature pyrolytic reaction to deposit a nitride film on GaAs and InP. AlN was chosen here because the ionicity and thermal expansion coefficient are very close to those of GaAs and InP and also its bandgap is large enough to yield high-resistivity. The typical deposition temperature of AlN by the pyrolysis of  $\text{NH}_3$ , however, has been reported to be more than  $1000^\circ\text{C}$ , which is too high<sup>3</sup> for the processing of GaAs and InP. Lower temperature pyrolytic CVD of nitrides is expected with hydrazine ( $\text{N}_2\text{H}_4$ ), instead of  $\text{NH}_3$ , because hydrazine is known to decompose at a much lower<sup>2</sup> temperature, therefore preserving the stoichiometric control of AlN.

## 2. Experimental

### a) Deposition procedures of AlN

Growth was carried out in a low-pressure MOCVD reactor. TMA (trimethyl aluminum) as an Al source and hydrazine as a N source were both held at  $20^\circ\text{C}$  and transported by hydrogen. n-GaAs(100) and n-InP(100) were used as substrates. Before the nitride growth, GaAs substrates were heated inductively up to  $620^\circ\text{C}$  with  $\text{AsH}_3$  flow. This is intended to remove oxides on the substrate surface. Flows of hydrazine and metalorganics, in this order, were then introduced to initiate growth. In some cases epitaxial GaAs was grown, prior to AlN, in the same reactor as an active layer. For the case of InP substrates, a pre-treatment (or removal of oxide) was undertaken by heating the substrate up to  $500^\circ\text{C}$  with  $\text{AsH}_3$  flow.

### b) Electrical measurements

A MIS diode was fabricated by evaporating Au or Al and soldering Indium for the back ohmic contact. Capacitance-voltage (C-V), Current-voltage (I-V) and ICTS (isothermal capacitance transient spectroscopy) were measured using HP 4280A and 4192A capacitance meters and 4140B picoammeter with a desk-top computer. C-V characteristics shown in this paper were taken with a voltage sweep rate of  $0.5\text{V/sec}$  from negative to positive gate voltage ( $V_G$ ).

## 3. Results and Interpretation

### a) Growth of AlN film

Figure 1 shows temperature dependence of growth rate and index of refraction for AlN with constant transport rates of TMA ( $2.5\ \mu\text{mol/min}$ ) and of hydrazine ( $56\ \mu\text{mol/min}$ ). Since the required value of the V/III (the ratio between number of N atom and Al atom in input source gases) has been reported as 1000 when  $\text{NH}_3$  is used, it is especially noted that V/III is less than 20 for the present growth condition.

At high temperature ( $T_d$  (deposition temperature)  $> 450^\circ\text{C}$ ) the growth rate reaches an approximately constant value where the rate was found linearly dependent on the transport rate of TMA and independent of hydrazine flow as long as  $V/III > 5$ . Therefore in this temperature region, mass-

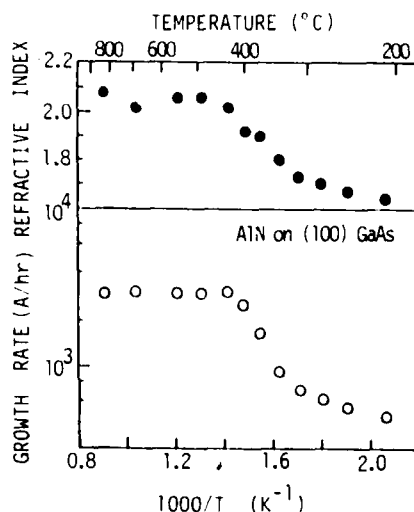


Fig. 1 Temperature dependence of growth rate and refractive index of AlN on (100) GaAs.

transport-limited growth takes place.

For  $450^\circ\text{C} > T_d > 350^\circ\text{C}$ , growth rate is thermally activated: dependent not only on the transport rate of TMA but on hydrazine as well, both with sub-linear relation. We found that this dependence is due to the surface-catalyzed decomposition of TMA rather than hydrazine (Mizuta 1986).

Further decreasing temperature, deposition of AlN proceeds without deterioration of surface morphology from  $350^\circ\text{C}$  down to  $220^\circ\text{C}$  as shown in Fig. 1. Preliminary SIMS (secondary ion mass spectrometry) measurements, however, show that the film contains more oxygen, which could be from the hydrazine source itself, than for films grown at higher temperature. Therefore, growth kinetics as well as the film composition may be quite different from at higher temperature.

Films grown in this study ( $220^\circ\text{C} < T_d < 860^\circ\text{C}$ ) presently show no evidence of crystallinity from the x-ray diffractometry.

#### b) Electrical characteristics of AlN film

From I-V characteristics of AlN on  $n^+$ -GaAs with  $T_d = 330$ – $860^\circ\text{C}$  it is revealed that the Pool-Frenkel type current results above  $1 \times 10^6 \text{ Vcm}^{-1}$  for both forward and reverse direction. Below this voltage I-V characteristics show ohmic nature. The resistivity is estimated, from this slope, to be  $> 10^{-6} \Omega \text{ cm}$ . However the measuring current is reaching the present instrument resolution and therefore the true resistivity would be larger. Dielectric breakdown, defined as current density of  $10^{-6} \text{ Acm}^{-2}$  occurs at  $4 \times 10^6 \text{ Vcm}^{-1}$ .

The dielectric constant of the film ranges from 5 ( $T_d = 300^\circ\text{C}$ ) to 7.5 ( $500^\circ\text{C}$ ), which is evaluated from the 1MHz capacitance of the Al/AlN/ $n^+$ -GaAs structure. Frequency dispersion of the capacitance is around 10% between 50Hz and 10MHz for  $T_d = 280$ – $490^\circ\text{C}$ .

#### c) Capacitance-Voltage characteristics

##### GaAs

The typical C-V and G-V characteristics for 700Å AlN on GaAs ( $n = 1.5 \times 10^{16} \text{ cm}^{-3}$ , LEC) are shown in Fig. 2, where the solid lines represent for data  $T_d = 370^\circ\text{C}$ . It is noted that the frequency dispersion of the capacitance between DC (quasi-static) and 1MHz at the accumulation side is fairly small (less than 20% at  $V_g = 10\text{V}$ ), evidence of low  $N_s$  from mid-gap to CB (see also Fig. 3).

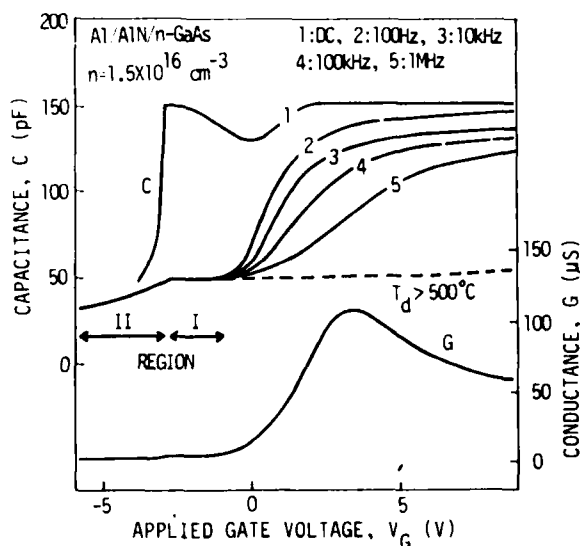


Fig. 2 C-V and G-V characteristics of GaAs MIS diodes for LEC GaAs as active layers. G-V curve is taken at 1MHz. Solid lines are for  $T_d = 370^\circ\text{C}$ . An abnormal C-V dependence appears in the region I and II.

On the other hand, for  $T_d > 500^\circ\text{C}$ , as represented by the dotted line, the C-V curve deteriorates badly, indicating little excursion of  $E_{fs}$ . The change in  $N_{ss}$  for different deposition conditions is observed as shown in Fig. 3; reduction in  $N_{ss}$  resulted when an active layer is epitaxial GaAs (curve 2) grown in the same reactor compared to LEC GaAs (curve 3). Further reduction was observed by the post-anneal of this diode at  $230^\circ\text{C}$  for 1 hr (curve 1): yielding  $N_{ss} < 10^{12} \text{ cm}^{-2} \text{ eV}^{-1}$ . On the other hand  $N_{ss}$  deteriorates when the pre-deposition treatment of  $\text{AsH}_3$  flow at  $620^\circ\text{C}$  was not employed for LEC GaAs sample (curve 4).

For the depletion to inversion side, every curve in Fig. 2 shows the same abnormal voltage dependence as has already been reported (Kohn 1978). There are two features in this voltage range: region I - a constant capacitance, which is not the inversion capacitance, upon  $V_g$  change and region II - a monotonic decrease in capacitance with decrease in  $V_g$ . In region II, a plot of  $C_D$  vs  $V_D$  ( $C_D$  the depletion layer capacitance:  $1/C_D = 1/C_{\text{measured}} - 1/C_{\text{insulator}}$  and  $V_D$  the voltage across semiconductor) shows a straight line, suggesting deep depletion. This decrease, however, disappears in both DC and 1MHz C-V by irradiating the sample with a sub-bandgap light.

#### InP

The results for AlN/n-InP ( $n = 6 \times 10^{15} \text{ cm}^{-3}$ ) are shown in Fig. 4. The frequency dispersion of the capacitance is quite small for the depletion-inversion side if the deposition AlN ( $T_d = 350\text{--}400^\circ\text{C}$ ) is followed by the pre-treatment of  $\text{AsH}_3$  flow at  $500^\circ\text{C}$ .  $N_{ss}$  distributions are also reflected by this pre-treatment as shown in the inset. The remarkable fact is that drastic reduction of  $N_{ss}$  resulted from the post-anneal of the MIS diode at  $290^\circ\text{C}$  for 1 hr yielding

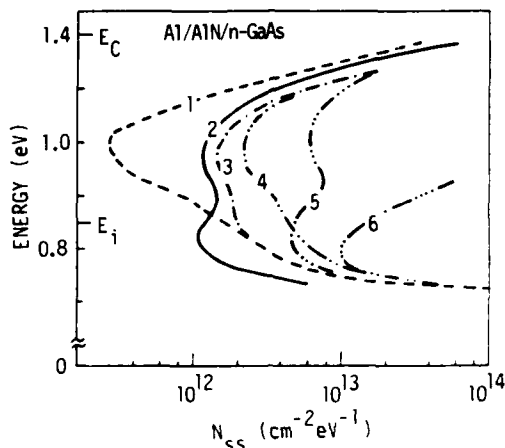


Fig. 3  $N_{ss}$  distribution for different deposition and treatment conditions. 1,2: epitaxial GaAs ( $n = 5 \times 10^{15} \text{ cm}^{-3}$ ), 3-6: LEC GaAs ( $n = 1.5 \times 10^{16} \text{ cm}^{-3}$ ) as active layers. 1: post-annealed, 4: no  $\text{AsH}_3$  pre-treatment. 1-4:  $T_d = 370^\circ\text{C}$  5:  $T_d = 450^\circ\text{C}$ , 6:  $T_d = 500^\circ\text{C}$ .

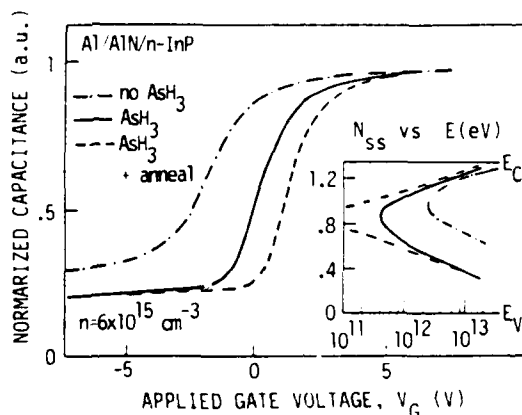


Fig. 4 C-V characteristics for InP MIS diodes with different pre- and post-treatment: — pre-treatment with  $\text{AsH}_3$  at  $500^\circ\text{C}$ , - - no pre-treatment, - · - post-annealed at  $300^\circ\text{C}$  (1 hr) for the pre-treated sample.

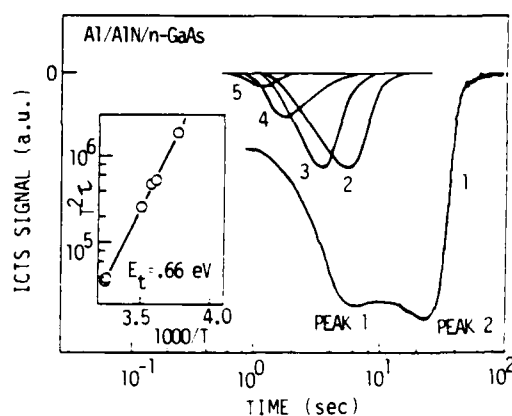


Fig. 5 ICTS spectra for GaAs MIS. Traces are taken at room temperature. Reduced signal scale for traces 2-5. Measurement conditions are: 1:  $V_G=0$ , 2:  $V_G=2$ , 3:  $V_G=2.5$ , 4:  $V_G=3$ , 5:  $V_G=3.5$ . Pulse voltages are 10V for 1 and 2V for 2-5.

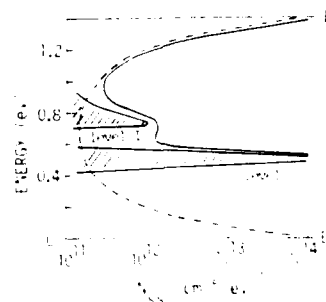


Fig. 6 A model for  $N_{ss}$  distribution for GaAs MIS. Hatched peaks are semi-discrete levels corresponding to peak 1 and 2. The dotted line represents U-shape surface state. The solid line is the sum of these states to simulate the present result.

less than  $10^{11} \text{ cm}^{-2} \text{ eV}^{-1}$ . The abnormal capacitance change at the depletion-inversion side observed for GaAs did not manifest itself here.

#### 4. Discussion of the GaAs MIS diodes

As described above  $N_{ss}$  seems to be quite reduced between midgap and CB. However this is rather contradictory to the previous understanding (Hasegawa 1983); the minimum of  $N_{ss}$  is located between midgap to valence band (VB). We, therefore, performed the transient capacitance measurement to determine the  $E_F$  at which  $N_{ss}$  is reduced. An example of the ICTS is shown in Fig. 5. Here  $C_{fs}$  capacitance transients were recorded (and processed (Tomokage 1985)) at  $V_G=0V$  after a pulse with its amplitude of +10V was applied (curve 1). This clearly indicates that at least two levels are involved for electron emission. The peak 1, which has a shorter time constant, disappears both when increasing  $V_G$  more than 4V and decreasing  $V_G$  less than 0V with constant pulse voltage of 2V. The width of the envelope of peak 1 for traces 2-5 is fairly small as seen in the figure. These results suggest that the peak 1 corresponds to a energetically semi-discrete level. We deduced the depth ( $E_t$ ) of this level to be 0.66eV as shown in the inset. These facts indicate that  $N_{ss}$  is low enough to change  $E_{fs}$  around  $E_C-0.7V$  and above. Therefore, low  $N_{ss}$  at midgap to CB is confirmed.

Furthermore, with the above fact in mind, this level can be seen in Fig. 3 as a hump located at  $E_C-0.7V$ . This hump apparently decrease its magnitude with decreasing  $T_d$ . Together with this decrease in the discrete level concentration, the density of the continuous surface state towards CB (corresponding to fast state) is also reduced as clearly seen in the figure. The reduction of the frequency dispersion of the capacitance is probably due to the reduction of the fast surface state rather than of the discrete level.

For the peak 2, it disappears when  $V_G > 0$ . But upon decrease in  $V_G$  it appears, even at  $V_G$  corresponding to deep-depletion condition. The onset of the gate

bias, at which the peak 2 appears, roughly corresponds to right hand side of the region I in Fig. 2 (this corresponds to  $E_{fs}=E_c-.9V$ ). The capacitance value of the region I, however, is always larger than the expected value of the inversion capacitance. Therefore in the region I where the C-V curve is flat, the surface is not inverted but is pinned.

Now we can construct a model to explain the abnormal C-V behavior of GaAs MIS structure. From Fig. 2 under a large negative  $V_G$ , semiconductor is subjected to deep-depletion. Even under such a condition surface is still pinned because charging and/or discharging of the level (peak 2), probably electron emission, cannot follow the  $E_{fs}$  change. Therefore deep-depletion resulted in order to keep the charge balance. This assumption perfectly explains C-V behavior under the sub-bandgap light illumination and a sudden decrease for the quasi-static measurement shown in Fig. 2; light illumination enhances the electron emission from the level, therefore keeping the charge balance and preventing the occurrence of deep-depletion. Also under deep-depletion, voltage across the insulator does not increase since almost all the voltage is used to develop the depletion width, resulting in the very small net charge flow which corresponds to a sudden decrease in the quasi-static measurement.

For p-type GaAs, although we have not tried MIS structure presently, several reports show quite similar abnormal C-V characteristics (Kohn 1978), however, symmetrical to the gate bias. This strongly suggests that when  $E_{fs}$  is scanned from VB to midgap,  $E_{fs}$  is pinned to the same level as peak 2. Further increase in  $V_G$  results in the deep-depletion because charging and/or discharging, in this case probably hole emission, cannot follow. Therefore our proposed model consists of two discrete-like levels and U-shape fast surface states as shown in Fig. 6. The concentration of level 1 (peak 1) deduced from the ICS measurement and that of level 2 (peak 2) is estimated to be more than  $10^{14} \text{ cm}^{-3} \text{ eV}^{-1}$  from C-V characteristics. These non-steady state behaviors of the discrete level have already been proposed in Si and GaAs (Wei 1974, Kazior 1983) to account for the abnormal C-V curve as well as large frequency dispersion. However, for GaAs we think anomalous dispersion is not due to this discrete level but due to the fast surface state located near CB.

#### Acknowledgments

The authors wish to thank Drs. S. Shinoda, F. Saito and H. Watanabe of NEC corporation for their continuing encouragement.

#### References

- Hasegawa H. and Sawada T. 1983 Thin Solid Films 103 119.
- Kazior T. E., Lagowski J. and Gatos H. C. 1983 J. Appl. Phys. 54 2533.
- Kohn E. and Hartnagel H. L. 1978 Solid State Electron. 21 409.
- Mizuta M., Fujieda S., Matsumoto Y. and Kawamura T. to be published.
- Pankove J. I., Berkeyheiser J. E., Kilpatrick S. J. and Magee C. W. 1983 J. Electron. Mater. 12 359.
- Pearton S. J., Haller E. E. and Elliot A. G. 1984 Appl. Phys. Lett. 44 684.
- Sankey O. F., Allen R. E., Ren S-F. and Dow J. D. 1985 J. Vac. Sci. Technol. B3 1162.
- Schwartz G. P. 1983 Thin solid Films 103 3.
- Spicer W. E., Lindau I., Skeath P. R., Su C. Y. and Chye P. W. 1980 Phys. Rev. Lett. 44 420.
- Tersoff J. 1985 J. Vac. Sci. Technol. B3 1157.
- Tomokage H. and Miyamoto T. 1985 Jpn. J. Appl. Phys. 24 381.
- Wei L. S. and Simmons J. G. 1974 Solid State Electron. 17 1021.



## **Ordered structures in OMVPE grown $\text{GaAs}_{1-x}\text{Sb}_x$ and $\text{Ga}_{1-x}\text{In}_x\text{As}_{1-y}\text{Sb}_y$ alloys**

H. R. Jen, M. J. Cherng, M. J. Jou, and G. B. Stringfellow

Department of Materials Science and Engineering, University of Utah, Salt Lake City, Utah 84112, USA

**Abstract.** Electron microscopy results for (001) oriented  $\text{GaAs}_{1-x}\text{Sb}_x$  layers with  $x=0.5$  and  $0.75$  and  $\text{Ga}_{1-x}\text{In}_x\text{As}_{1-y}\text{Sb}_y$  grown by organometallic vapor phase epitaxy indicate that ordered phases are formed during growth. For ternary alloys with  $x=0.5$ , two ordered phases are observed. The simple tetragonal, CuAu-I type phase consists of alternating {100} oriented GaAs and GaSb layers. Only the 2 variants with tetragonal c axes perpendicular to the growth direction are observed. Two variants are observed for the chalcopyrite,  $\text{E1}_1$  structure with alternating {210} oriented GaAs and GaSb layers. For ternary layers with  $x=0.75$ , an  $\text{L1}_3$  ordered structure is observed. This 3:1 structure consists of alternating superlattice planes along {100}, one of which is GaSb and the other a 50/50 mixture of GaAs and GaSb. For a  $\text{Ga}_{0.63}\text{In}_{0.37}\text{As}_{0.98}\text{Sb}_{0.02}$  layer, a 20-30Å periodicity is superimposed on the ordered CuAu-I and chalcopyrite structures.

$\text{GaAs}_{1-x}\text{Sb}_x$  alloys are potentially important materials for applications such as tandem solar cells (Bedair et al 1982 and Fraas et al 1982) and detectors in the wavelength range from 1.3 to 1.6  $\mu\text{m}$  (Law et al 1981). The quaternary  $\text{Ga}_{1-x}\text{In}_x\text{As}_{1-y}\text{Sb}_y$  alloys have an even wider range of band gaps, ranging from 1.43 to 0.1 eV. However, these alloy systems also contain large miscibility gaps (Stringfellow 1983). All III/V alloys with lattice parameter differences between the end components ( $\Delta a > 0$ ) have positive enthalpies of mixing, with the deviation from ideality increasing with  $\Delta a^2$  (Stringfellow 1974) for disordered alloys, i.e., those with random mixing on the respective sublattice(s). Molecular beam epitaxy (MBE) (Waho et al 1979) and organometallic vapor phase epitaxy (OMVPE) (Bedair et al 1983, Stringfellow et al 1983, Cherng et al 1984a, 1984b, 1986a, 1986b) techniques can be used to grow these metastable alloys inside the region of solid immiscibility because of kinetic limitations on the speed with which the constituents can redistribute themselves on the surface during growth. High quality  $\text{GaAs}_{1-x}\text{Sb}_x$  lattice matched to InP substrates,  $x=0.47$ , has been successfully grown by OMVPE by Cherng et al (1984b, 1986a).  $\text{Ga}_{1-x}\text{In}_x\text{As}_{1-y}\text{Sb}_y$  alloys over the entire range of solid composition have also been grown by OMVPE (Cherng et al 1986b).

Recently, Jen et al (1986a) reported the occurrence of ordering in  $\text{GaAs}_{1-x}\text{Sb}_x$  alloys, normally a sign of a negative deviation from ideality (Swalin 1962). This seeming contradiction was anticipated by Srivastava et al (1985). Based on a first-principles local-density total energy minimization calculation, they predicted that III-V semiconductor  $\text{A}_x\text{B}_{1-x}\text{C}$  pseudobinary alloys, where A and B are group III elements and C is a group V element, should have thermodynamically stable ordered structures for the compositions

$A_3B_1C_4$ ,  $ABC_2$  and  $A_1B_3C_4$ . The stability of these ordered structures is mainly due to a reduction in strain energy. In a random alloy, the strain energy is the major factor leading to the large positive enthalpy of mixing. The ordered structures are able to accommodate the two dissimilar bond lengths when  $\Delta a \neq 0$  with a minimum of distortion. The ordered phases were predicted to be observed if the surface mobility during growth is high enough, and the growth temperature is lower than the critical temperature for the order transformation ( $T^0$ ) (Srivastava 1985). Similarly  $AB_{1-x}C_x$  alloys, with mixing on the group V sublattice, are also expected to have stable ordered structures.

Srivastava et al (1985) predicted that for  $GaInP_2$ , an alloy with a moderate positive deviation from ideality for the disordered alloy, two ordered structures, the  $CuFeS_2$ -type chalcopyrite structure ( $E1_1$ ) and the simple tetragonal,  $CuAu$ -I, structure ( $L1_0$ ) would have nearly identical energies, and would thus both be expected to occur under the appropriate growth conditions. This prediction apparently describes very well the experimental observations of Jen et al (1986a) for the  $GaAs_{0.5}Sb_{0.5}$  alloy.

In this paper we report further observations of the ordered structures in  $GaAs_{1-x}Sb_x$  with  $x=0.5$  and describe for the first time the occurrence of a new ordered phase in this material with  $x=0.75$ . Initial results on ordering in the more complex quaternary alloy  $Ga_{1-x}In_xAs_{1-y}Sb_y$  are also presented.

The  $GaAs_{1-x}Sb_x$  and  $Ga_{1-x}In_xAs_{1-y}Sb_y$  epilayers were grown OMVPE in a horizontal, IR heated reactor at atmospheric pressure. The sources were trimethylgallium (TMGa), trimethylindium (TMIn), trimethylarsine (TMAs), and trimethylantimony (TMSb). The substrate was InP oriented  $3^\circ$  off (001) toward (110).  $GaAs_{1-x}Sb_x$  with  $x=0.5$  is lattice matched to the InP substrate and the epilayer with  $x=0.75$  has a large mismatch. The quaternary epilayer studied is slightly mismatched. The growth temperature was in the range from  $550$  to  $680^\circ C$ . The V/III ratio was about 4 for the ternary sample with  $x=0.5$ , 1.5 for  $x=0.75$ , and 4.6 for the quaternary sample, assuming complete pyrolysis of all reactants. The growth rate was typically  $0.09 \mu m/min$  and the thickness of the epilayers was about  $1.5 \mu m$ . The detailed growth technique has been described previously (Cherng et al 1984b, 1986a, 1986b).

The composition was determined by x-ray diffraction for ternary samples by comparing the relative position of the (400) peak for the epilayer to that of the InP substrate. For the quaternary sample the composition was determined by the electron microprobe analysis (EMPA) technique using GaSb and InAs as standards.

The transmission electron microscope (TEM) samples were prepared by first mechanically thinning the sample to about  $60 \mu m$ . Chemical etching with a solution  $H_3PO_4(1) : HCl(1)$  was used to remove the remainder of the InP substrate. The etching solution attacks InP much faster than the  $GaAs_{1-x}Sb_x$  and  $Ga_{1-x}In_xAs_{1-y}Sb_y$  layers. Final etching using a  $< 1\%$   $Br_2/CH_3OH$  solution brought the samples to transparency. A JEM-200CX scanning transmission electron microscope (STEM) was used at 200kV.

The [001] electron diffraction pattern for a sample of  $GaAs_{0.53}Sb_{0.47}$  grown at  $600^\circ C$  with a layer thickness of  $1.5 \mu m$  is shown in Fig.1. In addition to the normal zincblende spots with Miller indices being all even or all odd, extra, zincblende-forbidden,  $\{100\}$  and  $\{1,1/2,0\}$  spots appear. Fig. 2 shows the dark field image formed by  $4 \times \{1,1/2,0\}$  order induced spots. A rough estimate of the domain size of the ordered regions is approximately  $50$  to  $100 \text{ \AA}$ . Similar diffraction patterns and TEM images have been observed for other

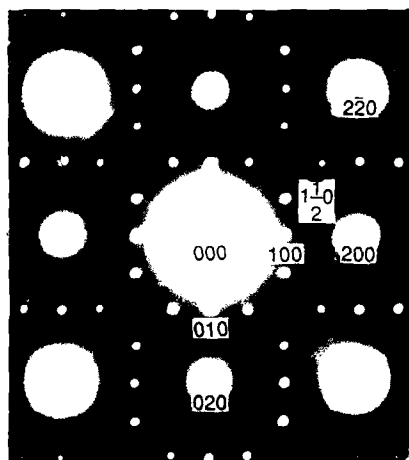


Fig. 1 [001] pole electron diffraction pattern of  $\text{GaAs}_{0.5}\text{Sb}_{0.5}$

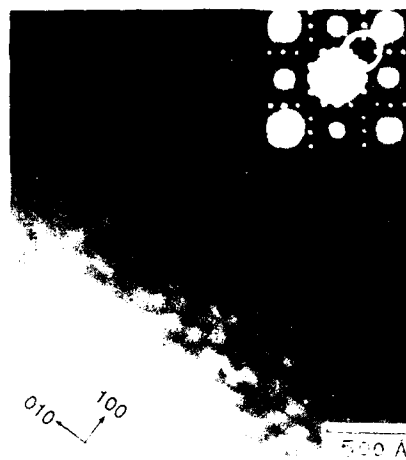


Fig. 2 Dark field image of  $\text{GaAs}_{0.5}\text{Sb}_{0.5}$  formed from  $E1_1$  spots

samples grown at 580 and 600°C. However, not all samples grown in this range show evidence of ordering, and all samples grown at either higher or lower temperatures show only the normal zincblende diffraction patterns.

The superlattice spots indicate the presence of both  $L1_0$  (CuAu-I) and  $E1_1$  (chalcopyrite) anion superlattices (Srivastava et al 1985), with the As and Sb atoms arranged in alternating planes,  $\{100\}$  for  $L1_0$  and  $\{210\}$  for  $E1_1$ . This ordering doubles the period of translational symmetry, giving rise to reciprocal lattice spots spaced  $1/2$  as far apart in the  $\langle 100 \rangle$  and  $\langle 110 \rangle$  directions for  $L1_0$  and in the  $\langle 210 \rangle$  directions for  $E1_1$ . The diffraction pattern shown in Fig. 1 contains all the diffraction spots for a mixture of  $L1_0$  and  $E1_1$  except the  $\{110\}$  spots. The  $L1_0$  ordered structure has 3 variants, with 6 for  $E1_1$ . For example the  $L1_0$  structure is tetragonal, thus there are 3 variants depending on the orientation of the tetrahedral  $c$  direction in the lattice. For the variant with periodicity along the  $[001]$  growth direction, the superlattice spots will appear for Miller indices with either  $l$  odd and  $h, k$  even or  $l$  even and  $h, k$  odd. This would give rise to  $(\pm 1 \pm 10)$  spots, which are missing. This indicates that only 2 variants of  $L1_0$  are present. The absence of the  $\{110\}$  type spots in the  $[112]$  pole electron diffraction pattern confirms the absence of the 3rd variant of the  $L1_0$  structure (Jen et al 1986b).

The chalcopyrite structure has 2 variants along each of the  $[100]$ ,  $[010]$ , and  $[001]$  axes, which give rise to:  $(\pm 1/2, 0, \pm 1)$  and  $(\pm 1/2, \pm 1, 0)$ ;  $(0, \pm 1/2, \pm 1)$  and  $(\pm 1, \pm 1/2, 0)$ ; and  $(0, \pm 1, \pm 1/2)$  and  $(\pm 1, 0, \pm 1/2)$  spots, respectively. The presence of only 2  $E1_1$  variants could account for the superlattice spots observed in Fig. 1. The absence of  $(0, \pm 1, \pm 1/2)$  and  $(\pm 1, 0, \pm 1/2)$  spots in the  $[112]$  diffraction pattern suggests that the 2 variants of  $E1_1$  with  $c$  axes parallel to the growth direction are missing.

This analysis indicates that we have a mixture of  $L1_0$  and  $E1_1$  ordered structures. However, the variant of  $L1_0$  with the  $c$  axis parallel to the growth direction is missing. This is exactly what is expected from simple kinetic considerations. Since diffusion in III/V solids is extremely slow, any ordering must occur at the interface during growth. The As and Sb

atoms are adsorbed on the surface in a random arrangement, and any ordering must occur before the deposition of the next layer. The formation of the variants with the tetragonal  $c$  axis perpendicular to the growth direction requires a diffusion distance of less than one lattice constant. The formation of the 3rd variant with its  $c$  axis parallel to the growth direction would require diffusion distances of as large as  $1/2$  the domain size of approximately  $50\text{ \AA}$  seen in Fig. 2. Since the diffusion time is proportional to the square of distance, the 3rd variant would require approximately 100 times as long to form.

The only other report of ordering in  $\text{GaAs}_{1-x}\text{Sb}_x$  alloys, was that of Murgatroid et al (1986) for layers grown at  $540^\circ\text{C}$  by MBE. They reported results similar to those for our OMVPE grown layers. However, their electron diffraction patterns indicated the ordering to occur on  $\{111\}$  oriented planes. The  $\{112\}$  diffraction patterns, would clearly show the  $1/2\{111\}$  spots. Their absence shows that we have no  $\{111\}$  type ordering present in our OMVPE grown samples (Jen et al 1986b).

In Fig. 3, we show the  $[001]$  diffraction pattern for a sample of  $\text{GaAs}_{0.25}\text{Sb}_{0.75}$ . The pattern is very simple and distinct from that for the sample with  $x=0.5$  shown in Fig. 1. Only  $\{001\}$  and  $\{012\}$  spots are seen. This diffraction pattern is indicative of a structure with  $\{001\}$  layers in the fcc anion sublattice composed alternately of all Sb atoms and of  $1/2$  Sb and  $1/2$  As atoms. We conclude this alloy has the  $L1_3$  ordered structure. This type of structure has been reported for the  $\text{Cu}_3\text{Pt}$  system (Schneider et al 1944). The structure is orthorhombic, but only slightly shifted away from cubic. We see evidence of this from electron diffraction patterns which show that the high index spots begin to divide into two spots.

Fig. 4 shows the  $L1_3$  structure for the anion sublattice. As atoms sit on the positions  $(000)$ ,  $(1/2\ 1/2\ 0)$ ,  $(1/2\ 0\ 1/2)$ ,  $(0\ 1/2\ 1/2)$ ,  $(1/4\ 1/4\ 0)$ ,  $(3/4\ 3/4\ 0)$ ,  $(3/4\ 1/4\ 1/2)$ , and  $(1/4\ 3/4\ 1/2)$  which forms two fcc lattices with one translated by  $(1/4\ 1/4\ 0)$  relative to the other. 24 Sb atoms occupy the remaining sites.

There are two variants along the  $\langle 100 \rangle$  direction giving  $\{110\}$  spots, which are missing. This indicates that, again, the variants with their  $c$ -axes along the growth direction are not

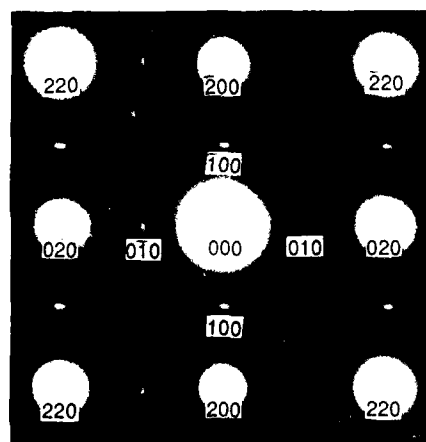


Fig. 3  $[001]$  pole electron diffraction pattern of  $\text{GaAs}_{0.25}\text{Sb}_{0.75}$

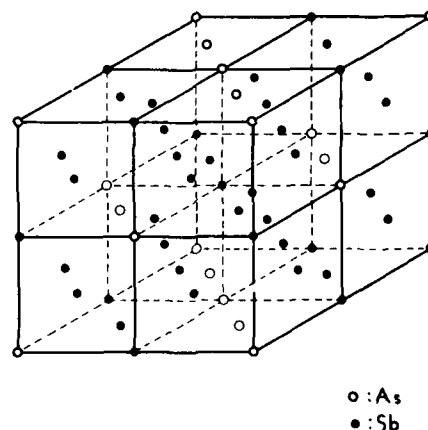


Fig. 4  $L1_3$  crystal structure

formed. This has been substantiated by electron diffraction patterns taken from other poles. In Fig. 5, the dark field images taken using the two order induced spots (120) and (300) are shown. The order induced spots are contributed by different order domains (i.e. variants) with sizes of about 60 Å by 120 Å. The domains are perpendicular to each other. The narrowed shape of the domains may explain the elongation of the order induced spots.

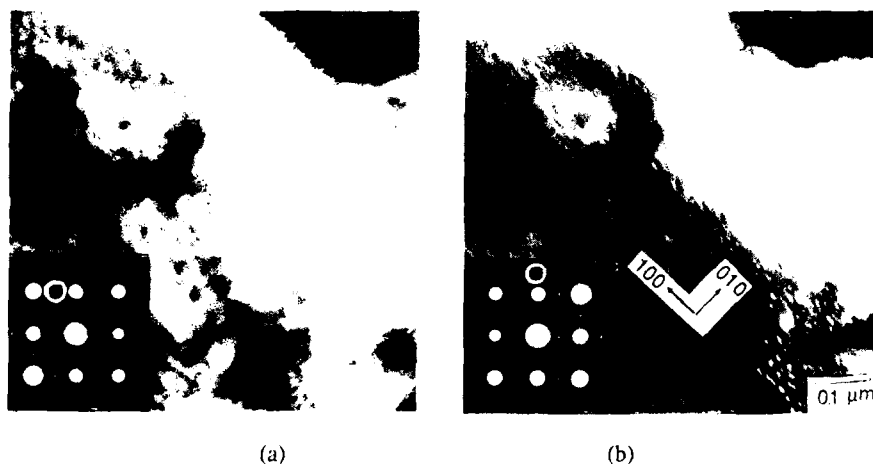


Fig. 5 Dark field images of  $\text{GaAs}_{0.25}\text{Sb}_{0.75}$  obtained using the (120) (a) and (300) (b) order induced spots.

The ordered structure (Fig. 6) found in the  $\text{Ga}_{0.63}\text{In}_{0.37}\text{As}_{0.98}\text{Sb}_{0.02}$  sample grown at 600°C is virtually the same as for the ternary  $\text{GaAs}_{0.5}\text{Sb}_{0.5}$  sample. However, a doubling of some spots is observed. From the dark field image we observe a lamellar structure composed of approximately 20–30 Å thick, (110) oriented parallel layers. The size is consistent with the separation of the doubled superlattice spots in the electron diffraction pattern.

In summary, we observe ordering in OMVPE grown  $\text{GaAs}_{1-x}\text{Sb}_x$  samples with  $x=0.5$ . This is remarkable in that the random solid alloy is known to have a large positive enthalpy of mixing. The chalcopyrite ( $\text{E1}_1$ ) and simple tetragonal ( $\text{L1}_0$ ) ordered phases are both present. Only the 2 variants of  $\text{L1}_0$  which have their tetragonal  $c$  axes perpendicular to the growth direction, and 2 of the 6  $\text{E1}_1$  variants are observed. For layers with  $x=0.75$  we have observed for the first time an ordered structure,  $\text{L1}_3$ , composed of alternating  $\{100\}$  layers of GaSb and a regular 50/50 mixture of GaAs and GaSb. For quaternary  $\text{Ga}_{1-x}\text{In}_x\text{As}_{1-y}\text{Sb}_y$  samples we observed a 20–30 Å layered structure, in addition to the localized ordered structures observed for  $\text{GaAs}_{0.5}\text{Sb}_{0.5}$ .

#### Acknowledgements

The authors gratefully acknowledge the valuable discussions with Dr. A. Virkar and Dr. T. Hsu, and the support of the Department of Energy through grant number DE-FG02-84ER45061.

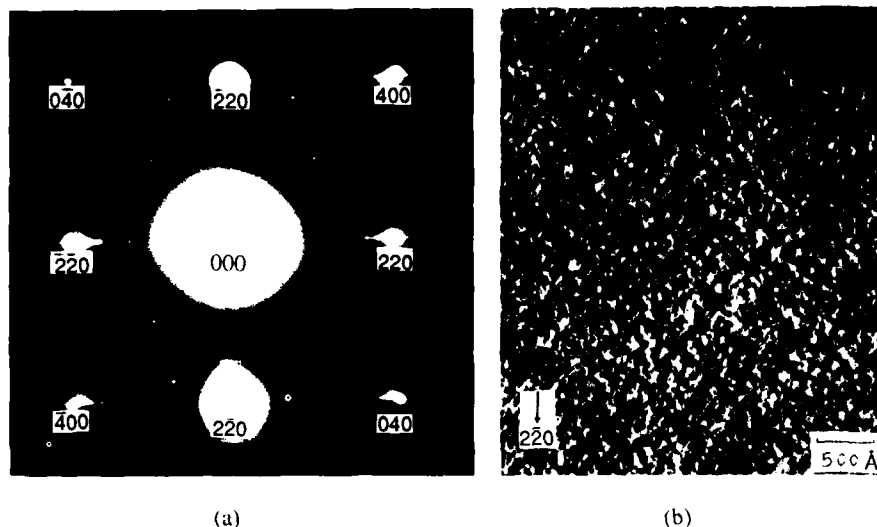


Fig. 6 (a) [001] pole electron diffraction pattern for  $\text{Ga}_{0.63}\text{In}_{0.37}\text{As}_{0.98}\text{Sb}_{0.02}$ ; (b) two beam dark field image using  $(\bar{2}20)$  spot

### References

- Bedair S M, Timmons M L, and Chiang P K 1981 Inst. Phys. Conf. Ser. 56, 403; Timmons M L, Bedair S M, Markunas R J, and Hutchby J A 1982 Proc. 16th IEEE Photovoltaic Specialists Conf., San Diego, 663.
- Bedair S M, Timmons M L, Chang P K, Simpson L, and Hauser J R 1983 J. Electron. Mater. **12**, 959.
- Cherng M J, Stringfellow G B, and Cohen R M 1984a Appl. Phys. Lett. **44**, 550.
- Cherng M J, Cohen R M, and Stringfellow G B 1984b J. Electron. Mater. **13**, 799.
- Cherng M J, Cherng Y T, Jen H R, Harper P, Cohen R M, and Stringfellow G B 1986a J. Electron. Mater. **15**, 79.
- Cherng M J, Jen H R, Larsen C A, Stringfellow G B, Lundt H, and Talyor P C 1986b 3rd Int. Conf. OMVPE, Universal City, California, April.
- Fraas L M, Shin B K, Cape J A, Ransom R A, and Sawyer D E 1982 Proc. 16th IEEE Photovoltaic Specialists Conf., San Diego, 655.
- Jen H R, Cherng M J, and Stringfellow G B 1986a Appl. Phys. Lett. **48**, 1503.
- Jen H R, Cherng M J, Jou M J, and Stringfellow G B 1986b Proceedings of 7th Int. Conf. on Ternary and Multinary Compounds, Snowmass, Colorado, 10-12 Sep..
- Khachatryan A G 1973 Phys. Stat. Sol. (b) **60**, 10.
- Law H D, Chin R, Nakano K, and Milano R A 1981 IEEE J. Quantum Electron. **QE-17**, 275.
- Murgatroyd I J, Norman A G, and Booker G R 1986 Phys. Rev. Lett. (submitted).
- Schneider V A and Esch U 1944 Z. Electrochem. **50**, 290.
- Srivastava G P, Martins J L, and Zunger A 1985 Phys. Review B **31**, 2561.
- Stringfellow G B 1974 J. Crystal Growth **27**, 21.
- Stringfellow G B and Cherng M J 1983 J. Cryst. Growth **64**, 413.
- Stringfellow G B 1983 J. Crystal Growth **65**, 454.
- Swalin R A, *Thermodynamics of Solids*, (John Wiley and Sons, New York, 1962), Chapter 9.
- Waho J, Ogaqa S, and Maruyama S 1979 Jpn. J. Appl. Phys. **16**, 1875.

## **Growth behaviors and characterization of plasma-assisted epitaxial InSb and InAs on different substrates**

T. Hariu, S.F. Fang, K. Shida and K. Matsushita

Department of Electronic Engineering, Tohoku University  
Sendai 980, Japan

**Abstract.** InSb and InAs epitaxial layers with mirror surface were grown at relatively low temperatures by plasma-assisted epitaxy in hydrogen plasma with less supply ratio of anions relative to cations than in MBE. Electron densities and mobilities of  $1 \times 10^{16} \text{cm}^{-3}$  and  $39000 \text{cm}^2/\text{Vs}$  for InSb, and  $4 \times 10^{16} \text{cm}^{-3}$  and  $21000 \text{cm}^2/\text{Vs}$  for InAs were obtained. Growth behaviors and electronic properties of layers grown on different lattice mis-matched substrates were compared.

### **1. Introduction**

InSb, InAs and their alloys are attractive semiconductor materials for application to high-speed devices and to optoelectronic devices and IC's in the longest wavelength infrared region of all III-V compound semiconductors. These optoelectronic devices can be discrete, as some of them have already been in practical application, but they are desired to be integrated on the same chip of Si IC or higher speed GaAs IC to achieve more intelligent functions with higher sensitivity and higher speed. It is then required to develop technologies which can grow these materials epitaxially at low temperatures even on lattice mis-matched substrates, as in the case of GaAs on Si which recently has been extensively investigated.

The purpose of this paper is to comparatively describe the growth behaviors and electronic properties of InSb and InAs grown on different substrates by plasma-assisted epitaxy (PAE) in hydrogen plasma.

### **2. Plasma-Assisted Epitaxy**

PAE has been developed for the low temperature epitaxial growth of semiconductor crystals by supplying atoms with enhanced internal energy to activate chemical reaction and kinetic energy for migration on the growing surface (Takenaka et al 1980). Several other advantages of PAE, including the cleaning effect of substrate surface at low temperatures (Hariu et al 1981), have already been confirmed (Hariu et al 1984).

Similar PAE apparatuses as described elsewhere (Hariu et al 1982) were used for the growth of the present InSb and InAs layers. 6-nine purity elemental sources were used and supplied from resistively heated crucibles through hydrogen plasma to substrates. The use of hydrogen plasma was found to give epitaxial layers of much better quality compared with other plasma gases (Sato et al 1984).

Different substrates including GaAs, InP, GaP and Si were used to compare the relaxation of lattice mis-match and the electronic properties of grown layers. They are usually  $\langle 100 \rangle$  oriented, but sometimes substrates with orientation 3 and 8 degrees off  $\langle 100 \rangle$  toward  $\langle 111 \rangle$  were also used. After chemical etching to obtain mirror surfaces, the substrates are treated in hydrogen plasma at a temperature of epitaxial growth or below, to remove native oxide layers before the growth of IAE layers.

### 3. Results

It was first confirmed that mirror surfaces of grown layers can be obtained in IAE with less supply ratio of anions relative to cations than in MBE, most likely due to the supply of excited atoms or molecules in IAE (Matsumita et al 1984). For example, Merritt et al (1978) complained that in MBE growth of InAs on GaAs, As/In supply ratio larger than 20/1 is required for mirror-like surface, but in IAE As/In ratio around 5/1 is sufficient as far as the surface morphology is concerned. Surface morphologies of layers grown on lattice mis-matched substrates with orientation just on  $\langle 100 \rangle$  and off  $\langle 100 \rangle$  did not show remarkable differences as far as they were observed under a Nomarski microscope, however, conclusive evaluation has not been derived yet.

Epitaxial layers were obtained in quite a wide range of substrate temperature: 250-440°C for InSb and 300-550°C for InAs. It was also possible to grow epitaxial InAs on  $\langle 100 \rangle$  Si after the surface cleaning was achieved in hydrogen plasma at 530°C, while poly-crystalline layers grew on Si without this treatment.

Figs.1 and 2 show the variation of lattice constants and half-widths of  $\langle 400 \rangle$  X-ray diffraction lines of InSb and InAs, respectively, grown on different substrates, as a function of the thickness of grown layers. In both cases, the thickness above 1  $\mu\text{m}$  is required for the growth restoring the lattice constants of bulk, except the case of InSb on GaSb. In the latter case, the difference of thermal expansion coefficients is considered to be responsible for the strain even in thick layers. However, the deviation of lattice constants of grown layers cannot be systematically explained only in terms of the difference of thermal expansion and/or of lattice constants.

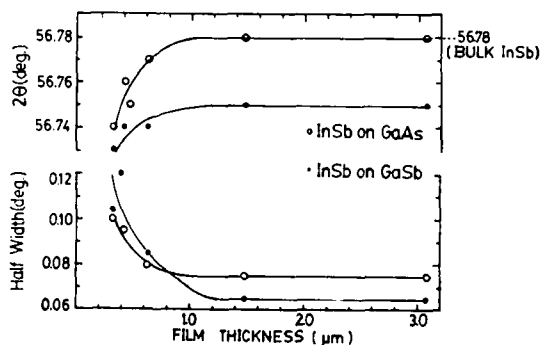


Fig.1 The variation of lattice constants (shown by X-ray diffraction angles) and half-widths of diffraction lines of InSb on different substrates as a function of thickness of grown layers.



It can be suggested that the combination of different anions between substrate and a grown layer leads to easier relaxation.

The smaller half-widths of InSb on GaSb than on GaAs and of InAs on InP than on GaAs can be attributed to the smaller lattice mismatch during the growth.

Fig.3 shows the similar variation for InAs layers with thickness of about 2 $\mu$ m as a function of growth temperature. This variation does not come from the difference of thermal expansion coefficients, but from the difference of growth behaviors at different temperatures.

Undoped layers of both PBE-InSb and -InAs showed n-type conduction. As shown in Fig.4, layers of similar electronic property were obtained in a wide range of supply ratio, compared with MBE (Miggitt et al 1978, Yano et al 1979, Kubiak et al 1984). It is also observed that the electronic properties of InAs layers grown on InP are less sensitive to the growth conditions including this supply ratio, compared with InAs on GaAs.

The dependence of electronic properties of InSb and InAs on substrate temperature are shown for layers grown on (100) semi-insulating GaAs in Figs.5 and 6,

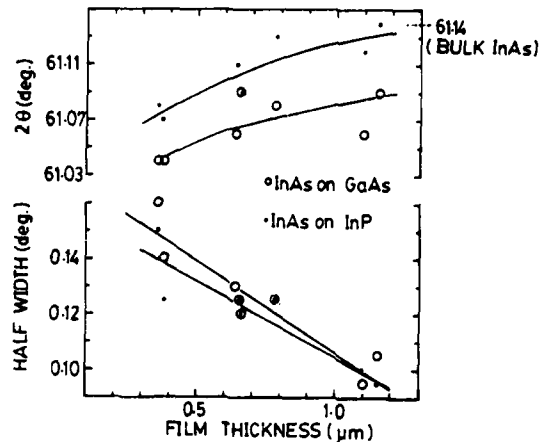


Fig.2 The variation of lattice constants (shown by X-ray diffraction angles) and half-widths of diffraction lines of InAs on different substrates as a function of thickness of grown layers.

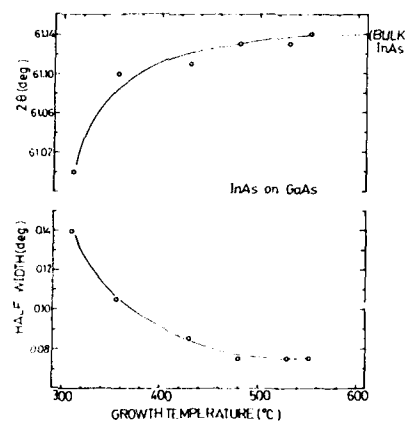


Fig.3 The variation of lattice constants (shown by X-ray diffraction angles) and half-widths of diffraction lines of InAs grown on GaAs as a function of growth temperature.

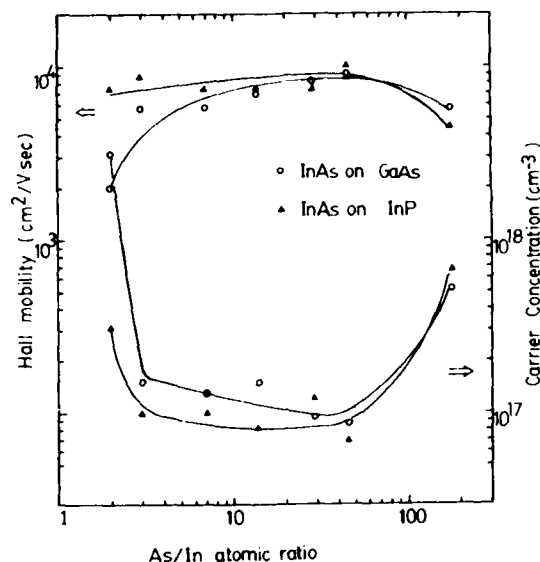


Fig.4 Carrier concentrations and Hall mobilities of n-type undoped InAs grown on semi-insulating (100) GaAs and InP at 450°C, as a function of supply ratio As/In.

respectively. In Fig.5, the dependence of 1/4-widths of (400) X-ray diffraction lines of InSb layers on substrate temperature is also included. The corresponding dependence for InAs has already been shown in Fig.3. The variation of the electronic properties has the same tendency with the crystallographic property in both cases, and the optimum substrate temperature with applied rf power of 20W in this case are about 380°C for InSb and 500°C for InAs.

Table I summarizes the electronic properties of the best InSb and InAs layers on different substrates. Further optimization of deposition conditions is expected to result in further reduction of epitaxial growth temperatures and improvement of electronic properties.

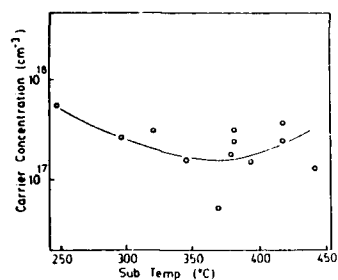
#### 4. Conclusions

InSb and InAs epitaxial layers with mirror surface were grown on (100) GaAs, InP, GaSb and Si at relatively low temperatures by plasma-assisted epitaxy in hydrogen plasma with less supply ratio of anions relative to cations than in MBE. Electron densities and mobilities of  $1 \times 10^{16} \text{ cm}^{-3}$  and  $39000 \text{ cm}^2/\text{Vs}$  for InSb, and  $4 \times 10^{16} \text{ cm}^{-3}$  and  $21000 \text{ cm}^2/\text{Vs}$  for InAs were obtained. The electronic properties were not so critically sensitive to the supply ratio. It is suggested that the combination of different

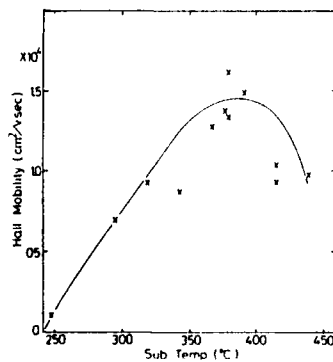
anions between substrates and grown layers can contribute to easier lattice relaxation in epitaxial growth on highly lattice mis-matched substrates.

#### Acknowledgement

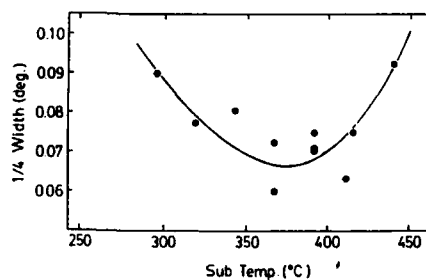
This work was supported in part by the Scientific Research Grant-in-Aid #61114004 for Special Project Research on "Alloy Semiconductor Physics and Electronics" from the Ministry of Education, Science and Culture. The authors wish to thank Y. Kashiwayanagi of Furukawa Electric for the supply of several GaAs wafers and partial support, Professors S. Ono and N. Miyamoto for stimulating discussions.



(a)



(b)



(c)

Fig.5 (a) Carrier concentrations, (b) Hall mobilities and (c)  $1/4$ -widths of (400) X-ray diffraction lines of PAE-InGa grown on semi-insulating GaAs, as a function of substrate temperature.

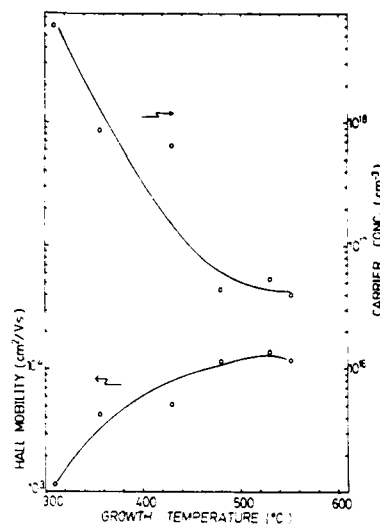


Fig.6 Carrier concentrations and Hall mobilities of PAE-InAs grown on semi-insulating GaAs, as a function of substrate temperature.

Table I Electronic properties of FAE-InSb and -InAs on different substrates.

|      |          | Film<br>substrate thickness<br>( $\mu\text{m}$ ) | carrier<br>density<br>( $\text{cm}^{-3}$ ) | Hall<br>mobility<br>( $\text{cm}^2/\text{Vs}$ ) | growth rate<br>( $\mu\text{m/h}$ ) | substrate<br>temp.<br>( $^{\circ}\text{C}$ ) |
|------|----------|--|--|---|------------------------------------|--|
| InSb | GaAs     | 3.5  | $1.1 \times 10^{16}$                       | $3.9 \times 10^4$                               | 0.5                                | 390  |
|      | sapphire | 3.5  | $1.0 \times 10^{16}$                       | $1.7 \times 10^4$                               | 0.5                                | 390  |
| InAs | GaAs     | 3.0  | $3.6 \times 10^{16}$                       | $1.5 \times 10^4$                               | 2.0                                | 550  |
|      | InP      | 3.7  | $7.0 \times 10^{17}$                       | $2.1 \times 10^4$                               | 1.2                                | 450  |

## References

- Hariu T, Takenaka K, Shibuya S, Komatsu Y and Shibata Y 1981 Thin Solid Films **80** 235  
 Hariu T, Matsushita K, Komatsu Y, Shibuya S, Igarashi S and Shibata Y 1982 Inst. Phys. Conf. Ser. **65** 141  
 Hariu T, Matsushita K, Sato Y, Sugiyama Y and Shibata Y 1984 Inst. Phys. Conf. Ser. **74** 193  
 Kubiak R A A, Parker E H C, Newstead S and Harris J J 1984 Appl. Phys. A (Germany) **35** 61  
 Matsushita K, Sato T, Sato Y, Sugiyama Y, Hariu T and Shibata Y 1984 IEEE Trans. Electron Devices **ED-31** 1092  
 Miggitt B T, Parker E H and King R M 1978 Appl. Phys. Lett. **33** 528  
 Sato Y, Matsushita K, Hariu T and Shibata Y 1984 Appl. Phys. Lett. **44** 592  
 Takenaka K, Hariu T and Shibata Y 1980 Jpn. J. Appl. Phys. Suppl. **19-2** 183  
 Yano M, Takase T and Kimata M 1979 phys. stat. sol.(a) **54** 707

## **Laser selective deposition and direct writing of single crystal III – V compounds films**

N H Karam N A El-Masry and S M Bedair

Electrical and Computer Engineering Department, North Carolina State University,  
Raleigh, North Carolina 27695-7911

**Abstract.** Laser induced chemical vapor deposition (LCVD) has been used for the first time to selectively grow and directly write single crystalline GaAs and its ternary alloys with P and Al on GaAs substrates. Deposition parameters were adjusted to reach growth rates low enough, typically 20 Å/s, for epitaxial growth to take place. Multiple scanning was found to improve the quality of the deposited films and give a better control of the deposition thickness.

### **1. Introduction**

Laser induced chemical vapor deposition (LCVD) has been the subject of growing interest due to its potential in selective epitaxy of optical and electronic components. The deposition process may be characterized as either pyrolytic or photolytic in nature (Allen, et.al., 1984) depending on the reactants, substrate and the laser wavelength. In a pyrolytic (thermal) process the laser wave length is selected such that the reactants are transparent and the substrate is absorbent. Hence, focusing the laser beam at the substrate creates a localized hot spot where deposition occurs and direct-writing is achieved by scanning the laser beam. Examples for such a pyrolytic process were reported for C, Si and Ni by Allen (1981, 1984), Bauerk, et.al. (1982) and Leyendecker, et.al. (1981). On the other hand, a deposition is photolytic in nature when the substrate is transparent while the reactants are absorbent to the laser power. In this case the deposition can be achieved at lower temperatures as for the case of Cd, Zr and Al demonstrated by Ehrlich, et.al. (1981a, 1981b, 1982) and Froidevaux, et.al. (1982, 1984).

The utilization of LCVD direct writing has been largely directed towards the deposition of metallic elements and compounds. Much less work has been reported on LCVD of III-V compound semiconductor. For example, InP was deposited on InP, GaAs and quartz substrates by Donnelly, et.al. (1984) using ArF excimer laser while GaAs was deposited on GaAs and Si substrates (Bedair, et.al., 1986 and Karam, et.al. (in press)) More recently Christou (1986) reported the use of an excimer laser to recrystallize amorphous GaAs deposition on Si. In this paper we will elaborate on some of the results we have obtained on laser induced chemical vapor deposition of GaAs and its alloys with P and Al on GaAs substrates. Particular emphasis is directed toward the control of the growth parameters for epitaxial deposition of the above compounds.

## 2. Experimental

The experimental set-up for LCVD is illustrated schematically in Figure 1. The experiment was carried out in a specially designed vertical MOCVD system operated at atmospheric pressure and was previously described by Bedair, et.al. (1984). GaAs substrates oriented  $2^\circ$  off the  $\langle 100 \rangle$  towards  $\langle 110 \rangle$  were irradiated with an  $\text{Ar}^+$  laser. The laser beam was focused on the substrate, that is thermally biased to a temperature  $25^\circ\text{C} \leq T_b \leq 500^\circ\text{C}$ , using a lens (focal length = 2cm). Laser beam scanning was achieved by translating the focusing lens at the desired speed using a computer controlled stepping motor.

Trimethyl Gallium, TMG ( $-13^\circ\text{C}$ ) or Triethyl Gallium, TEG ( $-5^\circ\text{C}$ ), Trimethyl Aluminum, TMA ( $20^\circ\text{C}$ ),  $\text{PH}_3$  (5% in  $\text{H}_2$ ), and  $\text{AsH}_3$  (5% in  $\text{H}_2$ ) were the sources used for Ga, Al, P and As, respectively. The flow rate of  $\text{H}_2$  through the TMG bubbler was in the range 1-2.5 sccm, TEG bubbler was 5-10 sccm and TMA 0-40 sccm. The  $\text{AsH}_3$  and  $\text{PH}_3$  flow rates were in the range 20-200 sccm with  $\text{H}_2$  as the carrier gas which maintains the total flow in the reactor at  $\sim 4000$  sccm.

## 3. Results and Discussions

Laser induced chemical vapor deposition (LCVD) and direct writing of GaAs and its alloys with P and Al was achieved by scanning the focused laser beam relative to the sample, resulting in deposition in the area that is locally heated by the  $\text{Ar}^+$  laser. The deposition rate and composition are a function of the mole fraction of the reactants, the laser power density ( $\rho$ ), scanning speed ( $S$ ) and substrate bias temperature ( $T_b$ ). LCVD allows the growth rate to be several orders of magnitude larger than the conventional CVD. For the same TMG mole fraction (2.5 sccm) in the gas phase the growth rate achieved by low-scanning speeds is about  $400 \text{ \AA}/\text{sec}$  (Bedair, et.al., in press). This is fifty times larger than that achieved in our conventional MOCVD experiments. Such an extremely high growth rate is accompanied by poor crystalline quality and grainy surface. This may be a result of the inefficient out diffusion of the reaction products (methane, ethane, TMG complexes and carbon) and probably their incorporation in the deposited film.

Several approaches were employed to decrease the growth rate of GaAs and GaAsP in order to be comparable to that of conventional MOCVD and eliminate the effect of reaction products on grown films. Low growth rates can be achieved by reducing the TMG mole fraction in the gas phase. Figure 2 shows two single scans (A and B) of GaAs on a GaAs substrate at  $\rho = 3.8 \times 10^4 \text{ W}/\text{cm}^2$ ,  $S = 20 \text{ \mu m}/\text{s}$  and  $T_b = 350^\circ\text{C}$ .

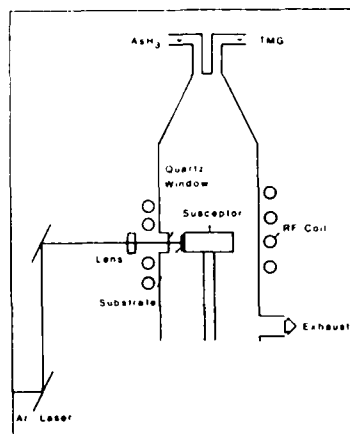


Figure 1. Schematic diagram of a laser chemical vapor deposition apparatus.

The  $H_2$  flow in the TMG bubbler for lines (a) and (b) is 2.5 and 1 sccm. It was found that even close to the minimum bubbler temperature ( $-13^\circ\text{C}$ ) and minimum reliable flow rate of TMG ( $\sim 1\text{cc/min}$ ) the growth rate was only reduced to  $300 \text{ \AA/s}$  which is an order of magnitude higher than conventional growth.

A second approach to reduce the growth rate was to reduce the laser power density. However, for a given power density, the quality of the deposition is improved by reducing the exposure time or increasing the laser scanning speed. This may cause some difficulty in achieving lines of reproducible thickness when very low laser power density is used. For example, at  $p$  of the order of  $10^2 \text{ W/cm}^2$ ,  $T_b$  in the range of  $375\text{--}500^\circ\text{C}$  and  $S = 0$  no laser deposition is observed for long exposure times (15 mins.). On the other hand for  $p = 3.8 \times 10^4 \text{ W/cm}^2$ ,  $S = 20 \text{ }\mu\text{m/sec}$  and  $T_b = 350^\circ\text{C}$ , rough deposition is achieved that is several microns thick.



Figure 2. LCVD single scans of GaAs on GaAs substrate at  $p = 3.8 \times 10^4 \text{ W/cm}^2$ ,  $T_b = 350^\circ\text{C}$  and  $S = 20 \text{ }\mu\text{m/s}$ ; a) TMG flow = 2.5 sccm, b) TMG flow = 1 sccm.

The third approach, which we believe is the most successful is accomplished by using fast scanning speeds  $S = 100\text{--}200 \text{ }\mu\text{m/s}$ , at moderate power densities  $p = 1.5 \times 10^3 \text{--}3.3 \times 10^4 \text{ W/cm}^2$  and  $T_b$  in the range  $375\text{--}500^\circ\text{C}$ . Shiny lines with good morphology at growth rates as low as  $20 \text{ \AA/s}$  have been obtained and by multiple scanning any desired thickness can be achieved. According to Lax (1977), the estimated substrate temperature at the center of the scanned line is  $\sim 600\text{--}700^\circ\text{C}$  depending on the surface reflectivity. Fast scanning does remove the growth (deposition region) surface away from the reaction products. Using a diffusion coefficient for the reaction products of about  $0.1 \text{ cm}^2/\text{sec}$  and laser spot size  $500 \text{ }\mu\text{m}$  these species will take about 10 sec to diffuse away to distance that is to say twenty times the size of the reaction region (twenty times is just an arbitrary number). At a scanning speed of  $200 \text{ }\mu\text{m/s}$ , for example, the laser beam crosses the  $500 \text{ }\mu\text{m}$  reaction region in 2.5 sec which is shorter than the time required for the reaction product to diffuse away from the deposition region. Thus reaction products will not interfere with the deposition process. However, on the other hand, for low scanning speed of  $10 \text{ }\mu\text{m/sec}$ , the laser beam crosses the deposition region in 50 sec. In this case the reaction products do not have enough time to diffuse away from this region, and thus they will influence the quality of the deposited films.

The optimum scanning speed depends also on the laser power density. For example, as shown in Figure 3, at a scanning speed of  $200 \text{ }\mu\text{m/s}$ , films with good surface morphology are obtained at laser powers of 4 and 5 watts (Figure 3a and 3b); however, 6 watts power gave a poor surface morphology as shown in Figure (3-C). The maximum thickness of the deposited film per scanning cycle is found to depend on the laser

TABLE I. GaAs growth rate per scan as a function of laser power at  $T_b = 375^\circ\text{C}$ ,  $s = 200\mu\text{m/s}$ , and laser spot size  $= 500\mu\text{m}$ .

|  | GaAs(1) | GaAs(2) | GaAs(3) |
|--|---------|---------|---------|
| Laser power (W)                              | 4       | 5       | 8       |
| Number of scans                              | 60      | 60      | 40      |
| Deposited thickness/scan ( $\text{\AA}$ )    | 65      | 130     | 400     |
| Max. growth rate ( $\text{\AA}/\text{sec}$ ) | 26      | 52      | 160     |

power density as shown in Table I. This indicates that the deposition process is controlled by the surface reaction kinetics and the surface temperature rather than the mass transport as in the case of the conventional

MOCVD.

Transmission electron microscopy (XTEM) was used to study the crystal quality of this new LCVD technique. Figure 4 shows a bright field image of a epitaxially grown LCVD line at  $g = 400$ . This line was grown at  $p = 15 \times 10^3 \text{ W/cm}^2$ ,  $T_b = 500^\circ\text{C}$  and  $S = 200 \mu\text{m/s}$ . More work is under way to study the structural defects associated with this technique.

**3.1 GaAsP:** The surface temperature of heated spots or lines can affect the spatial composition of ternary alloys.  $\text{GaAs}_{1-x}\text{P}_x$  compound is a good candidate to show such effect. This is because in a conventional MOCVD,  $x$  depends critically on the growth temperature for a given  $\text{AsH}_3$  to  $\text{PH}_3$  mole fraction in the gas phase

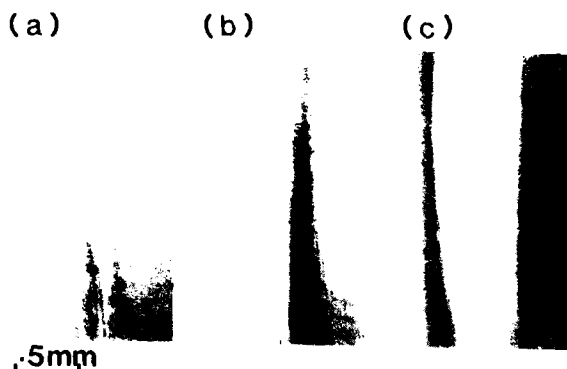


Figure 3. The variation of the deposited GaAs layer thickness with laser power density at  $T_b = 375^\circ\text{C}$ ,  $S = 200\mu\text{m/s}$  and laser spot size of  $500\mu\text{m}$ ; a) 4W, b) 5W and c) 6W.

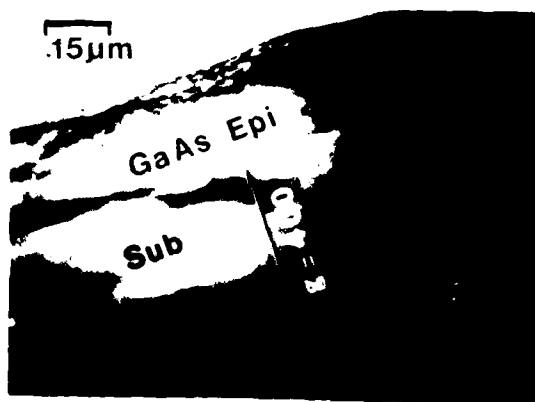


Figure 4. TEM image of a GaAs Epi layer grown on a substrate.

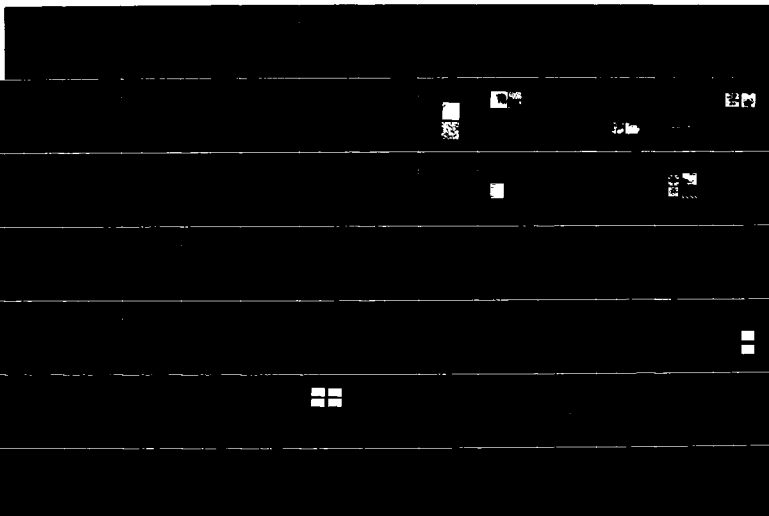


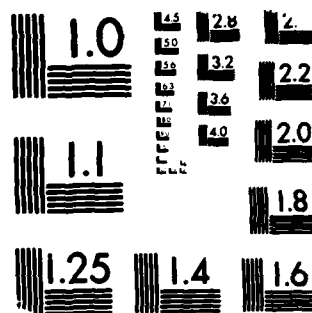
AD-A189 673

GALLIUM ARSENIDE AND RELATED COMPOUNDS 1986(U) ILLINOIS 3/7  
UNIV CHAMPAIGN W T LINDLEY 1986 AFOSR-1A-87-1888  
AFOSR-86-0169

UNCLASSIFIED

F/G 20/2 NL





MICROCOPY RESOLUTION TEST CHART  
NATIONAL BUREAU OF STANDARDS-1963-A

High growth temperatures allows more efficient cracking of  $\text{PH}_3$  and thus increases the value of  $x$ . The spatial distribution of P across a deposited GaAsP line (500  $\mu\text{m}$  wide) using SIMS is shown in Figure 5. As shown in this Figure the incorporation of P in the deposited film is not uniform and decreases at the boundaries where the surface temperature falls to that of the substrate bias temperature ( $T_b = 375^\circ\text{C}$ ). This temperature is too low to crack  $\text{PH}_3$  and the value of  $x$  should be close to zero. This nonuniform composition across the scanned GaAsP line can cause some limitations for this LCVD process. Nonuniformity can be reduced by using a laser beam with uniform intensity rather than the gaussian profile.

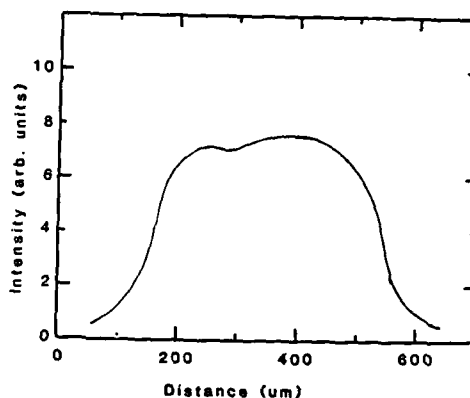


Figure 5. Phosphorous profile of GaAsP on GaAs by SIMS.

**3.2 AlGaAs:** Epitaxially AlGaAs was grown on GaAs substrates using the multiscan technique with compositions up to 25% Al measured by the electron micro probe (EMP). This was achieved at constant  $S = 200 \mu\text{m/s}$ ,  $\rho = 1.5 \times 10^3 \text{ W/cm}^2$ ,  $T_b = 500^\circ\text{C}$  and at flow rates of TMG and  $\text{As}_2\text{H}_3$  of 1 and 20 sccm respectively. Increasing the flow rate of TMA results in increasing Al concentration in the LCVD deposition with 40 sccm corresponding to 25% Al.

In conclusion, epitaxial GaAs and its ternary alloys with P and Al was selectively grown for the first time with LCVD direct writing technique. Photoluminescence and XTEM show that the material grown is comparable to that of conventional MOCVD. Controlling the growth parameters coupled with the multiscan technique provide better control over the grown crystal quality and the thickness. The deposition process is believed to be pyrolytic in nature and controlled by the surface kinetics.

#### References

- Allen, SD, J. Appl. Phys. 52, 6502 (1981).
- Allen SD, Jan, RY, Edwards, RH, Mazuk, SM and Vernon, SD, Proceedings of SPIE - The Inter. Soc. for Optical Engineering, LA California, vol. 459, p. 42 (1984).
- Aoyagi, Y, Masuda, S, Namba, S and Doi, A, Appl. Phys. Lett., 47, 95 (1985).
- Bauerk, D, Irsigler, D, Leyendecker, G, Noll, H and Wagner, D, Appl. Phys. Lett., 40, 9 (1982).
- Bedair, SM, Katsuyama, T, Chiang, PK, El-Masry, N, Tischler, M and Timmons, M., J. Cryst. Growth, 68, 477 (1984).
- Bedair, SM, Whisnant, JK, Karam, NH, Tischler, MA and Katsuyama, T, Appl. Phys. Lett., 48, 174 (1986).

- Bedair, SM, Whisnant, JK, Karam, NH, Griffis, D, El-Masry, N and Shadelmayer, HH, *J. Crystal Growth*, in press.
- Christou, A, *Appl. Phys. Lett.*, 48, 1516 (1986).
- Donnelly, VM, Geva, M, Long, J and Karliceck, RF, *Appl. Phys. Lett.*, 44, 10 (1984).
- Ehrlich, DJ, Osgood, Jr, RM, and Deutsch, TF, *Appl. Phys. Lett.* 38, 946 (1981a).
- Ehrlich, DJ, and Osgood, Jr, RM, *Thin Solid Films* 90, 287 (1981b).
- Ehrlich, DJ, Osgood, Jr, RM and Deutsch, TF, *J. Vac. Sci., Technol.* 21, 23 (1982).
- Froidevaux, YR, Salathe, RP, Gilgen, HH and Weber, HP, *Appl. Phys.*, A27, 133 (1982).
- Froidevaux, YR and Salathe, RP, *Proceedings of SPIE - The Inter. Soc. for Optical Engineering*, LA, California, vol. 459, p. 55 (1984).
- Karam, NH, El-Masry, NA and Bedair, SM, *Appl. Phys. Lett.*, (accepted for publication).
- Lax, M, *J. Appl. Phys.*, 48, 3919 (1977).
- Leyendecker, G and Baucerk, D, *Appl. Phys. Lett.*, 39, 11 (1981).

## **Optical characterisation of high purity GaAs and InP grown by vapor levitation epitaxy**

B J Skromme, H M Cox, and S G Hummel

Bell Communications Research, Red Bank, NJ 07701

**Abstract.** Low temperature photoluminescence measurements have been used to characterize GaAs and InP grown using chloride transport in conjunction with novel single phase source techniques in both VLE and conventional VPE reactors. Analysis of the exciton spectra indicates that the material is of high purity; selective pair luminescence and resonantly-excited two-hole transitions are used to identify residual C and Zn acceptors. Growth rates and residual acceptor incorporation are relatively insensitive to variations in growth parameters, rendering these techniques highly suitable for the controlled growth of alloys.

### 1. Introduction

Vapor levitation epitaxy (VLE) is a new approach to vapor phase epitaxy (VPE) in which the substrate is suspended above the growth apparatus by the flowing growth vapors (Cox 1984). As presently implemented, the VLE system requires a hot wall (exothermic) deposition process such as the trichloride or hydride techniques. In order to achieve high purity material while simultaneously avoiding the intrinsic instabilities of conventional saturated (two-phase) sources (Shaw 1971, Miers 1983), we have employed variants of the trichloride transport technique where only single phase sources of liquid Ga(In) and/or solid GaAs(InP) are used. These techniques are easily extended to the controlled growth of alloy materials with uniform and repeatable composition. In the following, we present the results of electrical and photoluminescence (PL) measurements which demonstrate that the material thus grown is of high electrical and optical quality. Under optimum conditions, the sensitivity of growth rates to variations in the growth parameters is shown to be weak. In addition, the residual shallow acceptor species are positively identified in each case and their incorporation is shown to be nearly independent of growth conditions.

### 2. Experimental

The design and construction of the VLE system used in this study have been described elsewhere (Cox et al. 1986); the conventional VPE system is similar to that described previously by Cox et al. (1985). Two different single phase sources were used for the GaAs growths. In the first technique,  $H_2$  and  $HCl$  obtained from the pre-cracking of  $AsCl_3$  at  $800^\circ C$  is passed over a liquid Ga source and the resulting  $GaCl$  is combined with a separate flow of  $AsCl_3$  in  $H_2$  which bypasses the source boat. The temperatures, mole fractions of the reactants, and other relevant growth parameters used with this technique are listed in the first column of Table I. It should be noted that the furnace temperature profile was varied from

Table I. Growth conditions

|   | GaAs                          |                        | InP                    |                                       |
|---|-------------------------------|------------------------|------------------------|---------------------------------------|
|   | 1st technique<br>(VPE)        | 2nd technique<br>(VLE) | 1st technique<br>(VLE) | 2nd technique<br>(VLE)                |
| T <sub>S</sub> (°C)                               | 700-800                       | 800                    | 750                    | 750, 650, 600                         |
| T <sub>G</sub> (°C)                               | 680-700                       | 700                    | 650                    | 650, 550, 500                         |
| [HCl] (Ga/In)                                     | $9.4 \times 10^{-3}$          | $6 \times 10^{-3}$     | ---                    | $0-1.0 \times 10^{-2}$                |
| [AsCl <sub>3</sub> ] (bypass)                     | $0.31-4.6 \times 10^{-3}$     | $1 \times 10^{-3}$     | ---                    | ---                                   |
| [AsCl <sub>3</sub> /PCl <sub>3</sub> ] (GaAs/InP) | ---                           | ---                    | $5 \times 10^{-2}$     | $0.74-1.7 \times 10^{-3}$             |
| III/V   | 2.0-30                        | 6.0                    | $\approx 0.67$         | 0.75-3.4                              |
| Total flow (sccm)                                 | 640                           | 1500                   | 2500                   | 1500                                  |
| Substrate type                                    | n <sup>+</sup> or Cr-doped SI | Cr-doped SI            | Cr-doped SI            | S-doped n <sup>+</sup> or Fe-doped SI |
| Substrate orientation                             | 6° off (100)                  | 6° off (100)           | 3° off (100)           | 3° off (100)                          |

approximately flat to a substantial gradient; the III/V ratio, which is directly controllable by changing the [HCl](Ga)/[AsCl<sub>3</sub>](bypass) ratio, was varied over a considerable range. It should be noted that the amount of HCl introduced to the deposition zone (from cracking of the AsCl<sub>3</sub> bypass flow) varies proportionally to the III/V ratio.

In the second technique, AsCl<sub>3</sub> in H<sub>2</sub> is simply passed directly over single crystal GaAs source material as described previously (Cox et al. 1985). The conditions employed in the VLE system using this technique are given in the second column of Table I. The III/V ratio with this technique is fixed by the source reaction efficiency which was taken to be 0.67 for the calculation (Shaw 1975).

The source technique employed for the InP growth in the VLE system was described previously by Cox et al. (1985). A flow of PCl<sub>3</sub> in H<sub>2</sub> is used to transport polycrystalline InP source material (MCP,  $n=3 \times 10^{15}$  cm<sup>-3</sup>). Additional InCl is generated by passing a separate flow of HCl in H<sub>2</sub> (derived from pre-cracking of AsCl<sub>3</sub>) over an In source; the III/V ratio can be adjusted by changing the ratio of the two flows. Growth conditions are listed in Table I. The III/V ratios were calculated assuming the source reactions go to completion (Shaw 1975). For one sample, HCl derived from PCl<sub>3</sub> was used to transport the In; comparable results were obtained.

The PL was excited using an Ar-pumped dye laser and LDS 821 dye; a 1.0 m double spectrometer, cooled GaAs and S-1 photomultipliers, and photon counting detection were employed. Resolution was typically 0.07 Å for the exciton spectra and 0.7 Å elsewhere. The data were acquired using a computer and corrections were made where necessary for system response as a function of wavelength. Samples were suspended strain-free in superfluid He.

### 3. GaAs Characterization Results

Electrical and PL characterization was employed to compare the quality of the best material produced with each of the single phase source techniques. In Fig. 1 we show exciton spectra recorded under the same measurement conditions for each of four samples. The peaks are labeled following Heim and Hiesinger (1974). The FWHM of the (D<sup>0</sup>,X) peaks for the VLE and VPE samples grown using a Ga source and AsCl<sub>3</sub> bypass (2nd and 4th spectra from top) are 0.17 and 0.13 meV, respectively, indicating very high purity. The PL data are particularly useful in evaluating these layers since Hall

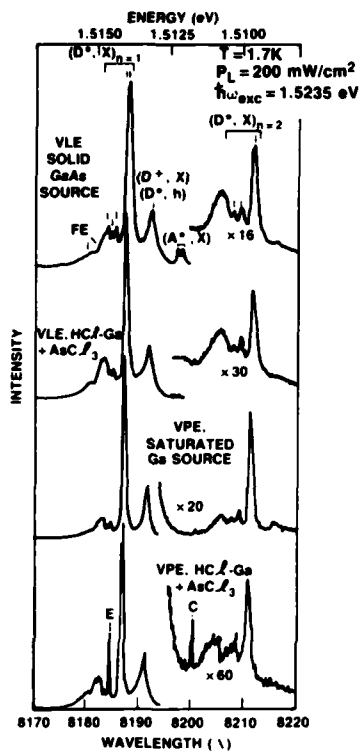
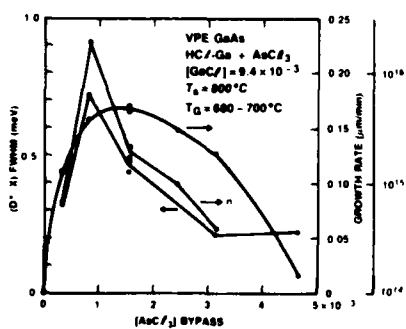
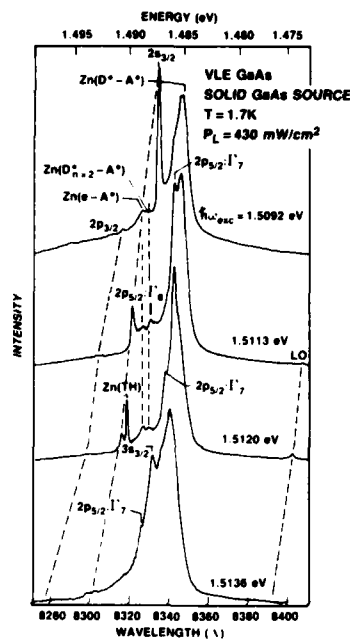


Fig. 1. Exciton spectra of four VLE and VPE GaAs samples



**Fig. 3. Mole fraction dependence using single-phase Ga source**



**Fig. 2. SPL spectra at four different excitation energies**

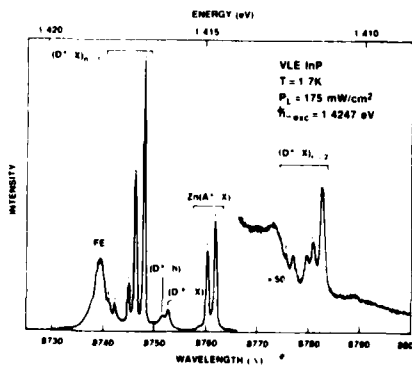


Fig. 4. Exciton spectrum of a high purity VLE InP sample

effect measurements were not possible on either (the former was grown on an  $n^+$  substrate and the latter was so thin as to be totally depleted). For comparison, a sample grown using a saturated Ga source in the same VPE reactor with the same source materials is shown in the 3rd spectrum. This sample has a  $(D^0, X)$  FWHM of 0.15 meV and a 77 K Hall mobility of 164,000  $\text{cm}^2/\text{Vs}$  for  $n=1.3 \times 10^{14} \text{ cm}^{-3}$ . The two-electron transitions  $(D^0, X)_{n=2}$  are somewhat better resolved in this reference sample, but otherwise the samples grown with the single phase Ga source appear to compare quite favorably in purity. The uppermost spectrum for a sample grown with the solid GaAs source has a  $(D^0, X)$  FWHM of 0.26 meV; the 77 K mobility is measured as 92,000  $\text{cm}^2/\text{Vs}$  and  $n=4 \times 10^{14} \text{ cm}^{-3}$ . This sample is significantly less pure than the others but is still to our knowledge the highest purity GaAs ever reported with this technique.

In order to positively identify the residual shallow acceptor species characteristic of the single phase source techniques, selective pair luminescence (SPL) measurements were employed (Tews and Venghaus 1979, Hunter and McGill 1982, Kisker et al. 1983). In Fig. 2 we show SPL spectra recorded for four different excitation wavelengths for a sample grown with a solid GaAs source. A full set of excited states of Zn acceptors are observed, with energies in excellent agreement with previous work (Kisker et al. 1983). No evidence is seen for other shallow acceptor species in this sample. Resonant enhancement of the very sharp Zn two-hole (TH) transition (Ashen et al. 1975) occurs as the laser is tuned through the  $(A^0, X)$  peaks. A doublet splitting of the  $2s_{3/2}$  state resulting from the axial donor-acceptor interactions at small separation distances is observed in the bottom spectrum; analogous observations were reported in InP (Dean et al. 1979) but this effect has not previously been reported in GaAs.

Similar SPL measurements were used to identify the principal residual shallow acceptors in samples grown with the single-phase Ga source as C and Zn. The Zn  $(D^0-A^0)$  peak is typically about 20X weaker than the C peak under non-selective excitation in samples grown with well-baked source materials. This result holds regardless of source temperature or III/V ratio, except at the lowest value of the latter where Zn incorporation is enhanced. In nearly all of these samples, the shallow acceptor peaks were roughly 50-100X weaker than the near band-edge exciton peaks, suggesting that deep acceptors may contribute most of  $N_A$ .

The variations of growth rate, carrier concentration (measured from C-V profiling), and  $(D^0, X)$  FWHM are plotted in Fig. 3 as a function of the mole fraction of  $\text{AsCl}_3$  introduced directly into the deposition zone. The drop in growth rate at low  $[\text{AsCl}_3]$  is due to insufficient mass transport of As, while the drop at high  $[\text{AsCl}_3]$  is a thermodynamic effect of the excess HCl, in agreement with Chatterjee et al. (1982). It is apparent that a large range exists where the growth rate is relatively insensitive to  $[\text{AsCl}_3]$ , which is highly desirable for reproducibility.

It appears that the donor incorporation, as indicated by the carrier concentration and the  $(D^0, X)$  FWHM, peaks sharply at a mole fraction of about  $8 \times 10^{-2}$ . However, the sharpness of the peak is probably exaggerated by the fact that the corresponding sample was the first layer ever grown in this reactor. Impurities such as S which later baked out of the source materials may therefore have contributed. The same growth conditions were not repeated in later runs. We speculate that the drop in donor incorporation as  $[\text{AsCl}_3]$  increases is due to a conventional "mole-fraction effect" on Si incorporation by the excess HCl (see Mullin (1977) and references therein).



The same three parameters as in Fig. 3 were measured as a function of source temperature ( $T_S$ ) with constant  $[AsCl_3]=1.56 \times 10^{-3}$ . The growth rate is constant to within 5% for  $T_S=708-800^\circ C$ , which is not surprising since the reaction with the Ga should be complete (Shaw 1975). The average value of  $n$  drops from  $2 \times 10^{15}$  to  $5 \times 10^{14}$  to  $4 \times 10^{14} \text{ cm}^{-3}$  as  $T_S$  drops from 800 to 750 to  $700^\circ C$ ; corresponding values of  $(n^0, X)$  FWHM are 0.46, 0.22, and 0.16 meV. This type of effect was previously noted in experiments with various single flat temperature zone methods (Koukutu et al. 1979) and is attributed to a reduction in the generation of chlorosilanes in the source zone which leads to a reduction in Si donor contamination.

#### 4. InP Characterization Results

An exciton spectrum for a moderately thick ( $8 \mu\text{m}$ ) InP layer grown on a semi-insulating substrate is shown in Fig. 4. Excellent resolution of the various peaks is observed, comparable to that achieved in very high purity layers grown using the conventional saturated In source (Dean and Skolnick 1983). This particular layer is totally depleted but a layer with a similar exciton spectrum has a 77 K mobility of  $75,300 \text{ cm}^2/\text{Vs}$  and  $n=2 \times 10^{14} \text{ cm}^{-3}$ . The exciton spectrum compares quite favorably with those recently reported for high purity InP samples grown by MOCVD which have considerably higher 77 K mobilities (Di Forte-Poisson et al. 1985 and Zhu et al. 1985). An accurate comparison, however, would require PL measurements performed under the same experimental conditions.

Exciton spectra were examined for a series of thin ( $1-2 \mu\text{m}$ ) layers grown on  $n^+$  substrates over the range of growth conditions described in Table I. None of the spectra of layers on  $n^+$  substrates were as well resolved as that of Fig. 4, possibly due to out-diffusion from the substrates. No consistent trends in spectral quality as a function of mole fractions were observed, indicating that impurity incorporation is apparently largely independent of III/V ratio, etc. The sample grown with  $T_S=650$  and  $T_G=550^\circ C$  fell within the range of those grown at higher temperatures, but the sample grown at  $600/500^\circ C$  displayed much weaker and broader peaks.

The residual acceptor in the InP layers was positively identified as Zn in all cases using SPL and resonantly-excited two-hole transitions. An example of both resonantly and non-resonantly excited spectra is given in Fig. 5. With above-band-gap excitation at moderately high intensities, the Zn (TH) peak is only just discernible (uppermost spectrum). As the laser is tuned into resonance with one of the  $(A^0, X)$  components, the corresponding sharp TH peak corresponding to Zn acceptors (White et al. 1972) is resonantly enhanced; weaker SPL peaks are simultaneously observed. As the laser is tuned

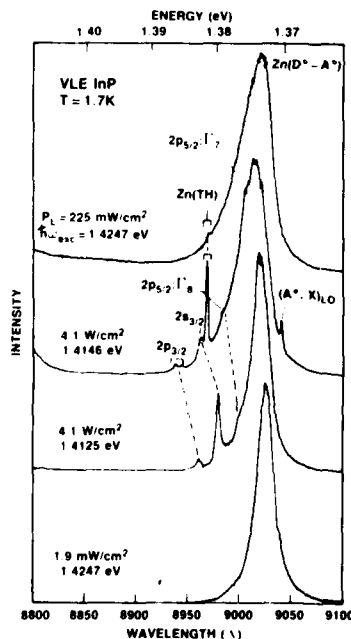


Fig. 5. Selective and non-selective pair luminescence in VLE InP

to lower energies, the broader SPL peaks corresponding to various excited states of Zn acceptors (Dean et al. 1979) become stronger. Under low-intensity above-band-gap excitation (bottom spectrum) the non-selective ( $D^0-A^0$ ) peak is quite narrow and no other acceptor peaks are observed.

The strength of the Zn-related peaks was found to be a strong function of the baking of the InP source material after loading. The ratio of Zn ( $A^0, X$ ) to ( $D^0, X$ ) peak heights decreased steadily in one case from 6.0 for the first run after loading a new source to 0.33 for the fourth run (total hot time=115 min at 750°C). Baking of the InP between runs is not performed because of the P loss that would result. The peak height ratio is reduced to around 0.06 after a large number of runs.

##### 5. Conclusions

We have demonstrated the capability of growing high purity GaAs and InP by both VLE and conventional VPE using novel single phase source techniques which can be readily extended to the controlled and reproducible growth of alloys. While not discussed here, these samples were grown under conditions which also yield excellent surface morphology and uniformity (Cox et al. 1986), and are thus quite practical for device production. We have shown that growth rates and residual acceptor incorporation are relatively insensitive to changes in growth conditions, which is highly desirable from the point of view of process control. The residual shallow acceptors have been identified and necessary baking steps after source loading have been noted. Finally, we note that no toxic gases or pyrophoric liquids are required for growth, in light of recent increased concern over safety.

##### 6. References

- Ashen D J, Dean P J, Hurle D T J, Mullin J B, White A M, and Greene P D 1975 *J. Phys. Chem. Solids* **36** 1041  
 Chatterjee A K, Faktor M M, Lyons M H, and Moss R H 1982 *J. Crystal Growth* **56** 591  
 Cox H M 1984 *J. Crystal Growth* **69** 641  
 Cox H M, Koza M A, Keramidas V G, and Young M S 1985 *J. Crystal Growth* **73** 523  
 Cox H M, Hummel S G, and Keramidas V G 1986 *Proc. 8th Int. Conf. Crystal Growth*, York, July 14-18, 1986, to be published in *J. Crystal Growth*  
 Dean P J, Robbins D J, and Bishop S G 1979 *Solid State Commun.* **32** 379  
 Dean P J and Skolnick M S 1983 *J. Appl. Phys.* **54** 346  
 Di Forte-Poisson M A, Brylinski C, and Duchemin J P 1985 *Appl. Phys. Lett.* **46** 476  
 Helm U and Hiesinger P 1974 *Phys. Stat. Sol. (b)* **66** 461  
 Hunter A T and McGill T C 1982 *Appl. Phys. Lett.* **40** 169  
 Kisker D W, Tews H, and Rehm W 1983 *J. Appl. Phys.* **54** 1332  
 Koukitu A, Seki H, and Fujimoto M 1979 *Jap. J. Appl. Phys.* **18** 1747  
 Miers T H 1983 *Gallium Arsenide and Related Compounds* Albuquerque 1982 ed G E Stillman (Bristol: Inst. Phys.) pp 125-132  
 Mullin J B 1977 *J. Crystal Growth* **42** 77  
 Shaw D W 1971 *J. Crystal Growth* **8** 117  
 Shaw D W 1975 *J. Phys. Chem. Solids* **36** 111  
 Tews H and Venghaus H 1979 *Solid State Commun.* **30** 219  
 White A M, Dean P J, Joyce B D, Clarke R C, and Taylor L L 1972 *Proc. 11th Conf. Phys. Semiconductors, Warsaw* (Warsaw: Polish Sci. Pub.) pp 190-195  
 Zhu L D, Chan K T, and Ballantyne J M 1985 *Appl. Phys. Lett.* **47** 47

## Growth of $\text{Ga}_{1-x}\text{In}_x\text{As}$ layers with excellent compositional uniformity on InP by OMVPE

H. Kamei, G. Sasaki, T. Kato, H. Hayashi, K. Ono and K. Yoshida  
Advanced Semiconductor Devices R & D Department,  
Sumitomo Electric Industries, Ltd.  
1-3 Shimaya 1-chome, Konohana-ku, Osaka 554, Japan

**Abstract.**  $\text{Ga}_{1-x}\text{In}_x\text{As}$  layers with excellent compositional uniformity have been obtained on 2 inch diameter InP substrates by reduced pressure organometallic vapor phase epitaxy. The reproducibility of composition in run-to-run was also excellent.

### 1. Introduction

$\text{Ga}_{1-x}\text{In}_x\text{As}$  lattice-matched to InP is a promising material for the fabrication of high speed transistors, optoelectronic devices operating in the wavelength of 1.3 - 1.55  $\mu\text{m}$ , and optoelectronic integrated circuits. For these applications, organometallic vapor phase epitaxy (OMVPE) is one of the most advantageous growth methods in respect of the controllability of layer thickness and composition (Razeghi et al. 1983, Smeets et al. 1986), large area growth, and high throughput. In this paper, we report OMVPE growth of  $\text{Ga}_{1-x}\text{In}_x\text{As}$  layers with excellent compositional uniformity on 2 inch diameter InP substrates. The compositional uniformity of the  $\text{Ga}_{1-x}\text{In}_x\text{As}$  epilayers was evaluated by double crystal x-ray diffraction and photoluminescence measurement.

### 2. OMVPE Growth

$\text{Ga}_{1-x}\text{In}_x\text{As}$  epilayers were grown directly on a 2 inch diameter Fe-doped InP substrate oriented  $2^\circ$  off the (100) in a water-cooled vertical reactor at reduced pressure. Triethylgallium (TEG), trimethylindium (TMI) and arsine ( $\text{AsH}_3$ , 10 % in  $\text{H}_2$ ) were used as the starting sources, and were introduced together with the carrier gas into the reactor from the top. The substrate was positioned perpendicular to the gas stream on a RF-heated carbon susceptor. Hydrogen was used as the carrier gas. 1 - 2  $\mu\text{m}$ -thick epilayers were typically grown under the conditions listed on Table 1.

Table 1. Typical growth conditions.

|                          |                               |
|--------------------------|-------------------------------|
| Growth temperature       | 600, 650 and 700°C            |
| Growth pressure          | 60 Torr                       |
| Total gas flow rate      | 3.4 slm                       |
| TEG flow rate            | $2.6 \times 10^{-6}$ mole/min |
| TMI flow rate            | $3.5 \times 10^{-6}$ mole/min |
| $\text{AsH}_3$ flow rate | $5.4 \times 10^{-4}$ mole/min |
| V/III                    | 90                            |
| Growth rate              | 1 $\mu\text{m/hr}$            |
| Substrate rotation rate  | 12 rpm                        |

As shown in Fig. 1, the controllability in composition of the epilayers was examined by measuring the lattice mismatch to the InP substrate for the epilayers grown at different TMI flow rates with the constant TEG flow rate. The linearity of the lattice mismatch against the composition broke due to the misfit dislocations at the large lattice mismatch in the InAs-rich region in Fig. 1.

The variation of epilayer thickness was less than  $\pm 4\%$  against the mean epilayer thickness over a 2 inch diameter wafer. The morphology of the epilayers showed a mirrorlike surface.

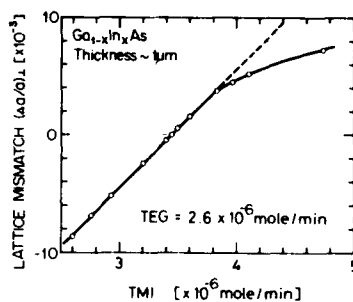


Fig. 1. The lattice mismatch as a function of TMI flow rate.

### 3. Results

Fig. 2 shows the variation of lattice mismatch to the InP substrate in each epilayer grown at different growth temperatures of 600, 650 and 700°C. Other growth conditions except for the growth temperature were kept constant in the growth of the epilayers shown in Fig. 2. The best compositional uniformity was obtained from the epilayer grown at 600°C. On the other hand, the epilayers grown at 650 and 700°C showed the unfavorable variation of composition in the GaAs-rich region although the tendencies of the variation in composition were different from each other. The variation of composition in the epilayers grown at 650 and 700°C was considered to be caused by the depletion of TMI in the gas phase above the hot substrate.

In order to evaluate the accurate variation of lattice mismatch in the epilayer grown at 600°C, we have grown an intentionally lattice-mismatched epilayer. In a lattice-mismatched epilayer, we can evaluate the accurate lattice mismatch of the epilayer to the substrate from the separated x-ray diffraction peaks of the epilayer and the substrate. As shown in Fig. 3, the variation of lattice mismatch to the InP substrate was less than  $1.5 \times 10^{-4}$  in the 2 inch diameter epilayer grown at 600°C, which corresponded to the variation in composition of less than 0.1 % mole fractions in consideration of the tetragonal distortion.

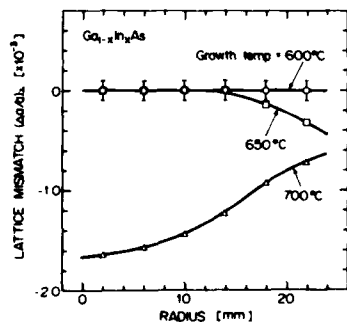


Fig. 2. The variation of lattice mismatch in  $\text{Ga}_{1-x}\text{In}_x\text{As}$  epilayers grown at 600, 650 and 700°C.

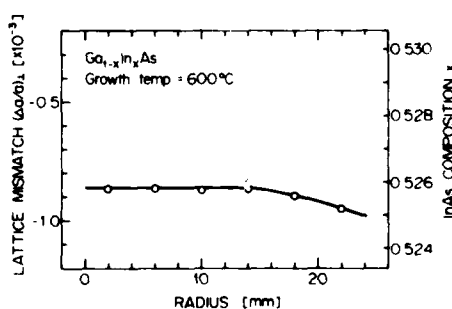


Fig. 3. The variation of composition in an intentionally lattice-mismatched  $\text{Ga}_{1-x}\text{In}_x\text{As}$  epilayer grown at 600°C.

A narrow x-ray diffraction peak of the epilayer was observed over the whole substrate area. The typical x-ray rocking curve of an intentionally lattice-mismatched epilayer on the InP substrate is shown in Fig. 4. The full width at half the maximum (FWHM) of the (400) reflection from a 2  $\mu\text{m}$ -thick epilayer was as narrow as 16 arcsec, and was comparable to the FWHM of the InP substrate. We also observed the FWHM of 20 arcsec for a 1  $\mu\text{m}$ -thick epilayer. These narrow FWHM of the epilayers indicate that the compositional uniformity of the epilayers depthwise was also excellent. In addition, so far as we are aware, these FWHM are the narrowest that were ever reported for  $\text{Ga}_{1-x}\text{In}_x\text{As}$  epilayers grown by any method.

We performed the photoluminescence measurements at 4.2 K for the epilayers with the excellent compositional uniformity. As shown in Fig. 5, an excitonic transition peak with the FWHM as narrow as 1.5 meV was observed. This narrow FWHM of the excitonic transition peak was consistent with the uniformity results obtained by x-ray diffractions.

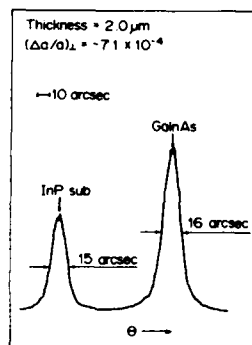


Fig. 4. The x-ray rocking curve of an intentionally lattice-mismatched  $\text{Ga}_{1-x}\text{In}_x\text{As}$  epilayer.

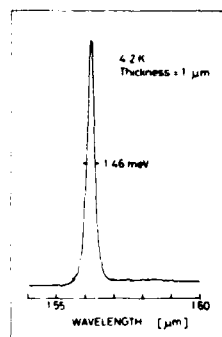
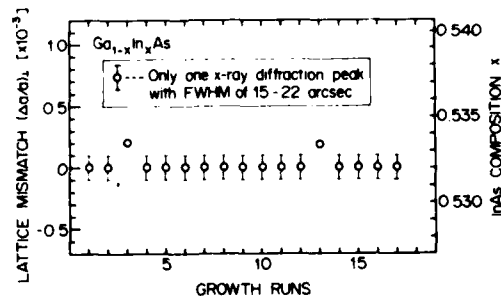


Fig. 5. The photoluminescence measurement of a  $\text{Ga}_{1-x}\text{In}_x\text{As}$  epilayer at 4.2 K.

Further, we evaluated the reproducibility of composition in run-to-run for 17 growth runs which were performed over a period of 4 months under the same lattice-matching growth conditions. As shown in Fig. 6, almost all epilayers except for 2 epilayers exhibited the only one double crystal x-ray diffraction peaks with the narrow FWHM of 15 ~ 22 arcsec. The variation of lattice mismatch in 17 growth runs was less than  $3 \times 10^{-4}$ , which corresponded to the variation in composition of less than 0.2 % mole fractions.

Fig. 6. The reproducibility of composition in run-to-run for 17 growth runs performed under the same lattice-matching growth conditions.



#### 4. Summary

We demonstrated the growth of  $\text{Ga}_{1-x}\text{In}_x\text{As}$  layers with excellent compositional uniformity over the area of a 2 inch diameter InP substrate by reduced pressure OMVPE using TEG, TMI and  $\text{AsH}_3$  in a vertical reactor. The compositional uniformity in a wafer and the reproducibility of composition in run-to-run of the  $\text{Ga}_{1-x}\text{In}_x\text{As}$  layers described here would be sufficient for the production of optoelectronic devices.

#### Acknowledgement

The authors would like to thank M. Maeda for photoluminescence measurements, and M. Murata for OMVPE growth.

#### References

- Razeghi M, Poisson M A, Larivain J P and Duchemin J P  
1983 J. Electron. Mater. 12 371  
Smeets E T J M and Cox A M W 1986 J. Cryst. Growth  
(Proceedings of 3rd Int. Conf. on Metalorganic Vapor Phase Epitaxy, to be published)

## **Double-injection induced conductivity between n and p contacts to semi-insulating GaAs: Experiment and numerical simulation**

L. D. Flesner, M. O'Brien, A. K. Nedoluha, R. Zuleeg\*, A. H. Guerrero+ and Claude M. Penchina+

Naval Ocean Systems Center, Code 56, San Diego, CA 92152-5000

\*McDonnell Douglas Microelectronics Center, Huntington Beach, CA 92647

+Physics Dept., University of Massachusetts, Amherst, MA 01003

**Abstract.** Two-dimensional simulations of current-voltage (I-V) and ionization induced current between co-planar n-type and p-type contacts on semi-insulating (SI) GaAs are compared with experimental data. Possible outdiffusion of deep levels in a thin layer near the surface is considered, although the surface interface is treated as ideal. Simulated and experimental results agree in many respects despite simplifying assumptions in the model.

### **1. Introduction**

Motivation for studying contact junctions to semi-insulating (SI) GaAs and conduction between contacts is provided by the need for electrical isolation between circuit elements in integrated circuits. A well-known problem is the so-called backgating/sidegating effect wherein a bias applied to a contact is observed to affect the current in a proximate transistor. Also there is a requirement for tolerance to ionizing radiation which might be encountered in space. The sidegating effect is dependent upon the properties of the channel-substrate junction [Kocot 1982] and upon the conductance between the contacts. The onset of sidegating has been associated with the onset of space-charge limited current [Lee 1982] but the threshold voltage is generally much less than would be expected from bulk properties, and one explanation which has been advanced is loss of deep-levels (EL-2) near the surface [Chang 1984a]. This effect has been modeled analytically [Chang 1984b] by assuming a thin layer with reduced trap density bounded top and bottom by uniform constant potentials. One-dimensional numerical simulations have also been reported [Horio 1984].

In this paper we describe two-dimensional simulations based on a model similar to that proposed by Chang and Lee. A two-dimensional simulation takes into account the trapping which occurs above and below a degraded layer, which would strongly influence the layer conductance if the thickness is less than the Debye length. For the initial work to be described the surface is treated as an ideal interface, with the sample effectively mirrored at the surface plane. The surface layer is therefore bounded by two SI bulk regions rather than by SI bulk below and surface states of surface states. This is unrealistic for GaAs, which is known to have a large density of surface states. However, this assumption does facilitate investigation of the effects of a thin layer with reduced impurities without additional complications.

The simulated results are compared with experimental measurements on devices fabricated by ion-implantation into nominally undoped

liquid-encapsulated Czochralski (LEC) substrates. The devices are coplanar n- and p- type contacts 100 micrometers wide with separations of 2, 4, 8 and 16 micrometers. They were fabricated by the McDonnell-Douglas Microelectronics Center using processing similar to that for junction field-effect transistor integrated circuits [Troeger 1979].

## 2. Mathematical Model

The steady state simulation uses the semi-classical drift-diffusion approach. This involves a simultaneous solution of three coupled non-linear differential equations: the Poisson Equation, and the Continuity Equations for electrons and for holes. The electron and hole currents are determined from field-dependent mobilities and the gradients of quasi-Fermi potentials [vanVliet 1980].

Generation and recombination processes at deep traps are handled by means of Shockley-Read-Hall statistics [Hall 1952, Shockley 1952]. Since for SI material the free carrier concentrations may be very small, space charge on the deep traps is fully accounted for in the Poisson equation. This important detail is frequently neglected in numerical modeling of semiconductor devices [Swierkowski 1984, Alvin 1976].

The SI properties of nominally undoped LEC GaAs are attributed to compensation of shallow acceptor impurities (primarily carbon) by intrinsic deep donors (primarily EL-2) [Holmes 1982]. The deep donor concentration is taken to be on the order of  $1 \times 10^{16} \text{ cm}^{-3}$  and the acceptor concentration to be the order of  $1 \times 10^{15} \text{ cm}^{-3}$ . The deep donors in the bulk are arbitrarily kept a factor of ten higher in concentration than the shallow acceptors. The energy level of the deep traps is taken to be 0.68 eV below the conduction band [Look 1983]. The deep donor cross-section of  $1 \times 10^{13} \text{ cm}^{-2}$  is the same as used by Horio [1984]. However, the acceptor cross-section of  $2 \times 10^{18} \text{ cm}^{-2}$  would give a hole lifetime of tens of microseconds, which is much longer than the nanosecond lifetimes actually observed in this material [Flesner 1985]. Therefore, we chose a hole cross-section of  $1 \times 10^{14} \text{ cm}^{-2}$  to get nanosecond time-scale recombination for assumed trap concentrations.

The sample is modeled as a rectangular parallelepiped with ion-implanted contact regions in the upper corners. See Fig. 1. The planar metal contacts to the ion-implanted n and p regions are treated as zero-resistance, ideal "Ohmic" contacts. The zero resistance is specified by fixed-potential Dirichlet boundary conditions; the "Ohmic" nature through the assumption of a fixed thermal-equilibrium concentration of electrons and holes. The other boundaries of the device are assumed to be symmetry planes across which there is no net current and zero normal electric field (Neumann boundary condition). This last assumption treats the surface as being ideal, and is equivalent to burying the surface between two mirror-image devices.

To simulate surface degradation either the deep donors only, or the deep donors and shallow acceptors are removed from a thin layer near the surface. The thickness of the degraded layer is taken to be of the order of 0.2 to 1 micrometer. [Chang 1984a]

Photoexcitation is simulated by pair generation which is uniform laterally and which decays exponentially away from the surface. Electron beam excitation is also modeled by increased pair generation, but it is confined to a vertical grid line with a depth of 1 micrometer.



The finite-difference method is used for discretization of the differential equations which are linearized by a modified version of the Newton method. The Successive Line Over-Relaxation (SLOR) method [Wachpress 1970] is used for an iterative solution to the linearized equations. To avoid numerical instabilities for the divergence of the current, we use the Scharfetter-Gummel [1969] method.

The electrostatic potential and charge concentrations are determined at the grid points shown in Fig. 1. Currents and electric fields are assumed uniform between grid points. The Poisson equation and the continuity equations use box integration surrounding the grid points.

### 3. Results

The dark I-V characteristics of p-SI-n devices with length  $L$  of the SI region as a parameter are shown in Fig. 2. The simulated curves were obtained assuming no surface degradation, and with impurity concentrations of  $7 \times 10^{15}$  EL-2 and  $7 \times 10^{14}$  C per cc. The simulations show an ohmic I-V at low voltage with a transition to recombination limited current proportional to  $\exp(qV/2kT)$  at higher voltage with the transition voltage increasing as the square of the contact separation  $L$ . In comparison, the data for the 2, 4, and 8 micrometer samples also show current proportional to  $\exp(qV/2kT)$  at higher voltages, but the scaling of voltage with  $L$  is more nearly linear than quadratic [Flesner 1986]. The 16 micrometer sample rises much more steeply. The data are ohmic at the lowest voltages, but the transition to non-ohmic behavior is more complex.

Outdiffusion of EL-2 (which produces a slightly p-like region) near the surface has been simulated, and found to lead to a lowering of the threshold voltage for transition to recombination limited current. This is illustrated in Fig. 3. For this figure larger concentrations of impurity levels were assumed to accentuate the effect. A strong dependence on layer thickness relative to depletion depth was found. The effect of creating a degraded surface layer is indistinguishable from decreasing bulk impurity concentrations, which increases diffusion lengths. This means that partial p-type surface conversion cannot be inferred from forward p-SI-n I-V data without additional information.

We also simulated the effect of removing both deep donors and shallow acceptors from a thin layer leaving an intrinsic region. Such a layer was found to have a negligible effect on the p-SI-n I-V. The reason for this is that charge trapped above and below an intrinsic layer, which has a large Debye length, still dominates the conductance. A p-type layer, on the other hand, provides a potential well and even though the conductance without injection may be negligible because of carrier depletion, hole transport can contribute significantly to the forward I-V.

Figure 4 shows simulation and data for photoconductivity in an 8 micrometer p-SI-n device. The induced current reverses sign when the bias equals the open circuit photovoltage. Simulation and data agree well, and this effect is useful experimentally to determine separately the junction voltages and the SI region voltage drop [Flesner 1986].

Simulated n-SI-n I-V without degraded layers were similar to those obtained by one-dimensional simulation [Rorio 1984]. Neither a p-type nor intrinsic layers were found to produce a significant effect on the n-SI-n I-V. Sidegating was also studied in simulation by monitoring the change in total number of electrons in the positively biased n-channel contact

junction region as a function of bias. The simulated sidegating is also insensitive to degraded p-like or trap-free intrinsic layers.

The effects of excitation by focused electron beam were simulated as shown in Fig. 5. No effort was made to adjust parameters for fitting to the data other than for amplitude scaling for convenient comparison. The zero bias simulation amplitude is multiplied by a factor of 2 and the 2 V bias simulation amplitude is divided by 15. Both the modeled and experimental spatial dependences reveal the presence of n-SI junction fields, which separate excited carriers and thereby induce current collection. At zero bias the n-SI junction is found both experimentally and in simulation to act as a photodiode. With applied bias the actual n-SI-n devices behave like back to back diodes with the current collected limited to less than the e-beam generated current. The simulation, on the other hand, shows a photoconductive gain of about 15 at 2 V. bias indicating that the junction barriers in simulation are less effective than the actual device barriers in suppressing photoconduction between n-type contacts. Such photoconductive gain between n-SI-n contacts is observed experimentally only at very high excitation levels [Flesner 1985]. Similar investigations are in progress on p-SI-p devices.

#### 4. Discussion and Conclusions

Although the forward I-V for the p-SI-n devices is strongly affected by the presence of a degraded p-like surface layer, similar results can be obtained by simply reducing the bulk impurity concentrations. Hence, no conclusions regarding the presence of such a layer can be made from I-V data without more information. Additional problems are the lack of quantitative agreement for the length scaling and the anomalous I-V of the 16 micrometer sample.

The n-SI-n I-V and the resulting sidegating phenomenon does not seem to be affected by either a p-like layer or by an intrinsic layer. This suggests that additional features, such as surface states, will have to be included in the model before progress can be made in understanding sidegating phenomena. Efforts are being made in this direction.

The agreement of the experiment and simulation regarding photo- and electron-beam induced currents suggests that the behavior of the contact-substrate junctions can be investigated using the assumed SI properties as a starting point. The presence of built-in fields at these junctions will influence the behavior of integrated circuits exposed to ionizing radiation. For example, the junctions are "blocking" contacts which suppress photoconductivity while inducing photodiode-like charge collection.

#### 5. Acknowledgements

This work was supported by the Defense Advanced Research Projects Agency. Summer 1986 tenure at the Naval Ocean Systems Center was provided for Prof. Petchina by the U. S. Navy-ASEE Summer Faculty Research Program. Assistance by K. W. Hwang in initial computer program development is also acknowledged.

# Characterisation

191

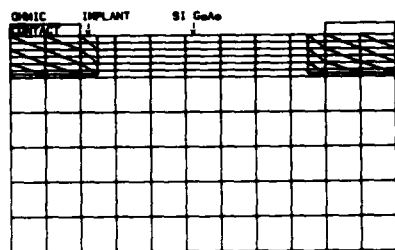


Figure 1.

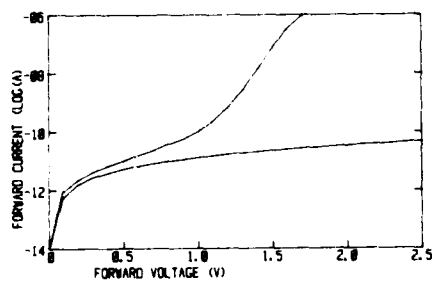


Figure 3.

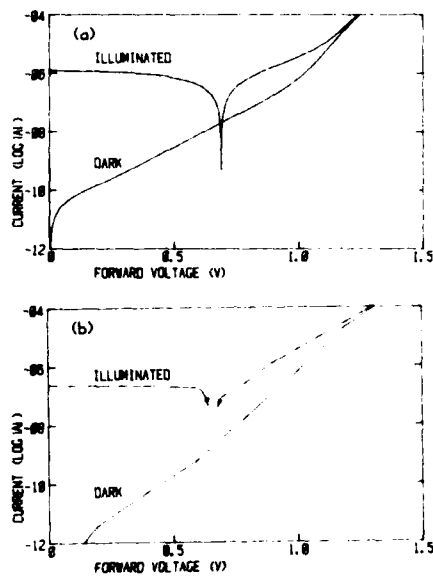


Figure 4.

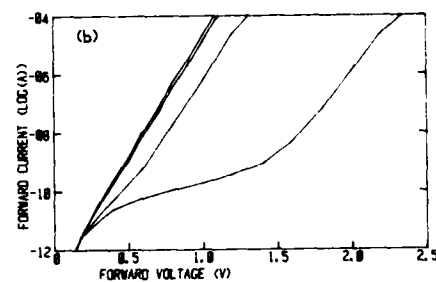
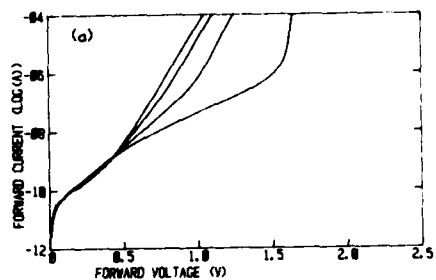


Figure 2.

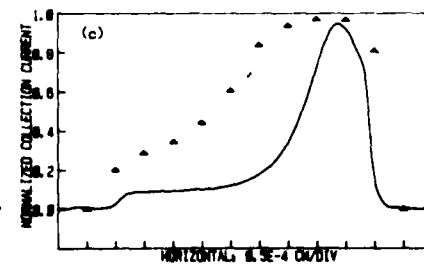
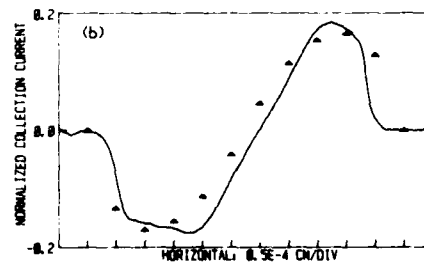
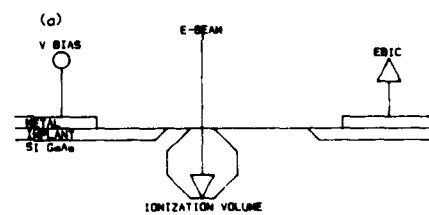


Figure 5.

## 6. References

- Alvin V K 1976 Ph.D. Dissertation, Univ. of Mass., Amherst MA  
 Chang M F, Lee C P, Hou L D, Vahrenkamp R P and Kirkpatrick C G 1984a Appl. Phys. Lett. **44** pp 869-871  
 Chang M F, Lee C P, Vahrenkamp R P, Hou L D, Holmes D E and Kirkpatrick C G 1984b Semi-Insulating III-V Materials, Kah-nee-ta 1984, ed D C Look and J S Blakemore (Cheshire U.K.: Shiva Publishing Ltd.) pp. 378-385  
 Flesner L D, 1985 IEEE Trans. Nucl. Sci. NS-32 pp. 4110-4114  
 Flesner L D, Nedoluha A K, Zuleeg R, Penchina C M 1986 J. Appl. Phys. **59** pp. 3298-3301  
 Hall R N 1952 Phys. Rev. **87**, p. 387  
 Holmes D E, Chen R T, Elliot K R and Kirkpatrick C G 1982 Appl. Phys. Lett. **53** pp. 149-151  
 Horio K and Ikoma T 1984 Semi-Insulating III-V Materials, Kah-nee-ta 1984 ed D C Look and J S Blakemore (Cheshire U.K., Shiva Publishing Ltd.) pp. 378-385  
 Kocot C and Stolte C A 1982 IEEE Trans. Electron Dev. ED-29 p. 1059  
 Lee C P, Lee S J and Welch B M 1982 IEEE Electron Dev. Lett. EDL-3 p. 97  
 Look D C 1983 Semiconductors and Semi-metals **19**, ed. R K. Willardson and A C Beer (New York: Academic Press) pp. 75-170  
 Scharfetter D L and Gummel H K 1969 IEEE Trans. Electron Dev. ED-16, pp. 64-77  
 Shockley W and Read W T 1952 Phys. Rev. **87**, p. 835  
 Swierkowski S P, Dease C G and Jelsma L F 1984 Lawrence Livermore Rept. No. UCID-20109  
 Troeger G L, Behle A F, Freibertshauser P E, Hu K L, and Watanabe S H 1979 IEEE International Electron Dev. Meeting Tech. Dig., IEEE Cat. No. CH1504-OED, pp. 497-500  
 van Vliet K M and Marshak A H 1980 Solid State Electron. **23**, pp. 49-53  
 Wachpress E L 1970 Iterative Solutions of Elliptic Systems (New York: Prentice-Hall)

## 7. Figure Captions

Figure 1. 12x12 grid used in device simulation.

Figure 2. Forward I-V for p-SI-n devices, experiment (a) and simulation (b). Contact separations are 2, 4, 8 and 16 micrometers from left to right.

Figure 3. Effect of p-like layer on p-SI-n forward I-V. L = 16 micrometers and the trap density is  $4 \times 10^{16}$  EL-2,  $4 \times 10^{15}$  C. The upper curve is for a p-like layer 0.2 micrometer deep.

Figure 4. Effect of uniform illumination on an 8 micrometer p-SI-n device I-V, data (a) and simulation (b). The log of the absolute value of current is plotted.

Figure 5. In (a) a schematic of the EBIC experiment is shown and (b) and (c) illustrate results for a 4 micrometer n-SI-n device. For (b) the applied bias is zero and the simulated results (triangles) have been multiplied by a factor of two. For (c) a bias of 2 V is applied and the simulated amplitudes have been divided by 15. The scale is normalized to the e-beam generated current. Assumed EL-2 and C concentrations are  $1 \times 10^{16}$  and  $1 \times 10^{15}$ , respectively.

## **Scanning laser photoluminescence imaging technique for nondestructive evaluation of direct bandgap materials**

D.L. Parker and Nathan Moon

Department of Electrical Engineering, Texas A&M University, College Station Texas 77843.

**Abstract.** A commercial laser trimming system with an adapted, AO modulated, Argon ion laser is used to serpentine raster scan direct bandgap semiconductor wafers. The photoluminescence radiation is synchronously detected and used to generate a two dimensional yield map for display and recording as with an SEM. The technique has been successfully applied to a variety of GaAs wafers. Image features have been correlated with crystal defects.

### **1. Introduction**

Photoluminescence (PL) analysis is currently widely used to study the electronic effects of various defects and impurities on direct bandgap semiconductor materials. This powerful tool usually requires that the sample be cooled to very low temperatures and further the sampled area is relatively large, allowing no conclusion about microscopic distributions of impurities and defects. Cathode luminescence (CL) offers high spatial resolution however the technique requires special sample preparation and is somewhat destructive. The imaging method described in this paper has relatively high spatial resolution (better than 10 microns); is compatible with thin dielectric films such as  $\text{SiO}_2$  or  $\text{Si}_3\text{N}_4$ ; and is nondestructive. The latter feature allows analysis of the same sample before and after each of several processing steps. The method may prove to be a useful complement to conventional analytic methods in device-process-defect-reliability studies.

### **2. Experimental**

A block diagram of the imaging system is shown in figure 1. The laser trimming system has an  $80 \times 80 \text{ mm}^2$  xy beam positioning capability with 2.5 micron accuracy. An AO switched Argon ion laser has been added to the system so that this radiation may be substituted for the Nd:YAG which is usually used for resistor trimming or link blowing. The blue green line square wave modulated at frequencies from 200Hz to 40kHz is usually used for PL imaging. This wavelength is absorbed in the first micron or so of most semiconductors producing essentially one excess hole-electron pair per absorbed photon.

The software which controls the system allows entry of scanning speed from  $1 \text{ mm/sec}$  to  $1000 \text{ mm/sec}$  and scanned size areas in binary steps from  $2.5 \times 2.5 \text{ mm}^2$  up to  $80 \times 80 \text{ mm}^2$ . The scan mode is always serpentine raster with 1000 lines and the x-y analog signals are automatically adjusted to fill the monitor and scan converter screens regardless of the scan size.

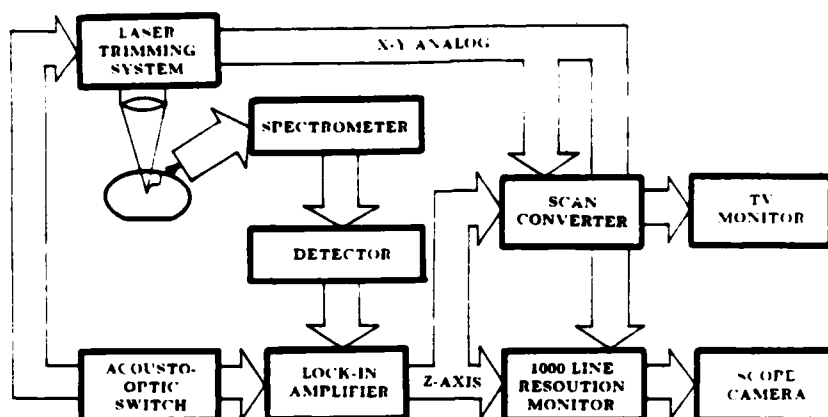


Fig. 1 Block diagram of scanning laser photoluminescence imaging system

The PL light is picked up by a fiber bundle moving with the laser beam. Three different positions have been used for the fiber bundle termination: 1.) near the front wafer surface at 45° to the wafer surface and the laser beam; 2.) on the backside looking normal to the wafer; and 3.) in the TV illuminator beam path through the final objective lens which delivers the laser beam. The first position was used to generate all images shown in this paper and comparisons with the other two positions are still underway. A filter is used in front of the fiber bundle to reject the laser light and the spectrometer is operated in a low resolution mode (slits removed) to maximize the signal. The detector is an S-1 photomultiplier with useful sensitivities out to about 11000 Å in the infrared.

Gain and offset controls on the lock-in amplifier are used as brightness and contrast controls to enhance image features. In some cases total black to saturated white may represent only a 10% change in the PL signal. All images to date have been made with the sample at room temperature and with the spectrometer set to pass the maximum band-to-band luminescence radiation (about 8700 Å for GaAs).

The scan converter stores an image as it is generated for viewing on a TV monitor at the end of the scan. The high resolution monitor with a scope camera attached is used to record hard copies. All features seen in the PL images are very reproducible and none are visible by optical microscope inspection.

### 3. Results

Figure 2 is a PL image of a 75mm LEC GaAs wafer after a source-drain Si implant ( $\sim 10^{13} \text{ cm}^{-2}$ ). Figure 3 is a  $2.5 \times 2.5 \text{ mm}^2$  zoom near the center of this wafer. The small black geometries are regions which received the Si implant and the white honeycomb is typically seen over the entire wafer. The white areas will be shown to be pinned to dislocation clusters. Figure 4 is a PL image of the same wafer after a capped thermal anneal. (850°C 30 min.) The white splotches are probably due to pinholes in the capping film or localized contamination. Although the

PL imaging technique can be nondestructive the Argon laser can produce changes in the GaAs material if the power is too high. The square boxes in this image were produced by prior laser scans at too much power. These damaged areas are not visible and have been observed to "flake away" after several weeks of storage in air at room temperature.

After annealing the honeycomb structure is in exactly the same place as before; however the white bands are wider. Before annealing the bands are 40-100 microns and about 150 microns after annealing. These results are consistent with the work of T. Kamejima et al and suggest that dislocations getter radiation killing impurity and/or defect states.

Fig. 2 PL image of 75mm  
LEC GaAs wafer after  
Si implant



Fig. 3 PL image of  
 $2.5 \times 2.5 \text{ mm}^2$  portion near  
the center of the wafer  
shown in Fig. 2





Fig. 4 PL image after anneal



Fig. 5 PL image before anneal

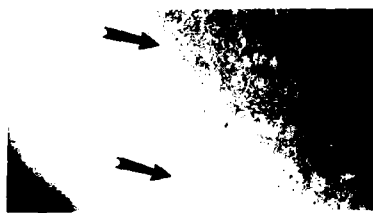


Fig. 6 XRT image of above

Figure 5 is a PL image of a portion of the wafer near the lower left edge taken before annealing. Figure 6 is an x-ray topograph (XRT) of the same region shown in figure 5. The black arrows in each image indicate unique features to assist the reader in confirming the complete correlation of the honeycomb structures with dislocation networks shown in the XRT image.

#### 4. Conclusions

The scanning laser photoluminescence imaging technique has been shown to nondestructively produce high contrast reproducible images of the distribution of dislocation clusters in GaAs wafers. Work is in progress to improve the spectral resolution by cooling the wafer specimen and the photomultiplier tube. Further comparisons of the luminescence radiation received at each of the three pickup points are being made. Also work is in progress to attempt to correlate PL features with device characteristics such as threshold voltage and backgateing effects in MESFET transistors.

#### 5. Acknowledgments

The authors wish to thank Honeywell Optoelectronics Division and TriQuint Semiconductor for GaAs material and other assistance. They also wish to thank Electro Scientific Industries and Spectra Physics for equipment donations.

#### 6. Reference

T. Kamejima, F. Shimura, Y. Matsumoto, H. Watanabe, and J. Matsui, "Role of dislocations in semi-insulation mechanism in undoped LEC GaAs crystal," *Jpn. Appl. Phys.*, vol. 21, pp. L721-L723, 1982.



## **GaAs wafer investigation by near-infrared transmission and photoluminescence topography techniques**

J. Windscheif and W. Wettling

Fraunhofer-Institut für Angewandte Festkörperphysik, Eckerstr. 4,  
D-7800 Freiburg, W.-Germany

### Abstract

Two optical topographical methods for homogeneity control of GaAs wafers are presented. The first one (NIRtop) monitors the transmission of near infrared light, while the other one (PLtop) records the room temperature photoluminescence. The topograms are displayed as false colour pictures of high resolution. By comparison a remarkable resemblance for both methods is found when applied to undoped s.i. LEC material. The two methods in combination are very useful for the inspection of surface quality and of various technological processes as annealing, ion implantation, activation and epitaxial growth of thin films.

### 1. Introduction

Various topographical methods have been developed during the past few years to measure the spatial inhomogeneity of s.i. LEC GaAs wafers with respect to almost any physical property (Fillard 1985, Hakone 1986). Of special interest are methods that correlate different properties because they allow a deeper insight into the physical mechanisms that lead to the inhomogeneities. Optical topographical techniques are especially useful because they are fast and nondestructive and can, therefore, be used as a routine characterization.

The present paper concentrates on the aspect of correlating the two topographical methods near infrared transmission topography (NIRtop) and photoluminescence topography (PLtop). Both methods have been used by a number of workers separately (Brozel et al. 1984, Dobrilla and Blakemore 1985, Hovel et al. 1986), but not much work has been done to compare the two methods (Wettling and Windscheif 1986, Löhnert et al. 1986).

We have investigated s.i. LEC GaAs wafers, n- and p- doped wafers, MBE layers and ion implanted layers. It will be shown that the two techniques in combination are a valuable tool for routine characterization of GaAs material and also of technological processes as etching, polishing, annealing, implantation and activation.

### 2. Experimental Set-up

Our experimental set-up was similar to that described earlier (Wettling and Windscheif 1986) but with some improvements. In short: The NIR topograms were performed by moving the wafer perpendicular to a fixed illuminated slit and focussing the image of the slit to a 256 diode Si detector array. Transmitted light between 1.18 and 1.38 eV is recorded, a spectral range where the optical absorption is closely related to the

concentration of deep donor EL2 defects (Martin 1981). The signal from the detector array is transferred to a computer (HP 217) and stored line by line in a 256 x 256 data file as 16 bit integers. All topograms shown were recorded from standard thickness wafers (0.3 to 0.5 mm).

In the PLtop experiment Argon laser light (514.5 nm, chopped at 500 Hz) is focussed to the wafer and the band edge luminescent light (870 nm) is recorded through several filters by a cooled Si photomultiplier, a lock-in detector and a digital storage oscilloscope. The wafer is scanned by a computer controlled x-y stage. The data (512 x 512 pixels) are stored in the same format as the NIRtop data in the computer.

Two dimensional images of the absorption and the luminescence data are composed using a false colour mapping technique. One-dimensional traces of absorption and luminescence along a line through the wafer can also be extracted from the data. Thus a direct comparison of the two methods can easily be performed.

In the following section we discuss topograms of whole 2 inch wafers (spatial resolution 100 to 200  $\mu\text{m}$ ) and of enlarged sections of about 15 x 15 mm (resolution 30 to 60  $\mu\text{m}$ ). In the NIR absorption measurements also a microscope can be used to record enlarged images with a resolution down to 1  $\mu\text{m}$ . In this configuration the diode array is moved while the wafer is fixed. Upon reproducing the coloured topograms in black and white the different colours are represented as different grey values. It is emphasized that the coloured mappings are much more illustrative and impressive.

### 3 Results

For s.i. undoped LEC GaAs it was shown in a previous paper that NIRtop and PLtop mappings exhibit almost identical pictures of the macroscopic inhomogeneity ("W"-shape) as well as of the cellular structures (Wetling and Windscheif 1986). This is demonstrated in Fig. 1. Areas of high absorption correspond to areas of increased PL intensity. This can be explained by assuming that the EL2 center exists in the material in two charge states,  $\text{EL2}^0$  and  $\text{EL2}^+$ . The  $\text{EL2}^+$  concentration is higher and therefore the  $\text{EL2}^0$  concentration is lower in areas of larger net acceptor concentration due to compensation of the shallow acceptor states. As NIR absorption is caused by the  $\text{EL2}^0$  states and an

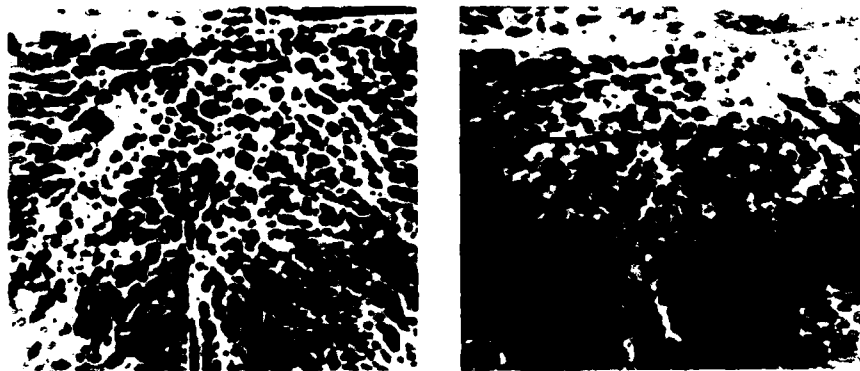


Fig. 1 NIR topogram (left) and PL topogram (right) of the central section of a s.i. undoped LEC grown GaAs wafer. The section is 19 x 19 mm<sup>2</sup> for NIRtop and 16 x 16 mm<sup>2</sup> for PLtop. Dark areas correspond to low absorption and low emission, respectively. The dark horizontal line in the right figure was bleached by repetitive scanning with the laser

increased nonradiative recombination can be assumed to result from the  $EL2^+$  states the observed correlation of PL topograms and NIR topograms is understandable. It should, however, be recalled that the NIRtop measures bulk properties through the full thickness of the wafer, whereas PLtop measures surface-near properties to a depth of about 200 to 300 nm.

Indium alloyed LEC grown wafers are, as expected, much more homogeneous than undoped wafers. In addition they exhibit remarkable differences in their topograms. Fig. 2 gives a NIR topogram and a PL topogram of the central section of an In alloyed wafer. There is no cellular structure of the inhomogeneity. Instead one observes dark areas which consist of isolated dots or accumulations of dark dots. These dots are dark also in PL (in contrast to the situation in undoped material mentioned above). In NIR transmission microscope pictures they show a higher definition than the more "cloudy" cellular structures of the undoped material. This is demonstrated in Fig. 3 where small sections of as-grown and In alloyed wafers are compared. It seems therefore that the inhomogeneous absorption mechanism is somewhat different in In-alloyed wafers.

The PLtop technique can also be used to study the homogeneity of MBE or MOCVD layers. In general, in PL topograms MBE films show larger intensity and better homogeneity than their s.i. substrates (Hovel and Guidotti 1985). Fig. 4 shows two PL traces of a 200 nm n-doped MBE layer and of its substrate after removing the MBE layer.

It was recently observed that the PL intensity varies nonlinearly with the incident laser power and that the PL intensity decreases (bleaches) with time upon illumination of one spot of the wafer with constant laser power (Hovel and Guidotti 1985, Wettling and Windscheif 1986). We find these two effects always in combination but not in all samples that we have studied. Superlinear power dependence and bleaching of PL intensity is observed in s.i. undoped LEC substrates, in In-alloyed s.i. substrates and in high ohmic MBE films with donor and acceptor concentration  $[N_d - N_a] < 10^{13} \text{ cm}^{-3}$ .

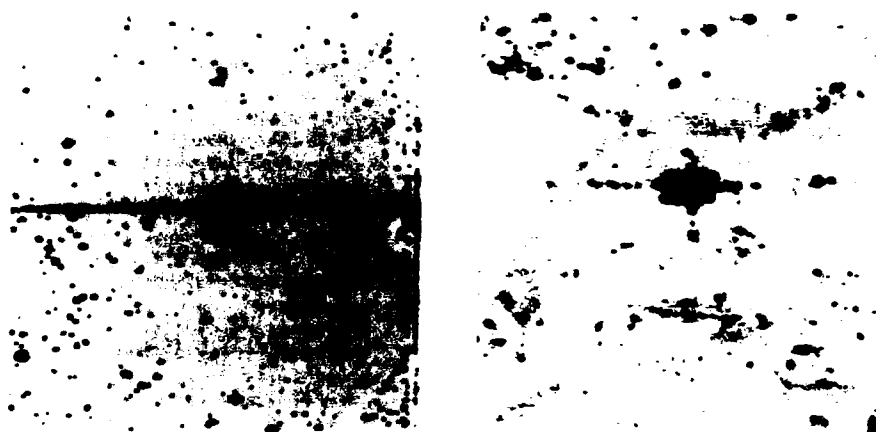


Fig. 2 NIR topogram (left) and PL topogram (right) of the central section of an indium alloyed s.i. GaAs wafer. Dark areas correspond to high absorption and low emission, respectively. The dark horizontal line results from a crack in the wafer

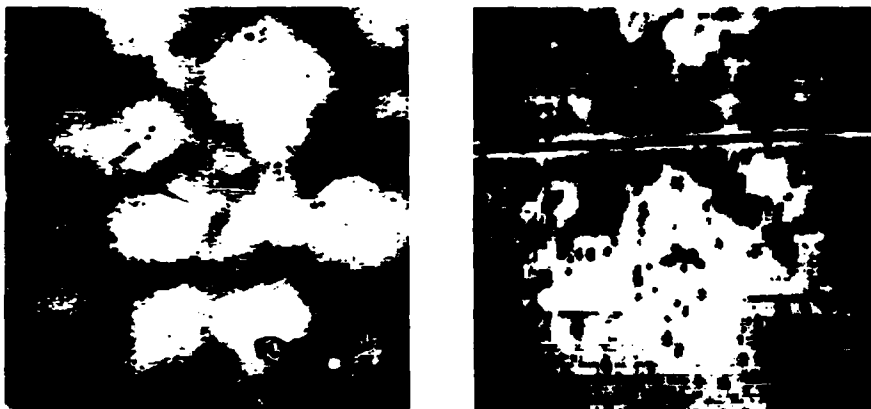


Fig. 3 Comparison of microscopic transmission topograms of "cellular" structures of a s.i. undoped wafer (left) and "cluster"-like structures in an In-alloyed s.i. wafer (same wafer as in Fig. 2). The measured section is  $2 \times 2 \text{ mm}^2$ . Dark areas: high absorption

The two effects are not -or only weakly- found in n-doped and p-doped wafers and in n-doped MBE films, as shown in Fig. 5. Therefore these two effects are related to the high resistivity of material or to the midgap position of the Fermi-level, rather than to the growth method. Further investigations are necessary to prove whether they are related to surface states and band bending effects at the surface. As also shown in Fig. 5, a 200 nm thick n-doped ion implanted and activated layer shows a "mixed" behaviour, namely a linear power dependence of the PL intensity up to 50 mW and a quadratic power law for larger laser powers. This finding fits well to the other observations if one assumes that the PL is generated to a larger part in the n-type layer (which has a linear power law and no bleaching) and to a smaller extend in the s.i. substrate material (which shows a superlinear power law and strong bleaching).

We have also used NIRtop and PLtop to study ion implanted layers in s.i. wafers before and after activation. After implantation the NIR absorption is increased by orders of magnitude in the implanted layer. The PL intensity is completely quenched after implantation but it is recovered by thermal activation. After the activation process the

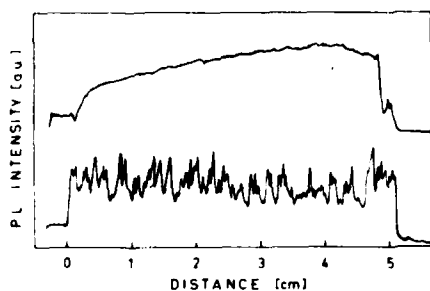


Fig. 4 One dimensional PLtop trace of a 200 nm thick n-doped MBE layer (upper trace) and of its substrate (lower trace) to demonstrate the good homogeneity of MBE layers. The PL intensity of the MBE layer is four times larger than that of the substrate. The reason for the increase from left to right is not yet clear

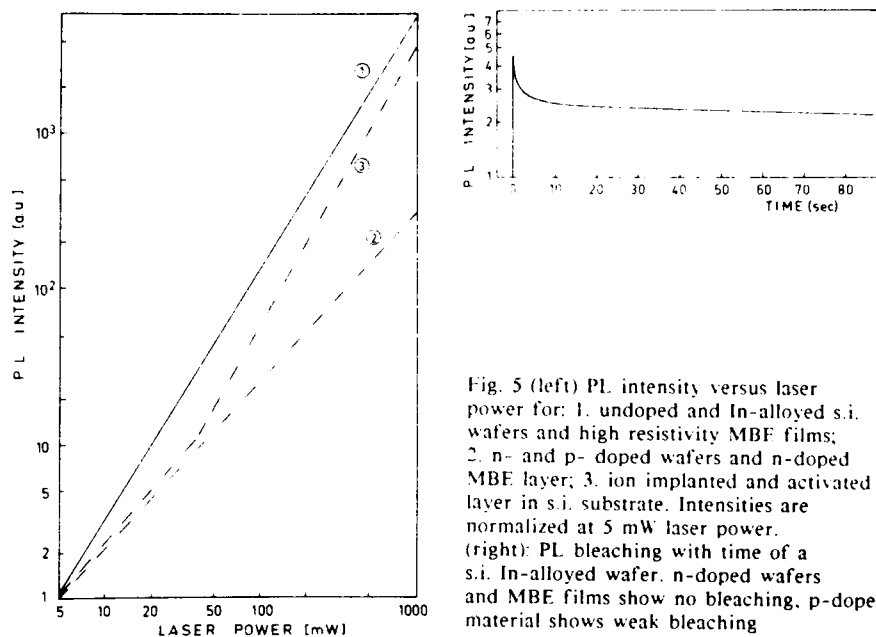


Fig. 5 (left) PL intensity versus laser power for: 1. undoped and In-alloyed s.i. wafers and high resistivity MBF films; 2. n- and p-doped wafers and n-doped MBE layer; 3. ion implanted and activated layer in s.i. substrate. Intensities are normalized at 5 mW laser power. (right): PL bleaching with time of a s.i. In-alloyed wafer. n-doped wafers and MBE films show no bleaching. p-doped material shows weak bleaching

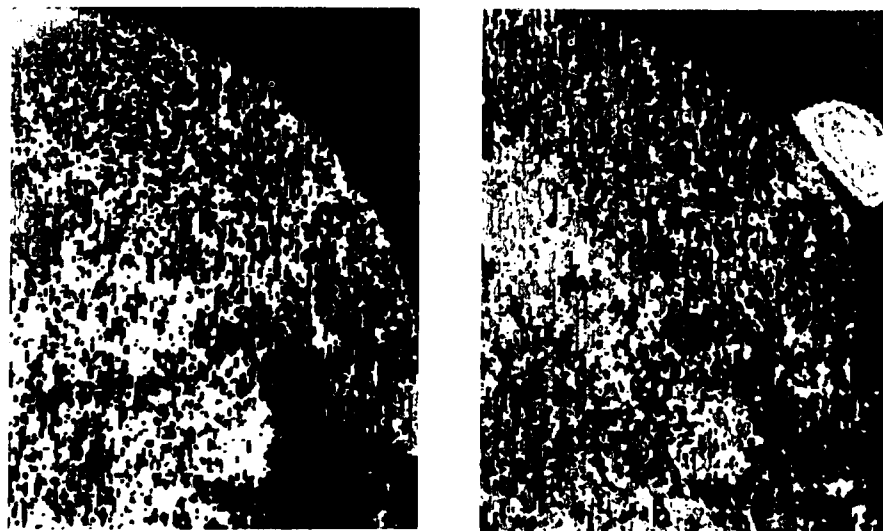


Fig. 6 PL topograms of a section of a wafer before ion implantation (left) and after implantation (Si,  $5 \cdot 10^{12} \text{ cm}^{-2}$ ) and thermal activation (right)

original cellular structure of the wafer is observed again (see Fig. 6). It remains to be determined to which extent this structure is due to the n-doped layer or to the substrate. Furthermore, the PLtop can be utilised to monitor the homogeneity of the temperature profile during the activation process. Details of the investigation of ion implanted layers will be published in a subsequent paper.

#### 4. Conclusions

The two topographical methods NIRtop and PLtop used in combination are well suited to study inhomogeneities of bulk GaAs wafers and of epitaxial and ion implanted layers. As the PLtop method measures a layer near the surface only it can also be used to probe the quality of the surface preparation (polishing, oxide films) and of technological processes.

It had been shown by several authors that these optically detected inhomogeneities are closely related to structural inhomogeneities (dislocations, internal strain) and to inhomogeneities of electrical properties of the bulk of the wafer and of devices fabricated on them (Nanishi et al. 1985). A detailed understanding of the correlation of all these complicated observations is still lacking although progress in this field is very rapid. It is hoped that topographical techniques will serve as powerful tools for these investigations.

#### 5. Acknowledgement

The authors appreciate many valuable discussions with U. Kaufmann, J. Schneider, H.S. Rupprecht, K.H. Bachem, R.S. Smith and W. Jantz. The project is supported by the Bundesministerium für Forschung und Technologie.

#### 6. References

- Brozel M R, Grant I, Ware R M, Stirland D J and Skolnick M S 1984 *J. Appl. Phys.* **56**, 1109
- Dobrilla P and Blakemore J S 1985 *J. Appl. Phys.* **58**, 208
- Fillard J P (editor) 1985 *Defect recognition and image processing in III-V compounds* (Amsterdam, Oxford, New York Tokyo: Elsevier)
- Hakone 1986, *Proceedings of the 4<sup>th</sup> conference on semi-insulating III-V materials*, to be published
- Hovel H J and Guidotti D 1985 *IEEE Transact. Electron. Devices* **ED-32**, 2331
- Hovel H J, Albert M, Farrel E, Guidotti D and Becker J 1986 in *Proc. of the 4<sup>th</sup> conf. on semi-insulating III-V materials*, (Hakone, Japan), to be published
- Löhnert K, Wettling W and Koschek G 1986 in *Proc. of the 4<sup>th</sup> conf. on semi-insulating III-V materials* (Hakone, Japan), to be published
- Martin G M 1981, *Appl. Phys. Lett.* **39**, 747
- Nanishi Y, Miyazawa S and Matsuoka Y 1985 in *Defect recognition and image processing in III-V compounds* (Amsterdam, Oxford, New York, Tokyo: Elsevier) p225
- Wettling W and Windscheif J 1986, *Appl. Phys.* **A40**, 191

## Characteristics of deep electron-traps in Te-doped AlGaSb on GaSb substrate

Y. Takeda, Y. Zhu\*, and A. Sasaki

Department of Electrical Engineering, Kyoto University  
Kyoto 606, Japan

**Abstract.** DLTS and C-V measurements of Te-doped GaSb and  $\text{Al}_{1-x}\text{Ga}_x\text{Sb}$  were conducted in a wide range of  $x$  to investigate the characteristics of deep electron-traps and their composition dependence in this alloy system. No deep electron-traps were detected in the range  $0 \leq x \leq 0.2$  by DLTS measurement to the detection limit of  $\sim 1 \times 10^{13} \text{ cm}^{-3}$ . In the higher range of  $x$ , deep electron-traps were detected and its concentration increased steeply with  $x$  and saturated. The trap characteristics were found to be very similar to the DX-center in AlGaAs.

### 1. Introduction

It is well known that a donor forms a deep electron-trap center, i.e., the DX-center, in  $\text{Al}_{1-x}\text{Ga}_x\text{As}$  with a certain range of  $x$  (Lang 1979). Dominance of the deep electron-trap concentration and occurrence of persistent photoconductivity have raised much interest in the origin of the DX-center from both view points of physics and device applications.

Many models have been proposed for the origin of the DX-center. As for X of DX, As-vacancy was originally proposed (Lang 1979), and later, a bond reconstruction between donor and host atoms (Kobayashi 1985), crystal field formed with a mixture of Al and Ga (Iwata 1986), association with L- or X-band (Saxena 1982, Chand 1984, Schubert 1984, Mizuta 1985), band crossing (Lifshitz 1980), central cell potential of donors (Yamaguchi 1986), and others have been proposed. A complex formation with As-vacancy has almost been excluded from the origin because it was found that the sum of the concentration of electrons trapped by the DX-center and by the shallow levels was constant over a wide range of Al composition (Watanabe 1984).

To understand the behavior of the DX-center more widely and deeply, deep donor levels in other alloy semiconductors have been started to be investigated (Tachikawa 1985, Nojima 1986, Watanabe 1986). Among them, GaSb and AlGaSb are thought to be a good test material for those several models for the DX-center. From the L-band associated donor model, GaSb is predicted to have deep donor levels from its band structure, and if it is the case, all the models which are related to the constituent Al atom are excluded from the origin.

In this paper, we will report the DLTS and C-V measurements of Te-doped GaSb and AlGaSb Schottky diodes. No deep electron traps were

detected in GaSb and  $\text{AlGa}_{1-x}\text{Sb}$  with lower  $x$  ( $<0.2$ ), but in the higher  $x$  range, deep electron-traps with high concentration, drastic change in capacitance with temperature, and persistent photocapacitance were observed.

## 2. Experiments

GaSb and AlGaSb were grown by LPE at 400°C and 500°C on Te-doped n-type GaSb substrates (Takeda 1984). Crystal orientation was (100) and the dopant was Te. Czochralski-grown Te-doped GaSb substrates were also used for the measurements. The behavior of amphoteric Si and Ge as a donor would be interesting, but group IV elements are acceptors in this alloy system, at least in the lower Al range. Al composition in AlGaSb was determined by EPMA and double crystal X-ray diffraction considering the lattice distortion. For the C-V and DLTS measurements, Schottky diodes with Au as a contact were formed on GaSb and AlGaSb wafers. Al composition was varied from 0 to 0.77. Conditions for DLTS measurements are summarized in Table 1.

Table 1 DLTS measurement conditions

|                   |  |
|-------------------|--|
| Capacitance Meter | Boonton, 72B                               |
| Sampling          | NF, Digital Boxcar Integrator BP-10        |
| Injection Pulse   | 0 V, 20 ms - 25 ms                         |
| Emission Pulse    | -0.5 V                                     |
| Temperature       | 77 K - 300 K                               |
| Rate Window       | $27 \text{ s}^{-1}$ - $215 \text{ s}^{-1}$ |

## 3. Results

Electron-traps were not detected, to the detection limits shown in Table 2, in Te-doped GaSb and AlGaSb with Al composition up to 0.20. The energy range covered was approximately between 0.1 and 0.9 eV.

On the other hand, deep electron-traps were detected in  $\text{AlGa}_{1-x}\text{Sb}$  with  $x > 0.20$ . A series of DLTS signals for electron emission are shown in Fig. 1. Half widths become larger at higher compositions and at  $x=0.7$  double peaks were observed. The ratio of the electron-trap concentration ( $N_t$ ) to the shallow donor concentration ( $n$ ) increased steeply in the composition range from 0.2 to 0.5 and then almost saturated at higher compositions. These data points are plotted in Fig. 2 in conjunction with reported band structures (Cheng 1976, Alibert 1983).

Table 2 In this composition range no deep electron-traps were detected by DLTS to the detection limits shown in the parentheses.

| Al composition<br>(EPMA)                | LEC<br>GaSb                            | LPE<br>GaSb                            | LPE<br>0.07                            | LPE<br>0.18                            | LPE<br>0.20                            |
|---|--|--|--|--|--|
| $n \text{ (cm}^{-3}\text{)}at RT$       | $\sim 2 \times 10^{17}$                | $3 \times 10^{17}$                     | $1 \times 10^{17}$                     | $1 \times 10^{17}$                     | $6 \times 10^{17}$                     |
| Detection limit<br>( $\text{cm}^{-3}$ ) | Not detected<br>( $2 \times 10^{13}$ ) | Not detected<br>( $2 \times 10^{13}$ ) | Not detected<br>( $4 \times 10^{13}$ ) | Not detected<br>( $1 \times 10^{13}$ ) | Not detected<br>( $8 \times 10^{13}$ ) |



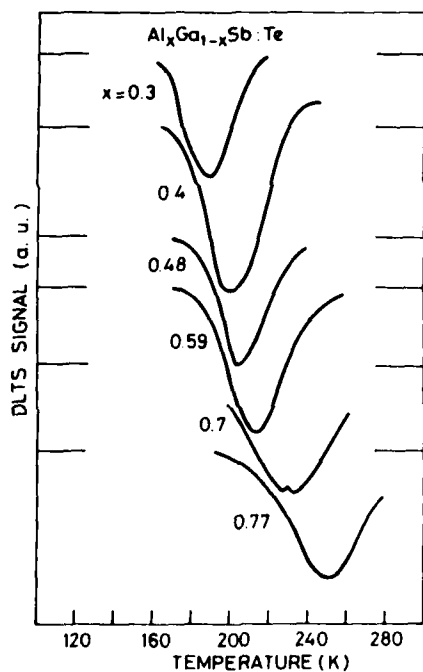


Fig. 1 DLTS signals of electron traps in  $\text{Al}_x\text{Ga}_{1-x}\text{Sb}$  with several Al compositions. For  $x=0.3$  and  $0.4$  the signal is of C-DLTS and for the rest of compositions the signal is of  $\text{C}^2$ -DLTS. The rate window is  $126.7 \text{ s}^{-1}$ .

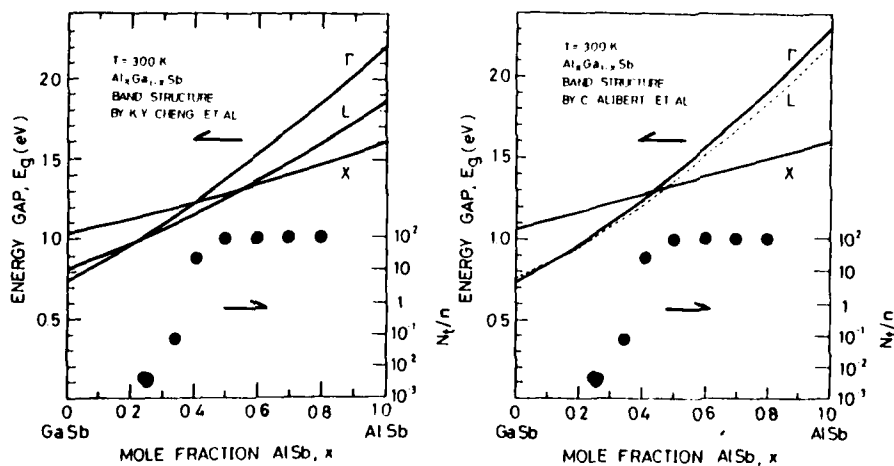


Fig. 2 The Al composition dependence of the ratio  $N_t/n$  (deep electron-trap concentration to shallow donor concentration) is superimposed on the reported band structures. If the deep electron-trap is the donor level associated with the L-band, it should be detected even in GaSb. In both band structures the  $\Gamma$ - and L-band cross-over is at  $0.20$ . Deep electron-traps were detected beyond this composition.

In  $\text{AlGa}_{1-x}\text{Sb}$  Schottky diodes with higher  $x$ , several characteristics related to a deep electron-trap were observed. Figure 3 shows a DLTS signal observed in a Schottky diode of  $\text{Te-Al}_{0.4}\text{Ga}_{0.6}\text{Sb}$ . A large peak of  $\Delta C$  and a long injection pulse width ( $\sim 20$  ms) required to fill the traps are observed here. In the  $\text{AlGa}_{1-x}\text{Sb}$  diodes with a lower  $x$  than 0.4 the activation energy for thermal electron-emission and cross section of the trap were calculated to be 0.39 eV and  $\sim 10^{-13} \text{ cm}^2$ , respectively, and at  $x$  higher than 0.4 the activation energy for thermal electron-emission and cross section of the trap were 0.49 eV and  $10^{-12} \sim 10^{-11} \text{ cm}^2$ , respectively. The activation energy for electron-capture was obtained as 0.30-0.32 eV at  $x=0.4$  and 0.38 eV at  $x=0.6$ , from the  $C^2$ -DLTS during the injection pulse and from the injection pulse width dependence of  $\Delta C$ .

A temperature cycle of the  $\text{Te-Al}_{0.4}\text{Ga}_{0.6}\text{Sb}$  diode capacitance is shown in Fig. 4. Increase of the capacitance by light illumination and persistency of the increased capacitance are quite similar to those observed in donor doped  $\text{AlGaAs}$  (Lang 1979).

#### 4. Discussion

In our experiments deep electron-traps were not detected in Te-doped  $\text{AlGa}_{1-x}\text{Sb}$  with  $x$  between 0 and 0.2. Gouskov et al. reported two electron-traps with thermal activation energies of 0.145 and 0.39 eV in Te-doped  $\text{Al}_{0.15}\text{Ga}_{0.85}\text{Sb}$ , though the concentrations were low ( $N/\text{m}^3 \times 10^{-3}$ ) (Gouskov 1985). Since we are now interested in the origin of the DX-center of which concentration is quite high, we neglect a low concentration electron-traps. If a donor is associated with the L-band to form a high-concentration deep electron-trap, even GaSb should have an electron-trap like the DX-center since the energy separation between the  $\Gamma$ -band minimum and the L-band minima in GaSb is as small as 0.078-0.0919 eV (Neuberger 1971) and the density-of-states effective mass (0.7 $m_0$ ) (Neuberger 1971) of the L-band of GaSb is even heavier than that of  $\text{Al}_{0.45}\text{Ga}_{0.55}\text{As}$  (0.6 $m_0$ ) (Casey 1978). The result appears to deny the L-band association model of the DX-center. The band crossing of the  $\Gamma$ - and L-bands has also nothing to do with the DX-center, since electron-traps were not detected at  $x=0.2$  where the  $\Gamma$ - and L-bands cross. However, the steep increase of the deep electron-trap concentration was observed near  $x=0.4$  where the  $\Gamma$ - and X-bands cross.

In the higher Al-composition range, high density electron-traps were detected and most of the donors were found to form deep levels. Such characteristics as differences in the activation energies for the electron-capture and emission, the slow capture rate, the temperature dependence of capacitance and the persistency of photocapacitance at a low temperature are very similar to those observed for the DX-center in  $\text{AlGaAs}$ . Other characteristics such as persistent photoconductivity and anomalous composition dependence of the thermal activation energy of free electrons should be examined to prove the detected deep traps to be the same as the DX-center. The conductivity measurements and Hall effect measurements are not easy for  $\text{AlGaSb}$  since a semi-insulating substrate is not available. In bulk crystals of Te-doped  $\text{Al}_{0.31}\text{Ga}_{0.69}\text{Sb}$ , persistent photoconductivity was observed (Konczewicz 1983).

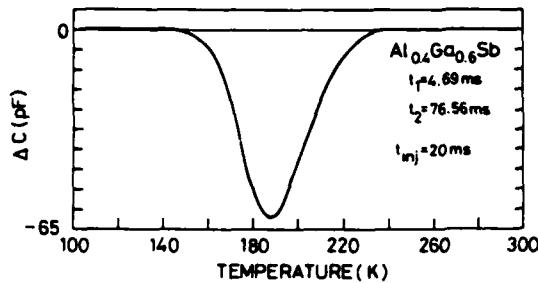


Fig. 3 A C-DLTS spectrum observed in Te-doped  $\text{Al}_{0.4}\text{Ga}_{0.6}\text{Sb}$ . A long injection pulse (20 ms) was necessary to fill the electron-trap.

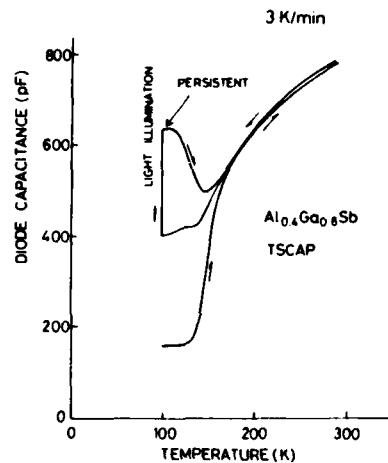


Fig. 4 TSCAP in Te-doped  $\text{Al}_{0.4}\text{Ga}_{0.6}\text{Sb}$ . Cooling and heating speed was 3 K/min. Increased capacitance by light illumination was persistent at 100 K.

##### 5. Summary

- 1) Deep electron-traps were not detected in Te-doped GaSb and  $\text{Al}_x\text{Ga}_{1-x}\text{Sb}$  with  $x$  up to 0.2.
- 2) Deep electron-traps were detected in Te-doped  $\text{Al}_x\text{Ga}_{1-x}\text{Sb}$  with  $x$  beyond 0.2, and its concentration increased steeply and saturated.
- 3) Considering the composition dependences of the electron-trap and band structure, the deep electron-trap is not formed simply by the association with the L-band.
- 4) In the higher  $x$  range the activation energy for thermal electron-emission was 0.49 eV and that for electron-capture was 0.38 eV.
- 5) Thermally stimulated capacitance and persistency of the photocapacitance were similar to those observed in donor doped AlGaAs.

**Acknowledgment.** This work was supported in part by the Scientific Research Grant-in-Aid #61114007 for Special Project Research on "Alloy Semiconductor Physics and Electronics," from the Ministry of Education, Science and Culture.

\* On leave from Shanghai Jiao Tong University.

# References

- Alibert C, Joullie A, Joullie A M and Ance C 1983 Phys. Rev. B 27 4946
- Casey Jr H C and Panish M B 1978 Heterostructure Lasers Part A (New York:Academic Press) p 192
- Chand N, Henderson T, Klem J, Masselink W T, Fischer R, Chang Y C, and Morkoc H 1984 Phys. Rev. B 30 4481
- Cheng K Y, Pearson G L, Bauer R S and Chadi D J 1976 Bull. Am. Phys. Soc. 21 365
- Gousskov L, Boustani M, Luquet H and Bougnot G, Bastide L and Baya'a D 1985 J. Appl. Phys. 58 3211
- Iwata N, Matsumoto Y, Baba T and Ogawa M 1986 Japan. J. Appl. Phys. 25 L349
- Kobayashi K L I, Uchida Y and Nakashima H 1985 Japan. J. Appl. Phys. 24 L928
- Konczewicz L, Litwin-Staszewska E, Porowski S, Iller A, Aulombard R L, Robert J L and Joullie A 1983 Physics 117B & 118B 92
- Lang D V, Logan R A and Jaros M 1979 Phys. Rev. B 19 1015
- Lifshitz N, Jayaraman A, Logan R A and Card H C 1980 Phys. Rev. B 21 670
- Mizuta M, Tachikawa M, Kukimoto H and Minomura S 1985 Japan. J. Appl. Phys. 24 L143
- Neuberger M 1971 III-V Semiconducting Compounds (New York:IFI/Plenum) p 37 and p 39
- Nojima S, Tanaka H and Asahi H 1986 J. Appl. Phys. 59 3489
- Saxena A K 1982 Solid-St. Electron. 25 127
- Schubert E F and Ploog K 1984 Phys. Rev B 30 7021
- Tachikawa M, Mizuta M, Kukimoto H and Minomura S 1985 Japan. J. Appl. Phys. 24 L821
- Takeda Y, Noda S, Nakashima K and Sasaki A 1984 J. Electron. Mat 13 855
- Watanabe M O, Morizuka K, Mashita M, Ashizawa Y and Zohta Y 1984 Japan. J. Appl. Phys. 23 L103
- Watanabe M O and Ohba Y 1986 J. Appl. Phys. 60 1032
- Yamaguchi E 1986 Japan. J. Appl. Phys. 25 L643

## **Correlation of structural, chemical and optical properties of GaInAs quantum wells**

R. Hull<sup>1</sup>, F.W. Carey<sup>2</sup>, J.E. Fouquet<sup>2</sup>, G.A. Reid<sup>2</sup> and S.J. Rosner<sup>2</sup>; D. Bimberg<sup>1</sup> and D. Bertel<sup>1</sup>

<sup>1</sup>Hewlett Packard Laboratories, 3500 Deer Creek Road, Palo Alto, CA 94304

<sup>2</sup>Institut für Festkörperphysik, Technische Universität Berlin, Hardenbergstrasse 36, 1 Berlin 12, Germany

**Abstract** Optical spectra are correlated with structural and chemical properties in GaInAs quantum wells grown between InP and AlInAs barriers by organo-metallic vapour phase epitaxy. Thick (3 micron) layers of AlInAs and GaInAs lattice-matched to InP are also studied and exhibit non-random distributions of Al and In upon the Column III sub-lattice in AlInAs, and periodic compositional modulations in GaInAs.

### **1. Introduction**

Experimental methods for determining the detailed effects of structural and chemical properties on recombination spectra in quantum well systems have hitherto been lacking. In this paper, we report new methods for investigating these relationships, and report on correlations of optical, structural and chemical properties in GaInAs quantum wells grown between InP and AlInAs barriers by organo-metallic vapour phase epitaxy (OMVPE).

### **2. Experimental**

Samples were grown by atmospheric pressure OMVPE using tri-methyl sources for the Column III elements and arsine and phosphine for the Column V. Growth rates were of the order of 4 Angstroms/sec for ternary compounds and 2 Angstroms/sec for InP. GaInAs/AlInAs structures were grown at 640 C on InP substrates with surface normals oriented to within 0.2 degrees of [100] (as measured by X-ray diffraction). GaInAs/InP structures were grown on InP wafers whose surface normals were rotated by 3 degrees from [100], also at a temperature of 640 C. All ternary alloys were nominally grown with compositions such that their lattice parameters matched those of the InP substrate. This was confirmed for thicker (3 micron) layers to an accuracy  $< 0.1\%$  average lattice mismatch by X-ray diffraction. The corresponding compositions are  $\text{Ga}_{0.47}\text{In}_{0.53}\text{As}$  and  $\text{Al}_{0.48}\text{In}_{0.52}\text{As}$ .

Atomic-scale structural measurements of quantum well structure were made by careful analysis and quantification of high resolution transmission electron microscope (HRTEM) lattice images. It is well known that for the special case of an extremely thin periodic specimen, imaged at an optimum electron microscope objective lens defocus, the image intensity is proportional to the crystal potential projected along the electron beam direction for specimen spatial frequencies less than the microscope

point-to-point resolution (Spence, 1981). Thus with accurate quantification of HRTEM image intensities, there is chemical, as well as structural information inherent in the image. Under more general experimental conditions, especially in the present case of a potential discontinuity at an interface, it is necessary to accurately calculate the specimen interaction and instrumental transfer functions using a numerical technique known as the multislice method (Goodman and Moodie, 1974). In this work we carefully analysed the range of experimental conditions under which the experimental image could be related to the chemistry and structure of the specimen. Accurate quantification of image intensities was performed using a scanning microdensitometer, as indicated schematically in Figure 1. By repeated scanning of different areas of a given structure, we derived distribution functions of well widths and accurate measurements of mean well width for GaInAs quantum well structures.

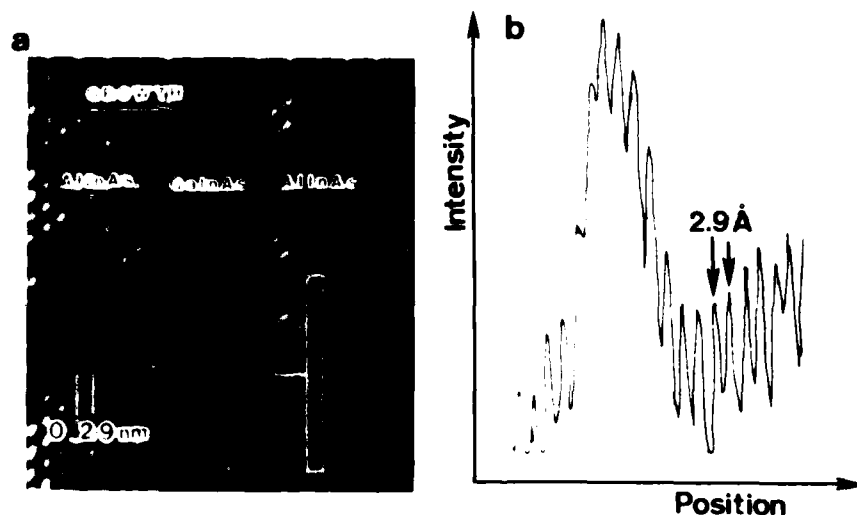


Fig. 1. (a) Representative  $\langle 110 \rangle$  HRTEM lattice structure image of a GaInAs quantum well between AlInAs barriers. (b) Corresponding microdensitometer trace recorded from a negative of the image shown in (a).

Photoluminescent (PL) spectra of structures with AlInAs barriers were recorded at the Technische Universität, Berlin using the  $647 \text{ nm}$  line of a cw  $\text{Kr}^+$  laser, with excitation intensities of  $0.7 \text{ W/cm}^2$ . PL spectra of InP barrier structures were recorded at Hewlett Packard Laboratories also using the  $647 \text{ nm}$  line of a cw  $\text{Kr}^+$  laser, at an excitation intensity of  $0.3 \text{ W/cm}^2$ . The usual corrections for grating and spectrometer response were performed.

Rutherford backscattering (RBS) was performed using  $2.0 \text{ MeV He}^+$  ions. Compositions of thin GaInAs quantum wells between InP barriers were determined by subtraction of the background In signal, giving a measurement of the integrated number of Ga and As atoms per unit area.

This number was then converted to chemical composition by reference to the quantum well width measured by HRTEM.

### 3. Results from quantum well structures

Figure 2(a) shows results from detailed HRTEM investigations of three samples each consisting of five extremely thin ( $< 30$  Angstrom) GaInAs quantum wells between 200 Angstrom AlInAs barriers. The well widths within a given sample were nominally identical, but varied from sample to sample. Experimental points are derived from combinations of PL and HRTEM measurements. The theoretical curve corresponds to the solution of the Schrodinger equation for  $n=1$  electron - heavy-hole transitions in a one-dimensional finite square quantum well. Effective mass and band gap parameters used are for GaInAs: zone center effective mass:  $0.041m_0$  (electron),  $0.47m_0$  (heavy hole); band gap (4K):  $0.811$  eV; for AlInAs: zone center effective mass:  $0.073m_0$  (electron),  $0.62m_0$  (heavy hole); band gap (4K)  $1.55$  eV, where  $m_0$  is the electron rest mass. The conduction band discontinuity used was  $70\%$  and the confinement energy dependence of the effective mass in the GaInAs well was calculated as by Welch et al (1986), with the equation  $m^*(E) = m(k_0)[1+2aE]$  where  $m(k_0)$  is the zone center effective mass and  $a$  is  $1.13$  for electrons and  $0.346$  for holes. Although there is uncertainty in some of these parameters (particularly the hole effective masses and the conduction band discontinuity), we note a reasonable quantitative agreement between experimental measurement and theoretical predictions of peak recombination energy.

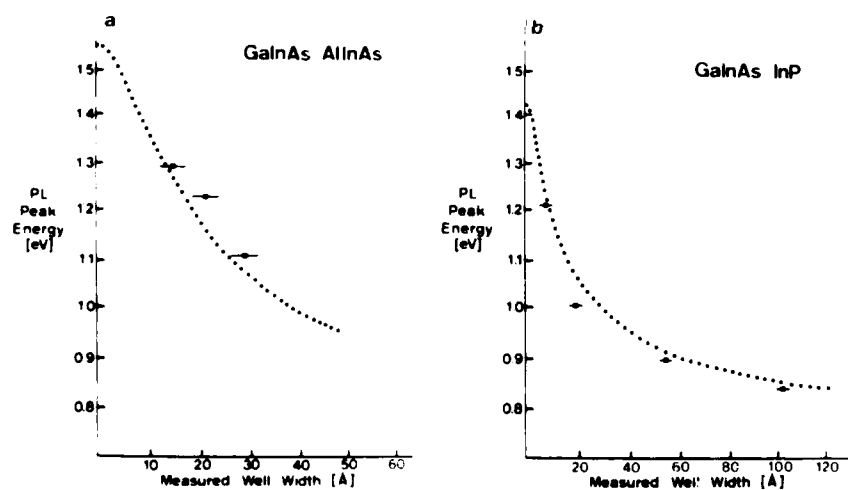


Fig. 2: Theoretical calculations (shown by dotted lines) of  $n=1$  electron - heavy hole recombination energies at 4K for GaInAs quantum wells between (a) AlInAs barriers and (b) InP barriers. Input parameters are given in the text. Experimental measurements (from PL and HRTEM) are shown by squares, with error bars.

For GaInAs/InP quantum well samples, we find a small systematic discrepancy between experimental PL and HRTEM measurements and theoretical predictions of recombination energies in that, as shown in Figure 2(b).

theoretical calculations generally imply a slightly higher recombination energy than we measure. The GaInAs parameters used in this calculation are the same as those used in Figure 2, for InP we use: effective mass,  $0.080m_0$  (electron),  $0.61m_0$  (heavy hole); band gap, 1.42 eV. The conduction band discontinuity was taken as 40%. The 4K PL halfwidths of these samples are among the lowest reported, varying from 8 meV for the 103 Angstrom well to 26 meV for the 10 Angstrom well. Note that these structures contained a single GaInAs quantum well.

This apparent slight discrepancy between theory and experiment could be modified by using a significantly lower conduction band discontinuity and/or much higher quantum well effective masses (these parameters have considerable experimental uncertainty), but we also wanted to investigate whether compositional effects could reconcile experiment and theory. Compositions of the thicker wells were measured using the RBS and HRTEM techniques outlined in section 2, yielding for samples indicated in Figure 2(b) with mean well thicknesses of 54 and 103 Angstroms, In concentrations of 22.4 and 24.1 atomic percent respectively, assuming perfect square well profiles. This apparent In deficit with respect to the lattice-matched composition of 26.5 atomic percent In might relate to either (i) a corresponding Ga increase, i.e. a  $Ga_xIn_{1-x}As$  alloy with  $x$  greater than the 0.47 value for lattice matching to InP (note, however that this would produce a higher quantum well band gap, and thus a higher recombination energy which would increase the discrepancy between experiment and theory) or (ii) an excess of As, with respect to the exactly 50% atomic concentration expected for a perfect square well profile, caused by an As tail into the InP barrier material, due to non-abrupt switching of the As source. This could result in apparent excess of both In and Ga in the quantum well if a perfect square well profile is assumed. Microdensitometer traces of HRTEM lattice images of GaInAs/InP structures do indicate slight deviations from square well profiles. We are currently investigating whether these deviations in the quantum well profile can reconcile experiment and theory.

#### 4. Results from Thick (3 micron) Epitaxial Ternary Layers

In an effort to better understand thin film structures, we decided also to study thicker ternary layers lattice-matched to InP substrates, such that radiative recombination in the ternary layers was essentially bulk-like. In particular, we were interested in resolving the discrepancy between PL halfwidth measurements in these thicker layers: low temperature PL halfwidths in GaInAs layers have been measured to be as low as 1.5 meV at 1.4 K (Garcia et al., 1986) which is close to the theoretical limit, whilst corresponding PL halfwidths in thick AlInAs layers have been of the order of 20-30 meV.

Structural and chemical studies of these thicker layers revealed significant deviations from random distributions of atoms over the Column III sublattice. For thick AlInAs layers, it was found that although the ternary compound was closely lattice-matched to the substrate (from X-ray diffraction), there was a high density (about  $10^7/cm^2$ ) of crystalline defects. Also, electron diffraction indicated a non-random distribution of Al and In atoms. Similar ordering phenomena have been noted in other ternary III-V alloys (e.g., Kuan et al., 1985; Jen et al., 1986). In this work, plan-view electron diffraction (i.e. electron beam parallel to growth direction) reveals ordering of Al and In atoms on alternate (110) planes, as indicated by the strong appearance of the forbidden (110)



reflections in the electron diffraction pattern of Figure 3(a). Diffraction patterns recorded in the cross-sectional mode (electron beam perpendicular to growth direction), show ordering of Al and In atoms on alternate (111) planes as shown by the electron diffraction pattern of Figure 3(b). A similar phenomenon, with two different ordered phases in the same material has been observed in OMVPE-grown  $\text{GaAs}_{0.5}\text{Sb}_{0.5}$  (Jen et al, 1986).

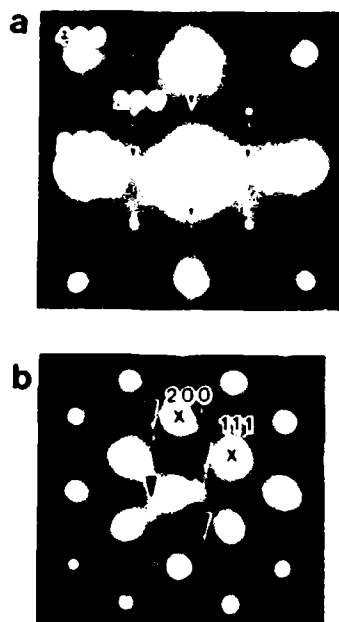


Fig. 3: Electron diffraction patterns from a 3 micron layer of AlInAs. (a) plan view along [100], showing extra (110) spots (arrowed) (b) Cross-sectional along <011> showing extra  $1/2(111)$  and  $1/2(311)$  spots (arrowed).



Fig. 4: Cross-sectional TEM [400] dark-field image showing periodic compositional modulations (arrowed) along the [100] growth axis of a 3 micron layer of GaInAs on an InP substrate. The fringe contrast running at an angle to the sides of the image is due to specimen thickness effects.

Cross-sectional electron diffraction patterns of 3 micron GaInAs layers exhibited no ordering-related electron diffraction spots. A weak periodic modulation in image intensity was noted, however, along the growth direction with a modulation wavelength of about 2000 Angstroms (see Figure 4). It is difficult to quantify this periodicity in terms of a compositional modulation, but the observed variations in image intensity probably correspond to chemical variations of the order of a few percent

change in Ga and In composition. RBS also revealed shorter periodicity variations near the surface of the ternary layer, with a periodicity of approximately 500 Angstroms and a chemical modulation of about  $\pm 1\%$  Ga or In concentration. No comparable fluctuation effects were noted in TEM measurements of AlInAs layers. These apparent composition modulations may arise from periodic variations in the OMVPE source temperatures during growth.

These structural effects do not appear to give a definitive explanation of the difference in bulk recombination halfwidths in GaInAs and AlInAs layers. Compositional fluctuations of the type illustrated in Figure 4 might be expected to affect spectral broadening, depending upon the modulation wavelength and amplitude, but no evidence for such fluctuations were found in the higher halfwidth AlInAs material. The existence of Column III ordering in AlInAs might produce an additional broadening mechanism if the degree of ordering varied from point to point in the sample (we have evidence of this from electron diffraction), and if the band gaps of the ordered and random materials significantly differed. Atomic relaxation and stress around defects could also produce a broadening mechanism. Finally we note that electrical measurements indicate significant impurity concentrations in the thick AlInAs films (of the order of  $10^{16}/\text{cm}^2$  using Van der Pauw, and  $10^{17}/\text{cm}^2$  using C-V techniques), which might also be expected to produce spectral broadening.

##### 5. Conclusions

Unified measurements of the structural, chemical and optical properties of GaInAs quantum wells have enhanced our understanding of these materials. For GaInAs quantum wells grown between AlInAs barriers, we are able to reconcile experimental measurements and theoretical predictions of peak recombination energies. A slight systematic discrepancy is noted between experiment and theory for recombination energy in the GaInAs/InP system, which is consistent with evidence for non-abrupt switching of As during OMVPE growth. Studies of thicker ternary layers have revealed non-uniform distribution of Column III atoms, specifically ordering within the unit cell in AlInAs layers and periodic compositional modulations in GaInAs layers.

##### 6. Acknowledgements

We wish to acknowledge X-ray measurements by S.L. Ladermann, the technical assistance of Mark Juanitas and Tina Reyes, and illuminating discussions with K.K. Bajaj, G. Dohler, S.S. Laderman, G. Trott and R. Weissman

##### References

- K.W. Carey, S.Y. Wang, R. Hull, J.E. Turner, D. Oertel, R. Bauer and D. Bimberg 1986, to be published in the Proceedings of ICMVPE III (Hollywood, Ca)
- P. Goodman and A.F. Moodie 1974, *Acta. Cryst. A* **30** 280
- H.R. Jen, M.J. Cherng and G.B. Stringfellow 1986, *Appl. Phys. Lett.* **48** 1603
- T.S. Kuan, T.F. Kuech, W.I. Wang and E.L. Wilkie 1985, *Phys. Rev. Lett.* **54** 201
- J.C.H. Spence 1981, *Experimental High Resolution Electron Microscopy* (Clarendon Press, Oxford)
- D.F. Welch, G.W. Wicks and L.F. Eastman 1986, *J. Appl. Phys.* **55** 3176

## **Photoluminescence studies of single GaAs quantum wells with extended monolayer-flat regions**

B. A. Wilson, R. C. Miller, S. K. Sputz, T. D. Harris, R. Sauer, M. G. Lamont, C. W. Tu and R. F. Kopf

AT&T Bell Laboratories, Murray Hill, New Jersey 07974

**Abstract** We present low-temperature photoluminescence (PL) and excitation (PLE) spectra for single GaAs/ $\text{Al}_{0.37}\text{Ga}_{0.63}\text{As}$  MBE-grown quantum wells for which growth was interrupted at each interface for 2 minutes. The multiple lines observed in PL and PLE are ascribed to free-exciton emission from extended ( $> 300\text{\AA}$ ) monolayer-flat regions of the wells differing in thickness by one monolayer. The individual lines are the sharpest and best-resolved ever reported for narrow wells. The remaining inhomogeneous widths place limits on the range of alloy fluctuations in the barrier material. Systematic differences in the relative intensity of the multiple peaks in PL and PLE spectra point to rapid lateral transfer from narrower to wider regions of the wells. PLE spectra also imply efficient transfer of excitation through the  $300\text{\AA}$  barriers separating individual wells. Lower-energy bands due to lightly-bound excitons are also observed, indicating a slight increase in neutral-acceptor incorporation.

### **1. Introduction**

In some cases the photoluminescence spectra of GaAs quantum wells exhibit a multiple peak structure associated with emission from extended monolayer-flat regions which differ in thickness by single monolayer (ML) steps,  $2.83\text{\AA}$ . Although structure has been reported in continuous-growth samples (Deveaud et al 1984, Goldstein et al 1983, Reynolds et al 1985), the use of growth interruption at the heterointerfaces has been shown to enhance this structure (Bimberg et al 1986, Fukunaga et al 1985, Hayakawa et al 1985, Juang et al 1986, Miller et al 1986, Ohta et al 1986, Sakaki et al 1985, Tanaka et al 1985, Voillet et al 1986), presumably by allowing additional surface atom migration to smooth out local roughness. In this paper we present low-temperature photoluminescence (PL) and photoluminescence excitation (PLE) spectra of interrupted-growth single GaAs quantum wells in which the individual lines of the multiplets are the narrowest for a given well width and the best-resolved reported to date. The narrowness and clear separation of the monolayer lines permit an unambiguous identification of the transitions involved, and provide new information on inter- and intra-well energy transfer within these structures.

### **2. Samples and experimental results**

The samples were deposited at  $600^\circ\text{C}$  on a (100) semi-insulating GaAs substrate in a Gen II MBE station. The interrupted-growth sample consisted of 4 single GaAs wells of nominal widths  $100\text{\AA}$ ,  $50\text{\AA}$ ,  $25\text{\AA}$  and  $15\text{\AA}$  grown in that order and separated by  $300\text{\AA}$  barriers composed of  $\text{Al}_{0.37}\text{Ga}_{0.63}\text{As}$ . A buffer region consisting of  $5000\text{\AA}$  GaAs followed by  $1000\text{\AA}$   $\text{Al}_{0.37}\text{Ga}_{0.63}\text{As}$  was deposited on the substrate prior to the growth of the wells, and the top well was capped with  $1000\text{\AA}$  of  $\text{Al}_{0.37}\text{Ga}_{0.63}\text{As}$ . The growth was interrupted for 2 minutes at each well/barrier interface to allow smoothing of the surface. A reference sample of identical nominal structure was deposited under the same growth conditions, but without interruption at the interfaces. The PL spectra were excited with an Argon ion laser operating at  $5145\text{\AA}$ , and detected through a monochromator with an S1-response photomultiplier using lock-in techniques. Excitation power densities were varied over 6 decades from  $10\text{ }\mu\text{W}/\text{cm}^2$  to  $10\text{ W}/\text{cm}^2$ . A tunable cw dye laser was used to obtain the PLE spectra. For all measurements the samples were mounted in a variable-temperature cryostat.

In Fig. 1a we contrast the cw PL spectra of the interrupted and continuous-growth samples. While the latter exhibits a single broad line for each of the 4 wells, the spectrum from the interrupted-growth sample consists of pairs or triplets of much narrower lines for each well with individual components associated with monolayer-flat regions differing in width by 1 ML. The estimated thicknesses in ML units are given in the figure. A comparison of the linewidths (FWHM) for transitions attributed to free exciton emission are plotted in Fig. 1b. Even in the absence of local surface roughness, variations in the confining barrier heights will still exist due to local compositional fluctuations in the barrier alloy. The linewidths of the three narrowest wells provide a consistent upper limit of  $\Delta x = 0.006 \pm 0.001$  on the range of alloy composition within the diameter of the exciton, which is thought to be  $\sim 300\text{\AA}$  (Miller et al 1981).

Free-exciton and defect-related PL lines were distinguished on the basis of PLE measurements described previously by Miller et al (1986). Figure 2 shows PL and PLE spectra for the single well of 50Å nominal width in the interrupted-growth sample. The PLE spectrum was obtained by monitoring the emission at the low-energy side of the peak labeled D in the PL spectrum. Substructure associated with the ML steps is evident in both the light- and heavy-hole regions designated  $E_{11}$  and  $E_{1h}$  respectively. The absence of PLE signal in the region of D itself as well as the quenching of this line by 20K indicate that it is due to a lightly-bound exciton. The other two PL lines are attributed to free-exciton transitions, and we estimate the well thicknesses to be 21 and 22 ML. A very weak 20 ML line is also observed, but is not evident in this linear plot. Any Stokes shifts between the free-exciton PLE and PL peaks are smaller than the 0.2 meV resolution of the measurements. Such small shifts are again consistent with the absence of short-range surface roughness. For comparison, a 2 meV Stokes shift is observed in the emission of the equivalent well in the continuous-growth reference sample.

A significant difference between the PLE and PL spectra is apparent, however, in the relative strengths of the transitions associated with different ML regions. The emission is consistently weighted more heavily towards the lower-energy peaks in the multiline spectra. Since the PLE spectra provide a measure of the fractional area of each ML thickness region within the exciting laser spot, this shift of the intensity to lower energy lines reflects rapid lateral motion of the excitons to wider regions of the wells. Presumably it is the same lateral motion that leads to significant Stokes shifts in quantum wells with short-range surface roughness, but is more readily identified here where there are discrete and well-resolved emission lines associated with different spatial regions in the well.

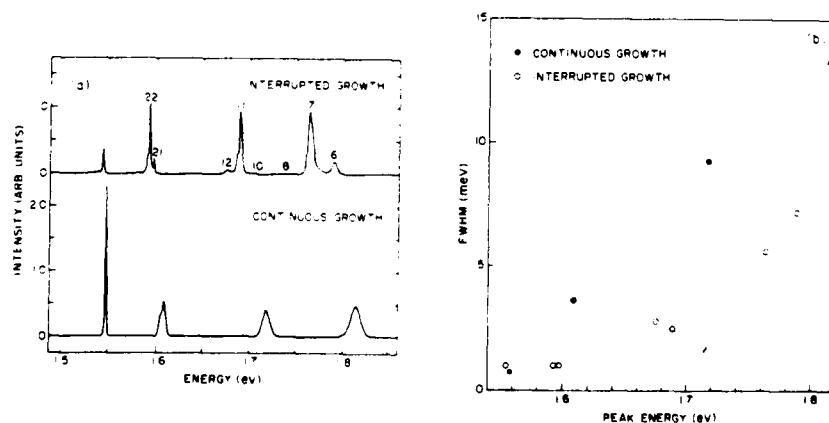


Fig. 1. Part a displays a comparison of 6K photoluminescence spectra for an interrupted growth and a continuous-growth sample grown under identical conditions. Both samples contain 4 single GaAs quantum wells of nominal thicknesses 100Å, 50Å, 25Å and 15Å between 300Å  $\text{Al}_{0.37}\text{Ga}_{0.63}\text{As}$  barriers. The interrupted-growth sample shows multiple narrow PL lines corresponding to recombination in monolayer-flat regions larger than the exciton diameters which differ in thickness by one monolayer. In part b the observed linewidths (FWHM) of free-exciton transitions are plotted versus peak energy.

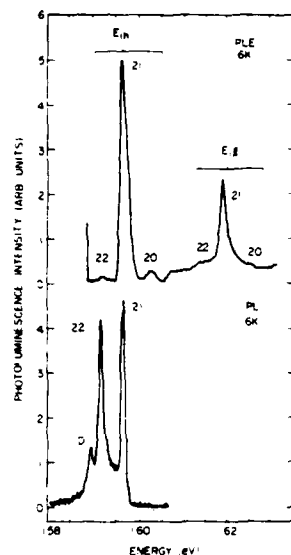


Fig. 2. 6K photoluminescence emission and excitation spectra for the 50Å nominal width well in the interrupted-growth sample. The PL spectrum exhibits 2 sharp lines attributed to recombination in 21 and 22 ML thick regions, and a third line ascribed to a lightly-bound exciton. Substructure associated with ML thickness differences is also evident in both the heavy hole ( $E_{1h}$ ) and light hole ( $E_{1l}$ ) regions of the PLE Spectrum.

The relative weight in the PL lines is also a function of the excitation intensity. This is apparent in the 6K PL spectra displayed in Fig. 3a which span 6 orders of magnitude in laser intensity. The two emission lines at  $\sim 1.765$  eV and  $\sim 1.79$  eV originate from the narrowest well of the interrupted-growth sample in regions we estimate to be 7 and 6 ML wide respectively. Although excitation spectra imply that the well is predominately 6 ML wide, the 7 ML line is consistently more intense in emission. The magnitude of this discrepancy depends on laser power, and is greatest at the lowest excitation densities. Higher intensities and higher temperatures increase the relative emission intensity from the narrower region. As shown in Fig. 3b, however,  $I_6/I_7$  does not continue to grow as the laser intensity is increased, but saturates at a value well below unity.

The relative strength of free to acceptor-bound exciton emission also depends on laser intensity. In Fig. 4a and b we display semilog plots of the 6K PL spectra from the two narrowest wells of the interrupted-growth sample, nominally 25Å and 15Å wide, again over 6 decades in excitation power. The 25Å (15Å) well spectrum shown in part a (b) exhibits peaks associated with 10-12 ML (6-8 ML) regions. Evident in the 10-12 ML peaks is a low-energy shoulder on each line which grows in relative strength as the laser intensity is lowered, and eventually becomes the dominant emission at the lowest powers. This emission is presumably due to a shallow defect which becomes saturated at higher intensities. This behavior is less well resolved in the spectra from the narrowest well shown in part b because the lines are slightly broader.

It is tempting to ascribe the change in the relative weights of the monolayer lines with intensity to a similar process. Namely, if one considers the wider parts of the well as "traps" for the excitons, then at low temperatures and intensities most of the excitons will recombine at these sites. Raising the temperature will allow thermally excited release back to narrow well regions and enhance the higher-energy lines, as observed. Similarly, since there is a somewhat smaller fractional area of these wider regions, they will saturate at high excitation densities and their relative contribution to the PL spectrum will be diminished. The analogy breaks down, however, in that the relative intensity of the higher-energy 6 ML line does not continue to grow with additional laser intensity, as it would if a simple saturation effect were responsible. Apparently the source of the branching ratio involves other processes. Since the change in the relative weights of the lines occurs at about the same low intensities as the cross over from defect-related to free-exciton emission, a more complicated interplay of defect-trapping, energy-transfer and recombination rates may be responsible for this behavior. One possibility is that the main recombination channel at low intensities involves free holes in the well donated by acceptors in the barrier layers. These holes have a relatively long time to thermalize, and will thus reside almost

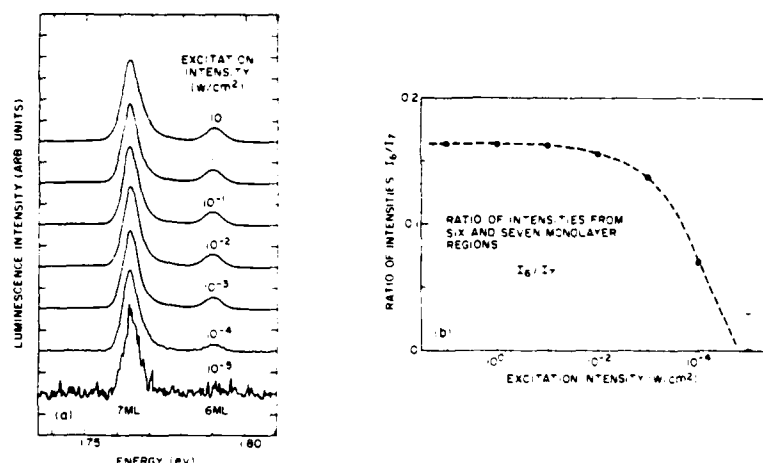


Fig. 3. Excitation-density dependence of the relative strengths of the 6 and 7 ML lines of the narrowest well in the interrupted growth sample. In part a the spectra are shown over a range of 6 decades in laser power. The peak heights have been normalized to the same magnitude. The ratio of intensities,  $I_6/I_7$ , is depicted in part b.

exclusively in the wider parts of the well. This model explains in a natural way why the onset of increased PL in the narrower region should occur when the optically-excited carrier population becomes comparable to the acceptor density.

Luminescence due to recombination in one well can also be excited by absorption at higher-lying states in other wells. This is evident in Fig. 5 where we display a PLE spectrum obtained by monitoring the emission from the widest (100Å nominal width) well in the interrupted growth sample. Individual ML lines are not resolvable in this well, and the only transitions associated with this well which appear in this PLE spectrum are the  $n = 1$  light hole ( $E_{11}^{(00A)}$ ) and  $n = 2$  heavy hole ( $E_{2h}^{(00A)}$ ). The other lines present in the spectrum replicate absorption peaks observed in the PLE spectra of the narrower wells. The peaks in the region enclosed by the dotted box are identified as the  $n = 1$  heavy and light hole absorption lines for 20-22 ML from the 50Å nominal-width well. Those within the dashed box represent absorption in the 10-12 ML regions of the 25Å nominal-width well. Since these additional peaks compete quite favorably with those associated with absorption in the same well, it is obvious that inter-well energy transfer is also quite efficient. Given that the intervening barriers are 300Å thick, it seems unlikely that a single-step tunnelling process is responsible. It is more probable that defect structures such as dislocation chains between the wells act as effective channels for this migration. Note that a radiative transfer process cannot be invoked since the 100Å well is below the narrower wells in the sample structure. Absorption in the narrower wells reduces the laser intensity reaching the wider well, and light reemitted by the narrower wells can only partially compensate for this loss. Thus photon recycling between wells cannot be responsible for peaks in the PLE spectrum. Although to our knowledge such effective transfer through thick barriers has not been reported before, we do not necessarily consider it a signature of interrupted-growth samples alone. We suggest that these features are merely easier to identify in this sample due to the narrowness of the transitions in the absence of short-range interface roughness.

Figure 6 shows a more extended PL spectrum of the narrowest well measured at 10 W/cm<sup>2</sup> excitation power. The semilog format highlights additional weaker structure in the spectrum. A lower-energy free-exciton emission associated with 8 ML-wide regions is observed with an intensity almost 3 orders of magnitude weaker than that of the 7 ML line. There is evidence of an unresolved defect-related line under the high-energy Boltzman tail of the 7 ML emission. This defect emission is apparently associated with the 6 ML regions as it is quenched in the same laser intensity range in which the 6 ML free-exciton line is lost. Additional weak defect-related structure is evident above and below the 6-8 ML

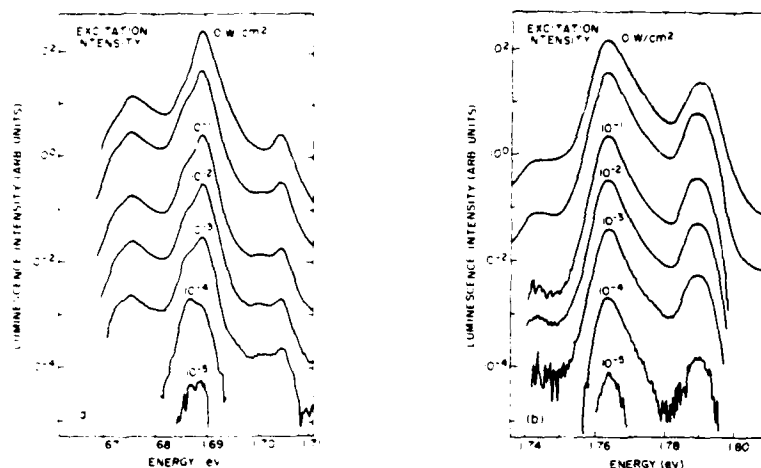


Fig. 4. 6K PL spectra as a function of excitation density for the 25Å (part a) and 15Å (part b) nominal-width wells of the interrupted-growth sample.

multiplet. The high-energy shoulder at 1.805 eV is approximately 10-15 meV below the position expected for the 5 ML free-exciton line, and we attribute it to a defect-related transition in the 5 ML regions. In fact, it is probably due to the same defect responsible for the unresolved line between the 6 and 7 ML peaks which also lies  $\sim 15$  meV below the associated free-exciton line, in that case the 6 ML peak. The lowest-energy peak, also labeled D in Fig. 6, is again attributed to the same defect, in this case associated with 8 ML-wide regions. The equivalent defect line for 7 ML would fall close to the same energy as the 8 ML free-exciton line, and the peak marked "8" may contain contributions from both sources.

The presence of a defect line associated with 5 ML regions, while the equivalent free-exciton line is absent, indicates that the trapping rate at these sites competes favorably with the transfer rate to other parts of the well, and that both are quite rapid in comparison to the radiative recombination rates. Thus only those excitons or carriers trapped at these sites, which are local minima in energy, remain long enough in these narrow regions of the well to recombine there. Although there is a somewhat higher level of defect incorporation in this interrupted-growth sample over its continuous growth counterpart as indicated by a slightly lower PL quantum efficiency, this pattern has not been consistently repeated in other sets of samples grown in our system (Miller et al 1986). In general this extensive study of defect-related transitions in the interrupted-growth sample was informative primarily because of the ability to resolve and identify these lines rather than because of the moderate enhancement of their intensities.

### 3. Conclusions

In this paper we have presented PL and PLE measurements on a sample with 4 single GaAs wells for which the growth was interrupted at each heterointerface. The growth interruption results in the elimination of short-range interface roughness so that excitons experience monolayer-flat regions at least as great as their 300Å diameter. The resulting PL and PLE spectra exhibit multiplets of discrete lines associated with these regions which differ in thickness by single ML steps. In the absence of interface roughness, the individual lines are extremely sharp and well-resolved. The remaining inhomogeneous widths place an upper limit of  $\Delta x = 0.006 \pm 0.001$  on fluctuations in the barrier alloy composition within the diameter of the exciton.

The narrow PL and PLE lines allow unambiguous identification of free and bound transitions. In comparison to the PL spectra, the dominance of higher-energy lines in the PLE spectra associated with absorption in narrower regions of the well reveals efficient lateral energy transfer. At the lowest

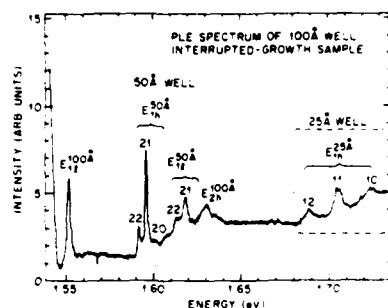


Fig. 5. PLE spectrum of the 100Å nominal-width well in the interrupted-growth sample. The spectrum contains absorption peaks associated with the 50Å and 25Å nominal-width wells, indicating effective inter-well energy transfer through the 300Å  $\text{Al}_{0.37}\text{Ga}_{0.63}\text{As}$  barriers.

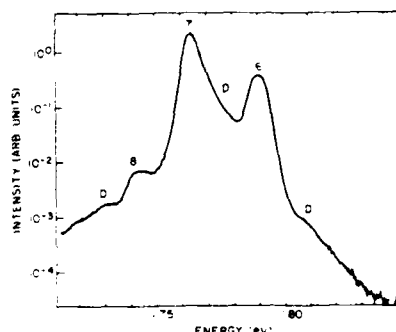


Fig. 6. Extended semilog plot of the 6K PL spectrum of the narrowest well in the interrupted-growth sample. Peaks labeled 6, 7 and 8 are attributed to free-exciton recombination in regions of 6, 7 and 8 ML thickness respectively. Additional defect-related structure is labeled D.

intensities the lower-energy lines completely dominate the PL spectra, which may reflect recombination with free holes donated by acceptors in the barriers layers. The presence of lines in the PLE spectra arising from absorption in other wells indicates that there is also rapid energy transfer between wells. The interrupted growth sample also exhibited a slight increase in defect incorporation.

The separation of the spectra into discrete and extremely narrow monolayer lines opens up many new avenues of investigation into the static and kinetic parameters of these quantum well structures. Time-resolved PL studies may provide clear measurements of lateral and well-to-well transfer rates. With the increased resolution and discrete ML lines, additional cw measurements should provide much more definitive values of system parameters such as effective masses and binding energies.

#### Acknowledgement

We wish to thank A. S. Jordan for his support of the project.

#### References

- Bimberg D, Mars D, Miller J N, Bauer R and Oertel D 1986 *J. Vac. Soc. Technol.* **B4** 1014
- Deveaud B, Emery J Y, Chomette A, Lambert B and Baudet M 1984 *Appl. Phys. Lett.* **45** 1078
- Fukunaga T, Kobayashi K L I and Nakashima H 1985 2nd Int. Conf. on Modulated Semiconductor Structures (to be published in *Surf. Sci.*)
- Goldstein L, Horikoshi Y, Tarucha S and Okamoto H 1983 *Jpn. J. Appl. Phys.* **22** 1489
- Hayakawa T, Suyama T, Takahashi K, Kondo M, Yamamoto S, Yano S and Hijokata T 1985 *Appl. Phys. Lett.* **47** 952
- Juang F-Y, Bhattacharya P K and Singh J 1986 *Appl. Phys. Lett.* **48** 290
- Miller R C, Kleinman D A, Tsang W T and Gossard A C 1981 *Phys. Rev. B* **24** 1134
- Miller R C, Tu C W, Sputz S K and Kopf R F 1986 *Appl. Phys. Lett.* (to be published)
- Ohta K, Funabashi H, Sakamoto T, Nakagawa T, Kawai N J, Kojima T and Kawashima M 1986 *J. Electron. Mat.* **15** 97
- Reynolds D C, Bajaj K K, Litton C W, Yu P W, Singh J, Masselink W T, Fischer R and Morkoc H 1985 *Appl. Phys. Lett.* **46** 51
- Sakaki H, Tanaka M and Yoshino J 1985 *J. Appl. Phys.* **58** L417
- Tanaka M, Sakaki H, Yoshino J and Furuta T 1985 2nd Int. Conf. on Modulated Semiconductor Structures (to be published in *Surf. Sci.*)
- Voillet F, Madhukar A, Kum J Y, Chen P, Cho N M, Tang W C and Newman P G 1986 *Appl. Phys. Lett.* **48** 1009



## **Spectroscopic investigation of the properties of III-V quantum well structures at high carrier densities**

G Tränkle, A Forchel, E Lach, F Scholz, M H Pilkuhn

4. Physikalisches Institut, University of Stuttgart,  
7000 Stuttgart 80, Germany

G Weimann

Forschungsinstitut der Bundespost, 6100 Darmstadt, Germany

H Kroemer, S Subbanna, G Griffiths<sup>+</sup>

Dept. of Elec. and Comp. Engineering, UCSB, CA 93106, USA

M Razeghi

Thomson-CSF, F-91401 Orsay, France

**Abstract.** Using photoluminescence we investigated the properties of the electron-hole plasma in quasi-twodimensional GaAs/GaAlAs-, InGaAs/InP- and GaSb/AlSb- quantum well structures. In all systems strong bandfilling and large band renormalizations are observed. Pronounced structures in the luminescence spectra reflect the particular subband structure of the quantum wells. The emission lineshapes can be described quantitatively assuming recombination between electron- and hole subbands including forbidden but parity-allowed transitions. From the analysis we obtain the plasma parameters and determine the dependence of band renormalization on plasma density in two-dimensional systems.

### I. Introduction

Due to their new physical properties and due to a wide variety of possible applications especially in optoelectronic devices quantum well structures have attracted a large amount of research both in the fields of material technology and characterization (Dow 1986).

In this paper we report high excitation luminescence measurements in III-V multiple quantum well structures at temperature, between 2 K and 300 K. We used GaAs/GaAlAs- samples grown by MBE with well widths  $L_z$  between 21 Å and 180 Å (Al-content between 19 % and 43 %), GaSb/AlSb- samples grown by MBE with  $L_z$  between 58 Å and 121 Å and lattice-matched InGaAs/InP- samples grown by MOVPE (using adducts (Scholz 1986) as well as alkyls (Razeghi 1983) as metal precursors) with  $L_z$  between 30 Å and 210 Å. In all samples the barrier widths were large enough to avoid coupling between the wells. In the high excitation experiments we excited an EHP using a pulsed dye laser (in the case of GaAs/GaAlAs;  $\tau \approx 10$  ns) or a frequency-doubled Nd:YAG-laser;  $\tau \approx 100$  ns) with excitation powers  $P_{ex}$  between  $100\text{W}/\text{cm}^2$  and  $1\text{ MW}/\text{cm}^2$ . The pulse widths were large enough to provide

quasi-stationary conditions. Backscattering geometry was used to avoid the observation of stimulated emission.

## II. Experimental results

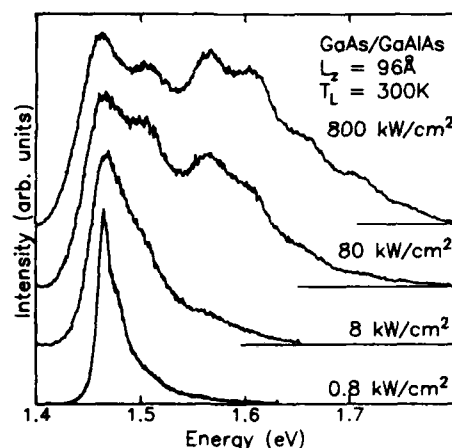


Fig.1 Dependence of plasma luminescence on excitation intensity

To show the general behaviour of the plasma luminescence we depict in figure 1 a series of spontaneous emission spectra recorded in a GaAs/Ga<sub>0.57</sub>Al<sub>0.43</sub>As-MQW sample with  $L_z = 96 \text{ Å}$  at a lattice temperature of 300 K. With increasing excitation power the spectra broaden drastically (up to 400 meV). Pronounced new structures appear at the high energy sides due to the band filling and the occupation of higher subbands. The high energy sides of the spectra become flat as a consequence of the heating of the carriers by the nonresonant excitation. The low energy edges shift to smaller energies due to the band gap renormalization in the dense EHP.

The features of the plasma spectra are quite sensitive to the particular subband structures of the quantum wells. Therefore they depend strongly on the well width within one material system (Tränkle 1985). In GaAs/GaAlAs- samples, e.g., for  $L_z < 50 \text{ Å}$ , where only the lowest subbands (1e, 1h, 1l) are occupied even for the highest excitation intensities, we observe a single broad emission line. For samples with  $50 \text{ Å} < L_z < 150 \text{ Å}$  the spectra show the strongly modulated structures like in figure 1. The energetic differences between the structures in the spectra decrease strongly with increasing well width and for  $L_z > 150 \text{ Å}$  broad unstructured emission bands remain.

For comparable well widths the luminescence lineshapes are quite sensitive to the properties of the material system. In figure 2 we compare spectra from samples of about 100 Å obtained at comparable excitation intensities. We observe large differences between the systems:

- i) The spectrum obtained from the GaAs/Ga<sub>0.57</sub>Al<sub>0.43</sub>As- sample shows up to seven structures. In this system the relatively large conduction band discontinuity leads to three electron levels for  $L_z = 96 \text{ Å}$ . In the potential well of the valence band there are four heavy hole and three light holes levels. Transitions between occupied subbands are responsible for the structures in the spectra.
- ii) The spectrum obtained from the InGaAs/InP- sample shows still four structures. In this material system only one third of the band discontinuity is in the conduction band, leading to a relatively flat potential well for the electrons. Therefore only two subband levels in the conduction band can be expected and fewer transitions should be observable.

Qualitatively in this system the dependence of the luminescence lineshape on the well width is comparable to that observed for GaAs/GaAlAs samples. With decreasing well width the splitting between the structures increases (Tränkle 1986a) and for very narrow and very broad wells single emission bands remain.

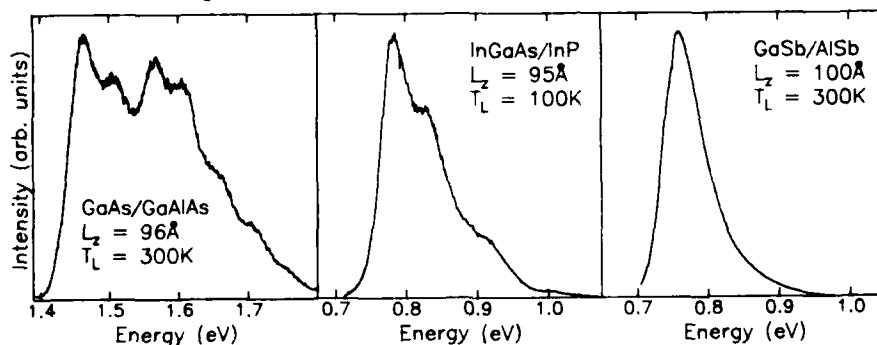


Fig.2 Dependence of plasma luminescence on material parameters. The spectrum of the InGaAs/InP- sample is measured at a lattice temperature  $T_L = 100$  K. At higher  $T_L$  the structures are not that pronounced anymore.

iii) The spectrum obtained in the GaSb/AlSb- sample shows only one broad line without further structures. In this material system the potential well in the conduction band is very deep ( $\approx 1.2$  eV), leading to a large splitting of the subband levels even for relatively thick quantum wells. Therefore higher subbands are not occupied and in our set of samples we observe no change in lineshape with increasing well width (Tränkle 1986b).

### III. Lineshape analysis

In order to quantitatively describe the spontaneous plasma luminescence we performed a lineshape analysis calculating spectra for allowed transitions between two-dimensional subbands. Neglecting any broadening effects the emission spectra should be described by:

$$I(\hbar\omega) \sim \omega^2 f_e(k) f_h(k) \int \frac{d\mathbf{l}}{V_k(E_e(k) + E_h(k))}$$

Here  $\hbar\omega$  is the transition energy;  $f_e, f_h$  denote the electron and hole Fermi functions; the integral describes the joint density of states. We assumed the electrons and holes to be distributed in parabolic subbands according to Fermi statistics using a common quasi-Fermi level for electrons and holes respectively. In order to account for the experimentally observed low energy tail the calculated spectra have been broadened using a Landsberg type formalism (Landsberg 1966). Previously this has been applied successfully to different 3D-systems and relates the broadening to relaxation processes. In this simple analysis we neglected the complicated dispersion relation in the valence band due to the subband mixing (Altarelli 1985). We approximated the mean curvature of the dispersion relation by the three-dimensional masses in the cases of GaAs/GaAlAs and InGaAs/InP. Using a realistic dispersion relation for the case of GaAs/GaAlAs (Broido 1986) we have shown that this approach is rea-

sonable especially for the lower subbands. In the case of the highly stressed GaSb/AlSb-layers (lattice mismatch 0.65%) we took into account the stress effects (Bir 1974) and calculated the in-plane masses assuming the high stress limit (Tränkle 1986b). A summary of the in-plane masses used in our analysis is given in table 1:

|          | GaAs/GaAlAs | InGaAs/InP | GaSb/AlSb |
|----------|-------------|------------|-----------|
| $m_e$    | 0.0665      | 0.041      | 0.047     |
| $m_{hh}$ | 0.45        | 0.465      | 0.071     |
| $m_{lh}$ | 0.38        | 0.05       | 0.124     |

Tab.1 In-plane masses (in units of the free electron mass  $m_0$ ) used in the lineshape analysis of the high excitation spectra

In figure 3 we depict three exemplary results for our analysis:

- i) a rather thin GaSb/AlSb- sample ( $L_z = 58 \text{ \AA}$ ): Only the lowest subbands are involved in the transitions (1hh,1lh) and the agreement between the experiment and the calculation is very good.
- ii) a rather thick GaAs/Ga<sub>0.78</sub>Al<sub>0.22</sub>As- sample ( $L_z = 180 \text{ \AA}$ ): Many subbands contribute to the lineshape (1hh,1lh,...,3hh). The energetic difference between the subbands is rather small, the transitions merge to a single broad line. Again this behaviour is modelled by our lineshape analysis quite well.
- iii) a InGaAs/InP- sample with a well width in the range of 100 \AA ( $L_z = 95 \text{ \AA}$ ). In this case the agreement seems to be poor, especially the second structure in the experimental spectra is not explained at all.

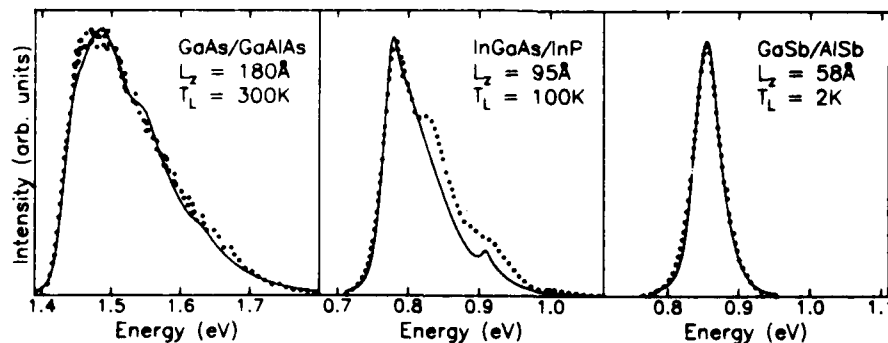
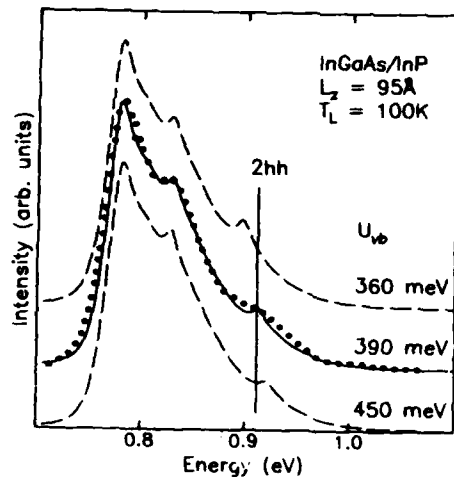


Fig.3 Lineshape analysis of plasma spectra for different material systems, different well widths and different lattice temperatures

To overcome this problem we have to include forbidden- but parity-allowed transitions ( $\Delta n = \pm 2, \pm 4$ ) in our analysis (Tränkle 1985). In figure 4 we depict the result for the InGaAs/InP- sample with  $L_z = 95 \text{ \AA}$  (solid line). Now the agreement between experiment and theory is very satisfactory and explains the second structure in the spectrum as a transition between the first electron and the third heavy hole subband (13h).

This agreement between the experimental spectra and the calculated lineshapes can now be used to determine basic parameters of the quantum well structures. As an example the dashed lines in figure 4 show calculated spectra assuming different depths of the potential well in the valence band of 450 meV and 360 meV, respectively.



Especially the energetic position of the structure assigned to the 2hh- transition is very sensitive to the change in well depth. The best fit (solid line) is obtained for a potential well depths of 390 meV, which is equivalent to 65% of the banddiscontinuity appearing in the valence band. This value is in good agreement with those obtained in other experiments (Vilela 1986).

Fig.4 Lineshape fit including forbidden but parity-allowed transitions (solid and dashed lines). The dashed lines illustrate the sensitivity of fit to the well depth  $U_{vb}$  in the valence band.

#### IV. Band gap renormalization.

From the lineshape analysis we obtain the plasma densities, temperatures and renormalized band gaps. Therefore we are able to determine the density-dependence of the band gap renormalization, which is due to many-body effects in the carrier plasma.

The band gaps for very low densities can be measured in absorption or excitation spectroscopy taking into account the appropriate exciton binding energies. In the case of the GaAs/GaAlAs- samples we take binding energies obtained from excitation spectroscopy (Dawson 1986). In our samples of the other material systems the exciton binding energies are negligible because the electron-hole interaction is largely screened by a relatively high background carrier concentration ( $\approx 10^{16} \text{ cm}^{-2}$ ; Kleinman 1985).

In figure 5 we show the dependence of the band gap renormalization on the carrier density for well widths smaller than 120 Å in the three material systems.

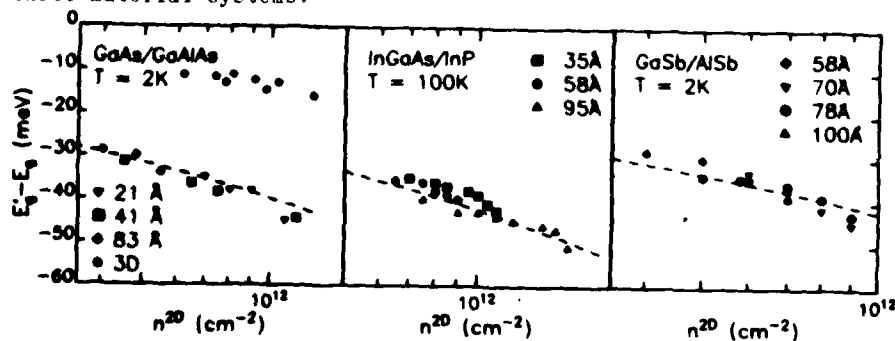


Fig.5 Band gap renormalization in quasi-two-dimensional systems ( $T_L = 2\text{K}$  for GaAs/GaAlAs and GaSb/AlSb;  $T_L = 100\text{K}$  for InGaAs/InP)

In all systems the relation between the plasma density and the band gap renormalization is close to  $\Delta E_g \propto n^{1/3}$ . This agrees with theoretical expectations (Schmitt-Rink 1984). In the GaAs/GaAlAs-samples the renormalization reaches values between 25 meV and 40 meV for densities between  $4 \cdot 10^{11} \text{ cm}^{-2}$  and  $1.5 \cdot 10^{12} \text{ cm}^{-2}$ ; in the InGaAs/InP-samples they are between 35 meV and 50 meV for densities between  $6 \cdot 10^{11} \text{ cm}^{-2}$  and  $2 \cdot 10^{12} \text{ cm}^{-2}$ . Finally in the GaSb/AlSb-samples we observe a band gap renormalization between 30 meV and 50 meV for carrier densities between  $4 \cdot 10^{11} \text{ cm}^{-2}$  and  $9 \cdot 10^{11} \text{ cm}^{-2}$ . In any system we observe no systematic dependence of the band renormalization on the well width. This is a clear evidence that the two-dimensional limit is reached in our samples.

The absolute values of the band renormalization in the 2D-systems are much larger than those obtained in 3D-structures of comparable materials (figure 5a shows for example the values obtained in GaAs-mesa structures at comparable densities (Capizzi 1984)) This is a consequence of the increase in excitonic Rydberg due to the confinement of the carriers in the quantum wells.

In summary we have demonstrated that high excitation luminescence measurements in quantum well structures yield information on basic material properties like band discontinuity distribution as well as insight in many-body effects in reduced dimensionality.

We acknowledge the collaboration of H Leier, P Wiedemann and G Laube and discussions with K W Benz. We are grateful for the financial support by the Deutsche Forschungsgemeinschaft (contract P71/20) and the Stiftung Volkswagenwerk and the Office of Naval Research.

#### References

- + now at C S I R O, Div of Radio Physics, Epping, NSW 2121 Australia
- Altarelli M 1985, *J Lumines* **30**, 472
- Bir G L, Pikus G E 1974, *Symmetry and Strain-induced Effects in Semiconductors* (New York : Wiley)
- Broido D A, Reinicke T L 1986, calculation of  $E(k)$ , private communication
- Capizzi M, Modesti S, Fropa A, Staehli J L, Guzzi M, Logan R A 1984, *Phys Rev B* **29**, 2028
- Dawson P, Moore K J, Duggan G, Ralph H I, Foxon C T B 1986, to be published in *Phys Rev B*, rapid communications
- Dow J D 1986, ed. *Proc. 2nd Int Conf on Superlattices, Microstructures, Microdevices*, to be published in *Superlattices and Microstructures*
- Kleinman D A 1985, *Phys Rev B* **32**, 3766
- Landsberg P T 1966, *Phys stat sol* **15**, 623
- Razeghi M, Hirtz J P, Ziemelis U D, Delalande C, Etienne B, Voos M 1983, *Appl Phys Lett* **43**, 585
- Schmitt-Rink S, Ell C 1985, *J Lumines* **30**, 585
- Scholz F, Wiedemann P, Benz K W, Tränkle G, Lach E, Forchel A, Laube G, Weidlein J 1986, *Appl Phys Lett* **48**, 911
- Tränkle G, Leier H, Forchel A, Weimann G 1985, *Proc. MSS-II*, to be published in *Surface Science* **172**
- Tränkle G, Lach E, Forchel A, Scholz F, Wiedemann P, Benz K W 1986a, *Proc. 2nd Int Conf Superlattices, Microstructures, Microdevices*
- Tränkle G, Lach E, Forchel A, Kroemer H, Subbanna S 1986b, to be published
- Vilela J M, Marten H W, Klötzer N, Kühn E, Eisele H, Pilkuhn M H, Kuphal E, *IEEE J Quant Elec*, to be published

## **Magneto-luminescence measurements in InGaAs/GaAs single-strained-quantum-wells**

E.D. Jones, I.J. Fritz, J.E. Schirber, M.C. Smith and T.J. Drummond

Sandia National Laboratories, Albuquerque, New Mexico 87185

**Abstract.** We report low-temperature magneto-luminescence studies on p-type and n-type single-strained-quantum-well InGaAs/GaAs structures. These structures exhibit a large strain-induced energy splitting between the in-plane "light-" and "heavy-" hole valence bands and thus effects due to valence-band mixing are minimal. From an analysis of the magneto-luminescence spectrum, the in-plane valence-band masses are found to be in the range of 0.14 to 0.17 $m_0$  in agreement with transport data on the p-type samples. Hydrostatic-pressure magneto-luminescence data for pressures up to 4 kbar and magnetic fields to 6T at 4K are also presented.

Single-strained-quantum-well (SSQW) structures comprise a thin strained-layer material sandwiched between thick layers of another material. The present work is concerned with magneto-luminescence measurements with In<sub>x</sub>Ga<sub>1-x</sub>As as the strained SSQW and GaAs as the unstrained thick-layered material. The unusual valence-band properties of semiconductors resulting from such a biaxial stress have been previously discussed (Bir and Pikus 1974 and Fritz et al 1986). Magneto-luminescence studies for the InGaAs/GaAs strained-layer-superlattice (SLS) structures have been previously presented (Jones et al 1985a and 1985b). For both the SSQW and SLS structures, the InGaAs layer is under compression, has the smaller band gap energy and also is the active layer. SSQW structures have the maximum amount of planar compression (71.4%). Hence the "heavy" and "light" hole valence bands are well separated reducing effects of valence-band mixing prominent for GaAs/GaPAs SLS structures (Jones et al 1985b).

In this paper, we report the results of low-temperature magneto-luminescence measurements on MBE grown  $x = 0.7$ , p-type (T0100) and  $x = 0.35$ , n-type (T0104 & T0106) SSQW In<sub>x</sub>Ga<sub>1-x</sub>As/GaAs structures with well widths of 79 Å. The 4K mobilities and  $10^{18}$  carrier concentrations were  $1.0 \times 10^4$  cm<sup>2</sup>/Vsec and  $1.6 \times 10^{18}$  cm<sup>-3</sup> for T0100 and  $3.0 \times 10^4$  cm<sup>2</sup>/Vsec and  $5.4 \times 10^{18}$  cm<sup>-3</sup> for T0104. We report the preliminary results of low-temperature hydrostatic pressure-dependent magneto-luminescence measurements on the two n-type InGa structures.

The experimental apparatus and techniques for performing hydrostatic-pressure-dependent magneto-luminescence measurements at low temperatures

and high magnetic fields has been previously described (Jones et al 1985b) and only a brief description will be presented here. Magnetic fields to 6.5T were provided by a superconducting solenoid and luminescence data were obtained in the 1.6 - 4K range by pumping on the helium bath in which the sample was immersed. The magnetic field direction was normal to the SLS layers. The [100] face of the sample was attached to one end of a 100- $\mu\text{m}$  core-diameter quartz fiber by GE 7031 varnish. The sample was illuminated by the 514.5 nm line of an Argon-ion laser through the fiber-optic cable. Hydrostatic pressures, to 4 kbar, were generated using the solid helium technique (Schirber 1970). For analysis, the luminescence signal, returning back through the fiber, was directed by a beam splitter to a monochromator, a Si-photocathode photomultiplier and a CAMAC-based data acquisition system (Jones and Wickstrom 1985).

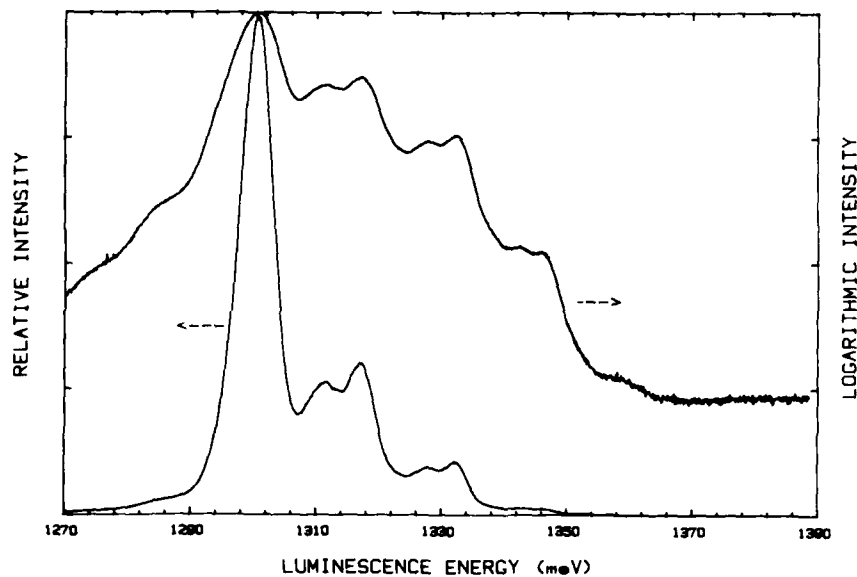


Figure 1. Luminescence spectrum for the n-type SSQW T0195 at 4K and 6.3T. The 4th order logarithmic intensity is also plotted. Note the double peak structure for the  $n > 0$  Landau-level transitions at 1315 meV, etc.

Figure 1 shows a typical magneto-luminescence spectrum for the n-type SSQW T0195 at 4K and 6.3T. For more detail, the logarithmic intensity is also displayed in Fig. 1. Several Landau-level transitions are clearly evident. The double peak structure, discussed in the figure caption, is probably the luminescence from excited states of either excitons and/or shallow bound donor states. Because of space



limitations, these data and conclusions will be presented at a later date. For this paper, only those transitions associated with the interband Landau-levels will be used in the present data analyses.

The luminescence energy in the presence of a magnetic field  $B$ , is given by (cgs units)

$$E = E_g + (n + 1/2) e\hbar B/\mu c \quad (1)$$

where  $E_g$  is the band gap energy,  $n$  is the Landau-level index,  $e$  is the electronic charge,  $\hbar$  is Plank's constant over  $2\pi$  and  $\mu$  is the reduced mass ( $1/\mu = 1/m_e + 1/m_h$ ) where  $m_e$  is the conduction-band mass and  $m_h$  is the valence-band mass. All masses will be expressed in units of the free electron mass  $m_0$  and will refer to their in-plane values.

Values for the band gap energy  $E_g$  and the reduced mass  $\mu$  can be obtained by plotting the Landau-level luminescence energies as a function of magnetic field  $B$  and performing a two parameter "best fit" of Eq. 1 to the data. The resulting "fan" diagram for the data shown in Fig. 1 is displayed in Fig. 2. The straight lines drawn through the data are calculated with the best-fit-values  $1/\mu = 21.5$  and  $E_g = 1289$  meV. Analyses of the magneto-luminescence spectra for the other two structures yields  $1/\mu = 21.8$  and  $E_g = 1300$  meV for the n-type SSQW T0196 and  $1/\mu = 20.1$  and  $E_g = 1374$  meV for the p-type SSQW T0160.

In order to calculate the plane valence-band mass  $m_h$  from the reduced mass  $\mu$ , knowledge of the conduction mass  $m_e$  is required. For all three samples, below-band-gap luminescence from a conduction-band to acceptor-level transition was observed. An analysis of the magnetic field dependence for this transition yielded a conduction-band mass  $m_e = 0.069 \pm 2\%$ . Similar values for the conduction-band mass  $m_e$  were obtained for InGaAs/GaAs SLS structures (Jones et al 1985a). However, as noted by these authors, a value of  $m_e = 0.069$  for the conduction-band mass is larger than the value obtained from magneto-transport measurements, where  $m_e$  ranges from 0.056 to 0.060. The reason for these differences is not understood. Using the optically determined conduction-band mass of  $m_e = 0.069$ , the valence-band masses  $m_h$  for each structure are calculated from the reduced mass data presented above and are respectively  $m_h = 0.17$ , 0.14 and 0.14 ( $\pm 6\%$ ) for T0160, T0195 and T0196.

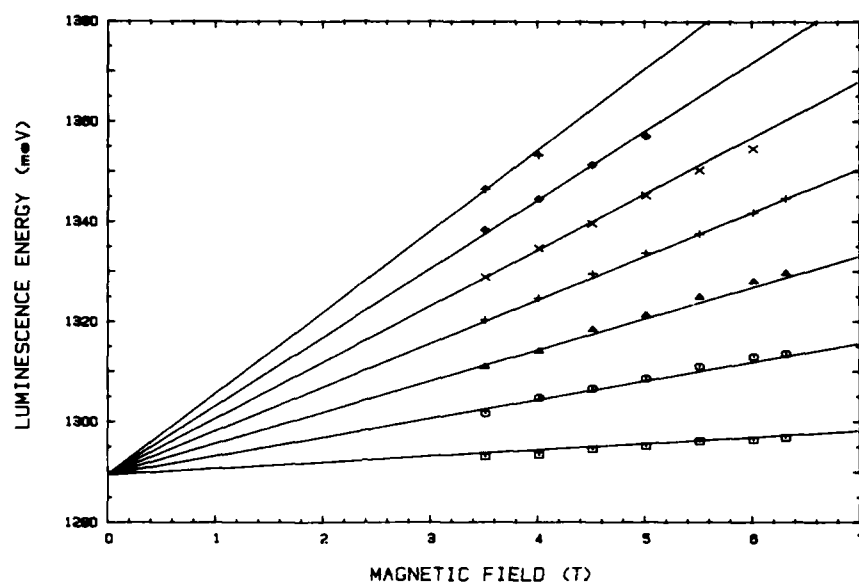


Figure 2. Magnetic field dependence of the luminescence energy of the Landau-level transitions for the n-type SSQW sample T0195. The index  $n$ , top to bottom, runs from 6 to 0.

These values are in good agreement with the magneto-transport data for p-type InGaAs/GaAs SSQW structures of Fritz et al 1986. The differences between these valence-band mass values may be consistent with the predictions of Osbourn et al (1986) which, because of valence-band nonparabolicity, show that the valence-band mass is concentration dependent. It is to be noted here that, in contrast to the difference between the magneto-luminescence-determined and magneto-transport-determined conduction-band mass  $m_e$ , the valence-band masses determined by these techniques do not appear to be significantly different. This result suggests that further investigation concerning the determinations of the conduction-band mass using optical methods is needed.

Figure 3 shows the pressure dependence of the luminescence spectrum for the n-type SSQW T0195 at atmospheric and 3.8 kbar pressures at 4K and 6T. Besides the shift in energy, both spectra are identical, and this is indicative of the hydrostatic quality of the He pressure medium. The double peak structure in the spectra is clearly evident and again will not be discussed here. The pressure-coefficient for the band gap energy  $E_g$  is 10.0 meV/kbar. For n-type SSQW T0196, the pressure-coefficient for the band gap energy was found to be 10.5 meV/kbar. The pressure-coefficients for the band gap energy for these SSQW structures are in good agreement with those obtained for the InGaAs/GaAs SLS structures

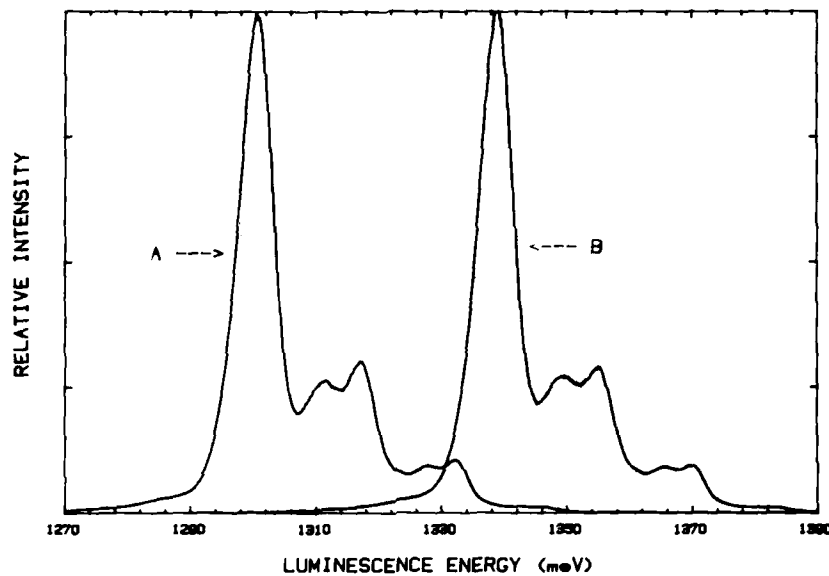


Figure 3. Pressure dependence of the luminescence spectrum for the n-type SSQW T0195 at 4K and 6T. Curve A is atmospheric pressure and curve B is for 3.8 kbar.

(Jones et al 1985b, 1985c) Because the valence-band mass  $m_h$  is determined by subtracting two large numbers, the pressure-coefficient for this parameter is difficult to determine due to the experimental uncertainties.

In conclusion, we have presented magneto-luminescence data for p-type and n-type InGaAs/GaAs SSQW structures which allowed determinations of the valence-band mass. It was found that the values for these masses are "light" and are in agreement with those obtained by magneto-transport methods and also with theoretical expectations. It is noted here that in contrast to the magneto-transport method, magneto-luminescence determinations of valence-band masses are not restricted to p-type samples.

The authors wish to acknowledge Dr. G. C. Osbourn and Professor A. Elci for many important conversations and D. L. Overmyer and R. J. Blake for excellent technical assistance. This work was performed at Sandia National Laboratories supported by the U.S. Department of Energy under contract number DE-AC04-756DP00789

References

- Bir G L and Pikus G E 1974 Symmetry and Strain-Induced Effects in Semiconductors (New York: Wiley) Chapter 5
- Fritz I J, Schirber J E, Jones E D, Drummond T J and Osbourn G C 1986 Proc. 13th Int'l. Symp. on GaAs, Las Vegas, USA
- Jones E D and Wickstrom G L 1985 SPIE SW Conf. on Optics 540 362
- Jones E D, Ackerman H, Schirber J E, Drummond T J, Dawson L R and Fritz I J 1985a Sol. State Comm. 55 525
- Jones E D, Ackerman H, Schirber J E, Drummond T J, Dawson L R and Fritz I J 1985b Appl Phys Lett 47 492
- Jones E D, Schirber J E, Fritz I J, Gourley P L, Biefeld R M, Dawson L R and Drummond T J 1985c Mat. Res. Soc. Symp. Proc 56 241
- Jones E D, Biefeld R M, Fritz I J, Gourley P L, Osbourn G C, Schirber J E, Heiman D and Foner S 1986 - to be published Appl Phys Lett
- Osbourn G C, Schirber J E, Drummond T J, Dawson L R, Doyle B L and Fritz I J 1986 to be published Appl Phys Lett
- Schirber J E 1970 Cryogenics 10 1

## **Hole transport and charge transfer in GaAs/InGaAs/GaAs single strained quantum well structures**

I.J. Fritz, J.E. Schirber, E.D. Jones, T.J. Drummond and G.C. Osbourn

Sandia National Laboratories, Albuquerque, New Mexico 87185

**Abstract.** We report studies of MBE-grown single strained quantum-well structures with  $\text{In}_{0.2}\text{Ga}_{0.8}\text{As}$  wells and GaAs barriers. Structures with selective p-type doping were investigated using Hall-effect, magnetoresistance and magnetoluminescence measurements. Measured carrier densities were fit to a simple charge-transfer model. Directly measured effective masses confirm the prediction of a strain-induced, density-dependent light hole mass for planar conduction. Mobilities comparable to electron mobilities were attained.

### **1. Introduction**

High-quality strained-layer epitaxy (the epitaxial growth of lattice-mismatched crystalline films without misfit dislocations) is possible for film thicknesses less than a mismatch-dependent critical value (Van der Merwe and Ball 1975, Matthews and Blakeslee 1974). This phenomenon has been utilized in the development of strained-layer superlattices in a variety of compound-semiconductor material systems. The present work is concerned with the use of strained-layer epitaxy for fabricating single strained quantum-well (SSQW) structures, which comprise a thin, strained layer sandwiched between thick layers of the substrate material or possibly another material which is lattice-matched to the substrate (Fritz, et al 1986a).

We report results of experiments on SSQW structures with  $\text{In}_{0.2}\text{Ga}_{0.8}\text{As}$  wells and GaAs barriers. A series of MBE-grown structures with well widths of  $\sim 90\text{\AA}$  and selective p-type doping has been investigated using Hall effect, magnetoresistance and magnetoluminescence measurements. We have chosen to study p-type doping because of the interesting changes in the valence band structure produced by the built-in strain in the quantum well. For the present samples the InGaAs layers are under biaxial compression of 1.4%. The effect of biaxial compression on bulk material (Bir and Pikus 1974) is illustrated schematically in Fig. 1. The volumetric component of strain  $\epsilon_v$  increases the bandgap whereas the axial component  $\epsilon_a$  splits the normally degenerate heavy and light hole bands. As indicated by the dispersion curves, the uppermost valence band has a light mass [ $m_h^* = (0.1-0.2)m_e$ , where  $m_e$  is the free electron mass] near the zone center, a phenomenon which is expected to lead to enhanced electrical transport for holes in our SSQW structures compared to GaAs. Recent calculations have suggested that the planar light hole mass depends strongly on carrier density due to band nonparabolicity

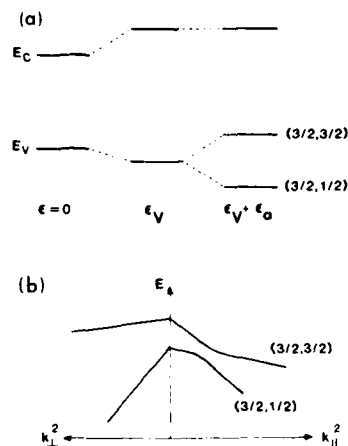


Fig. 1. Effect of built-in strain on (a) energy levels and (b) valence-band dispersion. Strain is caused by biaxial stress (compressive) due to lattice mismatch between GaAs and InGaAs.

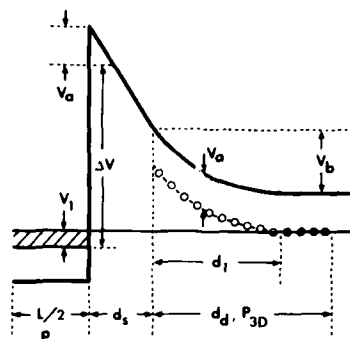


Fig. 2. Schematic illustration of simple model for band bending and charge transfer in SSQW structures. Half of the symmetrically doped structure is shown.

(Osbourne et al 1986). Therefore it is of interest to study properties over a range of densities.

## 2. Charge Transfer

Control of carrier density in the quantum well requires an understanding of the charge transfer process, which depends strongly on the details of the doping profile, due to the rather small band offset ( $\sim 60$ - $70$  meV for the present structures) and deep acceptor levels ( $V_a \approx 30$  meV for Be in GaAs). A simple model has been developed to estimate charge transfer. In Fig. 2 half of a symmetric SSQW structure is shown. The quantum well of width  $L$  confines a carrier gas of areal density  $p$ . The region of width  $d_s$  adjacent to the well is an undoped spacer layer, beyond which is a region of width  $d_d$  doped at a volume density of  $P_{3D}$ . Our simple model ignores band-bending in the well and assumes zero space charge in the spacer layer. We denote  $V_b$  as the band bending in the depletion region and  $V_1$  as the Fermi energy relative to the bottom of the subband. We consider two limiting situations. The first ("partial transfer") is under conditions where the depletion width  $d_s$  is less than  $d_d$ , and the second ("full transfer") is in the limit where the depletion width is wide enough for all charge to transfer. In the partial transfer regime we use the depletion width approximation to model the space charge. A simple analytical expression then describes the charge transfer:

$$\Delta V = \frac{\pi \hbar^2}{em^*} p + \frac{ep^2}{8\epsilon P_{3D}} \left( 1 + \frac{4d_s P_{3D}}{p} \right) \quad (1)$$

where  $\hbar$  is the reduced Planck's constant,  $e$  is the electronic charge magnitude, and  $\epsilon$  is the GaAs dielectric constant. Here  $\Delta V$ , which is the difference between the band offset and the sum of the confinement energy and  $V_0$ , is taken as an adjustable parameter, due to uncertainty in the offset.<sup>a</sup> Note that we have assumed a parabolic band with mass  $m^*$  to approximate the band filling. A value of  $m^* = 0.14 m_0$  was used. In the full transfer regime we have the simple relation  $p = \frac{e}{2d} P_{3D}$ .

In Fig. 3 results for measured carrier density (from Hall data below 77K) are plotted vs  $P_{3D}$  (from nominal growth conditions) for a series of nine samples with nominal dimensions of  $d_s = 125 \text{ \AA}$  and  $d = 150 \text{ \AA}$ . Good fits of the charge transfer model are obtained for dimensions about 20% smaller than these as indicated by the lines on the figure. The 20% difference is within experimental uncertainty. A value of  $\Delta V \approx 35 \text{ meV}$  is obtained from the fit. This value is consistent with the value of  $\sim 30 \text{ meV}$  predicted from simple modeling (Osborn 1983, Fritz, et al 1986b) based on a valence-band offset of  $0.235 \text{ eV}$  between GaAs and InAs.

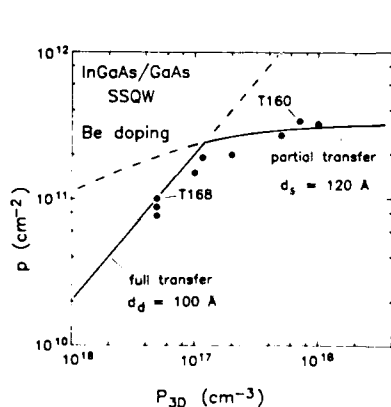


Fig. 3. Measured charge transfer characteristics for a series of samples with nominal spacer thicknesses of  $150 \text{ \AA}$  and doping spikes of  $125 \text{ \AA}$  (solid circles). Best fits of the charge transfer model (solid and dashed lines) are obtained with somewhat thinner layers, as indicated.

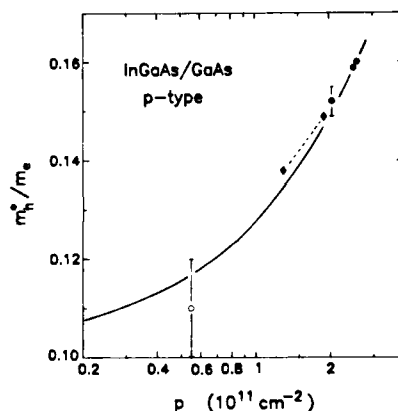


Fig. 4. Directly-measured hole effective mass for SSQW samples. Dashed line represents variation of single sample with optical excitation. Solid curve is fit to theoretical tight-binding model.

### 3. Mass Measurements

Strong quantum oscillations of magnetoresistance were observed at 4K and below for samples with  $p > 1 \times 10^{11} \text{ cm}^{-2}$  (Fritz et al 1986a). Samples with lower carrier density generally had mobilities which were too low for observation of oscillations. Effective masses were determined from the temperature dependence of the amplitude of oscillation in field regions where the oscillations were sinusoidal (Schirber et al 1985). Results for (reduced) effective mass  $m_h^*/m_0$  as a function of  $p$  are shown in Fig. 4 for five SSQW samples.<sup>n</sup> Data obtained on one sample with

density varied by optical excitation are indicated by a dashed line. The solid line represents a model tight-binding calculation which has been fitted to the data at high density (Osborn et al 1986). Agreement with experiment is within experimental uncertainty.

Confirmation of the light planar hole mass has also been obtained from magnetoluminescence measurements (Jones et al 1985). Typical data for an SSQW sample are shown in Fig. 5. The single band-edge luminescence peak observed at zero field becomes a series of peaks due to transitions between Landau levels at high field. Three levels are observed at 6.3T. From the level splitting, a reduced mass may be determined, from which a hole mass may be calculated, provided the (effective) electron mass is known. For the sample of Fig. 5 a mass of  $m_h^*/m_e = 0.17$  is obtained, in good agreement with the value of 0.16 obtained from magnetoresistance data.

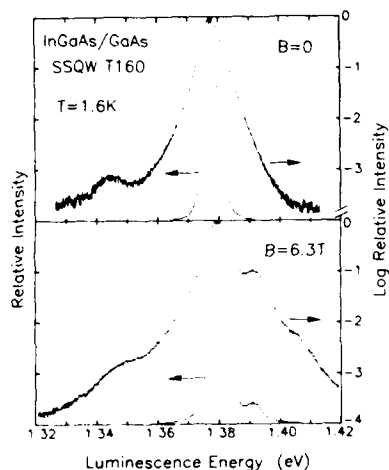


Fig. 5. Magnetoluminescence data at  $B = 0$  and  $6.3T$ . Both linear and logarithmic traces are given. Three Landau level transitions are observed at high field.

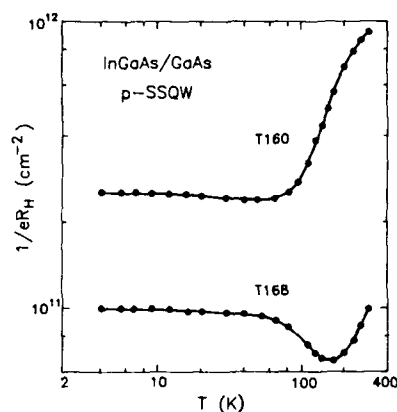


Fig. 6. Hall carrier density  $B$  versus temperature for two SSQW samples.

#### 4. Hall Effect

Hall-effect data between 4K and 300K are shown in Figs. 6 and 7 for two SSQW samples, T160 and T168. As can be seen from Fig. 3, our charge transfer model suggests that sample T160 is in the partial transfer regime, whereas T168 is in the full transfer regime. The data of Fig. 6 for the temperature dependence of the Hall density  $1/eR_H$  are consistent with this picture, as can be seen from the following argument. The measured Hall ratio for the present problem must generally be described by the theory of two-layer conduction (Kane et al 1985). However, at temperatures near 300K, the mobilities of the InGaAs well and GaAs barrier are nearly equal, so that the measured Hall coefficient yields a



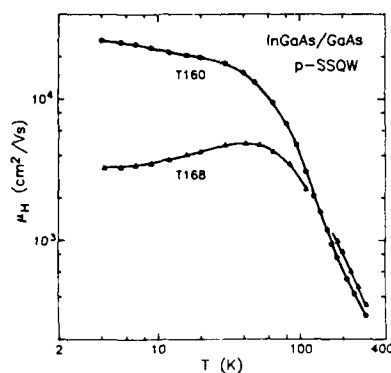


Fig. 7. Hall mobility versus temperature for two SSQW samples.

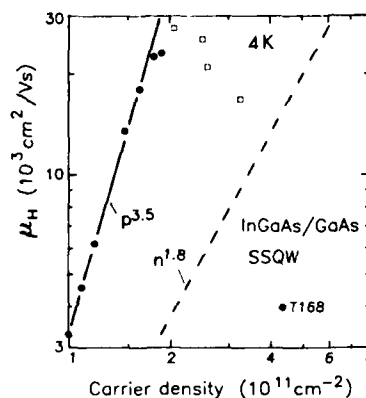


Fig. 8. Hall mobility versus carrier density at 4K for sample T168 at various levels of optical illumination (solid circles), for several p-type SSQW's in the dark (open squares), and for a gated n-type SSQW.

close approximation to the total carrier density. The total density is also measured correctly at low temperatures, where the carriers in the GaAs are frozen into the acceptor states. Thus the high- and low-temperature limits of the data in Fig. 6 suggest that about 25% of sample T160's carriers transfer into the well, whereas sample T168 appears to exhibit nearly total charge transfer.

Hall mobility data are shown in Fig. 7. The data for sample T160 are typical of our best samples, with mobility increasing monotonically with decreasing temperature to 4K. Mobilities at 4K of up to  $3 \times 10^4 \text{ cm}^2/\text{Vs}$  have been achieved. This value is comparable to the value of  $3.5 \times 10^4 \text{ cm}^2/\text{Vs}$  obtained for n-type selectively-doped InGaAs/GaAs superlattices grown in the same growth chamber. At 77K typical mobilities for the present samples were  $7 \times 10^3 \text{ cm}^2/\text{Vs}$  compared to  $3 \times 10^4 \text{ cm}^2/\text{Vs}$  for the n-type superlattices. Note that the ratio of n- to p-type mobilities (at 77K) is ~4.5 compared to a ratio of ~25 for high-quality GaAs/AlGaAs heterostructures. This may be taken as evidence of enhanced transport for holes in the strained InGaAs layers, even though present-day mobilities are less than have been achieved in the AlGaAs system.

Mobility data for sample T168 are also shown in Fig. 7. For this relatively lightly-doped sample, the low-temperature mobility is significantly degraded compared to samples with higher carrier density. We believe the degradation at low temperature is most likely due to residual impurities in the (nominally) undoped regions of the structure, although the exact nature of these impurities has not as yet been determined. We have investigated the dependence of the Hall effect in sample T168 at 4K under optical illumination and have obtained data for

mobility as a function of carrier density from the results. The data are shown in Fig. 8 as solid circles. Note that the mobility changes by a factor of  $\sim 9$  for a factor of 2 change in carrier density. Such a strong dependence does not appear to be interpretable in terms of current theories of screened Coulomb scattering (Drummond et al 1981), and may partly reflect changes in the charge state of impurities under illumination. By contrast, data obtained on an n-type selectively-doped SSQW with carrier density varied by an applied field showed a weaker dependence of mobility on density, as indicated by the dashed line in Fig. 8. The open squares in Fig. 8 represent data on four other p-type samples and show a fairly strong decrease of mobility for carrier densities greater than  $2 \times 10^{11} \text{ cm}^{-2}$ . Increases in the effective mass, intersubband scattering, and remote impurity scattering with density probably are important contributing factors in the reduction of mobility at high density. Further measurements on samples with a range of spacer thicknesses are needed to investigate these effects in more detail.

### 5. Conclusions

We have investigated p-type selective doping in GaAs/InGaAs/GaAs SSQW structures using electrical transport and optical techniques. A simple model appears adequate for describing charge transfer in these structures and should prove useful for designing structures for device and fundamental studies. Effective-mass measurements confirm the existence of a strain-induced light mass for planar transport, and Hall-effect studies indicate enhanced transport due to this light mass. Improvements in crystal-growth techniques to reduce impurities need to be made in order for the full potential for high hole mobility to be realized.

### Acknowledgements

We have benefited from technical assistance from R. F. Martinez, D. L. Overmyer and L. L. Stephenson. This work was performed at Sandia National Laboratories supported by the U.S. Department of Energy under contract number DE-AC04-76DP00789.

### References

- Bir G L and Pikus G E 1974 *Symmetry and Strain-Induced Effects in Semiconductors* (New York:Wiley) Ch 5
- Drummond T J, Morkoc H, Kess K and Cho A Y 1981 *J Appl Phys* **52** 5231
- Fritz I J, Drummond T J, Osbourn G C, Schirber J E and Jones E D 1986a *Appl Phys Lett* **48** 1678
- Fritz I J, Doyle B L, Drummond T J, Biefeld R M and Osbourn G C 1986b *Appl Phys Lett* **48** 1606
- Jones E D, Ackermann H, Schirber J E, Drummond T J, Dawson L R and Fritz I J 1985 *Solid State Commun* **55** 525
- Kane M J, Apsley N, Anderson D A, Taylor L L and Kerr T 1985 *J Phys C:Solid State Phys* **18** 5629
- Matthews J W and Blakeslee A E 1974 *J Cryst Growth* **27** 118
- Osborn G C 1983 *Phys Rev B* **27** 5126
- Osborn G C, Schirber J E, Drummond T J, Dawson L R, Doyle B L and Fritz I J 1986 to be published
- Schirber J E, Fritz I J and Dawson L R 1985 *Appl Phys Lett* **46** 187
- Van der Merwe J H and Ball C A B 1975 in *Epitaxial Growth* ed J W Matthews (New York:Academic) Ch 6 and references therein

## **Characterization of modulation-doped FET's using the Shubnikov – de Haas oscillations**

S.Y. Chou<sup>+</sup>, C.S. Lam<sup>\*</sup>, D.A. Antoniadis<sup>\*</sup>, Henry I. Smith<sup>\*</sup>, and C.G. Fonstad<sup>\*</sup>,

Massachusetts Institute of Technology, Cambridge, MA 02139, USA

**Abstract.** Novel uses of the Shubnikov-de Haas (SdH) oscillations in the characterization of AlGaAs/GaAs MODFET's are demonstrated. The SdH oscillations were used to measure the gate-to-channel capacitance, the density of two-dimensional electrons in the channel, and to detect the onset of parallel conduction in the AlGaAs layer. The characterization methods do not require knowledge of any device parameters, and are immune to parasitic capacitance and source-drain series resistances. One needs to know only the magnetic field, the gate voltage, and the SdH oscillation period. The characterization methods can be applied to MODFET's fabricated in other materials.

### **1. Introduction**

The gate-to-channel capacitance per unit area and the onset of parallel conduction in a modulation doped FET (MODFET) are the fundamental parameters for both device and circuit design. These parameters, however, cannot be determined accurately by conventional C-V and I-V measurements, due to the effects of parasitic capacitance and series resistance. This paper describes the use of the Shubnikov-de Haas (SdH) oscillations to measure directly the gate-to-channel capacitance and the onset of the parallel conduction in AlGaAs/GaAs MODFET's. The SdH oscillations refer to oscillations of the drain current or transconductance of an FET in a magnetic field, as the magnetic field or the gate voltage is swept respectively (Ando et al 1982). The SdH measurements are immune to the parasitic capacitance and source-drain series resistances. One needs to know only the magnetic field, the gate voltage, and the SdH oscillation period.

### **2. The Shubnikov-de Haas oscillations**

When a magnetic field  $B$  is applied normal to the electron conduction plane of an n-channel MODFET, the energy of the quasi-two dimensional electrons in the channel becomes quantized. The energy levels  $E_n$ , so-called the Landau levels, are given (Landau and Lifshitz 1965) by

$$E_n = (n + \frac{1}{2})\hbar\omega, \quad (1)$$

where  $n=0, 1, 2, \dots$ , are the Landau level numbers,  $\hbar$  is the Planck constant divided by  $2\pi$ ,  $\omega = qB/m^*$  is the cyclotron frequency,  $q$  is the absolute value of the electron charge, and  $m^*$  is the effective mass of the electron.

As the Fermi level is swept, by varying the gate potential in a fixed magnetic field, across the Landau levels, the drain current peaks when the Fermi level and a Landau level are lined up, and dips when the Fermi level is between the two Landau levels. Therefore the drain current oscillates with the gate voltage. The oscillation is referred as the Shubnikov-de Haas Oscillation with the gate voltage (SdH-G). Similarly, the drain current can oscillate with the magnetic field at a fixed gate potential (SdH-M) as well, as the Landau levels are swept, by changing the magnetic field, across the fixed Fermi level.

In the SdH-G, the maximum number of electrons per unit area that each Landau level can accommodate,  $\Delta N$ , is fixed and given by (Landwehr 1975)

$$\Delta N = \frac{g_v q B}{\pi \hbar} \quad (2)$$

where  $g_v$  is the valley degeneracy of a semiconductor, which is 1 for GaAs and 2 for (100) Si (Note). When the gate voltage,  $V_{GS}$ , is well above the threshold voltage,  $V_T$ , of the device, the number of electrons per unit area in the channel is related to the gate-to-channel capacitance,  $C$ , by

$$N = \frac{C}{q}(V_{GS} - V_T) \quad (3)$$

Thus,

$$\Delta N = \frac{C}{q} \Delta V_{GS} \quad (4)$$

where  $\Delta V_{GS}$  is the increment of gate voltage necessary to create  $\Delta N$ , and equals the spacing between adjacent oscillation peaks (Note that at low temperatures electrons fill energy states up to the Fermi level). Equating Eqs. (2) and (4), we have

$$C = \frac{g_v q^2}{\pi \hbar} \left( \frac{B}{\Delta V_{GS}} \right) \quad (5)$$

or

$$C = 7.72 \times 10^{-9} g_v \left( \frac{B}{\Delta V_{GS}} \right) \text{ F/cm}^2 \quad (5a)$$

where  $B$  is in tesla, and  $\Delta V_{GS}$  is in volts. Experimentally, both  $B$  and  $\Delta V_{GS}$  can be measured with good precision, and therefore the gate-to-channel capacitance,  $C$ , of a device can be extracted directly.

The gate-to-channel capacitance,  $C$ , of a MODFET consists of two parts: (1) the capacitance due to the thickness,  $Z_i$ , of the AlGaAs layer, and (2) the capacitance due to the average distance,  $Z_{av}$ , between the channel electrons and the semiconductor interface. It is important to note that  $Z_{av}$  is a function of gate bias, but for  $V_{GS} \gg V_T$  it does not vary appreciably. The capacitance is related to the above two distances by

$$\frac{1}{C} = \frac{Z_i}{\epsilon_i} + \frac{Z_{av}}{\epsilon_{ac}} \quad (6)$$

where  $\epsilon_{ac}$  is the dielectric constant of GaAs, and  $\epsilon_i$  is the dielectric constant of AlGaAs. Having measured  $C$  by the SdH, the  $Z_{av}$  can be extracted if  $Z_i$  is determined using other methods, or vice versa.

In the SdH-M measurement, the Fermi level,  $E_F$ , is fixed and so is the electron density in the channel. Then the period of  $1/B$  is, from Eq. (1), constant and given by

$$\Delta\left(\frac{1}{B}\right) \equiv \left(\frac{1}{B_n}\right) - \left(\frac{1}{B_{n+1}}\right) = \frac{q\hbar}{mE_F} = \frac{g_v q}{\pi\hbar N} \quad (7)$$

Rewriting Eq. (7), we have

$$N = \frac{g_v q}{\pi\hbar\Delta(1/B)} \quad (8)$$

or

$$N = 4.83 \times 10^{10} \frac{g_v}{\Delta(1/B)} \text{ cm}^{-2} \quad (8a)$$

which means that the electron density in the channel can be determined from the period  $\Delta(1/B)$ . By measuring  $V_{GS}$  and  $\Delta(1/B)$ , we can make a plot of  $N$  vs.  $V_{GS}$ . If  $C$  is independent of gate voltage, as can be seen from Eq. (3), the plot is a straight line and the slope is the gate-to-channel capacitance. When parallel conduction in the low mobility AlGaAs layer in a AlGaAs/GaAs MODFET begins,  $C$  becomes a function of gate voltage, and drops with increasing gate voltage. In this case, the  $N$  vs.  $V_{GS}$  curve deviates from a straight line. The onset of parallel conduction can thus be determined from the start of that deviation.

The requirements for observation of the SdH oscillations are that the thermal energy broadening,  $kT$ , and the scattering-induced energy broadening,  $\hbar/\tau$ , be smaller than the Landau level spacing,  $\hbar\omega$ , where  $k$  is the Boltzmann constant,  $T$  is the temperature, and  $\tau$  is the momentum relaxation time. This implies that the SdH measurement has to be carried out at low temperatures, and that a device has to have a reasonable mobility. The specific values of temperature and mobility that are necessary to observe the SdH oscillation can be estimated from  $\hbar\omega > kT$  and  $\hbar\omega > \hbar/\tau$  respectively. These expressions give the following two criteria for observing SdH oscillations:  $T < 1.3B/(m^*/m_0)$  K and  $\mu > 10^4/B$  cm<sup>2</sup>/V-sec, where  $B$  is in Tesla and  $m_0$  is the free electron mass.

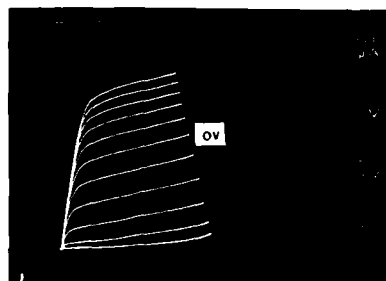
From the observation criteria, it can be seen that, except at extremely high magnetic fields, neither the electrons in the heavily doped AlGaAs layer nor the electrons in the  $n^+$  regions contribute to the SdH oscillation because of their low mobilities. The fact that electrons in  $n^+$  region move in a 3-dimensional space also prevents them contributing to the SdH oscillations. Therefore, the SdH measurements are immune to parasitic capacitance and series resistance.

### 3. Experimental

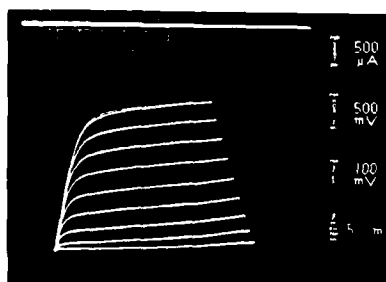
The modulation-doped layers used in this study was grown by molecular beam epitaxy (MBE) on Cr-doped semi-insulating (100) GaAs substrate. The growth temperature was 610 °C. The modulation-doped structure consists of a 1  $\mu\text{m}$  GaAs buffer, 5 nm thick undoped  $\text{Al}_{0.3}\text{Ga}_{0.7}\text{As}$  spacer, a 35 nm thick Si-doped ( $1 \times 10^{18} \text{ cm}^{-3}$ )  $\text{Al}_{0.3}\text{Ga}_{0.7}\text{As}$  layer, and a 15 nm thick  $n^+$ -GaAs cap layer. The grown layer has a Hall mobilities of 4500  $\text{cm}^2/\text{V-s}$  and 41,400  $\text{cm}^2/\text{V-s}$  at 300 K and 77 K respectively. AuGe(70 nm)-Ni(15 nm)-Au(60 nm) was deposited and alloyed to form ohmic contacts. Mesa isolation and gate recess were then performed by wet chemical etching. Finally, Ti(60 nm)-Pt(15 nm)-Au(80 nm) gate was deposited by lift-off technique. The drain I-V characteristics of a 1  $\mu\text{m}$  gate device at 300 K and 77 K are shown in Fig. 1. For 1  $\mu\text{m}$  gate devices, the maximum transconductances measured were 210 mS/mm and 310 mS/mm at 300 K and 77 K respectively. The highest transconductance for 5  $\mu\text{m}$  gate devices at 300 K was 120 mS/mm.

The SdH measurements were carried out at low temperatures ( $\sim 1.2\text{K}$ ) in a Bitter magnet. Both the conductance and the transconductance of devices were directly measured using a lock-in amplifier. The source-drain voltage was kept less than the Landau level spacing, i.e. a few millivolts, to avoid the electron transition between the Landau levels. The SdH-G oscillations of a 5- $\mu\text{m}$  gate-length AlGaAs/GaAs MODFET at different magnetic fields are shown in Fig. 2. When the gate voltage is below -0.1 V, the transconductance oscillates periodically with the gate voltage, and the spacing between the peaks is constant. From the spacing of the peaks, the gate-to-channel capacitance calculated from Eq. (5) are  $1.96 \times 10^{-7} \text{ F/cm}^2$  at  $B=2.5 \text{ T}$ , and  $1.90 \times 10^{-7} \text{ F/cm}^2$  at  $B=3\text{T}$ . As expected, the capacitance is independent of the magnetic field within the experimental error.

Having the gate-to-channel capacitance and knowing the total  $\text{Al}_{0.3}\text{Ga}_{0.7}\text{As}$  thickness,  $Z_i$ , from the growth parameters, one can calculate the average distance of electrons from the interface,  $Z_{av}$ , if the dielectric constants are known. The dielectric constant of  $\text{Al}_{0.3}\text{Ga}_{0.7}\text{As}$  was obtained by a linear interpolation between the dielectric constants of GaAs and AlAs



(a)



(b)

Fig. 1. The I-V characteristics of a 1  $\mu\text{m}$  gate MODFET, at (a) 300 K, and (b) 77 K.

(Casey and Panish 1978). The dielectric constants,  $\epsilon_s$ , of GaAs and AlAs at 1.3 K were obtained from (Strzalkowski et al 1976)

$$\epsilon_s = \epsilon_s(T=0) + 2.5 \times 10^{-3}T,$$

where  $\epsilon_{\text{GaAs}}(T=0)=12.35$  and  $\epsilon_{\text{AlAs}}(T=0)=9.31$ . Using  $C = 1.93 (\pm 0.03) \times 10^{-7} \text{ F/cm}^2$ ,  $Z_i = 40 \text{ nm}$ , and  $\epsilon_s$  of  $\text{Al}_{0.3}\text{Ga}_{0.7}\text{As} = 11.44$ , one finds that  $Z_{av} = 13.5 \pm 2 \text{ nm}$ .

In the SdH-M measurement, the  $B$  field was swept, while the gate voltage was fixed. Figure 3 shows the drain current of the  $5\text{-}\mu\text{m}$ -gate-length MODFET vs. magnetic field at two different gate voltages. The electron density was calculated from the oscillation period  $\Delta(\frac{1}{B})$ , and is plotted against  $V_{GS}$  in Fig. 4. It can be seen that once parallel conduction starts, the electron density in the channel almost ceases to increase with increasing  $V_{GS}$ . From the linear part of the curve, the gate-to-channel capacitance is determined to be  $1.65 \times 10^{-7} \text{ F/cm}^2$ , which is about 15% smaller than that measured by the SdH-G method. This difference can be explained by the fact that the parallel conduction starts before  $V_{GS}=0$ , as indicated in the SdH-G measurement, where the oscillation period of the transconductance becomes larger when  $V_{GS}$  is greater than the  $-0.1 \text{ V}$ . Had we had more data points below  $V_{GS}=-0.1 \text{ V}$ , the capacitances measured by the SdH-G and the SdH-M should be the same. Figure 5 shows the  $N$  vs.  $V_{GS}$  curves of an enhancement-mode  $5\text{-}\mu\text{m}$ -gate MODFET with a different threshold voltage and different threshold for onset of parallel conduction. Again, the  $N$  curve bends very sharply once parallel conduction starts.

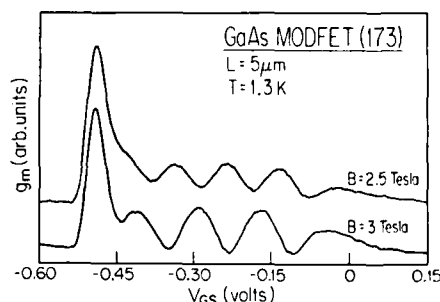


Fig. 2. The SdH oscillations of transconductance  $g_m$  with gate voltage  $V_{GS}$  for a  $5\text{-}\mu\text{m}$ -gate MODFET at different magnetic fields, and  $V_{DS} = 1 \text{ mV}$ .

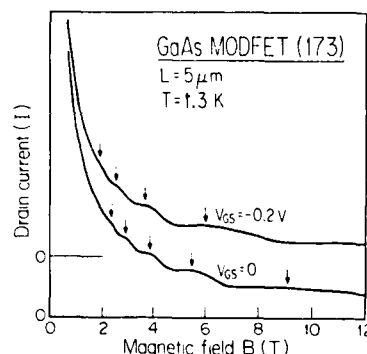


Fig. 3. The SdH oscillations of the drain current  $I$  with magnetic field  $B$  for a  $5\text{-}\mu\text{m}$ -gate MODFET at different gate voltages.

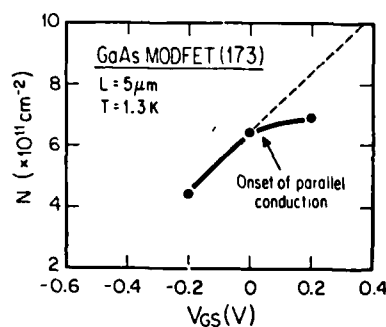


Fig. 4. The electron density  $N$  in the channel of a  $5\text{-}\mu\text{m}$ -gate MODFET vs. the gate voltages  $V_{GS}$ .

#### 4. Conclusion

We have demonstrated that the Shubnikov-de Haas oscillations can be used to measure directly the gate-to-channel capacitance, to measure the carrier density in the channel, and to detect the onset of parallel conduction in Al-GaAs/GaAs MODFET's. The SdH measurements do not require knowledge of device parameters, and are immune to the gate parasitic capacitance and source-drain series resistance. When the magnetic field is known, it is only required to measure the oscillation period with gate voltage to determine the gate-to-channel capacitance. Then the onset of parallel conduction can be determined from the  $V_{GS}$  at which  $C$  starts decreasing. The characterization methods can be applied to MODFET's fabricated in other materials.

#### Acknowledgment

The measurements were carried out at the National Magnetic Lab at M.I.T. D. Syphers, J. Brooks, L. Rubin and R. Higgins are acknowledged for their assistance. Helpful discussions with Z.Z. Gun, D. Syphers, M.A. Kastner and A.C. Warren are gratefully acknowledged. SYC would like to thank T.W. Sigmon, R.F.W. Pease, and R.W. Dutton for the encouragement and support during the manuscript preparation. CSL would like to thank K. Ismail for his helpful discussions. This work was sponsored by the Joint Services Electronics Program.

#### References

- Ando T, Fowler A B and Stern F 1982 "Electronic Properties of Two-Dimensional System," *Rev. Mod. Phys.*, **54**, No. 2, p437-672
- Casey H C and Panish M B 1978 "Heterostructure Lasers": Part A, Academic, New York
- Landau L D and Lifshitz E M 1965 *Quantum Mechanics*, Pergamon, 2nd ed., p424
- Landwehr G 1975 *Festkorperprobleme*, XV, *Advances in Solid State Physics*, ed. by H.J. Queisser, p9
- Note: The spin degeneracy equal to two is included in Eq. 2, and the interaction of spin and magnetic field (i.e. the spin splitting) is assumed to be negligible compared to Landau level spacing.
- Strzalkowski I, Joshi S and Crowell C R 1976 *Appl. Phys. Lett.* **28**, 350.

\* Department of Physics. Present address is Department of Electrical Engineering, Stanford University, Stanford CA 94305.

\* Department of Electrical Engineering and Computer Science.

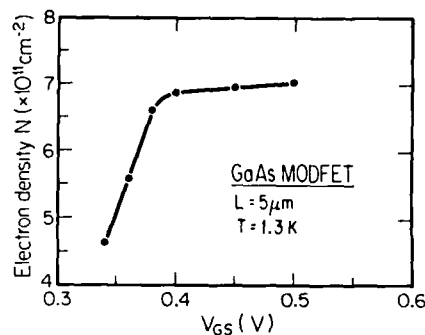


Fig. 5. The electron density  $N$  in the channel of an enhanced-mode 5- $\mu\text{m}$ -gate MODFET of different threshold voltage vs. the gate voltages  $V_{GS}$ .



## **Growth parameter dependence of 2DEG mobility in selectively doped n-AlGaAs/GaAs grown by MO-CVD**

H. Tokuda, A. Tanaka, H. Kawasaki, I. Inami, M. Higashiura, S. Hori and K. Kamei

Microwave Solid-State Department, Komukai Works, Toshiba Corporation  
1, Komukai Toshiba-cho, Saiwai-ku, Kawasaki 210, Japan

**Abstract.** Growth parameter dependence of 2DEG mobility in selectively doped n-AlGaAs/GaAs was investigated for wafers grown by MO-CVD. The most characteristic parameter on the 2DEG mobility was found to be  $[V]/[III]$  ratio. The mobility increased with increasing  $[V]/[III]$  ratio, while sheet carrier concentration was constant. A low noise HEMT fabricated on a wafer grown at optimized conditions showed minimum noise figures of 0.77 and 1.18 dB with associated gains of 11.5 and 9.7 dB at 12 and 18 GHz, respectively.

### **1. Introduction**

High electron mobility transistors (HEMTs) have shown the superiority to GaAs MESFETs as a microwave low noise devices (Kamei et al. 1985). Almost all of the developed HEMTs reported so far have been using wafers grown by MBE. MO-CVD is another approach for growing wafers for HEMT, and it is potentially superior to MBE in terms of surface morphology and productivity. Recently, Tanaka et al. (1986) reported on low noise characteristics of HEMT using the wafers grown by MO-CVD. The reported noise figure of 0.87 dB at 12 GHz is encouraging for the utilization of MO-CVD to the growth of HEMT wafers. Up to present, however, little is known on the relations between growth parameters and the performance of HEMTs, and more efforts toward the optimization of growth parameters are needed to improve the HEMT performance.

In this paper, growth parameter dependence of 2-dimensional electron gas (2DEG) mobility in selectively doped n-AlGaAs/GaAs structure grown by MO-CVD is described. HEMTs were fabricated on the wafers grown at different  $[AsH_3]/[TMG]$  or  $[AsH_3]/([TMG]+[TMA])$  ( $[V]/[III]$ ) ratios, and the relations between  $[V]/[III]$  ratios and dc and microwave characteristics of HEMTs are also described.

### **2. Epitaxial growth and measurements of 2DEG mobility**

The MO-CVD apparatus used through this work was a vertical type reactor operating under atmospheric pressure. The source materials were trimethyl gallium (TMG), trimethyl aluminum (TMA) and arsine ( $AsH_3$ ). Silane was used as a dopant gas. The growth temperature was monitored by the thermocouple which was placed in the graphite susceptor. To achieve an abrupt AlGaAs/GaAs interface, growth was carried out under high gas velocity of 50 cm/s and low growth rate of 3 Å/s.

A 0.5  $\mu\text{m}$ -thick undoped GaAs layer, 10 or 50  $\text{\AA}$ -thick undoped AlGaAs spacer layer, 300  $\text{\AA}$ -thick n-AlGaAs layer and 400  $\text{\AA}$ -thick n-GaAs cap layer were successively grown on semi-insulating Cr-doped GaAs substrates. The content of Al in the AlGaAs layers was fixed to be 0.3. In the growth, the following three growth parameters were varied and the dependences of 2DEG mobility and sheet carrier concentration on each parameter were investigated; (i)  $\text{SiH}_4$  mole fraction during the growth of n-AlGaAs and n-GaAs layers, (ii) growth temperature and (iii)  $[\text{V}]/[\text{III}]$  ratio (from now on,  $[\text{V}]/[\text{III}]$  ratio is defined as  $[\text{AsH}_3]/[\text{TMG}]$ ).

The mobility and sheet carrier concentration of the 2DEG were determined by the following procedure. The depth profiles of mobility and sheet carrier concentration ( $n_s$ ) were measured using van der Pauw method for each successive step etching. Figure 1 shows an example of the measured profiles. The mobility shows a peak when etched to a depth of 500  $\text{\AA}$  from the surface. The peak mobility and corresponding  $n_s$  are considered to be those of the 2DEG. This can be understood as follows. When the etching depth is shallow so that n-GaAs layer still remains, parallel conduction through n-GaAs, n-AlGaAs and 2DEG layers occur. Since the mobilities of n-GaAs and n-AlGaAs layers are lower than that of 2DEG (Hiyamizu et al. 1981), the measured mobility is lower than the 2DEG mobility itself. With further etching, the contribution of n-GaAs layer conduction decreases, hence the measured mobility increases and the measured  $n_s$  decreases. When the n-GaAs layer is etched off and electrons in the n-AlGaAs layer are depleted, the measured mobility and  $n_s$  coincide with those of 2DEG. The 2DEG mobility begins to decrease with further etching since it decreases with a decrease of  $n_s$  (Mimura 1982). Therefore, the depth profile of the mobility is expected to show a peak where the measured mobility and  $n_s$  correspond to those of 2DEG. The accuracy of measured sheet electron concentration was checked by using the simulation programs developed by Yoshida (1986). It was found that the difference between the measured values and calculated ones was within 30 % at most.

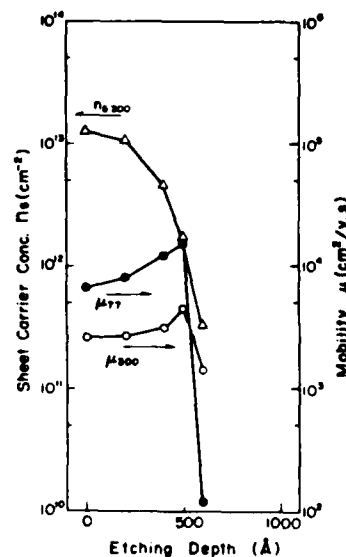


Fig. 1 Depth profiles of sheet carrier concentration at 300 K and mobilities at 300 K and 77 K for a selectively doped wafer.

### 3. Growth parameter dependences of 2DEG mobility and sheet carrier concentration

Dependences of the 2DEG mobility and  $n_s$  on  $\text{SiH}_4$  mole fraction are shown in Fig. 2. In this case, the spacer layer thickness, the growth temperature and  $[\text{V}]/[\text{III}]$  ratio were 10  $\text{\AA}$ , 640  $^\circ\text{C}$  and 120, respectively. The  $\text{SiH}_4$  mole fraction was varied from  $1 \times 10^{-7}$  to  $4 \times 10^{-1}$ , which corresponds to the carrier concentration of  $1 \times 10^{10}$  and  $4 \times 10^{18} \text{ cm}^{-3}$  in n-AlGaAs layer, respectively. With the increase of  $\text{SiH}_4$  mole fraction (carrier concentration of n-AlGaAs layer),  $n_s$  increased and the mobility decreased. This dependence is understood by considering the scattering of electrons by Si donors in AlGaAs layer (Ando 1982). From our experiments on fabricating HEMTs, it was found that

$n_s$  over  $1.5 \times 10^{12} \text{ cm}^{-2}$  was required to attain a low resistive ohmic contacts and high transconductance. Therefore,  $\text{SiH}_4$  mole fraction was chosen to be  $2 \times 10^{-1}$  for the HEMT wafers in order to keep  $n_s$  higher than  $1.5 \times 10^{12} \text{ cm}^{-2}$  and to make the mobility as high as possible.

Figure 3 shows the dependences of 2DEG mobility and  $n_s$  on the growth temperature, where the spacer layer thickness,  $[\text{V}]/[\text{III}]$  ratio and  $\text{SiH}_4$  mole fraction were 50 Å, 120 and  $2 \times 10^{-1}$ , respectively. Increasing the growth temperature,  $n_s$  increased while the mobility decreased. The measured carrier concentration of the AlGaAs layer was found to vary from  $2 \times 10^{18}$  to  $4 \times 10^{18} \text{ cm}^{-3}$  when the growth temperature increased from 640 to 680 °C. Therefore, the growth temperature dependence shown in Fig. 3 is due to the change of the carrier concentration in AlGaAs layer which was brought about by the change of doping efficiency with the growth temperature. For  $n_s$ ,  $1.5 \times 10^{12} \text{ cm}^{-2}$  was obtained by decreasing the spacer layer thickness to 10 Å.

The dependences of the 2DEG mobility and  $n_s$  on  $[\text{V}]/[\text{III}]$  ratio are shown in Fig. 4, where the spacer layer thickness, growth temperature and  $\text{SiH}_4$  mole fraction were 50 Å, 640 °C and  $2 \times 10^{-1}$ , respectively. The inter-dependent behavior between the mobility and  $n_s$  is quite different from those shown in Figs. 2 and 3. The 2DEG mobility increased with increasing  $[\text{V}]/[\text{III}]$  ratio while  $n_s$  was almost constant. To investigate the origin of the monotonic increase of mobility, van der Pauw and photo-

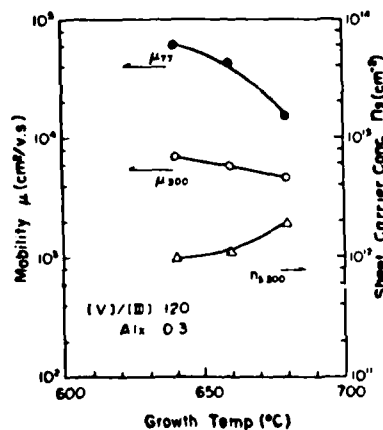


Fig. 3 Dependences of  $n_s$  and 2DEG mobility on the growth temperature. Spacer layer thickness is 50 Å.

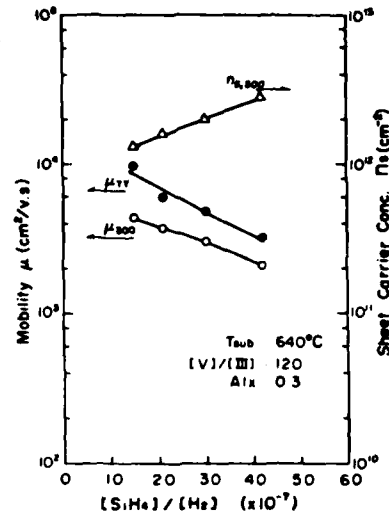


Fig. 2 Dependences of  $n_s$  and 2DEG mobility on  $\text{SiH}_4$  mole fraction. Spacer layer thickness is 10 Å.

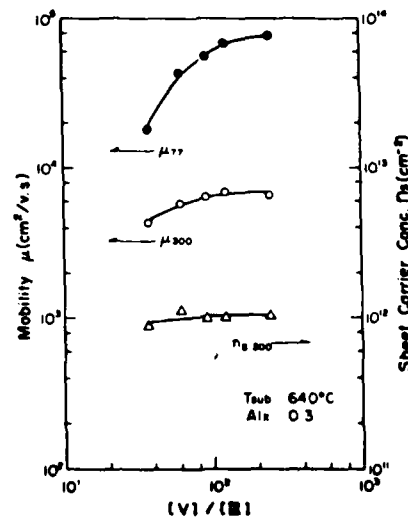


Fig. 4 Dependences of  $n_s$  and 2DEG mobility on  $[\text{V}]/[\text{III}]$  ratio. Spacer layer thickness is 50 Å.

luminescence (PL) measurements of undoped GaAs layers were performed. The measured samples were undoped GaAs layers with the thickness of 1  $\mu\text{m}$  grown at different [V]/[III] ratios, which were prepared independent of selectively doped wafers. Figure 5 shows the results of van der Pauw measurements. The carrier concentrations (conduction types) of  $5 \times 10^{13}$  (p-type),  $1 \times 10^{14}$  (p-type),  $7 \times 10^9$  (n-type) and  $7 \times 10^{15}$  (n-type) and the mobilities of 500, 750, 8100 and 3700  $\text{cm}^2/\text{V}\cdot\text{s}$  were observed at [V]/[III] ratios of 30, 60, 120 and 240, respectively, at room temperature. This result shows that the total impurity concentration in the layer becomes lowest at around [V]/[III]=120, and it increases at lower and higher [V]/[III] ratios than that (Nakanishi et al. 1981). From the PL measurements, carbon signal was detected for the wafers grown at [V]/[III]=30, 60, 120 and was not detected at [V]/[III]=240. The intensity of carbon signal decreased rapidly with the increase of [V]/[III] ratio. These results of van der Pauw and PL measurements suggest that the 2DEG mobility is dominated by the carbon acceptor concentration instead of total impurity concentration in undoped GaAs layer.

#### 4. [V]/[III] dependence of HEMT performance

As is discussed in the preceding section, [V]/[III] ratio seems to be a key parameter for the improvement of HEMT performance because it can increase the mobility while keeping  $n_s$  constant. Therefore, we have fabricated HEMTs using the wafers grown at [V]/[III]=30, 60, 120 and 240. All the wafers were grown at  $640^\circ\text{C}$ ,  $2 \times 10^{-3}$   $\text{SiH}_4$  mole fraction, and had the spacer layer thickness 15  $\text{\AA}$ . The n-GaAs cap layer was thickened to 600  $\text{\AA}$  to ensure the low resistive ohmic contacts. Each wafer showed the mobility at room temperature to be 2040, 340, 8910 and 4300  $\text{cm}^2/\text{V}\cdot\text{s}$  at respective [V]/[III] ratios. The sheet carrier concentration was  $1.5 \times 10^{13} \text{ cm}^{-2}$  for all the wafers. The fabrication process and the device structure were almost the same as those reported by Kamel et al. (1985). The gate length, gate width and source to drain spacing were 0.35  $\mu\text{m}$ , 100  $\mu\text{m}$  and 2  $\mu\text{m}$ , respectively. Ni/AuGe was used for source and drain electrodes and Al/Ti for gate electrode.

Figure 6 shows the drain current/voltage characteristics of HEMTs fabricated from the wafers grown at different [V]/[III] ratios. In the figures, one should notice that the gate voltage step for [V]/[III]=120 is 0.1 V, while others are 0.5 V. The transconductance ( $g_m$ ) at  $V_{DS}=3 \text{ V}$ ,  $I_{DS}=1 \text{ mA}$  are about 16, 16, 40 and 9  $\text{mS}$  for [V]/[III] ratio of 30, 60, 120 and 240, respectively. The reduction of  $g_m$  near the pinch-off at [V]/[III]=30 and 240 is marked. This reduction of  $g_m$  is supposed to be explained by considering the current flowing through the undoped GaAs layer beneath the 2DEG channel, and reflecting the increase of carrier concentration which was measured by van der Pauw in the undoped GaAs layer. To evaluate the current flowing through the undoped GaAs layer, current/voltage characteristics between a source electrode on a mesa and another source electrode on a neighbouring mesa was measured. The distance between mesas is 20  $\mu\text{m}$ . Figure 7 shows the result where the leakage current between the electrodes biasing at 30 V is plotted against [V]/[III] ratio of the wafers. As is clearly seen in the figure, four orders

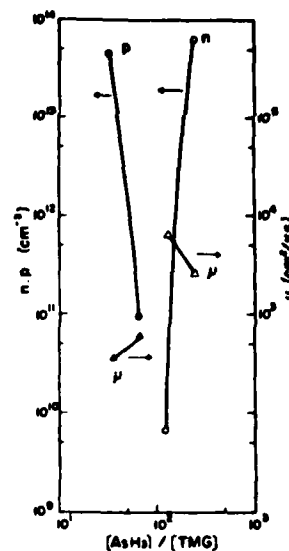


Fig. 5 Carrier concentration and Hall mobility at room temperature versus [V]/[III] ratio for undoped GaAs layers.

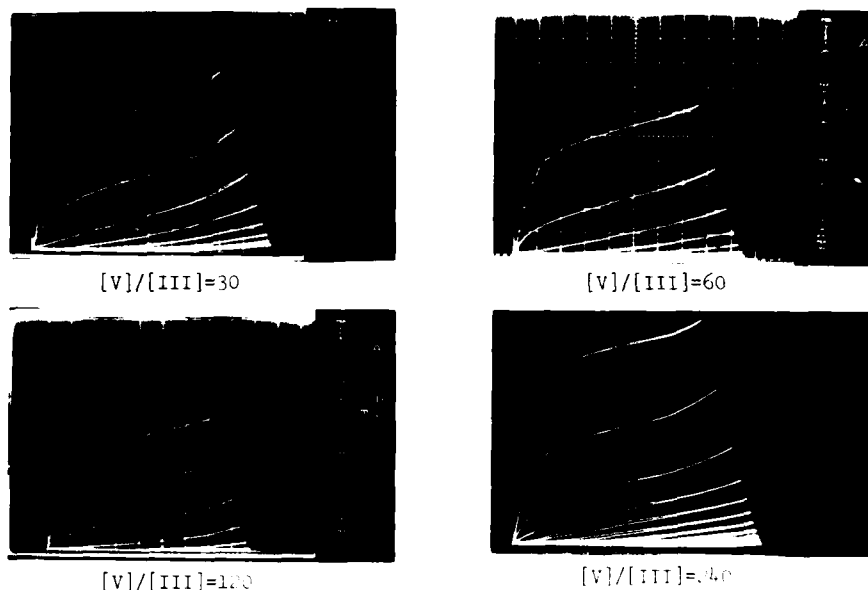


Fig. 6 Drain current-voltage characteristics of HEMTs fabricated from the wafers grown at different  $[V]/[III]$  ratios.

and three orders of magnitude higher current was observed for the wafers grown at  $[V]/[III]=4$ , and 1, respectively, as compared with  $[V]/[III]=10$ . Therefore, although the  $III$  mobility increased with increasing  $[V]/[III]$  ratio, the upper limit of  $[V]/[III]$  ratio should be determined by taking account of the undoped  $Si$  carrier concentration.

Microwave noise figures and associated gains at 1 GHz have been measured on each HEMT. The results are listed in Table 1. Reflecting the variation of  $\gamma$  near pinch-off shown in Fig. 1, noise figures become lower in order for the wafers grown at  $[V]/[III]=4, 10, 1$ , and 100. Minimum noise figure of 0.77 dB and associated gain of 11.5 dB were obtained for the wafer grown at  $[V]/[III]=10$ .

Measurements at 18 GHz were also carried out for the HEMTs of  $[V]/[III]=60$  and 100. The drain current dependence of noise figures and associated gains is shown in Fig. 2. Minimum noise figure of 1.15 dB and associated gain of 9.7 dB were obtained at  $I_{D0}=8$  mA for the HEMT of  $[V]/[III]=100$ . These are the best results ever reported on HEMTs fabricated from the wafers grown by Mo-CVD.

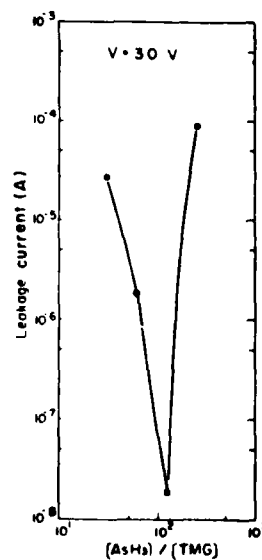


Fig. 7  $[V]/[III]$  ratio dependence of leakage current between source electrodes in the  $100^\circ\text{C}$  anneal period.

Table 1 Dependence of noise figures and associated gains of HEMTs at 18 GHz on [V]/[III] ratios.

| [V]/[III] | 30   | 60   | 120  | 240  |
|-----------|------|------|------|------|
| NF (dB)   | 1.35 | 0.81 | 0.77 | 2.18 |
| Ga (dB)   | 9.2  | 11.4 | 11.5 | 9.0  |

#### Conclusion

The optimization of the growth conditions by MO-CVD to improve the HEMT performance has been described. The key growth parameter for the optimization was found to be a [V]/[III] ratio, because [V]/[III] ratio is a parameter which makes it possible to increase the 2DEG mobility with keeping  $n_s$  constant. The highest value of [V]/[III] should be, however, limited so as not to increase the carrier concentration of undoped GaAs layer, which deteriorates pinch-off characteristics in the HEMTs. The fabricated HEMT using an optimized wafer exhibited an excellent low noise characteristics at 18 and 12 GHz. The obtained noise figures, though yet inferior to those obtained from the HEMTs grown by MBE, are very promising and show the possibility for applying the MO-CVD technique to the growth of HEMT wafers.

#### Acknowledgment

The authors would like to thank J. Okano for his encouragement throughout this work.

#### References

1. T. Itoh, *J. Appl. Phys.*, **61**, 379 (1987).
2. T. Itoh, T. Nishida, K. Mimura, T. Fujii, T. and Hashimoto, H. 1991 *Japan. J. of Applied Phys.*, **30**, L-77.
3. K. Kawanishi, H. Mori, K. Chikara, K. Higashimura, M. Watanabe, M. and Arai, Y. 1988 *Inst. Phys. Conf. Ser. No.*, **77**, 341.
4. T. Itoh, *J. Appl. Phys.*, **61**, 494 (1987).
5. T. Itoh, T. Nishida, T. Tanaka, A. and Kawanishi, K. 1991 *J. Cryst. Growth*, **95**, 177.
6. K. Kawanishi, H. Mori, K. Chikara, K. Higashimura, M. Watanabe, M. and Arai, Y. 1988 *Electron. Lett.*, **24**, 1400.
7. T. Itoh, *IEEE*, **EH-11**, 174 (1987).

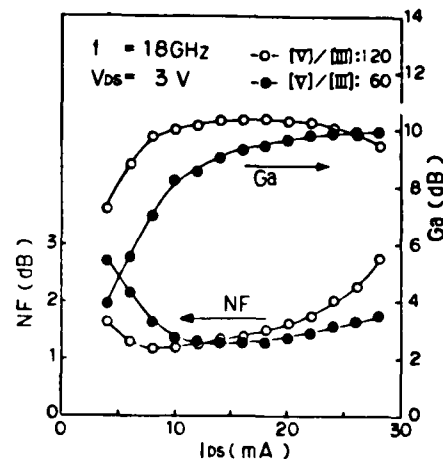


Fig. 2 Noise figures and associated gain versus drain current at 18 GHz for HEMTs grown at [V]/[III] = 20 and 60.

## **Characterization of simultaneous diffusions of zinc and indium into GaAs, and (AlAs)<sub>n</sub>(GaAs)<sub>m</sub> superlattice surfaces and its device applications**

J.R. Shealy\*, K. Kavanagh\*\* and P.M. Enquist  
School of Electrical Engineering, Phillips Hall  
\*\*Materials Science Department, Bard Hall

\* Cornell University, Ithaca, NY 14853  
\* and General Electric Company, Syracuse, NY 13221

**Abstract.** The characterization of a diffusion process which results in high concentrations of indium and zinc on GaAs and AlGaAs surfaces is described. These diffusions are carried out in a closed graphite box with InAs and ZnAs<sub>2</sub> sources in a H<sub>2</sub>/N<sub>2</sub> mixture. Under appropriate conditions large concentrations of Zn and In are obtained on the surface (approximately 10<sup>20</sup> cm<sup>-3</sup> of Zn and 10% InAs). The process has been used for obtaining low resistance p type contacts ( $\rho_c \sim 2 \times 10^{-7} \Omega \cdot \text{cm}^2$ ) to GaAs. This technique has also been applied to the fabrication of narrow stripe (3  $\mu\text{m}$ ) GRIN-SCH quantum well laser structures. These devices, which were diffused under conditions resulting in approximately 0.5  $\mu\text{m}$  of In penetration into the upper cladding regions, exhibit single mode operation over the full range of operating currents suggesting an index guiding mechanism originating from the In related strain field exists. Single mode output powers of 30 mW/facet (CW) were obtained on lasers with uncoated facets.

### Introduction

The simultaneous diffusion of zinc and indium into GaAs is a new approach for obtaining low resistance contacts to p type GaAs. The technique produces the alloy Ga<sub>0.9</sub>In<sub>0.1</sub>As on the diffused surface which results in the reduction of the bandgap, improving the tunneling probability at the metal semiconductor interface. Non-alloyed contacts to GaAs were measured to be as low as  $2 \times 10^{-7} \Omega \cdot \text{cm}^2$  after pulse annealing. [Shealy and Chinn 1985]

In this study, the diffusion profiles and concentrations of Zn and In have been examined using SIMS and RBS. Penetration depths have been controlled over a broad range from 1000 Å to several microns by varying the diffusion temperature over the range from 575 to 650°C.

A new type of index guided laser has been realized with a simple planar stripe geometry by diffusing Zn and In into the upper cladding region of a GRIN-SCH quantum well laser

structure through a  $3\ \mu$  opening in a pyrolytic  $\text{Si}_3\text{N}_4$  mask.

### Experimental

A series of diffusions were carried out on GaAs,  $(\text{AlAs})_{20}(\text{GaAs})_{100}$ ,  $(\text{AlAs})_2(\text{GaAs})_2$ , and  $\text{Al}_{0.5}\text{Ga}_{0.5}\text{As}$  surfaces. The surface concentrations and penetration depths of In and Zn were evaluated by RBS and SIMS data on each of these samples. When the diffused regions were selective, pyrolytic  $\text{Si}_3\text{N}_4$  was deposited as the mask by the decomposition of dichlorosilane and ammonia at  $675^\circ\text{C}$  and 100 mTorr in a nitrogen background gas. These films were of high quality compared to conventional plasma deposited  $\text{Si}_3\text{N}_4$  films as demonstrated by low pinhole densities on films as thin as  $200\ \text{\AA}$  and by low buffered HF etch rates ( $\sim 5\ \text{\AA}/\text{min}$ ) suggesting a high density  $\text{Si}_3\text{N}_4$  film. The index of refraction of the pyrolytic  $\text{Si}_3\text{N}_4$  was typically in the range from 2.0 to 2.1. The superlattice structures were produced by the multichamber OMVPE process discussed in an earlier publication. [Shealy 1986]

The GRIN SCH lasers were grown in a horizontal reactor at 76 Torr. The upper and lower cladding regions were  $1.75\ \mu\text{m}$  of  $\text{Al}_{0.6}\text{Ga}_{0.4}\text{As}$ . The GRIN regions were  $2500\ \text{\AA}$  of linearly graded  $\text{Al}_x\text{Ga}_{1-x}\text{As}$  ( $x = 0.60$  to  $x = 0.20$ ). The quantum well was  $150\ \text{\AA}$  of GaAs. Further details of the growth conditions and layer structure are reported in [Schaus et al 1985].

Narrow stripe lasers were processed by depositing pyrolytic  $\text{Si}_3\text{N}_4$  ( $700\ \text{\AA}$  thickness) and patterning  $3\ \mu\text{m}$  openings followed by plasma etching in  $\text{CF}_4/\text{O}_2$  and the In/Zn diffusion. The wafers were then thinned, metallized, cleaved into  $300\ \mu\text{m}$  cavities and tested.

The simultaneous diffusion of zinc and indium into these laser structures was performed in a sealed graphite box using InAs and  $\text{ZnAs}_2$  sources. Details of the experimental apparatus and conditions have been previously described. Three different diffusion temperatures ( $575^\circ\text{C}$ ,  $600^\circ\text{C}$  and  $650^\circ\text{C}$ ) were employed for 15 minutes to observe the effects of In and Zn penetration on laser performance. It was determined that the higher temperature diffusion resulted in  $0.5\ \mu\text{m}$  of In penetration and  $1.5\ \mu\text{m}$  of Zn penetration. It is important to note that the lateral Zn diffusion effectively broadened the stripe width from  $3\ \mu\text{m}$  to  $6\text{--}7\ \mu\text{m}$ .

### Results and Discussion

The results using this process and the masking ability of the pyrolytic  $\text{Si}_3\text{N}_4$  are illustrated by the SIMS data given in Figs. 1(a) and (b). The profile shown in Figure 1(a) represents a shallow Zn/In diffused GaAs surface. The diffusion conditions given resulted in a Zn penetration depth of approximately  $3000\ \text{\AA}$  while indium has diffused approximately  $800\ \text{\AA}$ . Also, the concentration of Zn is seen to be largest where the indium has diffused suggesting a strong interaction between the Zn and In diffusing species possibly due to strain.



In Fig. 1(b), the data given is that of a masked surface (1500 Å of  $\text{Si}_3\text{N}_4$ ) which has undergone the longest time and highest temperature cycle diffusion used in this study. A penetration of Zn and In into the  $\text{Si}_3\text{N}_4$  surface is barely visible and is estimated to be less than 200 Å. These conditions resulted in relatively deep Zn and In penetration in unmasked GaAs surfaces as shown by the corresponding data given in Fig. 2(a).

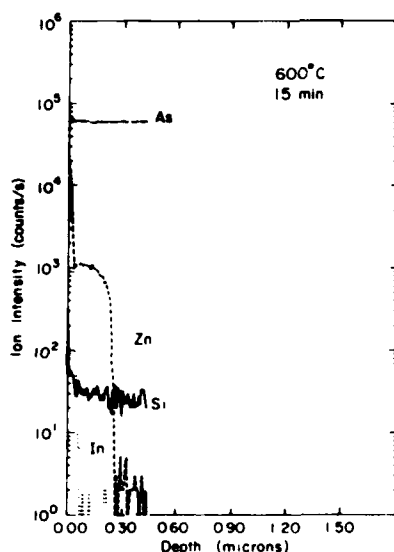


Fig. 1(a). Sims profile of a Zn/In diffused GaAs surface. The GaAs sample was doped  $2 \times 10^{18} \text{ cm}^{-3}$  with silicon.

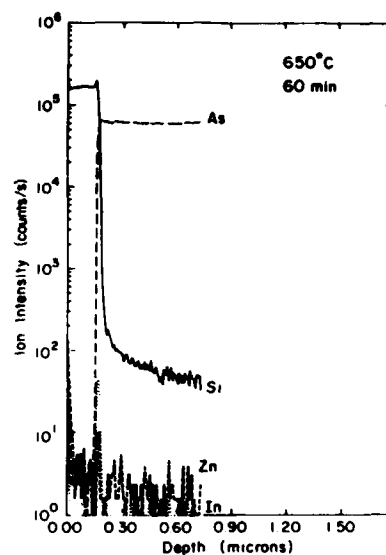


Fig. 1(b). Sims profile of a 2000Å thick pyrolytic  $\text{Si}_3\text{N}_4$  film deposited on GaAs after an anneal in the Zn/In diffusion apparatus.

A summary of the results of Zn/In diffused GaAs surfaces appears in Figures 2(a) and 2(b). The penetration depths are controlled over several thousand angstroms by varying the time-temperature cycle. Typically, the Zn is observed to penetrate approximately four times deeper than the In as shown. Although in Zn surface concentration was observed to be relatively constant with temperature (in the range of  $4 \times 10^{19} - 10^{20} \text{ cm}^{-3}$ ), a strong temperature dependence for the In surface concentration was observed as shown in Figure 2(b). It is interesting to note that the best p type ohmic contacts were obtained at 650°C where the In surface concentration is the highest.

In Figure 3, Rutherford backscattering spectra (75° tilt) are shown for a GaAs/AlAs superlattice comparing the as grown sample to a sample annealed at 575°C for 15 min. in the In/Zn diffusion apparatus. The superlattice consisted of 40 layers 5 of which are seen by RBS in the as grown case before beam straggling destroys the depth resolution. The superlattice period was 270/50 Å GaAs/AlAs, respectively. The anneal has clearly mixed the superlattice. The In peak is observable but expanded 40 times in the figure. The total In sheet concentration was  $1.3 \times 10^{15}$  atoms/cm<sup>2</sup> with a InAs surface concentration of approximately 0.02. The depth of the In was approximately 700 Å in reasonable agreement with the SIMS data. Also the indium penetration was less than the detectable mixing of the superlattice, presumably the work of the Zn as has been previously reported. [Laidig et al. 1981]

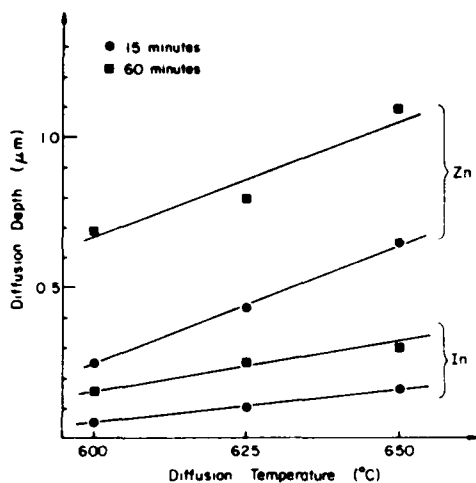


Fig. 2(a). Penetration depth of Zn and In in GaAs versus diffusion temperature at the indicated times.

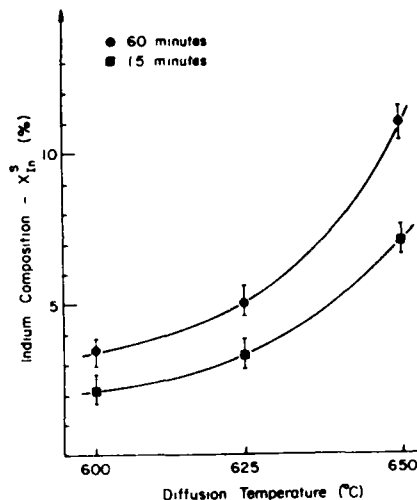


Fig. 2(b). Variation of InAs concentration on the diffused GaAs surface vs. diffusion temperature for the indicated times.

The diffusion rates in the superlattice structures and AlGaAs were observed to be significantly faster compared to those in GaAs as expected from the results of previous studies. [Blum et al. 1983; Ageno et al. 1985] The data shown in Figure 4, also indicates a higher Zn diffusion rate for an  $\text{Al}_{0.5}\text{Ga}_{0.5}\text{As}$  compared with the superlattice  $(\text{GaAs})_2(\text{AlAs})_2$ . Apparently the action of disordering the superlattice interfaces reduces the Zn diffusion rate. However, since the zinc diffuses much deeper than the indium, the indium diffuses through a mixed AlGaAs crystal in both cases and, as a result, no differences within experimental error were seen for indium penetration in bulk AlGaAs or superlattices of the same average Al content.

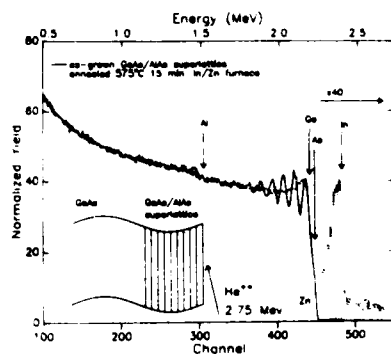


Fig. 3. Rutherford backscattering spectra comparing a superlattice of  $(\text{AlAs})_4(\text{GaAs})_4$  before and after a Zn/In diffusion for 15 min. at  $575^\circ\text{C}$ .

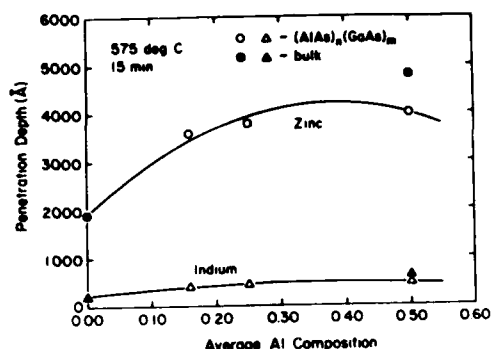


Fig. 4. Penetration depths of Zn and In in GaAs, AlGaAs and superlattice sample vs. average aluminum composition  $(n/(n+m))$ .

As mentioned earlier, this diffusion technique was applied to the fabrication of narrow stripe lasers using the pyrolytic  $\text{Si}_3\text{N}_4$  mask. The diffusion temperature had a strong influence on the electrical properties of these lasers above threshold. Namely, the specific "on resistance" was measured to be  $1.1 \times 10^{-5}$ ,  $5.5 \times 10^{-6}$ , and  $3.0 \times 10^{-6} \Omega \cdot \text{cm}^2$  for devices whose corresponding diffusion temperature was  $575^\circ\text{C}$ ,  $600^\circ\text{C}$ , and  $650^\circ\text{C}$ , respectively. This reduction in the diodes series resistance is attributed primarily to an improving p type ohmic contact as the diffusion temperature is increased (larger In surface concentration). The p type cladding layers' contribution to the series resistance was also reduced by the deep Zn penetration at the higher temperatures used. However, this contribution was small as the resistivity of the upper cladding region was approximately  $10^{-2} \Omega \cdot \text{cm}$  prior to the diffusion.

The lasers which were fabricated under the different diffusion conditions were tested p side up, pulsed ( $1 \mu\text{s}$ ) and CW, for their emission spectrum, far field pattern, and output power. The threshold currents and differential quantum efficiencies exhibited little dependence on the diffusion cycle used, and were typically 75 mA and 60%. These threshold currents were determined to reflect a significant amount of lateral current spreading as narrow mesa devices of the same cavity length had threshold current as low as 15 mA.

The devices diffused at  $650^\circ\text{C}$  exhibited single mode operation over the range of currents tested as shown in Figure 5. The In and Zn penetration in this case was  $0.5 \mu$  and  $1.5 \mu$  respectively. The lateral diffusion of the Zn through the mask resulted in producing an effective stripe width of  $6-7 \mu$  which resulted in the observed narrow far field angle of  $5^\circ$  and the high single mode output powers ( $30 \text{ mW/facet}$ ). The CW

spectra given in the figure indicates a significant amount of long wavelength shift due to heating ( $\sim 100^\circ\text{C}$ ) in the p side up configuration. Multimode operation was observed for the devices diffused at  $575$  and  $600^\circ\text{C}$ . The single mode operation is believed to originate from a lateral positive index guide from the strain field originating from the deep In penetration into the samples diffused at high temperature. The strain related effects are apparently large enough to overcome the carrier induced negative guiding effects from the Zn diffusion.

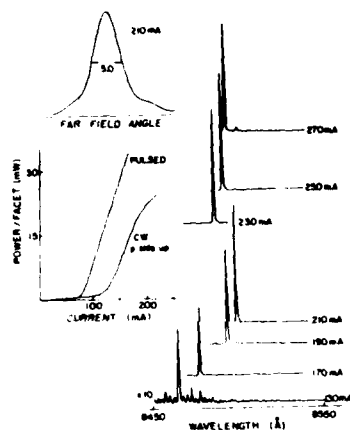


Fig. 5. Far field, emission spectra, and power-current curves for a narrow stripe laser diffused at  $650^\circ\text{C}$  for 15 min. The spectra and far field data are CW data.

In summary, the simultaneous diffusion of Zn and In into GaAs and  $(\text{AlAs})_n(\text{GaAs})_m$  superlattice structures has been characterized using SIMS and RBS. We have determined the diffusion depths and the In surface concentrations as the temperature time cycle is varied. These results suggest that the In concentration plays a dominant role for obtained improve ohmic contacts to narrow strip devices. Finally using this technique, with sufficient In introduced into the sample a strain related positive lateral index guide was produced resulting in high power single mode lasers.

The authors wish to acknowledge the contribution of J.W. Sprague, P. McDonald for assistance in the laser fabrication and G. Smith for the SIMS data.

Agno S K, Roedel R J, Mellen N, Escher J S 1985 Appl. Phys. Lett. **47** 1193.

Blum S E, Small M B, and Gupta D 1983 Appl. Phys. Lett. **42** 108.

Laidig W D, Holonyak N Jr., Camras M D, Hess K, Coleman J J, Dapkus P D, and Bardeen J 1981 Appl. Phys. Lett. **38** 776.

Schaus C F, Shealy J R and Eastman L F 1985 J. Cry. Growth **73**.

Shealy J R and Chin S R 1985 Appl. Phys. Lett. **47** 410.

Shealy J R 1986 Appl. Phys. Lett. **48** 925.

## **Characterization by Raman spectroscopy of GaInP, AlInP and GaAs single layers and superlattices**

G.W. Wicks, D.P. Bour, J.R. Shealy and J.T. Bradshaw

School of Electrical Engineering, Phillips Hall  
Cornell University, Ithaca, NY 14853 USA

**Abstract.** GaInP and AlInP layers and GaInP/GaAs superlattices are characterized with Raman spectroscopy. Raman features in the two ternaries have been identified and the compositional dependence determined. Raman measurements of GaInP at elevated temperatures determine the phonon energies vs. temperature and its maximum temperature of congruent sublimation. Superlattice Raman measurements allow estimates of intermixing and strain.

### Introduction

This paper is a study by Raman spectroscopy of GaInP and AlInP. Data are presented on the effects of the compositions of the two ternaries on their Raman features. Raman data at temperatures up to 505°C are presented for  $\text{Ga}_{0.5}\text{In}_{0.5}\text{P}$ , thus quantifying the shift of phonon energies with temperature and locating the maximum temperature of congruent sublimation in a vacuum. Finally, Raman data on strained and lattice matched superlattices of GaInP/GaAs are presented, allowing estimates of intermixing and strain.

### Experimental Methods

All samples in this study are epitaxial structures grown on (001) semi-insulating GaAs substrates by organometallic vapor phase epitaxy (OMVPE). The epitaxy occurred at a temperature of 650°C, under a hydrogen pressure of 76 Torr, and a growth rate of approximately 2 microns per hour. Trimethylgallium, trimethylindium, trimethylaluminum, arsine, and phosphine were the sources used.

The Raman spectra were measured with the samples at room temperature and excited by the 5145 Å line of an argon laser, unless otherwise indicated. The scattered light was spectrally dispersed with a 0.85 meter double spectrometer with a 4 cm<sup>-1</sup> resolution and detected with a photomultiplier with a GaAs photocathode in the photon counting mode. A backscattering geometry was used in which the incident light was polarized along a (100) direction. The polarization of the detected scattered light was either aligned parallel or perpendicular to the incident light, denoted  $z(x,x)z$  or  $z(x,y)z$ , respectively.

Compositional Dependence of Raman Features of GaInP

All GaInP samples in this study exhibited three Raman peaks between 300 and 420  $\text{cm}^{-1}$ . Figure 1 exhibits the energies of these peaks vs. GaInP composition. In addition, Fig. 1 plots the data from the literature of LO and TO phonon energies of the two binary end points, InP and GaP [Mooradian et al. 1966].

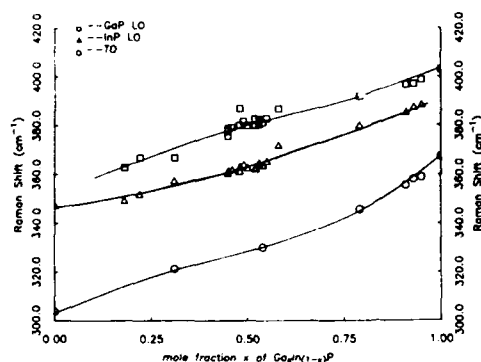


Fig. 1 Raman freq. of GaInP. As indicated by the different symbols, the three modes are identified as the GaP-like LO mode, the InP-like LO mode and a TO mode of GaInP.

As can be seen in Fig. 1, we have identified the highest energy peak as the GaP-like LO phonon, the middle energy peak as the InP-like LO phonon and the lowest energy peak as a TO phonon. This assignment is based on three considerations. First, the two highest energy peaks are approximately ten times more intense in the  $z(x,y)z$  configuration than in the  $z(x,x)z$  configuration, while the lowest energy peak is the same intensity in both configurations. These observations are consistent with the above peak assignments and the polarization selection rules [Hayes et al. 1978]. Second, the upper branch in Fig. 1 extrapolates toward the LO phonon of GaP, the middle branch toward the LO phonon of InP and the bottom branch toward both binaries' TO phonons. Third, the ratio of the intensity of the upper branch to that of the middle branch is observed to be approximately proportional to the ratio of Ga to In in the ternary.

The above assignments of the Raman features of GaInP are not in agreement with earlier studies of GaInP phonons [Lucovsky et al. 1971; Beserman et al. 1978], but are in agreement with more recent studies [Jusserand 1984].

Raman Features of Ga<sub>0.5</sub>In<sub>0.5</sub>P at Elevated Temperatures

Raman spectra of Ga<sub>0.5</sub>In<sub>0.5</sub>P were taken at temperatures up to 505°C by mounting the sample in a heater in a vacuum chamber pumped to  $10^{-3}$  Torr. The shifts with temperature of the GaP-like and InP-like LO phonons are displayed in Fig. 2. At

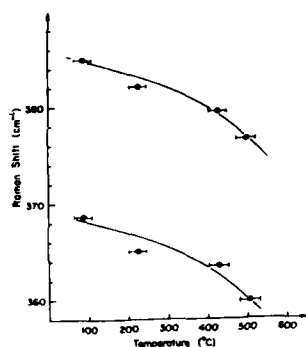


Fig. 2 LO phonon modes of  $\text{Ga}_{0.5}\text{In}_{0.5}\text{P}$  vs. temperature. The higher energy mode is the GaP-like LO mode and the lower energy mode is the InP-like LO mode.

temperatures below  $500^\circ\text{C}$ , the two LO phonons were clearly resolvable. Above  $500^\circ\text{C}$ , the Raman spectrum rapidly changes, indicating degraded crystallinity, as seen in Fig. 3. Apparently the maximum temperature of congruent sublimation is approximately  $500^\circ\text{C}$ , i.e. the material is stable against thermal decomposition in a vacuum below this temperature.

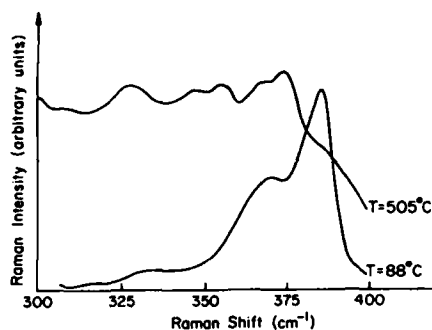


Fig. 3  $\text{Ga}_{0.5}\text{In}_{0.5}\text{P}$  Raman vs. Temperature. The features of the lower Raman spectrum is qualitatively similar to all spectra at temperatures less than  $500^\circ\text{C}$ . Above  $500^\circ\text{C}$  the spectrum changes as seen in the upper spectrum, indicative of degraded crystallinity.

#### Raman Features of AlInP

All AlInP samples in this study exhibited two clearly resolved Raman peaks, each with a partially resolved low energy shoulder. The four peak locations are plotted vs. composition in Fig. 4. Additionally the LO and TO phonons of the binary endpoints of AlP [Onton 1970] and InP [Mooradian et al. 1966] are plotted.

These four Raman features are assigned to be in order of decreasing energy, the AlP-like LO phonon, the AlP-like TO phonon, the InP-like LO phonon and the InP-like TO phonon.

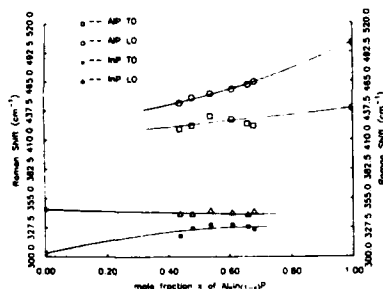


Fig. 4 Raman freq. of AlInP. As indicated by the different symbols, two LO modes and two TO modes are observed, each associated with one of the binary end points.

The basis for these identifications is simply that the phonon modes extrapolate well toward their respective binary compound endpoints. This ternary phonon picture, consisting of two sets of binary-like LO/TO phonon branches which meet as they vanish at the opposite binary endpoint, is similar to other ternaries. AlGaAs [Abstreiter et al. 1978], AlGaP [Tsu, 1981] and InAsP [Bedel et al. 1984] behave like the above phonon picture; GaInP having only a single TO phonon branch which does not join with either LO branch at the binary endpoints seems to be the exception.

Polarization selection rules were not found to be useful to identify which of the above phonon features were LO and which were TO related, as was done in the case of GaInP. The reason for this is that the available laser lines from the argon laser are energetically close to the direct bandgaps of these samples, thus resonant Raman scattering is occurring. Contrary to the non-resonant case in which the LO phonon is only allowed in the  $z(x,y)\bar{z}$  geometry, the LO phonon also appears in the  $z(x,x)\bar{z}$  geometry at resonance [Menendez et al. 1985]. The resonant Raman spectra are shown in Fig. 5. Also

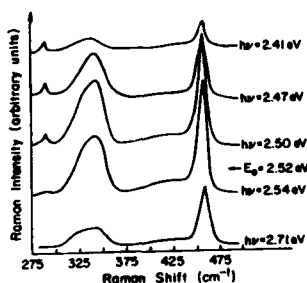


Fig. 5 AlInP resonant Raman spectra. The energy of the laser line ranges from 2.41 eV to 2.71 eV as indicated. The energy of the  $E_0$  band gap as determined by electroreflectance is also indicated. The two main Raman peaks are the AlP-like LO mode at 457  $\text{cm}^{-1}$  and the InP-like LO mode at 341  $\text{cm}^{-1}$ . A small GaAs LO peak at 292  $\text{cm}^{-1}$  from the substrate is also observed for sub-bandgap laser energies.

indicated is the  $E_0$  bandgap of the sample as determined by electro-reflectance. As the energy of the laser nears the energy of the  $E_0$  bandgap, the intensity of the two LO modes of the AlInP increase. Also seen in the figure is the appearance of the LO phonon of the GaAs substrate for laser energies less than the  $E_0$  bandgap of the AlInP, indicating that the AlInP becomes transparent to light less energetic than  $E_0$ , as expected.



Raman Measurements of GaAs/GaInP Superlattices

Three  $\text{Ga}_x\text{In}_{1-x}\text{P}/\text{GaAs}$  superlattices consisting of fifty  $75\text{\AA}/75\text{\AA}$  periods were grown for Raman measurements. In one sample, the  $\text{Ga}_x\text{In}_{1-x}\text{P}$  was lattice matched to GaAs ( $x \approx 0.52$ ); one sample contained indium rich  $\text{Ga}_x\text{In}_{1-x}\text{P}$  ( $x \approx 0.35$ ); one sample contained gallium rich  $\text{Ga}_x\text{In}_{1-x}\text{P}$  ( $x \approx 0.65$ ). The observed energies of the GaP-like phonon of the GaInP and the LO phonon of the GaAs are listed in Table 1 along with the expected values which neglect strain, intermixing, or phonon confinement effects. LO phonon confinements effects are negligible at  $75\text{\AA}$  thicknesses in AlGaAs/GaAs superlattices [Sood et al. 1985] and are assumed to be similar here. There is however strain or intermixing or both in these samples.

Intermixing can change the intended GaInP or GaAs layers into  $\text{Ga}_x\text{In}_{1-x}\text{As}_y\text{P}_{1-y}$  layers. Although there is some Raman data in the literature on GaInAsP compositions lattice matched to InP [Soni et al. 1986] and to GaAs [Inoshita and Usui 1984], the Raman features of arbitrary compositions of the quaternary are not known. Because of this situation, the complete aspects of intermixing cannot be determined, however some estimates can be made. Consider first the  $4\text{ cm}^{-1}$  discrepancy between the expected and observed GaAs LO phonon in the lattice matched sample. If this were caused by intermixing from the GaInP to the GaAs of indium only, Raman data on GaInAs [Kakimoto and Katoda 1982] would imply a composition of approximately 4% mole fraction of indium. Data on GaAsP would be necessary to determine the amount of phosphorous which could cause the  $4\text{ cm}^{-1}$  discrepancy. Now consider intermixing of Ga or As from the GaAs into the GaInP. The fact that the observed GaP-like phonon of the nominally lattice matched GaInP is very near the expected value implies either very little intermixing or that the GaP-like phonon of the resulting quaternary does not shift with composition. The former situation is thought to be more likely.

The shift of the LO phonon energy of GaAs,  $\Delta\omega$ , with the strain,  $\epsilon$ , is known to be given by [Weinstein and Cardona 1972]

$$\Delta\omega = - 380 \epsilon \text{ (cm}^{-1}\text{)}$$

A similar relation is not known for GaInP, but is expected to be very similar since the average of the elastic moduli of GaP [Weil and Groves 1968] and InP [Hickernell and Gayton 1966] are almost the same as that of GaAs [Garland and Fark 1962]. The magnitude of the total strain in the two mismatched superlattices studied here is approximately  $\epsilon = 1\%$ . Since the GaInP and GaAs are of each of similar thicknesses and have similar elastic constants, one might intuitively expect the strain to divide equally, thereby producing a strain shift of approximately  $2\text{ cm}^{-1}$  (but of opposite signs) in both layers. This does not occur. As Table 1 shows, after realizing that the GaAs LO is shifted by  $-4\text{ cm}^{-1}$  due to compositional intermixing, the magnitude of the strain shift in the GaAs layers is  $0-1\text{ cm}^{-1}$  and that in the GaInP is  $3-6\text{ cm}^{-1}$ . Thus most of the strain occurs in the GaInP with little in the GaAs. Similar results have been reported in strained AlInAs/GaAs superlattices [Nakayama et al 1986].

| x   | GaP-Like LO |          | GaAs LO  |          |
|-----|-------------|----------|----------|----------|
|     | observed    | expected | observed | expected |
| .35 | 376         | 373      | 287      | 292      |
| .52 | 381         | 382      | 288      | 292      |
| .65 | 383         | 389      | 288      | 292      |

Table 1. Energies of GaP-like LO phonon from GaInP and GaAs LO phonon in GaInP/GaAs superlattices. The mole fraction, x, of GaP in GaInP is also listed. All energies are in wavenumbers. The expected energies neglect intermixing and strain.

### Summary

GaInP has been shown to exhibit two LO phonons modes and one TO, whereas AlInP exhibits two LO and two TO phonons. GaInP phonon energies vs. temperature have been measured, and the maximum temperature of congruent sublimation is determined to be approximately 500°C. Intermixing in GaInP/GaAs superlattices was estimated and the strain was found to be primarily in the GaInP layers.

### Acknowledgements

This work was funded by SDI and Kodak. L.F. Eastman is acknowledged for support and W.J. Schaff for computerization of experiments.

### References

- Abstreiter G, Bauser E, Fischer A and Ploog K 1978 Appl. Phys. Lett. **16** 345.  
 Bedel E, Charles R, Zwick A, Renucci J, Renucci M, 1984 Phys. Rev. B **30** 5923.  
 Beserman R, Hirlimann C and Balkanski M 1978 Solid St. Commun. **20** 485.  
 Garland C, Park K 1962 J. Appl. Phys. **33** 759.  
 Hayes W and Loudon R 1978 Scattering of Light by Crystals (New York: Wiley).  
 Hickernell F, Gayton W 1966 J. Appl. Phys. **37** 462.  
 Inoshita T and Usui A, 1984 Jap. J. Appl. Phys. **23** L135.  
 Jusserand B and Slempek S 1984 Solid St. Commun. **49** 95.  
 Kakimoto K and Katoda T 1982 Appl. Phys. Lett. **40** 826.  
 Lucovsky G, Brodsky M, Chen M, Chicotka R and Ward A 1971 Phys. Rev. B **4** 1945.  
 Menendez, J Cardona M and Vodopyanov L 1985 Phys. Rev. B **31**, 3705.  
 Mooradian A, Wright G B 1966 Solid St. Commun. **4** 431.  
 Nakayama M, Kubota K, Kato H, Chika S and Sano N, 1986 Appl. Phys. Lett. **48** 281.  
 Onton A 1970 Proc. 10th Int. Conf. on Phys. of Semiconductors, Cambridge MA, USAC, Oak Ridge.  
 Soni R, Abbi S, Jain K, Balkanski M, Slempek, and Benchimol J 1986 Appl. Phys. Lett. **59** 2184.  
 Sood A, Menendez J, Cardona M, Ploog K 1985 Phys. Rev. Lett. **54** 2111.  
 Tsu R, 1981 SPIE 276 Optical Characterization Techniques for Semiconductor Technology.  
 Weil R, Groves W 1968 J. Appl. Phys. **39** 4049.  
 Weinstein B and Cardona M, 1972 Phys. Rev. B **5** 3120.

## **Effects of internal stress on the thermal stability of superlattice and alloy semiconductors**

Takashi Katoda and Naoki Hara

Institute of Interdisciplinary Research, Faculty of Engineering,

The University of Tokyo

4-6-1 Komaba Meguro-ku, Tokyo 153, Japan

### **I. Introduction**

The stability of superlattice and alloy semiconductors during fabrication or device operation is very important. Disordering of the superlattice induced by impurities has been discussed (Laidig et al. 1981, Coleman et al. 1983). It is reported that some kinds of alloy semiconductors have stress in their bonds and include clusters (Kakimoto et al. 1985). Some kinds of superlattices, such as GaAs-InAs strained layer superlattices, are known to include internal stress. However their thermal stability has been rarely discussed. Using laser Raman spectroscopy we estimated the stress in some superlattice and alloy semiconductors, and its effect on their thermal stability.

### **II. Experiment**

$(\text{GaAs})_m(\text{InAs})_m$  and  $(\text{GaAs})_n(\text{AlAs})_n$  superlattices, and  $\text{Ga}_{1-x}\text{In}_x\text{As}$  and  $\text{Ga}_{1-x}\text{Al}_x\text{As}$  alloy semiconductors were used as samples.

Raman spectra were obtained using an Ar laser operating at a wavelength of 514.5 nm in a backscattering geometry at room temperature.

Annealing of superlattice and alloy semiconductor was done in an atmosphere of nitrogen with 6% hydrogen. A  $\text{SiO}_2$  capping film was formed on the surface of superlattice and alloy semiconductor before annealing in order to protect the surface.

## III. Results and Discussion

Stress in the superlattice was estimated using the extra shift of the LO phonon frequency measured by laser Raman spectroscopy. Figure 1 shows the relation between the frequency of LO phonons from GaAs in GaAs-InAs superlattice and the number of monolayers. The solid line is the result calculated using the one-dimensional linear chain model (Barker Jr. et al. 1978). The LO phonon frequency decreases with the number of monolayers because of the zone folding effect. Dots in Fig.1 are experimental results obtained by laser Raman spectroscopy. The difference between calculated and experimental results is explained as resulting from stress. A value of stress was derived from the difference by using the modified relation (Eguchi et al. 1986) derived from the original model proposed by Cerdeira et al. (1972).

$(\text{GaAs})_m(\text{InAs})_m$  ( $m=1-4$ ) superlattices have stress in the order of  $10^{10} \text{ dyn/cm}^2$ . Stress in the  $(\text{GaAs})_2(\text{InAs})_2$  superlattice is about 10% larger than that in  $(\text{GaAs})_4(\text{InAs})_4$ . The value of stress in  $(\text{GaAs})_1(\text{InAs})_1$  includes a relatively larger error because no model which accurately explains the LO phonon frequency of  $(\text{GaAs})_1(\text{InAs})_1$  exists. Therefore we used  $(\text{GaAs})_m(\text{InAs})_m$  superlattice with  $m \geq 2$ .

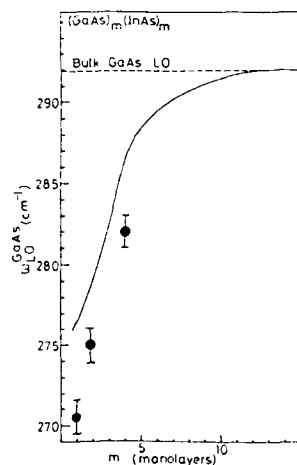


Fig.1 Relation between the frequency of LO phonons from GaAs in GaAs-InAs superlattice and the number of monolayers.

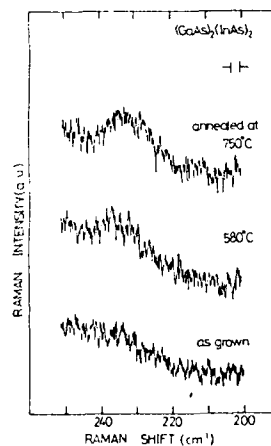


Fig.2 Raman spectra from  $(\text{GaAs})_2(\text{InAs})_2$  superlattice before and after annealing at 580°C for 30 min.

Figure 2 shows Raman spectra from  $(\text{GaAs})_2(\text{InAs})_2$  superlattice before and after annealing. A new peak at about  $235\text{cm}^{-1}$  is shown in the spectrum obtained after annealing at  $580^\circ\text{C}$  for 30 min. The new peak corresponds to InAs-mode LO phonon from  $\text{Ga}_{1-x}\text{In}_x\text{As}$  ( $x \sim 0.5$ ). The result means that disordering was induced by annealing at  $580^\circ\text{C}$ . Disordering was induced by annealing at a higher temperature in the case of the  $(\text{GaAs})_4(\text{InAs})_4$  superlattice which has a smaller stress than that in  $(\text{GaAs})_2(\text{InAs})_2$ . Figure 3 shows Raman spectra from  $(\text{GaAs})_4(\text{InAs})_4$ . A new peak at about  $270\text{cm}^{-1}$  was observed after annealing at  $800^\circ\text{C}$  for 30 min. The new peak corresponds to the GaAs-mode LO phonon from  $\text{Ga}_{1-x}\text{In}_x\text{As}$  ( $x \sim 0.5$ ). InAs-mode LO phonon whose peak is at about  $235\text{cm}^{-1}$  is considered to be included in the tail of GaAs-mode LO phonon.

The  $(\text{GaAs})_4(\text{AlAs})_4$  superlattice has negligibly small stress and showed no change in Raman spectra even with annealing at a temperature higher than  $800^\circ\text{C}$ .

Stress accumulated in each bond of ternary alloy semiconductor was estimated by the method we proposed (Kakimoto et al. 1985) using Raman spectra. Ga-As and In-As bonds in  $\text{Ga}_{1-x}\text{In}_x\text{As}$  ( $x=0.53$ ) have stresses of the order of  $10^{10}\text{dyn/cm}^2$  while Ga-As and Al-As bonds in  $\text{Ga}_{1-x}\text{Al}_x\text{As}$  have negligibly small stress. Figure 4 shows Raman spectra from  $\text{Ga}_{1-x}\text{In}_x\text{As}$

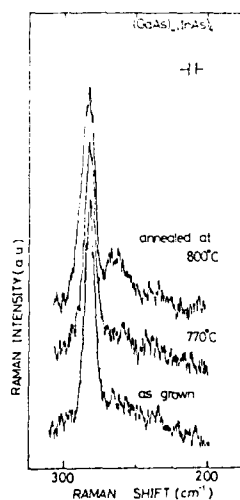


Fig.3 Raman spectra from  $(\text{GaAs})_4(\text{InAs})_4$  superlattice before and after annealing.

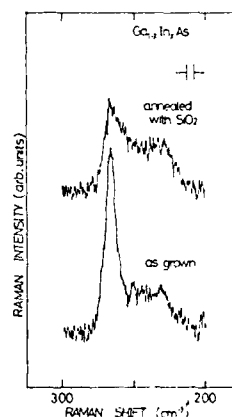


Fig.4 Raman spectra from  $\text{Ga}_{1-x}\text{In}_x\text{As}$  ( $x=0.53$ ) grown by MBE before and after annealing at  $480^\circ\text{C}$  for 8 hours.

( $x=0.53$ ) grown by MBE before and after annealing at  $480^\circ\text{C}$  for 8 hours. It is clear that Raman spectra changed by annealing at this condition. The change in Raman spectra from the ternary alloy is explained as due to rearrangement of atoms.

Impurities such as silicon which could be diffused from the  $\text{SiO}_2$  film by annealing might contribute to the introduction of disordering. However no local mode due to silicon or other impurities was observed.

#### IV. Summary

It was revealed by laser Raman spectroscopy that the effects of stress on the thermal stability of superlattice and alloy semiconductor are very large. It is speculated that stress promote interdiffusion of the host atoms constituting the superlattice and alloy semiconductor. Effects due to the difference in growth methods of superlattices or alloy semiconductors should be investigated. For example  $\text{Ga}_{1-x}\text{In}_x\text{As}$  ( $x=0.53$ ) grown by MBE always showed changes in Raman spectra resulting from annealing as described here. However,  $\text{Ga}_{1-x}\text{In}_x\text{As}$  grown by VPE or LPE did not show reproducible changes.

#### Acknowledgement

This work was supported in part by the Scientific Research Grant-in-Aid for Special Project Research on "Alloy Semiconductor Physics and Electronics," from the Ministry of Education, Science and Culture.

#### Reference

- Barker A S, Jr., Merz J L, and Gossard A C, 1978 Phys. Rev. B17, 3181.
- Cerdeira F, Buchenauer C J, Pollak F H, and Cardona M, 1972 Phys. Rev. B5, 580.
- Coleman J J, Dapkus P D, Kirkpatrick C G, Camras M D, and Holonyak N, Jr., 1982 Appl. Phys. Lett. 40, 904.
- Eguchi K and Katoda T, 1986 to be submitted.
- Kakimoto K and Katoda T, 1985 Jpn. J. Appl. Phys. 24, 1022.
- Laidig W D, Holonyak N, Jr., Camras M D, Hess K, Coleman J J, Dapkus P D, and Bardeen J, 1981 Appl. Phys. Lett. 38, 776.

## **Electron beam measurement of band discontinuities at heterostructure interfaces**

A. Lechner<sup>+</sup>, M. Kneidinger<sup>++</sup>, K. Lübke and H. Thim

University of Linz, Auhof, A-4040 Linz, Austria

<sup>+</sup> Siemens EZM, A-9500 Villach, Austria

<sup>++</sup> ITT Austria, A-1210 Wien, Austria

**Abstract.** An E-beam technique is described which allows directly measuring conduction band discontinuities  $\Delta E_c$  at heterostructure interfaces. This is achieved by probing the potential distribution across the discontinuity using a conventional scanning electron microscope. Measurements performed on isotype n-doped GaAs/Ga<sub>0.64</sub>Al<sub>0.36</sub>As structures have yielded  $\Delta E_c = 0.3\text{eV}$  and  $\Delta E_c : \Delta E_v = 66 : 34$  in good agreement with recently obtained results confirming that the previously measured ratio of 85 : 15 can no longer be considered correct.

### **1. Introduction**

The nondestructive experimental methods known for determining band discontinuities can be divided into two categories, optical and electrical. Duggan (1985), Hickmott (1986) and Heinrich (1986) have recently published excellent reviews on the various experimental techniques. They have given good insight into the difficulties of the different procedures and show that great care has to be taken in interpreting the experimental results. It is thus not surprising that the initial experimental result of  $\Delta E_c : \Delta E_v = 85 : 15$  by Dingle et al. (1974) obtained with GaAs/Ga<sub>0.8</sub>Al<sub>0.2</sub>As multiple quantum-well structures has not been questioned for many years until 1984 when several workers published the new value of 60 : 40 which is very close to the now generally accepted value of 65 : 35. Both, electrical and optical methods have yielded this result so that there is no urgent need for searching for a new technique unless it is both very simple and yet accurate.

The technique presented here is indeed very simple and has therefore been used for many years to study surface potentials of both metal and semiconductor surfaces. In contrast to the two other known electrical methods, the current-voltage (I-V) and the capacitance-voltage (C-V) techniques, its accuracy does not depend on the knowledge of structural details of the samples investigated and on the various assumptions made for calculating I-V and C-V as it allows directly measuring the potential distribution along semiconductor surfaces and, hence, conduction band discontinuities as will be shown below.

## 2. Theoretical considerations

Although several kinds of structures can be used for this experiment the isotype heterostructure which is certainly the simplest structure has been chosen for convenience. Fig. 1 shows a schematic view of the structure used. Also shown are the band diagrams for four different levels of applied bias voltage. By inspection of these diagrams it becomes evident that the magnitude of the conduction band discontinuity can be obtained only under forward bias condition for voltages equal to or larger than the built-in ("diffusion") voltage, i.e.,

$$V_B \geq V_{D1} + V_{D2} = V_{bi} \quad (1)$$

These cases are illustrated in Figures 1c and 1d.  $\Delta E_c$  can be obtained by simply probing the potential distribution at bias levels in accordance with equ. (1).

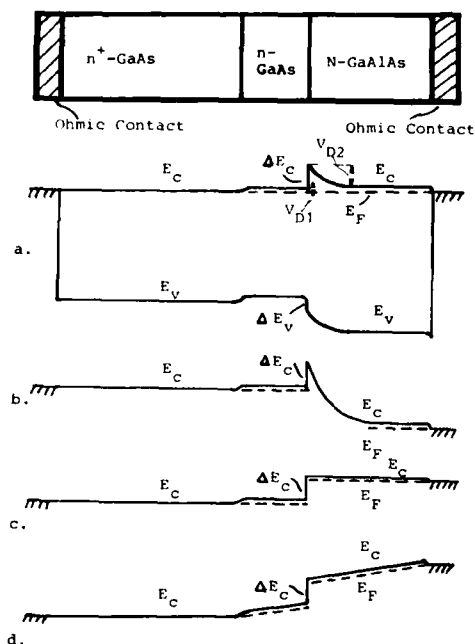


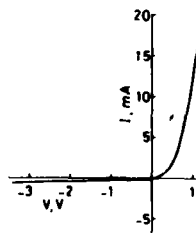
Fig. 1

Band diagrams of an n-doped isotype heterostructure at 4 different bias voltages. a. zero bias b. reverse bias c. forward bias at flat band condition d. large forward bias

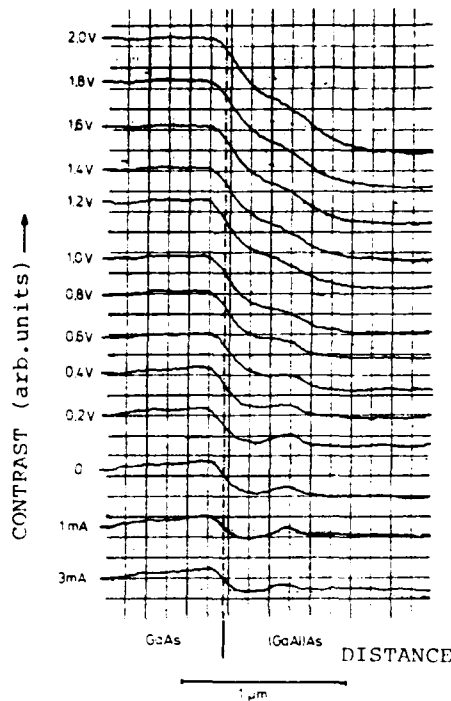
## 3. Experimental results

"Isotype"  $n^+$ -GaAs/ $n$ -GaAs(buffer) $N$ -Ga<sub>0.64</sub>Al<sub>0.36</sub>As heterojunctions grown by a step cooling LPE process (Lechner et al. 1979) have been contacted by evaporating Au Ge Ni Au layers onto both surfaces and alloying them at 420°C. Small area ( $A = 2.2 \times 10^{-4} \text{ cm}^2$ ) diodes prepared by cleaving have been mounted to a holder which was then placed into a conventional scanning electron microscope in a position to allow scanning the electron beam across a cleaved surface. The diodes investigated exhibited good rectifying behaviour as shown in Fig. 2.

Fig. 2 I-V characteristic of a typical  $n^+$ -GaAs/ $n$ -GaAs/ $N$ -GaAlAs heterojunction with  $N = 3 \cdot 10^{15} \text{ cm}^{-3}$ ,  $n \approx 10^{17} \text{ cm}^{-3}$







It should be pointed out that the shape of the I-V characteristics was generally such that a reliable derivation of the barrier height from I-V plots was not possible. By measuring the potential distribution across the heterointerface directly by means of the electron beam accurate determination of the barrier height  $\Delta E_c$  was indeed possible.

Figure 3 shows the video signal versus distance derived from the amplified low energy secondary electrons detector for different bias voltages. These "line scans" clearly show a depletion layer which exists within the lower doped N-GaAlAs region on the right hand side. Its length decreases with decreasing bias voltage.

Fig. 3 Potential line scans ("contrast") versus distance

The video signal which we simply call "contrast",  $K$ , consists of three contributions:

$$K(V) = K_{ch} + K_{bi} + K_{V_B} \quad (2)$$

$K_{ch}$  = chemical contrast proportional to  $\Delta E_c$

$K_{bi}$  = contrast due to built-in voltage, also called diffusion voltage

$K_{V_B}$  = contrast due to externally applied voltage  $V_B$

Equation (2) holds for bias voltages with negligible diode currents. Under forward bias conditions currents flow which cause additional voltage drops within the undepleted diode regions. They are not yet observable in Fig. 3 due to the low resistivity of the semiconducting materials used.

The conduction band discontinuity  $\Delta E_c$  can be obtained from that line scan which exhibits the same potential step as the line scans at higher forward bias voltages. At this voltage equation (2) reduces to

$$K(V) = K_{ch} \quad (3) \quad \text{and} \quad -V_B = V_{bi} = \Delta E_c / e \quad (4)$$

with  $e$  being the electronic charge. In Fig. 3  $K(V)$  assumes a constant value for forward current levels equal to 1mA and 3mA. The 1mA curve thus corresponds to flat band condition.

Although  $\Delta E_c$  can be calculated from equation (4) the accuracy for estimating the bias voltage at which  $K(V)$  assumes a constant value might not be sufficient. A more accurate way of determining  $\Delta E_c$  is obtained if  $K(V)$  is plotted against  $V$  as has been done in Fig. 4. As can be seen the contrast is a linear function of voltage. The voltage at which  $K$  intersects the constant value of  $K=K_{ch}$  is the built-in voltage  $V_{bi}$  and, hence, equal to  $\Delta E_c/e$ . The straight line allows better correction as it is fitted to a large number of experimental data:  $\Delta E_c = 0.3 \text{ eV}$  from Figure 4. Once  $\Delta E_c$  is known the valence band discontinuity  $\Delta E_v$  can be calculated using the well known band gap formula for  $\text{Ga}_{1-x}\text{Al}_x\text{As}$ :

$$\Delta E_v = 1.25x - \Delta E_c = 0.15 \text{ eV} \quad (5) \quad \text{for } x=0.36.$$

The ratio  $\Delta E_c : \Delta E_v$  is thus equal to 66:34 in good agreement with recently obtained values (Okumura et al. 1985, Watanabe et al. 1985), confirming that the previously measured value of 85:15 (Dingle et al. 1974) can no longer be considered correct.

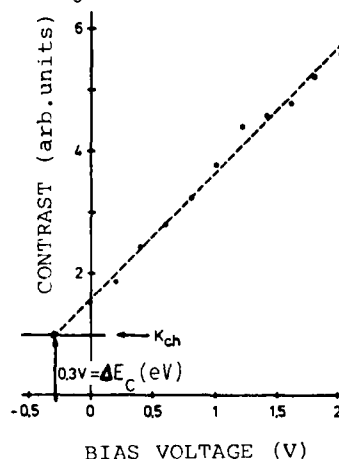


Fig. 4 Contrast  $K$  versus  $V$

#### 4. Conclusions

It has been demonstrated that conduction band discontinuities at heterostructure interfaces can be measured directly by probing the potential across the structure using a conventional SEM. In contrast to the other electrical methods, the I-V and C-V measurements, knowledge of structural details of the samples investigated is not essential and no assumptions need to be made for calculating band discontinuities. However, contacts must be applied to the structure for applying reverse and forward bias voltages but the contacts need not necessarily be ohmic as flat band condition can be established without drawing forward current as it is the case in MIS structures. The E-beam technique is thus a very convenient powerful method for characterizing single and multiple heterojunctions with sufficient electrical and spatial resolution in the order of 0.01 eV and 100 Å, respectively.

**Acknowledgements** Financial support by the Fonds zur Förderung der wissenschaftlichen Forschung and by the Ministry of Science and Research is gratefully acknowledged.

- Dingle R, Wiegmann W and Henry C H 1974 *Phys. Rev. Lett.* **33** 827  
 Duggan G 1985 *J. Vac. Sci. Technol.* **B3** 1224  
 Heinrich H and Langer J 1986 in: *Two Dimensional Systems* (Springer Series in Solid State Sciences) **67** 83  
 Hickmott T 1986 *ibid.* 72  
 Lechner A, Kneidinger M, Thim H, Kuch R and Wernisch J 1979 *El. Lett.* **15** 254  
 Okumura H, Misawa S, Yoshida S and Gonda S 1985 *Appl. Phys. Lett.* **46** 377  
 Watanabe M, Yoshida J, Mashita M, Takanishi T and Hojo A 1985 *J. Appl. Phys.* **57** 5340

AD-A189 673

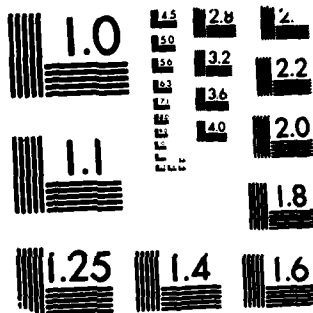
GALLIUM ARSENIDE AND RELATED COMPOUNDS 1986(U) ILLINOIS  
UNIV CHAMPAIGN W T LINDLEY 1986 AFOSR-TR-87-1800

4/7

UNCLASSIFIED

F/G 20/2

NL



MICROCOPY RESOLUTION TEST CHART  
NATIONAL BUREAU OF STANDARDS-1963-A

## **Activation and characterization of MeV n-type implants in GaAs**

Phillip E. Thompson and Harry B. Dietrich, Naval Research Laboratory,  
Washington DC 20375-5000

**Abstract.** The implantation and activation of Si and S having energies between 1 and 6 MeV have been studied. An activation study is reported in which both furnace and rapid thermal anneal were utilized. Extended layers 3  $\mu\text{m}$  deep have been formed having carrier concentrations ranging from  $1.5 \times 10^{16}/\text{cm}^3$  to  $2 \times 10^{18}/\text{cm}^3$ . Buried active layers have been produced at a depth of 3  $\mu\text{m}$ . Carrier profiles for a mixer diode and a voltage variable phase shifter are shown.

### **1. Introduction**

Selective ion implantation is one of the primary processing methods used in the fabrication of GaAs discrete devices and integrated circuits. Its use has become widespread because with selective implantation a variety of electrically isolated planar devices (for instance FET's) can be fabricated on the same chip. Selective implantation is the only processing approach which is genuinely compatible with monolithic integration. Through the years it has been used to develop a very sophisticated FET-based IC technology in GaAs. However, there are still many GaAs circuits, many of which are of an MMIC type which can only be made in a hybrid form. Higher levels of integration could be achieved in this area if it were possible to increase the number of device building blocks available to the circuit designer in a truly monolithic format. An example is the family of devices which require a buried n<sup>+</sup> layer: mixer diodes, vertical varactors and vertical PIN's to name a few. These devices and others could in principle be fabricated with the aid of higher energy implantation. Hence there is currently a push to develop an MeV implantation technology in the III-V's. This paper deals with implantation of Si and S, having energies between 1 and 6 MeV, in GaAs.

### **2. Experimental Procedures**

The MeV implantation was performed at Universal Energy Systems, Dayton, Ohio using a 1.7 MV Tandemron Accelerator. Using triply charged ions, energies up to 6 MeV were obtained with 1.5 MV on the terminal. In some of the device applications keV implantations were added using the 300 keV AI implanter at NRL. After implantation the samples underwent a high temperature anneal to remove implantation damage and to put the dopant atoms into active sites. Both furnace anneal (FA) and optical rapid thermal anneal (RTA) were investigated. For the 15 min. FA the samples were encapsulated with 1000Å of  $\text{Si}_3\text{N}_4$ , sandwiched between two pieces of Si, and kept in a forming gas (90%  $\text{N}_2$ , 10%  $\text{H}_2$ ) atmosphere. For the 10 s RTA, both  $\text{Si}_3\text{N}_4$  encapsulation and a capless procedure were employed. In both cases a piece

of GaAs was placed on the sample prior to anneal and a forming gas atmosphere was used. The atomic profiles were obtained by SIMS profiling. The electrical profiles were investigated using electrolytic CV profiling, bulk Hall measurements, and differential Hall profiling.

### 3. Results and Discussion

A uniformly doped layer is shown in Fig. 1. This carrier profile, obtained with a differential Hall technique, has an average carrier concentration of  $1.5 \times 10^{16}/\text{cm}^3$  and an average mobility of  $5500 \text{ cm}^2/\text{Vs}$ . The reported drift mobility at this concentration is  $6000 \text{ cm}^2/\text{Vs}$  (Sze 1981). The activation of low level implants in LEC material is constrained by inherent compensating centers which are required to make the material semi-insulating. If the carrier concentration is decreased below  $1.5 \times 10^{16}/\text{cm}^3$  the activation and mobility degrade significantly.

An activation study was made of Si implants in GaAs, having energies of 1 to 6 MeV. The sheet carrier concentration and mobility were measured with the Hall technique. The carrier concentration/mobility measurements for 2 and 6 MeV Si are presented in Figs. 2 and 3. As shown a  $850^\circ\text{C}$ , 15 min. furnace anneal is adequate for fluences up to  $10^{14}/\text{cm}^2$  for 2 and 6 MeV Si. After a  $850^\circ\text{C}$ , 15 min. anneal the 2 MeV Si implants had % activation/Hall mobility of 95/4730, 98/4570, and 29%/2940  $\text{cm}^2/\text{Vs}$  for  $5 \times 10^{12}$ ,  $10^{13}$ , and  $10^{14}/\text{cm}^2$ , respectively. Similarly, the 6 MeV Si implants had 98/4600, 95/4400, and 50%/3300  $\text{cm}^2/\text{Vs}$  for  $5 \times 10^{12}$ ,  $10^{13}$ , and  $10^{14}/\text{cm}^2$ , respectively. The activation percentages are greater than those typically reported for keV energy Si implants and the mobilities are at least as high. For 1 MeV Si,  $10^{14}/\text{cm}^2$ , implants it was necessary to anneal at higher temperatures. High dose implantation will be discussed later in this paper.

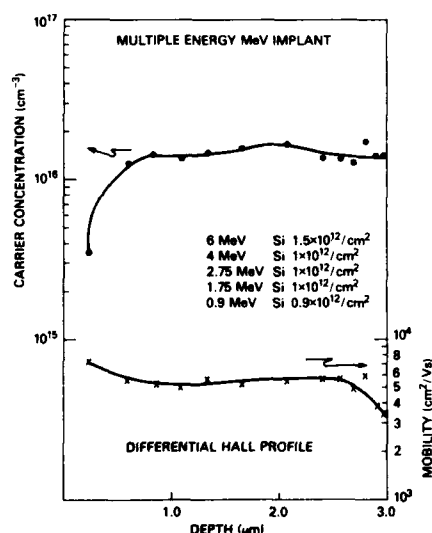


Fig. 1. 3  $\mu\text{m}$  deep, uniform, n-type implant. Average carrier concentration of  $1.5 \times 10^{16}/\text{cm}^3$  and average mobility of  $5500 \text{ cm}^2/\text{Vs}$ .

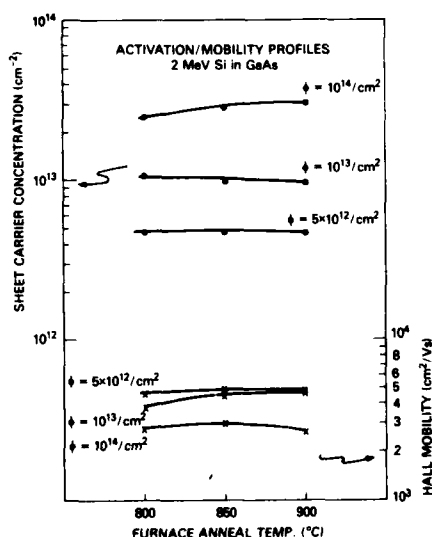


Fig. 2. Activation study of 2 MeV Si in GaAs using 15 minute furnace anneal.

Bulk Hall measurements of an implanted layer, used above, yield sheet carrier concentration and average mobility. By employing a differential technique, i.e., thin layer removal and multiple Hall measurements, the carrier concentration and carrier mobility at a given depth is obtained (Mayer et al. 1970). Differential Hall profiles were made of the 6 MeV Si implants annealed at 850°C for 15 min. ( $\phi=10^{13}$ ,  $10^{14}$ ,  $5 \times 10^{14}/\text{cm}^2$ ) to further understand the activation process of these buried implanted layers, Figs. 4-6. The profiles are considered in order of ascending dose. The  $10^{13}/\text{cm}^2$  implant yields a peak carrier concentration of  $10^{17}/\text{cm}^3$ . The mobility of the carriers at the depth of the maximum in the carrier concentration is 4000  $\text{cm}^2/\text{Vs}$ . When the fluence is increased to  $10^{14}/\text{cm}^2$  the peak carrier concentration is  $5.5 \times 10^{17}/\text{cm}^3$  with a corresponding mobility of 2600  $\text{cm}^2/\text{Vs}$ . The mobility increases on either side of the concentration maximum. The reduced activation efficiency with increasing dose is due to the amphoteric doping nature of Si in GaAs (Bhattacharya et al. 1983). In both cases the activation percentage and mobilities are comparable to those achieved with lower energy implantation and successfully used in device fabrication. When the fluence is further increased to  $5 \times 10^{14}/\text{cm}^2$ , the maximum carrier concentration is  $6 \times 10^{17}/\text{cm}^3$ . The carrier mobility at the location of the maximum is 3000  $\text{cm}^2/\text{Vs}$ , but there is an anomalous dip in the carrier mobility 0.5  $\mu\text{m}$  in front of the maximum. This reduction can be understood by considering the theoretical ion range and displacement profiles of 6 MeV Si in GaAs calculated using TRIM 2.0 (Ziegler et al. 1985). While the peak in the ion distribution is at 3  $\mu\text{m}$ , the maximum in the displacements caused by the implant is at 2.5  $\mu\text{m}$ . The anomalous dip in the mobility profile observed for the  $5 \times 10^{14}/\text{cm}^2$  Si implant, annealed at 850°C, 15 min., is due to residual implantation damage. High temperature activation, such as RTA (1050°C, 10 s) is used to anneal out the damage.

The advantage of using RTA on high dose implants is demonstrated in Fig. 7. In this case multiple MeV Si implants were used to form a layer 3  $\mu\text{m}$  thick with an implant concentration of  $5 \times 10^{18}/\text{cm}^3$ . When FA is used, even at temperatures as high as 900°C for 15 min., the activation is 6 % or less. By using RTA the activation has increased to 20%.

S implantation has also been used to form n-layers. However, it has been observed that S rapidly diffuses during high temperature furnace activation (Wilson et al. 1983). By minimizing the exposure to high temperature through the use of RTA the diffusion of the S is controlled. The carrier profile of 1.15 MeV S,  $10^{14}/\text{cm}^2$ , obtained with electrolytic CV profiling, and the atomic distribution profile prior to anneal, obtained with SIMS, are shown in Fig. 8. A S diffusion coefficient of  $3.7 \times 10^{-12} \text{ cm}^2/\text{s}$  was calculated, which is similar to those reported for FA (Pearton and Cummings 1985). The redistribution is reduced since the exposure time to high temperature is down by three orders of magnitude compared to FA.

Co-implantation of S and Si has been used to form  $n^+$  layers having carrier concentrations of  $2 \times 10^{18}/\text{cm}^3$ . An example of the use of co-implantation are substrates implanted for mixer diodes. The carrier profile is shown in Fig. 9. The vertical mixer diode structure requires low n-type doping on the surface, suitable for the fabrication of a Schottky barrier diode, and a deep  $n^+$  region for an ohmic contact. The transition between the two regimes should be as abrupt as possible to minimize the series resistance of the diode. Mixer diodes are currently being fabricated.

Another example of a device application is a implanted voltage variable phase shifter. The doping layer requirements are a surface layer having a

carrier concentration of  $10^{17}/\text{cm}^3$  and a thickness between 1.5 and 2  $\mu\text{m}$  and a subsurface layer of equivalent thickness and a carrier concentration of  $10^{18}/\text{cm}^3$ . The original voltage-variable phase shifter concept was demonstrated using VPE substrates (Neidert and Krowne 1985). A "first cut" was made to duplicate this doping structure using MeV implantation, Fig. 10.

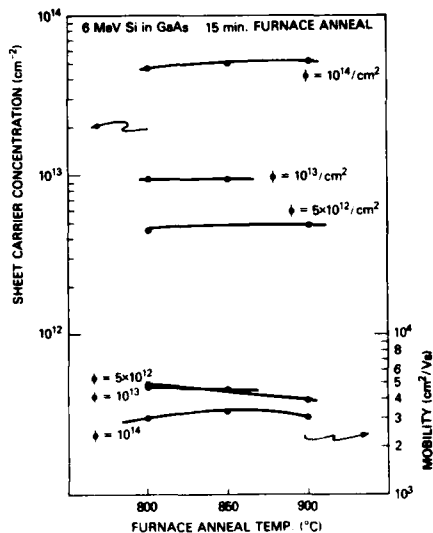


Fig. 3. Activation study of 6 MeV Si in GaAs using 15 minute furnace anneal.

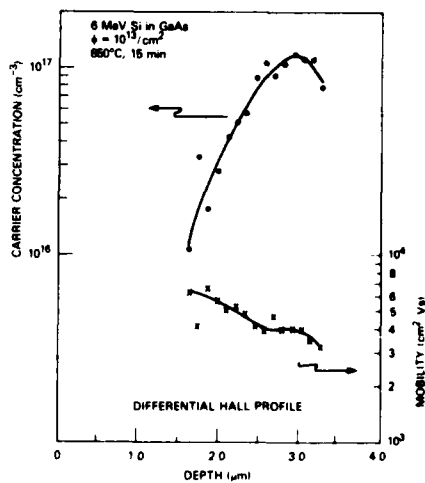


Fig. 4. Differential Hall profile of 6 MeV Si,  $10^{13}/\text{cm}^2$ , in GaAs annealed at  $850^\circ\text{C}$ , 15 minutes.

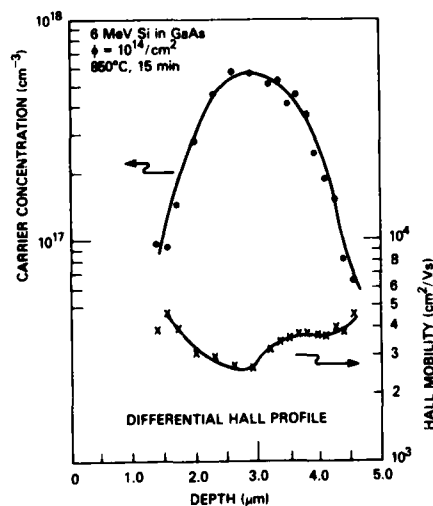


Fig. 5. Differential Hall profile of 6 MeV Si,  $10^{14}/\text{cm}^2$ , in GaAs annealed at  $850^\circ\text{C}$ , 15 minutes.

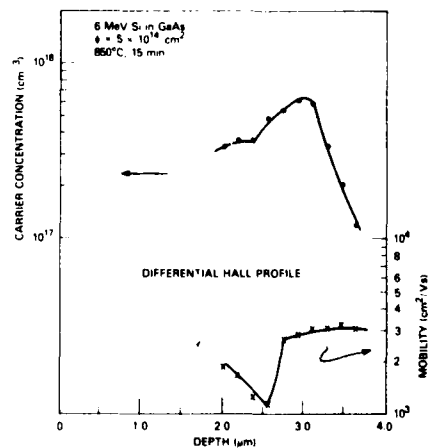


Fig. 6. Differential Hall profile of 6 MeV Si,  $5 \times 10^{14}/\text{cm}^2$ , in GaAs annealed at  $850^\circ\text{C}$ , 15 minutes.



Devices have been fabricated and phase shift,  $\theta$ , and insertion loss,  $L$ , measurements were performed for frequencies 2-18 GHz at room temperature. Comparison of the ion-implanted device results to epitaxial device results indicates comparable electrical performance, with no more than a 30% reduction in gain but with an improvement in loss behavior up to 40%. These differences are attributed to differences in doping profiles.

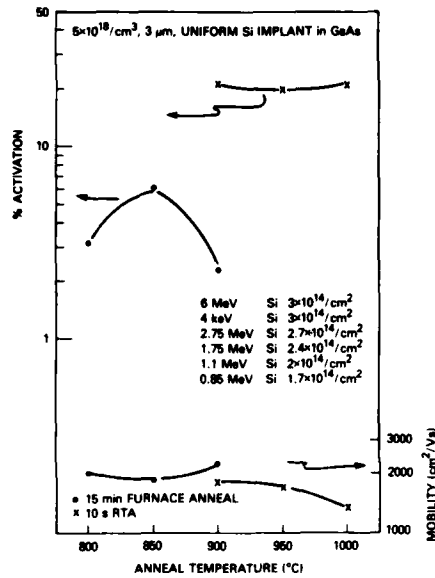


Fig. 7. Activation study of a 3  $\mu\text{m}$  deep, uniformly implanted layer. Average implant concentration of  $5 \times 10^{18}/\text{cm}^3$ .

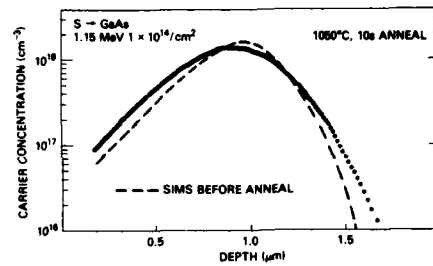


Fig. 8. Comparison of the carrier profile to the initial implanted profile of 1.15 MeV S in GaAs.

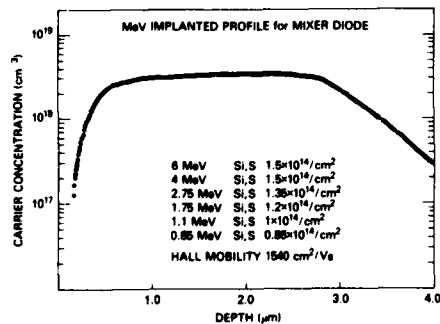


Fig. 9. Carrier profile for mixer diode fabrication obtained with MeV implantation.

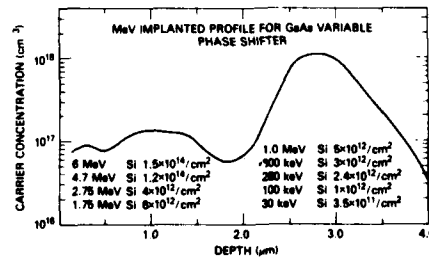


Fig. 10. Carrier profile for variable voltage phase shifter obtained with MeV implantation.

## 4. Conclusion

3  $\mu\text{m}$  thick uniform n-layers have been formed in GaAs using MeV implantation. The doping concentrations ranged from  $1.5 \times 10^{16}/\text{cm}^3$  to  $2 \times 10^{18}/\text{cm}^3$ , with carrier mobilities of 5500 and  $1500 \text{ cm}^2/\text{Vs}$ , respectively. Buried n-layers have been formed 2  $\mu\text{m}$  below the surface using 6 MeV Si implantation. Both FA and RTA have been investigated. For implant concentrations of  $5 \times 10^{17}/\text{cm}^3$  or less,  $850^\circ\text{C}$  furnace anneal with a  $\text{Si}_3\text{N}_4$  encapsulation proved adequate. At higher implant concentrations RTA proved to be superior. Implanted profiles for mixer diodes and voltage variable phase shifters have been produced. The implanted phase shifter devices have electrical characteristics equivalent to epitaxial devices.

## References

- Bhattacharya R S, Pronko P P and Ling S C 1983 *Appl. Phys. Lett.* **42** 880  
 Mayer J W, Eriksson L and Davies J A 1970 *Ion Implantation in Semiconductors* (New York: Academic Press) pp 192-3  
 Neidert R E and Krowne C M 1985 *Electronics Lett.* **21** 636  
 Pearton S J and Cummings K D 1985 *J. Appl. Phys.* **58** 1500  
 Sze S 1981 *Physics of Semiconductor Devices* 2nd Ed. (New York: John Wiley & Sons) p 29  
 Wilson R G, Jamba D M, Deline V R, Evans C A Jr and Park Y S 1983 *J. Appl. Phys.* **54** 3849  
 Ziegler J F, Biersack J P and Littmark U 1985 *The Stopping and Range of Ions in Solids* (New York: Pergamon Press)

## **High activation transient annealing of Si- and Mg-implanted GaAs using improved graphite heater**

Wei Dong Fan, Xin Yuan Jiang, Guan Qun Xia, Wei Yuan Wang

Shanghai Institute of Metallurgy, Academia Sinica  
865 Chang Ning Road, Shanghai 200050, China

**Abstract.** Experimental method and results for high activation and low redistribution transient annealing (TA) of ion-implanted GaAs are described. Samples covered with Si-wafer were preheated to 420°C and raised to 900-1220°C (graphite temperature) or higher within 4 sec using improved graphite heater in purified N<sub>2</sub> atmosphere with annealing time of 20 sec. Undoped SI GaAs samples were implanted with 150KeV Si to a dose of  $3 \times 10^{13} \text{cm}^{-2}$  and 200KeV Mg<sup>+</sup> to a dose of  $1 \times 10^{14} \text{cm}^{-2}$ . When TA temperature is 1220°C for Si-implanted sample and 1170°C for Mg-implanted sample, the activation efficiencies are 92 and 100% respectively. After compared with LSS theoretical distribution and SIMS measured Mg atomic profile, the redistribution of Mg-implanted sample after TA is negligible. The Si-implanted TA GaAs wafers were used for fabrication of GaAs MESFETs with better DC performances.

### **1. Introduction**

Ion implantation has widely been used for impurity doping of wafers in fabrication of GaAs MESFETs and it's ICs with good uniformity and reproducibility, but there still exist some problems to be solved. The conventional post-implantation annealing, furnace annealing (FA), with encapsulated films or intimately contacted wafer is usually carried out at about 800°C for 30min. The electrical properties of implanted GaAs layer, such as activation efficiency and carrier concentration profile are affected due to redistribution of atoms which results in poor controllability for the device characteristics.

In recent years, a new annealing method, transient annealing (TA), using radiation heat from halogen lamps (Kohzu et al 1983), arc lamps (Tabatabaie-Alavi et al 1983), tungsten lamps (Ezis et al 1984), graphite strip heater (Chapman et al 1982), was used for GaAs annealing, is characterized by high temperature annealing within several sec. The preliminary results indicated that high activation and low redistribution can be expected.

In this paper, a new design of transient annealing apparatus with improved graphite heater is described. The electrical properties of Si- and Mg-implanted GaAs layer after TA are discussed and GaAs MESFETs were fabricated.

### **2. TA Apparatus**

The schematic diagram of the new designed infrared TA apparatus is shown in Fig.1. A concave graphite block placed on a quartz pedestal and situated at the middle of high frequency coil is heated by high frequency

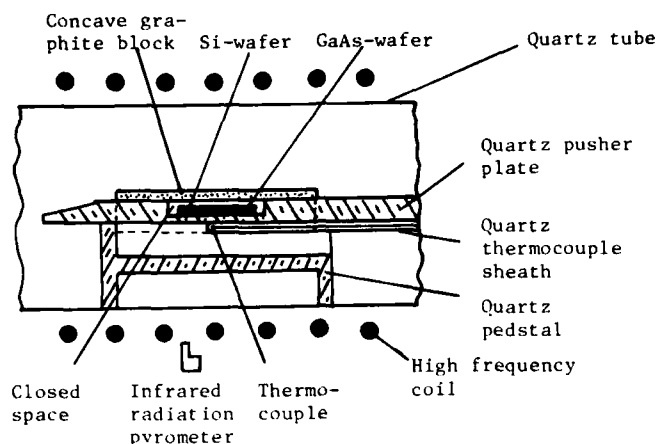


Fig. 1 Schematic diagram of the graphite heater

generator. GaAs sample covered with Si wafer is put on a polished quartz pusher plate which can be moved in and out the graphite block quickly along the horizontal direction. When the wedge-shaped head of the pusher moves into the graphite heater, actually the concave graphite block is pressed on the pusher and a small closed annealing space is formed.

The temperature of the graphite block is measured by optical pyrometer and the sample temperature is measured by infrared radiation pyrometer and thermocouple as shown in Fig.1.

Before annealing, the graphite block was heated to experimental temperature and the GaAs sample was placed in a position near the graphite block where the sample was preheated to  $420^{\circ}\text{C}$ . Then the preheated sample was moved into the graphite heater and its temperature can be raised to 90% of the graphite block temperature within 4 sec. After annealing, the sample was pulled out as quickly as possible. The typical relationship between the sample temperature and time in GaAs TA process is shown in Fig.2. In this paper, for convenience, the graphite temperatures were regarded as the annealing temperature.

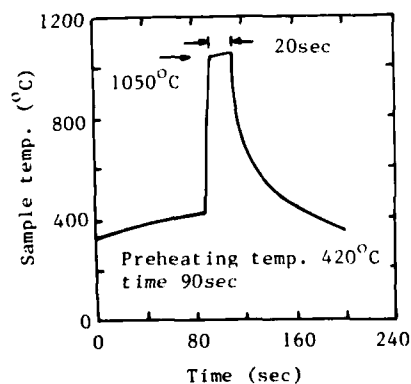


Fig. 2 The typical relationship between the sample temperature and time in GaAs TA process,  $\square$  to annealing temperature or graphite temperature  $1170^{\circ}\text{C}$  (see text)

### 3. Experimental Procedures

Samples used in this work were undoped LEC SI (100) GaAs single crystal wafers. Prior to implantation, the wafers were chemically cleaned and etched in  $3\text{H}_2\text{SO}_4:1\text{H}_2\text{O}_2:1\text{H}_2\text{O}$  solution at  $50^\circ\text{C}$  for 5 min to remove polishing damage.  $\text{Si}^+$  and  $\text{Mg}^+$  implantations were performed at room temperature at  $7^\circ$  off the  $\langle 100 \rangle$  crystal axis. TA was performed in purified  $\text{N}_2$  atmosphere and the GaAs sample was closely contacted with Si-wafer to prevent GaAs dissociation. For comparison, the close-contact capless furnace annealing was also used.

After annealing, Hall effect and sheet resistivity measurements were made using Van der Pauw method to examine the activation efficiency and mobility of implanted wafers. Also, carrier and atomic concentration profiles were obtained by Polaron automatic concentration profilemeter and SIMS measurements respectively.

### 4. Results

#### 4.1 Si-implanted GaAs layer characteristics

Fig.3 shows the dependence of activation efficiency and mobility on TA temperature for Si-implanted GaAs. The activation efficiency increases with increasing of TA temperature and amounts to 92% at  $1220^\circ\text{C}$ , higher than that of FA, 50% at  $800^\circ\text{C}$  for 30 min. The mobility increases with increasing TA temperature from  $1050^\circ\text{C}$  to about  $1120^\circ\text{C}$ , after then it decreases with increasing of TA temperature.

Fig.4 shows the relationship between the activation efficiency and TA time at annealing temperature of  $1170^\circ\text{C}$ . When the annealing time increases to more than 20 sec, the activation efficiency decreases.

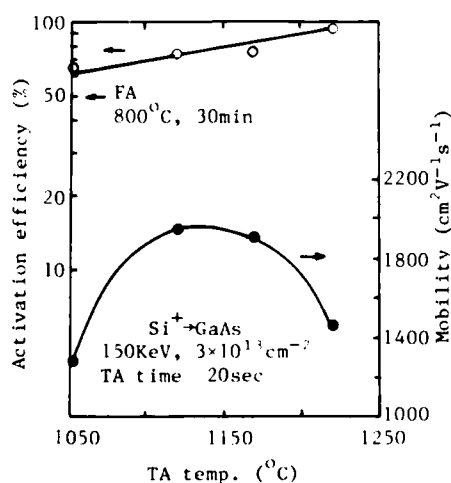


Fig. 3 Dependence of activation efficiency and mobility on TA temperature

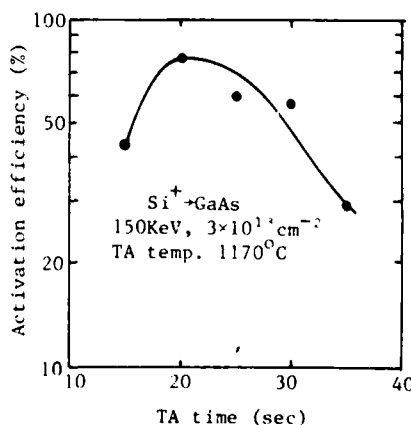


Fig. 4 Relationship between activation efficiency and TA time

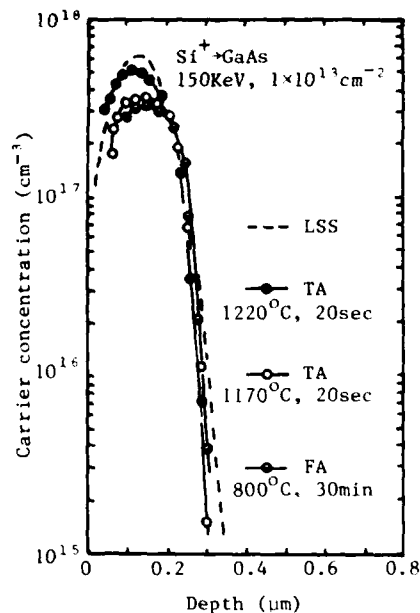


Fig. 5 Carrier concentration profiles

Carrier concentration profiles of Si-implanted n-GaAs layer annealed by TA and FA are shown in Fig.5. It can be seen that higher peak concentration with negligible redistribution can be achieved after TA at 1220°C for 20 sec.

#### 4.2 Mg-implanted GaAs layer characteristics

Fig.6 shows the dependence of activation efficiency and mobility on TA temperature. The activation efficiency increases with increasing of TA temperature and reaches 100% at 1170°C, but the mobility saturates at more than 1120°C. For comparison, the activation efficiency of the sample annealed by FA at 800°C for 15 min is only 53%.

The concentration profiles for Mg-implanted GaAs wafer are shown in Fig.7. It shows that the carrier concentration profile after TA is in good agreement with SIMS Mg atom profile and LSS theoretical distribution, and exhibits negligible Mg-redistribution. On the other hand, the carrier concentration profile after FA at 800°C for 15 min exhibits wide Mg-redistribution.

#### 4.3 GaAs MESFET characteristics

The TA samples were used in fabrication of GaAs MESFETs with gate length of 1.5 μm and width of 40 μm. The GaAs active layer was performed using Si<sup>+</sup> implantation at 150KeV to a dose of  $4.5 \times 10^{12} \text{ cm}^{-2}$  and 50KeV to a dose of  $8 \times 10^{12} \text{ cm}^{-2}$ , followed by TA at 1170°C for 20 sec. The source and drain ohmic contact were made by evaporated Ni/Au-Ge metal and alloyed at 450°C for 1.5 min, the metal gate was made by evaporated Al using lift off technique after recessing the n<sup>+</sup>-layer.

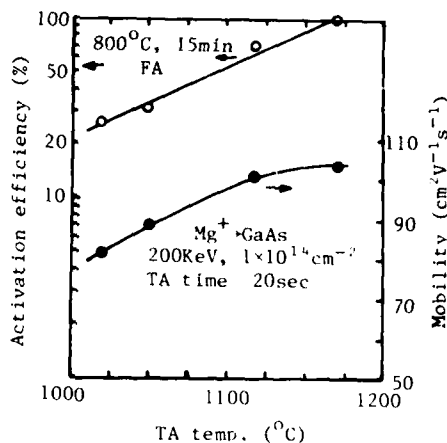


Fig. 6 Dependence of activation efficiency and mobility on TA temperature

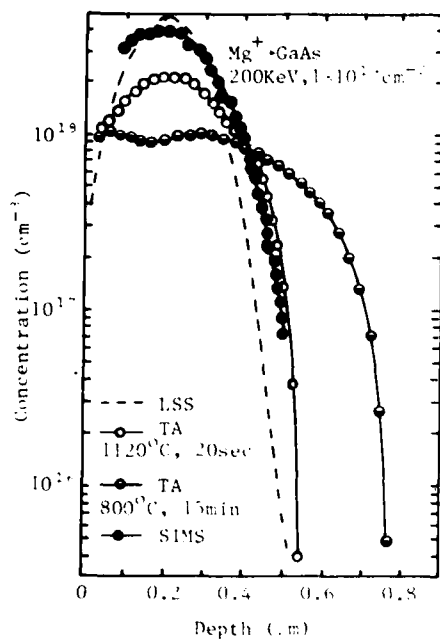


Fig. 7 SIMS atomic and electrical carrier concentration plotted as a function of depth

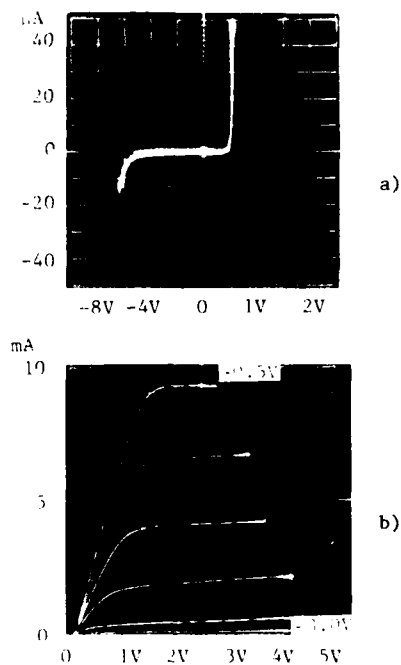


Fig. 8 GaAs gate-source diode I-V characteristics (a) and GaAs MESFET output characteristics (b)

The electrical characteristics of GaAs MESFET are as follows:  $I_{DSS0}=12\text{mA}$ ,  $g_m=166\text{mS/mm}$ ,  $V_p=-3.0\text{V}$ , and  $V_B=-6\text{V}$  as shown in Fig.8.

### 5. Discussion

We have obtained the successful results, high carrier activation and low atom redistribution by the new designed TA apparatus. AES measurements of Si-implanted GaAs sample indicate that the surface composition of GaAs is stoichiometric after TA at 1170°C for 20 sec (Fan et al 1986). The improved graphite heater and optimum TA conditions make the suppressing of GaAs dissociation feasible and the obtaining of higher activation efficiency possible.

The results similar to Fig.4 were obtained by Hiramoto et al (1985). It is well known that the mobility and carrier concentration of ion implanted materials depend on damage defects and ionized impurities in the material. The damage defects decrease and the ionized impurities increase with increasing of TA temperature, which result in increasing of carrier concentration, and increasing of mobility in a certain temperature range and decreasing of mobility at higher temperature.

The implanted Mg atom distribution shown in Fig.7 is different from the results by Yeo et al (1982). It seems that if the channeling effect could be avoided and a lower target temperature could be kept, the Mg

distribution should be fitted to LSS theoretical distribution.

Chapman et al (1982) had carried out RBS measurements in Se-implanted TA GaAs samples, and obtained the minimum channeling yield  $\chi_{\min}$  of 7.2 and 5.5% at TA temperature of 1010°C and 1040°C, respectively. The  $\chi_{\min}$  of undamaged GaAs crystal is about 4%. It will be worth to carry out RBS measurements on our Si-implanted GaAs in order to identify the residual damage defects. It is possible that still higher activation efficiency can be achieved in Si-implanted GaAs at higher TA temperature shown in Fig.3.

Although Mg is a fast diffusion element at high temperature, Mg has negligible redistribution after TA treatment as verified in this experiments. We believe that the deep level impurities in SI GaAs have a lower redistribution in TA than FA treatment. Besides a very high carrier activation can be obtained using TA technique. The above advantages are of benefit to obtain highly homogeneous implanted GaAs for MESFET ICs.

The TA samples were used for fabrication of GaAs MESFETs with better performances as shown in Fig.8 and in published literature (Kohzu et al 1983). But the stress in large diameter GaAs wafer after TA treatment and how to avoid it should be further investigated in future for application of TA technique in GaAs ICs.

#### Acknowledgement

The authors would like to acknowledge their indebtedness to 200KeV, 600KeV ion implanter group and GaAs MESFET group of our institute for their efficient cooperation in ion implantation and GaAs MESFET fabrication.

#### References

- Chapman R L, Fan John C C, Donnelly J P and Tsaur B Y 1982 Appl. Phys. Lett. 40 805  
 Ezis A, Yeo Y K and Park Y S 1984 Mat. Res. Soc. Symp. Proc. 23 681  
 Fan W D, Jiang X Y, Xia G Q and Wang W Y 1986 to be published  
 Hiramoto Toshiro, Saito Toshio and Ikoma Toshiaki 1985 Jpn. J. Appl. Phys. 24 L193  
 Kohzu H, Kuzuhara M, Takayama Y 1983 J. Appl. Phys. 54 4998  
 Tabatabaie-Alavi K, Masum Choudhury A N M, Fonstad C G, and Gelpey J C 1983 Appl. Phys. Lett. 43 505  
 Yeo Y K, Park Y S, Pedrotti F L and Choe B D 1982 J. Appl. Phys. 53 6148



## **Regrowth of amorphized InP**

G. Bahir and J. L. Merz  
Department of Electrical and Computer Engineering  
University of California, Santa Barbara, CA 93106

J. R. Abelson and T. W. Sigmon  
Stanford Electronics Laboratories  
Stanford University, Stanford, CA 94305

**Abstract** Epitaxial regrowth is investigated for layers of InP amorphized by ion implantation at 77° K and room temperature. Experimental criteria for amorphization and limitation of regrowth are correlated with damage calculated by a Boltzmann transport equation approach to ion-implant modeling. Conditions for complete epitaxial regrowth as determined by channeled Rutherford backscattering are presented. The limitation of solid phase epitaxy in InP is discussed in terms of the atomic imbalance induced by In and P recoils.

### **1. Introduction**

A number of papers in the literature deal with ion implantation in InP, an area of considerable interest because of its potential use in a wide variety of microwave, high-speed integrated circuits and electro-optical devices. An understanding of defects resulting from ion-implant damage in compound semiconductors is vital for the effective employment of ion implantation for high density III-V integrated circuits or optical devices. A technique has been developed by Christel *et al* (1981a,b) for the modeling of lattice displacements and stoichiometric imbalances resulting from implant damage in compound semiconductors. This technique, which employs the Boltzmann transport equation (BTE) approach to ion implantation in compound semiconductors, is used in this work to correlate experimental observations with physical damage mechanisms. Damage profiles from Rutherford backscattering spectrometry (RBS) are correlated with features of BTE calculations to develop a physical understanding of the defect formation processes.

The particular application of the correlation of experiment with BTE calculations that is addressed in this work is the amorphization and solid phase epitaxial regrowth of compound semiconductors. The motivation for an amorphizing ion implant followed by solid phase epitaxy (SPE) is as follows: it has been known for some time that in Si this technique results in activation of implanted dopants at significantly lower temperatures (<600°C) than those required to remove implant defects when the target is not amorphized (Crowder 1970). The lower temperature required for the anneal and activation of an amorphising implant would be attractive for compound semiconductor devices from the standpoint of minimizing material decomposition as well as reducing impurity redistribution. In the following sections amorphization criteria are proposed for InP, followed by observations on the correlation of SPE results with BTE calculations.

### **2. Amorphization**

The sequence of structural changes that occur during conversion of a crystalline semiconductor to an amorphous state when subjected to ion damage is still not well understood. The models for amorphization can be summarized in two categories: (i) The

so-called "heterogeneous" model, which suggests that individual damage clusters are amorphous, and that complete amorphization occurs as a result of accumulation and merging of individual damage clusters (Gibbons 1968). (ii) The "homogeneous" model, which suggests that when the defect concentration reaches some critical value in single crystal material, the crystal becomes unstable and transforms to an amorphous state (Swanson *et al* 1971). The first model leads to the conclusion that when the energy density deposited into elastic atomic processes exceeds a certain threshold, a continuous amorphous layer is formed. Although this is a useful criterion for the production of an amorphous layer, such estimates suffer from the fact that they do not account for the spatial distribution of the energy deposited into atomic processes.

By using the BTE calculation, it is possible to determine fairly accurately the fraction of the lattice which is displaced as a function of depth during implantation, from the number of atom recoils produced per unit volume at each depth. Dividing this number by the atomic density yields the fractional displacement of the lattice. The results of these calculations can be correlated with the depth of implantation-induced amorphous layers which have been measured experimentally by ion channeling and backscattering.

### 3. Solid Phase Epitaxy

It is well established from RBS/channeling measurements that the recrystallization of an amorphous layer occurs by solid phase epitaxy (SPE). Atoms in the amorphous region make bonds with those in the single crystal substrate at the amorphous-crystalline interface during the recrystallization process. The interface therefore advances in a layer-by-layer manner. However, the recrystallization behavior of III-V compounds (and consequently their electrical properties) is quite different from that of Si. For example, the regrowth of an amorphous layer in (100) Si tends to be free of secondary defects, especially microtwins and stacking faults. In contrast, the regrowth of such layers in (100) III-Vs leaves a large amount of disorder, as observed with a variety of techniques. Nevertheless, it is known from these measurements that an amorphous layer produced by ion implantation can be made to recrystallize, under certain conditions, at a much lower temperature (150-250°C) for GaAs and InP than an analogous amorphous layer of Si (450-500°C) (Sadana 1985).

Detailed accounts of the regrowth of amorphous InP have been given by Auvray *et al* (1982) for Cr and Se implants at room temperature (RT), Woodhouse *et al* (1984) for Se implants at liquid nitrogen temperature (LNT), and Bahir *et al* (1986) for Si implants at both LNT and RT. A linear relationship between the thickness of the disordered layer following annealing and the initial amorphous thickness has been established. This relationship was found to be independent of ion species and implant dose, so long as the dose was high enough to create an amorphous layer that extended to the surface, with thickness above  $\approx 2000$  Å. A similar relationship was found for GaAs by Grimaldi *et al* (1981).

In elemental semiconductors, the recoil of substrate atoms causes the displacement of indistinguishable atoms from one region to another. In compound semiconductors, on the other hand, the constituent species are distinguishable, and because they have different masses, they do not recoil equally, which leads to local perturbations in stoichiometry. This process is simulated by the BTE calculations. The major quantity of interest here is the resulting imbalance of the normal stoichiometry of the substrate, i.e., the excess concentration of one substrate element over the other. The calculations yield directly four concentration profiles, namely the indium and phosphorous vacancy distributions, and the indium and phosphorous recoil distributions.

The first step in determining the imbalance is to subtract the vacancy distribution from the recoil distribution for each atom type, in order to obtain the net displaced-atom distribution. The second step is to subtract the net displaced phosphorous distribution from the net displaced indium distribution to obtain the net excess atom distribution, which is a true measure of the stoichiometric imbalance. This procedure has been implemented in this work for different implant doses.

#### 4. Experimental

Highly-polished, (100) oriented, 300  $\mu\text{m}$  thick, non-intentionally-doped single crystals of InP were used for these experiments. For comparison, some experiments were done on Fe-doped semi-insulating material. The Si ion implantations were performed at RT or LNT, with fluences between  $10^{13}$  and  $10^{15}$  ions/ $\text{cm}^2$  at an energy of 180 keV and a constant current density of  $0.1 \mu\text{A}/\text{cm}^2$ . Furnace annealing at temperatures between 250° and 750°C was performed in a conventional open tube furnace under flowing dry Ar mixed with 10%  $\text{H}_2$  gas (Bahir *et al* 1986). The implantation-induced disorder and recrystallization following annealing were analyzed by RBS and channeling of 2.2 MeV He ions. A solid state detector placed at a laboratory angle of 170° was used to collect the backscattered particles.

#### 5. Results and Discussion

##### 5.1 Amorphization

Profiles of damage energy density and lattice displacement as calculated by the BTE have been compared with the results of amorphizing Si implants into InP. Fig. 1 shows the experimental results obtained by channeling and backscattering of 2.2 MeV He ions for the disorder distribution resulting from implantation of 180 keV Si into InP held at room temperature, for three different doses:  $10^{13}$ ,  $5 \times 10^{13}$  and  $10^{14}$  Si ions/ $\text{cm}^2$ . A value of unity indicates complete randomness of the sample; this is taken to mean that the sample is amorphous at this depth. Because of the large mass difference between phosphorous and indium, we can completely resolve the He ions that were scattered from In atoms to a depth greater than 5000 Å, from those that were scattered from P atoms. Thus, such a RBS spectrum represents only the displaced In atoms. The crystal became amorphous for doses between  $5 \times 10^{13}$  and  $10^{14}$  ions/ $\text{cm}^2$ ; from these data we estimate that the critical energy density for amorphization is between  $2.5$  and  $5 \times 10^{20}$  keV/ $\text{cm}^3$ .

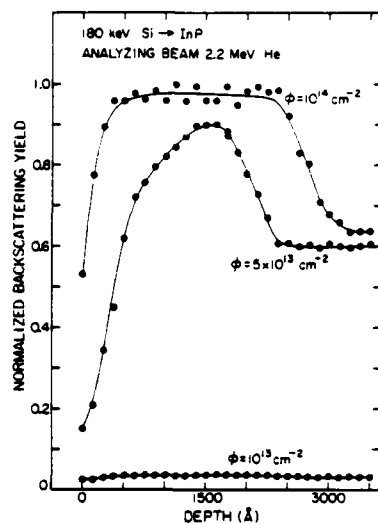


Fig. 1 Normalized aligned RBS spectrum (reversed direction) of 2.2 MeV He ions on InP implanted at room temperature with  $10^{13}$ ,  $5 \times 10^{13}$ ,  $10^{14}$  180 keV Si  $\text{cm}^{-2}$ .

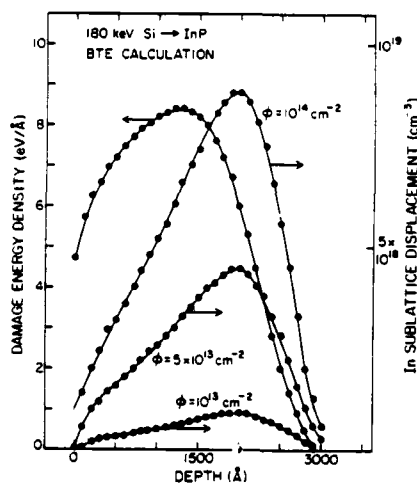


Fig. 2 BTE calculations for damage density and number of In sublattice displacement for InP implanted with  $10^{13}$ ,  $5 \times 10^{13}$ ,  $10^{14}$  180 keV Si  $\text{cm}^{-2}$ .

Fig. 2 shows the results of the BTE calculation for the number of displaced In atoms as a function of depth under the same implant conditions presented at Fig. 1, assuming a displacement energy  $E_d=11$  eV. By integrating these curves, the results indicate that the number of displaced atoms is proportional to the dose. The calculation assumes that the damage is stable and there is no self-annealing during implantation, which we know to be an incorrect assumption at RT. Comparison between experimental results and the BTE calculation shows that for a dose of  $5 \times 10^{13}/\text{cm}^2$  the calculated profile is similar to the experimental result, whereas for the higher dose the measured damage is not proportional to implant dose, and the crystal is transformed to an amorphous layer. This change could support the homogeneous model for amorphization; i.e., relaxation to the amorphous state at a certain dose, because the relation between dose and damage does not appear to be linear, Fig. 1. The position of the edge of amorphous interface is taken to be the point at which the normalized yield drops half the distance to the lowest yield outside the amorphous region (yield of about 0.8 at depth of 2600 Å). Comparison of the calculated number of displaced atoms of this depth with experimental results (including the calculated data for phosphorous atom displacement, not shown in Fig. 2) indicates that the fractional lattice displacement for amorphization is approximately 0.1% for  $E_d=11$  eV, or 0.5% if  $E_d=6.4$  eV is used in the BTE calculation.

## 5.2 Solid phase epitaxy

The typical annealing behavior of a thick layer ( $>2000\text{Å}$ ) of ion-induced damage can be seen in Fig. 3. In this figure we show the damage distribution for a LNT implant of  $10^{15}$  Si ions/ $\text{cm}^2$  as-implanted at 180 keV, and following different annealing schedules (250°C and 400°C for 120 minutes, and 750°C for 15 minutes), each of which represents the time for maximum regrowth thickness for the given temperature. For all temperatures the regrowth is incomplete. We found that the regrowth rate is nonlinear, characterized by an initial rapid growth that slows and eventually stops at a given amorphous depth for each temperature.

For low annealing temperature,  $<250^\circ\text{C}$ , there is SPE, since there is no reduction in the damage level of the un-regrown region. There may also be SPE at higher temperatures, but it is not uniform judging by the reduced yield near the surface, which indicates that the regrowth ended with a high density of extended defects, or with slightly misoriented crystallites. These results differ from those of Wruck et al (1981), for  $77^\circ\text{K}$ ,  $10^{15}\text{ cm}^{-2}$ , 200 keV implanted phosphorous, who reported complete regrowth following annealing at  $400^\circ\text{C}$  for 24 hours.

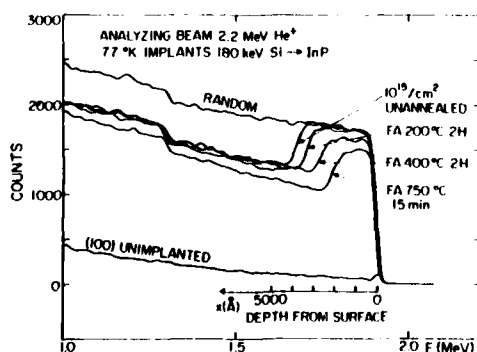


Fig. 3 Aligned and random RBS spectra for un-annealed InP implanted at  $77^\circ\text{K}$  with  $180\text{ keV } 10^{15}\text{ Si}/\text{cm}^2$ , and following FA at  $250^\circ\text{C } 2\text{ hr.}$ ,  $400^\circ\text{C } 2\text{ hr.}$  and  $750^\circ\text{C } 15\text{ min.}$

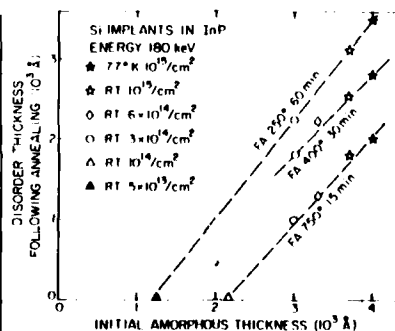


Fig. 4 Residual damage thickness, following different FA temperatures, as function of initial amorphous thickness for room temperature and  $77^\circ\text{K}$  implanted InP.

The regrowth behavior of a disordered sample with an amorphous layer less than 2000Å thick is different. Following furnace annealing at 750°C the samples do not completely reorder but remain relatively free of damage. Furnace annealing at a temperature of 250°C for 60 minutes can induce epitaxial regrowth of damage induced by 170 keV RT implant of  $5 \times 10^{13}$  Si ions/cm<sup>2</sup>. There is epitaxial regrowth from crystalline InP both underlying and overlying the amorphous layer, leaving a small residual disorder peak (Bahir *et al* 1986).

The channeling results for samples implanted at RT and LNT, followed by furnace annealing at different temperatures (250°, 400° and 750°C) are summarized in Fig. 4, where the thickness of the residual disorder following annealing is plotted against the thickness of the amorphous layer in the as-implanted samples. We show that for each annealing temperature there is a characteristic linear relationship between the damage thickness of the as-implanted layer and the residual thickness following annealing. Possible reasons for the difficulties encountered in obtaining defect-free regrowth of the amorphous layer in InP are primarily due to the binary nature of the system.

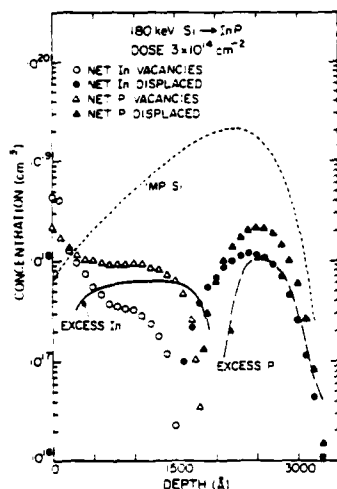


Fig. 5 BTE calculations of the stoichiometry distribution in InP implanted with 180 keV Si ions to a dose of  $3 \times 10^{14}$  cm<sup>-2</sup>.

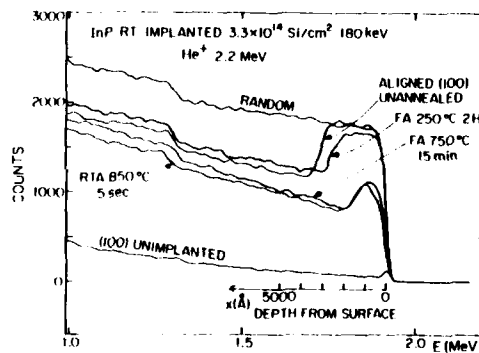


Fig. 6 Aligned and random RBS spectra for unannealed InP implanted with 180 keV  $3.3 \times 10^{14}$  Si/cm<sup>2</sup> and following FA at 750°C or RTA at 850°C.

Fig 5 shows the results of BTE calculations for the case of 180 keV Si implanted to a dose of  $3 \times 10^{14}$  ions/cm<sup>2</sup>. The results indicate that there will be an imbalance in stoichiometry resulting from the implant. At shallow depth an excess of In is present, while at greater depth an excess of P exists. The distance between the region of excess vacancies (introduced primarily between the surface and the projected range,  $R_p$ ) and the region of excess interstitials (introduced deeper than  $R_p$ ) is approximately 1000Å. In a solid-phase epitaxial process the proper reconstruction of the damaged lattice is dependent on the availability of elements in the correct proportions near the interface between the damage and recrystallized regions. Thus, In and P interstitials and vacancies must diffuse hundreds of angstroms in order to satisfy the requirement for epitaxial lattice growth. The self diffusion coefficients of In and P in InP at 750°C are  $10^{-13}$  and  $3 \times 10^{-16}$  cm<sup>2</sup>/sec, respectively (Goldstein 1961). These numbers were measured in a single crystal; we assume that they give at least the correct order of magnitude for the real diffusion coefficients in amorphous material. From these numbers

it is clear that the P diffusion coefficient is small and does not allow such long range diffusion for the time and temperature conditions used in these experiments. For example, the characteristic diffusion distance  $l=\sqrt{Dt}$  for  $T=750^{\circ}\text{C}$  and  $t=15$  minutes will be about  $50\text{\AA}$ . Thus, successful reordering of the lattice can not be accomplished. To the extent that reordering is not completed, processes which are dependent on disorder will be enhanced. Correlating the depth at which regrowth stops ( $\approx 1500\text{\AA}$ , as shown by the  $750^{\circ}\text{C}$  FA curve in Fig. 6) with the BTE calculations shown in Fig. 5, indicates that the regrowth stops at a net vacancy concentration on the order of  $10^{18}/\text{cm}^3$ . Some preliminary experiments were done in order to reduce the stoichiometry perturbation induced by the implantation. Phosphorous was implanted at low energy (100 keV) to a dose of  $5 \times 10^{13}$  ions/ $\text{cm}^2$  following a Si implant at 180 keV. To date, however, this technique has not yielded any better results than those reported above.

The mechanism for the results we have observed, namely that we can recrystallize a thin amorphous layer, but not an amorphous layer exceeding a certain critical thickness, is not well understood. Recently published results, based on high-resolution TEM performed at the interface of Se-implanted GaAs, describe this process as the creation of two transition regions, one near the surface and the other at the interface between the damaged region and the single crystal, with an amorphous layer between them. The different annealing behavior of these two regions can explain the regrowth of InP or GaAs (Sadana *et al* 1984).

#### 6. Conclusions

The thresholds for amorphization of InP in terms of the damage density deposited by the nuclear process, and the fraction of lattice atoms displaced, has been determined by the correlation of RBS measurements with BTE damage calculations. A limitation of SPE in InP appears to be correlated with a transition from a net excess of interstitials deep in the implanted material to net vacancies near the surface.

#### Acknowledgments

The authors would like to thank to L. Magel for help with the BTE calculations. This work is supported by the Air Force, ROME/RADC, Hanscom Air Force Base, Massachusetts.

#### References

- Auvray P, Guivarch A, Lharidon H, Pelous G, Salvi M and Henoc P 1982 *J. Appl. Phys.* **53** 6202
- Bahir G, Merz J L, Abelson J R and Sigmon T W 1986 *Proceedings of SPIE* **623** 149
- Christel L A, Gibbons J F 1981a *J. Appl. Phys.* **52** 5050
- Christel L A, Gibbons J F and Sigmon T W 1981b *J. Appl. Phys.* **52** 7143
- Crowder B L 1970 *J. Electrochem. Soc.* **117** 671
- Gibbons J F 1968 *Proc. IEEE* **56** 295
- Goldstein B 1961 *Phys. Rev.* **121** 1305
- Grimaldi M G, Paine B M, Nicolet M A and Sadana D K 1981 *J. Appl. Phys.* **52** 4038
- Sadana D K, Sands T, and Washburn J 1984 *Appl. Phys. Lett.* **44** 623
- Sadana D K 1985 *Nucl. Instr. and Meth.* **B7** 375
- Sawanson M L, Parsons J R and Hoelke C W 1971 *Rad. Effects* **2** 249
- Woodhouse J D, Donnelly J P, Nitishin P M and Owens E B and Ryan J L 1984 *Solid-St. Electron.* **27** 677
- Wrick V L, Choyke W J and Tzeng C F 1981 *Electron. Lett.* **17** 752

## Hydrogen passivation of shallow level impurities and deep level defects in GaAs

S. J. PEARTON, W. C. DAUTREMONT-SMITH, C. W. TU, J. C. NABITY, V. SWAMINATHAN, M. STAVOLA AND J. CHEVALLIER

AT&T Bell Laboratories, Murray Hill, New Jersey 07974

**ABSTRACT.** Hydrogen plasma exposure of GaAs leads to a near surface passivation of shallow donors and shallow acceptors. Detailed results are presented for the passivation depth of Si donors in n-GaAs as a function of plasma exposure temperature (100-350°C) and Si dopant level ( $8 \times 10^{13}$ – $1.5 \times 10^{18}$  cm $^{-3}$ ). The activation energy for recovery of the donor electrical activity is around 2.1 eV for each of the different species (Si, Se, S, Sn, Te and Ge), but varies as the strength of an isolated hydrogen-donor species bond. Chemical bonding models based on the charge states of hydrogen in n- and p-type material are proposed to account for the deactivation. Hydrogenation of MBE GaAs completely passivates the common M1, M2 and M4 deep level defects, and can increase room temperature photoluminescence by a factor of 30. Thermal restoration of the carrier concentration without loss of deep level passivation has been achieved.

### INTRODUCTION

The ability of atomic hydrogen to passivate the electrical activity of shallow donor (Chevallier et. al. 1985a, Pearton et. al. 1986, Chung et. al. 1985) and acceptor (Johnson et. al. 1986) impurities in GaAs has recently been demonstrated. Previous work has already shown the feasibility of neutralizing deep level centers such as EL2 present in bulk material (Lagowski et. al. 1982), and passivating impurities associated with grain boundaries in polycrystalline GaAs (Pearton 1982, Pearton and Tavendale 1983). In this paper we detail microscopic models for the deactivation by hydrogen of both shallow donors and acceptors, based on evidence that suggests hydrogen has a donor level in the upper half of the GaAs bandgap. The reactivation kinetics of all of the donor species have also been determined. The effect of hydrogenation on the common defects in Molecular Beam Epitaxy (MBE) GaAs is investigated, and compared with that of the shallow donor passivation.

### EXPERIMENTAL

A wide variety of material was used in the passivation studies. To investigate the shallow dopant deactivation, samples of single crystal, Bridgman grown GaAs doped with either Si ( $n = 8 \times 10^{16}$ – $2 \times 10^{18}$  cm $^{-3}$ ) or Zn ( $p = 2 \times 10^{16}$ – $1 \times 10^{19}$  cm $^{-3}$ ), LPE grown, undoped layers ( $n = 8 \times 10^{13}$  cm $^{-3}$ ) or Si doped, MBE grown layers ( $n = 2 \times 10^{15}$ – $2 \times 10^{18}$  cm $^{-3}$ ) on semi-insulating substrates were used. The chemical dependence of the deactivation effect was determined from semi-insulating, Liquid Encapsulated Czochralski (LEC) substrates implanted with Si, Ge, Sn, S, Se or Te donors, or Be, Mg, Zn or Cd acceptors, and annealed at 850°C for 20 min under an As-H $_2$  ambient to produce doped layers with peak carrier densities around  $3 \times 10^{17}$  cm $^{-3}$  for each of the different species. For deep level studies, Si-doped ( $1 \times 10^{15}$  cm $^{-3}$ ), 3  $\mu$ m thick, MBE grown layers on n $^+$  GaAs substrates were utilized.

Hydrogen or deuterium plasma exposures were performed in parallel plate reactors operating either at 30 KHz or 13.56 MHz, with power densities 0.08 and 0.4 W·cm $^{-2}$  respectively. The pressure in each system was kept constant at 750 mtorr with the samples held at 100-300°C for 30-180 minutes in the plasma. Deuterium was used to facilitate secondary ion mass spectrometry (SIMS) measurements.

Doping profiles in the samples were obtained by standard capacitance-voltage (C-V) profiling using the Schottky contact. Deep level transient spectroscopy (DLTS) was performed in the usual manner (Lang

1974). The reactivation kinetics of the passivated dopants or defects were obtained by measuring samples isochronally annealed (5 min) in a rapid thermal annealing system to minimize rise and fall times.

## RESULTS AND DISCUSSION

### SHALLOW LEVEL DEACTIVATION

Figure 1 shows carrier concentration profiles after hydrogen plasma exposure of bulk samples with initially uniform Si doping levels. The hydrogenation causes a strong reduction in the carrier concentration in the near surface region, with the actual depth of this modification being inversely dependent on the initial Si doping level (Chevallier et. al. 1985a). At least some of the carrier removal in a thin layer ( $\leq 500\text{\AA}$ ) from the surface may be due to plasma bombardment effects, but from electrolytic hydrogen insertion experiments it is clear that the donor neutralization at depths beyond this are due to the presence of atomic hydrogen alone (Chevallier et. al. 1985a). The passivation depth also varies as the square root of the plasma exposure time, indicating an indiffusion process.

The shallow acceptors in GaAs are also neutralized by association with atomic hydrogen (Johnson et. al. 1986). Figure 2 shows carrier concentration profiles in bulk, Zn-doped material, before and after hydrogenation at  $250^\circ\text{C}$ . Under our plasma conditions the passivation of donors is more complete than that of acceptors, though other workers see the reverse (Johnson et. al. 1986).

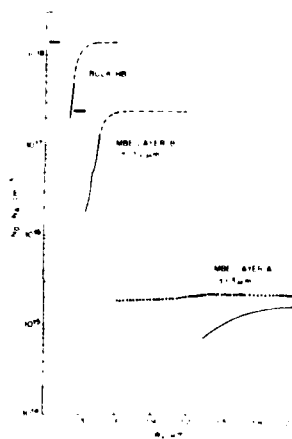


Figure 1 Carrier concentration profiles of GaAs(Si) of three different doping levels before (dotted line) and after (continuous line) hydrogen plasma exposure.

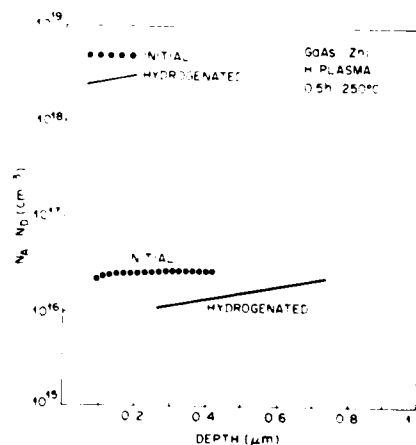


Figure 2 Carrier concentration profiles in GaAs(Zn) before and after hydrogenation at  $250^\circ\text{C}$  for 0.5h.

The role of hydrogen in the passivation process is clear from the SIMS and C-V data of Figure 3. There is a good correlation between the incorporation depth of deuterium and the Si donor neutralization depth, obtained from successive chemical etching, C-V measurements (Chevallier et. al. 1985b). It should be pointed out that the net electrically active Si donor profiles under some deuteration conditions do not always correlate well with the total D profile, indicating that much of the D is stabilized by trapping at other sites, possibly other D atoms, forming deuterium molecules. We have noticed that changes in the plasma parameters and sample exposure temperature can cause very significant variations in both the total amount of deuterium incorporated into the GaAs, and the efficiency of that deuterium in passivating the shallow dopants.

The thermal stability of the donor neutralization was examined as a function of chemical species. The degree of electrical activity returning after each anneal was measured by integrating under the free carrier profile, and checked by comparing the sheet carrier concentration of companion Hall samples as a



function of annealing temperature. Assuming the complex to which the hydrogen is bonded becomes dissociated at these temperatures, and that this is the rate limiting step obeying first order kinetics, then we can obtain the dissociation energy for each donor from (Pearton et. al. 1986)

$$E_D = kT \ln \left[ \frac{1}{\nu} \ln \left( N_D/N \right) \right] \quad (1)$$

where  $N/N_0$  is the integrated fraction of the donor-hydrogen complexes remaining after annealing for time  $t$  at temperature  $T$ , and  $\nu$  is the dissociation attempt frequency. Figure 4 shows the experimental data obtained after annealing the Si, Se, S, Te, Sn and Ge implanted GaAs. The solid lines are generated from equation (1) using an attempt frequency of  $10^{14} \text{ s}^{-1}$  and dissociation energies of 2.1 eV for Si, 2.04 eV for Te and Sn, 2.13 eV for Ge, 2.09 eV for Se and 2.16 eV for S respectively. Excellent fits to the experimental data are seen in all cases, with an uncertainty in the absolute activation energies of  $\sim 0.04$  eV. Similar experiments on Zn doped material yielded  $E_D \sim 1.6$  eV, so the acceptor passivation is less stable than that for the donors.

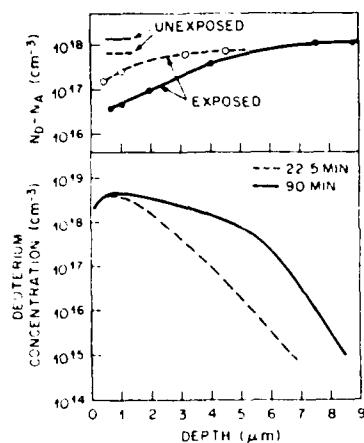


Figure 3 Carrier and deuterium profiles in GaAs(Si) deuterated for 22.5 or 90 min at 250°C in a 13.56 MHz plasma.

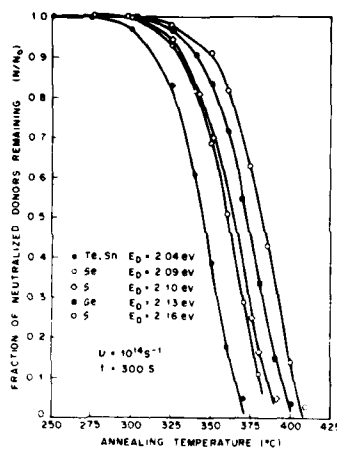


Figure 4 Reactivation of various donor species in implanted hydrogenated GaAs. The integrated fraction of neutralized donors remaining is shown after 5 min annealing of separate samples at progressively higher temperature. The solid lines are the expected fractions remaining calculated from eqn (1) assuming  $\nu = 10^{14} \text{ s}^{-1}$  and the various  $E_D$  values indicated.

SIMS measurements on deuterated samples as a function of annealing temperature show a rapid redistribution of the deuterium around 400°C where the donor electrical activity is restored. However, little deuterium actually leaves the GaAs until heating near 600°C. This argues for a mechanism in which the D is released from the bond with the donor, and diffuses until trapped by another impurity (Pearton et. al. 1986). This probably leads to the formation of relatively stable  $D_2$  molecules, i.e.



The reactivation data on the donors gives some clues as to the passivation mechanism. In Figure 5 we plot the reactivation energy for each donor against the hydrogen-donor element bond strength expected for an isolated molecule. The linear relationship suggests the donor neutralization is due to the formation of a H-donor bond which utilizes the extra electron from the donor (Pearson et. al. 1986). The passivation mechanism must obviously be different for acceptors — one possibility is the formation of an As-H bond for Ga site dopants like Zn.

The depth to which shallow impurities can be neutralized by atomic hydrogen is of obvious interest. The data in Figure 6 clearly show that for Si doped material it is a function of donor concentration, with an inverse square root dependence. This is indicative of a hydrogen trapping mechanism. The effective neutralization depth for a given profile is taken as the distance at which the free carrier concentration has returned to within  $e^{-1}$  of its original value. The ordinate in Figure 7 has the same dimensions as a diffusion coefficient. From limited data we obtain an activation energy of  $\sim 0.5$  eV for the lowest donor concentration, in reasonable agreement with the value estimated by Zavada et. al. (1985) from the redistribution of implanted H in GaAs. We should mention of course that our value is equivalent to the activation energy for H diffusion only if there is a one-to-one correspondence between the neutralized donor concentration, and the H concentration, which is not always the case, as described earlier.

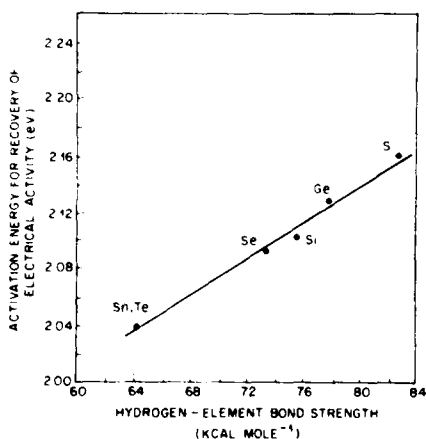


Figure 5 Plot of experimentally determined reactivation energies for each donor element vs. hydrogen-donor species bond strength for each element. The correlation suggests the donor neutralization is due to the formation of a H-donor bond.

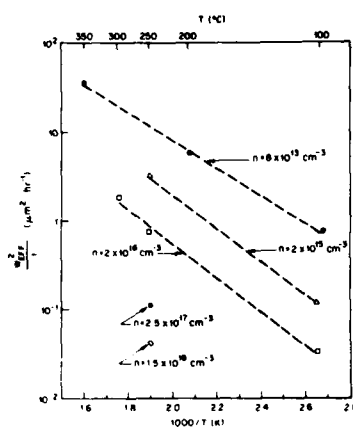


Figure 6 Effective neutralization depth squared per hour of H plasma exposure (30 KHz) plasma of Si-doped GaAs as a function of doping concentration and inverse temperature.

We have also found that the diffusion depth and total amount of D evaporated in GaAs during plasma exposure depends strongly on the conductivity type of the surface (Pearson et. al. unpublished). Thin ( $0.15 \mu\text{m}$ ) highly doped  $p^+$  or  $n^+$  layers were formed on some bulk samples by implantation of Si or Be, followed by rapid annealing. The inhibiting effect of an  $n$ -layer on deuterium diffusion in  $p$ -GaAs is shown in the SIMS profiles of Figure 7. Both the depth and total amount of D incorporation is reduced in the  $n^+p$  sample compared to either a  $p^+p$  or a bulk  $p$ -type specimen. The C-V profiles showed a factor of 2 less acceptor removal in the  $n^+p$  sample, and a shallower deactivation distance compared to the  $p^+p$  or  $p$  samples. Similar retardation by thin  $n^+$  layers is seen on  $n$ -type material.

#### DEEP LEVEL PASSIVATION IN MBE GaAs

Lightly doped ( $n \sim 10^{15} \text{ cm}^{-3}$ ) MBE grown GaAs typically shows three dominant deep levels with activation energies of 0.17, 0.28 and 0.45 eV, respectively below the conduction band (Lang et. al.

1976). These were labeled M1, M3 and M4 respectively by Lang et. al. (1976) Figure 8 shows the DLTS spectra from as-grown and hydrogenated (0.5h, 250°C) samples from the same wafer. There is complete passivation of the three main levels, and partial passivation of a fourth feature at  $E_c - 0.68$  eV. The defect deactivation is stable to annealing at 500°C, while there is a partial reappearance of the deep levels after 600°C annealing (Dautremont-Smith et. al. 1986). It should be noted that the shallow levels are reactivated at 400°C (Chevallier et. al. 1985a, Pearton et. al. 1986). Thus there is a wide temperature window within which it is possible to regain the carrier concentration without loss of passivation of the deep level defects. The stability of this passivation can be estimated in a similar way to that described above, leading to a dissociation energy of  $\sim 2.9$  eV. This corresponds to a room temperature lifetime of the defect passivation of  $10^{27}$  years, or 200 h at a typical maximum device processing temperature of 450°C.

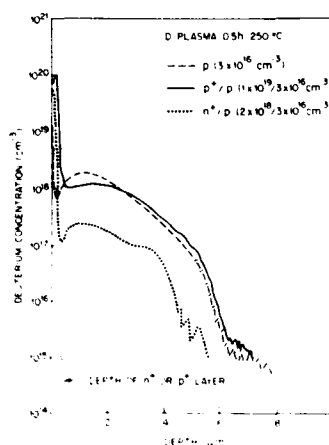


Figure 7 SIMS depth profiles of deuterium in p-type GaAs (Zn doped,  $3 \times 10^{16} \text{ cm}^{-3}$ ) with a thin  $p^+$  or  $n^+$  layer on the surface. Deuteration was for 30 min at 250°C.

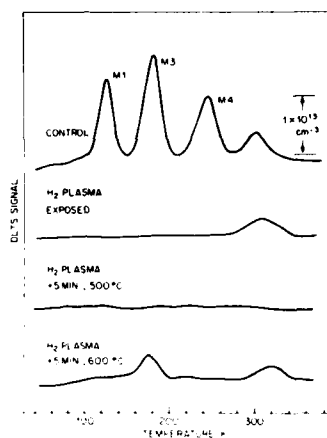


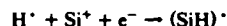
Figure 8 DLTS spectra from MBE GaAs samples before and after hydrogenation (0.5h, 250°C), and after post-hydrogenation annealing treatments at 500°C and 600°C (DLTS time constant = 8 ms, fill pulse width 5  $\mu$ s).

Hydrogenation also gave rise to increased band-to-band photoluminescence (PL) efficiency. Room temperature increases of 60-90% were recorded for n- and p- layers with doping levels in the range  $1-9 \times 10^{15} \text{ cm}^{-3}$ . In samples capped by a thin AlGaAs layer, the increase in RT PL yield was typically 300%, and at 77K between 800-1000%. These improvements are consistent with passivation of deep levels present in the material at the concentrations deduced from the DLTS data. At these low defect densities we could not detect any mobility increase related to the defect passivation.

#### CONCLUSIONS AND SUMMARY

The diffusion behaviour of hydrogen in GaAs reveals key information about its charge states in n- and p-type material, and hence on the chemical reactions responsible for the impurity passivation. While hydrogen diffuses rapidly in both conductivity types, the diffusivity is faster by approximately a factor of four in p-GaAs under our experimental conditions. Indeed at 250°C the diffusion distance of H is enhanced by increased levels of acceptor doping, while being retarded for increased donor doping (Pearton et. al. unpublished). The diffusion is also inhibited by the presence of a thin  $n^+$  region at the surface of n- or p-type material. This is consistent with hydrogen having a donor level in the upper half of the GaAs bandgap, as is postulated for H in Si (Tavendale et. al. 1986, Pantelides 1986).

Based on this assumption, H is always neutral in n-type GaAs, leading to a significant amount of molecule formation (i.e.  $H^{\cdot} + H^{\cdot} \rightarrow H_2$ ). This means there will be a slower effective diffusivity in n-type material because it is widely accepted that the non-reactive  $H_2$  molecules are far less mobile than the atomic species. Donor passivation will then occur by a reaction of the type



In p-type GaAs, the hydrogen will be in ionized form ( $H^{\cdot} + h^+ \rightarrow H^+$ ), inhibiting molecule formation. The deactivation of acceptors is then due to a compensation reaction



Obviously more direct investigation of the bonding reactions in both n- and p-GaAs are needed, but the above model is consistent with all of our experimental observations. In summary, we have shown that shallow donors and acceptors in GaAs are passivated by association with atomic hydrogen, as are the common deep level centers in MBE GaAs. The deep level passivation is considerably more stable than that of the shallow level impurities, making available a wide temperature window, within which the carrier concentration is restored, leaving the deep levels passivated. The ability of hydrogen to modify the carrier profile in the near surface region of both n- and p- GaAs can clearly be a factor when using dry processing involving  $H_2$ , or in normal cleaning procedures because hydrogen is a common constituent of most semiconductor reagents.

*Acknowledgements.* The authors acknowledge the expert technical assistance of J. Lopata and R. Kopf.

#### REFERENCES

- Chevallier J., Dautremont-Smith W. C., Tu C. W. and Pearton S. J. 1985a, *Appl. Phys. Lett.* **47**, 108
- Chevallier J., Dautremont-Smith W. C., Pearton S. J., Tu C. W. and Jalil A., 1985b 3rd Int. Symp. Dry Etching and Plasma Deposition in Microelectronics, Cachan France, Nov.
- Chung Y., Langer D. W., Becker R. and Look D. C. 1985 *IEEE Trans. Electron Devices* ED-32 40
- Dautremont-Smith W. C., Nabity J. C., Swaminathan V., Stavola Michael, Chevallier J., Tu C. W. and Pearton S. J. 1986 *Appl. Phys. Lett.* (in press).
- Johnson N. M., Burnham R. D., Street R. A., and Thornton R. L. 1986 *Phys. Rev. B* **33** 1102
- Lagowski J., Kaminska M., Parsey J. M. Jr., Gatos H. C. and Lichtensteiger M. 1982 *Appl. Phys. Lett.* **41** 1978
- Lang D. V. 1974 *J. Appl. Phys.* **45** 3023
- Lang D. V., Cho A. Y., Gossard A. C., Illegens M. and Weigman W. 1976 *J. Appl. Phys.* **47** 2558
- Pantelides S. T., August 1986 Proc. 18th Int. Conf. Physics Semicond, Stockholm
- Pearton S. J. 1982 *Appl. Phys.* **53** 4509
- Pearton S. J. and Tavendale A. J. 1983 *J. Appl. Phys.* **54** 1154
- Pearton S. J., Dautremont-Smith W. C., Chevallier J., Tu C. W. and Cummings K. D. 1986 *J. Appl. Phys.* **59** 2821
- Pearton S. J., Dautremont-Smith W. C., Lopata J., Tu C. W., and Abernathy C. R. 1986 (to be published).
- Tavendale A. J., Williams A. A., Alexiev D., Pearton S. J., 1986 *Mat. Res. Soc. Symp. Proc.* **59** 469
- Zavada J. M., Jenkinson H. A., Sarkis R. G., Wilson R. G., 1985 *Appl. Phys.* **58** 3731

## **Submicron processing of III-V semiconductors by focused ion beam technology**

Toshiro Hiramoto, Takahide Odagiri, Philip Oldiges, Toshio Saito and Toshiaki Ikoma

Institute of Industrial Science, University of Tokyo,  
7-22-1, Roppongi, Minato-ku, Tokyo 106, Japan

### **1. Introduction**

Fabrication of submicron devices is now very important in the semiconductor industry. At present, optical lithography using masks which are made by electron-beam lithography is widely used for submicron processing. In future, however, focused-ion beam (FIB) technology will become an important technique which will be able to eliminate the mask-alignment process. The FIB technique can be used for direct implantation of various impurities into a localized area in a semiconductor (Kubena et al. 1981), submicron etching (Ochiai et al. 1984) and submicron lithography (Seliger et al. 1979). Furthermore, the FIB technique can be used to fabricate novel modulated semiconductor structures such as a surface-nipi and a surface-superlattice.

In this paper we demonstrate various submicron-processing techniques such as fine-line implantation and fabrication of modulated structures and fine gratings with arbitrary shapes.

### **2. FIB technique**

The FIB equipment used in the experiment is JIBL-100L made by JEOL. A liquid-metal ion-source of Au-Si-Be eutectic alloy is used with a mass separator, by which both n- and p-type impurities can be selectively implanted. The beam is focused to 0.1  $\mu\text{m}$  diameter and controlled by a micro-computer which enables us to draw any desired pattern. The vacuum is about  $1 \times 10^{-9}$  Torr during implantation.

To activate implanted species, rapid thermal annealing (RTA) (Hiramoto et al. 1985) is employed to suppress spreading of implants by diffusion. The RTA furnace is composed of four halogen lamps with reflecting mirrors. The heating rate and the cooling rate are  $100^\circ\text{C}/\text{sec}$  and  $10^\circ\text{C}/\text{sec}$ , respectively.

### **3. Profile of line-implanted impurity**

Understanding of a carrier profile induced by impurity implantation and subsequent annealing is very important for practical usage of the FIB technique. Therefore, shapes of pn-junction boundaries were investigated for various implantation and annealing conditions with scanning-electron microscopy (SEM) after stain-etch. Although the beam diameter is about

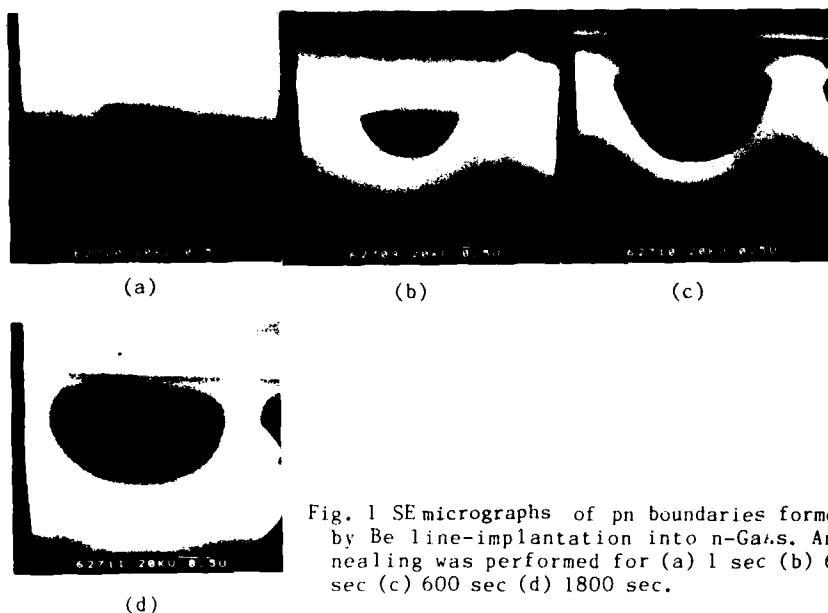


Fig. 1 SEMicrographs of pn boundaries formed by Be line-implantation into n-GaAs. Annealing was performed for (a) 1 sec (b) 60 sec (c) 600 sec (d) 1800 sec.

0.1  $\mu\text{m}$ , it is expected that the implanted species are scattered into a larger volume and also diffusion during annealing spreads the implanted impurities. It is also anticipated that the activation efficiency may vary according to the annealing conditions, affecting carrier profiles.

$\text{Be}^{2+}$  was line-implanted into Si-doped horizontal Bridgman (HB) GaAs substrates with a carrier density of  $5 \times 10^{17} \text{ cm}^{-3}$ . The implantation energy was 200 keV, the line dose was varied from  $3 \times 10^9$  to  $1 \times 10^{10} \text{ cm}^{-1}$  and the scanning rate was 0.34 cm/sec. The wafer was annealed in the RTA furnace at  $800^\circ\text{C}$ . The annealing time was varied from 1 to 1800 sec. During annealing As-pressure was applied by placing GaAs powder in a graphite boat (Hiramoto et al. 1985).

For observation of pn-junction boundaries, the wafer was cleaved and stain-etched with  $\text{HF}:\text{H}_2\text{O}_2:\text{H}_2\text{O} = 1:1:10$  under white light illumination. Under this condition only the p-region is etched. The pn-boundary appeared with a clear contrast in SE micrographs.

Figure 1 shows SE micrographs of pn-boundaries formed after 1, 60, 600 and 1800 sec annealing. In this case, the line-dose is  $1 \times 10^{10} \text{ cm}^{-1}$ . Even after 1 sec annealing the pn-boundary is spread laterally to 1.1  $\mu\text{m}$  and in depth to 1.1  $\mu\text{m}$ . For longer annealing the lateral spreading is 1.7  $\mu\text{m}$  (60 sec), 2.3  $\mu\text{m}$  (600 sec) and 2.6  $\mu\text{m}$  (1800sec). Correspondingly, the depth is 1.3  $\mu\text{m}$  (60sec), 1.8  $\mu\text{m}$  (600 sec) and 1.7  $\mu\text{m}$  (1800sec). Apparently, the behavior indicates anomalous diffusion of Be is taking place.

From a simple theory which assumes a Gaussian shape for the ion beam with the standard deviation of 0.05  $\mu\text{m}$  and a simple diffusion equation with a

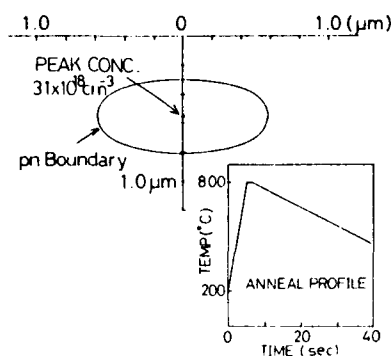


Fig. 2 Calculated pn boundary after Be line-implantation and 1 sec annealing. The line dose is  $1 \times 10^{10} \text{ cm}^{-1}$ . The carrier concentration of the substrate is  $4 \times 10^{17} \text{ cm}^{-3}$ . The inset shows the anneal profile.

and hence the pn-junction should disappear. However, in the experiment, a pn-junction still remains after 600sec annealing and the pn-boundary deviates largely from the oval shape. This suggests that more acceptors are created in the p-region or the background donors are reduced. It was found that the thermal conversion near the surface region was not significant in the unimplanted region. It should be also noted that the observation of a crystal facet of (111) orientation (Fig. 1(c)) indicates a preferential diffusion taking place.

We have made the similar experiment using an epitaxial substrate where the dopant is S. The spreading of the pn-boundary was much smaller than that in the case of Si-doped HB materials, and closer to the calculation which considers the reduction of activation efficiency.

The aforementioned results indicate that the anomalous diffusion of Be is dependent on the substrate quality. Also it is suggested that during annealing Si might transfer from Ga sites to As sites to create more acceptors in a HB substrate which contains a rather high density of Si.

#### 4. Surface nipi-structure

A surface nipi-structure is an interesting form of modulated semiconductor. To test the feasibility of FIB technique, Si and Be were alternatively line-implanted into semi-insulating (SI) GaAs substrates. The period was changed from 1 to 4  $\mu\text{m}$ . The annealing was performed at 800°C for 60 sec. The structure was observed with electron-beam-induced current (EBIC) mode and SE mode.

Figure 3(a) shows a SE micrograph of the nipi-structure reverse-biased at 5V. The separation of the n and p regions are 2  $\mu\text{m}$  in this case. A black region corresponds to n-type and a white region to p-type. A clear

temperature dependent diffusivity of Be ( $D=7.3 \times 10^{-6} \exp(-1.2/kT)$ ) (Poltoratski and Stuchechnikov 1966), the expected pn-boundary is calculated and shown in Fig. 2. After 1 sec annealing the peak density of Be is  $3.1 \times 10^{18} \text{ cm}^{-3}$  and the lateral spreading and the depth of the pn-boundary are 1.2  $\mu\text{m}$  and 0.82  $\mu\text{m}$ , respectively. In this case the discrepancy between the experiment and the calculation is not large but the shapes are apparently different. In the SE micrograph a half-moon shape is observed while in theory an oval shape is expected. We think that the surface depletion region affected the stain etching and the upper half of the oval shape in Fig. 1(a), (b) was obscured.

The calculation shows that the peak concentration of Be should become lower than the background donor density after annealing longer than 600 sec,

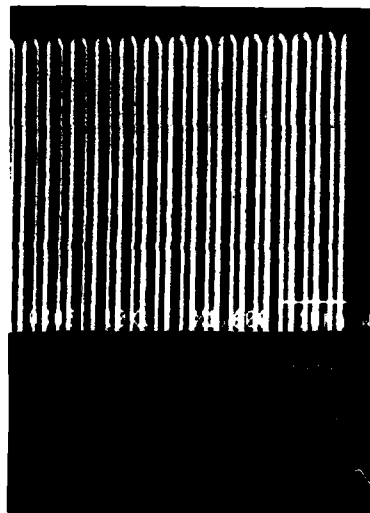
contrast in the two regions is observed. Figure 3(b) shows an EBIC image and a line profile. The white region represents the depletion region. In the line profile, the lowest and the second lowest currents correspond, respectively, to p- and n-regions. It was found that the perfect nipi-structure was fabricated by FIB implantation.

When the separation of the two regions is decreased to  $0.5\text{ }\mu\text{m}$ , the contrast of the EBIC image becomes unclear, as shown in Fig. 4. This is considered to result from the resolution limit of the EBIC technique. We conclude that a nipi-structure with down to  $0.5\text{ }\mu\text{m}$  separations can be formed by FIB. To

realize a quantum effect in a surface nipi-structure, the separation must be made much smaller. It will be possible to realize such structures by optimizing implantation and annealing conditions.

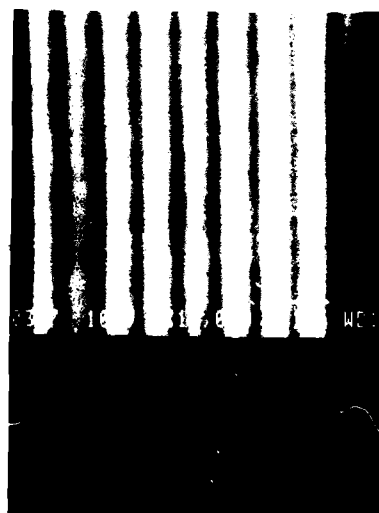


(a)  $50\text{ }\mu\text{m}$



(b)  $10\text{ }\mu\text{m}$

Fig. 3 (a) A SE micrograph of a nipi-structure reverse-biased at 5 V. The separation and p and n regions is  $2\text{ }\mu\text{m}$ . (b) An EBIC image and line profile.



$1\text{ }\mu\text{m}$

Fig. 4 EBIC image and line profile of a nipi-structure. The separation is  $0.5\text{ }\mu\text{m}$ .



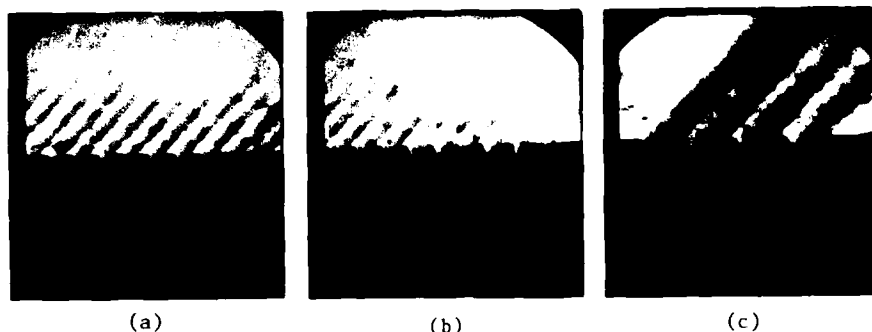


Fig. 5 SE micrographs of fine gratings fabricated by FIB implantation and etching. Si line doses were (a)  $3.0 \times 10^9 \text{ cm}^{-1}$  (b)  $3.5 \times 10^9 \text{ cm}^{-1}$  (c)  $4.1 \times 10^{10} \text{ cm}^{-1}$ .

#### 4. Gratings with arbitrary shapes

To produce a grating with an arbitrary shape, we applied enhanced etching of damaged regions induced by FIB. Focused Si-ions were line-implanted into a Si GaAs substrate. When the line-dose is high enough, amorphous regions are created (Taguchi et al. 1986). Such amorphous-regions cannot be created by conventional Si-implantation (Nakamura and Katoda 1984). Amorphous regions can be selectively etched with hot HCl (70°C) and submicron gratings were fabricated as shown in Fig. 5. When a line-dose

was just above the critical dose for forming amorphous, the width of the groove was about  $0.2 \mu\text{m}$  with a period of  $0.4 \mu\text{m}$  (Fig. 5(a)). The width and shape of grooves can be varied by changing the line-dose as shown in Fig. 5(b),(c).

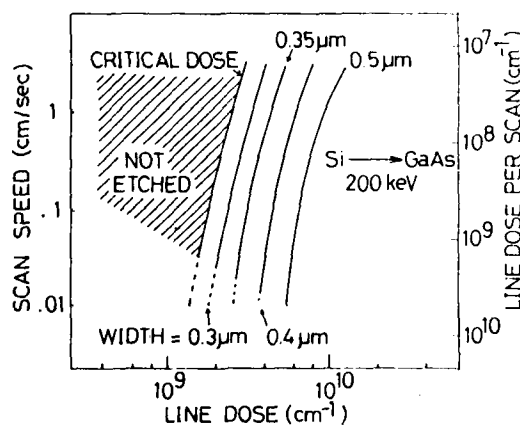


Fig. 6 Dependence of critical dose for formation of an amorphous region on the line dose and scan speed. The width of the groove is also shown.

The critical dose for formation of an amorphous depends on the scanning speed even for the same line dose. The slower the scanning rate, the lower the critical dose as shown in Fig. 6. The groove width becomes wider for larger line-dose. The separation of each groove can be controlled with a precision of  $0.1 \text{ nm}$  and therefore we can fabricate, for instance, a chirping grating.

Since FIB is precisely controlled by computer, we can draw a grating pattern with an arbitrary shape on target materials. As an example, circular gratings were fabricated as shown in Fig. 7. The fabrication process is the same as described above. The shape of the groove is, however, different from those in the line scanned grating. The difference may be due to difference in the line dose and scanning speed. We can also fabricate a Fresnel lens by this method. This technique will find various applications in optoelectronics.

#### 5. Summary

Submicron processing of III-V semiconductors by FIB was demonstrated. Concentration profiles of Be line-implanted by FIB were investigated by SEM. Anomalous diffusion is found to take place after long time annealing, suggesting that RTA is strongly required for post annealing. A surface nipi-structure was formed in SiGaAs by FIB implantation. EBIC observations showed that a nipi-structure with 0.5  $\mu\text{m}$  separation was successfully fabricated. An enhanced etching of damages induced by FIB was applied to form gratings with arbitrary shapes, such as fine gratings with 0.2  $\mu\text{m}$  wide grooves and circular gratings. These results show the feasibility of FIB technology for fabricating various modulated semiconductors and optoelectronic devices.

#### Acknowledgments

This work is partly supported by Grant-in Aid for Special Project Research "Alloy Semiconductor Electronics" from The Ministry of Education, Science and Culture. The authors would like to thank Mr. Ogura and Mr. Suzuki of JEOL for carrying out EBIC observations.

#### References

- Hiramoto T, Saito T and Ikoma T 1985 Jpn. J. Appl. Phys. **24** 193
- Kubena R L, Anderson C L, Seliger R L, Jullens R A and Stevens E H 1981 J. Vac. Sci. Technol. **19** 916
- Nakamura T and Katoda T 1984 Jpn. J. Appl. Phys. **23** 552
- Ochiai Y, Gamo K and Namba S 1984 Jpn. J. Appl. Phys. **23** 400
- Poltoratski E A and Stuchebnikov V M 1966 Sov. Phys. Solid State **8** 770
- Seliger R L, Kubena R L, Olney R D, Ward J W and Wang V J. Vac. Sci. Technol. **16** 1610
- Taguchi T, Nakamura T, Horiuchi K and Ishikawa H 1986 17th Symp. on Ion Implantation and Submicron Fabrication (Wako, Japan) pp 165-8

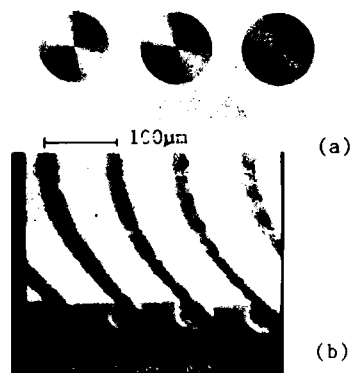


Fig. 7 (a) photograph of circular gratings fabricated by FIB implantation and etching. The separation of each circle is 1.0  $\mu\text{m}$ . (b) SE micrograph of the surface and cleaved surface of the circular grating.

## **A self-aligned technology using refractory metals for GaAs/GaAlAs heterojunction bipolar transistors**

K. DAOUD-KETATA, J.F. BRESSE, C. DUBON-CHEVALLIER  
Centre National d'Etudes des Télécommunications  
Laboratoire de Bagneux  
196 Avenue Henri Ravera - 92220 Bagneux - France

**ABSTRACT :** A new self-aligned technology for GaAs/GaAlAs Heterojunction Bipolar Transistors is presented. Self-alignment is obtained between the emitter ohmic contact and the p type implantation. This technology uses refractory metals to contact the emitter layer, in order to withstand the annealing process subsequent to the p type implantation, while also providing a mask for the implantation. Transistors processed with this new technology exhibit DC current gain of 25 showing the feasibility of the process.

### **1. INTRODUCTION**

Interest in a self-aligned processing technology has been demonstrated for Si bipolar applications, for it allows a decrease of the parasitic elements by scaling down the device dimensions. In the case of GaAs/GaAlAs heterojunction bipolar transistors (HBT's), a self-aligned technology is expected to enable a decrease of both the collector capacitance and the base access resistance which are the limiting parameters for high speed operation. Three self-aligned processes for HBT's have recently been reported. The first one (Fisher 1986) only involves a self-alignment between the emitter layer etch and the base ohmic contact deposition while the others, which provide a real self-alignment between the emitter ohmic contact and the p type implantation (Chang 1986) or between the emitter and base ohmic contacts (Nagata 1985), are rather sophisticated. This paper describes a new self-aligned technology using refractory metals. A single annealing step permits the formation of the emitter ohmic contact and activation of the p-type implant.

### **2. DEVICE STRUCTURE**

The multilayers are grown by molecular beam epitaxy (MBE) or by metalorganic vapour phase epitaxy (MOVPE) on semi-insulating GaAs wafers. The structure (Dubon-Chevallier 1986a) consists of a  $0.5 \mu\text{m}$   $n = 5 \times 10^{18} \text{ cm}^{-3}$  collector contact layer, a  $0.4 \mu\text{m}$   $n = 5 \times 10^{16} \text{ cm}^{-3}$  collector layer, a  $0.15 \mu\text{m}$   $p = 5 \times 10^{18} \text{ cm}^{-3}$  base layer, a  $0.35 \mu\text{m}$   $\text{Al}_{0.25}\text{Ga}_{0.75}\text{As}$   $n = 2 \times 10^{17} \text{ cm}^{-3}$  emitter layer and finally a  $0.1 \mu\text{m}$   $n = 10^{18} \text{ cm}^{-3}$  emitter contact layer. A 500 Å thick layer with a grading in Al composition from 0.08 to 0.25 is included on both sides of the emitter layer.

A schematic description of the self aligned process is shown in Fig. 1. The emitter ohmic contact is deposited first and delineated using reactive ion etching. The profile obtained after etching is a T-shape structure where the undercut determines the distance between the emitter ohmic contact and the p type implantation. The p type implantation is then performed with the emitter contact acting as a mask. The following annealing step forms the ohmic contact and activates the p-type dopant. Then a light wet etch is used to remove the lateral diode between the  $n^+$  cap layer and the p-type implantation. A deeper wet etch is performed down to the collector layer for contacting. Then a high energy  $B^+$ ,  $H^+$  implantation takes place in order to obtain electrical isolation between the transistors. AuGeNi/Ag/Au delineated by lift off and annealed at  $450^\circ\text{C}$  is classically used for the collector ohmic contact, while AuMn (Dubon-Chevallier 1986 b) is deposited to form the base ohmic contact.

This processing technology is quite simple, does not require any critical registration and leads to a decrease of the base access resistance and the collector capacitance.

### 3 - DEVICE FABRICATION

To realize this self-aligned structure, new fabrication techniques-refractory ohmic contact and reactive ion etching of the contact-have been developed.

The first step is to realize and to optimize a refractory ohmic contact for the emitter. We have investigated the feasibility of a molybdenum germanide (GeMo) ohmic contact which has also been studied by other workers (Tiwari

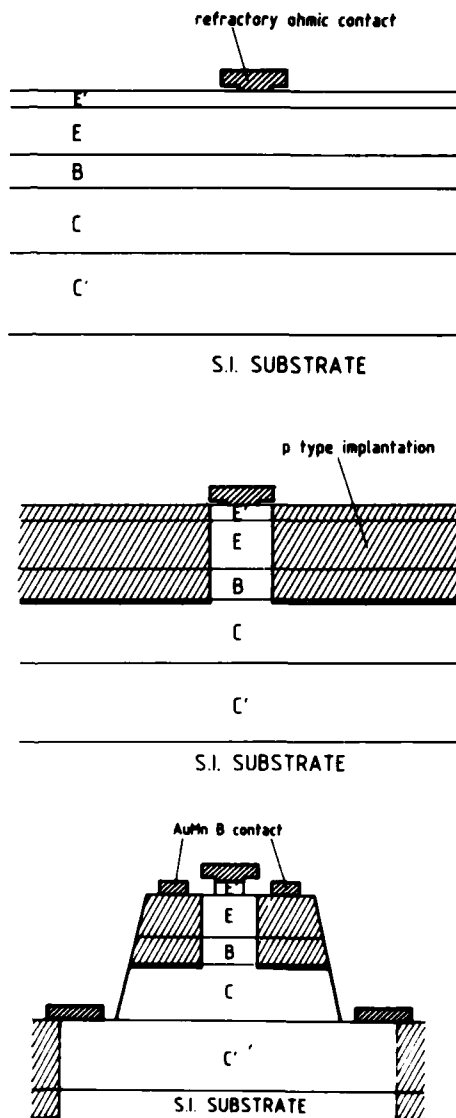


Fig. 1 : Schematic processing steps of the self-aligned technology.

150 Å Ge layer is deposited first using e-beam evaporation with a deposition rate of 10 Å/s, then a 150 Å Mo layer is RF sputtered with a deposition rate of 2 Å/s. Two different annealing techniques have been used to optimize the contact resistivity: rapid thermal annealing (RTA) and classical annealing in a sealed ampoule under an As overpressure. It is found that when using RTA, the electrical behaviour is non ohmic whatever the annealing conditions. In the second case, an ohmic contact is obtained. Specific contact resistivities as low as  $3 \cdot 10^{-6} \Omega \text{cm}^2$  are obtained on  $5 \cdot 10^{18} \text{ cm}^{-3}$  doped samples, at the optimum annealing conditions (800°C, 15 min). The As overpressure should reduce the creation of As vacancies and thus limit compensation mechanisms. Auger spectroscopy (AES) combined with an ion-beam sputtering technique was used to analyse the in-depth diffusion of the different species.

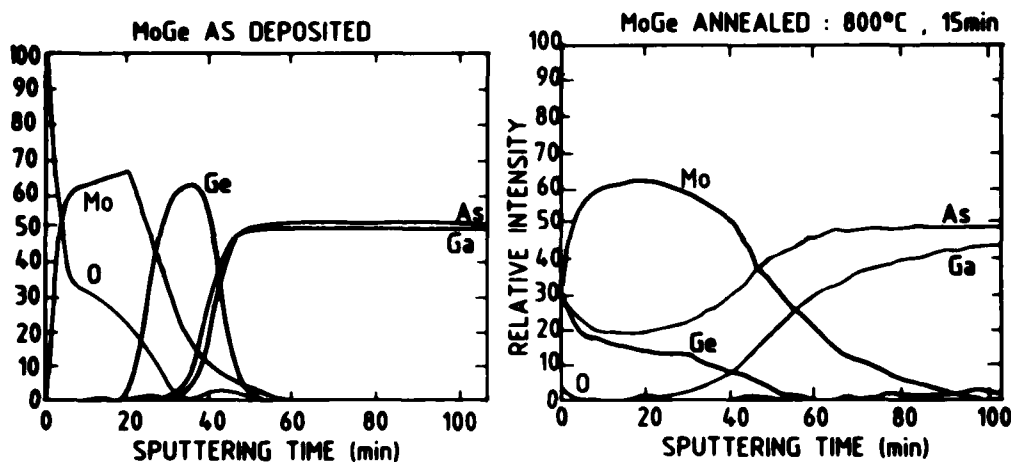


Fig 2 (a) Auger profiles before alloying. Ge is deposited first followed by Mo. (b) Auger profiles after alloying at 800°C under an As overpressure show the interdiffusion of Ge and Mo and the diffusion of Ge into the GaAs layer.

AES was conducted on as-deposited (Fig 2-a) and annealed (Fig. 2-b) samples. During the heat treatment, Ge and Mo interdiffuse and the comparison of the two curves a) and b) proves a diffusion of Ge and Mo in GaAs. A light diffusion of Ga in the metallic film can also be noted. There is an As accumulation in the metallic layer, but this may be due to the As overpressure. Before annealing, an important oxygen content is observed into the Mo film: oxygen is certainly incorporated in the Ar plasma. After annealing, nearly all the oxygen is eliminated. These results prove that the formation of the contact is due both to a  $n^+$  layer created at the metal/GaAs interface by Ge diffusion and to the formation of a stable phase between Ge and Mo which was identified as  $\text{Mo}_3\text{Ge}_3$  by transmission electron microscopy. Taking into account the results showing the influence of the As overpressure, contacts including As doped Ge instead of pure Ge

have been investigated : preliminary results show that ohmic contact can then be obtained without an As overpressure, which is more convenient for wafer processing. However, the best contact resistivity obtained up to now is  $10^{-5} \Omega\text{cm}^2$  which is too high and prevent the integration of this step in the HBT process.

Etching of the contact has also been investigated using reactive ion etching. Mo, Ge and W can be etched selectively on GaAs using a  $\text{SF}_6$  plasma discharge. The first step is to determine a convenient etching mask. Metallic films are found to be more suitable than photoresist and among the metallic films Pt was found to be the most convenient. In Fig 3, the etch rate is plotted as a function of pressure for GaAs, W, Pt and photoresist at a power density of  $0.6 \text{ W/cm}^2$ . The etch rates of GaAs and Pt are very low because GaAs and Pt do not form any volatile compounds. Moreover their etch rates become negligible when the pressure increases as the sputtering mechanisms disappear. The etch rates of W and photoresist are relatively high. At low pressure, the self bias voltage is high and the dominant mechanism is ion assisted chemically enhanced sputter etching. When the pressure increases, the sputtering mechanism becomes negligible and the etch rate decreases to a minimum. At higher pressure, the dominant mechanism is the free radical process. In order to obtain a T-shape profile two steps are necessary. During the first one the anisotropic etch, using Pt as a mask, is achieved (fig.4a). The conditions are chosen to obtain an anisotropic etch and also to prevent GaAs damage ( $p = 30 \text{ mT}$ ,  $P = 0.6 \text{ W/cm}^2$ ). These values lead to a self-bias voltage of  $170 \text{ V}$ , and the etching rates of Ge, Mo and W are respectively  $2000 \text{ Å/min}$ ,  $1000 \text{ Å/min}$  and  $1350 \text{ Å/min}$ . During the second step, the undercut of the contact is achieved. The etch is isotropic that is to say there is only a side etch, Pt being the upper part of the T-shape structure. The conditions are chosen to obtain an isotropic etch and to prevent the formation of residues ( $p=60 \text{ mT}$ ,  $P = 0.4 \text{ W/cm}^2$ ). These values lead to a self bias voltage of  $50\text{V}$ , and the side etching rates of Ge, Mo and W are respectively  $550 \text{ Å/min}$ ,  $450 \text{ Å/min}$  and  $250 \text{ Å/min}$ . The resulting profile is shown in Fig. 4b.

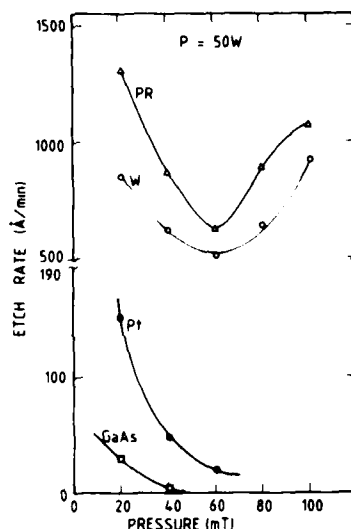


Fig 3 : The etch rates of W, photoresist, Pt and GaAs are plotted as a function of pressure for a power density of  $0.6 \text{ W/cm}^2$ . Pt which does not form any volatile compound is a suitable mask.



Fig 4 a) first step : anisotropic etch, b) second step : isotropic etch, the undercut is  $0.5 \mu\text{m}$ .

#### 4 - RESULTS

HBT's structures have been processed with this new self aligned technology to prove the feasibility of this technology. For this purpose relatively large area ( $80 \times 80 \mu\text{m}^2$ ) test transistors were fabricated. Common emitter characteristics are shown in Fig.5. The DC current gain is 25 at a collector current density of  $0.3 \text{ A/cm}^2$ . Such values are similar to those obtained with a classical technology. Using the same self aligned technology, it is expected that, with emitter dimensions of  $2 \times 20 \mu\text{m}^2$ , transition frequency and maximum frequency as high as 60GHz and 58GHz respectively can be obtained.

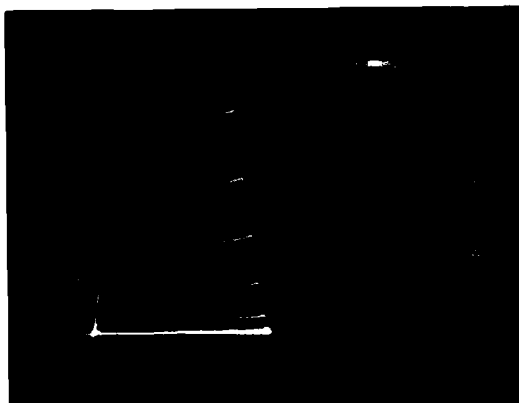


Fig 5 : Common emitter dc characteristics of a typical HBT.

#### CONCLUSION

A new self-aligned technology for GaAs/GaAlAs HBT's, which permits to decrease the base resistance and the collector capacitance has been presented. This technology requires new fabrication techniques-refractory ohmic contact, reactive ion etching of the contact-. HBT's exhibiting D.C current gain of 25 have been processed along this new technology.

#### ACKNOWLEDGEMENTS

The authors wish to thank P. HENOC for Transmission Electron Microscopy and C. GERARD for device simulation. This work was partly supported by Esprit project 971.

#### REFERENCES

- Chang M F , Asbeck P M, Miller D L and Wang K C 1986 IEEE Elect. Dev. Lett. EDL7 8
- Dubon-Chevalier C, Desrousseaux P, Duchenois A M, Besombes C, Dangla J Bacot C and Ankri D 1986a High Speed Electronics Conf. Stockholm Sweden
- Dubon-Chevalier C, Gauneau M, Bresse J F, Izraël A and Ankri D 1986b . J. Appl. Phys. 59 (11) 3783
- Fischer R and Morkoç H 1986 IEEE Elect. Div. Lett. EDL-7 359
- Nagata K, Nakajima O, Yamauchi Y and Ishibashi T 1985 Inst. Phys. Conf Ser. 79 (11) 589
- Tiwari S, Kuan T S and Tierney E 1983 Proc. IEDM



## **Low resistance refractory metal WAg/W gate self-aligned GaAs MESFETs**

Guan Qun Xia, Wei Yuan Wang

Shanghai Institute of Metallurgy, Academia Sinica 865 Chang Ning Road  
Shanghai 200050, China

**Abstract.** In this paper, the microstructure, electrical characteristics of sputtered WAg and WAg/W refractory metal films and its interaction with GaAs at high temperature were studied. After annealing at 800°C for 30 min the resistivity of WAg (30 at%) films with thickness of 4000Å is 18.9μΩcm, lower than that of any other reported refractory W alloy films with similar thickness. The fully ion-implanted self-aligned GaAs MESFETs were fabricated by using of 4000Å WAg/800Å W metal gate. The sputtered WAg/W double refractory metal films have the advantages of good thermal stability, low resistance and easy fabrication, and are of benefit to GaAs microwave MESFETs and digital ICs.

### 1. Introduction

After the first paper of refractory metal Ti-W gate self-aligned GaAs MESFETs was reported by Yokoyama et al (1981), the papers on refractory metal WTiSi<sub>2</sub>, WSi<sub>2</sub>, W, TaSi<sub>2</sub> and WAl gate (Yokoyama et al 1981, Matsumoto et al 1982, Nakamura et al 1983) were reported in succession. The results show that such refractory metal films deposited on GaAs have good thermal stability and high reliability at high temperature, and were used to form Schottky contact in fully ion-implanted GaAs digital ICs (Yokoyama et al 1983).

But the higher resistivity of these refractory metal films influences the noise of GaAs MESFETs, the speed and the power consumption of digital GaAs ICs, and is still a problem to be solved.

In this paper, the microstructure, resistance of sputtered WAg and WAg/W refractory metal films and its interaction with GaAs at high temperature were studied. We first confirm that WAg films are refractory metal with the lowest resistance, the low resistance refractory metal WAg/W gate self-aligned GaAs MESFETs with better performances were fabricated.

### 2. Experiments

WAg films were deposited by RF sputtering on n-type GaAs substrates. WAg target used for sputtering was inlaid by Ag in W, and the purity of Ag and W is 5N and 4N, respectively. Adjusting the Ag area of WAg target the different compositions of WAg films were obtained. Double WAg/W films were sputtered in order of W and WAg, and the W target was hot pressed from high purity W powder.

During sputtering, high purity (99.999%) Ar gas at the pressure of  $3 \times 10^{-2}$  Torr was used. The typical RF power was 0.5 KW, substrate temperature

was less than  $100^{\circ}\text{C}$  and the deposition rate was  $400\text{\AA}/\text{min}$ .

We observed and analysed the microstructure and compositions of WAg films with high voltage transmission electron microscope (TEM), scanning electron microscope (SEM) and electron probe, analysed the longitudinal atom profiles of WAg/GaAs and WAg/W/GaAs interface with auger electron spectroscopy (AES), measured the sheet resistance of metal films with four-point probe, and measured the thickness of metal films with interferential microscope and Talystep.

The substrates used for GaAs MESFETs were LEC undoped SI-GaAs with crystal orientation of [100] and  $10^{-2}\text{cm}$ . The selective  $\text{Si}^{+}$  implantation at an energy of 150 KeV to a dose of  $3.5 \times 10^{12}\text{cm}^{-2}$  was used to form active layer using photoresist AZ 1350J and  $\text{Si}_3\text{N}_4$  as a mask, then capless annealing at  $800^{\circ}\text{C}$  for 30 min. The self-aligned WAg/W gate with length of  $2\mu\text{m}$  and width of  $40\mu\text{m}$  was sputtered in order of W and WAg on cooled GaAs substrates and defined by a lift-off technique. The second selective and self-aligned  $\text{Si}^{+}$  implantation was used at energy of 100KeV and dose of  $2 \times 10^{13}\text{cm}^{-2}$ , and annealing was carried out at  $750^{\circ}\text{C}$  for 30 min, to form the source and drain  $\text{n}^{+}$  layer. The S and D ohmic contact was formed by alloying the evaporated AuGeNi.

### 3. Results

#### 3.1 The compositions and microstructure of WAg films

Fig.1 shows the relationship between the area ratio of  $S_{\text{Ag}}/S_{\text{WAg}}$  of WAg target and the Ag atomic percent in sputtered WAg films as measured by electron probe. It is clear that the  $S_{\text{Ag}}/S_{\text{WAg}}$  is linear with Ag atomic percent in WAg film.

Fig.2 is the W and Ag atomic distribution as determined by line scanning photo of electron probe, (a) and (b) is the  $\text{W}(\text{K}_{\alpha})$  and  $\text{Ag}(\text{L}_{\alpha})$  x-ray line scanning, respectively, in the same sample. Obviously the distribution is quite homogeneous.

Shown in Fig.3 are the TEM micrographs and transmission electron diffraction patterns on the same WAg (30 at%) films before and after annealing. Before annealing, Fig.3(a), the W and Ag are two independent phases, the Ag grains are oval in shape, about  $500\text{\AA}$  in size and well-distributed

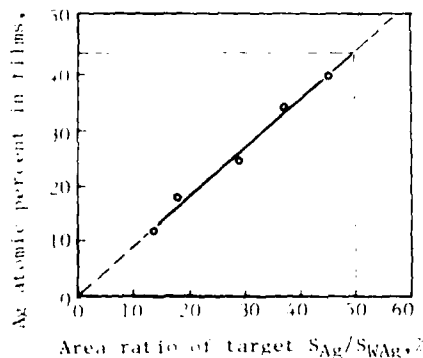


Fig. 1 Relationship between area ratio  $S_{\text{Ag}}/S_{\text{WAg}}$  of WAg target and Ag atomic percent in sputtered WAg films

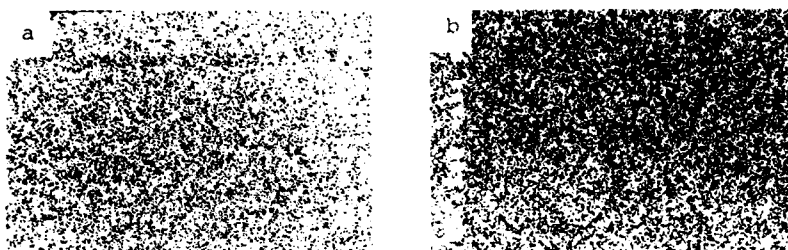


Fig. 2 W and Ag atomic distribution on WAg (30 at%) films  
(a) W( $K_{\alpha}$ ) x-ray line scanning (b) Ag( $L_{\alpha}$ ) x-ray line scanning

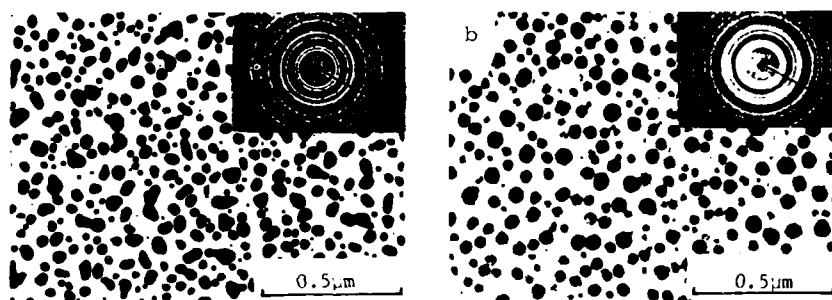


Fig. 3 TEM micrographs and TED patterns of WAg (30 at%) films  
(a) before annealing (b) after annealing at 800°C for 30 min

in bulk W. After annealing at 800°C for 30 min, Fig.3(b), the Ag grains appear as hexagonal in shape, and are still well-distributed in bulk W. According to the results calculated from electron diffraction pattern, only Ag poly-crystals are found in WAg films before annealing, Fig.3(a), but both Ag and W poly-crystals are found in WAg films after annealing, Fig.3(b). The W in WAg films is amorphous solid before annealing and becomes poly-crystals after annealing without change the distribution, which also confirm that W and Ag are two independent phases in the WAg films.

### 3.2 The resistivity of WAg films

Fig.4 shows the dependence of the resistivity of RF sputtered pure W and WAg (30 at%) films with thickness of 4000Å on annealing temperature. It can be seen from Fig.4 that the resistivity of sputtered W and WAg film is high before annealing, decreases slowly with increasing of annealing temperature to about 400°C, drops quickly when annealing temperature of 400-750°C, and tends to be even up to 750°C. The resistivity of WAg films at 800°C for 30 min is 18.9μΩcm and that of W films at 1000°C for 30 min is 25.1μΩcm.

### 3.3 The interface interaction between WAg/GaAs and WAg/W/GaAs

Shown in Fig.5 are the longitudinal composition profiles of 1000Å WAg/GaAs and 600Å WAg (30 at%)/800Å W/GaAs films after annealing at 800°C for 30

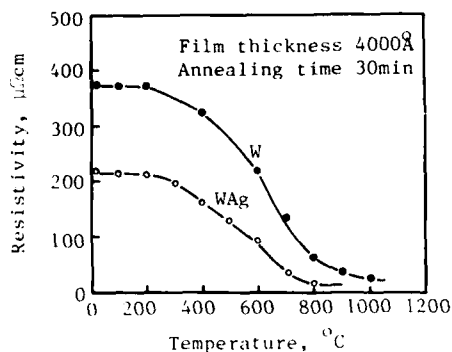


Fig. 4 Dependence of the resistivity of sputtered 4000Å W and 4000Å WAg (30 at%) films on annealing temperature

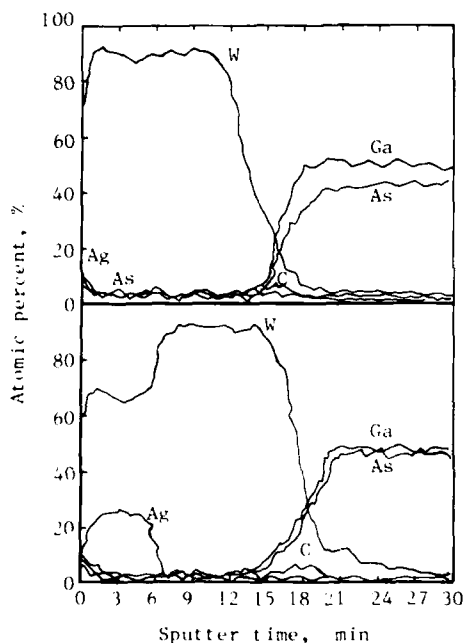


Fig. 5 AES longitudinal profiles of films after annealing at 800°C for 30 min  
(a) 1000Å WAg (30 at%)/GaAs  
(b) 600Å WAg (30 at%)/800Å W/GaAs

min as determined by AES. The mutual diffusion of Ag in WAg and As in GaAs is observed in interface of WAg/GaAs, Fig.5(a). In this case, metal-semiconductor Schottky barrier no longer exists, and a poor ohmic contact is formed. Inserting 800Å W layer between WAg and GaAs, the mutual diffusion of Ag in WAg and As in GaAs are effectively prevented, Fig.5(b), and the metal-semiconductor contact shows good Schottky barrier characteristics with forward built-in voltage and reverse breakdown voltage of 0.7V and >4V, respectively (see below).

#### 3.4 GaAs MESFETs

Self-aligned low resistance refractory metal 4000Å WAg (30 at%)/800Å W gate GaAs MESFETs with gate length of 2μm and width of 40μm were successfully fabricated. Fig.6 shows the I-V characteristics of GaAs MESFET

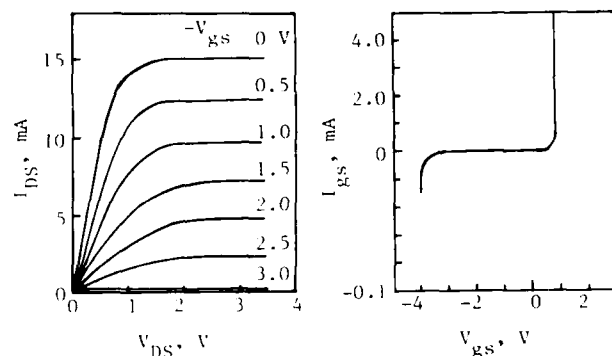


Fig. 6 I-V characteristics of WAg/W gate self-aligned GaAs MESFET

as well as the GaAs Schottky diode. The parameters of the experimental devices are as follows:  $I_{DSS0}=15\text{mA}$ ,  $V_p=-3\text{V}$  and  $g_m=140\text{mS/mm}$ .

#### 4. Discussion

The resistivity of refractory W alloys developed by Yokoyama et al and other scientists, whether W or  $\text{WSi}_2$ ,  $\text{WTiSi}_2$  and  $\text{WAl}$  alloy films etc., applied to fabricate self-aligned GaAs MESFETs are generally higher than that of pure W due to the electron scattering resulted from lattice periodicity deformation of bulk crystal by solute atoms. It is well known that W and Ag, solid or liquid, are mutual unsoluble, but homogeneous solid WAg mixture can be obtained by special techniques. Such is found to be the case in sputtered and annealed WAg (30 at%) films as shown in Fig.2 and 3. The resistivity of homogeneous mixture alloys, according to Berry et al (1968), is equal to an average-weighted value of resistivity of component metals. Ag is a metal of the lowest resistivity and unsoluble in W, we can expect that the resistivity of WAg films decreases continuously with increasing of Ag content in WAg films.

From Fig.3, the W appears as amorphous state in sputtered WAg films, but changes to poly-crystal state after annealing at  $800^\circ\text{C}$  for 30 min. Combined with Fig.4, the changing temperature must be over about  $400^\circ\text{C}$ . Besides, only after high temperature annealing can the stable and low resistivity of WAg films be obtained. The resistivity of  $25.1\mu\Omega\text{cm}$  of  $4000\text{\AA}$  W films determined in this paper is higher than that of  $5.6\mu\Omega\text{cm}$  of bulk W (Ross 1980) and  $6000\text{\AA}$  W films (Wilson and Terry 1970), and lower than that of  $40\mu\Omega\text{cm}$  of  $1000\text{\AA}$  W films (Nakamura et al 1983). The calculated resistivity of pure  $4000\text{\AA}$  Ag films using the method developed by Berry et al (1968) and the experimental data is  $4.4\mu\Omega\text{cm}$ , higher than that of  $1.6\mu\Omega\text{cm}$  of bulk Ag and  $6000\text{\AA}$  Ag films (Ross 1980, Wilson and Terry 1970). The discrepancy in resistivity of W materials may be due to the difference in material thickness or existing residual amorphous in W films, which results in discrepancy in resistivity between calculated and published Ag materials. The resistivity of WAg (30 at%) films decreases to  $18.9\mu\Omega\text{cm}$  after annealing at  $800^\circ\text{C}$  for 30 min, and is lower than that of any other published refractory W alloy.

We have tried to investigate higher Ag content WAg films with lower resistivity. But the shrinkage and segregation of Ag grains are found

in WAg (50 at%) films after annealing at 800°C for 30 min.

For fabrication of refractory metal-nGaAs Schottky barrier and self-aligned gate GaAs MESFETs with better performances (Fig.6), from the result of Fig.5, it is necessary to put a thin layer of W films between WAg and GaAs in order to inhabiting the mutual diffusion of Ag and As, which results in poor device performances.

The WAg alloys have widely been used in relays as a conducting contact materials, but this is the first time for the sputtered WAg (30 at%) films to be used in fabricating self-aligned gate GaAs MESFETs with better performances.

#### Acknowledgements

The authors wish to thank many of colleagues of high speed device group at Shanghai Institute of Metallurgy for fabricating the GaAs MESFETs, Dr. Xiang Yun Song of Shanghai Institute of Ceramic for TEM analysis and Dr. Hui Liang Zou of Shanghai Institute of Testing Technology for AES analysis. Thanks are also due to financial aid from Ion Beam Laboratory, Shanghai Institute of Metallurgy, Academia Sinica.

#### References

- Berry R W, Hall P M and Harris M T 1968 Thin Film Technology (Bell Telephone Lab. Series) Chapter 5
- Matsumoto K, Hashizume N, Tanoue H and Kanayama K 1982 Japanese J. Appl. Phys. 21 L393
- Nakamura H, Sano Y, Nonaka T, Ishida T and Kaminishi K 1983 GaAs IC Symposium pp134
- Ross R B 1980 Metallic Materials Specification Handbook (E. & F.N.Spon Ltd) pp279 and 611
- Wilson R W and Terry L E 1970 Electronic Packaging and Production 10 No.10 MC29
- Yokoyama N, Mimura T, Fukuta M and Ishikawa H 1981 ISSCC Digest of Technical Papers pp218
- Yokoyama N, Ohnishi T, Odani K, Onodera H and Abe M 1981 IEDM pp80
- Yokoyama N, Ohnishi T, Onodera H, Shinoki T, Shibatomi A and Ishikawa H 1983 ISSCC Digest of Technical Papers pp44

## **Influence of the InAs-GaAs miscibility gap on the In/GaAs reaction**

J. Ding, J. Washburn, T. Sands\* and V.G. Keramidas\*

Lawrence Berkeley Laboratory, University of California, Berkeley, CA 94720

\*Bell Communications Research, Inc., 331 Newman Springs Road, Red Bank, NJ 07701

**Abstract.** The In/GaAs reaction in the temperature range 350-650°C has been studied by analytical and high resolution electron microscopy and electron and x-ray diffraction. Histograms of the compositions of the  $\text{In}_{1-x}\text{Ga}_x\text{As}$  precipitates formed during annealing confirm the existence of a miscibility gap in the InAs-GaAs pseudo-binary system. Implications of these results for the fabrication of graded layer  $\text{In}_{1-x}\text{Ga}_x\text{As}/\text{n-GaAs}$  ohmic contacts by thermal reaction are discussed.

### **1. Introduction**

Graded  $\text{In}_{1-x}\text{Ga}_x\text{As}$  layers on GaAs grown by molecular beam epitaxy (MBE) have been shown to make low-resistance ohmic contacts to n-GaAs (Woodall *et al.* 1981). Woodall *et al.* argue that the grading is necessary to smooth out the conduction band discontinuity so that ohmic conduction can occur. Previous Auger electron spectroscopy studies by Lakhani (1984a, 1984b) suggest that a graded  $\text{In}_{1-x}\text{Ga}_x\text{As}/\text{GaAs}$  heterojunction ( $0 \leq x \leq 1$ ) can also be formed by heat treating thermally-evaporated indium films on GaAs substrates at 350°C. Recently, the interface structures and morphologies of In on GaAs after annealing at 350°C were investigated by Ding *et al.* (1986) using transmission electron microscopy techniques. The result of this study demonstrated the abrupt nature of the interface between the GaAs substrate and the  $\text{In}_{1-x}\text{Ga}_x\text{As}$  islands. Contrary to the results of Lakhani (1984a, 1984b), the  $\text{In}_{1-x}\text{Ga}_x\text{As}/\text{GaAs}$  interfaces were not graded. Furthermore, only islands with  $x \leq 0.2$  or  $x \geq 0.8$  were observed. Ding *et al.* (1986) proposed that the absence of precipitates with  $0.2 < x < 0.8$  is direct evidence for a miscibility gap in the InAs-GaAs pseudo-binary system at 350°C. This interpretation is consistent with the calculations of de Cremoux *et al.* (1981) which suggest the existence of a miscibility gap with a critical temperature between 500°C and 700°C in the InAs-GaAs system. Other theoretical analyses with similar conclusions were reported by Stringfellow (1982) and Onabe (1982). Quillec *et al.* (1982) grew a series of InGaAsP thin films from the liquid phase on both (100) GaP and (100) InP substrates at relatively high temperatures (610°C ~ 670°C). The experimental results from electron microprobe analyses indicated the existence of a miscibility gap in the  $\text{In}_x\text{Ga}_{1-x}\text{As}_y\text{P}_{1-y}$  system, supporting the previous theoretical results. The miscibility gap originates from an enthalpy of mixing ( $\Delta H_{\text{mix}}$ ) which is greater than the absolute temperature multiplied by the entropy of mixing ( $T\Delta S_{\text{mix}}$ ) at temperatures below some critical temperature,  $T_c$ . Atomistically, immiscibility in a system such as InAs-GaAs

implies that In and Ga atoms repel so that a random distribution of Ga and In on the cation sites of the zincblende structure is not energetically favorable.

In this paper, we extend our previous study of the In/GaAs reaction to include the temperature range 350°C-650°C. Data obtained by electron diffraction, energy dispersive x-ray analysis (EDS) and x-ray diffraction (XRD) clearly demonstrate the extent of the InAs-GaAs immiscibility and suggest a critical temperature between 575°C and 650°C.

## 2. Experiment and Data Analysis Procedure

Liquid encapsulated Czochralski (LEC) semi-insulating wafers were prepared for In deposition by an ultra-high vacuum (UHV) technique that was described in detail by Ding *et al.* (1986). Following this UHV cleaning procedure, In was deposited onto the rotating substrate (8RPM) to a thickness of 57 nm (~5.7 nm/min.) at 25°C. In order to investigate the miscibility gap in the pseudo-binary InAs-GaAs system, the samples were divided into four groups and annealed for 10 minutes at 350°C, 500°C, 575°C and 650°C respectively in an atmosphere of flowing forming gas (95% Argon, 5% Hydrogen). Both cross-sectional and plan-view TEM samples were prepared by standard techniques (Sands 1986). Observations of each sample were made in a scanning electron microscope (SEM), a Philips 301 TEM and a JEOL 200CX TEM. Energy dispersive x-ray spectrometry (EDS) was performed in a Philips 400ST TEM/STEM, and x-ray diffraction in a Siemens D500 x-ray diffractometer. The  $\text{In}_{1-x}\text{Ga}_x\text{As}$  phases formed at the In/GaAs interface after annealing at the various temperatures were identified by electron diffraction analysis and energy dispersive x-ray spectra. Since the ternary  $\text{In}_{1-x}\text{Ga}_x\text{As}$  phases exhibit a linear dependence of lattice spacing with composition (Woolley *et al.* 1958), i.e., they obey Vegard's law, the compositions of the precipitates studied can be determined by electron diffraction analysis, especially for In-rich  $\text{In}_{1-x}\text{Ga}_x\text{As}$  precipitates. Due to the overlap of diffraction spots from GaAs and Ga-rich  $\text{In}_{1-x}\text{Ga}_x\text{As}$ , the estimation of composition by electron diffraction was not straightforward for  $x \sim 1$ . Instead, the compositions of these Ga-rich precipitates were estimated by applying the EDS technique to cross-sectional samples. The EDS spectra were quantitatively analyzed by determining the proportionality factors  $K_{x/y}$  which relate the height ratios  $H_x/H_y$  of the x-ray peaks (proportional to the total counts or intensities) to the concentration ratios  $[X]/[Y]$  of the elements X,Y. The relationship between the concentration ratio and the peak height ratio is expressed as:

$$[X]/[Y] = K_{x/y} \cdot H_x/H_y$$

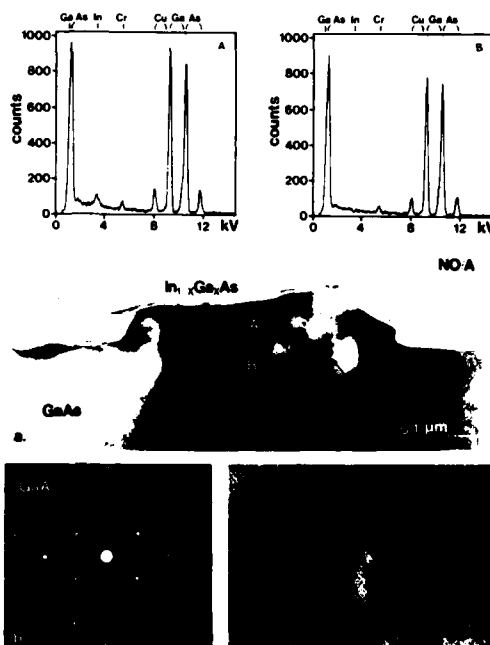
where the proportionality factor  $K_{\text{Ga/As}}$  relates the heights of the Ga and As  $K\alpha$  peaks in spectra taken from the adjacent GaAs substrate. The value of  $x$  in the  $\text{In}_{1-x}\text{Ga}_x\text{As}$  is then given by the ratio  $[X]/[Y]$  determined from spectra taken from the  $\text{In}_{1-x}\text{Ga}_x\text{As}$  precipitate.

## 3. Results

The interface morphology of the In/GaAs sample after annealing at 350°C for 10 minutes is depicted in Fig. 1. The two beam bright field TEM image is shown in Fig. 1a. A thin film of indium oxide can be seen to cover the reacted island. This precipitated phase has been identified structurally by electron diffraction analysis and compositionally by energy dispersive spectrometry. The EDS spectra from the island A and the substrate B



Fig. 1. (a) HRTEM image of the annealed oxide-free sample. The misfit dislocations can be seen at the interface. The indium oxide shell appears on the surface of the  $\text{In}_{1-x}\text{Ga}_x\text{As}$  phase. Quantitative microanalysis of the energy dispersive x-ray spectrum A indicates the patch A to have the composition of  $\text{In}_{0.02}\text{Ga}_{0.98}\text{As}$ . (b) Diffraction pattern taken from the island A and the substrate B shows only the reflections from the GaAs [011] zone axis orientation. (c) Lattice image of a misfit dislocation (arrowed in (a)) at the interface.



(shown above the image) yield a composition of  $\text{In}_{0.02}\text{Ga}_{0.98}\text{As}$  for the Ga-rich ternary phase with the zincblende structure. The diffraction pattern from the interface region shown in Fig. 1b indicates that it is almost impossible to distinguish the diffraction spots of this ternary phase from those of the GaAs substrate because of the small concentration of indium in this epitaxial island. The high resolution lattice image in Fig. 1c reveals the detailed interface morphology. A misfit dislocation can be seen at the interface due to the mismatch (0.16%) between the Ga-rich ternary phase  $\text{In}_{0.02}\text{Ga}_{0.98}\text{As}$  and the GaAs substrate. Another example of a precipitate from the same sample is shown in the cross-sectional high resolution micrograph in Fig. 2. The misfit dislocations and moiré fringes appear at the interface, where they result from the two distinct lattice parameters of the epitaxial island and the GaAs substrate. This indicates that the interface is abrupt, i.e., no graded  $\text{In}_{1-x}\text{Ga}_x\text{As}$  layer exists at the interface. Based on Vegard's law, the epitaxial island was identified from the diffraction analysis to be the In-rich ternary phase  $\text{In}_{0.9}\text{Ga}_{0.1}\text{As}$ . The EDS data also confirm that the island is In-rich  $\text{In}_{1-x}\text{Ga}_x\text{As}$ . Precipitates with compositions ( $0.2 < x < 0.8$ ) were not observed.

According to the theoretical calculations of de Cremoux *et al.* (1981), a miscibility gap exists in the InAs-GaAs pseudo-binary system with a critical temperature between 500°C and 700°C. To investigate the effect of immiscibility on the In/GaAs reaction, a statistical study was performed by annealing the In/GaAs samples at 350°C, 500°C, 575°C and 650°C. Several cross-sectional specimens from each sample were investigated by TEM and STEM. The distributions of precipitate compositions were determined by electron diffraction and EDS analyses. As can be seen in Fig. 3, three histograms from three different annealing temperatures reveal the extent of immiscibility in this system. It is also clear from the histograms

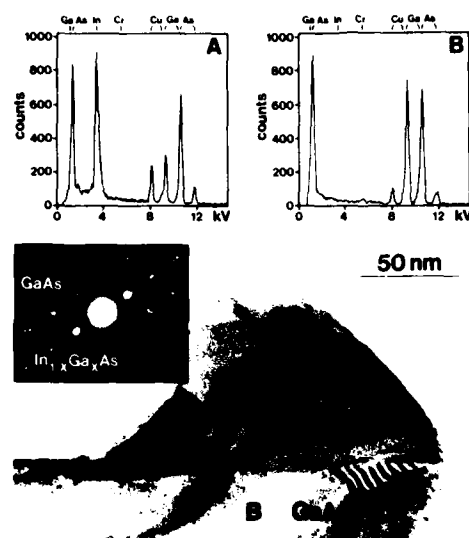


Fig. 2. High resolution image of the annealed cross-sectional oxide-free sample. The misfit dislocations and the moiré fringes indicate an abrupt interface. Inset diffraction pattern was taken from the region including the reacted patch A and the substrate B. The patch A was estimated to be  $\text{In}_{0.9}\text{Ga}_{0.1}\text{As}$  by diffraction analysis. The energy dispersive x-ray spectra obtained from the patch A and the substrate B are also shown to identify the patch as  $\text{In}_{1-x}\text{Ga}_x\text{As}$ .

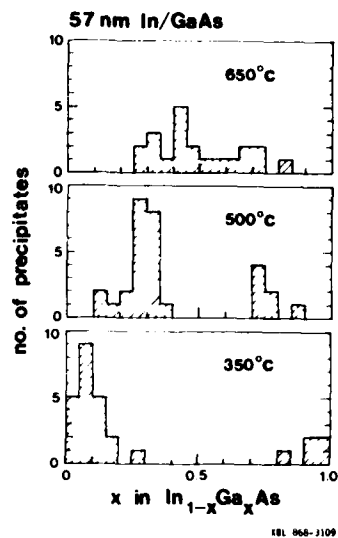


Fig. 3. Histograms of the numbers of the  $\text{In}_{1-x}\text{Ga}_x\text{As}$  precipitates with respect to composition  $x$  from the three samples annealed at the different temperatures (350°C, 500°C and 650°C).

that the critical temperature (i.e., the temperature above which InAs and GaAs are completely miscible) is between 500°C and 650°C. This miscibility gap in the InAs-GaAs pseudo-binary system was also revealed experimentally by x-ray diffractometry. The x-ray results from this system are shown in Fig. 4. Slow traces of the 400 peaks of the GaAs substrate and  $\text{In}_{1-x}\text{Ga}_x\text{As}$  ( $0 < x < 1$ ) precipitates were obtained by employing  $\text{CuK}\alpha$  radiation in an x-ray diffractometer. When compared with the spectrum from the as-deposited sample, the spectrum from the sample annealed at 350°C shows an additional peak corresponding to In-rich  $\text{In}_{1-x}\text{Ga}_x\text{As}$  and a shoulder on the GaAs 400 peak corresponding to Ga-rich  $\text{In}_{1-x}\text{Ga}_x\text{As}$ . This result is in agreement with EDS and electron diffraction data in Fig. 3. As the annealing temperature is increased, the In-rich  $\text{In}_{1-x}\text{Ga}_x\text{As}$  400 peak shifts toward the direction of increasing Ga content (i.e., increasing  $x$ ). The diffraction peak from the In-rich  $\text{In}_{1-x}\text{Ga}_x\text{As}$  ternary phase peak merges with the Ga-rich shoulder at 650°C, suggesting that the critical temperature is close to 650°C. Furthermore, it is apparent from the broad Ga-rich shoulder in the x-ray data that significant interdiffusion is taking place at 650°C.

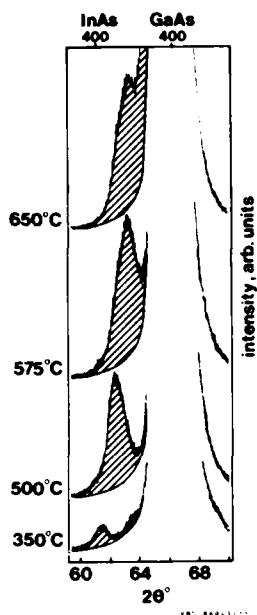
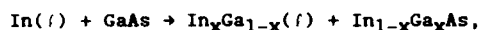


Fig. 4. Slow trace XRD patterns of the 400 reflections of as-deposited In on (100) GaAs, and after annealing for 10 minutes at 350°C, 500°C, 575°C and 650°C, respectively (CuK $\alpha$  radiation). Each trace is compared with the trace from the as-deposited sample (broken line).

#### 4. Discussion

The assumption is that the system rapidly approaches equilibrium. The observation that there is extensive reaction even at temperatures as low as 350°C excludes solid state interdiffusion between In and Ga as the reaction mechanism for temperatures <650°C. This is in agreement with a previous study (Ding *et al.* 1986) where the reaction involving the dissolution of Ga and As into the molten In (melting  $T \sim 156^\circ$ ) and the subsequent precipitation of  $\text{In}_{1-x}\text{Ga}_x\text{As}$  was discussed. In the reaction of the form



the presence of a liquid phase ensured that mixing was rapid and that the final states of the system, after annealing is close to equilibrium.

Such a reaction can be qualitatively understood by reference to a hypothetical isothermal section of the In-Ga-As phase diagram for  $T < T_c$  (Fig. 5). From this schematic diagram, it is apparent that when a limited amount of GaAs is involved in the reaction, as many as three phases, namely In-Ga( $l$ ), In-rich  $\text{In}_{1-x}\text{Ga}_x\text{As}$  and Ga-rich  $\text{In}_{1-x}\text{Ga}_x\text{As}$  can result. We propose that in the initial stages of the reaction, Ga and As are dissolved into the molten In so that the average composition of the system remains on the vertical line connecting In and GaAs. As more Ga and As are incorporated

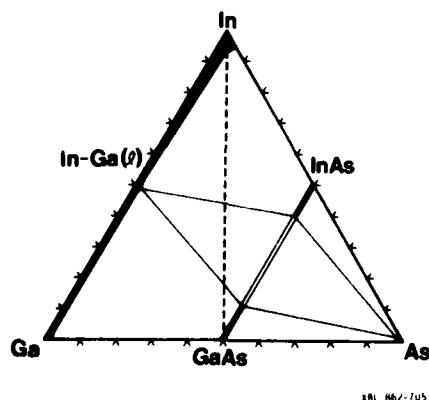


Fig. 5. Schematic isothermal sections of In-Ga-As phase diagram at a temperature below  $T_c$ . Assuming no loss of arsenic during annealing, the average composition of the system remains on the vertical dashed line.

into the molten material, i.e., as the molten In-Ga-As becomes supersaturated in Ga and As, the driving force for nucleation increases. Nucleation of  $\text{In}_{1-x}\text{Ga}_x\text{As}$  occurs at some time during the annealing treatment, most likely during cooling. The compositions of the phases formed depend on the degree of supersaturation at the time of nucleation. Misfit dislocations were observed only at the  $\text{In}_{1-x}\text{Ga}_x\text{As}/\text{GaAs}$  interface and no diffraction spot streaking (indicative of compositional grading) was detected. These observations suggest that once a precipitate is nucleated, it continues to grow at the same composition. The strain energy or dislocation energy associated with spatial variations in composition will inhibit compositional grading.

### 5. Conclusion

The experimental results described in this paper provide direct evidence for the existence of a miscibility gap in the InAs-GaAs pseudo-binary system. It follows that the formation of graded  $\text{In}_{1-x}\text{Ga}_x\text{As}$  ( $0 < x < 1$ ) layers by thermal reaction of In on GaAs is not possible under furnace annealing conditions (slow heating and cooling) unless the annealing temperature is above the critical temperature, estimated in this study to be between 575°C and 650°C. If a graded layer is indeed necessary to form a low-resistance In-base ohmic contact to n-GaAs (i.e. to smooth out the InAs-GaAs conduction band discontinuity), our results suggest that fabrication of graded  $\text{In}_{1-x}\text{Ga}_x\text{As}/\text{GaAs}$  ohmic contacts by thermal reaction must involve annealing at temperatures above the critical temperature. Observation of ohmic conduction in In/GaAs samples annealed at temperatures significantly below  $T_c$  (Lakhani 1984a, 1984b) can only be attributed to other mechanisms such as thermionic-field emission at small diameter protrusions in the  $\text{In}_{1-x}\text{Ga}_x\text{As}/\text{GaAs}$  interface (see Fig. 2).

### Acknowledgments

It is a pleasure to acknowledge the expert technical assistance of Tom Brennan of Bell Communication Research, Inc. for the thin film deposition. This work was supported by the Director, Office of Energy Research, Office of Basic Energy Sciences, Materials Science Division of the U.S. Department of Energy under Contract No. DE-AC03-76SF00098.

### References

- Cremoux, B. de, Hirtz, P. and Ricciardi, J., 1981 Inst. Phys. Conf. Ser. **56** 115.
- Ding, J., Washburn, J., Sands, T. and Keramidas, V.G., 1986 Appl. Phys. Lett. **49** 818.
- Lakhani, A.A., 1984a J. Appl. Phys. **56** 1888.
- Lakhani, A.A. 1984b Materials Lett. **2** 508.
- Onabe, K., 1982 Japan J. Appl. Phys. **21** L323.
- Quillec, M., Daguet, C., Benchimol, J.L. and Launois, H., 1982 Appl. Phys. Lett. **40** 325.
- Sands, T., 1986 Mat. Res. Soc. Symp. Proc. **62** in press.
- Stringfellow, G.B., 1982 J. Crystal Growth **58** 194.
- Woodall, J.M., Freeouf, J.L., Pettit, G.D., Jackson, T. and Kirchner, P., 1981 J. Vac. Sci. Technol. **19** 626.
- Woolley, J.C. and Smith, B.A., 1958 Proc. Phys. Soc. Lond. **72** 214.

## **Observation of coupled states in AlGaAs/GaAs coupled quantum well**

H Q Le, J J Zayhowski, W D Goodhue and J Bales

Lincoln Laboratory, Massachusetts Institute of Technology  
Lexington, Massachusetts 02173-0073, U S A

### 1. Introduction

AlGaAs/GaAs quantum well structures have been extensively studied for their potential device applications. However, the intrinsic simplicity of a square quantum well (SQW) does not provide much of the needed flexibility for the task of engineering. More complicated structures offer this advantage. One class of structures that has attracted a great deal of interest is coupled quantum wells (CQW) [Dingle, 1975; Delalande et al 1984; Kawai et al 1985; Yariv et al 1985; Austin et al 1986]. While theoretical speculation on these structures is abundant, their experimental realization remains scarce. In this work, evidence of QW coupling in AlGaAs/GaAs heterostructures is presented. The main evidence consists of the observation of confined excitonic states via conventional optical spectroscopy. In the presence of an externally applied electric field, these states exhibit behavior that is markedly different from those of SQWs, and is consistent with a CQW model.

### 2. Experiment

The term coupled quantum well can be generically used to refer to any ensemble of local QWs whose quantized state wavefunctions extend throughout the ensemble rather than being strongly localized. The CQW model reported here consists of two SQWs of the same potential depth, separated by a thin potential barrier. Two samples grown by MBE are studied. Sample 1, as depicted in the inset of Fig. 1, consists of a symmetric CQW structure. Sample 2, depicted in Fig. 3, is asymmetric and narrower. It is grown in a p-i-n structure to facilitate the study of the Stark effect. The ability to engineer large asymmetries is one of the advantages of CQW.

The experimental techniques employed are photoluminescence and luminescence-excitation spectroscopy. The principal measured quantities are the energy levels of various optical excitonic states as a function of the Stark perturbation. A more qualitative observation, but still useful for the study of CQW is the oscillator strengths of these states. In the effective mass approximation (EMA), the oscillator strength of an approximately two-dimensional excitonic state is proportional to

$$|\phi_{2D}(0)|^2 / Z_e(z) Z_h(z) dz, \quad (1)$$

where  $Z_e(z)$  and  $Z_h(z)$  are, respectively, the quantum well envelope wavefunctions of the electron in the conduction band and the hole in the

---

\*This work was sponsored by the Department of the Air Force.

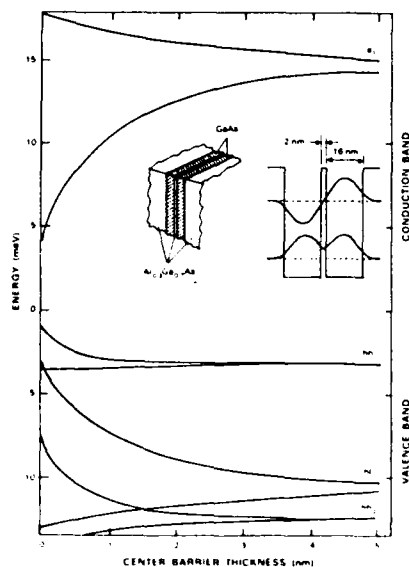


Fig. 1 Calculated confinement energy vs separation between CQW subwells. The insets show a diagram of sample 1, and the calculated electron wavefunctions. The well depth is 190 meV.

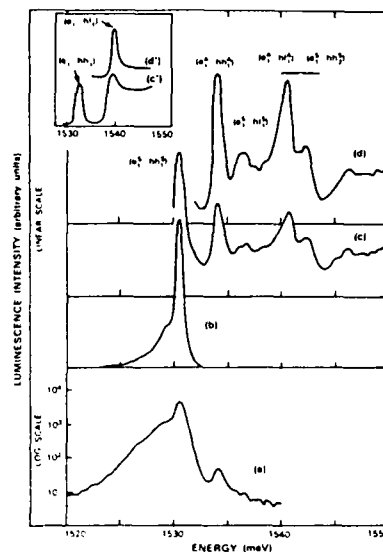


Fig. 2 (a) and (b) Luminescence spectra from sample a; (c) and (d) excitation spectra. Peaks are identified according to the model in Fig. 1. Splitting of electron coupled states is evidenced in the two lowest energy peaks. Inset [(c') and (d')] show typical excitation spectra of SOWs.

valence band, in the well normal dimension;  $\psi_{2D}(\rho)$  is the excitonic wavefunction in the other two dimensions. In expression (1), the term most relevant to the study of CQW is the inner product of  $Z_e(z)$  and  $Z_h(z)$ . Selection rules for this product consist of nodal quantum number conservation and parity conservation. Nodal number selection, referred to as the  $\Delta n$  selection rule, allows transitions only between states with the same number of nodes in the wavefunction. However, due to the intrinsic differences in the effective mass and the band potential profile seen by the electron and the hole for the AlGaAs/GaAs system, the  $\Delta n$  selection rule is not absolute. For structures without reflection symmetry, there is no parity selection rule, and practically all transitions are allowed.

### 3. Results and Discussion

The main result from the symmetric CQW sample is the observation of a set of closely spaced excitonic lines in the excitation spectra, shown in Fig. 2. Traces (a) and (b) are the luminescence spectra; traces (c) and (d) are the excitation spectra with luminescence monitored at two different energies. The inset of Fig. 2 [traces (c') and (d')] shows typical excitation spectra for a SQW structure whose width is about the same as that of the wells in the CQW. In (c') and (d'), only the heavy hole and the light hole exciton are observed. The spectral richness of traces

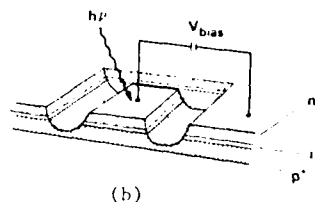
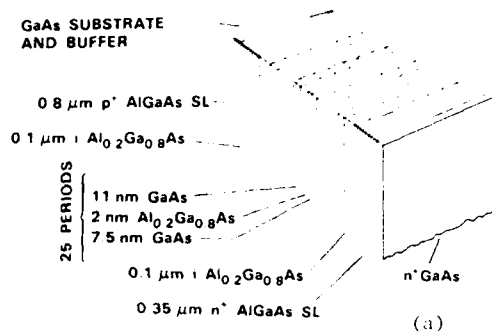


Fig. 3 Sample 2 diagram.  
Drawing is not to the scale.

(c) and (d) demonstrates the difference between the number of optical states in CQW and SQWs. Interpretation of this result is provided in Fig. 1, in which the energy levels of pairs of opposite parity in the conduction band and the valence band are calculated as a function of the separation between two SQW structures. The electron wavefunctions for the two lowest levels are calculated and shown in the inset to give a qualitative idea of the extent of the coupling. According to these calculations, various peaks labeled in Fig. 2 (c) and (d) correspond to various parity-allowed excitonic recombinations. The superscripts S and A refer to the symmetric and the antisymmetric character, respectively. Qualitatively, the observed level splittings of a few meV agree with the calculated electron and light hole energy splittings. The dimensions used in the model are estimates derived from the known MBE growth-rate.

Unlike sample 1, where the heavy hole remains strongly localized resulting in small energy splittings, the dimensions of the CQW in sample 2 are reduced (Fig. 3) to force the heavy hole to assume a larger kinetic energy, and thus to penetrate more readily through the center barrier. Asymmetry is also introduced to provide a mechanism for the first order Stark effect. Luminescence-excitation spectra from sample 2 are shown in Fig. 4. The absolute intensities of various traces are not on the same scale. The labels on the right vertical axis indicate the voltage applied to the p-i-n structure [Fig. 3 (b)]. The labels follow the same vertical order as the traces. The label "open" indicates the absence of external circuitry. The traces labeled from 0 V to 4 V on the left-hand side are luminescence spectra. The energy positions of various peaks are plotted vs bias voltage in Fig. 5.

The most salient features of the spectra in Fig. 4, besides the abundance of spectral lines, are the crossings of two or more levels, the positive energy shift of some levels and the overall sensitivity of the spectra with respect to applied bias. These features are uncharacteristic of SQWs, but readily understood with a CQW model. The spectral richness is a result of the increase of states and the relaxation of  $\Delta n$  and parity selection rules. The sensitivity to the Stark perturbation, as seen in Fig. 4, where the spectrum markedly changes its profile for bias voltages between 0 and 0.25 V, directly reflects the electric susceptibility of the CQW extended wavefunctions. Not only do the peak positions shift, but the oscillator strengths also vary greatly. The calculated results for the CQW model are presented in Figs. 6 and 7. In Fig. 6, the levels of various electron-hole pairs are plotted vs field. Curves (a), (b), (c), (d)

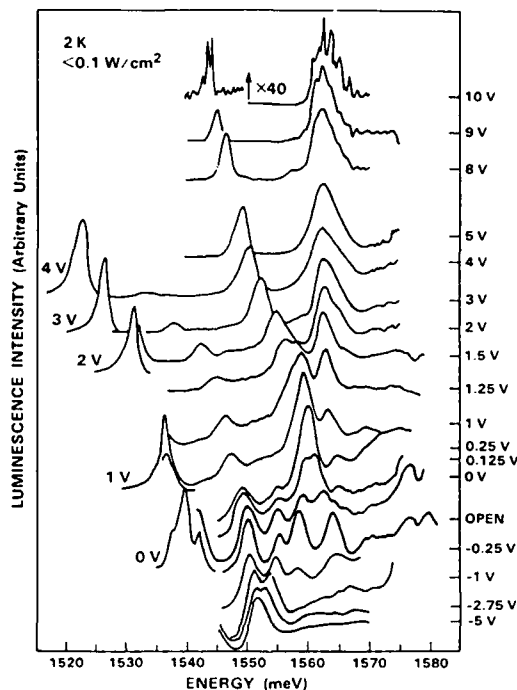


Fig. 4 Excitation and luminescence spectra for different bias voltages. Traces marked from 0 V to 4 V are luminescence spectra. All others are excitation spectra. Right vertical labels denote the applied voltages, arranged in the same vertical order as the associated traces.

and (e) correspond to  $(e_1, h_1)$ ,  $(e_1, h_2)$ ,  $(e_2, h_1)$ ,  $(e_2, h_2)$  and  $(e_1, l_1)$ , respectively, where e, h and l denote electron, heavy hole and light hole states; subscripts 1 and 2 refer to the lowest and the next lowest energy levels. These levels account for the experimental results. Since applied voltage is the experimental parameter while the calculations are based on electric field, direct comparison between experiment and theory is not possible. However, this can be done by assuming a linear relationship between the two parameters. It is important to keep in mind that this relationship is only approximate. In fact, there is a large leakage current for biases greater than 5 V. Also, due to the p-i-n diode structure, there exists a large internal field at 0 V bias; and when the bias is negative, the internal field is only slightly reduced. The dotted vertical line in Fig. 6 is the best theoretical estimate of the internal field that corresponds to 0 V bias. From the theory, two experimental features can be understood. Transitions  $(e_1, h_2)$  and  $(e_2, h_1)$  where  $\Delta n$  conservation is strongly violated, become allowed as a result of both CQW structural asymmetry and odd-parity Stark perturbation. Second, the upward energy shift of the  $(e_1, h_2)$  transition [curve (b)] reflects the presence of both the linear and quadratic Stark effect.



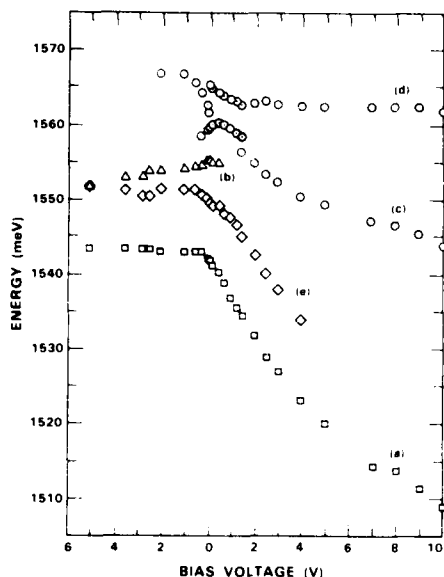


Fig. 5 Observed peak shift vs applied voltage. Different symbols are used to help distinguish well-traced peaks.

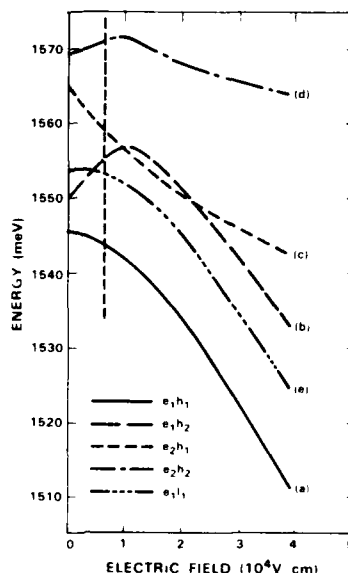


Fig. 6 Calculated Stark shift of CQW states. Traces (a), (b), (c), (d) and (e) correspond to transitions  $(e_1, h_1)$ ,  $(e_1, h_2)$ ,  $(e_2, h_1)$ ,  $(e_2, h_2)$  and  $(e_1, l_1)$ , respectively.

Although luminescence-excitation in this work does not provide an absolute measurement, or even an accurate relative measurement, of the oscillator strengths, the relative intensities of various lines provide useful insight for a qualitative understanding of the CQW model. The calculated inner products of the CQW wavefunctions in Eq. (1) for 4 transitions,  $(e_1, h_1)$ ,  $(e_1, h_2)$ ,  $(e_2, h_1)$  and  $(e_2, h_2)$ , are shown in Fig. 7, labeled (a), (b), (c) and (d), respectively. The calculated wavefunctions at different Stark fields are shown in Fig. 8. Qualitatively, these results are consistent with experiment. In particular, the maximum of (b) in Fig. 7 at a field close to  $1 \times 10^4$  V/cm offers an explanation for the observed strong line at about 1560 meV (Fig. 4) for the bias range from 0 to 1.5 V. This non-monotonic behavior characterizes CQW. At low fields [Fig. 8 (a)]  $e_1$  and  $h_2$  occupy opposite ends of wells with little spatial overlap ( $\Delta n$  is well conserved). As the field increases, they first move toward each other, and achieve maximum spatial overlap [Fig. 8 (b)]; at higher fields, they again become spatially separated [Fig. 8 (d)]. This type of wavefunction modulation underscores the potential of CQW as device structures.

#### 4. Conclusions

Luminescence-excitation spectroscopy of the Stark effect on excitonic states in AlGaAs/GaAs heterostructures evidences the realization of CQW structures. The observed spectral richness, the upward energy shifts, and the level crossings are radically different from the monotonic behavior

associated with SQWs. The interpretation is based on an approximate theory, in which the subtle differences in excitonic binding energies of various states with different CQW envelope wavefunctions are ignored, and the hole 3/2-spinor is approximated with two scalar particles. Despite the approximations, major features of the experimental results are accounted for.

We thank B. E. Burke and V. Diadiuk for valuable collaboration, B. Lax for stimulating discussion, R. C. Hancock and L. J. Belanger for valuable assistance, and G. D. Johnson for the critical processing of the samples.

#### References:

- Austin E J and Jaros M 1986 *J. Phys. C* **19** 533-541  
 Delalande C, Ziemelis U O, Bastard G, Voos M, Gossard A C and Wiegmann W 1984 *Surf. Sci.* **142** 498-503  
 Dingle R, 1975 *Festkörperprobleme* **15** 21-48  
 Kawai H, Kaneko J and Watanabe N, 1985 *J. Appl. Phys.* **58** 1263-1269  
 Yariv A, Lindsey C and Sivan U, 1985 *J. Appl. Phys.* **59** 3669-3672

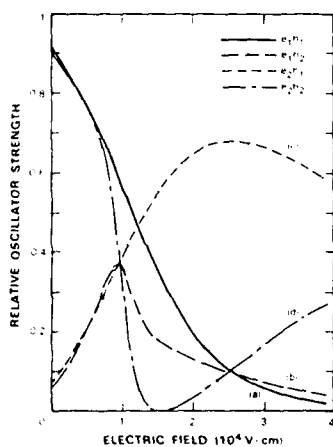


Fig. 7 Calculated relative oscillator strength of CQW states vs electric field. Traces (a), (b), (c) and (d) correspond to the same transitions labeled in Fig. 6.

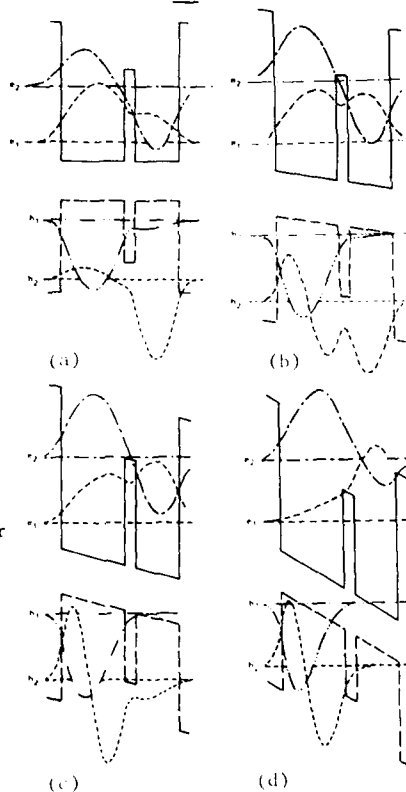


Fig. 8 Calculated CQW wavefunctions for the two lowest energy states of the electron and the heavy hole. (a), (b), (c) and (d) correspond to fields of 0, 1, 1.5 and  $4 \times 10^4$  V/cm. The wavefunction baselines do not correspond to the energy of the state with respect to the CQW.

## Magneto-optical studies of GaAs-Al<sub>x</sub>Ga<sub>1-x</sub>As multi-quantum-well structures

K K Bajaj<sup>\*</sup>, D C Reynolds<sup>\*</sup>, C W Litton<sup>\*</sup>, Ronald L. Greene<sup>§</sup>, P W Yu<sup>†</sup>,  
C K Peng<sup>‡</sup> and H Morkoc<sup>‡</sup>

<sup>\*</sup> Air Force Wright Aeronautical Laboratories, Avionics Laboratory,  
AFWAL/AADR, Wright-Patterson AFB, Ohio 45433, USA

<sup>§</sup> Department of Physics, University of New Orleans, New Orleans LA 70148,  
USA

<sup>†</sup> Wright State University, Dayton OH 45435, USA

<sup>‡</sup> Department of Electrical Engineering and Coordinated Science  
Laboratory, University of Illinois, Urbana IL 61801, USA

**Abstract.** We report measurements of the diamagnetic shifts of heavy and light-hole excitons as a function of the well size and the magnetic field in MBE grown GaAs-AlGaAs multi-quantum-well (MQW) structures using high resolution optical spectroscopy at liquid helium temperatures. The applied field is parallel to the plane of the MQW structures. We have also determined the variation of the effective g-values of the heavy and the light-holes as a function of the well size.

### 1. Introduction

The study of the properties of excitons in quantum well structures has attracted a great deal of interest in the last few years. Recently several groups (Mann et al. 1984, Tarucha et al. 1984, Miura et al. 1985, Ossau et al. 1985, Sakaki et al. 1985) have investigated the behavior of both the heavy-hole and the light-hole excitons in GaAs-AlGaAs multi-quantum-well (MQW) structures in the presence of a magnetic field. In all these studies the magnetic field is applied perpendicular to the plane of the MQW structures. However, in one of these investigations (Sakaki et al. 1985), the field is also applied parallel to the plane of the structures. From these measurements they determine the variations of the ground-state energies of these excitons (from hereon referred to as diamagnetic shift) as a function of the magnetic field. Sakaki, et al. (1985) have determined the diamagnetic shifts of heavy-hole excitons in GaAs-Al<sub>0.3</sub>Ga<sub>0.7</sub>As structures with different well sizes using photoluminescence spectroscopy. In their experiments they apply the magnetic field both perpendicular and parallel to the plane of the MQW structure and measure the diamagnetic shifts in both field configurations. In all of these measurements the widths of the excitonic transitions are typically 2-3 meV or more for 100 Å GaAs quantum wells. The magnetic field measurements have all been made at relatively high magnetic fields. Since one can observe sharp line structure from MQW systems in both photoluminescence (PL) and reflection spectra, (Reynolds et al. (1985), Reynolds et al. (1986)), it is possible to investigate the magneto-optical properties of these systems at relatively low magnetic fields (0-36 kG). In this study, we

have investigated the diamagnetic shift of both the light hole and heavy hole free excitons as a function of magnetic field, with the field applied parallel to the MQW layers. The diamagnetic shift of the light hole free excitons with the magnetic field oriented in this direction has not previously been measured. The diamagnetic shift of the light and heavy hole free excitons was also determined as a function of well size. The quadratic dependence of the diamagnetic shift as a function of magnetic field was observed, while a nearly linear variation in diamagnetic shift with well size was observed. The binding energies of both the heavy-hole and the light-hole excitons in a GaAs quantum well as a function of well size in the presence of an arbitrary magnetic field applied parallel to the plane of the quantum well structure have recently been calculated by Greene and Baja, (unpublished). The variational approach was used in these calculations. The experimentally measured results of this experiment are compared with the above calculation.

The light and heavy hole g-values were determined for the first time for different well sizes. To determine the hole g-values it was assumed that the electron g-value remained constant and essentially the same as in bulk GaAs. The observation of the magnetic field splitting of the excitonic transitions was possible because of the very narrow line widths associated with these transitions.

**2. Growth Conditions** The MQW structures used in this investigation were grown on (100) oriented Si-doped GaAs substrates by molecular beam epitaxy. The substrates were prepared and loaded in the growth chamber as previously described (Sum et al. 1984). The MQW structures were grown at 600°C. A five period superlattice consisting of 20A  $\text{Al}_{0.2}\text{Ga}_{0.8}\text{As}$  and 20A GaAs was grown between the substrate and a 0.5  $\mu\text{m}$  thick GaAs buffer layer on which the MQW structure was then grown. This structure produced MQWs with excellent optical properties.

### **3. Experimental Technique**

The experimental apparatus employed in this investigation permitted high-resolution photoluminescence and reflection measurements to be performed at 2K and in magnetic fields up to 36 kG. In the intrinsic region of GaAs a dispersion of 0.54 A/mm was achieved using a 4-meter spectrometer. Data were collected on Kodak-type 1-N spectrographic plates. The photoluminescence was excited with the 6471-A line of a Krypton ion laser; for reflection the broad spectrum of a Zr-lamp was used.

### **4. Experimental Results and Discussion**

The samples used in this study were MQW structures which consisted of  $\text{Ga}_{0.75}\text{Al}_{0.25}\text{As}$  barrier layers of thickness 100A and GaAs well thickness of 90, 135, 180, 300, and 400A. The total number of cycles in the 400 and 300A thick MQW samples was 20, whereas the 180A sample had 33 cycles and the 135 and 90A MQWs had 50 cycles. The light-hole free exciton transitions were observed in PL in only the widest wells, the heavy-hole free exciton transitions were seen in photoluminescence for all of the MQW structures. The reflection spectra were observed for both the light- and the heavy-hole free excitons for all of the MQWs. A typical reflection spectra for both the light and heavy hole free excitons at zero magnetic field and at an applied field of 31kG is shown in Fig. 1.

Some of the lines are extremely narrow, no more than 0.05 meV full width at half maximum (FWHM). The fine structure is observed over an energy

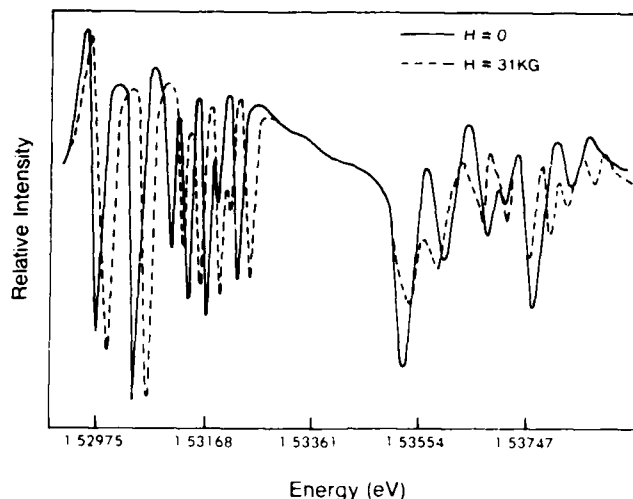


Fig. 1. Reflection spectra for both the light and heavy hole free excitons in a MQW  $L_z = 135\text{\AA}$  at  $H = 0$  and  $H = 31\text{ kG}$ .

spread corresponding to a well size fluctuation of about two monolayers. The heavy hole free excitons show a shift to higher energy with very little splitting when the magnetic field is applied. The light hole free excitons show a much smaller shift in energy with magnetic field however, they show a larger magnetic field splitting.

Similar experiments with different well sizes show that the diamagnetic shift increases as the well size increases for both the light and heavy hole excitons. It was also observed that the magnetic field splitting of the heavy hole exciton was smaller as the well size decreased while the magnetic field splitting of the light hole exciton was larger as the well size decreased. Variations of the diamagnetic shifts for both the light- and the heavy-hole free excitons as a function of well size for a magnetic field of 36 kG are shown in Fig. 2. A nearly linear relationship is observed, with the heavy-hole exciton having a considerably larger diamagnetic shift than the light-hole exciton. Also plotted in Fig. 2 is the variation of the diamagnetic shift of the two exciton systems as a function of the well size as calculated by Greene and Bajaj (unpublished) using Luttinger valence band parameters proposed by Skolnick et al. (1976) from their cyclotron resonance studies. Though the theory predicts the correct trends, namely the diamagnetic shift of the heavy-hole exciton is larger than that of the light-hole exciton and that the diamagnetic shifts of both excitons increase with well size, the theoretical values are considerably larger than the measured ones. For 135\AA MQW structure our measured value of the

diamagnetic shift of the heavy-hole excitons at 36kG agrees with the one determined by Sakaki et al. (1985). It is not clear why the theoretical values are considerably larger than the experimental values. In their variational calculation of the diamagnetic shift Greene and Bajaj

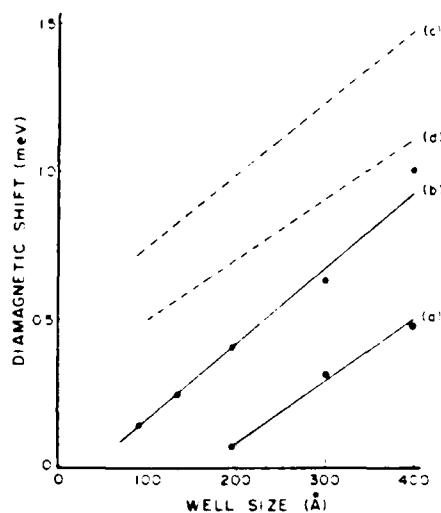


Fig. 2. Variation of the diamagnetic shift of light-hole exciton (solid line (a), experiment, dashed line (d), theory), and heavy-hole exciton (solid line (b), experiment, and dashed line (c), theory) as a function of well size at a magnetic field of 36 kG. Solid lines drawn through the experimental points are just aids to the eye.

(unpublished) have assumed that the heavy-hole and the light-hole bands are completely decoupled. Recently, Sanders and Chang (1985) and Briodo and Sham (unpublished) have calculated the exciton binding energies as a function of the well size using valence band mixing at zero magnetic field. Both these groups find that for the range of the well sizes used in the present work the binding energies are slightly larger than those calculated assuming decoupled bands. It is therefore highly unlikely that the diamagnetic shifts calculated using valence band mixing will be significantly different from those calculated using decoupled bands. Sakaki et al. (1985) have also measured the diamagnetic shift of the heavy-hole excitons in  $\text{GaAs-Al}_{0.3}\text{Ga}_{0.7}\text{As}$  MQW structures for the case of a magnetic field applied perpendicular to the plane of the structure. They find that for a given value of the well size and magnetic field the value of the diamagnetic shift for the perpendicular field case is about three times larger than that for the parallel field case. Their values of the diamagnetic shifts agree rather well with those calculated by Greene and Bajaj (1985) for the perpendicular field case. For the case of parallel field Greene and Bajaj (unpublished) calculate diamagnetic

shifts which are only twenty to thirty-percent smaller than those calculated for the perpendicular field for the range of well widths considered in the present study.

We have determined the variation of the g-values of the heavy- and the light-holes as a function of well size and display it in Fig. 3. We have assumed that the magnetic field splittings of the free excitons in

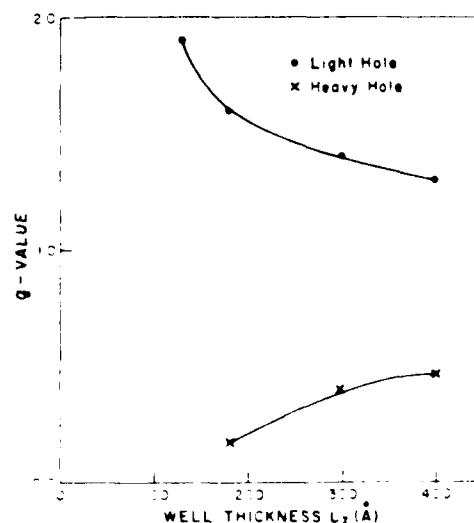


Fig. 3. The light- and heavy-hole g-values as a function of well thickness for a fixed magnetic field of 36 kG.

MQW structures are analogous to those in bulk semiconductors with nondegenerate valence bands (i.e. II-VI semiconductors with wurtzite structure) where the light-hole free exciton splits as the sum of the electron and hole g values and the heavy hole free exciton splits as their difference. Assuming that the g-value of the electron is the same in the quantum wells as in bulk GaAs (0.5) the g-values of the holes are determined from the magnetic field splittings. It is noted that the g-value of the light-hole approaches the GaAs bulk value as the wells get wider. Theoretical models are not available to compare the experiment with at this time.

##### 5. Concluding Remarks

We have measured the diamagnetic shifts of heavy- and light-hole excitons as a function of well size and magnetic field in GaAs-AlGaAs multi-quantum-well structures using high resolution optical spectroscopy. The applied magnetic field is parallel to the plane of the MQW structures. Some of the transitions have linewidths as small as 0.05 meV. For the range of magnetic fields (0-36 kG) studied the diamagnetic shift varies quadratically with the field and for a given value of the field, varies linearly with the well size. We have also determined the variation of the effective g-values of the heavy- and light-holes as a function of the well size. We have compared the values

of the diamagnetic shifts we measure with those determined by Sakaki et al. (1985) and with the results of a variational calculations (Greene and Bajaj, unpublished). We find that our results agree with those of Sakaki et al. (1985) but are considerably smaller than those predicted by theory.

#### References

- Briodo D A and Sham L J (to be published)  
 Greene R L and Bajaj K K Phys. Rev. B31 2494 (1985)  
 Greene R L and Bajaj K K (to be published)  
 Maan J C, Belle G, Fasolino A, Artarelli M and Ploog K Phys. Rev. B30 2253 (1984)  
 Miura N, Iwasa Y, Tarucha S and Okamoto H in Proc. 17th Int. Conf. on the Physics of Semiconductors ed J D Chadi and W A Harrison (Springer-Verlag, New York, 1985) p. 359  
 Ossau W, Jakel B, Bangert E., Landwehr G and Weimann G Proc. 2nd Int. Conf. on Modulated Semiconductor Structures Kyoto (Japan) September 1985 to be published in Surface Science  
 Reynolds D C, Bajaj K K, Litton C W, Yu P W, Singh J, Masselink W T, Fischer R and Morkoc H Appl. Phys. Lett. 46 51 (1985)  
 Reynolds D C, Bajaj K K, Litton C W, Singh J, Yu P W, Pearah P, Klem J and Morkoc H Phys. Rev. B33 5931 (1986)  
 Sakaki H, Arakawa Y, Nishioka M, Yoshino J, Okamoto H and Miura N Appl. Phys. Lett. 46 83 (1985)  
 Sanders G D and Chang Y C Phys. Rev. B32 5517 (1985)  
 Skolnick M S, Jain A K, Stradling R A, Leotin J, Ousset J C and Askenazy S J. Phys. C. Solid State Phys. 9 2809 (1976)  
 Sum Y L, Masselink W T, Fischer R, Klein M V, Morkoc H and Bajaj K K J. Appl. Phys. 55 3554 (1984)  
 Tarucha S, Okamoto H, Iwasa Y and Miura N Solid State Commun. 52 815 (1984)



## **GaAs/In<sub>x</sub>Al<sub>1-x</sub>As ( $0 \leq x \leq 0.006$ ) indirect bandgap superlattices**

T. J. Drummond, E. D. Jones, Harold P. Hjalmarson and B. L. Doyle

Sandia National Laboratories, Albuquerque, New Mexico 87185

**Abstract.** To explain transport data in unipolar superlattice diode structures it is necessary to assume that, for a sufficiently short period, AlAs/GaAs superlattices have an indirect bandgap. By using appropriately designed superlattices grown by molecular beam epitaxy, the superlattice  $\Gamma$  band is moved sufficiently far above the X bands that luminescence from these bands is clearly observed for the first time.

### 1. Introduction

In this paper we report the first unambiguous demonstration of photoluminescence from an X derived ground state in a series of GaAs/AlAs and GaAs/InAlAs superlattices. In previous studies the only evidence for indirect GaAs/AlAs superlattices is derived from absorption spectra of (GaAs)<sub>1</sub>(AlAs)<sub>1</sub> and (GaAs)<sub>3</sub>(AlAs)<sub>3</sub> superlattices (van der Ziel 1977) although pressure induced transitions have been observed in GaAs/AlGaAs superlattices at pressures of 18 kbar (Wolford 1986). Our investigation was motivated by the fact that earlier photoluminescence studies (Wang 1986, Okamoto 1985) provided no clear evidence for an X derived ground state in thin layer superlattices although assuming such a ground state was crucial to the interpretation of transport data for n-type unipolar superlattice barrier diodes (Drummond et al. 1984). The diode data also implies that an entirely new type of band structure may be achieved, i.e., the bulk ellipsoidal X minima with their long axis parallel to the superlattice axis are folded into an essentially cylindrical energy surface. This implies that the ground state cannot be clearly classified as being either direct or indirect and has a nearly infinite mass along the superlattice axis.

### 2. Experimental

Superlattices of GaAs/In<sub>x</sub>Al<sub>1-x</sub>As with  $x < 0.006$  were grown by molecular beam epitaxy in a Varian<sup>®</sup> MBE 360. Growth rates were 0.8  $\mu\text{m/hr}$  for GaAs and 0.3  $\mu\text{m/hr}$  for AlAs and the growth temperature for the superlattice was 565°C. Small amounts of In were in some cases added to the AlAs layer under the assumption that it would help maintain a smooth surface during the growth of the AlAs. We have noted in the past that clear (3x1) HEED (high energy electron diffraction) patterns were more easily obtained during the growth of thick AlAs layers when a small In flux was incident on the surface. The superlattices were nominally 0.5  $\mu\text{m}$  thick and the top 0.3  $\mu\text{m}$  were Si doped, in the GaAs layers only, to a level of  $1 \times 10^{16}/\text{cm}^3$ .

Specific superlattice parameters used in the theoretical analysis were derived from an x-ray analysis using a double crystal diffractometer. Table I lists individual layer thicknesses for the GaAs layers,  $L_a$ , and the InAlAs layers,  $L_b$ , in nm and the nearest integer number of monolayers (monolayer is approximately 0.283 nm for either material). Table I also gives the percent In in the AlAs layers as determined from the x-ray analysis and the percent perpendicular strain in the AlAs layers.

| SAMPLE # | $L_a$ (nm/ml) | $L_b$ (nm/ml) | % In | % STRAIN |
|----------|---------------|---------------|------|----------|
| 149      | 1.3/5         | 3.4/12        | 0    | 0.20     |
| 150      | 0.9/3         | 3.6/13        | 0.2  | 0.23     |
| 182      | 1.3/5         | 3.8/13        | 0.3  | 0.24     |
| 151      | 1.0/4         | 3.8/13        | 0.6  | 0.27     |
| ERROR    | 0.5/2         | 0.5/2         | 0.1  | 0.01     |

Table I GaAs layer thickness,  $L_a$ , AlAs layer thickness,  $L_b$ , percent In in the AlAs layers and percent strain in the AlAs layers. Layer thicknesses are given in both nm and nearest integer number of monolayers (ml).

Luminescence measurements were made at 4 and 11 K in a system capable of applying both hydrostatic pressure and high magnetic fields (Jones et al. 1985). Figure 1 shows the zero pressure, zero magnetic field luminescence response from sample 149 at 11 K. This sample is a GaAs/AlAs superlattice with no In in the AlAs layers. For all samples in this study (149-151, 182), the superlattice peak energy fell in the range 1798-1809 meV and the full width at half maximum (FWHM) was 10-12 meV. In all cases the intensity of the superlattice peak relative to the substrate peak more than doubled with the incorporation of In. This was the only observable effect of the In. No new features or energetic shifts were detectable. However, because the FWHM did not decrease as the intensity increased the difference may be a bulk effect (Beneking et al. 1985) with the interfacial quality being controlled by the GaAs layers (Singh and Bajaj 1985).

In Figure 1 there are five significant peaks in addition to the broad peak spanning the interval 1600 to 1700 meV. The dominant peak is assigned to transitions associated with the on axis X minima quantized according to the longitudinal mass and designated  $X_1$ . The two low energy peaks  $I_1$  and  $I_2$  are thought to be due to impurities. Because the GaAs layers are doped with Si, it is very likely that one peak may be a donor-related transition. Another candidate for an impurity related transition is carbon. A carbon-related impurity peak is clearly seen on the low energy side of the substrate peak. More sophisticated experiments are required to positively identify the origin of  $I_1$  and  $I_2$ . In addition to the problem of identifying the responsible impurity, the  $X_1$  bands are expected to give rise to impurity levels which may lie within the superlattice bandgap. Two weak features above the main superlattice peak

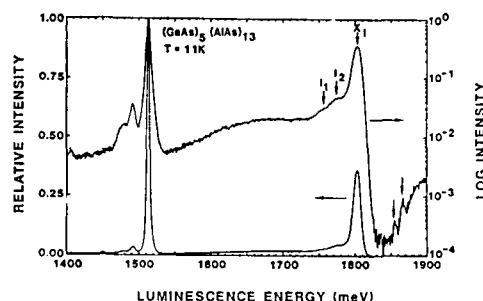


Fig. 1 Photoluminescence response of 149 at 11K.

are indicated but not labeled. They are possibly due to impurity related transitions to a light hole valence band state.

To demonstrate that the observed photoluminescence features are transitions derived from the bulk X point conduction band minima, photoluminescence spectra were recorded with 3.5 kbar of hydrostatic pressure applied and also with up to 65 kG magnetic field applied perpendicular to the superlattice. Figure 2 shows spectra from sample 182 at zero pressure (bottom) and under 3.5 kbar pressure (top). We see that the substrate peak has shifted upward in energy at a rate of 12.7 meV/kbar and that the superlattice peaks shift downward in energy at a rate of 2 meV/kbar. For GaAs the pressure dependences of the principle conduction band minima are 12.6 meV/kbar for  $\Gamma$ , 5.5 meV/kbar for L and -1.5 meV/kbar for X (Blakemore 1986). Because AlAs is similar to GaP in ordering of the conduction band minima as well as bandgap energies, the pressure dependence of the X point in AlAs should be approximately -2.4 meV/kbar. Thus, the pressure dependence of the superlattice peaks are characteristically negative and the exact value of the derivative is bracketed by the values associated with the two binary constituents of the superlattice. Finally, we found that application of a magnetic field had no effect on the energy of the peak  $X_1$ . This is consistent with the large effective mass of an X-driven state.

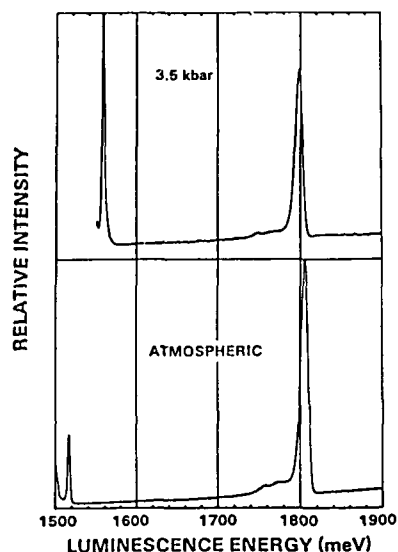


Fig. 2 Photoluminescence response of 182 at 4K, at atmospheric pressure and under 3.5 kbar of pressure.

### 3. Theoretical

The photoluminescence spectra were analyzed by both a Kronig-Penney (KP) method and a tight-binding (TB) method. These spectra depend primarily on band structure and dipole matrix elements. The KP technique was used to obtain the band offset from the experimental peak positions. An important consideration is the accuracy of the KP method near the  $\Gamma$ -X crossover. At present there is no analytic approximation which allows for coupling between direct and indirect conduction bands. The superlattice TB method was used to assess the degree of band mixing at the  $\Gamma$ -X crossover. It was also used to estimate the dependence of the luminescence intensity on GaAs/AlAs layer thickness ratio.

The KP method employed here allows for different effective masses in the binary constituents of the superlattice (Bastard 1981) and all inputs to the KP model listed in Table II for  $T = 0$  K are drawn from the current

literature references as discussed elsewhere (Hjalmarson and Drummond). Temperature dependences for the  $\Gamma$  and X bandgaps as well as for the  $\Gamma$  point effective electron and light hole masses are also incorporated into the model. The only adjustable parameter is the heterojunction band alignment.

The TB superlattice method (Hjalmarson and Drummond) utilizes an  $sp^3$  method which has been extensively applied to semiconductor, semiconductor alloy, semiconductor interface, and semiconductor superlattice problems (Vogl et al. 1983). The Hamiltonian  $H(k,g)$  depends on the individual Hamiltonians for layers  $m$  and  $n$  as well as the band edge discontinuity between  $m$  and  $n$ . Each semiconductor Hamiltonian has its matrix elements adjusted such that the zero of energy occurs at the valence band edge. Accordingly, the superlattice Hamiltonian is merely shifted by the valence band discontinuity.

|      | $E^v(\text{eV})$ | $E^c(\text{eV})$ | $m_e^*$ | $m_{lh}^*$ | $m_{hh}^*$ | $m_{hh}^*$ |
|------|------------------|------------------|---------|------------|------------|------------|
| GaAs | 1.519            | 1.981            | 0.067   | 1.2        | 0.27       | 0.51       |
| AlAs | 3.145            | 2.250            | 0.150   | 1.1        | 0.19       | 0.75       |

Table II Input parameters to the Kronig-Penney calculation. Bandgap energies for AlAs assume free-exciton energies for  $\Gamma$  and X to be the same as in GaP.

The dipole matrix elements for optical transitions depend on the wavefunctions and the atomic dipole matrix elements. The dipole matrix elements were approximated in terms of the overlap of the wavefunctions. To this end, the projection operator,

$$P = \sum_R |a(R,x)\rangle \langle a(R,s)|$$

was used to pick out the overlap of the  $s$  and  $p$  orbitals for the parallel polarized light used in the experiment. In the remainder of this paper we will refer to matrix elements of  $P$  as dipole matrix elements.

#### 4. Discussion

Having used x-ray analysis to determine GaAs and AlAs layer thicknesses in our superlattices, the KP method was used to obtain the band offset by fitting the data. The convention of aligning the direct bandgaps with a fraction  $\alpha$  of the bandgap energy difference appearing in the conduction band was used in the KP calculation. Positions of the longitudinal  $X_1$ , the transverse  $X_2$ , and the  $\Gamma$  superlattice bandgaps were calculated as a function of  $\alpha$  for a  $(\text{GaAs})_5(\text{AlAs})_{13}$  superlattice at 11K. By this analysis, we find that  $\alpha = 0.63 \pm 0.005$  in excellent agreement with other recent studies (Wilson 1986). This sets a lower limit on the value of  $\alpha$  as the main PL peak is likely an excitonic transition and thus the actual bandgap may be 10 to 50 meV larger.

Having determined an offset rule of 63/37, KP theory is used to compute the bandgap of a  $(\text{GaAs})_m(\text{AlAs})_n$  superlattice in which  $m+n=18$ . Figure 3 shows the bandgap as a function of superlattice composition varying from GaAs ( $n=0$ ) to AlAs ( $n=18$ ). The enhanced nonlinearity for these superlattice alloys (SLAs) is due to the shift of the conduction band ground state from the GaAs to the AlAs layers with the  $\Gamma$ -X crossing while

the valence band states remain localized in the GaAs layers. To further understand the data, the TB bandstructure and projection operator matrix elements as a function of the number of AlAs layers is shown in Figure 4. For this case, the superlattice period is again  $m + n = 18$ . The TB bandgap agrees with the KP bandgap to within 0.05 eV. Much of this discrepancy can be traced to the overly large bandgap incorporated in the  $sp^3$  matrix elements. In another publication we will present results using modified matrix elements. The most important point is that the  $\Gamma$ -X transition is well defined and "validates" the use of the KP method in this regime.

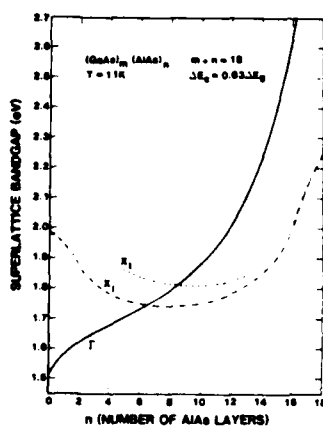


Fig. 3 Kronig-Penney superlattice bandstructure as a function of the number of AlAs monolayers per period with a period of 18 monolayers total.

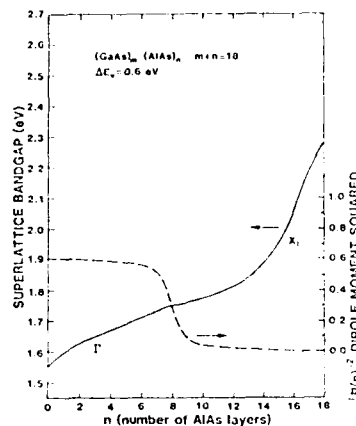


Fig. 4 Tight-binding superlattice bandstructure and dipole matrix element as a function of the number of AlAs monolayers per period with a period of 18 monolayers total.

The dipole matrix elements  $|P(n)|^2$  change magnitude due to the  $\Gamma$ -X crossover at  $n \sim 8$ . In the GaAs limit ( $n = 0$ ),  $|P(0)|^2 \sim 0.61$  and in the AlAs limit ( $n = 18$ ),  $|P(18)|^2 = 0.0$ . In the GaAs limit, both the electrons and the holes are localized in the GaAs layers and the dipole moment is large because the wavefunctions have appreciable overlap. In approaching the AlAs limit, the electrons become localized in the AlAs layers which leads to a smaller dipole moment because the overlap is reduced. Figure 4 also shows that the  $\Gamma$ -X transition is not discontinuous. Thus, even though the bandgap has become X-like for  $n > 8$ , the dipole moment is still large. Accordingly, the experimental observation of photoluminescence is consistent with zone folded X-point transitions.

## 5. Conclusions

We have clearly demonstrated that a strong luminescence signal which derives from X symmetry states can be obtained in GaAs/AlAs superlattices. A simple Kronig-Penney analysis is shown to be very successful in describing the position of the superlattice bandstructure. A more

sophisticated tight-binding calculation was used to demonstrate that although there is very little mixing between  $\Gamma$  and X conduction band states, the dipole matrix element does not immediately go to zero as the superlattice becomes indirect. From this, we conclude that our observation of luminescence from X-derived conduction band states is consistent with having zone-folded the on-axis X-minima to zone center.

#### 6. Acknowledgements

The authors would like to acknowledge the expert technical assistance of L.L. Stephenson, R.J. Blake and D.P. Wrobel in growing the crystals and in performing luminescence and x-ray measurements. This work was performed at Sandia National Laboratories and supported by the U.S. Department of Energy under Contract Number DE-AC04-76DP00789.

#### 7. References

- Bastard G 1981 Phys. Rev. B 24 pp 5693-97  
 Beneking H, Narozny P and Emeis N 1985 Appl. Phys. Lett. 47 pp 828-30  
 Blakemore J S 1982 J. Appl. Phys. 53 pp R123-81  
 Drummond T J, Hjalmarson H P, Pearah P and Morkoc H 1984 Proc. IEEE IEDM pp 528-31  
 Hjalmarson H P and Drummond T J, unpublished  
 Jones E D, Ackermann H, Schirber J E, Drummond T J, Dawson L R and Fritz I J 1985 Appl. Phys. Lett. pp 492-4  
 Okamoto H 1985 J. Vac. Sci. Technol. B 3 pp 687-93  
 Schulman J N and Chang Y C 1985 Phys. Rev. B 31 pp 2056-68  
 Singh J and Bajaj K K 1985 Appl. Phys. Lett. 47 pp 594-96  
 van der Ziel J P and Gossard A C 1977 J. Appl. Phys. 48 pp 3018-23  
 Ves S, Strosser K, Kim C K and Cardona M 1985 Sol. St. Commun. 55 pp 327-31  
 Vogl P, Hjalmarson H P, Dow J D, J. Phys. Chem. Solids 44, 365 (1983)  
 Wang W I 1986 Sol. St. Elect. 29 pp 133-9  
 Wilson B A, Dawson P, Tu C W and Miller R C 1986 J. Vac. Sci. Technol. B 4 pp 1037-40  
 Wolford D J, Kuech T F, Bradley J A, Gell M A, Ninno D and Jaros M 1986 J. Vac. Sci. Technol. B 4 pp 1043-50

## **The observation of the expansion of electron – hole plasma in GaAs – Al<sub>x</sub>Ga<sub>1-x</sub>As multiple quantum well structures**

K.T. Tsen

Physics Department, Arizona State University  
Tempe, AZ 85287

H. Morkoc

Coordinated Science Laboratory, University of Illinois  
Urbana, IL 61801

### 1. Introduction

Because of the development of laser annealing as a tool for eliminating the surface damage caused by ion-implantation, the evolution of the electronic and thermal energy following the creation of the photoexcited electron-hole plasma (EHP) in semiconductors becomes the subject of great interest and controversy (Wautelet et al. 1981, Forchel et al. 1983, Steranka et al. 1985). The expansion of EHP has been studied on the picosecond time scale in bulk GaAs (Collins et al. 1984, Huang et al. 1986) and in bulk CdSe (Junnarkar et al. 1986). In recent years, tremendous interest in layer structures such as GaAs-Al<sub>x</sub>Ga<sub>1-x</sub>As multiple quantum wells (MQW) has made the study of the expansion of EHP in those materials particularly important. In this paper, we present the first experimental evidence of the rapid plasma expansion in GaAs-Al<sub>x</sub>Ga<sub>1-x</sub>As MQW structures. The spatial expansion of the photoexcited EHP in GaAs-Al<sub>x</sub>Ga<sub>1-x</sub>As MQW structures was investigated by time-resolved Raman scattering on a picosecond time scale. The drift velocity of the plasma was estimated and found to be comparable to its Fermi velocity. These measurements show that at low intensity excitations thermodiffusion governs the transport of the photoexcited EHP in GaAs-Al<sub>x</sub>Ga<sub>1-x</sub>As MQW structures.

### 2. Experimental Technique and Sample

The experimental set up is shown in Fig. 1. The Excitation source is DCM dye laser which is synchronously pumped by the second harmonic of an actively mode-locked cw YAG laser. It produces a pulse train of ~3ps light pulses at a repetition rate of 76 MHz. These pulses are split into two beams of different intensity (with 10:1 ratio) and orthogonal polarizations. The more intense beam is used to pump the photoexcited plasma and the weaker one probes these non-equilibrium excitations by spontaneous intersubband Raman scattering. The photon energy from the dye laser is chosen to be ~1.870 eV, consequently, we would expect that the photoexcited carriers come mainly from excitations of electrons from (a) the heavy and light hole subbands to the continuum states; (b) the split-off hole subband to the first or second electronic subbands. However, as shown in Fig. 2, we do not observe any appreciable intersubband contributions from second or higher subbands to their next higher subbands in our Raman spectra taken under the excitations of (1) the probe pulse

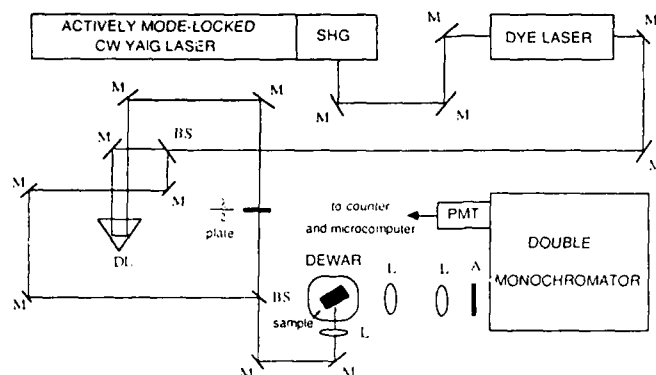


Fig. 1: Experimental setup for observing the spatial expansion of EHP in GaAs-Al<sub>x</sub>Ga<sub>1-x</sub>As MQW Structures. SHG--second harmonic generation system, M--mirror, BS--beam splitter, DL--delay line, L--lens, A--analyzer, PMT--photomultiplier tube.

alone and of (2) the pump and the probe pulses with different time delay  $\Delta t$ , we conclude that the photoexcited carriers primarily populate the first electronic subband for the parameters used in our experiments. The pump pulse is variably delayed before being recombined with the probe pulse and focused to the surface of the sample. The carrier density generated by the pump pulses was about  $4 \times 10^{10} \text{ cm}^{-2}$ . Raman scattering experiments were carried out in a backscattering geometry and in a pump/probe configuration. The undoped GaAs-Al<sub>x</sub>Ga<sub>1-x</sub>As MQW structure studied in this work was grown by MBE on (001) oriented undoped GaAs substrate. It consists of  $\approx 30$  periods of 100Å-thick Al<sub>x</sub>Ga<sub>1-x</sub>As ( $x=0.3$ ) and 300Å-thick GaAs layers. The sample was kept in contact with cold

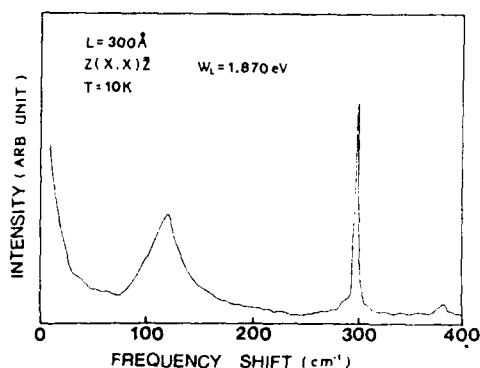


Fig. 2: A typical Raman spectrum taken at  $T=10 \text{ K}$  and for probe beam only. This spectrum demonstrates that the photoexcited carriers primarily populate the first electronic subband in our experiments. The sharp feature at  $\approx 300 \text{ cm}^{-1}$  is the first order Raman scattering signal from LO phonons and the broad peak at  $\approx 125 \text{ cm}^{-1}$  is from collective inter-subband excitations.



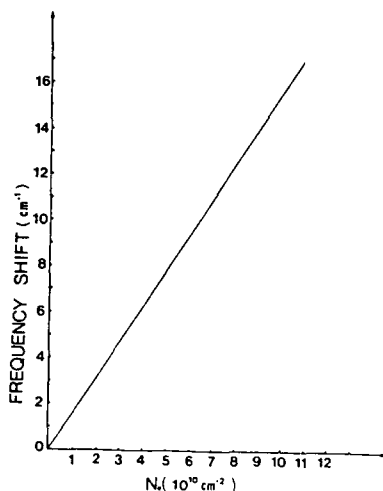


Fig. 3: Theoretical prediction of the frequency shift as a function of electron density for collective intersubband excitation (from equations 1 and 2, Pinczuk et al. 1980).

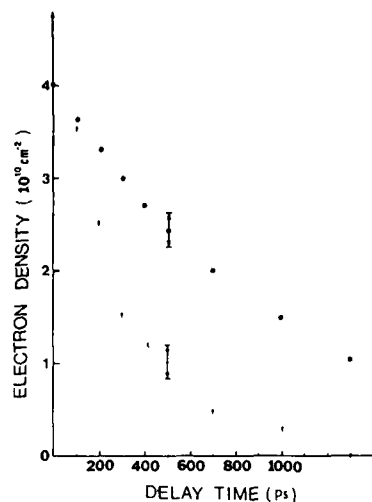


Fig. 4: The electron density vs. time delay  $\Delta t$  between the pump and the probe pulses. The solid circles are experimental data for GaAs- $\text{Al}_x\text{Ga}_{1-x}\text{As}$  MQW which has a diameter of  $\approx 500 \mu\text{m}$  and the spot size is  $\approx 500 \mu\text{m}$ . The crosses are for GaAs- $\text{Al}_x\text{Ga}_{1-x}\text{As}$  MQW and the spot size is  $\approx 100 \mu\text{m}$ .

( $\approx 10\text{K}$ ) He gas. The intersubband Raman scattering signal from photoexcited electrons confined inside the MQW is made up of two parts which can be separated by a proper selection rule. The first part consists of light scattering from spin-density fluctuation or single-particle excitations, the peak positions in the spectra reflect roughly (aside from the final state interactions) the difference in subband energies which are involved in the transition. The second part comes from the scattering from charge-density fluctuations or collective intersubband excitation; because of the depolarization effect and coupling to LO phonons, its peak positions will shift in proportion to the carrier concentration. As shown in Fig. 3, for carrier concentration  $n < 1 \times 10^{11} \text{ cm}^{-2}$  this shift has been found (Pinczuk et al. 1981, Pinczuk et al. 1980) to be linear in  $n$  and is about  $1.55 \text{ cm}^{-1}$  per  $10^{10} \text{ cm}^{-2}$  for our experimental situation. The shift of the peak position associated with the scattering of light from collective intersubband excitations was therefore utilized to determine the concentration of the photoexcited carriers in our measurements.

In our experiment, the analyzer was placed along (011) crystal direction, the pump and the probe beams were polarized along (0 $\bar{1}$ 1) and (011)

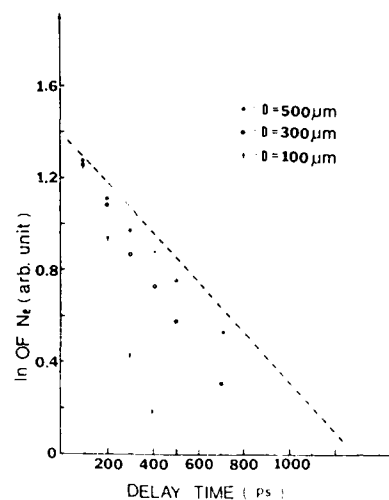


Fig. 5: The logarithm of the electron density vs. the time delay  $\Delta t$  for three different laser spot sizes  $D=500, 300, 100 \mu\text{m}$  in  $\text{GaAs-Al}_x\text{Ga}_{1-x}\text{As}$  MQW; although the spot size changes, the average power density in each cases is kept the same. The dashed line (which corresponds to the experimental data for  $\text{GaAs-Al}_x\text{Ga}_{1-x}\text{As}$  MQW having a diameter of  $\sim 500 \mu\text{m}$  and a spot size of  $\sim 500 \mu\text{m}$ ) is also plotted for comparison (See text for discussion)

directions, respectively. According to the selection rule, the probe beam will scatter collective intersubband excitations and the pump beam will have a contribution coming from single-particle excitations. However, due to the weakness of the latter at  $n=4 \times 10^{10} \text{cm}^{-2}$ , only the signal from collective intersubband excitations is observed in the spectra. The Raman signal is detected by a computer-controlled Raman system.

### 5. Experimental Results and Discussions

In Fig. 4, we have plotted the concentration of the photoexcited carriers as a function of time delay  $\Delta t$  between the pump and the probe pulses for two samples: (a) a  $\text{GaAs-Al}_x\text{Ga}_{1-x}\text{As}$  MQW with 300 Å-thick GaAs layers; (b) a  $\text{GaAs-Al}_x\text{Ga}_{1-x}\text{As}$  MQW with 300 Å-thick GaAs layers, but the total dimension of the sample has been tailored to  $\sim 500 \mu\text{m}$  by chemical etching. The laser beams were focused to a spot of diameter  $\sim 100 \mu\text{m}$  and  $\sim 500 \mu\text{m}$  on samples (a) and (b), respectively. We observe that the rate of decrease in the carrier concentration is much larger for sample (a) than for sample (b). Because the existence of the deep impurities in the GaAs sample has been shown to decrease the lifetime of the carriers (Weiner et al. 1982), one possible explanation is that sample (a) contains more deep impurities than sample (b). However, the following experimental observation rules out this possibility. In Fig. 5, the logarithm of the concentration of the photoexcited carriers is plotted against the time delay for sample (a) for three different laser spot sizes. We have deliberately kept the power density the same although we varied the spot size. These measurements show that the rate of decrease of the carrier concentration becomes smaller as the size of the focused spot increases and eventually, it approaches the value given in sample (b) of Fig. 4, which is indicated by the dashed line in Fig. 5. If deep impurities in the GaAs quantum wells are responsible for the observed data as shown in Fig. 4, we would expect that the rate of the decrease in the carrier concentration should be independent of the size of the focus spot. Therefore, in order to explain our measurements, some other intrinsic dissipation mechanism has to be invoked. We attribute the observed phenomena to the expansion of EHP. Qualitatively, the experimental data in Fig. 5 can be realized as follows:

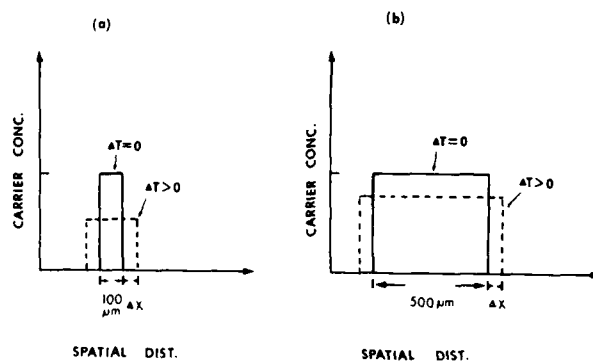


Fig. 6: Carrier concentration as a function of spatial distribution for EHP. Because  $\Delta x = V_D \cdot \Delta t$  where  $V_D$  is drift velocity of the plasma,  $\Delta t$  is the time delay and  $\Delta x$  is the distance the plasma expands, the lowering of the electron-hole pair density will be more efficient for a smaller excited spot such as (a) than a larger one such as (b) (see text for discussion).

As shown in Fig. 6, if we start with the same excitation power density and, consequently, the same electron-hole concentration in the plasma, then because the initial velocity of the expanding plasma (which is comparable to its Fermi velocity) is the same, the lowering of the electron-hole pair density is more efficient for a smaller excited spot. Quantitatively, the observed data can be understood, provided that the plasma is expanding at a velocity of about  $8 \times 10^6 \text{ cm/sec}$ . This measured plasma drift velocity is comparable to its Fermi velocity (which is about  $8.6 \times 10^6 \text{ cm/sec}$  for  $n = 4 \times 10^{10} \text{ cm}^{-3}$ ). Consequently, our experimental results demonstrate that at low intensity excitations the transport of EHP in  $\text{GaAs-Al}_x\text{Ga}_{1-x}\text{As}$  MQW structures is thermodiffusive and are consistent with the fast-diffusing model of Forchel et al. (1983). We have tried to make the measurements at higher laser power density, but at these high level excitations, the background signal (presumably resulting from the radiative recombination of hot electrons and holes excited through non-linear processes) becomes so large that we cannot confidently analyze our data.

#### 4. Conclusion

In brief, we have used picosecond time-resolved Raman scattering to investigate the spatial expansion of photoexcited EHP in  $\text{GaAs-Al}_x\text{Ga}_{1-x}\text{As}$  MQW structures. The experimental results show that the measured drift velocity of the plasma is comparable to its Fermi velocity, and therefore demonstrate that the transport of the photoexcited EHP in  $\text{GaAs-Al}_x\text{Ga}_{1-x}\text{As}$  MQW structures is thermodiffusive.

References:

- Burstein E, Pinczuk A and Bucher S 1978 Phys. of Semiconductors, edited by  
B L H Wilson (The Institute of Physics, London) p. 1231  
Collins C L and Yu P Y 1984 Solid State Comm. 51 123  
Forchel A, Schweitzer H and Mahler G 1983 Phys. Rev. Lett. 51 501  
Huang Y H and Yu P Y 1986 Bull. Am. Phys. Soc. 31 400  
Junnarkar M R and Alfano R R 1986 Bull. Am. Phys. Soc. 31 350  
Pinczuk A, Shah J, Gossard A C and Weigmann W 1981 Phys. Rev. Lett. 46  
1341  
Pinczuk A, Worlock J M, Stormer H L, Dingle R, Wiegmann W and Gossard A C  
1980 Solid State Comm.  
Steranka F M and Wolfe J P 1985 Phys. Rev. Lett. 55 95  
Wautelet M and Van Vechten J A 1981 Phys. Rev. B23 5551  
Weiner J S and Yu P Y 1982 Bull. Am. Phys. Soc. 27 335

## **Surface emitting lasers with slant edge mirrors and multilayer reflectors**

M. Ohshima, N. Takenaka, N. Hirayama, Y. Toyoda and N. Hase

Kawasaki Laboratory, Optoelectronics Development Center,  
Matsushita Electric Industrial Co., Ltd.  
3-10-1 Higashimita, Tama-ku, Kawasaki, 214 JAPAN

**Abstract.** We have developed new InP/InGaAsP surface emitting etched mirror laser diodes. This laser has a cavity consisting of slanted facets with a high reflectance dielectric coating and an InP/InGaAsP multilayer reflector. A threshold current as low as 65mA is obtained. The far field pattern has two strong intensity peaks in directions deflected by 20 and 40 degrees from the substrate plane. In addition, the single longitudinal mode operation is also observed.

### 1. Introduction

Monolithic formation of the Fabry-Perot resonators of semiconductor lasers are important for integrating laser diodes into optoelectronic circuits. It is also of considerable interest for a variety of applications such as two dimensional light sources for image processing and optical computers. In particular, facet formation by etching is potentially advantageous for batch processing and on-wafer testing since it eliminates the processes of cleaving or dicing. Various types of etched facet lasers have been proposed in the InP/InGaAsP (Iga and Miller 1982, Wright et al 1982) and GaAs/GaAlAs (Hurwitz et al 1975, Wada et al 1985) materials systems. In etched mirror lasers, the vertical facets which can be produced by wet chemical etching on (100) substrates, however, are generally nearly parallel to the (111) planes. As a result, the etched mirror lasers reported to date showed threshold currents considerably higher than those of cleaved mirror lasers.

Here, we report the fabrication and properties of a new type of etched mirror laser (SEM-LD) which has slant-edge mirrors and semiconductor multilayer reflectors.

### 2. Laser Structure

A schematic diagram of the SEM-LD is shown in Fig. 1. The facets nearly parallel to the (111) planes are used as the cavity mirrors. Since the facets are slanted, dielectric films for coating can be deposited by evaporation from the top of the wafer. A third mirror of the cavity consists of the InP/InGaAsP multilayer

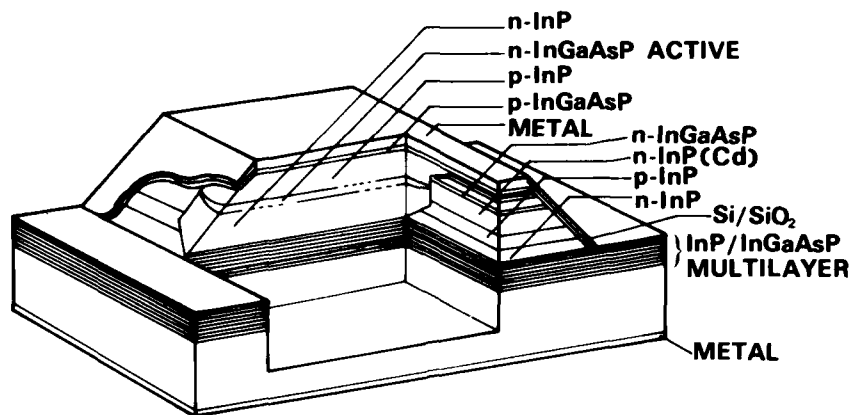


Fig. 1 Schematic diagram of the RFM-LI.

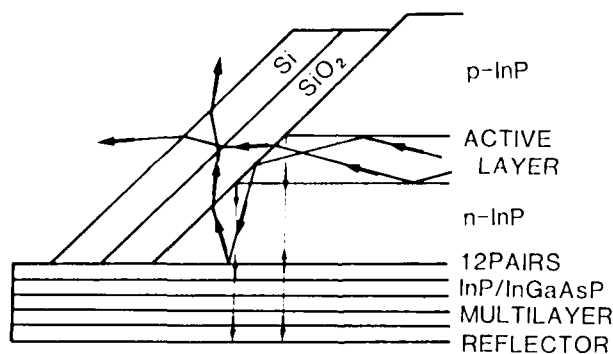


Fig. 2 The beam reflection and emission at the slant edge.

reflectors (MLK). Fig. 2 shows schematically the details of the slant edge mirror with dielectric coatings of thin Si and SiO<sub>2</sub> layers. The emission beam from the active layer is reflected at the slant edge mirror to the direction of MLK. The MLK has a reflectivity of typically about 40%. Therefore, an optical cavity is constructed by the active layer, the slant edge and the MLK. The output power can be extracted from the active layer edge through the dielectric coating which has a designed reflectance.

#### 3. Fabrication

Fig. 3 shows the fabrication process of the RFM-LI. This process includes three steps of LPE growths. First, the multilayer structure, consisting of twelve pairs of InP/InGaAsP (E<sub>g</sub> 1.0 eV) layers with constant compositions are grown by LPE using a horizontal sliding boat. One of the major problems with LPE growth when the substrate wafer is slid repeatedly back and forth between the InP and InGaAsP growth melts is the mixing of the two melts. This melt mixing can cause poor control of the layer composition and the layer thickness.

To avoid this, we designed a horizontal boat which has 25 melt containers. By sliding the boat only in one direction, reflectances as high as 40-45% at  $1.3\mu\text{m}$  wavelength were obtained with good reproducibility. In the second LPE growth, layers of n-InP(Te-doped), p-InP(Zn-doped),  $^{15}_{-3}$  n-InP(Cd-doped, Nd-Na= $5 \times 10^{-3} \text{ cm}^{-3}$ ) and n-InGaAsP(undoped,  $E_g=0.95\text{eV}$ ) were grown successively as shown in Fig. 3(a).

After the second LPE growth, a  $\text{SiO}_2$  film was deposited on the surface. The standard photolithographic technique was applied to open a  $2\mu\text{m}$ -wide window. Then, the stripe channels were preferentially etched into the three layers using solutions of  $\text{H}_2\text{SO}_4:\text{H}_2\text{O}_2:\text{H}_2\text{O}(3:1:1)$  for the top InGaAsP and concentrated HCl for the InP layers. After removal of the  $\text{SiO}_2$  film and the photoresist, the layer of n-InP(Te-doped), n-InGaAsP(undoped, the active layer), p-InP(Zn-doped) and p-InGaAsP(Zn-doped, the cap layer) were grown on the channeled substrate.

After the crystal growth, the p-side electrode(Au/AuZn) was evaporated on the cap layer and patterned into rectangles of  $200\mu\text{m} \times 150\mu\text{m}$ . Then, a CVD- $\text{SiO}_2$  film was deposited to cover the p-side electrodes during etching (Fig. 3(b)). Smooth slanted mirrors were obtained using  $\text{H}_2\text{SO}_4:\text{H}_2\text{O}_2:\text{H}_2\text{O}$  for InGaAsP and concentrated HCl for InP. The etched depth was about  $7\mu\text{m}$ . Magnified observation of the edge of the active layer profiles revealed that the slant plane formed an angle of about 47 degrees with the (001) plane. We note that the etching characteristics of InP and InGaAsP can be different. In fact, however, the slant planes of these layers (Fig. 2) were in the range 40-50 degrees from the wafer plane, leading approximately to the structure of Fig. 2. After the mirror etching,  $\text{SiO}_2$  and Si layers were evaporated using an electron-beam evaporation system as shown in Fig. 3(c). When the  $\text{SiO}_2$  and Si layers were respectively 2320Å and 930Å thick, the reflectivity measured was about 80% at  $1.3\mu\text{m}$  wavelength. This value would be improved to 95% if the coating is doubled using Si- $\text{SiO}_2$  layers of the same thickness as used above.

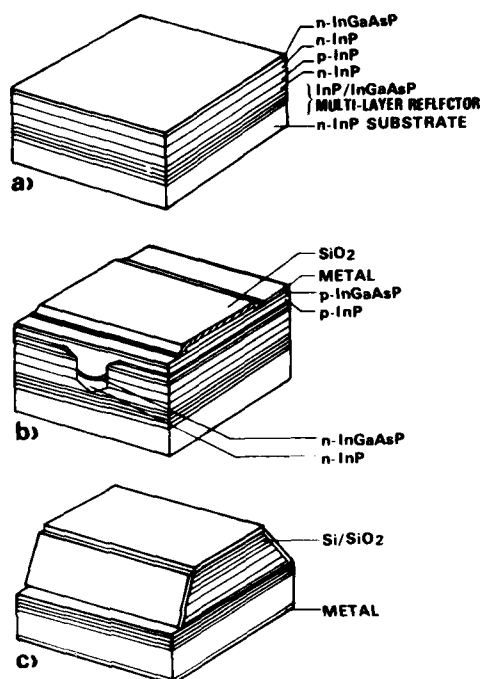


Fig. 3 Fabrication process of the SEM-LD. a) Epitaxial growth of the MLR and current confinement layers. b) Epitaxial growth of the cladding layer, active layer, and cap layer and metallization. Ohmic metal is covered by  $\text{SiO}_2$  as an etching mask. c) Formation of the slanted plane and evaporation of the Si/ $\text{SiO}_2$  coating.

#### 4.Characteristics

##### 4.1 L-I Characteristics

Fig. 4 shows a typical optical output power versus current(L-I) characteristics of the SEM-LD in pulsed operation, measured before separation into individual chips. The length of the active layer was about 200 $\mu$ m. The threshold current is as low as 65mA, and no kinks are seen. On the other hand, the threshold currents of the lasers with two cleaved facets and a 200 $\mu$ m-long cavity fabricated from the same wafer were typically about 20mA, which is about 1/3 of the threshold currents of SEM-LD. This difference is ascribed to the beam broadening which occurs between the slant edge and MLR.

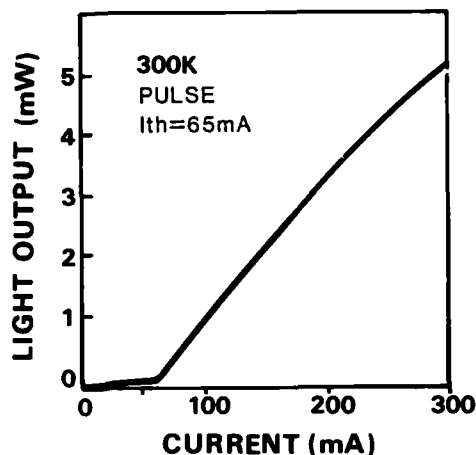


Fig. 4 Room-temperature output power versus pulse injection current for a SEM-LD before cleaving.

##### 4.2 Far Field Patterns

Fig. 5(a) shows the far field patterns, perpendicular to the junction plane, measured when the laser is rotated up to about 90 degrees. The three curves correspond to laser diode currents of 150, 200, and 300mA. Three intensity peaks are observed. Two of them are strong and narrow, at angles of about 20 and 40 degrees with respect to the (001) plane. Their full widths at half maximum are both about 10 degrees. Fig. 5(b) is a far-field pattern nearly parallel to the junction plane; the detector was fixed at peak at about 20 degrees in Fig. 5(a) and the laser was rotated around an axis a normal to the rotate axis of Fig. 5(a). The full width at half maximum in Fig. 5(b) is about 25 degrees and the fundamental mode oscillation is obtained. These far-field patterns are considerably narrower than those of the conventional edge-emitting lasers (Oomura et al 1981).

##### 4.3 Longitudinal Mode Behavior

Fig. 6 shows the typical longitudinal mode behavior of the SEM-LD. The longitudinal mode behavior with increasing current is quite similar to that of a multi-cavity laser (Suematsu et al 1975, Garmire et al 1981, Ohshima et al 1985). As shown in Fig. 6(a), at a low injection current of about 1.1I<sub>th</sub>, the envelope of the emission spectrum has peaks separated by a constant interval of 22Å. As the current is increased to 1.4I<sub>th</sub> (Fig. 6(b)), the dominant mode grows and the other modes are almost suppressed. As the current is increased to 1.6I<sub>th</sub>, the single mode operation is achieved (Fig. 6(c)).

The reason for this longitudinal mode behavior is believed to be as follows;



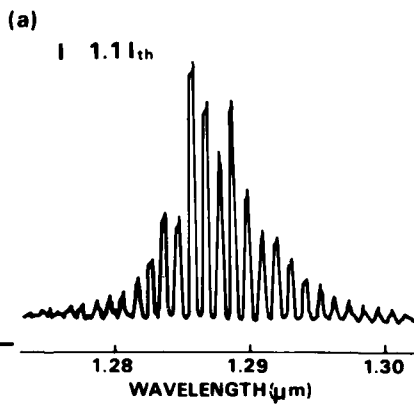
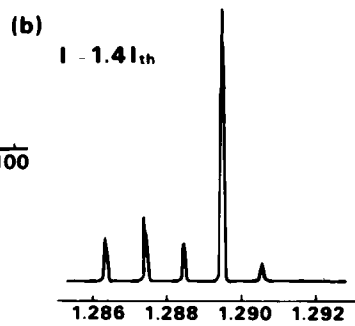
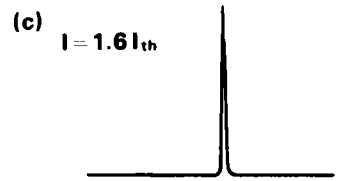
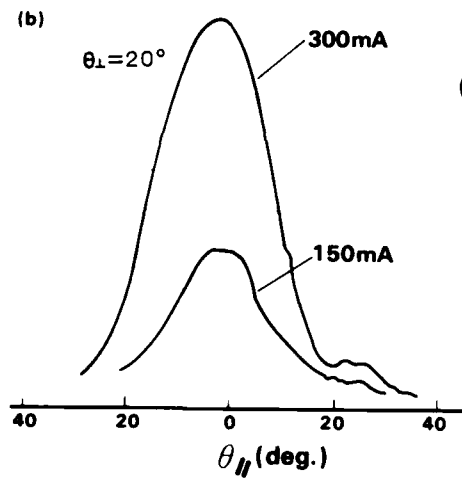
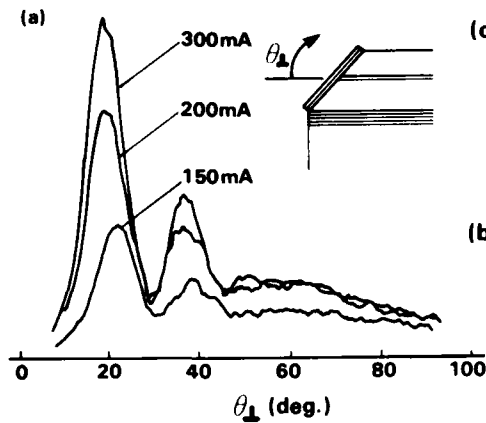


Fig. 5 Far field patterns at various light output powers, a) perpendicular and b) nearly parallel to the junction plane(see text). The transverse mode is stable even at current levels up to 300mA.

Fig. 6 Emission spectrum at operating currents of a) 1.1 I<sub>th</sub>, b) 1.4 I<sub>th</sub>, c) 1.6 I<sub>th</sub>.

- 1) The MLR acts as a waveguide.
- 2) Part of the lasing power in the active layer is sustained also in the MLR waveguide. Accordingly, the longitudinal mode spacing is determined also by the MLR length.
- 3) The constructive interference between the modes of these two resonators (the active stripe layer and the MLR) can enhance a

specific longitudinal mode and result in the mode selectivity.

Therefore, the SEM-LD is essentially a double cavity laser so that the stable longitudinal mode operation can be achieved.

#### 5. Summary

We have developed a new etched cavity laser, which has a cavity formed with slant edges and semiconductor multilayer reflectors. A threshold current as low as 65mA has been obtained. Two intensity maxima are observed, with full widths at half maximum of about 10 degrees perpendicular to the junction. In addition, this laser can operate in a single longitudinal mode due to the MLR acting as a waveguide. The present results indicate that this laser is promising for applications in integrated optoelectronic circuits.

#### Acknowledgments

The authors are grateful for the continuous support and encouragement by I. Senbokuya and Y. Kino. They also thank M. Mihara, Y. Takeuchi, T. Tsuruta and K. Idota for useful discussions.

#### References

- Garmire E, Evans G, and Niesen J 1981 Appl. Phys. Lett. 39, 789
- Hurwitz C E, Rossi J A, Hsieh J J, and Wolte C M 1975 Appl. Phys. Lett. 27, 241
- Iga K, and Miller B I 1982 IEEE J. Quantum Electron. QE-18, 22
- Ohshima M, Toyoda Y, Hirayama N, Takenaka N, Matsuki M, Kobayashi H, and Kino Y 1985 IEEE J. Quantum Electron. QE-21, 563
- Omura E, Murotani T, Higuchi H, Namizaki H, and Susaki W 1981 IEEE J. Quantum Electron. QE-17, 56
- Suematsu Y, Yamada M, and Hayashi K 1975 IEEE J. Quantum Electron. QE-11, 457
- Wada M, Hamada K, Shibutani T, Shimizu H, Kume M, Itoh K, Kano G, and Teramoto I 1985 IEEE J. Quantum Electron. QE-21, 658
- Wright P D, Nelson R D, and Wilson R B 1982 IEEE J. Quantum Electron. QE-18, 249

## Angular chlorine ion-beam-assisted etching of GaAs and AlGaAs

W. D. Goodhue, G. D. Johnson and T. H. Windhorn

Lincoln Laboratory, Massachusetts Institute of Technology, Lexington, Massachusetts 02173

**Abstract** We have used chlorine ion-beam-assisted etching to produce channels with sloping walls in GaAs and AlGaAs layers. Contours have been generated by tilting the substrate with respect to the etching beams at an angle that is either fixed or varied by means of a computer-controlled stage. This technique is potentially useful for a wide variety of electronic and optical GaAs/AlGaAs applications. The first application of the technique was to fabricate  $45^\circ$  deflecting mirrors in combination with vertical laser cavity mirrors to produce surface-emitting diode laser arrays. This paper will focus on the procedures involved in the angular etching process.

A variety of electronic and optical GaAs/AlGaAs-based devices require channels with sloping walls in GaAs and AlGaAs layers. Windhorn and Goodhue (1986) have used chlorine ion-beam-assisted etching (IBAE) to control wall slopes. In the IBAE process an argon ion beam and a jet of chlorine gas are simultaneously incident on the sample. Etching is a chemical process involving the chlorine, but is highly anisotropic because of the argon ion beam. In fact, the wall slope is determined by the angle at which the sample is tilted with respect to the ion beam. Contours have been generated both by using fixed tilt angles and by computer-controlled dynamic tilting. We have used the technique to fabricate  $45^\circ$  deflecting mirrors in combination with vertical laser cavity mirrors to produce surface-emitting laser arrays and are presently applying the technique to fabricate two-dimensional GaAs/AlGaAs diode laser arrays and columns 10 - 20 nm wide for quantum confinement studies.

In this paper we will focus on the angular etching process itself rather than specific devices. The basic chlorine ion-beam-assisted etching process has been described by Geis *et al* (1981). Since their paper, a cryopump, Meissner coil, second chlorine tube, load-lock and tiltable sample holder have been added to the apparatus. A schematic of the present system is shown in Fig. 1. The cryopump, Meissner coil, and load-lock provide a clean vacuum system that routinely reaches a background pressure of  $1 \times 10^{-7}$  Torr 15 minutes after a

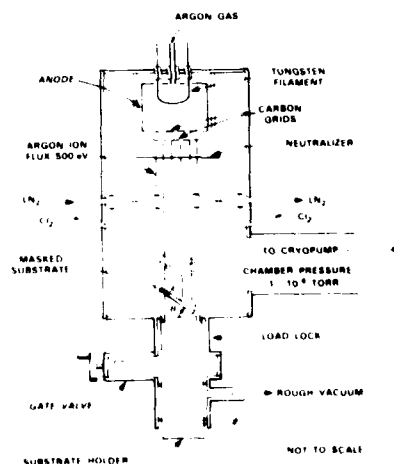


Fig. 1 Schematic of the  $\text{Cl}_2$ -IBAE etching system.

sample is transferred into the system. Samples are etched approximately 30 minutes after transfer.

For this work we adjusted the system operating parameters to give a normal-incidence etch rate of 40 to 50 nm min<sup>-1</sup> in GaAs. As in the earlier work by Geis *et al* (1981), we operated the system with a 500-eV argon ion beam at a current density of 1.4 mA cm<sup>-2</sup> and an argon beam pressure of 10 mTorr at the sample surface. The chlorine beam pressure at the sample surface was 2.8 mTorr. With these parameters the normal-incidence etch rates for Al<sub>x</sub>Ga<sub>1-x</sub>As with *x* from 0.08 to 0.80 were, to within 10%, 40 nm min<sup>-1</sup>. No roughness was observed at GaAs-AlGaAs heterointerfaces.

The masking materials used in this work were baked AZ-1470 photoresist, pyrolytically deposited phosphosilicate glass (PSG) and evaporated nickel. The respective etch rates for these materials were 4.7 nm min<sup>-1</sup>, 1.2 nm min<sup>-1</sup>, and 0.4 nm min<sup>-1</sup>. Chrome lithographic masks were used in preference to emulsion and iron oxide masks since they were found to minimize ripple of the etched walls.

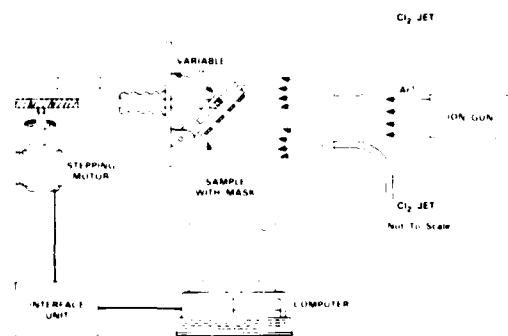


Fig. 2 Schematic showing the etching geometry for the computer-controlled stage.

A schematic of the etching geometry and computer-controlled sample stage used for angular etching is shown in Fig. 2. Figure 3 shows SEM micrographs of etched walls in (100) GaAs with the edge alignment along the (011) cleavage plane. The first micrograph shows a sidewall etched at four different tilt angles for four different time intervals. The tilt-angle schedule was 30° for 20 min, 40° for 10 min, 50° for 5 min, and 60° for 2.5 min. The etched sidewall angles are identical to the tilt angles of the substrate with respect to the ion beam and the etch rate is constant in the direction of the ion beam independent of tilt angle. The second micrograph shows a curved sidewall obtained by computer-controlled etching using 800 discrete tilt angles. Etching was initiated with the ion beam 35° from the normal to the sample, and the angular motion of the sample holder was accelerated during the run. As the angle between the ion beam and the sample normal increases, the top edge of the mask shadows areas with more vertical sidewalls so that virtually any concave shape can be generated. Convex sidewalls could be obtained by combining substrate tilting with computer-controlled variation in the argon ion beam current density. However, the motion required to generate convex shapes is more complicated because the entire sidewall is etched during the entire run.



Fig. 3 SEM micrographs of etched sidewalls in GaAs. (a) Sidewall contour generated by four discrete angle runs at varying times. (b) Sidewall contour generated by computer-controlled continuous angle variation.

The system can also be used to generate smooth vertical sidewalls. Figure 4 is an SEM micrograph of a 3- $\mu\text{m}$ -deep channel with vertical walls that was etched in an  $\text{Al}_{0.30}\text{Ga}_{0.70}\text{As}$  double heterostructure with a 100 nm GaAs active layer. During the etch the sample was rocked under computer control with the ion beam parallel to the channel sidewall plane. The lower 2  $\mu\text{m}$  portion of the sidewall is extremely smooth. The roughness on the upper sidewall of the channel is due to PSG mask edge failure 2  $\mu\text{m}$  into the etch. Better masks will be required to produce optically smooth walls. We hope to investigate the use of both x-ray and high-resolution electron-beam lithography in the masking process.



Fig. 4 SEM micrograph of the vertical sidewall of a channel etched 3  $\mu\text{m}$  deep in a  $\text{Al}_{0.30}\text{Ga}_{0.70}\text{As}$ -GaAs double heterostructure.

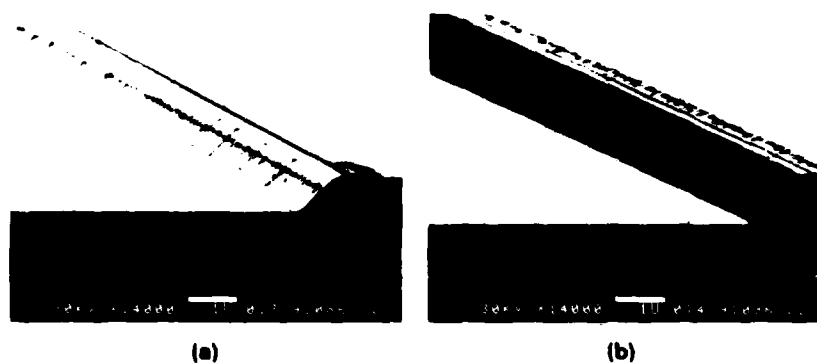


Fig. 5 Composite showing 45° sidewall variations when oriented a) along  $(0\bar{1}1)$  toward  $(1\bar{1}1)$ . b) along  $(011)$  toward  $(11\bar{1})$  and

Several orientations were checked for variations in angular etching. A grating was placed along the  $(0\bar{1}1)$ ,  $(01\bar{1})$ ,  $(001)$ , or  $(010)$  plane of a portion of a  $(100)$ -oriented substrate. The tilt angle was adjusted to 45° and a set of channels was etched for each of eight orientations (each of the four samples was cleaved into two so that both 45° directions could be etched). All orientations etched at 45° with some minor variations in the sidewall ripple. The sidewall oriented along  $(0\bar{1}1)$  toward  $(11\bar{1})$  was the smoothest, while the sidewall oriented along  $(01\bar{1})$  toward  $(\bar{1}11)$  had the most ripple (Fig. 5).

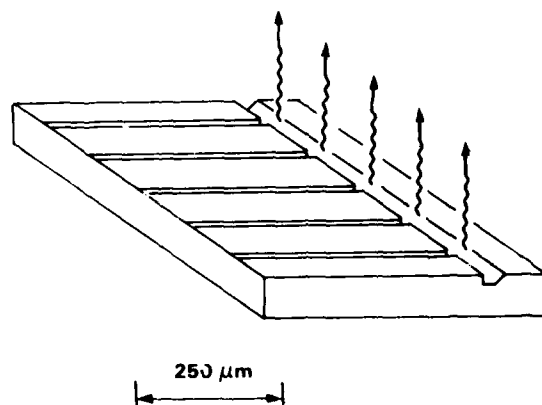


Fig. 6 Schematic of a surface-emitting laser device showing the relationship between the etched facet and deflecting mirror.

We have used the angular etching technique to produce surface-emitting diode lasers. The processing techniques used to prepare the wafers for etching have been described previously by Windhorn and Goodhue (1986). Figure 6 is a schematic of a surface-emitting laser which shows the relationship between the etched facet and  $45^\circ$  deflecting mirror. We plan to replace the  $45^\circ$  deflecting mirror with a curved mirror to add focusing capability and permit the fabrication of two dimensional cw room-temperature arrays for high-power applications. Since the technique produces minimal surface damage, (Geis *et al* (1981)) we are also investigating its use in combination with molecular beam epitaxy overgrowth and as a method for etching relatively easily fabricated 80-nm-wide quantum wires or boxes down to 10-20 nm for quantum confinement studies (Fig. 7). The results of our first effort to make 10-20 nm wide quantum wires is shown in (Fig. 8). The columns shown in a) were fabricated using ion beam lithography, a nickel lift off and vertical  $\text{Cl}_2$ -IBAE. The columns of a) were then angle etched after the nickel mask was removed. As shown in b) not all of the mask was removed, so the angle etch left the upper portion of the columns wedge shaped. The lower portions, however, were not masked from the angled beam so that sub-20-nm-wide column base regions were produced.

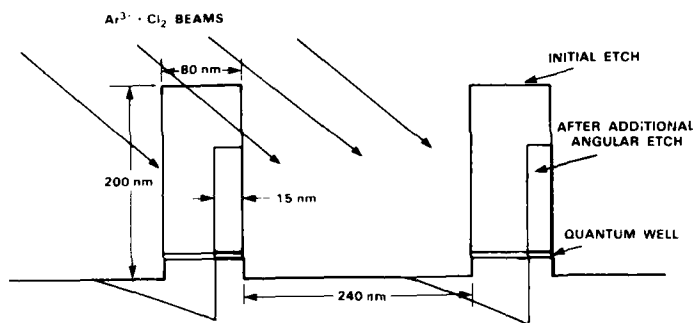


Fig. 7 Schematic showing how quantum lines or boxes could be generated in a two-step etching process. After the initial etch the masking layer is removed and a second angular etch is used to thin the columns.



Fig. 8 SEM micrographs of columns etched in GaAs showing a) the initial etch which produce 80-nm-wide columns on 320 nm centers and b) the results of angular etching the columns at  $20^\circ$ . The bases of the columns are less than 20 nm wide.

In summary, chlorine IBAE has been used to etch channels in GaAs and AlGaAs, producing sidewalls tilted at the same angle as the substrate is tilted with respect to the ion beam. Both planar and curved sidewalls have been generated. Only minor orientation effects have been observed for the limited number of orientations investigated. Masking materials and patterning techniques still need to be improved to eliminate edge ripple on the sidewalls. The etching technique is potentially very useful for a variety of electronic and optical GaAs/AlGaAs devices.

The authors thank Dr. S. W. Pang for preparing the quantum wire test samples used in this work. The expert technical assistance of L. Krohn, Jr., W. F. DiNatale and P. M. Nitishin is also gratefully acknowledged. This work was sponsored by the Department of the Air Force and the Defense Advanced Research Projects Agency.

#### References

- Geis M W, Lincoln G A, Efremow N, and Piacentini W J 1981,  
J. Vac. Sci. Technol. **19**, 1390  
Windhorn T H and Goodhue W D 1986, Appl. Phys. Lett. **48**, 1675



## **GaAs/AlGaAs double-heterostructure diode lasers on (110) GaAs substrates**

H. K. Choi and M. K. Connors  
Lincoln Laboratory, Massachusetts Institute of Technology  
Lexington, Massachusetts 02173-0073

**Abstract.** Operation of GaAs/AlGaAs double-heterostructure diode lasers fabricated on (110) GaAs substrates is reported for the first time. Structures composed of a 0.1- $\mu\text{m}$ -thick GaAs active layer and 1- $\mu\text{m}$ -thick  $\text{Al}_{0.28}\text{Ga}_{0.72}\text{As}$  confinement layers were grown by organometallic vapor phase epitaxy. Broad-area lasers with a cavity length of 350  $\mu\text{m}$  have exhibited pulsed threshold current densities as low as 730  $\text{A}/\text{cm}^2$ . A stripe-geometry, gain-guided laser has exhibited pulsed threshold current of 60 mA and differential quantum efficiency of 33% per facet.

### **1. Introduction**

There has been no report of GaAs/AlGaAs heterostructure devices fabricated on (110) GaAs substrates, apparently because of the difficulty encountered in growing device-quality epilayers with this orientation. Both the surface morphology and crystal quality, which are strongly dependent on growth parameters, have generally been poor (Nakanisi 1984, Reep and Ghandi 1983, Wang 1983). In addition, alloy clustering or segregated growth has been observed for AlGaAs (Petroff et al. 1982, Wang et al. 1986), resulting in a fairly broad linewidth in low-temperature photoluminescence (PL). Although mobility enhancement was observed by Wang et al. (1986) in GaAs/AlGaAs modulation-doped structures grown on (110), no device results were reported. In this paper we report the first (110) GaAs/AlGaAs diode lasers, which have been fabricated in double heterostructures (DH) grown by organometallic vapor phase epitaxy (OMVPE) on substrates oriented  $2^\circ$  off (110) toward (112). These devices have characteristics comparable to those reported for lasers with similar structures on (100) substrates.

Our work on (110) diode lasers is motivated by their potential for utilization in monolithic two-dimensional surface-emitting laser arrays. Such arrays could be fabricated from edge-emitting devices having etched facets that are coupled with mirrors deflecting the laser radiation by  $90^\circ$  so that it emerges normal to the wafer surface (Walpole and Liao 1986, Windhorn and Goodhue 1986). For (110) substrates, there are {111} planes that are normal to the substrate surface. Since (111A) and (111B) are respectively the slowest and fastest etching planes for many wet-chemical etchants, facet-deflector pairs can be obtained by wet-chemical etching.

### **2. Epitaxy of GaAs and AlGaAs on (110) GaAs Substrates**

The GaAs and AlGaAs layers were grown in a horizontal OMVPE system at atmospheric pressure. Trimethylgallium and trimethylaluminum were used as

Ga and Al sources and arsine as the As source. The reactor is equipped with a vacuum load-lock for substrate introduction. The GaAs substrates, which were doped with Si to  $\sim 2 \times 10^{18} \text{ cm}^{-3}$ , were degreased and free etched to remove polishing damage. Before growth most of the substrates were etched *in situ* with gaseous HCl at  $900^\circ\text{C}$  for a few minutes for further cleaning. An *in situ* HCl etch was used after every few runs to remove thick deposits from the reactor wall.

The surface morphology of the epitaxial layers was very sensitive to the direction of substrate misorientation. Figure 1 shows Nomarski photomicrographs of GaAs layers grown on substrates tilted  $2^\circ$  toward (110), (112) or (112). (For convenience, in the following discussion the (112) and (112) planes will be designated as (112A) and (112B), respectively.) All these layers were grown at  $780^\circ\text{C}$  with a V/III ratio of about 60. Tilting toward (110) gave very fine terraces, while tilting toward (112B) produced a very rough surface. The best surface morphology was obtained when the substrate was tilted toward (112A). For this orientation shallow surface defects elongated along  $\langle 111 \rangle$  were observed. For comparison, GaAs was also grown on an  $n^+$  (100) substrate under the same conditions. Featureless surfaces were obtained in this case.

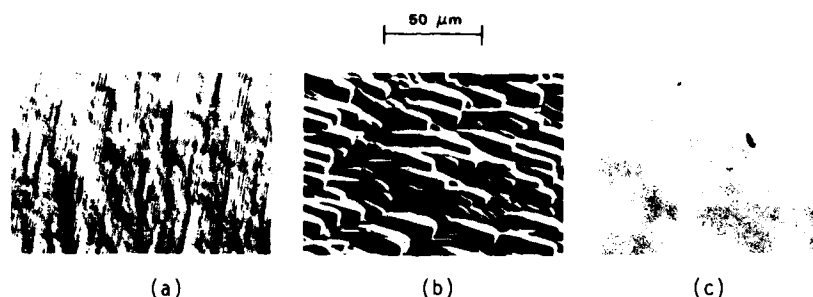


Fig. 1. Nomarski photomicrographs showing the surface morphology of GaAs grown on substrates oriented (a) (110) + (110), (b) (110) + (112B) and (c) (110) + (112A). The substrate temperature was  $780^\circ\text{C}$ .

The quality of the layers of Fig. 1 was characterized by PL measurements at 5 K. Figure 2 shows the PL spectra excited by an Ar ion laser emitting at 647 nm with a power density of about  $7.5 \text{ W/cm}^2$ . The strongest and sharpest exciton peak was obtained for the layer grown on the substrate tilted toward (112A). The full width at half maximum (FWHM) of this peak was about 3 meV. By reducing the power density to  $0.75 \text{ W/cm}^2$ , we could

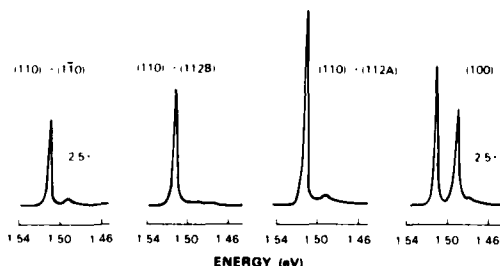


Fig. 2. Low-temperature photoluminescence (PL) spectra of GaAs layers grown on substrates with four different orientations.

resolve the free, donor-bound and acceptor-bound exciton peaks, indicating the high purity and crystal quality of the material. Despite its poor morphology, the layer grown on the substrate tilted toward (112B) had a stronger exciton peak than the one grown on the substrate tilted toward (110). All the layers on near-(110) substrates showed smaller carbon peaks than the one grown on (100). The dependence of carbon incorporation on substrate orientation has been reported by Kuech and Veuhoff (1984). Because the smoothest morphology and strongest PL were obtained for (110) tilted toward (112A), further experiments were confined to that orientation.

The GaAs layers were much less sensitive to substrate temperature and V/III ratio than to orientation. The surface morphology was not much changed for substrate temperatures up to 820°C, but the surface was slightly rougher for growth at 850°C. With increasing substrate temperature the FWHM of the exciton peak increased, reaching about 5 meV for 850°C, and the carbon peak became larger. At a substrate temperature of 780°C, the surface morphology was slightly degraded when the V/III ratio was changed from 60 to either 30 or 90. At higher substrate temperatures, however, better surface morphology was obtained with V/III ratios larger than 60.

The surface morphology of AlGaAs layers was very sensitive to the substrate temperature. The most serious problem was large surface defects, as shown in Fig. 3(a) for a layer grown at 820°C with a V/III ratio of about 30. The size of the defects was fairly uniform, indicating that they originated from the substrate. The density of these defects increased with decreasing substrate temperature. The density was significantly reduced by *in situ* HCl etching prior to growth, showing that surface contamination contributed to defect generation. Under optimum conditions, AlGaAs with very smooth morphology and few defects could be obtained at a substrate temperature of 850°C, as shown in Fig. 3(b). Figure 4 shows the low-temperature PL spectra of an  $\text{Al}_{0.28}\text{Ga}_{0.72}\text{As}$  layer excited by an Ar ion laser at 568 nm with power densities of 7.5 and 30 W/cm<sup>2</sup>. Both an exciton peak and strong carbon peak were observed. The FWHM of the exciton peak was about 13 meV, much smaller than the value of 52 meV obtained by Wang *et al.* (1986) for  $\text{Al}_{0.3}\text{Ga}_{0.7}\text{As}$  grown on (110) GaAs by molecular beam epitaxy.

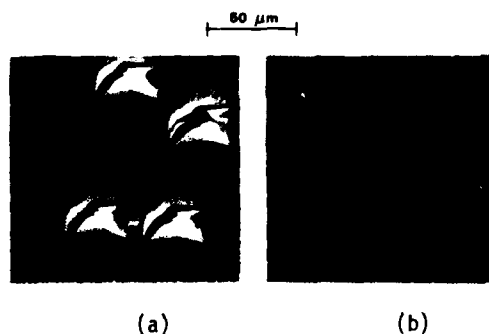


Fig. 3. Nomarski photomicrographs showing the surface morphology of AlGaAs grown at substrate temperatures of (a) 820°C and (b) 850°C. The substrate orientation was (110) + (112A).

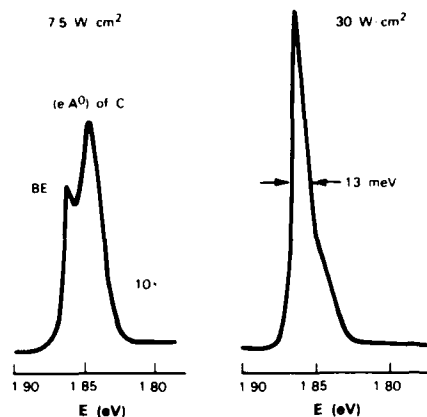


Fig. 4. Low-temperature PL spectra of  $\text{Al}_{0.28}\text{Ga}_{0.72}\text{As}$  for excitation power densities of 7.5 and 30  $\text{W}/\text{cm}^2$ .

### 3. Double-Heterostructure Diode Lasers

A DH laser structure consisting of the following layers was grown by OMVPE on a GaAs substrate oriented  $2^\circ$  off (110) toward (112A): 1- $\mu\text{m}$ -thick  $\text{n-Al}_{0.28}\text{Ga}_{0.72}\text{As}$  confinement, 0.1- $\mu\text{m}$ -thick nominally undoped GaAs active, 1- $\mu\text{m}$ -thick  $\text{p-Al}_{0.28}\text{Ga}_{0.72}\text{As}$  confinement, and 0.2- $\mu\text{m}$ -thick  $\text{p}^+\text{GaAs}$  cap. Dimethylzinc and hydrogen selenide were used as the sources of p and n dopants, respectively. All the layers were grown at  $850^\circ\text{C}$  in order to minimize the density of the large surface defects in the AlGaAs layers. Broad-area lasers were fabricated with cleaved facets. Figure 5 shows the pulsed threshold current density  $J_{\text{th}}$  as a function of cavity length  $L$ . The lowest  $J_{\text{th}}$  for  $L = 350 \mu\text{m}$  was  $730 \text{ A}/\text{cm}^2$ , which approximates the lowest values reported for lasers of similar structure on (100) substrates. The absorption coefficient  $\alpha$  was found to be  $14 \text{ cm}^{-1}$  by fitting the data to the standard expression

$$J_{\text{th}} = \frac{1}{\beta} \left[ \alpha + \frac{1}{2L} \ln \left( \frac{1}{R_1 R_2} \right) \right],$$

where  $R_1 = R_2 = 0.32$  are the facet reflectivities and  $\beta$  is a constant equal to  $0.059 \text{ cm}/\text{A}$ .

Oxide-defined stripe-geometry lasers with a stripe width of  $6 \mu\text{m}$  were also fabricated. Figure 6 shows the current vs light output characteristic of a laser with  $L = 210 \mu\text{m}$  that was operated with 100-ns pulses at a duty cycle of 0.1%. The threshold current was 60 mA, and the differential quantum efficiency was 33% per facet. Light output of more than 20 mW was obtained without kinks for many of the lasers, indicating uniform material quality. Figure 7 shows the data for threshold current as a function of  $L$ , together with data reported by Burnham *et al.* (1981) for DH stripe-geometry lasers with an  $\text{Al}_{0.07}\text{Ga}_{0.93}\text{As}$  active region and  $\text{Al}_{0.45}\text{Ga}_{0.55}\text{As}$  confinement layers that were grown by OMVPE on (100) substrates. For the same cavity length, the threshold current of the (110) lasers was about 20 mA higher than that of the (100) lasers.

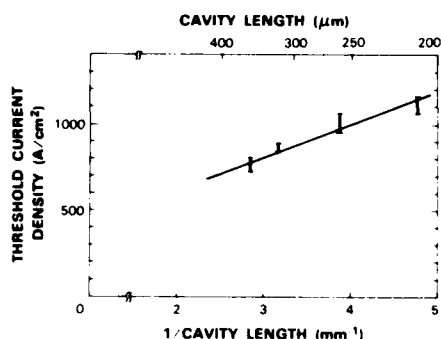


Fig. 5. Threshold current density as a function of cavity length for broad-area (110) DH diode lasers.

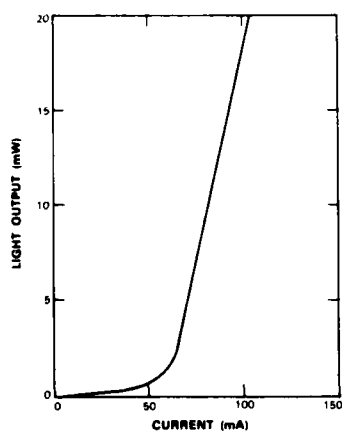


Fig. 6. Light output vs current for a stripe-geometry (110) DH laser. The threshold current is 60 mA, and the differential quantum efficiency is 33% per facet.

However, the AlAs mole fraction difference between the active and confinement layers is 0.38 for the (100) lasers and only 0.28 for (110) lasers. For the same difference in AlAs mole fraction, the difference in threshold current should be much smaller.

#### 4. Etching of Facet-Deflector Pairs

In order to demonstrate the potential usefulness of (110) lasers for monolithic two-dimensional surface-emitting arrays, facet-deflector pairs were formed by wet-chemical etching of a double heterostructure consisting of the following layers grown by OMVPE: 1-μm-thick n AlGaAs, 0.1-μm-thick GaAs, 3-μm-thick p AlGaAs, and 0.2-μm-thick p<sup>+</sup> GaAs. Silicon dioxide was deposited on the wafer, stripes 2 μm wide were opened perpendicular to the [111] direction, and the sample was etched with Br/CH<sub>3</sub>OH. Figure 8 is a scanning electron micrograph showing a facet-deflector pair in cross section. In the (111A) direction, a vertical facet was obtained because the (111A) plane is the slowest etching plane. However, since there is no slow etching plane in the opposite direction, the profile of the opposite wall was determined by etchant diffusion, resulting in a semicircular shape. The facet and deflector surfaces were both very smooth. To obtain light emission normal to the substrate from a semicircular deflector, the active layer should be located about 2/3 of the etch depth below the surface. The divergence of the beam is expected to be slightly larger after the deflector. In order to complete laser fabrication, it would be necessary to form the other facet by a dry etching technique such as reactive-ion or ion-beam-assisted etching.

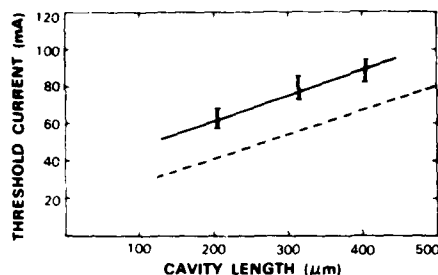


Fig. 7. Threshold current as a function of cavity length for stripe-geometry (110) DH lasers. The dotted line represents data reported by Burnham et al. (1981) for  $\text{Al}_{0.07}\text{Ga}_{0.93}\text{As}/\text{Al}_{0.45}\text{Ga}_{0.55}\text{As}$  DH lasers.

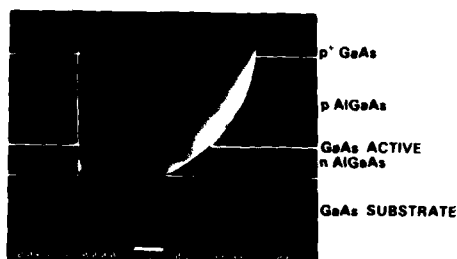


Fig. 8. Scanning electron micrograph showing the cross section of a facet-deflector pair formed by  $\text{Br}/\text{CH}_3\text{OH}$  etching.

## 5. Conclusion

We have fabricated (110) GaAs-AlGaAs DH diode lasers with performance comparable to lasers of similar structure on (100) substrates. Facet-deflector pairs with very smooth surfaces have been obtained by wet-chemical etching. We believe that it should be possible to fabricate monolithic two-dimensional laser arrays with good performance on (110) substrates.

## 6. Acknowledgements

We would like to thank C. O. Bozler and G. W. Turner for helpful discussions, J. W. Chludzinski for photoluminescence measurements, E. L. Mastromattei for crystal orientation, P. M. Nitishin for SEM micrographs, and D. F. Kolesar and P. D. Nader for technical assistance. We are also grateful to A. J. Strauss and B-Y. Tsaur for encouragement and critical reading of the manuscript. This work was sponsored by the Department of the Air Force and the Defense Advanced Research Projects Agency.

## 7. References

- Burnham R D, Scifres D R and Streifer W 1981 *Electron Lett.* **17** 714
- Kuech T F and Veuhoff E 1984 *J. Cryst. Growth* **68** 148
- Nakanisi T 1984 *J. Cryst. Growth* **68** 282
- Petroff P M, Cho A Y, Reinhart F K, Gossard A C and Wiegmann W 1982 *Phys. Rev. Lett.* **48** 170
- Reep D H and Ghani S K 1983 *J. Cryst. Growth* **61** 449
- Walpole J N and Liao Z L 1986 *Appl. Phys. Lett.* **48** 1675
- Wang W I 1983 *J. Vac. Sci. Technol.* **B1** 630
- Wang W I, Kuan T S, Tsang J C, Chang L L and Esaki L 1986 *J. Vac. Sci. Technol.* **B4** 517
- Windhorn T H and Goodhue W D 1986 *Appl. Phys. Lett.* **48** 1675

## Si-induced disordering and its application to fabrication of index-guided AlGaAs MQW lasers

Koji Ishida, Kazunori Matsui, Toshiaki Fukunaga, Takeshi Takamori,  
Junji Kobayashi, Koichi Ishida and Hisao Nakashima

Optoelectronics Joint Research Laboratory  
1333 Kamikodanaka, Nakahara-ku, Kawasaki, 211 Japan

**Abstract** Compositional disordering of Si ion implanted AlGaAs-GaAs superlattices has been studied by secondary ion mass spectrometry for various ion implantation and annealing conditions. It is found that when the Si concentration exceeds  $3 \times 10^{18} \text{ cm}^{-3}$ , Si diffuses rapidly and the disordering of superlattices directly correlates to this rapid diffusion. The results are successfully applied to the fabrication of transverse mode controlled AlGaAs-GaAs multi-quantum well (MQW) lasers with buried MQW optical guide. It is observed that the laser oscillates in a single mode, both spectrally and spatially up to 60 mW. These facts show that the Si induced disordering is very useful for optoelectronic device fabrication.

### 1. Introduction

Compositional disordering of AlGaAs-GaAs superlattices (SL's) is promoted by diffusion of impurities, such as Zn (Laidig et al. 1981), Si (Meehan et al. 1984), S (Rao et al. 1985) etc., Si ion implantation and subsequent annealing (Coleman et al. 1982) and Si doping during growth followed by heat treatment (Kawabe et al. 1984). Because of the potential for application to novel optoelectronic devices (Fukuzawa et al. 1984, Nakashima et al. 1985, Deppe et al. 1985), this phenomenon has been studied by various methods such as Auger-electron-spectroscopy (Kawabe et al. 1984), cross-sectional transmission electron microscope (Ishida et al. 1985), and photoluminescence (Hirayama et al. 1984). Although the results have demonstrated Al-Ga intermixing, it has been very difficult to obtain quantitative relationship between the Al-Ga intermixing and the diffusion of impurities because of the lower sensitivities of the above detecting techniques for the impurities. The knowledge of this relationship is thought to be very important for the application to optoelectronic device fabrication.

We have studied Si-induced disordering of SL's by secondary ion mass spectrometry (SIMS) and clarified the role of the Si diffusion in the disordering (Kobayashi et al. 1986). In this paper, we present detailed SIMS results which show the annealing condition dependence of the disordering induced by Si ion implantation and subsequent annealing. Furthermore, we describe its application to the fabrication of transverse mode controlled multi-quantum well (MQW) lasers with buried MQW optical guide (MQW-BOG).

## 2. Correlation between Si diffusion and Si-induced disordering in AlGaAs-GaAs superlattices

The samples used for SIMS studies were  $\text{Al}_{0.5}\text{Ga}_{0.5}\text{As-GaAs}$  SL's with 30nm-30nm periodicity grown by molecular beam epitaxy (MBE). Si ions were implanted at 80 keV with doses of  $10^{14}$  to  $10^{16} \text{ cm}^{-2}$ . Annealing was carried out at  $850^\circ\text{C}$  for 1 h in three different conditions, i.e. (1) in face to face contact with another GaAs wafer, (2) under  $\text{As}_4$  pressure of about 100 Torr and (3) with an  $\text{SiO}_2$  cap in  $\text{H}_2$  atmosphere.

$^{28}\text{Si}$  and  $^{27}\text{Al}$  depth profiles were taken by SIMS (CAMECA IMS-3F spectrometer).  $\text{Cs}^+$  ions were used as primary ions, and the acceleration energy was 14.5 keV. The signals from  $60 \mu\text{m}^2$  area centered in the raster scanned area of  $500 \times 500 \mu\text{m}^2$  were detected with an ion-optic system. Since the mass number of  $^{28}\text{Si}$  is close to that of  $^{28}\text{AlH}$  and  $^{28}\text{CO}$ , Si ions were detected under the high resolution mode ( $M/\Delta M = 2200$ ). The absolute value of the Si concentration was determined by comparing the integrated area of the obtained Si profile with the implanted doses. Depth scales were established by measuring crater depths with a calibrated surface profilometer and the thickness of each SL layer.

Figure 1 shows Si and Al depth profiles for the as-implanted ( $1 \times 10^{16} \text{ cm}^{-2}$ ) and annealed (under  $\text{As}_4$  pressure) SL. Since no disordering is observed for the Al profile of the as-implanted sample, the knock-on effect during Si ion implantation does not induce the disordering of SL. After annealing, Si diffuses remarkably deeper into SL layer to a definite depth ("diffusion edge") where the Si concentration abruptly decreases. This means that Si diffuses rapidly above

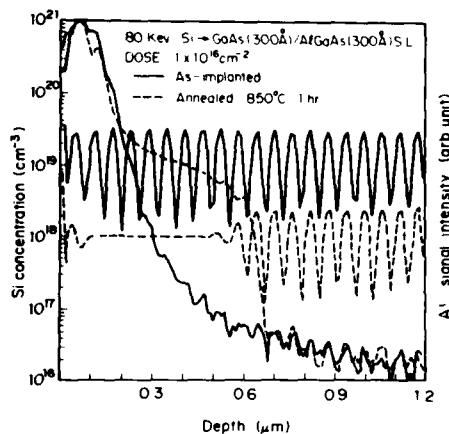


Fig. 1. Si and Al depth profiles for as-implanted and annealed SL.

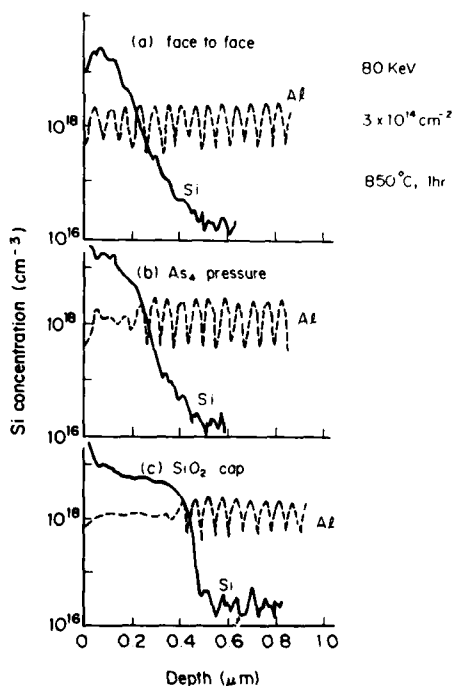


Fig. 2. Si and Al depth profiles of SL annealed in various conditions.



the critical concentration of about  $3 \times 10^{18} \text{ cm}^{-3}$ . The disordered region expands to this diffusion edge.

For a lower dose of  $3 \times 10^{14} \text{ cm}^{-2}$ , the induced disordering depends on the annealing condition, as shown in Fig. 2. The sample annealed in face to face contact with another GaAs wafer does not show the rapid Si diffusion and disordering. Some trace of SL is observed for the sample annealed under  $\text{As}_4$  pressure, showing incomplete disordering. Complete disordering and rapid Si diffusion are clearly observed for the sample annealed with an  $\text{SiO}_2$  cap. Comparing the Si and Al SIMS profile, the distinct correlation and the induced disordering is obtained.

The rapid Si diffusion at high concentration has been explained by the substitutional exchange of  $\text{Si}_{\text{III}}\text{-Si}_{\text{V}}$  pairs with the matrix vacancies (Greiner et al. 1984, Gavrilovic et al. 1985, Kavanagh et al. 1985). The formation of Si pairs was observed for highly Si doped MBE-grown GaAs layers by channeling PIXE measurements (Narusawa et al. 1984). Consequently, the vacancy flow enhanced by the paired Si atom movement is considered to cause the Al-Ga intermixing. Both types of the vacancy (Ga and As vacancy) of sufficient concentration are required for the rapid Si diffusion. The Si pairs cannot diffuse but rotate around  $\text{Si}_{\text{III}}$  at the condition of too much As vacancies, which means too little Ga vacancies. This corresponds to the annealing in face to face contact with another GaAs wafer. Annealing with an  $\text{SiO}_2$  cap causes the out-diffusion of Ga and pile-up of As at the interface which introduce the high concentration of Ga and As vacancies (Gyulai et al. 1970). The introduced Ga and As vacancies are considered to induce the deeper Si diffusion and complete disordering. Consequently, it is confirmed that the disordering of SL's is caused by vacancy flow enhanced by the Si-Si pairs.

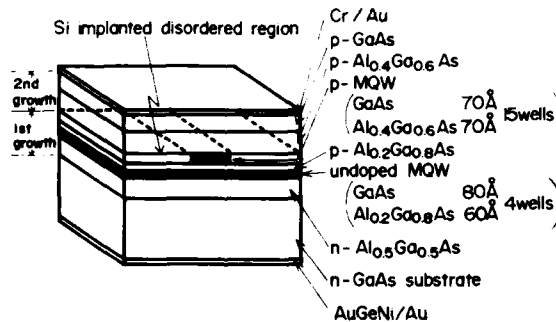


Fig. 3. Schematic illustration of the MQW-BOG laser structure.

### 3. Device Application

Here, we give an example of application of Si induced disordering to the fabrication of MQW lasers with buried MQW optical quid (MQW-BOG). The structure of MQW-BOG lasers is schematically illustrated in Fig. 3.

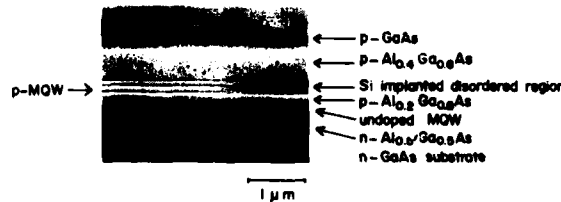


Fig. 4. SEM micrograph of a cleaved facet of an MQW-BOG laser.

A two-stage epitaxial growth was carried out on n-GaAs (100) substrate by MBE at 680 °C. Silicon ions were implanted before 2nd growth. In the first growth, n-GaAs and n-MQW buffer layers, an n-Al<sub>0.5</sub>Ga<sub>0.5</sub>As cladding layer, an undoped MQW active layer and p-Al<sub>0.2</sub>Ga<sub>0.8</sub>As and p-MQW guide layers were grown successively. After the 1st growth, the surface of the sample was coated with a 0.1 µm thick SiO<sub>2</sub> layer by plasma CVD and a 1 µm thick photoresist which was masked and etched to give stripes of 2 to 5 µm wide. Silicon ions were implanted through the SiO<sub>2</sub> layer at 80 keV with a dose of  $3 \times 10^{14}$  cm<sup>-2</sup>. Implantation parameters and thicknesses of the p-MQW optical waveguide layer and p-Al<sub>0.2</sub>Ga<sub>0.8</sub>As layer were designed not to deteriorate the undoped active MQW layer by the Si ion implantation, based on the above mentioned experiments. After implantation, the photoresist was removed by dry etching and the SiO<sub>2</sub> was etched by buffer HF. Cladding and cap layers were grown on the implanted samples after thermal cleaning at 700 °C for 5 min. The wafer was annealed in H<sub>2</sub>/N<sub>2</sub> atmosphere at 850 °C for 60 min in face to face contact with another GaAs wafer. This annealing induced the disordering of the implanted MQW layer outside the stripe to form a buried MQW optical guide. The MQW-BOG structure controls the transverse mode, because the refractive index of AlGaAs MQW structure is larger than that of the averaged AlGaAs alloys (Suzuki and Okamoto 1983). In addition, the pnpn structure formed by Si implantation confines current flow to the stripe region. Contacts of Au-Ge-Ni/Au and Cr/Au were then applied to the n- and p-side, respectively.

These processes are completely planar and do not require any etching procedure for the formation of buried optical guide structure. An endview of the etched cross section of the laser is shown in the scanning electron microscope (SEM) image of Fig. 4.

Typical light output power versus current (L-I) characteristic for MQW-BOG lasers under pulsed operation at room temperature is shown in Fig. 5. The width of the optical guide and cavity length of the lasers are 3.5 µm and 500 µm, respectively. The threshold current is 26 mA. The

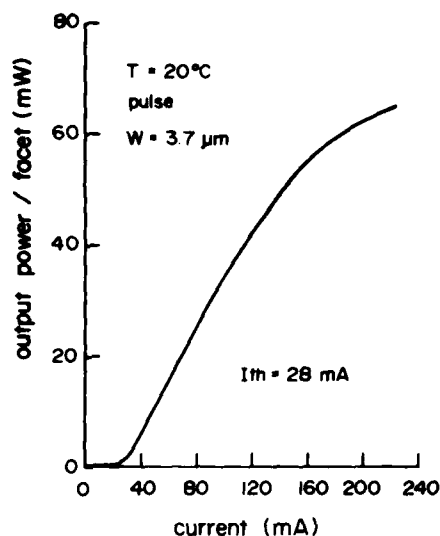


Fig. 5. Light-output power vs current characteristics for an MQW-BOG laser.

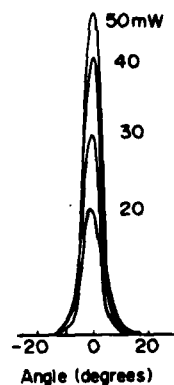


Fig. 6. Far-field patterns of an MQW-BOG laser.

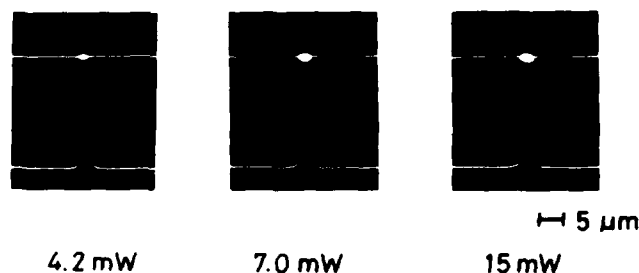


Fig. 7. Near-field patterns of an MQW-BOG laser for optical output at 15 mW.

differential quantum efficiency reaches 70% which is rather high compared with MQW-BOG lasers fabricated by Zn diffusion-induced disordering (Semura et al. 1985). The L-I characteristic is linear up to 40 mW.

The far-field patterns of an MQW-BOG laser are shown in Fig. 6. The beam width (full width at half maximum) parallel and perpendicular to the junction plane are  $10^\circ$  and  $37^\circ$ , respectively. The laser operates stably in a fundamental transverse mode even at about 60 mW. The near-field patterns of an MQW-BOG laser at different output powers are shown in Fig. 7. Even at a high current, the first-order mode has not been observed. These results show that the MQW-BOG laser acts as an index-guided laser.

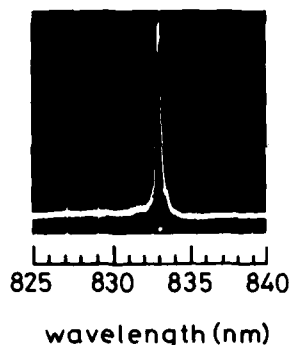


Fig. 8. Lasing spectrum of an MQW-BOG laser under pulsed operation for optical output at 8 mW.

The lasing spectrum for an MQW-BOG laser under pulsed operation (1  $\mu$ s of pulse duty and 30 ns of width) is shown in Fig. 8. Lasing wavelength is around 833 nm. In spite of the pulsed operation, a single longitudinal mode is obtained above the threshold current. This result suggests that the longitudinal mode of the MQW-BOG laser fabricated by Si ion implantation is more stable than conventional index-guided lasers.

#### 4. Conclusion

We have studied the Si-induced disordering of  $\text{Al}_{0.5}\text{Ga}_{0.5}\text{As-GaAs}$  SL's by SIMS. Distinct correlation was found between the induced disordering and the rapid Si diffusion. Annealing condition dependence of the disordering suggests that the Al-Ga intermixing is induced by the vacancy flow enhanced by the  $\text{Si}_{\text{III}}\text{-Si}_{\text{V}}$  pair movement which causes the rapid Si diffusion. These results are successfully applied to the fabrication of AlGaAs MQW lasers with buried MQW optical guide. Fabricated laser has shown a stable fundamental transverse mode at light-output as high as 60 mW. The fundamental transverse and single longitudinal mode operation indicate that the MQW-BOG laser acts as an index-guided laser. These fabrication

processes combined with the focused ion beam technology will be useful in the fabrication of micro-optoelectronic devices.

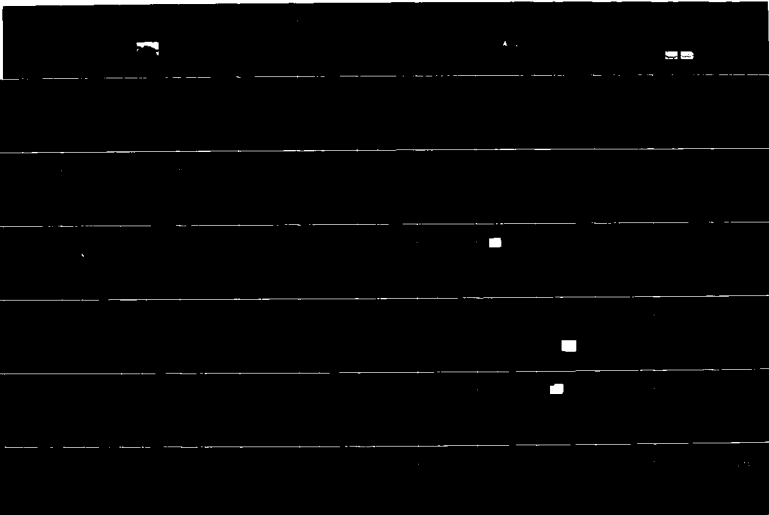
### References

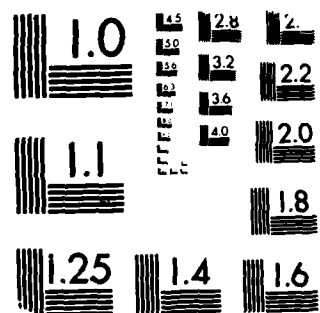
- Coleman J J, Dapkus P D, Kirkpatrick C G, Camras M D and Holonyak N Jr.  
1982 Appl. Phys. Lett. 40 904.
- Deppe D G, Hsieh K C, Holonyak N Jr., Burnham R D, and Thornton R L 1985  
J. Appl. Phys. 58 4815.
- Fukuzawa T, Semura S, Saito H, Ohta T, Uchida Y, and Nakashima H 1984  
Appl. Phys. Lett. 45 1.
- Gavrilovic P, Gavrilovic J, Meehan K, Kaliski R W, Guido L J, Holonyak N  
Jr., Hess K, and Burnham R D 1985 Appl. Phys. Lett. 47 710.
- Greiner M E and Gibbons J F 1984 Appl. Phys. Lett. 44 750.
- Gyulai J, Mayer J W, Mitchell I V and Rodriguez V 1970 Appl. Phys. Lett.  
17 332.
- Hirayama Y, Horikoshi Y, and Okamoto H, Jpn. J. Appl. Phys. 1984 23  
1568.
- Ishida K, Ohta T, Semura S, and Nakashima H 1985 Jpn. J. Appl. Phys. 24  
L620.
- Kavanagh K L, Mayer J W, Magee C W, Sheets J, Tong J, and Woodall J W  
1985 Appl. Phys. Lett. 47 1208.
- Kawabe K, Matsuura N, Shimizu N, Hasegawa F, and Nannichi Y 1984 Jpn.  
J. Appl. Phys. 23 L623.
- Kobayashi J, Nakajima M, Bamba Y, Fukunaga T, Matsui K, Ishida K,  
Nakashima H, and Ishida K 1986 Jpn. J. Appl. Phys. 25 L385.
- Laidig W D, Holonyak N Jr., Camras M D, Hess K, Coleman J J, Dapkus P.P,  
and Bardeen J 1981 Appl. Phys. Lett. 38 776.
- Meehan K, Holonyak N Jr., Brown J M, Nixon M A, Gavrilovic P, and  
Burnham R D 1984 Appl. Phys. Lett. 45 549.
- Nakashima H, Semura S, Ohta T, and Kuroda T 1985 Jpn. J. Appl. Phys.  
24 L647.
- Narusawa T, Uchida Y, Kobayashi K L I, Ohta T, Nakajima M, and Nakashima  
H 1984 Proc. 11th Int. Symp. on GaAs and Related Compounds 127.
- Rao E V K, Thibierge H, Brillouet F, Alexandre F, and Azoulay R 1985  
Appl. Phys. Lett. 46 867.
- Semura S, Ohta T, Kuroda T, and Nakashima H 1985 Jpn. J. Appl. Phys. 24  
L463.

AD-A189 673 GALLIUM ARSENIDE AND RELATED COMPOUNDS 1986(U) ILLINOIS 5/7  
UNIV CHAMPAIGN W I LINDLEY 1986 AFOSR-IR-87-1800  
AFOSR-86-0169

UNCLASSIFIED

F/G 20/2 NL





MICROCOPY RESOLUTION TEST CHART  
NATIONAL BUREAU OF STANDARDS-1963-A

## **GaAs/AlGaAs waveguide with grating coupler fabricated by selective superlattice intermixing**

J.D. Ralston, L.H. Camnitz\*, G.W. Wicks, and L.F. Eastman

School of Electrical Engineering and National Research  
and Resource Facility for Submicron Structures,  
Cornell University, Phillips Hall, Ithaca, NY 14853 USA

\* Present address: HP Laboratory, Palo Alto, CA 94304

**Abstract.** Grating couplers have been fabricated in a GaAs/Al<sub>0.32</sub>Ga<sub>0.68</sub>As superlattice slab waveguide. The grating "teeth" are impressed into the superlattice by selective Se implantation-induced intermixing of the GaAs and Al<sub>0.32</sub>Ga<sub>0.68</sub>As layers, yielding a planar, rather than corrugated, surface. Intermixing of the implanted and annealed superlattice layers is characterized by TEM and Raman spectroscopy. Grating coupling is demonstrated using a HeNe laser operating at  $\lambda = 1.15 \mu\text{m}$ .

### **1. Introduction**

Localized intermixing of semiconductor superlattices via ion implantation and diffusion of both donor and acceptor impurities [Laidig et al. 1981; Coleman et al. 1982; Camras et al. 1983; Meehan et al. 1984a], as well as by impurity-free vacancy diffusion during high temperature annealing in the presence of an SiO<sub>2</sub> capping layer [Deppe et al. 1986], has recently found application in the design of a variety of novel laser structures [Deppe et al. 1986; Meehan et al. 1984b; Fukuzawa et al. 1984; Gavrilovic et al. 1985a; Deppe et al. 1985; Gavrilovic et al. 1985b; Thornton et al. 1986; Laidig et al. 1984; Ogura et al. 1984]. In the present work, laterally selective intermixing of GaAs/Al<sub>x</sub>Ga<sub>1-x</sub>As superlattices is demonstrated on a submicron scale via masked ion implantation, and the technique is utilized to fabricate a planar grating coupler [Dakss et al. 1970] in a GaAs/Al<sub>x</sub>Ga<sub>1-x</sub>As optical waveguide structure. Grating couplers have previously been fabricated in GaAs/Al<sub>x</sub>Ga<sub>1-x</sub>As waveguide structures by physically corrugating the surface via ion milling or chemical etching [Somekh and Casey 1977].

### **2. Grating Fabrication**

The asymmetric 3-layer slab waveguide structure used in these experiments consists of an 8000 Å superlattice core region (40 periods of 100 Å GaAs layers alternating with 100 Å

$\text{Al}_{0.32}\text{Ga}_{0.68}\text{As}$  layers) grown on top of a 1.0 micron  $\text{Al}_{0.32}\text{Ga}_{0.68}\text{As}$  cladding layer by molecular beam epitaxy. A 1700 Å layer of CVD deposited  $\text{SiO}_2$ , along with a 4000 Å layer of PMMA resist serve as the implantation mask. Using electron beam lithography, a 3500 Å period grating pattern was generated in the PMMA and then transferred into the  $\text{SiO}_2$  via reactive ion etching in a  $\text{CHF}_3$  plasma. The waveguide sample was then implanted through the mask with Se ions at an energy of 100 keV and a dose of  $7 \times 10^{14} \text{ cm}^{-2}$ . Following removal of the mask, the sample was annealed at  $720^\circ\text{C}$  for 2 hrs. in a capless annealing system. The resulting selective intermixing of the GaAs and  $\text{Al}_{0.32}\text{Ga}_{0.68}\text{As}$  layers gives rise to a planar, rather than corrugated, grating with "teeth" consisting of an  $\text{Al}_{0.16}\text{Ga}_{0.84}\text{As}$  alloy whose refractive index is slightly less than that of the as-grown superlattice [Leburton et al. 1983]. Figure 1 shows a Transmission Electron Microscope (TEM) cross-sectional image of the resulting profile - the grating depth is roughly 500-600 Å, which corresponds well to the 400 Å projected range of 100 keV Se ions in GaAs [Gibbons et al. 1975]. Although the intermixing profile appears to be somewhat irregular, the grating period is exceedingly uniform, and strong diffraction in the visible wavelength region can be observed with the naked eye. Corrugated grating samples were also fabricated for comparison by ion-milling to a depth of approximately 800 Å into the superlattice through the PMMA/ $\text{SiO}_2$  mask.

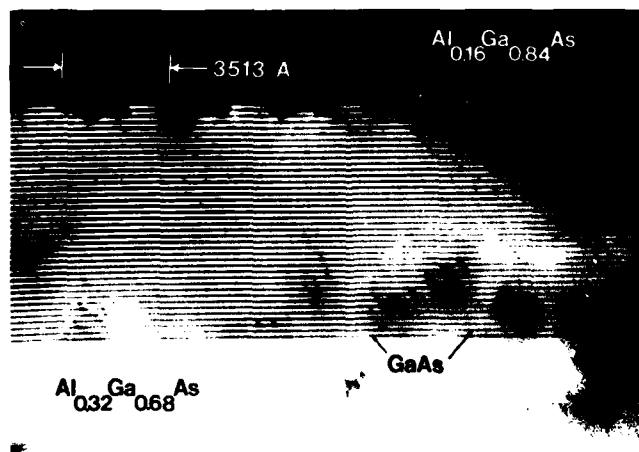


Figure 1. Cross-sectional dark-field TEM image of the selectively Se implanted superlattice-core waveguide sample after  $720^\circ\text{C}$  2 hr. anneal.



### 3. Raman Scattering

In order to confirm the presence of both as-grown superlattice and intermixed alloy in the grating region, room temperature Raman scattering experiments were performed on as-grown, uniformly implanted and annealed, and selectively implanted and annealed samples using the 5145 Å line of an Ar<sup>+</sup> laser. The frequency of the lattice vibrational modes can be used to determine the composition  $x$  of  $\text{Al}_x\text{Ga}_{1-x}\text{As}$  alloy samples [Ilegems and Pearson 1970]. In addition, Raman scattering yields the vibrational spectra of individual layers in a superlattice [Merz et al. 1970]. Results are shown in Figure 2. The spectrum of the as-grown sample (Fig. 2(a)) clearly shows LO phonon peaks from both the pure GaAs layers (292  $\text{cm}^{-1}$ ) and the  $\text{Al}_{0.32}\text{Ga}_{0.68}\text{As}$  layers (279  $\text{cm}^{-1}$ ). Following uniform Se implantation (no mask) and annealing at 720°C for 2 hours, the Raman spectrum (Fig. 2(b)) shows only a single LO phonon peak whose frequency corresponds to an  $\text{Al}_{0.16}\text{Ga}_{0.84}\text{As}$  alloy (287  $\text{cm}^{-1}$ ), indicating extensive intermixing of the original superlattice layers. The Raman spectrum of the selectively implanted sample (Fig. 2(c)) closely resembles a superposition of the above 2 spectra, indicating the presence of both intermixed and unmixed regions within the epitaxial layers, in agreement with the TEM image of Fig. 1. In the backscattering geometry used in the above experiments, with both incident and scattered light being normal to the <001> crystal surface, symmetry selection rules [Hayes and Loudon 1978] forbid optical coupling to the TO modes of a perfect

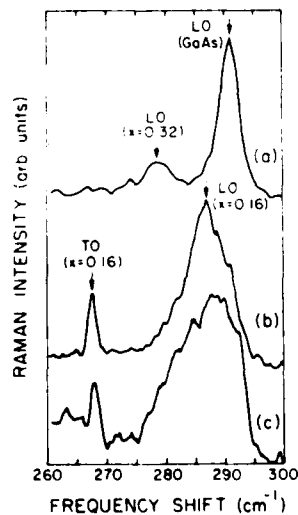


Figure 2. Room temperature Raman spectra of (a) as grown superlattice-core waveguide sample; (b) uniformly Se implanted sample following 720°C 2 hr anneal; (c) selectively Se implanted sample following 720°C 2 hr anneal ( $\lambda_0 = 5145$  Å).

zincblende crystal. The symmetry-forbidden TO peak observed at  $268\text{ cm}^{-1}$  in Figs. 2(b) and 2(c) is evidence of residual post-anneal damage in both of the implanted samples, which agrees with previous studies of Se implanted and annealed superlattices [Ralston et al. 1986].

#### 4. Coupling Measurements

Grating coupling to the waveguide modes has been evaluated using a HeNe laser operating at a wavelength of 1.15 microns. At this wavelength, waveguide dispersion calculations predict that the structure will support fundamental and first order modes with both TE and TM polarizations. The coupling characteristics of both planar and corrugated samples were studied by monitoring the guided mode output intensity from a cleaved facet as a function of the incident laser beam angle with respect to the sample normal [Dakss et al. 1970]. Results are shown in Fig. 3. The incident beam polarization has been oriented  $30^\circ$  out of the reflection plane, as shown in the inset of Fig. 3, in order to excite both TE and TM modes. The mode assignment agrees with 3-layer (AlGaAs cladding, superlattice, air) waveguide dispersion calculations. Mode polarizations have been confirmed by placing a polarization analyzer between the output facet and the detector. The discrepancy between coupling angles for the two different grating structures may be related to the different loading of the waveguide by the gratings. Grating efficiencies will be the subject of further study.

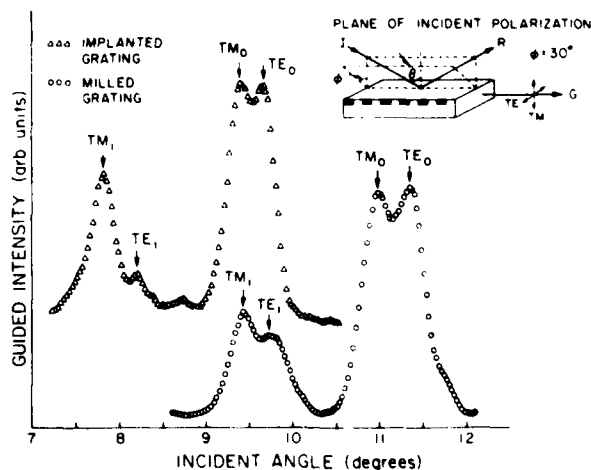


Figure 3. Coupling characteristics of planar (intermixed) and corrugated (ion-milled) grating samples. The scattering geometry is illustrated in the inset: I = incident beam, R = reflected beam, G = guided mode output from cleaved facet,  $\theta$  = incident angle,  $\phi$  = angle between incident polarization and reflection plane.

## 5. Summary

Laterally selective intermixing of GaAs/Al<sub>0.32</sub>Ga<sub>0.68</sub>As superlattices on a submicron scale has been demonstrated via masked Se implantation and annealing. Raman spectroscopy and TEM have been used to characterize the intermixing profiles. As an application of the process, a planar grating coupler has been fabricated in a GaAs/AlGaAs optical waveguide and tested successfully at  $\lambda = 1.15 \mu\text{m}$ .

## Acknowledgements

The authors wish to thank Mr. Mike Skvarla of the National Research and Resource Facility for Submicron Structures for maintenance of and assistance with the ion implanter, J. Wendt and B. de Cooman of Cornell for their ion milling and TEM expertise, respectively, A. Moretti of Amoco Corporation for access to Raman apparatus, and J.R. Shealy of General Electric for additional waveguide measurements. This research was supported by the Joint Services Electronics Program and the Amoco Corporation.

## References

- Camras M D, Coleman J J, Holonyak N Jr., Hess K, Dapkus, P D and Kirkpatrick C G Proc. 10th Internat. Symp. on GaAs and Related Compounds, Albuquerque, 1982, edited by G.E. Stillman (Inst. Phys. Conf. Ser. No. 65, London, 1983), p. 233.
- Coleman J J, Dapkus P D, Kirkpatrick C G, Camras M D, and Holonyak N Jr. 1982 Appl. Phys. Lett. **40** 905.
- Dakss M L, Kuhn L, Heidrich P F, and Scott B A 1970 Appl. Phys. Lett. **16** 523.
- Deppe D G, Hsieh K C, Holonyak N Jr., Burnham R D, and Thornton R L 1985 J. Appl. Phys. **58** 4515.
- Deppe D G, Guido L J, Holonyak N Jr., Hsieh K C, Burnham R D, Thornton R L, and Paoli T L 1986 Appl. Phys. Lett. **49** 510.
- Fukuzawa T, Semura S, Saito H, Ohta T, Uchida Y, and Nakashima H 1984 Appl. Phys. Lett. **45** 1.
- Gavrilovic P, Meehan K, Guido L J, Holonyak N Jr., Eu V, Feng M, and Burnham R D 1985a Appl. Phys. Lett. **47** 903.
- Gavrilovic P, Meehan K, Epler J E, Holonyak N Jr., Burnham R D, Thornton R L, and Streifer W 1985b Appl. Phys. Lett. **46** 857.
- Gibbons J F, Johnson W S, and Mylroie S W 1975 Projected Range Statistics (Stroudsburg, PA: Dowden, Hutchinson, and Ross).
- Hayes W and Loudon R 1978 Scattering of Light by Crystals (New York: Wiley).
- Ilegems M and Pearson GL 1970 Phys. Rev. **B1** 1576.
- Laidig W D, Holonyak N Jr., Camras M D, Hess K, Coleman J J, Dapkus P D and Bardeen J 1981 Appl. Phys. Lett. **38** 776.
- Laidig W D, Lee J W and Caldwell P J 1984 Appl. Phys. Lett. **45** 485.
- Leburton J P, Hess K, Holonyak N Jr., Coleman J J and Camras M 1983 J. Appl. Phys. **54** 4230.

- Meehan K, Holonyak N Jr., Brown J M, Nixon M A, Gavrilovic P and Burnham R D 1984a Appl. Phys. Lett. 45 549.
- Meehan K, Brown J M, Holonyak N Jr., Burnham R D, Paoli T L and Streifer W 1984b Appl. Phys. Lett. 44 700.
- Merz J L, Barker A S Jr., and Gossard A C 1977 Appl. Phys. Lett. 31 117.
- Ogura M, Hata T, and Yao T 1984 Jap. J. Appl. Phys. 23 L512.
- Ralston J D, Wicks G W, Eastman L F, de Cooman B C, and Carter C B 1978 Mat. Res. Soc. Symp. Proc. Vol. 56 ed. J M Gibson, G C Osbourne, and R M Tromp p. 327.
- Somekh S and Casey H C Jr. 1977 Appl. Optics 16 126 and references therein.
- Thornton R L, Burnham R D, Paoli T L, Holonyak N Jr. and Deppe D G 1986 Appl. Phys. Lett. 48 7.

## **Device structures for high power 0.83 $\mu\text{m}$ superluminescent diodes**

J. Niesen, C. Morrison, and L. Zinkiewicz

TRW Electro Optics Research Center, El Segundo, CA 90245

**Abstract** Three modifications of the twin channel laser structure have been fabricated and characterized for continuous wave power and spectral limitations in superluminescent diode (SLD) behavior. The conventional antireflective coating technique produced lasing - limited power less than 10mW. Fabry-Perot spectral modulation was typically greater than 50 percent at 7mW. The angle stripe approach yielded thermal - rollover limited powers of 30mW. Spectral halfwidth of 160 Å and 5% Fabry-Perot modulation were typical.

### **1. Introduction**

Conventionally, SLDs are fabricated by coating the front facet of a laser diode chip with a quarter wave thickness of material whose refractive index equals the square root of gallium arsenide's refractive index (N. Dutta et al, 1983). The diode output power useful for gyro applications is typically limited by Fabry-Perot modulation to 5mW.

Two different approaches to SLD fabrication are described that discriminate more strongly against lasing. Each technique used the twin channel laser (TCL) structure (C. Morrison et al, 1985) has produced at least 15mW cw output with 1 and 30 percent Fabry-Perot modulation for the methods of angled stripe and truncated stripe, respectively.

### **2. Antireflective Facet Coating**

Theoretical limits for facet reflectivity resulting of a quarter wave thickness of dielectric are model dependent, ranging from  $10^{-4}$  (R. Clarke et al, 1983) to  $10^{-5}$  (Kaplan et al, 1985). Detailed model results show a non-zero, quarter wave reflectivity due to the spread of angles that make up the waveguide mode. The best single layer antireflective coating reported to date has a reflectivity of  $10^{-4}$  (Paoli et al, 1985).

Cleaved bars and soldered chips were coated with silicon monoxide or titanium zirconium dioxide. For some coating runs an in situ optical monitor was used to determine when a quarter wave thickness had been obtained. For other coating runs on soldered chips, the increase in the pulsed laser threshold, monitored during deposition, was used to determine

the quarter wave thickness. The threshold and optical monitoring technique produced similar device reflectivities as evidenced by the coating-induced change in pulsed laser threshold (Table 1). Contrary to theory, (Kaplan et al, 1984) we did not find that optimal thicknesses were higher for pulsed threshold monitoring (minimal modal reflectivity) than for optical monitoring (minimal plane wave reflectivity).

Table 1. Antireflective Coating Results

| SLD Process Level | Material           | Refractive Index at .63 $\mu\text{m}$ | Monitor   | Change in Laser Threshold |
|-------------------|--------------------|---------------------------------------|-----------|---------------------------|
| Soldered chip     | TiZrO <sub>2</sub> | 1.9                                   | Optical   | 2                         |
| Soldered chip     | TiZrO <sub>2</sub> | 1.9                                   | Threshold | 2                         |
| Cleaved bar       | SiO                | 1.86                                  | Optical   | 2.5                       |

Silicon monoxide was superior to TiZrO<sub>2</sub> but CW lasing still occurred. The larger changes in pulsed thresholds (three times uncoated) achieved by Xerox (Paoli et al, 1985) are attributed to their material (ZrO<sub>2</sub>) better matching the desired film refractive index. Characteristic spectral behavior for antireflective coated laser chips is that the Fabry - Perot modulation increase and the spectral half-width decrease as the power is increased (Figure 1).

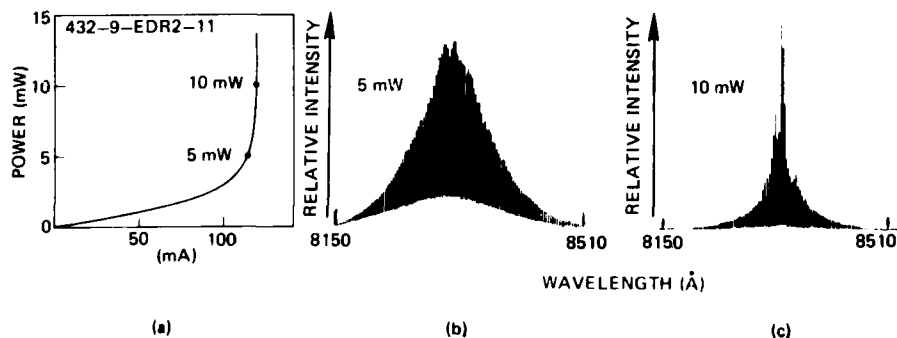


Figure 1. Power-Spectra characteristics for a laser chip with TiZrO<sub>2</sub> on its front facet. a. Power-current relationship, b. 5 mW spectra, c. 10 mW spectra.

To suppress lasing at higher optical powers, a quarter-wave thickness of silicon monoxide was simultaneously applied to the facet and to a small length of the conducting stripe. Die shear testing exposed the SLD chip for wetting length correlation with power-spectra. For too much non-wetting, unpumped absorption is too severe and SLD power reduced. For too little non-wetting, the device performs as a laser. Spectra at 13mW for conditions of proper truncation and insufficient truncation are shown in Figures 2a and 2b, respectively. At 18mW, the truncated stripe SLD spectral width decreases with normally 50% Fabry-Perot modulation.

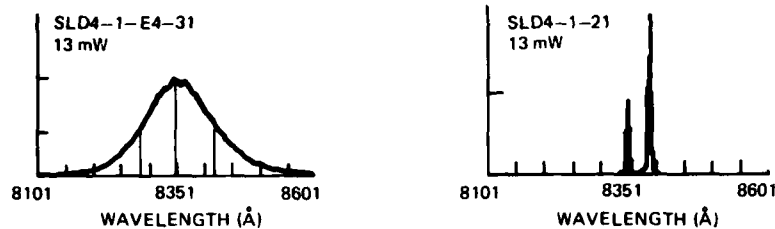


Figure 2. Wetting length influence on spectra, a. Spectra for SLD with proper truncation, b. Spectra for SLD with improper truncation.

### 3. Angled Stripe SLD

Angle stripe SLDs are fabricated by photolithographically misaligning the stripe waveguide of the twin channel laser with respect to the SLD chip's cleavage plane. Single pass amplified spontaneous emission upon Fresnel reflection from the cleave will not be captured by the transverse waveguide. To prevent cleave reflected light from coupling back into the gain stripe, the misalignment angle ( $\theta$ ) must be greater than half the critical angle of the transverse waveguide. The SLD output refracts at angle of arcsin ( $\sin \theta / 3.6$ ) with respect to the cleave. The angular relationships of angle stripe SLD behavior are summarized in Figure 3.

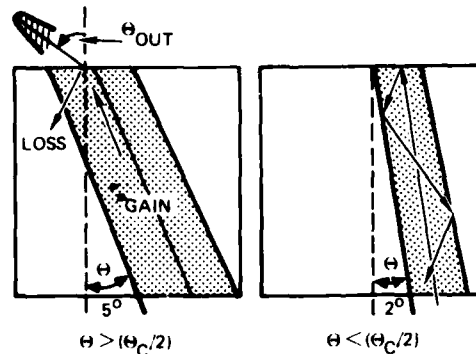


Figure 3. Conditions of angle stripe SLD operation

The parallel far field for a device with 5° stripe misalignment with respect to the cleave's normal (0° reference) had a maximum beam intensity at 18° (Figure 4). Devices from this particular wafer had a curved active layer which reduced the spot size parallel to the epilayers yielding a far-field full width at half maximum of 12°. Flat active layer angle stripe SLDs were typically 9° wide in the parallel far field. For the angle stripe SLD, power nonlinearly increases as a function of drive current to 1 to 5mW with linear operation above this power (Figure 5). The analytical relationship between power  $P$  and current  $I$  is:

$$P(I) = \frac{\beta R_{sp}}{G(I)} (e^{\Gamma G(I)L} - 1) \quad \text{where the gain} \quad G(I) = \frac{A(I-b)}{(1 + \frac{P}{P_{sat}})}$$

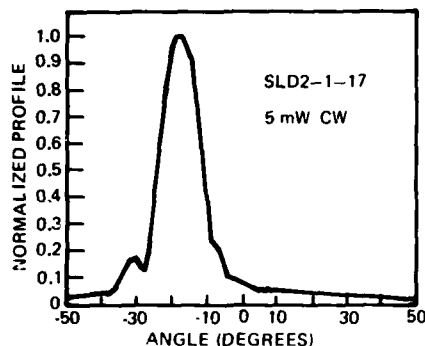


Figure 4. 5° angle stripe SLD parallel far-field

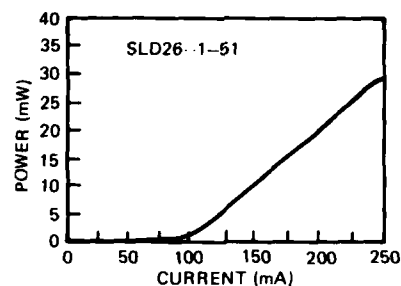


Figure 5. Power as a function of current for an angle stripe SLD.

$R_{sp}$  is the total spontaneous emission rate per unit volume,  $\Gamma$  is the fraction of light intensity overlap with the active layer,  $P_{sat}$  is the gain saturation intensity, and  $\beta$  is the fraction of that spontaneous emission captured by the waveguide.

In the expression for gain dependence on current,  $A$  is typically 0.045 cm/Amp and  $b$  is typically 4kAmp/cm<sup>2</sup> at room temperature.  $A$  varies with temperature as  $1/T$  and  $b$  changes as  $\sqrt{T}$  (Thompson, 1980). The experimentally strong temperature dependence of angle stripe SLD power-current slope is due to the small value of  $A$ , to heterobarrier current leakage, and to the need for improved heat sinking. All reported devices were soldered epitaxial side down to silicon submounts with AuSn solder. The 10mW power level  $T_0$  for SLDs is normally 60°K.

To prove the independence of the angle stripe's power output upon back facet reflectivity, we deposited a high reflectance coating (two stacks of aluminum oxide and silicon) on the back facet of a cleaved bar angle stripe SLDs. There was no post deposition change in the SLD power or spectral performance.

Comparing the TCL and Xerox's angle stripe device (Scrifres, 1973), the distinguishing device property is the absence of lasing for a properly grown TCL angle stripe SLD. The Xerox structure does not suppress between cleave lasing. This results in a lasing beam at 0° to the cleave's normal in addition to the expected refracted SLD beam. The two effects compete for the same drive current reducing the SLD efficiency. Lasing is suppressed by structurally forcing substrate absorption for the between-cleave waveguide mode.

Characteristically, the spectral halfwidth narrows and peak wavelength decreases with increased drive current (Figure 6a). Spectral data concerning peak wavelength and halfwidth was recorded and analyzed by an Ando spectrum analyzer (Figure 6b). Heating shifts the peak to longer wavelengths as the current squared while the current-induced (band filling) peak shift changes linearly to shorter wavelengths. Heating narrows and current broadens the gain spectra. The power spectra narrows for mostly due to the increased amplification by gain center wavelengths



(Thompson, 1980). Higher resolution spectra (Figure 6c) shows a detection-limited 3% Fabry-Perot modulation at 10mW.

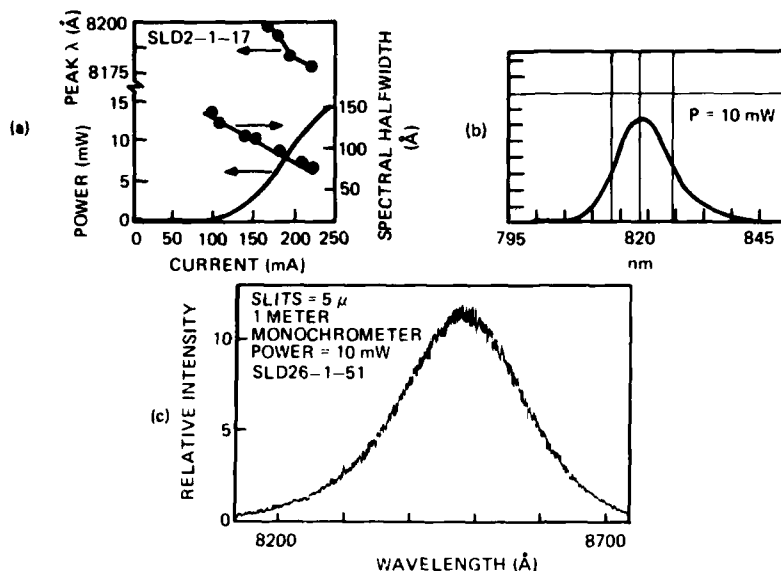


Figure 6. Angle stripe SLD spectral characteristics, a. Peak and halfwidth dependence on drive current, b. Typical low resolution Ando spectra, c. High resolution spectra.

The spectra were measured by a one meter monochromator with cooled S1 photomultiplier. Data was taken at 5  $\mu$ m (0.2 Å resolution) slit width.

Collimating the SLD with a 0.2 NA microscope objective and passing it through a Glan-Thompson prism polarizer, the polarization parallel to the epilayers was three times greater than that perpendicular to the epilayers. This ratio was the same for four different angle stripe SLDS. Crystal growth runs of angle stripe SLDS with curved (Figure 7a) and flat (Figure 7b) active layers were compared for power performance. The power distribution from evaluation sample diodes of both lots are shown in (Figure 7c).



Figure 7. a. SEM microphotograph of curved active layer angle stripe, b. SEM microphotograph of flat active layer angle stripe.

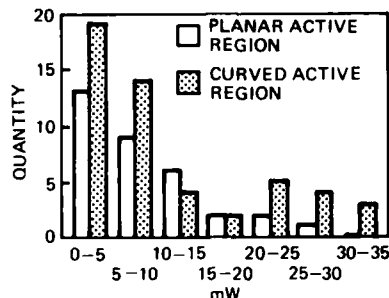


Figure 7c. Power distribution for curved and flat active layer wafers.

The yield was higher for the curved active layer wafer. Average slope efficiency was .25mW/mA for the curved active layer devices and .15mW/mA for the flat active layer devices.

#### 4. Conclusion

Tight fabrication tolerances on matching the chip modal index to the coating's desired refractive index results in a low yield process for the technique of antireflectively coating a laser chip to make an SLD. By angling the gain stripe at 5° to the cleaved facet normal, modal facet reflectivities of 0.1% were achieved. The angle stripe TCL has suppressed lasing, in all devices to date, up to thermal rollover powers as high as 30mW. The spectral halfwidth, typically 150 Å, narrowed with increased power.

#### REFERENCES

- Clarke R.H., 1983, *Int. J. Electron.* **53**, 495.  
 Dutta N.K. and Deimel P.P., 1983, *IEEE J. Quantum Electronics* **QE - 19**, 496.  
 Kaplan D.R. and Deimel P.P., 1984, *AT&T Bell Lab Tech. J.* **63**, 857.  
 Lee T., 1973, *IEEE J. Quantum Electronics* **QE - 9**, 820.  
 Morrison C., Zinkiewicz L.M., Burghard A., and Figueroa L., 1985, *Electron Lett.* **21**, 337.  
 Paoli T.L., Thornton R.L., Burnham R.D. and Smith D.L., 1985, *Appl. Phys. Lett.* **47**, 450.  
 Scifres D.R., Streifer W. and Burnham R.D., 1978, *IEEE J. of Quantum Electronics* **QE-14**, 223.  
 Thompson G.H.B., 1980, *Physics of Semiconductor Laser Devices*, J. Wiley, New York, pp. 82-84 and pp. 121-124.

## Reliable high power 1.3 micron DCPBH laser diodes

E.A. Rezek, D. Tran, and L. Yow

TRW-Electro Optics Research Center, El Segundo, CA 90245

**Abstract** 1.3 micron wavelength laser diodes have been fabricated which operate at 90 mW CW junction-side-up. 110 mW CW has been achieved at 8°C. Accelerated aging tests have been performed on unscreened diodes at 50°C at 5 and 10 mW CW. 20 mW CW testing has been performed at room temperature. No significant degradation is observed during the 2000 hr test period.

### 1. Introduction

The double channel planar buried heterostructure (DCPBH) laser diode (Mito 1982) is one of the most efficient laser structures operating at 1.3 microns. The narrow mesa active layer and p-n-p-n InP blocking layers combine to provide high quantum efficiency. With special modifications the DCPBH structure is also capable of high power operation. Several modifications have been implemented and are described below. Fig. 1 shows the output power attained as a function of development time. Up to 200 mW has been demonstrated (100 mW/facet) at 1.3 microns. A diode reliability program has been carried out in parallel with the demonstration of high power. Accelerated aging has been performed at constant output power to assess device MTTF. No significant degradation has been observed after  $10^4$  device -hours at 20mW CW.

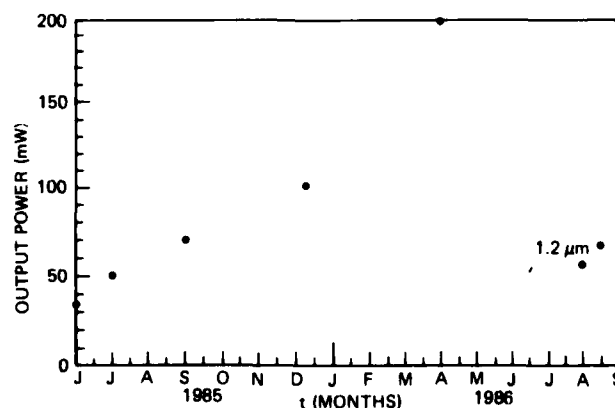


Figure 1. DCPBH diode power versus time

## 2. Background

The DCPBH device structure is the baseline diode for high power and high reliability demonstration. The emitting area of the diode is defined by chemically etching a narrow mesa active region. Current confinement is provided by p-n-p-n blocking layers grown around the mesa. The mean threshold current for 53 devices fabricated from a typical wafer is 24.04 mA with a 3.3 mA standard deviation. Threshold currents as low as 10 mA have been measured, and quantum efficiencies as high as 35%/facet have been demonstrated. The DCPBH structure was initially optimized for low threshold and high quantum efficiency. Standard devices were tested for maximum output power and up to 33 mW CW was achieved. On the basis of these results, special consideration was given to improving the output power of the DCPBH laser diode geometry. The results are described below.

## 3. High Power 1.3 Micron Laser Diodes

The refractive index difference between the InGaAsP active layer and air provides a natural laser diode facet reflectivity of 32%, meaning that only a portion of the stimulated emission actually exits the diode cavity. Application of an anti-reflection (AR) coating to the output facet reduces the amount of power reflected back into the cavity and increases the power emitted from that facet. A high reflectivity coating deposited on the back facet of the diode forces all the light out of the AR coated facet, again increasing the power emitted from that facet.

Electron beam evaporation was used to deposit an AR coating of  $\text{Al}_2\text{O}_3$  on the output facet. The refractive index was controlled to yield a facet reflectivity of roughly 5%. A dielectric mirror was developed for the high reflectivity coating. A 4-layer composite film of alternating layers of  $\text{Al}_2\text{O}_3$  and amorphous Si (a-Si) was used to increase the back facet reflectivity to over 95%. Fig. 2 demonstrates the output power improvement due to the application of facet coatings to the DCPBH structure. A maximum CW output power of 55 mW is measured from a device mounted junction-up on a Si heat sink. An uncoated diode from the same wafer saturates at 33 mW CW. Since the comparison of Fig. 2 is between champion diodes from the same wafer, the 67% increase in output power is due entirely to the facet coating.

Increasing the diode cavity length is also effective in increasing the output power. A longer cavity exploits the high internal gain of the device and directly reduces the operating current density. Fig. 3 demonstrates the effect of a longer diode cavity on output power. As the length is increased from 250 to 500 microns, the maximum CW power is increased from 33 to 44 mW. The diodes of Fig. 3 are uncoated and are mounted

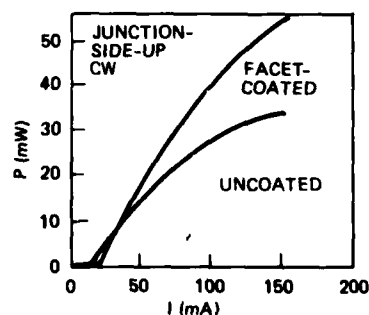


Fig. 2 Effect of facet coating on CW output power.

junction-up on Si. Diodes from the same wafer are compared so that the only experimental variable is cavity length. Note that as expected the efficiency is lower for the longer diode; the 250  $\mu\text{m}$  long device has an efficiency of 0.33 mW/mA while the 500  $\mu\text{m}$  long device efficiency is 0.22 mW/mA. Also, as the cavity length is doubled, the threshold current is increased by 70% from 13 to 22 mA.

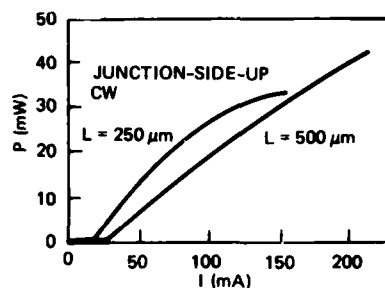


Fig. 3. Effect of cavity length on CW output power.

Fig. 4 shows the P-I versus temperature characteristics of a 500 micron long facet coated device. At room temperature 70 mW CW is measured; at 0°C, the output power is increased to over 100 mW. Additional external modifications to the DCPBH diode resulted in minimal increases in output power. To increase output power beyond the data of Fig. 4, internal modifications to the DCPBH structure were required. A parametric study was carried out to improve the doping profile of the diode structure. Five distinct doping modifications were implemented and correlated with maximum output power. Furthermore, changes were made in device processing to determine the effect of variations in channel width and channel depth on output power. As a result, an improved DCPBH geometry was identified. Fig. 5 shows the improvement in output power resulting from internal diode modifications. At room temperature over 90 mW CW is measured from a 500 micron long facet coated diode mounted junction-up on Si.

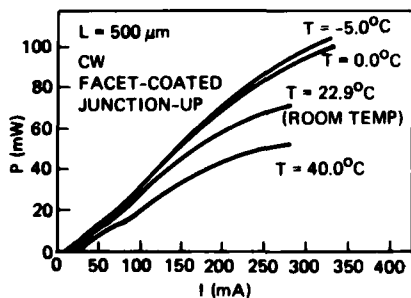


Fig. 4. P-I vs T characteristics 500 micron long facet coated diode.

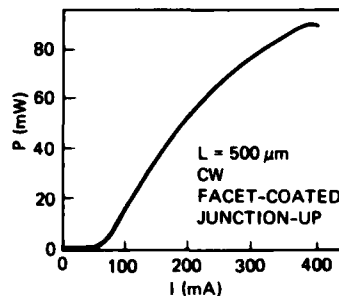


Fig. 5. Output power of improved DCPBH diode.

Higher power is achieved using 50% duty cycle excitation, due to the reduced diode heating. At 50% duty cycle, over 90 mW is measured from a 500 micron long device without facet coatings as shown in Fig. 6. This corresponds to 90 mW/facet. At 16°C, the diode of Fig. 6 is capable of over 100 mW/facet of output power. The diode is also mounted junction-side up on Si. Proper application of facet coatings would result in 200 mW of usable power. The maximum CW power obtained from a DCPBH diode is shown in Fig. 7.

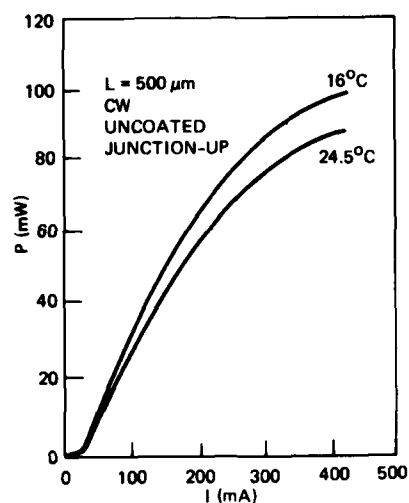


Fig. 6. 50% duty cycle operation uncoated diode.

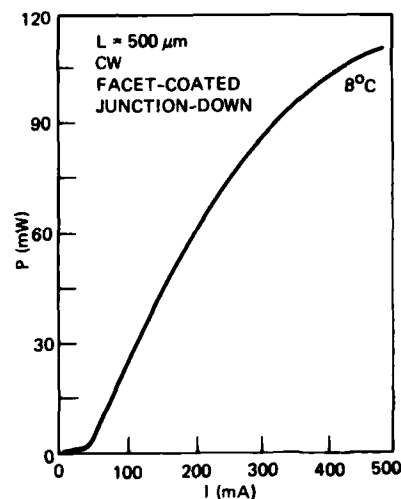


Fig. 7. Maximum CW DCPBH output power.

Over 110 mW has been demonstrated from a 500 micron long facet coated diode mounted junction-down on a synthetic diamond heat sink. The diode was cooled to 8°C. Over 120 mW was obtained at 50% duty cycle. Further junction-down mounting development is underway and is expected to result in significantly higher output power. Diodes mounted junction-up on Si operate CW to 95°C. Junction-down mounting increases the maximum CW temperature to 115°C. Junction-up mounting results in a more reliable diode (Fujita 1985), but highest output power will be obtained from a device mounted junction-down.

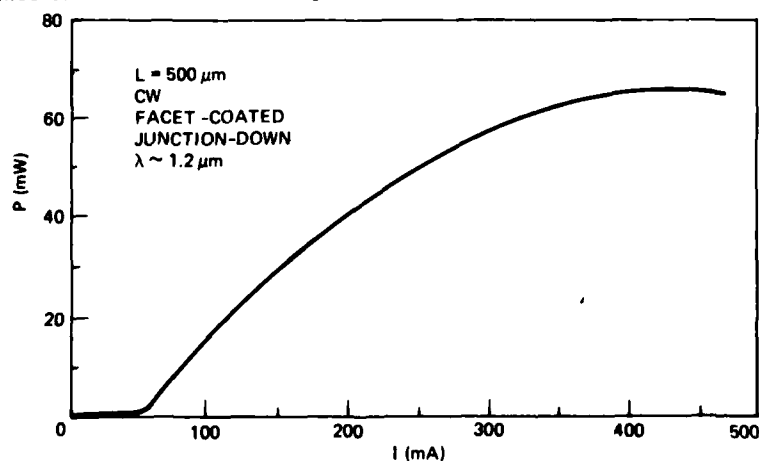


Fig. 8. Maximum CW power at 1.2 micron wavelength

Many systems applications for high power InGaAsP laser diodes require bi-directional data transfer. This is easily accomplished if the laser diodes operate at two distinct wavelengths. For these applications, DCPBH laser diodes operating at a wavelength of 1.2 microns have been developed and optimized for high power operation. Fig. 8 shows the maximum power demonstrated at 1.2 microns. Over 65 mW CW is measured from a 500 micron long facet coated diode mounted junction-down on Si. Without facet coating a 500 micron long device mounted junction-up on Si saturates at 37 mW CW.

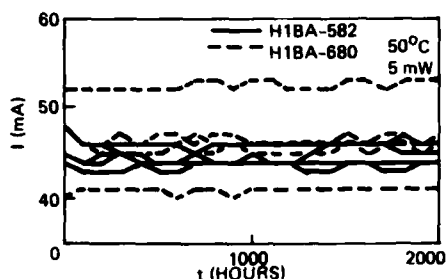


Fig. 9. 50°C 5mW lifetest data un-screened diodes.

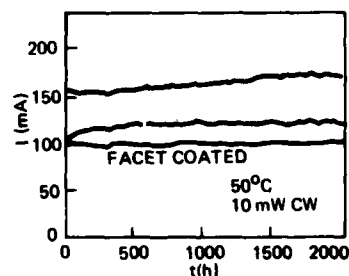


Fig. 10. 50°C 10mW lifetest data for un-screened diodes.

#### 4. Reliability

The evaluation of diode lifetime is simplified by the fact that the degradation of the device can be thermally accelerated. Using a known activation energy, the room temperature meantime to failure (MTTF) can be extrapolated. DCPBH reliability was assessed by operating the units at constant power. Fig. 9 shows data for 2000 hr of operation of 10 diodes at 50°C and 5 mW. Diodes were selected from two different wafers. The tested units were not pre-screened or burned-in prior to accelerated aging. At 2000 hr the test was terminated. There is no evidence of device degradation during the test. Fig. 10 shows accelerated aging data for 3 un-screened diodes operating at 50°C and 10 mW CW. The population degradation rate was  $6.45 \times 10^{-5}$  A/hr. Using a 50% increase in operating current as the failure criterion, the MTTF at 50°C and 10 mW CW is  $9.5 \times 10^3$  hr.

The highest power lifetesting was performed at room temperature at a constant CW power of 20 mW. The data generated by 5 un-screened devices is shown in Fig. 11. After 2000 hrs of operation, no significant increase in the operating current is measured. One tested diode was facet coated; no difference in performance is observed. The data of Fig. 11 shows that the DCPBH diodes are extremely reliable under high power operation. It is important to note that the diodes were not pre-screened in any manner. Additional lifetesting has been performed and data is available on over  $10^5$  device-hours. Even without pre-screening no device failures have been recorded. Lower degradation rates and longer MTTFs will be attained by implementation of a rigorous pre-screening test to eliminate inferior devices (Ikegami 1983, Nakano 1983, Nakano 1984, Kuindersma 1985, Fujita 1985).

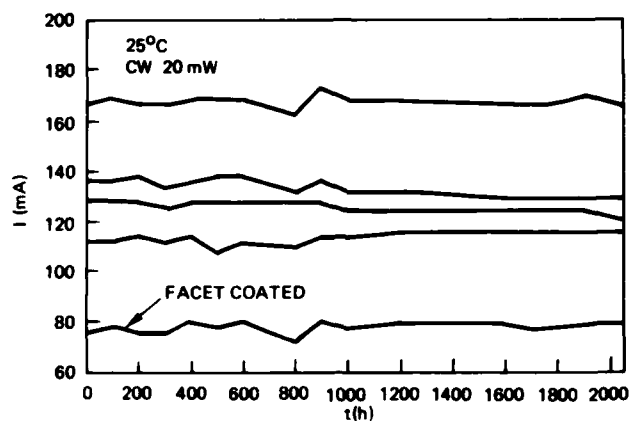


Fig. 11. 20 mW room temperature lifetest data

Acknowledgements

The authors would like to thank L. Figueroa for technical direction, and are indebted to N. Adachi, E. Anderson, D. Artiaga, S. Comings, P. Higgins, M. Moore, and T. Pham for technical assistance.

References

- Fujita O, Nakano Y, and Iwane G 1984 IEEE J. Lightwave Technol. **LT-3** 1211  
 Fujita O, Nakano Y, and Iwane G 1985 Electron. Lett. **21** 1172 Ikegami T, Takahei K, Fukuda M, and Kuroimu K 1983 Electron. Lett. **19** 282 Kuindersma P.I., Valster A, and Baks W 1985 IEEE J. Quantum Electron. **QE-21** 726 Mito I, Kitamura M, Kobayashi Ke, and Kobayashi Ko 1982 Electron. Lett. **18** 953  
 Nakano Y, Fukuda M, Sudo H, Fujita O, and Iwane G 1983 Electron. Lett. **19** 567 Nakano Y, Iwane G, and Ikegami T, 1984 Electron. Lett. **20** 397



## **Growth and modelling of InAsPSb/InAs double heterostructures**

J.L. BENCHIMOL, B. SERMAGE and J. PRIMOT

Laboratoire de Bagneux - CNET  
196 Avenue Henri Ravera - 92220 Bagneux - FRANCE

C. ALIBERT

Equipe de Microelectronique de Montpellier - USTL  
34060 Montpellier Cedex FRANCE

### 1. Introduction

Fluoride glasses are promising materials for optical fibers since an intrinsic attenuation of  $10^{-3}$  db/Km is predicted (Shibata et al 1981) at a wavelength of  $3.44\mu\text{m}$  as compared to 0.16db/Km at  $1.6\mu\text{m}$  for silica. The present state of art is only at 0.7db/Km, at a wavelength of  $2.5\mu\text{m}$ ; but if progress in these new fibers is as fast as for silica-based fibers, studies on adapted sources must start now.

The  $3\mu\text{m}$  wavelength range requires new materials for sources. Among III-V compounds semiconductors, there are only two candidates, InGaAsSb and InAsPSb quaternary alloys, both lattice matched to either GaSb or InAs substrates. We have chosen to study the latter system, because the miscibility gap present in that alloy is outside the range of interest for emission. Moreover, the refractive index decreases when the bandgap increases, so that the same alloy can be used as confinement layer. However, this miscibility gap, which extends on the high bandgap side, is troublesome for the confinement layer, because it limits the energy gap barrier between the active and confinement layers.

We propose to study in this paper the limitations of the InAsPSb/InAs system. We present first solid phase instability and liquid-solid phase equilibrium calculations in the quaternary alloy. Liquid phase epitaxial (LPE) growth conditions are then described and limitations on high bandgap alloy growth are determined. Monolayers and double heterostructures are characterized, and a model is proposed to estimate the threshold current density of such a laser structure.

### 2. Solid phase instability and liquid-solid phase equilibrium calculations

The spinodal curves, separating the unstable from the stable or metastable  $\text{In}(\text{As}_{1-x-y}\text{P}_x\text{Sb}_y)$  solid regions were calculated using the delta lattice parameter (DLP) model of Stringfellow (1974). This calculation shows that, as in other III-V compounds with miscibility gap, the extension of the immiscibility domain is reduced when the temperature is increased. Thus high temperatures are necessary to obtain phosphorous rich alloys, ie large bandgap alloys. The spinodal curve is represented on fig.1 (curve A), where the maxima of solid composition  $x(\text{InP})$  lattice

matched to InAs ( $y(\text{InSb})=0.47x(\text{InP})$ ) are plotted as a function of temperature.

Using the same DLP model, the liquid-solid phase equilibrium of the quaternary alloy was calculated. Fig.2 shows the isotherms of solid composition lattice matched to InAs as a function of liquid composition. A peculiar result is that all these curves pass through a maximum in  $x(\text{InP})$ , and that the lower the temperature, the higher the maximum. Curve (B) of fig.1 represents these  $x(\text{InP})$  maxima as a function of temperature.

Curves (A) and (B) are the frontiers of the allowed composition region for LPE growth. Their intersection represents the highest bandgap alloy which can be grown :  $x(\text{InP})=0.45$  ; the corresponding growth temperature is  $T=810\text{K}$ .

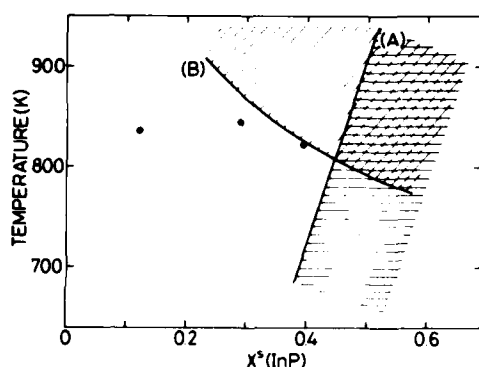


Fig. 1 Plot, as a function of temperature, of solid composition maxima  $x(\text{InP})$  lattice matched to InAs, allowed from (A) solid phase instability calculations and (B) from liquid-solid phase equilibrium calculations. The experimental points are also represented.

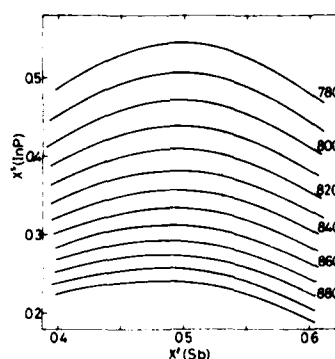


Fig. 2 Isotherms of lattice matched solid compositions  $x(\text{InP})$ , versus liquid compositions  $x^l(\text{Sb})$ .

### 3. Epitaxial growth and characterization

InAsPSb alloys were grown by LPE on (100) oriented InAs substrates, using the single phase technique. Liquidus temperatures were measured by direct observation through a transparent furnace, but were made difficult and inaccurate because of melt oxidation. Growth was performed at constant temperature, so that good composition homogeneity, measured by electron microprobe analysis, was achieved along the growth direction for thicknesses of up to  $5\mu\text{m}$  (Kobayashi et al 1981).

The different alloy compositions which have been grown are shown on fig.1. The highest phosphorous solid composition lattice matched to InAs which could be grown was  $x(\text{InP})=0.39$ . However, the sample surface was slightly rough and epitaxial growth was not reproducible. This composition is very close to the maximum value (0.45) calculated in the previous section. Proximity of the instability domain can explain the growth difficulties, which were also observed by Fukui et al (1981), using organometallic vapor phase epitaxy (OMVPE). This technique allows the growth of  $x(\text{InP})=0.46$ ; for higher values, surface degradation occurred, as in LPE. Easier was the LPE growth of the  $x(\text{InP})=0.30$  composition, which is characterized further below.

The lattice parameter in the direction perpendicular to the surface, measured by x-ray double diffraction using the (400) symmetric reflection, was found to be very sensitive to supersaturation. Fig.3 shows the relative lattice mismatch  $\Delta a/a$  as a function of growth temperature: a  $\Delta a/a$  variation of about  $5 \times 10^{-4}$  per degree is measured. It can be noticed that positive mismatches are mainly obtained, and that the lattice matching condition corresponds to a small supersaturation. Fig.4 shows the diffraction profile of a lattice matched layer: the full width at half maximum,  $\Delta\theta$ , of layer and substrate are comparable (29" and 21" respectively), which is a criteria of epilayer quality.  $\Delta\theta$  values between 20" and 30" were measured by Fukui et al (1981) on OMVPE layers.



Fig. 3 Variation of the relative lattice mismatch  $\Delta a/a$  with growth temperature  $T$ , at constant liquid composition.

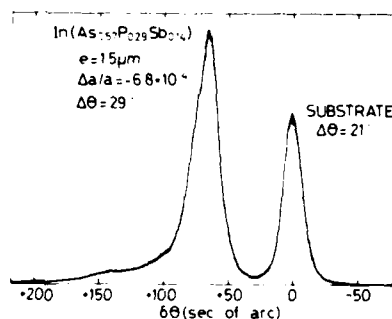


Fig. 4 X-ray diffraction profile of a 1.5  $\mu\text{m}$  thick InAsPSb layer.

The Schottky barrier electroreflectance technique (ER) was used on these samples (fig.5). The third derivative nature of the low field ER spectra allows a good resolution in energy. The ER was measured after deposition of a Cu<sub>2</sub>S film used as a biasing electrode. The experimental system has been described elsewhere (Alibert 1972). We find at  $T=24\text{K}$  a bandgap of  $E_0=545\text{meV}$  and a spin orbit splitting of  $\Delta_0=475\text{meV}$ ; at  $300\text{K}$ ,  $E_0=482\text{meV}$ . This is the first experimental determination of  $\Delta_0$  in this material. The  $E_0$  value is in close agreement with the result obtained by photoluminescence (PL) using the 514nm line of an argon laser. The PL peak for this sample occurs at an energy of 536meV at 77K and has a half width of 40meV.

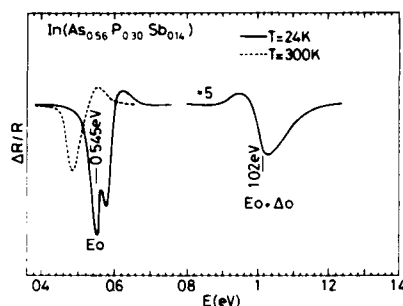


Fig. 5 Electoreflectance spectra of InAsPb at 300K and 24K.

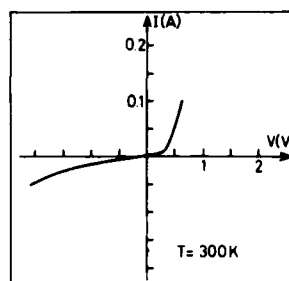


Fig. 6 Current-voltage characteristic of an In(As<sub>0.56</sub>P<sub>0.30</sub>Sb<sub>0.14</sub>)/InAs/In(As<sub>0.56</sub>P<sub>0.30</sub>Sb<sub>0.14</sub>) double heterostructure at 300K.

Double heterostructures were grown using In(As<sub>0.56</sub>P<sub>0.30</sub>Sb<sub>0.14</sub>) as confinement layer and InAs as active layer. There was no dissolution problem, and flat hetero-interfaces were obtained. Te and Zn were used as n and p type dopant respectively of the cladding layers. A room temperature current-voltage diode characteristic is shown on fig.6. At forward bias, the rise in current occurs at a voltage corresponding approximately to the bandgap energy of the InAs active layer. Using the electoreflectance measurements, we can determine the bandgap difference between the cladding and active layer:  $\Delta E_0 = 125 \text{ meV}$ . Calculation of the refractive index (Alibert et al 1986) leads to an optical confinement of  $\Delta \bar{n} = 0.2$ .

#### 4. Modelling of In(As<sub>0.56</sub>P<sub>0.30</sub>Sb<sub>0.14</sub>)/InAs double heterostructures

We have made a model to predict the threshold current density in a laser structure such as the experimental one described above. The electronic band structure of the active layer was taken as a spherical approximation of Kane's five band model (Kane 1957). The intervalence band absorption and the gain were calculated using Kane's model. The free carrier absorption and the mirror losses were obtained from standard formulae. The threshold carrier density,  $n_{th}$ , was determined as usual by equalizing losses and maximum gain in the cavity.

The threshold current density was calculated as the sum of the recombination in the active layer and the leakage current:

$$J_{th} = n_{th} q w (1/\tau_r + 1/\tau_a) + J_{leak}$$

$J_{leak}$  is the diffusion current of carriers having an energy larger than  $\Delta E_0$ . The radiative lifetime  $\tau_r$  was calculated from the Fermi Golden rule, and the Auger lifetime  $\tau_a$  was taken as  $1/\tau_a = C_a n^2$ .

The main uncertainty comes from the fact that the Auger coefficient  $C_a$  has not been measured in InAs. We think that the best estimation can be obtained by extrapolating the value which has been carefully measured in In<sub>0.53</sub>Ga<sub>0.47</sub>As ( $7.10^{-29} \text{ cm}^6 \text{ s}^{-1}$ , Sermage 1986) using Sugimura's formula (Sugimura 1983):

$$Ca \propto \exp \left[ \frac{-(E_0 - \Delta_0)/kT}{\{(2m_h + m_l)/m_s - 1\}} \right] \text{ for } E_0 > \Delta_0$$

$$Ca \propto \exp \left[ (E_0 - \Delta_0)/kT \right] \text{ for } E_0 < \Delta_0$$

We suppose that the dominant Auger process in InAs and InGaAs is CHHS because the difference between  $E_0$  and  $\Delta_0$  is small in these materials. This leads to  $Ca = 3.8 \cdot 10^{-28} \text{ cm}^6 \text{ s}^{-1}$  in InAs. The Auger coefficient is then supposed to be independent of temperature (Sermaige 1984).

The results of the calculation are summarized below:

- Due to the small conduction band mass, the threshold carrier density is small ( $n_{th} = 5.5 \cdot 10^{17} \text{ cm}^{-3}$ ) and the threshold current density without Auger recombination and leakage is small:  $J_{th} = 240 \text{ A/cm}^2$ .
- With Auger recombination,  $J_{th} = 1300 \text{ A/cm}^2$ .
- With Auger recombination and leakage over the barrier,  $J_{th} = 5500 \text{ A/cm}^2$ . The intervalence band absorption is small ( $23 \text{ cm}^{-1}$ ) and the characteristic temperature  $T_0$  at room temperature is about 65K. This calculation shows that in this structure, the largest part of the threshold current is the leakage current and not the Auger recombination and also that, reasonable  $T_0$  values can be expected.

## 5. Conclusions

We have shown, from thermodynamical calculations, that under lattice matching conditions to InAs substrates, LPE growth of InAsPSb is limited on the high bandgap side to a solid composition  $x(\text{InP}) < 0.45$ . As a consequence, the electrical confinement of double heterostructures based on this material will be small. With cladding layers made of the best alloy which could be grown by LPE ( $x(\text{InP}) = 0.30$ ), an energy gap barrier of 125meV is obtained using an InAs active layer. Double heterostructures with emission wavelengths shorter than that of InAs can be designed using InAsPSb low bandgap alloys as active layers; but this is to the detriment of electrical confinement.

The threshold current of the structure was calculated by taking into account radiative and Auger recombination, intervalence band absorption and leakage of carriers over the barrier. Due to the small value of the conduction band effective mass in InAs and to the small energy gap barrier, the largest part of the threshold current is the leakage current and not the Auger recombination current.

## List of parameters

### Active layer

Laser length :  $L = 200 \mu\text{m}$   
 Thickness :  $w = 1 \mu\text{m}$   
 Kane matrix element :  $E_p = 22.2 \text{ eV}$   
 Bandgap energy :  $E_0(300\text{K}) = 356 \text{ meV}$   
                    $E_0(0\text{K}) = 418 \text{ meV}$   
 Spin orbit splitting :  $\Delta_0 = 380 \text{ meV}$   
 Conduction band mass :  $m_e = 0.023 m_0$   
 Heavy hole mass :  $m_h = 0.33 m_0$   
 Light hole mass :  $m_l = 0.025 m_0$   
 Spin orbit splitted band mass :  $m_s = 0.14 m_0$   
 Auger recombination coefficient :  $Ca = 3.8 \cdot 10^{-28} \text{ cm}^6 \text{ s}^{-1}$   
 Refractive index :  $\bar{n} = 3.52$

**Confinement layer**

Bandgap energy :  $E_0(300K) = 482\text{meV}$   
 Electron mobility :  $\mu_e = 2000\text{cm}^2\text{V}^{-1}\text{s}^{-1}$   
 Hole mobility :  $\mu_h = 100\text{cm}^2\text{V}^{-1}\text{s}^{-1}$   
 Electron and hole lifetime :  $\tau_e = 3.10^{-9}\text{s}$   
 Doping :  $N_d = N_a = 10^{18}\text{cm}^{-3}$

**Acknowledgements**

The authors wish to thank C. Daguet for electron microprobe analysis, A. Godin for sample processing and A. Joullie for fruitful discussions. This work was supported by EEC under Race contract n° 1029.

**References**

- Alibert C, Bordure G, Laugier A and Chevallier J 1972 Phys. Rev. B6 1301
- Alibert C and Joullie A 1986 Private communication
- Fukui T and Horikoshi Y 1981 Jap. J. Appl. Phys. 20 587
- Kane EO 1957 J. Phys. Chem. Sol. 1 249
- Kobayashi N and Horikoshi Y 1981 Jap. Appl. Phys. 20 2301
- Sermage B, Heritage JP and Dutta NK 1984 J. Appl. Phys. 57 5443
- Sermage B, Chemla DS, Sivco D and Cho AY 1986 IEEE J. Quant. Electron. QE22 774
- Shibata S, Horiguchi M, Jinguji K, Mitachi S, Kanamori T and Manabe T 1981 Electron. Lett. 17 775
- Stringfellow GB 1974 J. Cryst. Growth 27 21
- Sugimura A 1983 J. Quant. Electron. QE19 930

## **First fabrication of CW high power phase-locked laser arrays emitting at 1.3 $\mu\text{m}$ grown by LP-MOCVD**

M. Razeghi and R. Blondeau  
THOMSON-CSF - Laboratoire Central de Recherches  
Domaine de Corbeville - BP N° 10  
91401 ORSAY CEDEX (FRANCE)

### Abstract

We report the first continuous wave high power GaInAsP-InP semiconductor phase-locked laser arrays fabricated on material grown by two step low-pressure metalorganic chemical vapor deposition growth technique.

Multiple-stripe GaAs-GaAlAs lasers have been shown to operate to pulsed output powers in excess of 1 W with stable output characteristics (1). Stripe-to-stripe coupling has been deduced in GaAs-GaAlAs system from the analysis of structure in the far fields caused by interference between the individual oscillating stripes in the arrays.

Razeghi et al. (2-3) previously showed that the LP-MOCVD growth technique is promising for large scale production of high quality GaInAsP-InP Buried-Ridge Structure (BRS) lasers emitting at 1.3  $\mu\text{m}$ , 1.55  $\mu\text{m}$  and DFB lasers. Recently we have been studying the phase-locked operation of GaInAsP InP semiconductor lasers, with the eventual goal of obtaining high powers into narrow, coherent beams.

In the case of GaAs-GaAlAs system, it has been shown that Index-guided lasers, are intrinsically more coherent, less astigmatic, and more stable than gain-guided devices (4). Here we report on phase-locked operation from a 7-unit array of new mixture of index-guided and gain-guided devices: Ridge-Island-Laser-Arrays (R.I.L.A.).

The high power laser phase locked arrays structure was manufactured as follows:

First the following layers were grown successively on InP(Sn) substrate with orientation (100) exact or (100)2° off.

- 1  $\mu\text{m}$  InP sulphur doped ( $n = 1 \times 10^{18} \text{ cm}^{-3}$ ) for confinement layer.
- 0.2  $\mu\text{m}$  undoped GaInAsP (1.3  $\mu\text{m}$  wavelength composition) for active layer
- 100 Å undoped InP as blocking layer.
- 100 Å undoped GaInAsP for waveguide layer.

Next, the arrays consisting of 7 stripes of 2  $\mu\text{m}$  and stripe-stripe spacing of 1  $\mu\text{m}$  was etched in the 100 Å GaInAsP layer, through a photolithographic resist mask, using a selective etchant composed of  $\text{SO}_4\text{H}_2\text{-H}_2\text{O}_2\text{-H}_2\text{O}$  (1:8=200).

After removing the resist mask, the arrays was then covered by a 1  $\mu\text{m}$  thick Zn doped InP confinement layer ( $N_A - N_D \approx 5 \times 10^{17} \text{ cm}^{-3}$ ) and 0.5  $\mu\text{m}$  Zn doped GaInAs contact layer with  $N_A - N_D \approx 10^{19} \text{ cm}^{-3}$ . In order to localize the injection only in the Ridge Island Laser Arrays (R.I.L.A.) active region, a shallow proton implantation was realized through a 20  $\mu\text{m}$  wide photoresist mask after the metallisation of the contacts (see Fig. 1). After cleaving and scribing into chips 300  $\mu\text{m}$  length and 300  $\mu\text{m}$  width, the lasers weremounted epi-side down, onto nickel-plated copper heatsinks using indium.

Room temperature pulsed and CW threshold of 220 mA, with a external quantum efficiency of 0.19 W/A (pulsed) and 0.13 W/A (CW) have been obtained (Fig. 2) output power more than 300 mW at 2 A pulse modulated (limited by the pulse generator), and 120 mW at 1.3 A (CW) have been measured with no facet coatings. The far field patterns parallel and perpendicular to the junction plane under CW operation for 10 mW was 3 and 45 degrees respectively (Fig. 3). These measurements confirmed the highly coherent output beam with strongly phase locked operation of these devices.

In conclusion, CW and pulsed phase-locked operations to high powers have been achieved for the first time from 7-unit arrays of new mixture of index-guided and gain-guided (R.I.L.A.) GaInAsP-InP lasers fabricated by two steps LP-MOCVD.

#### REFERENCE

- 1 - D.R. SCIFRES, W. STREIFER, and R.D. BURNHAM  
Appl. Phys. Lett. 34, 259, (1978).
- 2 - M. RAZEGHI, R. BLONDEAU, K. KAZMIERSKI, M. KRAKOWSKI and J.P. DUCHEMIN, Appl. Phys. Lett. 46, 131, (1985).
- 3 - M. RAZEGHI, R. BLONDEAU, K. KAZMCERSKI, M. KRAKOWSKI, B. DE CREMOUX, J.P. DUCHEMIN and J.C. BOULEY, Appl. Phys. Lett. 45, 784, (1984).
- 4 - D. BOTEZ, W.T. TSANG and S. WANG, Appl. Phys. Lett. 28, 234, (1976).



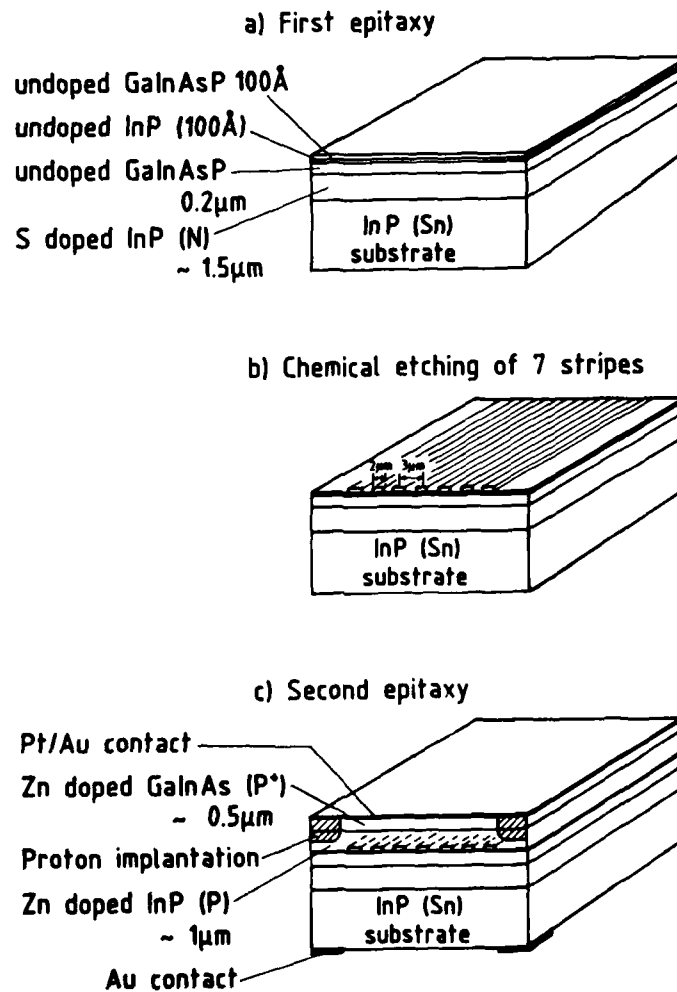


Fig. 1 Schematic diagram of Ridge-Island-Laser-Arrays (R.I.L.A.) structure :

a) first epitaxy,  
b) selective chemical etching of 7 stripes,  
c) after regrowth, metallisation and proton implantation.

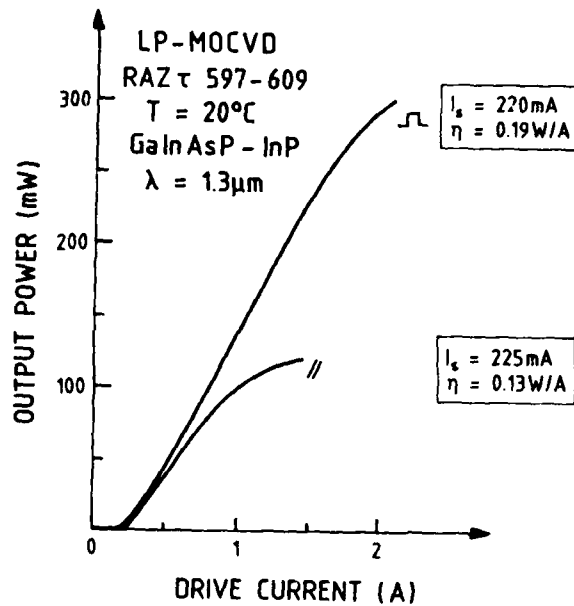


Fig.2 Typical light-current characteristics of the phase locked high power GaInAsP-InP laser arrays at  $20^\circ\text{C}$ , under pulsed and CW operations.

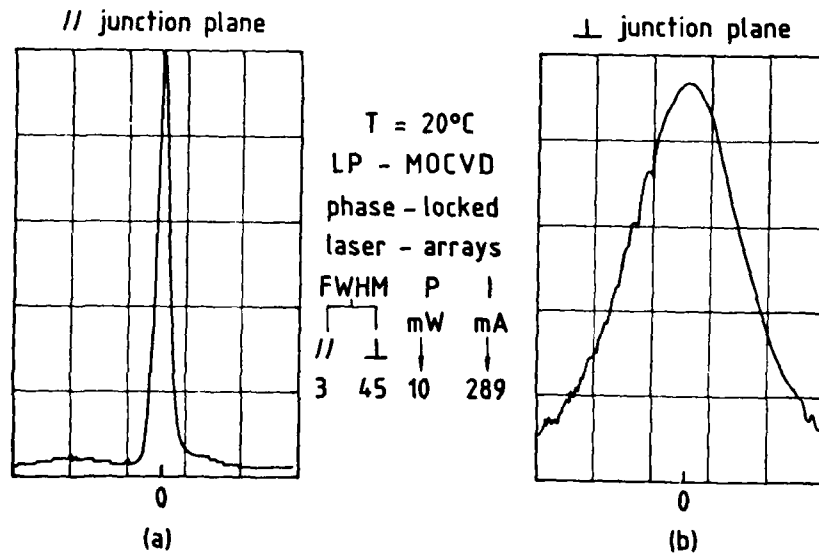


Fig. 3 CW longitudinal mode spectrum of a phase locked GaInAsP-InP laser arrays.

## **Fe-doped InP hydride vapor phase epitaxy for high speed buried heterostructure laser diodes**

Yoshitake Kato, Akira Usui\*, Taibun Kamejima\*\*  
Shigeo Sugou and Kenichi Kasahara

Opto-electronics Res. Labs., \*Fundamental Res. Labs.,  
\*\*Resources and Environment Protection Res. Labs., NEC Corporation  
4-1-1 Miyazaki, Miyamae-Ku, Kawasaki-City, Kanagawa 213, Japan

**Abstract.** Highly resistive Fe-doped InP hydride VPE has been developed for blocking layer growth in InGaAsP/InP BH lasers. Fe metal charged with In source was used for Fe doping source. Doped Fe concentration could be accurately controlled, simply through initial HCl partial pressure. Fe-doped InP layer resistivity obtained was as high as  $3.2 \times 10^8$  ohm-cm. Planar surface BH lasers selectively embedded with Fe-doped InP exhibited a modulation bandwidth exceeding 10CHz.

### **1. Introduction**

InGaAsP/InP buried heterostructure laser diodes (BH-LDs) have been developed for high bit rate optical fiber communication systems. In these BH-LDs, reverse biased p-n junctions are commonly used as the current blocking layers. However, laser frequency response is severely limited by high parasitic capacitance in the p-n junction current blocking layers. In order to achieve high speed response, the current blocking with high-resistive InP layers is more effective compared with that by the p-n junction structure.

Recently, Fe-doped InP growth using MOCVD method has been reported by several authors (Long et al. 1984, Hess and Zehr 1986, Huang and Wessels 1986, and Sugawara et al. 1986). However, the present VPE method has several advantages over MOCVD, that is, 1) less Fe concentration is necessary, because a purer InP layer can be grown, 2) excellent Fe doping controllability can be realized and 3) it is easy to fabricate planar surface BH-LDs.

This paper reports Fe-doped InP hydride VPE using iron chloride and the characteristics of a high speed BH-LDs fabricated with high-resistive current blocking layer.

### **2. Experimental**

#### **a) Fe-doped InP growth**

The hydride VPE apparatus for Fe-doped InP growth is shown in Fig. 1. For Fe doping, Fe metal charged with the In source was used. Another In source for the growth was set separately in the source region. Total HCl flow rate

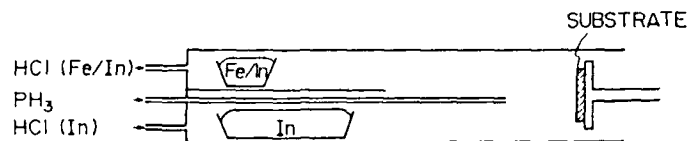


Fig. 1. Schematic diagram of hydride VPE system.

over these sources was kept constant at 10 cc/min.  $\text{PH}_3$  and total carrier  $\text{H}_2$  flow rate were 15 cc/min and about 3 l/min, respectively. The metal source temperature was  $830^\circ\text{C}$ . At a growth temperature of  $600^\circ\text{C}$ , background carrier concentration for undoped InP layers was in the range of  $6.8\text{--}8.0 \times 10^{14} \text{ cm}^{-3}$ . Therefore, Fe concentration as small as about  $10^{15} \text{ cm}^{-3}$  is enough to compensate the background carrier concentration and obtain high resistivity.

If pure Fe metal is employed as the Fe doping source with the transport gas of  $\text{HCl}$ , dominant species of iron chloride at the  $830^\circ\text{C}$  source temperature is  $\text{FeCl}_2$  and  $\text{FeCl}_2$  reaction efficiency is less than  $2 \times 10^{-3}$  under the present growth conditions by thermodynamic calculations. Therefore, almost all of  $\text{HCl}$  which does not react on the Fe metal will be transported to the substrate region and will result in making the embedded layer surface rough. For this reason, Fe-charged In source was employed to avoid the residual  $\text{HCl}$ . In the Fe/In source region, reactions are described as follows:



where  $K_1$  and  $K_2$  are equilibrium constants,  $p_i$  is partial pressure of species  $i$  and  $a_{\text{Fe}}$  is activity of Fe in In. From (1) and (2), we can obtain

$p_{\text{FeCl}_2} = (K_2/K_1^2) r_{\text{Fe}} x_{\text{Fe}} (p_{\text{InCl}})^2$   
 where  $r_{\text{Fe}}$  is activity coefficient of Fe, and  $x_{\text{Fe}}$  is dissolved Fe concentration in In. Under thermodynamic equilibrium condition of the reactions,  $p_{\text{InCl}}$  is nearly equal to the initial  $\text{HCl}$  partial pressure ( $p_{\text{HCl}}^0$ ). Therefore,  $p_{\text{FeCl}_2}$  is proportional to the  $x_{\text{Fe}}(p_{\text{HCl}}^0)^2$ .

The  $p_{\text{HCl}}^0$  dependence of doped Fe concentration was experimentally investigated. Fe concentrations were evaluated through Fe ion intensity in SIMS measurement. Figure 2 shows the obtained experimental results for two kinds of charged amount of Fe in the Fe/In source ( $N_{\text{Fe}}$ ). Doped Fe

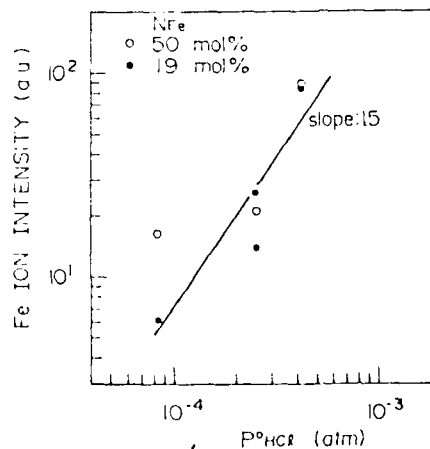


Fig. 2. Doped Fe concentration dependence on  $\text{HCl}$  partial pressure over Fe/In source. Doped Fe concentrations were evaluated by SIMS.  $N_{\text{Fe}}$  indicates charged amount of Fe in In.

concentration was proportional to the about 1.5 power of initial HCl partial pressure. Though  $N_{Fe}$  was reduced from 50 mol% to 19 mol%, doped Fe concentration remained to be unchanged. The  $x_{Fe}$  would be nearly constant, because the solubility of Fe in In is saturated under these charged amounts of Fe. Eventually, doped Fe concentration can be controlled simply by initial HCl partial pressure even if  $N_{Fe}$  changed. The difference between the experimental value, 1.5 and calculated value, 2 is considered to be due to insufficiency in the reaction time ( $\sim 0.2$  seconds) to achieve thermodynamic equilibrium condition between HCl and Fe/In source.

Figure 3 shows doped Fe concentration dependence of Fe-doped InP layer resistivity. Fe-doped InP layers were grown on  $n^+$  InP substrates. First, AuGe-Ni was deposited on the substrate side, and then samples were annealed at  $390^\circ\text{C}$ . Next, 0.5 mm  $\phi$  Au-dot electrode for epitaxial layer side was formed. The resistivity of layers were measured from ohmic region of current-voltage characteristics (Macrender et al. 1984). As the doped Fe concentration increased, the resistivity tended to saturate at about  $10^8$  ohm-cm. The maximum resistivity obtained was as high as  $3.2 \times 10^8$  ohm-cm.

#### b) BH-LDs embedded with Fe-doped InP

1.3  $\mu\text{m}$  InGaAsP/InP BH-LDs were fabricated using high-resistive layer as a current blocking layer. The schematic cross section of the device is shown in Fig. 4. In this experiment, LPE-grown double heterostructure (DH) wafer with an 0.16  $\mu\text{m}$  thick InGaAsP active layer grown on a Sn-doped InP substrate was used. Chemical etching was performed on the DH wafer to form the 6  $\mu\text{m}$  wide and 5

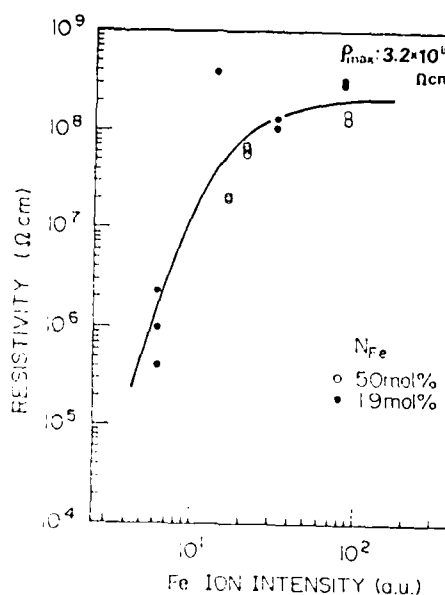


Fig. 3. Fe-doped InP layer resistivity as a function of doped Fe concentration. The maximum resistivity obtained was  $3.2 \times 10^8$  ohm-cm.

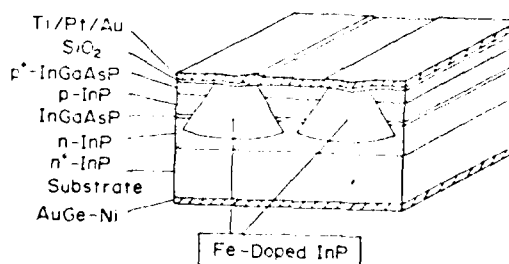


Fig. 4. Schematic structure of planar surface buried heterostructure InGaAsP/InP lasers with highly resistive current blocking layers.

$\mu\text{m}$  deep double channels using  $\text{SiO}_2$  masks. Then, using the present technique, the DH wafer was selectively embedded with Fe-doped InP through the same  $\text{SiO}_2$  masks on which no growth occurs during the epitaxy. Growth conditions were as follows;  $N_{\text{Fe}}$  was 19 mol% and initial HCl partial pressure over Fe/In source was  $2.5 \times 10^{-3}$  atm. Threshold current was 32 mA in the BH-LDs with an around 1  $\mu\text{m}$  active layer width.

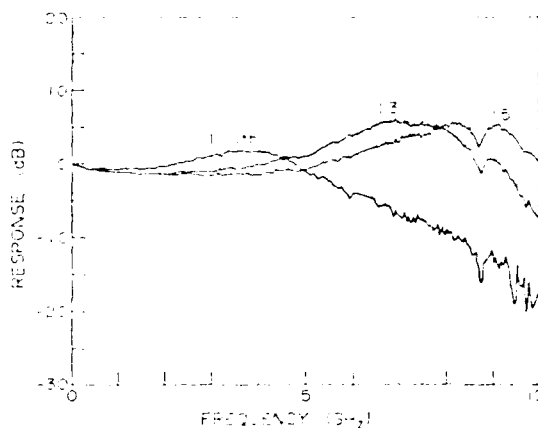


Fig. 5. Small-signal modulation response with several bias levels.

Figure 5 shows the small signal response for lasers with 200  $\mu\text{m}$  cavity length and 2.4  $\mu\text{m}$  active layer width. 3dB-down bandwidth of more than 10 GHz was achieved at  $1.5I_{\text{th}}$ . 3dB-down roll-off frequency due to electrical parasitics was as high as 6 GHz. The estimated parasitic capacitance was 8 pF, which was much smaller than that for ordinary BH-LDs with p-n junction in the current blocking region. The residual parasitic capacitance arising mainly from the electrode capacitance can be reduced by contact pad size reducing.

In summary, we have developed highly resistive InP hydride VPE method with high controllability and reproducibility. By applying this method to BH-LD embedding layers, high frequency response with the bandwidth over 10 GHz has been achieved. This result indicates that the present method is promising for high speed laser fabrication.

The authors acknowledge H. Watanabe, K. Kobayashi, R. Lang and T. Yanase for fruitful discussions and encouragement.

#### References

- Hess K. L. and Zehr S.W. 1986 Electron. Mater. Conf. Amherst USA abstract 23.
- Huang K. and Wessels B. W. 1986 Electron. Mater. Conf. Amherst USA abstract 27.
- Long J. A., Riggs V. G. and Johnston, Jr. W. D. 1984 J. Cryst. Growth **69** 10.
- Macrander A.T., Long J. A., Riggs V. G., Bloemeke A. F. and Johnston, Jr. W. D. 1984 Appl. Phys. Lett. **45** 1297.
- Sugawara M., Aoki O., Nakai N., Tanaka K. Yamaguchi A. and Nakajima K. 1986 4th conf. semi-insulating III-V Mater. Hakone Japan abstract 115.

## **Observation of novel step-like structure in the photocurrent and dark current of a superlattice: charge collection by successive depletion of quantum wells**

J Allam, F Capasso, M B Panish and A L Hutchinson

AT&T Bell Laboratories, Murray Hill, New Jersey 07974, U.S.A..

**Abstract.** We have observed novel manifestations of superlattice properties in a  $\text{Ga}_{0.47}\text{In}_{0.53}\text{As}/\text{InP}$  quantum well photodiode structure grown by gas source molecular beam epitaxy, evident as multiple steps in the reverse bias photocurrent and dark current. This striking effect is explained in terms of depletion of successive quantum wells as the reverse bias field is increased, while the diffusion of carriers generated in the undepleted region is suppressed by localization within the wells. As the electric field punches through into each well the carriers photogenerated and thermally generated in that well are collected by the field, while carriers generated in the undepleted wells remain localized and cannot contribute to the current. This causes a step-like increase in the photocurrent and the dark current.

### **1. Introduction**

Superlattice structures are of potential interest for devices in applications including avalanche photodiodes (See, for example, Capasso 1985) and tunneling devices (Capasso et al 1986a). Enhancement of ionization rates in avalanche photodiodes (Capasso 1985, Chin et al 1980) and the observation of tunneling require high quality heterojunction interfaces in terms of interface abruptness and uniformity.

For photodetector applications in optical fiber communications,  $\text{Ga}_{0.47}\text{In}_{0.53}\text{As}/\text{InP}$  is the material system of immediate interest. Gas source molecular beam epitaxy (GSMBE) is a promising growth technique enabling precise control of the As/P ratio in this material system (Panish and Sumski 1984) and accurate dimensional control for the growth of multilayer structures. Recently, superlattice pin photodetectors grown by GSMBE were shown to have good interface quality, exhibiting exciton structure in the spectral response at room temperature (Temkin et al 1985).

### **2. Device Structure and Experimental Results**

We have observed novel step-like structure in the reverse bias photocurrent and dark current in superlattice structures grown by GSMBE. The structure consists of a pin photodiode with the superlattice placed in the nominally undoped i-region. A  $1\text{ }\mu\text{m}$   $\text{n}^+\text{-InP}$  buffer layer was grown on the Sn-doped InP substrate, followed by a highly doped  $1.7\text{ }\mu\text{m}$   $\text{Ga}_{0.47}\text{In}_{0.53}\text{As}$  absorption layer and a  $2500\text{ }\text{\AA}$   $\text{Ga}_{0.47}\text{In}_{0.53}\text{As}$  undoped spacer layer. The latter was intended to prevent diffusion of dopants

into the superlattice from the substrate. The superlattice consists of 10 periods of 300 Å  $\text{Ga}_{0.47}\text{In}_{0.53}\text{As}$  wells and 500 Å InP barriers. The top p-type contact is a 1.5 µm InP window layer to allow absorption of long-wavelength light by the superlattice. The layers were processed into mesa devices (with an area of  $1.7 \times 10^{-4} \text{ cm}^2$ ) by chemical etching with Br-Methanol, and top and bottom contacts were made by evaporating Au-Be and Au-Sn-Au respectively and alloying at 420 °C for 2 seconds. The sides of the mesa were coated with Merck HTR3 polyimide for passivation and physical protection. The processed devices exhibited a soft breakdown with  $I_{\text{dark}} = 10 \text{ µA}$  at a reverse bias  $V_r = 10 \text{ V}$  at room temperature.

The diodes were illuminated with white light from a microscope lamp filtered through a 0.95 µm long pass filter, to ensure carriers are photo-generated in the narrow band-gap quantum wells. Figure 1(a) shows the current-voltage characteristic, with and without illumination, measured at room temperature on an HP 4145A parameter analyzer. A clear step-like structure is seen in the photocurrent as the reverse bias is increased. Five steps (plus one in forward bias) are seen before the dark current exceeds the photocurrent and obscures any further structure. The increase in photocurrent at each step is approximately constant. These steps are equally spaced when the photocurrent is plotted against  $(V_r + V_{bi})^{1/2}$  (Figure 1(b));  $V_{bi}$  is the built-in potential  $\approx 0.65 \text{ V}$  measured by plotting the square of the depletion region width,  $W(V_r)$ , against  $V_r$  on a Miller feedback depletion profiler. This clearly shows that the steps occur at multiple increments of the depletion width  $W(V_r) = \sqrt{(2\epsilon_s/qN)(V_{bi} + V_r)}$  for a single sided abrupt junction). Each increment corresponds, as we shall see, to the superlattice period. This immediately suggests

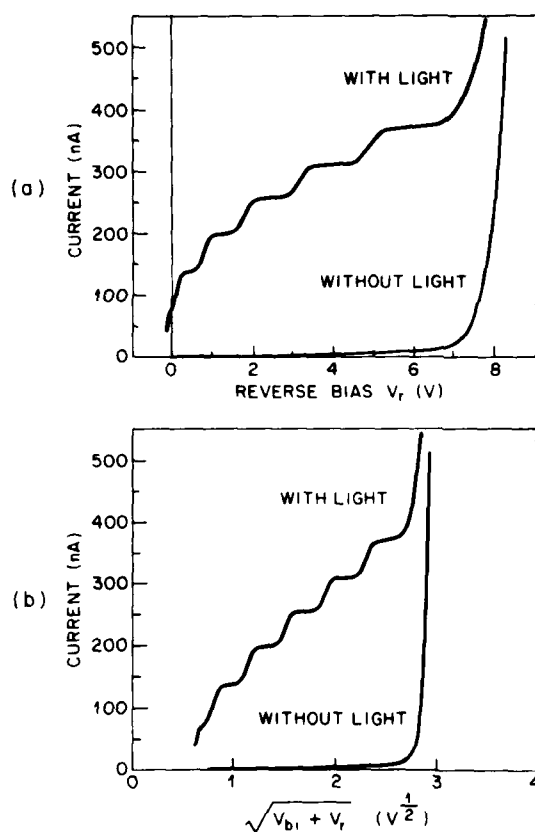


Figure 1. Current-voltage characteristic with illumination (upper trace) and in dark (lower trace) at room temperature, (a) versus reverse bias ( $V_r$ ), (b) versus  $\sqrt{(V_r + V_{bi})}$ .

the current-voltage characteristic, with and without illumination, measured at room temperature on an HP 4145A parameter analyzer. A clear step-like structure is seen in the photocurrent as the reverse bias is increased. Five steps (plus one in forward bias) are seen before the dark current exceeds the photocurrent and obscures any further structure. The increase in photocurrent at each step is approximately constant. These steps are equally spaced when the photocurrent is plotted against  $(V_r + V_{bi})^{1/2}$  (Figure 1(b));  $V_{bi}$  is the built-in potential  $\approx 0.65 \text{ V}$  measured by plotting the square of the depletion region width,  $W(V_r)$ , against  $V_r$  on a Miller feedback depletion profiler. This clearly shows that the steps occur at multiple increments of the depletion width  $W(V_r) = \sqrt{(2\epsilon_s/qN)(V_{bi} + V_r)}$  for a single sided abrupt junction). Each increment corresponds, as we shall see, to the superlattice period. This immediately suggests



that the steps are caused by the electric field punching through into successive wells. Similar results were obtained when  $1.55 \mu\text{m}$  light from a monochromator was focussed onto the mesa top with the photocurrent measured using a current-sensitive amplifier followed by a lock-in amplifier. At this wavelength the absorption length is about  $1.5 \mu\text{m}$  (Humphreys et al 1985) and absorption occurs in the quantum wells. The position of the steps did not change with light intensity (up to  $I_0=100 \text{ nA}$ ) or with chopping frequency. Figure 4(a) shows the photocurrent at a chopping frequency of  $1 \text{ kHz}$  and  $\lambda=1.55 \mu\text{m}$  at a light intensity of  $4.25 \text{ nW}$ . When the sample is illuminated with light from a He/Ne laser (which is absorbed in the top InP layer) no structure is observed and the photocurrent is constant with bias up to breakdown. A similar step-like structure is observed in the dark current, with the first three steps being observable at corresponding biases (Figure 4(b)).

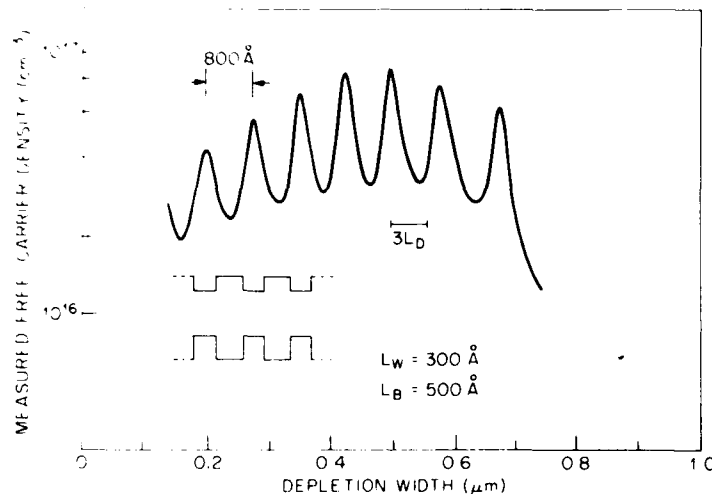


Figure 2. Measured free carrier density versus depletion width.

The carrier concentration profile was measured using a Miller feedback depletion profiler(7) (Figure 2). As the applied bias is increased from 0 to  $-10 \text{ V}$ , the depletion width increases from  $0.2 \mu\text{m}$  to  $0.7 \mu\text{m}$  and the measured free carrier concentration oscillates between  $2 \times 10^{16} \text{ cm}^{-3}$  and  $8 \times 10^{16} \text{ cm}^{-3}$  with a period of  $800 \text{ \AA}$ , equal to that of the superlattice. The 7 peaks observed correspond to the  $300 \text{ \AA}$  wide wells. It is important to realize what this figure represents. The method of depletion profiling (Miller 1972) measures the free carrier density via the movement of free carriers into and out of the depletion layer as an a.c. voltage modulation is applied. The spatial resolution is limited by Debye screening with a characteristic length given by  $L_D = \sqrt{(kT\epsilon_s/q^2N)}$  which is  $\approx 200 \text{ \AA}$  at a doping of  $N \approx 5 \times 10^{16} \text{ cm}^{-3}$ . This 'smears out' the charge distribution so that abrupt changes in the free carrier distribution cannot be resolved to better than several Debye lengths (Johnson and Panousis 1971). This smearing is thus of the order of the well widths in our superlattice, hence the high and low free carrier densities in figure 2 do not represent the true densities in the wells and barriers.

In order to obtain these values it would be necessary to simulate the profiling measurement using a numerical solution of Poisson's equation, and to vary the density to give the best fit to experimental data (Whiteaway 1983). However, the measured profile shows that the free carriers in the barriers spill over into the wells, similar to the process which occurs in modulation doping, and allows an estimation of the carrier concentration in the wells.

### 3. Discussion

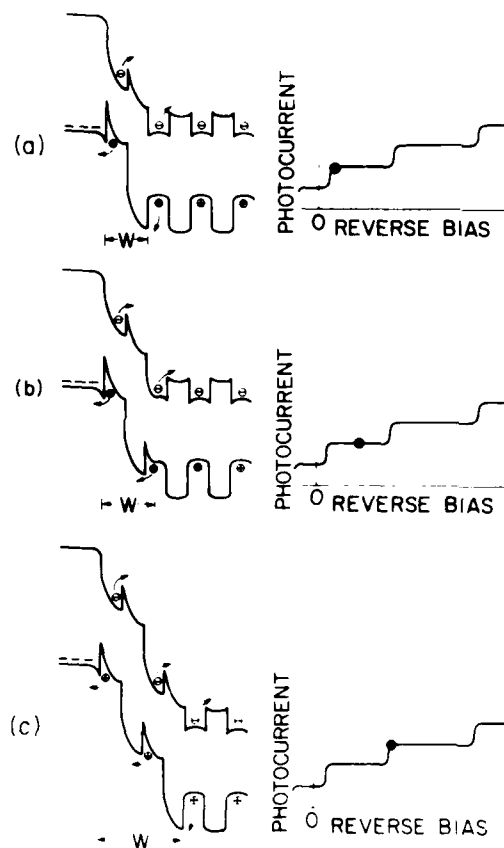


Figure 3. Band structure of partially depleted superlattice, showing:  
 (a) One period fully depleted.  
 (b) Depletion edge extending into second well. The carriers previously localized in that well are collected by the field.  
 (c) On reaching the barrier the depletion edge immediately punches through into the next well and collects the charge.

To better understand the charge collection process in a superlattice, consider an ideal case in which all the free carriers are in the wells and the barriers are depleted by carrier transfer into the wells (Figure 3). Electron-hole pairs will be generated in the wells by thermal processes and by photo-ionization across the band gap. In the undepleted region of the superlattice, the carriers are localized in the wells, perpendicular to the layers, due to the potential barriers. Thus their effective diffusion length is of the order of the well width, and carriers generated in this region cannot diffuse to the depletion region, be collected by the field and thus contribute to the total dark- and photocurrent. The first period is depleted at zero bias. At the point when the depletion edge punches through into the second well (Figure 3(a)), carriers thermally and photogenerated in the well can be collected by the field: the effective width of the absorbing region is thus two wells. As the bias is increased and the depletion edge sweeps through the second well, the photocurrent and the thermal generation component of the dark current

(which dominates the total dark current at low bias) remain constant (Figure 3(b)), until the depletion edge reaches the next barrier. Since the barrier has no free charges, the depletion edge immediately punches through into the next well (Figure 3(c)), where it can 'collect' the charge previously localized in the well. This gives rise to steps in the photocurrent. Note that the suppression of the diffusion current by localization is essential for the observation of photocurrent steps since the absorption length ( $\approx 1 \mu\text{m}$ ) is significantly greater than the depletion width in the bias range 0 to  $-10 \text{ V}$ . Diffusion currents would completely mask the steps.

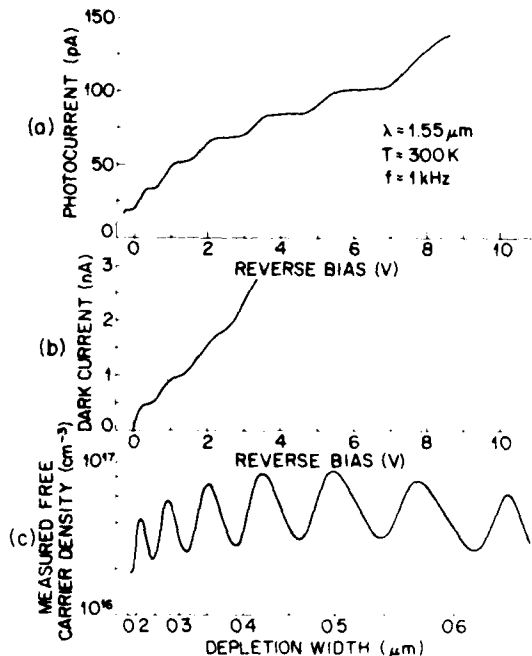


Figure 4.  
 (a) Photocurrent versus reverse bias at room temperature and  $\lambda = 1.55 \mu\text{m}$ , measured on lock-in amplifier at a chopping frequency of  $1 \text{ kHz}$ .  
 (b) Dark current at room temperature versus reverse bias.  
 (c) Measured free carrier density versus depletion width, plotted on the same bias scale as in (a) and (b).

In our data the photocurrent does not increase abruptly as soon as punch-through into the well occurs. Figure 4 shows the correlation between the structure in the photocurrent and dark current plotted as a function of bias and the doping profile plotted at a corresponding depletion depth. The features in the current can be seen to coincide with the periods of the superlattice. The photocurrent is constant while the depletion edge is sweeping through a given barrier because carriers are only photo-generated in the wells (note that a finite voltage is required to sweep through the barriers since not all the carriers have transferred into the wells). However, when the well is reached the current increases gradually with the field until it levels off at some point within the well. As the chopping frequency is increased, the current increase becomes more gradual and a higher field is

required for it to level off. This suggests that the efficiency of collection of carriers from the well is reduced by recombination processes in the well. In the absence of recombination, all the carriers generated in a given well will be collected as soon as the depletion edge punches through into that well. In practice, to achieve unity collection

efficiency, the average field in the well must be sufficiently high that the rate of thermionic emission over the barriers (which increases strongly with the field) exceeds the recombination rate.

Above about -5 V, the room temperature dark current is dominated by other mechanisms (surface leakage, tunneling, etc.) so the structure is no longer observed. For the photocurrent measurements, structure is obscured above  $\approx -8$  V by the presence of gain effects caused by ionization of the carriers in the wells over the band-edge discontinuity by carriers heated by the field in the barriers (Capasso et al 1986b).

#### Acknowledgement

One of the authors (J.A.) acknowledges financial support from the U.K. Science and Engineering Research Council.

#### References

- Capasso F 1985 in *Semiconductors and Semimetals*, edited by R.K. Willardson and A.C. Beer (New York: Academic Press) 22 D, 2
- Capasso F, Mohammed K and Cho A Y 1986a Appl. Phys. Lett. 48 478
- Capasso F, Allam J, Cho A Y, Mohammed K, Malik R J, Hutchinson A L and Sivco D L 1986b Appl. Phys. Lett. 48 1294
- Chin R, Holonyak N, Stillman G E, Tang J Y and Hess K 1980 Electron. Lett. 16 467
- Humphreys D A, King R J, Jenkins D and Moseley A J 1985 Electron. Lett. 21 1187
- Johnson W C and Panousis P T 1971 IEEE Trans. Electron Devices ED18 965
- Miller G L 1972 IEEE Trans. Electron Devices ED-19 1103
- Panish M B and Sumski S 1984 J. Appl. Phys. 55 3571
- Temkin H, Panish M B, Petroff P M, Hamm R A, Vandenberg J M and Sumski S 1985 Appl. Phys. Lett. 47 394
- Whiteaway J E A 1983 Proc. IEE. 130, 165

## Impact ionization across the band-edge discontinuity with very large ionization rate ratio in a superlattice with graded wells

J Allam<sup>‡</sup>, F Capasso, K Alavi<sup>\*</sup> and A Y Cho

AT&T Bell Laboratories, Murray Hill, New Jersey 07974, U.S.A..

**Abstract.** Two types of impact ionization mechanism occurring in superlattice avalanche photodiodes are reported. Conventional band-to-band ionization in a superlattice device indicates enhanced ionization rate ratios. A new ionization phenomenon, ionization over the band-edge discontinuity, is described. Very large ionization rate ratios have been measured for this mechanism in samples with graded wells.

### 1. Introduction

There is considerable interest in developing a low-noise long-wavelength (1.3 - 1.55  $\mu\text{m}$ ) avalanche photodiode (APD) for use in fiber-optic communications. For low-noise operation of an APD, the impact ionization rate for electrons ( $\alpha$ ) and holes ( $\beta$ ) should be very dissimilar, and the carrier with the larger ionization rate should be injected into the avalanche region.

Superlattice APD's have been proposed to artificially enhance the ionization rate ratio ( $K=\alpha/\beta$ ), and are discussed in detail by Capasso (1985). Such enhancement has been experimentally demonstrated in GaAs/ $\text{Al}_x\text{Ga}_{1-x}\text{As}$  superlattices, with values of  $K$  up to  $\approx 8$ , by Capasso (1985) and Juang et al (1985).

### 2. Band-to-band ionization: evidence of ionization rate ratio enhancement in an $\text{Al}_{0.48}\text{In}_{0.52}\text{As}/\text{Ga}_{0.47}\text{In}_{0.53}\text{As}$ superlattice APD.

We present evidence for enhancement of the ionization rate ratio in a long-wavelength APD fabricated in  $\text{Al}_{0.48}\text{In}_{0.52}\text{As}/\text{Ga}_{0.47}\text{In}_{0.53}\text{As}$ . We have previously reported on the high performance aspects of this device (Mohammed et al, 1985). The device structure is shown in Figure 1. The superlattice is placed in the nominally-undoped region of a pin photodiode structure. Ohmic contacts are made to the heavily doped p and n regions by evaporating and alloying Au-Be and Au-Sn, respectively. Individual devices are fabricated by mesa etching using conventional photolithographic techniques. The superlattice dimensions for this device (D418) are given in Table I.

The ionization rates are derived from the multiplication versus reverse bias under conditions of pure electron and pure hole injection into the

<sup>‡</sup>On leave from the University of Surrey, Guildford GU2 5XH, England.

<sup>\*</sup>Present address: Siemens Research and Technology Laboratory, Princeton, New Jersey 08540.

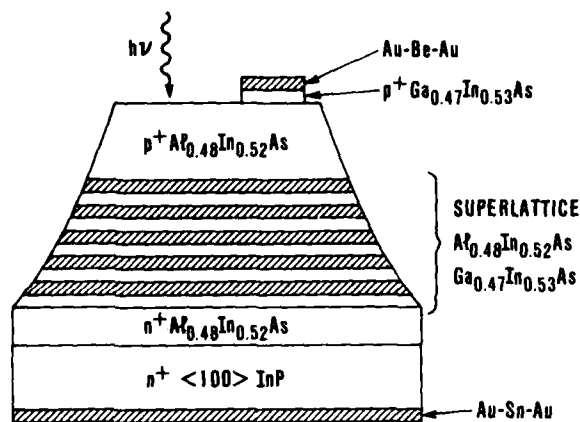


Figure 1. Structure of superlattice pin APD.

below -10 V is due to the large recombination rate of electrons and holes in the wells, compared to the rate of thermionic emission from the wells. The emission rate increases with reverse field due to hot carrier effects. The unity-multiplication photocurrent in the bias range -10 V to -20 V is extremely well fitted by a straight line. Avalanche multiplication occurs for reverse bias in excess of  $\approx 20$  V, which corresponds to a field of  $2 \times 10^5$  Vcm $^{-1}$ . Figure 3 shows the ionization rates calculated from the standard equations for a pin structure. The  $k$ -ratio,  $(\alpha/\beta) = (M_e - 1)/(M_h - 1)$ , varies from about 3 at a field of  $3.5 \times 10^5$  Vcm $^{-1}$  to 3.5 at  $2.5 \times 10^5$  Vcm $^{-1}$ . This suggests an enhancement of the  $k$ -ratio over the value of 2 in bulk In $_{0.53}$ Ga $_{0.47}$ As measured by Pearsall (1980).

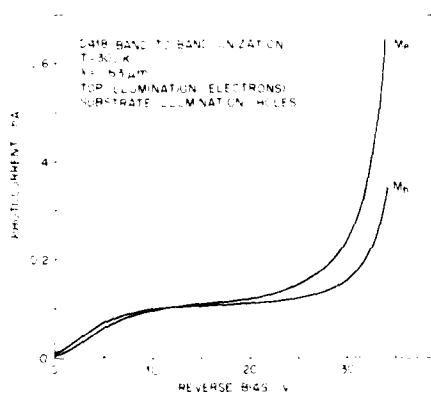


Figure 2. Multiplication as a function of reverse bias under conditions of pure electron ( $M_e$ ) and hole ( $M_h$ ) injection, for band-to-band ionization in sample D418 at 300 K.

avalanche region. This is achieved using the standard technique of injection of minority carriers by selective illumination of the p-type (electrons) or n-type (holes) sides of the device, with a mechanically chopped HeNe laser beam. The photocurrent is detected with a lock-in amplifier.

Figure 2 shows the photocurrent multiplication as a function of reverse bias for electrons ( $M_e$ ) and holes ( $M_h$ ) at 300 K. The low photocurrent

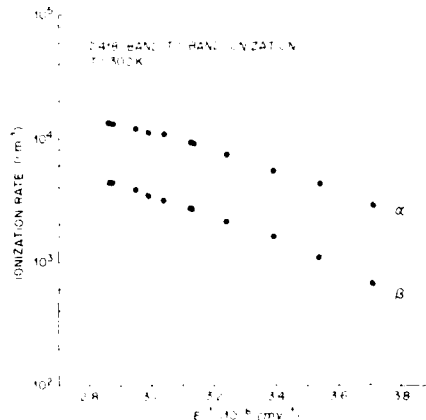


Figure 3. Ionization rate for electrons ( $\alpha$ ) and holes ( $\beta$ ) in sample D418 at 300 K, plotted against reciprocal field.

3. New avalanche multiplication effects in superlattices:  
impact ionization across the band-edge discontinuity.

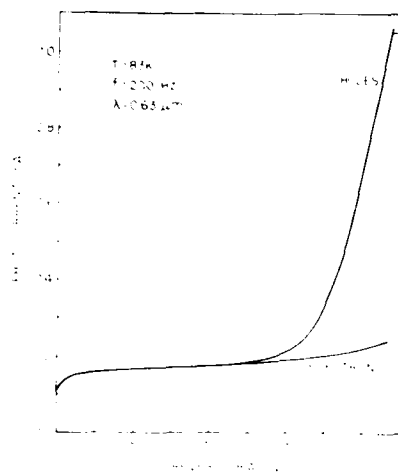


Figure 4. Photocurrent multiplication for pure hole and electron injection, due to ionization across the discontinuity in sample D622 at  $T \approx 85$  K.

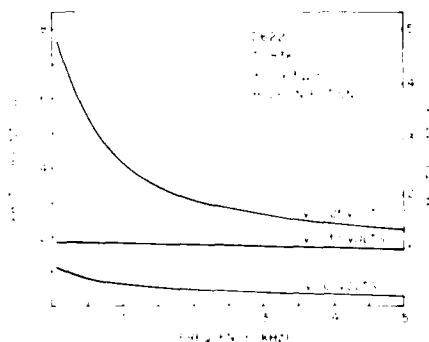


Figure 5. Photocurrent plotted against chopping frequency at unity gain ( $-10$  V) and in avalanche region ( $-21$  V) for D622.

We have observed new avalanche effects in superlattices, characterized by avalanche gain occurring at lower fields than band-to-band ionization, with much greater multiplication of holes than of electrons, and a strong frequency dependence in the kHz range.

Figure 4 shows the hole and electron multiplication for sample D622 at a temperature of  $\approx 85$  K. The device structure is similar to that of Figure 1 apart from the superlattice dimensions (see Table I). Multiplication occurs at fields of less than  $10^5$   $\text{Vcm}^{-1}$ . The hole multiplication is greater than that of electrons, with  $(M_h - 1)/(M_e - 1) \approx 20$ .

The frequency dependence was studied by varying the chopping frequency of the illumination. At unity gain ( $-10$  V) the photocurrent is constant between  $f = 0$  and  $6$  kHz (Figure 5). In the gain region ( $-21$  V) the photocurrent is strongly frequency dependent with a  $-3$  dB cutoff of  $\approx 1$  kHz. In contrast, we have reported microwave gains of  $\approx 12$  at frequencies of several GHz for band-to-band ionization in sample D418 (Mohammed et al, 1985).

The temperature dependence of this new ionization mechanism is directly opposite to that for band-to-band ionization. Figure 6 shows the photocurrent multiplication for holes at temperatures between  $90$  and  $300$  K for R397. There is a marked correlation between the temperature dependence of the dark current and multiplication curves. Diodes with very low dark currents do not show this effect but exhibit

band-to-band ionization at significantly higher bias (e.g. D418).

We have observed very similar behaviour in a number of materials grown by different techniques (Table I), including  $\text{InP}/\text{In}_{0.53}\text{Ga}_{0.47}\text{As}$  grown by gas source molecular beam epitaxy with very low density of deep levels

(Allam et al 1986). Homostructure pin diodes grown as control samples did not show such effects. This suggests that the behaviour is due to an intrinsic band-structure effect rather than ionization of deep levels.

The proposed mechanism is impact ionization across the band-edge discontinuity of carriers dynamically stored in the wells, by collision with carriers heated by the electric field in the barriers (Capasso et al 1985). Figure 7(a) shows a superlattice structure with n-type doped wells and undoped barriers. Electrons from the donor sites provide a dynamical reservoir of carriers in the wells. When a sufficiently high electric field is applied across the superlattice, electrons will be heated in the barrier regions with enough energy on entering the well to impact ionize a stored electron over the conduction band discontinuity, resulting in avalanche gain. This process can be viewed as ionization from deep "artificial traps", but has a much larger cross-section. Chuang and Hess (1985) have calculated the ionization rates for this process.

Our devices have undoped superlattice regions; the charge reservoir arises from thermally-generated dark current carriers (Figure 7(b)). Since there are both electrons and holes in the wells, both carrier types are multiplied. The threshold energy for the process is approximately twice the band-offset, thus the holes are multiplied at a greater rate than electrons in  $\text{Al}_{0.48}\text{In}_{0.52}\text{As}/\text{Ga}_{0.47}\text{In}_{0.53}\text{As}$  where the electron offset is about twice that for holes. The carriers lost by ionization are replaced

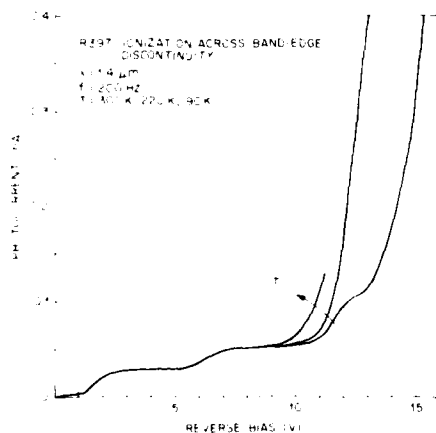


Figure 6. Temperature dependence of ionization across the discontinuity in R397: the arrow shows the direction of increasing temperature. The step-like structure in the photocurrent is due to successive depletion of the wells (Allam et al, 1986).

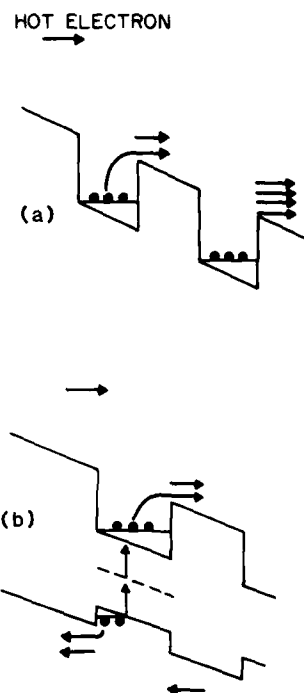


Figure 7. Mechanism of impact ionization across the band-edge discontinuity: (a) in n-type doped wells. (b) in undoped wells. The reservoir of carriers in the wells is supplied by thermally-generated dark-current carriers.



by dark current carriers generated via mid band-gap states, with a characteristic emission time  $\tau$  which may be of the order of  $10^{-3}$ s.

4. Very large ionization rate ratios in multiple graded-well superlattices.

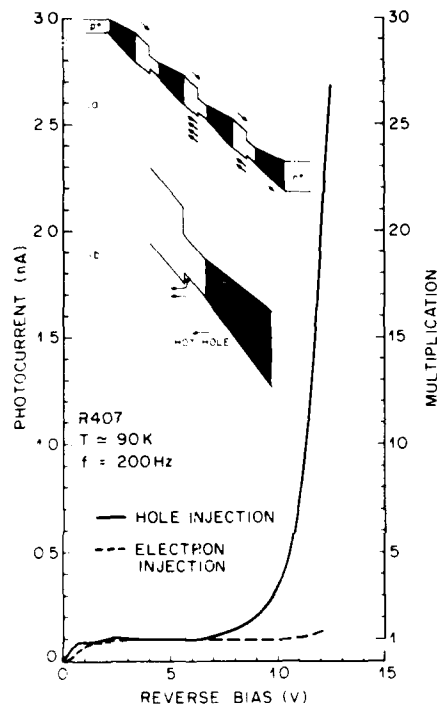


Figure 8. Impact ionization over the discontinuity in a superlattice with graded wells: Photocurrent multiplication of electrons and holes. The inset shows: (a) single carrier multiplication of holes for a solid-state photomultiplier. (b) mechanism for hole multiplication. Electrons are not multiplied as there is no storage of electrons within the graded wells. (The graded regions are shaded).

electron gain provides feedback resulting in a large hole gain (maximum measured gain  $\approx 50$  at 10Hz and -12 V). The onset of electron gain occurs at a field of  $1-2 \times 10^5$  Vcm $^{-1}$ , which is similar to the field at which band-to-band ionization occurs in bulk Ga $_{0.47}$ In $_{0.53}$ As. It therefore appears that multiplication of holes (only) occurs via ionization over

To further reduce the multiplication of electrons via ionization over the offset, we have utilized grading of the wells to reduce the density of electrons stored in the well. The Al $_{0.48}$ In $_{0.52}$ As / Ga $_{0.47}$ In $_{0.53}$ As superlattice pin photodiodes with compositionally graded interfaces at the exits of the wells were grown by computer-controlled MBE. Further details of the growth will be provided in a later paper. The dimensions of sample R407 are shown in Table 1.

Below a reverse bias of  $\approx 5$  V, there is storage of both electrons and holes in the wells. At higher fields the graded region becomes inverted thus there can be no storage of electrons or multiplication by ionization over the discontinuity.

Figure 8 shows the hole- and electron- initiated gain at a frequency of 200 Hz and a temperature of 90 K, for the sample with three periods. For pure hole injection, avalanche multiplication occurs at a reverse bias of -7 V and reaches  $M \approx 20$  at -12 V. For electron injection, the multiplication is less than 1.4 at -12 V, resulting in a value of  $(M_h - 1)/(M_e - 1)$  in excess of 50. This is, the highest value measured in a III-V material.

For the case of unity electron gain, the maximum hole multiplication would be 8 ( $2^3$ , corresponding to the 3 periods) (Figure 8 (a)). The presence of some

the band-edge discontinuity, and the feedback is accounted for by band-to-band impact ionization of electrons.

Table I. Dimensions of superlattices.

| Wafer # | Composition  | Number of Periods | Barrier width | Well width |
|---------|--|-------------------|---------------|------------|
| D418    | $\text{Al}_{0.48}\text{In}_{0.52}\text{As}/\text{Ga}_{0.47}\text{In}_{0.53}\text{As}$                              | 35                | 139 Å         | 139 Å      |
| D384    | $\text{Al}_{0.48}\text{In}_{0.52}\text{As}/\text{Ga}_{0.47}\text{In}_{0.53}\text{As}$                              | 48                | 104 Å         | 104 Å      |
| D620    | $\text{Al}_{0.48}\text{In}_{0.52}\text{As}/\text{Ga}_{0.47}\text{In}_{0.53}\text{As}$                              | 20                | 200 Å         | 200 Å      |
| D622    | $\text{Al}_{0.48}\text{In}_{0.52}\text{As}/\text{Ga}_{0.47}\text{In}_{0.53}\text{As}$                              | 20                | 465 Å         | 230 Å      |
| D676    | $\text{Al}_{0.48}\text{In}_{0.52}\text{As}/\text{Ga}_{0.47}\text{In}_{0.53}\text{As}$                              | 20                | 450 Å         | 450 Å      |
| A064    | AlSb/GaSb  | 25                | 200 Å         | 200 Å      |
| 25FebG6 | InP/ $\text{Ga}_{0.47}\text{In}_{0.53}\text{As}$   | 10                | 500 Å         | 300 Å      |
| R407    | $\text{Al}_{0.48}\text{In}_{0.52}\text{As}/\text{Ga}_{0.47}\text{In}_{0.53}\text{As}$<br>(1022 Å graded well exit) | 3                 | 292 Å         | 501 Å      |
| R397    | $\text{Al}_{0.48}\text{In}_{0.52}\text{As}/\text{Ga}_{0.47}\text{In}_{0.53}\text{As}$<br>(700 Å graded well exit)  | 5                 | 300 Å         | 700 Å      |

#### Acknowledgement

We would like to thank P.W.Foy and A.L.Hutchinson for device processing, and S.M.Abys for SIMS analysis. One of the authors (J.A.) acknowledges financial support from the U.K. Science and Engineering Research Council.

#### References

- Allam J, Capasso F, Panish M B and Hutchinson A L 1986 Appl. Phys. Lett. **49** 707
- Capasso F 1985 in *Semiconductors and Semimetals*, edited by R.K. Willardson and A.C.Beer (New York: Academic Press) **22** D 2
- Capasso F, Allam J, Cho A Y, Mohammed K, Malik R J, Hutchinson A L and Sivco D L 1986 Appl. Phys. Lett. **48** 1294
- Chuang S L and Hess K 1986 J. Appl. Phys. **59** 2885
- Juang F Y, Das U, Nashimoto Y, and Bhattacharya P K 1985 Appl. Phys. Lett. **47** 972
- Mohammed K, Capasso F, Allam J, Cho A Y and Hutchinsom A L 1985 Appl. Phys. Lett. **47** 597
- Pearsall T P 1980 Appl. Phys. Lett. **36** 218

### III-V superlattice photodiodes

F.-Y. Juang, W. Li, P.K. Bhattacharya, U. Das and A. Chin  
Solid State Electronics Laboratory  
Department of Electrical Engineering and Computer Science  
The University of Michigan, Ann Arbor, MI 48109

D.J. Jackson and D.L. Persechini  
Hughes Research Laboratories  
3011 Malibu Canyon Road, Malibu, CA 90265

**Abstract** Enhanced  $\alpha/\epsilon$  ratios  $\sim 2$ -10, are measured in GaAs/AlGaAs multiquantum wells at 300K. Measurement of  $M_n$ ,  $M_p$  and  $\alpha/\epsilon$  is difficult for InGaAs/InAlAs superlattices due to a monotonically increasing photocurrent with increase of reverse bias. Avalanche photodiodes made with both materials show responsivity  $\sim 0.3$ -1.0 A/W at 0.5V<sub>BR</sub>, avalanche gains  $\sim 10^3$  and bandwidths 12GHz at 0.5V<sub>BR</sub>. A modulated barrier photodiode using InGaAs/InAlAs small-period ( $\sim 80\text{\AA}$ ) superlattice in part of its structure gives extremely high responsivity  $\sim 50$  A/W.

#### 1. INTRODUCTION

It has been predicted and shown that GaAs-Al<sub>x</sub>Ga<sub>1-x</sub>As superlattices (SL) can exhibit enhanced ionization coefficient ratios  $\alpha/\epsilon$  (Chin et al 1980, Capasso et al 1982). This makes them attractive materials for fabricating low-noise avalanche photodiodes (McIntyre 1966) and some performance characteristics of such devices have been reported (Larsson et al 1985). We present here a detailed account of the measurement of these coefficients in GaAs/AlGaAs and InGaAs/InAlAs superlattices and multiquantum wells. Some performance characteristics of photodiodes made with these materials are also described and analyzed.

We have also studied the performance of InGaAs/InAlAs modulated barrier diodes with a superlattice incorporated in one part of the device. Extremely large responsivities are measured in these devices and it is thought that the recently proposed mechanism of effective mass filtering (Capasso et al 1985) may be partly responsible.

#### 2. MOLECULAR BEAM EPITAXIAL GROWTH AND DEVICE FABRICATION

The GaAs/Al<sub>x</sub>Ga<sub>1-x</sub>As and In<sub>0.53</sub>Ga<sub>0.47</sub>As/In<sub>0.52</sub>Al<sub>0.48</sub>As superlattice photodiodes were grown in a three-chamber RIBER 2300 Modutrac MBE growth system. Typical growth temperature of the GaAs and InP-based structures were 630 and 500°C, respectively. Three classes of superlattices were studied:

i)  $L_z, L_B \sim 30\text{-}50\text{\AA}$ ; ii)  $L_z, L_B \sim 100\text{-}200\text{\AA}$ ; and iii)  $L_z, L_B \sim 500\text{\AA}$ .

Two distinct types of  $p^+ - n^- - n^+$  diode structures were used for impact ionization studies and for measuring photodiode performance. In the former case the top  $p^+$  layer was at least  $2\text{ }\mu\text{m}$  thick to enable pure electron injection upon shining intrinsic light on the top surface. In the photodiodes, the top layer was  $\sim 0.5\text{ }\mu\text{m}$  thick and consisted of a wider bandgap material (AlGaAs or InAlAs). The superlattice multiplication/absorption region was typically  $2\text{ }\mu\text{m}$  thick. Mesa diodes with  $250\text{ }\mu\text{m}$  diameter were delineated by standard photolithography for the various measurements. The current-voltage characteristics in the superlattice photodiodes were measured at 300K and lower temperatures. Measured dark currents at half the breakdown voltage ( $V_{BR}$ ) are less than 1 nA in the GaAs/AlGaAs materials and are less than 30 nA in the InGaAs/InAlAs system. It was evident from the temperature dependence of  $V_{BR}$  that avalanching is the dominant breakdown mechanism in both material systems.

### 3. IMPACT IONIZATION PHENOMENA IN SUPERLATTICES

#### 3.1 GaAs/AlGaAs Superlattice:

The doping in the superlattice regions of all devices studied is  $\sim (1\text{-}3) \times 10^{15}\text{ cm}^{-3}$ , derived from capacitance-voltage data. The reverse breakdown voltage  $V_{BR}$  is in the range of 50-100 V. Electron and hole-initiated photomultiplication was generated by illuminating the diodes with a chopped He-Ne  $5\text{ }\mu\text{m}$  diam. laser ( $\lambda = 6328\text{ \AA}$ ) beam. Pure hole injection was achieved by illuminating the diode through a hole etched into the  $n^+$  substrate. Electron-initiated multiplication was achieved by illuminating the  $p^+$  layer on the top of the mesa structure. To obtain the electron and hole multiplication factors, appropriate stable values of the photocurrent at low bias values were considered. Measurements were first made on (001) GaAs whose impact ionization coefficients are fairly well known to calibrate the system. Since  $L_B, L_z$  are both much smaller than the usual values of  $\alpha^{-1}$  and  $\beta^{-1}$  measured in these wide band-gap semiconductors, the relationships between the multiplication factors and the impact ionization coefficients applicable for superlattices simplify to those that are used for bulk semiconductors (Stillman et al 1977).

Figure 1 depicts the electron and hole impact ionization coefficients in a sample with  $L_B = 570\text{\AA}$  and  $L_z = 424\text{\AA}$ . In the range of fields that these measurements were made  $\alpha/\beta \sim 10$ , which is in good agreement with data reported by Capasso et al (1982). Figure 2 depicts the measured impact ionization coefficients in superlattices with smaller wells and barriers. The values of  $\alpha(E)$  for all three samples shown in Fig. 2 remain fairly constant (represented by the cross-

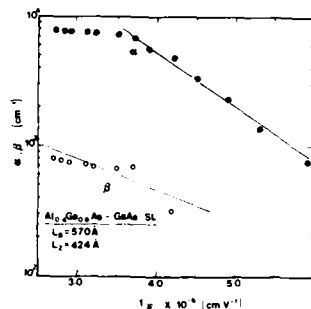


Fig. 1 Measured  $\alpha$  and  $\beta$  in GaAs/AlGaAs multi-quantum wells with large  $L_Z$  and  $L_B$ .

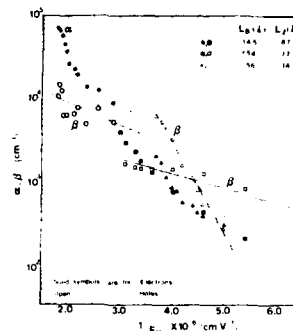


Fig. 2 Electron and hole impact ionization coefficients in GaAs/AlGaAs superlattices with varying  $L_Z$  and  $L_B$ .

hatched region) and can be approximately fitted by the equation,

$$\alpha(E) = 8.5 \times 10^5 \exp(-1.59 \times 10^6/E) \text{ cm}^{-1}$$

The values of  $\alpha(E)$ , on the other hand, are very sensitive to superlattice parameters. In quasi-two-dimensional systems carrier-phonon interactions can be greatly enhanced (Holonyak et al 1980). The electrons, however, with smaller effective mass are not truly confined in wells with  $L_B < 160 \text{ Å}$  and have fairly high energies relative to the GaAs conduction-band edge. Therefore, electron scattering in the quantum wells is very limited and the measured values of  $\alpha$  reflect, within limits of experimental error, bulklike behavior. The holes, on the other hand, have a much larger mass and a smaller scattering length. Therefore, it is expected that hole multiplication will be dependent on their confinement and scattering in the quantum wells, which in turn depend on the well widths. Furthermore, the coupling between the wells will also alter the degree of confinement. As expected, we see that at higher field values of  $\beta$  for the SL with  $L_B = 56 \text{ Å}$ ,  $L_Z = 34 \text{ Å}$  are higher than those for the superlattice with  $L_B = 145 \text{ Å}$ ,  $L_Z = 87 \text{ Å}$ . In uncoupled systems, with large wells and barriers, the mechanism of enhancement of  $\alpha/\beta$  has been discussed before (Capasso et al 1982). In this case the enhancement probably results from a periodic lowering of the threshold ionization energy of the electrons as they traverse an  $\text{Al}_x\text{Ga}_{1-x}\text{As}$  barrier and reach a GaAs well. The holes, by virtue of their large mass and greater confinement cannot participate in this process.

### 3.2 $\text{In}_{0.53}\text{Ga}_{0.47}\text{As} - \text{In}_{0.52}\text{Al}_{0.48}\text{As}$ Superlattice

Photocurrent measurements with very low levels of injection ( $I_{ph}=2\text{nA}$ ) were made on three types of superlattices, each distinguished by their well and barrier widths. Measurements in this case were done at 300 and 77K. The electron and hole photocurrents at -5V were made approximately equal by adjusting the light intensity. Measured electron and hole photocurrents for a typical diode at 300 and 77K are shown in Fig. 3(a) and (b), respectively. A distinct feature to be observed here is that the photocurrent increases monotonically with reverse bias at room and low temperatures, which is also true for other structures. This makes an accurate estimation of carrier multiplication and the impact ionization coefficients almost impossible in this material.

On examining the electron and hole multiplication processes as the temperature is lowered it is seen that for samples with  $L_z=L_B = 30\text{\AA}$ , the electron multiplication increases approximately by a factor of 4. On the other hand, in samples with  $L_B=L_z = 500\text{\AA}$ , both electron and hole multiplication are reduced as the temperature is lowered. For structures with  $L_z=L_B=90\text{\AA}$ , the electron multiplication is invariant, while that for hole increases slightly at lower temperatures. It is also to be noted that the multiplication process in the samples with large wells and barriers starts at fields almost half of that in samples with small wells and barriers. We conclude that in the former, multiplication is a mixed process, including band-to-band, and well-localized (Capasso et al 1986) single-carrier multiplication. For small wells and barriers, multiplication is dominated by a band-to-band process. The significant increase in electron multiplication at low temperatures in these samples is probably due to reduced phonon scattering.

### 4. PERFORMANCE OF SUPERLATTICE AVALANCHE PHOTODIODES

The spectral response of the photodiodes was measured at room temperature. External quantum efficiencies of  $\sim 86\%$  at  $V=-0.5V_{BR}$  are estimated from the measured responsivity in the GaAs/AlGaAs devices. The responsivities are generally smaller in diodes with large wells and barriers ( $L_z, L_B > 500\text{\AA}$ ) probably because photogenerated carriers in the wells recombine before they contribute to the photocurrent. Spectral response characteristics measured in the InGaAs/InAlAs devices are very similar and are shown in Fig. 4. The measured avalanche gains in GaAs/AlGaAs SL photodiodes are greater than 1000 near the breakdown voltage. From measured responsivities in InGaAs/InAlAs photodiodes, a.c. gains  $\sim 10$ -100 are estimated near the breakdown voltages. These high values of gains are extremely encouraging.

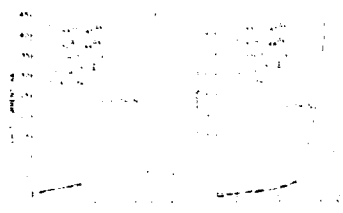


Fig. 3 Measured electron and hole photocurrents in InGaAs/InAlAs SL photodiode at (a) 300, and (b) 77K.

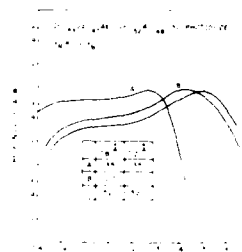


Fig. 4 Spectral response characteristics of photodiode with InGaAs/InAlAs superlattice and multiquantum well absorption regions.

The response of a large-area ( $A = 4.9 \times 10^{-4} \text{ cm}^2$ ) GaAs/AlGaAs superlattice device to 100 ps laser pulses, obtained by driving a GaAs laser with a comb generator is characterized by a temporal width (FWHM) of 250 ps. The capacitance of the device was  $\sim 3$  pF. Taking into account the diode and load resistance, and the length of the electron drift region (2  $\mu\text{m}$ ) it is clear that the response is limited by capacitance effects. As a comparison some preliminary measurements of the frequency response of smaller diodes ( $A = 5.4 \times 10^{-5} \text{ cm}^2$ ) under non-avalanche conditions with GaAs/AlGaAs and InGaAs/InAlAs superlattice absorption regions were also made. For these measurements the outputs of a pair of matched laser diodes were heterodyned to produce a microwave signal at the difference frequency. The detector response to this microwave input was then recorded with a microwave spectrum analyzer over the zero to 17GHz frequency range (Gee et al 1986). The capacitance of the devices was  $< 1$  pF at 0V bias. The data are shown in Fig. 5. Essentially, a 3-dB bandwidth of 11-12 GHz was measured in devices with large wells and barriers and the bandwidth decreased to  $\sim 8$ GHz as  $L_z$  and  $L_b$  decreased to 30Å. These results are very encouraging and indicate that high speed superlattice photodiodes can be realized.

##### 5. THE SUPERLATTICE MODULATED BARRIER DIODE

The modulated barrier diode (Chen et al, 1981) can be used as a detector with internal gain, which results from enhanced thermionic emission over a potential barrier. In addition, this diode also behaves as a majority carrier device. We have fabricated a photodiode in which an InGaAs/InAlAs superlattice ( $L_z = 45\text{\AA}$ ,  $L_b = 30\text{\AA}$ ) is incorporated in one arm (inset of Fig. 6). The

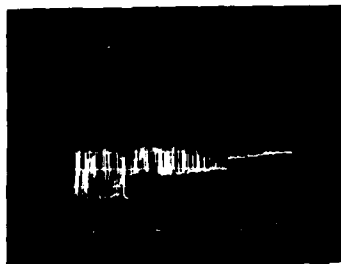


Fig. 5 Frequency response of GaAs/AlGaAs SL photodiode,  $L_z=417\text{\AA}$ ,  $L_B=556\text{\AA}$ .

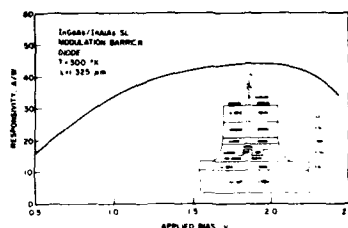


Fig. 6 Measured bias dependent responsivity of modulated barrier diode.

incorporation of the superlattice changes the spectral response and reduces the dark current. The measured bias-dependent responsivity of a typical device is shown in Fig. 6. Responsivities as high as 50 A/W are obtained at  $T = 300\text{K}$ . This high value of gain may be due to a combination of enhanced thermionic emission and effective mass filtering (Capasso et al 1985). The latter effect will particularly be operative if the adequate voltage drops across the superlattice and perpendicular electron transport occurs by miniband conduction. Further experiments and theoretical modeling of the current-voltage characteristics are in progress.

#### References

- Capasso F, Tsang WT, Hutchinson AL, and Williams GF 1982 Appl. Phys. Lett. 40, 38  
 Capasso F, Mohammed K, Cho AY, Hull R., and Hutchinson AL 1985 Phys. Rev. Lett. 55, 1152  
 Capasso F, Allam J, Cho AY, Mohammed K, Malik RJ, Hutchinson AL, and Sivco D 1986 Appl. Phys. Lett. 48  
 Chen CY, Cho AY, Garbinski PA, Bethea CG, and Levine BF 1981 Appl. Phys. Lett. 39, 340  
 Chin R, Holonyak N, Stillman Jr GE, Tang JY, and Hess K 1980 Electron Lett. 16, 467  
 Gee CM, Thurmond GD, Yen HW, and Blauvett H 1986 Proc. Integrated and Guided-Wave Optics Conference  
 Holonyak N, Kolbas Jr, RM, Dupuis RD, and Dapkus PD 1980 IEEE J. Quantum Electron QE-16 170  
 Larsson A, Yariv A, Tell R, Maserjian J, and Eng ST 1985 Appl. Phys. Lett. 47  
 McIntyre RJ 1966 IEEE Trans. Electron Devices ED-13 164  
 Stillman GE and Wolfe CM 1977 Semiconductors and Semimetals (Academic, New York) 12, 291



## **High quality lattice matched InGaAs/InP heterostructures prepared by atmospheric pressure MOVPE for high speed photodetectors**

**J.P. André, J.N. Patillon, J.L. Gentner, E.P. Menu, D. Moroni, G.M. Martin**

L.E.P.\* 3, avenue Descartes, 94451 LIMEIL-BRENNES CEDEX (FRANCE)

\* Laboratoires d'Electronique et de Physique appliquée :  
A member of the Philips Research Organization

**Abstract.** A simple but performant semi-planar PIN photodiode is described, based on a high quality AP.MOVPE heterostructure. The heterostructure interface is shown to be of very high quality, i.e. flat and sharp within 2-3 monolayers as deduced from sharp and intense photoluminescence from 140, 80, 26 and 14 Å wide quantum wells. Furthermore, this interface exhibits very high 2 DEG mobilities up to  $250\,000\text{ cm}^2/\text{Vs}$  at 4 K and almost free from interface states. The corresponding band offset is clearly demonstrated to be  $225 \pm 10\text{ meV}$ .

### **1. Introduction**

MetalOrganic Vapor Phase Epitaxy (MOVPE) is receiving a great deal of attention due to its ability to grow pure multiple heterostructures necessary for optoelectronic applications, and in particular for photodetectors (André et al 1985a, Poulain et al 1985, Wang and Carey 1985, Nelson et al 1985, Dupuis et al 1986). The purpose of this paper is to show the extremely high quality of bulk InP and GaInAs materials, and of their corresponding interfaces obtained by atmospheric pressure MOVPE. Then a new, called SEMI-PLANAR, PIN photodetectors structure, is described which takes advantage of that high quality material.

### **2. Experimental**

Most of the details concerning the used atmospheric pressure MOVPE growth technique have been given elsewhere (André et al 1985b, Menu et al 1986). TEI (TriEthylIndium) has been chosen as the In source because of its high purity and the growth temperature lies in the 570 - 640°C range. Special attention has been given in order to minimize both transient effects originating from the gas switching process during the growth of heterostructures, and depletion of In in the gas phase, due to parasitic quartz catalyzed side reaction. Only one composition of the ternary, i.e. Ga<sub>0.47</sub>In<sub>0.53</sub>As lattice matched on InP, has been grown and will later simply be referred to as (GaIn)As.

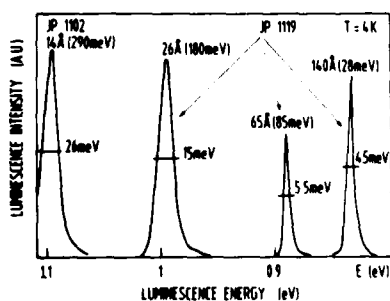
Photoluminescence properties have been analysed using an AR 1000 Jobin-Yvon Monochromator and a Ge cooled detector. Shubnikov-de Haas experiments have been performed in a 7 T magnetic field, He cooled Oxford

Cryostat. Accurate capacitance and current measurements were performed using a HP 4175 A digital capacitance meter and a 617 Keithley picoammeter.

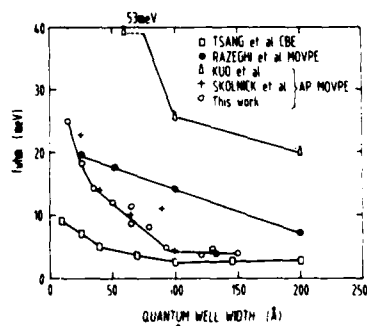
### 3. Material assessment

The high purity of materials has been evidenced (Menu et al 1986) by the low values of doping level ( $n = 2-5 \times 10^{14} \text{ cm}^{-3}$  for InP and  $n = 1-3 \times 10^{15} \text{ cm}^{-3}$  for InGaAs) and high corresponding values of mobilities  $\mu$ . In the case of InP,  $\mu$  is routinely between 80 000 to 100 000 and frequently reaching 120 -140 000  $\text{cm}^2/\text{Vs}$ . (GaIn)As lattice matched on InP is always grown with a thin InP buffer. Mobilities have always been deduced from thick (3  $\mu\text{m}$ ) (GaIn)As layers, and Hall values routinely exceed 10 000 (best value = 10 750) at 300°K and 78 000  $\text{cm}^2/\text{Vs}$  (best value = 86 300) at 77 K. These high values at low temperature might have been slightly boosted by the presence of a 2 dimension electron gas (2 DEG) at the GaInAs/InP interface (see below).

Thanks to very sharp transition of composition, (GaIn)As quantum wells (Q.W.) have been realized. An example of a photoluminescence (PL) from a Frijlink type series of 26 Å, 63 Å and 140 Å thick wells is given in fig. 1. They exhibit very strong and sharp peaks with FWHM equal to 15, 5.5 and 4.5 meV respectively. This is comparable to, or even better than the best results published so far by Atmospheric Pressure MOVPE (Kuo et al 1985, Skolnick et al 1986), by low Pressure MOVPE (Razeghi et al 1985) or Chemical Beam Epitaxy (Tsang et al 1976) as seen in fig. 2. Single wells located at a distance  $D = 500 \text{ Å}$  from the surface have also been grown. The thinnest well gave rise to a PL peak 290 meV up-shifted in energy (see fig. 1), which should correspond (Bastard 1983) to a thickness of about 18 Å. The PL intensity is very large and, in the case of single wells, increases by a factor of 10 with respect to bulk material when the QW thickness decreases down to 14 Å. PL excitation has been made using an argon laser light mostly absorbed in the InP top layer. The capture of carriers in those (GaIn)As wells is supposed to be very efficient in view of the above observations and also because no luminescence is detected from the InP cap layer as long as its thickness  $D$  is lower than 3000 Å!

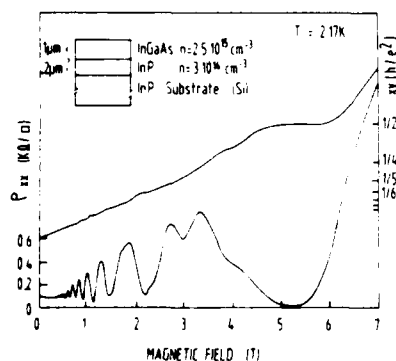


**Figure 1** : Photoluminescence spectra from two samples JP 1102 and 1119 recorded at 4 K. For each peak are given the well width and the energy shift (in bracket).

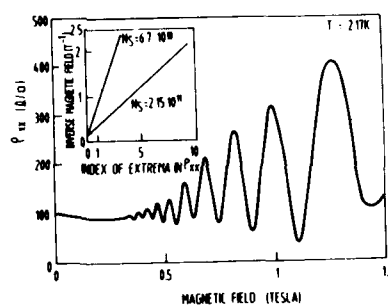


**Figure 2** : Photoluminescence Full width at Half maximum as a function of quantum well width at 4 K for different authors and growth techniques.

A detailed analysis of the PL behaviour of these wells will be given elsewhere (Moroni et al 1986). It demonstrates that the sum of roughness fluctuations of both interfaces of the wells is of the order of 4 to 6 mono-layers. The InP  $\rightarrow$  (GaIn)As interface, i.e. (GaIn)As grown on InP, has been extensively studied because the semi-planar photodiodes quality partly rely on it (see below). Fig. 3 presents the results of Shubnikov - de Haas measurements recorded from the usual bar configuration sample (2 current injecting contacts, 6 other as bias probes). Pronounced oscillations of magneto-resistance are detected as soon as the magnetic field  $B$  exceeds 0.3 T as seen in fig. 4. This complex oscillatory behaviour has been shown (Patillon et al 1986) to be related to the presence of two subbands distant by 8 meV from each other, with a sheet carrier concentration in the lower energy one  $NS_1 = 2.15 \times 10^{11} \text{ cm}^{-2}$  and  $NS_2 = 0.67 \times 10^{11} \text{ cm}^{-2}$  in the other. The Hall curve (fig. 3) exhibits quantified effects, as manifested by "plateaux", some corresponding to integer number index ( $n = 2, 5$ ), while some other integer index are missing. This more complex behaviour can be attributed to the presence of two subbands. The total sheet carrier concentration extracted in the usual way from these Hall data is equal to  $2.9 \times 10^{11} \text{ cm}^{-2}$ , a value similar to  $NS_1 + NS_2$  deduced from SdH analysis. The overall electron mobility in the 2 DEG has been calculated from  $\rho_{xx}$  at  $B = 0$ , using the value of  $NS_H$ , to be  $250\,000 \text{ cm}^2/\text{Vs}$ , which is a very high value for a 2 subband 2 DEG interface, and very much indicative of its quality. Such a high value also suggests that intersubband scattering for that material may not be as important as expected from general consideration.



**Figure 3** : Shubnikov de Haas and quantum Hall effect recorded at 2.17 K as a function of magnetic field  $B$



**Figure 4** : Magneto-resistance  $\rho_{xx}$  at low magnetic field on the same sample as that studied in figure 3.

Further analysis of that interface has been made from the point of view of perpendicular transport properties. The same interface material as above was used, but this time a blanket zinc diffusion, followed by a mesa etching, was made to obtain  $p^+/n$  mesa diode, the processing technology being the same as that used for the photodiode. Fig. 5 shows the variation of its dark reverse current (bias = -10 V) as a function of the inverse of temperature. Its behaviour is not any more a pure exponential and it cannot either be considered as a deep level related generation current (Patillon et al 1985), which is consistent with the fact that no deep

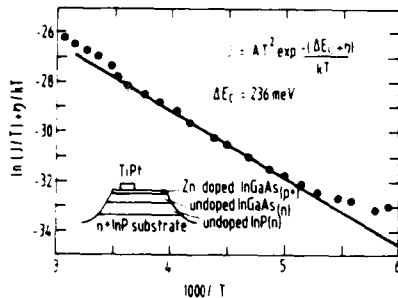
level has been detected by DLTS above  $10^{11} \text{ cm}^{-3}$ . But this behaviour very likely corresponds to the Fowler-Nordheim tunneling phenomena, which can be fitted by the following thermionic emission current equation (Wu et al 1979):

$$I = AT^2 \exp(\Delta E_c + \eta / kT)$$

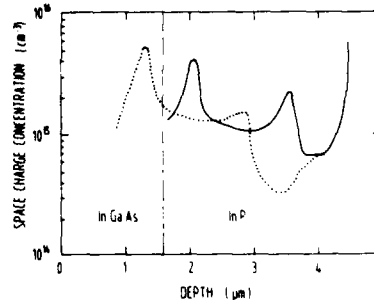
This equation takes into account a current flowing through an interface presenting a band off-set  $\Delta E_c$ , A being the Richardson constant and  $\eta$  the Fermi level energy in the (GaIn)As layer. From fig. 5, one obtains  $\Delta E_c = 0.236 \text{ meV}$ .

Capacitance measurements have also been proved to be very efficient in the characterization of the interface. As seen in fig. 6, the space charge concentration profile deduced from C-V curves present two peaks. The first peak P1 is detected at both 77 and 300 K and corresponds to the emptying of the 2 DEG under applied bias. The other peak P2 rises up in the range  $T < 100 \text{ K}$ , but smears out for  $T > 170$ . It corresponds to the emptying of a single electron trap. An iterative self-consistent approach has been used to solve the Poisson equation through the interface (Patillon et al 1986). It has led to the same value of band offset from 80 and 300 K data equal to  $\Delta E_c = 215 \pm 5 \text{ meV}$  and to parameters of the single electron trap (concentration =  $3.7 \cdot 10^{10} \text{ cm}^{-3}$ , activation energy =  $115 \text{ meV}$ ).

The small shift between the two C-V curves recorded at 77 and 300 K corresponds to a small change of doping in the layer in that temperature range.



**Figure 5** : Dark reverse current of a mesa junction diode made on a single hetero-junction.



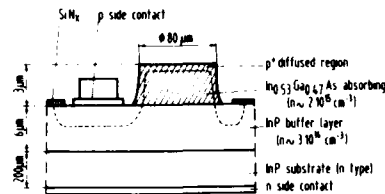
**Figure 6** : Space charge concentration profile deduced from C-V measurement recorded on mesa-junction diode made on a single hetero-junction, at low temperature (full curve) and high temperature (dotted curve).

Since this trap is not detected by DLTS as mentioned above, this means that it has a very low electron capture cross section and this suggests that it may be an acceptor. This is the first time that a single deep level, and not a band of deep states, is detected at one interface, and with a very low concentration. All these observations are coherent with the high value of the electron mobility in that 2 DEG interface.

It is worth noticing that the same value of  $\Delta E_c$ , i.e.  $225 \pm 10 \text{ meV}$ , has been measured from the behaviour of two different parameter i.e. the current and the capacitance, and in a wide range of temperature (80 to 400 K). This brings confidence to that value already estimated from photo-conductivity (Skolnick et al 1986).

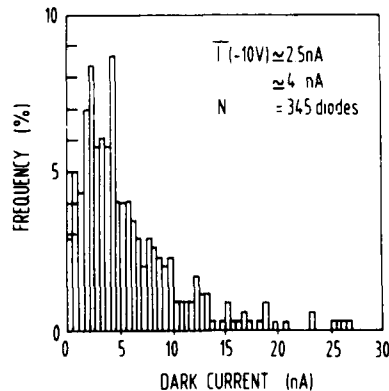
#### 4. Photodetectors

An optimized diode structure has been realized, called the SEMI-PLANAR structure. As shown in fig. 7, it consists in a single heterostructure with a mesa etching of the ternary layer. Then a single localized Zn diffusion, using a PECVD  $\text{SiN}_4$  mask, in a sealed ampoule, allows to make the p<sup>+</sup>/n junction, the p<sup>+</sup> layer being thin (0.7  $\mu\text{m}$ ) in (GaIn)As and large (2  $\mu\text{m}$ ) in InP. Then the Pt Au front side contact is evaporated on InP, instead of GaInAs in the usual process. This detector structure presents several combined advantages : i) reduction of surface leakage current originating at the junction edge since it is in the large gap InP material, ii) reduction of bulk leakage current essentially coming from the small band gap GaInAs material, the area of which is made minimal since it excludes the metallization pad, iii) increased reliability of the ohmic contact on a thick p<sup>+</sup> InP layer. Furthermore, the junction edge in InP is planar and

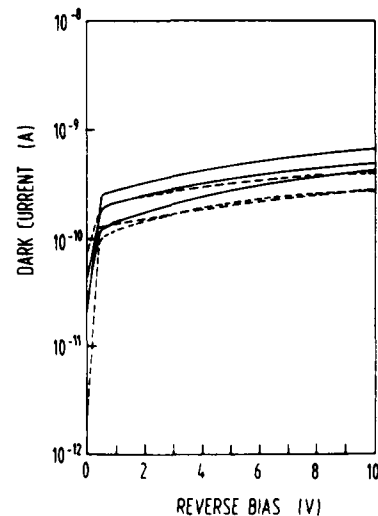


**Figure 7 :** Structure of semi-planar diodes. Diameter of active (GaIn)As area = 80  $\mu\text{m}$   
Surface of the overall junction area = 10 000  $\mu\text{m}^2$

thus easy to clean and passivate. As a matter of fact, very low dark current  $I_D$  is obtained as evidenced by the histogram shown in fig. 8, the best data being 200 pA at - 5 V and 300 pA at - 10 V for  $\text{SiO}_2$  passivated diodes as seen in fig. 9. These very good figures are also very much



**Figure 8 :** Histogram of semi-planar diode reverse dark current values at - 10 V bias. Mean value  $I$  and standard deviation  $\sigma$  are given in insert.



**Figure 9 :** Best reverse dark current curves recorded from semi-planar diodes.

coherent with the good quality of the MOVPE layers. This structure should also lead to very small capacitance value since the metallisation pad is on top of a very low doped ( $n \leq 3 \times 10^{14} \text{ cm}^{-3}$ ) region. The present value, close to 0.6 pF at -10 V, is expected to decrease as soon as a thicker InP buffer layer will be made. A detailed analysis of this semi-planar structure is to be given by Gentner et al, showing that the responsivity is as high as 0.9 A/W at 1.3  $\mu\text{m}$ , i.e. an external quantum efficiency at about 85 %. The speed of that device has not yet been measured. But one can already think that the small band offset  $\Delta E_c = 0.25 \text{ meV}$  is not a high barrier for fast electrons at  $T = 300 \text{ K}$  and that the cut-off frequency of these SEMI-PLANAR diodes should be similar to that of more classical mesa diode which reaches 3 GHz (André et al 1985a).

**Acknowledgement** : The authors wish to thank P. Gentric for growing one of the QW structures, and B.G. Martin and R. Duchesne for their skillfull assistance.

### References

- André J P, Chané J P, Gentner J L, Mallet-Mouko C, Martin B G, Martin G M, Menu E P, Patillon J N, 1985 a, presented at 5th IOOC, Venezia (Italy) October - Technical Digest vol 1, p. 541-544
- André J P, Menu E P, Erman M, Meynadier M H, Ngo T, 1985 b, presented at Electronic Material Conference, Boulder and published in J. Electron. Mat. 15, 71
- Bastard G, 1983, Proceedings NATO School on MBE and Heterostructures, Erice (Sicily) (Ed. L.L. Chang, K. Ploog, Amsterdam) p. 381
- Dupuis R D, Campbell J C, Velebir J R, 1986, Electron. Lett. 22, 49-50
- Gentner J L, Patillon J N, André J P, Martin B G, Mallet-Mouko C, Chané J P, Martin G M, 1986, to be published at the 12th European Conference on Optical Communications Barcelona, Spain).
- Kuo C P, Fry K L, Stringfellow G B, 1985, Appl. Phys. Lett. 47, 885
- Menu E P, Moroni D, Patillon J N, Ngo T, André J P, 1986, presented at ICCG-8 York (UK) July and to be published in J. Crystal Growth.
- Moroni D, André J P, Menu E P, Gentric P, Patillon J N, 1986, to be published in J. Appl. Phys.
- Nelson A W, Wong S, Ritchie S, Sargood S K, 1985, Electron. Lett. 21, 838-840
- Patillon J N, Makram-Ebeid S, Chané J P, Martin B G, Martin G M, 1985, Gallium Arsenide and Related Compounds, Inst. Phys. Conf. Ser., 74, 475-478.
- Patillon J N, Menu E P, André J P, Martin G M, 1986, to be published at the 2nd Conf. on Superlattices, Microstructures and microdevices, Göteborg (Sweden)
- Poulain P, Razeghi M, Kazmierski K, Blondeau R, Philippe P, 1985, Electron. Lett. 21, 441-442
- Razeghi M, Nagle O, Weisbuch C, 1985, Gallium Arsenide and Related Compounds, Inst. Phys. Conf. Ser. 74, 379-384
- Skolnick M S, Tapster P R, Bass S J, Pitt A D, Apsley N, Aldred S P, 1986, Semicond. Sci. Technol. 1, 29-40
- Tsang N T, Schubert E F, 1986, Appl. Phys. Lett., 49, 220
- Wang S Y, Carey K, 1986, Paper III A-8 presented at the 43rd Device Research Conference, Boulder (USA)
- Wu C.M. and Yang E.S., 1979, Solid State Electron. 22, p. 241

## Single-crystal integration of an optical interference filter and photodiode

P. L. Gourley, R. M. Biefeld, and T. E. Zipperian

Sandia National Laboratories, Albuquerque, NM 87185

**Abstract.** We have produced an all-semiconductor, single-crystal, integrated optical detector for the visible, in which a photodiode and an optical interference filter (high reflector) were integrated in a single growth run by metal-organic chemical vapor deposition. In this structure, the high reflector is both optically and electrically active, being composed of alternating, doped, quarter-wave layers of GaP and  $\text{GaAs}_{0.2}\text{P}_{0.8}$ . The diode is a p-n junction superlattice composed of much thinner layers of GaP and  $\text{GaAs}_{0.35}\text{P}_{0.65}$ . The photodiode responds to light from 460 to 600 nm, while the high reflector rejects a narrow 10 nm band centered near 500 nm. The rejection factor is ~7 dB for these prototype devices. The quantum efficiency, linearity, temperature and bias dependence of the spectral response are reported here.

### 1. Introduction

In recent years, increasing attention has been focused on the use of all-semiconductor optical integrated circuitry to perform switching, modulation, demodulation, waveguiding, and detection of photonic signals. The success of the all-semiconductor approach to integrated optics will depend on the ability to fabricate needed optical elements with existing and developing crystal growth methods. With existing growth techniques it has recently been demonstrated that it is possible to grow single-crystal III-V semiconductor multilayers with precision layer thicknesses corresponding to a quarter-wave of light in the visible and near infrared spectral regions (Gourley et al 1986a, 1986b). Although these semiconductor optical interference structures have not yet received much attention, they hold promise as a versatile new class of optically and electrically active interference filters which can be integrated with other device structures (Gourley 1985). Furthermore, these single crystal filters can be implemented with alternating layer materials which are either lattice-matched or lattice-mismatched in the bulk.

Here, we report the growth, fabrication, and characterization of a single-crystal, integrated high-reflector/photodiode (HRPD) optical detector for operation in the visible wavelength range. This device functions as a visible wavelength band optical detector with selective, narrow-wavelength band rejection for suppression of unwanted monochromatic light. The device was produced in a single growth run by metal-organic chemical vapor deposition of both a p-n junction  $\text{GaAs}_{1-x}\text{P}_x/\text{GaP}$  strained-layer superlattice photodiode and a quarter-wave high reflector composed of alternating layers of GaP (low index material) and  $\text{GaAs}_{1-x}\text{P}_x$  (high index material) with the high index material outermost. In these filters, the difference in refractive index between adjacent layers is relatively small

(~2-4%) so that the high reflectance zone is quite narrow (~ 100 Å). This feature is attractive for wavelength-selective enhancement or suppression of transmitted or reflected light at an interface. Although small index difference means lower interlayer reflectance, we show that the net reflectance can be controlled over a wide range of values with total numbers of layers and uniformity that are practicable to achieve.

## 2. Experimental Methods

The structures were grown by a metal-organic chemical vapor deposition process described elsewhere (Biefeld 1986). A schematic of the structure is illustrated in Fig. 1. The HRPD's were grown onto a step-graded, n-type buffer layer which was grown onto an n-type <100>-oriented GaP substrate. The HRPD's were grown in the sequence {n-SLS,p-SLS,p-HR}, where SLS is a strained-layer superlattice of GaP and  $\text{GaAs}_{0.35}\text{P}_{0.65}$ , HR is the high reflector with N=50 periods of GaP (400 Å) and  $\text{GaAs}_{0.2}\text{P}_{0.8}$  (400 Å), and n and p refer to the doping type. All doping concentrations were in the mid  $10^{17}$  to low  $10^{18} \text{ cm}^{-3}$  range. Oppositely doped HRPD structures were also grown although fabrication was slightly more difficult. The SLS p-n junction photodiode in this structure is similar to previously reported SLS photodiodes which demonstrated high external quantum efficiency (Biefeld et al 1983). The HR quarter-wave layer thickness was designed to position the high reflectance wavelength  $\lambda_0$  near the peak wavelength of the isolated photodiode spectral response.

The grown materials were characterized in several ways. The compositions and layer thicknesses determined by x-ray diffraction. The interlayer thickness uniformity for a given sample was generally very high as determined in a separate Auger profiling study (Chamberlain and Wallace 1985). Although the compositions were relatively easy to control, the quarter-wave thickness was subject to greater fluctuation from run to run. The present study required a very tight tolerance (<10%) on layer thickness, which would have greatly benefited from an in situ thickness monitor. Finally, we mention that the electronic properties (minority carrier diffusion lengths, energy band gap, and absorption coefficient) of these materials have previously been studied (Osbourne et al 1987).

The devices were fabricated in the following sequence. After cleaning the top surfaces, a AuBe/Au deposition and lift-off process was performed to form p-type annular contacts. Next, an n-type AuGe/Ni/Au metallization was deposited fully across the bottom surface, and the wafer was annealed for 2 minutes at 425 °C in hydrogen gas. To electrically isolate different devices, a  $\text{SiO}_2$  layer was deposited, patterned with photoresist, and plasma-etched to expose the unwanted surface regions. These regions were subsequently etched away with a GaP etchant to leave mesa structures (0.3, 1.0, and 1.5 mm in diameter) which isolated the high

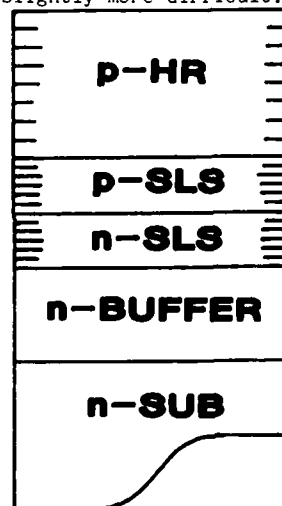


Fig. 1. Schematic diagram of the high-reflector/photodiode



reflector/photodiode layers. Finally, the remaining  $\text{SiO}_2$  was chemically removed, and the final surface cleaned. Before dicing, the electrical characteristics of the isolated devices were tested with an I-V curve tracer. In addition, the front surface reflectance of each device was measured in a microspectrophotometer. This enabled us to screen out devices with defective contacts or poor surface quality. As a last step, the best devices were scribed and mounted on carriers for subsequent testing.

In the I-V curves of a typical finished device (1.5 mm diameter), the forward turn-on voltage is about 1.6 V. For 6 decades of current below  $2 \times 10^{-8}$  A, the curve is logarithmic with ideality factor of 2.0. Above this range the forward series resistance can be approximated by a  $\sim 20 \Omega$  linear region which is determined by the contact resistance of the top metal annulus (area  $\sim 5\%$  of total). This demonstrates the thick HR is sufficiently conductive to avoid high series resistance. The reverse saturation current density is  $6.6 \times 10^{-9}$  A/cm<sup>2</sup> at  $-3$  V, and the reverse breakdown voltage is about  $-13$  V. These values are typical for p-n junctions fabricated with GaAs<sub>0.9</sub>P<sub>0.1</sub>/GaP SLS materials (Myers et al 1984). Thus, the electrical characteristics of these diodes are not degraded in any way due to the presence of the HR or the processing steps needed to fabricate the HRPD.

The optical response of the finished HRPD device was measured as a function of applied bias and temperature with a microspectrophotometer with beam diameter as small as 30  $\mu\text{m}$ . In addition, a laser beam of selected wavelength could be coupled into the microspectrophotometer for absolute radiometric measurements of the device quantum efficiency and response linearity. To measure absolute surface reflectance, uncalibrated reflectance spectra for the device and a reference mirror were separately measured. The two spectra were ratioed and corrected for the known absolute reflectance of the reference mirror. The error in this absolute measurement is less than a few percent.

### 3. Experimental Results

A measured reflectance spectrum of an HRPD is shown (solid curve) in Fig. 2a. The spectrum has a pronounced maximum of 0.86 near 500 nm due to coherent reflection of

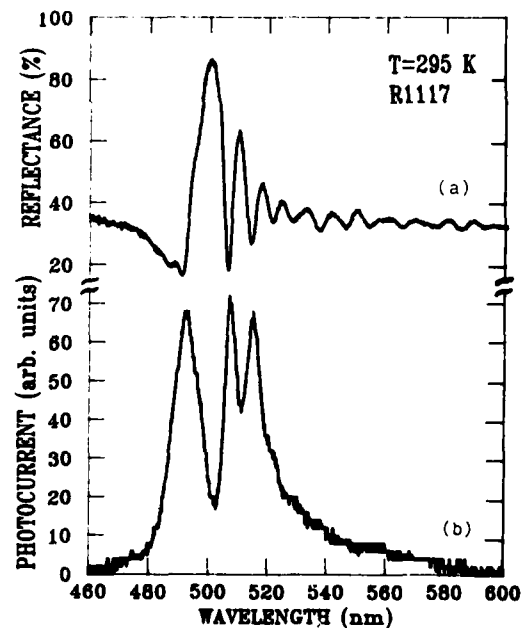


Fig 2. (a) Measured reflectance spectrum (solid line) of the front surface of a high-reflector/photodiode structure at room temperature. (b) Measured photocurrent versus wavelength for the same structure operated with no external bias.

light from the front surface and interior interfaces. The peak width is only 10 nm due to the small ~3% difference in the index of refraction between adjacent layers. According to the theory of optical interference filters (Macleod 1969), the wavelength of the central peak is given by  $\lambda_0 = 2(n_H d_H + n_L d_L)$  where  $n$  and  $d$  are the index and layer thickness, and  $H$  and  $L$  refer to high and low index layer, respectively. The peak reflectance is  $R_m = [(1-n^*)/(1+n^*)]^2$  where  $n^* = (n_H/n_L)^{2N}$  ( $n_H^2/n_L^2$ ) is an effective index of refraction. The width of the reflectance extremum is  $\Delta\lambda/\lambda_0 = 4(n_H - n_L)/\pi(n_H + n_L)$ . The characteristics of the high reflectance zone, peak position, height and width, predicted by these simple equations are in good agreement with the measured lineshape in Fig. 2a. As a side comment, we mention that we have fit spectra like these using theoretical spectra computed by the matrix field transfer method (Courley 1986a). We find that the refractive indices determined in the fit are within 2% of the literature values (Pikhtin and Yas'kov 1980) for indices of bulk GaP and GaAs  $\Gamma$ -X. We have estimated the effect of the doping and strain on the refractive index, and find that the change in index between adjacent layers is almost entirely due to the difference in composition.

In Fig. 2b., we show the measured HRPD spectral response at room temperature with zero external bias. The diode responds to light in the range 460 to 600 nm with peak response near 500 nm. In the HRPD spectrum, the effects of the high reflector are quite prominent. The photoresponse shows sharp minima near 502 and 515 nm corresponding to reflectance maxima in Fig. 2a. At 502 nm the HRPD response is suppressed by a factor of ~5, giving 7 dB rejection. Although this rejection factor of this prototype device is rather low for practical application, the result clearly demonstrates the concept of integrating an active device and interference filter by single crystal growth. Means of improving performance will be discussed shortly.

Using 5208 Å laser excitation, the HRPD response linearity and quantum efficiency was measured. We found a linear response over the range of irradiance levels investigated, encompassing 8 orders of magnitude from  $2 \times 10^{-7}$  W/cm<sup>2</sup> to 20 W/cm<sup>2</sup>. This data translates into a peak responsivity of 0.025 A/W or 13 % external quantum efficiency. The quantum efficiency is lowered slightly by absorption in the HR due to indirect X-point transitions. From the spectra in Fig. 1. (both (a) and (b)), it is evident that the HR starts to strongly absorb near 490 nm. This is due to a direct  $\Gamma$ -point transition. From spectrum (b) we determine a weak absorption onset near 600 nm and strong onset near 530 nm corresponding, respectively, to the X and  $\Gamma$  transition energies of the SLS in the junction region.

We have also measured the response characteristics over the temperature range 78 to 300 K. We find that the high reflectance peak  $\lambda_0$  shifts with temperature at a rate -0.02 nm/°C. This change is consistent with a decrease in refractive index of  $-2.3 \times 10^{-4}$ /°C for the HR. This value is typical for III-V semiconductors near a direct band edge. Over the same T-range, the photodiode peak response shifts faster, -0.10 nm/°C. This shift is explained by the temperature shift of the direct gap transition in the SLS junction. As a result of the difference in temperature shifts, the high reflectance band moves away from the peak of the diode response to longer wavelengths. Thus, for lower temperature operation, care must be taken to design HR wavelength to account for these temperature shifts. It should be noted that the T-shift for an all-semiconductor filter is

comparable to that in optical interference filters prepared with conventional materials by vacuum evaporation.

Finally, we have characterized the HRPD photoresponse at different values of applied reverse bias. With 1.5 volt reverse bias, we find an ~10% increase in the quantum efficiency accompanied by a small dark current of 17 pA. With 3 volts reverse bias, the quantum efficiency changes negligibly, and the dark current increases to about 200 pA. With the latter bias condition, the device noise increased substantially.

We have grown many other HR's with  $x=0.2$  corresponding to different layer thicknesses from 310 to 580 Å, including undoped and n and p-type structures. These data show that  $\lambda_0$  increases directly with layer thickness as expected from theory and can be varied over a wide range, 460 to 750 nm. The lower (upper) limit is imposed by absorption (layer critical thickness). It is important to note that this range includes the energy gaps for these multilayers (1.83-2.26 eV) as determined in separate absorption and photoluminescence experiments (Osborn et al 1987). Thus the HR wavelength and its energy bandgap can be varied independently. We have also grown and characterized several high reflectors corresponding to different numbers of periods  $N$ . The results are summarized in Fig. 3 by plotting the peak reflectance value against  $N$  (open points). The reflectance values extend from 0.30 for the bare GaP substrate to 0.90 for  $N=50$ . The calculated values for  $R_m$  (solid line) describe the data well. These data indicate that 100 periods must be grown to achieve  $R_m = 0.99$  which give 20 dB rejection for a practical HRPD device. There should be no fundamental problem in realizing these high reflectance values, provided strict control of uniformity of layer-to-layer thickness and doping is maintained. In addition, thicker structures with large  $N$  must be designed for longer wavelengths where absorption will be smaller.

#### 4. Discussion and Summary

Several important concepts are demonstrated with this device. First, we have demonstrated successful integration by a single growth process of a semiconductor optical interference filter with an active device. Second, this integration was carried out with materials which are lattice-

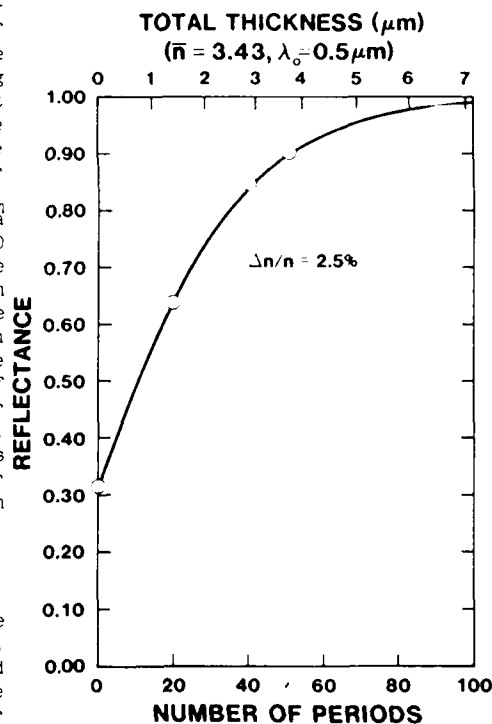


Fig. 3. Summary of measurements (open points) for several different structures corresponding to different numbers of periods  $N$ . For each structure, the measured peak reflectance  $R_m$  is plotted against  $N$ . The solid line is the calculated value of  $R_m$ .

mismatched in bulk. Third, we have demonstrated the concept of an electrically active optical interference filter: the high reflector is both electrically active (providing electrical contact to the buried junction) and optically active (providing enhanced reflectance from coherent, multiple interfacial reflections).

Single-crystal semiconductor multilayers for electrically active optical interference filters have a potentially very broad range of application, including detectors (as above), emitters, and bistable devices. They are technologically attractive because they can be integrated with other device structures. Furthermore, it should be possible to modify their optical properties by intense light or electric fields.

#### 6. Acknowledgements

The authors gratefully acknowledge the technical assistance provided by K. C. Baucom in the preparation of these structures, R. Caldwell, J. Clifton, and T. A. Plut in processing the devices, and A. E. McDonald in measuring the optical spectra. This work was supported by the U. S. Department of Energy under contract number DE-AC04-76DP00789.

#### 7. References

- Biefeld R M 1986 J. Electron. Mater. 15 193  
 Biefeld R M, Zipperian T E, Gourley P L and Osbourn G C 1983 Proceedings of the Electronic Materials Conference, Burlington, VT June 22-24 (Warrendale, PA:Metallurgical Society of AIME) p 60  
 Chamberlain M B and Wallace W O 1985 J. Vac. Sci. Technol. A3 2596  
 Gourley P L 1985 Superlattices and Microstructures 1 227, and references therein  
 Gourley P L Biefeld R M and Zipperian T E 1986a Appl. Phys. Lett. 49 242  
 Gourley P L and Drummond T J 1986b Appl. Phys. Lett. 49 489  
 Osbourn G C, Gourley P L, Fritz I J, Biefeld R M, Dawson L R, and Zipperian T E 1987 Semiconductors and Semimetals, edited by Willardson R K and Beer A C (New York: Academic, in press).  
 Macleod H A 1969 Thin film Optical Filters (London:Adam Hilger) chapter 5  
 Myers D R Biefeld R M Fritz I J Picraux S T and Zipperian T E 1984 Appl. Phys. Lett. 44 1052  
 Pikhtin A N and Yas'kov A D 1980 Sov. Phys. Semicond. 14 389

## **A (Ga,Al)As semiconductor scintillator with monolithically integrated photodiode: a new X-ray detector**

P. A. Glasow\*, W. W. Rühle\*\* and K. D. Schwarzmichel\*

\* Siemens AG, Central Research Laboratories, Erlangen, F.R.G.

\*\* Siemens AG, Medical Engineering Department, Erlangen, present address  
Max-Planck-Institut für Festkörperphysik, Stuttgart, F.R.G.

**Abstract.** A new type of a nuclear particle and X-ray detector with a (Ga,Al)As-GaAs heterojunction is demonstrated. A liquid phase epitaxial (Ga,Al)As layer of up to 200  $\mu\text{m}$  thickness with graded band gap acts as scintillator and the junction as photodiode with GaAs as absorbing layer. The detector can be arranged to hybrid or monolithical position sensitive arrays. Experimental results will be presented both for single detectors and linear arrays.

### 1. Introduction

In the last few years high internal luminescence efficiencies close to 100 % have been reported for various compound semiconductors used for infrared emitting diodes, in particular for GaAs and (Ga,Al)As (Roedel, Keramidas 1979, Leibenzeder, Heindl 1980). The band gaps of these semiconductors are four or five times smaller than the gaps of scintillators usually used for nuclear detectors. The mean energy for electron hole pair creation by high energetic particles or X-rays should therefore be strongly reduced in a "semiconductor scintillator".

However, two problems are inherent in this type of scintillator: Firstly, strong selfabsorption is expected in these direct gap semiconductors, and the absorbed photons are lost at least after several reabsorption steps if internal quantum efficiency is less than unity. Secondly, transmission of light out of the semiconductor surface is strongly reduced by the high refractive indices.

The first problem can be solved, at least partially, using a semiconductor with a graded band gap. The second difficulty can be overcome integrating monolithically a photodiode directly on the scintillator.

We want to show the concept of a new X-ray or nuclear radiation detector, the realization of the concept as well as experimental results with single detectors and detector arrays.

### 2. Concept and Operation Mode

A  $\text{p}^+-(\text{Ga,Al})\text{As}:\text{Si}$  epitaxial layer with a graded band gap acts as a scintillator with small average energy for electron hole pair creation (1) and high internal quantum efficiency. The expected self absorption of the scintillation light (2) within this "direct" semiconductor is avoided by two steps: first, the band gap increases in one direction due to a varying

Al mole fraction, and second, the Si doping causes a shift of the luminescence to lower energies relative to the absorption edge. A  $n^-$ -GaAs layer is monolithically integrated on the high energy gap side of the (Ga,Al)As layer, forming a  $p^+-n^-$  heterojunction. Photons propagating in direction of the increasing band gap (3) are absorbed (4) in the space

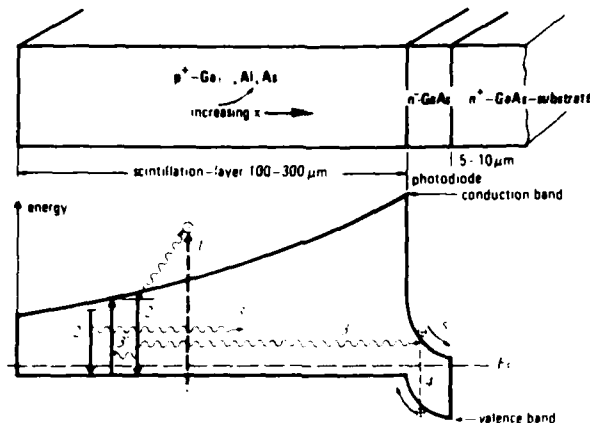


Figure 1: Structure and operation mode of the (Ga,Al)As-detector

charge region of the  $n^-$ -GaAs generating a photocurrent pulse. Photons propagating toward the decreasing band gap are reabsorbed (3'). However, due to "photon recycling" effects (Rühle, Hoffmann, Leibenzeder 1982) in these layers with high internal quantum efficiency, they are reemitted (3'') and can contribute to photocurrent.

The advantages of this new type of solid state detector are obvious: i) Smaller pair creation energy in comparison to ion crystal scintillators, ii) direct conversion of scintillation light into an electrical signal by the integrated photodiode, iii) high stopping power in contrast to Si, and iv) room temperature operation in contrast to Ge.

### 3. Sample Preparation

A high purity  $n^-$ -GaAs epitaxial buffer layer is grown on a  $n^+$ -GaAs substrate by liquid phase epitaxy. Subsequently, the  $p^+$ -(Ga,Al)As:Si doped layer is grown onto this buffer layer. Both steps are either performed in one graphite slider boat with different chambers for the two melts or in two completely separated procedures in different ovens. The second possibility results in a lower doping level of the buffer layer ( $n \sim 2 - 10 \times 10^{14} \text{ cm}^{-3}$ ).

The thicknesses vary between 70 and 150  $\mu\text{m}$  up to now. The Al mole fraction at the heterojunction is always about 30 % ensuring that the (Ga,Al)As at this point is still a direct gap semiconductor. Growth must be started at temperatures below the transition temperature (n to p) of the amphoteric Si in (Ga,Al)As in order to achieve p-type conduction. A graded band gap is obtained automatically due to the high distribution coefficient of Al, as revealed by a microprobe analysis.

#### 4. Experimental Results

First, we performed some photoluminescence experiments with "front" and "back" excitation in order to get some idea about selfabsorption in the (Ga,Al)As layers. For these experiments the substrate and the buffer layer are completely removed by chemical etching. Self supporting (Ga,Al)As:Si

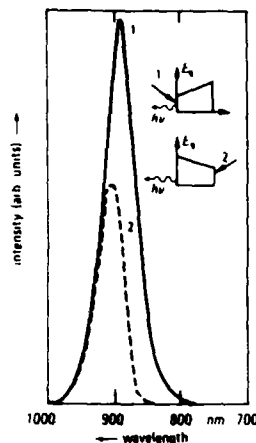


Figure 2  
Photoluminescence of a p-(Ga,Al)As layer  
(80  $\mu\text{m}$  thick) with "front" (1) and "back"  
(2) excitation

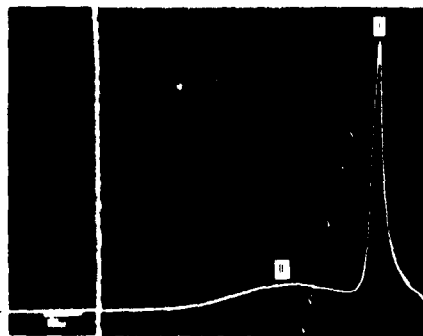
layers are obtained. In Fig. 2 the two spectra obtained with "front" and "back" excitation are shown. "Front" excitation means, that the laser hits the surface with low Al mole fraction, which is pointing towards the spectrometer. "Back" excitation means, that the excited surface with low Al mole fraction is pointing away from the entrance slit, i.e., the luminescence has to pass through the whole epitaxial layer suffering selfabsorption. Fig. 2 shows that selfabsorption reduces the intensity only by about a factor of two, although a quantitative comparison is rather difficult. The spectrum is however shifted to longer wavelengths.

In a second experiment we looked at the cleavage of the device with a scanning electron microscope (SEM). A picture of the cleaved surface is shown in Fig. 3. The situation corresponds to Fig. 1: the p-(Ga,Al)As layer is on the left side, the band

gap decreasing to the left. The p-region is slightly darker than the n-regions of the buffer layer and the substrate. This effect in the SEM is caused by the potential contrast due to the diffusion potential.

A line scan of the electron beam induced current (EBIC) is included. A strong EBIC signal, the peak in the line scan (I), is obtained at the pn-junction.

Additionally, a broad hump (II) is observed on the left side, i.e., when the electron beam hits the almost field free p<sup>+</sup>-(Ga,Al)As layer. This is a direct proof that the device works as expected: The electron beam generates electrons in the p-(Ga,Al)As ((1) in Fig 1).



They recombine (2) emitting photons (3) which are absorbed in the space charge region (4). A current is induced.

Third, we took pulse height spectra with this new detector using Am 241  $\alpha$ -particles (5.49 MeV). The  $\alpha$ -particles were incident almost perpendicular on the small band gap side of the (Ga,Al)As surface and have a range of  $\sim 15 \mu\text{m}$ . Parts of the smaller gap side of the scintillation layer are removed in order to study the spatial dependence of pair creation energy. The  $\alpha$ -particle spectra shown in Fig. 4 are taken with three different thicknesses of the (Ga,Al)As layers. From left to right 80, 30 and  $15 \mu\text{m}$  of the scintillation layer are left. The scale of the pulse height axis is labelled in Si-equivalent MeV. In the last case the  $\alpha$ -particles already cross the pn-junction. A mean net pair creation energy can be calculated from the peak position. 230, 29, and 14 eV are obtained respectively, i.e. the pair creation energy depends strongly on the spatial position.

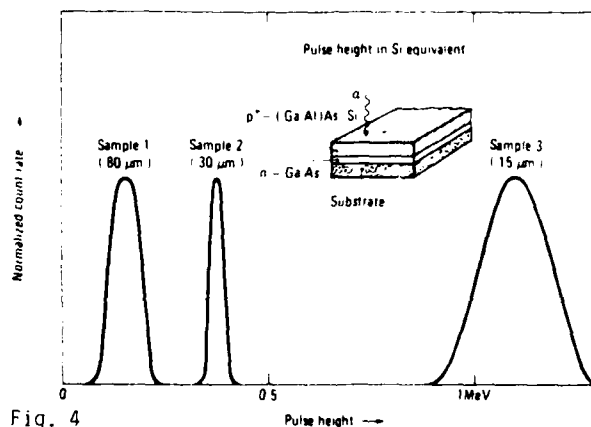


Fig. 4  
Pulse height spectra of Am 241  $\alpha$ -particles with 3 samples with different thickness of the (Ga,Al)As layer

The width of the peak is due to several contributions:

- i) Variation of the net pair creation energy  $E_i$  within the stopping path of the  $\alpha$ -particles.
- ii) Nonuniform thickness of the (Ga,Al)As layer and corresponding changes in  $E_i$ .
- iii) Deviations in the angle of incidence of the  $\alpha$ -particles.
- iv) Electrical noise due to the high capacitance of the devices.



Fourth, in Fig. 5 we show the results, obtained with X-ray pulses and a linear detector array (insert). The circles and crosses show the signal of 5 different stripes as a lead slit is scanned across the array.

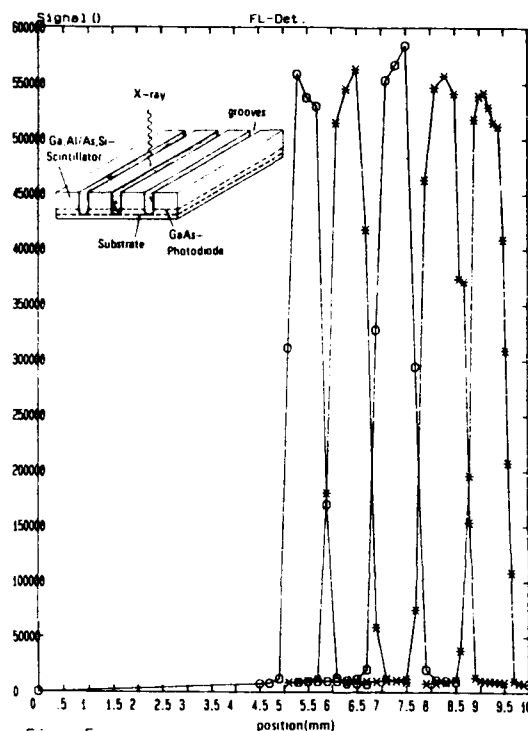


Fig. 5  
(Ga,Al)As-GaAs linear detector array scanned with 100 keV X-rays

Finally, a reverse bias does not change any of the demonstrated results giving more evidence that the device operates as expected.

### 5. Discussion

Figures 3 to 5 demonstrate that this new zero bias (Ga,Al)As detector works well, but it has a strong spatial variation of pair creation energy  $E_i$ . This variation is caused by:

- i) Variation of energy gap and hence the primary  $E_i$  of step 1 in Fig. 1 due to the varying Al mole fraction (increase of  $E_i$  to the right in Fig. 1).
- ii) Spatial variation of the internal quantum efficiencies. Space resolved photoluminescence experiments on cleaved devices show that quantum efficiency decreases to the right (increase of  $E_i$  to the right). This may be due to a decrease in hole concentration from left to right (amphoteric character of the Si-doping).
- iii) Differences in photon recycling effects: Photon recycling is certainly more expressed on the right (Rühle, Hoffmann, Leibenzeder 1982) (decrease of  $E_i$  to the right).

- iv) Selfabsorption without photon recycling leads to a decrease of  $E_i$  to the right.
- v) The luminescence at long wavelengths is not absorbed in the pn-junction, leading to a strong increase of  $E_i$  at the left side where only few Al is incorporated.

The last effect is mostly responsible for the high  $E_i$  for the regions with almost no Al: The energy gap of GaAs corresponds to about 865 nm whereas the luminescence arriving at the pn-junction and coming from the left side has wavelengths longer than 870 nm (see Fig. 2).

The overall spatial variation of  $E_i$  is therefore a mixture of several varying contributions which cannot be clearly separated. This spatial  $E_i$ -variation prevents the application of the device as an energy resolving nuclear radiation detector. However, in the field of X-ray imaging there are applications, where this inhomogeneity should be uncritical and where this new detector might be very useful.

#### 6. Conclusions

A new type of semiconductor, X-ray or nuclear particle detector with a net pair creation energy between 14 and 230 eV is presented. This pair creation energy covers the until now existent gap between conventional semiconductor detectors and scintillation detectors. This detector can still be improved: quantum efficiency can be maximized, homogeneity in pair creation energy can be improved and the thickness of the (Ga,Al)As layers must be increased.

#### Acknowledgements

We would like to thank C. Weyrich for helpful discussions. We thank Mrs. Nungässer for the  $\mu$ -measurements and Mr. Köppel from the Siemens Medical Department for the X-ray scans.

#### References

- Leibenzeder S and Heindl C 1980 Siemens Forsch.- u. Entwickl.-Ber. Bd. 9 Nr. 6 pp 339-346
- Roedel R J and Keramidas V G 10/1979 J. Appl. Phys. Vol. 50 No. 10 pp 6353-6362
- Rühle W, Hoffmann L and Leibenzeder S 5/1982 J. Appl. Phys. Vol. 53 No. 5 pp 3765-8

## Electro-optic effect in a GaAs/AlGaAs quantum well structure at room temperature

Y Kan, M Yamanishi, H Nagai and I Suemune

Faculty of Engineering, Hiroshima University, Saijocho, Higashi-Hiroshima, Japan

### 1. Introduction

One of the attractive features of the quantum well (QW) structures is the existence of excitons at room temperature (Ishibashi et al. 1983, Miller et al. 1982a), which was observed with absorption measurements. Excitonic nonlinear optical properties in QW structures, such as absorption saturation and the associated nonlinear refraction have been studied at room temperature by Miller et al. (1982b, Chemla et al. 1984). On the other hand, electric field effects on optical properties of the QW structures is attracting a great deal of practical interest with their high speed switching capability. The optical properties relevant to the exciton states, such as absorption coefficient and refractive index, are sensitively affected by electric field. Up to now, several field-controlled optical devices were proposed and/or demonstrated (Yamanishi et al. 1983, Wood et al. 1984, Miller et al. 1984a, Yamamoto et al. 1985). Experimental data on field-induced variations in refractive index and absorption coefficient of QW structures are quite important for designing such devices. Electroreflectance (ER) (Erman et al. 1984, Alibert et al. 1985) and electroabsorption (EA) (Wood et al. 1984) measurements are effectively available to understand the field effects on refractive index and absorption coefficient of QW structures over a wide wavelength range, particularly, involving the excitonic gap.

In this paper, we shall report ER spectra of a GaAs/AlAs multi-QW (MQW) structure at room temperature (Nagai et al. 1986a, 1986b). The measured ER data can be well interpreted in terms of the theoretically obtained dispersions of refractive index variation, which include the contributions of the excitonic transitions. This indicates that the observed data result in exciton-induced features on the variations in refractive index. A maximum variation of refractive index  $\Delta n/n$  in each QW at a photon energy near the lowest excitonic transition gap was obtained to be 4% in each QW, induced by the  $10^5$  V/cm field modulation. We shall also report ER and EA spectra in a GaAs/AlGaAs multi-QW (MQW) structure at room temperature, demonstrating a relation between dispersion curves of the field-induced variations in refractive index and absorption coefficient in the structure (Nagai et al. 1986c).

### 2. ER Dispersion for a GaAs/AlAs QW Structure

The sample configuration for the present ER measurements is shown in Fig.1. N-doped  $\text{Al}_{0.7}\text{Ga}_{0.3}\text{As}$  ( $\sim 1.0 \mu\text{m}$ ) and 20-period undoped superlattice composed of alternate 100 Å GaAs well and 300 Å AlAs barrier were sequen-

tially grown on an n-type GaAs substrate by molecular beam epitaxy. The couplings between the adjacent wells in the MQW structure might be negligible because of the thick AlAs barriers so that the MQW structure can be regarded as a collection of uncoupled quantum wells. Therefore, the theoretical estimations can be made by considering an isolated single well. Very thin ( $\sim 200$  Å) Au film, transmitting the monochromatic light, was deposited on the top surface of the MQW structure to form a Schottky contact. The electric field across the MQW structure perpendicular to the well plane could be applied by reverse biasing the Schottky diode. It was confirmed by capacitance-voltage measurements that the depletion layer spread over the MQW structure for reverse bias voltages, larger than 2 volts corresponding to an electric field of  $3 \times 10^4$  V/cm.

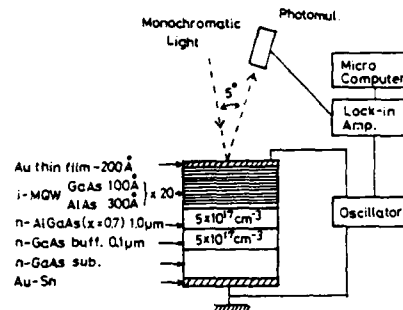


Fig.1 Sample configuration and experimental arrangements used in the ER measurements.

The monochromatic light is focused on the surface of the sample at an incident angle of about  $2.5^\circ$  and the reflected light intensity is measured by a photomultiplier. All data were obtained at room temperature at low light intensity ( $1.5 \times 10^{-4}$  W/cm<sup>2</sup>), so that the intensity does not have any effect on the obtained result.

Prior to description of experimental results on the ER spectra, we show the theoretical dispersions of the field-induced modulations of refractive index, making easy to understand the measured ER data. The imaginary parts of dielectric constant caused by the excitonic and free carrier-transitions were estimated and, then, their contributions to the real part of dielectric constant were obtained by Kramers-Kronig transformation of the imaginary parts (Nagai et al. 1986a). In the estimation of the free carrier contribution to the imaginary part, energy-dependent transition matrix elements (Yamanishi et al. 1984) and line broadenings were taken into account.

The calculated dispersions of the field-induced modulations of refractive index for a modulating field of  $6.25 \times 10^3$  V/cm are shown in Fig.2. The downward peaks of lower and higher energy side in the spectra are originated in the lowest electron to heavy hole (1e1hh) and the lowest electron to light hole (1e1lh)

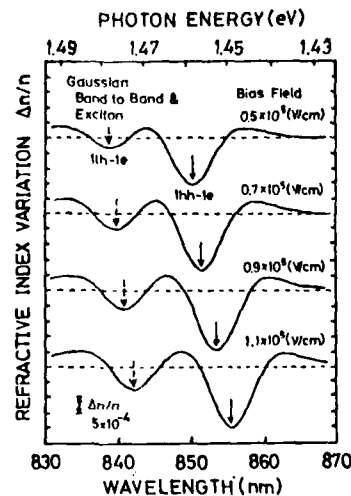


Fig.2 Estimated dispersions of field-induced variation in refractive index of the quantum well. The arrows show the excitonic transition energies of 1e1hh and 1e1lh transitions.

excitonic transitions, respectively. The obtained spectral shapes mainly result from the shift of the excitonic optical transition energy due to the applied field, i.e., the quantum-confined Stark shift (Miller et al. 1984b).

Figure 3 shows the measured ER spectra of the QW sample for a small modulating field of  $6.25 \times 10^3$  V/cm and for various bias fields. With conventional formulations (Seraphin et al. 1972) for reflectance modulations due to refractive index- and absorption coefficient-variations, it was confirmed that the observed ER spectra are almost dominated by refractive index-variation over the wavelength range (830 ~ 870 nm). Thus, the ER spectra permit us a rough estimation of the dispersion of refractive index-variations  $\Delta n/n$  by the following

relation (Nagai et al. 1986a),  $\Delta n/n = [(n^2 - 1)/4n] (\Delta R/R) = 0.75 \Delta R/R$ .

The refractive index variation  $\Delta n/n$  is proportional to the reflectance variation  $\Delta R/R$ , so that we can compare the experimental data of Fig.3 with the theoretical results of Fig.2 by suitably scaling the vertical axis in the figure. With respect to both the shapes and modulation depths of the dispersion curves, the observed ER data are satisfactorily fitted by the theoretical curves which are dominated at the excitonic gaps by the exciton contribution. The similar calculation of the refractive index variation, where the exciton contribution was ignored, was also performed. However, in this case, the estimated dispersion curves of the refractive index variation did not resemble the measured ER spectra, and the modulation depths of the theory was much smaller than that of experimental results. Above mentioned results mean that the excitonic transitions are mainly responsible for the field-induced modulations of refractive index in the GaAs/AlAs MQW structure at room temperature. Some discrepancy between the theory and the experiments in the value of  $\Delta n/n$  may be caused by the uncertainty on the value of line width, which sensitively affects the theoretical result, and by the under-estimation of the theoretical squared matrix elements (Kane et al. 1957, Casey et al. 1978).

In spite of significant red shifts of the peaks, the fundamental shapes of the spectra were not seriously changed with increasing field. This indicates that excitons in the MQW structure are quite stable under the high field (at least  $1.2 \times 10^5$  V/cm), perpendicular to the well plane, even at room temperature.

The downward peaks in the ER spectra have been assigned to the  $1e1h$  and  $1e1h$  exciton transitions. Clear shifts of the downward peaks with increasing bias field are caused by the mixture of the field-induced carrier separation and resultant perturbation with the reduction of the exciton binding energy due to the applied field. The shifted energies of the downward peaks as functions of the bias fields are shown in Fig.4.

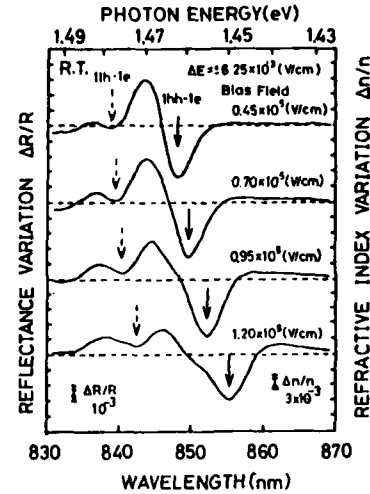


Fig.3 Electroreflectance spectra for a small modulating electric field and various bias fields at room temperature.

The theoretical field-induced shifts of the lowest subband (1e1hh, 1e1lh) free carrier- and excitonic-transition energies are, also, shown in the figure. The free carrier-transition energies were estimated by solving one-dimensional Schrödinger equation while the excitonic binding energies  $E_{ex}$  were estimated with variational technique for the trial exciton function (Miller et al. 1984b, Miller et al. 1985). The observed peak shifts are reasonably explained in terms of the excitonic transitions rather than free carrier transition.

Figure 5 shows the similarly measured ER spectra for large modulating fields. Also, in this case, similar dispersion curves of  $\Delta R/R$ , which are caused by the field effect on exciton, were observed even for such large modulation fields. The maximum variation in refractive index was deduced to be 4.4% in each QW from the measured value of  $\Delta n/n$  (1.1%) at downward peak with photon energy of 1.455eV for the variation in electric field ( $0 \rightarrow 1.2 \times 10^5$  V/cm), taking the volume-ratio of the well to barrier layers into account. The obtained rate for the field-induced variation of refractive index in each QW is thirteen times larger than a theoretical value in an InGaAsP/InP QW structure (Yamamoto et al. 1985), which was estimated on the basis of free carrier transitions without exciton contribution. This means that exciton transitions play an important role for field-induced refractive index-variations at photon energies close to the exciton gaps in the GaAs/AlAs MQW structure. The obtained large variation in refractive index may indicate a possibility of an field-controlled optical switch much more efficient than the previous prediction (Yamamoto et al. 1985).

### 3. Field-induced Modulations of Refractive Index and Absorption Coefficient in a GaAs/AlGaAs QW Structure

Recently, several external optical modulators (Miller et al. 1982b, Tarucha et al. 1985) using the field effect on absorption coefficient in QW structures were proposed and the high speed operation of the devices were demonstrated. From the practical viewpoints, one of the serious problems of the modulation scheme may be the frequency chirping (Koyama et al.

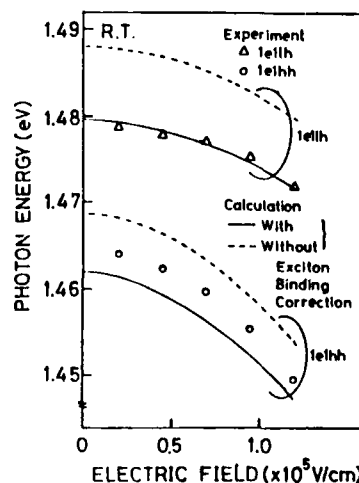


Fig.4 Downward peak shifts as a function of the bias field. The change of the estimated transition energies are, also, shown in solid and dashed line.

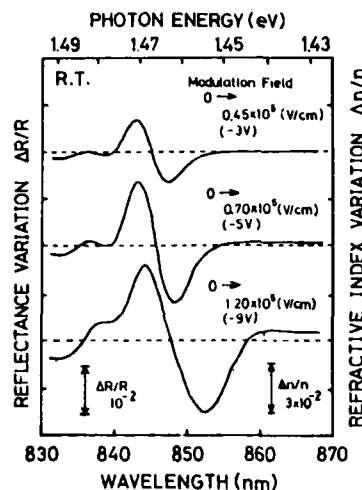


Fig.5 Electroreflectance spectra for large modulating fields at room temperature.

1985) which caused by undesirable phase modulation due to an simultaneous refractive index change. Therefore, it is desirable to know not only the field-induced change in absorption coefficient but also the accompanied refractive index change. We investigated a relation between dispersion curves of the field-induced variations in refractive index and absorption coefficient in a GaAs/AlGaAs QW structure with ER and EA measurements at room temperature, respectively (Nagai et al, 1956c).

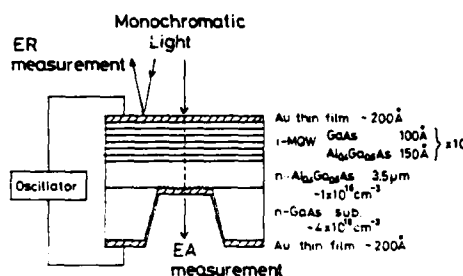


Fig.6 Sample configuration used in the ER and EA measurements.

The ER and EA measurements were performed with an experimental arrangements and a Schottky barrier samples with a 10 period MQW structure consisting of 100Å GaAs wells and 150Å  $\text{Al}_{0.4}\text{Ga}_{0.6}\text{As}$  barriers as shown in Fig.6. A part of the opaque GaAs substrate was selectively etched away by chemical etching. The exposed surface of the n-AlGaAs layer was intentionally roughened by another chemical etching to prevent Fabry-Perot interference with the obtained result. Finally, the roughened surface was covered with the deposited thin Au film.

The EA measurements were performed by measuring the intensity of transmitted monochromatic light beam. On the other hand, the ER measurements for the same sample were performed at a spot outside the central hole of the substrate, as shown in Fig.6, to avoid the influence of reflected light from the back surface of the sample. The dispersion of the refractive index variation  $\Delta n/n$  is approximately given from the measured ER dispersion  $\Delta R/R$  as mentioned in the former section, i.e.,  $\Delta n/n = 0.75\Delta R/R$ .

The dispersions of field-induced variations in refractive index and absorption coefficient of the QW structure, which are obtained with ER and EA measurements, are shown in Fig.7. As is expected from real and imaginary parts of the susceptibility near a resonance of a two-level system such as an exciton, the refractive index variation  $\Delta n/n$  takes the downward peaks around the null-wavelengths of the absorption variation  $\Delta\alpha$ . Also, the absorption variation  $\Delta\alpha$  takes the upward peaks around the null-wavelengths of the refractive index variation  $\Delta n/n$ .

The frequency chirping due to phase modulation is quantitatively expressed in terms of the  $\alpha$ -parameter (Koyama et al. 1985) defined as a ratio of the real to imaginary refractive index variations. The dashed line in Fig.8 shows the  $\alpha$ -parameter estimated from the data on  $\Delta\alpha$  and  $\Delta n$  of Fig.7. The  $\alpha$ -para-

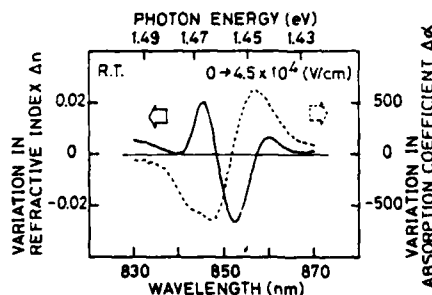


Fig.7 Dispersions of field-induced variation in refractive index and absorption coefficient of the QW structure, obtained with ER and EA measurements.

meter was obtained to be less than 1.5 around upward peaks of the absorption variation  $\Delta\alpha$ , allowing a 1 nm-deviation of the wavelength from the null-points of the refractive index variation  $\Delta n/n$ . The above result predicts that one can make use of the large modulation in absorption coefficient without significant refractive index change due to the field effect of QW structures, as an effective modulation scheme. In other words, one might realize an effective electro-absorption modulator free from a frequency chirping.

#### Acknowledgement

The authors express their thanks to Drs. Y. Ide and R. Lang, Opto-Electronics Research Laboratories NEC Corporation and Drs. T. Hijikata and T. Hayakawa, Central Research Laboratory, Sharp Corporation for kindly supplying the GaAlAs wafer used in the work and for stimulating discussions. This work was partially supported by the Scientific Research Grant-In-Aid for Special Distinguished Research from Ministry of Education, Science and Culture of Japan.

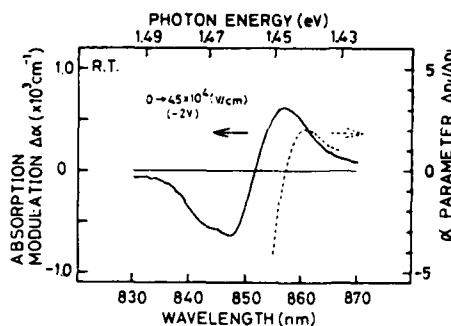


Fig.8 Dispersions of field-induced variation in absorption coefficient of the QW structure. The dashed line shows the dispersion of  $\alpha$ -parameter calculated from the data on  $\Delta\alpha$  and  $\Delta n$  of Fig.7.

- Alibert C et al. 1985 Solid State Comm. **53** 457  
 Casey H C Jr and Panish M B 1978 Heterostructure Lasers, Part A, Chap.3 (Academic Press) p.150-157  
 Chemla D S et al. 1984 IEEE J.QE **QE-20** 265  
 Erman M et al. 1984 J. Appl. Phys. **56** 3241  
 Ishibashi T et al. 1983 Int. Symp. GaAs and Related Compounds, Inst. Phys. Conf. Ser. **63** 587  
 Kane E O 1957 J. Phys. Chem. Solids. **1** 249  
 Koyama F and Iga K 1985 Electronics Lett. **21** 1065  
 Miller D A B et al. 1982a Appl. Phys. **B28** 96  
 Miller D A B et al. 1982b Appl. Phys. Lett. **41** 679  
 Miller D A B et al. 1984a Appl. Phys. Lett. **45** 13  
 Miller D A B et al. 1984b Phys. Rev. Lett. **53** 2173  
 Miller D A B et al. 1985 Phys. Rev. **B-32** 1043  
 Nagai H et al. 1986a extended abstract of Int.Conf. Solid State Devices and Materials, Tokyo  
 Nagai H et al. 1986b to be published in Japan. J. Appl. Phys. Letters  
 Nagai H et al. 1986c to be published in Electronics Lett.  
 Seraphin B O 1972 Semiconductors and Semimetals Vol.9, Chap.1, (Academic Press) p.8-13,  
 Tarucha S et al. 1985 Japan. J. Appl. Phys. **24** L442  
 Wood T H et al. 1984 Appl. Phys. Lett. **44** 16  
 Wood T H et al. 1984 Appl. Phys. Lett. **44** 16  
 Yamamoto H et al. 1985 Electronics Lett. **21** 579  
 Yamanishi M and Suemune I 1983 Japan. J. Appl. Phys. **22** L22  
 Yamanishi M and Suemune I 1984 Japan. J. Appl. Phys. **23** L35



## Very short channel GaAs MESFETs obtained using an overlapped gate configuration

A. Colquhoun and G. Ebert

TELEFUNKEN electronic GmbH, Heilbronn, West Germany

**Abstract.** MESFETs with a novel electrode configuration have been fabricated and characterised. By fabricating the source and drain contacts as buried layer contacts, the gate could be overlapped onto the source zone. The configuration allows the effective channel length of the device to be varied independent of the gate-metal contact length. The characteristics of the FETs were examined for various channel lengths. Channel lengths smaller than  $0.2 \mu\text{m}$  were obtained.

### 1. Introduction

The usual design of planar GaAs MESFET devices for analog applications, typically the "recessed" gate MESFET, has disadvantages caused by the exposure of active areas of the device to the semiconductor surface. Surface effects lead to reduced breakdown voltages, surface trapping etc. In addition, better performance can only be obtained by using very narrow gate-metal stripes leading to a) difficult lithography, b) mechanically instable structures and c) high metalisation resistances.

The advent of low temperature epitaxial growth using MBE or MOCVD makes it possible to configure a MESFET device with  $n^+$  buried layer contacts. This paper presents a novel configuration of MESFET device with buried layer source and drain contacts and the gate stripe overlapped onto the source buried layer zone. We have called the device an **OGFET** for **O**verlapped **G**ate **F**ET.

### 2. The OGFET Structure

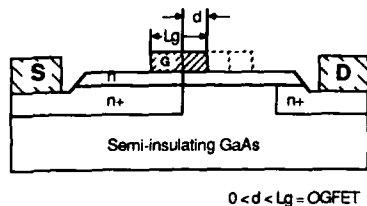


Fig.1 Schematic cross-section of an OGFET device with gate overlap  $d$

© 1987 IOP Publishing Ltd

The basic OGFET structure is shown in Fig. 1. The device is fabricated by selectively implanting the  $n^+$  source and drain zones and epitaxially growing the active layer onto the previously annealed substrate. Ohmic source and drain contacts are formed by etching through the active layer and contacting directly onto the  $n^+$  layer. The gate stripe is offset towards the source so that part of the metalisation overlaps onto the  $n^+$  source zone without making contact to the  $n^+$  layer because the active layer of the device separates the two contacts. The effective channel length of the device is independent of the gate metalisation length  $L_g$  and is

determined by the amount of overlap  $d$ . The basic OGFET does not require extremely fine lithography, it does require accurate alignment of the gate to the  $n^+$  buried layer.

Because the  $n^+$  source contact zone extends underneath the gate, the source resistance  $R_s$  of the device can be reduced to an absolute minimum. The gate metalisation resistance  $R_g$  can be substantially lower than in a conventional MESFET device with an equivalent channel length. Contact resistances can also be kept small due to the highly doped  $n^+$  regions. These parasitic resistances contribute substantially to the noise generated in MESFETs, so the OGFET structure should be particularly suitable for low noise devices (Pucel 1975, Fukui 1979). The gate-source capacitance of the OGFET is not larger than a conventional MESFET with an equivalent gate length because under normal operating conditions the depletion layer of the gate does not extend into the  $n^+$  buried layer. The cut-off frequency of the OGFET  $f_T = g_m/2\pi C_{gs}$  is equivalent to that of a conventional MESFET with the same  $L_g$ , however,  $f_T$  will be increased if  $g_m$  is increased by the reduction in  $R_s$  or an increase in the saturation velocity of the electrons in the active channel due to velocity overshoot (Shur 1981). Transit time effects at very high frequencies are determined by the effective channel length giving the OGFET an advantage over conventional MESFETs.

### 3. OGFETs with different gate displacements

We have examined the OGFET structure by fabricating an array of devices with different gate displacements. In this way the variation of the electrical parameters of the devices with channel length could be experimentally determined. Fig.2 shows schematically the variation of overlap  $d$  and  $n^+$ - $n^+$  separation along the array. The masks for the devices were fabricated using electron beam lithography with a raster of  $0.25 \mu\text{m}$  so that it was possible to accurately control the gate displacements of the individual devices. Standard uv-lithography was used for the fabrication of the devices.

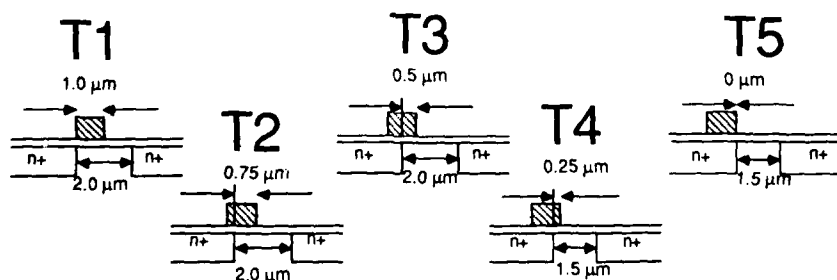


Fig. 2 An array of OGFETs with different gate displacements.

### 4. Fabrication Technology

The  $n^+$  zones were obtained by selectively implanting Si into undoped semi-insulating (S.I) substrates using silicon oxynitride as an implantation mask. A combination of singly and doubly ionised Si ions with different energies was used to obtain a deep, uniformly doped  $n^+$  layer.

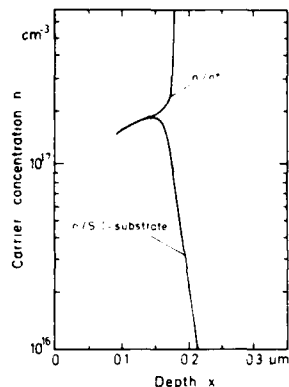


Fig.3 Carrier concentration profiles  $n/n^+$  and  $n/S.I.$

Sheet resistances of typically  $60\text{--}80 \Omega/\square$  were obtained after annealing. The  $n^+$  zones were aligned to alignment marks etched into the surface of the substrate. After a suitable surface preparation, the  $n$  doped active layer was grown using MOCVD. The etched alignment marks were reproduced in the epitaxial layer and were used for the further alignment of the device. The epitaxial layers were of good surface quality with reproducible doping profiles. Fig. 3 shows carrier concentration profiles derived from C/V measurements. The profiles show the epitaxial layer on the S.I. substrate and on the  $n^+$  buried layer. The average mobility, measured on test structures on the processed wafers was approx.  $4500 \text{ cm}^2\text{V}^{-1}\text{s}^{-1}$  for  $n \approx 1.5 \times 10^{17} \text{ cm}^{-3}$ . The epitaxial layers were designed to be  $0.15 \mu\text{m}$  thick giving a pinch-off voltage of  $2.5\text{--}3 \text{ V}$  and a sheet resistance of approx  $1 \text{ k}\Omega/\square$ . Source, drain and gate contacts were formed using a self-aligned technique with Al as gate metal and Au/Ge for the ohmic contacts (Baudet 1976). The bonding areas were thickened using Ti/Pt/Au metalisation followed by Au electrolytic plating. The active areas were passivated using PECVD  $\text{Si}_3\text{N}_4$ . Each device had a gate width of  $200 \mu\text{m}$ ,  $L_g = \text{approx. } 1 \mu\text{m}$  and the separations of the S-G and D-G metalisations were approx  $2 \mu\text{m}$ .

##### 5. Gate Position

The position of the gate electrode relative to the  $n^+$  buried layer contacts could be accurately determined by measuring  $C_{gs}$ ,  $C_{gd}$ ,  $R_{gs}$  and  $R_{gd}$ . The unintentional alignment error was determined by measuring  $R_{gs}$  and  $R_{gd}$  on structures with gates which were not intentionally displaced relative to the  $n^+$  contacts. Fig. 4 shows the variation of  $R_{gs}$  and  $R_{gd}$  with overlap  $d$  for a particular wafer. The step in  $R_{gd}$  is due to a change in the  $n^+ \text{--} n^+$  separation between the third and fourth elements in the array. On the wafer shown in Fig. 4, the gate mask was misaligned  $0.4 \mu\text{m}$  towards the source. The minimum resistance of  $5.5 \Omega$  is a combination of

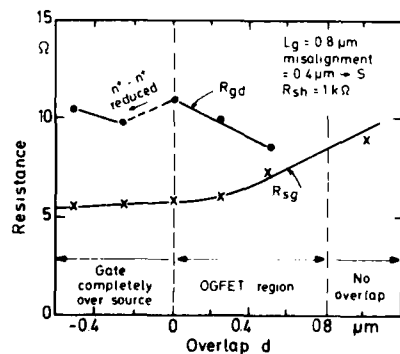


Fig.4  $R_{gs}$ ,  $R_{gd}$  as a function of  $d$

$1.5 \Omega$  contact resistance  $R_c$ ,  $1 \Omega$  source resistance  $R_s$  and  $3 \Omega$  gate resistance  $R_g$ .  $R_c$  corresponds to a specific contact resistance of  $6 \times 10^{-6} \Omega \cdot \text{cm}^2$ .  $R_g$ , for  $L_g = 0.8 \mu\text{m}$ , a metal thickness of  $0.7 \mu\text{m}$  and  $Z = 200 \mu\text{m}$  is the dominating component of  $R_{sg}$ .  $R_{sg}$  attains a minimum when more than  $0.5 \mu\text{m}$  of the gate overlaps onto the  $n^+$  zone. In this example,  $n$  was  $1.3 \times 10^{17} \text{ cm}^{-3}$ . Measurement of  $C_{gs}$  and  $C_{gd}$  can also accurately determine the position of the gate. Fig.5 shows  $C_{gs}$  vs.  $V_{gs}$  and  $C_{gd}$  vs.  $V_{gd}$  for different gate displacements. For  $|V| < |V_p|$ ,  $C_{gs}$  is independent of  $d$ . For  $|V| > |V_p|$  the part of the depletion layer

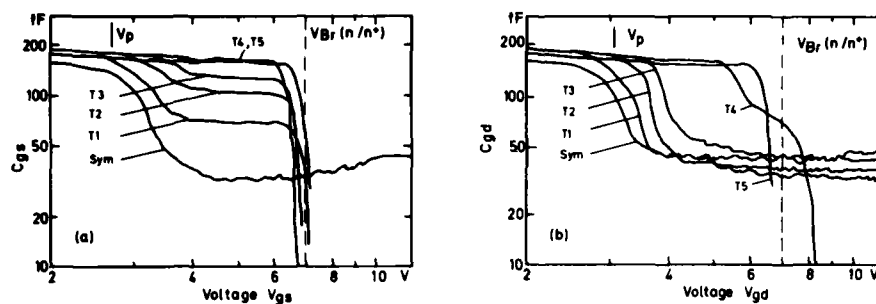


Fig.5 (a)  $C_{gs}$  vs  $V_{gs}$ , (b)  $C_{gd}$  vs  $V_{gd}$  for different transistors in an array

above the semi-insulating material cannot be modulated by the measurement signal and  $C_{gs}$  is reduced to the capacitance of the depletion layer over the  $n^+$  zone. Due to the very high doping in the  $n^+$  layer, the depletion layer width and hence  $C_{gs}$  remains essentially constant for further increase of the applied voltage. If any part of the depletion layer comes into contact with the  $n^+$  zone, the breakdown voltage is reduced (in the example in Fig. 5  $V_{br}$  is approx 7 V). If the gate is completely over the S.I. zone, then  $C_{gs}$  falls to a minimum consisting of the stray capacitance and the junction capacitance of the edge of the depletion layer exposed to the source. The breakdown voltage is then considerably higher (in the example in Fig. 5  $V_{br} > 15$  V).

At voltages smaller than pinch-off,  $C_{gd}$  is also independent of  $d$ . At voltages higher than pinch-off,  $C_{gd}$  is reduced to the stray capacitance plus the capacitance of the edge of the depletion layer exposed to the drain. In Fig. 5(b), the gates of T4 and T5 do not overlap onto the S.I. zone, a current path between source and drain is open and  $C_{gd}$  becomes the capacitance of the complete depletion layer over the source.  $V_{br}$  is then correspondingly reduced. The reverse breakdown voltage between gate and source or drain can also be used to determine the position of the gate.

#### 6. Low Frequency Measurements

The output characteristic of a typical short channel device and the transfer characteristics of an array of devices with different overlaps are shown in Fig 6. All the devices show stable well defined output characteristics with little looping or light sensitivity. Devices with short channels exhibit an increase in transconductance  $g_m$  at low values of  $I_{ds}$  and a reduction of  $g_m$  at high values of  $I_{ds}$ . The open gate saturation current  $I_s$  is only marginally higher than  $I_{dss}$ . Both  $V_p$  and  $I_{dss}$  increase as the channel length  $d$  is reduced.

The behaviour of the devices can be explained as follows: The buried layer has reduced  $R_s$  so that for  $V_g = 0$  the potential under the drain end of the gate is only marginally higher than the source potential and  $I_{dss} \approx I_s$ , assuming that the free surface potential is approximately the same as the built-in voltage of the Schottky barrier (Baek 1985). Due to velocity overshoot (Shur 1981), reduction of the channel length increases the saturation drift velocity of the electrons in the channel and hence the current through the channel. At high values of  $I_{ds}$ , the current is then limited by saturation in the parasitic gate-drain channel and  $g_m$  is lower

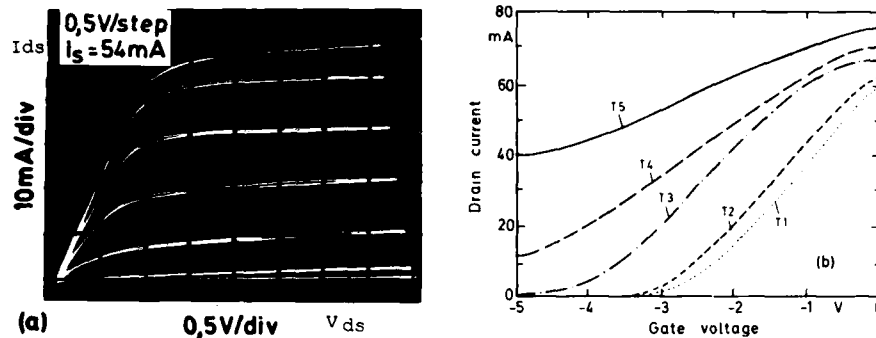


Fig.6 (a) output and (b) transfer characteristics of typical devices

(Chen 1983). An increase in  $V_p$  has been observed in many short channel MESFET devices (Chao 1982) and is thought to be a result of the vertical component of the S-D field in the pinch-off region.  $I_{dss}$  increases due to the reduction in  $R_s$ , the increase in  $v_s$  and additional substrate current.

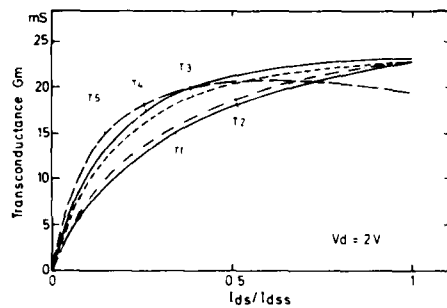


Fig.7 Transconductance vs.  $I_{ds}/I_{dss}$

acteristic is not symmetrical, the current is higher when the drain is positively biased.

#### 7. High Frequency Measurements

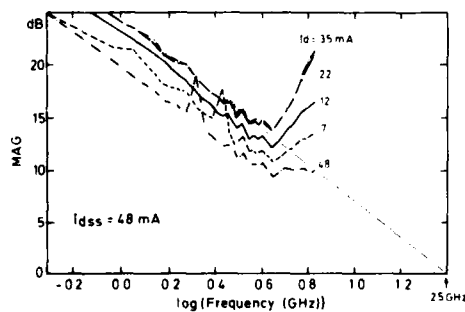


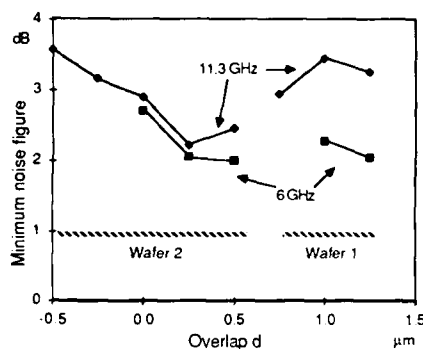
Fig. 8 MAG as a function of frequency

The effect of saturation can be clearly seen in Fig. 6(b) and in Fig 7 where  $g_m$  has been measured as a function of normalised drain current  $I_{ds}/I_{dss}$  for various transistors in an array. The increase in  $g_m$  at low values of  $I_{ds}/I_{dss}$  is more than can be expected from the reduction of  $R_s$ . Fig. 7 demonstrates clearly that saturation effects are reducing  $g_m$  in FETs with very short channels.

Because of the displaced gate the open gate source-drain I/V characteristic is not symmetrical, the current is higher when the drain is positively biased.

S parameter measurement of the devices was carried out by bonding the FETs into ceramic packages, measuring, and subsequently de-embedding to obtain the HF properties of the devices. The best devices achieved cut-off frequencies of  $f_{max} = 25\text{GHz}$ . For short channel devices, the variation in low frequency transconductance is reflected in the high frequency performance of the devices. In Fig. 8 the maximum available gain MAG of a short channel device is plotted as a function of frequency

for various values of  $I_{ds}$ . The maximum MAG, at  $I_{ds} \approx 50\% I_{dss}$  is consistent with the low frequency measurements. The higher MAG values at approx. 7 GHz are due to a resonance in the package used for the measurement. The extrapolated  $f_{max}$  of 25 GHz at  $50\% I_{dss}$  is higher than that (21 GHz) at  $100\% I_{dss}$  of a device with a  $0.75 \mu m$  longer channel.



The minimum noise figure of the packaged devices was measured at 6 GHz and 11.3 GHz and the values are plotted in Fig. 9 as a function of the channel length  $d$  for transistor arrays from two different wafers. On wafer 1,  $L_g = 1.5 \mu m$ , on wafer 2,  $L_g = 0.8 \mu m$ . The best value obtained was 2.25 dB at 11.3 GHz for a channel length of approx.  $0.25 \mu m$ . Devices with  $d < 0$  exhibited higher minimum noise figures. The 11.3 GHz measurements show a minimum noise figure at very short channel lengths, as would be expected.

Fig. 9 Minimum noise figure vs.  $d$

#### 9. Discussion and Summary

The results have demonstrated that buried layer MESFETs with very short channel lengths can be fabricated. However, the gain of the devices was reduced due to current saturation in the gate-drain channel. Two possibilities to increase the current saturation in this channel are: 1) the use of a recess in the epitaxial layer or 2) the reduction of the  $n^+-n^+$  separation to sub-micron dimensions so that the electron drift velocity in that part of the channel is increased due to velocity overshoot effects. The use of a recess complicates the fabrication, however, an  $n^+$  layer on the surface would not be essential. The noise figure measurements at 11.3 GHz are comparable to values obtained on  $1 \mu m$  recessed gate FETs. Optimisation of the devices by reducing the gate finger length, the contact resistance and the buried layer resistance should lead to even lower noise figures.

#### Acknowledgements

The Authors would like to thank B. Adelseck and K.E. Schmeider of AEG, Ulm, H. Renz, W. Mroczek, B. Wolfstatter, R. Stewasser and T. Sellers for their help in the preparation and evaluation of the samples, and the German Bundesverteidigungsministerium for financial support.

#### References

- Baudet P, Binet M and Buccon-Gibod D 1976 IEEE Trans. MTT MTT-24 372
- Baek J, Shur M S, Lee K W and Vu T 1985 IEEE Trans. Electron Devices ED-32 pp 2426-2430
- Chao P C, Ku W H and Nulman J 1982 IEEE Electron Device Letters EDL-3 187
- Chen C L and Wise K D 1983 IEEE Electron Device Letters EDL-4 341
- Fukui H 1979 IEEE Trans. Electron Devices ED-26 1032
- Pucel R A, Haus H A and Statz H 1975 Advances in Electron Physics (New York: Wiley) pp 195-265
- Shur M S 1981 IEEE Trans. Electron Devices ED-28 1120

## **Analysis of narrow channel effect in small-size GaAs MESFET**

Takeshi Uenoyama, Shinji Odanaka and Takeshi Onuma

Semiconductor Research Center,  
Matsushita Electric Co., Ltd.,  
3-15, Yagumo-Nakamachi, Moriguchi, Osaka, 570, Japan

**Abstract.** Narrow channel effect in small-size GaAs MESFETs was studied by three-dimensional analysis and experiments. The threshold voltage of FETs with 1.0  $\mu\text{m}$  gate length increases more than 150 mV with decreasing its channel width from 5.0  $\mu\text{m}$  to 1.0  $\mu\text{m}$ . From the simulation results, it was clarified that gate extension caused the narrow channel effect by spreading the depletion region to the channel area when supply voltage was applied to the gate electrode and that providing gate extension on the passivation film was effective to suppress the narrow channel effect.

### 1. Introduction

In recent high-speed and low-power GaAs ICs, utilization of 1.0  $\mu\text{m}^2$  (Hasegawa K et al. 1986) or 2.0  $\mu\text{m}^2$  (Ishii Y et al. 1984) well FETs has been reported. These FET structures are essentially three-dimensional, as shown in Fig. 1. In order to design GaAs LSIs, such as static random access memory, using these small-size FETs, it is necessary to understand the size dependences of the device characteristics, such as threshold voltage dependences on the channel lengths and channel widths. While short channel effect has been studied mainly for the self-alignment FETs by experiments and two-dimensional analyses, few works have been done on the narrow channel effect in GaAs MESFETs which requires three-dimensional analyses.

In this paper, we have studied the narrow channel effect in GaAs MESFETs by using the three-dimensional device simulator, in a similar way reported for Si MOSFETs (Shigyo n et al. 1982) and compared with the fabricated small-size FETs. Based on the simulated results, it was clarified that gate extension on the semi-insulating substrate caused the narrow channel effect and that providing the gate extension on the passivation film was effective in suppressing this effect.

### 2. Outline of three-dimensional device simulator

In this device simulator, the conventional finite-difference method is used along with the box integration method to solve the following

Poisson's equation(1) and steady-state current continuity equation(2), taking into account the electron velocity overshoot.

$$\nabla \cdot (\epsilon_s \nabla \Psi) = -q(N_D - n) \quad (1)$$

$$\nabla \cdot (\mu n \nabla \Phi) = 0 \quad (2)$$

$$n = N_c \exp\left(\frac{\Psi - \Phi}{kT}\right) \quad (3)$$

where  $N_D$  is impurity concentration and  $n$  is electron density.  $\Psi$  and  $\Phi$  are electrostatic potential and quasi-fermi level, respectively.  $q$  is the electron charge and  $\epsilon_s$  is the dielectric constant of GaAs. For an effective numerical calculation, a nonuniform mesh scheme is adopted. Impurity profiles of active layer and source-drain regions were given by superimposing the Gaussian profiles in vertical direction and error function profiles in lateral direction on the semi-insulating GaAs substrate, which was assumed to be  $n$ -type semiconductor ( $10^{18} \text{ cm}^{-3}$ ). Three-dimensional device simulation was performed for only a half of the channel width as shown in Fig. 1 to reduce the calculation time.

### 3. Analysis of narrow channel effect

Figure 2 shows the dependence of threshold voltage on channel width, in which the broken line shows the experimental results and the solid line shows the simulated one by three-dimensional analysis. In the experiment, these FETs, having gate length of  $1.0 \mu\text{m}$ , were fabricated by Si ion-implantations ( $100 \text{ keV}$ ,  $5 \times 10^{12} \text{ cm}^{-2}$  for active layer and  $150 \text{ keV}$ ,  $1 \times 10^{14} \text{ cm}^{-2}$  for source-drain regions). Annealing was performed in  $\text{AsH}_3$  ambient at  $800^\circ\text{C}$  for 20 min. Channel widths of these FETs were varied from  $1.0 \mu\text{m}$  to  $10.0 \mu\text{m}$ . Threshold voltage was defined as the gate voltage ( $V_{gs}$ ) at  $V_{ds} = 1.0 \text{ V}$  and  $I_{ds} = 1.0 \mu\text{A}$ ,  $2.0 \mu\text{A}$ ,  $5.0 \mu\text{A}$ ,  $10.0 \mu\text{A}$  for each  $W_{ch} = 1.0 \mu\text{m}$ ,  $2.0 \mu\text{m}$ ,  $5.0 \mu\text{m}$ ,  $10.0 \mu\text{m}$ . With the decrease of the channel widths from

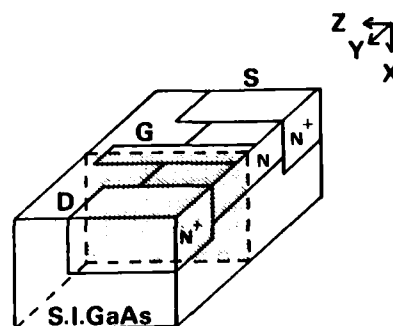


Fig. 1 Schematic explanation for three-dimensional structure.

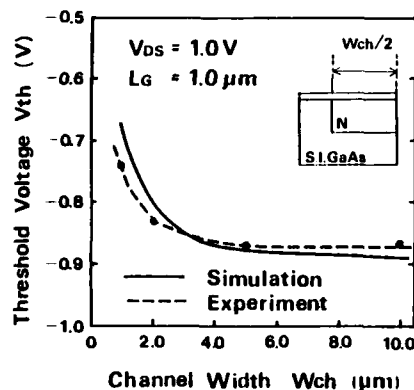


Fig. 2 Dependence of threshold voltage on channel width.



5.0  $\mu\text{m}$  to 1.0  $\mu\text{m}$ , threshold voltage varied from -0.86 V to -0.74 V as shown in Fig. 2. This characteristic was in good agreement with the simulated result.

The cause of this narrow channel effect seems to be originated from the gate extension ( $W_{ex}$ ) on the semi-insulating substrate. Thus, we have investigated the channel width dependence of threshold voltage, varying the length of gate extension which were provided on the semi-insulating substrate (Fig. 3(a)). Fig. 3(b) shows the potential profiles in X-Z cross sectional plane in the active layer for  $W_{ex} = 0.1 \mu\text{m}$  and  $0.5 \mu\text{m}$ . In this simulation, it was assumed that the boundary condition for electrostatic potential satisfies  $\nabla\psi \cdot \hat{n} = 0$  at the surface without electrode. It was found in Fig. 3(a) that the narrow channel effect was suppressed with the decrease of gate extension length, showing a drop of the threshold voltage. Fig. 3(b) indicates that the potential curvature at the interface between active layer and semi-insulating substrate is strongly deformed by gate extension. This pins the potential to the barrier height level at the surface of the substrate, and reduces the effective channel area.

Note that for the 0.1  $\mu\text{m}$  gate extension, the opposite channel width dependence of threshold voltage to the other three examples is seen. In these small-size MESFETs, threshold voltage is modified not only by the narrow channel effect but

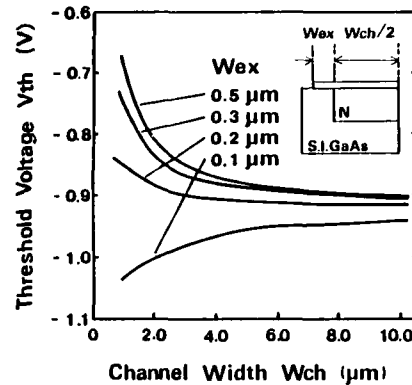
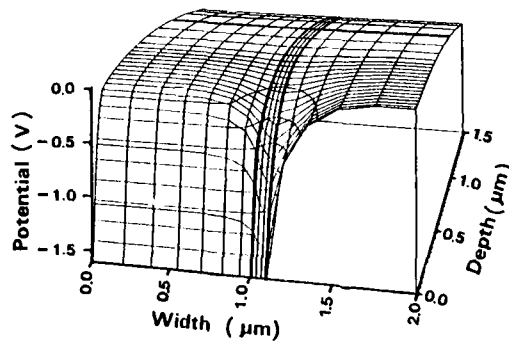
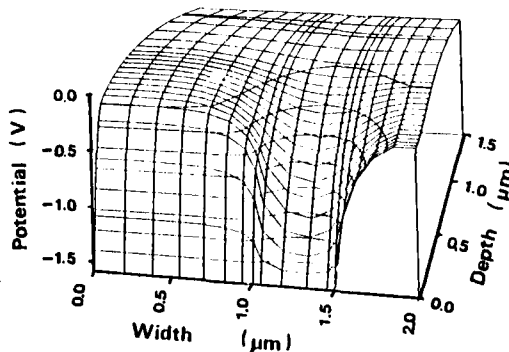


Fig. 3(a) Dependence of narrow channel effect on gate extension.



$W_{ex} = 0.1 \mu\text{m}$



$W_{ex} = 0.5 \mu\text{m}$

Fig. 3(b) Potential profiles in X-Z cross sectional plane in active layer.  $V_{ds} = 1.0$  V,  $V_{gs} = -0.8$  V.

also short channel effect. When the gate extension of the narrow channel FETs becomes extremely short and the FET is nearly off condition, the component of excess current that flow the periphery of active well region is considered to become comparable with the channel current because too short a gate extension cannot extend enough depletion region near the surface of the substrate. In such a case, the short channel effect may become predominant due to such "side excess current" around the active well region. This explains the fact that threshold voltage of the FET with 0.1  $\mu\text{m}$  gate extension is smaller at 1.0  $\mu\text{m}$  than at 10.0  $\mu\text{m}$ , as shown in Fig. 3(a).

In order to further understand this effect quantitatively, one dimensional profiles of active layer (A1) and semi-insulating substrate (A2) under the gate electrode are schematically shown in Fig. 4(a). Since both potentials (A1 and A2) must be coincident at the surface and in the deep region of substrate, the potential difference  $\delta V$  causes the potential curvature between the active layer and substrate, namely the region between boundary (A1') and boundary (A2'), which reduces the channel area and increases the threshold voltage.

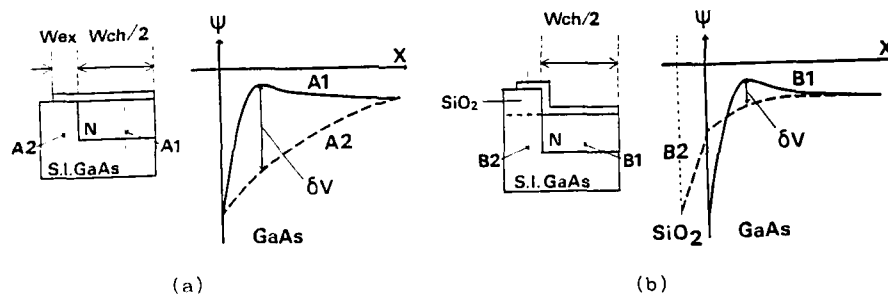


Fig. 4 Schematic potential profiles at active layer (A1, B1) and substrate (A2, B2). (a) conventional structure, (b) structure providing gate extension on the passivation film.

For real devices, however, it is impossible to eliminate the gate extension because of necessity of mask alignment margin. So we propose a device structure in which gate extension is provided on the passivation film, such as SiO<sub>2</sub>, to decrease the potential difference  $\delta V$  by increasing potential B2 at interface between passivation film and GaAs substrate, as shown in Fig. 4(b). Potential profile B1 is the same as A1. On the other hand, B2 is the MIS structure's potential profile. In this case, the potential B2 at the interface is determined by following boundary condition,

$$-\epsilon_p \frac{\partial \Psi}{\partial X} + \epsilon_s \frac{\partial \Psi}{\partial X} = -\sigma \quad (4)$$

where  $\sigma$  is the charge trap density at the interface.  $\epsilon_p$  is dielectric constant of passivation film. From the eq.(4), it is necessary to select the low dielectric constant material as the passivation film which should be formed as thick as possible, in order to decrease the potential difference  $\delta V$ .

Figure 5(a) and 5(b) show the channel width dependence of threshold voltage of FETs, of which gate extensions were provided on the passivation film, and potential profiles in X-Z cross sectional plane in active layer, respectively, using three-dimensional device simulator. In this simulation, it was assumed that dielectric constant of this passivation film was 3.5 and thickness was 2000 Å and charge trap density was neglected for simplicity. As has been expected, the increase of threshold voltage with the decrease of channel width is suppressed by providing the gate extension on the passivation film in Fig. 5(a) and the potential profile becomes more flattened in Fig. 5(b) than that of the conventional structure.

#### 4. Conclusion

Narrow channel effect that threshold voltage increases with the decrease of channel width, becomes remarkable within the 5.0  $\mu\text{m}$  channel width for 1.0  $\mu\text{m}$  gate length. By using the three-dimensional device simulator, it was clearly shown that the cause of this effect was the existence of gate extension on the semi-insulating substrate. To suppress the narrow channel effect, a gate extension on the thick passivation film with lower dielectric constant, than that of GaAs, is effective.

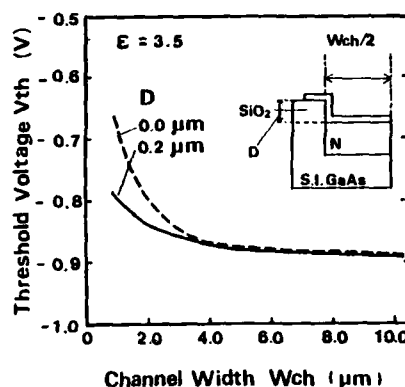


Fig. 5(a) Dependence of threshold voltage on channel width, providing gate extension on the passivation film.

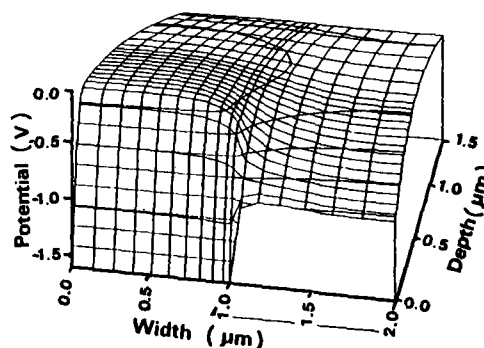


Fig. 5(b) Potential profile in X-Z cross sectional plane in active layer.  $V_{ds} = 1.0$  V,  $V_{gs} = -0.8$  V.

Acknowledgement

The authors would like to express their sincere thanks to Dr. H. Mizuno and T. Kajiwara for their encouragement. They also wish to thank K. Inoue for his helpful discussions, K. Nishii for fabrication of samples and J. Sato for her assist in developing the device simulator.

Reference

- Hasegawa K, Uenoyama T, Nishii K and Onuma T, 1986 Electron. Lett. Vol 22 pp. 251-252  
Ishii Y, Ino M, Idda M, Hirayama M and Ohmori M, 1984, GaAs IC symposium, pp.121-124  
Shigyo N and Dang R. L., 1982 Electron. Lett. vol 18, pp. 247-275

## **Characterization and physics of low-field electron transport in GaAs MESFETs**

Krishna Shenai,<sup>\*</sup> and Robert W. Dutton

Integrated Circuits Laboratory  
Stanford University, Stanford, CA 94305 (USA)

<sup>\*</sup> Present Address

General Electric Corporate Research and Development  
1 River Road, Schenectady, NY 12301 (USA)

### **Abstract**

The electron transport mechanism in the vicinity of channel-substrate (buffer) interfaces is studied in detail, both theoretically and experimentally. It is shown that considerable degradation in the low-field electron drift mobility occurs in the near pinchoff regime of GaAs MESFETs as a result of electron scattering from the steep channel walls and localized states at the channel-buffer interface.

### **1. Introduction**

The low-field electron mobility ( $\mu_n$ ) in the vicinity of channel-substrate (buffer) interfaces has been used to understand the quality of substrate and buffer layers (Das et al. 1982, Lee et al. 1984, Lehovec 1974, and Sites et al. 1980). A reduction in mobility in the near pinchoff regime of GaAs MESFETs was attributed to scattering of charged carriers from the localized states at the channel-substrate interface (Lehovec 1974), enhanced compensation of donor atoms resulting from the outdiffusion of Cr acceptors into the channel layer (Walukiewicz et al. 1979), and recently to increased ionized impurity scattering in the channel as a result of reduced electron concentration (Ford et al. 1982).

These studies, however, are not conclusive because the techniques used for mobility profiling have relied on depletion approximations to calculate the channel mobile charge and have neglected the space charge effects at the channel-substrate (buffer) interface (Houng et al. 1978). It has been shown that local band calculations do not conserve the overall charge in the device (Shenai et al. 1985 (a), and 1985 (b)). The problem is compounded because of the difficulties involved in profiling the impurity distribution in the vicinity of channel-substrate (buffer) interfaces, especially in channel layers formed by ion-implantation. In many instances, techniques used for mobility profiling do not necessarily profile the drift mobility (Sites et al. 1980). Theoretical calculations, on the other hand, pertain to

electron transport in a semiconductor sample and, therefore, do not directly apply to a working device (Walukiewicz et al. 1979). In a practical device such as the GaAs MESFET studied in this investigation, a number of local scattering mechanisms are found to play a significant role in determining the low-field carrier transport phenomena in the channel.

In this paper, a novel method of extracting an average value of low-field electron drift mobility ( $\bar{\mu}_n$ ) is presented based on an exact solution of the Poisson's equation. Comparison with previous electrical techniques is made using the experimental results obtained from long channel GaAs MESFETs in which atomically clean and nearly abrupt channel-buffer interfaces were fabricated by depositing the active channel layer *in situ* in an ultra-high vacuum environment of the MBE system. It is shown that previous techniques are unsuitable for mobility profiling in the near pinchoff regime as they rely on the depletion approximations; in a neutral channel, these techniques overestimate the channel mobile charge as there is no provision to account for the finite space charge at the channel-substrate (buffer) interface. Experimental results also show nearly 35% degradation in  $\bar{\mu}_n$  in the near pinchoff regime. This degradation in mobility is in good agreement with the scattering calculations made from the steady-state Boltzmann transport equation. The dominant scatterers are determined to be the steep channel walls and localized states at the channel-buffer interface; the interface states may correspond to any changes in the growth conditions in an MBE system. It is also shown that increased ionized impurity scattering plays a minimal role in the mobility degradation mechanism.

## 2. Sample Preparation

The device structure shown in Fig. 1 was fabricated entirely in the ultra-high vacuum environment of the MBE system. An undoped GaAs buffer layer (approximately  $0.5\mu\text{m}$  thick) was grown on top of undoped GaAs substrate (approximately  $200\mu\text{m}$  thick) under normal growth conditions ( $T_s = 585^\circ\text{C}$ ,  $\text{As}_4:\text{Ga} = 0.5:1$ ,  $r_g = 0.9\mu\text{m/hr}$ ). Following this, about  $2 \times 10^{17}\text{cm}^{-3}$  Si-doped n-type GaAs active channel layer

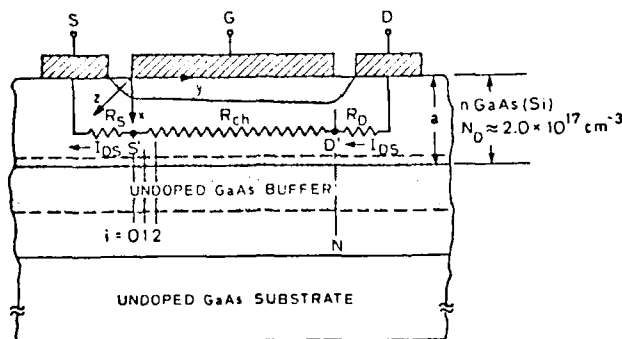


Fig. 1 Device structure of long channel MESFETs fabricated by MBE.

was deposited *in situ* in an ultra-high vacuum environment of the MBE system; thereby ensuring that the channel-buffer interface is atomically abrupt and nearly free of contaminations. This aspect of the growth technique is critical to develop a satisfactory theory for carrier transport in the channel or to understand the

physical mechanisms responsible for the low-field channel pinchoff mechanism (Shenai et al. 1985 (a), and 1985 (b)). Note that the undoped GaAs buffer layer in Fig. 1 is slightly  $p$ -type because of the incorporation of residual acceptor impurities in the MBE system during the crystal growth (Illegems et al. 1975). The channel-buffer interface is therefore an  $n$ - $p$  junction.

The spacing between the electrodes in Fig. 1 is  $2\mu\text{m}$  compared to a gate length of  $7\mu\text{m}$ . Further, no surface passivation was employed and, therefore, the free surface between the electrodes plays a minimal role in the channel charge control mechanism. In Fig. 1,  $R_S$  and  $R_D$  represent the parasitic source and drain resistances, respectively, and  $R_{ch}$  is the total channel resistance. In this study, devices with different pinchoff voltages were fabricated by etching out portions of GaAs active layer by wet chemical etching techniques; the qualitative mobility results are similar in different types of devices. The source and drain ohmic contacts were formed by alloying whereas the gate Schottky contact was deposited by electron beam evaporation of Ti and Au.

### 3. Mobility Characterization Technique

A value for  $\bar{\mu}_n$  was extracted from the measured  $I_{DS}$  vs.  $V_{DS}$  characteristics at low values of drain-source voltage (i.e.,  $V_{DS} < 100\text{mV}$ ) and the charge control model presented below. The conducting channel in Fig. 1 is partitioned into a number of two-dimensional charge sheets. At any cross-section along the channel, the drain current density  $J_n$  is obtained from (Shenai 1986)

$$J_n = -q\mu_n n \nabla \phi_n \quad (1)$$

where  $n$  is the local electron concentration and  $\phi_n$  is the local quasi-Fermi potential for electrons. The value of  $\phi_n$  is determined to account for a finite drift field following the gradual channel approximation. The resulting expression for the drain current is

$$I_{DS} = \frac{\epsilon_s \bar{\mu}_n Z}{L} \int_{V_S'}^{V_D'} \left[ E_B(\phi_n) - E_S(\phi_n) \right] d\phi_n - \frac{qN_{DC}^+ a Z \bar{\mu}_n}{L} (V_D' - V_S') \quad (2)$$

where  $E_B$  and  $E_S$  are the channel-buffer and gate Schottky barrier interface electric fields, respectively, and are determined from an exact solution of the one-dimensional Poisson's equation

$$\frac{dE}{dx} = \frac{q}{\epsilon_s} \left[ p(x) - n(x) + N_D^+(x) - N_A^-(x) \right] \quad (3)$$

where the electron and hole distributions are determined to obey the Fermi-Dirac statistics (Joyce et al. 1977). In Eq. (2), the potentials at the internal drain and source nodes are

$$V_D' = V_{DS} - I_{DS} R_D \quad (4)$$

$$V_S' = I_{DS} R_S \quad (5)$$

A value for  $\bar{\mu}_n$  is extracted from the measured drain-source current and Eq. (2) for a given gate voltage.

The measured mobility values are plotted in Fig. 2 using different electrical techniques at room temperature. In a charge neutral channel, previous methods overestimate the channel mobile charge because no provision was made to include the finite space charge at the channel-buffer junction. Further they are not applicable to mobility profiling in the near pinchoff regime because depletion layer approximations were used in the analysis.

The neutral channel mobility in Fig. 2 is in good agreement with the theoretical calculations of Rode (1970) and Wolfe, et al. (1970). The degradation in  $\bar{\mu}_n$  in the near pinchoff regime, however, cannot be explained from the conventional theoretical calculations. From the energy band diagram shown in Fig. 3 it is seen that the majority of conduction electrons travel in a narrow region close to the channel potential maximum and, therefore, are prone to local scattering effects. The interface states in Fig. 3 are hypothesized to originate from any changes in the growth conditions in an MBE system.

As the electron density is significantly lowered below the ionized donor density, ionized impurity scattering also increases. To understand the electron transport mechanism, a solution to the steady-state Boltzmann transport equation is obtained in the relaxation time approximation (Schrieffer 1955, Greene et al., 1960,

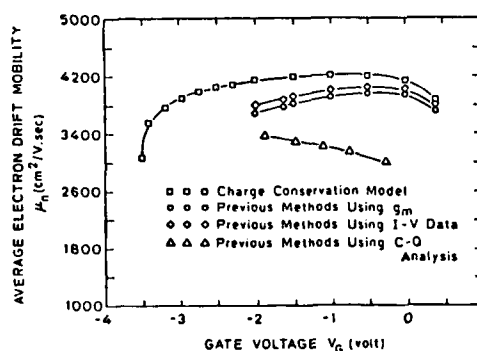


Fig. 2 Low-field electron drift mobility obtained from various electrical techniques.

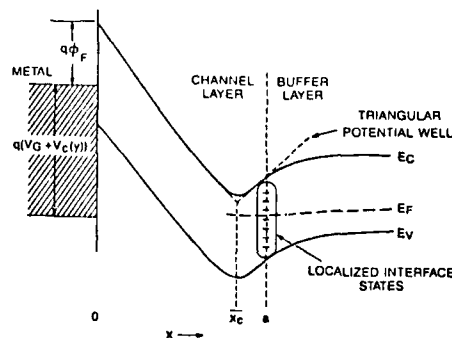


Fig. 3 Triangular potential well approximation of GaAs MESFET channel.



and Shenai 1986). In the calculations, the actual potential distribution in the channel is approximated by a triangular potential well and a parabolic band structure is assumed for the semiconductor. The scattering calculations show that for the range of electron densities under consideration, ionized impurity scattering is not the limiting factor in the mobility degradation mechanism. Instead, the dominant scatterers include the steep channel walls and localized interface states.

To obtain good agreement with the experimental results, about  $3 \times 10^{11} \text{ cm}^{-2}$  states are required as shown in Fig. 4.

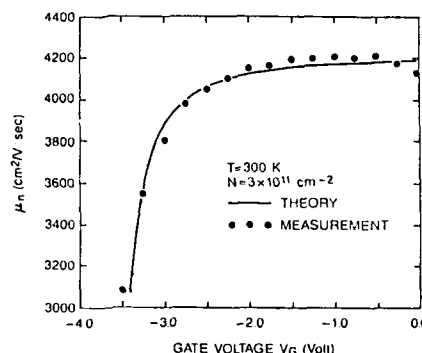


Fig. 4 Theoretical and experimental comparison of  $\mu_n$ .

To obtain good agreement with the experimental results, about  $3 \times 10^{11} \text{ cm}^{-2}$  states are required as shown in Fig. 4.

#### 4. Conclusions

The data presented here show that considerable degradation in  $\mu_n$  occurs in the near pinchoff regime in GaAs MESFETs. The experimental results are obtained from devices in which atomically clean channel- buffer interfaces were fabricated by MBE. These results are in excellent agreement with the transport calculations made from a solution of the steady-state Boltzman transport equation. It is shown that ionized impurity scattering plays a minimal role in the mobility degradation mechanism and that the electrons are predominantly scattered from the steep channel walls and localized interface states.

#### Acknowledgments

This research was supported through an industrial grant from Hewlett- Packard Microwave Technology Division, 1412 Fountain Grove Parkway, Santa Rosa, CA 95401, and also by SRC under contract 84-02-047. The authors are indebted to Marek Mierzwinski for assistance during device fabrication.

#### References

- Das M B, et al., 1982, IEEE Transactions on Electron Devices *ED-29* 205
- Ford W, et al., 1982, Semiinsulating III-V Materials (S. M. Ebeid and B. Tuck, Eds.) 352
- Greene R F, et al., 1960, Phys. Rev. *118* 967
- Houng Y M, et al., 1978, J. Appl. Phys. *49* 3348
- Illegems M, et al., 1975, Fifth Int. Symp. GaAs and Related Compounds, in Inst. Phys. Conf. *24* 1

- Joyce W B, et al., 1977, Appl. Phys. Lett. 31 354  
Lee K, et al., 1984, IEEE Transactions on Electron Devices ED-31 390  
Lehovec K, 1974, Appl. Phys. Lett. 25 279  
Rode D L, 1970, Phys. Rev. B2(15) 1012  
Schrieffer J R, 1955, Phys. Rev. 97 641  
Shenai K, et al., 1985 (a), IEEE Transactions on Electron Devices ED-32 2550  
Shenai K, et al., 1985 (b), IEEE Electron Device Letters EDL-6 528  
Shenai K, 1986, Ph. D Dissertation, Stanford University, Stanford, CA  
Sites J R, et al., 1980, IEEE Transactions on Electron Devices ED-27 2277  
Walukiewicz W, et al., 1979, J. Appl. Phys. 50 899  
Wolfe C M, et al., 1970, J. Appl. Phys. 41 3088

## **Effects of thin and high-carrier concentration active layer for GaAs MESFET performance**

Yutaka Matsuoka, Suehiro Sugitani, Naoki Kato and Hajime Yamazaki

NTT Electrical Communications Laboratories

3-1, Morinosato Wakamiya, Atsugi-shi, Kanagawa, 243-01, Japan

### Abstract

The reduction effects of channel-layer ion-implantation energy,  $E_n$ , on GaAs MESFET performance are investigated. A decrease in  $E_n$  from 67 to 30 keV produces an increase in K-value from 210 to 292 mA/V<sup>2</sup>mm and a decrease in  $\sigma V_{th}$  over an entire 2-inch In-doped low-EPD wafer from 49 to 30 mV, sufficiently suppressing short-channel effects in 0.5µm-gate-length FETs to permit LSI applications. Rapid thermal annealing (RTA) was successfully applied to another 2-inch wafer for further improvement of the carrier concentration profile. Diode C-V data are correlated with FET characteristics to clarify the RTA effects. The K-value of long-gate FETs is increased by RTA as well as the  $E_n$  reduction. The  $\sigma V_{th}$  of the FETs on a conventional substrate is as low as 18 mV for RTA, indicating RTA's effectiveness in suppressing dislocation effects.

### 1. Introduction

GaAs MESFETs fabricated on semi-insulating (SI) substrates by direct ion-implantation have advantages for the development of high-speed ICs, because they include a potential of high trans-conductance (Ueno et al 1985) and offer generally reproducible and controllable processes. It is essential for high-speed GaAs ICs to improve the FET performance. Various kinds of self-aligned FET structures and process technologies have been proposed to realize the improvements. There are three key requirements for the improvements; a reduction of source resistance, a reduction of gate length without short-channel effects and channel layer thinning combined with increasing carrier concentration.

High-performance GaAs MESFETs have been realized mainly by the reduction of source resistance and suppression of short-channel effects due to improvements in device structure and process technology. However, not much attention has been paid to the characteristics of FET channel layer. In addition, the quantitative correlation between FET characteristics and carrier profiles has not been investigated.

Rapid thermal annealing (RTA) for activation of implanted ions is useful in obtaining high activation efficiency and in suppressing diffusion of the implanted ions. The effectiveness of RTA has been demonstrated in  $n^+$ -layer formation. For example, Kuzuhara et al (1985) obtained an  $n^+$ -layer with a peak carrier concentration as high as  $9 \times 10^{18}/\text{cm}^3$ . However, few applications of RTA have been made to channel-layer formation on a 2-inch wafer maintaining uniformity of characteristics.

In this paper, the reduction effects of channel-layer ion-implantation energy,  $E_n$ , on the characteristics of submicron-gate-length FETs are studied. Successful application of RTA to a formation of a thin, high-carrier-concentration layer on a 2-inch wafer is described. Numerical calculations are made for correlating Diode C-V data with FET I-V data, to clarify the channel-layer-thinning effects of RTA.

## 2. Effects of Low-Energy Implantation on BP-SAINT FET Performance

Buried P-layer (BP-) Self-Aligned Implantation for  $N^+$ -layer Technology (SAINT) FETs (Yamasaki et al 1984) were fabricated on SI 2-inch diameter substrates. A cross section of BP-SAINT FET is shown in Fig. 1. For channel layers, Si ions were implanted at energy levels of 67 keV and 30 keV on separate wafers. Be ions of  $6 \times 10^{11}/\text{cm}^2$  were implanted to form buried p-layers at an energy level either 90 keV or 70 keV according to channel-layer implantation energies. For  $n^+$ -layers, Si ions of  $4 \times 10^{13}/\text{cm}^2$  were implanted at the relatively high energy of 200 keV because the implantations were through a 1500 Å SiN layer. The wafers were annealed at 800°C for 20 minutes to activate the implanted ions using the SiN layer as a cap. A gate length,  $L_G$ , of 0.5 μm was obtained starting from a 1 μm line width. A 10 to 1 reduction stepper was used in each lithography process. The standard deviation of the gate length was as small as 0.03 μm.

I-V characteristics and threshold voltage,  $V_{th}$ , uniformity were compared between the 30keV- and 67keV-implanted 0.5μm-gate length BP-SAINT FETs. The characteristics were measured in detail to obtain I-V fitting parameters. It is well known that short-channel effects appear in the  $V_{th}$  dependence on drain voltage,  $V_{DS}$ , and subthreshold-region drain current  $I_{DS}^{sbt}$ , passing through the substrate under the channel layer.  $I_{DS}^{sbt}$  is characterized by subthreshold factor  $N_G$  defined as  $I_{DS} \propto \exp(V_{GS}/N_G kT)$ , where  $V_{GS}$ ,  $k$ , and  $T$  are gate voltage, Boltzman constant and temperature, respectively.

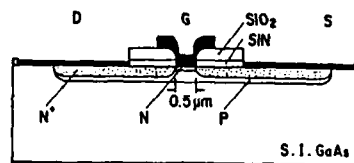


Fig. 1 Cross section of BP-SAINT FET.

Dependences of  $V_{th}$  and  $N_G$  on  $V_{DS}$  are shown in Fig. 2 for typical 30keV- and 67keV-implanted FETs. The  $N_G$ -value at a  $V_{DS}$  of 1V decreased from 1.5 to 1.4 due to the  $E_n$  reduction. This indicates that thinning the channel layer suppresses substrate leakage current as a result of suppression of short-channel effects. The  $N_G$ -value of 1.4, the smallest ever reported for submicron-gate length FETs, is sufficiently small even for LSI-applications because the  $N_G$ -value was larger than 1.5 for 1μm-gate length SAINT FETs without a buried p-layer used in a 16 kbit SRAM (Hirayama et al 1986).

Typical I-V characteristics for the 30keV implanted BP-SAINT FET are shown in Fig. 3, where solid lines indicate

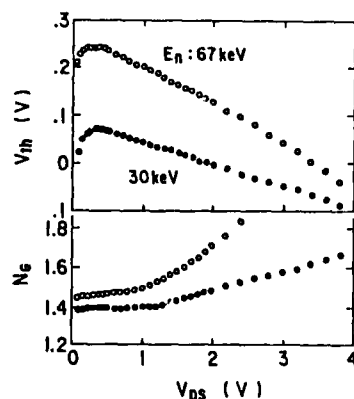


Fig. 2 Dependences of  $V_{th}$  and  $N_G$  on  $V_{DS}$ .

the measured data, and broken lines indicate calculated values. The dependence of saturation drain current  $I_{DS}^{sat}$  on  $V_{GS}$  and  $V_{DS}$  were calculated by the equation,

$$I_{DS}^{sat} = K (1 + \lambda V_{DS})^{-1} (V_{GS} - V_{th0} + \gamma V_{DS} - I_{DS} R_s)^2, \quad (1)$$

where  $V_{th0}$ ,  $\gamma$ ,  $K$ ,  $\lambda$  and  $R_s$  are fitting parameters. The parameters' values are listed in Table 1 not only for the I-V curves shown in Fig. 3 but also for I-V curves of a typical 67keV-implanted BP-SAINT FET and a typical 1 $\mu$ m-gate-length SAINT FET. The values of the first two parameters were determined by the linear relationship between  $V_{th}$  and  $V_{DS}$  shown in Fig. 2. The others were determined so as to fit the measured curves, on the basis of K-value dependence on  $V_{DS}$  and measured source resistance. The measured I-V curves are traced correctly by equation (1) when using the suitable fitting parameters, as shown in Fig. 3, and so in the other two cases. As a result of  $E_n$  reduction from 67 keV to 30 keV, the K-value increased from 210 mA/V<sup>2</sup>mm to 292 mA/V<sup>2</sup>mm, and a trans-conductance,  $g_m$ , as large as 270 mS/mm was obtained for the FET with a  $V_{th}$  of about 0.1V. The increase in K-value or  $g_m$  is attributed to both the channel layer thinning itself and short-channel effect suppression.

It is recognized from equation (1) that the  $\gamma$ -value is approximately equal to the ratio of drain-conductance,  $g_D$ , to  $g_m$ . Therefore the decrease in  $\gamma$ -value from 0.066 to 0.045 indicates a decrease in  $g_D$  due to the  $E_n$  reduction. Here emphasis should be put on the fact that, in spite of the short gate length the  $\gamma$ -value for the 30keV-implanted BP-SAINT FET is smaller than that for the FET used in the 16 kbit SRAM.

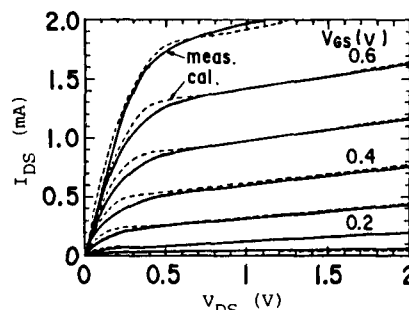


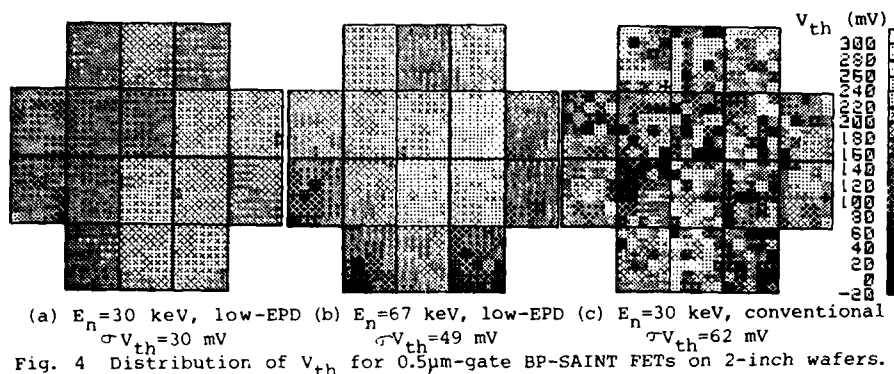
Fig. 3 Typical I-V characteristics of BP-SAINT FET.  
( $E_n$ :30 keV,  $L_G$ :0.5  $\mu$ m,  $W_G$ :20  $\mu$ m)

Table 1. I-V curve fitting parameters for three kind of FETs.

| FET      | $L_G$<br>( $\mu$ m) | $E_n$<br>(keV) | dose<br>( $\times 10^{12}/\text{cm}^2$ ) | K<br>(mA/V <sup>2</sup> mm) | $\lambda$<br>(1/V) | $V_{th0}$<br>(mV) | $\gamma$ | $R_s$<br>( $\Omega$ ) |
|----------|---------------------|----------------|--|-----------------------------|--------------------|-------------------|----------|-----------------------|
| BP-SAINT | 0.5                 | 30             | 4.0                                      | 292                         | 0                  | 100               | 0.045    | 40                    |
| BP-SAINT | 0.5                 | 67             | 2.2                                      | 210                         | 0                  | 268               | 0.066    | 40                    |
| SAINT    | 1                   | 67             | 1.1                                      | 185                         | 0.065              | 155               | 0.051    | 38                    |

Distributions of  $V_{th}$  of the BP-SAINT FETs on 2-inch wafers are shown in Fig. 4. There are 16 blocks on one wafer, and each block of 7.75mm x 9.2mm contains 30 FETs in an FET characteristic monitoring region of about 2 mm<sup>2</sup>. In the case of 30keV-implantation combined with In-doped low-dislocation density (or etch pit density, EPD) substrate (Fig. 4 (a)), 30 mV is the  $V_{th}$  standard deviation,  $\sigma V_{th}$ , in the entire wafer, while  $\sigma V_{th}$  is 49 mV in the 67keV-implantation case (Fig. 4 (b)). The  $\sigma V_{th}$  of 30 mV in the former case is the smallest in existence for submicron-gate-length high-performance FETs. In the small areas, extremely high uniformity was obtained for the 30keV-implantation. The  $\sigma V_{th}$ s in the 16 small areas are in the range of from 4 to 19 mV, and their mean value is only 11mV.

Threshold voltage scattering of IC-directed FETs is introduced mainly by dislocations in the substrate and  $L_G$  non-uniformity (Matsuoka et al 1984).



When a conventional wafer with dislocations on the order of  $10^4/\text{cm}^2$  was used as a substrate,  $V_{th}$  scattering was not decreased by the  $E_n$  reduction, as shown in Fig. 4 (c). This fact suggests that dislocation effects (Miyazawa et al 1983) are not suppressed by channel-layer thinning. The decrease in  $\sigma V_{th}$  resulting from the  $E_n$  reduction for the low-EPD wafer is attributable to the decrease in the contribution of  $L_G$ -scattering, which is related to the suppression of short-channel effects.

### 3. Improvements in active layer characteristics by rapid thermal annealing

Low-energy implantation is effective for obtaining high device performance as described above. However, as the energy decreases, activation efficiency is reduced and thermal diffusion of the dopants becomes dominant for carrier profile control. Rapid thermal annealing (RTA) was applied to overcome these situations. A schematic diagram of the RTA apparatus used in the experiments is shown in Fig. 5. There are 12 halogen lamps above the sample and 12 lamps below it at right angles to the upper group. The lamps on each side are divided into three zones, and the power ratio between the zones can be controlled independently. The sample wafer was sandwiched between Si wafers to maintain high uniformity and suppress slip-line formation, and was then put into the quartz chamber.

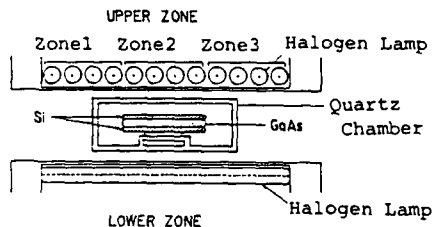


Fig. 5 Schematic diagram of the RTA apparatus.

Si ions were implanted into conventional 2-inch GaAs wafers. Patterning of the channel layer were made for each quarter of the wafers. Four dose levels were assigned to the quarters. For a comparison, activation was made either by RTA or by furnace annealing (FA) at  $800^\circ\text{C}$  for 20 min. In the case of RTA, the sample, which was implanted at  $E_n=30$  keV, was pre-heated to  $600^\circ\text{C}$ , then annealing power was supplied to the zones in a suitable ratio for 8 sec to obtain a maximum temperature of  $970^\circ\text{C}$ . In both cases, a  $1500\text{\AA}$  SiN layer was used as a cap during annealing. Diodes for C-V measurement and conventional FETs with various gate-lengths were fabricated on the wafers.

Carrier concentration profiles for three cases obtained by C-V measurements are shown in Fig. 6. Although the  $E_n$ -reduction effects can be observed in

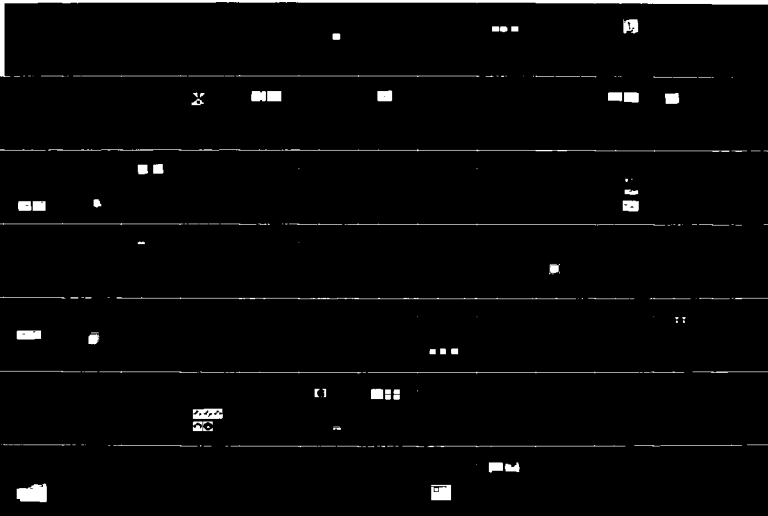
AD-A189 673

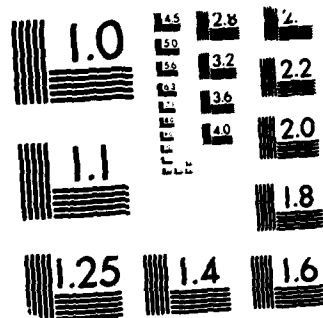
GALLIUM ARSENIDE AND RELATED COMPOUNDS 1986(U) ILLINOIS 6/7  
UNIV CHAMPAIGN W Y LINDLEY 1986 AFOSR-TR-87-1888

UNCLASSIFIED

AFOSR-86-0169

F/G 20/2 NL







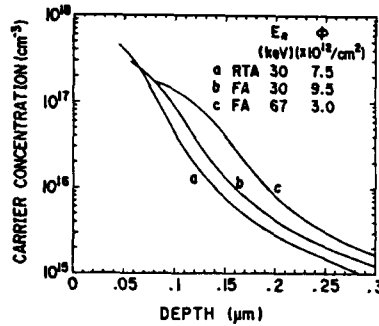
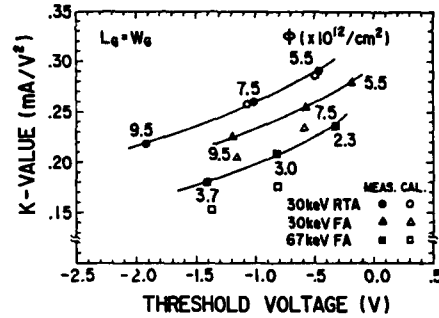
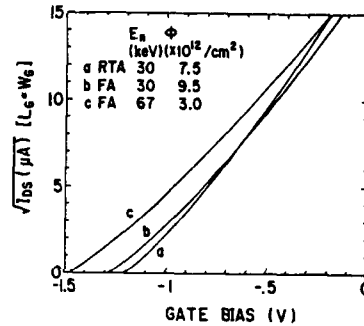


Fig. 6 Carrier concentration profile.

the case of FA, the effects are not as conspicuous as expected. Owing to the change from FA to RTA, the active layer became shallower and the carrier concentration became higher. Activation efficiency,  $\eta$ , and diffusion length  $L_D$  can be obtained by fitting the profile to the LSS curve. Using the projected range,  $R_p$ , and the projected standard deviation,  $\Delta R_p$ , given by Gibbons,  $\eta$  and  $L_D$  are estimated to be 53 % and 0.025  $\mu\text{m}$  for the 30keV-implanted RTA sample, and 35 % and 0.037  $\mu\text{m}$  for the 30keV-implanted FA sample. These values verify the superiority of RTA quantitatively.

Fig. 7 K-value versus  $V_{th}$ .Fig. 8 Calculated  $I_{DS}$  from C-V data versus  $V_G$ .

The relationship between K-value and  $V_{th}$  of the conventional FETs is shown in Fig. 7. The measured data of K-value and  $V_{th}$  in Fig. 7 are average values for more than 100 FETs. The K-value is normalized to the case of  $L_G = W_G$  since it was confirmed that the K-value is inversely proportional to  $L_G$  if short-channel effects do not appear. The change from FA to RTA shifted  $V_{th}$  to the negative direction as a result of high activation efficiency. For example,  $V_{th}$  of the FETs with a dose level of  $7.5 \times 10^{12}/\text{cm}^2$  was -1.04 V for the RTA sample but only -0.59 V for the FA sample. RTA also increased the K-value as a result of diffusion suppression. The increase in the K-value produced by the change from FA to RTA was nearly equal to that by the  $E_n$  reduction from 67 keV to 30 keV in the FA case.

C-V data were analytically compared to FET characteristics.  $I_{DS}$  can be calculated using charge density  $q(x)$  by the equation,

$$I_{DS} = W_G / L_G \int_{y_1}^{y_2} \mu [Q^{(s)} - Q(h)] h \varphi(h) dh \quad (2)$$

where  $Q(h) = \int_{y_1}^{y_2} (y) dy$ ,  $y_1, y_2$  are the depletion-layer widths on the source and drain side, respectively,  $\mu$  is electron mobility, and  $\epsilon$  is dielectric constant. Integration over the depletion-layer width,  $h$ , can be replaced by integration over the voltage variation of the depletion layer. Assuming that  $\mu$  is constant, we obtain the expression

$$I_{DS} = \mu W_G / L_G \int_{V_G}^{V_D} dV \int_{h(V)}^{\infty} (y) dy. \quad (3)$$

The right side of equation (3) can be numerically integrated using the C-V data. Figure 8 shows the dependence of  $I_{DS}$  on  $V_{GS}$  calculated by equation (3) using the data shown in Fig. 6. In the calculation,  $\mu$  is assumed to be  $3800 \text{ cm}^2/\text{Vsec}$ . It is possible to estimate  $V_{th}$  and the K-value using Fig. 8 and to correlate them to the measured FET data.

K-values and  $V_{th}$ s estimated by this method for the diode C-V data are also plotted in Fig. 7. It can be seen that the estimated values are very close to the measured values. So, important information can be drawn from C-V data even if carrier profile around peak position is unknown. A slight difference between the measured and calculated K-values noticed in Fig. 7 can be reduced if the dependence of the mobility on the carrier concentration is taken into account.

RTA has another beneficial effect. In the case of FA, the  $\sigma V_{th}$  of the FETs on the conventional substrate with dislocations was larger than several tens of mV even for  $6\mu\text{m}$  gate length FETs. On the other hand, a small  $\sigma V_{th}$  of 18mV was obtained for such FETs in the case of RTA. It is concluded that the undesirable dislocation effects generally observed in FA are suppressed by RTA. One of the possibilities of dislocation effect suppression by RTA is that the inhomogeneity of  $V_{As}$ -concentration around the dislocations might be decreased at high annealing temperatures.

#### 4. Conclusion

Low-energy ion implantations were successfully applied to  $0.5\mu\text{m}$ -gate length BP-SAINT FETs. A decrease in  $E_n$  from 67 keV to 30 keV produced an increase in K-value from  $210 \text{ mA/V}^2\text{mm}$  to  $292 \text{ mA/V}^2\text{mm}$ , and a decrease in  $\sigma V_{th}$  over an entire 2 inch wafer from 49 mV to 30 mV, sufficiently suppressing short-channel effects to allow LSI applications. Rapid thermal annealing (RTA) was successfully applied to a 30keV-implanted 2-inch wafer to raise activation efficiency and to produce a steeper carrier profile. Diode C-V data were quantitatively correlated with FET characteristics to clarify the RTA effects. It was also verified that RTA is effective for decreasing  $V_{th}$ -scattering by suppressing the dislocation effects. RTA, combined with the low-energy implantation is a very effective way to improve the performance and uniformity of FETs for LSI applications.

#### Acknowledgment

The authors wish to thank Dr. T. Sugeta and Mr. M. Hirayama for valuable discussions, and Drs. M. Fujimoto and T. Ikegami for their encouragement.

#### Reference

- Hirayama M, Togashi M, Kato N, Suzuki M, Matsuoka Y and Kawasaki Y 1986 IEEE Trans. Electron Devices ED-33 pp104-110
- Kuzuhara M, and Nozaki T 1985 J. Appl. Phys. 58 pp 1204-1209
- Matsuoka Y, Ohwada K, Hirayama M 1984 IEEE Trans. Electron Devices ED-30 pp 1062-1067
- Ueno K, Furutsuka T, Kanamori M, Higashisaka A 1985 Extended Abs. 17th Conf. Solid State Devices and Materials pp 405-408
- Yamasaki K, Kato N and Hirayama M 1984 Electron Lett. 20 pp 1029-1031

## **A GaAs high-electron-confinement transistor (HECT)**

S. P. Kwok, Milton Feng and H. B. Kim

Ford Microelectronics, Inc., Colorado Springs, Colorado, 80908, USA

**Abstract.** A self-aligned-gate GaAs High-Electron-Confinement-Transistor (HECT) using a thin insulator between Schottky barrier metal and n-implanted GaAs has been fabricated. The HECT exhibits square-law I-V characteristics. A super-high K-factor of 952 mS/(V\*mm) and a transconductance of 2200 mS/mm were measured in an enhancement HECT having a  $V_t$  equal to +0.98 V and gate length of 1.2 microns. The device exhibits stable hysteresisless I-V characteristics, which are independent of the sweep rate.

### **1. Introduction**

In this paper, we will report a self-aligned-gate GaAs MISFET having a thin interfacial insulator between the Schottky barrier metal and the n-implanted GaAs. The thin insulator was unintentionally formed but its presence was later verified by surface analyses. Its presence is also believed to be an important factor for the reported enhancement-mode FET having a large threshold voltage of +0.98 V and a super-high transconductance. The I-V and C-V characteristics are given and compared with those of self-aligned-gate MESFET. As will be shown later, both characteristics are consistent with a high-electron-confinement at the GaAs interface expected of a MIS structure with a thin insulator. We will refer to the device as a High-Electron-Confinement-Transistor (HECT). Our results are also consistent with the I-V characteristics of silicon and GaAs Schottky barrier diodes with thin interfacial oxides reported earlier by Card and Rhoderick (1971), Stirn and Yeh (1975 and 1977) and Meirheaghe et al (1980).

### **2. Device Fabrication and Structure**

Silicon ion (50 KeV and  $1.45 \times 10^{12}/\text{cm}^2$ ) was used for selective implantation on GaAs semi-insulating substrate to define the normally-off n-channel of FET; n+ implantation was done so that the drain and source regions are self-aligned to the gate metal. High-temperature annealing in arsine overpressure was used to activate the implanted channel. A thin insulator was formed under the gate. The presence of such thin insulator was verified using SIMS and Auger analyses but its thickness could not be measured accurately, as yet. An n-type Schottky barrier metal was used as the gate. The metal gate length was 1.2 microns. Ohmic contact was formed using commonly used AuGe metallization. The spacing between the gate metal and ohmic contact was 1.25 microns. Ti/Pt/Au was used as an overlay or interconnect metal. Figure 1 shows the cross section of the HECT.

## CROSS SECTION OF HECT

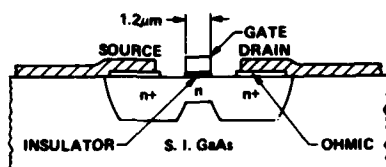


Figure 1  
(n: Si 50KeV 1.45E12/cm<sup>2</sup>)

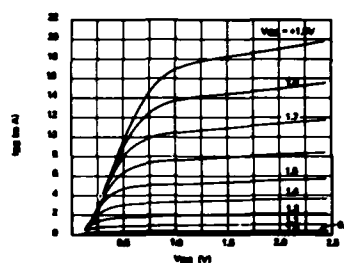
I-V CHARACTERISTICS OF HECT  
(1.2 X 20 MICRON GATE)

Figure 2  
(curve tracer 0.1-300 Hz)

## 3. Device I-V Characteristics

## 3.1 HECT I-V Characteristics

The room-temperature I-V characteristics of an enhancement-mode self-aligned-gate HECT with a 1.2 x 20 micron-gate are shown in Figure 2. The gate bias voltage is stepped from +0.9 V to +1.9 V at an increment of 0.1 V per step. The transconductance increases monotonically with positive gate-source bias voltage. At  $V_{GS} = +1.9$  V, a transconductance as high as 2200 mS/mm and drain current as high as 1 A/mm at  $V_{DS} = 2.5$  V were obtained. The corresponding drain-source output conductance was 80 mS/mm. Whence, the open-circuit voltage gain, which is the ratio of transconductance to output conductance, was 27.5. This value is comparable to that of a high-performance self-aligned gate MESFET. The transconductance value of 2200 mS/mm is, to our knowledge, the highest reported of any MESFETs or heterostructure FETs by Ueno et al (1985), Hiyamizu et al (1982), Solomon et al (1984), Sheng et al (1985) and Cirillo et al (1986). When the square root of the drain-source current at drain voltage equal to 2 V is plotted as a function of the gate voltage, as shown in Figure 3, the HECT exhibits a square-law relation with a threshold voltage equal to +0.98 V. From the gradient value of the plot, a K-factor of 952 mS/(V\*mm) is obtained, which is approximately a factor of 5 higher than the best value of enhancement MESFET reported by Kotera et al (1985). An average threshold voltage for a HECT of +0.98 V with a standard deviation of 25 mV over a 3" wafer was also demonstrated as shown in Figure 4.

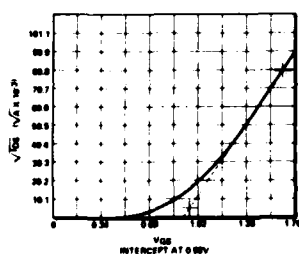
 $\sqrt{I_{DS}}$  VS  $V_{GS}$   
(1.2 X 20 MICRON GATE)

Figure 3

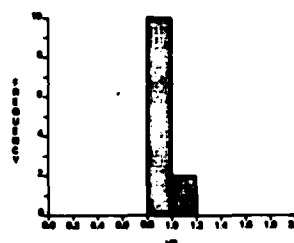
HECT THRESHOLD VOLTAGE  
DISTRIBUTION (3" WAFER)  
AVG=0.98V STD=25mV

Figure 4

the transconductance and the ratio of drain current to gate current (Beta) as functions of gate-source bias voltage above are given in Figure 5. The transconductance increases linearly at gate voltages above the threshold of +0.98 V and up to +1.9 V. To avoid the device burn out at higher currents, the gate voltage is limited to 1.9 V. These characteristics differ from those of MESFET, where the transconductance value starts to decrease at gate voltages above 0.7 V, which is due to the Schottky diode conducting a large current; hence, the voltage drop across the diode series resistance dominating the gate-source voltage. Although HECT exhibits a super-high transconductance at large positive gate voltages, the gate diode turns on and current increases significantly at voltages larger than 1.2 V. Consequently, the HECT is no longer operating in the normal voltage control mode of FET. As evident from Figure 5, Beta decreases from a value of 90 at  $V_{GS} = 0.75$  V to 3 at 1.9 V. However, HECT can still be operated under a normal FET mode of operation with very high transconductance. For example, at  $V_{GS} = 1.25$  V, a value of nearly 600 mS/mm can be realized with Beta equal to 10.

TRANSCONDUCTANCE & BETA VS  $V_{GS}$   
(1.2 x 20 MICRON-GATE)

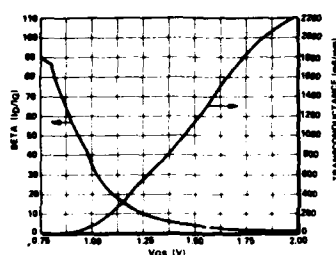


Figure 5  
(0.1-300 Hz)

GATE-SOURCE/DRAIN DIODE  
CHARACTERISTIC  
(1.2 x 20 MICRONS)

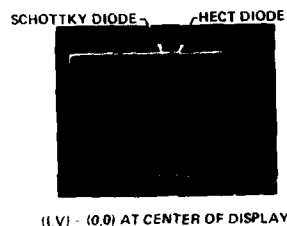


Figure 6

### 3.2 Gate to Source/Drain Diode Characteristics

The gate-source/drain diode of a HECT (1.2 x 20 microns) exhibits the well-known diode rectifying I-V characteristics as shown in the curve tracer picture of Figure 6. The apparent diode knee voltage is 1.2 V, which is approximately 0.5 V higher than the metal/GaAs Schottky diode of the same structure without the thin insulator. The detail of a semi-log plot of I-V characteristics, as shown in Figure 7, reveals the HECT diode ideality factor of 2.1, the equivalent Schottky saturation current of  $1E-12$  A and reverse leakage current of  $3.8E-8$  A at a bias voltage of -4 V.

The gate-source/drain capacitance measurement was done at 1 MHz. Figure 8 shows the C-V characteristics of the 1.2 x 20- micron gate structure as a function of gate bias. No attempt was made to separate the real part from the imaginary part of admittance in the capacitance measurement. To minimize the effect of leakage current, the gate bias voltage was limited to +0.8 V. As evident from Figure 8, the gate capacitance is relatively constant at 23 to 25 fF from reverse bias of -0.5 V to forward bias of +0.4 V, indicating that the channel is depleted of carriers. At higher forward bias voltages, the capacitance rises monotonically and reaches a maximum value at +0.8 V. At this point, the leakage current is in the order of  $1E-6$  A and the capacitance value is no longer valid.

## 4. Comparison of HECT and MESFET

The self-aligned-gate MESFET was fabricated using identical processes with the exception that the gate is a metal/GaAs Schottky barrier diode. Figure 9 shows the I-V characteristics of a high performance MESFET. The MESFET's threshold voltage is  $-0.4$  V. The transconductance at  $V_{GS} = 0.7$  V is  $260$  mS/mm for  $1.4 \times 20$  micron-gate. For convenience of comparison, the same I-V characteristics are replotted in Figure 10, using the scales identical to those of Figure 2. As evident in Figure 10, when biased above  $+0.8$  V, not only is there a significant gate current, but the transconductance value also decreases and approaches zero at gate voltage of  $+1.2$  V. Consequently, the current drive capability of MESFET is limited to  $4$  mA compared to  $20$  mA of HECT (Figure 2). Also, the HECT device exhibits linearly increasing transconductance up to  $+1.9$  V, which is similar to silicon MOSFET, where an increasing number of carriers are confined at the semiconductor accumulation/inversion interface. The silicon MOSFET transconductance increases linearly until reduction of carrier mobility or insulator breakdown dominates.

HECT & SCHOTTKY DIODE  
CHARACTERISTICS  
( $1.2 \times 20$  microns)

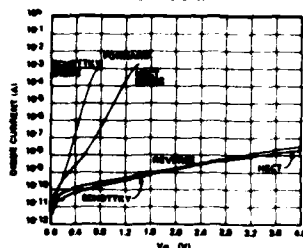


Figure 7

GATE-SOURCE DIODE C-V  
CHARACTERISTICS (1 MHz)  
( $1.20 \times 20$  micron)

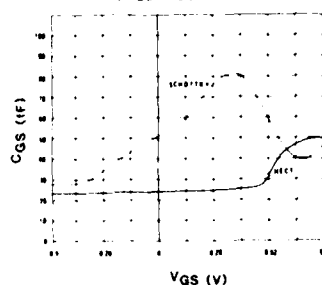


Figure 8

The gate-source diode characteristics of metal/GaAs Schottky barrier are also plotted in Figure 7 for comparison. The ideality factor of the Schottky diode was 1.18, while that of the HECT is 2.1. The significant increase in the ideality value reflects the presence of the insulator. The data are consistent with those reported by Card and Rhoderick (1971) and Meirhaeghe et al (1980). Unlike the Schottky diode, the HECT MIS diode, with a thin interfacial insulator, exhibits an excessive leakage current ( $1E-9$  A) at low forward bias voltages of less than  $0.4$  V.

The 1 MHz C-V characteristics of a gate-source Schottky diode are also plotted in Figure 8 for comparison. The capacitance decreases with reverse bias voltage and approaches an asymptotic value of  $27$  fF at  $-0.35$  V and beyond. The value increases monotonically with more positive bias voltages to  $82$  fF at  $+0.36$  V, above which the diode conduction current makes the capacitance measurement invalid. The HECT diode exhibits lower capacitance than the Schottky diode. Its capacitance reaches lower asymptotic value at approximately  $+0.4$  V and rises monotonically with more positive voltages and reaches its peak value at approximately  $+0.8$  V, above which the diode current conduction becomes dominant.

### 5. Stability of HECT Device Characteristics

HECT exhibits stable I-V characteristics with no hysteresis. Both the I-V and transfer characteristics of Figure 2 and 5 are unchanged when the sweep rate of the curve tracer is changed from 0.1 Hz to 300 Hz. At dc, the HECT also exhibits stable characteristics, as evident in the identical I-V characteristics of a HECT swept under normal curve tracer sweep rate and under dc 'sweep', as shown in Figure 11. Also, under the microscope's light there is no observable variation in its I-V characteristics, except currents at subthreshold levels. The C-V characteristics of the gate source diode measured at 1 MHz shown in Figure 8 are also stable and reproducible. The devices were tested over a period of more than 8 months and showed no instability of drift in its I-V characteristics.

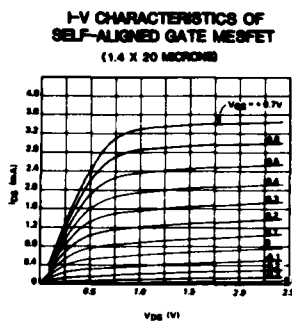


Figure 9

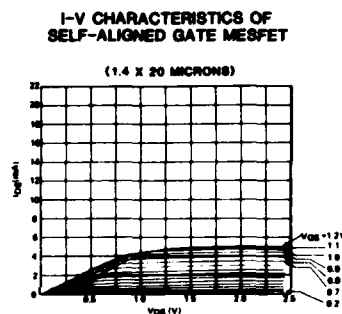


Figure 10

### 6. Discussion

Because the channel was implanted with a dosage of  $1.45 \times 10^{12}/\text{cm}^2$ , the maximum possible drain drift current, assuming 100% implantation activation and a saturation velocity of  $1 \times 10^7$  cm/s at 20 kV/cm, is 4.64 mA for a 20-micron wide channel. The HECT device of Figure 2 exhibits 20 mA drain current at  $V_{DS}$  equal to 2.5 V, which is more than a factor of 4 larger. In the absence of avalanche multiplication breakdown, which appears to be the case here, there are two possibilities which can account for such a high drain current: (1) The presence of high-electron-confinement in the accumulation layer at the GaAs/insulator interface under a large positive gate bias voltage, which makes the channel highly conductive. (2) The unintentional presence of highly doped  $p^+$  region between the Schottky gate metal and the  $n^-$  implanted region, which allows high injection of minority carrier holes into the  $n^-$  region. If hole injection dominates the current transport, the diode must exhibit minority carrier storage and recombination characteristics in its switching recovery. We have compared the turn-off transient currents of Schottky and HECT diodes when reverse bias step voltage is applied. As shown in Figure 12, the HECT diode not only shows no storage and recombination times but also recovers somewhat faster than the Schottky diode. This phenomenon appears to dispute the presence of larger minority carrier injection in the HECT device. Therefore, it appears that high-electron-confinement, whose surface concentration is significantly higher than the  $n^-$  implanted dosage, is responsible for the high current capability of HECT. The 1 MHz C-V characteristics, showing the capacitance rising with positive voltage to a maximum value at 0.8 V (Figure 8), is also consistent with the presence of such accumulation layer. Therefore, according to our present preliminary data, it appears that the Fermi level

at the GaAs/insulator interface is not pinned and the HECT device behaves partly as Schottky barrier and MIS. Unlike GaAs MIS reported thus far, for instance by Mimura et al (1980) and Weider (1984), HECT shows dc stable and frequency non-dispersive I-V characteristics at low frequencies.

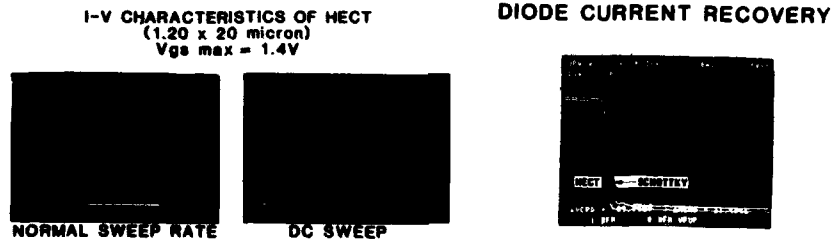


Figure 11

Figure 12

## 7. Conclusion

A GaAs High-Electron-Confinement-Transistor (HECT) using a thin insulator between Schottky barrier metal and GaAs as a gate was fabricated and its device characteristics given. An enhancement HECT having a room-temperature transconductance and K-factor as high as 2200 mS/mm and 952 mS/(V\*mm) was demonstrated with a 1.2 micron-gate length. A large average threshold voltage of +0.98 V with a standard deviation of 25 mV for a 3" wafer was demonstrated. The device shows stable, hysteresisless and frequency non-dispersive I-V characteristics, suggesting that the role of insulator/GaAs interface states in HECT is minimized. The large threshold voltage and high transconductance are highly desirable for high-speed LSI applications where large noise margin and current drive capabilities are needed.

## 8. References

- Card H C, Rhoderick E H 1971 Phys D V4 1589
- Cirillo Jr. N C, Shur M S and Abrokwhah J. K. 1986 EDL
- Hiyamizu S and Mimura T 1982 J Crystal Growth 56 455
- Kotera N, Shigeta J et al 1985 IEEE GaAs IC Sym Tech Digest 41
- Meirhaeghe van R L, Cardon F and Gomes W P 1980 Phys Stat Sol(a) 59 477
- Mimura T and Fukuta M 1980 IEEE Trans Electron Devices V27 1124
- Sheng N H, Lee C P, Chen R T et al 1985 IEEE EDL 6
- solomon P M, Knoedler C M and Wright S L 1984 IEEE EDL 5 379
- Stirn R J and Yeh Y C 1975 Appl Phys Lett 27 95
- Stirn R J and Yeh Y C 1977 IEEE Trans Electron Devices ED 24 476
- Ueno K, Furutsuka T et al 1985 17th Conf on Solid State Devices and materials Tokyo 405
- Wieder H H 1984 J Vac Sci Tech A2 (2) 97

**Acknowledgement:** The technical comments and suggestions of J. Harris and H. Wieder and C-V and transient measurements by P. Brusenback are appreciated.



## **Ion-implanted submicron MESFET's with high transconductance**

H Jaeckel, V Graf, B J Van Zeghbroeck, P Vettiger and P Wolf

IBM Research Division, Zurich Research Laboratory, 8803 Rüschlikon,  
Switzerland

**Abstract.** Fabrication of ion-implanted GaAs MESFET's with gate lengths down to  $0.1\ \mu\text{m}$  is reported. Key technological features are the use of electron-beam lithography and of shallow ( $1000\ \text{\AA}$ ) channel implants. Transconductance depends only weakly on gate length, and reaches a maximum value of  $370\ \text{mS/mm}$  for  $0.1\ \mu\text{m}$  gate length. Capacitance decreases and transit frequency increases with decreasing gate length. The transit frequency has a highest measured value of  $80\ \text{GHz}$  for a  $0.33\ \mu\text{m}$  device and is compatible with a drift velocity of  $1.5 \times 10^7\ \text{cm/s}$ , independent of gate length.

### **1. Introduction**

Over the years, many GaAs MESFET processes have been invented and investigated. Recently, various laboratories have developed fully-implanted GaAs MESFET processes because they look promising for the fabrication of LSI GaAs integrated circuits (Yamasaki *et al* 1982, Yokoyama *et al* 1983, Chang *et al* 1985, Ueno *et al* 1985). Most processes use  $1\ \mu\text{m}$  gate lengths, but the emphasis on submicron gate-length devices has increased (Ueno *et al* 1985, Yamasaki *et al* 1985, Kato *et al* 1983, Patrick *et al* 1985). We, too, have explored the extensibility of a fully ion-implanted process to submicron gate length, by characterizing the device performance, by addressing scaling and by investigating practical limitations.

In this paper, we present details of fabrication of submicron GaAs MESFET's with nominal gate length ranging from  $1\ \mu\text{m}$  down to  $0.1\ \mu\text{m}$ . Key features are the use of electron-beam lithography and of shallow channel implants with high doping density. To improve device performance, it is also important to reduce parasitic source and drain resistances for good access to the intrinsic device. Normally, a self-aligned MESFET structure (Yamasaki *et al* 1982, Ueno *et al* 1985) provides close spacing between  $n^+$  implant and the gate. Instead, we chose to use the high alignment capability of the electron-beam system ( $\approx 0.1\ \mu\text{m}$ ) to achieve dimensions comparable to self-aligned structures, and to gain a more flexible process.

## 2. Fabrication

Figure 1 shows the vertical structure of MESFET's and an SEM photograph. The devices were made with the following six-level process: first, 500 Å tungsten was sputtered onto the substrate and lifted off to form the alignment marks. Then the channel areas were masked and implanted with SiF(47) in the energy range of 40-60 keV. A deeper implant (100 keV) followed, also with SiF(47), to form the source and drain contact areas. Then the wafer was annealed at 850°C for 20 min in forming gas ( $N_2/H_2$ ). During annealing, the wafer was covered with a clean GaAs wafer (proximity anneal). The Ge/Au/Ni/Au (65 Å/110 Å/200 Å/90 Å) ohmic contact was lifted off and alloyed in  $N_2/H_2$  at 430°C for 40 sec. Before depositing the Schottky gate, the GaAs surface was cleaned in oxygen plasma and in HCl. Then the Ti/Pt/Au (150 Å/100 Å/950 Å) gate metal was lifted off. Finally, a Ti/Pt/Au (150 Å/100 Å/2650 Å) wiring layer was deposited.

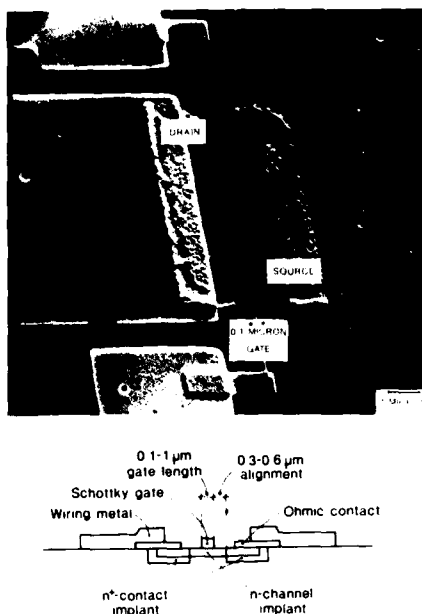


Fig. 1 Vertical structure and SEM photograph of the 0.1  $\mu m$  MESFET  
© 1986 IEEE

Lithography was done with an IBM Vector Scan E-Beam system (Chang *et al* 1986). For all lift-off steps, a double-layer resist system consisting of Terpolymer on PMMA was used. For masking the channel implant, a single layer of PMMA was chosen whereas the contact implant was masked with a double-layer resist. We were successful in scaling our gate length down to about 1000-1500 Å while still maintaining very smooth gate edges with variations of about 100-200 Å for a 1000 Å thick gate. Apart from the gate lithography, exposure of the contact implant, where a 0.7  $\mu m$  wide resist stencil remained between the two large drain and source openings, created a challenge with respect to proximity correction. It should be noted that alignment between contact implant and gate metal was done by layer-to-layer registration of each chip. In this way, a minimal alignment distance of 0.1  $\mu m$  was obtained. The nominal designed gate-source contact implant separations of 0.3  $\mu m$  and 0.6  $\mu m$  were reduced by 0.2-0.3  $\mu m$  owing to misalignment, lift-off profile overhang, lateral straggle, and implant diffusion. Our method allows for different alignment distances on the same wafer, as well as asymmetric alignment within one device.

Regarding implantation, our investigations showed that for vertical scaling of the devices simple reduction of the implant energy is not sufficient. Ion channeling effects broaden the doping profile. Partial ion-channeling tails are found for energies below 60-100 keV, and resulted in a significantly broader profile than predicted by LSS theory. This is illustrated in Fig.2 by the measured doping profiles with implant energies of 60 and 40 keV. The profiles were obtained from FATFET measurements. We also found that the channeling effects decreased slightly by increasing the ion-beam incidence angle during implantation from  $7^\circ$  to  $15^\circ$ . Since the critical angle for channeling increases sharply at lower energies and for heavier ions, we implanted the somewhat heavier ion SiF(47). From our electrical results, we conclude that vertical scaling of the channel thickness down to the desired range of about 30 nm and doping concentrations of  $10^{18} \text{ cm}^{-3}$  requires special implant and anneal techniques, such as rapid thermal annealing or the use of an amorphous capping layer (Onodera *et al* 1984, Graf *et al* 1986) during implantation, preferably together with a buried p-layer (Yamasaki *et al* 1985).

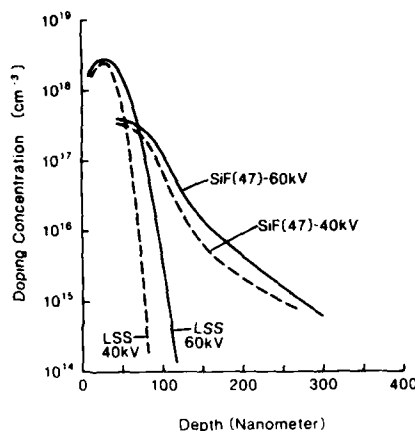


Fig. 2 Doping profile of different channel implants compared to LSS theory (© 1986 IEEE)

### 3. Results

Our submicron test vehicle contained process test sites to characterize the channel implant, surface leakage and contact resistance, as well as some transistor arrays. The general trends are the following: as the gate length is reduced by a factor 10 the maximum transconductance increases only by 45%. At the same time, the gate capacitance decreases, the transit frequency and the output conductance increase, and the threshold voltage becomes more negative.

Some of these trends are quantitatively summarized in Fig.3. The maximum transconductance ranges from 255 mS/mm for the  $1 \mu\text{m}$  device to 370 mS/mm for the  $0.1 \mu\text{m}$  device at  $V_{gs} = 0.7 \text{ V}$ . The weak increase of transconductance with

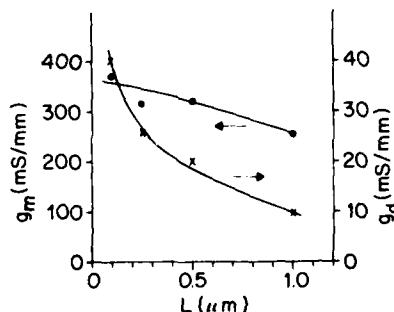


Fig. 3 Transconductance  $g_m$  and output conductance  $g_d$  versus nominal gate length for devices with  $0.3 \mu\text{m}$  nominal gate to  $n^+$  implant separation

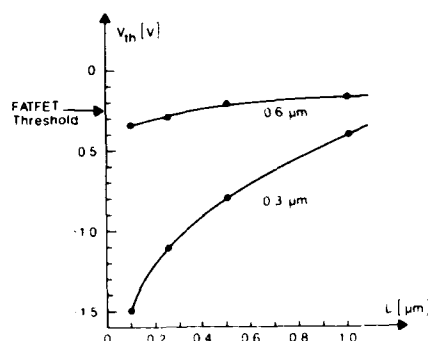


Fig. 4 Threshold voltage versus nominal gate length for devices with 0.3 and 0.6  $\mu\text{m}$  nominal gate to  $n^+$  implant separation

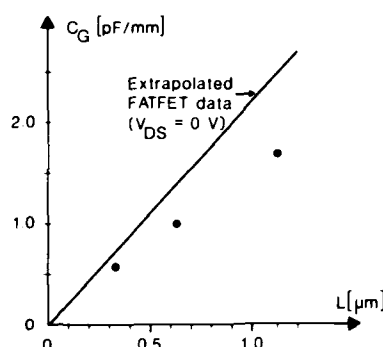


Fig. 5 Intrinsic gate capacitance versus measured gate length for 0.6  $\mu\text{m}$  nominal gate to  $n^+$  implant separation and  $V_{ds}=2\text{ V}$  and  $V_{gs}=0\text{ V}$ . The full line is an extrapolation of FATFET data for  $V_{ds}=V_{gs}=0\text{ V}$

decreasing gate length is partially expected because of drift velocity saturation. Another part is caused by the parasitic source resistance which, for the shorter gate devices, increasingly reduced the extrinsic transconductance. For the 0.1  $\mu\text{m}$  device, the intrinsic transconductance was estimated to be about 450 mS/mm. The output conductance increases from 10 mS/mm to 40 mS/mm with decreasing gate length, mainly a consequence of the reduced aspect ratio gate length over channel thickness. Threshold voltage dependence on gate length is shown in Fig.4 for devices with nominal alignment distance of 0.3  $\mu\text{m}$  and 0.6  $\mu\text{m}$ . For devices with 0.3  $\mu\text{m}$  nominal alignment, the threshold decreases from -0.45 V for the 1  $\mu\text{m}$  device to -0.8 V for the 0.25  $\mu\text{m}$  device. The 0.1  $\mu\text{m}$  device could not be turned off for  $V_{ds} > 0.6\text{ V}$ . For a nominal alignment of 0.6  $\mu\text{m}$ , a much weaker dependence on gate length is seen. This suggests that straggle and diffusion of the  $n^+$  implant underneath the gate occurred for devices with tighter alignment. A similar dependence of threshold voltage on alignment was observed in Ueno *et al* (1985).

Intrinsic gate capacitance  $C_{gi}$  of devices with nominal gate source alignment of 0.6  $\mu\text{m}$  is presented in Fig.5. It was computed from s-parameter measurements at 1, 2 and 4 GHz for a gate voltage of 0 V and a drain-source voltage of 2 V. The gate length of the devices was measured to be about 1.1, 0.56, and 0.33  $\mu\text{m}$ . To obtain  $C_{gi}$ , the parasitic capacitance of the pads, and the fringe capacitances on the left and right gate edges were determined and subtracted from the total gate input capacitance. As expected from one-dimensional theory, the capacitances scale fairly well with gate length. Extrapolation from FATFET measurements for  $V_{ds}=0\text{ V}$  yields the full line shown. The capacitance of the MESFET's is smaller, mainly because the depletion layer at the drain is thicker with a drain voltage applied. In addition, the source resistance, by its feedback effect, also decreases the measured gate capacitance.

The intrinsic transit frequency  $f_{ti}$  calculated according to the equation:  $f_{ti} = g_m / 2\pi C_{gi}$  is shown in Fig.6 for several devices as a function of gate length. Intrinsic gate capacitance was determined as previously described, and transconductance  $g_m$  is also computed from measured s-parameters. The  $f_{ti}$  values are independent of the measurement frequencies, so they are a good representation for our devices. For these MESFET's, the transit frequency usually peaks just above threshold and then drops again for more positive gate voltages. In Fig.6, the peak values are given. The spread in data points is due to device spread and not caused by measurement errors. In our devices, current saturation is mainly caused by drift velocity saturation and not so much by the channel pinch-off mechanism of the Shockley model. Under these circumstances, transit frequency  $f_{ti}$  can be written as  $f_{ti} = v_s / 2\pi L$ , with  $v_s$  the saturation drift velocity and  $L$  the gate length. As is obvious from Fig.6, our devices have a saturated drift velocity of roughly  $1.5 \times 10^7$  cm/s, independent of gate length. Velocity-overshoot effects which have been predicted theoretically (Ruch 1972, Yoshii *et al* 1983, Awano *et al* 1983, Fauquemberque and Pernisek to be published), are not visible in Fig.6, not even for the smallest gate length of  $0.33 \mu\text{m}$ . At present, we do not know whether this is a deficiency of our device structures or due to the assumptions made in the Monte Carlo device simulations.

#### 4. Conclusions

We have presented electrical data of submicron MESFET's made with implanted channels and electron-beam lithography. Transconductance increases weakly with decreasing gate length to a maximum of 370 mS/mm at  $0.1 \mu\text{m}$  gate length. Gate capacitance scales with gate length. Transit frequency increases nearly linearly with reciprocal gate length, indicating a saturated drift velocity of  $1.5 \times 10^7$  cm/s. We see no velocity-overshoot effects; a result which needs more clarification, both from the experimental and theoretical sides. These results show the potential of submicron MESFET's for high-speed applications. However, vertical scaling of the MESFET's is mandatory: because of increased two-dimensional effects (mainly caused by  $n^+$  implants) the  $0.1 \mu\text{m}$  device has increased output conductance, and cannot be pinched off for  $V_{ds} > 0.6$  V (see also Patrick *et al* 1985). Applying constant voltage scaling, the channel depth has to be reduced with gate length, and the channel doping to be increased with the inverse square of gate length, thus maintaining the pinch-off voltage. In addition, the depths of the  $n^+$  layers have also to be scaled. These measures should reduce the gate-length dependence of the threshold voltage and improve the transconductance and the output conductance. Our channels are typically

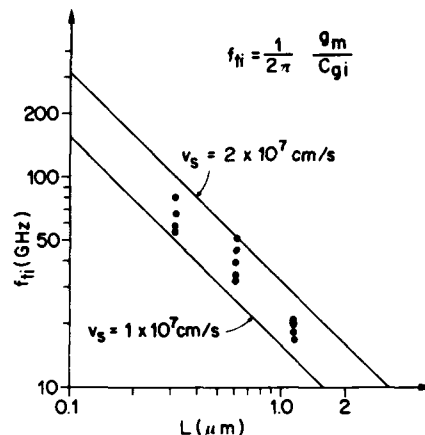


Fig. 6 Intrinsic transit frequency  $f_{ti}$  versus measured gate length

100 nm, whereas more shallow channels down to 30 nm should be obtained for a correct vertical scaling of the 0.1  $\mu\text{m}$  MESFET's. For an ion-implanted process, this remains a real challenge.

#### Acknowledgements

We should like to acknowledge the dedication and technical support of the people in our department who made this work possible : Kurt Daetwyler for the electron-beam lithography, Hans-Peter Gschwind for the chip lay-out, Willi Heuberger and Louis Perriard for ion implantation and annealing, Willi Walter, Hans-Peter Dietrich and Giovanni Sasso for the different metallizations, and Werner Bucher for his assistance during the microwave measurements. Finally, we thank Albert Oosenbrug for his support and encouragement during the course of this work, and Dr. Ronald F Broom for valuable comments.

#### References

- Awano Y, Tomizawa K, Hashizume N, Kawashima M, and Kanayama T, 1983, IEDM Technical Digest, 617
- Chang M F, Ryan F J, Vahrenkamp R P, and Kirkpatrick C G, 1985, *Electron. Lett.*, **21**, 354
- Chang T H P, Wilson A D, Speth A J, and Ting C H, 1976, *Proc. 7th Int. Conf. on Electron and Ion Beam Science and Technology*, p.392
- Fauquembergue R and Pernisek P, to be published
- Graf V, and W Heuberger, 1986, *Proc. IBBM86 in: Nuclear Instrum. & Methods in Phys. Res., Sect. B*, in print
- Ruch J G, 1972, *IEEE Trans. Electron Dev.* **ED-19**, 652
- Kato N, Yamasaki K, Asai K, and Ohwada K, 1983, *IEEE Electron Dev.* **ED-30**, 663
- Onodera H, Yokoyama N, Kawata H, Nishi H, and Shibatomi A, 1984, *Electronics Lett.*, **20**, 45
- Patrick W, Mackie W S, Beaumont S P, Wilkinson C D, and Oxley C H, 1985, *IEEE Electron Dev. Lett.* **EDL-6**, 471
- Ueno K, Furutsuka T, Kanamori M, and Higashisaka A, 1985, *Extended Abstracts 17th Conf. on Solid-State Devices and Materials*, Tokyo, p.405, 1985
- Yamasaki K, Asai K, and Kurumada K, 1982, *IEEE Trans. Electron Dev.* **ED-29**, 1772
- Yamasaki K, Kato N, and Hirayama M, 1985, *IEEE Electron Dev.* **ED-32**, 2420
- Yokoyama N, Ohnishi T, Onodera H, Shinoki T, Shibatomi A, and Ishikawa H, 1983 *IEEE J. Solid-State Circuits*, **SC-18**, 520
- Yoshii A, Tomizawa M, and Yokoyama K, 1983, *IEEE Trans. Electron Dev.* **ED-30**, 1376

## **Ultrahigh transconductance, tin doped, spike channel GaAs MESFETs grown by MOCVD**

K.H. Hsieh, J.D. Parsons, L.S. Lichtmann, L. Jelloian, and  
F.G. Krajenbrink

Hughes Research Laboratories, Malibu, CA 90265, USA

### **1. Introduction**

Low noise and high power GaAs MESFETs are of great technological importance for microwave and millimeter wave integrated circuits. Maximizing performance of these devices depends upon optimizing both material properties and device design.

Four growth-controlled characteristics are of paramount importance in attaining FET structures suitable for low noise, high power, high speed devices and integrated circuits. First, the buffer layer material must isolate the processed devices, and it must accomplish this without relying on deep levels for carrier reduction, in order to avoid capacitive coupling and light sensitivity. Second, the transition from undoped buffer layer to n-doped active channel must be very abrupt, to ensure complete channel pinch-off. Third, low resistance (i.e., high carrier concentration) contacts and high low-field electron mobility are mandatory for high transconductance and high speed device operation. Fourth, uniformities of better than  $\pm 1\%$  in layer thickness and carrier concentration over the entire chip area are required to achieve uniform pinch-off voltages and current gains.

Device design features which contribute to good performance are incorporated in our MESFET design. We have used spike channel doping to improve high frequency performance and minimize short channel effects (Daembkes et al. 1984).

Our efforts have been concentrated on development of an MOCVD growth process capable of achieving the material requirements reproducibly and consistently, and on development of a device fabrication process compatible with the epitaxial device structure. The results presented in this paper represent the successful culmination of these efforts: an MOCVD process capable of consistent growth of high quality materials and a spike channel doping profile, and a fabrication technology which yields state-of-the-art GaAs MESFETs.

### **2. Growth**

The epitaxial FET structures were grown by atmospheric-pressure MOCVD using an inverted-vertical (i.v.) reaction chamber (Parsons et al 1983, 1984a). In the i.v. arrangement, reactants enter at the bottom of the reaction chamber and are exhausted at the top, contrary to the usual

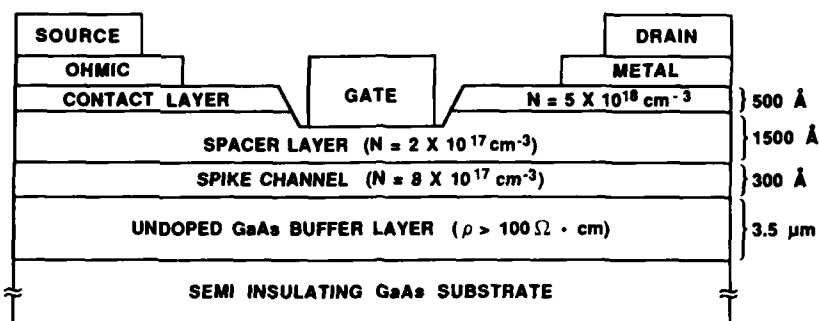


Fig. 1 Cross section of spike channel MESFET

practice with vertical chambers. A 51 mm (2 inch) diameter GaAs wafer is supported by placing its growth face downward on the inside bottom of a pyrolytic boron nitride (PBN) cup having a 44 mm diameter circular opening in its base. A 3 mm wide annulus at the wafer's outer rim is thus masked from growth. Heating is accomplished by RF induction in a graphite susceptor which rests directly on top of the back surface of the substrate and inside the PBN cup.

The purpose of the i.v. configuration is to achieve stagnation point flow characteristics and eliminate eddy-current recirculation of reactants without resorting to low pressures or substrate rotation. Epilayers grown in the i.v. reactor at atmospheric pressure and without substrate rotation exhibit thickness and carrier concentration uniformities better than +1% over a 2 inch wafer. The absence of recirculating eddies also facilitates the growth of hyperabrupt junctions (Leys et al 1984). The PBN cup shields the growth surface and reactant gases from the hot graphite susceptor. This eliminates epilayer impurity incorporation due to contamination from hot reactor components and permits reproducible growth of high purity GaAs (Parsons et al 1985).

N-type doped layers were grown using tetraethyltin (TET) as a tin source. Tin has several advantages as an n-dopant in MOCVD. Its vapor pressure is at least nine orders of magnitude lower than the more commonly used group VI elements. Its use, even at very high concentrations, does not produce a "memory effect" and contaminate subsequently-grown low-doped layers. Very abrupt high-to-low doping transitions are also possible. Tin also has a very high solubility and low diffusivity in GaAs and in III-V compounds in general, has less tendency towards amphoteric behavior and compensation than Si, and has the smallest activation energy of available n-dopants (Parsons et al 1984b). These attributes of Sn are important factors in achieving a low contact resistance and a spike channel doping profile.

Four identical GaAs spike channel FET structures, shown in Fig. 1, were grown in four consecutive growth runs. The structure consists of a semi-insulating undoped buffer layer, and Sn-doped channel, spacer, and contact layers, with thicknesses and dopings as shown in the figure. All layers were grown at 700 °C and at a rate of 7.0 μm/hr. The input



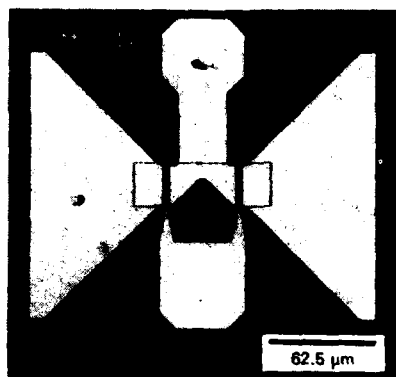
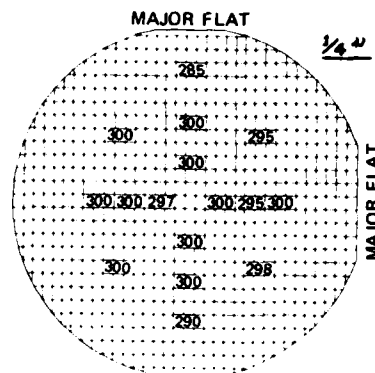


Fig. 2 Low noise MESFET layout

Fig. 3  $I_{Sat}$  (ma) uniformity map

molar ratio of  $AsH_3$  to trimethylgallium (TMG) was 8:1 during buffer layer growth and 10:1 during channel, spacer, and contact layer growth. The total flow rate of diluent, carrier, and reactant gases through the reactor was 2.9 slpm. Growth was stopped between layers in order to adjust flows and to allow flushing of reactants.

Sheet resistances of these wafers, measured with a Tencor M Gauge 200 resistivity meter, indicated very uniform doping and thickness across the wafer, consistent from run to run. Measured sheet resistances were 43.5, 56.2, 46.2, and 50.3  $\Omega$ /square for wafers from the four consecutive runs. These resistances represent the averages of measurements from five locations on the 2 inch wafers. The individual measurements were within 2% of the average value for the wafer. Defect counts on the wafers were approximately  $2000\text{ cm}^{-2}$ .

### 3. Device Fabrication

Two types of MESFETs were fabricated on each wafer using optical lithography. Devices with 5  $\mu\text{m}$  source to drain spacing (channel spacing), 1.0  $\mu\text{m}$  gate length, and 75  $\mu\text{m}$  gate width, referred to as "Test (T) FETs", were used in evaluation of material quality and in process monitoring. Devices with 2  $\mu\text{m}$  channel length, "low noise (LN) FETs", were also fabricated. These LN FETs had two gate fingers, each of dimensions 1  $\mu\text{m}$  x 25  $\mu\text{m}$ . This "50 2" layout is shown in Fig. 2.

Both types of devices were fabricated in the same process; from mesa isolation step to ohmic contact formation. Mesa isolation was achieved by wet chemical etching of the epilayers through to the semi insulating undoped GaAs buffer. Ohmic contacts were obtained with AuGeNi metals alloyed at 360  $^{\circ}\text{C}$  for one minute. After the alloying step, FET saturation currents were measured at sites across the wafer in order to examine uniformity. Results are shown in Fig. 3. Only a 1% variation was observed in a region within a 1 inch diameter of the wafer center, and a 3% variation in a 1.5 inch diameter region. The high uniformity of the saturation current reflects the good uniformity of the product of the doping concentration, epilayer thickness, and electron mobility across the wafer.

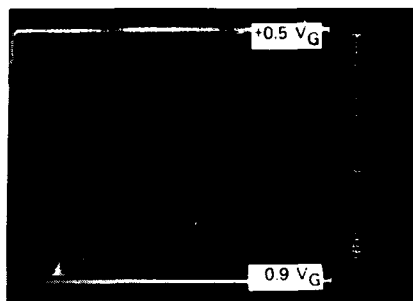


Fig. 4 Drain I-V for  $g_m = 440$  mS/mm MESFET

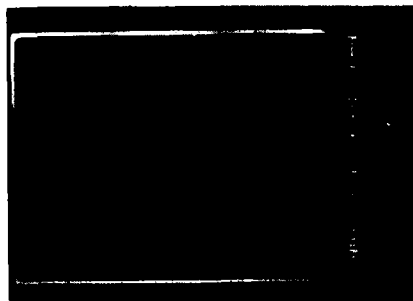


Fig. 5 Gate to source/drain I-V

Ti/Pt/Au was used for gate metallization. The gate metals were deposited after the gate channel was recessed to a distance of 20 nm above the spike channel layer, using an  $\text{NH}_4\text{OH}/\text{H}_2\text{O}_2/\text{H}_2$  etch. The small distance between the gate metal and the spike channel is a design feature which enhances the transconductance.

Both T FETs and LN FETs were tested in DC operation at room temperature using a curve tracer, an Accutest automatic DC test system, and an HP 4145A semiconductor parameter analyzer. Only high performance LN FET devices were selected for RF testing.

#### 4. Results

Most T FETs exhibited external transconductances ( $g_m$ ) above 200 mS/mm on each of the four wafers processed. On one wafer (MFET-3),  $g_m$  values as high as 392 mS/mm were measured. Two wafers out of the four were selected to have additional sections processed to fabricate LN FETs, as described above. Fig. 4 presents data from the best resulting device, an LN FET from wafer MFET 3. Drain I V curves for one finger of the two finger 50  $\Omega$  device are shown. A maximum  $g_m$  of 440 mS/mm was achieved with a gate bias of +0.5 V at room temperature. With no gate bias,  $g_m$  was over 300 mS/mm. A  $g_m$  of 440 mS/mm was seen on several other devices from this wafer.

This ultrahigh external transconductance, obtained with a spike doped channel MESFET produced by MOCVD, represents the state of the art for 1  $\mu\text{m}$  gate length devices, equaled only by MBE grown GaInAs/AlInAs HEMTs tested at room temperature (Hirose et al 1985). It is also much higher than the 330 mS/mm figure reported for MOCVD grown AlGaAs/GaAs HEMTs (Takanashi et al 1985).

The DC I V curves showed excellent saturation characteristics and were free of hysteresis and light sensitivity. Pinch off for the FET of Fig. 4 occurred at 0.9 V. Most devices tested showed complete pinch-off. A small drain current near pinch-off at high drain voltage in the drain I V for some devices was due to gate leakage. The gate leakage could be estimated from the gate to source/drain I V characteristics, shown in Fig. 5. At a gate to drain voltage of 2.5 V, the gate leakage was about 0.5 mA, which agrees with the drain I V characteristic near pinch-

A : 0-100    B : 100-200    C : 200-300  
D : 300-400    E : 400-500

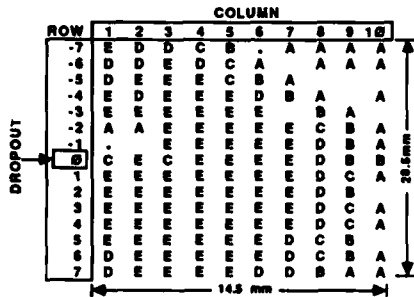


Fig. 6 Transconductance (mS/mm) uniformity map

A : 0-0.22    B : 0.22-0.42    C : 0.42-0.62  
D : 0.62-0.82    E : 0.82-1.0

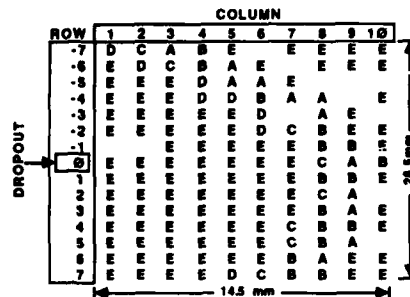


Fig. 7 Pinchoff voltage (volts) uniformity map

off in Fig. 4. This gate leakage was mainly due to the tunneling current between the heavily doped spike channel and the Schottky gate.

Fig. 6 shows the  $g_m$  values mapped across half of a 2 inch wafer (MFET-3) on which LN FETs were fabricated and tested. Of the 138 LN FETs tested, a very high fraction, 52%, exhibited  $g_m$  over 400 mS/mm (indicated by an "E" marker in the figure). The center of the 2 inch wafer is located at the dropout, hence the  $g_m$  values showed concentric uniformity. A total of 66% of the transistors exhibited  $g_m$  over 300 mS/mm, and 75% over 200 mS/mm. This data was obtained with the Accutest system. The measured values agreed with those obtained by the curve tracer and the HP 4145A parameter analyzer.

The pinch-off voltage map for LN FETs on this same wafer section is shown in Fig. 7. Most devices had pinch-off voltages between 0.82 and 1.0 V. Comparing these devices (marked "E") with the high transconductance devices in Fig. 6, we find that the  $g_m$  uniformity agrees with pinch-off uniformity in that both reveal similar concentric uniformity around the dropout.

There were minimal backgating effects on this wafer (MFET-3). Only a very small change of drain current was observed when -20 V was placed on a nearby backgate contact (Fig. 8).

##### 5. Discussion

We attribute the extremely high values of  $g_m$  for these MESFETs to the high material quality of the MOCVD epilayers and to the use of tin as the n-dopant. As mentioned above, tin produces a very shallow donor level and has comparatively little tendency towards self compensation in GaAs, even at high concentrations. Comparing materials grown in our laboratories, we have observed that Sn doped MOCVD GaAs epilayers have mobilities 10 to 20% higher than Si-doped MBE epilayers of the same carrier concentration.

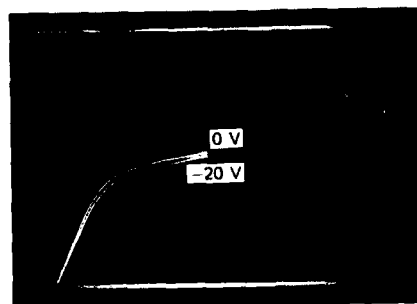


Fig. 8 Backgating characteristics

With regard to device characteristics, these high  $g_m$  devices exhibited very small contact resistances (0.037 to 0.040  $\Omega$  mm) and very small source resistances. For the 2  $\mu$ m channel LN FETs, source resistances as low as 0.13  $\Omega$  mm were observed. These small source resistances are the result of a heavily doped cap layer ( $n = 5 \times 10^{18}$  cm<sup>-3</sup>), a spike channel, and a small gate to source distance (0.5  $\mu$ m). In the deep gate recess process used for these devices, we were able to put the gate metals 20 nm above the spike channel layer, separated by a less heavily doped spacer layer. With such a short gate to channel distance, the transconductance was enhanced at the cost of gate tunneling leakage current.

Initial RF measurements have been carried out for selected high performance parts. S parameter measurements from 0.045 to 26 GHz gave a current gain cut off frequency  $f_T$  of 13 GHz and unity power gain frequency  $f_u$  of 38 GHz, respectable for 1  $\mu$ m gate length devices. Details of the RF characterization for these transistors and sub micron gate devices fabricated from the same wafers will be reported in other publications.

#### References

- Daembkes H, Brockerhoff W, Heime K 1984 IEEE Trans. Electron Devices **ED-31** 1032
- Hirose K, Ohata K, Mizutani T, Ogawa M 1985 Proc 12th Int. Symp. GaAs and Related Comp., Inst. Phys. Conf. Ser. 79 529
- Leys MR, Van Opdorp C, Viegiers MPA, Talen-Van Der Wheen HJ 1984 J. Cryst. Growth 68 431
- Parsons JD, Krajenbrink FG 1983 AACG West 7th Conf. Cryst. Growth, Fallen Leaf Lake, CA
- Parsons JD, Krajenbrink FG 1984a AACG-6/ICVGE-6 Atlantic City, NJ
- Parsons JD, Krajenbrink FG 1984b J. Cryst. Growth 68 60
- Parsons JD, Hunter AT, Reynolds DC 1985b Proc 12th Int. Symp. GaAs and Related Comp., Inst. Phys. Conf. Ser. 79 211
- Takanashi Y, Kobayashi N 1985 IEEE Electron Dev. Lett. **EDL-6** 154

## **High gain step-graded InGaAs(P)/InP heterostructure bipolar transistors for high current drive – high frequency applications**

R. N. Nottenburg, M. B. Panish\* and H. Temkin\*  
Bell Communications Research Red Bank, NJ 07701-5699

\* AT&T Bell Laboratories Murray Hill, NJ 07974

**Abstract.** We report on InGaAs(P)/InP double heterostructure bipolar transistors (DHBT) with step-graded emitter and collector junction interfaces. These devices exhibit high current gain  $h_{fe} \sim 1300$  and show no decrease in current gain for collector current densities up to  $1 \times 10^4 \text{ A/cm}^2$ . For a large area ( $1 \times 10^{-4} \text{ cm}^2$ ) transistor we measure an  $f_{max}$  (frequency of unity power gain) of 3.7GHz.

### **1. Introduction**

Double heterostructure bipolar transistors (DHBT), fabricated using the InGaAs/InP material system, are attractive candidates for integration in long wavelength (1.3-1.55 $\mu\text{m}$ ) fiber-optic communication systems and other high speed electronic applications. These devices already have demonstrated high current gain ( $\beta$ ) (Grote et al. 1985 and Kanbe et al. 1984) and high  $\beta$  at very low collector current levels (Nottenburg et al. 1986). In addition, these transistors should offer a combination of speed and high current capability uniquely suitable to integration with semiconductor lasers. A preliminary report (Shibata et al. 1984) has already demonstrated 1.6 Gbit/s modulation speed in a monolithically integrated laser driver.

To date however, the realization of high performance InGaAs/InP DHBT's has been impeded due to the limitations in materials growth and in particular the inability to compositionally grade the emitter and collector junction interface regions. Using gas source molecular beam epitaxy GSMBE (Panish 1986) we have fabricated step-graded interfaces by the incorporation of thin 0.02 $\mu\text{m}$  InGaAsP layers on both sides of the InGaAs base region. These devices have higher current gain than abrupt DHBT's and show no fall-off in  $\beta$  for collector current densities as high as  $1 \times 10^4 \text{ A/cm}^2$ . Furthermore, a large area ( $1 \times 10^{-4} \text{ cm}^2$ ) transistor is demonstrated with an  $f_{max}$  (frequency of unity power gain) of 3.7GHz.

### **2. Crystal Growth And Device Fabrication**

The InGaAs/InP double heterostructure bipolar transistors were grown by GSMBE on (100) oriented  $\text{N}^+$  substrates at a growth temperature of

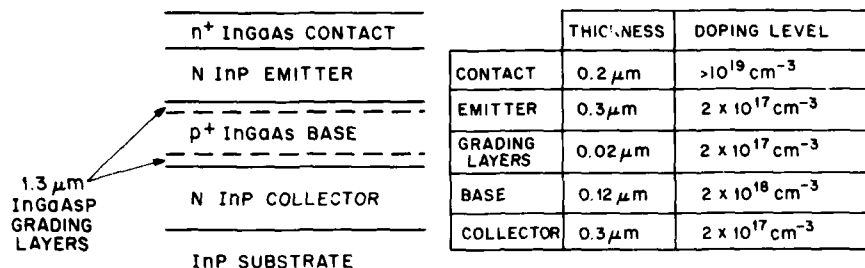


Fig. 1 Schematic representation of the step-graded DHBT device.

Table 1. Doping parameters and layer thicknesses for the step-graded DHBT with the lowest base doping.

500°C. Three device structures were grown. The first one, is a step-graded DHBT which is shown schematically in Fig. 1. The doping parameters and layer thicknesses for this device are given in Table 1. A second step-graded device with a much higher base doping level ( $p \sim 3 \times 10^{19} \text{ cm}^{-3}$ ) was also studied. The grading in both these devices was achieved by growing thin (0.02 μm) lattice matched InGaAsP ( $E_g \sim 0.95 \text{ eV}$ ) quaternary layers on both sides of the InGaAs base region. The third structure is identical to the first with the exception that the quaternary-step layers were omitted.

Devices were fabricated into mesa structures with emitter area  $40 \times 100 \mu\text{m}^2$  and collector area  $100 \times 100 \mu\text{m}^2$ . For high speed characterization individual transistors were bonded into conventional packages and power gain versus frequency was measured using a spectrum analyzer.

### 3. Material Quality

To assess the quality of the InGaAs/InP heterostructures the current-voltage characteristics of the emitter-base and base-collector diodes were measured and are shown in Fig. 2. A junction ideality factor  $n \sim 1.0$  is measured for both the emitter and collector diodes. The absence of any "2kT current" component demonstrates that these junctions are free of defects. In addition, the absence of any surface recombination current is predicted from the low intrinsic surface recombination velocity found in the InGaAs/InP system. Since both junctions show ideal behavior we can conclude that the growth sequence is unimportant. This is in contrast to the AlGaAs/GaAs system in which the AlGaAs to GaAs transition often results in lower junction quality. The common-emitter characteristics for this device are shown in Fig. 3. For a base current as low as 0.2 nA, a collector current  $I_C \sim 36 \text{ nA}$  is measured

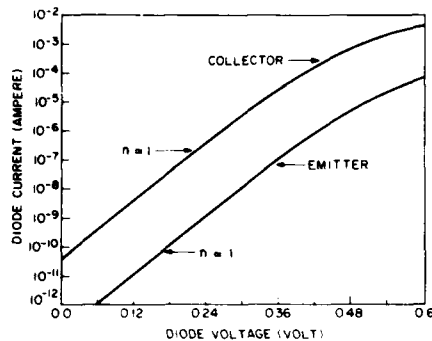


Fig. 2 Current-voltage characteristics of the emitter and collector junction diodes.

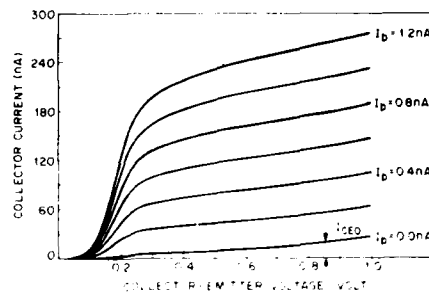


Fig. 3 Common-emitter characteristics for an abrupt DHBT at low collector current.

corresponding to a current gain of 180. It is also evident from Fig. 3 that the current gain at these low collector current levels is independent of  $I_C$ . From the high current gain and the small variation of  $\beta$  with  $I_C$ , we observe that the emitter injection efficiency for this device is close to unity over a wide range of emitter junction bias. These results are consistent with the current-voltage characteristics shown in Fig. 2.

The use of a wide band-gap InP collector also reduces the base-collector junction leakage current. With the emitter terminal open  $I_{CO} \sim 0.3 \text{ nA}$  is measured for  $V_{CB} = 1 \text{ V}$ . This is consistent with the collector saturation current  $I_{CBO}$  measured for the base terminal open ( $\beta \sim 100$ ,  $I_{CBO} \sim \beta I_{CO}$ ). Such a low value for the base-collector junction dark current further attests to the high quality of these materials.

#### 4. Step Graded Devices

##### 4.1 DC Characteristics

At high current levels the abrupt DHBT device exhibits (Fig. 4a) a soft turn-on and poor saturation characteristics. Similar characteristics have also been observed for abrupt InGaAsP/InP DHBT devices (Su et al. 1985) grown by liquid phase epitaxy. The dependence of  $I_C$  on collector bias has been shown to be due to the presence of a spike barrier in the base-collector conduction band (Hayes et al. 1984). By shifting the base-collector p/n junction into the narrow band-gap material (Su et al. 1985) transistors with low collector offset voltage and improved saturation characteristics were obtained. This approach, however, is not optimum for high speed transistor operation because of



Fig. 4a Common-emitter characteristics for the abrupt DHBT device at high collector currents.

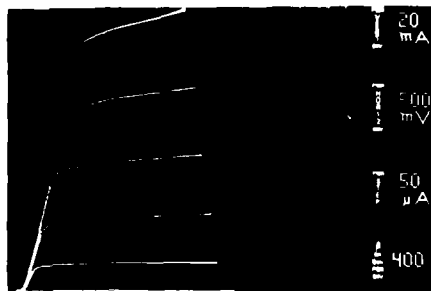


Fig. 4b Common-emitter characteristics for a step-graded DHBT.

the relatively low, high field drift velocity in the narrow band-gap material. In addition, this approach restricts the collector doping to fairly low values because of junction breakdown. A better solution is to step-grade the base-collector interface. This results in a low collector offset voltage and improved collection efficiency of injected base electrons. The common-emitter characteristics of a step-graded DHBT are shown in Fig. 4b. The addition of the grading layers reduces the collector offset voltage to less than 100mV and results in a nearly flat saturation region. In addition, the current gain (small signal current gain  $h_{fe} > 1300$ ) and the maximum current range are greatly improved as shown in Fig. 5. On the other hand, the introduction of InGaAsP step layers results in an increased dependence of the current gain on collector current ( $\beta \sim I_C^{0.3}$ ). These effects are presumably due to a slight lattice mismatch and varies from wafer to wafer. What is remarkable, however, is that even at very high base doping levels  $p \sim 3 \times 10^{19} \text{ cm}^{-3}$  where almost all the electrostatic potential drop is on the InP collector side, a single quaternary step provides sufficient grading. This is apparent from the common-emitter characteristics shown in Fig. 4c. This transistor exhibits flat saturation characteristics and shows a current gain  $h_{fe} \sim 120$  despite the very high base doping level. From the current gain of this device we can estimate a lower limit for the minority carrier diffusion length in the base  $\sim 1 \mu\text{m}$ .

#### 4.2 High Frequency Performance

The large area step-graded DHBT's are ideal for many applications requiring high current drive at moderate frequencies. In such devices the frequency response is limited by the charging time of the emitter and collector junction capacitances. Despite the relatively large



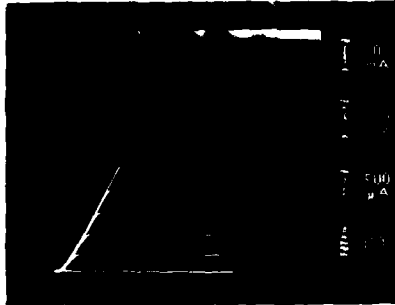


Fig. 4c Common-emitter characteristics for the step-graded DHBT with base doping  $p\text{-}3 \times 10^{19} \text{ cm}^{-3}$ .

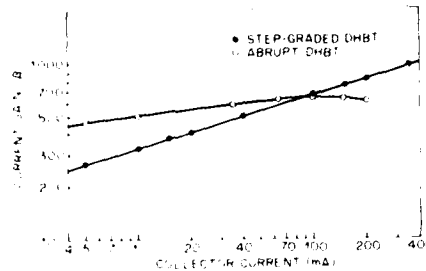


Fig. 5 Dependence of current gain ( $B$ ) on collector current.



Fig. 6 Dependence of power gain on frequency.

junction areas and associated capacitances ( $C_E=6\text{pf}$  and  $C_C=15\text{pf}$ ), we observe an  $f_{\text{max}} \sim 3.7\text{GHz}$  at a collector current of  $250\text{mA}$ . As shown in Fig. 5, the transistor (base doping  $p\text{-}2 \times 10^{18} \text{ cm}^{-3}$ ) exhibits a power gain of  $20\text{dB}$  at  $1\text{GHz}$ . This makes it an attractive device for a semiconductor laser driver where RF modulation currents on the order of  $50\text{mA}$  are required. In light of the high current capability of these transistors it should be possible to considerably reduce the device size and still have adequate laser drive capability.

### 5. Conclusions

InGaAs(P)/InP DHBT devices with high current gain ( $h_{fe} \sim 1300$ ) and low collector offset voltage  $\sim 100\text{mV}$  have been realized by step-grading the emitter and collector junction interfaces. The grading is achieved by the growth of thin ( $0.02\mu\text{m}$ ) lattice matched InGaAsP layers on both sides of an InGaAs base. These transistors show no decrease in current gain for collector current densities up to  $1 \times 10^4 \text{ A/cm}^2$  and exhibit an  $f_{\text{max}} \sim 3.7\text{GHz}$  making them attractive candidates for integrated

semiconductor laser driver applications.

#### Acknowledgements

The authors wish to thank R. Hamm, S. Hummel and S. Sumski for technical assistance during the course of this work and J. R. Hayes and R. F. Leheny for useful technical discussions.

#### References

- Grote N, Su L M and Bach H G 1985 Gallium Arsenide and Related Compounds Inst. Phys. Conf. Ser. 79 583  
Hayes J R, Gossard A C and Wiegmann W 1984 Electron. Lett. 20 766  
Kanbe H, Vlcek J C and Fonstad C G 1984 IEEE Electron Device Lett. EDL-5 172  
Nottenburg R N, Temkin H, Panish M B, Bhat R and Bischoff J C 1986 IEEE Electron Device Lett. (Nov.)  
Panish M B 1986 Progress in Crystal Growth (in press)  
Shibata J, Natao I, Sasai Y, Kimura S, Hase N and Serizawa H 1984 Appl. Phys. Lett. 45 191  
Su L M, Grote N, Kaumanns R and Schroeter H 1985 Appl. Phys. Lett. 47 28

## **GaAs E/D MESFET 1K-bit static RAM fabricated on silicon substrate**

H. Shichijo, J. W. Lee, W. V. McLevige and A. H. Taddiken

Central Research Laboratories  
Texas Instruments Incorporated  
P.O.Box 655936, MS 134  
Dallas TX 75265

### **ABSTRACT**

A GaAs E/D MESFET 1K-bit static RAM has been fabricated on a 2 inch GaAs-on-Si substrate. The GaAs layer is grown on a (100) silicon wafer by MBE. A row address access time of 6-14 nsec compares well with the 4-12 nsec for bulk GaAs devices fabricated concurrently using the identical E/D MESFET process. The total power dissipation of less than 500 mW and the memory array dissipation of 45 mW are also comparable to the bulk GaAs chips.

### **INTRODUCTION**

A recent success in growing high quality GaAs layers on silicon substrates has prompted an immediate interest in utilizing this material for device applications (Fisher et al. 1986). Besides the realization of GaAs/Si monolithic integrated circuits with high speed and optoelectronic GaAs circuits and high density silicon circuits on a chip (Choi et al. 1986), there exists a possibility of utilizing this material in place of bulk GaAs wafers for GaAs digital ICs. Some of the advantages of GaAs-on-Si wafers over bulk GaAs wafers include: 1) higher mechanical strength of silicon substrates compared to brittle GaAs substrates, which facilitates wafer handling and process automation, 2) availability of large diameter silicon wafers which is expected to reduce the cost of IC chips, and 3) three times higher thermal conductivity of silicon compared to GaAs, which helps in dissipating the heat from high speed circuits.

In spite of these expectations, however, the progress in applying this material for LSI-level digital circuits has been rather slow because of the limitations and uncertainties in material quality. The only reported result on circuit performance to date is a 17 stage ring oscillator (Nonaka et al. 1984) which contains no more than 50 transistors. Additionally, the compatibility of GaAs-on-Si wafers with GaAs wafers in a circuit fabrication process has not been demonstrated.

### **FABRICATION PROCESS**

The GaAs-on-Si wafers used in our studies are prepared by growing a 4  $\mu\text{m}$  thick GaAs layer on a 2 inch  $n^+$  doped (100) silicon substrate by MBE. The crystal orientation of the silicon substrate is tilted 4 degrees towards a (011) direction to avoid the formation of antiphase domains and to improve the surface morphology (Lee 1986). After the silicon substrate is heated to 1000°C

for 3 minutes in the MBE preparation chamber, the first 0.2  $\mu\text{m}$  of the GaAs layer is grown at 525°C at a growth rate of 0.3  $\mu\text{m/hr}$ . Subsequently the temperature is raised to 580°C, and the remainder of the GaAs layer is grown at a rate of 0.9  $\mu\text{m/hr}$ . The resulting GaAs surface layer is very smooth and shows an excellent surface morphology comparable to GaAs layers grown on GaAs substrates. A cross sectional TEM micrograph indicates that the dislocation density at the surface is approximately  $10^7$  to  $10^8/\text{cm}^2$ . The GaAs layer is left undoped in order to use a fully implanted MESFET process to examine the compatibility of the GaAs-on-Si material with a standard GaAs MESFET process and to compare directly with bulk semi-insulating LEC GaAs wafers. The background doping of the undoped layer is on the order of  $10^{14}\text{ cm}^{-3}$ .

The fabrication process for GaAs-on-Si wafers is identical to that for bulk semi-insulating GaAs wafers (McLevige and Chang 1985). It uses a fully implanted two-threshold process with a true double-level metal interconnection. All lithography is done using a 10x optical stepper with a resolution of 1  $\mu\text{m}$  which is also the minimum dimension of the MESFET gates. After three implants, the slices are annealed using a proximity arsenic overpressure system at 850°C for 15 minutes. It should be noted that after the annealing, the slices show no sign of cracking or peeling. On the contrary, the material quality is actually found to improve after this thermal annealing with a dramatic reduction of dislocations at the surface (Lee et. al. 1986). A cross sectional TEM shows that most of twins and slip lines are eliminated in the GaAs layer and that the dislocation density at the surface is reduced by several orders of magnitude. This improvement is attributed to the solid phase regrowth of the GaAs layer. After the annealing, the ohmic and Schottky metals are formed by evaporation and liftoff, followed by the formation of double-level metal interconnection to complete the circuit fabrication.

#### DEVICE PERFORMANCE

Fig.1 shows typical current voltage characteristics of enhancement and depletion GaAs MESFETs fabricated in a GaAs-on-Si wafer. The threshold voltages are 0.15 and -0.7 volts for enhancement and depletion devices, respectively. Maximum transconductances of 196 mS/mm for enhancement and 182 mS/mm for depletion devices have been obtained. The average values over a 2 inch wafer are 170 mS/mm and 147 mS/mm for enhancement and depletion devices, respectively. These values correspond to approximately 80% of those for devices fabricated in bulk GaAs wafers processed concurrently.

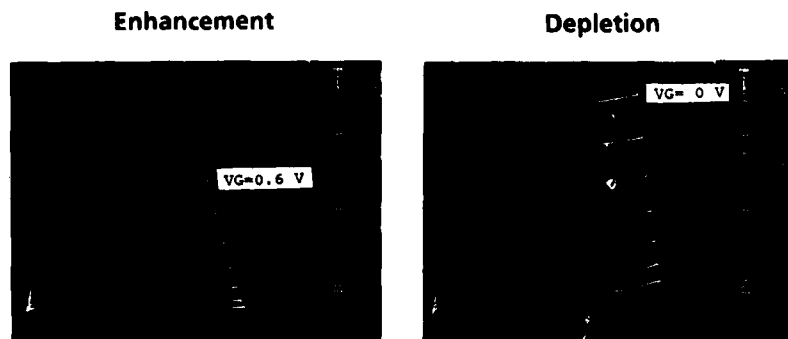


FIG. 1. I-V characteristics of fully implanted enhancement and depletion GaAs MESFETs fabricated in a GaAs-on-Si wafer.

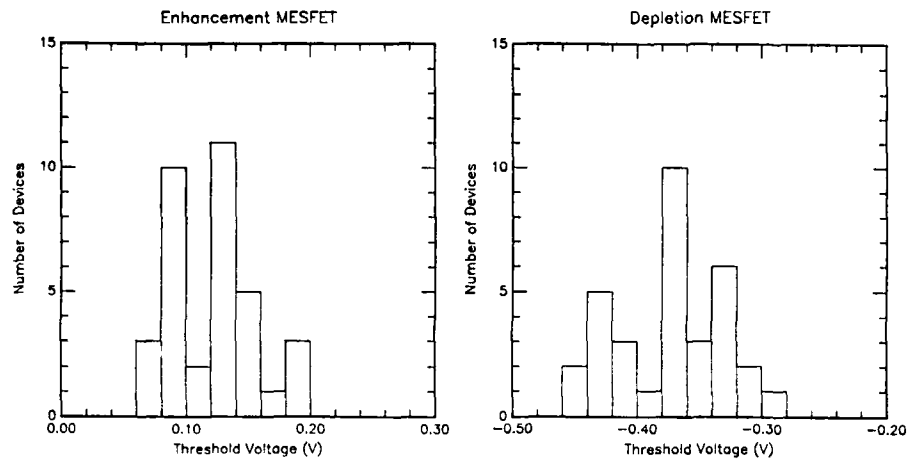


Fig.2. Threshold voltage uniformity of GaAs E/D MESFETs across a 2 inch GaAs-on-Si wafer.

Surprisingly, the uniformity of the threshold voltage is found to be excellent for GaAs-on-Si wafers. Fig.2 shows an example of the threshold voltage uniformity obtained across a 2 inch wafer. Standard deviations as low as 27 mV across a 2 inch wafer have been obtained with typical values of 30-70 mV. These uniformities are comparable to the best uniformity found for GaAs wafers. This excellent uniformity proves the excellent quality of the GaAs layer grown on a silicon substrate.

#### STATIC RAM PERFORMANCE

The circuit design of the 1K-bit static RAM fabricated in a GaAs-on-Si wafer is identical to the one used for bulk GaAs SRAM previously reported (McLevige and Chang 1985). The 1K SRAM uses DCFL for the memory array and BFL circuits for the peripheral circuits, and is fully ECL-compatible. The memory cell area is  $774 \mu\text{m}^2$  and the chip size is  $2.0 \times 1.75 \text{ mm}^2$ . Fig.3 shows a chip photograph of the 1K SRAM.

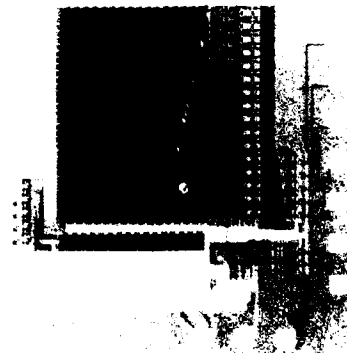


Fig.3. Chip photograph of 1K-bit static RAM.

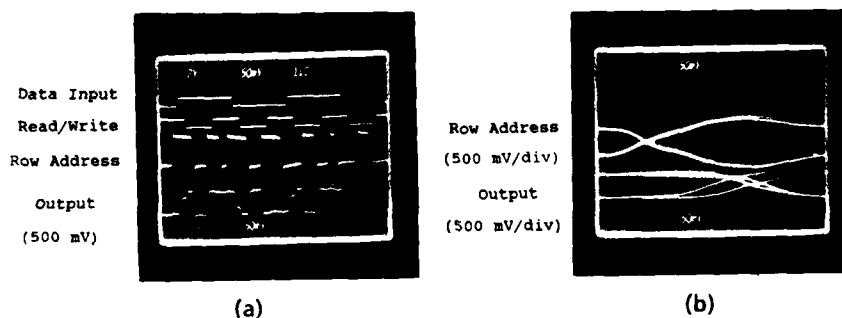


Fig.4. (a) Waveforms showing operation of two memory bits.  
 (b) Oscilloscope photograph of access time measurements. Horizontal scale is 2 ns/div. Both signals are measured using 0.1X picoprobe.

Fig.4 demonstrates the functionality of the SRAM. The input signal patterns in Fig.4(a) exercise the four possible permutations of address and data changes for two bits of memory. As shown in the waveforms in Fig.4(b), a minimum address access time of 6 nsec has been obtained. The measured access times for the GaAs-on-Si wafer range from 6 to 14 nsec compared to the 4 to 12 nsec observed for the bulk GaAs SRAMs fabricated concurrently using the same design. The power consumption is also very comparable. For both cases, the chip dissipates approximately 400 mW.

#### CONCLUSIONS

A 1K-bit static RAM with a minimum address access time of 6 nsec has been fabricated for the first time in GaAs-on-Si material. Comparable performances of LSI-level circuits between GaAs-on-Si wafer and bulk GaAs wafer indicate that the GaAs-on-Si technology is well suited for digital IC applications.

#### REFERENCES

- Choi H K, Turner G W, Windhorn, T H and Tsaur, B-Y 1986 IEEE Elect. Dev. Lett. EDL-7 500.
- Fisher R, Morkoc H, Choi C, Otsuka N, Longerbone M and Erickson L P 1986 J. Appl. Phys. 60 1640.
- Lee J W 1986 Materials Research Soc 1986 Spring Meeting, paper A1.3 Palo Alto.
- Lee J W, Shichijo H, Tsai H-L and Matyi R J 1986 7th Molecular Beam Epitaxy Workshop, Cambridge.
- McLevige W V and Chang C T M 1985 GaAs IC Symp. Tech. Digest 203.
- Nonaka N, Akiyama M, Kawarada Y and Kaminishi K 1984 Jap. J. Appl. Phys. 23 L919.

## **W-band characterization of high electron mobility transistor**

*J. Schaffner, K. Moeller, H. Fetterman*  
University of California, Los Angeles

*J. Berenz, K. Nakano*  
TRW Electronic Systems Group, Los Angeles

**Abstract:** The scattering parameters of high electron mobility transistors were measured at W-band using a six-port network analyzer. Connections to the transistors were made using microstrip and ridged waveguide transitions. Actual scattering parameters were then determined from the experimental data using a two-tier de-embedding process.

### **1. Introduction**

Technological advances in device fabrication have made it possible to develop field-effect transistors that operate at millimeter wave frequencies. In particular, high electron mobility transistors (HEMT) have received considerable attention for use in millimeter wave active circuits. Recently, HEMTs have been used in amplifiers at 70 GHz (Sholley 1986a) and at 94 GHz (Smith 1986b).

The design of these millimeter wave circuits is typically preceded by scattering parameter measurements of the transistor at microwave frequencies, from which a small signal transistor circuit model is derived. The performance of the transistor in a millimeter wave circuit is then obtained by extrapolating the model to the frequency of interest. The physical realization of the millimeter wave circuit usually requires extensive tuning.

This paper presents an approach to direct scattering parameter measurements of quarter-micron gate length HEMTs at W-band (75 GHz to 110 GHz). The measurements are achieved using a six-port network analyzer, along with a ridged waveguide to microstrip transition. The final results are obtained after de-embedding the transistors scattering parameters from the transition test fixture.

### **2. Six-Port Network Analyzer**

In order to measure scattering parameters at W-band, a six-port network analyzer was constructed using discrete commercially available waveguide components. The six-port junction allows the determination of a device's reflection or transmission coefficient by measuring the power at four ports (Enger 1977). In figure 1, the six-port network analyzer is configured for reflection measurements. The power measurements are taken at  $P_3$  through  $P_6$  in the figure by W-band thermistors which were chosen for their linearity. Power is supplied by a backward wave oscillator that has been frequency locked. The test fixture containing the device is connected to the remaining port. Power readings are acquired from each power meter using a computer controlled scanner and voltmeter. In addition to reflection measurements, the

transmission coefficients of the device can be obtained by a minor re-configuration of the input power and device connection ports.

### 3. Measurement of HEMT

A five section Chebyshev ridged waveguide transformer was fabricated to couple the waveguide of the six-port to 50  $\Omega$  microstrip transmission line, as shown in figure 2. The ridge was designed for a passband from 70 GHz to 110 GHz. Indium ribbon was placed between the end of the ridge and the microstrip line to ensure good electrical contact.

The HEMT was placed at the center of the test fixture and attached to the microstrip lines by ribbon bonds to the gate and drain, with the source grounded by ribbon bonds to the test fixture. Bias current was applied through 0.0007 inch bond wires, and microstrip chip capacitors with resonant frequencies at 75 GHz provided DC blocks.

Since good microstrip short circuits are difficult to achieve at millimeter wave frequencies, a two-tier de-embedding process was used to obtain the scattering parameter of the HEMTs. First, a test fixture comprising back-to-back waveguide to microstrip transitions separated by a length of microstrip line was characterized by measuring its transmission coefficient and reflection coefficient. Next, the reflection coefficient of a single transition was measured using a microstrip load. From these measurements the scattering parameters of the test fixture were determined. The next step was to measure the reflection and transmission coefficients of the test fixture with a HEMT. By assuming a symmetrical test fixture the device scattering parameters were determined by the method of Kupps and Sodomsy (1971).

Table 1 shows the de-embedded scattering parameters of a HEMT and bond ribbons at frequencies between 75 GHz and 85 GHz. In figure 3, the maximum available gain of the HEMT was calculated from the measured scattering parameters. It is apparent from this figure that the maximum frequency of oscillation of this HEMT occurred a little below 75 GHz.

At millimeter wave frequencies, the bond ribbons behave more like transmission lines rather than discrete inductances. Measurements are being planned on transistors with zero drain bias, which would simplify the small signal model enough to obtain an effective bond ribbon characteristic impedance (Curtice 1985).

It may be concluded from the transistors that have been characterized that it is difficult to predict from a device's DC behavior whether or not it will operate with gain at W-band. However, techniques are being developed which allow microwave characterization of devices that are still on a wafer. Thus, HEMTs which show promise of operation at W-band can be pre-selected for further characterization above 75 GHz of millimeter wave active circuits.

### References:

- Berenz, J.J., Nakano, K., and Weller, K., 1984, *IEEE MTT-S International Microwave Symposium Digest*, pp. 83-6



- Curtice, W.R. and Camisa, R.L., April 1985, *Test and Measurement World*, pp. 68-76.
- Engen, G.F., 1977, *IEEE Trans. Microwave Theory Tech.*, MTT-25, pp. 1075-80.
- Kupps, W and Sodamsky, K.F., Jan. 1971, *IEEE Trans. Microwave Theory Tech.*, MTT-19, pp. 122-3.
- Sholley, M. and Nichols, A., 1986a, *IEEE MTT-S International Microwave Symposium Digest*, pp. 463-5.
- Smith, P.M., Chas. P.C., Duh, K.H., Lester, L.F., and Lee, B.R., 1986b, *Electronics Letters*, vol. 22, 15, pp. 780-1.

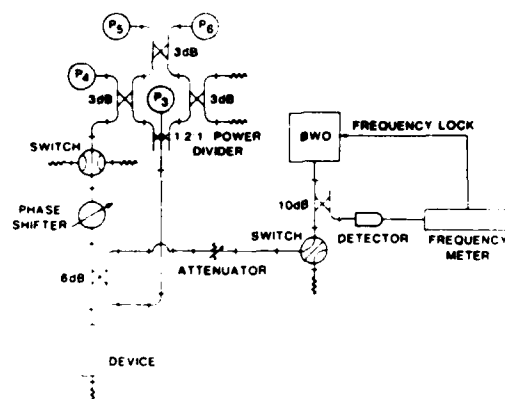


Figure 1

Six-port Network Analyzer in Reflection Measurement Configuration

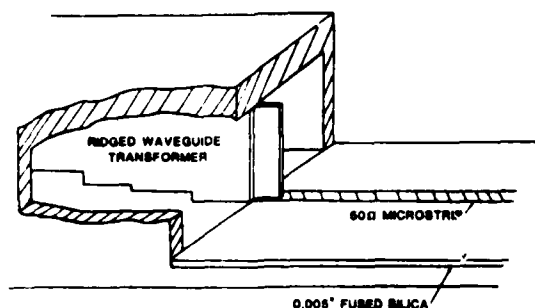


Figure 2

Ridged Waveguide to Microstrip Transition

|      | (11<br>MAG | PHASE  | MAG   | PHASE  | MAG   | PHASE  | MAG   | PHASE   |
|------|------------|--------|-------|--------|-------|--------|-------|---------|
| 75.0 | 0.303      | -75.3° | 0.477 | 9.4°   | 0.695 | -1.3°  | 0.109 | 103.8°  |
| 76.0 | 0.057      | 130.8° | 0.487 | 8.9°   | 0.593 | -2.1°  | 0.234 | 17.5°   |
| 77.0 | 0.221      | 129.7° | 0.430 | -16.2° | 0.545 | -24.6° | 0.170 | -160.4° |
| 79.0 | 0.409      | -41.6° | 0.467 | -27.4° | 0.551 | -24.2° | 0.219 | 2.6°    |
| 81.0 | 0.288      | 133.7° | 0.437 | -49.1° | 0.548 | -48.3° | 0.167 | -155.8° |
| 84.0 | 0.193      | -59.5° | 0.469 | -36.9° | 0.576 | -29.3° | 0.221 | -12.1°  |
| 85.0 | 0.137      | -15.1° | 0.368 | -30.5° | 0.440 | -22.8° | 0.240 | -11.6°  |

Table 1. De-Embedded Scattering Parameters of a HEMT and Bond Ribbons.

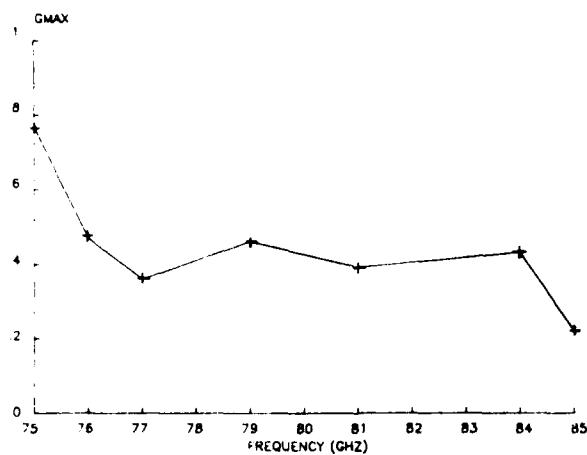


Figure 3

Maximum Available Gain of HEMT Connected with Bond Ribbons

## 15 GHz-band power InP MISFETs

H. Tokuda, H. Kamo, F. Sasaki and M. Higashiura

Microwave Solid-State Department, Komukai Works, Toshiba Corporation  
1, Komukai Toshiba-cho, Saiwai-ku, Kawasaki 210, Japan

**Abstract.** Power InP MISFETs have been developed using phospho-silicate-glass (PSG) as a gate insulator, which was deposited in situ at 300 °C after etching InP surface with HCl. Good interface properties with interface state density as low as  $2.5 \times 10^{12} \text{ cm}^{-2} \text{ eV}^{-1}$  were obtained. Fabricated MISFETs with gate length and width of 0.7  $\mu\text{m}$  and 800  $\mu\text{m}$ , respectively, exhibited maximum output power of 0.51 W with gain of 4.1 dB at 15 GHz.

### 1. Introduction

For microwave power device applications, InP is potentially superior to GaAs in terms of thermal conductivity and peak electron drift velocity. In fact, several results showing higher output power per gate width than that of GaAs MESFETs have been reported for InP MISFETs (Armand et al. 1983, Itoh and Ohata 1983). These results, however, are only limited to rather low frequencies and RF performance at the frequency higher than Ku-band has not been reported yet.

In this paper, we report on newly developed InP MISFETs and their RF performance at 15 GHz as well as 3 GHz. The MISFETs exhibited successful Ku band operation for the first time and higher output power per gate width than that of GaAs MESFETs was obtained. Section 2 describes the interface properties between a gate insulator and an InP substrate. The fabrication process and the device structure is shown in section 3. In sections 4 and 5, DC and RF characteristics are mentioned. Section 6 gives a summary.

### 2. Interface properties between insulator and InP

The improvement of the interface properties between a gate insulator and a substrate is a key factor for the successful operation of the MISFETs. In this work, a phospho-silicate glass (PSG) was used as a gate insulator. After an InP substrate was pretreated by etching with the solution of  $\text{H}_2\text{PO}_4/\text{H}_2\text{O}_2/\text{H}_2\text{O}$ , it was put into the reactor. The PSG film was deposited by the reaction of silane, oxygen and phosphine under atmospheric pressure. The deposition temperature was 300 °C. Before the deposition of PSG film, InP surface was slightly etched in situ in the reactor by HCl gas. The deposition rate was typically 250 Å/min.

MIS diodes were fabricated to investigate the interface properties between the PSG film and InP substrates. Undoped (n-type) InP (100) substrates with a carrier concentration of  $8.5 \times 10^{15} \text{ cm}^{-3}$  were used for this experiments. The thickness of the PSG film was 800 Å. Figure 1 shows the capacitance-voltage (C-V) curves of the diodes. The measuring frequency and the sweep rate of the bias voltage were 1 MHz and 0.1 V/s, respectively. In the figure, C-V curve for the PSG film without HCl etching is also shown to

clarify the effect of HCl etching. Comparing these two curves, the following differences are noticeable; (i) the width of the flat band ( $C_{FB}/C_{ox}=0.82$  in this case) voltage shift in the hysteresis loop reduces from 1 V (without HCl etching case) to 0.4 V (with HCl etching case), (ii) the interface state density obtained from Terman's method (shown in Fig. 2) is as high as  $1 \times 10^{12} \text{ cm}^{-2} \text{ eV}^{-1}$  at the bottom for the film without HCl etching, while it is as low as  $0.5 \times 10^{11} \text{ cm}^{-2} \text{ eV}^{-1}$  for that with HCl etching and (iii) the change of the surface potential is restricted from 0.1 V to -0.3 V for the film without HCl etching, while it becomes wider, from 0.1 V to -0.55 V (almost midgap) for that with HCl etching. These three improvements of the interface properties were essential on the fabricated MISFET operation for suppressing the drain current drift, increasing the transconductance and obtaining a good pinch-off characteristic. The frequency dispersion of the capacitance was also measured in the frequency range from 30 Hz to 1 MHz. The results showed that the dispersion at the biasing of 5 V was within less than 3 % throughout the measured frequencies, and this confirmed the attainment of the accumulation condition. The relative dielectric constant of the PSG film calculated from the accumulation capacitance was 4.9.

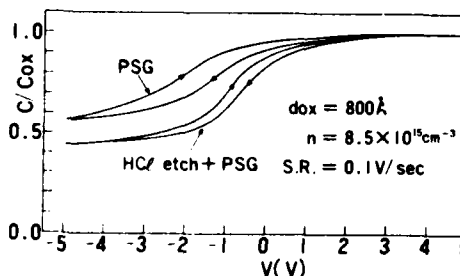


Fig. 1 C-V curves of MIS diodes.

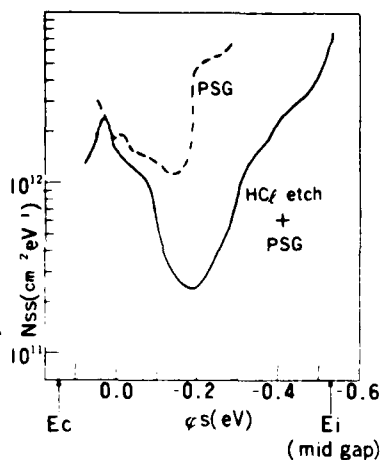


Fig. 2 Interface state density as a function of surface potential.

As is shown in the preceding paragraph, the effect of HCl etching before the PSG deposition is remarkable.

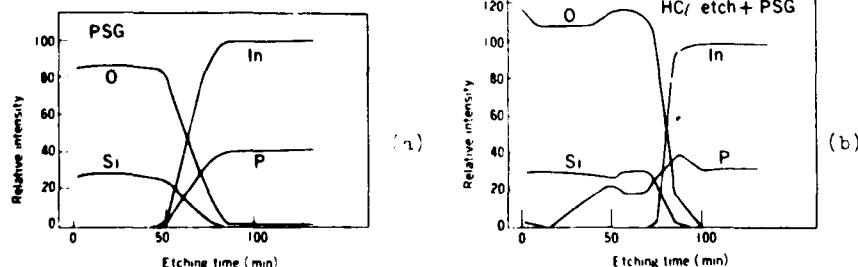


Fig. 3 AES depth profiles for PSG films deposited on InP. (a) Without HCl etching, (b) with HCl etching.

Okamura and Kobayashi (1980) have reported on the role of HCl etching as to remove the native oxide layer which exists inevitably on InP surface. Here, we propose another role of HCl etching for the deposition of PSG film. Figure 3 shows the AES depth profiles of the PSG films deposited without (Fig. 3(a)) and with (Fig. 3(b)) HCl etching. These two films were deposited under the same conditions except for the HCl etching. As is clearly seen, phosphorus signal was not detected for the film without HCl etching, while it was detected for that with HCl etching. However, SIMS measurement, which is more sensitive than AES, showed the existence of the phosphorus even in the film without HCl etching. The phosphorus concentration in the film with HCl etching was found to be 15-20 times higher than that in the film without HCl etching. These results suggest that HCl gas acts as a catalyst to make the phosphorus concentration high in the film. It is plausible that the higher concentration of phosphorus leads to the improvements of the interface properties, which was also reported by Pande and Gutierrez (1985). The role of HCl etching for the improvements of interface properties by making the phosphorus concentration high instead of removing the native oxide is also supported by the experiments shown below.

(i) The undoped  $\text{SiO}_2$  film was deposited in situ after InP surface was etched with HCl. The interface state density of the film was higher than that of the PSG film without HCl etching. This result indicates that the interface state density between the film and InP is dominated by the phosphorus concentration during the deposition of the film. (ii) The PSG film was deposited without HCl etching after the pre-treated InP surface was exposed to the air for 12 hours. The C-V curve was almost the same as that deposited immediately after the InP surface being pretreated. This result indicates that the native oxide does not affect the interface properties.

### 3. Fabrication process and device structure

Depletion-type InP MISFETs were fabricated. The fabrication process is shown in Fig. 4. An undoped buffer layer and an n-type active layer were successively grown on an Fe doped semi-insulating substrate by chloride ( $\text{In}/\text{PCl}_3/\text{H}_2$ ) VPE. The carrier concentration and the thickness of the active layer were  $1.5 \times 10^{17} \text{ cm}^{-3}$  and  $0.25 \mu\text{m}$ , respectively (Fig. 4(a)). After mesa-etching (Fig. 4(b)), source and drain electrodes were formed by alloying evaporated Ni/AuGe at  $400^\circ\text{C}$  for 2 minutes. The undoped  $\text{SiO}_2$  film was used as the spacer for the lift-off of Ni/AuGe metal (Fig. 4(c)). The gate pattern was delineated and recess-etching using a solution of  $\text{H}_2\text{PO}_4/\text{H}_2\text{O}_2/\text{H}_2\text{O}$  was performed to the depth where the drain to source current decreased to 120 mA. The gate insulator was deposited in the same process as described in section 2. The thickness of the PSG film was  $800 \text{ \AA}$  (Fig. 4(d)). The gate pattern was re-aligned precisely on the previously formed recessed pattern using the same photo-mask as used in the recess-etching. Al was evaporated with a thickness of  $7000 \text{ \AA}$  and lifted-off leaving the gate electrode (Fig. 4(e)). Finally, Au/Pt/Ti bonding pads were formed.

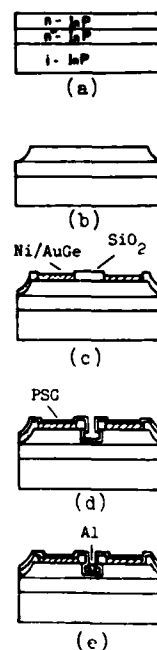


Fig. 4 Fabrication process of InP MISFET.

The top view of the fabricated chip is shown in Fig. 5. The gate width is  $800\text{ }\mu\text{m}$  ( $200\text{ }\mu\text{m} \times 4$  fingers) and the source to drain spacing is  $5\text{ }\mu\text{m}$ . A SEM magnified photograph near the gate electrode is shown in Fig. 6. The gate length was as short as  $0.7\text{ }\mu\text{m}$ , which enabled the successful operation at  $15\text{ GHz}$ . The shape of the recess was almost rectangular and the width of the bottom of the recess was  $1.2\text{ }\mu\text{m}$ . The obtained recess shape enabled to increase the drain breakdown voltage, though a slight increase of source and drain resistance was in trade.

#### 4. DC characteristics

Figure 7 shows the drain current/voltage characteristics of the fabricated MISFET, where the horizontal axis, vertical axis and the gate voltage step are  $1\text{ V/div.}$ ,  $20\text{ mA/div.}$  and  $1\text{ V}$ , respectively. In the figure, the left and the right show the gate bias being applied, negative and positive, respectively. The device showed a drain saturation current ( $V_{GS}=0\text{ V}$ ) of  $100\text{ mA}$  and a transconductance of  $40\text{ mS}$ . Clear pinch-off was observed with the pinch-off voltage of  $V_{GS}=-3.5\text{ V}$ . By positive biasing the gate to  $3\text{ V}$ , the drain current increased to  $200\text{ mA}$ . This indicates that the current dynamic range is larger than MESFETs, which is essential for higher output power operation.

The DC drain current drift was measured at room temperature. For the measurements, the gate bias was changed stepwise from  $0\text{ V}$  to  $-2\text{ V}$  or from  $0\text{ V}$  to  $2\text{ V}$ , while the drain bias was kept constant at  $3\text{ V}$ . For the former case, the decreasing current drift with a magnitude of  $10\%$  normalized with respect to the initial value was observed for the measurement time of  $30\text{ minutes}$ , while the increasing current drift with the magnitude of  $5\%$  was observed for the latter case. The decreasing or increasing current drift directions with gate biasing is inverse of that expected from the clockwise hysteresis loop measured in the C-V curves (Lile and Taylor 1983). The reason is not clear at present. Mobile ions may play a role in this phenomenon (Okamura and Kobayashi 1980).

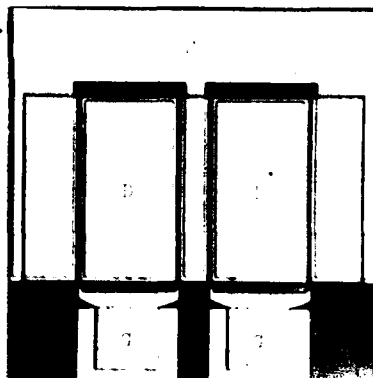


Fig. 5 Top view of the fabricated InP MISFET.



Fig. 6 A SEM magnified photograph near the gate electrode.

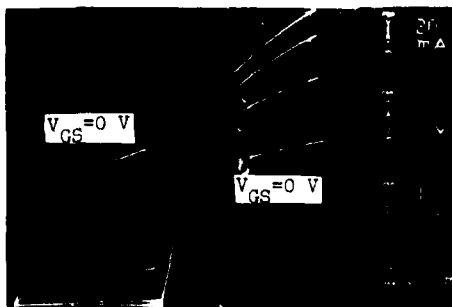


Fig. 7 Drain current/voltage characteristics of InP MISFET.

Though the degree of the drain current drift is larger than that reported by Pande and Gutierrez (1985), it seems to be improved by controlling the phosphorus concentration during the deposition.

### 5. Microwave performance

Microwave performance was evaluated on the fabricated InP MISFETs at 8 and 15 GHz. Chips were mounted and assembled in the ceramic packages. Figure 8 shows input-to-output characteristics of the device biasing at 18 and 0 V to the drain and the gate, respectively. The linear gains of 9.0 and 5.6 dB were obtained at 8 and 15 GHz, respectively.

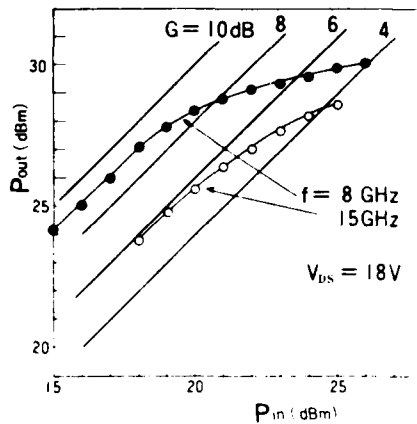


Fig. 8 Power input-to-output characteristics at 8 and 15 GHz.

The gain at 15 GHz seems to be small as compared with the reported values of GaAs MESFETs (Saito et al. 1983). This is because the gate finger in this device is too long for operation at 15 GHz (Kuvshinov 1980), and higher gains can be expected with further optimization in device design. At 8 GHz, the maximum output power of 1.0 W (1.25 W/mm) with gain of 4.2 dB was obtained. At 15 GHz, the dependence of output power on the drain voltage was also measured with gate biasing at 0 V. The drain-source voltage could be applied up to 20 V with negligible gate leakage current, typically 6.8  $\mu$ A. The result is shown in Fig. 9, where the power added efficiency is also shown. With the increase of drain voltage, output power increased. Output power of 0.81 W (1.0 W/mm) was obtained at the drain voltage of 20 V, with gain and power added efficiency of 4.1 dB and 21%, respectively. The value of 1.0 W/mm at 15 GHz is, to our knowledge,

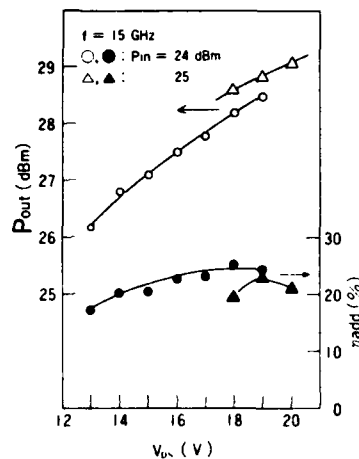


Fig. 9 Drain-voltage dependence of output power and power added efficiency at 15 GHz for different input powers.

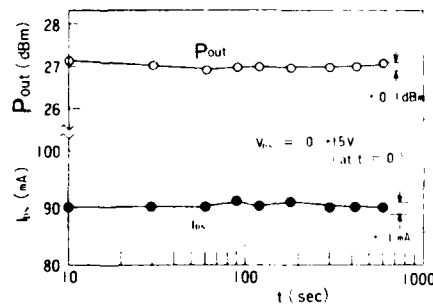


Fig. 10 Time dependence of output power and drain current after the drain voltage is switched on.

higher than the best results reported so far in GaAs MESFETs (DiLorenzo and Wisseman 1979). Figure 10 shows the gain and drain current drift in the RF measurements, where the drain voltage was applied stepwise with gate voltage being kept constant at 0 V. No gain and current drifts were observed during 10 minutes.

#### 6. Summary

InP MIS diodes and depletion-type InP MISFETs were fabricated and evaluated to clarify the feasibility for the high frequency microwave power devices. It was found from the C-V curves of MIS diodes that good interface properties were obtained by depositing PSG film in situ after etching InP surface with HCl. In the deposition process, HCl gas is supposed to act as a catalyst to increase the phosphorus concentration in the PSG film. And high concentration of phosphorus seems to lead to the improvements of the interface properties. The fabricated InP MISFETs with gate length of 0.7  $\mu\text{m}$  exhibited higher output power per gate width than GaAs MESFETs at 15 GHz. These results show that InP MISFET is very promising as a microwave power device.

#### 7. Acknowledgment

The authors would like to thank K. Kamei and S. Okano for their encouragement and helpful discussions.

#### References

- Armand M, Bui D V, Chevrier J and Linh N T 1983 *Electron. Letts.* **19** 433
- DiLorenzo J V and Wisseman W R 1979 *IEEE MTT-27* 367
- Itoh T and Ohata K 1983 *IEEE ED-30* 811
- Kuvas R L 1980 *IEEE ED-27* 1193
- Lile D L and Taylor M J 1983 *J. Appl. Phys.* **54** 260
- Okamura M and Kobayashi T 1980 *Japan. J. Appl. Phys.* **19** 2151
- Pande K P and Gutierrez D 1985 *Appl. Phys. Lett.* **46** 416
- Saito A, Kojima Y, Suzuki K, Kaneko Y and Aihara S 1983 *IEEE MTT-S International Microwave Symp. Dig.* 265



## **Correlation of undoped, In-alloyed and whole ingot annealed semi-insulating GaAs substrates for low noise microwave amplifiers**

H Kanber and D C Wang

Hughes Aircraft Company, Torrance Research Center, Torrance, CA 90509, USA

**Abstract.** The quality of LEC grown GaAs substrates critically affects the final low noise microwave device and circuit performance as evidenced by comparing Si implanted undoped, In-alloyed and whole-ingot annealed semi-insulating substrates. We investigated differences in Si implant activation, electrical profiles, and uniformity of material, device and circuit parameters. A noise figure of 2.0 dB with associated gain of 24 dB at 10 GHz was achieved for a monolithic two stage low noise amplifier.

### **1. Introduction**

Direct ion implantation technology is being widely used in GaAs integrated circuit fabrication. However, the final device and circuit performance still critically depend on the characteristics and quality of liquid encapsulated Czochralski (LEC) grown GaAs substrate materials. The role of dislocations on both digital and microwave device performance is also actively being researched by several laboratories. Active material parameters such as implant activation, sheet resistivity and saturated current may have quite different characteristics depending on the material growth technique. In this paper, we study the correlation between low noise device and circuit performance and material quality using undoped, In-alloyed and whole-ingot annealed semi-insulating GaAs substrates.

### **2. Device Fabrication**

Four types of semi-insulating GaAs substrates were selected: In-alloyed high pressure LEC, undoped standard low pressure LEC, undoped standard high pressure LEC and whole-ingot annealed high pressure LEC. The substrates were obtained commercially from different manufacturers and were 2-inch diameter crystals grown by the B<sub>2</sub>O<sub>3</sub> encapsulated high or low pressure LEC technique in pBN crucibles. The KOH defined average etch pit densities in the In-alloyed, standard high pressure, standard low pressure and the annealed high-pressure were 420,  $3.5 \times 10^4$ ,  $1.7 \times 10^4$  and  $5.8 \times 10^4$  cm<sup>-2</sup> respectively. The In content of the In-alloyed wafers was determined to be  $7.8 \times 10^{19}$  cm<sup>-3</sup> by the manufacturer. The as-grown resistivities of the above sequence of wafers were  $1.6 \times 10^8$ ,  $2.1 \times 10^7$ ,  $3.0 \times 10^7$  and  $4.6 \times 10^7$  ohm-cm respectively. After thermal conversion testing, the resistivity of the standard high-pressure substrates increased to  $2.7 \times 10^7$  ohm-cm, that of the standard low-pressure substrates increased to  $2.0 \times 10^8$  ohm-cm, and that of the annealed high pressure substrates decreased to  $3.5 \times 10^7$  ohm-cm. The implant and anneal parameters were chosen to fabricate the active channel layer in low noise GaAs monolithic microwave integrated circuits (MMICs). The substrates were implanted with 100 keV

$^{28}\text{Si}$  ions at a dose of  $5$  to  $6 \times 10^{12} \text{ cm}^{-2}$  and capless annealed in a  $\text{H}_2\text{-AsH}_3$  atmosphere for  $850^\circ\text{C}/30$  minutes. The sheet resistivity of these blanket implants was measured by a Tencor surface eddy current measurement gauge. The differential capacitance-voltage profiles were measured by the Miller feedback technique.

The MMIC fabrication procedure includes formation of the FET channel layer, device isolation, fabrication of ohmic contacts, Schottky gates, overlay metallization of the circuitry, MOM overlay capacitors, device passivation, airbridge interconnects, wafer thinning, via hole etching, and back metalization. Substrate related effects are monitored by using standard process control monitoring techniques such as C-V profiles,  $I_{\text{SAT}}$  current, sheet resistivity and FET characteristic measurements. An optical contact lithography process is used to produce high yield  $0.5 \mu\text{m}$  gates with high throughput (Wang). S-parameter characterization of the devices was carried out on an automatic network analyzer (ANA) over the 2-18 GHz frequency range to evaluate the effect of critical parameters in an equivalent circuit model in which the circuit elements are related to the physical device structure.

### 3. Performance Results

Material characteristics of the active channel in the four different types are summarized in Table I. By using ion-implant and capless anneal techniques, good activation of the Si implant and abruptness of the doping profile were achieved. The peak electron concentration was about  $2.6$  to  $2.9 \times 10^{17} \text{ cm}^{-3}$  at a depth of  $0.09 \mu\text{m}$ . The C-V profiles for the whole-ingot annealed, the undoped high pressure and the In-alloyed high pressure LEC are compared in Fig. 1 and show transition widths  $\Delta d$  of  $670$ ,  $770$ , and  $800 \text{ \AA}$ , respectively when the concentration drops from  $1 \times 10^{17}$  to  $1 \times 10^{16} \text{ cm}^{-3}$ . Higher implant activation of the whole ingot annealed wafer compared to the In-alloyed wafer is also indicated in Fig. 1. The importance of the transition width will be discussed later with device performance.

A high yield MMIC fabrication process necessitates uniform channel and FET characteristics. For microwave applications, the uniformity of the gateless saturation current  $I_{\text{SAT}}$  is monitored to reflect substrate material quality. By testing whole two-inch wafers using 180 data points on a  $15$  by  $200 \mu\text{m}$  gateless channel, we obtained global  $I_{\text{SAT}}$  uniformities of  $2.5$ ,  $3.1$ ,  $4.4$  and  $4.8$  percent for whole-ingot annealed, standard high pressure, In-alloyed high pressure and standard low pressure wafers. Fig. 2 shows the wafer map of the whole-ingot annealed wafer. The density of dislocations do not seem to affect the macroscopic and microscopic uniformity of  $I_{\text{SAT}}$  for the implant parameters used in MMIC fabrication. Whole ingot annealing has been shown by several researchers including Dobrilla et al, Ogawa, Otoki et al, Löhnert et al to homogenize substrate properties such as the

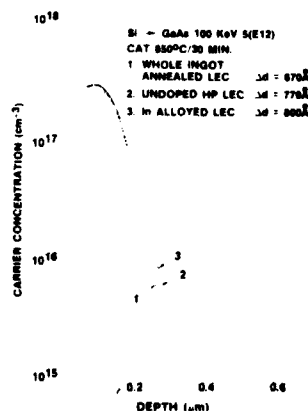


Fig. 1 Electrical C-V profiles of  $100 \text{ keV Si}$  implanted GaAs LEC substrates.

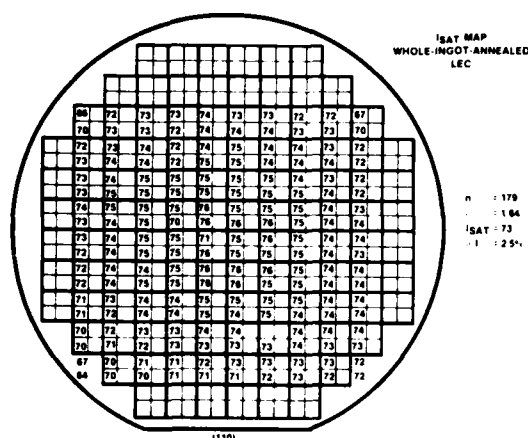


Fig. 2 ISAT uniformity map of whole ingot annealed LEC substrate.

EL2 distribution, stress, substrate resistivity, extrinsic photoconductivity, and photoluminescence intensity distribution of the carbon acceptor envelope. A decrease in the deep levels other than EL2 has also been observed. The improved uniformity of LEC substrate properties is reflected by the above ISAT uniformity of whole-ingot annealed wafers. As seen in Table I, FET saturation current uniformity of 1.1 percent has been achieved on the annealed high pressure substrate of lot MH697. The devices in our low noise amplifier are standard 0.5 x 300  $\mu\text{m}$  low noise GaAs MESFETs whose

structure is shown in Fig. 3 and consist of four 75  $\mu\text{m}$  gate fingers. The individual FET dc characteristics are summarized in Table II and show excellent FET  $I_{\text{DSS}}$  uniformity for ion implanted channels. The ratio of the transconductance to the pinch-off voltage,  $g_m/V_p$ , shows superior dc performance for the standard high pressure and the annealed high pressure substrates.

The low noise device performance from the four types of GaAs substrates is summarized in Table III where the average noise figure and associated gain is obtained from 8 measured FETs for each wafer. The best RF performance results are indicated in parentheses under the average numbers. The best noise figure of 1.33 dB with an associated gain of 9.20 dB at 10 GHz was measured on the whole-ingot annealed high pressure LEC wafer. The highest

TABLE I  
ACTIVE MATERIAL CHARACTERIZATION

| Lot #  | Descriptions              | $I^2$ Parameters                                 | $\rho_s (\Omega/\square)$ | $I_{\text{SAT}}(\text{mA})$ |
|--------|---------------------------|--|---------------------------|-----------------------------|
| MH694  | In-Alloyed<br>Hi-Pressure | $\text{Si}^+$ , 100 KeV<br>6E12 $\text{cm}^{-2}$ | 473 $\pm$ 8 (1.7%)        | 44.7 $\pm$ 1.9 (4.2%)       |
| MH 695 | Standard<br>Hi-Pressure   | $\text{Si}^+$ , 100 KeV<br>6E12 $\text{cm}^{-2}$ | 469 $\pm$ 8 (1.7%)        | 46.3 $\pm$ 0.9 (2.0%)       |
| MH696  | Standard<br>Low-Pressure  | $\text{Si}^+$ , 100 KeV<br>5E12 $\text{cm}^{-2}$ | 443 $\pm$ 6 (1.4%)        | 50.5 $\pm$ 1.3 (2.6%)       |
| MH697  | Annealed<br>Hi-Pressure   | $\text{Si}^+$ , 100 KeV<br>5E12 $\text{cm}^{-2}$ | 456 $\pm$ 5 (1.1%)        | 46.0 $\pm$ 0.5 (1.1%)       |

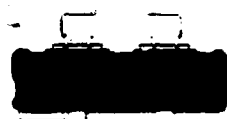


Fig. 3 0.5  $\mu\text{m}$  gate length by 300  $\mu\text{m}$  gate width low noise FET.

gain of 10.46 dB was measured on the standard undoped high pressure LEC wafer.

The final low noise monolithic amplifier consists of two 0.5  $\mu\text{m}$  gate FETs with 300  $\mu\text{m}$  gate width, five 10 pF overlay capacitors, microstrip lines and via holes to ground. The chip size is 1.9 x 2.0 mm. RF performance of 20 low noise amplifier chips selected from the four types of wafers is illustrated in Table IV. The noise

figure is measured without tuning and with a bias condition of  $V_D = 3.0$  volts and  $I_{DS} = 24$  mA. The noise figure is less than 3.0 dB and the associated gain is more than 20 dB across the frequency band from 9 to 10 GHz. A best noise figure of 2.0 dB with an associated gain of 24 dB has been measured at 9.5 GHz on standard high pressure undoped LEC material.

Equivalent circuit elements have been evaluated from S-parameters to identify the critical material parameters necessary to achieve the low noise results reported here. The equivalent circuit model used in this work has been described previously by Feng et al. The calculated equivalent elements are summarized in Table V. The ratio  $g_m/C_{gs}$  is a figure of merit which can be used to predict the noise figure and  $f_T$  as described by Fukui. Maximizing the ratio  $g_m/C_{gs}$  will minimize the noise figure and maximize  $f_T$ . Both the In-alloyed and the standard low pressure material lots have  $g_m/C_{gs}$  ratios that are 23-24 percent lower than the standard high pressure and the whole-ingot annealed high pressure material. The highest ratio is

TABLE II  
FET DC CHARACTERISTICS

| Lot # | Descriptions              | FET                  |                  |                 |                        |
|-------|---------------------------|----------------------|------------------|-----------------|------------------------|
|       |                           | $I_{DSS}(\text{mA})$ | $g_m(\text{mS})$ | $V_p(\text{V})$ | $g_m/V_p(\text{mS/V})$ |
| MH694 | In-Alloyed<br>Hi-Pressure | 15 $\pm$ 1.9         | 9.3 $\pm$ 0.3    | 1.8 $\pm$ 0.3   | 5.17                   |
| MH695 | Standard<br>Hi-Pressure   | 12 $\pm$ 1.5         | 9.4 $\pm$ 0.8    | 1.4 $\pm$ 0.1   | 6.71                   |
| MH696 | Standard<br>Low-Pressure  | 13 $\pm$ 1.3         | 9.1 $\pm$ 0.3    | 1.7 $\pm$ 0.2   | 5.35                   |
| MH697 | Annealed<br>Hi-Pressure   | 11 $\pm$ 0.9         | 8.4 $\pm$ 0.4    | 1.3 $\pm$ 0.03  | 6.46                   |

TABLE III  
LOW NOISE FET RESULTS FROM DIFFERENT GaAs MATERIALS AT 10 GHz

| Type of GaAs Materials           | Noise Figure* (dB)    | Associated* Gain (dB)   | Rating |      |
|----------------------------------|-----------------------|-------------------------|--------|------|
|                                  |                       |                         | N.F.   | Gain |
| Hi-Pressure LEC Undoped Standard | 1.49 ± 0.06<br>(1.41) | 10.13 ± 0.24<br>(10.46) | 2      | 1    |
| Hi-Pressure LEC Undoped Annealed | 1.44 ± 0.08<br>(1.33) | 8.83 ± 0.28<br>(9.20)   | 1      | 3    |
| Low-Pressure LEC Undoped         | 1.68 ± 0.05<br>(1.62) | 8.60 ± 0.26<br>(8.97)   | 4      | 4    |
| Hi-Pressure LEC In-Alloyed       | 1.63 ± 0.09<br>(1.50) | 9.24 ± 0.29<br>(9.68)   | 3      | 2    |

\* Average from 8 measured data

() Indicates the best results

calculated for the whole-ingot annealed material and confirmed by the measured lowest noise figure as shown in Table III. The material characteristics of the sharpest transition width and highest activation and the measured FET dc characteristics of largest  $g_m/V_p$  ratio can also be correlated to the best measured low noise figure for whole-ingot annealed LEC substrates.

##### 5. Conclusion

A high performance X-band monolithic low noise amplifier with low cost ion implanted MESFET technology has been demonstrated. We have compared In-alloyed high pressure, standard undoped low pressure, standard undoped high pressure and whole-ingot annealed substrates and correlated ion implanted material characteristics to FET dc and RF performance. An excellent noise figure of 2.0 dB with an associated gain of 24 dB was achieved

TABLE IV  
X-BAND TWO-STAGE LNA PERFORMANCE

| Lot #                         | N.F. (dB) | $G_A$ (dB) @ 9.5 GHz | Bias Conditions   |
|-------------------------------|-----------|----------------------|---|
| MH694<br>(In-Alloy)           | 2.4 - 2.8 | 23 - 24              | $V_D = 3.0$ V<br>$I_{DS} = 24$ mA<br>$V_G = -1.1$ to $-1.2$ V |
| MH695 High<br>(STD.) Pressure | 2.0 - 2.2 | 24 - 25              | $V_G = -1.0$ to $-1.05$                                       |
| MH696<br>(Low-Pressure)       | 2.3 - 2.5 | 23 - 24              | $V_G = -1.1$ to $-1.2$  |
| MH697<br>(Annealed)           | 2.2 - 2.5 | 23 - 24              | $V_G = -0.9$ to $-0.95$                                       |

TABLE V  
CALCULATED EQUIVALENT CIRCUIT ELEMENTS

| Device Lot         | MH694 | MH695 | MH696 | MH697 |
|--------------------|-------|-------|-------|-------|
| $g_m$ (mS)         | 22.7  | 28.3  | 23.3  | 29.6  |
| $C_d$ (m $\mu$ )   | 2.89  | 3.82  | 3.42  | 4.18  |
| $C_{gd}$ (pF)      | 0.024 | 0.021 | 0.024 | 0.023 |
| $C_{gs}$ (pF)      | 0.26  | 0.25  | 0.27  | 0.26  |
| $C_c$ (pF)         | 0.069 | 0.091 | 0.092 | 0.102 |
| $R_i$ ( $\Omega$ ) | 0.85  | 0.75  | 0.77  | 0.82  |
| $R_s$ ( $\Omega$ ) | 1.79  | 1.58  | 1.17  | 1.80  |
| $R_g$ ( $\Omega$ ) | 3.22  | 2.59  | 3.46  | 2.59  |
| $g_m/C_{gs}$       | 87.3  | 113.2 | 86.3  | 113.8 |

for a monolithic two stage low noise amplifier. In this study, both standard and whole-ingot annealed high pressure substrates show superior uniformity and dc and RF performance for microwave applications.

#### Acknowledgments

The authors would like to thank H. Yamasaki, J. M. Schellenberg and H. J. Kuno for their support and advice throughout this work. The contributions of R. Rush, P. Busted, G. Vitale, and M. Siracusa are also appreciated.

#### References

- Dobrilla M and Blakemore J S 1986 Appl Phys Lett **48** 1303  
 Feng M, Eu V K and Kanber H 1984 J Appl Phys **56** 1171  
 Fukui H 1979 IEEE Trans Electron Dev **ED-26** 1032  
 Löhnert K, Wettling W and Koschek G 1986 4th Conf on Semi-Insulating III-V Materials Hakone Japan 18-22 May 1986 paper PE-8 To be published  
 Ogawa O 1986 ibid paper VI-3  
 Otoki O 1986 ibid paper PE-11  
 Wang D C, Pauley R G, Wang S K and Liu L C T 1986 IEEE 1986 MTT-S Symposium Digest (New York:IEEE) pp 61-63

## **Evaluation of the theoretical maximum fabrication yield of GaAs 1K bit SRAM's**

**Christian ROCHER, José MALUENDA, Bertrand GABILLARD,  
Thierry DUCOURANT, Michel PROST, Marc ROCCHI**

L.E.P.\*\* 3, avenue Descartes, 94451 LIMEIL-BREVANNES CEDEX (FRANCE)

\*\* "Laboratoires d'Electronique et de Physique appliquée :  
A member of the Philips Research Organization"

### **Abstract**

Full operation and high fabrication yield of GaAs SRAM's with nanosecond access time requires accurate statistical simulations including the variations of the material and process parameters. The theoretical fabrication yield can be deduced from the stability condition of a memory cell, the local distribution (over  $1 \text{ mm}^2$ ) of the threshold voltages of FET's and the distribution function over the whole wafer of the local mean threshold voltage. The maximum simulated yield for 64 Bit and 1Kbit SRAM's for both conventional and dislocation free substrates is discussed theoretically and experimentally. Correlation between the fabrication yield measured on full operating 0.7 ns 64 bit and 1.4 ns 1Kbit SRAM's and the mean  $V_T$  over the whole wafer is presented.

### **1. Introduction**

In recent years the ultra high speed digital LSI's for super computers has attracted a great deal of attention. Many GaAs LSI's, including both logic devices and memories have been reported (N. Yokoyama), (F.S. Lee), (Y. Ikawa), (M. Hirayama). In order to achieve an high fabrication yield for such LSI devices, high quality GaAs substrates are required. The purpose of this paper is to evaluate for several kinds of LEC substrates, the theoretical maximum fabrication yield of 64 bit and 1Kbit SRAM's deduced from the microscopic and macroscopic distributions of the threshold voltages of FET's grouped in dense row patterns.

### **2. Yield analysis**

Full operation and high fabrication yield of GaAs SRAM's with nanosecond access time using the DCFL approach requires accurate statistical simulations including the non-uniformities of the material and the process parameters. A first analysis of all the parameters shows that the transistor threshold voltage  $V_T$  is the main parameter to be considered. The most sensitive part of a SRAM is the memory cell array.

\*This work is supported by ESPRIT contract.

The memory cell stability has been considered to be one of the main electrical features influencing the fabrication yield. A more detailed analysis would also have to include the interaction between memory cells. The memory cell (figure 1) consists of two  $100\text{ K}\Omega$  resistors, two access FET's and two driver FET's, with  $3\text{ }\mu\text{m}$  and  $9\text{ }\mu\text{m}$  gate width respectively.

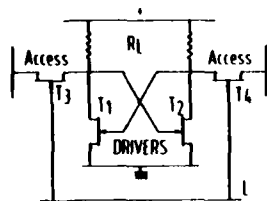


Figure 1 :  
Schematic of the memory cell

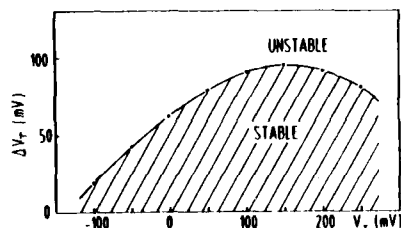


Figure 2 :  
Stability conditions of  
a memory cell

Computer simulations show that cell stability in the read mode is lower than in the write mode, and depends on three parameters : a) the ratio between the gate width of driver transistor to access transistor ; the greater the ratio, the higher the cell stability. b) the high level of the word-line voltage, which must be lower than .7 Volt. c) the threshold voltage difference between the two-cross coupled driver FET's of the memory cell. The first two parameters can be optimized and fixed at an optimum value. The last parameter is  $V_T$  dependent,  $V_T$  being a function of the electrical uniformity of the active layer and of the variations of the process parameters. In order that the memory cell does not lose its data during the read mode, the maximum allowable difference of threshold voltages  $\Delta V_T$  ( $V_T$ ) between the drivers is deduced from transient computer simulation on a worst case unbalanced memory cell (figure 2). A maximum  $\Delta V_T$  of 90 mV corresponds to  $V_T$ 's between 150 mV and 250 mV. However to ensure a significant differential voltage on the bit lines, or a CML compatibility output signal, the threshold voltage of peripheral circuits has to be less than 170 mV.

The fabrication yield "r" is expressed as follows :  $r = r_1 \times r_2 \times r_3$   
where :

- $r_1$  = corresponds to the electrical non-uniformity of the active layer,
- $r_2$  = corresponds to the electrical and geometrical non-uniformities of the process.
- $r_3 = e^{-\lambda s}$  where  $s$  is the chip area and  $\lambda$  the density of fatal defects.

The yield  $r_1$  of a SRAM which is design dependent, should be equal to 1. Theoretical calculations, presented in section 5, shows that  $r_1$  is smaller than 1 for a 1K SRAM, processed on GaAs material, and so gives a limit for the maximum fabrication yield. Consequently, for a given design and material there is a mean value for the  $V_T$  over the wafer which gives the maximum value for  $r_1$ .



### 3. Homogeneity qualification of GaAs substrates

To evaluate  $r_1$ , 30 GaAs wafers from various ingots have been processed. Some of the substrates considered are standard dislocated LEC semi-insulating substrates, others are In doped substrates in order to reduce the dislocation density.

The original pattern (figure 3) is a very dense row of 30 micro-FET's (J. Maluenda), ( $L_G = 2 \mu\text{m}$ ;  $W = 5 \mu\text{m}$ ; drain-source spacing =  $6 \mu\text{m}$ ; distance between two FET's =  $5 \mu\text{m}$ ). A  $2 \mu\text{m}$  long gate which is common to the 30 FET's, has been used in order to minimize the effect of gate length variation on the threshold voltage of the FET's.

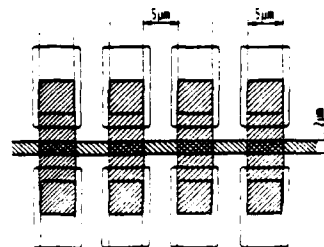


Figure 3 :  
Schematic of a part of the dense  
row of 30 micro-FET's

The test procedure is performed on 250 dense rows pattern (DRP) of 30 FET's distributed over a wafer.

For each dense row,  $V_T$  of each FET was measured and  $\sigma(V_T)$  and  $\bar{\sigma}(V_T)$  are calculated. These values show the microscopic distribution of  $V_T$  over the dense row pattern.

The  $V_T$  variation over the whole wafer is assessed by the overall mean value  $\langle V_T \rangle$  over the 250 dense rows on a wafer, and the standard deviation  $\sigma(V_T)$ .

The standard deviation  $\sigma(V_T)$  shows the macroscopic distribution from DRP to DRP. Standard GaAs, In doped, then standard annealed, In annealed have been considered. The following table shows the typical values obtained for several materials on all the processed wafers.

Table 1

| Material              | Microscopic (mV)     |               |                       | Macroscopic (mV) |
|-----------------------|----------------------|---------------|-----------------------|------------------|
|                       | $\sigma(V_T)_{\min}$ | $\sigma(V_T)$ | $\sigma(\sigma(V_T))$ | $\sigma(V_T)$    |
| Standard (worst)      | 44                   | 100           | 25                    | 100              |
| (best)                | 15                   | 40            | 20                    | 50               |
| Standard annealed     | 9                    | 25            | 15                    | 50               |
| In doped (typical)    | 11                   | 30            | 17                    | 50               |
| (best)                | 8                    | 15            | 8                     | 40               |
| In annealed (typical) | 8                    | 20            | 13                    | 40               |

where :

$\sigma(V_T)$  is the mean value of  $\sigma(V_T)$  for the 250 DRP's over a wafer,

$\sigma(\sigma(V_T))$  is the standard deviation of  $\sigma(V_T)$ .

The superiority of the In doped GaAs with low dislocation density over the standard GaAs is clearly demonstrated. The standard deviation of  $V_T$  inside the dense rows is remarkably improved. The average standard deviation inside one dense row is between 40 and 100 mV for a standard material and decrease below 20 mV for In doped GaAs. Post growth annealing seems to improve the homogeneity of both materials.

The standard deviation at the macroscopic scale is always superior to the microscopic one and seems to be limited by the technological process.

#### 4. Yield calculation

The theoretical fabrication yield  $r_1$  for a given wafer can be deduced from the stability condition of a memory cell and from the distribution functions of  $\sigma(V_T)$ ,  $V_T$  and  $\bar{V}_T$ . Each DRP is assumed to be representative of the  $V_T$  variation over an area of  $1 \text{ mm}^2$ . The distribution function  $h(\bar{V}_T)$  is centered around  $\bar{V}_T$  with a standard deviation  $\sigma(\bar{V}_T)$ . The 3 distribution functions  $f(\sigma(V_T))$ ,  $g(V_T)$ ,  $h(\bar{V}_T)$  are assumed to be independent  $g(V_T)$  and  $h(\bar{V}_T)$  are gaussian,  $f(\sigma(V_T))$  is assumed to be maxwellian. The probability of the memory cell to be operational is given by :

$$P_M = \left[ \int_{V_{T_1}=-\infty}^{V_{T_1}=\infty} \int_{V_T=V_{T_1}-\Delta V_T(V_{T_1})}^{V_T=V_{T_1}+\Delta V_T(V_{T_1})} \frac{1}{\sigma^2(V_T)2\pi} \times e^{-\frac{(V_T-\bar{V}_T)^2}{2\sigma^2(V_T)}} \times e^{-\frac{(V_{T_1}-\bar{V}_T)^2}{2\sigma^2(\bar{V}_T)}} dV_T dV_{T_1} \right]^2 \quad (1)$$

where  $\Delta V_T(V_{T_1})$  is deduced from figure 2. Thus  $r_1$  is expressed as :

$$r_1 = \frac{1}{A} \int_{\bar{V}_T=-\infty}^{\bar{V}_T=\text{max}} \int_{\sigma V_T=0}^{\sigma V_T=\infty} (P_M)^N \times e^{-\frac{(\bar{V}_T-\langle \bar{V}_T \rangle)^2}{2\sigma^2(\bar{V}_T)}} \times \sigma^2(V_T) \cdot e^{-\frac{\sigma^2(V_T)}{\sigma^2(\bar{V}_T)}} d\sigma(V_T) d\bar{V}_T \quad (2)$$

where  $\bar{V}_{T,\text{max}} = 170 \text{ mV}$ .  $N$  = number of memory cell.

$$A = \pi \cdot [\sigma(\bar{V}_T)]^3 \cdot \sigma(\bar{V}_T)$$

The optimum  $\langle \bar{V}_T \rangle$  which gives the highest yield can be deduced by plotting equation (2) (see figures 4 and 5).

#### 5. Theoretical results

##### 5.1. - 64 bit SRAM's

The figure 4 shows the yield  $r_1$  for a 64 bit SRAM versus  $\langle \bar{V}_T \rangle$  for 3 different processed material : a) an typical indium doped, b) an typical indium annealed, c) the best indium doped.

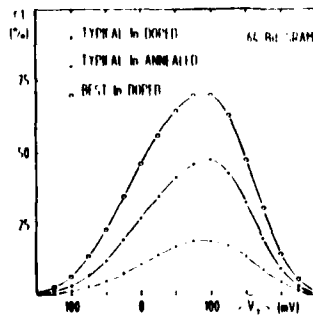


Figure 4

| 64 Bit SRAM Maximum Yield $r_1$ (%) |      |
|-------------------------------------|------|
| Standard (worst)                    | .4   |
| (best)                              | 9.4  |
| Standard annealed                   | 28.4 |
| n doped (typical)                   | 19   |
| (best)                              | 70   |
| n annealed (typical)                | 47   |

Table 2

The table 2 shows the theoretical maximum yield  $r_1$  at the 64 bit level calculated on six different materials.

### 5.2. - 1 KBit SRAM's

The figure 5 shows the yield  $r_1$  for a 1 KBit SRAM's versus  $\langle \bar{V}_T \rangle$  for the same processed material as for the 64 Bit.

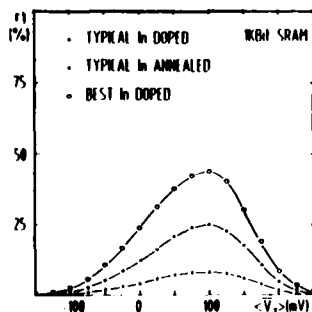


Figure 5

| 1KBit SRAM            | Maximum Yield $r_1$ (%) |
|-----------------------|-------------------------|
| Standard (worst)      | .2                      |
| (best)                | 3.8                     |
| Standard annealed     | 13.4                    |
| In doped (typical)    | 8                       |
| (best)                | 43                      |
| In annealed (typical) | 25                      |

Table 3

The maximum yield  $r_1$  is obtained with  $80 \text{ mV} < \langle \bar{V}_T \rangle < 100 \text{ mV}$ ; a reduction by a factor of 2 of  $\sigma(V_T)$  and  $\sigma(\sigma(V_T))$  on the indium doped material, enables an improvement  $r_1$  by a factor of 3.7. Table 3 shows the theoretical maximum yield calculated for six different materials.

## 6. Experimental results

### 6.1. Device fabrication

A 64 Bit and a 1 Kbit SRAM (Figure 6) have been fabricated using N-OFF E/R aligned gate FET technology, on In doped low dislocations substrate. The main technological features of the 1KBit are summarized in the table 4.

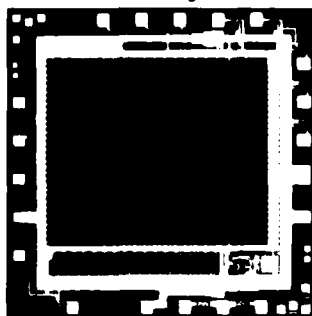


Figure 6

| Main Characteristics of the 1K SRAM's |  |
|---------------------------------------|--|
| Gate length                           | .7 $\mu\text{m}$ / 1 $\mu\text{m}$ memory cell |
| Line/space 1st Level                  | 2 $\mu\text{m}$ / 3 $\mu\text{m}$              |
| 2nd Level                             | 3 $\mu\text{m}$ / 3 $\mu\text{m}$              |
| Via                                   | 2 $\mu\text{m}$ x 2 $\mu\text{m}$              |
| Organization                          | 1024 x 1 Bit                                   |
| Cell size                             | 43 $\mu\text{m}$ x 43 $\mu\text{m}$            |
| Chip size                             | 2.5 mm x 2.5 mm                                |
| Supply voltage                        | + 1.5 V, - 1.5 V                               |
| Access time                           | 1.4 ns (best)                                  |

Table 4

### 6.2. Experimental yield

The table 5 and the figure 7 show the correlation between the theoretical maximum fabrication yield  $r_1$  and the experimental yield on 64 Bit and 1KBit SRAM processed on typical indium doped low dislocations substrate.

\* $Y_m$  is the percentage on the wafer of fully functional SRAM's in a marching test (10 MHz) for the 64 Bit and in a reduced marching test (10 MHz) for the 1 KBit. Batch 4 corresponds to an indium doped wafer with a  $\sigma(V_T)$  and a  $\sigma(\sigma(V_T))$  equal to 35 mV and 18 mV respectively.

| 64 Bit SRAM | $\langle V_T \rangle$ mV | $r_1$  | $Y_m^*$ |
|-------------|--------------------------|--------|---------|
| Batch 1     | 56                       | 16.8 % | 7.7 %   |
| Batch 2     | 90                       | 19 %   | 10.6 %  |
| Batch 3     | 115                      | 18 %   | 9.6 %   |
| Batch 4     | 63                       | 56 %   | 37 %    |
| 1 Kbit SRAM | $V_T$                    | $r_1$  | $Y_m^*$ |
| Batch 5     | 92                       | 8 %    | 5 %     |

Table 5

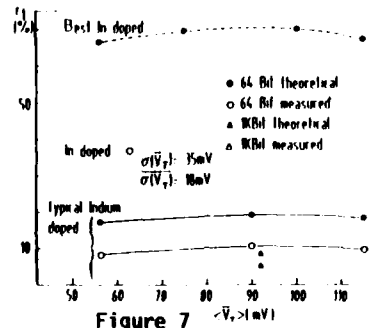


Figure 7

The figure 7 shows that the dependence of the measured yield versus  $\langle V_T \rangle$  is in good agreement with the theoretical results. Nevertheless, the difference between the two curves are due to the  $r_2$  and  $r_3$  parameters. The difference between the yield of the batches 1, 2, 3, 4 and the batch 5 has been achieved by reducing the density of particle contamination induced during the process.

### 7. Conclusion

As a general conclusion, DRP procedure provides a correct assessment tool for yield analysis on SRAM's. Today the first limitation is still due to the process, but we have seen that a limitation already exists with the material which gives a maximum theoretical yield. In order to achieve an ultimate yield, the best uniformity at the microscopic level is definitely required or new design tricks have to be developed.

### Bibliography

- N. Yokoyama, H. Onodera, T. Shinoki, H. Unnishi, H. Nishi, and A. Shibatomi, "A 3 ns GaAs 4 K x 1 b SRAM" in ISSCC Dig. Tech. Papers, Feb. 1984, pp. 44-45
- F.S. Lee, G.R. Kaelin, B.M. Welch, R. Zucca, E. Shen, P. Asbeck, C.P. Lee, C.G. Kirkpatrick, S.I. Long, and R.C. Eden, "A high-speed LSI GaAs 8 x 8 bit parallel multiplier", IEEE J. Solid-State Circuit, vol. SC-17, pp. 638-647, Aug. 1982
- Y. Ikawa, N. Toyoda, M. Mochizuki, T. Terada, K. Kanazawa, M. Hirose, T. Mizoguchi, and A. Hojo, "A 1K-gate GaAs gate array", in ISSCC Dig. Tech. Papers, Feb. 1984, pp. 40-41
- M. Hirayama, M. Togashi, N. Kato, M. Suzuki, Y. Matsuoka, Y. Kawasaki, "A GaAs 16 KBit static RAM using dislocation free crystal", IEEE Trans. on Electron Devices, vol. ED-33, n°1, Jan. 86
- J. Maluenda, G.M. Martin, H. Schink, G. Packheiser, "Homogeneity application of GaAs substrates for large scale integration applications", Appl. Phys. Lett., 48, (11), 17 March 1986, pp. 715-717

### Acknowledgments

The authors would like to thank M. Fichelson, J.M. Gibereau and G. Haldemann for the circuits fabrication, B. Bru for the measurements, and P. Deconinck and G.M. Martin for fruitful discussions.

## **High performance inverted HEMT and its application to LSI**

S.Nishi, T.Saito, S.Seki, Y.Sano, H.Inomata, T.Itoh, M.Akiyama and K.Kaminishi

Research Laboratory, Oki Electric Industry Co., Ltd.  
550-5, Higashiasakawa, Hachioji, Tokyo 193, Japan

**Abstract:** The growth condition of MBE and processing technique for inverted HEMT were studied. A high electron mobility ( $1.1 \times 10^5 \text{ cm}^2/\text{Vs}$ ), a high transconductance and a K-value ( $g_m = 400 \text{ mS/mm}$ ,  $K = 480 \text{ mA/V}^2 \text{ mm}$  at R.T. and  $g_m = 550 \text{ mS/mm}$ ,  $K = 860 \text{ mA/V}^2 \text{ mm}$  at 77K) were obtained. The minimum ring-oscillator propagation delay of 19.7ps was obtained at R.T. with the gate length of  $0.5 \mu\text{m}$ . A fully operational  $6 \times 6$  parallel multiplier was fabricated on a  $1\text{K}$  gate array using the inverted HEMTs with a gate length of  $0.8 \mu\text{m}$ . Multiply times of 6ns( $0.7\text{W}$ ) and 5.1ns( $1\text{W}$ ) were measured at R.T. and 77K, respectively.

### 1. Introduction

The selectively doped GaAs/N-AlGaAs single heterostructures was widely used for high speed devices (Kobayashi et al. 1985, Watanabe et al. 1986, Kinoshita et al. 1985). A high transconductance (Inomata et al. 1986) and an extremely short propagation delay time (Shah et al. 1986) were reported by this time. But these reports were using the heterostructure of a ternary on top of a binary (conventional HEMT) because of the difficulty in the growth of inverted heterostructure (binary on top of ternary) (Morkoç et al. 1982a,b). In the conventional HEMT, as the sheet resistance of 2 dimensional electron gas (2-DEG) is rather high, some processing techniques are required for the reduction of the source resistance to improve the FET performance at R.T. On the other hand, in the inverted heterostructure, the source resistance can be easily lowered at R.T. by the top  $n^+\text{GaAs}$  layer and recessed gate process. Then a high performance is expected at room temperature in an inverted HEMT.

In this report, we demonstrate the growth condition of MBE and the processing technique for inverted HEMT. A high electron mobility was obtained in the inverted heterostructure. The optimum layer structure was studied and an inverted HEMT with high performance was fabricated. A  $1\text{K}$  gate array was successfully fabricated using the inverted HEMTs with the gate length of  $0.8 \mu\text{m}$ .

### 2. Crystal Growth

The inverted heterostructures were grown by conventional III-V MBE system. The growth rate was about  $0.5 \mu\text{m/h}$ . A 2-inch HB semi-insulating GaAs was used as a substrate. After chemical etching, a substrate was immediately fixed to a substrate holder by In solder. A direct heating system without In solder was also used. Schematic cross section of an inverted

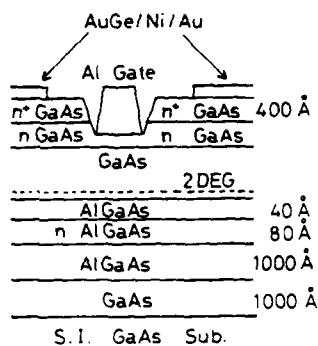


Fig.1 Schematic cross-section of inverted HEMT.

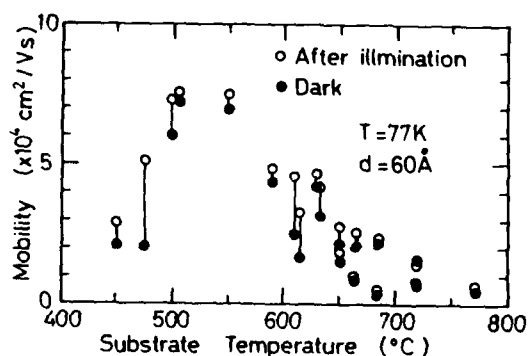


Fig.2 Dependence of 2-DEG mobility at 77K on substrate temperature.

HEMT is shown in Fig.1. An epitaxial layer consists of undoped GaAs and AlGaAs with both thicknesses of 1000Å, n-AlGaAs ( $1.1 \times 10^{18} \text{cm}^{-3}$ , 80Å), AlGaAs separation layer (40Å), undoped GaAs (200Å or 400Å), n-GaAs ( $5 \times 10^{17} \text{cm}^{-3}$ ) and n<sup>+</sup>-GaAs ( $4 \times 10^{18} \text{cm}^{-3}$ , 400Å). With this structure, the maximum carrier concentration of 2-DEG is  $8 \times 10^{11} \text{cm}^{-2}$ .

To fabricate a high performance inverted HEMT, it is important to grow a heterostructure with 2-DEG of high electron mobility. We studied the substrate temperature dependence of the mobility of 2-DEG at the inverted hetero-interface. In Fig.2, mobility of 2-DEG at 77K is shown as a function of a substrate temperature. In the experiment, the substrate temperature was monitored by a thermocouple behind a Mo substrate holder. The thickness of an AlGaAs separation layer was fixed to be 60Å. To suppress both a depletion of 2-DEG by surface potential and a parallel conduction in n-GaAs, thick undoped GaAs channel layer of 2000Å with thin top n-GaAs layer was grown on AlGaAs layer. The electron mobility was measured by van der Pauw method. The electron mobility increased gradually with decreasing the substrate temperature and it decreased rapidly with the substrate temperature below 500°C. The sheet carrier concentrations of 2-DEG were ranging between  $5 \times 10^{11} \text{cm}^{-2}$  and  $1.5 \times 10^{12} \text{cm}^{-2}$  above 500°C and decreased to about  $2 \times 10^{11} \text{cm}^{-2}$  below 500°C. The decrements of mobility and sheet carrier concentration below 500°C were due to the increase of the deep level concentration in the grown layer. The higher mobilities at fairly low substrate temperatures may be due to the improvement of AlGaAs surface morphology and the reduction of surface segregation of doped Si. The maximum mobility of  $1.1 \times 10^5 \text{cm}^2/\text{Vs}$  at 77K was obtained with a sheet carrier concentration of  $3.5 \times 10^{11} \text{cm}^{-2}$  when the separation layer thickness was increased to 250Å. As the sheet carrier concentrations were extremely low at low substrate temperatures and a control of substrate temperature is rather difficult, a little high substrate temperature (600–650°C) was used for inverted HEMT. In this temperature range, a sufficiently high electron mobility was obtained at R.T. ( $>6000 \text{cm}^2/\text{Vs}$ ).

For the inverted HEMT, the thickness of n-AlGaAs must be chosen to the proper value because the thicker n-AlGaAs causes a parallel conduction to a channel and degrades a FET performance. Fig.3 shows the relation between the sheet carrier concentration and the thickness of n-AlGaAs.

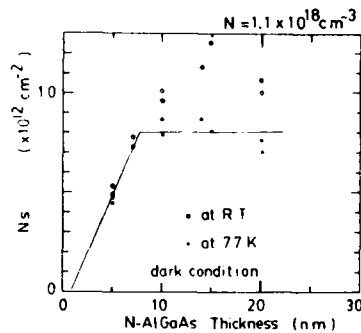
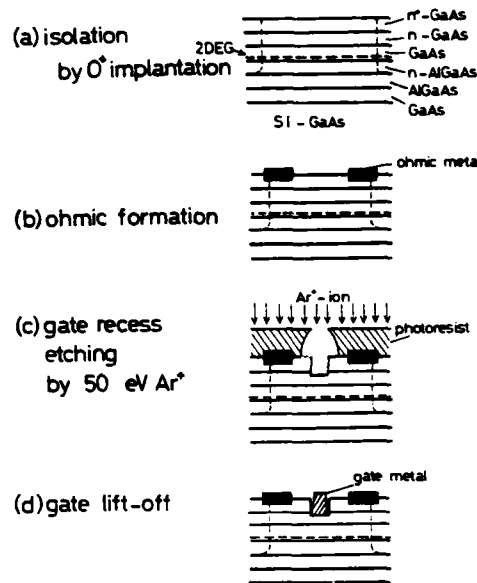


Fig.3 Relation between  $N_s$  and thickness of n-AlGaAs.

Fig.4 Process flow of inverted HEMT.

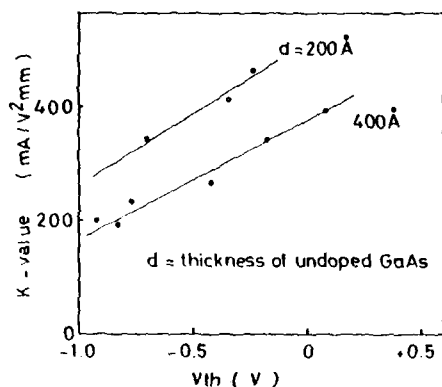
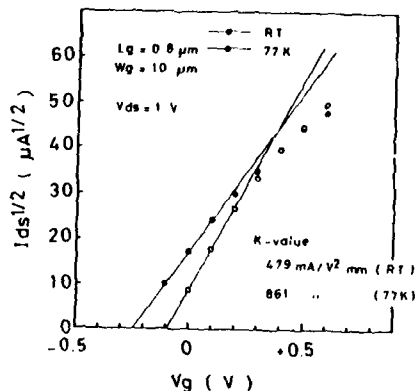


The thickness of AlGaAs separation layer was 40Å. The sheet carrier concentration increased to  $8 \times 10^{11} \text{ cm}^{-2}$  with increasing the thickness of n-AlGaAs to 80Å. Above the thickness of 80Å, the sheet carrier concentration saturated to the same value at 77K, indicating the parallel conduction at R.T. occurred in n-AlGaAs layer.

### 3. Device Fabrication and Characteristics

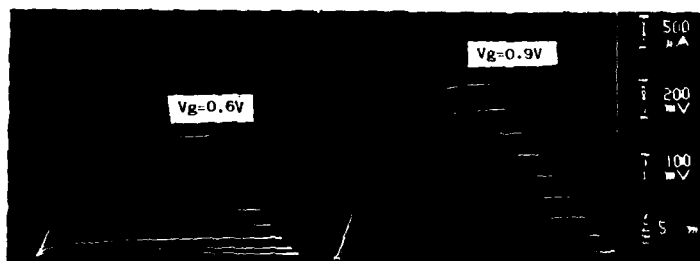
The fabrication process flow is shown in Fig.4. At first, devices were isolated by ion implantation of oxygen to form a planar structure (Fig.4(a)). Source and drain contacts were formed by AuGe/Ni/Au (Fig.4(b)). Gate regions were recessed by 50eV Ar ion-beam (Fig.4(c)). Al metal was deposited into the recessed region by a self-alignment technique using LMR deep-UV photoresist (Fig.4(d)) (Yamashita et al. 1985). The threshold voltage was controlled by the recessed depth.

To improve the performance of an inverted HEMT, a short distance from the gate electrode to 2-DEG was desirable. Two different thicknesses (200Å and 400Å) of the undoped GaAs channel layers were compared in FET performance. In Fig.5, K-values at R.T. are shown as a function of threshold voltage for two different thicknesses. The gate length and the width were 0.8μm and 10μm, respectively. K-values were much improved by reducing the thickness of undoped GaAs. At the threshold voltage of 0V, the distances from the gate electrode to the hetero-interface are calculated to be 460Å and 590Å for the undoped GaAs thickness of 200Å and 400Å. K-value at the threshold voltage of 0V was improved about 40%. This larger improvement may be explained if the distribution of 2-DEG in GaAs layer is considered. In Fig.6, square roots of saturation current at R.T. and 77K are shown as a function of a gate voltage. The thickness of an undoped GaAs was 200Å. Extremely high K-values of 480mA/V<sup>2</sup>mm at R.T.

Fig. 5 Relations between K-value and  $V_{th}$  for  $d=200\text{\AA}$  and  $400\text{\AA}$ .Fig. 6  $I_{ds}$  versus  $V_g$  relations at R.T. and 77K.

at R.T.

at 77K

Fig. 7 I-V characteristics of inverted HEMT.  $L_g=0.8\mu\text{m}$  and  $W_g=10\mu\text{m}$ .

and  $860\text{mA/V}^2\text{mm}$  at 77K were obtained. I-V characteristics of the inverted HEMT at R.T. and 77K are shown in Fig. 7. The maximum transconductances at R.T. and 77K were  $400\text{mS/mm}$  and  $550\text{mS/mm}$ , respectively. The source resistances were as low as  $0.7\Omega\text{mm}$  and  $0.54\Omega\text{mm}$  at R.T. and 77K. Drain current saturation characteristics were fairly good, showing the small short channel effect.

To fabricate LSI using inverted HEMTs, the threshold voltage must be uniform on the microscopic scale as well as on the full wafer. On a whole area of a 2-inch wafer, the very uniform threshold voltage distribution was obtained with the gate length of  $1.5\mu\text{m}$  at R.T. The standard deviation was  $11.8\text{mV}$  at the threshold voltage of  $0.1\text{V}$ . The microscopic uniformity was studied at R.T. using the  $50\mu\text{m}\times 50\mu\text{m}$  pitch FET array (Nakamura et al. 1985). The histogram of the threshold voltages is shown in Fig. 8. The gate length and width were  $0.8\mu\text{m}$  and  $10\mu\text{m}$ , respectively. The threshold voltages of 780 samples, in the area of  $0.5\text{mm}\times 3.9\text{mm}$ , were included in the figure. The standard deviation of  $19\text{mV}$  at the mean threshold voltage of  $-0.38\text{V}$  was obtained, which was sufficiently small to fabricate LSI.

The propagation delay time of an inverted HEMT E/D DCFL circuit was



measured at R.T. using the 21-stage ring-oscillator (R/O). The gate length was reduced to  $0.5\mu\text{m}$  and the minimum propagation delay times of 19.7ps/gate with the power dissipation of 0.2mW/gate and 20ps/gate with 2mW/gate were obtained. No dependence of a propagation delay time on a power dissipation may be due to the good saturation characteristics of drain current.

#### 4. 1K Gate Array

To confirm the ability of the inverted HEMT for LSI, we fabricated 1K gate array using the inverted HEMTs with the gate length of  $0.8\mu\text{m}$ . 1K gate array consisted of 1000 basic cells and 52 I/Os. The basic cell was 3-input NOR gate by E/D DCFL circuit and I/O was constructed by SBFL circuit (Tanaka et al. 1984). The chip size was  $3.8\text{mm} \times 4.2\text{mm}$ . On this masterchip a 6x6 parallel multiplier using the carry save algorithm and the R/Os under various load conditions were fabricated. Fig.9 shows the photograph of a 1K gate array.

Functional check was performed on a 6x6 parallel multiplier. All 4096 bit patterns were tested at 10kHz and full operation was observed. The multiply time was measured from the delay time through critical path (26-stage internal gates and 5-stage I/O gates). The multiply times at R.T. and 77K were 6.0ns (0.7W), and 5.1ns (1W), respectively. Table 1 shows increments of delay times due to various loads calculated from the results of R/Os under various loads at R.T. The multiply time of 26-stage internal gates could be calculated from the actual fan in, fan out, line length and crossovers, using the data of Table 1, which was 4ns at R.T. The difference between the measured and calculated ones is due to the delay at I/O. The transconductance of inverted HEMT used to fabricate the gate array was  $240\text{mS/mm}$ , which was not improved yet. The multiply time will be shortened if the improved inverted HEMTs are used.

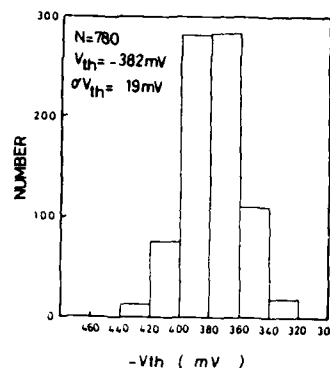


Fig.8 Histogram of threshold voltages of  $50\mu\text{m} \times 50\mu\text{m}$  pitch inverted HEMTs.  $L_g = 0.8\mu\text{m}$ .

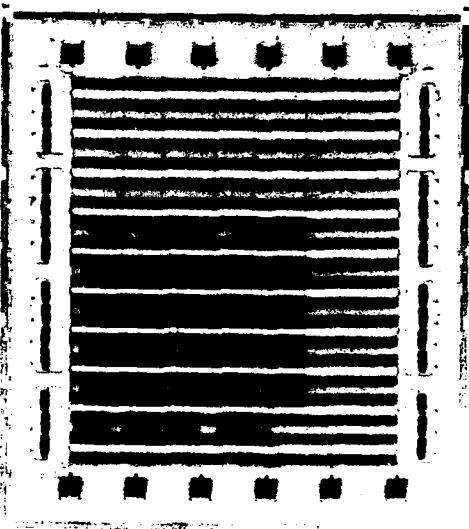


Fig.9 Photograph of 6x6 parallel multiplier on 1K gate array.  $L_g = 0.8\mu\text{m}$ .

5. Summary

MBE growth condition and processing technique for inverted HEMT were optimized. High performance inverted HEMT was fabricated and short propagation delay time was obtained at R.T. Fully operating 6x6 parallel multiplier was fabricated on 1K gate array. These results confirm an inverted HEMT is a promising FET for high speed LSI at R.T.

|                   |                       |                 |
|-------------------|-----------------------|-----------------|
| delay time        | $\tau_0$ (ps/gate)    | 70.6            |
| fan-in delay      | $\tau_{fi}$ (ps/F.O.) | 37.2<br>(0.528) |
| fan-out delay     | $\tau_{fo}$ (ps/F.I.) | 12.5<br>(0.177) |
| line load delay   | $\tau_l$ (ps/mm)      | 56.8<br>(0.804) |
| crossover delay   | $\tau_c$ (ps/c.o.)    | 0.90<br>(0.013) |
| power dissipation | P (mW/gate)           | 0.86            |

6. Acknowledgement

The present research effort is part of the National Research and Development program on "Scientific Computing System", conducted under a program set by the Agency of Industrial Science and Technology, Ministry of International Trade and Industry.

Table 1 The increments of delay time due to various load conditions.

7. References

- Inomata H, Nishi S, Takahashi S and Kaminishi K 1986 Jpn. J. Appl. Phys. 25 L731
- Kobayashi N, Notomi S, Suzuki M, Tsuchiya T, Nishiuchi K, Odani K, Shibatomi A, Mimura T and Abe M 1985 GaAs IC Symp. Tech. Dig. 207
- Kinoshita H, Nishi S, Akiyama M and Kaminishi K 1985 Jpn. J. Appl. Phys. 24 1061
- Morkoç H, Drummond T J and Fischer R 1982a J. Appl. Phys. 53 1030
- Morkoç H, Drummond T J, Fischer R and Cho A Y 1982b J. Appl. Phys. 53 3321
- Nakamura H, Matuura H, Egawa T, Sano Y, Ishida T and Kaminishi K 1985 Extended Abstracts 17th Conf. Solid State Devices and Materials, Tokyo, 429
- Shah N J, Pei S S, Tu C W, Tiberio R C 1986 IEEE Trans. Electron Devices ED-33 543
- Tanaka K, Nakamura H, Kawakami Y, Akiyama M, Ishida T and Kaminishi K 1984 Extended Abstracts 16th Conf. Solid State Devices and Materials, Kobe. 399
- Watanabe Y, Kajii K, Nishiuchi K, Suzuki M, Hanyu I, Kosugi M, Odani K, Shibatomi A, Mimura T, Abe M and Kobayashi M 1986 IEEE ISSCC Tech. Dig. 80
- Yamashita Y, Kawazu R, Kawamura K, Ohno S, Asano T, Kobayashi K and Nagamatsu G 1985 J. Vac. Sci. Technol. 3 314

## **Multiple-input and -output OR/AND circuits for VLSI GaAs ICs**

Tho Vu, Kang Lee, Andrzej Peczalski, Gary Lee, Herpetap Somal, William Betten  
Honeywell Systems and Research Center  
3660 Technology Drive, Minneapolis, Minnesota 55418

**Abstract.** Novel OR/AND circuits with multiple input and output have been demonstrated experimentally for low-power 2K and 6K GaAs gate arrays with two levels of logic at approximately a 155% increase in speed and power product. The proposed multiple-logic levels process in parallel some complex logic functions with only one gate delay. Two proposed bootstrap techniques have shown an improvement of typically 12% in speed without an increase in power for low-power applications.

### **1. Concept and Design**

Multiple-input and -output OR/AND circuits have been developed for VLSI GaAs ICs. Figure 1 shows the OR/AND circuit for Schottky diode FET logic (SDFL). The multiple-input AND function is done in parallel instead of in series (Vu et al., February 1984, and Vu et al., May 1985). Each AND input is realized by a diode along with a pull-up (PU) current source. Therefore, multiple AND functions are easily achievable with multiple diodes. Similarly, multiple OR functions are implemented in parallel using a diode for each input along with a pull-down (PD) current source. The number of level shifting diodes required depends upon the FETs' threshold voltages.

Circuit simulations have shown that 6 AND inputs in coupling with 8 OR inputs per branch is achievable. Figures 2 and 3 show the simulated plots of the output voltage and the transition time versus the FET ratio of PU and PD devices for different AND/OR functions. The transition times here are the fall time and the rise time, which are required to change the output voltage from 90% of high state to 10% of low state or vice versa. The simulations were done with a fixed PD FET size of  $1 \times 3 \mu\text{m}^2$  and then with a fixed PU FET size of  $2 \times 3 \mu\text{m}^2$ . A comparison of simulated data for OR/AND/INVERT and NOR gates has shown a 40% increase in gate delay and an 80% increase in power dissipation. This results in an 152% increase in power-delay product.

The key concept here is that the OR/AND functions are isolated from the inverting stage so that the inverter can be designed to provide multiple fanout. Figure 1 shows an optional output push-pull stage that can handle large fanout. This feature was not available in the series stacking approach, which has limited the SDFL family to less than VLSI level (Vu et al., February 1984, and Vu et al., May 1985).

### **2. Experimental Performance**

The OR/AND/INVERT SDFL circuits have been designed and fabricated using depletion-mode, non-self-aligned GaAs MESFETs (Vu et al., February 1984). Figure 4 shows the layout of OR/AND/INVERT and NOR gates with and without buffering stages in the 2K and 6K SDFL gate arrays.

Table 1 shows the measured noise margin of SDFL OR/AND gates from five different wafers determined by the maximum square method (Hill, April 1968). The measured circuit was a 4-OR input NAND gate with a fanout of 2 and having a -0.9V threshold voltage. As shown, this OR/AND circuit has better noise margin and is more tolerant to the FET's threshold voltage than a series gating circuit (Vu et al., February 1984, and Vu et al., May 1985). These features are very desirable for high radiation hardness and manufacturability. Figures 5 and 6 show the transfer curves of this OR/NAND SDFL gate at  $V_{DD} = 1.3V$  and  $2.0V$ , respectively.

Table 2 summarizes measured dc and ac characteristics of the single-input OR/AND/INVERT SDFL ring oscillators. The data include with and without bootstrap enhancement versus various fanouts, capacitance loadings, and power dissipations. The bootstrap here includes two diodes that are added in parallel to the PU transistor (PUU). This bootstrap increases the PU current when the output goes high, and hence, improves the gate speed by 21% with an increase of 17% in power dissipation (Peczalski, May 1986, and Vu and Lee, June 1984).

Another bootstrap enhancement, which has shown improvement in gate delay by 8% without an increase in power, has a large diode connected in reverse across the level shifting diodes (DS) and logic diodes (DL) (Vu and Lee, June 1984). This bootstrap is very useful for low-power applications. Figure 7 shows the circuit diagram of a SDFL NOR gate with these two bootstrap enhancements.

Figure 8 shows the measured SDFL gate delay versus fanout and includes OR/AND/INVERT and NOR gates with and without buffering stages. The unbuffered gate is used for fanouts of 1 to 4, and the buffered gate for fanouts up to 8. The buffering stages were designed by doubling each FET, which improves the driving capability by 30% at high loading. The buffered gate drives 250 fF on an average of 0.6 ns faster than the unbuffered gate. Also, the buffered gate has better noise margin than the unbuffered gate because of higher gain.

These OR/AND structures also have been implemented successfully in the 2K and 6K gate arrays (Peczalski, May 1986, and Peczalski, to be presented). The OR/AND circuit used in the 6K SDFL gate array has a proprietary, temperature-compensated, level shifting element to improve the temperature operation of the SDFL circuit family.

Table 3 shows the measured data of OR/AND/INVERT and NOR gates from ring oscillators of 2K and 6K SDFL gate arrays. Table 4 compares the performance of NOR and OR/AND/INVERT gates. Basically, the average measured data from the 2K and 6K gate arrays show a match within 3% with the simulated data in power and delay product. Also, simulated data from the 6K gate array have shown a good match with the measured data for the buffered gates with an increase of 106% in power delay product. Essentially, the buffered OR/AND/INVERT gate has a performance of 50% better in power delay product than the unbuffered gate in the 6K gate array. The tradeoff of speed and power in designing OR/AND circuits is up to the designer for each application.

In summary, the SDFL gate can be easily configured into an OR/AND/INVERT gate, which performs two logic levels at an increase of roughly 155% in power delay product.

### 3. Macrocells

The series gating of OR/AND gates has been shown to be unreliable in the 8-bit counter implemented in the 2K SDFL gate array, as described by Vu et al. (May 1985). Two 8-bit counters implemented with the parallel OR/AND structure have been shown to be reliable in two different SDFL gate arrays (Peczalski et al., May 1986). One 8-bit counter was tested on the 2K gate array. Figure 9 shows the output waveform of this test. A yield of 40% was measured. Another 8-bit counter implemented on the bootstrap SDFL gate array is shown at 100 MHz in Figure 10. A yield of 52% was measured. The 8-bit counter consists of 7 OR/NAND gates, 76 buffered NOR gates, 3 input buffers, and 8 output buffers. The longest delay path in the counter is 11 gate delays. The average gate power was 56  $\mu$ W with a gate delay of 2.4 ns.

A pipelined 12 x 12 multiplier implemented with both the unbuffered and buffered OR/AND/INVERT gates has also been shown working in the 6K SDFL gate array (Peczalski et al., to be presented). This multiplier includes the following microcells: a 12-bit ripple counter, a 12-bit synchronous counter, a 24-bit inverting multiplexer, a 12 x 12 multiplier, a 24-bit parallel-to-serial shift register, and a 24-bit multiplexer. A total of 48 unbuffered OR/AND/INVERT gates were used in the 24-bit inverting and noninverting multiplexers. Twelve buffered OR/AND/INVERT gates were used in the 12 x 12 multiplier microcell. Figure 11 shows the output waveform of the pipelined 12 x 12 multiplier in the self-test mode.

### 4. Applications

The concept of the OR/AND structure can be expanded to three logic levels of OR/AND/OR, or the logic order can be interchanged to AND/OR. These multiple-logic circuits can be designed for any GaAs bipolar or FET logic family, including ECL, CML, SDFL, BFL, DCFL, SCFL, etc. For example, a two-level of OR/AND/AMPLIFIER was implemented in the SCFL family with an increase of 25% in gate delay, 100% in power, or 150% in power delay product (Vu et al., May 1986). These OR/AND circuits are very useful in implementing logic functions like multiplexer, demultiplexer, encoder, counter, ALU, etc., which require multiple input and multiple output. This is essentially applicable for VLSI which implements more logic functions in less chip area, higher speed, and lower power.

### 5. Acknowledgments

We acknowledge the staff of Honeywell Optoelectronics Division for processing and the staff of Honeywell Systems and Research Center for testing. This work was partially supported by the Defense Advanced Research Projects Agency under Contract No. F29601-84-C-0010. This paper was approved for public release with unlimited distribution.

### 6. References

- Hill, C.F., April 1968, "Noise Margin and Noise Immunity in Logic Circuits," *Microelectronics*, pp. 16-21.
- Peczalski, A., et al., May 1986, "The Design and Performance of GaAs 2K Gate Array," *Proceedings of Custom Integrated Circuit Conference*, pp. 517-520.
- Peczalski, A., et al., to be presented at 1986 GaAs IC Symposium, "A 6K GaAs Gate Array with Fully Functional LSI Personalization."

- Vu, T., and Lee, K., June 1984, "Study of SDFL Family for Low-Power Applications--New Ideas," Honeywell memo.
- Vu, T., et al., February 1984, "A Gallium Arsenide SDFL Gate Array with On-Chip RAM," *IEEE Journal of Solid-State Circuits*, Vol. SC-19, No. 1, pp. 10-22.
- Vu, T., et al., May 1985, "Low Power Logic Gate with Active Pull-Down Push-Pull Output for GaAs SDFL Circuits," *CICC*, pp. 429-433.
- Vu, T., et al., May 1986, "GaAs Source Coupled FET Logic," *Proceedings of the International Conference on Circuits and Systems*, pp. 1129-1130.

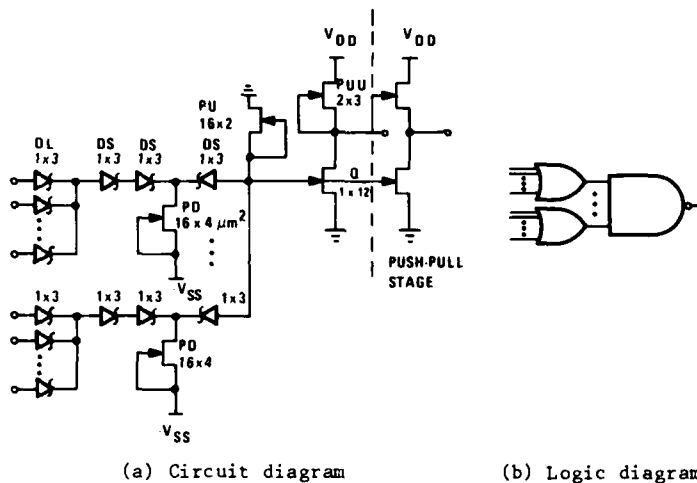


Figure 1. Multiple Input/Output OR/AND/INVERT SDFL

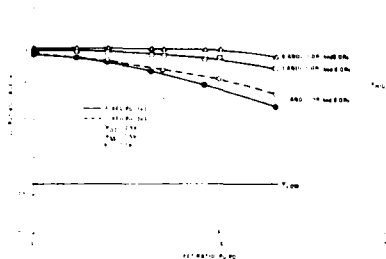


Figure 2. Output Voltage versus FET Ratio of PU to PD Devices for Different AND/OR Functions

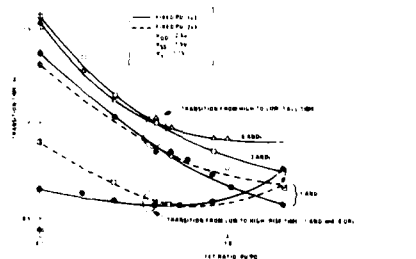


Figure 3. Transition Time versus FET Ratio of PU to PD Devices for Different AND/OR Functions

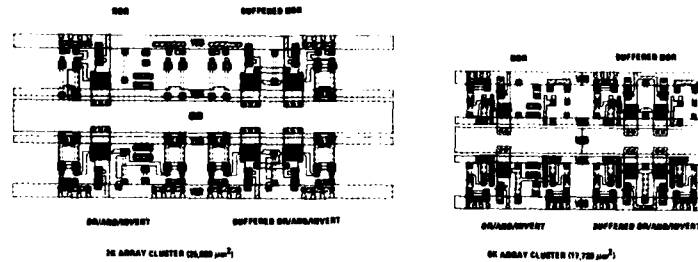


Figure 4. Layout of SDFL Cluster and Its Area Decrease from a 2K to a 6K Gate Array

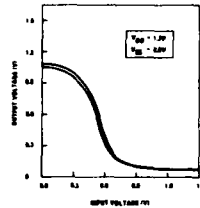


Figure 5. Transfer Curves of an OR/NAND SDFL Gate with Each AND Input Exercised; Each AND Input Has 2 OR Inputs

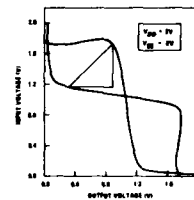


Figure 6. Noise Margin Curve of an OR/NAND SDFL Gate with 2-AND Input and a Fanout of 2; Each AND Input Has 2 OR Inputs

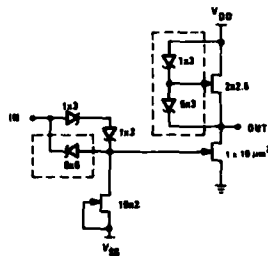


Figure 7. SDFL NOR Gate with Bootstrap Enhancements

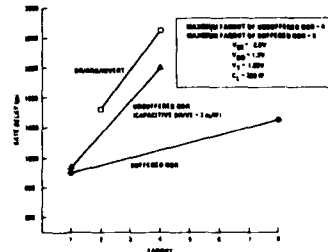


Figure 8. SDFL Fanout Sensitivity



Figure 9. Output of 8-Bit Counter on 2K Gate Array



Figure 10. Output of 8-Bit Counter from the Bootstrap Gate Array at 100 MHz



Figure 11. Output of Pipelined 12 x 12 Multiplier in the Self-Test Mode

TABLE 1. NOISE MARGIN AND YIELD OF A 4-INPUT OR/AND/INVERT SDFL WITH A FANOUT OF 2 AT  $V_{SS} = -2V$ 

| Parameter         | Wafer Number |        |       |        |       |
|-------------------|--------------|--------|-------|--------|-------|
|                   | 1            | 2      | 3     | 4      | 5     |
| $V_{DD} = 2V$     |              |        |       |        |       |
| Noise margin (mV) | 492.4        | 403.29 | 323.8 | 489.4  | 223.8 |
| Voltage swing (V) | 1.52         | 1.58   | 1.53  | 1.56   | 1.03  |
| Yield (%)         | 49.0         | 57.1   | 80.1  | 67.0   | 34.7  |
| $V_{DD} = 1.3V$   |              |        |       |        |       |
| Noise margin (mV) | 183.5        | 191.5  | 198.9 | 313.27 | 132.1 |
| Voltage swing (V) | 1.03         | 0.948  | 0.954 | 1.06   | 0.593 |
| Yield (%)         | 49.0         | 55.1   | 81.6  | 67.0   | 26.5  |

Note: 1. Noise margin was calculated using the maximum square method.  
 2. Voltage swing =  $V_{out}(\text{high}) - V_{out}(\text{low})$ .  
 3. Yield was based on 40 die per wafer with a 50-mV pass/fail criterion.

TABLE 2. DC AND AC CHARACTERISTICS OF OR/AND/INVERT GATE FROM SDFL RING OSCILLATOR AT  $V_{SS} = -2V$ 

| Variable          | Fanout | Capacitance Loading (fF) | $V_{DD}$ (V) | $I_{DD}$ ( $\mu A$ ) | $I_{SS}$ ( $\mu A$ ) | P ( $\mu W$ ) | $T_d$ (ns) | $P \times T_d$ (fJ) | $V_{SW}$ (V) |
|-------------------|--------|--------------------------|--------------|----------------------|----------------------|---------------|------------|---------------------|--------------|
| Without bootstrap | 2      | --                       | 1.3          | 154.4                | 72.7                 | 346           | 1.65       | 571                 | 0.34         |
|                   | 2      | --                       | 2            | 171.4                | 83.6                 | 510           | 2.27       | 1158                | 0.50         |
|                   | 4      | 250                      | 1.3          | 237.3                | 67.2                 | 443           | 1.38       | 612                 | 0.7          |
|                   | 4      | 250                      | 2            | 492.7                | 69.9                 | 1125          | 1.10       | 1233                | 0.8          |
| With bootstrap    | 2      | --                       | 1.3          | 197.9                | 72.7                 | 373           | 1.25       | 466                 | 0.28         |
|                   | 2      | --                       | 2            | 498.5                | 73.1                 | 1143          | 1.04       | 1189                | 0.34         |
|                   | 4      | 250                      | 1.3          | 145.7                | 64.5                 | 304           | 2.71       | 823                 | 0.9          |
|                   | 4      | 250                      | 2            | 155.4                | 65.2                 | 441           | 3.10       | 1365                | 1.4          |

TABLE 3. PERFORMANCE OF OR/AND/INVERT AND NOR GATES FROM RING OSCILLATORS OF 2K AND 6K GaAs SDFL GATE ARRAYS

| Gate      | Fanout | Capacitance Loading (fF) | $V_{DD}$ (V) | $I_{DD}$ ( $\mu A$ ) | $I_{SS}$ ( $\mu A$ ) | P ( $\mu W$ ) | $T_d$ (ns) | $P \times T_d$ (fJ) | $V_{SW}$ (V) |
|-----------|--------|--------------------------|--------------|----------------------|----------------------|---------------|------------|---------------------|--------------|
| 2K OR     | 2      | --                       | 1.3          | 154.4                | 72.7                 | 346           | 1.65       | 571                 | 0.34         |
| 2K AND    | 2      | --                       | 2            | 171.4                | 83.6                 | 510           | 2.27       | 1158                | 0.50         |
| 2K INVERT | 2      | --                       | 1.3          | 197.9                | 72.7                 | 373           | 1.25       | 466                 | 0.28         |
| 2K NOR    | 2      | --                       | 2            | 498.5                | 73.1                 | 1143          | 1.04       | 1189                | 0.34         |
| 6K OR     | 4      | 250                      | 1.3          | 237.3                | 67.2                 | 443           | 1.38       | 612                 | 0.7          |
| 6K AND    | 4      | 250                      | 2            | 492.7                | 69.9                 | 1125          | 1.10       | 1233                | 0.8          |
| 6K INVERT | 4      | 250                      | 1.3          | 145.7                | 64.5                 | 304           | 2.71       | 823                 | 0.9          |
| 6K NOR    | 4      | 250                      | 2            | 155.4                | 65.2                 | 441           | 3.10       | 1365                | 1.4          |

TABLE 4. PERFORMANCE COMPARISON OF OR/AND/INVERT AND NOR GATES

| Gate  | Average % Increase in Gate Delay, $T_d$ | Average % Increase in Power, P | Average % Increase in $P \times T_d$ |
|---|---|--------------------------------|--------------------------------------|
| 2K gate array, unbuffered gates               | 32.5                                    | 129.5                          | 204.5                                |
| 6K gate array, buffered gates                 | 92                                      | 6.5                            | 105.5                                |
| Average of 2K and 6K                          | 62                                      | 68                             | 155                                  |
| Simulation (Vu and Lee)                       | 40                                      | 80                             | 152                                  |
| Simulation of 6K gate array, unbuffered gates | 68.3                                    | 47.4                           | 150                                  |
| Simulation of 6K gate array, buffered gates   | 53                                      | 35                             | 106                                  |



## Total dose effects of gamma ray on GaAs ICs

K. AONO, T. SHIMURA, M. KOMARU, M. KATSUMATA, O. ISHIHARA  
AND K. FUJIKAWA

LSI RESEARCH AND DEVELOPMENT LABORATORY  
MITSUBISHI ELECTRIC CORPORATION  
4-1 Mizuhara, Itami, Hyogo 664 Japan

**ABSTRACT** Gamma ray total dose effects on electrical properties of X-band two-stage MMIC amplifier have been studied. Typical gain and noise figure of the MMIC are 19.5dB and 4.7dB at 9.7GHz, respectively. The MMIC is exposed to gamma radiation ranging from  $10^6$  to  $10^9$  rad(GaAs). No significant change is observed up to  $10^8$  rad. However, at  $10^9$  rad, gain and noise figure are seriously degraded to 17.5dB and 8dB, respectively. Crystal defect level (0.32eV) induced by gamma ray irradiation is found to cause these degradations.

### 1. INTRODUCTION

GaAs monolithic microwave IC's (MMIC's) are becoming one of the most promising devices in radar and communication systems. Especially in satellite communication systems, highly reliable and radiation hardened MMIC's are required. It has been already reported that high dose gamma ray irradiation causes degradation of GaAs FETs and MMICs [Kadowaki and Aono]. However, the degradation mechanism has not been clarified. In this paper described are gamma ray irradiation effects on X-band two-stage MMIC amplifier, and the degradation mechanism is discussed.

### 2. X-BAND TWO-STAGE AMPLIFIER

An X-band two-stage amplifier has been developed. Figure 1 shows a microphotograph of the amplifier. The chip size is 4.2mm X 2mm. The amplifier is composed of 2 FETs, 4 resistors, 11 capacitors and transmission lines as shown in Fig. 2. FET's and resistors are fabricated using selective Si ion implantation. Gate length and width are 1µm and 150µm, respectively. Capacitors have a MIM(Metal-Insulator-Metal) structure. A plasma-CVD SiN film having 4,000Å thickness is used as an insulator. Typical RF characteristics are shown in Fig. 3. Gain and noise figure are 19.5dB and 4.7dB at 9.7 GHz, respectively.

### 3. IRRADIATION EFFECTS ON MMIC

The MMIC is exposed to gamma ray ranging from  $10^6$  to  $10^9$  rad. Cobalt 60 is used as gamma ray source. Dose rate is  $5.4 \times 10^6$  rad/hour. Figure 4 shows gamma dose dependence of RF characteristics of the MMIC. The gain is initially 19.5dB and gradually decreases and reaches to 17.5dB at  $10^9$  rad. On the other hand, the noise figure does not remarkably change up to  $10^8$  rad. However, it is seriously degraded with additional dose and

increases to 8dB at  $10^{11}$  rad. To clarify the degradation mechanism, gamma dose effects on FET, capacitor and resistor are investigated using these monitors fabricated in the vicinity of the MMIC on the same wafer. Figure 5 shows gamma dose dependence of MIM capacitor and resistor. No change in capacitance is observed up to  $10^{11}$  rad. On the contrary, remarkable increase in the n-doped layer resistance is observed above  $10^8$  rad. Figure 6 shows gamma dose dependence of DC characteristics of FET. No remarkable change in both  $I_{ds}$  and  $g_m$  is observed up to  $10^8$  rad. However, drain current  $I_{ds}$  and transconductance  $g_m$  rapidly decreased to 60 and 80% of the initial value, respectively. Gamma dose dependence of the gain is calculated using measured S-parameters of FET. Figure 7 shows the calculated gain. There is a good agreement between the experiment and calculation. Using these measured S-parameters, circuit parameters of FET are obtained from the equivalent circuit shown in Fig. 8. The results are shown in Table 1. The increase in resistances shown in Table 1 agrees well with both the increase in monitor's resistance and the decrease in  $I_{ds}$  and  $g_m$ . From these results, the degradation of the MMIC is caused by the increase in resistive components of the equivalent FET circuit.

#### 4. IRRADIATION INDUCED DEFECTS

The increase in the resistance is expected to be due to radiation induced defects. Therefore, gamma dose effects on GaAs crystal is studied using DLTS. Figure 9 shows typical DLTS spectra before and after irradiation of  $10^8$  rad. Before irradiation, only one peak, denoted as G-4, is observed. This level is well known as EL2. On the other hand, three peaks, G-1, G-2 and G-3, appear after irradiation. The activation energies of G-1, G-2 and G-3 level are 0.32, 0.8 and 0.93 eV, respectively. Among these three types of defects, the density of G-3 level is neglected in this paper, because this is relatively small. Densities of G-1 and G-2 levels are shown as a function of gamma dose in Fig. 10. Below  $10^8$  rad, G-2 level is dominant, while density of G-1 level more rapidly increases with gamma dose and becomes dominant above  $10^8$  rad. The decrease in carrier concentration and the increase in the defect densities of G-1 and G-2 levels are shown in Fig. 11. Fairly good agreement is found between the decrease in carrier concentration and the increase in the defect densities. This result means that irradiation induced defects act as electron traps and remove free carriers.

#### 5. CONCLUSION

Total dose effects of gamma ray on GaAs MMIC's are studied. From this study, the degradation of X-band two-stage amplifier is found to be caused by crystal defects induced by gamma ray irradiation. The following is concluded.

- (1) No remarkable degradation of two-stage amplifier performance is observed for gamma dose up to  $10^8$  rad. However above  $10^8$  rad, a degradation mechanism was demonstrated.
- (2) The degradation of two-stage amplifier is mainly caused by the increase in the resistance of FET.
- (3) Three types of crystal defects, G-1, G-2 and G-3 are induced in GaAs crystal by gamma ray irradiation. The increase in the resistance of FET is due to the increase of these defects.
- (4) Among these three defects, G-1 level plays an important role in the degradation of the amplifier.

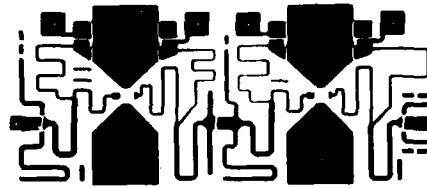


Fig.1 A microphotograph of X-band two-stage MMIC amplifier.

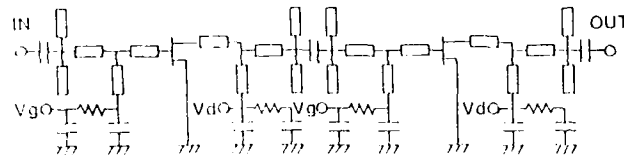


Fig.2 An equivalent circuit of the MMIC two-stage amplifier.

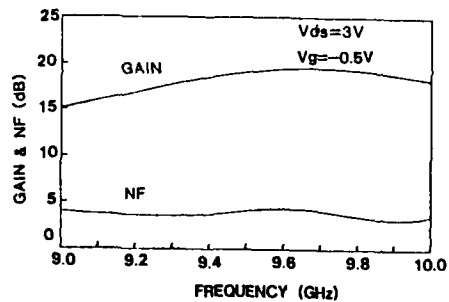


Fig.3 Typical RF characteristics of the MMIC two-stage amplifier.

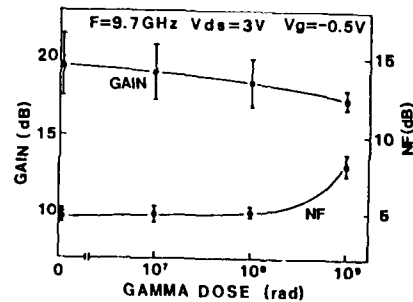


Fig.4 Gamma dose dependence of RF characteristics of the MMIC two-stage amplifier.

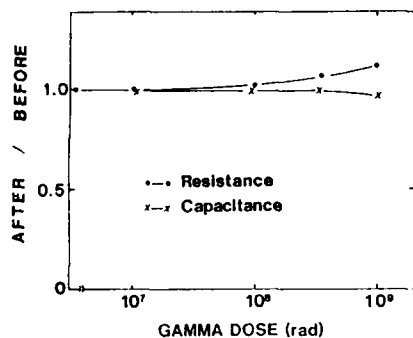


Fig.5 Gamma dose dependence of MIM capacitor and resistor.

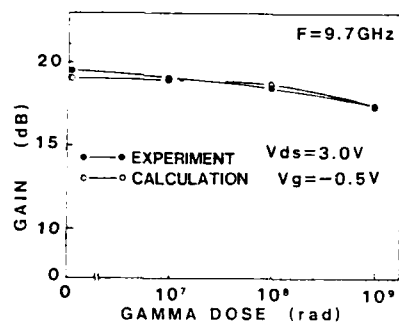


Fig.7 Gamma dose dependence of calculated and experimental gain of the MMIC.

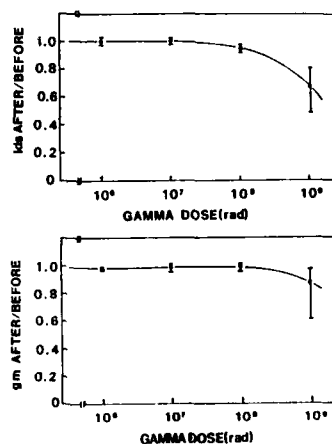


Fig.6 Gamma dose dependence of DC characteristics of FET.

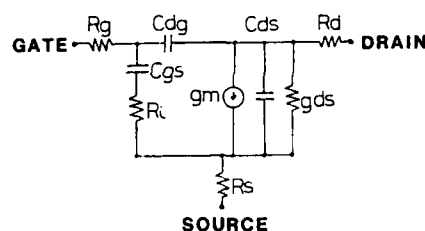


Fig.8 Equivalent circuit of FET.

Table.1 Gamma dose dependence of circuit parameters of FET.

|         | GAMMA DOSE (rad) |                 |                 |                     |                 |
|---------|------------------|-----------------|-----------------|---------------------|-----------------|
|         | 0                | 10 <sup>7</sup> | 10 <sup>8</sup> | 3.5×10 <sup>8</sup> | 10 <sup>9</sup> |
| Cgs(pF) | 0.21             | 0.21            | 0.21            | 0.21                | 0.21            |
| Cgd(pF) | 0.020            | 0.020           | 0.020           | 0.021               | 0.023           |
| Cds(pF) | 0.006            | 0.006           | 0.005           | 0.008               | 0.006           |
| Rg (Ω)  | 1.54             | 1.54            | 1.58            | 1.50                | 1.54            |
| Ri (Ω)  | 7.2              | 7.2             | 6.9             | 6.4                 | 7.2             |
| Re(Ω)   | 6.1              | 5.9             | 6.1             | 6.9                 | 8.8             |
| Rd (Ω)  | 7.5              | 7.5             | 8.0             | 9.3                 | 9.6             |
| Rs (Ω)  | 640              | 640             | 640             | 667                 | 720             |
| gm(mS)  | 19.9             | 19.9            | 20.3            | 19.5                | 19.1            |

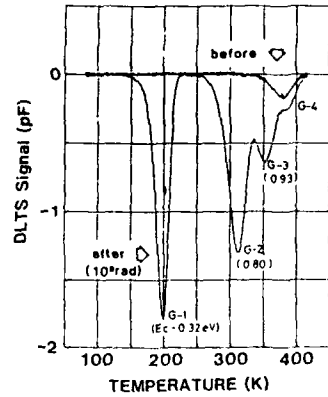


Fig.9 Typical DLTS spectra before and after irradiation.

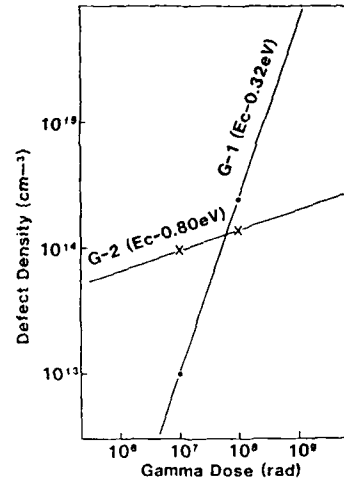


Fig.10 Defect densities of G-1 and G-2 levels as a function of gamma dose.

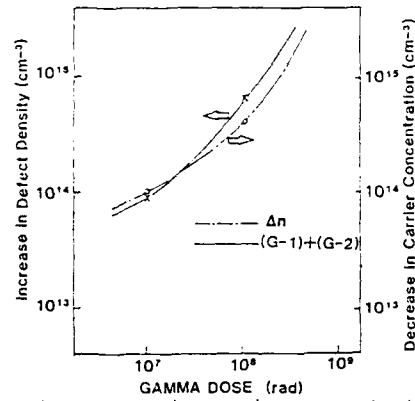


Fig.11 Decrease in carrier concentration and increase in defect densities of G-1 and G-2 levels.

ACKNOWLEDGMENTS

The experiments of gamma ray irradiation have been carried out using Cobalt 60 source facility of Radiation Center of Osaka Prefecture. Authors are grateful to Dr.M. Kitagawa et. al. for their cooperation. Authors would like to thank Dr. K. Nishitani for the useful discussion.

REFERENCES

- Y. KADOWAKI et. al; "Effects of Gamma Ray Irradiation on GaAs MMICs"  
Tech. Dig., 1982. GaAs IC Symp., p.83.
- K. AONO et. al; "Gamma Ray Radiation Effects on MMIC's Elements"  
Tech. Dig., 1984 GaAs IC Symp., p.139.

## **A novel rapid thermal annealing for GaAs digital ICs**

A. Tamura, T. Uenoyama, K. Inoue and T. Onuma

Semiconductor Research Center  
Matsushita Electric Industrial Co., Ltd.  
3-15 Yagumo-Nakamachi, Moriguchi, Osaka 570, Japan

**Abstract.** A novel rapid thermal annealing (RTA) method using GaAs guard rings has been developed. The method has effectively suppressed slip line generation and offered uniform annealing characteristics over 2-inch diameter GaAs wafer. Using this RTA method, GaAs digital ICs (dual-modulus prescaler) have been fabricated with high yield.

### **1. Introduction**

Rapid thermal annealing (RTA) using radiation from halogen lamps is very promising annealing method for ion-implanted GaAs. The great advantages of this method are a short annealing time and its relative simplicity as compared with the conventional furnace annealing. The diffusion of implanted dopants and surface degradation of GaAs wafer due to As dissociation are expected to be suppressed by this short annealing time. In spite of those advantages, only a few papers have been reported so far (Badawi et al. 1984, Cummings et al. 1986) on the application of RTA method to annealing large-size (2- or 3-inch diameter) GaAs wafers. This is probably because considerable crystallographic slips are induced during RTA. Therefore, not only overcoming this problem but also uniform annealing characteristics over the wafer are needed in order to apply RTA method to GaAs IC processing.

In this paper, we report a new RTA method using GaAs guard rings and successful fabrication of GaAs digital ICs with high yield using this RTA method.

### **2. Experimental**

The RTA system used in this work was a commercial Heatpulse 210T system manufactured by A.G.Associates. The wafers used in this work were undoped (100) semi-insulating 2-inch diameter GaAs crystals grown by liquid encapsulated Czochralski (LEC) method. Si<sup>29</sup> and Si<sup>28</sup> were implanted selectively at 100keV and 150keV for n-type layers of FETs and n<sup>+</sup>-type layers of source/drain regions, respectively.

The wafers were annealed caplessly using the proximity method (i.e., face down on another 2-inch diameter GaAs wafer) under Ar atmosphere in order to prevent the surface degradation during RTA. These GaAs wafers were supported by 4-inch diameter Si wafer. The wafers were firstly kept at

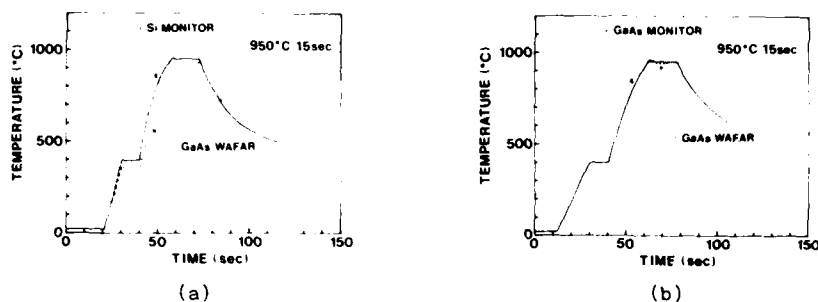


Fig. 1. Temperature cycles of monitor and GaAs wafer on RTA (950°C, 15sec) using (a) Si monitor and (b) GaAs monitor.

400°C for 10sec in order to improve the reproducibility of annealing.

The temperature of annealed wafer is usually monitored via thermocouple embedded in a small piece of Si wafer (Si monitor) attached to periphery of Si supporting wafer. This monitor temperature is controlled as to be programmed value by closed loop control. We have investigated the temperature difference between monitor and the annealed GaAs wafer using two kinds of monitors. One is usually used Si monitor and the other is GaAs monitor, which is made of a GaAs block in which thermocouple was embedded. The GaAs block has the same thermal capacity as that of two 2-inch diameter GaAs wafers. The GaAs wafer temperature was measured via thermocouple embedded between two 2-inch diameter GaAs wafers.

The results are shown in Fig. 1 (a) and (b) for Si monitor and GaAs monitor, respectively, at the annealing condition of 950°C for 15sec. The large temperature difference between Si monitor and the GaAs wafer was observed due to the difference of thermal capacity as shown in Fig. 1 (a). On the other hand, the difference between them was diminished for GaAs monitor as shown in Fig. 1 (b). Therefore, it is possible to control accurate temperature cycle using GaAs monitor.

After annealing, the slip lines in 2-inch diameter GaAs wafers were observed by X-ray transmission topography. The uniformity of annealing characteristics was evaluated by the drain saturation current ( $I_{dss}$ ) distribution of gateless FETs over 2-inch diameter GaAs wafer. GaAs digital ICs (dual-modulus prescaler) were fabricated using RTA.

### 3. Reduction of slip lines in GaAs wafer during RTA

The most likely cause of the slip generation is a relief of stress developed as a result of small temperature nonuniformity across the wafer. Blunt et al. (1985) have reported reduction of slip lines by using Si guard rings during RTA. Taking thermal match between the guard rings and the GaAs wafer into account, the GaAs guard rings will be more desirable (Tamura et al. 1986, Cummings et al. 1986). Thus, we have investigated the following annealing methods using GaAs guard rings. Their experimental arrangements are shown in Fig. 2.

- A) no guard ring arrangement
- B) one GaAs guard ring arrangement
- C) two GaAs guard rings arrangement
- D) three GaAs guard rings arrangement



The annealing temperature and time are 950°C and 15sec, respectively. A GaAs guard ring was made from a 3-inch diameter GaAs wafer (800 $\mu$ m-thickness).

After annealing, the GaAs wafers were examined by X-ray transmission topography using MoK $\alpha$  radiation. The results are shown in Fig. 3. As-grown wafer without heat treatment is also shown as a reference. The method A, B, and C resulted in the generation of extensive slip networks toward the center from the periphery of the wafer. A clear improvement in the reduction of slip lines is seen for the method D in which three GaAs guard rings were used. These results indicate that the uniformity of temperature distribution across the wafer is improved using three GaAs guard rings.

Therefore, we selected this RTA method D using three GaAs guard rings for the following experiments.

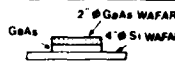

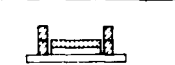

| ANNEALING METHOD | EXPERIMENTAL ARRANGEMENT  |
|------------------|---|
| A                |  |
| B                |  |
| C                |  |
| D                |  |

Fig. 2. Experimental arrangements for different kinds of RTA methods.

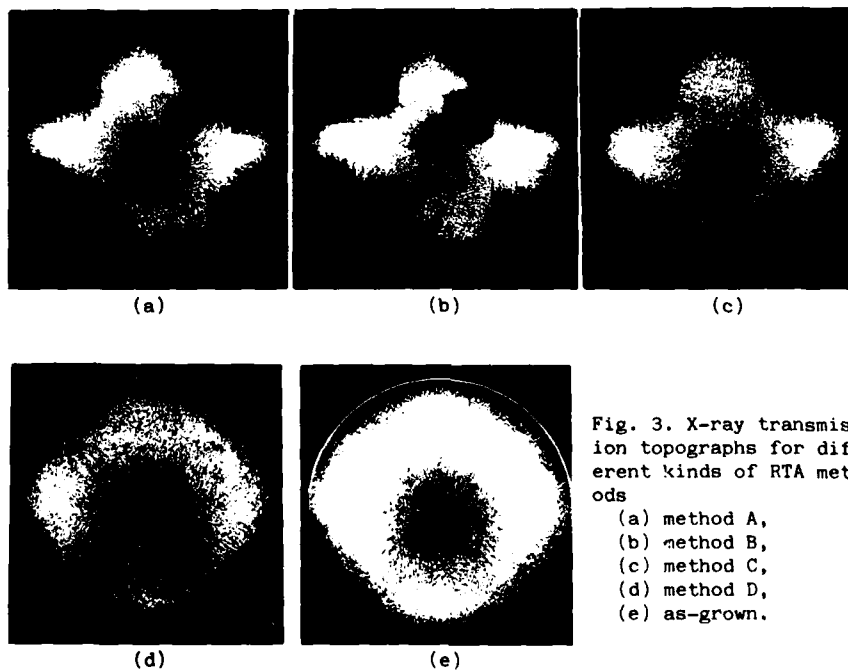


Fig. 3. X-ray transmission topographs for different kinds of RTA methods

- (a) method A,
- (b) method B,
- (c) method C,
- (d) method D,
- (e) as-grown.

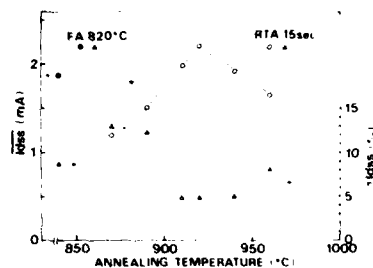


Fig. 4. Annealing temperature dependence of  $\overline{Idss}$  and  $\sigma Idss$ .

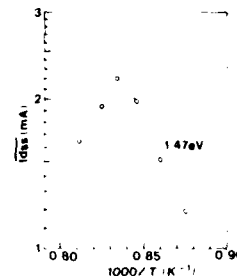


Fig. 5. Arrhenius plot of  $\overline{Idss}$ .

#### 4. Annealing temperature dependence of uniformity and activation

The uniformity of annealing characteristics and activation by RTA were investigated as changing annealing temperature with the aim of its application to the device fabrication. GaAs FETs have been fabricated on 2-inch diameter GaAs wafers.  $Si^{28}$  and  $Si^{28}$  were selectively implanted at 100keV with a dose of  $5 \times 10^{12} \text{ cm}^{-2}$  and at 150keV with a dose of  $1 \times 10^{14} \text{ cm}^{-2}$  for active layers and source/drain regions of FETs, respectively. The source-drain spacing and channel width of FET are  $3\mu\text{m}$  and  $5\mu\text{m}$ , respectively. The uniformity of annealing characteristics was evaluated by drain saturation current ( $Idss$ ) distribution of about 1100 gateless FETs, which were measured using computer controlled automatic probing system by 1.2mm-pitch over 2-inch diameter wafer.

Fig. 4 shows the annealing temperature dependence of  $\overline{Idss}$  (mean value of  $Idss$ ) and  $\sigma Idss$  (standard deviation of  $Idss$ ). Annealing time was 15sec. As a reference, the result obtained by conventional furnace annealing (FA, capless annealing at 820°C for 15min in  $AsH_3/Ar$  atmosphere) was also shown in this figure. The  $\overline{Idss}$  increases almost linearly with annealing temperature and has a maximum value at around 920°C. Over that temperature, the  $\overline{Idss}$  decreases linearly due to the surface degradation or the increase of compensation ratio because of amphoteric nature of Si.  $\sigma Idss$  has a minimum value at around 920°C. The values of  $\overline{Idss}$  and  $\sigma Idss$  at 920°C show higher activation and more uniform annealing characteristics than those of furnace annealing.

Fig. 5 shows the Arrhenius plot of  $\overline{Idss}$ . From this figure, the activation energy of 1.47eV for  $\overline{Idss}$  was obtained. That value is about three times higher than that reported in the case of high-dose ( $> 3 \times 10^{13} \text{ cm}^{-2}$ ) Si-implantation (Hiramoto et al. 1985, Cummings et al. 1986). The reason is not clear at present, but it may be due to the difference of implanted dose.

Fig. 6 and 7 show the typical  $Idss$  distribution and the histogram of  $Idss$  over 2-inch diameter wafer by RTA at 920°C, respectively.

From the above results, the annealing condition at 920°C for 15sec was selected as optimum, and this annealing condition was adopted for fabrication of GaAs digital ICs.



Fig. 6.  $I_{dss}$  distribution of gateless FETs by RTA (920°C, 15sec).

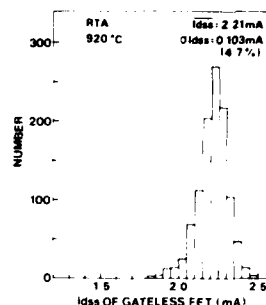


Fig. 7. Histogram of  $I_{dss}$  for gateless FETs by RTA (920°C, 15sec).

#### 5. Application of RTA to GaAs digital IC processing

Using RTA, GaAs digital ICs (dual-modulus prescaler) were fabricated on 2-inch diameter GaAs wafer. Fig. 8 shows the block diagram of fabricated dual-modulus prescaler IC for the use of mobile telecommunication systems designed as to have low dissipation current (Hasegawa et al. 1986). By the two mode control signals MC1 and MC2, it operates as a 256/258/128/130 variable frequency divider. This prescaler is consisted of 334  $\mu\text{m}$ -gatelength enhancement-mode MESFETs (E-MESFETs), 56 load resistors and 104 shift diodes using source-coupled FET logic (SCFL) with a fully complementary operation (Katsu et al. 1982, Idda et al. 1984). Fig. 9 shows the photograph of IC chip.

The  $n^+$ -type source/drain regions of FETs and n-type layers of FETs, load resistors and shift diodes were formed by selective  $\text{Si}^{28}$  (150keV,  $1 \times 10^{14} \text{ cm}^{-2}$ ) and  $\text{Si}^{29}$  (100keV,  $\sim 4 \times 10^{12} \text{ cm}^{-2}$ ) ion implantations, respectively. RTA (method D) was carried out with optimum annealing condition (920°C, 15sec). The gate electrode was Pt/Ti/Au and the threshold voltage ( $V_{th}$ ) of FET was adjusted to 0.1~0.2V by sintering at 380°C in Ar atmosphere using Pt buried gate technology (Onuma et al. 1983). Typical value of  $\sigma V_{th}$  (standard deviation of  $V_{th}$ ) over 2-inch diameter wafer was about 40~60mV, of which value is lower than that of furnace annealing (60~80mV), at  $V_{th} \sim 0.1\text{V}$  in the case of using conventional LEC crystals. The first and second interconnection lines were formed with about 2 $\mu\text{m}$ -thick Ti/Pt/Au by a plating technique. 2 $\mu\text{m}$ -thick polyimide was formed as the cross-over

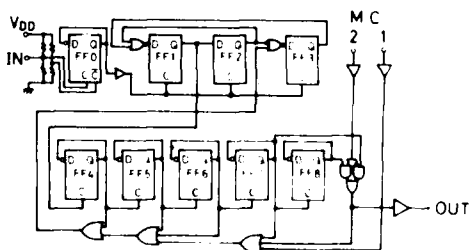


Fig. 8. Block diagram of prescaler IC.

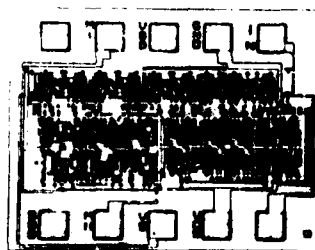


Fig. 9. Photograph of IC chip.



Fig. 10. Dissipation current distribution of prescalers operating at 1GHz fabricated by RTA.

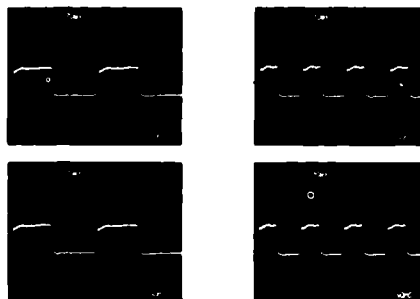


Fig. 11. Output waveforms of prescaler at input frequency of 1GHz.

insulator to reduce the interconnection capacitance.

Fig. 10 shows the dissipation current distribution of the operated prescalers at input frequency of 1GHz with 5V supply voltage obtained by on-wafer measurement. The chip yield was as high as 69% for 1GHz operation, which is higher than that of furnace annealing (typical 40 ~ 60%). Fig. 11 shows the output waveforms of divide-by-258/256/130/128 mode for input frequency of 1GHz. The lowest dissipation current was 3.1mA with 5V supply voltage for 1GHz operation. These results have proved that this RTA method is very promising for GaAs digital IC processing.

#### 6. Summary

A novel RTA method using GaAs guard rings has been developed. This method has shown to provide reduced slip line generation and uniform annealing characteristics over 2-inch diameter GaAs wafer. Using this RTA method, high-yield fabrication of GaAs digital ICs has been achieved.

#### Acknowledgments

The authors wish to thank Dr. H. Mizuno and T. Kajiwara for their continuous encouragement throughout this work. They also wish to thank H. Yagita and K. Utsumi for helpful discussions, K. Nishii for fabrication and K. Hasegawa for on-wafer measurement.

#### References

- Badawi M H and Mun J 1984 *Electron. Lett.* **20** 125
- Blunt R T, Lamb M S M and Szweda R 1985 *Appl. Phys. Lett.* **47** 304
- Cummings K D, Pearton S J and Vella-Coleiro G P 1986 *J. Appl. Phys.* **60** 163
- Hasegawa K, Uenoyama T, Nishii K and Onuma T 1986 *Electron. Lett.* **22** 251
- Hiramoto T, Saito T and Ikoma T 1985 *Jpn. J. Appl. Phys.* **24** L193
- Idda M, Takada T and Sudo T 1984 *IEEE Trans. MTT-32* 5
- Katsu S, Nambu S, Shimano A and Kano G 1982 *IEEE Electron Device Lett.* **EDL-3** 197
- Onuma T, Tamura A, Uenoyama T, Tsujii H, Nishii K and Yagita H 1983 *IEEE Electron Device Lett.* **EDL-4** 409
- Tamura A, Inoue K and Onuma T 1986 presented at 4th Conference on Semi-Insulating III-V Materials in Japan

## **Hot electron resonant tunneling through a quantum well: a new electron spectroscopy**

Federico Capasso, Susanta Sen\*, A Y Cho and A L Hutchinson

AT&T Bell Laboratories, Murray Hill, N.J. 07974

### **1. Introduction**

In recent years there has been an increasing research activity in the field of hot electron or ballistic electron spectroscopy in semiconductors. The principle as well as the name of this technique were first introduced in theoretical papers by Hesto, Pone and Castagne' (1982, 1983). The idea is to use a double barrier transistor structure, one of the barriers being used as the electron injector (emitter) and the other as the collector. The derivative of the collector current  $I_c$  with respect to the base-collector voltage  $V_{bc}$ , i.e.,  $dI_c/dV_{bc}$ , is measured as a function of  $V_{bc}$ . This quantity is directly related to the momentum distribution function  $n(p_\perp)$  in the base region, where  $p_\perp$  is the component of the electron momentum perpendicular to the base-collector interface. Hot electron spectroscopy was first experimentally demonstrated by groups at Bellcore - Bell Labs (Hayes et al. 1984-85) and Fujitsu (Yokoyama, et al. 1984) using respectively planar doped barriers (Malik et al. 1980) and tunneling hot electron transistors (Heiblum et al. 1985a, b). These structures were subsequently employed for the study of ballistic transport by the Bellcore - Bell Labs group (Levi et al. 1985a,b) and IBM group (Heiblum et al. 1985a,b, 1986). A theoretical analysis of hot electron spectroscopy has been recently performed (Wang et al. 1986).

In this paper we demonstrate a new electron spectroscopy technique based on resonant tunneling. The key difference compared to conventional hot electron spectroscopy (Hayes and Levi (1986)) is the use of a resonant tunneling double barrier in the collector of the structure (Fig. 1). The advantage of this new feature is that it allows one to obtain information on the electron momentum distribution  $n(p_\perp)$  directly from the measured resonant tunneling collector current, without requiring the use of derivative techniques.

### **2. Resonant Tunneling Spectroscopy**

Figure 1 illustrates the energy band diagrams of two possible structures for resonant tunneling electron spectroscopy. The first one (Fig. 1a) realized by us in the present experiment consists basically of a reverse biased pn heterojunction and can be used to investigate hot minority carrier transport. Incident light is strongly absorbed in the wide-gap  $p^+$  layer. Photo-generated minority carrier electrons diffuse to an adjacent low-gap layer. Upon entering this region

\* On leave from Institute of Radio Physics and Electronics - University of Calcutta, Calcutta, India

electrons are ballistically accelerated by the abrupt potential step and gain a kinetic energy  $\cong \Delta E_c$ . Collisions in the low gap layer tend to randomize the injected, nearly mono-energetic distribution, making it "hot". Hot electrons subsequently impinge on the double barrier in the collector. From simple considerations of energy and lateral momentum  $p_{||}$  conservation in the tunneling process (Luryi, 1985) it can be shown that only those electrons with a perpendicular energy  $p_{\perp}^2/2m_e^*$  equal (within the resonance width) to the energy of the bottom of one of the subbands (i.e., a resonance) of the quantum well, resonantly tunnel through the quantum well and give rise to a current. Thus by varying the applied bias (i.e., changing the energy difference between the resonance of the quantum well and the bottom of the conduction band in the low gap  $p^+$  layer) and measuring the current, one directly probes the electron energy distribution  $n(E_1)$  or, equivalently the momentum distribution  $n(p_1)$  (Fig. 2). Identical arguments apply to the case of the transistor structure of Fig. 1(b) which can be used to analyse the electron distribution in the base layer by measuring the collector current as a function of the collector-base voltage.

In the above arguments we have assumed that thermionic currents above the double barrier can be minimized. This can be done by operating the structure at sufficiently low temperature and by suitably designing the double barrier (Tsuchiya et al. 1985).

The steady state current density flowing through the double barrier via resonant tunneling is therefore given by, for the case of a parabolic band:

$$J_1 = \frac{e}{m_e^*} \int_0^{\infty} \sqrt{2m_e^* E_1} \, n(E_1) T(E_1) dE_1 \quad (1)$$

where we have considered resonant tunneling through one resonance only.  $T(E_1)$  is transmission of the double barrier. If the latter is designed in such a way that  $T(E_1)$  is high over a narrow energy range (resonance width  $\leq 1$  meV) and negligible elsewhere, Eq. (1) can be rewritten as

$$J_1 = e \sqrt{\frac{2E_1}{m_e^*}} \, n(E_1) T_R \Delta E_R \quad (2)$$

where  $T_R$  is the peak transmission of the double barrier (i.e., at an incident perpendicular energy  $E_1$  equal to the energy of the bottom of the first subband of the quantum well  $E_1$ ) and  $\Delta E_R$  is the full width at half maximum of the resonance. The energy  $E_1$  (which is measured with respect to the bottom of the  $p^+$  low gap layer (Fig. 1a) or the base layer (Fig. 1b)) is linearly related to the electric field applied to the double barrier. For the structure of Fig. 1(a) one has

$$E_1 = E_1 - \frac{e(V + V_{bi})(L_B + L_W/2)}{L_c} \quad (3)$$

where  $V$  is the reverse bias voltage,  $V_{bi}$  the built-in potential of the pn-junction,

$L_c$  the total collector layer thickness,  $L_B$  and  $L_W$  the barrier and well layer thickness respectively.  $E_1$  is the energy of the bottom of the ground state resonance measured with respect to the bottom of the center of the well. (Note that  $E_1$  is assumed to be independent of the electric field  $F$  which is a good approximation as long as  $E_1$  is significantly greater than  $eFL_W$ ). It is clear from Eq. (2) and (3) that by measuring the current as a function of voltage, rather than its derivative, one probes directly the energy distribution  $n(E_1)$  of the electrons incident on the double barrier. Note that the term  $T_R \Delta E_R$  can be rigorously calculated (assuming no inelastic current) for a given double barrier and is monotonically dependent on the applied field. Note that also in conventional hot electron (derivative) spectroscopy the collector current depends in general on the transmission at the collector base interface, due to quantum mechanical reflections of electrons emitted near the top of the barrier (Wang et al. 1986).

### 3. Experimental Results

The structures were grown by Molecular Beam Epitaxy on a  $\langle 100 \rangle$   $p^+$  GaAs substrate and consist of  $p^+n$  heterojunctions. Their band diagram is shown in Fig. 1a at a given reverse bias. The growth starts with a 2000 Å thick  $n^+ = 2 \times 10^{17} \text{ cm}^{-3}$  buffer layer followed by an undoped 5000 Å GaAs layer and an AlAs/GaAs/AlAs double barrier, with barrier and well thicknesses of 20 Å and 80 Å respectively. The parameters of the double barrier were chosen in such a way that over the applied voltage range (0–10 V) the electron energy distribution is probed essentially by only one resonance at a time. In this way at any given bias the current is due to resonant tunneling through a single resonance. For our double barrier the first resonance is at  $E_1 = 60 \text{ meV}$  from the well bottom and the second at  $E_2 = 260 \text{ meV}$  (Tsuchiya et al 1985). Thus it is easily shown (see later in text) that the first peak in the current (Fig. 3 and 4) is obtained from probing the low energy tail of the distribution with the first resonance while the second one is obtained from sampling the higher energy portion of the distribution with the second resonance. A 20 Å undoped GaAs spacer layer separates the double barrier from the  $p^+$  ( $= 3 \times 10^{18} \text{ cm}^{-3}$ ) GaAs layer. Different thicknesses were used for this region (250 Å, 500 Å, 1800 Å) while keeping everything else the same. The last layer consists of 2 μm thick  $\text{Al}_{0.3}\text{Ga}_{0.7}\text{As}$  doped to  $p = 3 \times 10^{18} \text{ cm}^{-3}$ . Light from a He-Ne laser ( $\lambda = 6328 \text{ Å}$ ) heavily absorbed in this region was used to achieve pure electron (minority carrier) injection.

The devices were mounted in a Helitran dewar and the photocurrent was measured as a function of reverse bias in the temperature range from 70 to 9 K. Fig. 3 and 4 illustrate the measured photocurrent for two different thicknesses of the GaAs  $p^+$  layer. Consider first the data for the structure with the 500 Å thick layer (Fig. 3). Two distinct features are present at 1.2 V and 7 V respectively. Using Eq. (3) one can easily see that the first peak corresponds to electrons with perpendicular energy of a few tens of meV ( $\approx 17 \text{ meV}$  at the maximum) that have resonantly tunneled through the first resonance of the quantum well. The second peak, clearly visible only at the lower temperature is much broader and corresponds to incident electrons with energy  $E_1 \approx 122 \text{ meV}$  which have resonantly tunneled through the second resonance of the well. It is therefore clear that the energy distribution of the electrons in the  $p^+$  GaAs layer, following high energy injection (0.233 eV, i.e. the conduction band discontinuity between

GaAs and the  $\text{Al}_{0.3}\text{Ga}_{0.7}\text{As}$ ) consists of two parts. One is strongly thermalized, with energies close to the bottom of the conduction band, while the other one is much hotter. Thus the distribution is strongly non maxwellian similar to what has been found, by conventional electron spectroscopy, in the case of majority carrier electrons in the base of hot electron transistors (Hayes and Levi 1986).

Similar results are found by decreasing the GaAs  $p^+$  layer thickness from 500 Å to 250 Å (Fig. 4). The first peak is located at somewhat lower voltage (corresponding to 25°C - 30°C higher energies) implying that the thermalization of carriers is somewhat less, due to the thinner layer, as expected. Overall however, the shape of the energy distribution has not changed significantly which implies that already over a length of a few hundred Å the near ballistic injected distribution has been strongly randomized by scattering. Additional manifestation of strong scattering comes from the fact that no evidence is found in the data of Fig. 4 of the quantized subbands of the 250 Å  $p^+$  well into which electrons are injected. Since this subband structure should be reflected on the electron distribution, one would expect to observe peaks in the photocurrent at such voltages, that the resonances of the double barrier coincide in energy with the resonances of the 250 Å thick layers. The fact that this is not observed implies that the collisional broadening due to scattering  $\hbar/\tau$  must be comparable to the typical energy separation between the resonances of the  $p^+$  layers. The latter varies with the quantum number. For the  $n=3$  and  $n=4$  levels the energy separation is  $\approx 60$  meV. By the above criteria this implies a scattering time of  $\approx 10^{-14}$  sec for hot electrons with an energy  $\gtrsim 0.1$  eV. This order of magnitude estimate is not unreasonable. Note that at high p-type doping levels ( $>10^{18}\text{cm}^{-3}$ ) in GaAs impurity scattering plays an important role in randomizing the momentum of hot electrons traversing the GaAs layer. Scattering from optical phonons ( $\hbar\omega \approx 36$  meV), plasmons ( $\hbar\omega_p \approx 10$  meV) and single particle scattering between an electron and a hole also play a very important role. In fact recent electron spectroscopy measurements by Hayes et al. (1986) in heterojunction bipolar transistors with base thicknesses  $\gtrsim 400$  Å shows that electrons undergo strong relaxation in the  $p^+$  ( $\approx 2 \times 10^{18}\text{cm}^{-3}$ ) base. Recent experimental determinations of the scattering rates of hot electrons with comparable energies in heavily doped  $n^+ = 1 \times 10^{18}\text{cm}^{-3}$  GaAs give a scattering time in the  $3 \times 10^{-14} - 5 \times 10^{-14}$  sec. (Hayes and Levi 1986) range.

We have also performed measurements in similar structures with a thicker  $p^+$  region (1800 Å). From the photo current IV we found that electrons undergo resonant tunneling through the double barrier starting from a few meV energy from the bottom of the conduction band in the  $p^+$  GaAs layer, and that there is not a hot electron distribution at higher energy. This is to be expected since by making the  $p^+$  layer much thicker electrons have had time to thermalize at the bottom of the band before undergoing resonant tunneling.

One final important point should be noted. To obtain the energy distribution  $n(E_e)$  from the current, the latter must be properly normalized by taking into account the increase of the tunneling probability with increasing electric field (more precisely the product  $T(E_R)\Delta E_R$  in Eq. (2)) and by subtracting any background due to thermionic emission over the barrier. In any case, the main qualitative features of the electronic transport can be obtained directly from the current, as previously shown.



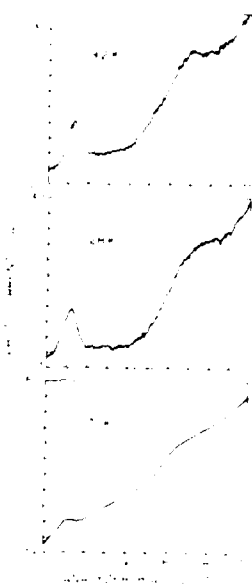
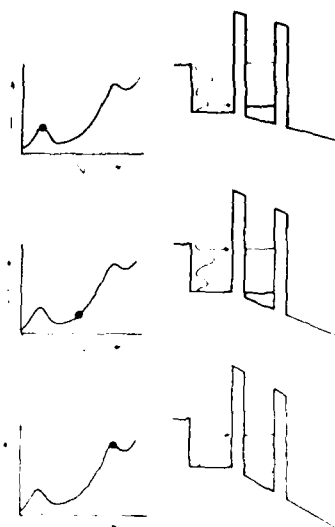
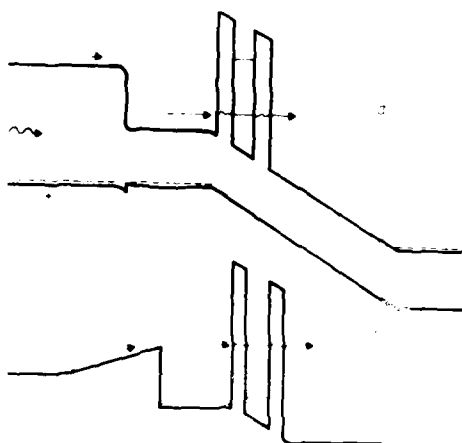


Fig. 3 Photocurrent vs reverse bias voltage of the structure of Fig. 1a with a low gap GaAs p layer of thickness = 500 Å. The wavelength of the incident light is 6328 Å.

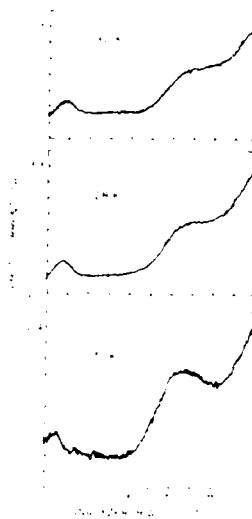


Fig. 4 Photocurrent vs reverse bias voltage of the structure of Fig. 1a with a low gap GaAs p layer of thickness = 250 Å. The wavelength of the incident light is 6328 Å.

## REFERENCES

- Hayes J R, Levi A F J and Wiegmann W 1984 *Electron Lett.* **20**, 851-52.
- Hayes J R, Levi A F J and Wiegmann W 1985 *Phys. Rev. Lett.* **54**, 1570-72.  
Hayes J R and Levi A F J 1986 *IEEE J. Quantum Electron.* **QE-22**, 1744-52.
- Hayes J R, Levi A F J, Gossard A C and Wiegmann W 1986 *Technical Digest of the Device Research Conference*.
- Heiblum M, Nathan M I, Thomas D C and Knoedler C M 1985a *Phys. Rev. Lett.* **55**, 2200-03.
- Heiblum M, Thomas D C, Knoedler C M and Nathan M I 1985b *Appl. Phys. Lett.* **47**, 1105-07.
- Heiblum M, Calleja E, Anderson I M, Dumke W P, Knoedler C M and Osterling L 1986 *Phys. Rev. Lett.*, **56**, 2854-56.
- Hesto P, Jone J F and Castagne R 1982 *Appl. Phys. Lett.* **40**, 405-7.
- Hesto P 1983 *Surface Sci.* **132**, 623-36.
- Levi A F J, Hayes J R, Platzman P M and Wiegmann W 1985a *Physica*, **134B**, 480-86.
- Levi A F J, Hayes J R, Platzman P M and Wiegmann W 1985b *Phys. Rev. Lett.* **55**, 2071-73.
- Luryi S 1985 *Appl. Phys. Lett.* **47**, 490-97.
- Malik R J, AuCoin T R, Ross R L, Board K, Wood L E C and Eastman L F 1980 *Electron. Lett.* **16**, 836-38.
- Shah J 1986 *IEEE J. Quantum Electron.* **QE-22**, 1728-43.
- Tsuchiya M, Sakaki H and Yoshino J 1985 *Jpn. J. Appl. Phys.* **24**, L417-19.
- Yokoyama N, Imamura K, Oshima T, Nishi H, Muto S, Kondo K, and Hiyamizu S 1984 *Proc. IEEE International Electron. Devices Meeting*, 532-35.
- Wang T, Hess K, and Iafate G J 1986 *J. Appl. Phys.*, **59**, 2125-28.

## **Resonant tunneling in a double GaAs/AlAs superlattice barrier heterostructure**

M A Reed and J W Lee

Central Research Laboratories  
Texas Instruments Incorporated  
Dallas, Texas 76265 USA

**Abstract.** Resonant tunneling has been demonstrated through a double barrier, single quantum well heterostructure in which the barriers have been replaced by thin, short period binary superlattices. The structure exhibits an anomalously low barrier height and a peak to valley tunnel current ratio of 1.8:1 at 300°K.

### **1. Introduction**

The phenomena of resonant tunneling in double barrier heterostructures, first investigated in the seminal work of Chang, Esaki, and Tsu (1974), has recently undergone a renaissance due to recent improvements in epitaxial growth techniques. The DC and high frequency transport in these structures has been the subject of intense investigation following the remarkable submillimeter wave experiments of Sollner et al (1983) which has been interpreted as coherent resonant tunneling through the heterostructure. This renewed interest has led to the observation of large room temperature peak to valley tunnel current ratios (Shewchuk et al 1985), resonant tunneling of holes (Mendez et al 1985), the observation of multiple negative differential resistance (NDR) peaks due to resonant tunneling (Reed 1986) and the observation of sequential resonant tunneling through a multi-quantum well (MQW) superlattice (Capasso et al 1986).

The initial investigations of this structure, typically in the GaAs/Al<sub>x</sub>Ga<sub>1-x</sub>As system, have utilized "square" (i.e., constant Al mole fraction) barriers to confine the central quantum well. A number of intriguing physical phenomena can be examined by tailoring the barrier(s) in real space, such as equally spaced resonant peaks arising from a parabolic quantum well. However, the variety of tunneling structures that can be investigated is limited by the practical constraints on the Al<sub>x</sub>Ga<sub>1-x</sub>As barrier (or well) growth and the rate the Al mole fraction can be changed over the region of interest, typically ~100Å. A possible solution to the Al mole fraction gradient constraint is the emulation of the desired Al<sub>x</sub>Ga<sub>1-x</sub>As alloy barrier structure with a GaAs/Al<sub>x</sub>Ga<sub>1-x</sub>As superlattice of fixed (even 100%) Al mole fraction (Laidig 1983 and Sakaki 1985). In this letter we report the first study of resonant tunneling through a double barrier, single quantum well heterostructure in which the barriers have been replaced by thin, short period binary superlattices. This is the first demonstration that quantum well states can be confined by very thin, short period superlattices and that resonant tunneling transport through a compositionally modulated barrier is possible.

## 2. Experimental procedure

The samples used in this study were grown by molecular beam epitaxy in a Riber MBE-2300 on a 2-inch (100) n+ Si-doped Sumitomo GaAs substrate utilizing a directly heated rotating substrate holder. Following a highly doped (n-type, Si @  $1 \times 10^{18} \text{ cm}^{-3}$ ) buffer layer, the active resonant tunneling structure region was then grown. For comparison, a conventional  $\text{Al}_x\text{Ga}_{1-x}\text{As}$  alloy barrier structure of similar barrier and quantum well dimension was fabricated, as well as one with a larger quantum well size. The conventional  $\text{Al}_x\text{Ga}_{1-x}\text{As}$  barrier sample consisted of an undoped  $\text{Al}_x\text{Ga}_{1-x}\text{As}$  barrier (50 Å,  $x = .35$ ), followed by an undoped GaAs quantum well (50 Å or 100 Å), similar barrier, and a top contact  $\sim 0.5$  micron thick. For the binary superlattice barrier structure, each barrier consists of three 7 Å layers of AlAs separated by two 7 Å layers of GaAs. The GaAs quantum well in this sample is 45 Å and the remainder of the structure is identical to the  $\text{Al}_x\text{Ga}_{1-x}\text{As}$  barrier samples. A cross-sectional transmission electron micrograph of the superlattice barrier structure is shown in Figure 1. Devices were fabricated by defining mesas on the surface with conventional photolithography techniques, bonded for mechanical stability, and inserted into a variable-temperature helium-flow Janis cryostat or into a stabilized oven for variable temperature measurements.



Figure 1 Cross-sectional transmission electron micrograph of the superlattice barrier resonant tunneling structure. The width of the GaAs quantum well is 45 Å and the widths of the two GaAs and three AlAs superlattice barrier components are 7 Å.

### 3. Results

Figure 2 shows the room temperature static current-voltage (I-V) characteristics of a typical conventional alloy barrier, 50 Å wide quantum well, resonant tunneling structure. This structure exhibits a room temperature peak to valley tunnel current ratio of 1.75:1 which increases typically to 7:1 at low temperatures ( $\leq 100^\circ\text{K}$ ). We have plotted the negative bias data reflected into the first quadrant to emphasize the observed asymmetry in the current-voltage characteristics of these structures. This asymmetry has been ascribed to the inferior inverted interface morphology of the quantum well and contact region (Shewchuk et al 1985). This is consistent with our observations; our convention of positive bias means electron injection from the backside superior GaAs contact. A higher resonant bias for the inverted configuration would be expected from an extended inverted region. The room temperature I-V characteristics for the superlattice barrier structure, designed to have the same resonant bias voltage, is shown in Figure 3. The symmetry for positive and negative bias is excellent. This observation suggests that the inverted interface is indeed responsible for the observed asymmetry in the alloy barrier structure and that the superlattice barrier improves the interface by lessening trapping of undesired impurities and/or prevents surface roughening. This improvement has been observed previously in photoluminescence experiments (Sakaki et al 1985). The superlattice barrier structure exhibits a 1.8:1 peak to valley ratio at room temperature and exhibits NDR up to  $100^\circ\text{C}$ .

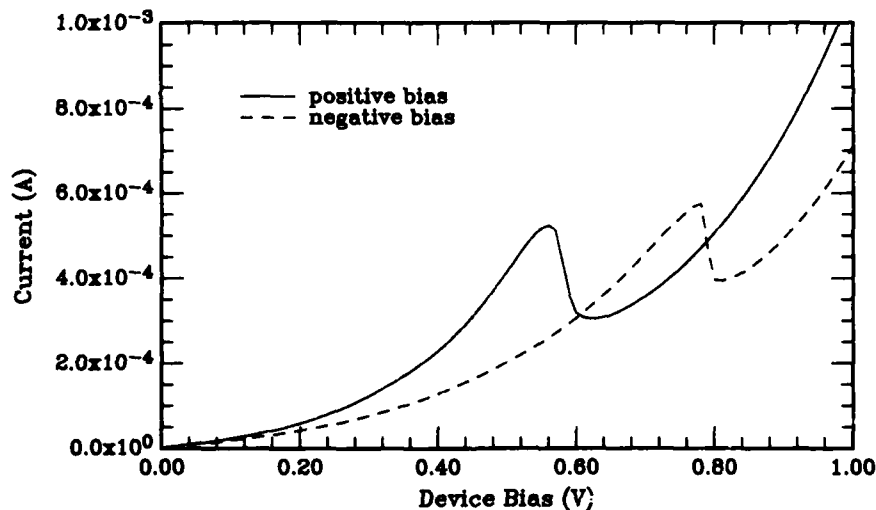


Figure 2. Room temperature static I-V characteristics of a typical conventional 50 Å alloy barrier, 50 Å wide quantum well, resonant tunneling structure. Device mesa area =  $25 \mu\text{m}^2$ . Positive and negative bias are shown.

The observed resonant bias positions can be compared to the theoretical predictions of a transfer matrix model (Ricco and Azbel 1984) if the parasitic resistances in the structure are independently known. Since this is unknown for the structures, we employ the technique (Gossard et al 1982) of low bias thermal activation of carriers over the effective barrier to determine the position of the quantum well bound state relative to the Fermi level of the contact. In this case the effective thermal barrier presented to the electrons, at low bias, is not the full barrier but the  $\Gamma$ -point of the quantum well bound state. This is demonstrated in Figure 4 for the alloy barrier structure with a 50 Å quantum well, which yields an

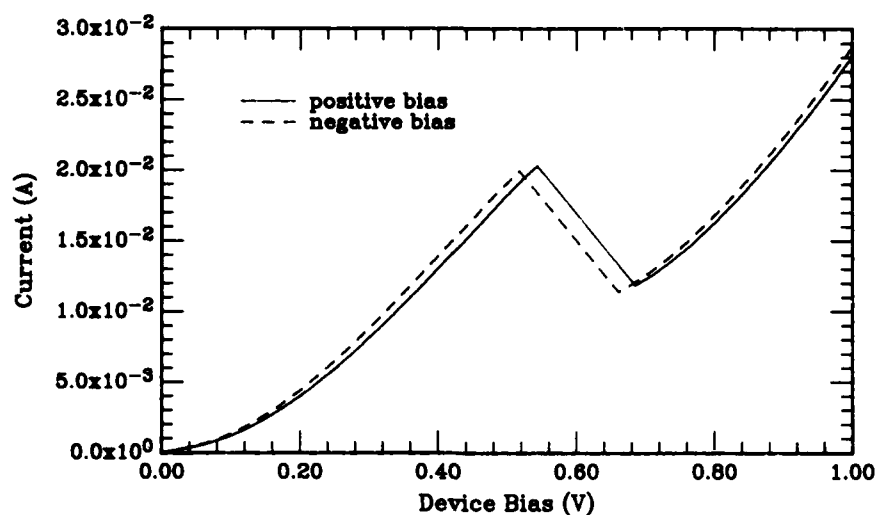


Figure 3. Room temperature static I-V characteristics for the superlattice barrier structure. Device mesa area =  $25 \mu\text{m}^2$ . The symmetry for positive and negative bias is excellent.

activation energy of 70 meV. Similar measurements on an alloy barrier structure with a quantum well width of  $\sim 100 \text{\AA}$  gave an activation energy of 15 meV, demonstrating that the activation energy decreases with increasing well size as expected. It should be noted that the ground state only is observed due to the large energetic separation of the excited state.

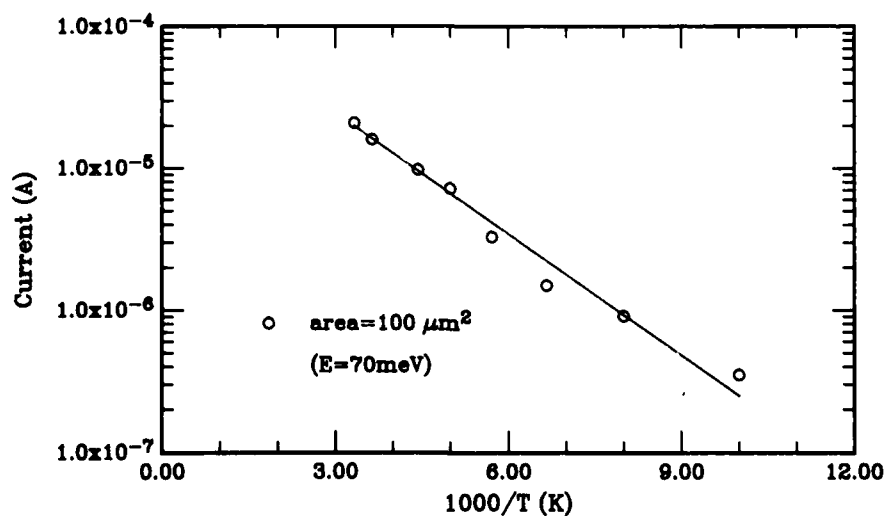


Figure 4. Low bias thermally activated current for the  $50 \text{\AA}$  quantum well alloy barrier structure. The thermal activation measurement gives  $E = 70 \text{ meV}$ .

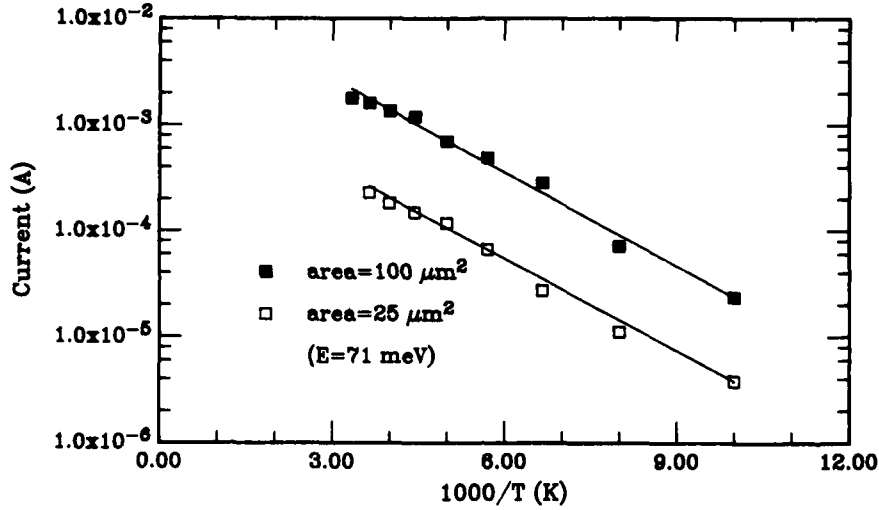


Figure 5. Low bias thermally activated current for the superlattice barrier structure, showing identical activation energies independent of current density. The current does not exactly scale with top mesa dimension due to mesa undercut. The thermal activation measurement gives  $E = 71$  meV.

The activation energy gives the quantum well energy relative to the conduction band edge when corrected for the assumed degeneracy in the contact due to the high doping ( $N_D \approx 1 \times 10^{18} \text{ cm}^{-3}$ , which gives  $E_F \approx 55$  meV). The derived quantum well state is 120 meV which is in excellent agreement with the values of 116 meV predicted from an envelope function approximation (Bastard 1981) using a 60% conduction band offset. This technique was used to derive the position of the center quantum well state for the superlattice barrier structure and is shown in Figure 5 for two devices of different mesa dimension. The thermal activation measurement for both gives a quantum well state of 121 meV, the same as for the 50 Å alloy barrier structure which was expected from the identical resonant bias positions of Figures 2 and 3.

There are two independent approaches to determine the effective barrier height  $\Delta E_c^*$  of the superlattice barrier once the quantum well energy is known. First, we can use the energy of the quantum well state (determined above) to derive the effective barrier height  $\Delta E_c^*$  assuming that the envelope function approximation for thick barriers is valid. Using a 45 Å quantum well, we obtain an effective barrier height  $\Delta E_c^* = 290$  meV, or an equivalent alloy composition of 0.296. Secondly, we can compare the transmitted resonant current densities of the conventional alloy barrier structure and the superlattice barrier structure. Considering single particle transmission coefficients, it can be shown that the effective barrier height  $\Delta E_c^*$  can be expressed as

$$\Delta E_c^* = E_{QW,0}^{SL} + \frac{\hbar^2}{8m^* d_{SL}^2} \left\{ \ln \frac{J_{SL}}{J_A} + \frac{2d_A}{\hbar} \left| 2m^* (\Delta E_c^A - E_{QW,0}^A) \right| \right\} \quad [1]$$

where  $d_{SL}$  is the width of the superlattice barrier,  $d_A$  is the width of the alloy barrier,  $J_A$  and  $J_{SL}$  are the measured current densities for the alloy barrier and superlattice barrier, respectively,  $\Delta E_c^A$  is the conduction band offset for the alloy barrier case, and the  $E_{QW,0}^A$  are the ground state energies of the quantum wells.

Using a 60% conduction band offset and a 35Å superlattice barrier width, we get  $\Delta E_c^* = 240$  meV, slightly lower than the barrier computed above. A monolayer fluctuation at the interfaces of the barrier gives  $\Delta E_c^* = 275$  meV, in good agreement with the envelope function prediction.

The superlattice barrier height is much lower than would be expected from an averaged alloy composition of 0.60, which gives a barrier height of 587 meV. Photoluminescence experiments on thick superlattice barrier confined isolated quantum wells (Sakaki et al 1985) also found disagreement with an averaged alloy composition model, though an equivalent alloy composition higher than the average alloy composition was found. An envelope function approximation to a superlattice of infinite extent to determine the effective barrier height as the first conduction minizone edge gives an even greater discrepancy. Thus the superlattice barrier allows appreciable wavefunction penetration while maintaining a high energy quantum well state, as has been previously suggested. The observation of an anomalously low barrier height to transport is indicative of the enhanced evanescent tail.

#### 4. Summary

In summary, we report the first study of a double short period binary superlattice barrier, single quantum well heterostructure. This is the first demonstration that quantum well states can be confined by very thin, short period superlattices. The superlattice structure does not exhibit the asymmetry around zero bias in the electrical characteristics normally observed in the conventional  $\text{Al}_x\text{Ga}_{1-x}\text{As}$  barrier structures, and exhibits an anomalously low barrier height demonstrating an enhanced evanescent tail in the superlattice barrier. The ability to emulate barriers with superlattices permits a number of intriguing suggested investigations for tunneling structures, such as equally spaced resonances from a parabolic well, an increase in transmission coefficient from a structure symmetric at resonant bias, bandgap engineered contacts, an increase in sequential multiquantum well resonant current, and the investigation of the influence of barrier symmetry on resonant bias and transmission. The flexibility of design and enhanced evanescent tail are also important to MQW lasers and high frequency resonant tunneling devices.

We are thankful to R. T. Bate, W. R. Frensley and C. H. Hoel for discussions and R. Aldert, R. Thomason, and J. Williams for technical assistance. This work was supported in part by the Office of Naval Research and the U. S. Army Research Office.

#### 5. References

- Bastard G 1981 Phys. Rev. **24B** 5693
- Capasso F, Mohammed K, and Cho A Y 1986 Appl. Phys. Lett. **48** 478
- Chang L L, Esaki L, and Tsu R 1974 Appl. Phys. Lett. **24** 593
- Gossard A C, Brown W, Allyn C L, and Wiegmann W 1982 J. Vac. Sci. Technol. **20** 694 (1982).
- Laidig W D, Caldwell P J, Kim K, and Lee J W 1983 ELD **4** 212
- Mendez E E, Wang W I, Ricco B, and Esaki L 1985 Appl. Phys. Lett. **47** 415
- Reed M A 1986 Superlattices and Microstructures **2** 65
- Ricco B and Azbel M Ya 1984 Phys. Rev. **29B** 1970
- Sakaki H, Tsuchiya M, and Yoshino J 1985 Appl. Phys. Lett. **47** 295
- Shewchuk T J, Chapin P C, Coleman P D, Kopp W, Fisher R, and Morkoç H 1985 Appl. Phys. Lett. **46** 50
- Sollner T C L G, Goodhue W D, Tannenwald P E, Parker C D, and Peck D D 1983 Appl. Phys. Lett. **43** 588



## **New quantum interference effects in GaAs/AlAs resonant tunneling structures**

N Tabatabaie and M C Tamargo

Bell Communications Research, Red Bank, New Jersey 07701-7020

**Abstract.** A remarkable split is observed in the ground state resonance energy of electrons in a GaAs/AlAs resonant tunneling structure placed in the intrinsic region of an  $n^+/i/n^+$  diode. The 11 meV splitting is observed through a pair of Negative Differential Resistance Regions (NDRRs) in the current-voltage characteristics of the diode at room temperature ( $kT=25$  meV). The existence of the doublet and the apparent lack of thermal broadening of the eigenvalues is explained by quantum mechanical reflection from the edge of the intrinsic region as well as reflections from the two AlAs layers.

### **1. Introduction**

Resonant tunneling in heterostructured semiconductors (Tsu 1973) has received considerable attention during the past three years. The interest in these structures has been primarily stimulated by the speculations regarding the possibility of realizing new high speed electronics and optoelectronics devices based on the resonant tunneling phenomenon. Recently, we have demonstrated that resonant tunneling can also be used as a high resolution spectroscopic technique at elevated temperatures (Tabatabaie 1986). In this paper we describe the origin of newly observed resonance peaks in the I-V spectra of our resonant tunneling structures.

### **2. Extended field structures**

Ricco and Azbel (1984) have pointed out that the strength of the resonant tunneling current through a double barrier structure is maximized only if the reflection coefficients of the individual barriers are the same. Such a condition does not exist for the conventional symmetrically grown double barrier structures under external bias. The obvious approach to maximizing the resonant tunneling transmission coefficient for a specific resonance energy level is the use of carefully designed asymmetrically grown structures. Alternatively, the composition of the emitter electrode

can be chosen so that the bottom of its conduction band is degenerate with one of the resonance levels inside the quantum well (Capasso 1986).

One partial solution proposed by us is to extend the electric field resulting from the applied external bias, beyond the barriers region. This is accomplished by placing the resonant tunneling barriers inside the intrinsic region of an  $n^+/i/n^+$  diode structure as is shown in Fig. 1. If the thickness of the undoped spacer layers outside the heterobarriers region is kept small, quantum size effects prevent charge pile-up adjacent to the first AlAs heterobarrier. Instead, the accumulation region forms at the  $n^+/n^-$  homojunction doping barrier as is the case for conventional  $n^+/i/n^+$  structures. In theory, electrons injected over the small homobarrier are heated by the electric field prior to impact with the heterobarriers, resulting in smaller overall field strengths required to achieve resonance. Later in this paper, we show that the preferred path is for the electrons to directly tunnel through the entire three barrier, double quantum well structure.

### 3. Experimental results

Room temperature I-V characteristics of 50  $\mu\text{m}$  diameter double quantum well structures of the type described above are shown in Figs. 2, 3, and 4. The structures are grown by MBE and consist of two 20  $\text{\AA}$  AlAs barriers separated by a 70  $\text{\AA}$  GaAs well. The spacer layer on the collector side is 50  $\text{\AA}$  thick while the emitter side spacer is 70  $\text{\AA}$  for the device of Fig. 2 and 100  $\text{\AA}$  for the devices of Figs. 3 and 4. The above layers are all undoped and have a net n-type background impurity concentration of less than  $2 \times 10^{15} \text{ cm}^{-3}$ . The emitter and collector electrodes are degenerately doped (mid  $10^{18}$  range) n-type GaAs layers. The layer thicknesses have not been directly measured and are therefore approximate. They are inferred from previously grown calibration standards.

Fig. 2 shows a pair of transmission peaks at 250 and 285 mV and a third peak at 470 mV. The inset of this figure is the I-V plot of another diode from the same wafer clearly showing the relative strengths of the two peaks in the doublet. The wafer of Fig. 3 also exhibits three NDRRs at 600 mV, 2.7 V and 3.3 V. Fig. 4 shows an expanded plot of the I-V characteristics of another diode from the same wafer near the lowest energy NDRR. This figure shows the presence of yet another transmission peak observed as a shoulder in the I-V data at 400 mV but too weak to produce an NDRR at room temperature. The observation of four transmission peaks in the structure of Figs. 3 and 4 and the presence of the doublet in the ground state resonance of Fig. 2 have not been previously observed or explained.

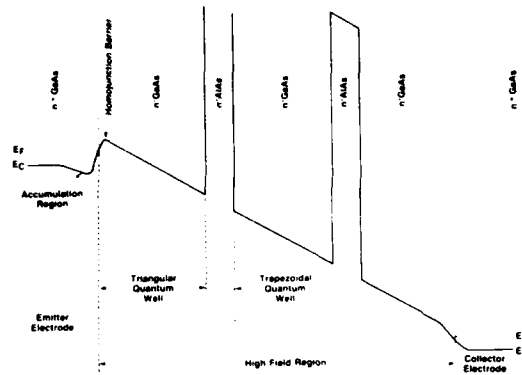


Fig. 1. Extended field double barrier resonant tunneling structure.

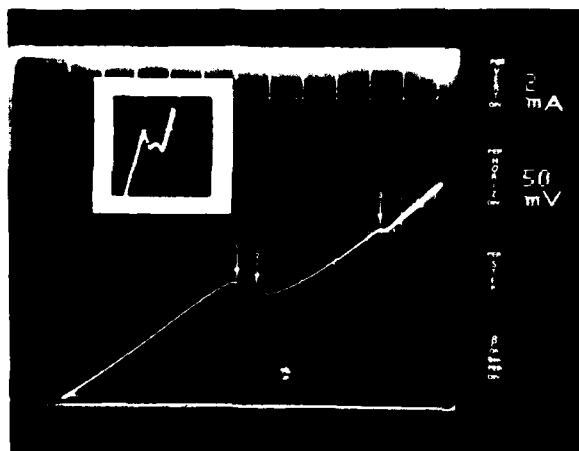


Fig. 2. I-V characteristics of a 50  $\mu$ m diode having an emitter spacer width of 70  $\text{\AA}$ .

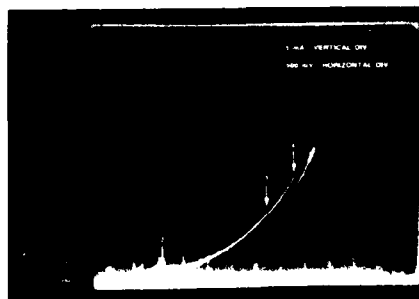


Fig. 3. I-V characteristics of a 50  $\mu\text{m}$  diode having an emitter spacer width of 100 Å.

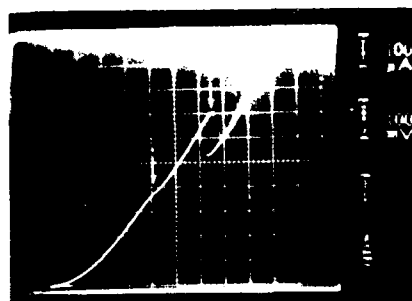


Fig. 4. Expanded scale I-V data of a device similar to that of Fig. 3.

#### 4. Shape of the I-V characteristics

Early theoretical calculations by Tsu and Esaki (1973) predicted NDRRs in the I-V plots of multilayered AlGaAs/GaAs structures based on the resonant transmission of charge carriers in response to an applied external electric field. In most experimental structures, the electron fermi energy in the emitter electrode is considerably larger than the breadth of the resonant tunneling transmission. Mendez et al. (1986), Coon and Liu (1986), and we (Tabatabaie 1986) have shown that at low temperatures, the above results in a triangular resonant tunneling I-V signature having a near right angle at the high bias side. The transmission maximum and minimum occur almost side by side, immediately before and after the resonance energy level is pulled down below the bottom of the emitter electrode conduction band. The above is shown schematically in Fig. 5. This sudden termination of the resonance condition is a consequence of the conservation of transverse momentum and is responsible for the NDRR.

Luryi (1985) has proposed that a similar I-V behavior is expected even if phase coherence is not maintained throughout the barriers region. Furthermore, we have proposed that the breadth of the NDRR is determined by the homogeneous broadening of the quasistationary states within the barriers region alone and does not depend on temperature. The above is significant since it leads to the use of resonant tunneling as a powerful spectroscopic technique with sub-kT resolution at elevated temperatures. The observation of the doublet in Fig. 2 is proof to that effect.

Given the I-V signature of a single resonance (Fig. 5), it is interesting

to consider the case where two approximately equal strength resonances occur closely in energy as shown in Fig. 6. If the two processes are independent, the sum resonant tunneling current through the structure has the shape reminiscent of the observed doublet in Fig. 2. Two possible mechanisms which could result in such a resonance configuration are discussed in section 6.

### 5. Resonant tunneling spectroscopy

In order to ascertain the energy levels of the observed eigenstates, an energy reference must be defined. The center of the trapezoidal quantum well has been customarily used in the literature as the reference level with respect to which other energy levels are stated. This choice is not always a good one specially for the extended field structures described here. The ideal approach is to directly calibrate the I-V spectra with an energy scale in order to eliminate the need for an energy reference as well as eliminating errors due to resistive voltage drops. We have used determining such an energy scale near the ground state resonance of the structure exhibiting the doublet. Using this technique, the peak-to-peak energy separation between the two resonances was found to be 11 meV.

### 6. The origin of the doublet and the weak resonances

In this section we discuss two mechanisms which are capable of producing the observed doublet in the I-V plot of Fig. 2. One possible mechanism is the effect of monolayer step variations on the resonance energies of the

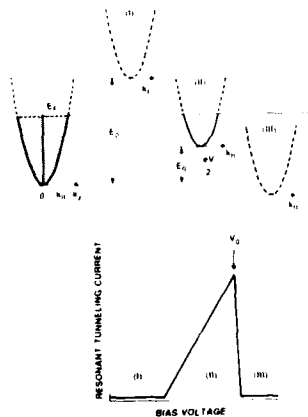


Fig. 5. Dispersion curves of the emitter electrode and the quantum well showing various resonant tunneling transmission regions.

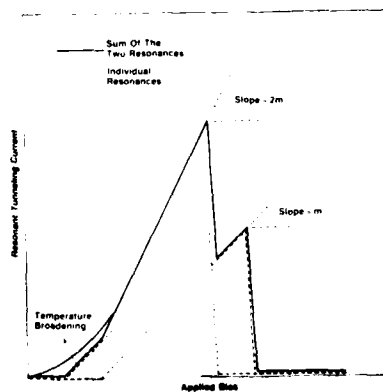


Fig. 6. The asymmetric I-V plot resulting from the combination of two identical resonances shifted in energy.

quantum well. Since the width of the quantum well is always an integral number of monolayers, if it is varied by one step accross the latteral surface of the device, the result is a doublet with two distinct resonance energies. If the area covered by each of the two possible thicknesses is approximately equal, the resulting resonant tunneling current will have a signature similar to that shown in Fig. 6. The thickness of a monolayer in GaAs based structures is  $2.8 \text{ \AA}$  and the effective width of the trapezoidal well (one half of the particle wavelength at ground state) in our structures is  $90 \text{ \AA}$ . This yields an energy splitting of roughly 4 meV, in good agreement with the observed 11 meV splitting. This mechanism, however, does not explain the existance of the weak resonances, peak #3 in Figs. 2 and 3 and peak #1 in Fig. 4, observed in these structures.

We propose that the triangular quantum well depicted in Fig. 1, participates fully in the tunneling process. We further propose that for the wafer with the  $70 \text{ \AA}$  spacer layer thickness (Fig. 2), the ground state resonances of the two wells are degenerate. This leads to symmetric and antisymmetric extended eigenstates in the wells resulting in the observed split in the eigenvalue spectrum. Peak #3 in Fig. 2, therefore, corresponds to the first excited state resonance of the triangular well alone. According to this model, the increased spacer width in the structure of Figs. 3 and 4 results in th lowering of the ground state resonance energy of the triangular well with respect to that of the trapezoidal well. The two wells are no longer degenerate and the four peaks in the two figures correspond to individual well resonances. The peaks #1 and #3 are identified as the ground state and the first excited state resonances of the triangular well, respectively. Similarly, peaks #2 and #4 are the ground state and the first excited state resonances of the trapezoidal well. We can estimate the expected energy split due to the coupling permutations from simple quantum mechanics. Following Kane's approach (Kane 1969) and using the effective mass approximation, we obtain a coupling split of 1.3 meV. This value is substantially less than the observed 11 meV splitting. The discrepancy even though unfortunate is not too disturbing given the exponential nature of the tunneling formulas.

## 7. References

- Capasso F, Sen S, Gossard A C, Hutchinson A L and English J H 1986 IEEE Electron Device Lett. EDL-7 573
- Coon D D and Liu H C 1986 Appl. Phys. Lett. 49'94
- Kane E O 1969 Tunneling Phenomenon in Solids (New York:Plenum) Chap. 1
- Luryi S 1985 Appl. Phys. Lett. 47 490
- Mendez E E, Esaki L and Wang W I 1986 Phys. Rev. B 33 2893
- Ricco B and Azbel M Y 1984 Phys. Rev. B 29 1970
- Tabatabaie N and Tamargo M C 1986 Submitted for publication
- Tsu R and Esaki L 1973 Appl. Phys. Lett. 22 562

## **Mobility and parasitic resistance measurements in AlGaAs/GaAs and AlGaAs/InGaAs MODFET structures**

D C Look<sup>†</sup>, T Henderson\*, C K Peng\*, and H Morkoc\*

<sup>†</sup>University Research Center, Wright State University, Dayton, OH 45435.

\*Department of Electrical Engineering, University of Illinois, Urbana IL 61801.

**Abstract.** Geometric magnetoresistance techniques are used to measure mobility at 296 and 77°K in AlGaAs/GaAs and AlGaAs/InGaAs MODFET devices, and a GaAs MESFET device. The measurements are corrected for parasitic resistance, which is determined by a new method based on the source-drain voltage dependence of the gate current. Multi-band and multi-layer effects are considered. The mobility in the 2-D electron gas varies with carrier concentration in the expected way for ionized-impurity scattering, but the situation is unclear for polar-optical-phonon scattering.

### 1. Introduction

Mobility is an important parameter for determining material quality and predicting device performance. Usually mobility is measured by means of the Hall effect, but this technique requires a special test pattern. It is more advantageous to make the measurement in an actual device structure, such as a field-effect transistor (FET), because, for example, the material may have been modified by the device processing. In recent years the geometric magnetoresistance (GMR) technique for mobility measurements has been developed for metal-semiconductor FET's (MESFET's) (Jay and Wallis 1981, Look 1985) and modulation-doped FET's (MODFET's) (Look et al 1985). Although this method is quite simple and convenient to use, the results can be influenced by parasitic resistances, because voltages are measured at current-carrying contacts. It has been shown that parasitic-resistance effects are not very important for typical MESFET devices (Look 1985) but the situation may be different for very-short-channel MESFET's and MODFET's, especially at low temperatures for the latter. In this paper we will discuss a new method for measuring parasitic resistances, and apply it to GMR measurements in a promising new MODFET material,  $\text{Al}_{0.15}\text{Ga}_{0.85}\text{As}/\text{In}_{0.15}\text{Ga}_{0.85}\text{As}$  (Ketterson et al 1986). By using a Schottky gate to control the channel conductance, the dependence of mobility on carrier concentration can be determined.

### 2. Theory

A generalized test structure, appropriate for FET or contact-resistance measurements, is shown in figure 1. The ohmic contacts, which are shaded, are of length  $l_c$  and width  $w$ . The semiconductor regions between the ohmic contacts are of lengths  $l_{S1}$ ,  $l_{S2}$ ,  $l_{S3}$ , etc., and the Schottky-barrier

gates have lengths,  $\ell_{G1}$ ,  $\ell_{G2}$ ,  $\ell_{G3}$ , etc. When a voltage is applied between two of the adjacent ohmic contacts, current will typically flow out of only a small region of characteristic length  $\ell_T$  (the "transfer length"), near the inner edge of each contact. In the transmission line model (TLM), normally used for analysis of planar contacts, it is assumed that the current flows vertically through the metal/semiconductor (M/S) barrier into the semiconductor material below the contact, and then horizontally into the main semiconductor body (Berger 1972). The total resistance between the two ohmic contacts separated by  $\ell_{Sk}$  is

$$R_k = 2R_{MS} + 2R_T + R_S \frac{\ell_{Sk} - \ell_{Gk}}{w} + R_{SG} \frac{\ell_{Gk}}{w} \quad (1)$$

where  $R_{MS}$  and  $R_T$  are, respectively, the M/S-barrier and "transfer" resistances, together making up the total contact resistance, and  $R_S$  and  $R_{SG}$

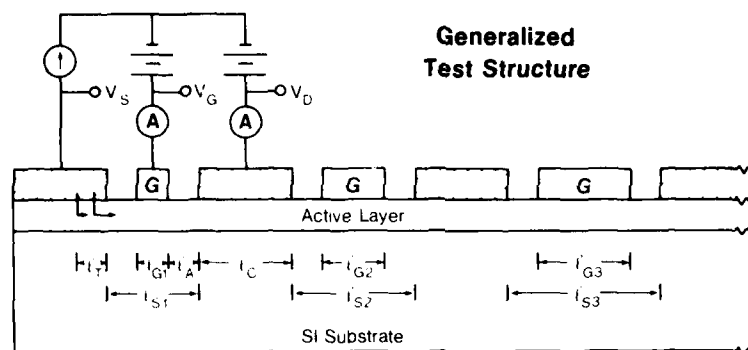


Figure 1. A generalized test structure useful for mobility, sheet resistance, and contact resistance measurements.

are, respectively, the ungated and gated portions of the semiconductor sheet resistance. (It is assumed here that the applied voltage is small enough that  $R_{SG}$  is uniform along the length of the gate.) For the FET case, we note that  $\ell_{Sk} - \ell_{Gk} = 2\ell_A$  for all  $k$ , where  $\ell_A$  is the "access" length. Then, by defining the "parasitic" resistance as  $R_P = 2R_{MS} + 2R_T + 2R_S \ell_A/w$ , we get

$$R_k = R_P + R_{SG} \frac{\ell_{Gk}}{w}$$

so that the slope of an  $R_k$  vs.  $\ell_{Gk}$  plot has y-axis intercept  $R_P$ , slope  $R_{SG}/w$ . Similarly, for the contact-resistance-measurement there are no gates (standard "TLM" pattern), so that

$$R_k = 2R_{MS} + 2R_T + R_S \frac{\ell_{Sk}}{w}$$

Then,  $R_C = R_{MS} + R_T$  is determined from the intercept, and the slope. If the TLM is truly valid, then the "contact resistance" by  $\rho_C = wR_C/R_G$ , and the transfer length  $\ell_T = \sqrt{R_C R_G}$ . The normalized contact resistance,  $r_C = R_C/w$ , which



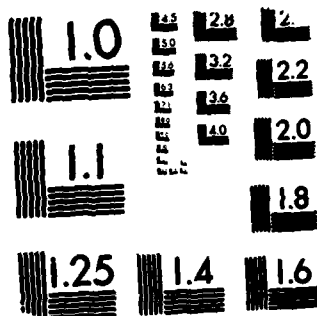
AD-A189 673

GALLIUM ARSENIDE AND RELATED COMPOUNDS 1986(U) ILLINOIS 7/7  
UNIV CHAMPAIGN W T LINDLEY 1986 AFOSR-IR-87-1800

UNCLASSIFIED

F/G 20/2 NL

END  
DATE  
- MAR 84  
- 484



MICROCOPY RESOLUTION TEST CHART  
NATIONAL BUREAU OF STANDARDS-1963-A

quantity for device considerations, is independent of the TLM. These questions are discussed further elsewhere (Ketterson et al 1985).

If a perpendicular magnetic field is now applied, then equation 1 becomes

$$R_k = 2R_{MS} + 2R_{T0}(1 + \mu_B^2) + \frac{l_{Sk} - l_{Gk}}{w} R_{SO}(1 + \mu_S^2) + \frac{l_{Gk}}{w} R_{SG0}(1 + \mu_{SG}^2) \quad (4)$$

where, in the case of more than one band or conducting region (Look et al 1985),

$$\mu_S^2 = \frac{\sum_i \frac{n_i \mu_i^3}{1 + \mu_i^2}}{\sum_i \frac{n_i \mu_i}{1 + \mu_i^2}} \quad (5)$$

with similar equations for  $\mu_T$  and  $\mu_{SG}$ . Equation 5 is valid if the electrons are degenerate, quantum effects are negligible, and  $w/l_{Sk} \gg 1$ . The latter inequality insures that the GMR conditions are met. The validity of equation 4 for TLM-pattern analysis (called the "magneto-TLM" analysis) has been verified recently (Look 1986) for GaAs MESFET's. In this paper, we are mainly concerned with MODFET properties.

Equations 2-4 can be used to determine  $R_S$  or  $R_{SG}$  only if there are at least two different spacings ( $l_{Sk}$  or  $l_{Gk}$ ) available on the test structure. If, however, only one discrete device is being studied, then another method must be used. We will discuss here a new technique based on the fact that the ends of the Schottky-barrier gate of an FET are biased by the source and drain currents flowing, respectively, through the source and drain contact (and access) resistances,  $r_S$  and  $r_D$  (Look and Cooper 1985, Look 1986, Yang and Long 1986). It can be shown (Look 1986) that

$$I_G = I_{G0} [e^{\beta V_{SG} F(V_{SD}, r_S, r_D)} - 1] \quad (6)$$

where

$$F = \frac{e^{-\beta I_S r_S} \left\{ 1 - e^{-[V_{SD} - I_S r_S - I_D r_D]} \right\}}{\beta [V_{SD} - I_S r_S - I_D r_D]} \quad (7)$$

where  $\beta = (q/nkT)$ ,  $n$  is the ideality factor, and  $V_{SD} = V_D - V_S$ . If  $\beta [V_{SD} - I_S r_S - I_D r_D] \ll 1$ , then

$$F = e^{-\frac{1}{2} \beta [V_{SD} + I_S r_S - I_D r_D]} \quad (8)$$

and, therefore, for two different values of some parameter, equation 6 yields

$$\frac{2nkT}{q} \ln \frac{I_{G2}}{I_{G1}} = 2(V_{SG2} - V_{SG1}) - (V_{SD2} - V_{SD1}) - (I_{S2} - I_{S1})r_S + (I_{D2} - I_{D1})r_D \quad (9)$$

The quantity  $r_S - r_D$  can be determined by changing  $I_G$  and  $I_D$ , with either a current source or power supply (cf. figure 1), while simultaneously varying  $V_G$  to hold  $I_G$  constant. Then, the full equation 7 can be applied, with  $r_S$  as the only unknown. Once  $R_P = r_S + r_D$  is known, the true channel resistance  $R_{SG}$  can be obtained, and  $\mu_{SG}$  calculated from the relationship

$$\mu_{SG} = \frac{1}{B} \left[ \frac{R_{SG}(B)}{R_{SG}(0)} - 1 \right]^{1/2}. \quad (10)$$

By making measurements at several values of  $B$ , multi-band and multi-layer effects can be studied via equation 5. For a two-band (or layer) problem, equation 5 becomes

$$\mu_{SG}^2 = \mu_0^2 \frac{1 + \frac{n_1}{n_0} \frac{\mu_1^3}{\mu_0^3} \frac{1 + \mu_0^2 B^2}{1 + \mu_1^2 B^2}}{1 + \frac{n_1}{n_0} \frac{\mu_1}{\mu_0} \frac{1 + \mu_0^2 B^2}{1 + \mu_1^2 B^2}}. \quad (11)$$

If  $n_0$  and  $n_1$  denote, respectively, two subband concentrations in a MODFET hetero-interface region, then their ratio can be determined analytically by the following technique. It can be shown that

$$\frac{e^{n_1/n_C} - 1}{e^{n_0/n_C} - 1} = e^{(E_0 - E_1)/kT} \quad (12)$$

where  $n_C \equiv m^*kT/\pi\hbar^2$  is the 2-D density of states, and where we assume  $n_0 + n_1 = n_S$  in this two-band model. The energies may be approximately determined from

$$E_i = \gamma_i [n_S + \alpha_i n_A]^{2/3} \quad i = 0, 1 \quad (13)$$

where  $n_A$  is the background acceptor concentration in the low-bandgap material. The most accurate values of the  $\gamma_i$  and  $\alpha_i$  are obtained from a fit of theoretical curves such as those given by Stern and Das Sarma (1984). (We get  $\gamma_0 = 6.15 \times 10^{-7}$ ,  $\gamma_1 = 8.80 \times 10^{-7}$ ,  $\alpha_0 = 1.68$ ,  $\alpha_1 = 2.93$ ,  $E_i$  in meV.) Other approximations are also available.

### 3. Results

We will apply these techniques to three samples: (A) a GaAs MESFET, with a  $4 \times 10^{12} \text{ cm}^{-2}$ , 100 keV  $\text{Si}^+$  implant; (B) a standard  $\text{Al}_{0.3}\text{Ga}_{0.7}\text{As/GaAs}$  MODFET; and (C) a recently-introduced  $\text{Al}_{0.15}\text{Ga}_{0.85}\text{As/In}_{0.15}\text{Ga}_{0.85}\text{As}$  pseudomorphic MODFET (Ketterson et al 1986). First the magneto-TLM method was used with a standard, ungated TLM pattern to study the initial, unetched material of samples A and C. The sample C data were analyzed by equation 11, with  $\mu_0$ ,  $\mu_1$ , and  $n_1/n_0$  as fitting parameters. These results will be discussed in detail elsewhere, but basically the values obtained for  $\mu_1$  and  $n_1/n_0$  suggested parallel conduction in the high-bandgap material rather than effects of higher subbands. Thus, we consider that the value of  $\mu_0$  in this case represents all of the subbands in the 2-D region. However, the lowest subband tends to dominate, especially at low temperatures, according to equations 12 and 13. To determine carrier concentration in this model, we use the relationship  $R_S^{-1} = e(n_0\mu_0 + n_1\mu_1)$  to get

$$n_0^{-1} = eR_S\mu_0 \left( 1 + \frac{n_1\mu_1}{n_0\mu_0} \right). \quad (14)$$

Then  $n_1$  and  $n_S = n_0 + n_1$  can also be calculated.

To vary  $n_0$  it is necessary to use a gated structure. Our test pattern includes a structure such as that shown in figure 1 with gate lengths of 4, 6, and 10  $\mu\text{m}$ . Parasitic resistances calculated from equation 2 agree

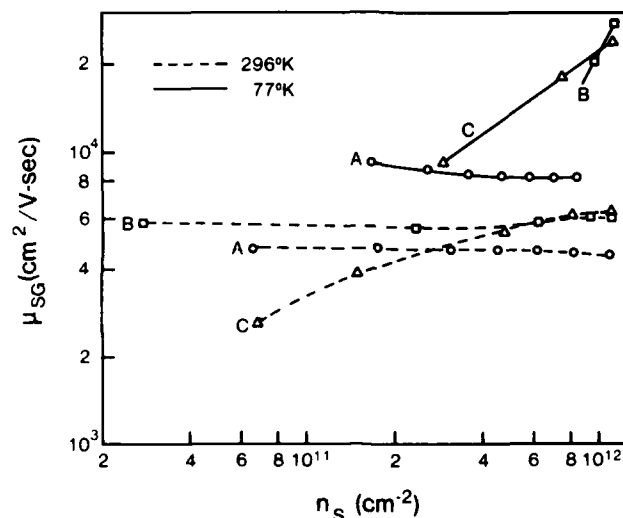


Figure 2. Mobility vs. sheet carrier concentration data for three FET-type structures: (A) a GaAs MESFET; (B) an  $\text{Al}_{0.3}\text{Ga}_{0.7}\text{As}/\text{GaAs}$  MODFET; and (C) an  $\text{Al}_{0.15}\text{Ga}_{0.85}\text{As}/\text{In}_{0.15}\text{Ga}_{0.85}\text{As}$  MODFET.

reasonably well with those calculated from equation 9. The mobilities for various  $B$  and  $V_G$  were calculated from equation 10 and fitted with equation 11. However, because  $n_1\mu_1$  was in general small, it was difficult to get accurate values of  $n_1$  and  $\mu_1$ . Thus, to study  $\mu_i$  vs.  $n_S$  in this case, we simply approximate  $n_1\mu_1 \approx \mu_{SG}(9\text{kG})$  at 296°K, and  $n_1\mu_1 \approx \mu_{SG}(4.5\text{kG})$  at 77°K, with  $n_S \approx (e\mu_{SG}R_S)^{-1}$ . At these magnetic fields,  $\mu_{SG}B < 1$  for most of the data.

The data are presented in figure 2. Sample A, the MESFET, shows increasing  $\mu_{SG}$  as  $n_S$  decreases. This phenomenon is due to the fact that the undepleted region moves toward the substrate/active-layer interface in a MESFET, as the gate is biased more negatively. Since the ionized impurity concentration is tailing off in the interface region, the mobility should increase, although somewhat mitigated by the loss of screening. (In some

cases, however, a poor interface can actually lead to a decreased mobility.)

The MODFET material differs in that the ionized-impurity scattering is mainly due to distant donors in the high-bandgap material. Furthermore, the electrons being sampled at a given gate bias are not much farther from these donors than the electrons which are sampled at a more positive bias (the MODFET's also have 30Å spacer layers). However, the numbers of electrons are changing with gate bias, so that Fermi-wave-vector and screening effects tend to be more important, as evidenced by the strong dependences of  $\mu_{SG}$  on  $n_s$  at 77°K. These effects have been studied in detail before, and are fairly well understood (Hirakawa and Sakaki 1986).

At 296°K, however, polar-optical-phonon scattering is dominant in MODFET-type devices, and this mechanism is not well understood as yet. For example, there seems to be disagreement on whether  $\mu_{p0}$  should increase or decrease as  $n_s$  increases (Hirakawa and Sakaki 1986, Das Sarma and Mason 1985). In figure 2 we see that for sample C at 296°K,  $\mu_s$  increases strongly with  $n_s$ , at low  $n_s$ , while for sample B, no definite pattern is apparent. A detailed discussion of this behavior is not possible in this paper but it is clear that both theoretical and experimental aspects of this problem need to be studied further.

#### Acknowledgements

We wish to thank T. A. Cooper for performing the electrical measurements and J. R. Sizelove for computational assistance. The work of DCL was performed at the Avionics Laboratory, Wright-Patterson AFB, under Contract F33615-84-C-1423.

#### References

- Berger H H 1972 Solid-State Electronics 15 145
- Das Sarma S and Mason B A 1985 Annals of Physics 163 78
- Hirakawa K and Sakaki H 1986 Phys. Rev. B 33 8291
- Jay P R and Wallis R H 1981 IEEE Trans. Electron Dev. Lett. EDL-2 265
- Ketterson A A, Ponce F, Henderson T, Klem J, Peng C K and Morkoc H 1985 IEEE Trans. on Electron Dev. ED-32 2257
- Ketterson A, Masselink W T, Gedymin J S, Klem J, Kopp W, Morkoc H and Gleason K R 1986 IEEE Trans Electron Dev. ED-33 564
- Look D C 1985 J. Appl. Phys. 57 377
- Look D C and Cooper T A 1985 Solid-State Electronics 28 521
- Look D C, Norris G B, Kopp W, Henderson T and Morkoc H 1985 Appl. Phys. Lett. 47 267
- Look D C 1986 unpublished
- Stern F and Das Sarma S 1984 Phys. Rev. B 30 840
- Yang L and Long S 1986 IEEE Electron Dev. Lett. EDL-7 75

### **Improved 77K performance of AlAs/GaAs superlattice heterostructure field-effect-transistors (SLHFET)**

M. Heuken, W. Prost, S. Kugler, K. Heime, Universität Duisburg  
D-4100 Duisburg 1, FRG

W. Schlapp, G. Weimann, FI der Deutschen Bundespost  
D-6100 Darmstadt, FRG

#### **Abstract:**

Conventional AlGaAs doped HFETs show degradation of their 77K performance in darkness. This paper reports the 77K performance of HFETs with undoped AlAs/ doped GaAs superlattices grown by MBE. The 77K Hall mobility is  $130000\text{cm}^2/\text{Vs}$  in the dark and under illumination. The mobility in the highest subband of the 2DEG exceeds  $200000\text{cm}^2/\text{Vs}$ . Device degradation in darkness is strongly reduced. Low frequency noise and Photo-FET investigations were carried out in order to study the trap influence on device behaviour. The concentration of deep donors and the number of different deep acceptors is lower than in conventional AlGaAs/GaAs HFETs. This result supports a model (KASTALSKY et al. 1985) on 77K HFET degradation.

#### **1. Introduction**

High electron mobilities are achievable in a two dimensional electron gas (2DEG) at the interface between doped AlGaAs and undoped GaAs due to the reduced Coulomb scattering, especially at low temperatures. However in a heterostructure field-effect transistor (HFET) with high electric fields in the channel device degradations are reported at cryogenic temperatures (Fischer et al. 1983), e.g. persistent photoconductivity, I-V characteristic collapse and threshold voltage shift. A deep trap related to a donor-Al complex (DX-center) is responsible for these effects in HFET with homogenous AlGaAs: Si doping layer. In addition recent results (Kastalsky et al. 1985) indicate that deep acceptors contribute to the degradation, too.

Device improvement is possible by using a superlattice (SL) doping layer consisting of a series of thin layers of undoped AlAs and Si-doped GaAs (Baba et al. 1983). In this structure the DX-center formation and the large binding energy of Si donors in AlGaAs are avoided. Such SLHFETs were fabricated and investigated by several electronic and optoelectronic methods. Donor and acceptor-like traps were detected and their influence on device performance was studied.

#### **2. SLHFET Structure and Device Fabrication**

Figure 1 illustrates the layer sequence and the corresponding

band diagram. Two different configurations were investigated. A  $1\mu\text{m}$  thick undoped GaAs buffer layer is grown on a (100) oriented semiinsulating substrate by MBE for both samples. Samples of type 1 consist of a three period AlAs (1.6nm)/GaAs (2.0nm) undoped spacer layer followed by seventeen GaAs (2.0nm)/AlAs (1.6nm) layers, which form the superlattice. Only the GaAs is doped ( $1.2 \times 10^{18} \text{ cm}^{-3}$ ) by silicon. Samples of type 2 consist of two period AlAs (1.0nm)/GaAs (1.7nm) undoped spacer layer and a superlattice of twenty Si doped ( $1.2 \times 10^{18} \text{ cm}^{-3}$ ) GaAs (1.7nm)/undoped AlAs (2.0nm) layers. A 20.0nm undoped GaAs top layer serves as surface protection and facilitates ohmic contact formation. Gate length and gate width of the SLHFET were  $1.3\mu\text{m}$  and  $200\mu\text{m}$ , respectively. Au/Ge/Ni ohmic contacts with a contact resistivity below  $0.2\Omega\text{mm}$  were used.

### 3 Experimental Results and Discussion

Figure 2 shows the I-V characteristic of a SLHFET of type 1 at  $T=300\text{K}$ . The saturation drain-source current is  $6\text{mA}$  and the transconductance is  $g_{\text{mmax}}=50\text{mS/mm}$ . The sheet carrier concentration  $n_s$  of this device is only  $4.4 \times 10^{11} \text{ cm}^{-2}$ , which is constant in the 300-77K temperature range. Higher values of  $n_s$  are possible by increasing the doping concentration in the GaAs layers. Devices of sample 2 with a two period spacer layer show a sheet carrier concentration of  $6.1 \times 10^{11} \text{ cm}^{-2}$  at 300K and  $7 \times 10^{11} \text{ cm}^{-2}$  at 77K with identical doping concentration in the GaAs. This may be an effect of the thinner spacer layer. The other characteristics of these devices are comparable to that of sample 1.

If the device is cooled down in the dark, an I-V collapse, which is typical for electron capture by DX centers, does not occur (see fig. 3). Simultaneously the threshold voltage is shifted by 0.2V only. The drain source current saturates at  $15\text{mA}$  in the dark. If the device is illuminated by white light the saturation current increases to  $17\text{mA}$  due to band-band generation of electrons but the transconductance remains almost unchanged at  $g_{\text{mmax}} = 120 \text{ mS/mm}$ . The light sensitivity was studied in more detail using ungated FET structures ( $L_{\text{DS}}=5\mu\text{m}$ ). The devices were cooled down in the dark and single sweep I-V measurements were carried out while the device was illuminated with light of various photon energies. Figure 4 shows that the main current increase appears in the range  $0.44\text{eV} < h\nu < 0.52\text{eV}$ . That means the trap level responsible for the remaining light sensitivity has an activation energy in this energy range. The current increase is not persistent if the illumination is interrupted. The absence of both persistent photoconductivity and I-V characteristic collapse indicate that due to the superlattice the influence of deep levels is strongly reduced. Further trap investigations were carried out by Photo-FET and low frequency noise measurements in fully processed devices. With the Photo-FET technique (Heuken et al. 1985, Tegude et al. 1984) optically induced drain current variations are measured. Activation energies of deep levels can be deduced from thresholds in the drain current variation at certain photon energies. A typical spectrum of a SLHFET is shown in fig. 5. The investigations were carried out at different bias combinations. The detected trap levels appear



nearly independent of the applied gate-source and drain-source voltages. This indicates that the traps responsible for the effects are located outside the gate space charge region. Donor-like levels with an activation energy of 0.43 and 0.47 eV were detected at room temperature. By means of the DLTS technique a thermal activation energy of the main electron level of about 0.5 - 0.6 eV were detected by Baba et al. (1985) in similar AlAs/n-GaAs superlattice structures. Since the amplitude of the Photo-FET signal is correlated to the trap concentration the 0.47 eV donor like trap is the main electron trap in this sample. This trap level is responsible for the remaining light sensitivity of the sample (see fig. 4). The two acceptor-like trap levels detectable in this samples have activation energies of 0.39 and 0.60 eV. The number of different acceptor like trap levels is strongly reduced compared with conventional AlGaAs/GaAs HFETs. This fact and the excellent device performance at low temperatures in the dark support a model (Kastalsky et al. 1986) according to which acceptor-like trap levels are responsible for the threshold voltage shift at low temperatures. In addition low frequency noise measurements at low fields in the channel were performed.

Generation-recombination processes at deep levels result in low frequency noise with Lorentzian-type spectra. Trap activation energies can be deduced from the temperature dependence of these spectra (Loreck et al. 1984). At room temperature SLHFETs have a low frequency noise power which is an order of magnitude smaller than that of conventional HFETs. By measurements in the temperature range 50-400 K and frequency range 1 Hz-25 KHz electron trap levels with  $\Delta E_T = 0.36$  eV and  $\Delta E_T = 0.59$  eV were detected. When comparing the results of the Photo-FET, DLTS (Baba et al.) and noise measurements it has to be recognized that there is a difference in the optical and thermal activation mechanism of traps (Frank-Condon shift) and usually the measuring temperatures are different. In addition nothing is known about trap behaviour in such thin superlattice layers. At present it is not possible to correlate the measured activation energies with transitions from traps into energy levels in the superlattice. Deep traps in the GaAs buffer layer may also contribute to Photo-FET and noise signals.

With these problems in mind a trap level  $\Delta E_T = 0.37$  eV only detected with the Photo-FET technique at low temperatures and the trap level  $\Delta E_T = 0.36$  eV detected with LF noise measurements are in good agreement. The trap level  $\Delta E_T = 0.43$  eV is only weak and probably not detectable with the LF noise method. The optically detected threshold of 0.47 eV and the thermal activation at 0.59 eV may correspond to the same trap. This conclusion is supported by the fact that no other transitions are observed between 0.47 and 0.59 eV neither by optical nor by thermal activation. Hall measurements gave 77 K Hall mobility values of  $130000 \text{ cm}^2/\text{Vs}$  and  $123000 \text{ cm}^2/\text{Vs}$  for sample 1 and 2, respectively. Carrier transport properties especially mobility, transconductance and gate-modulated carrier concentration were monitored by the magnetotransconductance profiling method extended to HFETs (Prost et al. 1985). The measurements represent the carrier concentrations and mobilities, which are available for the ac operation of the device for a given dc gate voltage.

The room temperature mobility ( $8000\text{cm}^2/\text{Vs}$ ) is almost independent of the gate voltage  $V_{\text{GS}}$ . Under forward bias  $V_{\text{GS}}$  no mobility degradation is observed, indicating that parallel conductance in the superlattice is absent. This is supported by the I-V characteristic of fig. 3. The mobility versus gate bias at cryogenic temperatures is plotted in fig. 6. At 77K the mobility increases rapidly at forward bias up to  $2 \times 10^5\text{cm}^2/\text{Vs}$ , representing the mobility in the highest subband of the 2DEG. Again no parallel conductance in the superlattice appears.

#### 4. Conclusion

To ensure proper operation of HFETs at cryogenic temperatures several drawbacks such as persistent photoconductivity, collapse of the I-V characteristic and high low-frequency noise level have to be solved. Improvement of HFETs is possible by a spatial separation of Al and Si atoms using AlAs/n-GaAs:Si superlattices as doping layer in a FET. Electronic and optoelectronic investigations reported here underline the high device quality obtainable with these structures. A reduced light sensitivity, no persistent photoconductivity and a low threshold voltage shift were achieved using these superlattices. The extremely low concentration of donor-like trap levels was experimentally proved by low frequency noise measurements and by Photo FET investigations. The small number of acceptor-like levels detected with the Photo FET technique is another characteristic of this novel structure. Properly designed superlattice layer sequences and excellent quality of MBE grown layers result in high mobility devices with good pinch off behaviour.

#### Acknowledgement

Authors are thankful to G. Howahl and M. Böhm for device preparation. The technical assistance by R. Tilders is very much appreciated.

#### References

- Baba T., Mizutani T., Ogawa M., 1983, J.J.Appl.Phys. 22, 627
- Fischer R., Drummond T.J., Kopp W., Morkoc H., Lee K., Schur M.S., 1983, Electr. Lett., Vol.19, No.19, 789
- Baba T., Mizutani T., Ogawa M., 1986, J.Appl.Phys. 59, 526
- Heuken M., Loreck L., Heime K., Ploog K., Schlapp W., Weimann G., 1986, IEEE Trans. Electron Dev., ED-33, No.5, 693
- Kastalsky A., Kiehl R., 1986, IEEE Trans.Electron.Dev., ED-33, No.3, 414
- Loreck L., Dämbkes H., Heime K., Ploog K., Weimann G., 1984, IEEE Electr. Dev. Lett., EDL-5, No.1, 9
- Prost W., Bockerhoff W., Heime K., Ploog K., Schlapp W., Weimann G., Morkoc H., 1986, IEEE Trans.Electron Dev., ED-33, No.5, 646
- Tegude F., Heime K., 1984, Inst. Phys. Conf. Ser. No.74, 305

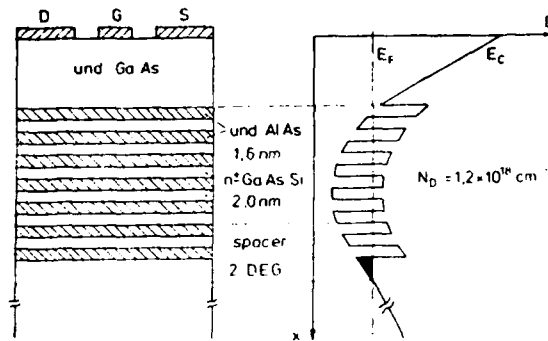


Fig. 1: Layer sequence and band diagram of a SLHFET

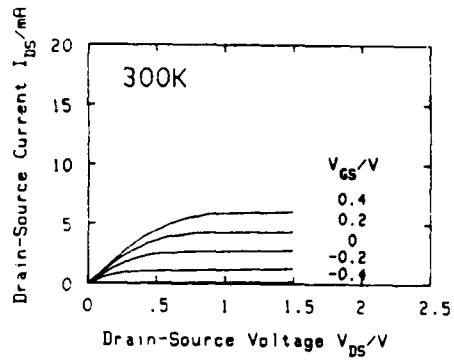


Fig. 2: I-V characteristic at  
 $T = 300\text{K}$   
 $(L_G = 1.3 \mu\text{m}, w = 200 \mu\text{m})$   
 $n_s = 4.4 \times 10^{11} \text{cm}^{-2}$

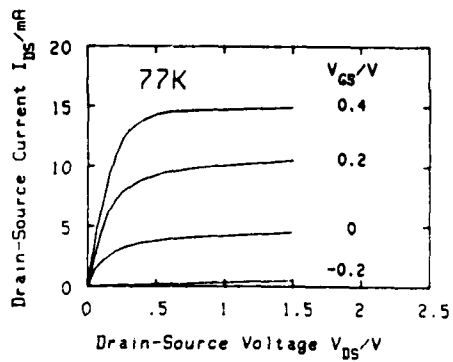


Fig. 3: I-V characteristic of  
 a SLHFET at 77K

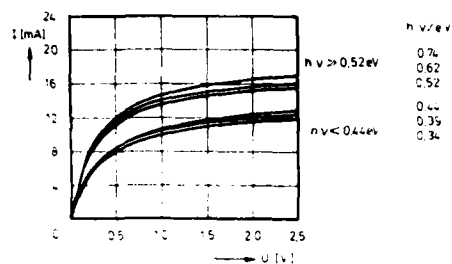


Fig. 4: Ungated SLHFET illuminated with monochromatic light of varying energy

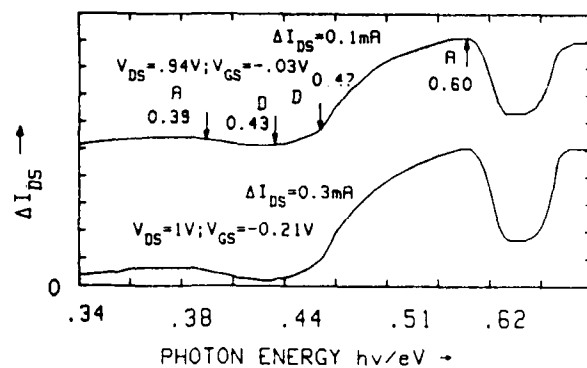


Fig. 5: Photo-FET Spectra at  $T = 300\text{K}$

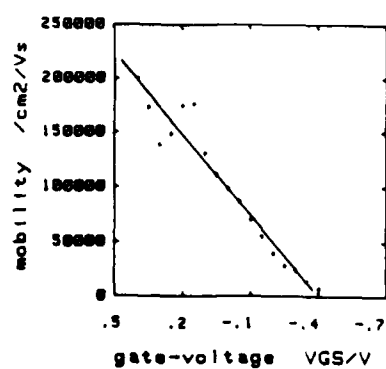


Fig. 6: Mobility profile at  $T = 77\text{K}$

## Strained N-Ga<sub>0.7</sub>Al<sub>0.3</sub>As/In<sub>0.23</sub>Ga<sub>0.77</sub>As/GaAs 2DEG FET with large band offset

A. Okamoto, H. Toyoshima and K. Ohata

Microelectronics Research Laboratories,  
NEC Corporation, 4-1-1, Miyamae-ku, Kawasaki 213 Japan

**Abstract** Strained N-Ga<sub>0.7</sub>Al<sub>0.3</sub>As/In<sub>0.23</sub>Ga<sub>0.77</sub>As/GaAs 2DEG FETs with large bandoffset were fabricated and high gm values of 275 and 425 mS/mm were obtained for FETs of 0.5  $\mu$ m-gate at 300 K and 77 K, respectively. By using strained InGaAs layers, sheet resistance is reduced to be about 500 ohm i.e., about two third of that in conventional N-GaAlAs/GaAs modulation-doped structures. The FETs with 0.5  $\mu$ m-gate exhibited a minimum noise figure of 1.2 dB with the associated gain of 11.6dB at 12 GHz.

### 1. Introduction

N-GaAlAs/GaAs modulation-doped FETs have been demonstrating excellent performance as low noise or high speed devices. However, their disadvantage, that the sheet carrier density of the two dimensional electron gas (2DEG) is rather low, causes high source resistance and low saturation current for FETs. The authors introduced a strained InGaAs layer between GaAs and GaAlAs layers to increase bandoffset, and observed high 2DEG density of about twice more than that of conventional modulation-doped structures. Furthermore, FETs were fabricated and good performance was achieved.

The lattice constant of InAs is larger than that of GaAs or AlAs by 7 %, and thus, InGaAs is lattice-mismatched to GaAs. However, an epilayer without dislocations can be grown on GaAs substrate when the thickness of InGaAs layer is thinner than the critical layer thickness given by Matthews et al (1974). Although InGaAs strained layers have been employed for FETs (Zipperian et al 1985, Rosenberg et al 1985, Masselink et al 1985, Morkoc et al 1986, Henderson et al 1986), the importance of large band discontinuity has not been studied yet. This paper describes the electrical properties of the strained modulation-doped structures, FET performances, and their advantages.

### 2. Experimental

Molecular Beam Epitaxy (MBE) was employed to fabricate the modulation-doped structures with large band discontinuity shown in Fig. 1, where Al composition of GaAlAs is fixed as 0.3 and In composition was varied. On semi-insulating GaAs substrate, grown were an undoped GaAs of 8000 Å, an InGaAs layer, an undoped GaAs or GaAlAs spacer layer, a Si-doped Ga<sub>0.3</sub>Al<sub>0.7</sub>As of 500 Å and an undoped GaAs cap layer of 100 Å. Doping concentration was  $2 \times 10^{18} \text{ cm}^{-3}$ . In composition and spacer thickness were varied to study the electrical properties for the strained modulation-doped structures. The In composition and the layer thickness of InGaAs

are shown in Table I. The thickness of InGaAs was chosen to be slightly less than the calculated critical layer thickness derived by Matthews et al (1974). The spacer thickness was varied between 0 to 80 Å. The growth temperature was 550°C and other procedures were quite similar to those for the growth of conventional GaAlAs/GaAs modulation-doped structures. Growth rate of 1 micron per hour for GaAs was used and no apparent variation in morphology was detected.

For FET fabrications, planar p+ gate technology was chosen to achieve high performance of planar FETs (Ohata et al 1985). The actual structure of epitaxial layers for FET fabrication is shown in Fig. 2. The n+ graded GaAlAs layer and GaAs surface layer were employed to obtain low resistance ohmic contact.

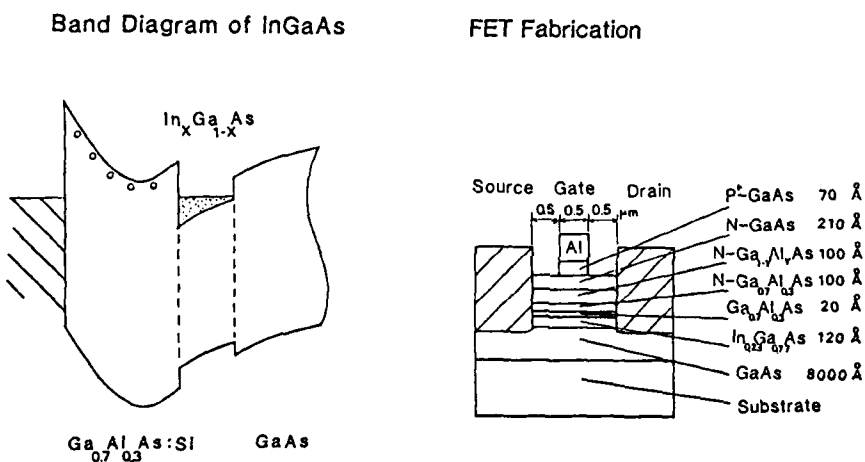


Fig. 1 Modulation-doped Structure using a strained InGaAs layer.

Fig. 2 Structure of the fabricated FET.

Table. I In composition and thickness of InGaAs layers.

| In Composition | Thickness(Å) | Critical layer thickness(Å) |
|----------------|--------------|-----------------------------|
| 0.15           | 200          | 217                         |
| 0.23           | 120          | 130                         |
| 0.30           | 80           | 88                          |

### 3. Results and discussion

#### 3.1 Two dimensional electron gas of strained heterostructure

Hall effect measurements were carried out for the modulation-doped structures with different In compositions. Figure 3 shows the mobility, 2DEG density and sheet resistance as a function of In composition. No spacer layer was employed. While mobility decreases with increasing In composition, the sheet carrier density increases and high value of  $2.2 \times 10^{12} \text{ cm}^{-2}$  was obtained at 0.3 In composition. The sheet resistance is minimized at In composition of 0.23, and the magnitudes, 480 ohm at RT and 220 ohm at 77K, are about two third of those for conventional structures. The dashed line indicates the calculated sheet carrier concentration by solving Poisson's equation with simple triangle potential approximation for InGaAs region. Furthermore, the conduction bandoffset between InGaAs and GaAlAs is assumed to be two third of the energy bandgap difference. The figure shows the measured  $N_s$  is slightly more than the calculated one. The simple estimation of bandoffset suggests that the bandoffset between  $\text{In}_{0.23}\text{Ga}_{0.77}\text{As}$  and  $\text{Ga}_{0.7}\text{Al}_{0.3}\text{As}$  be more than 0.40 eV.

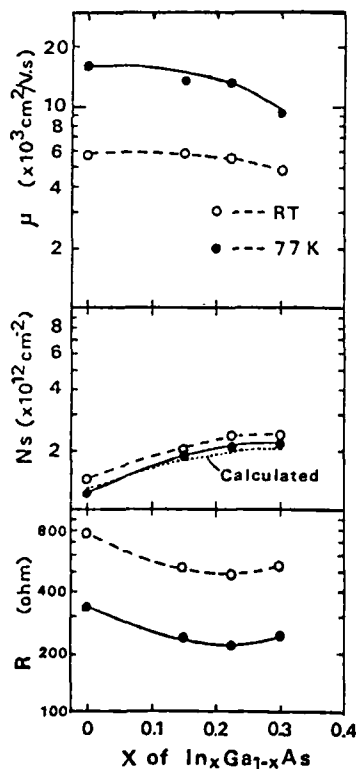


Fig. 3  $\mu$ ,  $N_s$  and  $R$  as a function of In composition.

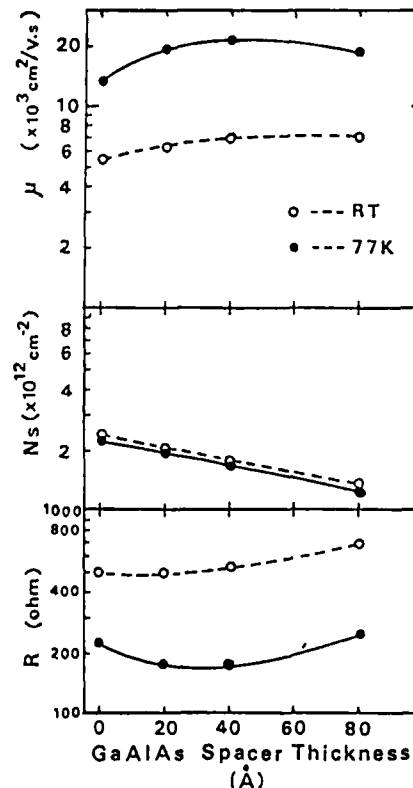


Fig. 4  $\mu$ ,  $N_s$  and  $R$  as a function of GaAlAs spacer.

The introduction of undoped spacer layers separates 2DEG from donors in the doped region and enhances the mobility. We studied the spacer effect on undoped GaAlAs, for the modulation-doped structures with 120 Å  $\text{In}_{0.23}\text{Ga}_{0.77}\text{As}$  layers. Figure 4 shows the dependence of  $N_s$  on GaAlAs spacer layer. The mobilities for 20 Å spacer were  $6300\text{cm}^2/\text{Vs}$  at room temperature and  $19,000\text{cm}^2/\text{Vs}$  at 77 K. However, the mobility at 77 K does not increase more than  $20,000\text{cm}^2/\text{Vs}$  with the increase of the spacer thickness. It is not clear at this stage how the strain influences the electron scattering mechanism. The sheet carrier density decreases monotonously with the spacer thickness and, consequently, the sheet resistance, 170 ohm, was obtained for a 40 Å spacer at 77 K. It is concluded from these results that the strained modulation-doped structure of In composition of 0.23 with a 20 to 40 Å GaAlAs spacer layer is the most promising as an epitaxial layer structure for FETs.

### 3.2 Device Characteristics

Figure 5 shows DC characteristics of the fabricated FET at room temperature, where the gate length and the width are 0.5  $\mu\text{m}$  and 200  $\mu\text{m}$ , respectively. Although pinch-off voltage is somewhat deep, 2.0 V, and  $g_m$  compression with gate voltage near 0 V is observed, maximum transconductance,  $g_{m\text{max}}$ , was 275 mS/mm. Furthermore,  $g_{m\text{max}}$  of 425 mS/mm was obtained for the 0.5  $\mu\text{m}$  gate FETs at 77 K. Figure 6 shows the dependence of  $g_m$  on gate length. The FET performance of short gate length is dominated by the saturation velocity of electrons. On the other hand, I-V characteristics are dominated by the electron mobility for long gate FETs and  $g_m$  tends to be inversely proportional to gate length. Compared with the conventional GaAlAs/GaAs or AlInAs/InGaAs 2DEG FETs,  $g_m$  of the FETs decreases with gate length more significantly at 77 K, and the behavior is due to rather low 2DEG mobility in the strained quantum wells at low temperature. In spite of the performance of the long gate FETs, short gate FETs are promising because of large sheet carrier density and high saturation velocity of electrons.

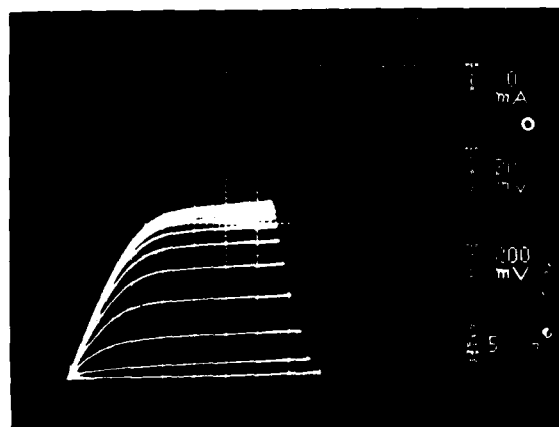


Fig. 5 DC characteristics of 0.5  $\mu\text{m}$ -gate FET.



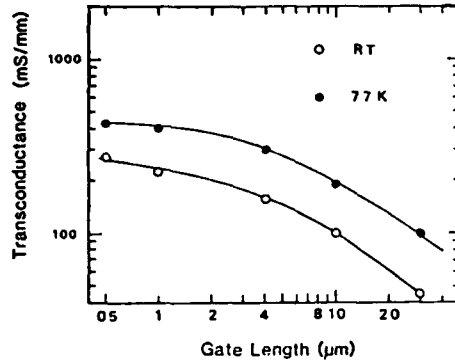


Fig. 6  $g_m$  as a function of gate length.

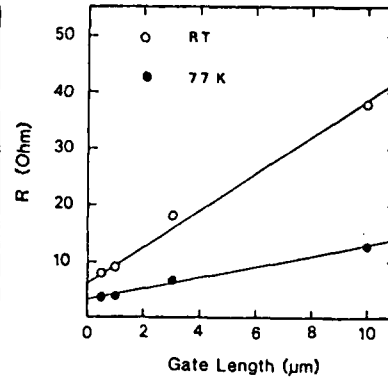


Fig. 7 Resistance between source and drain of FETs as a function of gate length.

Resistance,  $R$ , between source and drain of FETs with various gate length gives the source resistance  $R_s$  as shown in Fig. 7. Since the geometry of source and drain is symmetric,  $R$  is expressed by

$$R = 2R_s + (L_g / W_g) \times R_{ch}$$

where  $R_{ch}$  is sheet resistance under the gate,  $L_g$  is gate length and  $W_g$  is gate width. The estimated  $R_s$  was 0.61 ohm mm and 0.31 ohm mm at RT and 77 K, respectively. Since the sheet resistance is about 550 ohm, the contact resistance must be rather high, more than 0.33 ohm.

From the obtained  $g_m$  and  $R_s$ , intrinsic transconductance  $g_{m0}$  is evaluated by the equation:

$$g_{m0} = g_m / (1 - g_m R_s),$$

and they were 330 mS/mm and 490 mS/mm at room temperature and 77 K, respectively. Furthermore, the average electron velocity,  $V_a$ , is estimated assuming the short channel approximation:

$$V_a = g_{m0} / C_g$$

where  $C_g$  is gate capacitance, which is calculated by considering the GaAlAs thickness, 430 Å, and the distance from the heterointerface to the center position of 2DEG, 60 Å. The average electron velocity,  $V_a$ , was found to be  $1.5 \times 10^7$  and  $2.3 \times 10^7$  cm/sec at room temperature and 77 K, respectively. They are nearly equal to those for the conventional GaAlAs/GaAs 2DEG FETs and good transport properties were shown. Since large  $N_s$  and good transport of 2DEGs are proved,  $g_m$  compression shown in Fig. 5 might be due to the nonlinear I-V characteristics of ohmic contact.

RF performance was measured by the p-i-n FET with two gate pads at 12 GHz and gain and noise figure were, respectively, 11.6 dB and 1.2 dB

Further process improvement leading to lower contact resistance and lower threshold voltage will enhance performance of these FETs using the proposed strained modulation-doped structures.

#### 4. Conclusions

Strained N-GaAs/In<sub>0.23</sub>Ga<sub>0.77</sub>As/Ga<sub>0.7</sub>Al<sub>0.3</sub>As modulation-doped structures were fabricated by MBE and high 2DEG concentration of  $2 \times 10^{12} \text{ cm}^{-2}$  was observed. With increasing In composition, mobility decreases while 2DEG density increases, and it is found that the sheet resistance is minimized at In composition of 0.23. Strained N-Ga<sub>0.7</sub>Al<sub>0.3</sub>As/In<sub>0.23</sub>Ga<sub>0.77</sub>As/GaAs 2DEG FETs were fabricated and high  $g_m$  value of 275 and 425 mS/mm were obtained for FETs of 0.5  $\mu\text{m}$ -gate at 300 K and 77 K, respectively. By using strained InGaAs layers, sheet resistance is reduced to be about 500 ohm i.e., about two-third of that in conventional N-GaAlAs/GaAs modulation-doped structures. The FETs with 0.5  $\mu\text{m}$ -gate exhibited a minimum noise figure of 1.2 dB with 11.6 dB associated gain at 12 GHz. The proposed modulation-doped structures and FETs demonstrated in this paper clearly indicate the possibilities for better performance of 2DEG FETs compared to the conventional GaAlAs/GaAs FETs.

#### Acknowledgment

The authors would like to thank M. Ogawa, T. Mizutani, H. Baba, A. Furukawa, and K. Nishi for fruitful discussions and help. The authors also thank Y. Takayama, T. Itoh, H. Hida and H. Miyamoto for their helpful suggestions and encouragement. They are grateful to S. Tahara for her experimental assistance.

#### References

- Henderson T, Klem J, Peng C K, Gedymin J S, Kopp W and Morkoc H 1986 Appl. Phys. Lett. 48 1080
- Masselink W T, Ketterson A, Klem J, Kopp W and Morkoc H 1985 Electronics Lett. 20 939
- Matthews J W and Blakeslee A E 1974 J. Cryst. Growth, 27 118
- Morkoc H, Henderson T, Kopp W and Peng C K 1986 Electronics Lett. 22 578
- Ohata K, Ogawa M, Hida H and Miyamoto H 1984 GaAs and Related Compounds 1984 Inst. Phys. Conf. Ser. 74 653
- Rosenberg J J, Benlamri M, Kirchner P D, Woodall J M and Pettit G D 1985 IEEE Trans. Electron Devices Lett. EDL-6 491
- Zipperian T E and Drummond T J 1985 Electronics Lett. 21 823

## Selectively doped AlInAs/GaInAs heterostructures grown by MOCVD and their application to HIFETs (Hetero-Interface FETs)

M. Kamada, H. Ishikawa, M. Ikeda, Y. Mori, and C. Kojima

SONY Corporation Research Center  
174 Fujitsuka-cho, Hodogaya-ku, Yokohama, JAPAN 240

**Abstract.** Selectively doped AlInAs/GaInAs heterostructures lattice-matched to InP were successfully grown by atmospheric-pressure MOCVD using trimethylmetals. Mobility as high as  $11700 \text{ cm}^2/\text{Vs}$  at room temperature with a sheet carrier density of  $2.6 \times 10^{12} \text{ cm}^{-2}$  was obtained. We fabricated a HIFET (Hetero-Interface FET)  $1 \mu\text{m}$  in gate length using the heterostructure, and it showed a transconductance of  $404 \text{ mS/mm}$  at room temperature.

### 1. Introduction

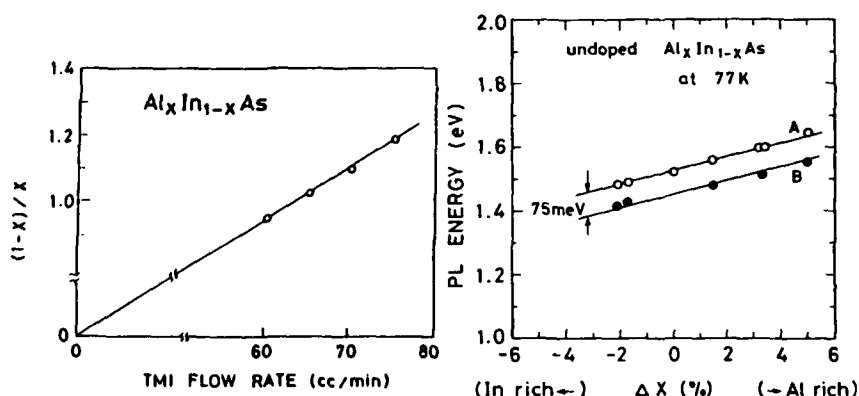
Selectively doped AlInAs/GaInAs heterostructures have attractive features for high speed devices such as high electron mobility, large saturation velocity, and large discontinuity of the conduction band edge (Pearsall 1984). The crystal growth of this system has mainly been done by MBE (Hirose et al 1985), however, we reported the first MOCVD growth of this system (Kamada et al 1986). In the previous paper, we used triethylmetals as source materials and demonstrated the high mobility of the selectively doped heterostructures. In this study, we report the crystal growth using trimethylmetals to obtain purer and more uniform epitaxial layers.

### 2. MOCVD growth

We used the atmospheric-pressure MOCVD method. The substrates were 2-inch-diameter (100) Fe-doped semi-insulating InP. They were etched by a mixture of  $\text{H}_2\text{SO}_4:\text{H}_2\text{O}:\text{H}_2\text{O}_2=5:1:1$  heated at  $100^\circ\text{C}$  for 2min before the MOCVD growth. The source materials of group III (trimethylmetals: TMA, TMG, and TMI) and of group V (arsine,  $\text{AsH}_3$ ) were mixed near the leading edge of the substrate to minimize parasitic gas-phase reactions. To obtain abrupt heterostructures, the gas flow had a very high speed of about  $1 \text{ m/sec}$ . The growth was continuous without any interruption. The substrates were rotated during the growth to obtain good uniformity of the epitaxial layers. The growth temperature was  $640^\circ\text{C}$ , and excellent morphology was obtained. The typical growth rate was about  $5 \text{ \AA/sec}$ .

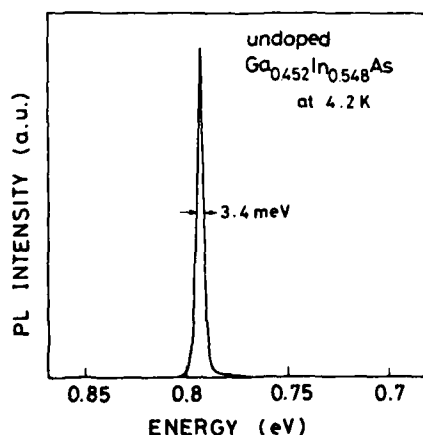
Figure 1 shows the relation between the TMI flow rate and the compositional ratio  $(1-x)/x$  in the  $\text{Al}_x\text{In}_{1-x}\text{As}$  epitaxial layers. The composition of the epitaxial layer was evaluated by measuring the lattice mismatch  $(\Delta a/a)$  between the epitaxial layer and the substrate by an X-ray diffractometer assuming Vegard's law. The linear relation in this figure indicates that the compositional ratio of In to Al is

proportional to the ratio of the gas flow rate of TMI to TMA. By controlling the gas flow rates, we suppressed the lattice mismatch within  $\pm 1.5 \times 10^{-4}$ . The value corresponds to a deviation of 0.2% in composition. To examine the energy gap change caused by the compositional change, we performed photoluminescence measurements of the undoped AlInAs layers at 77K. Figure 2 shows the relation between the photoluminescence energy and the deviation of the Al composition ( $\Delta x$ ) of the epitaxial layer from the composition corresponding to lattice matching ( $x=0.479$ ). Each layer has two photoluminescence peaks — labeled A (open circles) for the higher energy peaks, or B (closed circles) for the lower energy peaks. Both peaks increase in energy as  $\Delta x$  increases, corresponding to the increase in the energy gap of the AlInAs layers. This dependence of the higher energy peaks is quantitatively the same as the data of the AlInAs layers grown by MBE (Wakefield et al 1984). The lower peak may be an acceptor-related peak.



**Fig.1** Relation between the TMI flow rate and the compositional ratio  $(1-x)/x$  in the  $\text{Al}_x\text{In}_{1-x}\text{As}$  layers.

**Fig.2** Relation between the photoluminescence energy of undoped AlInAs layers and the deviation of the Al composition ( $\Delta x$ ) of the epitaxial layer from the composition corresponding to lattice-matching ( $x=0.479$ ).



The undoped GaInAs layer was n type with a carrier density of about  $1 \times 10^{18} \text{ cm}^{-3}$ , and it showed a mobility as high as  $10100 \text{ cm}^2/\text{Vs}$  at 300K. Figure 3 shows the photoluminescence spectrum from an undoped GaInAs layer measured at 4.2K. Only an exciton-related peak with a full width at half maximum (FWHM) of 3.4 meV is observed, and there is no acceptor-related peaks.

**Fig.3** Photoluminescence spectrum from an undoped GaInAs layer measured at 4.2K.

Disilane (5ppm  $\text{Si}_2\text{H}_6$  in  $\text{H}_2$  base) was used for n type doping to AlInAs. Figure 4 shows the relation between the  $\text{Si}_2\text{H}_6$  flow rate and the carrier density. The relation is almost linear. But there is a saturation behavior in the case of high doping, and the maximum doping density is  $6 \times 10^{18} \text{ cm}^{-3}$ . Even with such a high doping, there was no degradation of the surface morphology.

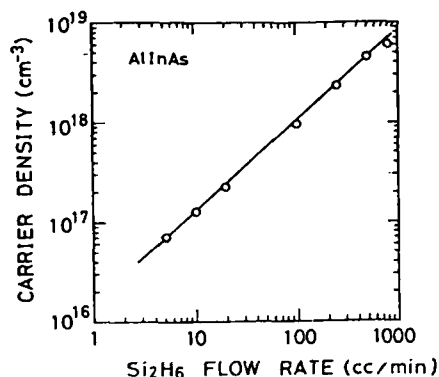


Fig.4 Relation between the  $\text{Si}_2\text{H}_6$  flow rate and the carrier density.

### 3. Abruptness of the heterostructures

To confirm the abruptness of the heterostructures, we performed two experiments. One was an Auger analysis of an AlInAs/GaInAs superlattice. The other was photoluminescence measurements of single quantum wells. Figure 5 shows the Auger profiles of an AlInAs/GaInAs superlattice, which consisted of 10 periods of  $47\text{\AA}/47\text{\AA}$  superlattice and 5 periods of  $94\text{\AA}/94\text{\AA}$  superlattice. We can observe a clear oscillation of Al and Ga and perfect periodicity was observed. Although the depth resolution of the Auger analysis was not sufficient (about  $50\text{\AA}$  or less), this result confirms the very sharp interfaces of the AlInAs/GaInAs heterostructures.

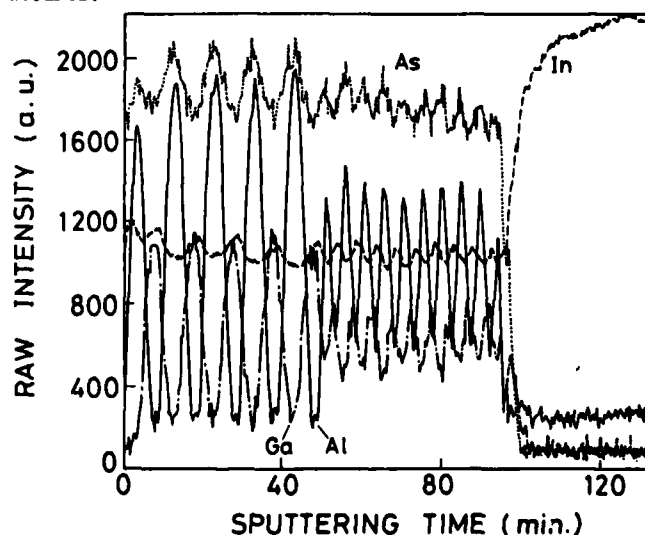


Fig.5 Auger profiles of an AlInAs/GaInAs superlattice, which consisted of 10 periods of  $47\text{\AA}/47\text{\AA}$  superlattice and 5 periods of  $94\text{\AA}/94\text{\AA}$  superlattice.

Figure 6 shows the photoluminescence spectrum at 4.2K from the single quantum wells, whose width was 11.7, 23.5, 35.2, 47.0, 93.6, and 1000Å with barrier layers 500Å thick. Six photoluminescence peaks from different wells are clearly observed. In fig.7, we plotted the photoluminescence peak energy as a function of the well width. Open circles show our data, and closed circles show the data in the case of the MBE growth (Welch et al 1983). Our data are nearly the same as the data of MBE growth. The calculated curve is also shown as a solid line. In the calculation, we assumed the continuity of the probability current density on two sides, and ignored the effect of non-parabolicity. The physical parameters used in the calculation were summarized in table 1. The calculated curve nearly fits the experimental data, and it suggests that the designed abrupt heterostructures were essentially realized in this experiment.

|        | effective mass |             |
|--------|----------------|-------------|
|        | $m(e)/m_0$     | $m(hh)/m_0$ |
| GaInAs | 0.041          | 0.50        |
| AlInAs | 0.086          | 0.58        |

$$\Delta E_c = 0.5 \text{ eV}, \Delta E_v = 0.2 \text{ eV}$$

Fig.6 Photoluminescence spectrum at 4.2K from the single quantum wells with barrier layers 500Å thick.

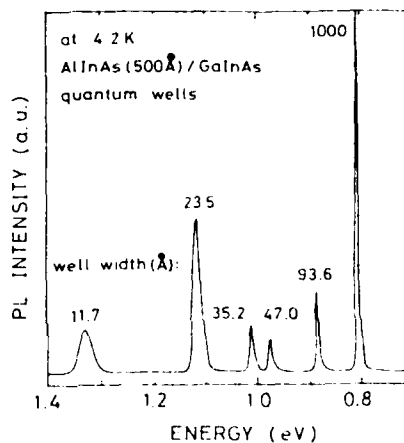
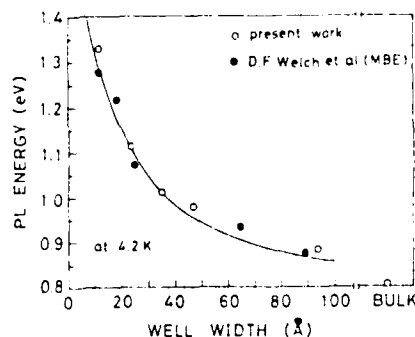


Fig.7 Relation between the photoluminescence peak energy of the single quantum wells as a function of the well width.



#### 4. Selectively doped heterostructures

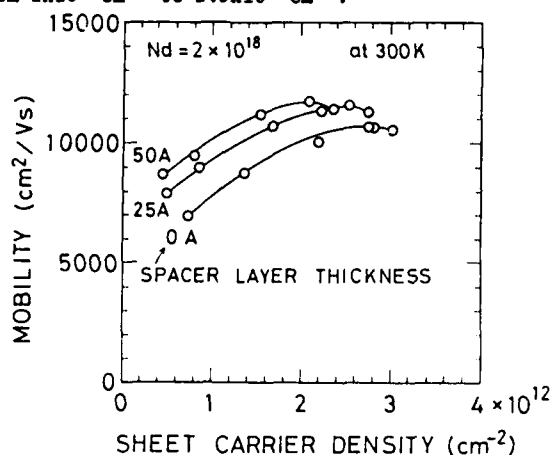
Selectively doped AlInAs/GaInAs heterostructures with three different spacer-layer thicknesses were grown. There was an undoped AlInAs buffer layer 2000Å thick, and the undoped GaInAs layer was 1000Å thick. The spacer layer thicknesses were 0, 25, and 50Å, and the doping density in n AlInAs was  $2 \times 10^{18} \text{ cm}^{-3}$ . We evaluated the electron mobility of the selectively doped heterostructures at room temperature. To obtain the data as a function of the sheet carrier density, we repeated Hall measurements after a brief chemical etching of the n AlInAs layers. Figure 8 shows the electron mobility of selectively doped heterostructures with varying sheet carrier density at room temperature.

Higher mobilities are obtained in samples of larger spacer layer thickness. This is natural behavior because the Coulomb scattering caused by the ionized impurities in the n AlInAs layers is reduced by increasing the spacer layer thicknesses. Mobility beyond 10000  $\text{cm}^2/\text{Vs}$  was obtained for the sample with a spacer layer of 50Å in the range of sheet carrier density from  $1 \times 10^{12} \text{cm}^{-2}$  to  $2.5 \times 10^{12} \text{cm}^{-2}$ .

**Fig.8** Electron mobility of selectively doped heterostructures as a function of the sheet carrier density measured at 300K.

**Table 2**

|      | $\mu$<br>( $\text{cm}^2/\text{Vs}$ ) | $n$<br>( $\text{cm}^{-2}$ ) |
|------|--------------------------------------|-----------------------------|
| 300K | 11700                                | $2.6 \times 10^{12}$        |
| 77K  | 57200                                | $2.6 \times 10^{12}$        |



The maximum electron mobility of the sample is summarized in table 2. These values are nearly the same as those of the selectively doped heterostructures grown by MBE, and higher than those in crystals grown by MOCVD using triethylmetals as source materials (Kamada et al 1986).

##### 5. HIFETs (Hetero-Interface FETs)

We fabricated HIFETs using selectively doped heterostructures with a spacer layer 50Å thick. The n AlInAs was 500Å thick with a doping density of  $2 \times 10^{18} \text{cm}^{-3}$ . Figure 9 shows the cross-sectional view of a HIFET. The channel layers were separated by mesa etching. The Al gate metals were evaporated and lifted off. The barrier height of the Schottky junction of Al and n AlInAs ( $N_d = 2 \times 10^{18} \text{cm}^{-3}$ ) obtained from C-V measurements was 0.63eV, and the value obtained from I-V measurements was 0.55eV. These values are somewhat smaller than those of GaAs, but this is not a problem for device operation. The ohmic metals were AuGe(1900Å)-Ni(520Å), which were evaporated, lifted off, and alloyed in an  $\text{H}_2/\text{N}_2$  atmosphere ( $\text{H}_2$ , 4%) at 300°C. The alloying temperature was optimized and is lower than the temperature used in the case of the AlGaAs/GaAs HIFETs. The ohmic contact resistance, measured by the transmission line method, was about 0.3Ωmm.

**Fig.9** Cross-sectional view of a HIFET.

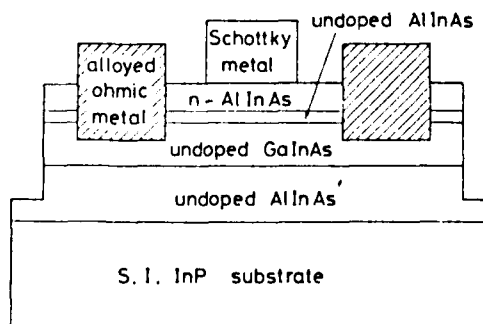
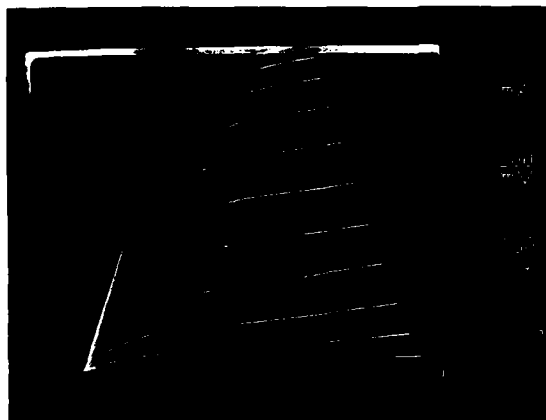


Figure 10 shows the FET characteristics of a  $1\mu\text{m}$  gate HIFET operated at room temperature. The HIFET shows good pinch-off characteristics, and a maximum transconductance of  $404\text{mS/mm}$  was obtained. This value is very high compared with that of an AlGaAs/GaAs HIFET with the same gate length (Tanaka et al 1986), and nearly the same as in the case of MBE growth (Hirose et al 1985).



**Fig.10** FET characteristics of a  $1\mu\text{m}$  gate HIFET operated at 300K. The maximum gate voltage is 0V.

#### 6. Conclusion

Selectively doped AlInAs/GaInAs heterostructures lattice-matched to InP were grown by atmospheric-pressure MOCVD using trimethylmetals. The composition of the epitaxial layers were successfully controlled by varying the gas flow rates of the source materials. High flow speed was used to obtain sharp hetero-interfaces, and the abruptness was confirmed from an Auger analysis and from the well width dependence of the photoluminescence energy of single quantum wells. A selectively doped AlInAs/GaInAs heterostructure with a spacer 50Å thick showed mobility as high as  $11700\text{cm}^2/\text{Vs}$  at 300K, and  $57200\text{cm}^2/\text{Vs}$  at 77K, with a sheet carrier density of  $2.6 \times 10^{13}\text{cm}^{-2}$ . A HIFET,  $1\mu\text{m}$  in gate length, showed a high transconductance of  $404\text{mS/mm}$  at room temperature. These results confirm the very high potential of our technology for high speed devices.

#### Acknowledgments

We wish to thank Miss. T.Shimada and Miss. M.Ema for their help in device fabrication and measurement, and also Dr. N.Watanabe and Dr. M.Kikuchi for their support of this work.

#### References

- Hirose H, Ohata K, Mizutani T, Itoh T, and Ogawa M 1985 GaAs and Related Compounds(Karuizawa) 1985 Inst.Phys.Conf.Ser. No.79 529
- Kanada M, Ishikawa H, Ikeda M, Mori Y, and Kojima C Extended Abstract of the 18th Conference on Solid State Devices and Materials, Tokyo, 1986, pp.777
- Pearsall Thomas P 1984 Surface Science 142 529
- Tanaka K, Takakuwa H, Nakamura F, Mori Y, and Kato Y 1986 Electron.Lett. 22 487
- Wakefield B, Halliwell M A G, Kerr T, Andrews D A, Davies G J, Wood D R, 1984 Appl.Phys.Lett. 44 341
- Welch D F, Wicks G W, Eastman L F, 1983 Appl.Phys.Lett. 43 762



## **DC and RF characterization of a planar-doped double heterojunction MODFET**

Y.K. Chen, D.C. Radulescu, P.J. Tasker, G.W. Wang  
and L.F. Eastman

School of Electrical Engineering, Cornell University  
Ithaca, NY 14853 USA

**Abstract.** A GaAs/AlGaAs double heterojunction MODFET structure with atomic planar doping layers prepared by Molecular Beam Epitaxy (MBE) was fabricated and characterized. FET structures of  $0.5 \times 200 \mu\text{m}$  gate geometry demonstrated a DC transconductance of  $135 \text{ mS/mm}$  over a broad gate bias range and a zero gate bias current of  $350 \text{ mA/mm}$  with a maximum channel current of  $430 \text{ mA/mm}$ . Both are extrinsic values measured at room temperature. Results obtained from microwave measurements show the cut-off frequency of short circuit current gain ( $f_T$ ) of  $24 \text{ GHz}$ , and the maximum oscillation frequency of  $50 \text{ GHz}$  been achieved. At  $10 \text{ GHz}$ , the device gave the maximum efficiency of  $47$  percent with  $5.5 \text{ dB}$  gain and  $0.5 \text{ W/mm}$  output power at a drain bias of  $6.5 \text{ volts}$ .

### **Introduction**

Gallium arsenide MODFETs (Modulation-Doped Field-Effect Transistors) have demonstrated excellent microwave performance with very high cut-off frequency and very good noise performance [Camnitz 1984; Chao 1985; Berenz 1984; Smith 1985]. However, the current driving capability of conventional single heterojunction MODFETs is limited by the amount of sheet charge density in the two dimensional channel, usually less than  $1 \times 10^{12}/\text{cm}^2$ . Therefore, their power performance and switching speed, which are directly related to the current driving capability, were not much better than MESFETs. In order to achieve high sheet charge density, a high doping concentration in AlGaAs is generally used. This leads to problems such as low breakdown voltage, low activation efficiency of dopants, and process control problems such as poor pinch-off characteristics and threshold voltage uniformity. Double and multiple heterojunction devices were then investigated [Hikosaka 1986; Gupta 1985; Saunier 1986] to increase the current density. The highest maximum channel current reported so far is  $600 \text{ mA/mm}$  from a multiple heterojunction device [Saunier 1986]. However, all multiple heterojunction structures built so far, were still based on uniformly doped AlGaAs layers to support the two dimensional electron gases. So the problems with heavily doped AlGaAs layers still persist.

In 1979, Wood [1979] reported a GaAs power FET structure of which the dopants were deposited on one atomic plane by interrupting MBE growth. The ultra-thin doped layer resulted in a FET structure with very constant transconductance and gate-to-source capacitance over a wide bias range. We present here a double heterojunction MODFET structure which utilizes two Si planar-doped AlGaAs layers. This provides us with good charge control of the two-dimensional electron sheet charge density in comparison to the uniformly doped layers as well as better device performances. From those double planar-doped MODFET structures, we observed enhanced FET performance such as higher breakdown voltage, broader  $g_m$  and gate capacitance curves, reduced light sensitivity and threshold voltage shifts at low temperature.

#### Device Structure

The fabricated AlGaAs/GaAs structure is shown in Fig. 1, and the corresponding energy band diagram under the gate is shown in Fig. 2. Since the donor atoms are confined in a two-dimensional plane, the band bending is linear and resulting in broad  $g_m$  and  $C_{gs}$  characteristics. The structure is grown by MBE on top of a semi-insulating GaAs substrate in the following sequence: 5000 Å superlattice buffer layer, 200 Å undoped AlGaAs, Si planar doped layer of  $4 \times 10^{12}/\text{cm}^2$ , 100 Å undoped AlGaAs, 200 Å undoped GaAs channel, 50 Å undoped AlGaAs spacer layer, Si planar doped layer of  $4 \times 10^{12}/\text{cm}^2$ , 400 Å undoped AlGaAs, and 400 Å GaAs capping layer doped to  $1 \times 10^{18}/\text{cm}^3$ . The mole fraction of aluminum is 30% throughout all the AlGaAs layers.

#### Device Fabrication

The double heterojunction MODFETs were fabricated by using a deep-UV contact lithography and a lift-off technique. After mesa etching, source and drain ohmic contacts were formed with Ni/AuGe/Ag/Au alloyed at 750 C furnace temperature on the cap layer. Using the photoresist as mask, the gate recess was performed by wet chemical etching. Finally, Ti/Pt/Au gate metal was evaporated and lift-off to form complete FET structure. The gate length of FETs is either 1  $\mu\text{m}$  or 0.5  $\mu\text{m}$  measured on the mask with distance of 1.5  $\mu\text{m}$  between gate and source and gate to drain.

#### Results and Discussion

Minimum breakdown voltage measured between two adjacent mesa pads placed 7  $\mu\text{m}$  away on the superlattice buffer layers was 40 volts. Specific ohmic contact resistance obtained from transmission line patterns was typically 0.4 ohms-mm. Since a phosphoric acid/peroxide/DI aqueous solution was used for gate recess etching, it left residues underneath the Schottky gate metal and caused variations in gate breakdown voltages ranged from 3.5 to 19 volts as shown in Figs. 3 and 4. Despite this processing related problem, we demonstrated that the high gate breakdown voltages of 19 volts can be

|   |
|---|
| 400 Å $n^+$ - GaAs $2 \times 10^{18}/\text{cm}^3$   |
| 400 Å undoped $\text{Al}_{0.3}\text{Ga}_{0.7}\text{As}$                                     |
| ATOMIC PLANAR DOPING $\text{Si-}4 \times 10^{18}/\text{cm}^3$                               |
| 50 Å undoped $\text{Al}_{0.3}\text{Ga}_{0.7}\text{As}$                                      |
| 200 Å GaAs QUANTUM WELL   |
| 100 Å undoped $\text{Al}_{0.3}\text{Ga}_{0.7}\text{As}$                                     |
| ATOMIC PLANAR DOPING $\text{Si-}4 \times 10^{18}/\text{cm}^3$                               |
| 200 Å undoped $\text{Al}_{0.3}\text{Ga}_{0.7}\text{As}$                                     |
| 5,000 Å Superlattice Buffer<br>(16 Å GaAs/200 Å $\text{Al}_{0.3}\text{Ga}_{0.7}\text{As}$ ) |
| Si. GaAs  |

Figure 1. Layer structure of an atomic planar doped double heterojunction MODFET.

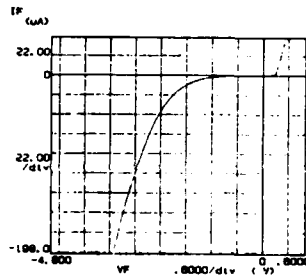


Figure 3. Breakdown characteristics of a bad Schottky diode.

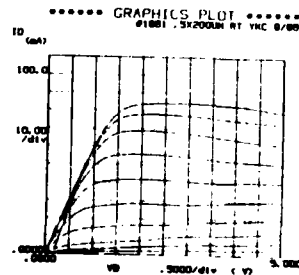


Figure 5. Drain current-voltage characteristics for a  $0.5 \times 200 \mu\text{m}$  MODFET.

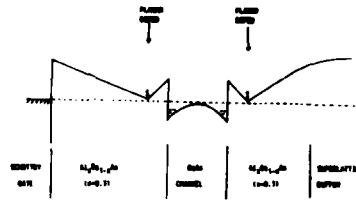


Figure 2. Band diagram of the APD double heterojunction MODFET.

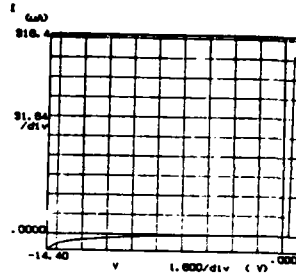


Figure 4. Breakdown characteristics of a good Schottky diode.

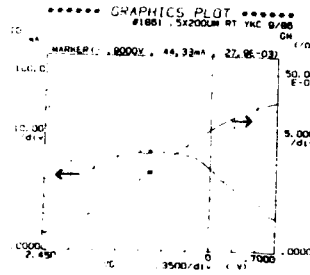


Figure 6.  $g_m$ ,  $I_{DS}$  characteristics versus gate bias variation.

accomplished by the planar doping technique.

Figure 5 shows the drain current-voltage characteristics of a  $0.5 \times 200 \mu\text{m}$  FET at room temperature. It shows very good pinch-off characteristics as well as very low output conductance. The relation of DC transconductance and drain current versus gate bias were plotted in Fig. 6 with drain biased at 2.5 volts. A very broad peak of transconductance over the bias variations was observed. By combining the flat gate-to-source capacitance curve in Fig. 7, this double planar doped technique will yield MODFETs with very good RF power performance in terms of high  $f_{\text{max}}$ , high efficiency, low intermodulation distortion, and fairly constant input impedance at different power levels. The maximum extrinsic  $g_m$  measured at room temperature is 139.5 mS/mm with a source resistance of 1.6 ohms-mm from the end-resistance measurement. This yields an intrinsic  $g_m$  of 179 mS/mm. Fig. 8 shows the drain I-V characteristics of a  $1 \times 200 \mu\text{m}$  FET at 77K under the light and in the dark. Despite the oscillations from the probe station, we can see very little I-V collapse which is very pronounced and commonly seen in MODFETs with uniformly-doped AlGaAs layers. This can be seen better in the 77K transconductance and drain current curve as depicted in Fig. 9.

Data obtained from small signal s-parameter measurements from 1 to 19 GHz of a packaged FET with  $0.5 \times 200 \mu\text{m}$  gate geometry shows a short-circuit current gain cut-off frequency ( $f_T$ ) of 24 GHz with an associated maximum oscillation frequency ( $f_{\text{max}}$ ) of 50 GHz. The data were extrapolated from the low frequency measurements with a slope of 6 dB per octave. Power measurements were performed at 10 GHz with the diced device mounted and wire-bonded in a microwave fixture. At a maximum efficiency of 47 percent, the tuned device delivered a corresponding power of 0.5 W/mm and 5.5 dB gain with the drain biased at 6.5 volts. The device also exhibited a soft output power compression curve as shown in Fig. 10, hence it was difficult to determine the 1 dB compression point. At low power level, the tuned device gave 12.4 dB gain. The maximum output power can be delivered by this device could not be measured on our test system which is limited by the low available input power level from the signal source.

#### Summary

We have demonstrated a double heterojunction MODFET structure that utilizes a MBE growth suspension technique to confine all the dopants within a ultra-thin plane in the otherwise unintentionally doped AlGaAs layers. The fabricated FETs with  $0.5 \times 200 \mu\text{m}$  gate geometry shows an  $f_T$  of 24 GHz and corresponding  $f_{\text{max}}$  of 50 GHz. The room temperature DC characteristics shows a very broad  $g_m$  peak of 135 mS/mm with a maximum channel current of 350 mA/mm. Power measurements on this device at 10 GHz shows a maximum efficiency of 47 percent with 5.5 dB associated gain and 0.5 W/mm. At 77K, the fabricated MODFET showed very little light sensitivity and no

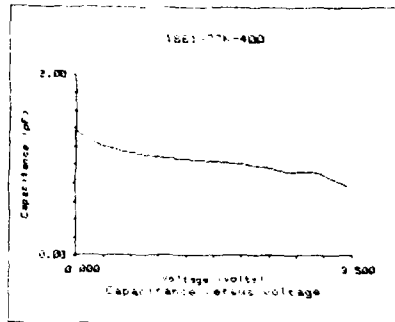


Figure 7. (a) 10MHz C-V characteristics of Schottky Gate Diode at 77°K.

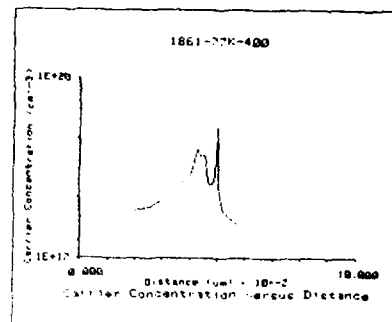


Figure 7. (b) Corresponding carrier concentration at 77°K.

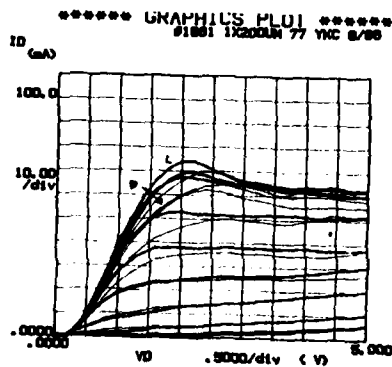


Figure 8. Drain current-voltage characteristics of 1 x 400  $\mu\text{m}$  FET at 77°K.

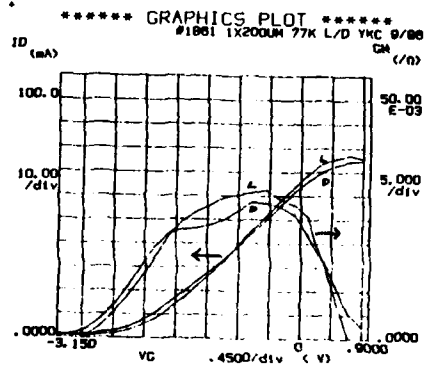


Figure 9.  $g_m$ ,  $I_{DS}$  characteristics at 77°K with/without light.

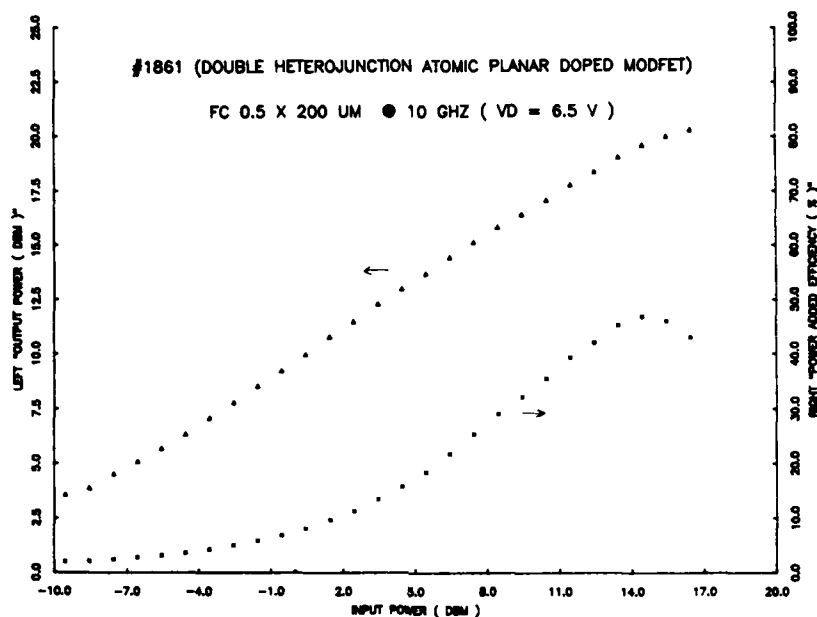


Figure 10. Power Performance of a  
0.5 x 200 μm FET at 10 GHz.

I-V collapse was observed. Therefore, the double atomic planar doped structure will be a very good candidate for the high speed digital and high power microwave applications.

#### Acknowledgements

The authors wish to thank A. Lepore for E-beam mask generation, J. Berry for technical advise, NRFSS and the Electronics Laboratory (General Electric Co., Syracuse, NY) for facility usage. Some 1 μm MODFETs were evaluated at Cascade Corps. (Beaverton, OR) microwave probe station, help from D. Carlton, J. Marron, and K. Jones are deeply appreciated. The work was supported in part by JSEP, ONR, GE and McDonnell-Douglas Co.

- Berenz J J et al. 1984 Proc. IEEE MMIC Symp. 93.  
 Camnitz L H et al. 1984 Proc. IEEE IEDM 360.  
 Chao P C 1985 Proc. IEEE/Cornell Conf. 163.  
 Gupta A K et al. 1985 Proc. IEEE MMIC Symp. 50-53.  
 Henderson T et al. 1986 Appl. Phys. Lett. 48 1080.  
 Hikosaka K et al. 1986 IEEE Elec. Dev. ED-33 583.  
 Saunier P et al. 1986 IEEE EDL-7 503.  
 Smith P M et al. 1985 Proc. IEEE/Cornell Conf. 189.  
 Wood C E C et al. 1979 Proc. IEEE IEDM 388.

## **Novel resonant tunneling diodes with an $\text{In}_x\text{Ga}_{1-x}\text{As}$ strained layer deep quantum-well**

Hideo Toyoshima, Yuji Ando, Akihiko Okamoto and Tomohiro Itoh

Microelectronics Research Laboratories, NEC Corporation  
4-1-1, Miyazaki, Miyamae-ku, Kawasaki, 213 Japan

**Abstract** This paper presents the first successful fabrication of double barrier resonant tunneling diodes with an  $\text{AlAs}/\text{In}_x\text{Ga}_{1-x}\text{As}/\text{AlAs}$  strained layer deep quantum-well. The threshold voltage for the onset of negative differential resistance was controlled down to near zero volt. The diode with an  $\text{In}_{0.1}\text{Ga}_{0.9}\text{As}$  quantum-well exhibited the peak-to-valley current ratio of 13 at 77K, which is the highest value ever reported for double barrier structures.

### **1. Introduction**

Resonant tunneling transport has been attracting much interest because of its characteristics, such as pronounced negative differential resistance (Tsu and Esaki 1973) and high speed charge transport (Sollner et al 1983). It has also been shown to be applicable to ultra high frequency devices or new functional devices (Yokoyama et al 1985, Bonnefoi et al 1985, Capasso et al 1985). In order to improve negative differential resistance (NDR) characteristics, much effort has been made by changing structure parameters of the double barrier resonant tunneling diodes (RTD's). Its main parameters are quantum-well width, barrier layer thickness and barrier height (Sollner et al 1983, Schewchuk et al 1985, Tsuchiya et al 1986a,b). In this work, another structure parameter, quantum-well depth was changed and deep quantum-well RTD's were successfully fabricated by introducing an  $\text{InGaAs}$  strained layer quantum-well.

### **2. Principle**

Figure 1(a) shows an energy band diagram for a conventional RTD with double barriers. Quantum states are formed in a well and their energy  $E_n$  is described as follows:

$$E_n = \frac{\hbar^2}{2m^*} (n\pi/L_w)^2 \quad (n = 1, 2, \dots) \quad (1)$$

where  $\hbar$  is the reduced Planck's constant,  $m^*$  the effective electron mass and  $L_w$  the well thickness. It is known that threshold voltage  $V_t$  for the onset of NDR corresponds approximately to twice  $E_n$ ,

$$V_t = 2E_n/q \quad (2)$$

where  $q$  is the electronic charge. In order to apply resonant tunneling transport to high frequency devices or functional devices, a high P/V ratio and the capability of attaining threshold voltage control are crucial factors. In conventional structures, threshold voltage is

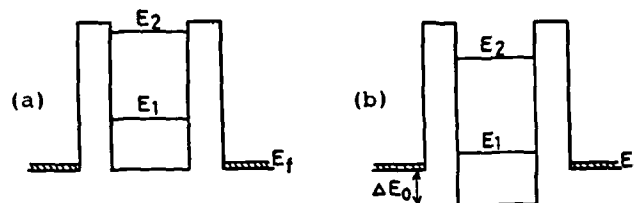


Fig.1. Energy band diagram for (a) a conventional RTD, (b) a deep quantum-well RTD.

determined mainly by well thickness according to eqs.(1) and (2). In order to reduce threshold voltage it is essential to employ a thicker well. However, the energy separation between the resonant states becomes smaller and, when electrons are injected by the resonant tunneling through the first state, another excess current through the higher energy states becomes larger, resulting in P/V ratio degradation.

As another approach to threshold voltage control without changing well thickness, we study a deep quantum-well structure. Figure 1(b) shows an energy band diagram for a deep quantum-well RTD, where a quantum-well conduction band edge is lower than those of contact regions by  $\Delta E_0$ . In this case, threshold voltage  $V_t$  is given approximately by:

$$V_t = 2(E_n - \Delta E_0)/q. \quad (3)$$

Thus in the deep quantum-well structure, a thinner well is chosen to keep the large energy separation between the resonant states. Then threshold voltage is reduced by lowering the conduction band edge of the quantum-well by  $\Delta E_0$ , which leads to the reduction of threshold voltage by  $2\Delta E_0/q$ . Hence in the deep quantum-well RTD, threshold voltage can be controlled while retaining a high P/V ratio.

### 3. Device Fabrication

In order to fabricate a deep quantum-well RTD, InGaAs was used for the quantum-well. Figure 2 shows the epitaxial layer structure of the fabricated RTD. It consists of 70Å quantum-well, 30Å AlAs barriers, 50Å undoped spacer layers and 1000Å Si doped N-GaAs layers ( $N_d = 5 \times 10^{17} \text{ cm}^{-3}$ ). Four kinds of RTD's with indium composition of 0, 0.1, 0.2 and 0.3 were fabricated. Although an InGaAs quantum-well is lattice mismatched to AlAs barriers, a dislocation-free epilayer, so called strained layer, quantum-well can be grown when the thickness of an InGaAs layer is thinner than the critical layer thickness given by Matthews et al (1974). The present quantum-well thickness of 70 Å is set to be within the critical thickness. On both sides of the epitaxial layers as shown in Fig.2, heavily doped  $N^+$ -GaAs contact

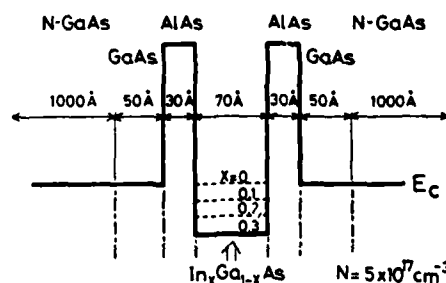


Fig.2. Epitaxial layer structure for fabricated RTD's.



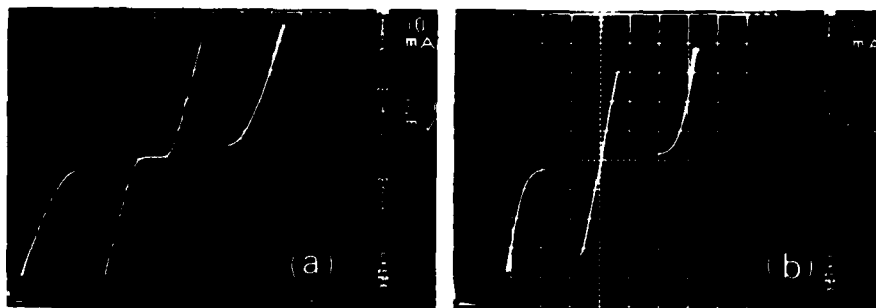


Fig.3. I-V characteristics for diodes at 77K, (a) with a GaAs quantum-well, (b) with an  $\text{In}_{0.1}\text{Ga}_{0.9}\text{As}$  quantum-well.

layers ( $N_d = 3 \times 10^{18} \text{ cm}^{-3}$ ) were put to reduce the series resistance. These structures were grown on semi-insulating GaAs substrates by MBE at growth temperature of 600 °C. The diameter of diodes is 100  $\mu\text{m}$ .

#### 4. Results and Discussions

Figure 3(a) and 3(b) show I-V characteristics for the diodes with a GaAs quantum-well and an  $\text{In}_{0.1}\text{Ga}_{0.9}\text{As}$  quantum-well at 77K, respectively. They exhibited clear NDR even at room temperature. When they were cooled down to 77K, the valley current was significantly reduced, resulting in a very high P/V ratio. The I-V characteristics for both diodes were symmetric with respect to the voltage origin, confirming the symmetry of grown heterostructures. The P/V ratio for the GaAs quantum-well structure was 10. That for the  $\text{In}_{0.1}\text{Ga}_{0.9}\text{As}$  quantum-well structure was as high as 13, which is the highest value ever reported for double barrier RTD's. It is confirmed that even when the strained layer is used for the quantum-well, very sharp hetero junction interface is obtained. Threshold voltage for the GaAs quantum-well structure was 340mV and that for the  $\text{In}_{0.1}\text{Ga}_{0.9}\text{As}$  quantum-well structure was reduced to 150mV. It is noted that the I-V characteristics around zero bias for the  $\text{In}_{0.1}\text{Ga}_{0.9}\text{As}$  quantum-well structure is fairly linear compared with the nonlinear characteristics for the GaAs quantum-well structure.

In Fig.4, the peak current and the valley current of the fabricated diodes, and their ratio are plotted against indium composition of the quantum-well. The peak current decreases monotonously with the increase of the indium composition. The valley current decreases more steeply than the peak current does from the indium composition of 0 to 0.1. Then it tends to saturate. Therefore, the P/V ratio has a peak at the indium composition of 0.1 and

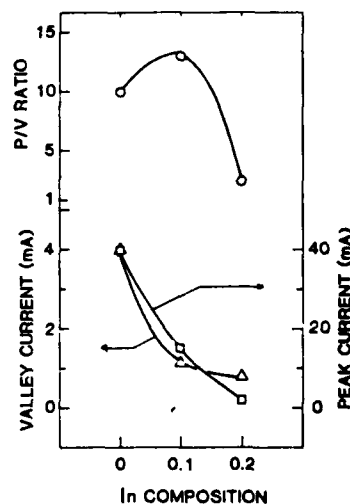


Fig.4. Peak current, valley current and P/V ratio vs. quantum-well indium composition.

its value is as high as 13. It is also noted that a high P/V ratio is obtained at the indium composition between 0 and 0.2.

The threshold voltage for the fabricated diodes is plotted against the indium composition of the quantum-well in Fig.5. The increase in the indium composition from 0 to 0.2 reduces the threshold voltage from 340 to 30 mV. The diode with indium composition of 0.3 exhibited no NDR. The possible reason is that the first resonant state lies below the conduction band edge of the N-GaAs layers. A theoretical estimation from the obtained threshold voltage shift indicates that a conduction band offset between  $\text{In}_{0.2}\text{Ga}_{0.8}\text{As}$  and GaAs corresponds to about 60% of the band gap difference calculated from Vegard's law. The details of discussion will be published elsewhere. It is thus demonstrated that threshold voltage can be controlled down to near zero volt by using the present InGaAs deep quantum-well structure, still retaining a large P/V ratio.

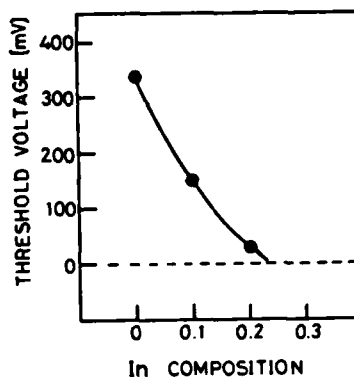


Fig.5. Threshold voltage vs. quantum-well indium composition.

##### 5. Summary

The resonant tunneling diode with a deep quantum-well structure was fabricated by introducing an InGaAs strained layer for the quantum-well. The peak-to-valley current ratio of 13 was obtained at 77K, which is the highest value ever reported for double barrier resonant tunneling diodes. In addition, the threshold voltage can be controlled from 340 to 30 mV by changing the indium composition of the InGaAs quantum-well.

##### Acknowledgements

The authors would like to thank M.Ogawa and T.Baba for their fruitful discussions and help. Thanks are also due to Y.Takayama and K.Ohata for their helpful suggestions and encouragement.

##### Reference

- Bonnefoi A R, Chow D H and McGill T C 1985 *Appl.Phys.Lett.* **47** 888
- Capasso F and Kiehl R A 1985 *J.Appl.Phys.* **58** 1366
- Matthews J W and Blakeslee A E 1974 *J.Cryst.Growth* **27** 118
- Schewchuk T J, Chapin P C, Coleman P D, Kopp W, Fischer R and Morkoç H 1985 *Appl.Phys.Lett.* **46** 508
- Sollner T C L G, Goodhue W D, Tannenwald P E, Parker C D and Peck D D 1983 *Appl.Phys.Lett.* **43** 588
- Tsu R and Esaki L 1973 *Appl.Phys.Lett.* **22** 562
- Tsuchiya M and Sakaki H 1986a *Jpn.J.Appl.Phys.* **25** L185
- Tsuchiya M and Sakaki H 1986b *Appl.Phys.Lett.* **49** 88
- Yokoyama M, Imamura K, Muto S, Hiyamizu S and Nishi H 1985 *Jpn.J.Appl.Phys.* **24** L185

## Author Index

- Abelson J R, 283  
 Ahizawa Y, 105  
 Akiyama M, 515  
 Alavi K, 405  
 Allam J, 399, 405  
 Anderson N G, 135  
 Ando Y, 587  
 André J P, 417  
 Antoniadis D A, 239  
 Aono K, 527  
 Armiento C A, 141  
  
 Bahir G, 283  
 Bajaj K K, 325  
 Bales J, 319  
 Bedair S M, 135, 171  
 Benchimol J L, 385  
 Beneking H, 147  
 Berenz J, 493  
 Betten W, 521  
 Bhattacharya P K, 411  
 Biefeld R M, 423  
 Bimberg D, 209  
 Blondeau R, 391  
 Bour D P, 257  
 Bourret E, 51  
 Bradshaw J T, 257  
 Bresse J F, 301  
 Burnham R D, 9  
  
 Camnitz L H, 367  
 Capasso F, 17, 399, 405, 539  
 Carey K W, 209  
 Caruso R, 57  
 Chen C H, 75  
 Chen Y K, 581  
 Cherng M J, 159  
 Chevallier J, 289  
 Chin A, 411  
 Chiu T H, 93  
 Cho A Y, 405, 539  
 Choi H K, 355  
 Chou S Y, 239  
 Choudhury A N M, 141  
 Chu S N G, 93  
 Colquhoun A, 441  
 Connors M K, 355  
 Cox H M, 177  
 Cunningham J E, 93  
 Curless J A, 117  
  
 Daoud-Ketata K, 301  
 Das U, 411  
 Dautremont-Smith W C, 289  
 Desnica U V, 33  
 Dietrich H B, 271  
 Ding J, 313  
 Ditzemberger J A, 93  
 Doyle B L, 331  
 Drummond T J, 227, 233, 331  
 Dubon-Chevallier C, 301  
 Ducourant T, 509  
 Duncan W M, 39  
 Dutton R W, 453  
  
 Eastman L F, 367, 581  
 Ebert G, 441  
 El-Masry N A, 171  
 Ermeis N, 147  
 Enquist P M, 251  
 Epler J E, 9  
  
 Fan W D, 277  
 Fang S F, 165  
 Feng M, 465  
 Fetterman H, 493  
 Flesner L D, 187  
 Fonstad C G, 239  
 Forchel A, 221  
 Fouquet J E, 209  
 Fritz I J, 227, 233  
 Fujieda S, 153  
 Fujikawa K, 527  
 Fukunaga T, 361  
  
 Gabillard B, 509  
 Gentner J L, 417  
 Glasow P A, 429  
 Goodhue W D, 319, 349  
 Gorman R L, 69  
 Gourley P L, 423  
 Graf V, 471  
 Greene R L, 325  
 Griffiths G, 221  
 Gronsky R, 51  
 Guerrero A H, 187  
  
 Hara N, 263  
 Hariu T, 165  
 Harris T D, 215  
 Hase N, 343

Hayashi H, 183  
Heime K, 563  
Henderson T, 557  
Henry R L, 69  
Heuken M, 563  
Higashiura M, 245, 497  
Hiramoto T, 295  
Hirayama N, 343  
Hjalmarson H P, 331  
Holonyak N, 9  
Hori S, 245  
Hsieh K H, 477  
Hull R, 209  
Hummel S G, 177  
Hutchinson A L, 399, 539

Ikeda M, 575  
Ikoma T, 295  
Inami I, 245  
Inomata H, 515  
Inoue K, 533  
Ishida Koichi, 45, 361  
Ishida Koji, 361  
Ishihara O, 527  
Ishikawa H, 575  
Ishikawa T, 99  
Itoh T, 515, 587

Jackson D J, 411  
Jaeckel H, 471  
Jagannath C, 141  
Jelloian L, 477  
Jen H R, 159  
Jiang X Y, 277  
Jitsukawa T, 153  
Johnson G D, 349  
Jones E D, 227, 233, 331  
Jou M J, 159  
Juang F Y, 411

Kafalas J, 63  
Kamada M, 575  
Kamei H, 183, 245  
Kamejima T, 395  
Kaminishi K, 515  
Kamo H, 497  
Kan Y, 435  
Kanber H, 503  
Karam N H, 171  
Kasahara K, 395  
Kato N, 459  
Kato T, 183  
Kato Y, 395  
Katoda T, 263  
Katsumata M, 527

Kavanagh K, 251  
Kawasaki A, 27  
Kawasaki H, 245  
Kawase T, 27  
Keramidas V G, 313  
Kikuta T, 45  
Kim H B, 465  
Klapper H, 147  
Kneidinger M, 267  
Kobayashi J, 361  
Kojima C, 575  
Komaru M, 527  
Komeno J, 99  
Kondo K, 99  
Kopf R F, 215  
Koteles E S, 63, 141  
Krajenbrink F G, 477  
Kramer G D, 117  
Kroemer H, 221  
Kugler S, 563  
Kwok S P, 465

Lach E, 221  
Lam C S, 239  
Lambert G, 141  
Lamont M G, 215  
Larsen C A, 75  
Le H Q, 319  
Lechner A, 267  
Lee B T, 51  
Lee G, 521  
Lee J W, 111, 489, 545  
Lee K, 521  
Lichtmann L S, 477  
Li W, 411  
Litton C W, 325  
Look D C, 557  
Lubke K, 267

McLevige W V, 489  
Maluenda J, 509  
Martin G M, 417  
Matsui K, 361  
Matsumoto Y, 153  
Matsuoka Y, 459  
Matsushita K, 165  
Menu E P, 417  
Merz J L, 283  
Miller R C, 215  
Missous M, 123  
Mizuta M, 153  
Moeller K, 493  
Moon N, 193  
Mori Y, 575  
Morkoc H, 325, 337, 557

- Moroni D, 417  
Morrison C, 373
- Nabity J C, 289  
Nagai H, 435  
Nakagome H, 87  
Nakanisi T, 105  
Nakano K, 493  
Nakashima H, 361  
Narozny P, 147  
Nedoluhu A K, 187  
Niesen J, 373  
Nishi S, 515  
Norris P, 63, 81, 141  
Nottenburg R N, 483
- O'Brien M, 187  
Odagiri T, 295  
Odanaka S, 447  
Oertel D, 209  
Ohata K, 569  
Ohshima M, 343  
Okamoto A, 569, 587  
Oldiges P, 295  
Ono K, 183  
Onuma T, 447, 533  
Osbourne G C, 233
- Panish M B, 399, 483  
Paoli T L, 9  
Parker D L, 193  
Parsons J D, 477  
Patillon J N, 417  
Pawlowicz L M, 33  
Pearson S J, 57, 289  
Peczalski A, 521  
Peffley M S, 117  
Penchina C M, 187  
Peng C K, 325, 557  
Persechini D L, 411  
Pilkun M H, 221  
Primot J, 385  
Prost M, 509, 563
- Radulescu D C, 581  
Ralston J D, 367  
Razeghi M, 221, 391  
Reed M A, 545  
Reid G A, 209  
Reynolds D C, 325  
Rezek E A, 379  
Rocchi M, 509  
Rocher C, 509  
Rosner S J, 209  
Rühle W W, 429
- Saito T, 295, 515  
Sands T, 51, 313  
Sano Y, 515  
Sasaki A, 203  
Sasaki F, 497  
Sasaki G, 183  
Sauer R, 93, 215  
Schaffner J, 493  
Schirber J E, 227, 233  
Schlapp W, 563  
Scholz F, 221  
Schubert E F, 93  
Schummers R, 147  
Schwarz-michel K D, 429  
Seki S, 515  
Sen S, 539  
Sermage B, 385  
Shastry S K, 81, 141  
Shealy J R, 251, 257  
Shenai K, 453  
Shibatani A, 99  
Shichijo H, 489  
Shida K, 165  
Shimura T, 527  
Sigmon T W, 283  
Singer K E, 123  
Skromme B J, 177  
Smith H I, 239  
Smith M C, 227  
Somali H, 521  
Sputz S K, 215  
Stavola M, 57, 289  
Stringfellow G B, 75, 159  
Subbanna S, 221  
Suemune I, 435  
Sugitani S, 459  
Sugiyama N, 105  
Sugou S, 395  
Sunakawa H, 129  
Swaminathan V, 289
- Tabatabaie N, 551  
Tada K, 27  
Taddiken A H, 489  
Tai K C, 93  
Takahei K, 87  
Takamori T, 361  
Takeda Y, 203  
Takenaka N, 343  
Tamargo M C, 551  
Tamura A, 533  
Tanaka A, 245  
Tasker P J, 581  
Temkin H, 483  
Thim H, 267

Thompson P E, 271  
 Thornton R L, 9  
 Tilli T, 147  
 Tischler M A, 135  
 Tokuda H, 245, 497  
 Toyoda Y, 343  
 Toyoshima H, 569, 587  
 Tran D, 379  
 Tränkle G, 221  
 Tsang W T, 93  
 Tsen K T, 337  
 Tsui R K, 117  
 Tu C W, 215, 289

Uenoyama T, 447, 533  
 Usui A, 129, 395  
 Usui S, 1  
 Uwai K, 87

Van Zeghbroeck B J, 471  
 Vettiger P, 471  
 Von Neida A R, 57  
 Vu T, 521

Wang D C, 503  
 Wang G W, 581  
 Wang W Y, 277, 307

Washburn J, 313  
 Watanabe H, 1  
 Watanabe M O, 105  
 Weimann G, 221, 563  
 Westphal G H, 39  
 Wettling W, 197  
 Wicks G W, 257, 367  
 Wilson B A, 215  
 Windhorn T H, 349  
 Windscheif J, 197  
 Wolf P, 471

Xia G Q, 277, 307

Yamamoto T, 99  
 Yamanishi M, 435  
 Yamazaki H, 459  
 Yoshida K, 183  
 Yow L, 379  
 Yu P W, 325

Zayhowski J J, 319  
 Zemon S, 63, 81, 141  
 Zhu Y, 203  
 Zinkiewicz L, 373  
 Zipperian T E, 423  
 Zuleeg R, 187

DATE  
~~FILMED~~  
4 8